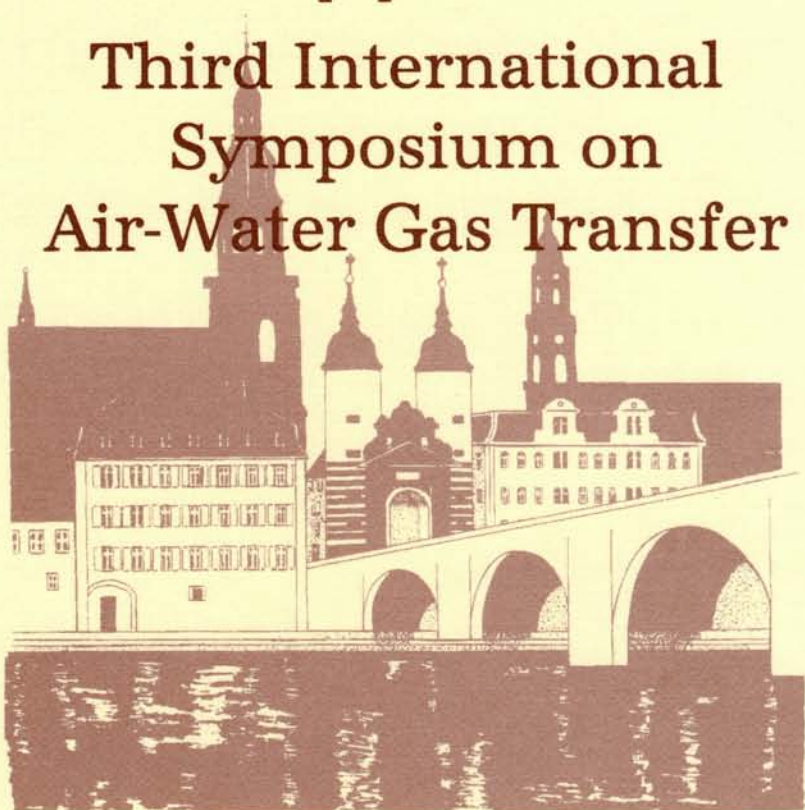




Air-Water Gas Transfer

Selected papers from the
Third International
Symposium on
Air-Water Gas Transfer



B. Jähne and E.C. Monahan
editors

Aeon

Air-Water Gas Transfer

**Selected papers from the
Third International
Symposium on
Air-Water Gas Transfer
July 24-27, 1995, Heidelberg University**

**edited by
B. Jähne and E. C. Monahan**

AEON Verlag & Studio, 63454 Hanau

Editors

Prof. Bernd Jähne
Interdisciplinary Center for Scientific Computing (IWR)
University of Heidelberg
Im Neuenheimer Feld 368
69120 Heidelberg, Germany
and
Scripps Institution of Oceanography
University of California, San Diego
La Jolla, CA 92093-0230, USA
E-mail: bjaehne@ucsd.edu

Prof. Edward C. Monahan
Marine Science Institute
University of Connecticut
Avery Point
Groton, Connecticut 06340, USA

Note: released by contract signed on June 5, 2014 by AEON-Verlag & Studio and B. Jähne to Creative Commons Licence CC BY 3.0 DE
doi: 10.5281/zenodo.10571

ISBN 3-9804429-0-x AEON Verlag & Studio Hanau

This work is subject to copyright. All rights are reserved, whether the whole or part of the material is concerned, specifically the rights of translation, reprinting, reuse of illustrations, recitation, broadcasting, reproduction on microfilm or in other ways, and storage in data banks. Duplication of this publication or parts thereof is permitted only under the provisions of the German Copyright law of September 9, 1965, in its current version, and permission for use must always be obtained from AEON Verlag & Studio. Violations are liable for prosecution act under German Copyright Law.

This work relates to Department of Navy Grant N00014-95-1-0199 issued by the Office of Naval Research. The United States Government has a royalty-free license throughout the world in all copyrightable material contained herein.

© AEON Verlag & Studio, Hanau 1995
Printed in Germany

The use of general descriptive names, registered names, trademarks, etc. in this publication does not imply, even in the absence of a specific statement, that such names are exempt from the relevant protective laws and regulations and therefore free for general use.

Foreword

We are pleased to present in this volume a comprehensive record of what transpired at the Third International Symposium on Air-Water Gas Transfer, which was held in the University of Heidelberg, Germany, on July 24-27, 1995.

This is the third volume arising from this series of symposia. The first such volume, "Gas Transfer at Water Surfaces", edited by W. Brutsaert and G. H. Jirka and published by D. Reidel (now Kluwer) in 1984, contained the papers contributed at the First International Symposium on Gas Transfer at Water Surfaces, which had been held at Cornell University, Ithaca, New York, in June, 1983. The second such volume, "Air-Water Mass Transfer", edited by S. C. Wilhelms and J. S. Gulliver, and published in 1991 by the American Society of Civil Engineers, incorporated, as its subtitle indicated, "selected papers from the Second International Symposium on Gas Transfer at Water Surfaces". This second symposium was held at the University of Minnesota, Minneapolis, in September, 1990.

Much of the volume arising from the first symposium was given over to papers dealing with the fundamental mechanisms of interfacial gas transfer, with numerous contributions involving the various relevant physical and chemical processes, for example, with turbulence, interfacial motions, and fluid instabilities. At the Second Symposium, and in the resulting volume, fundamental mechanisms were again discussed, but greater emphasis was given to appropriate experimental techniques, and to a wide range of environmental and engineering applications.

The reader of the present volume will again find numerous papers on the traditional physical and chemical mechanisms acknowledged to play important roles in the transfer of gases between air and water. But, reflecting one of the major themes of the Third Symposium, our volume also contains many contributions that deal with bubbles and breaking waves. This new emphasis results from the quite recent recognition of the major role of breaking waves, and of the bubbles thereby generated, in facilitating the transfer of gases across the sea surface, and at the air-water interface of other large natural and artificial water bodies.

This volume, like its predecessors, contains numerous papers on measurement techniques, and applications of these techniques in the laboratory and in the field, but the reader will find that many of the techniques

discussed in the current volume are non-invasive, and particularly suited to remote sensing applications.

While many of the papers in earlier volumes dealt with oxygen and water vapor, an emphasis on the air-water transfer of carbon dioxide and other radiatively important gas will be detected in the present volume, reflecting the current interest of the scientific community in the issue of the "greenhouse effect" and potential global warming.

The third symposium accommodated 105 contributions spread among 15 plenary and 8 poster sessions. The program committee selected 81 of these contributions for publication in this volume. The major topics, and areas of focus, of the Third Symposium are clearly reflected in the titles of the parts into which the volume is divided, which are as follows:

-
- Part I: Physical and Chemical Mechanisms
 - Part II: Waves and Turbulence
 - Part III: Breaking Waves and Bubbles
 - Part IV: Measuring Technology: Reaeration
 - Part V: Laboratory Measurements
 - Part VI: Field Measurements
 - Part VII: Remote Sensing and Global Modelling
-

The editors of this volume, and co-chairs of the Third Symposium, wish to join their colleagues on the Organizing and Program Committees, and all of the participants in this symposium, in thanking the funding agencies whose support was vital to the conduct of these meetings. We gratefully acknowledge financial support provided by

-
- U.S. Office of Naval Research (ONR), via Grant N00014-95-1 -0199
 - Office of Global Programs of the National Oceanic and Atmospheric Administration (NOAA) of the U.S. Department of Commerce via Award # 43AANA500128
 - U.S. Department of Energy (DOE)
 - International Association for the Physical Sciences of the Oceans (IAPSO)
 - German Science Foundation (DFG)
 - State of Baden-Württemberg
 - University of Heidelberg
 - Connecticut Sea Grant College Program via its Program Development Account
-

We are also grateful for the formal professional endorsements of the Third International Symposium on Air-Water Gas Transfer provided by the American Geophysical Union and the International Association for Hydraulic Research.

We wish to acknowledge with heartfelt thanks the efforts on behalf of the Symposium put forth by our fellow members of the Organizing Committee, and likewise by our colleagues who served on the Program Committee. The memberships of these committees are listed forthwith:

Organizing Committee

Bernd Jähne, Scripps Institution of Oceanography (General Chair)
Edward Monahan, University of Connecticut (Co-Chair)
Karl Otto Münnich, Local Chair
William Asher, Battelle Northwest
Rik Wanninkhof, NOAA/AOMI, Miami

Program Committee

Eric Bock, Woods Hole Oceanographic Institution, USA
Michel Coantic, IMST, Universite de Marseille, France
Mark Donelan, Canada Centre for Inland Waters, Canada
Thomas Hanratty, University of Illinois, USA
Martin Heimann, Max Planck Institute for Meteorology, Hamburg, Germany
Norden Huang, NASA, Goddard Space Flight Center, USA
John Gulliver, University of Minnesota, USA
Gerhard Jirka, Cornell University, USA
Ralph Keeling, Scripps Institution of Oceanography, USA
Bryan Kerman, Canada Centre for Inland Waters, Canada
Peter Liss, University of East Anglia, United Kingdom
Ken Melville, Scripps Institution of Oceanography, USA
Liliane Melivat, Universite Marie and Pierre Curie, Paris, France
Wiebe Oost, Royal Dutch Meteorological Office (KMNI), the Netherlands
Erich Plate, University of Karlsruhe, Germany
Steve Thorpe, University of South Hampton, United Kingdom
Shizuo Tsunogai, Hokkaido University, Japan

We are pleased to have been able to bring this volume to print so soon after the close of the Symposium. The willingness of the above committees to meet in editorial session in Ladenburg immediately after the Heidelberg symposium ended helped us attain this goal, and the now almost universal use of electronic means for transmitting texts, figures, and revisions contributed in no small measure to the early publication of this volume. But we wish to particularly acknowledge the efficient performance of the dedicated staff of AEON Verlag of Hanau as a crucial factor in moving this book forward to publication in this fashion.

The editors want to recognize the efforts of Thomas Scholz, who, in his capacity as Symposium Secretary, worked diligently to see that things went smoothly. Mr. Scholz exerted himself on behalf of this Symposium not only in Heidelberg, but in La Jolla, California, and Groton, Connecticut, as well. He was ably assisted by students of the institute for Environmental Physics and the Interdisciplinary Center for Scientific computing. Their work “behind the scenes” contributed in substantial measure to the success and stimulating atmosphere at the symposium.

We are most grateful for the efforts of Ms. Peg Stewart van Patten and others in the U.S. point-of-contact office at the University of Connecticut

at Avery Point. Ms. van Patten assisted with early editorial matters and prepared and distributed the several Symposium announcements. She is also responsible for the revised logo and the cover design for this book, using an illustration of Heidelberg by Judy Ricketts-White.

The second of these symposia was held some seven years after the first, and the third followed five years after the Second. We are confident that these meetings have become established events on the academic landscape, and project that the Fourth International Symposium on Air-Water Gas Transfer will be held in the year 2000, probably in Canada.

We hope to see many of the readers of this volume at this next symposium.

Bernd Jähne and Edward C. Monahan, Editors

Contents

I Physical and Chemical Mechanisms

- B. Jähne*, Impact of Quantitative Visualization and Image Processing on the Study of Small- Scale Air-Sea Interaction 3
- D. B. King, W. J. De Bryun, M. Zheng, and E. S. Saltzman*, Uncertainties in the Molecular Diffusion Coefficient of Gases in Water for Use in the Estimation of Air-Sea Exchange 13
- S. Emerson*, Enhanced Transport of Carbon Dioxide During Gas Exchange 23
- E. V. Yakushev and G. E. Mikhailovsky*, Mathematical Modeling of the Influence of Marine Biota on the Carbon Dioxide Ocean-Atmosphere Exchange in High Latitudes 37
- P. Prinios, M. Atmane, and J. George*, Gas Flux Measurements and Modelling below an Air-Water Interface 49
- D. K. Woolf*, Vertical Mixing in the Upper Ocean and Air-Sea Gas Transfer 59
- J. George, B. Caussade, and L. Masbemat*, Conceptual Modelling of Interfacial Gas-Liquid Mass Transfer 69
- C. R. Chu and G. H. Jirka*, Reaeration in Combined Wind/Stream Driven Flows 79
- D. B. Moog and G. H. Jirka*, Macroroughness Effects on Stream Reaeration 89
- D. B. Moog and G. H. Jirka*, Analysis of Reaeration Equations Using Mean Multiplicative Error 101

II Waves and Turbulence

- M. L. Banner and W. L. Peirson*, An Observational Study of the Aqueous Surface Layer Structure Beneath a Wind-Driven Air-Water Interface 115
- F. Hering, D. Wierzymok, and B. Jähne*, Measurements of Enhanced Turbulence in Short Wind-Induced Water Waves 125
- E. A. Cowen, S. G. Monismith, and J. R. Koseff*, Digital Particle Tracking Velocimetry Measurements Very Near a Free-Surface 135

- P. A. Hwang*, Spatial Measurements of Small-Scale Ocean Waves 153
- J. Klinke and B. Jähne*, Measurements of Short Ocean Waves during the MBL ARI West Coast Experiment 165

III Breaking Waves and Bubbles

- Y. Toba and H. Kawamura*, Wind-Wave Coupled Downward-Bursting Boundary Layer Below the Sea Surface — In Relation to Penetration Depth of Bubble Clouds 177
- D. K. Woolf*, Energy Dissipation through Wave Breaking and the Air-Sea Exchange of Gases 185
- C. Kraan, W. A. Oost, and P. A. E. M. Janssen*, Whitecap Measurements and Whitecap Dissipation Modelling 197
- W. E. Asher, B. J. Higgins, L M. Karle, P. J. Farley, C. R. Sherwood, W. W. Gardiner, R. Wanninkhof, H. Chen, T. Lantry, M. Steckley, E. C. Monahan, Q. Wang, P. M. Smith*, Measurement of Gas Transfer, Whitecap Coverage, and Brightness Temperature in a Surf Pool: An Overview of WABEX-93 205
- Q. Wang, E. C. Monahan, W. E. Asher, and P. M. Smith*, Correlations of Whitecap Coverage and Gas Transfer Velocity with Microwave Brightness Temperature for Plunging and Spilling Breaking Waves 217
- W. E. Asher, L M. Karle, B. J. Higgins, P. J. Farley, I. S. Leifer, and E. C. Monahan*, The Effect of Bubble Plume Size on the Parameterization of Air-Seawater Gas Transfer Velocities 227
- R. Wanninkhof, W. E. Asher, and E. C. Monahan*, The Influence of Bubbles on Air-Water Gas Exchange: Results from Gas Transfer Experiments during WABEX-93 239
- A. S. Ogston, C. R. Sherwood, and W. E. Asher*, Estimation of Turbulence-Dissipation Rates and Gas-Transfer Velocities in a Surf Pool: Analysis of the Results from WABEX-93 255
- Ira S. Leifer, William E. Asher, and Paul J. Farley*, A Validation Study of Bubble Mediated Air-Sea Gas Transfer Modeling for Trace Gases 269
- W. K. Melville, E. Terrill, and L. Ding*, Field Measurements of Air Entrainment by Breaking Waves 285
- D. Farmer*, Breaking Waves, Bubbles and Langmuir Circulation: a Measurement Strategy for Studying Bubble Enhanced Air-Sea Gas Transfer 297
- M.-Y. Su and J. Cartmill*, Effects of Salinity on Breaking Wave Generated Void Fraction and Bubble Size Spectra 305
- A. Gnanadesikan*, Effects of Waves and Heat Fluxes on Bubble Patch Structure and Gas Exchange 313

<i>G. de Leeuw and L. H. Cohen</i> , Bubble Size Distributions in Coastal Seas	325
<i>M. R. Loewen, M. A. O'Dor, and M. G. Skafel</i> , Laboratory Measurements of Bubble Size Distributions Beneath Breaking Waves	337
<i>P. Geißler and B. Jähne</i> , Measurements of Bubble Size Distributions with an Optical Technique Based on Depth from Focus	351
<i>W. R. McGillis, E. J. Bock, and N. M. Frew</i> , Mass Transfer from Gas Bubbles in Fresh and Seawater	363
IV Measuring Technology; Reaeration	
<i>M. D. DeGrandpre, W. R. McGillis, N. M. Frew, and E. J. Bock</i> , Laboratory Measurements of Seawater CO ₂ Gas Fluxes	375
<i>C. McNeil, D. Farmer, M. Trevorrow, and B. Johnson</i> , Development and Testing of In Situ N ₂ ,O ₂ and Gas Tension Sensors for Oceanographic Studies	385
<i>B. E. Boumansour, H. Jupsin, and J. - L Vasel</i> , Propane as a Tracer Gas for Reaeration Tests	393
<i>H. Hausbecke, S. Reinelt, and B. Jähne</i> , Heat as a Proxy Tracer for Gas Exchange Measurements in the Field: Principles and Technical Realization	405
<i>W. McKeown</i> , Radiometric Measurement of Diffusion Zone Thickness	415
<i>J. S. Smith, K. T. Valsaraj, and L. J. Thibodeaux</i> , An Innovative Air-Water Exchange Process for the Treatment of Waste Waters	425
<i>T. Etoh and K. Takehara</i> , Development of Visualization Techniques for Motion of Surface Water Induced by Collision of a Vortex Ring	435
<i>T. Etoh and K. Takehara</i> , High-Speed Video Capture of the Motion of Surface Water Induced by the Collision of a Droplet and the Collapse of a Bubble	447
<i>P. T. Weiss, J. S. Gulliver</i> , A Bubbleless Hollow Fiber Membrane Aerator for Surface Waters	461
<i>y. Hosoi and H. Murakami</i> , Model of Reaeration at Permeable Breakwaters	473
V Laboratory Measurements	
<i>E. C. Monahan, Q. Wang, and M. B. Wilson</i> , UConn's Sea Surface Physics Laboratory	487
<i>D. B. Moog and G. H. Jirka</i> , Tilting Wind-Water Tunnel	495
<i>P. van Vliet, F. Hering, and B. Jähne</i> , Delft Hydraulic's Large Wind-Wave Flume	499
<i>W. J. Cooper, M. A. Donelan, and M. Alaei</i> , Gas Transfer Flume Facility at CCIW	503

<i>D. Schmundt, T. Münsterer, H. Lauer and B. Jähne</i> , The circular wind/wave facilities at the University of Heidelberg	505
<i>W. E. Asher and R. Wanninkhof</i> , The Effect of Breaking Waves on the Analysis of Dual-Tracer Gas Exchange Measurements	517
<i>N. M. Frew, E. J. Bock, W. R. McGillis, A. V. Karachintsev, T. Hara, T. Münsterer, and B. Jähne</i> , Variation of Air-Water Gas Transfer with Wind Stress and Surface Viscoelasticity	529
<i>F. J. Ocampo-Torres, M. A. Donelan</i> , On the Influence of Fetch and the Wave Field on the CO ₂ Transfer Process: Laboratory Measurements	543
<i>S. Komori and T. Shimada</i> , Gas Transfer across a Wind-Driven Air-Water Interface and the Effects of Sea Water on CO ₂ Transfer	553
<i>W. N. L. Roma</i> , Surface Deformation Measurement with Optical Sensor and Correlation with Reaeration Coefficient	571
<i>S. Kakuno, M. Saitoh, Y. Nakata, and K. Oda</i> , The Air-Water Oxygen Transfer Coefficients with Waves Determined by Using a Modified Method	577
<i>J. S. Gulliver and A. Tamburrino</i> , Turbulent Surface Deformation and Their Relationship to Mass Transfer in an Open-Channel Flow	589
<i>A. T. Jessup, C. J. Zappa, V. Hesany, M. R. Loewen, and M. G. Skafel</i> , Dependence of the Skin Layer Recovery Rate on Heat Flux and Turbulence	601
<i>Tetsu Hara, Erik J. Bock, Nelson M. Frew, Wade R. McGillis</i> , Relationship between Air-Sea Gas Transfer Velocity and Surface Roughness	611
<i>M. Alaei, M. A. Donelan, and W. M. J. Strachan</i> , Wind and Wave Effects on Mass Transfer Velocities of Halomethanes and SF ₆ Measured in a Gas Transfer Flume	617
<i>S. R. Duke and T. J. Hanratty</i> , Measurement of the Concentration Field Resulting from Oxygen Absorption at a Wavy Air-Water Interface	627
<i>T. Münsterer, H. J. Mayer, and B. Jähne</i> , Dual-Tracer Measurements of Concentration Profiles in the Aqueous Mass Boundary Layer	637
<i>A. Hirska, L. M. Logory, S. Kim, G. M. Korenowski, and C. D. Judd</i> , Surfactant Effects on Vortex Flows at a Free Surface and the Relation to Interfacial Gas Transfer	649
<i>F. Minel, J. George</i> , Hydrodynamics in a Jet-Agitated Vessel Close to the Gas-Liquid Surface	665

VI Field Measurements

- M. A. Donelan and W. M. Drennan*, Direct Field Measurements of the Flux of Carbon Dioxide 677
- G. J. Kunz, G. de Leeuw, S. E. Larsen, and F. Aa. Hansen*, Over-Water Eddy Correlation Measurements of Fluxes of Momentum, Heat, Water Vapor and CO₂ 685
- S. D. Smith, R. J. Anderson, O. Hertzman, W. A. Oost, W. Kohsiek, G. de Leeuw, and G. Kunz*, New Measurements of Eddy Fluxes at the Sea Surface in ASGASEX 703
- S. IV. Kholouiski*, Radon-222 Transfer Coefficients in Atlantic and Pacific Oceans. The Influence of Temperature and Wind 713
- W. A. Oost, W. Kohsiek, G. de Leeuw, G. J. Kunz, S. D. Smith, R. J. Anderson, and O. Hertzman*, On the Discrepancies between CO₂ Flux Measurement Methods 723
- E. Plate, T. Stahlschmidt, M. Schulz, and W. Dannecker*, The Influence of Air-Sea-Exchange on the Partitioning of N-Species during Transport over Sea 735
- M. Schulz, E. Plate, T. Stahlschmidt, and W. Dannecker*, The Potential of Vertical Profiling of Particulate Nitrogen Species to Investigate Air-Sea-Exchange of Nitrogen Species 745
- J. J. Ridal, B. Kerman, and W. Drennan*, Estimating Air-Water Transfer of Hexachlorocyclohexanes in Lake Ontario 753
- H. P. J. de Wilde and J. Duyzer*, Methane Emissions off the Dutch Coast: Air-Sea Concentration Differences Versus Atmospheric Gradients 763
- H. Haußecker and B. Jähne*, In Situ Measurements of the Air-Sea Gas Transfer Rate during the MBL/CoOP West Coast Experiment 775
- J. F. Clark, P. Schlosser, H. J. Simpson, M. Stute, R. Wanninkhof, and D. T. Ho*, Relationship between Gas Transfer Velocities and Wind Speeds in The Tidal Hudson River Determined by the Dual Tracer Technique 785
- E. J. Bock, J. B. Edson, N. M. Frew, A. Karachintsev, W. R. McGillis, R. K. Nelson, K. Hansen, T. Hara, M. Uz, B. Jähne, J. Dieter, J. Klinke, and H. Haußecker*, Description of the Science Plan for the April 1995 CoOP Experiment, 'Gas Transfer in Coastal Waters', Performed from the Research Vessel New Horizon 801
- W. A. Oost*, The ASGASEX'93 Experiment 811
- B. D. Johnson*, The Joint Global Ocean Flux Study: Role of Gas Exchange 817

VII Remote Sensing and Global Modelling

<i>J. Boutin and J. Etcheto</i> , Estimating the Chemical Enhancement Effect on the Air-Sea CO ₂ Exchange Using the ERS1 Scatterometer Wind Speeds	827
<i>P. Suntharalingam andj. L. Sarmiento</i> , Modeling Global Air-Sea N ₂ O Fluxes. A Sensitivity Analysis of the Gas-Exchange Formulation	843
<i>Y. Sugimori, C. Zhao, M. Akiyama, N. Itoh, and M. He</i> , The Determination of CO ₂ Difference of Partial Pressure in the North Pacific Ocean using SST by Ship and Satellite Data	855
<i>B. Chapron, K. Katsaros, T. Elfouhaily, D. Vandemark</i> , A Note on Relationships between Sea Surface Roughness and Altimeter Backscatter	869
<i>J. P. Jasper, E. L. Sikes, and J. M. Hayes</i> , Transfer of CO ₂ from Equatorial Latitudes to High Latitudes During the Late Quaternary	879
Author Index	889
Index	893
Color Plates	901

Impact of Quantitative Visualization and Image Processing on the Study of Small- Scale Air-Sea Interaction

Bernd Jähne

Interdisciplinary Center for Scientific Computing, University of Heidelberg
Im Neuenheimer Feld 368, 69120 Heidelberg, Germany
Scripps Institution of Oceanography, Physical Oceanography Res. Div.
La Jolla, CA 92093-0230, USA
email: bjaehne@ucsd.edu

doi: 10.5281/zenodo.10326

Abstract

Non-intrusive image measuring methods based on modern photonics and digital image processing techniques provide and continue to provide an unprecedented quantitative insight into small-scale air-sea interaction processes.

1 Introduction

From the early beginnings, scientists tried to record their observations in pictures. In early times, they could do this only in the form of drawings. Remarkable examples are known, for instance, from Leonardo da Vinci. Any visual observation, however, was limited to the capabilities of the human eye. The invention of photography triggered the first revolution in the usage of images for science and extended the possibilities for visual observation to non-visible radiation such as ultraviolet light, X-rays, and various particulate radiation. However, the cumbersome manual evaluation of photographs restricted the quantitative analysis. Nowadays, we experience a second revolution of scientific imaging. Images can be converted into electronic form, digital images, that are analyzed quantitatively using computers to perform exact measurements.

In this paper, we discuss the impact of these techniques for the experimental investigation of small-scale air-sea interactions. These processes are a key example for the application of imaging techniques in two respects. First, large scale processes become visible in aerial and satellite images by their interaction with small-scale processes that themselves cannot be resolved in the images but influence the imaging mechanism. A classical example are *sun glitter* images (Figure 1). The brightness of the sun glitter is directly related to the two-dimensional wave slope distribution which to a large extend is influenced by short wind waves. These short wind waves are modulated by slicks, swell, internal waves, tidal currents, etc. In this way, these phenomena become visible in sun glitter images as well as in



Figure 1: Sun glitter image from coastal Pacific waters taken on a flight from Los Angeles to San Diego by the author. It shows the variation of the micro-surface roughness constituted by gravity/capillary waves by slicks, swell, and internal waves. (For color figure, see Plate 1.)

synthetic aperture radar (SAR) images. Second, the boundary layers at the wavy ocean surface are very difficult to investigate by conventional intrusive probes. This is especially true for air-sea gas transfer. The thin aqueous mass boundary layer which is at most a few $100\ \mu\text{m}$ thick can hardly be profiled by any intrusive probe, especially under field conditions.

Therefore, all conventional techniques do not take any measurements in aqueous mass boundary layer that controls air-sea gas transfer. Based on mass balance methods, they only measure the mean flux through the aqueous mass boundary layer integrated over large temporal (hours to days) and spatial scales. It is obvious that no direct insight into the mechanisms of air-sea gas exchange can be gained in this way. At best, an empirical parameterization can be obtained.

The plan of this review paper is to give a brief summary of the current state of the art of imaging techniques that are of importance for an experimental investigation of small-scale air-sea interaction processes with emphasize on air-sea gas exchange (*section 2*). Based on the expected developments in photonics and digital image processing one the one hand, and the experimental data needed mostly for a better understanding of small-scale air sea interaction processes one the other hand, we discuss the imaging techniques that can be envisioned to be developed within the next five years (*section 3*).

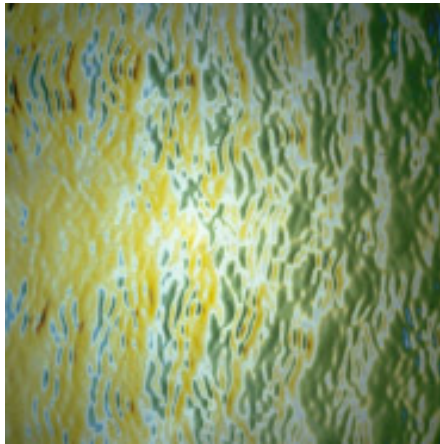


Figure 2: Wave slope images taken in the large IMST wind/wave flume, University of Marseille, at 4.6 m fetch and 4 m/s wind speed. The sector shown is about $0.4 \times 0.4 \text{ m}^2$. The wind is blowing from the left to the right. Slope color key: white means a flat surface, from yellow to red the slope is increasing into wind direction, from green to blue against the wind direction. From Jähne [1985]. (For color figure, see Plate 2.)

2 State of the Art

In recent years, tremendous progress has been made with imaging measuring techniques that take spatially resolved measurements of various key parameters involved in small-scale air-sea interaction.

2.1 Imaging of Short Wind Waves

The foundation for optical techniques to measure short waves was laid by the pioneering work of Cox. He not only used sun glitter images to infer the wave slope distribution and *mean square slope* [Cox and Munk, 1954], but also introduced the usage of optical techniques based on light refraction for the measurement of *wave slope* [Cox, 1958]. Keller and Gotwols [1983] were the first to use refractive optical techniques to capture wave slope images.

Figures 2 and 3 show some of the first wave slope images taken by the author in the Marseille wind/wave flume in 1984; Figures 4 and 5 illustrate the equipment used later in this facility by the author. Jähne and Riemer [1990] conducted the first systematic study of 2-D wave number spectra of short wind waves from the Delft wind/wave flume. The first spatial wave slope measurements taken at sea are reported in this volume [Klinke and Jähne, 1995]. The two most promising techniques used nowadays both in the field and laboratory are the *Scanning Laser Slope Gauge* (SLSG) [Bock et al., 1995; Hwang, 1995] and the *Imaging Slope Gauge* (ISG) [Klinke and Jähne, 1995]. A detailed comparative study of optical wave imaging techniques can

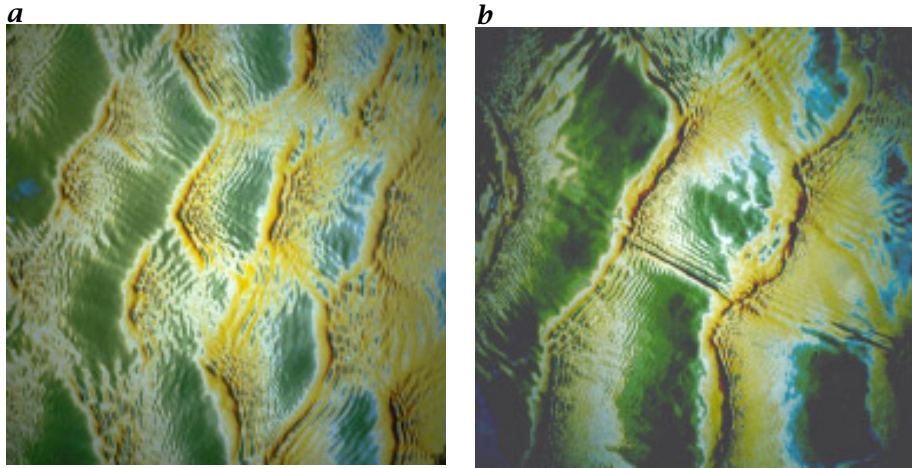


Figure 3: As Figure 2 at **a** 6.3 m/s and **b** 8 m/s wind speed. From Jähne [1985]. (For color figure, see Plate 3.)



Figure 4: Wave slope visualization system used by the author in the large wind/wave flume of the IMST, University of Marseille. A large screen close to the ceiling is illuminated from aside by two rows of lamps (see Figure 5) to produce an intensity wedge in wind direction. In this way, the along-wind wave slope can be made visible. Through the plane water surface, the submerged optical parts can be seen. In order to increase the distance of the camera to the water surface, the optical path is folded two times by mirrors. Slope calibration is — as shown in the figure — performed by using an artificial wave consisting of a Perspex foil bent by a frame into a sinusoidal shape. The whole system is mounted onto a carriage so that it can be moved through the facility. (For color figure, see Plate 4.)



Figure 5: Wave slope visualization system in operation at high wind speeds in the large wind/wave flume of the IMST, University of Marseille, France. The system is viewed through one of the large glass windows of the facility. In the upper right corner, some of the lamps can be seen used to illuminate the large screen. (For color figure, see Plate 5.)

be found in Jähne *et al.* [1994].

2.2 Imaging of Flow Fields Close to the Water Surface

Flow visualization techniques are as old as experimental studies in hydrodynamics but quantitative techniques such as *Particle Imaging Velocimetry (PIV)* and *Particle Tracking Velocimetry (PTV)* became available only recently. The many papers published in this volume indicate that this field is meanwhile well established [Banner and Peirson, 1995; Cowen *et al.*, 1995; Dieter *et al.*, 1995; Etoh and Takehara, 1995; Gulliver and Tamburrino, 1995; Hering *et al.*, 1995] and that the spatial resolution is sufficient to perform even measurements within the aqueous viscous boundary layer.

2.3 Imaging of Bubbles

Besides acoustic techniques, optical techniques are widely used to measure *bubble size distributions*. This volume contains the works of De Leeuw and Cohen [1995], Geißler and Jähne [1995], and Loewen *et al.* [1995]. Optical bubble concentration measurements have also been used in the WABEX'93 experiment [Asher *et al.*, 1995].

2.4 Thermal Imaging

Infrared imaging provides very promising opportunities to gain more insight into small-scale air-sea interaction processes. *Jessup et al.* [1995] study the skin layer recovery rate, while *Haußecker et al.* [1995] and *Haußecker and Jähne* [1995] report first in situ measurements of the air-sea gas exchange rate using heat as a proxy tracer. The *heat flux* at the ocean surface can be inferred from temperature gradient measurements using infrared spectral radiometry [McKeown, 1995].

2.5 Imaging of Concentration Fields of Dissolved Gases

Almost 30 years ago, *Hiby* [1968] used acid and alkaline gases and fluorescent pH indicators to investigate the transport mechanisms in falling films. He demonstrated that both mean and fluctuating concentrations can be measured successfully. Similar techniques have successfully been transferred to wind/wave tunnel studies (see Figure 6). Today, two techniques are available to perform high-resolution *concentration field* measurements within the aqueous mass boundary layer: *quenching* of the fluorescence of *PBA* by dissolved oxygen [Duke and Hanratty, 1995] and the fluorescent pH indicator method [Münsterer et al., 1995].

3 Envisioned Imaging Techniques

Still some key parameters cannot be measured and remain a challenge for future instrumentation development. Here a prediction is given what key quantities might be within the reach of novel techniques until the turn of the century.

3.1 Local Measurements of the Gas Transfer Rate

Although the controlled flux technique using heat as a proxy tracer (see above) does not only provide fast local measurements of the transfer rate but also gives direct insight into the mechanisms by taking images of the surface, it has the disadvantage that the Prandtl number (around 7) is about two decades lower than the Schmidt number for dissolved gas tracers (400 - 1000). Therefore, the development of similar techniques as the controlled flux technique but with a tracer of higher Schmidt number is very desirable.

3.2 Measurements of the Wind Stress at the Water Surface

One of the key problems to understand the mechanisms of air-sea gas transfer is the lacking knowledge of the spatial and temporal distribution of *wind stress* at a wavy water surface. More than twenty years ago, *Braun et al.* [1971] used it to measure the surface velocity in falling films. If techniques

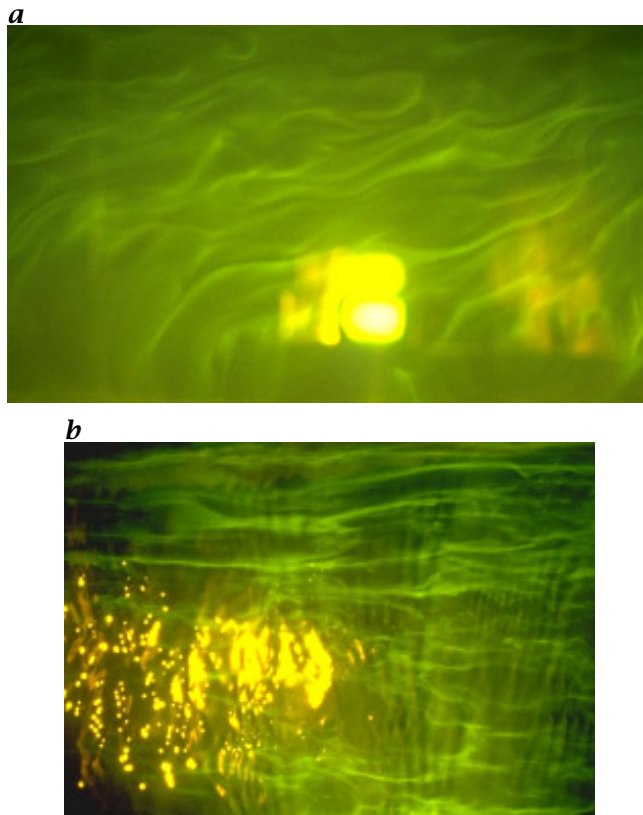


Figure 6: Visualization of the mass boundary layer in the large circular wind/wave flume at Heidelberg University. Shown is an image sector of about $0.12 \times 0.17 \text{ m}^2$ at the water surface viewed from above. The mass boundary is made visible by absorbing NH_3 gas in a 10^{-3} molar HCl solution. Absorption of NH_3 gas makes the mass boundary layer alkaline. This alkaline layer is made visible by the fluorescent pH indicator fluorescein. Therefore, the brightness in the image is directly proportional to the instantaneous thickness of the mass boundary layer. From Jähne [1991]. (For color figure, see Plate 6.)

became available to measure the velocity in different short distances from the surface, a direct determination of the wind stress from the velocity gradient at the water surface would be feasible.

3.3 3-D Imaging of Flow Fields at the Wavy Water Surface

Currently, the flow field can — except for very slow flows — only be taken in 2-D cross sections. With faster imaging sensors utilizing parallel outputs and compact laser-diode pumped solid state lasers, it can be expected that 3-D flow fields may become feasible soon. Other techniques might include

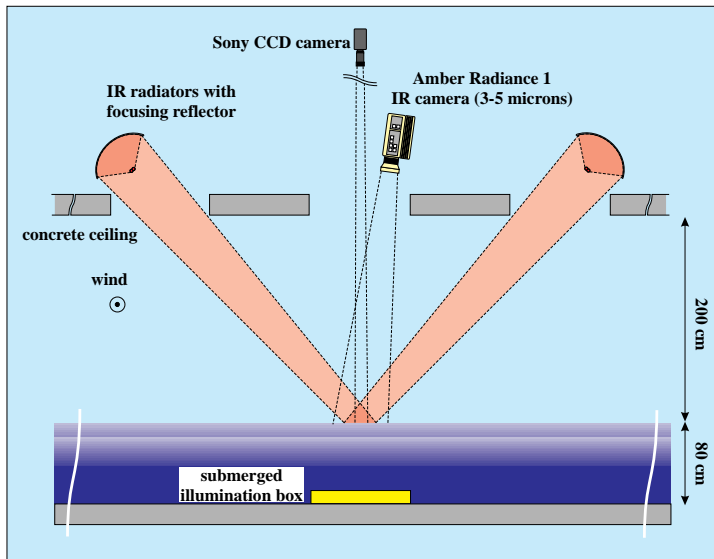


Figure 7: Schematics of a setup recently used by the author's research group [Haußecker and Beyer] in the Delft wind/wave flume to image simultaneously and at the same footprint the wind/wave slope using an imaging slope gauge, and the surface micro turbulence using an active thermal technique. With the latter technique, the water surface is heated up with two infrared radiators and the resulting temperature patterns — reflecting the spatial turbulence structure at the water surface — is observed by an infrared camera. (For color figure, see Plate 7.)

multi-camera setups using photogrammetric techniques to measure 3-D positions or colored light illumination systems.

3.4 3-D Imaging of Concentration Fields

Once measuring techniques for fast scanning of volumes are available for flow measurements, it is only a small step to measure 3-D concentration fields. The real challenge is the required high spatial resolution of better than $10\ \mu\text{m}$ for measurements within the mass boundary layer. At higher wind speeds/wave heights, sophisticated optical wave followers will be required.

3.5 Synoptic Imaging

Of most importance are simultaneous imaging measurements of flow fields, concentration fields, and short wind waves. Simultaneous measurements of flow and concentration provide a direct way to measure fluxes by cross-correlation. An experimental setup for simultaneous measurements of wave slope and surface turbulence is shown in Figures 7 and 8.

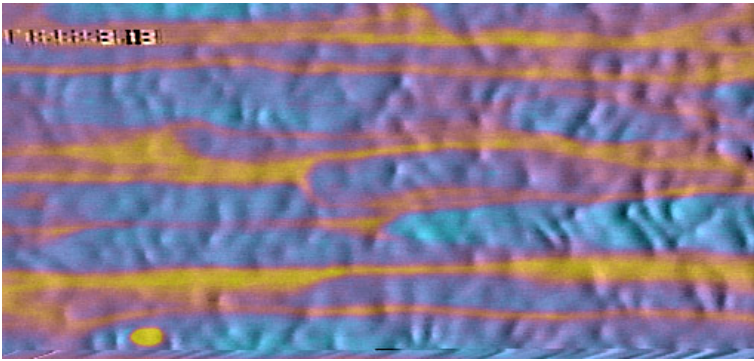


Figure 8: Example of a composite image taken with the setup shown in Figure 7. The wave slope is shown in blue, and the water surface temperature in red colors. The image sector is about $0.14 \times 0.20 \text{ m}^2$. (For color figure, see Plate 8.)

4 Conclusions

If only a few of the envisioned techniques become reality, they will have a significant impact on the understanding of small-scale air-sea interaction processes. It is obvious, however, that further development in this area critically depends on our ability to perform interdisciplinary research crossing the boundaries between classical research areas.

References

- Asher, W. E., B. J. Higgins, L. M. Karle, P. J. Farley, C. R. Sherwood, W. W. Gardiner, R. Wanninkhof, H. Chen, T. Lantry, M. Steckley, E. C. Monahan, Q. Wang, and P. M. Smith, Measurement of gas transfer, whitecap coverage, and brightness temperature in a Surf Pool: An Overview of WABEX-93, *This volume*.
- Banner, M. L., and W. L. Peirson, An observational study of the aqueous surface layer structure beneath a wind-driven air-water interface, *This volume*.
- E. J. Bock, J. B. Edson, N. M. Frew, A. Karachintsev, W. R. McGillis, R. K. Nelson, K. Hansen, T. Hara, M. Uz, B. Jähne, J. Dieter, J. Klinke, and H. Haußecker, Description of the science plan for the April 1995 CoOP experiment, 'Gas Transfer in Coastal Waters', performed from the research vessel New Horizon, *This volume*.
- Braun, D., Eckstein, H., and Hiby, J. W., Messung der Oberflächengeschwindigkeit von Rieselfilmen, *Chem.-Ing.-Techn.*, 43, 324-329, 1971.
- Cowen, E. A., S. G. Monismith, and J. R. Koseff, Digital particle tracking velocimetry measurements very near a free-surface, *This volume*.
- Cox C., and W. Munk, Measurement of the roughness of the sea surface from photographs of the sun's glitter, *J. Optical Soc. Amer.*, 44, 838-850, 1954.
- Cox C., Measurement of slopes of high-frequency wind waves, *J. Marine Res.*, 16, 199-225, 1958.
- Dieter, J., F. Hering, R. Bremeyer, and B. Jähne, Measurements of velocity profiles in the aqueous boundary layer at a wind-driven water surface, *This volume*.

- Duke, S. R., and T. J. Hanratty, Measurement of the concentration field resulting from oxygen absorption at a wavy air-water interface, *This volume*.
- Geißler, P., and B. Jähne, Measurements of bubble size distributions with an optical technique based on depth from focus, *This volume*.
- Gulliver, J. S., and A. Tamburrino, Turbulent surface deformation and their relationship to mass transfer in an open-channel flow, *This volume*.
- Haußecker, H., and B. Jähne, In situ measurements of the air-sea gas transfer rate during the MBL/COOP West Coast Experiment, *This volume*.
- Haußecker, H., S. Reinelt, and B. Jähne, Heat as a proxy tracer for gas exchange measurements in the field: principles and technical realization, *This volume*.
- Hering, F., D. Wierzimok, and B. Jähne, Measurements of enhanced turbulence in short wind-induced water waves, *This volume*.
- Hiby, J.W., Eine Fluoreszenzmethode zur Untersuchung des Transportmechanismus bei der Gasabsorption im Rieselfilm, *Wärme- und Stoffübertr.*, 1, 105-116, 1968.
- Hiby, J.W., The chemical indicator: a tool for the investigation of concentration fields in liquids, *Ann. N.Y. Acad. Sci.*, 404, 348-349, 1983.
- Hwang, P. A., Spatial measurements of small-scale ocean waves, *This volume*.
- Jähne, B., *On the transfer processes at a free air-water interface*, Habilitation thesis, Faculty of Physics and Astronomy, Univ. Heidelberg, 1985
- Jähne, B., From mean fluxes to a detailed experimental investigation of the gas transfer process, *Air-Water Mass Transfer*, selected papers from the 2nd International Symposium on Gas Transfer at Water Surfaces, September 11-14, 1990, Minneapolis, Minnesota, S. C. Wilhelms and J. S. Gulliver, eds, pp. 244-256, ASCE, New York, 1991.
- Jähne, B., J. Klinke, and S. Waas, Imaging of short ocean wind waves: a critical theoretical review, *J. Optical Soc. Amer. A*, 11, 2197-2209, 1994.
- Jessup, A. T., C. J. Zappa, V. Hesany, M. R. Loewen, and M. G. Skafel, Dependence of the skin layer recovery rate on heat flux and turbulence, *This volume*.
- Keller, W., and B. L. Gotwols, Two-dimensional optical measurement of wave slope, *Appl. Opt.*, 22, 3476-3478, 1983.
- Klinke, J., and B. Jähne, Measurements of short ocean waves during the MBL ARI West Coast Experiment, *This volume*.
- De Leeuw, G., and L. H. Cohen, Bubble size distributions in coastal seas, *This volume*.
- Loewen, M. R., M. A. O'Dor, and M. G. Skafel, Laboratory measurements of bubble size distributions beneath breaking waves, *This volume*.
- McKeown, W., Radiometric measurement of diffusion zone thickness, *This volume*.
- Münsterer, T., H. J. Mayer, and B. Jähne, Dual-tracer measurements of concentration profiles in the aqueous mass boundary layer, *This volume*.
- Wolff, L.M., Z.-C. Liu, and T.J. Hanratty, A fluorescence technique to measure concentration gradients near an interface, *Air-Water Mass Transfer*, selected papers from the 2nd International Symposium on Gas Transfer at Water Surfaces, September 11-14, 1990, Minneapolis, Minnesota, S. C. Wilhelms and J. S. Gulliver, eds, pp. 210-218, ASCE, New York, 1991.

Uncertainties in the Molecular Diffusion Coefficient of Gases in Water for Use in the Estimation of Air-Sea Exchange

D. B. King, W. J. De Bryun, M. Zheng, and E. S. Saltzman

Rosenstiel School of Marine and Atmospheric Science
University of Miami, Miami, FL

Abstract

Measurements of the molecular diffusion coefficient of several environmentally important gases in pure water are summarized and used to test the accuracy of estimates based on semi-empirical relationships. These estimates agree with the corresponding measured diffusivities to within about 17% (1σ), with a maximum difference of 36%. The uncertainty associated with estimating the molecular diffusion coefficient of a gas in seawater from the value in pure water is also discussed. The correction of the pure water molecular diffusion coefficient to the seawater value is shown to be variable, demonstrating our lack of understanding of the effect of salinity on diffusion. The total uncertainty in the molecular diffusion coefficient of a gas is relatively small compared to other uncertainties in the air-sea exchange process, so estimates made using the semi-empirical relationships can be used with reasonable confidence where measurements have not been made.

1 Introduction

Air-sea exchange is an important component in the biogeochemical cycling of many gases in the environment. It is used extensively in the estimation of both oceanic and atmospheric lifetimes and in models which predict the behavior of various chemical species. The flux of a gas (F) is quantified in terms of a gas exchange coefficient (k) and the concentration difference across the air-sea interface:

$$F = k(C_l - C_g\alpha) \quad (1)$$

where C is the concentration in the liquid (l) or gas (g) phase and α is the dimensionless *solubility* of the gas in seawater [Liss and Slater, 1974]. For slightly soluble gases, the liquid phase component of the gas exchange coefficient dominates air-sea exchange [Liss, 1973]. This is the case for many gases of environmental interest. The liquid phase gas exchange coefficient (k_l) can be expressed as a function (f) of the molecular *diffusion coefficient* (D) of the gas according to the following relationship:

$$k_l = f(Sc^{-n}) = f(D^n) \quad (2)$$

where Sc is the *Schmidt number* (kinematic viscosity/molecular diffusion coefficient), and n may vary from 2/3, for a smooth surface, to 1/2, in the presence of waves [Liss and Merlivat, 1986; Jähne et al., 1987b]. A variety of expressions have been developed to estimate the magnitude of the gas exchange coefficient, primarily through its relationship to wind speed [Smettie et al., 1985; Liss and Merlivat, 1986; Wanninkhof, 1992; Erickson, 1993]. The estimation of the gas exchange coefficient introduces uncertainties in F which vary in magnitude depending on which method is used. Since D has not been measured for many environmentally important gases, researchers are often forced to use an estimate and thus add increased uncertainty into the calculation of both the gas exchange coefficient and the flux.

Even when the molecular diffusion coefficient of a gas has been measured, the results are often unreliable. Jähne et al. [1987a] observed that there are large discrepancies between published values of D . While most values of D are reported with uncertainties on the order of 5–10%, the discrepancy between measurements by different authors is often much larger.

When measurements are not available, D of the gas can be estimated through the use of semi-empirical relationships which fit molecular diffusion coefficient data for nonelectrolytes in dilute solutions as a function of the *molar volume* of the diffusing gas and the viscosity of the solvent. The relationship developed by Wilke and Chang [1955] primarily used measurements made prior to 1950. In 1974, Hayduk and Laudie refit two existing relationships to measurements made in the 1950s and 60s. The reported uncertainty in these relationships is about 6–10% [Wilke and Chang, 1955; Hayduk and Laudie, 1974]. However, these relationships are only as accurate as the diffusivities used to derive them. The disagreement between the older data strongly suggests that measurements of D would be preferable to relying on these semi-empirical relationships fit to that data. Recent measurements have been limited to those published by Jähne et al. [1987a] and those made in our laboratory.

2 Determination of the Diffusion Coefficient of a Gas

2.1 Technique for Measurement of the Molecular Diffusion Coefficient

Diffusion coefficients were measured in our laboratory using a technique based on the method developed by Barrer [1941] and modified by Jähne et al. [1987a] for measurements in water. The technique was further modified for the measurement of D for more reactive gases [Saltzman et al., 1993]. The technique involves monitoring the flux of the gas through an aqueous gel membrane. If the *solubility* of the gas is known, the flux can be expressed in terms of the gas phase concentrations above and below the

gel. The apparatus used in these measurements was developed from a design by *Jähne et al.* [1987a] and consists of a stainless steel housing with a chamber above and below an aqueous gel membrane. The cell is submerged in a circulating, thermostatted water bath to maintain constant temperature throughout the course of the experiment. At the onset of each experiment, the pure gas, or a highly concentrated mixture of the gas in an inert gas, is introduced into the lower chamber while the upper chamber is flushed with an inert gas. The pure gas is then allowed to diffuse through the membrane, and the concentration in the upper chamber is monitored until it reaches a constant, steady-state, value. The steady-state concentration is then used to calculate the flux across the gel. This technique has been used to determine the molecular diffusion coefficient of the following gases: *dimethyl sulfide* (DMS), *sulfur hexafluoride* (SF₆), *methyl bromide* (CH₃Br), *trichlorofluoromethane* (F-11) and *dichlorodifluoromethane* (F-12). Results were also obtained for *methane* in order to test the reliability of the technique [*Saltzman et al.*, 1993]. Methane was chosen because *Jähne et al.* [1987a] had recently published diffusivities for methane with very good precision. The values of D obtained for methane were within 5% (1σ) of those published by *Jähne et al.* [1987a], which is within the stated uncertainty of both sets of measurements.

2.2 Semi-Empirical Relationships for the Estimation of the Molecular Diffusion Coefficient

The two most commonly used expressions for the estimation of the molecular diffusion coefficient were proposed by *Wilke and Chang* [1955] and *Hayduk and Laudie* [1974], equations (3) and (4), respectively:

$$D_{W-C} = \frac{7.4 \times 10^{-8} (\phi M_B)^{1/2} T}{\eta_B V_A^{0.6}} \quad (3)$$

$$D_{H-L} = \frac{13.26(10^{-5})}{\eta_B^{1.4} V_A^{0.589}} \quad (4)$$

where ϕ is a dimensionless “association factor” equal to 2.6 for water, M_B is the molecular weight of solvent B , T is temperature (in degrees kelvin), η_B is the dynamic viscosity of solvent B (in centipoise), and V_A is the *molar volume* (the volume of a mole of the pure liquid at its normal boiling point in cm³ mole⁻¹) of the solute A . The relationship attributed to *Hayduk and Laudie* [1974] was not actually developed by them. Using a larger and more recent data set, they reevaluated the constants in the relationship developed by *Othmer and Thakar* [1953]. *Hayduk and Laudie* [1974] also recalculated the association factor for water in the Wilke-Chang expression using the newer data set and recommended a change in the value from 2.6 to 2.26.

The major difference between these two relationships is the inclusion of temperature as an explicit parameter in the Wilke-Chang relationship, while the temperature dependence of D is expressed solely in terms of the change in η_B as a function of temperature in the other relationship.

3 Results and Discussion

3.1 Comparison of Measurements and Estimates

The *diffusion coefficients* of several gases at 5 and 25 °C (Figure 1, A and B, respectively) are plotted as a function of *molar volume*. Measurements of D plotted in the figure were reported in the following studies: *Jähne et al.* [1987a], *Saltzman et al.* [1993], *King and Saltzman* [1995], *De Bruyn and Saltzman* [submitted], and *Zheng and Saltzman* [unpublished data]. Also plotted are the corresponding estimates of D using the *Hayduk-Laudie* [1974] and *Wilke-Chang* [1955] relationships.

As can be seen from the figures, the estimates are able to predict the diffusion coefficient of gases in water with reasonable accuracy at both 5 and 25 °C. The exceptions are the estimates of D for gases with a low molar volume (H_2 , He, and Ne). Excluding those three gases, these estimates are all within 36% of the measured values. Both expressions yield similar estimates for D at 25 °C, but Wilke-Chang appears to better represent D at 5 °C. The fact that temperature is an additional parameter in the Wilke-Chang expression suggests that there is temperature dependence in the molecular diffusion coefficient beyond the effect on viscosity.

While the Wilke-Chang expression is better able to predict the temperature dependence of the molecular diffusion coefficient for most gases, this is not the case for all gases. This implies that the dependence of D on temperature is more complicated than that suggested by the semi-empirical relationships. An analysis of the recent data provides some insight, however. All of the recent studies have measured D over a range of temperatures. The temperature dependence of the diffusion coefficient data was expressed using the following equation:

$$D = Ae^{-E_a/RT} \quad (5)$$

where E_a is the “*activation energy*” for diffusion in water (in kJ mole^{-1}), R is the gas constant ($8.314 \times 10^{-3} \text{ kJ mole}^{-1} \text{ K}^{-1}$), and T is temperature in Kelvin [*Eyring*, 1936]. Table 1 gives the constants for this equation for several gases, along with the corresponding molecular mass. An examination of the noble gases shows a clear trend with an increase in the activation energy as a function of increasing molecular mass. However, for the remainder of the gases listed in Table 1, the activation energy remains relatively constant despite large variations in the molecular mass. This indicates that the role

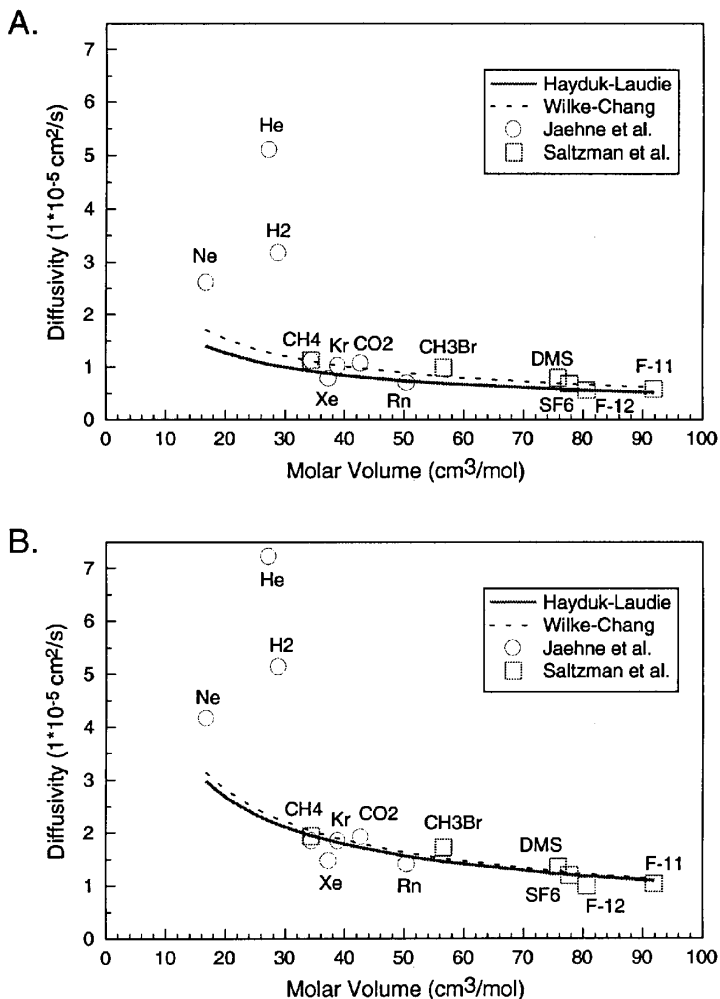


Figure 1: (A,B). Measured and estimated diffusion coefficients for a variety of gases at 5°C (A) and at 25°C (B) as a function of molar volume. The measured diffusivities were reported by Jähne et al. [1987a] (circles), Saltzman et al. [1993] (squares-CH₄ and DMS), King and Saltzman [1995] (square-SF₆), De Bruyn and Saltzman [submitted] (square-CH₃Br), and Zheng and Saltzman [unpublished data] (square-F-11, F-12). The estimated diffusivities were calculated using the semi-empirical relationships: Hayduk and Laudie [1974] (solid line) and Wilke and Chang [1955] (dotted line).

Table 1: List of constants for the temperature-dependent fit of recent molecular diffusion coefficient data

Compound	Molecular Mass	A (cm ² /s)	Ea (kJ/mole)	Reference
He	4.00	0.008	11.7	Jähne et al. [1987a]
Ne	20.18	0.016	14.8	Jähne et al. [1987a]
Kr	83.80	0.064	20.2	Jähne et al. [1987a]
Xe	131.30	0.090	21.6	Jähne et al. [1987a]
Rn	222.00	0.159	23.3	Jähne et al. [1987a]
H ₂	2.02	0.033	16.1	Jähne et al. [1987a]
CH ₄	16.04	0.030	18.4	Jähne et al. [1987a]
CH ₄	16.04	0.031	18.3	Saltzman et al. [1993]
CO ₂	44.01	0.050	19.5	Jähne et al. [1987a]
DMS	62.13	0.020	18.1	Saltzman et al. [1993]
CH ₃ Br	94.94	0.038	19.1	De Bruyn and Saltzman [submitted]
F-12	120.91	0.041	20.5	Zheng and Saltzman [unpublished data]
F-11	137.37	0.034	20.0	Zheng and Saltzman [unpublished data]
SF ₆	146.05	0.029	19.3	King and Saltzman [1995]

of temperature in diffusion is influenced by the interaction between the diffusing gas and the water molecules. Until a theory is developed which can explain the observations, the Wilke-Chang relationship should be used to predict the temperature dependence of the molecular diffusion coefficient of a gas, where measurements are not available.

While the Wilke-Chang expression appears to provide more accurate estimates for most gases which have been measured, either expression will provide a value for D which can be used in calculations of the flux of a gas across the air-sea interface. Since air-sea exchange is a function of the square root of D , the differences between estimates made with either expression and the corresponding measured values are minor for all of the gases other than H₂, He, and Ne. An uncertainty of less than 6% in the square root of D is going to be a minor component of the total uncertainties in the estimation of the rates of air-sea exchange. *Wanninkhof* [1992] discussed the effect of several parameters on the calculation of the gas exchange coefficient. He found that different methods of estimating the gas exchange coefficient responded differently to changes in each parameter. However, the uncertainty in D was not a large contributor to the overall uncertainty for any method. Until the agreement between the various methods of predicting the gas exchange coefficient is improved, the semi-empirical expressions can be used to estimate the molecular diffusion coefficient of a gas in water.

When estimating the molecular diffusion coefficient of a gas, it is impor-

tant to use an accurate value for the molar volume of the gas. Both semi-empirical estimates define the molar volume at the normal boiling point. However, molar volumes and/or densities are not always reported at the boiling point. If this is the case, the molar volume at the boiling point must be estimated to avoid the introduction of large uncertainties in the molecular diffusion coefficient. *Reid et al.* [1987] present methods for estimating both the molar volume (Le Bas; Tyn and Calus) and the liquid density (modified Rackett). While these techniques are accurate to within 5% of the desired value in most cases, the error can be as large as 20%. Therefore, measured molar volumes should always be used when available.

3.2 Molecular Diffusion Coefficient in Seawater

There have been relatively few direct measurements of the molecular *diffusion coefficient* of gases in seawater or other high ionic strength aqueous solutions. It is expected that D in seawater should be lower than in pure water, due to the increase in *viscosity* with ionic strength. The viscosity difference between pure water and seawater is about 6% at 25 °C [Miller, 1974]. The observed differences between D in pure water and seawater are plotted in Figure 2. *Ratcliff and Holdcroft* [1963] measured the molecular diffusion coefficient of *carbon dioxide* (D_{CO_2}) in pure water and in several salt solutions of various ionic strengths at 25 °C. An interpolation from their data to a 35‰ NaCl solution yields an estimate of D_{CO_2} about 6% lower than the pure water molecular diffusion coefficient. *Jähne et al.* [1987a] measured the diffusivities of H_2 and He in both pure water and 35.5‰ NaCl over the temperature range 5 to 35 °C. The diffusion coefficients in the NaCl solutions were observed to be lower by 3–8%. Based on these results, *Jähne et al.* [1987a] recommended an average decrease of 6% for the conversion of pure water diffusivities to seawater. *Saltzman et al.* [1993] measured D of *methane* at 15 °C in 35‰ NaCl and in pure water and found the values in NaCl to be 4% lower than in pure water. The molecular diffusion coefficient of F-12 was measured at 10 °C in pure water and in seawater (salinity 35‰) and was found to be 6% lower in seawater [*Zheng and Saltzman*, unpublished data].

Several recent studies, however, have failed to observe this difference. *King and Saltzman* [1995] observed no difference between D of SF_6 in 35‰ NaCl at 25 °C and the corresponding pure water value. Measurements of the molecular diffusion coefficient of *methyl bromide* in pure water and 35‰ NaCl solution at 13 °C showed no statistically significant difference [*De Bruyn and Saltzman*, submitted]. Similarly, no difference was observed in the molecular diffusion coefficient of F-11 in pure water versus seawater of salinity 35‰ at 10 °C [*Zheng and Saltzman*, unpublished data].

The difference in behavior between F-11 (CCl_3F) and F-12 (CCl_2F_2) is particularly surprising. We do not know why similar molecules like F-11 and F-12 should behave differently. Further work is needed to investigate whether

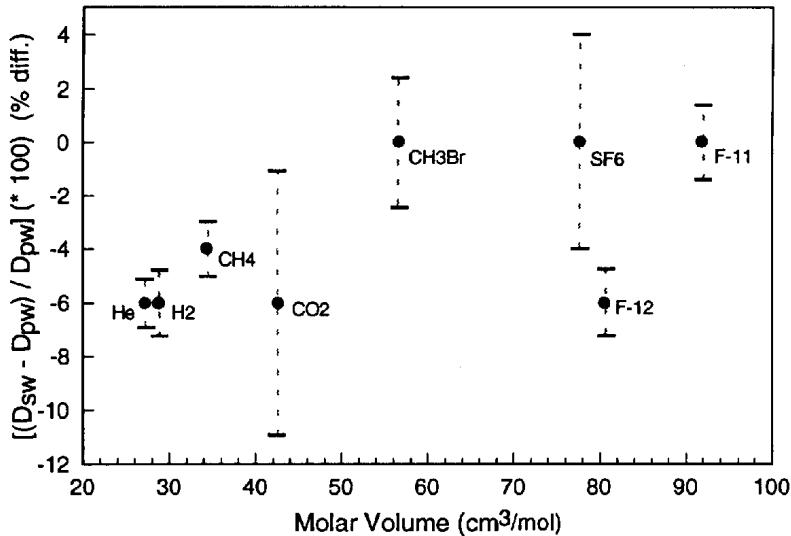


Figure 2: Percent difference between molecular diffusion coefficient in pure water and seawater, or 35% NaCl, plotted as a function of molar volume. The CO₂ data is interpolated from Ratcliff and Holdcroft [1963]. The other data are reported in the following papers: He and H₂ [Jähne et al., 1987a], CH₄ [Saltzman et al., 1993], CH₃Br [De Bruyn and Saltzman, submitted], SF₆ [King and Saltzman, 1995], and F-11 and F-12 [Zheng and Saltzman, unpublished data].

this difference is indeed real or an experimental artifact of some kind. One of the principle difficulties in studying this phenomenon is demonstrated by the large uncertainties shown in Figure 2. The error bars were calculated using the precision in both the pure and seawater measurements and show that the difference between D in pure and seawater is close to, if not larger than, the experimental uncertainty in magnitude. Work at higher ionic strengths may help overcome this problem.

4 Conclusions

Both semi-empirical relationships [Wilke and Chang, 1955; Hayduk and Laudie, 1974] provide estimates of the molecular diffusion coefficient of a gas in pure water which are in good agreement with measured values, although the Wilke-Chang relationship appears to better predict the temperature dependence. Increased measurements of the molecular diffusion coefficient of gases in both seawater and pure water will help to improve the ability to estimate D in seawater when only pure water measurements or semi-empirical estimates are available. However, neither the uncertainty in the estimates

of the molecular diffusion coefficient in pure water nor the uncertainty introduced in the calculation of D in seawater appears to have a significant effect on the resulting air-sea exchange calculations.

Acknowledgements

The authors would like to acknowledge Kim Holmen and Caroline Leck for their work towards development of the apparatus used to measure diffusion coefficients. The authors would also like to thank Rik Wanninkhof and Frank Millero for helpful scientific discussion.

References

- Barrer, R. M., *Diffusion in and through solids*, 464 pp., Cambridge University Press, London, 1941
- De Bruyn, W. J. and E. S. Saltzman, Diffusivity of methyl bromide in water, *Geophys. Res. Lett.*, submitted.
- Erickson, III, D. J., A stability dependent theory for air-sea exchange, *J. Geophys. Res.*, 98, 8471-8488, 1993
- Eyring, H., Viscosity, plasticity, and diffusion as examples of absolute reaction rates, *J. Chem. Phys.*, 4, 283-291, 1936
- Hayduk, W. and H. Laudie, Prediction of diffusion coefficients for nonelectrolytes in dilute aqueous solutions, *Am. Inst. Chem. Eng. J.*, 20, 611-615, 1974
- Jähne, B., G. Heinz, and W. Dietrich, Measurement of the diffusion coefficients of sparingly soluble gases in water, *J. Geophys. Res.*, 92, 10767-10776, 1987a
- Jähne, B., K. O. Münnich, R. Bosinger, A. Dutzi, W. Huber, and P. Libner, On the parameters influencing air-water gas exchange, *J. Geophys. Res.*, 92, 1937-1949, 1987b
- King, D. B. and E. S. Saltzman, Measurement of the diffusion coefficient of sulfur hexafluoride in water, *J. Geophys. Res.*, 100, 7083-7088, 1995
- Liss, P. S., Processes of gas exchange across an air-water interface, *Deep Sea Res.*, 20, 221-238, 1973
- Liss, P. S. and L. Merlivat, Air-sea gas exchange rates: introduction and synthesis, in *The Role of Air-Sea Exchange in Geochemical Cycling*, P. Buat-Ménard (ed.), D. Reidel Publishing Company, New York, 113-127, 1986
- Liss, P. S. and P. G. Slater, Flux of gases across the air-sea interface, *Nature*, 247, 181-184, 1974
- Millero, F. J., Seawater as a multicomponent electrolyte solution, in: *The Sea*, vol. 5, *Marine Chemistry*, ed. by E. D. Goldberg, pp. 3-80, John Wiley, New York, 1974
- Othmer, D. F. and M. S. Thakar, Correlating diffusion coefficients in liquids, *Ind. Eng. Chem.*, 45, 589-593, 1953
- Ratcliff, G. A. and J. G. Holdcroft, Diffusivities of gases in aqueous electrolyte solutions, *Trans. Instn. Chem. Engrs.*, 41, 315-319, 1963
- Reid, R. C., J. M. Prausnitz, and B. E. Poling, *The Properties of Gases and Liquids*, 4th ed., 741 pp., McGraw-Hill Book Company, New York, 1987

- Saltzman, E. S., D. B. King, K. Holmen, and C. Leck, Experimental determination of the diffusion coefficient of dimethylsulfide in water, *J. Geophys. Res.*, 98, 16,481-16,486, 1993
- Smethie, W. M., Jr., T. Takahashi, D. W. Chipman, and J. R. Ledwell, Gas exchange and CO₂ flux in the tropical Atlantic Ocean determined from ²²²Rn and pCO₂ measurements, *J. Geophys. Res.*, 90, 7005-7022, 1985
- Wanninkhof, R., Relationship between wind speed and gas exchange over the ocean, *J. Geophys. Res.*, 97, 7373-7382, 1992
- Wilke, C. R. and P. Chang, Correlation of diffusion coefficients in dilute solutions, *A.I.Ch.E. Journal*, 1, 264-270, 1955

Enhanced Transport of Carbon Dioxide During Gas Exchange

Steven Emerson

School of Oceanography, University of Washington
Seattle, Washington 98195-7940

Abstract

I present calculations of the degree of chemical enhancement of the carbon dioxide gas exchange rate at the air-water interface in lakes and the ocean using a general model that considers pH and charge gradients in the diffusive boundary layer. To a first approximation the enhancement factor in lakes of widely different chemical properties is dependent on the turbulent rate of physical exchange and the pH of surface waters. Chemical enhancement in the ocean should be negligible unless the rate of CO₂ hydrolysis is catalyzed. Conditions may be favorable for catalysis by carbonic anhydrase in coastal waters, but there is no evidence that it occurs. Isotope fractionation during gas exchange will be important where chemical enhancement occurs because of the different rates of ¹²CO₂ and ¹³CO₂ reaction with hydroxyl ion. Even in the ocean where the mean global surface water CO₂ is near saturation, isotopic fractionation by this mechanism could be significant because sea water departs from saturation by tens of percent locally, and chemical enhancement factors are greater when surface waters are undersaturated (pH is relatively high) than when they are supersaturated.

1 Introduction

The exchange of carbon dioxide across the air-water interface involves both physical transport and chemical reaction. The extent of completion of the reaction or "chemical enhancement" depends on the reaction kinetics and the rate of physical transport near the interface. In lakes which are often somewhat protected from strong winds and which have a wide variation of water chemistry, the effect of chemical enhancement ranges from unimportant to a dominant [Emerson, 1975; Quay *et al.*, 1986]. Gas transfer rates between the air and sea are on average faster than in lakes and the pH rarely reaches values greater than 8.4, diminishing the importance of enhanced CO₂ transfer, so long as the reaction rate is uncatalyzed [Broecker and Peng, 1974, Bolin, 1960]. The possibility of reaction rate *catalysis* is an important problem to resolve because global gas exchange rates determined by ¹⁴C-CO₂ mass balance are 20-50% greater than those determined by inert tracers [Watson, 1993] and one of the possible explanations is that there is some level of CO₂ chemical enhancement during ¹⁴CO₂ invasion. While the studies performed to test the level of CO₂ reaction catalysis in the ocean

revealed no evidence for enhanced transport [Goldman and Dennett, 1983], the level of accuracy and generality of this result was not sufficient to rule out the possibility of its importance.

I present results of enhancement factors calculations determined by a completely general model for a variety of physical conditions in different lakes and the ocean. An assessment is made of the feasibility of catalysis necessary to enhance the global $^{14}\text{CO}_2$ gas exchange rate over that determined from inert gas exchange experiments. And, an argument is presented that stable isotope fractionation by chemical reaction during gas exchange causes a small but possibly significant fractionation of anthropogenic CO_2 that currently invades the ocean.

2 Theory

Models of gas exchange across air-water interfaces assume that the driving force for the transfer of a relatively insoluble gas is the concentration gradient between the atmospheric saturation value and that in the water [Dankwertz, 1970]. If the gas reacts with water during the transfer, the gradient at the interface will be steeper than assumed by the macroscopic concentration difference and a gradient will be formed in the reaction product. This is called enhanced (or facilitated) transport and must be calculated as gradients on this scale at the interface cannot be measured. Carbon dioxide is the most important gas in nature with a hydrolysis rate that is relatively slow (that is on the order of tens of seconds rather than micro seconds). The reaction rate is in fact of the same order as the transit time of CO_2 between the atmosphere and water, making the question of facilitated transport an important one in nature.

There are two CO_2 hydrolysis reaction path ways [Johnson, 1982]:



In our calculation of the chemical enhancement factors we use the stagnant boundary layer gas exchange model that assumes the flux across the interface, F ($\text{mol m}^{-2} \text{ s}^{-1}$), is described by molecular diffusion (with the diffusion coefficient, D , $\text{m}^2 \text{ s}^{-1}$) in a stagnant layer of thickness, z (m), times the concentration gradient in the layer:

$$F = \frac{D}{z}(\alpha pC - [C_w]) \quad (3)$$

where pC (atm) is the gas partial pressure in the atmosphere, α ($\text{mol m}^{-2} \text{ atm}^{-1}$) is the gas solubility, and $[C_w]$ is the concentration (mol m^{-3}) of gas

in surface waters. It has been shown that the transfer of gases is more realistically described by more elaborate surface renewal models [Ledwell, 1984]; however, enhancement factors calculated by both methods are very similar [Dankwertz, 1970; Keller, 1994] indicating that our results should be generally applicable.

The chemical aspects of the model presented here are general because there are no assumptions about constancy of pH across the boundary layer or the importance of coupled diffusion of charged dissolved species. The model is identical to that described twenty years ago [Emerson, 1975], but the computer scheme has been streamlined to calculate enhancement factors for all natural conditions. The equations controlling the enhancement factor calculation are outlined in detail in Emerson [1975]. Briefly, the one dimensional diffusion equation is solved for CO_2 and all ionic species present. Equations for the carbonate system species include a reaction rate term that describes the mechanisms in (1 and 2). Instantaneous equilibria are assumed between HCO_3^- and CO_3^{2-} ($K'_2 = [\text{CO}_3^{2-}] a_{\text{H}^+} / [\text{HCO}_3^-]$) and dissociation of water ($K'_w = [\text{H}^+] [\text{OH}^-]$). The *alkalinity* is defined as the difference in concentration between cations and anions that are likely to protonate in the pH range 7-10 and is equal to: $(\text{HCO}_3^- + 2\text{CO}_3^{2-} + \text{OH}^- - \text{H}^+)$. Because the mobility of H^+ and OH^- are 8 and 5 times that for bicarbonate and carbonate, charge gradients are established where reaction produces gradients in these and the carbonate species. Macroscopically the solution must maintain electroneutrality, so ions of high mobility speed up the slower ones and vice versa. If the reacting species are minor component of the total ionic strength, as in sea water, the trace ions diffuse nearly with their own mobility because of the availability of other ions in solution (e. g., Na^+ and Cl^-) to maintain charge balance. However, if the carbonate species and OH^- ion are a significant portion of the ionic strength (as in dilute fresh waters) then the effect can not be neglected and will cause gradients in alkalinity across the boundary layer [Emerson, 1975]. The charged species diffusion effect is incorporated into the model by considering that the flux of an individual ion is a function of the concentration and concentration gradients of all ions in solution [Vinograd and McBain, 1941].

Fluxes of CO_2 , HCO_3^- , and CO_3^{2-} across the boundary layer are calculated numerically using the above constraints in a finite difference scheme to determine the total inorganic carbon transfer. Approximate analytical solutions to the enhancement factor problem have been derived [Bolin, 1960; and later Hoover and Berkshire, 1969] by assuming ionic species diffuse with their own mobilities and that pH is constant across the boundary layer. The first of these assumptions is valid in the swamping electrolyte of sea water; however, the constant pH assumption violates electroneutrality. Quin and Otto [1971] pointed this out and solved the sea water problem numerically with the assumption that the reaction in (2) is unimportant at these pHs. (The latter assumption is inappropriate for higher pHs and in fact even at $\text{pH} = 8.2$, 30-40 percent of the reaction is accounted for by direct combi-

Table 1: Temperature dependence of equilibrium and kinetic constraints of the CO₂ system in pure water and seawater. Apparent equilibrium constraints for sea water are on the NBS scale to be consistent with the rate constants. Johnson's [1982] sea water value for $k_{OH}K_W$ was multiplied by the activity coefficient of OH⁻ (0.2; see text).

	Pure Water					Sea Water 35%				
	10	15	20	25	30 (°C)	10	15	20	25	30(°C)
K_O (mol l ⁻¹ atm ⁻¹) × 10 ² (a)	5.37	4.56	3.92	3.41	3.00	4.39	3.74	3.24	2.84	2.52
K_1 (mol l ⁻¹) × 10 ⁷ (b)	3.44	3.80	4.15	4.45	4.71	8.12	8.88	9.56	10.2	10.7
K_2 (mol l ⁻¹) × 10 ¹¹ (c)	3.24	3.72	4.20	4.69	5.13	47.6	53.9	65.5	75.8	86.7
K_w (mol l ⁻¹) ² × 10 ¹⁴ (d)	0.29	0.45	0.68	1.01	1.47	-	2.00	-	6.00	-
k_{CO_2} (s ⁻¹) × 10 ² (e)	0.8	1.4	2.4	3.7	5.4	0.8	1.4	2.4	3.7	5.4
$k_{OH} K_W$ (mol l ⁻¹) ⁻¹ × 10 ⁻⁴ (e)	1.2	2.1	3.8	7.1	13.4	0.5	0.8	1.5	2.7	5.1
$k_{H_2} CO_3$ (mol l ⁻¹) ⁻¹ × 10 ⁴ (f)	2.3	3.7	5.8	8.3	11.5	0.8	1.2	1.9	2.6	3.4
k_{HCO_3} (s ⁻¹) × 10 ⁵ (f)	3.5	5.5	9.2	16.0	26.3	0.6	0.9	1.6	2.6	4.8

(a) Weiss, 1974

(b) K_1 (I = 0) Harned and Davis, 1943; K'_1 (s.w.) Mehrbach's values [Dickson and Millero, 1987]

(c) K_2 (I = 0) Harned and Scholes 1941; K'_2 (s.w.) same as K'_1

(d) K_w (I = 0) Harned and Owen, 1958; K'_w (s.w.) Culberson and Pytkowicz, 1973, converted to molal scale ($K_w = K_w$ (C & P)/(1.025))²

(e) Johnson, 1982

(f) $k_{CO_2}/k_{H_2CO_3} = k_{OH}K_W/k_{HCO_3} = K_1$

nation of OH⁻ with CO₂.) The approximate solution of Hoover and Berkshire [1969] is often used to determine chemical enhancement factors because of its simplicity.

Carbonate system equilibrium and reaction rate constants as a function of temperature are presented in Table 1. The kinetic data were determined by Johnson [1982] in pure water and sea water. He used the NBS scale for equilibrium constants and I have conformed to his practice in the table. Because rate constants are written in terms of concentrations rather than activities, I believe Johnson determined the value, $K_{OH}K_w/\gamma_{OH^-}$, (where γ_{OH^-} is the activity coefficient of hydroxyl ion) rather than $K_{OH}K_W$ as stated in his paper. This correction has been incorporated into Table 1.

Table 2: Chemical conditions for enhancement factor calculations in a range of lakes. Average cation, AC, and anion, AA, concentration; equilibrium and rate constraints.

Lake	AC	AA (meq/l)	T (°C)	K' ($\times 10^7$)	K'2 ($\times 10^{11}$)	K'w ($\times 10^{14}$)	k _{CO₂} ($\times 10^2$)	k _{OH} ($\times 10^{-3}$)
A) ELA ^(a)	.18	.12	20	4.15	4.20	.68	2.4	5.6
B) Lake Wash- ington ^(b)	.50	.15	25	4.51	4.74	.68	2.4	5.6
C) Lake Erie ^(c)	2.00	1.05	20	4.80	5.80	.80	2.4	5.6
D) Greifen- see ^(d)	3.20	1.00	20	4.94	5.92	.80	2.4	5.6
E) Mono Lake ^(e)	895	600	20	9.21	65.0	3.20	2.4	2.5

(a) Hesslein et al., 1980

(b) Quay et al., 1986

(c) Kramer, 1967

(d) H. Ambuhl (EAWAG/ETH, Zürich Switzerland; unpublished data)

(e) Simpson and Takahashi, 1973

3 Enhancement Factors

Enhancement factor calculations were made for lakes of widely different chemical composition, and sea water. Each case was solved for a variety of stagnant boundary layer thicknesses so that the values in the experiments or in nature would be bracketed.

3.1 Lakes

Gas exchange enhancement factors were determined for five lakes with a range in carbonate chemistry compositions that span those found in nature (Table 2). Alkalinities range from 0.1 for the dilute lakes of the Canadian Shield to 550 meq/l in the alkaline *Mono Lake*. Apparent constants for the carbonate system were determined by evaluating activity coefficients and ion pairs for carbonate, bicarbonate, and hydroxyl ion. The extended Debye-Huckel equation and ion pair equilibrium constants were used with published chemical compositions except for *Mono Lake* where the high concentrations pose special problems and the total activity coefficients were determined by *Simpson and Takahashi* [1973]. It was assumed that the rate constant, k_{OH}, in *Mono Lake* is similar to that in sea water, although this is clearly an approximation because of the high ionic strength [*Wanninkhof*, 1986].

Enhancement factors are presented as a function of boundary layer thickness (a reasonable mean value for the gas exchange rate in lakes is 150 microns; *Emerson* [1975], *Wanninkhof et al.* [1985]) and CO₂ concentration in Figure 1. These two variables and the alkalinity are the major factors deter-

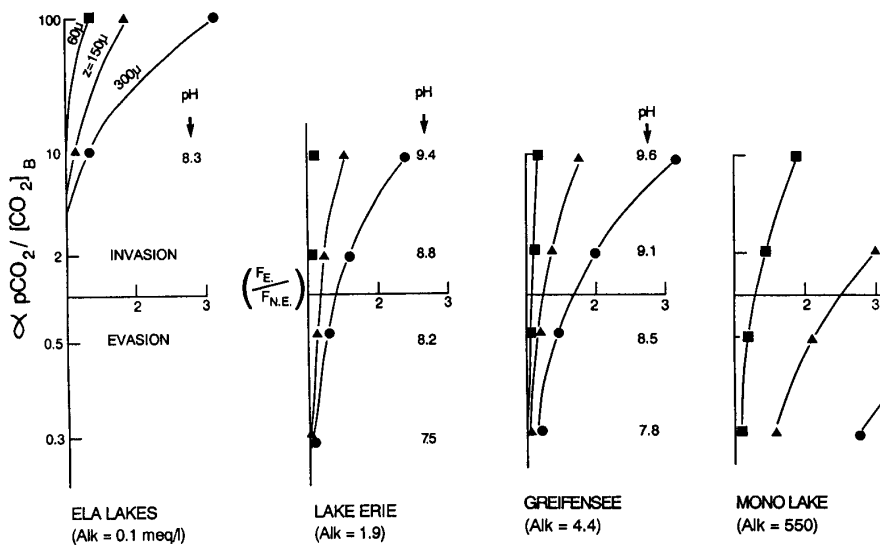


Figure 1: The CO₂ enhancement factor (enhanced flux/unenhanced flux, $F_E/F_{N.E.}$) plotted against the degree of CO₂ saturation ($\alpha pCO_2/[CO_2]_B$) for different boundary layer thicknesses, z . Values were calculated for lakes of different alkalinity, and surface water pH is indicated (see Table 2)

mining the extent of chemical enhancement. In waters with low alkalinity there is essentially no possibility for enhanced transfer during CO₂ evasion because of the low bicarbonate concentrations at $pH \leq 7$ when CO₂ is greater than atmospheric equilibrium concentrations. As the alkalinity increases (Figure 1) the possibility for enhancement becomes greater at higher CO₂ concentrations because the HCO_3^-/CO_2 ratio is larger (indicated by higher pH) and conditions are more favorable for the CO₂-OH⁻ reaction (Eq. 2). When the alkalinity is as high as that in Mono Lake the pH at atmospheric CO₂ saturation is near 10. To a first approximation the trend in enhancement as a function of pH (Figure 2) for a given boundary layer thickness is followed relatively independently of alkalinity. This result (Figure 2) serves as a rough guide to the estimation of enhancement factors in lakes if the pH and stagnant boundary layer thickness are known.

Charged ion diffusion effects are important only in dilute solutions where the sum of the ion concentration changes across the boundary layer is significant compared with the sum of all the ion concentrations in the water. This happens when bicarbonate and carbonate are major anions and when the bicarbonate gradient is significant compared to the total alkalinity. For example, a 10 μ mol/l gradient in bicarbonate is roughly equivalent to the maximum CO₂ concentration gradient during invasion and would cause an enhancement factor of 2. If the carbonate species are the major anions

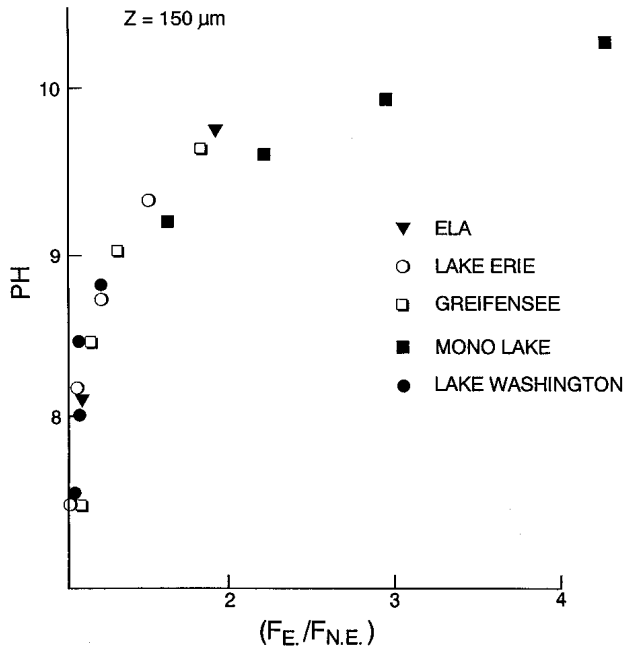


Figure 2: The CO_2 enhancement factor ($F_E/F_{N.E.}$) versus surface water pH at a boundary layer thickness of 150μ for five different lakes with widely different alkalinities. (see Table 2)

and have concentrations of less than a few hundred micromolar, this gradient would be significant compared to the total ion concentration, and the charged ion effect would be important. Dilute lakes of the Canadian Shield are an example of chemical conditions in which this effect is important [Emerson, 1975].

3.2 Sea Water

Enhancement factors calculated for oceanic conditions as a function of boundary layer thickness and degree of CO_2 saturation (Figure 3) are a few percent for boundary thicknesses of 30–60 microns and between 20 and 30% for thickness of 150 microns. The mean boundary layer thickness determined from inert gas measurements in the ocean is on the order of 40 ± 20 microns [Broecker and Peng, 1974] and the total integrated rate of exchange is highly weighted to the lower range of boundary layer thicknesses (Figure 3). It is clear that the maximum oceanic enhancement in this calculation is less than 10% which is consistent with previous assessments [Bolin, 1960; Hoover and Berkshire, 1969; Quinn and Otto, 1971; Wanninkhof, 1992]. Since the amount of enhancement needed to explain the discrepancy

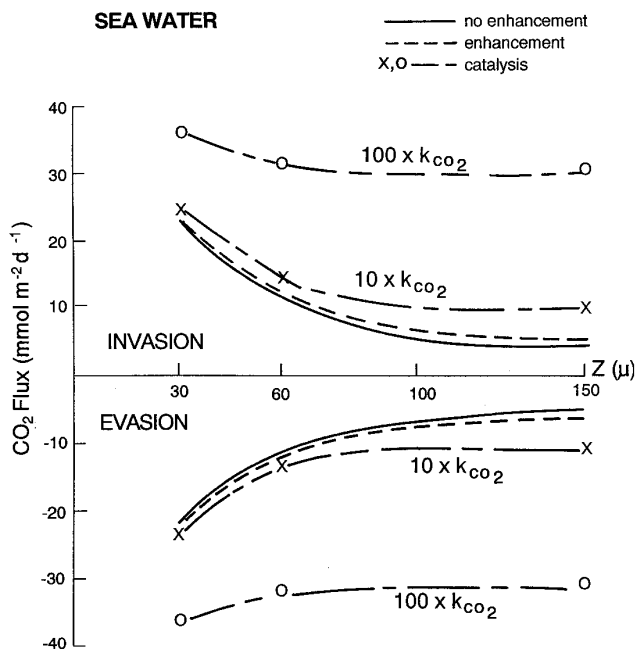


Figure 3: The CO₂ gas exchange flux versus boundary layer thickness for the cases of: no enhancement (solid line), chemically enhanced flux (broken line), and chemically enhanced flux with reaction rate catalysis.

between ¹⁴C-CO₂ exchange and the inert gas estimates is on the order of 50%, enhancement via the uncatalyzed reaction cannot be the answer. I found that enhancement factors determined for these conditions using the general model differed from those determined by the *Hoover and Berkshire* [1969] approximation by less than 10%.

Enhancement factors for the *hydration rate constant* ten and one hundred times the uncatalyzed value (Figure 3) increase the exchange rate by 10-50% and 50-100%, respectively. Since it is known that marine diatoms produce *carbonic anhydrase* [Morel et al., 1994], one can make a first order assessment of whether a 10-100 times enhancement is feasible by determining the amount of carbonic anhydrase (CA) it would require in solution. The turn over number (the number of substrate molecules transformed per enzyme molecule) for human carbonic anhydrase is $0.6 \times 10^6 - 1.5 \times 10^6$ s⁻¹ [Khalifah, 1971]. As the uncatalyzed rate of CO₂ reaction at 25 °C and a CO₂ concentration at equilibrium with the atmosphere is 3.7×10^{-7} mol l⁻¹ s⁻¹ ($R = k_{CO_2} [CO_2] = .037 [10 \times 10^{-6}]$), one pico mole l⁻¹ of CA would increase the gas exchange rate by 3 times and 0.1 nanomole l⁻¹ by 300 times at these turnover numbers. *Silverman and Tu* [1976] measured a catalysis rate of 30 times for 5 nanomolar CA at pH 8.35. This is a lower limit for

our purposes as the rate of catalysis increases with decreasing pH [Silverman and Tu, 1976]. Thus, nanomolar levels of CA are necessary to create sufficient CO₂ catalysis.

No one has attempted to measure the carbonic anhydrase concentration at this level, so I assess the possibility of its presence at this concentration by the zinc content of sea water. Human carbonic anhydrase is about 0.3% zinc and has a molecular weight of about 30,000 [Coleman, 1973]. Some estimates suggest that the 80% of Zn in diatoms is bound by this enzyme. Given the differences in their molecular weights, the number of moles of complexed zinc and carbonic anhydrase should be about the same (3×10^4 gCA (mol CA)⁻¹ 3×10^{-3} g Zn (gCA)⁻¹ / 65 g Zn (mol Zn)⁻¹ = 1.4). Bruiland [1989] measured total zinc concentrations of 0.3 nanomolar in open ocean surface waters and determined that it is nearly all complexed by an organic ligand of concentration 1.2 nM concentration. Thus, the range of zinc concentrations, if it is all bound as carbonic anhydrase with the properties suggested above, is just sufficient to indicate CA concentrations great enough to cause the necessary catalysis. This is not a very strong case, but there are a couple of unknown factors that might strengthen the possibility. The first is that zinc, like other metals, may be concentrated at the air-water interface where one might expect relatively high concentrations of the partially hydrophobic carbonic anhydrase [Coleman, 1973], and the second is that the zinc concentration in surface sea waters is somewhat greater in coastal waters because of upwelling and atmospheric inputs. Since diatom blooms are also most prevalent in near shore waters, it may be possible for significantly enhanced CO₂ transport in these locations during high productivity periods. This calculation indicates the region of the ocean where the catalysis is most likely to occur, but whether it actually happens will require further experimentation.

3.3 Carbon Isotope Fractionation

The effect of chemical enhancement during gas exchange on *carbon isotope fractionation* between atmosphere and ocean could be significant because of the asymmetry in the relatively small (on the order of one percent) enhancement during evasion and invasion. Keller [1994] pointed out the potential importance of this effect on the global mass balance of carbon-14. In today's ocean the global mean undersaturation required to accommodate the invasion of anthropogenic CO₂ is 2–3% [Siegenthaler and Sarmiento, 1993]. This small departure from equilibrium would create negligible chemical enhancement if it were uniform. To calculate the effect of chemical enhancement; however, one must consider observations that indicate large annual swings from under to over saturation and vast regions of the ocean that are tens of percent under and over saturated [Takahashi, 1991]. For example, sea water 30% depleted in CO₂ with respect to atmospheric saturation has a pH 0.2 higher than the same water 30% enriched in CO₂ (Table 3). The enhance-

Table 3: Calculation of the kinetic isotope fractionation factor. CO_2 concentrations $[CO_{2,B}]$ are for surface waters. The atmospheric equilibrium value is $[CO_{2,A}] = 10.2 \times CO^{-6}$ mol/kg. pH was calculated for an alkalinity of 2.277 meg/kg and 25°C. Fluxes, F , are net fluxes, i. e., the difference between the invasion and evasion flux, for a stagnant boundary layer thickness of 30 μ m. Superscripts 12 and 13 indicate the isotope of carbon and subscripts U and E indicate unenhanced and enhanced fluxes. Flux ratios indicate the isotope effect for the net CO_2 flux. The last column is an estimate of the atmosphere-ocean isotope difference caused by this effect (see text).

$[CO_{2,B}]$ (mmol/kg $\times 10^6$)	$\frac{[CO_2]_W-A}{[CO_2]_A}$	pH	F_u^{12}	F_E^{12}	F_u^{13}	F_E^{13}	$\frac{(F^{13}/F^{12})_E}{(F^{13}/F^{12})_U}$	$\Delta\delta$
			(mol $cm^{-2}s^{-1} \times 10^{11}$)					
8.7 11.6	.15	8.15 8.01	.06100	.06252	.06093	.06240	.9995	.02
7.1 13.2	.30	8.20 7.98	.06100	.06480	.06090	.06460	.9986	.07
5.1 15.2	.50	8.31 8.93	.06100	.07170	.06090	.07130	.9960	.20

$$K_1^{12}K_1^{13} = .9905 \text{ [Mook et al, 1974]}$$

$$\alpha_{CO_2}^{13} / \alpha_{CO_2}^{12} = .9989 \text{ [Vogel et. al., 1970]}$$

$$k_{OH}^{13} / k_{OH}^{12} = .973 \text{ [Siegenthaler and Münnich, 1981]}$$

$$k_{HCO_3}^{13} / k_{HCO_3}^{12} = k_{OH}^{13} / k_{OH}^{12} (K_1^{12} / K_1^{13}) = .973 (.9905) = .964$$

$$D_{HCO_3}^{13} / D_{HCO_3}^{12} = .9991 \text{ [Siegenthaler and Münnich, 1981]}$$

ment factor during invasion is about 1% and during evasion roughly 0.9% because of the pH dependence of CO_2 hydrolysis via reaction (2).

I demonstrate the effect of this asymmetry on the isotope fractionation of anthropogenic CO_2 entering the ocean (Table 3) by assuming that the ocean is split into equal regions, one undersaturated in CO_2 with respect to the atmosphere and the other supersaturated to nearly the same degree. The departure from equilibrium in the undersaturated region is slightly greater in order to create a net undersaturation necessary for anthropogenic CO_2 invasion. Examples in Table 3 assume 15, 30, and 50% departures from atmospheric equilibrium. Gas exchange fluxes of CO_2 were calculated for both the undersaturated and supersaturated cases using the boundary layer model and stagnant layer thickness of 30 microns. Enhanced fluxes were determined using the formula of Hoover and Berkshire [1969] because it results in values nearly identical to those of the more elaborate model for these cases. Carbon 13 fluxes were calculated using the equilibrium and rate constant ratios presented in the footnotes of table 3. Net global fluxes (i. e., the difference between the invasion and evasion fluxes in the under and supersaturated regions) are presented in the table. The discrimination against carbon 13 in the net invasion of CO_2 caused by chemical enhancement is

indicated in the second to last column as the relative $^{13}\text{C}/^{12}\text{C}$ flux ratio for the enhanced and unenhanced cases.

The relevance of this fractionation factor to observed values is realized by calculating the stable isotope difference between the atmosphere and ocean caused by the enhancement factor. I determined this value using a simple mass balance model of the fate of anthropogenic CO_2 in the atmosphere and surface ocean, and data for the difference in carbon and isotope inventories between 1970 and 1990 presented by *Tans et al.* [1993]. The change in the atmospheric CO_2 concentration, $[C_a]$ (mole m^{-3}), due to the influx of fossil fuel, J_f (mole yr^{-1}), and moderated by the flux to the ocean, F (mole $\text{m}^{-2} \text{yr}^{-1}$), is:

$$V_a d[C_a]/dt = J_f - A_o F \quad (4)$$

where V_a is the volume of the atmosphere, A_o is the ocean area, and the atmosphere-ocean flux is parameterized by equation (3). For carbon 13 the relationship is:

$$V_a d[^{13}C_a]/dt = J_f R_f - A_o (D_{13}/z) [\alpha^{13} p \text{CO}_2 R_a - [\text{CO}_2] R_w] E \quad (5)$$

where R is the $^{13}\text{C}/^{12}\text{C}$ ratio, α^{13} is the solubility of $^{13}\text{CO}_2$, and E is the fractionation effect in the second to last column of Table 3. The net CO_2 difference between the atmosphere and surface waters used in the calculation was 2.5% of the equilibrium value and the $\delta^{13}\text{C}$ difference was 0.7 per mil. The isotope effect in the final column of Table 3 is the atmosphere-surface ocean difference in $\delta^{13}\text{C}$ caused by the enhancement effect between 1970 and 1990. The total atmosphere-ocean isotope difference is believed to be on the order of 0.4–0.7 per mil [*Tans et al.*, 1993; *Quay*, personal communication] and each 0.1 per mil difference is equivalent to about 0.5 gigatons of fossil fuel carbon uptake [*Tans et al.*, 1993] indicating that the enhancement effect, while small, could be significant.

I would like to point out a few caveats to the result in the final column of Table 3. The first is that my calculation assumes a single linear change in the atmosphere between 1970 and 1990 and constant ocean carbon dioxide concentration and isotope ratios. Initial results from a more realistic model in which the ocean and atmospheric concentrations respond to fossil fuel input results in an enhancement isotope effect that is about half the value presented in Table 3 [*Paul Quay and Jianrong Zhang*, personal communication]. Furthermore, the calculation was made for 25 °C and constant stagnant boundary layer thickness. In reality a large portion of CO_2 evasion from the ocean occurs at the equator with invasion spread over a larger area at higher latitudes. Lower temperature, smaller gradients, and more turbulent conditions for invasion all tend to favor a smaller enhancement effect. My calculation represents an upper limit on the air-water isotope difference

caused by chemical enhancement, and it is probably safe to say, until a more elaborate attempt is made, that the effect is less than 0.1 per mil.

Acknowledgements

I would like to thank Pavo Kovala for helping to streamline my computer program for calculating enhancement factors and Ray Hesslein for helping me transfer it to a desktop computer version. Discussions with Paul Quay about the stable isotope fractionation have been very helpful.

References

- Bolin, B., On the exchange of carbon dioxide between the atmosphere and the sea, *Tellus*, 12, 274-281, 1960
- Broecker, W. S., and T. H. Peng, Gas exchange rates between air and sea, *Tellus*, 26, 21-35, 1974
- Bruland, K. W., Complexation of zinc by natural organic ligands in the central North Pacific, *Limnol. Oceanogr.*, 34, 269-285, 1989
- Coleman, J. E., Carbonic Anhydrase. In G. L. Eichorn (Eds.), *Inorganic Biochemistry* pp. 489-548, Amsterdam: Elsevier, 1973
- Dankwertz, P. V., *Gas-Liquid Reactions*. New York: McGraw-Hill, 1970
- Culbertson, C. H. and Pytkowicz, R. M., Ionization of water in seawater, *Marine Chemistry*, 1, 309-316, 1973
- Dickson, A. G. and F. J. Millero, A comparison of the equilibrium constants for the dissociation of carbonic acid in seawater media, *Deep-Sea Res.*, 34, 1733-1743, 1987
- Emerson, S., Chemically enhanced CO₂ gas exchange in a eutrophic lake: A predictive model, *Limnol. Oceanogr.*, 20, 743-753, 1975
- Goldman, J., and M. Dennett., Carbon dioxide exchange between air and seawater: No evidence for rate catalysis. *Science*, 220, 199-201, 1983
- Hesslein, R. H., W. S. Broecker, P. D. Quay, and D. W. Schindler, Whole-lake radiocarbon experiment in an oligotrophic lake at the Experimental Lakes Area, Northwest Ontario. *Can. J. Fish. Aquat. Sci.*, 37, 454-463, 1980
- Harned, H. S. and R. Davis, The ionization constant of carbonic acid in water and the solubility of CO₂ in water and aqueous salt solution from 0 to 50, *C. J. Am. Chem. Soc.*, 65, 2030-2037, 1943
- Harned, H. S., and B. B. Owen, *The Physical Chemistry of Electrolyte Solutions*, pp 803, Reinhold, New York, 1958
- Harned, H. S. and S. R. Scholes, The ionization constraint of HCO₃⁻, *J. Am. Chem. Soc.*, 63, 1706.- 1709, 1941
- Hoover, T. E., and D. C. Berkshire, Effects of hydration on carbon dioxide exchange across an air-water interface, *J. Geophys. Res.*, 74, 456-464, 1969
- Johnson, K. S., Carbon dioxide hydration and dehydration kinetics in seawater, *Limnol. Oceanogr.*, 27, 849-855, 1982
- Khalifah, R. G., The carbon dioxide hydration activity of carbonic anhydrase, *J. Bio. Chem.*, 246, 2561-2573, 1971

- Keller, K., Chemical enhancement of carbon dioxide transfer across the air-water interface, Masters Thesis, MIT, Cambridge, Mass., 1994
- Kramer, J. R., Equilibrium models and composition of the Great Lakes, in *Equilibrium Concepts in Natural Water Systems*, edited by R.F. Guild, pp. 243-254, Am. Chem. Soc. Pub., Wash. D.C., 1967
- Ledwell, J. J., The variation of the gas transfer coefficient with molecular diffusivity. In W. B. a. G.H. Jirka (Eds.), *Gas transfer at water surfaces* (pp. 293-302). Norwell, Mass.: D. Reidel, 1984
- Mook, W. G., J. C. Boommerson, and W. H. Stavermann, Carbon isotope fractionation between dissolved bicarbonate and gaseous carbon dioxide, *Earth Planet. Sci. Letters*, 22, 169-176, 1974
- Morel, F. M. M., J. R. Reinfelder, S. B. Roberts, C. P. Chamberlain, J. G. Lee, and D. Yee, Zinc and carbon co-limitation of marine plankton, *Nature*, 369, 740-742, 1994
- Quay, P., B. Tilbrook and C. S. Wong, Oceanic uptake fo fossil fuel CO₂: Carbon-13 evidence. *Science*, 256, 74-79, 1992
- Quay, P. D., S. R. Emerson, B. M Quay, and A. H. Devol, The carbon cycle for Lake Washington - A stable isotope study , *Limnol. Oceanogr.* 31, 596-611, 1986
- Quinn, J. A., and N. C. Otto, Carbon dioxide exchange at the air-sea interface: flux augmentation by chemical reaction, *J. Geophys. Res.*, 76, 1539-1549, 1971
- Siegenthaler, U., and K. O. Münnich, ¹³C/¹²C fractionation during CO₂ transfer from air to sea, in *Carbon Cycle Modeling*, edited by B. Bolin, pp. 249-257, John Wiley and Sons, New York, 1981
- Siegenthaler, U., and J. Sarmiento, Atmospheric carbon dioxide and the ocean, *Nature*, 365, 119-125, 1993
- Silverman, D. N., and C. K. Tu, Buffer dependence of carbonic anhydrase catalyzed oxygen-18 exchange at equilibrium, *J. Am. Chem. Soc.*, 97, 2263-2269, 1976
- Simpson, H. J., and T. Takahashi, Interstitial water studies, Leg 15—Chemical model of seawater and saline waters, in *Initial Reports of the Deep Sea Drilling Project*, 20, 877-886, U.S. Govt. Printing Office, 1973
- Takahashi, T., J. Goddard, D. W. Chipman, S. G. Sutherland, and G. Mathieu, Assessment of carbon dioxide sink/source in the North Pacific Ocean: Seasonal and geographic variability, 1984-1989, *Technical Report*, Lamont-Doherty Earth Observatory, 1991
- Tans, P., J. Berry and R. Keeling, Oceanic ¹³C/¹²C Observations: A new window on Ocean CO₂ Uptake, *Global. Biogeochem. Cycles*, 7, 353-368, 1993
- Vinograd, J., and McBain, J., Diffusion of electrolytes and ions in their mixtures. *J. Am. Chem. Soc.*, 63, 2008-2015, 1941
- Vogel, J. C., P. M. Grootes, and W. G. Mook, Isotope fractionation between gaseous and dissolved carbon dioxide, *Z. Physic*, 230, 225-238, 1970
- Wanninkhof, R., Gas exchange across the air-water interface determined with man-made and natural tracers, Ph. D. thesis, Columbia University, New York, 1986
- Wanninkhof, R., Relationship between wind speed and gas exchange over the ocean. *Jour. Geophys. Res.*, 97, 7373-7382, 1992
- Wanninkhof, R., Ledwell, J., and W. Broecker, Gas exchange-wind speed relation measured with sulfur hexafluoride on a lake. *Science*, 227, 1224-1226, 1985
- Watson, A., Air-sea gas exchange and carbon dioxide. In M. Heimann, ed., *The Global Carbon Cycle* pp 397-411. Heidelberg: Springer-Verlag, 1993

Mathematical Modeling of the Influence of Marine Biota on the Carbon Dioxide Ocean-Atmosphere Exchange in High Latitudes

E. V. Yakushev and G. E. Mikhailovsky

P. P. Shirshov Institute of Oceanology
23 Krasikova St., Moscow 117218 Russia

Abstract

On the basis of numerical experiments with a mathematical model, it was shown that in high latitudes of the ocean, the amplitudes of annual variability of parameters such as oxygen, pH, and the partial measure of carbon dioxide ($p\text{CO}_2$), are caused by hydrophysical processes for two-thirds of their values (about 2.5 ml l^{-1} for oxygen, 0.10 for pH, 130 ppm for $p\text{CO}_2$), and caused by chemico-biological processes for one-third of their values (about 2 ml l^{-1} for oxygen, 0.05 for pH, 60 ppm for $p\text{CO}_2$). The influence of biota resulted first in changes in pH values during the phytoplankton bloom period, followed by displacement of the carbonate system balance: that is, the temporary increase of carbonate ion and decrease of free carbon dioxide contents. Because of these changes, a temporary anomaly in the ocean-atmosphere flux rate took place. It was estimated that the total value of CO_2 consumed by the ocean during the phytoplankton bloom period was about 1200 mmol m^{-2} . According to the model assumptions, this result could be typical of all the high latitudes.

1 Introduction

Study of the global carbon cycle is very important in the context of its impact on the Earth's climate. According to up-to-date information, the global carbon cycle is not balanced, and therefore, so-called *missing sinks* must exist [Siegenthaler and Sarmiento, 1993]. Identification of these sinks is one of the most important tasks in the context of global climate change. All of the methods describing the exchange processes are based on the idea that the intensity of seawater flux is proportional to the difference of the gas content in the contiguous water and air layers. The CO_2 concentrations in the atmosphere are characterized by more uniform temporal and spatial variability compared with those in seawater, caused by different density of these two media. The direction and intensity of fluxes are connected primarily with the seawater carbonate system parameter values. Therefore, it is necessary to study the peculiarities of the variability and distribution of the water CO_2 content.

According to the observation data [Conway *et al.*, 1994], CO_2 distribution in the atmosphere is characterized by an absence of significant latitudinal

differences and by seasonal variability in the northern hemisphere with an amplitude of 10–15 ppm. According to the archive data of observations from 1970 to 1990 [Makkaveev and Yakushev, 1995], surface seawater CO₂ is characterized by significant latitudinal variability. The equatorial region has pCO₂ values of 440–480 ppm, tropical regions have 300–350 ppm, and moderate and high latitude regions are characterized by year-averaged concentrations approximately equal to those of the atmosphere and by seasonal variability with amplitude of 15–20 ppm. Therefore, the equatorial region appears to be a constant source of CO₂, tropical latitudes are regions of intensive influx [Murray *et al.*, 1994; Makkaveev and Yakushev, 1995], and moderate and high latitudes are characterized by evasion or invasion, depending on the season.

These generalized studies do not take into account the intensity and the short duration of the vegetational period in high latitudes. As it will be shown below, these processes could be significant in the global carbon cycle, and they could act as the alleged "missing sinks." The goal of this work was to use a *mathematical model* to obtain numerical estimates of the exchange processes.

The concentrations of the *ocean carbonate system* compounds are ruled by several complex processes, the most important of which are the following:

- the hydrophysical processes of advection and turbulence;
- the chemical transformation in the carbonate system from the formation and dissolution of the carbonates to the appearance of free carbon dioxide gas;
- the chemical-biological processes of the formation and decay of suspended organic and inorganic matter;
- the gravitational flow of the particulate forms into the deeper layers;
- the exchange processes on the air-sea border.

Finally, all these processes should be parameterized in the model to be used for concrete numerical estimates. To do this, however, it is necessary to understand the individual roles of these concrete processes. Therefore, this paper investigates first the role of *marine biota* in the ocean carbon (C) compounds' transformation.

2 Model Description and Equations

Since phytoplankton growth is generally not carbon-limited in natural conditions, it is necessary to describe the cycles of limiting photosynthesis nutrients. The carbon model was therefore incorporated into a previously proposed model of the *nitrogen* (N) and *phosphorus* (P) cycles [Yakushev and Mikhailovsky, 1994]. The N and P model was calibrated using data obtained during several *White Sea* expeditions in 1991 and also literature known data [Bruevich, 1960, Yakushev & Mikhailovsky, 1994].

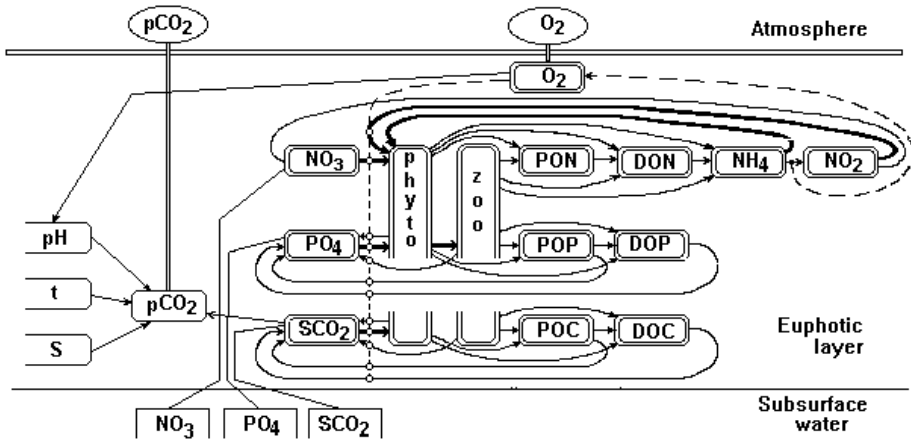


Figure 1: Model scheme of the transformation of biological components, nutrients, and carbonate system elements, where phyto = phytoplankton, zoo = zooplankton, O_2 = oxygen, NO_3 = nitrates, NO_2 = nitrites, NH_4 = ammonia, PON = particulate organic nitrogen, DON = dissolved organic nitrogen, PO_4 = phosphates, POP = particulate organic phosphorus, DOP = dissolved organic phosphorus, SCO_2 = total inorganic carbon, POC = particulate organic carbon, DOC = dissolved organic carbon, pCO_2 = carbon dioxide partial pressure, t = temperature, S = salinity, pH = pH value.

The scheme of the model is shown in Figure 1. The following parameters were considered: phytoplankton (F), zooplankton (Z), dissolved oxygen (O_2), nitrates (NO_3), nitrites (NO_2), ammonia (NH_4), particulate organic nitrogen (PON), dissolved organic nitrogen (DON), phosphates (PO_4), particulate organic phosphorus (POP), dissolved organic phosphorus (DOP), total inorganic carbon (SCO_2), particulate or suspended organic carbon (POC), dissolved organic carbon (DOC), carbonate ion (CO_3), bicarbonate ion (HCO_3), gaseous carbon dioxide (CO_2) and its partial pressure (pCO_2). The oxygen concentrations change due to the chemico-biological processes, according to the Redfield ratio. The carbonate system parameters were calculated based on the carbonate system equations.

This model describes the annual variability of the nutrient parameters in the euphotic zone of the White Sea. This sea, however, could possibly be not the best research example for an initial modeling simulation because of its complex chemical balance due to a large volume of freshwater river influence. However, this situation allows us to examine the model under very extreme conditions.

For the numerical integrations, the following equation was used:

$$\frac{dC_i}{dt} = R_{C_i} - \frac{1}{h_k} w_{C_i} C_i + w_a (C_0 - C_i) + Q_{C_i} \quad (1)$$

where $C_i = F, Z, PO_4, POP, DOP, NO_3, NO_2, NH_4, DON, PON, O_2, SCO_2, POC, DOC$; R_{C_i} = chemico-biological sources; w_{C_i} = rate of sedimentation of suspended matter, accepted non zero for particulate matter parameters; w_a = intensity of exchange with intermediate waters (C_0) of phosphates, nitrates and total carbon; Q_{C_i} = flux of oxygen and carbon dioxide on the sea-air surface; and h_k = thickness of the upper mixed layer.

This model assumes that the euphotic layer has the same depth as the upper mixed layer. Since the focus of this paper is to analyze the biota influence on the CO_2 exchange, this model will parameterize R_{C_i} sources. Therefore, the following proposed equations describe the processes shown in the scheme (Figure 1) by arrows:

$$\begin{aligned}
R_F &= C_F(1 - K_{FN})F - K_{FP}F - K_{FD}F - C_Z^F \\
R_Z &= C_Z U_Z - K_{ZP}Z - K_{ZN}Z \\
R_{POP} &= S_P(K_{FP}F + K_{ZD}Z + C_Z(1 - U_Z)(1 - H_Z) - C_Z^P) - K_{PD}POP - K_{PN}POP \\
R_{PON} &= S_N(K_{FP}F + K_{ZD}Z + C_Z(1 - U_Z)(1 - H_Z) - C_Z^P) - K_{PD}PON - K_{P4}PON \\
R_{DOP} &= S_P(K_{FD}F + C_Z(1 - U_Z)H_Z) + K_{PD}POP - K_{DN}DOP \\
R_{DON} &= S_N(K_{FD}F + C_Z(1 - U_Z)H_Z) + K_{PD}PON - K_{DN}DON \\
R_{PO_4} &= S_P(C_F(K_{FN} - 1)F - K_{ZN}Z) + K_{PN}POP + K_{DN}DOP \\
R_{NH_4} &= S_N(C_F(K_{FN} - 1)f(NH_4, NO_3 + NO_2)F + K_{ZN}Z) \\
&\quad + K_{P4}PON + K_{D4}DON - K_{42}NH_4 \\
R_{NO_2} &= S_N(C_F(K_{FN} - 1)f(NH_4, NO_3 + NO_2)f'(NO_3, NO_2)F \\
&\quad + K_{42}NH_4 - K_{23}NO_2 \\
R_{NO_3} &= S_N(C_F(K_{FN} - 1)f(NH_4, NO_3 + NO_2)f'(NO_3, NO_2)F + K_{23}NO_2 \\
R_{O_2} &= s_O R_{PO_4} + c'_{O_2} K_{42}NH_4 - c''_{O_2} K_{23}NO_2 \\
R_{POC} &= s_C(K_{FP}F + K_{ZD}Z + C_Z(1 - U_Z)(1 - H_Z) - C_Z^P) - K_{PD}POC - K_{PC}POC \\
R_{DOC} &= s_C(K_{FD}F + C_Z(1 - U_Z)H_Z) + K_{PD}POC - K_{DC}DOC \\
R_{SO_2} &= s_C(C_F(K_{FN} - 1)F - K_{ZN}Z) + K_{PC}POC + K_{DC}DOC
\end{aligned} \tag{2}$$

where

$$C_F = K_{NF} f_t(t) F_i(i) \min [f_P(PO_4), f_N(NO_3, NO_2, NH_4)] \tag{3}$$

is the phytoplankton specific growth rate; $F_t(t)$ is the dependence of that rate on temperature; $f_i(i)$ is the dependence of that rate on the illumination.

$$\min [f(PO_4), f(NO_3, NO_2, NO_3)] \tag{4}$$

is the influence of nutrients' concentrations, where for phosphorus

$$f(PO_4) = PO_4 / (K_{PO_4} + PO_4); \tag{5}$$

and for nitrogen [*Fasham et al.*, 1990]

$$f_N(NO_3, NO_2, NH_4) = f'_N(NO_3, NO_2) + f''_N(NH_4) = \frac{(NO_3 + NO_2) \exp(-K_{psi}NH_4)}{K_{NO_3} + (NO_3 + NO_2)} + \frac{NH_4}{K_{NH_4} + NH_4}. \quad (6)$$

$C_Z = C_Z^F + C_Z^P$ is the zooplankton specific growth rate, with

$$C_Z^F = K_{FZ} \frac{F}{F + K_F} Z; \quad (7)$$

$$C_Z^P = K_{PZ} \frac{P}{P + K_P} Z \quad (8)$$

The non-linear Michaelis-Menten-Mono formula was used to describe the consumption of the inorganic nutrients' forms by phytoplankton and of phytoplankton by zooplankton. To describe the possibility of choice among the different forms of N, an approach proposed by *Fasham et al.*, 1990] was used in the nitrogen cycle model. The first-order formula was used with a constant for the remaining processes connected with metabolism and regeneration of particulate (POM) and dissolved (DOM) organic matter. The influence of temperature was considered for the processes of photosynthesis rate and organic matter oxidation rates [*Yakushev and Mikhailovsky*, 1993]. Due to accepted differences in organic P, N, and C oxidation rates, the Redfield ratio in the model differed between the organisms and dead organic matter.

In Table 1, the numerical values and the names of the coefficients are shown. Their values were selected either from published data or from numerical experiments. The more complete description of the model is presented in *Yakushev and Mikhailovskiy* [1994].

The following formula by *Lyahin* [1981] was used to calculate pH values as a function of the O₂ concentration:

$$pH = 3.429 + 0.074O_2 + 0.015T^\circ K. \quad (9)$$

On the basis of obtained values of pH, SCO₂, temperature (t), and salinity (S), values were calculated for CO₃, HCO₃, CO₂, pCO₂ and alkalinity (Alk) using the following equations system [*Alekin*, 1979]:

$$\begin{aligned} Alk_C &= SCO_2(1 + 2K_2/a_{H^+}) - (1 + a_{H^+}/K_1 + K_2/a_{H^+}) \\ HCO_3 &= SCO_2/(1 + a_{H^+}/K_1 + K_2/a_{H^+}) \\ CO_3 &= K_2SCO_2/a_{H^+}(1 + a_{H^+}/K_1 + K_2/a_{H^+}) \\ CO_2 &= SCO_2a_{H^+}/(1 + a_{H^+}/K_1 + K_2/a_{H^+}) \\ pCO_2 &= CO_2/a_s \end{aligned} \quad (10)$$

Table 1: The Values of the Model Coefficients

Symbol	Name	Units of measurements	Value
K_{NF}	maximal specific rate of the phytoplankton growth	day ⁻¹	5.5
K_{PO_4}	phosphate half-saturation constant	$\mu\text{mol l}^{-1}$	0.25
F_P	threshold phytoplankton concentration	mg m^{-3}	1.6
K_{FN}	specific rate of phytoplankton respiration	day ⁻¹	0.15
K_{FP}	specific rate of phytoplankton death	day ⁻¹	0.05
K_{FD}	specific rate of phytoplankton excretion	day ⁻¹	0.15
K_{FZ}	maximum rate of phytoplankton consumption by zooplankton	day ⁻¹	0.9
K_F	half saturation constant for phytoplankton	...	5.0
K_{ZN}	specific rate of zooplankton respiration	day ⁻¹	0.10
K_{ZP}	specific rate of zooplankton mortality	day ⁻¹	0.05
K_{PZ}	maximum rate of POM consumption by zooplankton	day ⁻¹	0.2
K_{PP}	half-saturation constant for POM	...	0.5
P_{por}	threshold POM concentration	$\mu\text{molP l}^{-1}$	0.0001
K_{PD}	specific rate of POM autolysis	day ⁻¹	0.13
U_Z	food digestion for zooplankton	...	0.7
H_Z	liquid-to-solid excrement ratio for zooplankton	...	0.4
K_{PN}	phosphatofication coefficient for POM	day ⁻¹	0.002
K_{DN}	phosphatofication coefficient for DOM	day ⁻¹	0.01
K_{PSI}	Fasham formula coefficient	day ⁻¹	1.5
K_{NO_3}	half-saturation constant for nitrates	$\mu\text{mol l}^{-1}$	0.3
K_{NH_4}	half-saturation constant for ammonia	$\mu\text{mol l}^{-1}$	0.3
K_{NP_4}	ammonification coefficient for POM	day ⁻¹	0.05
K_{ND_4}	ammonification coefficient for DOM	day ⁻¹	0.08
K_{N42}	specific rate of first stage nitrification	day ⁻¹	0.09
K_{N23}	specific rate of second stage nitrification	day ⁻¹	0.04
w_F	specific rate of phytoplankton sinking	m day^{-1}	1.8
w_Z	specific rate of zooplankton sinking	m day^{-1}	0.1
w_D	specific rate of POM sinking	m day^{-1}	2.0
w_{a1}	coefficient of surface-subsurface waters exchange for summer	day ⁻¹	0.001
w_{a2}	coefficient of surface-subsurface waters exchange for winter	day ⁻¹	0.007
s_N	N content per biomass unit	$\mu\text{mol mg}^{-1}$	0.014
s_P	P content per biomass unit	$\mu\text{mol mg}^{-1}$	0.001
s_O	O content per biomass unit	ml mg^{-1}	0.005

where Alk_C — carbonate alkalinity; $Alk = Alk_C + 0.022Cl$, where $Cl = S/1.80655$ — chlorinity. The apparent ionization constants (K_1, K_2) by Edmond-Gieskes [Edmond and Gieskes, 1976] were used, and the solubility of carbon dioxide in the water (a_S) was calculated on the basis of the Weiss formula [Weiss, 1974]. To describe the exchange of gases between the atmosphere and the ocean, the following formulas were used [Liss, 1973; Lyahin, 1975]: For carbon dioxide

$$Q_{CO_2} = W_d A_C (pCO_{2w} - pCO_{2a}), \quad (11)$$

where W_d = wind coefficient; $AC = 3.60 + 0.046S + 4.793$; Alk — invasion-evasion coefficient [Lyahin, 1975]; pCO_{2w} = partial pressure of CO_2 in water; pCO_{2a} = partial pressure of CO_2 in air. pCO_{2a} was assumed to equal 350 ppm. For oxygen sea-air flux

$$Q_{O_2} = W_d A_O O_2 (100 - O_2\%) / O_2\%, \quad (12)$$

where $O_2\%$ = oxygen saturation as function of O_2 , t, S; $A_O = 10^{-4}$ = coefficient.

The rates of exchange of PO_4 , NO_3 and SCO_2 between the euphotic zone and the intermediate waters (1) was described using the concentration gradient with coefficient w_a . The w_a coefficient is rather conditional, since it reflects both the processes of advection and of turbulence. Furthermore, it should significantly change in the regions of convergence and divergence. w_a values were assumed to be 0.001 for summer and 0.005 for winter to reflect the process of winter pycnocline destruction. The changes of illumination, temperature, salinity, and depth of the upper mixed layer were accepted as external parameters.

The annual variability of light was a simple sinusoid curve with a maximum in June. The temperature fluctuated between $+12^\circ C$ in the summer to $-2^\circ C$ in winter. Since carbon concentrations and the Alk/Cl values in freshwater are higher than in the seawater, this model assumed that the content of total carbon in intermediate waters was a constant, and that salinity changed, according to observations, from 23 promille in winter to 12 in early spring. The depth of the upper mixed layer changed from 2 m in May, when the White Sea haloclyne forms, to 60 m in winter.

3 Results

The numerical simulations were conducted with a time scale of 0.25 days. Iterations were repeated until the difference of the succeeding years disappeared. Results are shown in Figure 2. In spring, a very sharp phytoplankton bloom peak took place, with concentration about 3000 mg m^{-3} . Maximum primary production value was $800 \text{ mgCm}^{-2}\text{day}^{-1}$. Following the scheme (Figure 1) this resulted in a decrease in PO_4 and NO_3 concentrations and an increase in concentrations of the organic forms of these elements (Figure 2).

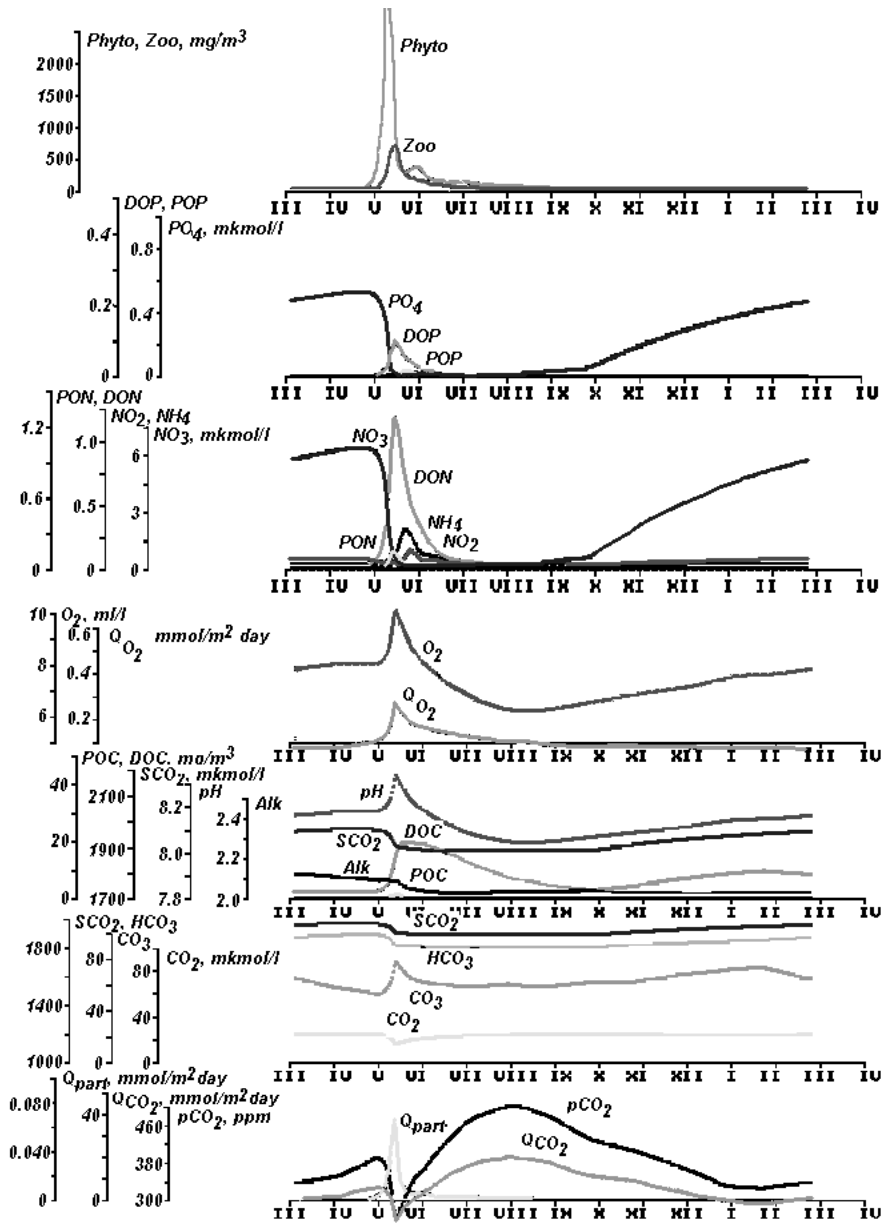


Figure 2: Seasonal variability of the model components. Explanations are in the text. Q_{CO_2} and Q_{O_2} are fluxes of gases through the ocean-atmosphere boundary, Q_{part} = flux with POM sedimentation.

The *phytoplankton bloom* peak was followed by a *zooplankton bloom* peak. During the summer months, a quasi-equilibrium took place, when sufficient light and temperature conditions and constant low PO_4 and NO_3 flux from the intermediate layer resulted in quasi-constant phytoplankton and zooplankton concentrations. As illumination and temperature decreased in autumn, photosynthesis also decreased. After decrease of the phytoplankton and zooplankton concentrations, PO_4 and NO_3 concentrations increased up to the previous winter values.

This model observed N as a limiting nutrient for photosynthesis in spring, whereas P was the limiting nutrient during the summer months. This fact can be explained by the different oxidation rates of these two elements. These results compare well to similar data obtained during a 1991 White Sea expedition [Yakushev and Mikhailovsky, 1993].

The concentrations of O_2 (Figure 2) were characterized by the concentrations of 9 ml l^{-1} in winter and 7 ml l^{-1} in summer. During the phytoplankton bloom period, the concentrations roughly increased, reaching 11 ml l^{-1} . The saturation of O_2 was about 100% throughout the year, with a rough maximum of 130% in early spring. The O_2 flux through the ocean-atmosphere surface was directed from air into water from September to May with values less than $0.03 \text{ mmol m}^{-2} \text{ day}^{-1}$, and from water into air from May to September with a maximum of $0.15 \text{ mmol m}^{-2} \text{ day}^{-1}$ during the phytoplankton bloom period.

According to the Lyahin formula, the pH changes were similar to those of O_2 . This parameter was characterized by values of 8.20 in winter, 8.05 in summer, and up to 8.30 in the bloom period. In the model, phytoplankton consumed SCO_2 ; therefore, to fulfill the neutrality equation, the pH changes took place. The consummation of the negatively charged ions was compensated by the decrease of free CO_2 . The SCO_2 annual variability curve followed the PO_4 and NO_3 curves, because it was caused by similar factors.

The anomaly in pH values during the phytoplankton bloom period was caused by the temporary increase of CO_3 content from 0.055 to $0.080 \text{ mmol l}^{-1}$, and decrease of the gaseous CO_2 concentrations from 0.022 to 0.017 . The annual variability of *Alk* with values of $2.100 \text{ mg-eq l}^{-1}$ in winter and 2.050 in summer corresponded to the observed data [Bruevich, 1960]. The White Sea, unlike the other seas of the Polar basin, is characterized by a whole-year surface water oversaturation of CO_2 and its evasion. This is connected with the dominant freshwater influence on the chemical balance of this sea. The same situation took place in the model: the pCO_2 changed from 340 ppm in winter to 480 ppm in summer, caused by the influence of temperature on CO_2 solubility. The obtained values corresponded to the observed limits – about $380\text{--}540 \text{ ppm}$ [Maksimova, 1993]. During the short phytoplankton bloom period, the pCO_2 decreased to 280 ppm .

The flux of the CO_2 through the air-water surface practically throughout the year was directed from water to the air and was characterized by values of $10 \text{ mmol m}^{-2} \text{ day}^{-1}$ in winter and $45 \text{ mmol m}^{-2} \text{ day}^{-1}$ in summer. In the

phytoplankton bloom period, the flux changed its direction to invasion and had values of $-10 \text{ mmol m}^{-2} \text{ day}^{-1}$.

4 Discussion

This model allowed us to provide a numerical experiment, the goal of which was to obtain the picture of annual variability without the influence of biota. Therefore it was assumed that $R_O = 0$. In this case, the content of O_2 is determined only by the variations of t and S , because only these characteristics affected O_2 solubility and water-air flux of this gas. The pH values, calculated on the basis of the Lyahin formula, were also influenced only by hydrophysical parameters. And correspondingly, the curves of the all other carbonate system characteristics reflected only the hydrophysical processes.

In this situation, the behavior of SCO_2 and HCO_2 scarcely changed, but the other carbonate system parameters changed significantly: The early spring period of pH decrease and the resulting period of decrease of pCO_2 were absent. Correspondingly, the short period of CO_2 evasion was also absent. On the basis of this experiment, one can estimate that during the spring phytoplankton bloom, changes of pH from 0.20 to 0.25 and decrease of pCO_2 to 60 ppm take place. It was also possible to calculate the total value of CO_2 consumed by the ocean: about 1200 mmol m^{-2} during the White sea spring phytoplankton bloom period.

The *sedimentation flux* of carbon (Q_{part}) in the particulate organic matter was characterized by values less than $0.005 \text{ mmol m}^{-2} \text{ day}^{-1}$ and had a short maximum with values of $0.040 \text{ mmol m}^{-2} \text{ day}^{-1}$ in early spring, connected with the intensification of the organic matter synthesis processes. As is obvious from the model, even the maximum values of this flux are three orders of magnitude less than the water-air flux intensity.

The phytoplankton bloom's influence on pCO_2 is well known, but perhaps the more interesting result of this phenomenon is the increase of the CO_3 ion content (on $0.030 \text{ mmol l}^{-1}$ or on 50% in model). This can affect the carbonate system physical-chemical processes of the formation and dissolution of particulate inorganic C, which can play a large role in the ocean carbon balance.

5 Conclusion

The significance of biota could be not only in aggregation of the inorganic carbon compounds, but also in changing of the carbonate system balance and forming of the conditions that can change the inorganic carbonates' formation intensity in both biogenic and nonbiogenic pathways. The significance of the processes of suspended inorganic carbonate's formation can be extremely large, and as shown in these model estimates, can serve as a background for future investigations. The maximum value of the flux of carbon in

the POM consisted of $0.040 \text{ mmol m}^{-2} \text{ day}^{-1}$, which is 1000 times less than the intensity of flux of free carbon dioxide through the ocean-atmosphere surface (about $40 \text{ mmol m}^{-2} \text{ day}^{-1}$).

On the basis of numerical experiments, it was shown that in the high latitudes of the ocean, the amplitudes of annual variability of such parameters as O_2 , pH, and pCO_2 are caused by hydrophysical processes for two-thirds of their values (about 2.5 ml/l for O_2 , 0.10 for pH, 130 ppm for pCO_2), and caused by chemical-biological processes for one-third of their values (about 2 ml/l for O_2 , 0.05 for pH, 60 ppm for pCO_2). The influence of biota resulted first in changes in pH values during the phytoplankton bloom period, followed by displacement of the carbonate system balance: the temporary increase of CO_3 ion and decrease of gaseous CO_2 contents. Because of these changes, a temporary anomaly in the ocean-atmosphere exchange flux rate took place. It was estimated that the total value of CO_2 consumed by the ocean during the phytoplankton bloom period was about 1200 mmol/m^2 . According to the model assumptions, this result could be typical of all the high latitudes. If we multiply the average value of carbon consumption (up to 30 g/m^2) by square meter of ocean for the region with latitude of more than 40N, equal to $1.25 \cdot 10^{14} \text{ m}^2$ [Vinogradov and Shushkina, 1987], we shall have $3.75 \cdot 10^{15} \text{ g C}$ during the bloom for the entire globe. Therefore, the "belt" of under-ice phytoplankton bloom moves every spring from south (in March in the White Sea) to north (in July in high latitudes) and can serve as an intensive pump of atmospheric CO_2 directly into the waters of ocean.

Acknowledgements

This work was supported by the International Science Foundation, grant N JJ8100 and the Russian Foundation for Basic Research, grant N 95-05-14779.

References

- Bruevich, S. V., Hydrochemical investigations of the White Sea. *Trudy IOAN SSSR*, Moscow 199-254, 1960 (in Russian)
- Conway J. J., P. P. Tans, L. S. Waterman, K. W. Thoring, D. R. Kitzis, K. A. Masaric, and N. Zhi, Evidence for interannual variability of the carbon cycle from National Oceanic and Atmospheric Administration Climate Monitoring and diagnosis Laboratory Global Air Sampling. *Journal of Geoph. Res.*, 99(D11), 20, 22831-22855, 1994
- Edmond, J. M., and T. H. Gieskes, On the degree of saturation of sea water with respect to calcium carbonate under in situ conditions. *Geochem. et Cosmoch. Acta*, 34, 1261-1291, 1976
- Fasham, M. J. R., H. V. Ducklow, and S. H. Mckelvie, A nitrogen-based model of plankton dynamics in the ocean mixed layer. *Journal of Mar. Res.*, 48,591-639, 1990
- Liss, P. S., Processes of gas exchange across an air-water interface. *Deep-Sea Res.*, 20(3), 221-238, 1973

- Lyahin, Yu. I., Estimation of CO₂ exchange rate between sea water and atmospheric air. *Okeanologiya*, 15(3), 458-464, 1975 (In Russian)
- Lyahin, Yu. I., On the correlation between dissolved oxygen and carbonate system in ocean waters. In: V.N. Ivanenkov (ed.), *Exchange of chemical elements on the marine environment borders*, Shir. Inst. of Ocean. Press, Moscow, 115-125, 1981 (In Russian)
- Makkaveev, P. N., and E. V. Yakushev, On the role of the Pacific Ocean's equatorial-tropical system in the Carbon Cycle. In press, 1995
- Maksimova, M. P. *Hydrochemistry of the White Sea*, VNIRO Press, Moscow, 52, 1991 (in Russian)
- Millero, F. J., The thermodynamics of the carbonate system in sea water, *Geochem. et Cosmoch. Acta*, 43, 1651-1661, 1979
- Murray J. V., R. T. Barber, M. R. Roman, M. P. Bacon, and R. A. Feely, Physical and biological controls on Carbon Cycling in the Equatorial Pacific. *Science*, 266, 58-65, 1994
- Siegenthaler, U., and J. L. Sarmiento, Atmospheric Carbon Dioxide and the Ocean. *Monthly Nature*, 1(9), 48-54, 1993
- Vinogradov, M. E., and E. A. Shushkina, Functioning of the ocean epipelagic plankton communities. *Nauka, Moscow*, 240, 1987 (in Russian)
- Weiss R. F., Carbon dioxide in water and seawater: the solubility of a non-ideal gas. *Marine Chemistry*, 2(3), 203-215, 1974
- Yakushev, E. V., and G. E. Mikhailovsky, Simulation of chemico-biological cycles in the White Sea. Calculations of nitrogen, phosphorus and oxygen annual variability. *Oceanology*, English translation, 33(5), 611-617, 1993

Gas Flux Measurements and Modelling below an Air-Water Interface

*P. Prinos*¹, *M. Atmane*², and *J. George*²

¹ Hydraulics Lab., Civil Eng. Department
Aristotle University Thessaloniki, 54006. Greece

² INP-ENSEEIH - Institut de Mécanique des Fluides URA 005 CNRS
Avenue du Professeur Camille Soula 31400 Toulouse. France

Abstract

Mean and fluctuation concentration profiles were carried out in a jet-agitated vessel in the absence of mean shear at the interface. Present experimental measurements, and previous ones obtained by *Chu and Jirka* [1992] in a grid-stirred tank, are compared with numerical results obtained from the second order modelling of the transport equation for the mean and fluctuation concentration, the gas flux as well as the normal stresses $\overline{u^2}$ and $\overline{w^2}$ and the turbulence characteristics k and ε .

1 Introduction

In order to understand better the gas-liquid mass transfer phenomenon at an agitated surface both numerical and laboratory experiments were carried out.

Laboratory experiments were carried out in the *jet-agitated vessel* designed by *Grisenti* [1991]. Turbulence inside the liquid phase is generated by upflowing microjets and there is no mean shear at the interface. Numerical experiments were carried out using a the *second order modelling* of the normal stresses $\overline{u^2}$, in the horizontal plane, and $\overline{w^2}$, in the vertical direction, in conjunction with transport equations for k , the turbulent kinetic energy, and ε , the dissipation rate of k , as described below.

2 Numerical Modelling

The *numerical modelling* of gas mean concentration C , rms concentration c' and flux $\overline{w\overline{c}}$ below a shear-free gas-liquid interface is based on the transport equations for the respective quantities C , c' and $\overline{w\overline{c}}$. The modelled transport equations for the above quantities in shear free turbulence (absence of convective terms) are written as follows:

$$\frac{dC}{dt} = \frac{d}{dz} \left(\frac{\nu}{Sc} \frac{dC}{dz} - \overline{w\overline{c}} \right) \quad (1)$$

$$\frac{d\overline{c^2}}{dt} = c_\theta \frac{d}{dz} \left(\frac{\overline{w^2} k}{\varepsilon} \frac{d\overline{c^2}}{dz} \right) - 2\overline{w\overline{c}} \frac{dC}{dz} - \frac{1}{R} \frac{\overline{c^2}}{k} \varepsilon \quad (2)$$

$$\frac{d\overline{w\overline{c}}}{dt} = -\overline{w^2} \frac{dC}{dz} + c_{s\theta} \frac{d}{dz} \left(\frac{k}{\varepsilon} \overline{w^2} \frac{d\overline{w\overline{c}}}{dz} \right) - c_{1\theta} \frac{\varepsilon}{k} \overline{w\overline{c}} \quad (3)$$

where C is the mean concentration, $\overline{c^2}$ the mean square concentration fluctuation, $\overline{w\overline{c}}$ the gas flux, ν the liquid kinematic viscosity, Sc the Schmidt number, $\overline{w^2}$ the normal stress in the vertical z -direction, $c_{s\theta}$, $c_{1\theta}$ and c_ε are constants (respectively equal to: 0.15, 2.9, 0.11), and R a scalar to dynamic time-scale ratio ($R = 0.8$). The above equations are considered as modelled equations of the exact transport equations after the suggestions of *Gibson and Launder* [1978].

The calculation of the above characteristics is based on either a known turbulence structure below the interface or a calculated one from a hydrodynamic model which models the turbulence characteristics, below the gas-liquid interface, appearing in equations (2) and (3).

The vertical distribution of the horizontal and vertical turbulence intensities u' , w' in nearly isotropic turbulence produced by either oscillating grids [*Hopfinger and Toly*, 1976; *Brumley and Jirka*, 1987; *De Silva and Fernando*, 1994 among others] or upflowing microjets of water [*George et al.*, 1994] has been found experimentally and theoretically to follow the relationships:

$$u' = c_1 f S^{1.5} M^{0.5} z^{-1} \quad (4)$$

$$w' = c_2 f S^{1.5} M^{0.5} z^{-1} \quad (5)$$

where f , S are the frequency (in Hz) and stroke of the grid oscillations, M the grid mesh size, z the vertical distance (measured from a virtual origin) and c_1 , c_2 constants which depend on the grid geometry. The above equations hold in the bulk of the homogeneous fluid far from free or solid boundary surfaces. Experimental measurements of u' , w' near the gas-liquid interface [*Brumley and Jirka*, 1987; *George et al.*, 1994] have indicated a strong anisotropy of u' , w' with increased values of u' and respective decreased values of w' . This is due to the interaction of the turbulence with the free surface and may affect the distribution of the gas flux and the rms concentration near the interface, as well as the turbulence kinetic energy and its rate of dissipation. Hence a detailed modelling of the turbulence characteristics is required which is possible through the second order modelling of the normal stresses $\overline{u^2}$ and $\overline{w^2}$ in conjunction with transport equations for k and ε .

These equations are written as follows

$$\frac{d\bar{u}^2}{dt} = c_s \frac{d}{dz} \left(\frac{\bar{w}^2 k}{\varepsilon} \frac{d\bar{u}^2}{dz} \right) - \frac{1}{3} \varepsilon - c_1 \varepsilon \left(\frac{\bar{u}^2}{k} - \frac{1}{3} - \frac{c_1'}{c_1} \frac{\bar{w}^2}{k} f_s \right) \quad (6)$$

$$\frac{d\bar{w}^2}{dt} = c_s \frac{d}{dz} \left(\frac{\bar{w}^2 k}{\varepsilon} \frac{d\bar{w}^2}{dz} \right) - \frac{1}{3} \varepsilon - c_1 \varepsilon \left(\frac{\bar{w}^2}{k} - \frac{1}{3} + \frac{c_1'}{c_1} \frac{\bar{w}^2}{k} f_s \right) \quad (7)$$

$$\frac{dk}{dt} = c_s \frac{d}{dz} \left(\frac{\bar{w}^2 k}{\varepsilon} \frac{dk}{dz} \right) - \varepsilon \quad (8)$$

$$\frac{d\varepsilon}{dt} = c_\varepsilon \frac{d}{dz} \left(\frac{\bar{w}^2 k}{\varepsilon} \frac{d\varepsilon}{dz} \right) - c_{2\varepsilon} \frac{\varepsilon^2}{k} + 3.9 \frac{\varepsilon^2}{k} \frac{a_{ij} a_{ij}}{1 + 15 \sqrt{a_{ij} a_{ij}}} \quad (9)$$

where $c_s, c_1, c_1', c_\varepsilon, c_{1\varepsilon}, c_{2\varepsilon}$ are constants (respectively equal to 0.22, 1.8, 0.6, 0.2, 0.15, 1.90 [Gibson and Launder, 1978], f_s is a free surface proximity function and a_{ij} the anisotropy tensor $a_{ij} = \frac{\bar{u}_i \bar{u}_j}{k} - \frac{2}{3} \delta_{ij}$. The last term of equations (6) and (7) is a pressure-strain model of the exact pressure-strain term and the surface proximity function is defined assuming that the redistributive effect of the free surface on \bar{w}^2 is physically similar to that of a solid wall. Hence, the f_s function is the one proposed by Gibson and Rodi [1989]. The last term of equation (9) needs special attention since it describes the rate of generation of ε by turbulence interaction in the absence of mean velocity gradients which may be significant in the region near the free surface [Zeman and Lumley, 1976].

Hence the solution of equations (1) to (3) and (6) to (9) has as a result the complete calculation of the turbulence and concentration characteristics in the vertical direction from the virtual origin up to the free surface.

The above equations are solved with a finite volume method, described extensively by Patankar [1980], using appropriate initial conditions and boundary conditions at the virtual origin and the free surface. The applied boundary conditions are discussed into some detail in the following paragraphs.

Appropriate boundary conditions for all unknown variables are applied at the virtual origin and the free surface. At the virtual origin the mean concentration is set equal to bulk concentration C_b while the rms concentration and the gas flux are set equal to zero. With regard to turbulence quantities, the intensities u', w' are defined according to equations (4) and (5) respectively and hence the normal stresses can be estimated accordingly. The turbulence kinetic energy k is defined as $k = \frac{2\bar{u}^2 + \bar{w}^2}{2}$ and the dissipation ε is estimated as $\varepsilon = \frac{u'^3}{2L_U}$ where L_U is the horizontal integral length scale which increases linearly with distance from the virtual origin ($L_U = 0.1z$).

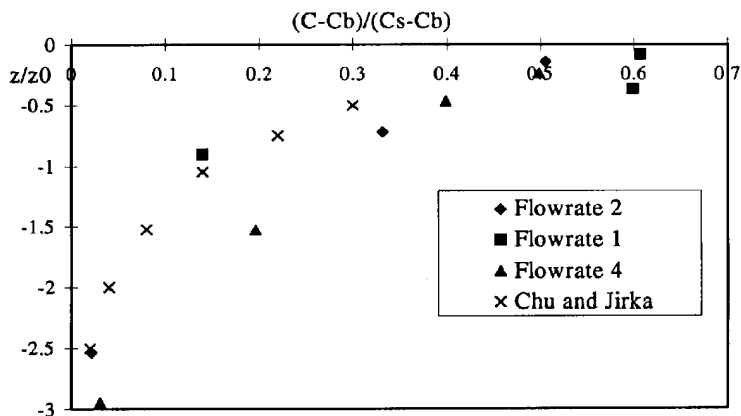


Figure 1: Normalised vertical mean concentration profile

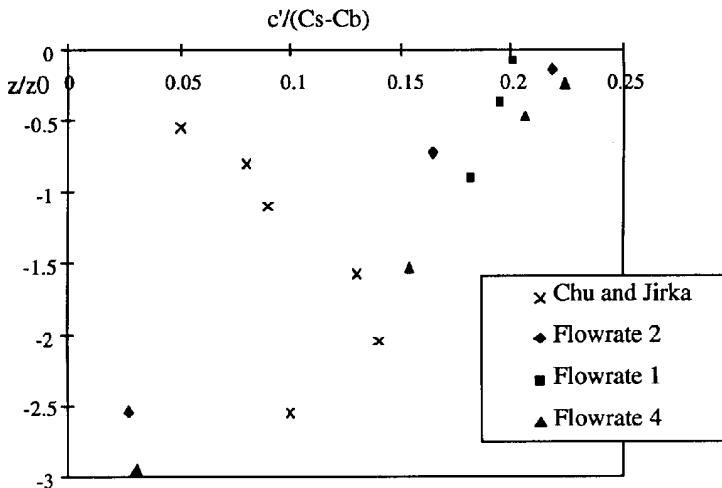


Figure 2: Normalised vertical fluctuation concentration profile

At the *free surface* the mean concentration is known as C_s (concentration at interface) while the values of the rms concentration and gas flux are given. Finally the gradients of all turbulence parameters with regard to the vertical direction are set to zero ($d/dz = 0$). Computed results, based on the above procedure, are compared against the experimental measurements of *Chu and Jirka* [1992].

3 Local Gas Concentration Measurements

Experiments were carried out in the jet-agitated vessel designed by *Grisenti* [1991]. This vessel consists of an Altuglass tank, with a square base ($0.45 \times 0.45 \text{ m}^2$) bottom and a height of 0.80 m. The square section was used in order to prevent the occurrence of preferential flows, in particular mean rotating flows. An array of one hundred microjet nozzles ($0.7 \cdot 10^{-3} \text{ m}$ in diameter) is built in an injection-evacuation device. The jet nozzles are regularly distributed in the injection plane and are distant from each other by $4.3 \cdot 10^{-2} \text{ m}$ in each direction as described by *Minel and George* [1995]. The liquid depth in the vessel is maintained constant using a constant head tank which allows the interfacial turbulence level to be adjusted.

Gas absorption experiments were meant to provide information on the local gas concentration and gas fluxes. Experimental profiles for C and c' are obtained using an oxygen microprobe designed by *Head* [1994], which is very similar to the one designed by *Chu* [1991].

A significant contrast between the Oxygen bulk concentration and that of the interface was obtained by introducing pure nitrogen above the free surface in order to remove air from the gas phase.

As shown in Figures 1 and 2, mean and fluctuating *concentration profiles* are comparable to those obtained by *Chu and Jirka* [1992] (only averaged values of Chu and Jirka's results are plotted) except for one trend: no damping was observed in our experiments in the value of c' close to the free surface. Two different hypotheses can be formulated with regard to this problem. The first one is to consider that in our case, the higher value is measured below the interfacial region, region in which concentration damping occurs. The second one is to consider that in our case there is no such damping, concentration fluctuations being present right at the interface.

In order to analyse the two different possibilities we have drawn concentration frequency spectra (Figure 3) and compared previous horizontal velocity fluctuation profiles obtained under the same hydrodynamic conditions. First, concentration density spectra show a large increase in the lower frequency range close to the free surface, time dependent concentration records showing large intermittent peaks. Second, horizontal velocity fluctuation profiles show an increase close to the free surface, in our case, while *Brumley and Jirka* [1987] showed a damping. Therefore, we can reasonably assume that, when the interface is agitated enough (hence when horizontal eddies can develop freely), an intermittent interfacial renewal occurs which leads to low frequency concentration fluctuations and an increase in mass transfer.

4 Analysis of Computed and Experimental Results

The computed distributions of mean concentration C , its *rms* value c' and the gas flux $\overline{w\bar{c}}$ below the gas-liquid interface are compared with respective

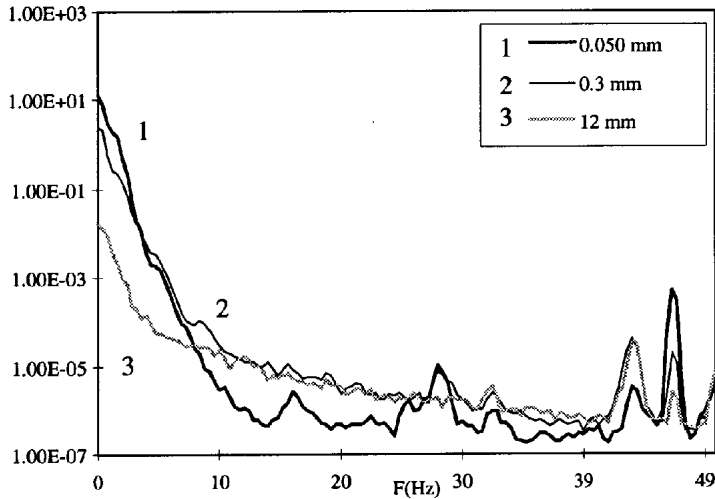


Figure 3: Concentration power density spectra

ones based on experimental measurements of *Chu and Jirka* [1992].

Figure 4 shows the computed and experimental distribution of the normalized gas mean concentration against the normalized depth (z/z_0). It is shown that the agreement between experimental and computed results is satisfactory with the exception of the smoother transition in the computed concentration values from 0.1 down 0.0. This may be due to the number of nodes used in this region although a high number of nodes was used in the whole vertical (up to 10.000) with highly non-uniform grid near the interface.

Figure 5 shows the computed distribution of the rms *concentration fluctuation* c' together with the experimental data of *Chu and Jirka* [1992].

The maximum values of the experimental c' occur below the interface while the computed one is at the interface which, however, has been set at the above value as a boundary condition. Below the interface there is a continuous decrease of c' with a satisfactory agreement between experimental and computed results for z/z_0 less than -5.0. A similar distribution of c' has been observed in our experimental measurements which is analysed in the previous section.

In Figure 6, computed *gas flux* below the gas-liquid interface is compared against direct flux measurements based on simultaneous measurements of turbulent velocity and oxygen concentration. The flux $-\overline{w\bar{c}}$ has been made dimensionless by the absolute value of the mean flux J ($J = K_L/(C_s - C_b)$).

The dashed line represents the turbulent flux profile estimated by subtracting the molecular flux due to the mean concentration distribution while the solid line represents the computed values from equation (3). Due to difficulties and shortcomings of the measuring technique near the interface

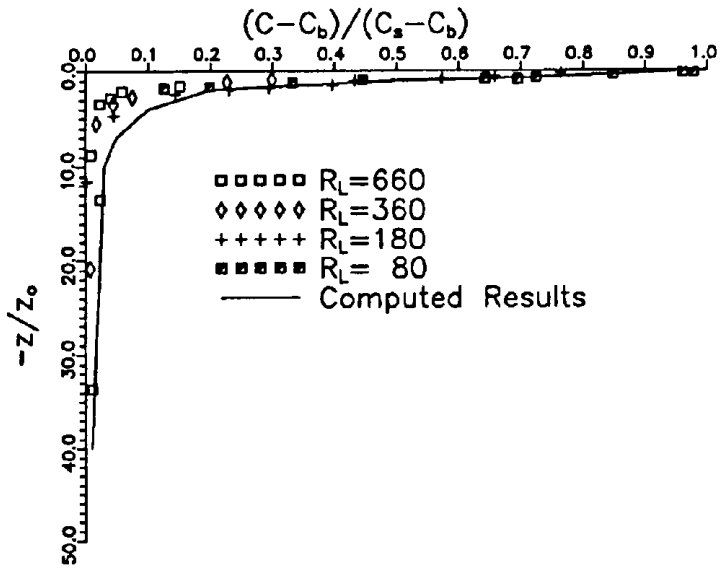


Figure 4: Experimental and computed distribution of mean concentration

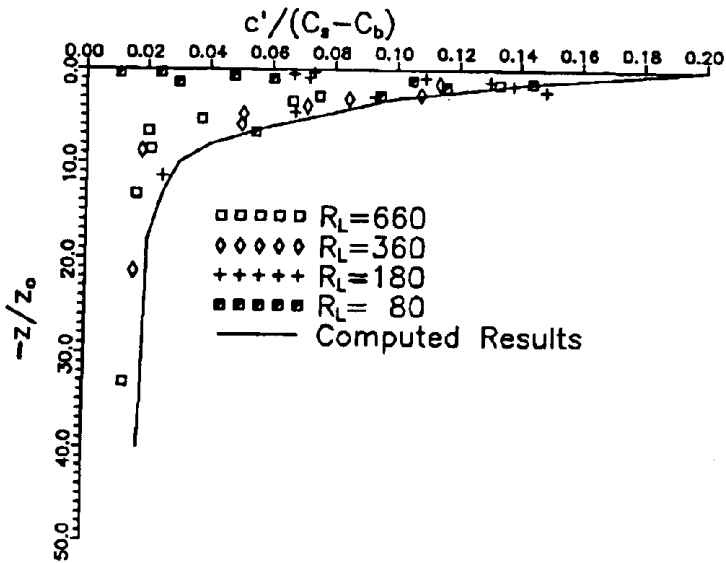


Figure 5: Experimental and computed distribution of rms concentration

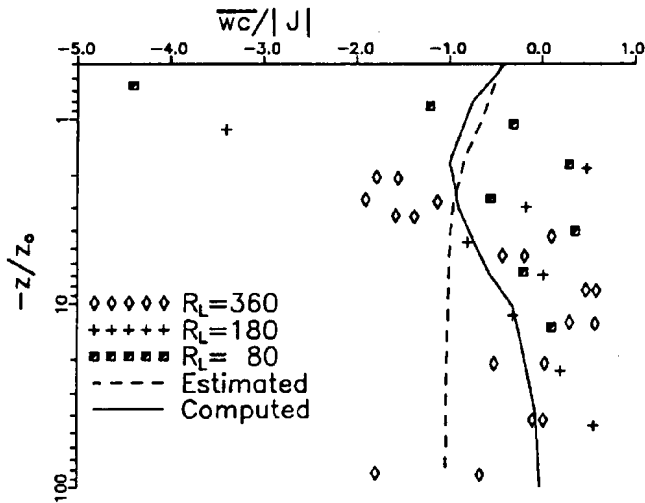


Figure 6: Experimental and computed distribution of gas flux.

the experimental data can be considered with caution and provide only a qualitative insight [Chu and Jirka, 1992]. It is shown that the maximum computed gas flux is found around $-z/z_0$ equal to 2 which is associated with high production due to mean concentration gradient. The maximum estimated flux is found a little deeper while direct measurements of gas flux indicate also high values in this region.

The computed gas flux starts to decrease below $-z/z_0$ approximately equal to 3.0 and tends to zero at approximately equal to 40.0 where the production of gas flux is low (low mean concentration gradient). Similar tendency is observed for the experimental measurements in the region below $-z/z_0$ equal to 4.0 in which measurements of gas flux are spread around the zero value.

Certainly more refined measurements are required for assessing the performance of second moment turbulence models in predicting the scalar fluxes in such flow conditions.

5 Conclusions

The numerical modelling of mean concentration, rms concentration fluctuation and gas flux using second moment closure indicates the satisfactory performance of such a methodology in the region below the *air-water interface* of nearly isotropic turbulence field (grid-stirred tank or upflowing microjets).

Further experiments are certainly required for establishing the values

of c' close to the interface, under various experimental conditions, while direct measurements of the gas flux are needed for further refinement of turbulence models which are based on the transport equations for the unknown quantities. However, it can be noted that the dimensionless value of c' ($\frac{c'}{C_s - C_b} \approx 0.22$), observed experimentally, is in excellent agreement with the boundary condition which much be imposed numerically. This last result tends to acknowledge the fact that, when the liquid phase is agitated by any means, the interface is renewed by intermittent turbulent events responsible for a large increase in the gas transfer velocity values.

Acknowledgements

Authors are grateful to the Franco-Greek Programme Platon n° 94028 for its partial support.

References

- Brumley B. H. and Jirka, G. H, Near-Surface turbulence in a grid-stirred tank, *J. Fluid Mech.*, 183, 235-263, 1987
- Chu C. R., Ph. D. Thesis, Cornell University, 1991
- Chu C. R. and G. H. Jirka, Turbulent gas flux measurements below the air-water interface of a grid-stirred tank, *Int. J. Heat Mass Transfer*, 35, 1957-1968, 1992
- De Silva I. P. D. and Fernando, H. J. S. Oscillating grids as a source of nearly isotropic turbulence, *Phys. Fluids*, 6(7), 2455-2464, 1994
- George J., F. Minel, M. Grisenti, Physico-chemical and hydrodynamical parameters controlling gas-liquid mass transfer, *Int. J. Heat Mass Transfer*, 37, pp. 1569-1578, 1994
- Gibson M. M. and Launder B. E. Ground effects on pressure fluctuations in the atmospheric boundary layer. *J. Fluid Mech.*, 86, 491-511, 1978
- Gibson M. M and Rodi., W., Simulation of free surface effects on turbulence with a Reynolds stress model, *J. Hydraulic Res.*, IAHR, 27, 233-244, 1989
- Grisenti M., Etude de l'hydrodynamique et des transferts en cuve agitée par microjets, Thèse de Doctorat de l'INP - Toulouse, 1991
- Head M. J., Calibration of a dissolved oxygen microsensor, Technical note : Precision Measurement Engineering, Encinitas, CA, USA, 1994
- Hopfinger E. J., Toly J. A., Spatially decaying turbulence and its relation to mixing across density interfaces, *J. Fluid Mech.*, 78, pp. 155-175, 1976
- Launder B. E., Second-moment closure: present... and future? *Int. J. Heat and Fluid Flow*, 10, no 4, pp. 282-300, 1989
- Minel F., George, J. Hydrodynamics in a jet-agitated vessel close to the gas-liquid surface, *This volume*
- Patankar S. V. Numerical Heat Transfer and Fluid Flow. Hemisphere Publ., 1980
- Shir C. C. A preliminary study of atmospheric turbulent flows in the idealized planetary boundary layer. *J. of Atmos. Science*, 30, 1327-1339, 1973
- Zeman , O and Lumley, J. L. Modelling buoyancy - driven mixed layers, *J. of Atmospheric Sci.*, 33, 1974, 1976

Vertical Mixing in the Upper Ocean and Air-Sea Gas Transfer

D. K. Woolf

Department of Oceanography, University of Southampton,
Southampton Oceanography Centre, Waterfront Campus, European Way,
Southampton, SO14 3ZH, United Kingdom email: dkw@willow.soton.ac.uk

Abstract

A numerical model describing both the hydrodynamics of individual bubbles and, in a parameterised form, upper ocean mixing is used to investigate how variations in upper ocean mixing may affect sub-surface bubble populations and the associated transfer of gases. Oceanic bubble populations are often characterised as showing little variation in size distribution with depth, and an exponentially attenuating concentration. The observed size distribution of bubbles at various depths can be mimicked most effectively by the model with strong advection (≥ 10 cm/s) in fixed cells, but bubble concentrations only attenuate exponentially when advection velocities are quite low (≈ 5 cm/s), when the size distribution is rather sensitive to depth. Gas fluxes generally increase steadily with increasing vertical mixing, and are especially sensitive to the representation of initial injection and near-surface mixing.

Measurements with upward-looking 248 kHz sonar suggest that the penetration of bubble clouds is quite variable. The scattering measured by this sonar should usually be dominated by small bubbles and so the results will generally reflect the behaviour of these bubbles, but without giving any indication of the size distribution.

1 Introduction

The influence of bubbles on air-sea gas exchange is very sensitive to the time for which the bubbles are submerged and the depth to which they are entrained, and thus upon *vertical mixing processes* in the upper ocean. In this paper, these relationships are investigated with both numerical models and field data. The sensitivity of bubble dispersion to vertical mixing parameters, and the corresponding variations in air-sea gas flux are investigated using a version of the numerical model described by *Woolf and Thorpe* [1991]. The actual penetration of oceanic bubble clouds including its dependence on environmental conditions has been investigated using vertically-pointing sonar.

2 Numerical Model

The *numerical model* describes the changes in individual bubbles in small time steps from injection until the bubble either surfaces or totally dissolves. Equations for the buoyant rise of each bubble (relative to the surrounding water), the motion of the water, gas exchange between each bubble and the surrounding water, and the hydrostatic pressure balance are applied at each time step so that the bubble evolves in position, size and content. The initial injection of the bubble is only represented by a “starting position”. The motion of the water following injection is represented by random walk (representing small-scale turbulence) and advection in a fixed field of streamlines (representing Langmuir circulation).

Individual bubbles are followed from injection until they surface or dissolve, while the position, size and composition of each bubbles is continually collated. The behaviour of an ensemble of bubbles is found by choosing the size and initial position of individual bubbles by Monte-Carlo selection and repeating the procedure until statistical uncertainties are reduced sufficiently. In this paper, we describe results where bubbles are initially between 50 and 500 μm in radius, r , selected according to a r^{-4} distribution; bubbles are injected randomly over the sea surface, in the “standard” case at up to 0.5 m in depth in a “triangular” distribution. Many results from the model in this form have been reported by *Woolf and Thorpe* [1991] and by *Thorpe et al.* [1992]. In this paper, we also present some results where all bubbles are introduced at only 1 cm depth. The principal focus here is on the influence of the mixing parameters — both the downwelling velocity in the fixed “*Langmuir cells*” and the *turbulent diffusion constant* (the size of the random walk) — on time-averaged bubble distributions and gas fluxes in near-saturation conditions. In all the model runs presented here, gas saturations were fixed at 100%, in seawater of 10 °C and 35 ppt salinity.

Langmuir cells are represented by cells of 10 m depth, and 14 m width with streamlines of a simple formulation introduced by *Stommel* [1949]. These streamlines are not very close to the observed form [*Weller and Price*, 1988] and the natural variety of cells is not mimicked. Only the maximum downwelling velocity is varied. Figure 1 shows the variation of concentration of bubbles with depth for a standard source of 10,000 bubbles, a turbulent diffusion constant of 20 cm^2/s and various downwelling velocities. At moderate or large downwelling velocities, the variation of concentration with depth deviates significantly from a simple exponential attenuation: near the surface concentration gradients are high, while they are remarkably low at depths of a few metres. In the same cases, the mean concentration of bubbles at every depth is quite sensitive to the maximum downwelling velocity in the Langmuir cell (high velocities reduce concentrations as bubbles are swept around quickly), but the attenuation with depth is remarkably insensitive to this parameter. Only at low Langmuir velocities (≈ 5 cm/s) does the bubble concentration attenuate exponentially.

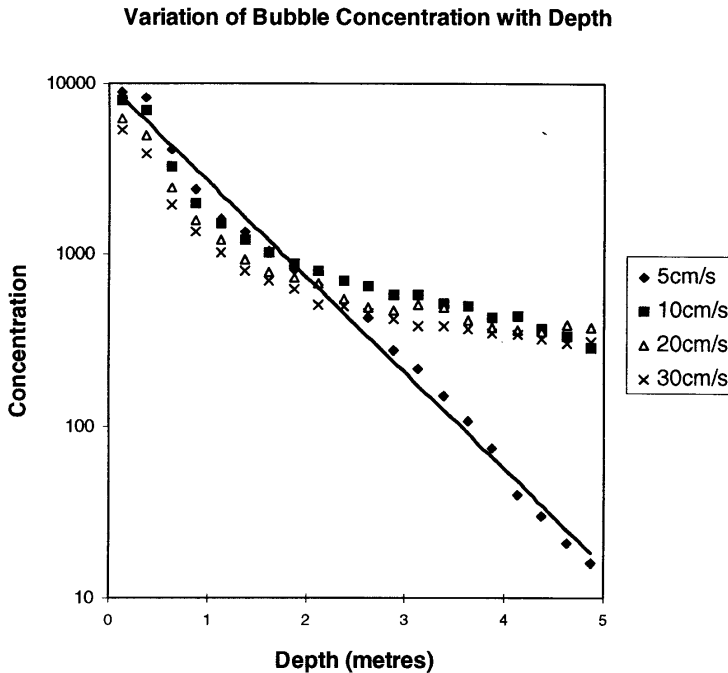


Figure 1: Variation of bubble concentration with depth at various Langmuir downwelling velocities (10,000 bubbles are injected and sampled in twenty 0.25 m deep bins every 10 seconds). The results for downwelling of 5 cm/s are fitted by an exponential model, the attenuation depth is 0.78 m.

It may appear at first sight that oceanic bubble populations — which typically exhibit an approximately exponential attenuation with depth [e.g., Johnson and Cooke, 1979; Vagle and Farmer, 1992] — may be explained by low Langmuir cell velocities; however, on examining the size distribution of the bubbles, the situation appears more complicated. The size distribution of bubbles at 4 m depth for various Langmuir cell velocities are shown in Figure 2. Size distributions near the surface are fairly insensitive to downwelling velocities, and reflect the source distribution. At high downwelling velocities, the size spectrum shifts with increasing depth to generally smaller bubbles, but only gradually and in line with oceanic observations. At low downwelling velocities, the size distribution is highly modified at a few metres depth with few bubbles $>50 \mu\text{m}$ in radius, which is inconsistent with observations.

In Figure 1, it is shown that the attenuation of bubble concentrations (counting all bubbles) and the concentration of bubbles at 4 m is fairly insensitive to downwelling velocity for velocities $\geq 10 \text{ cm/s}$. The size distribution is sensitive to the downwelling velocities however, so a different picture

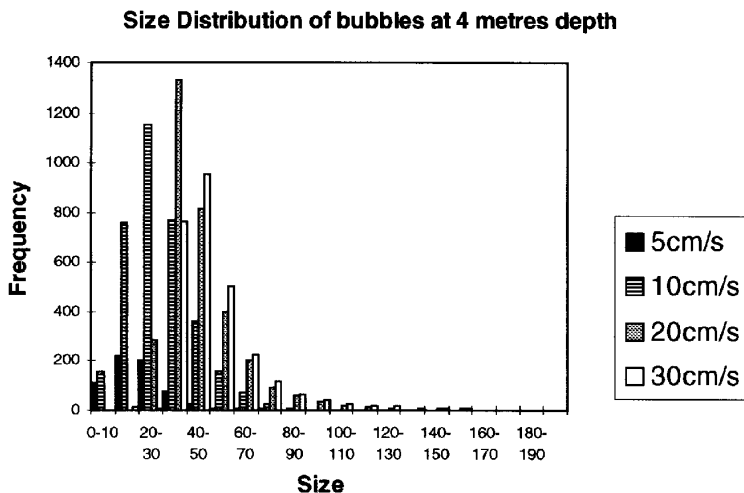


Figure 2: The size distribution of bubbles at 4m depth for various Langmuir cell velocities (10,000 bubbles of the standard source are injected and every 10 seconds bubbles between 3 and 5 metres depth are counted in twenty radius bins from 0-200 μm).

emerges if one instead looks at specific size classes of bubbles. For instance, if one is measuring bubbles optically then there will be a minimum bubble radius that is resolvable. It is shown in Figure 3 that the number of bubbles larger than 50 μm radius at 4 m depth is much more sensitive to downwelling speed than the total number of bubbles.

When the gases are saturated in the upper ocean, the advection of bubbles to depth and their consequent compression drives a gas flux from the bubbles into the water. This gas flux can be simply calculated as an integral part of the bubble dispersion model. The effect of variations in Langmuir advection velocities and the turbulent diffusion constant are investigated both for the standard source, and when all the bubbles are injected at 1 cm depth. The results are plotted in Figure 4. When the bubbles are injected at 1 cm, the turbulent diffusion constant is paramount in the dispersion of bubbles away from the surface and the consequent injection of gas, however Langmuir circulation can carry bubbles yet deeper and enhance the injection of gas (upper panel). For the standard source, a steady increase in the injection of gases at 100% saturation is found with increasing Langmuir circulation velocities (lower panel). In the presence of strong Langmuir circulation, increased turbulence slightly decreases the penetration of bubbles and gas fluxes, if the initial injection of the bubbles is reasonably deep. Small-scale turbulence increases the likelihood of a bubble being drawn from near the sea surface, but can also lead to a bubble straying out of the downward jet of a Langmuir cell. Note that the treatment of bubbles very near the surface

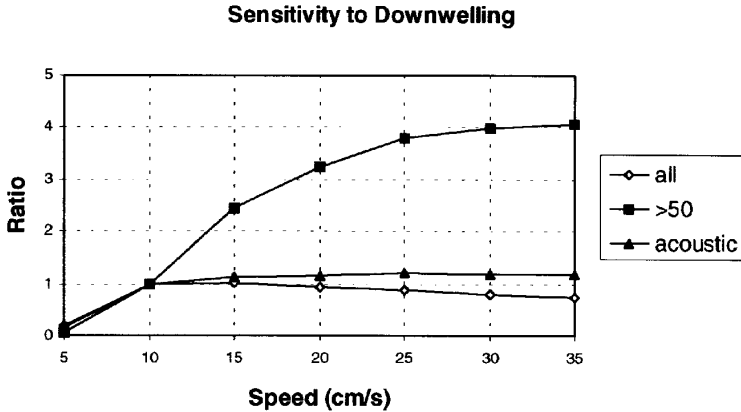


Figure 3: The sensitivity of the bubble concentration at 4 m to downwelling speed, expressed as a ratio of the concentration for a downwelling speed of 10 cm/s. Modelled as in Figure 2; total bubble numbers (“all”), bubbles larger than 50 mm radius (“>50”), and total 248 kHz acoustic backscattering cross-section (“acoustic”).

is unrealistic, being limited to defining an initial injection depth and a constant turbulent diffusion constant; therefore, the role of large near-surface bubbles cannot be investigated effectively.

3 Field Measurements

Measurements of near surface bubble clouds were made with an automatically recording inverted echo sounder (ARIES) in deep waters of the North East Atlantic in the Spring of 1990, during the onset of the Spring Phytoplankton Bloom in the region. The acoustic scattering cross-section of the bubble clouds as a function of depth, $M(z)$, and the concurrent meteorological and sea state data are generally consistent with a surface injection of bubbles proportional to whitecap coverage [Monahan and O’Muircheartaigh, 1980]. We can characterise the mean profile of the *bubble clouds* by,

$$M(z) = M_0 \exp(-z/d_e)$$

or

$$\ln M(z) = \ln M_0 - z/d_e$$

where M_0 and the *attenuation depth*, d_e can be calculated from a linear regression of $\ln M$ on z . Data from this study conformed very well to this exponential model (but note the minimum measurement depth, next paragraph), and values of the attenuation depth, d_e , calculated from the profile are plotted versus wind speed in Figure 5. The attenuation depth generally increases with wind speed but the correlation is quite poor.

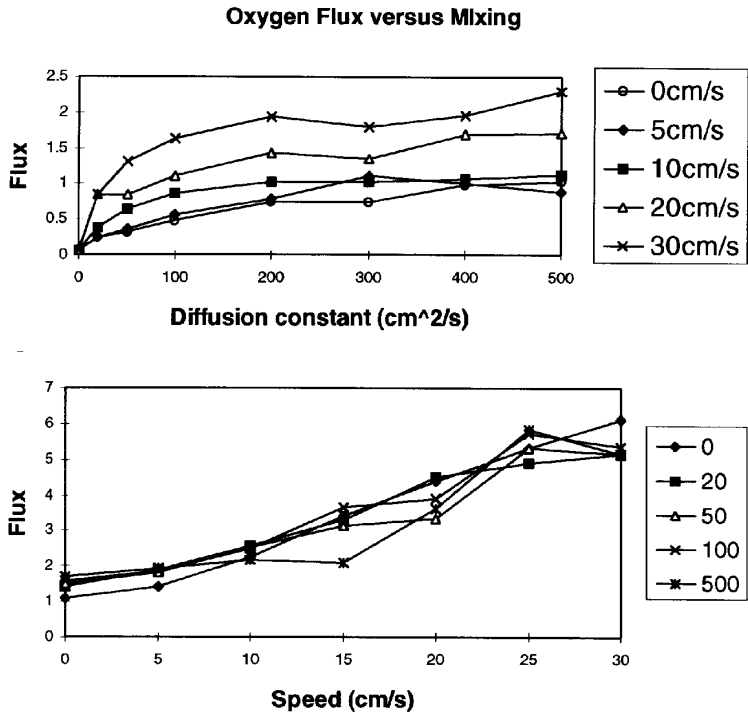


Figure 4: The influx of gas ($\times 10^{-9}$ moles of oxygen) resulting from an injection of 1000 bubbles ($50\text{--}500\ \mu\text{m}$ radius, r^{-4} distribution) as a function of upper ocean mixing. Upper panel: Source at 1cm, plotted versus turbulent diffusion constant (invariant with depth) for various downwelling speeds. Lower panel: Standard source, plotted versus downwelling speed for various turbulent diffusion constants (cm^2/s).

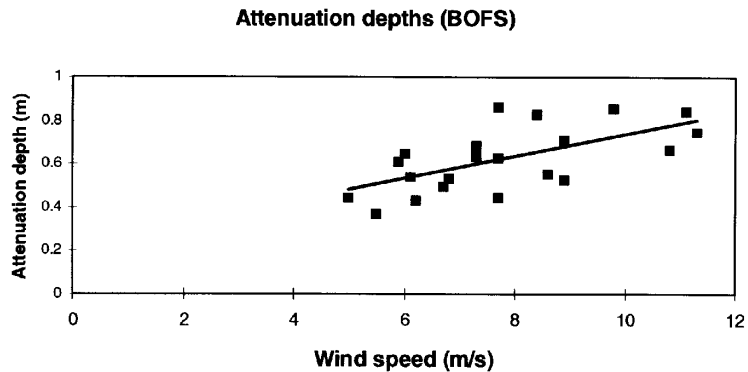


Figure 5: The attenuation depth of bubble clouds as measured by the 248 kHz sonar, ARIES, in the 1990 BOFS experiment plotted versus wind speed. The equation of the regression line is included in the Table.

Table 1: Statistics of the attenuation depth of bubble clouds measured by ARIES in a number of deployments. The last column shows results of a linear regression of attenuation depth, d_e , on wind speed, U .

Deployment	Temperature Range, °C	Number in Sample	d_e [mean \pm std.dev.] metres	$d_e(U)$ metres
BOFS (this study)	12.2-12.6	22	0.62 (± 0.14)	0.22 + 0.051U
DB2 Sept-Oct '84	14.7-17.3	23	1.57 (± 0.45)	0.92 + 0.057U
DB2 Dec '84-Feb '85	10.7-11.6	18	0.85 (± 0.14)	0.48 + 0.035U
Irish Sea	6.1-6.6	4	1.08 (± 0.34)	-0.33 + 0.131U

Statistics of d_e from this experiment are shown in Table 1 together with similar statistics from previous studies with ARIES. The penetration depths of the clouds were generally lower than those measured with the same instrument in the Winter and especially Fall on the continental shelf [Thorpe, 1986]. The variation in the attenuation depth of the clouds is probably partly, but not wholly, related to variations of the water temperature. Other seasonal factors (e. g., buoyancy flux) may be significant. It should be noted that the measurement of acoustic bubble scattering by ARIES is generally limited to below the deepest wave trough [Thorpe, 1986] and in the latest study to below 3.5 m depth. Almost all the measured profiles follow quite closely a simple exponential attenuation, but the attenuation in the surface layer should not be inferred.

4 Synthesis

There is a narrow resonance in 248 kHz acoustic backscatter for bubbles of approximately 14 μm radius, for larger bubbles the acoustic cross-section is proportional to their geometric cross-section, while very small bubbles have a very small acoustic cross-section. The numerical model together with oceanic measurements of bubble size distribution and acoustic theory suggest that the acoustic cross-section at 248 kHz (the operating frequency of ARIES) beneath the surface layer will almost invariably be dominated by small (<100 μm radius) bubbles. Also the attenuation of the smaller size classes and the *acoustic scattering* cross-section are generally quite similar, so the acoustic results are a genuinely useful indication of the characteristics of the bubble population. This general conclusion should be qualified, since there are quite significant variations in the size distribution of bubbles (Figure 2), [Vagle and Farmer, 1992]. The contribution of bubbles of different size classes is shown in Figure 6. The most important size class is quite variable; at low downwelling speeds the resonance is predicted to be very important, but is insignificant in strong circulation (it remains significant if very small bubbles are injected). As shown in Figure 3, the sensitivity of the

**Acoustic cross-section of bubble population
at 4 metres depth**

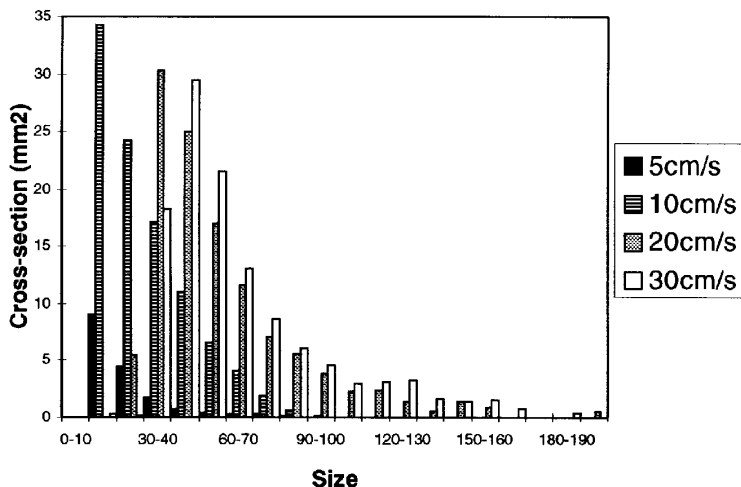


Figure 6: Contribution to 248 kHz acoustic backscattering cross-section of bubbles of various size classes (as in Figure 2).

248 kHz backscatter to downwelling speed is much closer to that of total bubble number than to that of the larger bubbles. The resonance condition is dependent on acoustic frequency. Lower frequency sonar will be relatively sensitive to bubbles of a larger resonant radius. For high frequency sonar (say, 500 kHz) the resonance is unlikely to be significant.

5 Discussion and Conclusions

It is difficult on the basis of the model results to give a satisfactory explanation of reported characteristics (e.g., exponential attenuation and fairly invariant size spectra) of oceanic bubble distributions. More work needs to be done on oceanic bubble distributions and their relationship to upper ocean mixing. Even less is known about the initial injection depth of bubbles, the number of large (≈ 1 mm radius) bubbles, and the dispersion of the bubbles within the surface layer (≈ 1 m), but it is likely [Rapp and Melville, 1990], that near-surface dispersion is closely related to the characteristics of the breaking waves. Variability in vertical mixing should be parameterised in models of the seasonal variation of dissolved gases such as oxygen and the inert gases, but this variability and its causes must first be determined. Substantial variations in gas fluxes and the forced supersaturations of gases must be expected at a given wind speed, unless the characteristics of Langmuir circulation and other phenomena responsible for vertical mixing are

remarkably consistent. The limited work described here is insufficient to establish the relationship of vertical dispersion to environmental parameters, or to describe with any accuracy, the sensitivity of air-sea fluxes and dissolved gas supersaturations to vertical mixing, but does show that there is indeed a significant sensitivity, and that this is a complicated problem. Further measurements with vertically-pointing sonar, preferably of several frequencies [Vagle and Farmer, 1992], should improve our understanding of both upper-ocean mixing processes and air-sea gas transfer.

Acknowledgements

Our research on bubbles and air-sea gas exchange is currently conducted as part of an EC MAST project (contract MAS2-CT93-0056). Earlier work, including the deployment of ARIES described here, was supported by the Natural Environment Research Council and supervised by Steve Thorpe. The technical support of Alan Hall and others at IOSDL is gratefully acknowledged.

References

- Johnson, B. D. and R. C. Cooke, Bubble populations and spectra in coastal waters: A photographic approach, *J. Geophys. Res.*, 84, 3761-3766, 1979
- Monahan, E. C. and I. O'Muircheartaigh, Optimal power-law description of oceanic whitecap coverage dependence on wind speed, *J. Phys. Oceanogr.*, 10, 2094-2099, 1980
- Rapp, R. J. and W. K. Melville, Laboratory measurements of deep-water breaking waves, *Phil. Trans. R. Soc. London*, A331, 735-800, 1990
- Stommel, H., Trajectories of small bodies sinking slowly through convection cells, *J. Mar. Res.*, 8, 24-29, 1949
- Thorpe, S. A., Measurements with an automatically recording inverted echo sounder; ARIES and the bubble clouds, *J. Phys. Oceanogr.*, 16, 1462-1478, 1986
- Thorpe, S. A., P. Bowyer and D. K. Woolf, Some factors affecting the size distributions of oceanic bubbles, *J. Phys. Oceanogr.*, 22, 382-389, 1992
- Vagle, S. and D. M. Farmer, The measurement of bubble-size distributions by acoustical backscatter, *J. Atmos. Oceanic Technol.*, 9, 630-644, 1992
- Weller, R. A. and J. F. Price, Langmuir circulation within the oceanic mixed layer, *Deep-Sea Res.*, 35, 711-747, 1988
- Woolf, D. K. and S. A. Thorpe, Bubbles and the air-sea exchange of gases in near-saturation conditions, *J. Mar. Res.*, 49, 435-466, 1991

Conceptual Modelling of Interfacial Gas-Liquid Mass Transfer

J. George, B. Caussade, L. Masbernat

INP-ENSEEIH - Institut de Mécanique des Fluides URA 0005 CNRS
Avenue du Professeur Camille Soula 31400 Toulouse. France

Abstract

An analysis of experimental results concerning gas absorption under different physico-chemical and hydrodynamic conditions is presented. The role played by turbulent eddies which develop close to the free surface is emphasized. A conceptual model, using a velocity scaling based on the turbulent kinetic energy value present at the interface, is proposed for K_L , the gas transfer velocity. As gas absorption is an interfacial phenomenon, this model seems suitable for situations as different as laboratory or environmental ones.

1 Introduction

The knowledge of interfacial gas-liquid mass transfer is of fundamental importance in environment as well as in chemical or biochemical engineering. Concerning interfacial absorption of weakly soluble gases, for which resistance to transfer takes place inside the liquid phase, prediction of the mass transfer coefficient K_L depends on the modelling of the interfacial dynamic phenomena and on the knowledge of physico-chemical properties.

Most conceptual models of K_L found in the scientific literature consist in the determination of K_L by introducing the effective diffusivity or by determining the size of the most efficient eddies (*large eddies* [Fortescue and Pearson, 1967] or *dissipative structures* [Lamont and Scott, 1970]).

All models can be written in a non-dimensional form [Aisa et al., 1981]:

$$K_L/u_0 \propto Sc^n Re^\alpha We^\beta \quad (1)$$

The velocity u_0 is a characteristic velocity and the non-dimensional numbers are the Reynolds number ($Re = u_0 l_0/\nu_L$), the Schmidt number ($Sc = \nu_L/D\mu$) and the Weber number ($We = \rho_L l_0 u_0^2/\sigma$).

For environmental conditions, the interfacial *liquid friction velocity* u_{SL} , which accounts for the interfacial agitation, is generally chosen as *characteristic velocity* u_0 and one can make use of the following relation:

$$K_L/u_{SL} = 0.12Sc^{-1/2} \quad [\text{Hanratty, 1991}] \quad (2)$$

Unfortunately, the use of u_{SL} as a characteristic velocity scaling does not permit a correct prediction of situations for which there is little or no mean shear stress at the interface, for which there exist large developing waves or for which wall turbulence directly governs interfacial turbulence.

The aim of this paper is to analyse the possibility of scaling K_L , under various situations, by using a characteristic velocity based on local interfacial agitation parameters.

2 Interfacial Turbulent Kinetic Energy

As will be analysed in the following sections, the square root of the interfacial turbulent kinetic energy inside the liquid phase, at the gas-liquid interface, seems to be a good velocity scaling for K_L .

The fundamental difference between a gas-liquid interface and a solid wall is that velocity fluctuations may exist at the very surface. Therefore, one can define an interfacial liquid *turbulent kinetic energy* k_I .

In the laboratory, in the case the interface is flat, an experimental value of k_I can be directly obtained when measurements are carried out very close to the *free surface*. There, as was shown, by *Brumley and Jirka* [1987] or by *Grisenti and George* [1991], the value of k_I remains roughly constant inside an upper region developing a few millimetres below the interface.

In the case of a wind stressed interface, with waves, it is of course impossible to reach the free surface, even in the laboratory. However, studies have shown that the turbulent kinetic energy present at the lower limit of the wavy region accounts for the effect of wind and also for the extra turbulence generated by orbital motions (wave-turbulence interactions). Therefore, the *interfacial turbulent kinetic energy* concept k_I can be extended to the value of k measured right below the wave region.

Let us now examine the possible relations between k_I and K_L .

3 Data Analysis

The large amount of experimental data, provided by literature, covers very different interfacial physico-chemical and hydrodynamic conditions. It is therefore of great interest to analyse the main features controlling the gas transfer process.

3.1 Wind Sheared Interfaces

In the case of *wind-sheared interfaces*, as was shown by various authors, the characteristic velocity u_{SL} fits, relation 2 can generally be used and u_{SL} is convenient.

However, in the case of large developing waves, which occurs very often under environmental conditions, when turbulence produced under waves

is greatly enhanced (there the ratio k_I/u_{SL}^2 , which generally equals 3 to 16, can reach values up to 50 or more - see for example *Kitaigorodskii et al.* [1983]), K_L is underestimated by relation 2 (see figure 1) and a better fitting can be obtained using a velocity scaling based on the dominant wave energy [*Caussade et al.*, 1990]. Therefore, under such conditions, the square root of the interfacial turbulent kinetic energy $\sqrt{k_I}$ can be preferred to u_{SL} and the non dimensional mass transfer coefficient is shown to range between:

$$0.028Sc^n \leq K_L/\sqrt{k_I} \leq 0.056Sc^n \quad [\text{Magnaudet et al., 1990}] \quad (3)$$

The *Schmidt number* power value was shown to be varying between $n = -1/2$ (for clean interfaces) and $n = -2/3$ for dirty surfaces or for winds weaker than 4 m/s [*Jähne et al.*, 1987, *Caussade et al.*, 1990].

3.2 Free Falling Films

In the case of *free-falling films*, K_L can be modelled using an intermediate velocity based on the interfacial and on the wall liquid friction velocities [*Henstock and Hanratty*, 1971] but not on u_{SL} alone. In fact, a large amount of turbulence generated at the wall is responsible for a certain agitation of the free surface, even if there is no co- or counter-current wind (in this last case the ratio k_I/u_{SL}^2 tends towards infinity).

Therefore, as was shown by *Caussade et al.*, [1990], the liquid friction velocity u_{SL} is not representative of K_L for weaker winds when K_L remains important due to the role bottom turbulence plays on the free surface behavior (Figure 1). Hence, turbulence responsible for the interfacial agitation seems to play a major role on gas absorption. It is important to emphasize the fact that the interfacial agitation level seems to be directly related to K_L , not depending on its origin (local origin, i.e., wind-wave interactions or diffusion from a bottom wall) and again one can think of using $\sqrt{k_I}$ as characteristic velocity.

3.3 Agitated Vessels

The case of grid-stirred vessels is fully documented. Hydrodynamic conditions described by *Thompson and Turner* [1975], *Hopfinger and Toly* [1976] and *Brumley and Jirka* [1987] show that turbulence, which is roughly isotropic and homogeneous in horizontal planes, decays regularly towards the free surface. There, the rapid distortion due to splatting effects (agitation is increasing greatly in the horizontal plane while it is rapidly damping in the vertical direction), described by *Hunt* [1984], is hardly observed in the immediate vicinity of the free surface. As mentioned by *Brumley and Jirka* [1987], the absence of turbulence redistribution is probably due to the fact that, under their experimental conditions, interface was not clean enough and a viscous layer could develop in the water.

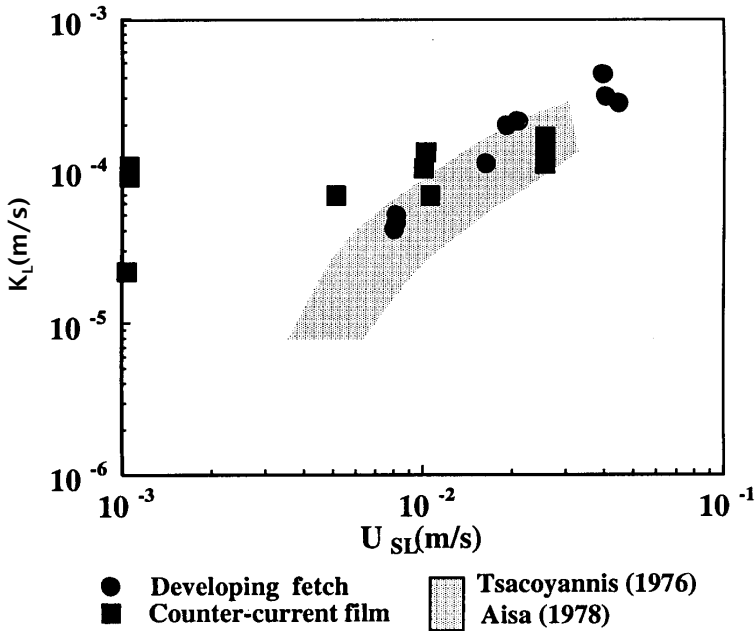


Figure 1: Absorption coefficient under different interfacial turbulence conditions: shaded area: laboratory wind sheared interfaces, circles: developing fetch with large wind driven waves, boxes: free falling films and counter-current films

Of course, as there is no mean shear stress, one has to look for velocity scaling different from the liquid friction velocity at the interface. Gas transfer measurement results, reported by *Asher and Pankow* [1976], show it is possible to relate K_L to parameters such as global turbulence parameters, or such as ε , the dissipation rate of the turbulent kinetic energy.

In an agitated vessel in which turbulence is produced by upflowing liquid microjets, *Grisenti and George* [1990] have shown that the value of the turbulent kinetic energy present at the interface is well related to mass transfer and K_L can be modelled as:

$$K_L/\sqrt{k_I} = 0.03Sc^n \quad (4)$$

As is shown in figure 2, K_L is reduced for weaker agitation levels, in presence of Hexadecanol, and $n = -2/3$. This is probably due to the fact that, while surface tension is damped, a reduction of the horizontal mobility of the free surface simultaneously exists [*George et al.*, 1994]. However, when horizontal agitation remains large without being damped at the surface (i. e., when k_I is important and when the film of surfactant is broken), K_L values become large and n tends towards $-1/2$.

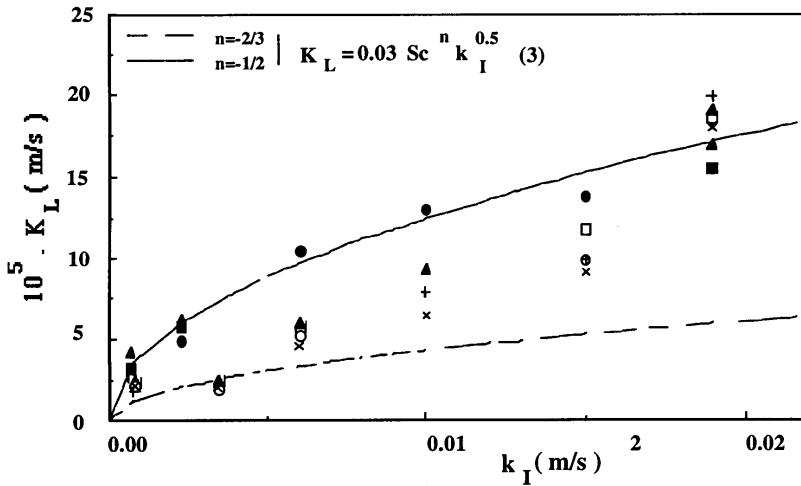


Figure 2: K_L values with (open symbols) and without (solid symbols) Hexadecanol Films after [George et al., 1994]

Recent experiments concerning the characteristic length scales and frequencies of interfacial turbulent eddies have shown that the existence of large horizontal structures seems to be of great importance [Minel and George, 1995]. Also, as shown by Prinos et al. [1995], an increase in the value of concentration fluctuations seems to correlate with the existence of such eddies. It can be added that these horizontal structures correspond to a development of the spectrum density power towards the lower frequencies and may represent intermittent phenomenon.

3.4 Freely Falling Drops

Experiments with *freely falling droplets* were carried out by Amokrane [1993] in a specially designed vertical absorption column. In that case [Amokrane et al., 1994], for freely falling drops which diameters range between 0 and 6 mm.

As can be seen in figure 3 which represents the variation of the Sherwood number Sh versus the droplets diameter ($Sh = \frac{K_L d}{D\mu}$, where d is the droplet diameter), the best fitting can be obtained using the large eddy model ($K_L = \alpha u_{SL} Re^{-0.5} Sc^{-0.5}$) proposed by Fortescue and Pearson [1967] for wind stressed surfaces. However, to fit experimental results, the coefficient α has to be empirically changed from $\alpha = 1.46$ to $\alpha = 0.8$. It means that one cannot be using the same law for wind stressed surfaces and for droplets. Let us note here that K_L is reduced in the case of falling droplets.

On the contrary K_L can be modelled using relation (4), with $n = -2/3$, without changing any coefficient. The knowledge of the droplets terminal

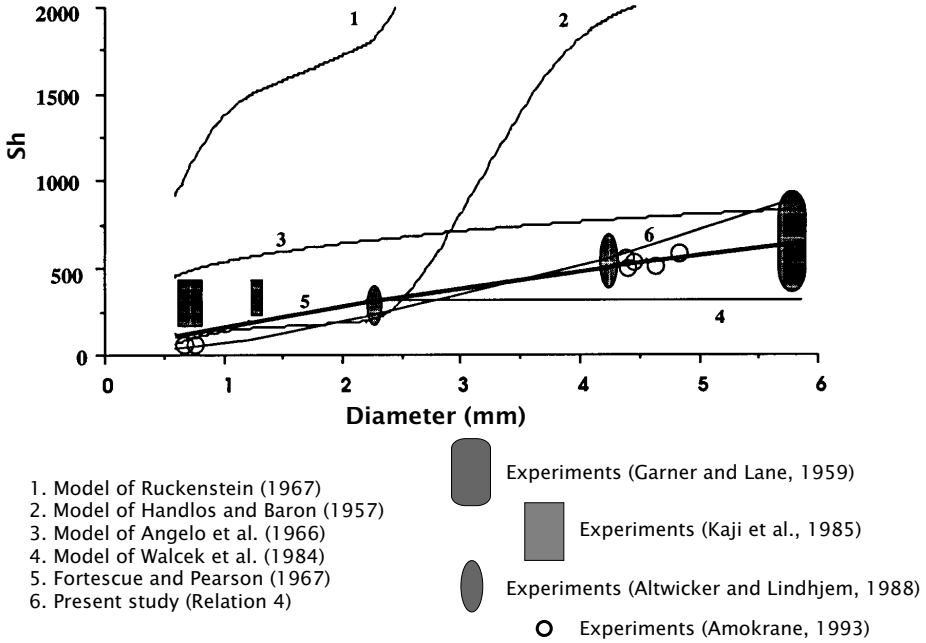


Figure 3: Sherwood number vs. droplet diameter [Caussade, Amokrane, Saboni, 1994]

velocity allows to calculate the friction velocity u_{SL} and to deduce a value for k_I using the relation $k_I/u_{SL}^2 \cong 10$ (the value of the ratio k_I/u_{SL}^2 depends on the level of deformation of the interface and, for smooth interfaces, it has been shown in laboratory experiments in channels that it is approximately equal to 10).

In fact, it seems that there is not only a problem of coefficient. When the coefficient value is adjusted, the Schmidt number power remaining equal to $n = -1/2$, it is implicitly assumed that large eddies can develop. On the contrary, the value of $n = -2/3$ corresponds to the fact that large eddies cannot develop freely inside the drops. Hence, in relation with absorption, each droplet seems to behave more like a solid wall than like a free surface and it seems preferable to use relation 4 without trying to adjust any coefficient.

In that last case, relation 4 can be written:

$$K_L = 0.03\sqrt{k_I}Sc^n = 0.095u_{SL}Sc^n \quad (5)$$

which is roughly equivalent to the classical relation 2 with $n = -2/3$ or $-1/2$ depending on the interfacial behavior.

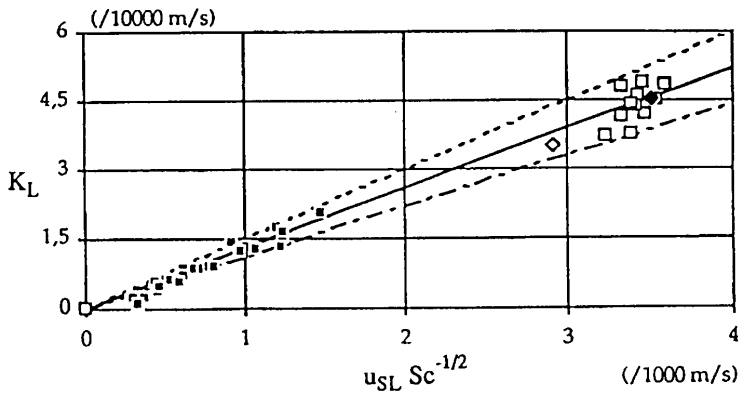


Figure 4: K_L versus $u_{SL} Sc^{-1/2}$ (filled box: stratified flow, open box: deep U-tube, open rhombus: bubble column ozone, filled rhombus: bubble column oxygen, solid and broken lines: correlation $K_L = (0.13 \pm 0.02) u_{SL} Sc^{-1/2}$) after [Cockx et al., 1994]

3.5 Bubbly Flows

In the case of *bubbly flows*, when large turbulent eddies can develop freely around *bubbles*, again relations (2) and (4) collapse into one single relation (with $k_I/u_{SL}^2 \cong 16$) and give good results (Figure 4). One can observe here that K_L values are very large due to the fact that the drag coefficient of bubbles C_D is important [$C_D = 0.16$, Cockx et al., 1994] and the liquid is strongly agitated when it flows past bubbles. The large value of C_D corresponds to a large value of u_{SL} and, as bubbles are deformed by the liquid agitation, the ratio $k_I/u_{SL}^2 \cong 16$, corresponding to a surface with small waves, is adequate.

In this case, as turbulence can develop freely inside the liquid phase, mass transfer rate is more important than in the case of droplets. We can also underline the fact that, mass transfer occurring at the surface itself, this phenomenon is controlled by the interfacial agitation inside the liquid phase.

4 Discussion

As can be seen from above, when K_L is modelled using the turbulent kinetic energy at the surface, all experiments can be represented by the same empirical law. When results are examined in more detail, it can be noted that the role played by *horizontal eddies* which develop at the surface seems important.

Let us now focus on the mechanism of mass transfer itself. According to Perkins et al. [1990] particles are carried to the surface and then back down again, that is the matter released from the interior which reaches the surface in bursts or surface boils [Komori et al., 1989], traps matter diffusing from

the interface and melts with the inner fluid in downward sweeps [Pankow *et al.*, 1986].

For Komori *et al.* [1989], who showed that organised motions in the air flow intermittently appear on the front of the wave crest and induce surface-renewal motions in the water, K_L is found proportional to the root of this surface-renewal frequency, which corresponds to downward bursts, and increases with increasing the wind shear (but tends to saturate when it reaches approximately 100 Hz).

For others, the major role is played by *small eddies*. For Banerjee [1990] the ejection frequency, which coincides with the peak in the wave spectrum for sheared interfaces, gives a characteristic frequency that allows absorption to be calculated using the small eddies concept when in Danckwerts formulation the renewal frequency is equal to the capillary-gravity wave frequency peak, which is in agreement with the model developed by Coantic [1986].

Our results tend to acknowledge the role played by large structures in the horizontal plane. When a surfactant is added, large horizontal structures tend to disappear and mass transfer is reduced even if the turbulence level remains important close to the surface. For dispersed flows, absorption is different depending on the dispersed phase: mass transfer is reduced when the liquid phase is trapped into droplets and when large eddies cannot develop freely inside the liquid phase due to the small dimension of droplets, on the contrary, mass transfer is large in presence of bubbles when large eddies can develop inside the liquid phase.

In the case of wind-stressed interfaces, Wolf and Hanratty [1994] showed that the existence of capillary waves enhances mass transfer and concluded that small structures play a dominant role. In fact, the existence of small ripples on top of the waves is not in contradiction with what was noticed above: capillary waves on top of gravity waves are the signature of a high level of surface friction, and hence, one can assume that when capillary waves are present, the turbulence level under waves is important and large horizontal eddies can develop allowing water particles to reach the free surface and to remove quantities of dissolved gas.

5 Conclusion

We can emphasize the fact that in most situations the square root of the interfacial turbulent kinetic energy value $\sqrt{k_I}$ can be chosen as characteristic velocity u_0 and in all situations listed above, as the mass transfer rate ranges as indicated by (3), relation (4) can be used. As showed above, the interfacial turbulent kinetic energy inside the liquid phase is closely related to the interfacial mass transfer velocity and can be directly measured in the case of flat interfaces. In the case of wavy surfaces or dispersed flows k_I can be estimated from the value of k below the waves or from the drag coefficient of bubbles or droplets.

We can add that models based on the dissipation rate [Asher and Pankow, 1986] give also rather good results. However, a direct estimation of the dissipation rate ε and of the characteristic length scales have shown [Minel and George, 1995] that large horizontal eddies develop with increasing K_L values and hence that large eddies seem to be more efficient than dissipative structures.

From a practical point of view, K_L can be modelled using relation (4) and in the case of bubbles, one can use relation (2) which is then equivalent to relation (4) with $\sqrt{k_I} \cong 4u_{SL}$.

References

- Aisa L., B. Caussade, J. George and L. Masbernat, Echanges de gaz dissous en écoulements stratifiés de gaz et de liquide, *Int. J. Heat Mass Transfer*, 24, 1005-1018, 1981
- Amokrane H., Etude expérimentale et modélisation de l'absorption de dioxyde de soufre en milieu dispersé liquide, Thèse de doctorat de l'INP Toulouse, 1993
- Amokrane H., Saboni A., Caussade B., Experimental study and parameterization of gas absorption by water drops, *AIChE J.*, 40, part 12, 1950-1960, 1994
- Asher W. E. and J. F. Pankow, The interaction of mechanically generated turbulence and interfacial films with a liquid phase controlled gas/liquid transport process, *Tellus*, 38B, 305-318, 1986
- Banerjee S., Turbulence/Interface Interactions, Proceedings of the ICHMT International Seminar Phase-Interface Phenomena in Multiphase Flows. Dubrovnik. Yugoslavia, 1990
- Brumley B., Jirka G. H., Near-surface turbulence in a grid-stirred tank, *J.Fluid Mech.*, 183, 253-263, 1987
- Caussade B., J. George and L. Masbernat, Experimental Study and Parameterization of Interfacial Gas Absorption, *AIChE J.*, 36(2), 265-274, 1990
- Coantic M., A model of gas-transfer across air-water interfaces with capillary waves, *J. of Geophysical Res.*, 91, 3925, 1986
- Cockx A., M. Roustan, A. Line, G. Hebrard, Modelling of mass transfer coefficient K_L in bubble columns, to appear in *Chem. Eng. Research and Design*, 1995
- Danckwerts P. V., Significance of liquid-film coefficients in gas absorption, *Ind. Eng. Chem.*, 43, 1460, 1951
- Fortescue G. E. and J. R. A. Pearson, On gas absorption into a turbulent liquid, *Chemical Eng. Sci.*, 22, 1163-1176, 1967
- George J., F. Minel, M. Grisenti, Physico-chemical and hydrodynamical parameters controlling gas-liquid mass transfer, *Int. J. Heat Mass Transfer*, 37, 1569-1578, 1994
- Grisenti M. and J. George, Hydrodynamics and mass transfer in a jet -agitated vessel, *Air-water mass transfer*, S. C. Wilhelms & J.S. Gulliver Eds, ASCE, 1991
- Hanratty T. J., Effect of gas flow on physical absorption, *Air-water mass transfer*, S. C. Wilhelms & J. S. Gulliver Eds, ASCE, 1991
- Henstock W. H. and T. J. Hanratty, Gas absorption by a liquid layer flowing on the wall of a pipe, *AIChE J.*, 25, 122-131, 1979

- Hopfinger E. J., Toly J.-A., Spatially Decaying Turbulence and its Relation to Mixing across Density Interfaces. *J.Fluid Mech.*, 78, part 1, pp. 155-175, 1976
- Hunt J. C. R., Turbulence structure in thermal convection and shear-free boundary layers. *J.Fluid Mech.*, 138, 161-184, 1984
- Jähne B., Münnich K. O., Böisinger R., Dutzi A., Huber H., Libner P., On the parameters influencing air-water gas exchange. *J. Geophys. Res.*, C2, 92, 1937-1949, 1987
- Kitaigorodskii S. A., Donelan M. A., Lumley J. L., Terray E. A., Wave-turbulence interactions in the upper ocean. Part II : Statistical characteristics of wave and turbulent components of the random velocity field in the marine surface layer *J. of Physical Oceanography*, 13, 1988-1999, 1983
- Komori S., Murakami Y., Ueda H., The relationship between surface-renewal and bursting motions in an open channel flow *J.Fluid Mech.*, 203, 103-123, 1989
- Lamont J. C. and D. S. Scott, An eddy cell model of mass transfer into the surface of a turbulent liquid, *AIChE J.*, 16, 513-519, 1970
- Magnaudet J., J. George, L. Masbernat and B. Caussade, Turbulence below the waves and its relation to absorption, *Air-water mass transfer*, S. C. Wilhelms & J. S. Gulliver Eds, ASCE, 1991
- Minel F. and George J., Hydrodynamics in a jet-agitated vessel close to the gas-liquid surface, *this volume*
- Perkins R. J., Carruthers D. J., Drayton M. J., Hunt J. C. R., Turbulence and Diffusion at Density Interfaces. Proceedings of the ICHMT International Seminar Phase-Interface Phenomena in Multiphase Flows. Dubrovnik. Yugoslavia, 1990
- Prinos P., Atmane M., George J., Gas Flux Measurements and Modelling below an Air-Water Interface, *this Volume*
- Thompson S. M., Turner J. S., Mixing across an Interface due to Turbulence Generated by an Oscillating Grid. *J.Fluid Mech.*, 67, pp. 349-368, 1975
- Wolf L. M., Hanratty T. J., Instantaneous concentration profiles of Oxygen accompanying absorption in a stratified flow, *Experiments in Fluids*, 16, 385, 1994

Reaeration in Combined Wind/Stream Driven Flows

*Chia R. Chu*¹ and *Gerhard H. Jirka*²

¹ Department of Civil Engineering
National Central University Taiwan, R.O.C.

² School of Civil and Environ. Engineering
Cornell University, U.S.A.

Abstract

Reaeration in combined wind/stream driven flows was studied experimentally in a laboratory wind-water tunnel. Wind velocities, stream flow properties and oxygen transfer rates were measured under a variety of co- and counter-current flows. For pure open channel flows and pure wind-driven flows, the results of oxygen transfer experiments show good agreement with other laboratory studies. For wind/stream combined flows, the transfer velocity depends on the stream flow condition and wind speed. Based on the magnitude of the bottom-shear induced transfer velocity and the wind-shear induced transfer velocity, a criterion was suggested to determine the dominant mechanism for reaeration in combined wind/bottom driven flows. A predictive model was proposed to calculate the transfer velocity of combined wind/stream driven flows.

1 Introduction

Correct prediction of oxygen transfer across the air-water interface is crucial for the modeling of water quality. In traditional engineering analyses, reaeration in rivers is computed as a function of stream flow parameters and neglects the effects of surface wind shear. In contrast, gas transfer rates in *lake*, *reservoir* and *ocean* are calculated as a function of surface wind speed, without considering the influence of water current. However, in places like *estuaries*, mild-slope streams and coastal regions with current, the flow condition in the water is strongly influenced by water current and surface wind simultaneously. In these kinds of environments, there is considerable uncertainty on which physical mechanism — and to what extent — affects the interfacial transfer process. Existing knowledge of the transfer process under the joint action of stream flow and surface wind is seriously deficient [Cerco, 1989]. First, there is no clear guidance to the determination of the process that dominates the oxygen transfer in such a combined regime. Second, the lack of reliable experimental information has hampered the development of a predictive model for the interfacial transfer process.

Customarily, the interfacial transfer rate of low solubility gases, such as oxygen, is parameterized by the liquid phase gas transfer velocity (or transfer coefficient) K_L :

$$J = K_L(C_s - C) \quad (1)$$

where J is the gas flux per unit interfacial area into or out of the water column, C_s and C are the saturated and bulk concentration of dissolved gas, respectively. For low solubility gases, the transfer velocity K_L depends on the molecular and turbulent transport processes in the water layer immediately below the surface. While the molecular transport is directly affected by the molecular diffusivity of dissolved gas in water, the turbulent transport is governed by the forcing that may be active in the natural environment. In estuaries, the most important forcing on the surface transfer mechanism are bottom-shear and wind-shear generated turbulence.

There has been some awareness of the fact that wind shear may considerably affect the transfer velocity of natural streams. For example, *Eloubaidy & Plate* [1972] and *Mattingly* [1977] carried out laboratory experiments to study the reaeration rates of stream flows under surface wind. Their results showed a slight but definite dependence of K_L on stream flow velocity in addition to the primary dependence on wind velocity. However, their studies did not give a quantitative criterion to the determination of the dominant mechanism in combined driven flows. A comprehensive and detailed investigation of the gas transfer process in *wind/stream combined flows* is urgently needed for the water quality modeling of estuarine environments.

In this study, a laboratory experiment was carried out to investigate the influence of different turbulence sources on the reaeration. Wind velocities, stream flow properties and oxygen transfer rates were measured under a variety of co-current and counter-current flow conditions. The goal of this study is to improve our understanding of gas transfer mechanism in combined wind/stream driven flows and to develop a predictive model for the gas transfer rate.

2 Experimental Setup

The experiments were performed in the *Tilting Wind-Water Tunnel* (TWWT) at Cornell University. The TWWT is composed of a recirculating tilting water flume and an open-ended wind tunnel (see Figure 1). The overall length of the TWWT is 29.6 m with a test section 20.0 m long, 1.0 m wide and 0.8 m high. The air flow in the flume can progress from headbox to tailbox through suction, or in the opposite direction by blowing. The water was deaerated by bubbling nitrogen through a pipe line system into the water in the reservoir for approximately one hour. The initial concentration of dissolved oxygen was, on the average, 4.0 mg/l. The water was then circulated into the flume, and the water depth, slope, and pump speed were adjusted to give uniform flow at the condition desired.

Water samples were taken from taps on the bottom of the upstream and downstream ends of the flume, separated by 20.0 m. Nine samples, spaced

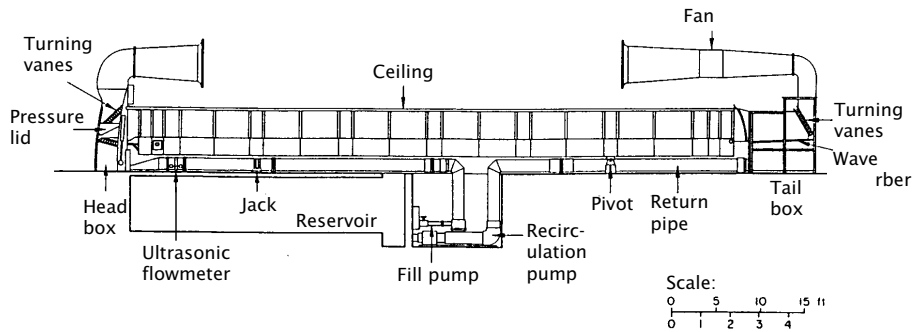


Figure 1: Schematic diagram of the Tilting Wind-Water Tunnel

at 15 minute interval were taken at each station. The dissolved oxygen (D. O.) concentrations of samples were determined by the Winkler titration method (Standard Method, 1989). The water temperature and D.O. concentration were monitored continuously at the downstream end by a dissolved oxygen meter (YSI model 58). The saturation value of D.O. was calculated based on Standard Method for zero chlorinity. The reaeration coefficient $K_2 (= K_L/h)$ was calculated by the two-station method suggested by Rathbun [1988].

The experimental conditions were chosen to cover the range of flow conditions in the estuarine environment. Five different stream flow conditions (Case S1 - S5) and one stagnant water condition (Case S0) were studied. The stream flow condition of Case S1 and Case S3 are the same, but Case S1 is co-current flow whereas Case S3 is counter-current flow. The channel bed (stainless steel) was smooth for all cases. The mean water velocity U_w was obtained from an ultrasonic flowmeter in the return pipe of TWWT. The friction velocity of stream flow was calculated from $u_{*b} = (gRS)^{1/2}$, where g is the gravitation acceleration, R is the hydraulic radius and S is the slope of channel bed. Each stream flow condition is combined with four to five different wind speeds (ranging form 1.0-10.0 m/s). The air friction velocity u_{*a} was determined by best-fitting the wind velocity profile to the logarithmic distribution. No significant surface breaking was observed during the experiment in all cases. Further details regarding the experimental setup and the uncertainty analysis of the measurements can be found in Chu [1993].

3 Results and Discussion

All the measured K_L values were corrected to 20°C by the empirical temperature-correction equation

$$K_{L_T} = K_{L_{20}} \theta^{T-20} \quad (2)$$

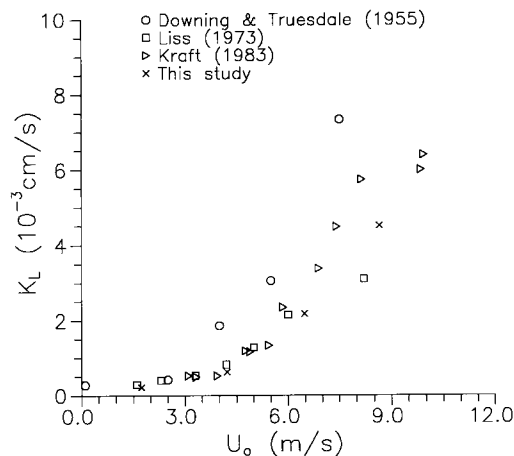


Figure 2: Transfer velocity K_L vs. U_o for pure wind driven flows (Case S0).

where T is the water temperature in $^{\circ}\text{C}$, and θ is the temperature correction coefficient. The value of θ used in this study is 1.024, which was suggested by *Elmore and West* [1961]. The measured gas transfer velocities K_L for pure wind-driven flows and pure open channel flows are presented first, then the results of combined wind/stream driven flows are shown. Based on the experimental results, a criterion is suggested to determine the dominant mechanism in a combined wind/stream driven flow. Furthermore, a predicted model is proposed and compared with the reaeration data in the natural environments.

3.1 Pure Wind-Driven Flows

The oxygen transfer velocity K_L for pure *wind-driven flows* (Case S0) is plotted against mean wind velocity U_o in Figure 2. Also plotted in the figure are the laboratory reaeration experiments of *Downing & Truesdale* [1955], *Liss* [1973] and *Kraft* [1983]. As can be seen, although this comparison shows some scattering among different experiments, all the measured K_L increases as much as an order of magnitude as the wind speed increases from low (1–3 m/s) to high (6–10 m/s). The transfer velocities K_L for Case S0 are plotted as a function of air friction velocity u_{*a} in Figure 3. Because *Downing & Truesdale* [1955] did not present the friction velocity u_{*a} of their study, their results are not shown in Figure 3. As can be seen, the quantitative agreement among different studies is much better than in Figure 2. This indicates that the air friction velocity is a better parameter than the mean wind velocity in describing the transfer mechanism of pure wind-driven flow. However, note that there is a discontinuity around $u_{*a} = 15$ cm/s for the power law

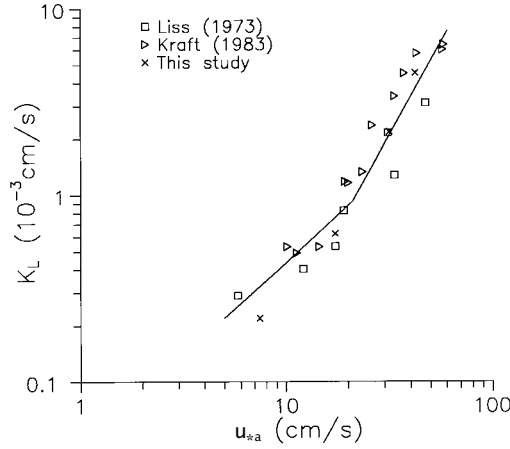


Figure 3: Transfer velocity K_L vs. u_{*a} for pure wind driven flows (Case S0). The solid line is the prediction of (3) and (4).

dependency of K_L on u_{*a} . This discontinuity corresponds to the change of surface roughness condition from smooth to rough [Jähne *et al.*, 1987].

For aerodynamically smooth surfaces, Deacon [1977] suggested the wind-shear induced transfer velocity

$$K_{Lw} = \alpha u_{*a} \tag{3}$$

where both K_{Lw} and u_{*a} are in [cm/s]. The coefficient $\alpha = 4.38 \times 10^{-5} \pm 0.67 \times 10^{-5}$ (95% confidence interval) determined from the data of Liss [1973], Kraft [1983] and this study compares favorably with $\alpha = 4.60 \times 10^{-5}$ reported by Deacon [1977] and $\alpha = 4.10 \times 10^{-5}$ by Jähne *et al.* [1987]. For rough surfaces, a least square fit of the data that $u_{*a} > 15$ cm/s yields

$$K_{Lw} = 2.12 \times 10^{-6} (u_{*a})^2 \tag{4}$$

The coefficient is within $\pm 0.12 \times 10^{-6}$ (95% confidence interval). The quadratic power dependence agrees with several laboratory studies [Kanwisher, 1963; Liss, 1973]. The transitional velocity for the smooth and rough regimes is around $u_{*a} = 15$ cm/s, which is close to the observation of Jähne *et al.* [1987] $u_{*a} = 11.5$ cm/s.

3.2 Pure Open Channel Flows

For reaeration in pure *open channel flows*, numerous models have been proposed to correlate the transfer velocity K_L with mean flow parameters.

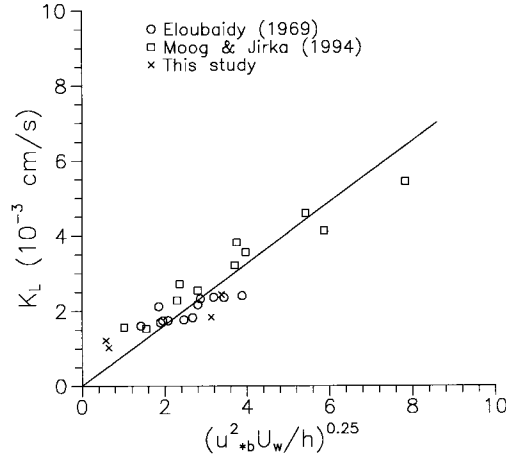


Figure 4: Transfer velocity K_L vs. $((u_{*b})^2 U_w / h)^{1/4}$ for pure open channel flows. The solid line is the prediction of (5).

However, all these competing models have very limited general accuracy. In this study, no attempt was made to do a comprehensive study on this problem and the model suggested by *Moog & Jirka* [1994] was used. In their model, the transfer velocity K_L is related to the energy of mean flow $((u_{*b})^2 U_w / h)^{1/4}$. The one quarter power law is from the scaling relation of small eddy model [*Lamont & Scott*, 1970]. Figure 4 shows the transfer velocities K_L for the pure open channel flows (Cases S1, S2, S4, and S5) plotted against $((u_{*b})^2 U_w / h)^{1/4}$. Also plotted in the figure are the results of laboratory experiments of *Eloubaidy* [1969], *Moog & Jirka* [1994]. An empirical relation for bottom-shear induced transfer velocity K_{Lb} is compiled from all the data shown in Figure 4.

$$K_{Lb} = 1.23 \times 10^{-3} \left(\frac{u_{*b}^2 U_w}{h} \right)^{1/4} \quad (5)$$

where the unit of K_{Lb} , u_{*b} and U_w are in [cm/s], h is in [cm], and the coefficient is within $\pm 4.48 \times 10^{-5}$ (95% confidence interval).

3.3 Combined Wind/Stream Driven Flows

The values of transfer velocity K_L for all cases are plotted as a function of the mean wind velocity U_o in Figure 5. Also plotted in the figure are the results of the laboratory study of *Eloubaidy & Plate* [1972]. As can be seen in Figure 5, the transfer velocity shows little or no increase at low wind speeds (1–3 m/s), but increases significantly with increasing wind velocity

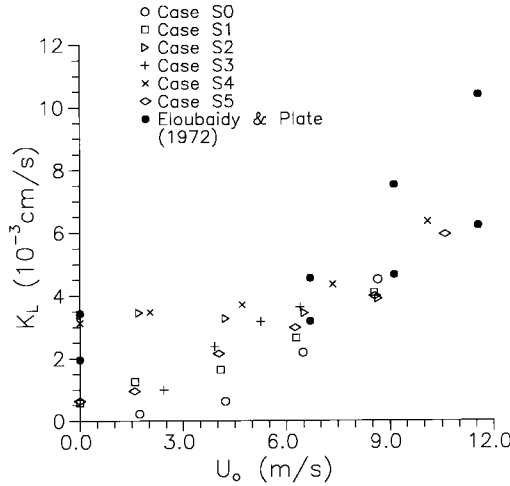


Figure 5: Transfer velocity K_L vs. U_o for all cases.

at high wind speeds (6–10 m/s). However, the threshold for the wind effect depends on the stream flow condition. For example, wind can enhance the transfer process in the slow-flowing stream flows (Cases S1, S3, and S5) even at low wind speeds (2–4 m/s), but does not show noticeable effects on K_L for fast stream flows (Cases S2 and S4) until in higher wind speeds (>7 m/s). By comparing Cases S1 and S3, one can see that under similar wind speed, the transfer velocity of counter-current flow is larger than that of co-current flow. The transfer velocity K_L is plotted against u_{*a} in Figure 6, which has a similar behavior as that shown in Figure 5. Due to the fact that *Eloubaidy & Plate* [1972] did not present the values of u_{*a} for their experiment, their results are not shown in Figure 6.

The magnitude of the bottom-shear induced transfer velocity K_{Lb} and the wind-shear induced transfer velocity K_{Lw} can be used as indicators for the regimes of dominance. The condition $K_{Lb} \gg K_{Lw}$ indicates a bottom-shear turbulence controlled transfer process, while $K_{Lb} \ll K_{Lw}$ represents wind-shear turbulence domination. The condition $K_{Lb} \approx K_{Lw}$ is the transition between two regimes, where both the bottom-shear and wind-shear are important. By using (3), (4) and (5) the transition regime happens when $u_{*a} > 15$ cm/s and

$$\left(\frac{U_w u_{*b}^2}{h} \right)^{1/8} \approx 0.042 u_{*a} \tag{6}$$

where u_{*a} , u_{*b} and U_w are in [cm/s], and h is in [cm].

Even with a criterion for the determination of the process that dominates the surface transfer, a predictive model is still needed for the transfer ve-

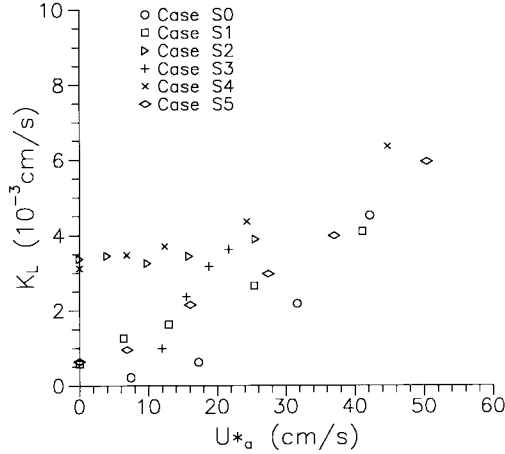


Figure 6: Transfer velocity K_L vs. u_{*a} for all cases.

locity in combined wind/bottom driven flows, especially for the transition regime, when both bottom-shear and wind-shear are important. The predictive model should consider the relative contributions of wind-shear and bottom-shear forcing on the gas transfer process. A mechanistic model is constructed by adding the transfer velocities caused by the bottom-shear and the wind-shear induced turbulence

$$K_{Lp} = K_{Lb} + K_{Lw} \quad (7)$$

Figure 7 shows the predicted K_L compared with the measured data K_L . As can be seen, this model shows reasonably good prediction compared with the measured data.

4 Conclusion

The dynamic coupling between wind and water plays an important role in the interfacial transfer of momentum, heat and mass between atmosphere and ocean. Most of the previous studies are concerned with the cases of water current without surface wind and surface wind blows over stagnant water. However, in many situations, such as slow-flowing streams, estuaries and coastal regions, water flow is driven by the bottom-shear and wind-shear at the same time. In this study, oxygen transfer in combined wind/stream driven flows was investigated experimentally in a laboratory wind-water tunnel. Reaeration rates were measured for a variety of co- and counter-current flow conditions. The results of pure wind-driven flows and

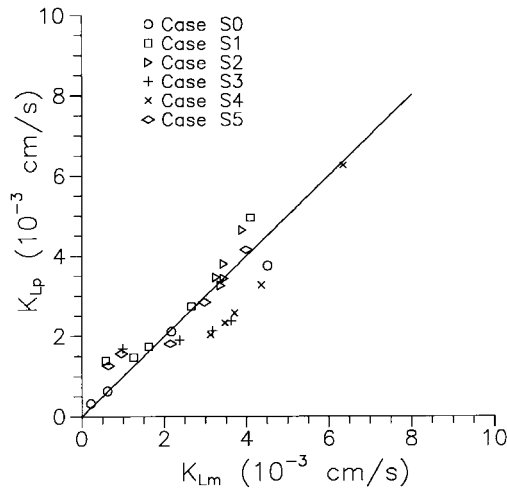


Figure 7: Predicted transfer velocity K_{Lp} compared with measured transfer velocity K_{Lm} .

pure open channel flows show good agreement compared with other similar laboratory studies. For pure wind-driven flows, air friction velocity u_{*a} is found to be a better parameter than the mean wind speed to describe the surface transfer mechanism. For pure open channel flows, transfer velocity is correlated with the energy of stream flow $((u_{*b})^2 U_w / h)^{1/4}$.

For wind/stream combined flows, transfer velocity shows little or no increase at low wind speeds range (1-3 m/s), but increases significantly with increasing wind velocity at high wind speeds range (6-10 m/s). However, the threshold for the wind effect depends on stream flow condition. Based on the magnitude of the bottom-shear induced transfer velocity and the wind-shear induced transfer velocity, a criterion was suggested to determine the dominant mechanism for reaeration in a combined wind/bottom driven flow. Furthermore, a predictive model to calculate the oxygen transfer velocity for combined wind/stream driven flows was proposed.

Acknowledgment

The authors would like to acknowledge support from the New York State Sea Grant program.

References

Cerco, C. F., Estimating estuarine reaeration rates, *J. of Environ. Eng.*, ASCE, Vol. 115, No. 5, 1066-1070, 1989

- Chu, C. R., Experiments on gas transfer and turbulence structure in free surface flows with combined wind/bottom shear, Ph. D. Dissertation, Cornell University, 1993
- Downing, A. L. and G. A. Truesdale, Some factors affecting the rate of solution of oxygen in water, *J. Appl. Chem.*, No. 5, 570-581, 1985
- Elmore, H. L. and W. F. West, Effect of water temperature on stream reaeration, *J. of Sanitary Eng.*, ASCE, Vol. 87, 59-71, 1961
- Eloubaidy, A. F., Wind waves and the reaeration coefficient in open channel flow, Ph. D. thesis, Colorado State Univ. Fort Collins, Colorado, 1969
- Eloubaidy, A. F. and E. J. Plate, Wind shear turbulence and reaeration coefficient, *J. of Hydraulics Div.*, ASCE, Vol. 98, No. HY1, 153-170, 1972
- Jähne, B., K. O. Münnich, R. Bösinger, A. Dutzi, W. Huber, and P. Libner, On the parameters influencing air-water gas exchange, *J. Geophys. Res.*, Vol. 92, No. C2, 1937-1949, 1987
- Kraft, K., Der Sauerstoffeintrag in eine windinduzierte Kanalströmung, Diploma thesis, Univ. of Karlsruhe, 1983
- Lamont, J. C. and D. S. Scott, An eddy-cell model of mass transfer in the surface of a turbulent liquid, *AIChE J.*, V. 16, 513-519, 1970
- Liss, P. S., Processes of gas exchange across an air-water interface, *Deep-Sea Res.*, 20, 221-238, 1973
- Mattingly, G. E., Experimental study of wind effects on reaeration, *J. of Hydraulics Div.*, ASCE, Vol. 103, No. HY3, 311-323, 1977
- Moog, D. B. and G. H. Jirka, Marco-roughness effects on stream reaeration, *Proceedings of Hydraulic Engineering National Conference*, Buffalo, G. V. Cotroneo and R. R. Rumer eds., 994-998, 1994
- Rathbun, R. E., Discussion of "Flume tests on hydrocarbon reaeration tracer gases", by J. D. Bales and E. R. Holley, *J. of Environ. Eng.*, ASCE, Vol. 114, No 2, 473-475, 1988

Macroroughness Effects on Stream Reaeration

Douglas B. Moog and Gerhard H. Jirka

DeFrees Hydraulics Lab., School of Civil & Environmental Engineering
Cornell University, Ithaca, NY 14853, USA

Abstract

The gas transfer coefficient is key to modeling dissolved oxygen levels in streams. Engineers commonly calculate it as a function of mean flow depth, velocity, and slope, with large predictive errors common. A set of laboratory studies measures oxygen absorption in flows over both smooth and large-roughness beds. It is found that the larger coefficients measured in the latter case may be explained by the greater rates of turbulent energy dissipation expected near the free surface — supporting a physically-based predictive equation incorporating bed roughness.

1 Introduction

Depressed *dissolved oxygen* (DO) levels in *streams* recover primarily through “*reaeration*”, the absorption of atmospheric oxygen. To model streams and allocate wasteloads, it is necessary to estimate the gas transfer coefficient K_L , relating the absorption flux F and DO deficit D :

$$F = H \frac{dD}{dt} = K_L D \quad (1)$$

where D is saturation minus bulk concentration, and H is mean flow depth.

Numerous studies have correlated K_L to mean stream parameters — slope S , velocity V , and depth H — generating a large number of competing equations with limited accuracy. Some commonly-employed equations are off by a factor of two or greater at least half the time [Moog & Jirka, 1995a]. The unsuitability of such simple correlations would seem to arise largely from the complex geometry of natural streams. One of the primary differences between simple, uniform flows and natural streams is that the resistance in many natural streams arises not only from shear friction at the channel bed, but also from drag produced by “*macroroughness elements*”, involving all or most of the flow depth. This study examines the effects of macroroughness by measuring K_L in both uniform and macrorough flows, evaluating theories of gas transfer in describing the uniform cases, and adapting the successful theory to the physics of macrorough flows.

2 Renewal Theory

The resistance to absorption at a free surface lies in a very thin, fluctuating concentration boundary layer near the air-water interface, within which the DO level varies from saturation to the bulk concentration. Its mean thickness, of order K_L/D_m (where D_m = molecular diffusivity) is smaller than the smallest turbulent motions, of scale $(\nu^3/\varepsilon)^{1/4}$ (where ν = kinematic viscosity and ε = turbulent energy dissipation rate), as shown by *Chu & Jirka* [1992] and found to hold for the experiments presented below.

This thinness means that the usual “mixing” mode of turbulent diffusion is replaced by one in which eddies from below impinge upon the concentration boundary layer, “renewing” it to the bulk concentration, after which molecular diffusion through the interface returns it toward saturation. One version of this theory is the renewal model of *Danckwerts* [1951], in which each impinging eddy reaches the free surface. Its result may be expressed as

$$K_L = \sqrt{D_m r} \quad (2)$$

where r is the mean frequency of *surface renewal*.

The parameter r has been estimated in various ways. The *large eddy model*, [*Fortescue & Pearson*, 1967] views renewal as governed by the largest-scale, energy-containing turbulent motions. Accordingly, r may be estimated as:

$$r = \frac{u'}{L} \propto \frac{u_*}{H} \quad (3)$$

where u' and L are turbulent macroscales for velocity and length, and u_* is the shear velocity. In the *small eddy model* [*Lamont & Scott*, 1970], the smallest turbulent motions control renewal. The free surface tends to filter out larger motions, and the thinness of the concentration boundary layer eliminates their size advantage. Having the smallest time scales, the smallest eddies should be able to most frequently renew the boundary layer. Estimating r as proportional to the inverse of the Kolmogorov time scale,

$$r \propto \left(\frac{\varepsilon}{\nu}\right)^{1/2}; \quad \varepsilon_s \sim \frac{u_*^3}{H} \quad (4)$$

where ε is the near-surface turbulent energy dissipation rate, estimated as ε_s for smooth, uniform flows (e. g., [*Nezu & Nakagawa*, 1993]). Nondimensionalizing K_L by u_* , both models result in

$$\frac{K_L}{u_*} \equiv K_L^+ \propto R_*^n S C^{-1/2} \quad (5)$$

where $R_* = u_*H/\nu$, the shear Reynolds number; and $Sc = D_m/\nu$, the Schmidt number. The large eddy model predicts $n = -1/2$, while the small eddy model predicts $n = -1/4$.

3 Smooth Channel Experiments

3.1 Procedures

The difference in R_* exponents provides a basis for testing, which formed one objective of a series of experiments in the *Tilting Wind-Water Tunnel* (TWWT) in the DeFrees Hydraulics Laboratory (described by [Moog & Jirka, 1995b]). The TWWT is a straight, recirculating flume with variable slope and a rectangular test channel of width 1 m and length 20 m. A pressure lid in the headtank lies above a series of turning vanes mounted on hinged, sliding parallelogram supports which move as the channel tilts - maintaining rectilinear flow upon entrance to the channel. Followed by boundary layer generating devices, this design minimizes entrance effects in the channel. The plexiglass and stainless steel channel and tanks, with 12-16" PVC return pipes, minimize the possible corrosion area.

Water was deoxygenated by bubbling nitrogen through a reservoir, in contrast to all similar previous studies, which used chemical deoxygenation. The prepared water was then pumped into the test loop and steady, uniform flow established. After enough time to attain a steady gradient of $\ln D$, nine to ten samples were taken at each end of the channel. The upstream samples were taken 3 m from the channel entrance, to permit further flow development prior to the test section. Sample DO levels were measured by the azide modification of the Winkler test, in calibrated 125 ml flasks to eliminate pouring - and using a diluted titrant, platinum-tipped microburet, and amperometric detection to attain high precision. With channel time-of-travel values derived from flow rates provided by an ultrasonic flowmeter (checked by salt tracers), these values permit calculation of K_L from (1).

4 Results

A series of tests was performed in a smooth channel at uniform flow depth from 2.5 to 10 cm and slope S from 0.00025 to 0.0010. Friction velocities were determined as $u_* = (gR_hS)^{1/2}$, where R_h = hydraulic radius. Results are shown in Figure 1, which includes the small-bed-roughness studies of Lau [1975], Gulliver & Halverson [1989], and Thackston & Krenkel [1969]. "Small bed roughness" was taken as $(k_s u_*)/\nu < 136$ (where k_s is the uniform roughness height) for which $\epsilon H u_*^{-3}$ has been shown to be invariant with roughness in the upper 70% of the flow depth [Nezu & Nakagawa, 1993]; for larger roughnesses, (4) may not be valid.

The TWWT data are about twice the magnitude of the other studies, including nearly identical runs of Lau [1975]. The reason is unknown. With

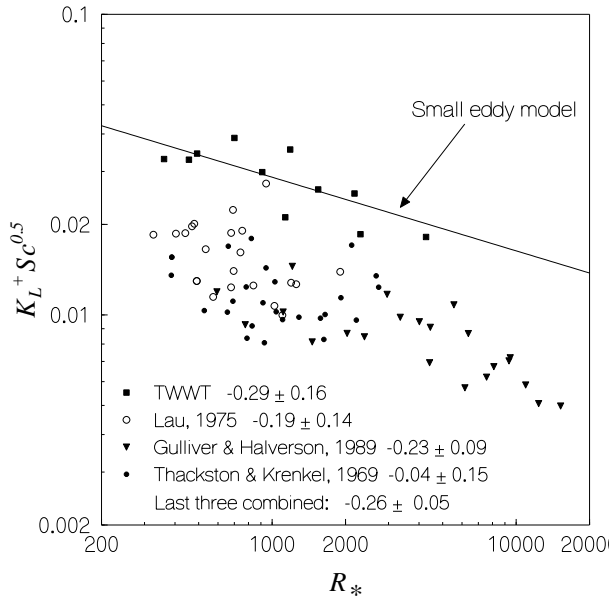


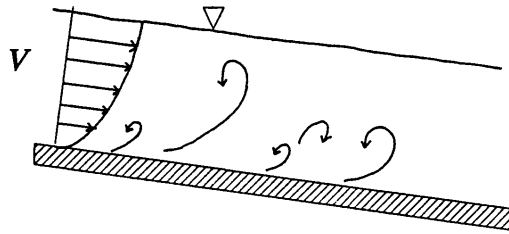
Figure 1: Oxygen absorption data for smooth and small-scale roughness channels. The small eddy model was evaluated with a coefficient calibrated to the TWWT data. Ranges indicate 95% confidence intervals for n in (5).

this caveat, the trends of the TWWT data and the other studies should be examined separately. Regression-based values for n listed in Fig. 1 show that, in all but the case of *Thackston & Krenkel*, it is close to the small eddy model value of $-1/4$. All preclude the large eddy model value of $-1/2$. On the basis of this and other evidence presented by *Moog* [1995], it is concluded that (4) provides proper scaling for the penetration model in smooth, uniform channel flow. By (2) and (4), K_L is controlled by the near-surface dissipation rate as

$$K_L = 0.161Sc^{-1/2}(\epsilon\nu)^{1/4} \quad (6)$$

where the coefficient of 0.161 was determined from the TWWT runs. This conclusion does not mean that large eddies are not active in surface renewal — they certainly carry turbulent energy to the surface — but rather that their influence is likely to be relatively invariant with Reynolds number.

Smooth or Small-Roughness Bed:



Large-Roughness Bed:

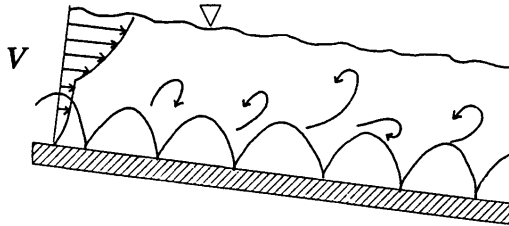


Figure 2: Establishment of steady, homogeneous mean velocity profiles in uniform flows over both smooth and large-roughness beds (schematic diagrams).

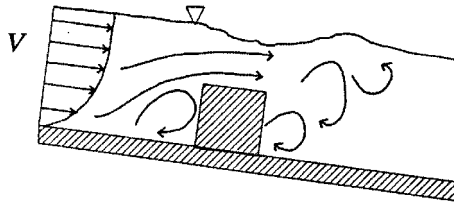
5 Macrorough Experiments

5.1 Characteristics of Macrorough Flow

Another series of runs was performed with bricks of height 5.7 cm placed in the channel, for flow depths from 2.5 to 20 cm. Fig. 2 depicts typical velocity profiles in uniform flows. Even when the bed roughness is large, a fairly steady velocity profile develops if the roughness is sufficiently uniform. By contrast, the brick flows, as in Fig. 3, were characterized by strong spatial variations in resistance, resulting in wakes, jets, and recirculation zones. Both depth and the mean velocity field varied in the spanwise and streamwise directions. This nonuniformity arose not only from the large size of the bricks, but from strong spatial variations in resistance. As illustrated in Fig. 3, high velocities could develop over the smooth bed before colliding with a brick, creating localized energy losses and distortions in velocity profiles, affecting most or all of the flow depth.

Macroroughness elements need not be individual rocks sitting on a flat bed; they may arise from any variations in the boundary comparable to the depth scale.

Submerged Macroroughness, Side View:



Unsubmerged Macroroughness, Plan View:

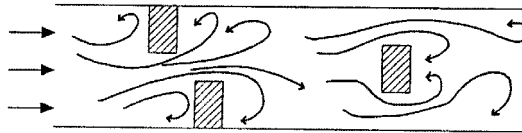


Figure 3: Nonuniformities created by variations in flow geometry and resistance, due to macroroughness elements in both submerged and unsubmerged flows.

6 Procedures

For the macrorough runs, the bricks were placed randomly upon the channel floor in two different concentrations, comprising 18.2% (“high density”) and 9.1% (“low density”) areal coverage of the original steel floor, in such a way as to avoid pooling. The entire 20 m test section was used, since there was no development of uniform flow. However, the macrorough flows were “globally” uniform in that the mean depth remained constant over distances exceeding the flow depth. For flows with unsubmerged bricks, the overall depth H was taken as the elevation of the mean water surface over the steel bed; for submerged flows, the mean displacement of the bricks was subtracted from this quantity. In calculating hydraulic radii, flow areas and perimeters were traced around the bricks. Use of these hydraulic radii - as opposed to those based on the smooth, rectangular bed - has a barely noticeable effect on the results (e. g., a 2% difference in the regression of K_L vs. $\varepsilon^{1/4}$).

7 Results and Analysis

The gas transfer coefficients for the macrorough runs are contrasted to the smooth-bed runs in Figure 4.

Four of the macrorough runs exhibited bubble entrainment; these are marked by crosses (\times). Their deviation is explained by *Moog* [1995] in terms of the Froude numbers of the over-brick flows. These point to a possible en-

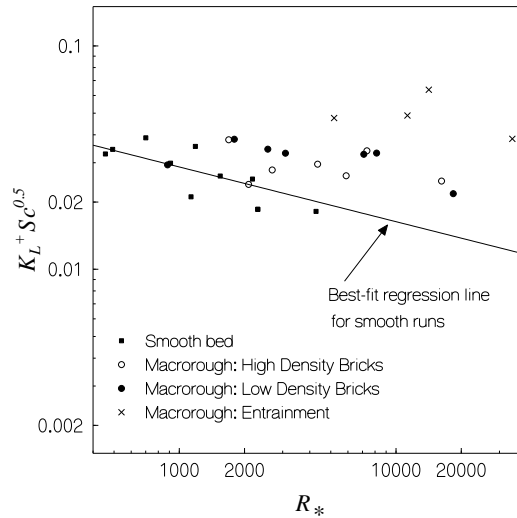


Figure 4: Dimensionless gas transfer coefficients for macrorough runs, compared to smooth-bed data.

hancement mechanism in stream flows not accounted for by renewal theory. The remainder of the present analysis will focus on the unentrained cases.

In Figure 5, K_L values for these are plotted against the small eddy model dissipation rate dependence, using (4) to estimate ε . They are seen to lie above the corresponding smooth-bed results. The smallest turbulent motions should behave independently of channel-scale geometry, reflecting only the local ε . The brick results may be reconciled to the small eddy model only if (4) tends to underpredict their near-surface dissipation rates.

Indeed, such is the case. In the wall region, where most production occurs, transport rates of turbulent energy are much smaller than production rates [Nezu & Nakagawa, 1993, pg. 80]. Therefore, most dissipation occurs close to the zone of production, where mean velocity gradients are largest. Thus, in smooth-channel flow, most dissipation occurs near the bed, well away from the free surface. In uniform, large-roughness flows, production by wakes or shear stresses is also greatest close to the bed, so most dissipation again takes place far from the free surface. Consequently, in uniform flow, the near-surface dissipation rate, which provides the energy for gas transfer, is much smaller than the mean rate of dissipation in the channel.

By contrast, turbulent production in the brick flows is not preferentially located near the bed. In these cases, resistance is dominated by local form drag. The energy dissipation occurs primarily in wakes and jets which typically involve the entire flow depth, as in Figure 3. *Turbulence* production — and thus dissipation — should occur much more uniformly throughout the flow depth. The near-surface ε would then exceed the estimate (4) for

smooth and small-roughness flows.

Since most of the energy dissipated by the stream passes through the turbulent cascade, and since this energy should be fairly uniformly distributed, ε might be estimated simply as the *total stream power* gSV . Indeed, using this expression in (7) brings the macroroughness predictions into close agreement with the smooth runs. Since gSV is a factor of V/u_* larger than ε_S , 2 to 20 times in streams, K_L could be as much as doubled by form drag.

Actual streams may reflect a more even partitioning of resistance between friction at the bed (i. e., “skin friction”) and form drag. Separation of these sources of resistance has long been an active area of research in fluvial hydraulics (e. g., [Karim, 1995]), in which the Darcy-Weisbach coefficient f and friction slope S_f are divided into contributions from *skin friction* (f' , $S_{f'}$) and *form drag* (f'' , $S_{f''}$): $f = f' + f''$ and $S_f = S_{f'} + S_{f''}$. The main difficulty for discharge prediction is the form drag contribution, but in the case of reaeration prediction, we presume to know f and S_f *a priori*. Thus, an estimate of f' is sufficient to estimate the fraction of total resistance attributable to form drag as

$$\phi = \frac{S - S_{f'}}{S} = 1 - \frac{f'V^2}{8gR_hS} \quad (7)$$

where ϕ is a “resistance partition coefficient” and $S = S_f$. If ϕ is calculated as negative for a stream, it may be set to zero as a case of pure skin friction. Applying (7) to the brick runs, with f' taken as the smooth-wall limit (as indicated by the smooth-bed runs), shows that over 90% of the total work performed against resistance is due to form drag, except for about 85% in the two cases with 20 cm flow depth.

8 Modified Small Eddy Model

It is desirable to modify the estimate of ε , to incorporate cases more evenly balanced between skin friction and form drag. This goal is accomplished by interpolating ε , between the extremes of pure skin friction ($\phi = 0$) and pure form drag ($\phi = 1$) as

$$\varepsilon_M = (1 - \phi)\varepsilon_S + \phi gSV \quad (8)$$

where the “macrorough near-surface dissipation rate” ε_M may be substituted for ε in (6) to predict K_L . The success of this modification is illustrated by contrasting Figure 5 to Figure 6, in which the smooth-bed dissipation rate estimate is replaced by ε_M from (8). The regression line for the macrorough runs drops from 38% above the smooth bed regression to within 1%. (For the smooth-bed runs, $\varepsilon_M = \varepsilon_S$.)

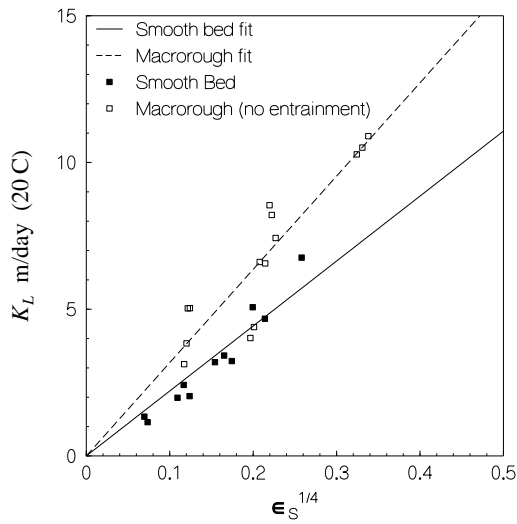


Figure 5: K_L scaled by small eddy model with smooth-bed dissipation rate estimated by (4).

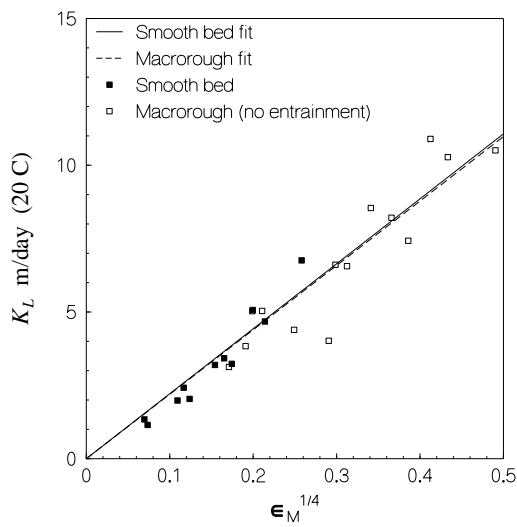


Figure 6: K_L scaled by small eddy model with macroroughness-modified dissipation rate.

In the modified small eddy model, (6) and (8), the only basic variable added to S , V , and H is f' in (7). Its determination may be left open. One good estimate for f' should be the formula of *Griffiths* [1981], obtained in straight, uniform gravel-lined channels with immobile beds:

$$\sqrt{f'} = 1.33D_{50}^{+0.287} \quad (9)$$

where D_{50}^+ is the median bed particle size divided by R_h . This scale should characterize skin friction, while the largest particles may contribute form drag similar to the bricks. To gain some insight into the likely degree of macroroughness enhancement, (6), (7), (8), and (9) were applied to roughness and flow data for 437 discharges in 78 New Zealand streams [*Hicks & Mason*, 1991]. For 34% of the cases, ϕ was set to zero. Examining the overall enhancement (i. e., K_L calculated using ε_M as opposed to ε_S), it is, perhaps surprisingly, greatest not for the largest D_{50}^+ but for the smallest. With ε_M , K_L is between 1 and 1.5 times larger for $D_{50}^+ > 0.01$, but is between 1.5 and 2 times larger for $D_{50}^+ > 0.01$. The reason is that streams with large median particles have low V/u_* ; velocities are too small to create strong depth-scale form drag. However, smoother beds permit greater acceleration and larger velocities between macroroughness elements, leading to large form drag. Additionally, sand-bed streams may generate bedforms which can act as macroroughness elements.

9 Conclusions

The small eddy model provides the proper Reynolds number dependence for oxygen transfer in smooth, uniform channels. Predictions may be improved by accounting for the increase in near-surface turbulent energy dissipation rates resulting from depth-scale form drag, i. e., macroroughness. The modified small eddy model provided this accounting accurately for experiments using bricks as macroroughness elements. The success of this modification is powerful for several reasons. It worked without specification of the macroroughness concentration (i. e., brick density). The macroroughness runs involved a number of very distinct flow types, from nearly braided flow around unsubmerged bricks to choppy flow over submerged bricks, as well as some backwatering, spillage, and recirculation. Excepting those involving bubble entrainment, the modification worked well for all flow types. It involved no fitted coefficients. The only additional field parameter is the bed particle size, a measurement well-established in stream resistance studies.

Further data are needed from combined roughness and reaeration studies. By estimating bed roughness and applying the above theory, engineers should be able to account for some of the complexity of natural streams, improving the accuracy of reaeration predictions and DO models.

Acknowledgements

The authors gratefully acknowledge the support of the U.S. Geological Survey and the DeFrees Family Foundation.

References

- Brumley, B. H. and G. H. Jirka, Near-surface turbulence in a grid-stirred tank, *J. Fluid Mech.*, 183, 235-263, 1987
- Chu, C. R. and G. H. Jirka, Turbulent gas flux measurements below the air-water interface of a grid-stirred tank, *Int. J. Heat Mass Transfer*, 35, 1957-1968, 1992
- Danckwerts, P. V., Significance of liquid-film coefficients in gas absorption, *Indust. & Eng. Chem.*, 43, 1460-1467, 1951
- Fortescue, G. E. and J. R. A. Pearson, On gas absorption into a turbulent liquid, *Chem. Engrg. Sci.*, 22, 1163-1176, 1967
- Griffiths, G. A., Flow resistance in coarse gravel bed rivers, *J. Hydraulics Div., Proc. ASCE*, 107, 899-918, 1981
- Gulliver, J. S., and M. J. Halverson, Air-water gas transfer in open channels, *Water Resources Res.*, 25, 1783-1793, 1989
- Hicks, D. M. and P. D. Mason, *Roughness Characteristics of New Zealand Rivers*, Water Resources Survey, Kilbirnie, Wellington, NZ, 1991
- Karim, F., Bed configuration and hydraulic resistance in alluvial-channel flows, *J. Hydr. Engrg.*, 121, 15-25, 1995.
- Lamont, J. C. and D. S. Scott, An eddy cell model of mass transfer into the surface of a turbulent liquid, *A.I.Ch.E. Jl.*, 16, 513-519, 1970
- Lau, Y. L., An experimental investigation of reaeration in open-channel flow, *Prog. in Water Tech.*, 7, 519-539, 1975
- Moog, D. B., Stream Reaeration and the Effects of Large-Scale Roughness and Bed-forms. Ph. D. Thesis, Cornell University, Ithaca, NY, 1995
- Moog, D. B. and G. H. Jirka, Analysis of reaeration equations using mean multiplicative error, *This volume*
- Moog, D. B. and G. H. Jirka, Tilting Wind-Water Tunnel, *This volume*
- Nezu, I. and H. Nakagawa, *Turbulence in Open-Channel Flows*, A. A. Balkema, Rotterdam, Netherlands, 1993
- Thackston, E. L. and P. A. Krenkel, Reaeration prediction in natural streams, *J. Sanitary Engrg. Div., Proc. ASCE*, 95, 65-93, 1969

Analysis of Reaeration Equations Using Mean Multiplicative Error

Douglas B. Moog, Gerhard H. Jirka

DeFrees Hydraulics Lab., School of Civil & Environmental Engineering
Cornell University, Ithaca, NY 14853, USA

Abstract

Modeling stream quality requires estimation of the “reaeration coefficient”, which controls the absorption rate of atmospheric oxygen. Numerous equations have been developed using depth, velocity and slope. This study shows that error metrics used to evaluate these equations in the past are biased toward underprediction. The “mean multiplicative error”, defined herein, overcomes this and other defects and provides a direct assessment of accuracy in predicting critical dissolved oxygen deficits. Application of this metric to selected equations and field data shows that predictability improves with slope, and that, compared to a constant coefficient, current equations are of little or no value below certain slopes. Additionally, some frequently-used equations are shown to have little general value. Those which perform well tend to employ the square root of the stream power.

1 Introduction

Sufficient *dissolved oxygen (DO)* levels are required in streams to maintain aquatic life. DO is most commonly depressed below equilibrium by biochemical oxidation, often in response to an organic waste discharge. Levels recover primarily through “*reaeration*”, the absorption of atmospheric oxygen. These opposing processes lead to a minimum DO value at some point downstream from a wastewater discharge. To model streams and allocate wasteloads, it is necessary to estimate the reaeration coefficient K_2 or the gas transfer coefficient K_L ; these are related to the reaeration rate dD/dt by:

$$K_2 = \frac{1}{D} \frac{dD}{dt} = \frac{K_L}{H} \quad (1)$$

where the “DO deficit” D is saturation minus bulk concentration, t is stream travel time, and H is mean depth. K_2 is the practical form, but as the inverse of the interfacial flux resistance, K_L provides a better basis for physical analysis and modeling.

K_2 is frequently determined by predictive equations employing mean stream parameters - generally depth H , velocity V , and slope S . Dozens of such equations have been developed and applied. While this abundance

Table 1: Commonly-used reaeration equations tested in this study.

	Authors	K_2 Equation (day ⁻¹ at 20 ° C)
OD	O'Connor and Dobbins [1958]	$K_2 = 3.90V^{0.5}H^{-1.5}$
CEB	Churchill et al. [1962]	$K_2 = 5.01V^{0.969}H^{-1.673}$
KO	Krenkel and Orlob [1962]	$K_2 = 173(SV)^{0.404}H^{-0.66}$
OEG	Owens et al. [1964]	$K_2 = 5.35V^{0.67}H^{-1.85}$
LD	Langbein and Durum [1967]	$K_2 = 5.14VH^{-0.67}$
CM	Cadwallader and McDonnell	$K_2 = 186(SV)^{0.5}H^{-1.0}$
TK	Thackston and Krenkel [1969]	$K_2 = 24.9(1 + F^{0.5})u_*H^{-1.0}$
PP	Parkhurst and Pomeroy [1972]	$K_2 = 23(1 + 0.17F^2)(SV)^{0.375}H^{-1}$
TN	Tsvoglou and Neal [1976]	$K_2 = \begin{matrix} 31, 200SV & Q < 0.28m^3/s \\ 22, 500SV & Q > 0.28m^3/s \end{matrix}$
SM	Smoot [1988]	$K_2 = 543S^{0.6236}V^{0.5325}H^{-0.7258}$
0	null model	$K_2 = 4.46$

Q , u_* , and F are discharge, friction velocity and Froude number.

K_2 is in base e units per day, H in m, and V and u_* in m/s.

Null model is K_2 set to the geometric mean of the full data set.

Evaluation of SM excluded data used to derive it.

reflects a great deal of effort, it also reflects the lack of an accurate general formula. This lack would appear to arise from the tremendous variability of channel beds and bed types, as well as nonhydraulic variables. *Parker and DeSimone* [1992] indicated that at lower slopes, surfactants and wind may be expected to play increasing roles, so that the performance of equations based on purely hydraulic variables should improve with slope.

In this study, the types of error metric generally used to assess equation performance are shown to be biased, and a proper standard is developed. Then this metric is applied to selected sets of predictive equations and field data - to evaluate them individually, identify successful patterns, and assess the variation of predictability with stream slope. A more detailed analysis is provided by *Moog* [1995].

2 Databases and Equations

Commonly-applied formulae are listed in Table 1. All are temperature-corrected to 20 °C. Also included is a “null model”, with K_2 set to a constant; an equation should be able to outperform it in order to be useful. KO, CM, TN, PP, and to a degree SM employ the product SV , which is proportional to the total energy dissipation rate, or “stream power”.

To evaluate these, a set of field data (331 points) was selected from tracer-based studies reporting slope, velocity, and depth, as listed in Table 2. Four of them, comprising Subset A, are known to employ high-accuracy hydraulic parameter measurements. For example, *Smoot* [1988] showed that the ap-

Table 2: Sources for data set

Parker and Gay* [1987]	Wilcock [1988]
Parker and DeSimone* [1992]	Genereux & Hemond [1992]
Ruhl and Smoot* [1987]	Shindala & Truax** [1980]
Smoot* [1988]	NCASI expert system** [Whittemore, 1991]
Stedfast and Draper [1986]	
* part of Subset A	** Consist of data from earlier studies

parent performance of a predictive equation improved dramatically when multiple cross-sections were used to determine depth and velocity for the field data. Another subset of 53 points was formed from reaches identified as riffle-pool type. Too few were identified as channel-controlled to form a contrasting set.

3 Error Metrics

3.1 Traditional

Previous studies evaluating *reaeration equations* (e. g., *Wilson and MacLeod* [1974]; *Rathbun* [1977]; *Parker and DeSimone* [1992]) have generally used normalized mean error (NME) or standard error (SE) to evaluate predictive performance:

$$NME = \frac{100\%}{N} \sum_{i=1}^N \left(\frac{K_P - K_M}{K_M} \right)_i; \quad SE = \left(\sum_{i=1}^N \frac{(K_P - K_M)_i^2}{N} \right)^{1/2} \quad (2)$$

where N is the number of reaeration measurements, K_P is the predicted value of K_2 or K_L , and K_M is the measured value. These metrics suffer from several important defects. One is the lack of scaling in the standard error; the residual $(K_P - K_M)$ which produces a small error in large K_2 (or K_L) values would be relatively large at small K_2 . It has also been criticized (*Wilson and Macleod* [1974]) for the squared residual, which causes it to focus on eliminating the largest errors. Since outliers and large errors (>100%) are very common in reaeration prediction, this criticism is warranted. The standard error's oversensitivity and lack of scaling are eliminated by *NME* — at the cost of measuring precision, since positive and negative errors cancel.

Probably the greatest defect in both is that they are based on the differential residuals $(K_P - K_M)$. Given the large errors common in reaeration prediction, such residuals create unintended distortions. While overestimates ($K_P > K_M$) are unbounded and often well over 100%, underestimates are limited to 100%. As a consequence, the distribution of residuals is skewed. An equation which tends to underpredict by a factor of two would be highly

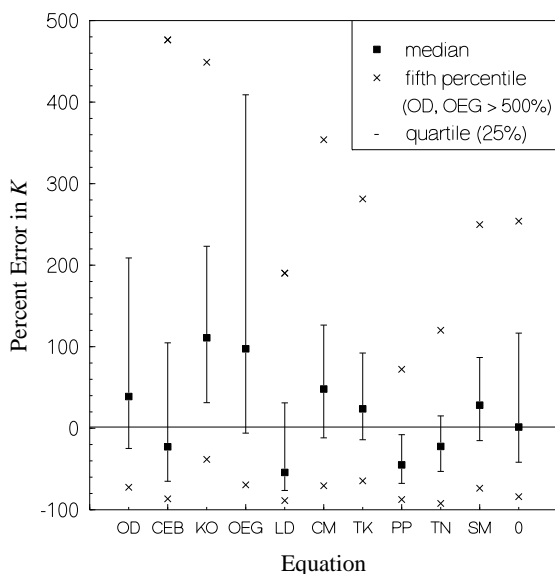


Figure 1: Distribution of differential residuals for equations compared to the full data set. Bars reach from lower to upper quartiles. Note Skew.

avored over one which tends to overpredict by a factor of two. Indeed, most predictive equations could be “improved” through multiplication by a constant less than one, i. e., intentional underprediction.

This skew is demonstrated in Figure 1 by plots of the residuals of the equations, as applied to the database described above. Half the errors lie beyond the bars, with 10% beyond the crosses (×). Generally, the lower quartile lies closer to the median than does the upper quartile. In effect, underpredictions are “compressed”, artificially improving the performance of equations which tend to underpredict, such as PP and TN. Equation PP was judged as a top performer in each of the fore-mentioned comparative studies despite - or because of - large, consistent underprediction.

3.2 Mean Multiplicative Error

The error metric should be based on what really matters in applying reaeration predictions. The primary goal is the prediction of the “critical deficit” D_{CR} , the maximum deficit downstream of a wastewater discharge. The solution for D presented by *Bennett and Rathbun* [1972] may be differentiated to provide D_{CR} for an initial deficit of zero. Defining L_a as the carbonaceous BOD of the discharge and K_1 as the deoxygenation coefficient, a plot of D_{CR}/L_a versus K_2/K_1 , as in Figure 2, shows a nearly logarithmic dependence of D_{CR} on K_2 .

Thus, errors in $\ln(K)$ are better measures of errors in D_{CR} than are errors

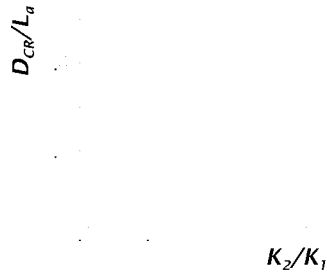


Figure 2: Variation of the critical DO deficit with K_2 .

in K . Overprediction by a factor m produces the same error as underprediction by m . A logarithmic residual, $\{\ln(K_P) - \ln(K_M)\}$, correctly equates these errors. *Bennett and Rathbun* [1972] defined E_{SL} , a version of the standard error using logarithmic residuals mapped asymptotically into the range 0 to 100, to define a “percent” error. Alternatively, the mean *multiplicative error* may be defined:

$$MME \equiv \exp \left[\frac{\sum_{i=1}^N |\ln(K_P/K_M)_i|}{N} \right] \quad (3)$$

It may be shown directly that the MME is the geometric mean of K_P/K_M . One may thus say that on average a certain equation is in error by a factor equal to the MME . An advantage over SE is that $MME(K_2) = MME(K_L)$. Then, equations which are judged most consistent with the physics are those which best predict reaeration. Also, the MME avoids squaring residuals, unlike E_{SL} and SE . Cancellation of residuals is avoided by the absolute values. In the following analysis, the MME is employed as the error metric, owing to its significant advantages: scaling, proper sensitivity, lack of bias in determining critical deficit, invariance with coefficient choice, and direct measurement of mean multiplicative error.

3.3 Calibration

Though variation with discharge limits the applicability of a measured K_2 , it could be used to calibrate the multiplicative coefficient in a predictive equation. The rest of the equation based on S , V , and H should reflect the contribution of the mean hydraulics to reaeration and thus to some degree account for the discharge dependence. Calibration would then partially account for the influence of heterogeneity and other variables.

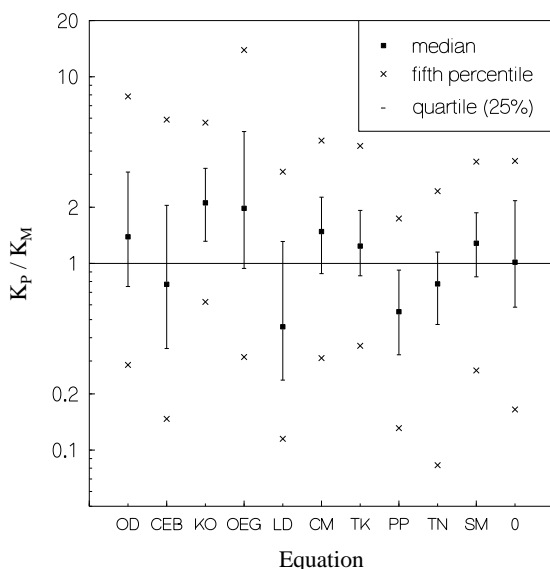


Figure 3: Distribution of multiplicative errors for equations compared to the full data set. Bars reach from lower to upper quartiles.

Consequently, one goal of evaluating equations should be to determine those with the best functional dependence. Figure 1 shows that much of the error in K_2 prediction arises from the deviation of the median prediction from that of the data set - i.e., miscalibration. To isolate functional dependence, MME 's were evaluated for calibrated forms, in which the multiplicative constants were adjusted to agree with the geometric mean of the data set.

4 Analysis of Predictive Equations

4.1 Uncalibrated Performance

The performance of the equations with original coefficients is illustrated in Figure 3 using mean multiplicative error, which shows much less skew. Calibration would simply shift the medians of the error ranges to unity. It is seen that errors in excess of a factor of two are commonplace. One typically has a greater than 10% chance of predicting a coefficient at least three times off. The underpredictive equations no longer appear superior.

4.2 Slope and Predictability

Figure 4 demonstrates the effect of slope on predictability by plotting MME 's of the calibrated equation KO versus various high-slope subsets, which con-

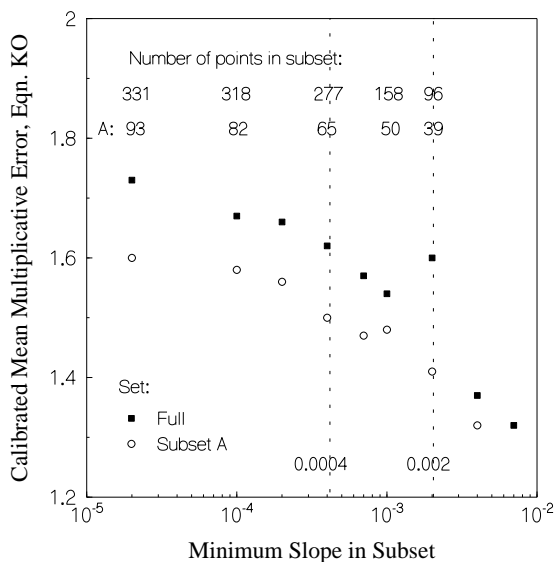


Figure 4: Each point represents the calibrated MME for equation KO applied to all points above the slope indicated on the horizontal axis.

tain all points above the “transition slope”. KO is typical of the best performers after calibration. It may be seen that error decreases steadily with transition slope (with one exception). This plot suggests three slope ranges for testing equations, delineated by $S = 0.0004$ and 0.002 , the latter being the transition slope of *Parker and DeSimone* [1992] and a common criterion used by hydrologists to denote *high-slope streams*.

The mean multiplicative errors of the calibrated equations are shown in Figure 5. The full data set has been divided into three subsets by slope, with a fourth overlapping set formed by reaches identified as “riffle-pool” type. Their slopes are almost entirely above 0.002 . The null model has been calibrated so that K_2 is equal to different values in each slope range, as listed at the top of the figure.

The accuracy and usefulness of predictive equations increase substantially with slope. For $S < 0.0004$, there appears to be little reason to use any of the tested equations, since the null model value of $K_2 = 2.14 \text{ day}^{-1}$ works better than any of them. For $0.0004 < S < 0.002$, six equations improve on the null model, but not by much. In the absence of hydraulic data, use of $K_2 = 3.27 \text{ day}^{-1}$ in this range is acceptable. For $S > 0.002$, a number of the equations improve substantially upon the null model. The thesis of *Parker and DeSimone* [1990] is supported.

Repeating Figure 5 for high-quality Subset A yields very similar results. The improvement in predictability with slope is steadier, and errors are lower. The same equations again perform best, with one exception; the per-

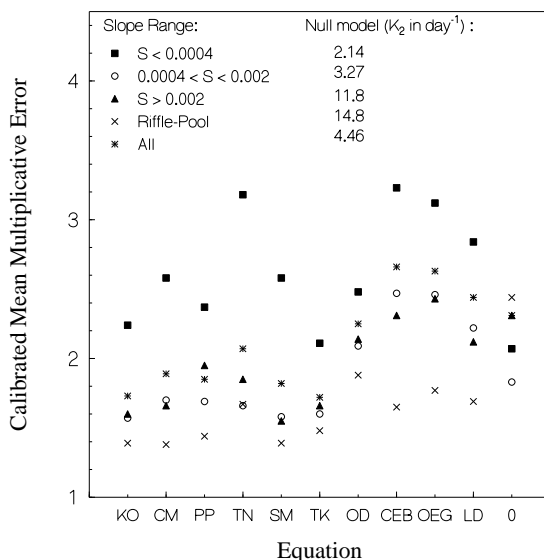


Figure 5: Mean multiplicative error of the equations calibrated separately to the slope ranges. The null model value for each slope range is listed at the top.

formance of TN is much poorer and shows no improvement over the null model in any slope range.

Even when a constant K_2 (null model) may be recommended, this does not mean that it is accurate; it means that predictive equations based solely on hydraulic variables are not adequate at low slopes. Since slopes below 0.002 are common, effective prediction of reaeration coefficients will require improved formulae. Clearly, these will require an expansion of variables beyond S , V , and H . Candidates include bed type, roughness, wind shear, and surfactants.

4.3 Comparative Performance

Equations KO, CM, SM, and TK were among the top performers regardless of slope range, bed type, calibration, or data set. Outperformed by the null model, OD, CEB, OEG, and LD have little or no predictive value, though they are among the most frequently applied. Most of the rest employ $(SV)^n$, with the best (KO, CM, SM) having n around 0.5. KO had a particularly large calibration adjustment, whereas SM worked well with its original coefficient. When applied to Subset A, CM performs best and TN much worse. With its greater sensitivity to stream slope, TN tends to be subject to more extreme errors. Since it exhibits no clear advantage on the average, its use is not recommended.

4.4 Stream Power

Physically, this comparison stresses the importance of the stream power SV , but at a lower sensitivity than in TN, for which $n = 1$. To check this dependence, linearized multiple regression was used to relate the natural logs of SV and H to that of K_L . (While this technique is biased in terms of K_L , $\ln(K_L)$ is in fact the variable of interest.) For $S > 0.002$,

$$K_L = 321(SV)^{0.530}H^{0.348} \quad \text{for } S > 0.002 \quad (4)$$

for which $r^2 = 0.687$. ANOVA indicates that SV dominates the regression, with the influence of H relatively minor ($F(SV) = 127; F(H) = 9.2$). For Subset A, accurate parameter measurements are more assured. For $S > 0.002$, depth is insignificant, and regression yields

$$K_L = 215(SV)^{0.526} \quad \text{for Subset A and } S > 0.002 \quad (5)$$

for which $r^2 = 0.615$, and the exponent has a 95% confidence interval (0.387 to 0.665) which coincides well with the range of exponents encountered in the SV models other than TN.

This last subset is the most likely to isolate hydrodynamic effects. Since riffle-pool bedforms are more prevalent at higher slopes, it may be that increasing depth dependence at lower slopes arises from correlation of slope to channel type (riffle-pool vs. channel-controlled). Other possible factors correlated to slope include bubble entrainment, surfactants, and wind. It is recommended that these phenomena be examined in field studies.

5 Conclusions

Mean multiplicative errors correct several defects of other metrics, including a bias toward underprediction, and provide the best gauge of errors in the critical dissolved oxygen deficit. Their application to a selected database reveals that predictability improves with stream slope. For slopes below 0.004, none of the tested equations improve upon a constant K_2 - nor do several of the most popular equations at any slope. The most successful equations generally employ the stream power, with an exponent of order 0.5. The poor or marginal performance of predictive equations compared to a constant K_2 for slopes below 0.002 indicates that effective prediction for most streams will require improved formulae and additional variables.

Acknowledgements

The authors appreciate the assistance of Ray C. Whittemore and the National Council of the Paper Industry for Air and Stream Improvement, Inc. in supplying reaeration data.

References

- Bennett, J. P. and Rathbun, R. E., *Reaeration in Open-Channel Flow*, U.S. Geological Survey Professional Paper 737, 1972
- Cadwallader, T. E. and A. J. McDonnell, A multivariate analysis of reaeration data, *Water Res.*, 3, 731-742, 1969
- Churchill, M. A., H. L. Elmore, and E. A. Buckingham, The prediction of stream reaeration rates, *J. Sanitary Engrg. Div.*, Proc. ASCE, 88, 1-46, 1962
- Genereux, D. P. and H. F. Hemond, Determination of gas exchange rate constants for a small stream on Walker Branch Watershed, Tennessee, *Water Res. Resch.*, 28, 2365-2374, 1992
- Krenkel, P. A. and G. T. Orlob, Turbulent diffusion and the reaeration coefficient, *J. Sanitary Engrg. Div.*, Proc. ASCE, 88, 53-116, 1962
- Langbein, W. B. and W. H. Durum, *The Aeration Capacity of Streams*, U.S.G.S. Circular 542, 1967
- Moog, D. B., *Stream Reaeration and the Effects of Large-Scale Roughness and Bed-forms*, Ph. D. Thesis, Cornell University, Ithaca, NY, 1995
- O'Connor, D. J. and W. E. Dobbins, Mechanism of reaeration in natural streams, *ASCE Transactions*, 123, 641-684, 1958
- Owens, M., R. W. Edwards, and J. W. Gibbs, Some reaeration studies in streams, *Int. J. Air Water Polln.*, 8, 469-486, 1964
- Parker, G. W. and F. B. Gay, *A Procedure for Estimating Reaeration Coefficients for Massachusetts Streams*, U.S.G.S. Report WRI 86-4111, 1987
- Parker, G. W. and L. A. DeSimone, *Estimating Reaeration Coefficients for Low-Slope Streams in Massachusetts and New York*, 1985-88, U.S.G.S. Report WRI 91-4188, 1992
- Parkhurst, J. D. and R. D. Pomeroy, Oxygen absorption in streams, *J. Sanitary Engrg. Div.*, Proc. ASCE, 98, 101-124, 1972
- Rathbun, R. E., Reaeration coefficients of streams - state-of-the-art, *J. Hydr. Div.*, Proc. ASCE, 103, 409-424, 1977
- Ruhl, K. J. and J. L. Smoot, *Mean Velocity, Longitudinal Dispersion, and Reaeration Characteristics of Selected Streams in the Kentucky River Basin*, U.S.G.S. Report WRI 87-4179, 1987
- Shindala, A. and D. T. Truax, *Reaeration Characteristics of Small Streams*, prep. for Miss. Dept. of Nat. Res., Bureau of Pollution Ctrl., Jackson, Miss., 1980
- Smoot, J. L., *An Examination of Stream Reaeration Coefficients and Hydraulic Conditions in a Pool-And-Riffle Stream*, Ph. D. Thesis, Virginia Poly. Inst. and State Univ., Blacksburg, VA., 1988
- Stedfast, D. A. and R. E. Draper, *Reaeration Coefficients of Six Streams in New York*, U.S.G.S. Report WRI 85-4028, 1986
- Thackston, E. L. and P. A. Krenkel, Reaeration prediction in natural streams, *J. Sanitary Engrg. Div.*, Proc. ASCE, 95, 65-93, 1969
- Tsivoglou, E. C. and L. A. Neal, Tracer measurement of reaeration: part III - predicting the reaeration capacity of inland streams, *Water Poll. Ctrl. Fed. J.*, 48, 2669-2689, 1976
- Whittemore, R. C., Development of an expert system for estimating stream reaeration rates, 378-385 in *Air-Water Mass Transfer*, S. C. Wilhelms and J. S. Gulliver, eds., publ. ASCE, NY, 1991

Wilcock, R. J., Study of river reaeration at different flow rates, *J. Env. Engrg.*, 114, 91-105, 1988

Wilson, G. T. and N. Macleod, A critical appraisal of empirical equations and models for the prediction of the coefficient of reaeration of deoxygenated water, *Water Research*, 8, 341-366, 1974

An Observational Study of the Aqueous Surface Layer Structure Beneath a Wind-Driven Air-Water Interface

Michael L. Banner and William L. Peirson

School of Mathematics, University of New South Wales
Sydney, Australia

Abstract

The detailed structure of the aqueous surface layer flow immediately adjacent to the wind-driven air-water interface is investigated in a laboratory wind-wave flume using Particle Image Velocimetry (PIV) techniques. An initial goal is to investigate quantitatively the character of the flow in this crucial, very thin region and in particular to examine critically the conclusions of *Okuda et al.* [1977], henceforth O77. These authors have argued that for very short, strongly forced wind wave conditions, shear stress is the dominant mechanism for transmitting the atmospheric wind stress into the water motion - waves and surface drift currents. In contrast, other authors have more recently observed very substantial normal stress contributions on the air side. O77 also reported that the breaking (without air entrainment) of these wind waves resulted in strong downward convective motions. The availability of PIV and associated image technology now permits a timely re-examination of their results, which have been influential in shaping present perceptions of the physics of this dynamically important region. The PIV technique used in the present study overcomes many of the inherent shortcomings of hydrogen bubble measurements.

Initial results obtained here cast considerable doubt on the conclusions of O77 and suggest a reconciliation for the question of relative importance of normal and tangential stresses at the interface.

1 Introduction

Nearly twenty years ago, *Banner and Melville* [1976] reported laboratory observations of *air flow separation* over breaking wave crests. It was concluded that flow separation and *wind stress enhancement* were directly associated with wave breaking. This work indicated that form drag (consistent with the 'sheltering hypothesis' of *Jeffreys* [1924, 1925] was an important contributor to the flux of momentum between the atmosphere and the surface wave field. About the same time, detailed laboratory studies were undertaken to examine the structure of the aqueous boundary layer at the air-sea interface by *Okuda et al.* [1977], henceforth O77. These studies were directed at quantifying the tangential stresses at the interface by estimating the near

surface shear. The near surface shear was deduced from flow visualisation using hydrogen bubble lines created by a surface-piercing wire. It was concluded that for strongly wind-forced wavelets at relatively short fetches (2.85 m), the wind stress was predominantly supported by the skin friction or *tangential stresses*. Consequently, it was concluded that the contribution of *form drag* (or *normal stresses*) was limited to but a few percent of the total stress. Somewhat later, a detailed study of surface pressure distributions over laboratory wind-ruffled, mechanically triggered waves was reported by *Banner* (1990). Measured surface pressure distributions were used to compute the form drag over wind waves. In contrast with the results of O77, it was concluded that, for such conditions, the form drag was dominant, being equal to approximately $O(0.7 \text{ to } 0.8)$ of the total wind stress.

We have undertaken further studies here in an effort to reconcile the disparities between these two conflicting conclusions. In particular, particle image velocimetry (PIV) has presented an opportunity to review the estimates of tangential stresses near the interface. In this contribution, previous studies of surface tangential stresses are reviewed, the experimental equipment used for the present investigation is described, a comparison of PIV results is made with previous results inferred from hydrogen bubble analyses, and initial conclusions are drawn on the relative importance of normal and tangential stress contributions to the overall *interfacial wind stress*. A brief discussion of the role other small scale free-surface processes is included.

2 Previous Free Surface Studies

Whilst many studies have examined surface wind driven velocities with relatively large ($>1 \text{ mm}$) tracers, few investigators have attempted experiments with particle tracers of sufficiently small scale to reliably measure the near-surface shear in the aqueous *viscous sublayer*.

The earliest experimental studies of surface shear were initiated by *McLeish and Putland* [1975]. These were not intended to be comprehensive but to support conclusions about surface heat transfer. Hydrogen bubbles were used in a laboratory flume to visualise flow within the near-surface layer, whose motion was captured by photographs of 62.5 ms exposure. At very short (unspecified) fetch before wind waves had developed, the tangential stresses at the water were reported to be 0.1 and 0.2 Pa for wind speeds of 5.5 and 9.0 m/s respectively. Further downwind in a region of initial wind wave development, they reported a reduction in the indicated stress (0.07 Pa) for a 5.5 m/s wind. A second and far more detailed study was undertaken shortly afterwards by O77. This was conducted in a wind-wave tunnel 50 mm wide and 4.55 m long with an air section 170 mm high and a water depth of 530 mm. Observations were made of wind waves generated at a fetch of 2.85 m with a mean wind speed of 6.2 m/s. The characteristic wave period, length and height of the generated wavelets at this fetch were 0.23 s, 83 mm and 9.4 mm respectively. Hydrogen bubbles were used to visualise

and quantify the flow field. These were generated using a $50\ \mu\text{m}$ diameter platinum wire and generated every 40 ms with a pulse of 2 ms duration. The bubbles were illuminated by a stroboscope and the images captured by a cine camera with 24 ms between exposures. The authors made a number of significant improvements in their technique over that used by McLeish and Putland. In particular, the size of the generated bubbles was recorded, the rise velocities were inferred and corrections were made to the bubble trajectories for the buoyant rise of the bubbles. The near-surface shear along the wave profile was assessed in terms of its magnitude and the thickness of the viscous layer. Strong tangential stresses were indicated on the upwind face of the waves, increasing in intensity towards the crest. On the lee face of the waves, the tangential stresses were assessed as being negligible. The stress supported by the tangential shear was estimated to be between 0.36 and 0.40 Pa. These stresses were shown to increase from about 0.1 Pa in the trough to a value of between 1.2 and 1.6 Pa just upwind of the crest. The total stress computed from the mean wind profile was given as 0.30 Pa. It was therefore concluded by O77 that the normal stresses were negligible and the tangential stresses dominated the interfacial wind stress. Their results also imply a dominant contribution of the shear stresses to the wave-coherent stress.

These results have led other authors to speculate on the dominant role of shear stress contributions (e. g., *Csanady* [1985, 1990] amongst others) in air-sea momentum exchange. However, as attractive as this viewpoint may seem, there are potentially serious problems associated with the underlying supportive data provided by O77. In particular, difficulties appear to arise with the quantitative use of hydrogen bubble measurements. These are well documented in the literature [e. g., *Wilkinson and Willoughby*, 1981]. In the case of O77, there seems to have been no account taken of wire wake effects, the unknown interaction of bubbles with a rapidly varying free surface meniscus and the relatively large bubble size ($\sim 140\ \mu\text{m}$ dia.) in relation to the viscous sublayer thickness. It may be reasonably argued that such previous studies of the aqueous surface boundary layer using hydrogen bubbles may have had some serious problems with their methodology and their conclusions are open to question. The next section describes a laboratory study designed to overcome some of these shortcomings.

3 Experimental Configuration

The experimental facility used is similar to that used by *Banner* [1990]. The wind-wave tank is 220 mm wide and 8 m long, with a wind tunnel section transitioning smoothly over the water surface. For the experiments described here the depth of water was 200 mm with a 650 mm air space above, with two fetches of 2.45 m and 3.1 m used in the present study. The wind waves generated at these very short fetches have wavelengths of $O(100\ \text{mm})$, and are overdriven by the wind input and describable as generally in a state

of *micro-scale breaking*. An attempt was made to quantify the microscale breaking level by recording the percent passage rate of breaking wavelets past the measurement site.

To carry out the primary goals of this study, a specialised high resolution *particle image velocimetry (PIV)* system has been developed to examine near-surface currents beneath wind generated wavelets with wavelengths of $O(10\text{ cm})$ that are comparable in scale with those examined by O77. This wavelet scale is commonly associated with wind gusting over the ocean. The PIV system consists of:

Light sheet generator and tracers. A 6W water-cooled argon ion laser with its beam directed at a rotating wheel with high quality optical mirrors mounted on its periphery has been used to provide a pulse light generator with a pulse period of approximately 2 ms. A pulsed *light sheet* about 1 mm thick and 80 mm wide was formed by illumination of the flow through a glass panel in the floor of the wave tank. The tracers used were fluorescent particles with diameters of 20 to 60 μm and a relative density of 1.2.

Velocity field image capture. A Kodak Megaplug CCD camera with an effective resolution of 1280 (horizontal) \times 1028 (vertical) pixels was used to capture images of velocity fields below the water surface. The camera was fitted with a telephoto zoom lens (focal length 80 to 200 mm) and an extension bellows so that a region approximately 15 \times 10 mm on the flume centre-line could be imaged. The CCD camera has attendant hardware to enable single images to be downloaded rapidly to a controlling PC. This camera was mounted looking slightly upward at 7.5° to allow a clear view of the sub-surface interface.

Detection of the free surface. The laser light sheet created a well-defined line in the water surface when viewed from above. This optical property of the interface was used to provide measurements of the water surface profile and hence the phase location for the sub-surface images. This was achieved with a second CCD camera, fitted with a 25 mm focal length lens, mounted rigidly above the first and viewing the surface at 12.5° from above. A frame grabbing card mounted in the PC bus was used to capture these images. Considerable testing and software development were required to align the two camera images in both time and space. This was achieved using an opto-coupler trigger mounted on the mirrored wheel.

Image analysis. A system was developed to examine the very near surface region within 2 mm of the local interface. This required software that enabled direct displacement measurements to be made on captured particle images at the camera resolution. This technique relied on identifying near surface particles by their reflections in the underside of the wave surface. As noted by O77, relatively clear reflections of subsurface particles can be observed under the relatively smooth rear face of the wave. As may be seen in Figures 1a and 1b, particles at varying distances from the surface can be identified by their multiple point images and subsurface reflections produced by the multiple pulsing of the laser beam.

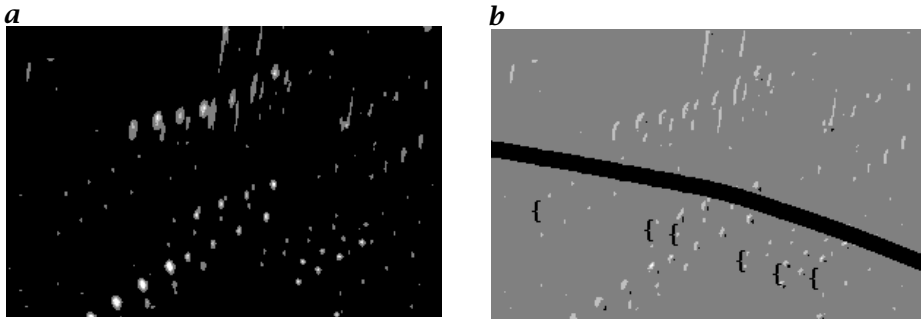


Figure 1: **a** A subimage of a region $3.75 \text{ mm} \times 2.5 \text{ mm}$ containing a number of particles in close proximity to the surface of a wind-driven wavelet. **b** As for **a** but with each near-surface particle image-reflection pair associated with the fourth light pulse indicated by a brace. The estimated free surface position for the first light pulse is represented by the heavy line.

Calculations have shown that for small angles of view, the position of the interface can be reliably located as being at the mid-point between a particle and its reflection. Given the laser pulsing frequency, both the velocity and location of individual particles could be determined. By differencing the velocities and depths of the two centre images of each of the two proximate particles, the shear stress could be determined by division of velocity difference by vertical particle separation. It is recognised that the differencing inherent in this methodology may generate potentially large errors. To examine this in detail we calculated shear stress estimates from ten typical particle pairs. We calculated the shear amongst all combinations of points from the four-point particle images and found an RMS uncertainty of $\pm 0.04 \text{ Pa}$. However, it is noted that the variations in the computed velocities include local flow unsteadiness. A second method was therefore used to estimate error levels. With our standard technique, we made 36 measurements of near surface shear stresses for paddle generated waves with no wind forcing. A mean tangential stress of 0.002 Pa was observed with an RMS variability of 0.022 Pa . This would appear to be more indicative of error levels inherent in the method.

4 Results and Discussion

The experiments reported here are for three short fetch cases: 0.13 m , 2.45 m and 3.1 m with the same nominal centreline wind speed $U_c = 6.2 \text{ m/s}$. The relevant details of wind and wave properties are summarised in Table 1. In this table, the wind friction velocity u_{*a} and the air roughness length z_{0a} were determined from mean velocity profiles measured with a miniature Pitot-static probe connected to a high resolution electronic manome-

Table 1: Experiment wind and wave conditions. O77 conditions are shown in fifth column.

		Present study		O77
fetch (m)	0.13	2.45	3.10	2.85
peak observed frequency (Hz)	0.0	4.46	3.81	4.34
approx. mean wavelength (mm)	0.0	77	120	83
mean char. wave height (mm)	0.0	6.0	7.2	9.4
mean wave energy (mm ²)	0.0	5×10^{-6}	10.4×10^{-6}	-
wind friction velocity u_* (m/s)	0.25	0.37	0.43	0.497
wind stress t (Pa)	0.08	0.17	0.23	0.30
roughness length z_o (mm)	0.0033	0.07	0.17	0.33
mean tang. stress τ_{tang} (Pa)	0.07	0.07	0.05	0.36
mean surface current (m/s)	0.120	0.093	0.073	-
mean $\tau_{tang} * u_{orb}/c$ (Pa)	0.0	0.008	0.006	-
estimated breaking fraction	0.0	0.7	0.6	-
number of observations	20	151	139	80 waves

ter. The measurements at 0.13 m fetch served the dual purpose of verifying the reliability of the technique and confirming that the entire wind stress is supported by the tangential stresses in the absence of waves. For the longer fetch cases, the wave properties were recorded using a high resolution impedance wire probe digitised at a rate of 1 kHz. This high digitisation rate was used for the detection of microscale breaking passage rate, which followed the procedure used by *Banner* [1990]. The propagation of these short fetch waves is influenced to an extent by advection by the drift current. Consequently, the mean wavelength in each case was determined using elevation profile measurements based on optical techniques. The drift current correction to the phase speed was found to be zero at fetches less than 2.45 m and approximately $0.1u_{*a}$ for the 3.1 m fetch.

The shear stress distributions along the wave profile and related results are shown in Figures 2 and 3, in which Figure 2 is for the shorter (2.45 m) fetch. In each of these composite figures, the uppermost panel shows the measured average wave surface profile. The second panel shows the individual data points in the surface velocity distribution. The third panel shows the distribution of the surface shear stress data points relative to the wave crest, based on about 140 measurements located within 1 mm of the interface. No data is shown in the trough regions because of the presence of transient patches of capillary waves. These created very substantial variability associated with their strong shear levels [e. g., see *Longuet-Higgins* [1992] and this made it impossible to characterise the local wind-induced shear stress. Because of this effect and the results of previous studies [O77, *Banner*, 1990] that the leeward side airflow is separated, the tangential stress is assumed to vanish and τ_{tang} was set to zero in this region. The fourth panel shows

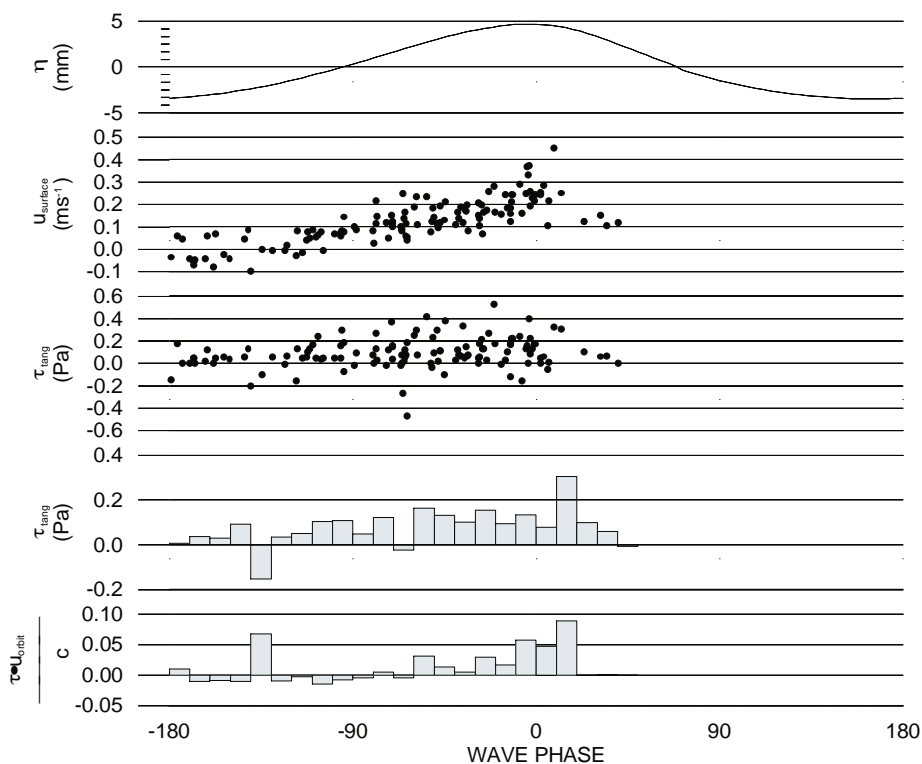


Figure 2: Fetch: 2.45 m – Wave profile with distributions of surface velocity, shear stress, 10° binned shear stress, and 10° binned wave-coherent shear stress.

the same shear stress data binned over 10° of phase. The fifth panel shows the wave-coherent shear stress $\langle \tau u_o / c \rangle$, in which the local surface orbital velocity u_o was generated by subtracting the overall mean velocity $\langle u_s \rangle$ from the measured surface velocity distribution along the wave. Finally, a comparison of the present shear stress results with O77 is given in Figure 4, which shows the distribution of dimensionless shear stress using $U_{\lambda/2}$ as the normalising velocity (where λ is the spectral peak wavelength). It is very evident in this figure that the present results represent significantly reduced relative shear stress levels.

5 Conclusions

We have successfully measured representative shear stress levels in the aqueous viscous sublayer immediately below strongly forced, very short wind-driven wavelets in a laboratory wind wave tank, together with complementary properties of the wind stress based on logarithmic mean velocity

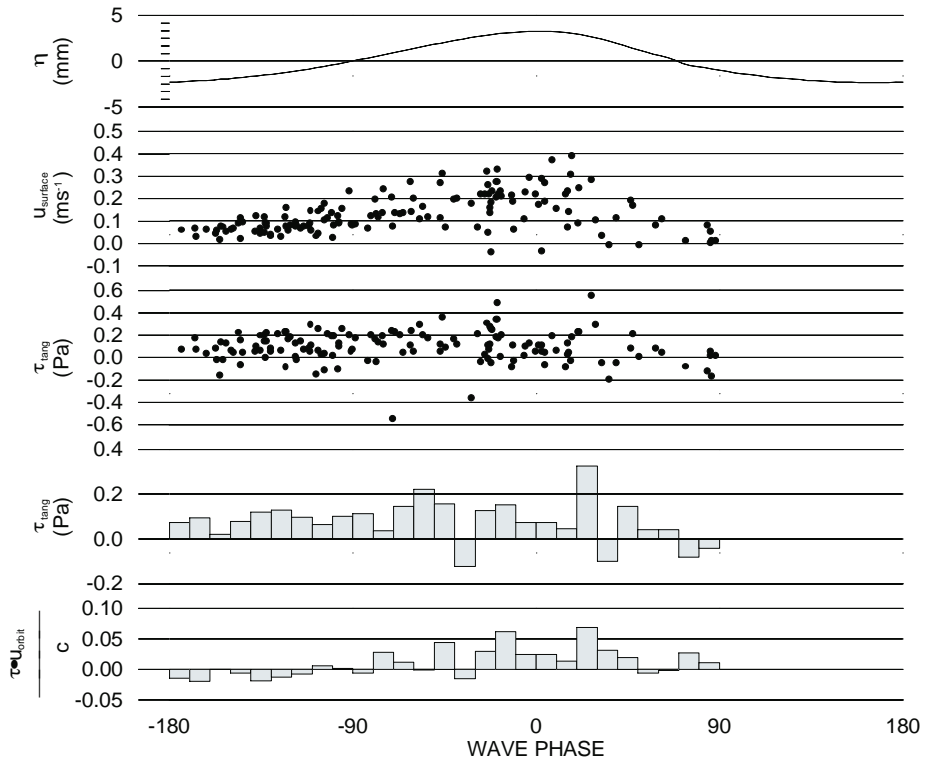


Figure 3: Fetch: 3.1 m —Wave profile with distributions of surface velocity, shear stress, 10° binned shear stress, and 10° binned wave-coherent shear stress.

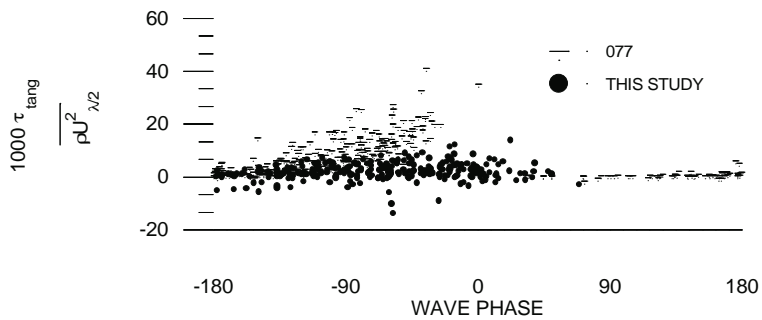


Figure 4: Normalised surface shear stresses as recorded by O77 compared with data gathered within this investigation.

profiling. The initial results obtained in this study provide the following conclusions:

1. tangential stress in the surface layer immediately beneath a wind-driven wavy interface contributes significantly to the interfacial stress for very short fetch conditions in the absence of any background large-scale waves. Indeed, in the absence of waves the entire wind stress is supported by the tangential stresses. However, tangential stress in the aqueous viscous sublayer does not account for the entire wind stress in the presence of waves, contrary to the conclusions of O77. We attribute their conclusion to experimental errors inherent in their hydrogen bubble methodology.
2. the relative contribution that tangential stress makes to the overall wind stress depends strongly on the stage of development of the wind waves. Before the onset of wind waves, the wind stress is entirely supported by tangential stress. As the wave field develops, the wave form drag component becomes increasingly important and provides the dominant contribution. From the present results, at a fetch of 2.45 m, the fraction of the total wind stress that is supported by tangential stress in the viscous sublayer is $O(0.4)$. This decreases to about $O(0.2)$ at 3.1 m fetch. This is consistent with the results of Banner [1990], who reported that at longer wave tank fetches with further developed waves, the fraction of tangential stress to the overall wind stress decreases to about $O(0.25)$.
3. our preliminary larger scale PIV measurements of the flow surrounding microscale breaking events produced no evidence of the deep convective motions reported by O77. Rather, the influence of these regions was locally compact, resulting in enhanced turbulent diffusion below and rearward of the spilling region, rather than deep convection. Further work on quantifying this important aspect of interfacial transport is in progress.
4. there was evidence of modulated tangential stress in phase with the wave elevation. However the associated wave-coherent shear stress levels were estimated here as typically only a small [$O(0.05)$] fraction of τ , indicating that form drag dominates the wave-coherent momentum flux. This is consistent with conclusion (2) above.
5. we observed variability in the PIV-inferred shear values in the aqueous viscous sublayer. This is believed to be associated with several potential sources including turbulent fluctuations and transient capillary waves.

Acknowledgements

The authors gratefully acknowledge the support provided for this research project by the Australian Research Council and the use of facilities at the University of NSW, Water Research Laboratory.

References

- Banner, M. L. The influence of wave breaking on the surface pressure distribution in wind-wave interactions, *J. Fluid. Mech.* 211, 463-495, 1990
- Banner, M. L. and Melville, W. K. On the separation of air flow over water waves, *J. Fluid. Mech.* 77, 825-842, 1976
- Csanady, G. T. Air-sea Momentum transfer by means of short crested wavelets, *J. Phys. Oceanogr.* 15, 1486-1501, 1985
- Csanady, G. T. Momentum flux in breaking wavelets, *J. Geophys. Res.* 95, 13289-13299, 1990
- Jeffreys, H. On the formation of waves by wind, *Proc. Roy. Soc.* A107, 189, 1924
- Jeffreys, H. On the formation of waves by wind, II *Proc. Roy. Soc.* A 110, 341, 1925
- McLeish, W. and Putland, G. E. Measurements of wind-driven flow profiles in the top millimeter of water, *J. Phys. Oceanogr.* 5, 516-518, 1975
- Longuet-Higgins, M. S. Capillary rollers and bores, *J. Fluid Mech.* 240, 659-679, 1992
- Okuda, K. Kawai, S. and Toba, Y. Measurement of skin friction distribution along the surface of wind waves, *J. Oceanogr. Soc. Jap.* 30, 190-198, 1977
- Wilkinson, D. L. and Willoughby, M. A. Velocity measurements with hydrogen bubbles - the wake effect, *J. Hydraulic Res.* 19, 141-153, 1981

Measurements of Enhanced Turbulence in Short Wind-Induced Water Waves

Frank Hering¹, Dietmar Wierzimok^{1*}, and Bernd Jähne²

¹Institute for Environmental Physics, University of Heidelberg
Im Neuenheimer Feld 366, D-69120 Heidelberg, Germany
email: fhering@davinci.uphys.uni-heidelberg.de

²Scripps Institution of Oceanography, Physical Oceanography Res. Div.
La Jolla, CA 92093-0230, USA
email: bjaehne@ucsd.edu

doi: 10.5281/zenodo.10328

Abstract

Particle Tracking Velocimetry was used to study turbulence beneath short wind-induced water-waves at the circular wind-wave facility of the Institute for Environmental Physics. Recording image sequences at up to 200 Hz allow an extensive study of the flow field. An automatic tracking algorithm was developed for the evaluation of the trajectories. Monte Carlo simulations show that Lagrangian flow field measurements offer an ideal approach to the study of drift profiles (mass transport) in the turbulent wave region. Also bulk velocity and surface velocities can be calculated. A measure for the turbulence was gained by the calculation of the friction velocity profile by correlating horizontal and vertical velocity components (eddy correlation technique).

1 Introduction

A *particle tracking* technique working with a high particle concentration for the measurement of flow fields beneath water waves was used. It features a 1–4 cm thick light sheet parallel to the main wave propagation direction so that the seeding particles stay long enough in the illuminated area to enable tracking over several wave periods (Figure 1). An area of $10.0 \times 10.0 \text{ cm}^2$ is observed by a CCD camera (Dalsa CA-D1-0256) with up to 200 images/s (Figure 2). An automatic tracking algorithm was developed allowing particles to be individually tracked over more than 400 images at particle concentrations up to 800 particles/image. As a result both the Lagrangian and the Eulerian vector field is measured. Details on technique and algorithms are reported by *Hering et al.* [1995]. This paper describes the appliance of *PTV* to the study of turbulence beneath short wind-Induced water waves. In section 2 various Monte Carlo simulations show, that mean properties of a flow (such as drift or friction velocity) can more easily and accurately be extracted close to the wavy free water surface from the Lagrangian flow

*Now affiliated to IBM Research Center Heidelberg

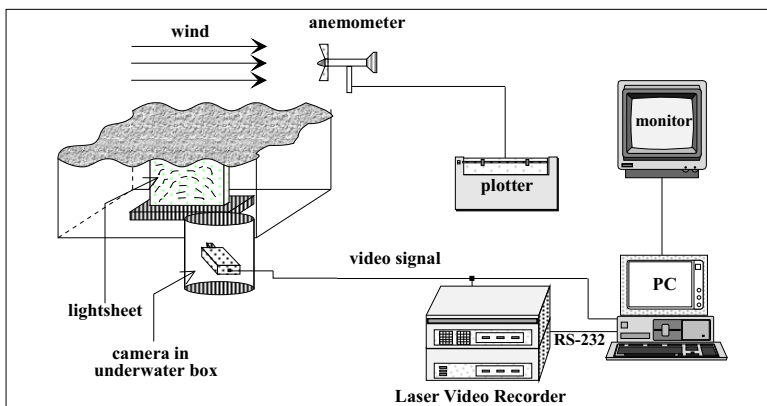


Figure 1: Scheme of the optical instruments used for flow visualization: A camera in an underwater box is looking perpendicular on a light sheet, illuminating seeding particles.

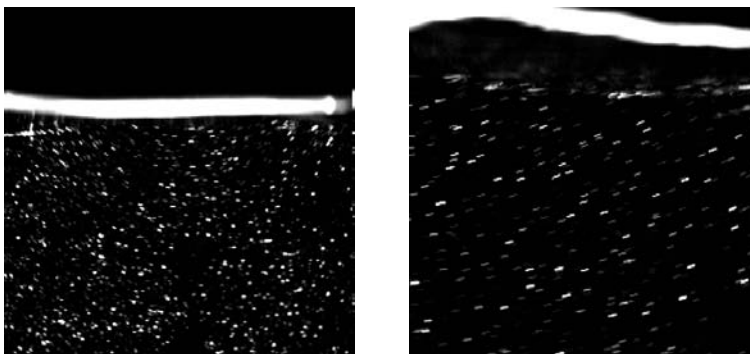


Figure 2: Seeding particles at a wind speed of 4.2 m/s (left) and 6.4 m/s (right) beneath the water surface in a light sheet illumination. Due to the exposure time of the camera particles in motion are visualized as streaks.

field, than from the Eulerian flow field. These simulations therefore form the basis for the resulting drift- and friction velocity computations (section 3).

2 A Study of the Eulerian vs. the Lagrangian Approach to the Calculation of Mean Properties of a Flow

The basic idea of the following *Monte Carlo simulations*, is to simulate the flow field with certain properties (such as a drift velocity) according to a model at various random grid points in space and time. These properties are then reextracted from the flow field, and the dependency of validity of

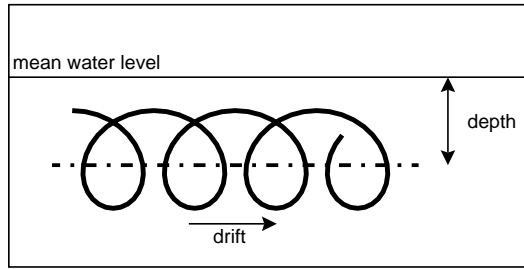


Figure 3: In contrast to point measurements (Eulerian), the exact location of the wavy water surface, is not required to be known if trajectories are measured (Lagrangian), as the mean height is calculated for each trajectory. The mean height of the trajectory in respect to the mean water level is calculated (see text).

the extraction on various parameters (such as the number of particles being tracked) is measured. Especial attention is directed to the problem of the moving free water surface, which may lead to an averaging at wrong heights (Figure 3). Eulerian measurements always require the simultaneous measurement of wave elevation and velocity to separate random orbital motions out of a random fluctuating motion [Thais and Magnaudet, 1995].

2.1 The Calculation of the Drift Velocity Profile

The information from the PTV is used for the study of momentum transport near the free boundary layer. Two approaches exist for calculating drift velocities, one using the *Eulerian flow field* data the other the *Lagrangian trajectory* information. The drift velocity is gained from the Eulerian flow field, by dividing the depth beneath the mean water level into a number of bins: By integrating over all vectors of a height bin the mean Eulerian drift $u_e(z)$ is gained:

$$u_e(z) = \frac{1}{t_1 - t_0} \int_{t_0}^{t_1} u_x(z) dt, \quad \text{for all vectors in that bin,} \quad (1)$$

$t_1 - t_0$ being the sequence length of the observation.

In contrast the drift velocity $u_l(z)$ is gained from the Lagrangian trajectory data, by integrating over all vectors belonging exactly to **same** trajectory. In addition the mean depth is calculated as the reference depth z' . Concluding from this data the drift is the mean of all previously calculated drift values assigned to each trajectory belonging to a depth bin:

$$u_l(z') = \frac{1}{n} \sum_{i=1}^n \frac{1}{t_{i0} - t_{i1}} \int_{t_{i0}}^{t_{i1}} u_x(z) dt, \quad \text{for all trajectories in that bin,} \quad (2)$$

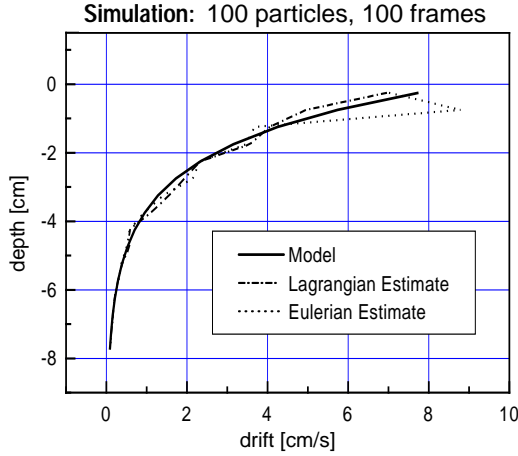


Figure 4: Drift velocity curves reconstructed from simulated flow fields (100 particles tracked over 100 image frames) by via Eulerian and Lagrangian averaging. Especially close to the water surface the Eulerian approach shows poorer results.

n being the number of trajectories in the height bin and $t_{i0} - t_{i1}$ the length of the i -th trajectory. The summation goes over all n trajectories in a depth bin.

Extensive Monte Carlo simulations have been undertaken to verify the errors on the velocity profile from the Eulerian respectively the Lagrangian averaging. A vector field generated at random grid points was simulated by:

$$\begin{aligned} u(x, z, t) &= A_0 e^{kz} \sin(kx - \omega t) + u_d(z) \\ v(x, z, t) &= A_0 e^{kz} \cos(kx - \omega t), \end{aligned} \quad (3)$$

A_0 being the amplitude of the wave, k the wave number, ω the frequency, and u_d the drift velocity profile function. It was therefore assumed that no Stokes drift is present and as a consequence Lagrangian and Eulerian drift velocities are identical.

Hence the Eulerian and Lagrangian vector field is known. The Eulerian drift velocity can then be reconstructed via eq. 1, the Lagrangian via eq. 2 and then compared to the input $u_d(z)$. The effect of various parameters, like particle density, sequence length, frequency of the wave, maximum drift etc. on the velocity profile can be studied. Figure 5 shows the effect of the number of trackable particles (particle density) and the period over which the particles are tracked (image sequence length) on the velocity profile. As measure of confidence a normalized χ^2 -function was chosen and plotted in

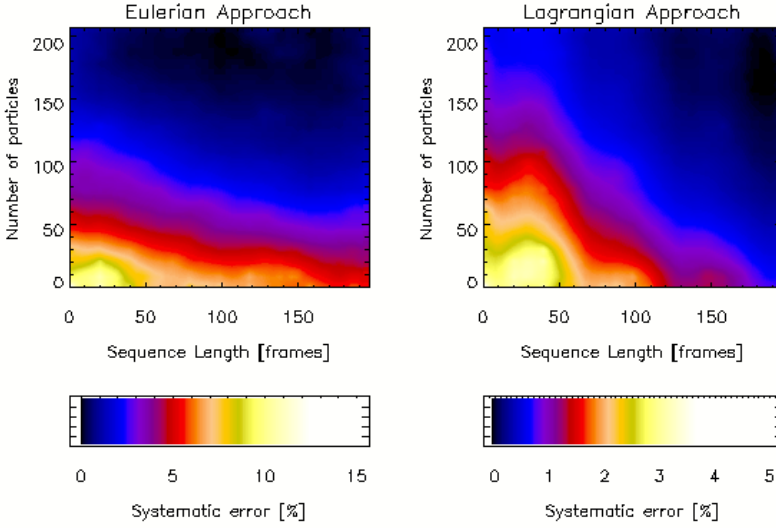


Figure 5: Monte Carlo simulation: The effect of particle density and image sequence length on the velocity profile calculations. (For color figure, see Plate 9.)

the figures:

$$\chi^2 = \sum_{z=1}^n \frac{(u_d(z) - u_{el})^2}{n}, \quad (4)$$

n , being the number of bins of the Eulerian, or respectively Lagrangian horizontal velocity component u_{el} .

Especially at low particle concentrations and short image sequences, the Lagrangian approach yields 2-3 times better results than the Eulerian. This is not very surprising as in this approach an additional information, namely the trajectorial data of a particle path, is taken into account. In addition the effect of the moving water surface much more important in the Eulerian reconstruction of the drift (Figure 4).

2.2 The Calculation of the Turbulent Reynolds Stress

To study the transport near the interface by fluctuating velocity the flow field is commonly represented in the form:

$$\vec{u} = \langle \vec{u} \rangle + \vec{u}', \quad (5)$$

$\langle \vec{u} \rangle$ being the average of the velocity over the time and \vec{u}' the deviation from the average. The contributions of the fluctuating velocities to the momentum flux form the *Reynolds stress tensor* τ_{ij} :

$$\tau_{ij} = -\rho \overline{v'_i v'_j}, \quad (6)$$

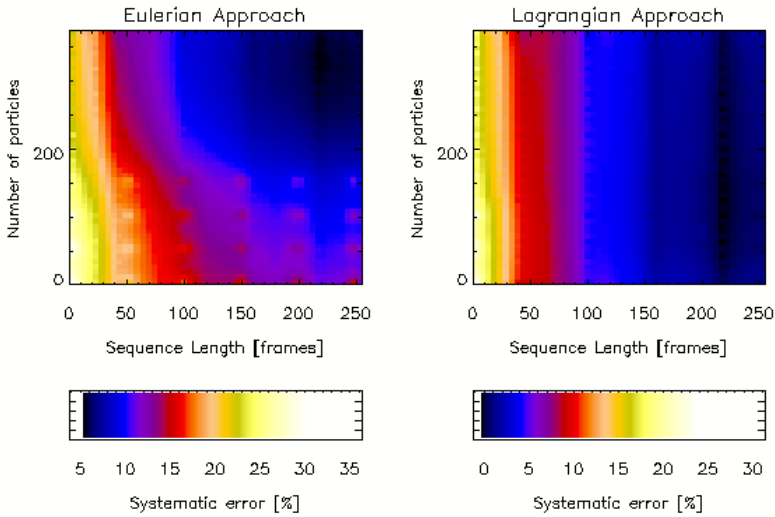


Figure 6: Monte Carlo simulation: The effect of particle density and image sequence length on the Reynolds stress calculation of 2 Hz wave. (For color figure, see Plate 10.)

v'_j and v'_j being the fluctuating velocity components of \vec{u}' . Of special importance for *friction velocity* calculations is the correlation of horizontal and vertical velocity fluctuations. The Monte Carlo simulations focuses on the question, whether the orbital movement beneath the water surface contributes significantly to the calculation of the stress component. For a monochromatic wave the additional offset to the stress component can be computed by integrating over a period T of the orbital wave motion and assuming no horizontal and vertical drift:

$$\begin{aligned}
 \overline{u'_x u'_z} &= \frac{1}{T} \int_0^T u'_x u'_z dt & (7) \\
 &= \frac{1}{T} \int_0^T A(z) \sin(kx - \omega t) B(z) \cos(kx - \omega t) dt \\
 &= \frac{A(z)B(z)}{T} \sin(2kx) \int_0^T [\cos(2\omega t) - \sin(2\omega t)] dt \\
 &= 0.
 \end{aligned}$$

Therefore when integrating $u'_x u'_z$ over one wave period no additional offset to the friction velocity computation is expected. When integrating over t , and t not being the wave period T the offset τ_{off} is of the order:

$$\tau_{off} = \mathcal{O}\left(\frac{A(z)B(z)T}{t}\right) \quad \text{assuming } t \gg T; \quad (8)$$

a long integration time (in comparison to the period of the wave) therefore

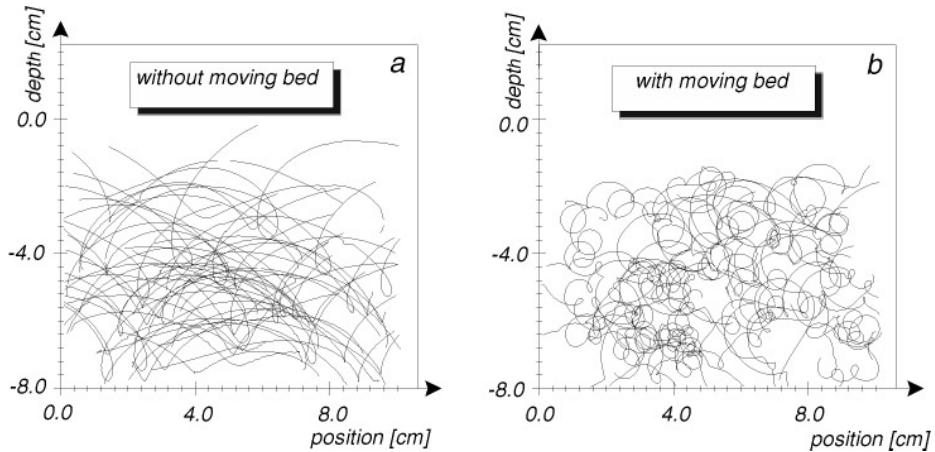


Figure 7: Trajectories of wind induced water waves without (a) and with (b) moving bed.

yields a neglectable offset. The effects of integration time (\equiv observation length), particle density, Eulerian and Lagrangian averaging were studied in a Monte Carlo simulation. As in the previous drift reconstruction the flow field was modelled using equation 3 at random observation points. The stress component was computed and then compared to the expected value (Eq. 7). Figure 6 shows the effect of the number of trackable particles (particle density) and the period over which the particles are tracked on the stress computation. The Lagrangian averaging approach yields superior results to the Eulerian as no dependency on particle density is found.

2.3 Results: PTV Beneath Water Waves

Figure 7 shows two typical trajectories measured at the circular wind/wave facility in Heidelberg. The wind wave flume was equipped with a moving bed installed at the bottom of the flume, moving against the wind induced currents. With this feature the main horizontal drift velocity can be reduced significantly. Particles stay longer in the light sheet, thus enabling the measurement of longer particle trajectories (Figure 7b). After now having studied the influences on the computation of drift profiles, the curves were calculated for various conditions at circular channel in Heidelberg. The wind speed was varied between 4–6 m/s and the fetch between 3–6 m. The fetch was limited by putting a 2 m long bubble foil on the water surface.

Figure 8 shows typical drift profiles for 5.2 m fetch at three different wind speeds. The observed trajectories ($x(t), z(t)$) were then used for a radius estimation (Figure 8d). As a first step *natural cubic splines* $S_x(t)$ and $S_z(t)$

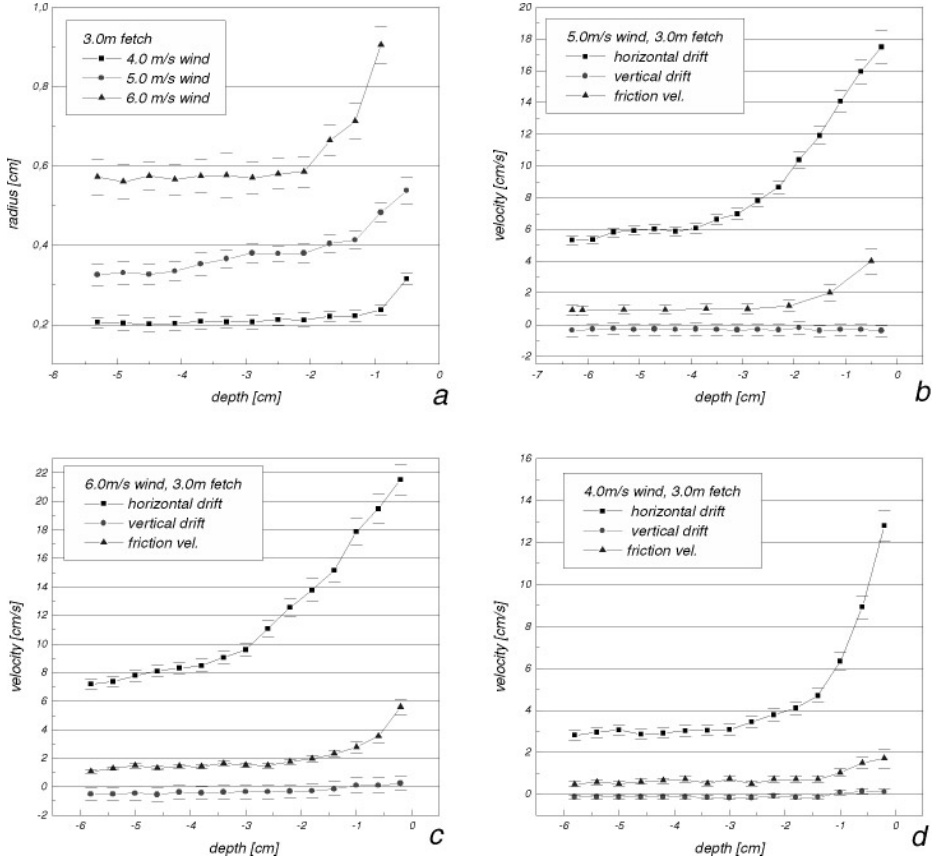


Figure 8: Horizontal and vertical drift velocities and turbulent friction velocity at three different wind speeds (a-c). Dependency of orbital radius on depth (d).

were fitted to the trajectory for all $t \in \{t_i, t_{i+1}\}$:

$$\begin{pmatrix} S_x^i(t) \\ S_z^i(t) \end{pmatrix} \equiv \begin{pmatrix} a_i + b_i(t - t_i) + c_i(t - t_i)^2 + d_i(t - t_i)^3 \\ a'_i + b'_i(t - t_i) + c'_i(t - t_i)^2 + d'_i(t - t_i)^3 \end{pmatrix} \approx \begin{pmatrix} x(t) \\ z(t) \end{pmatrix}. \quad (9)$$

The big advantage of the spline interpolation is that immediately the first and second temporal derivatives of $x(t)$ and respectively $z(t)$ are known. With this input the radius R can be computed for each trajectory:

$$R = \frac{(\mathcal{X}^2 + \mathcal{Z}^2)^{(3/2)}}{\mathcal{X}\ddot{z} - \ddot{x}\mathcal{Z}}. \quad (10)$$

In addition an eddy correlation technique was used to determine the friction velocity and its profile. In the bulk of the water the viscous transport

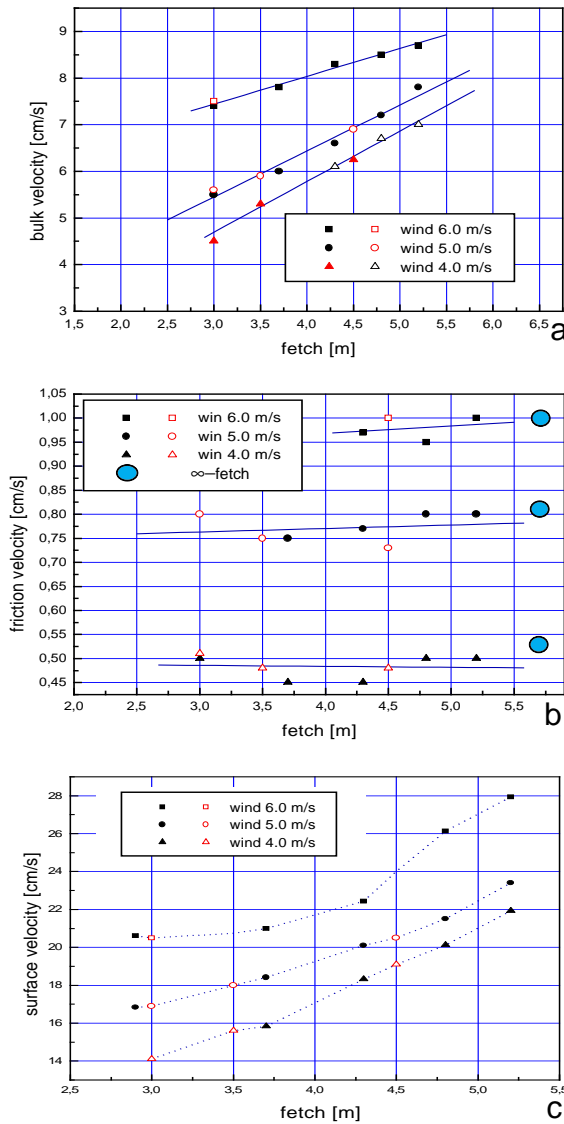


Figure 9: Dependency of bulk (a), friction velocity (b) and extrapolated surface velocity (c) on wind speed and fetch, measured at the circular in Heidelberg. Closed symbols denote measurements without the moving bed, the hollow ones with. Measurements of bulk and surface velocities with the moving bed have been corrected for the drift induced by the bed.

term can be neglected. The friction velocity profile $u_*(z)$ and its dependency on the water depth can therefore be directly determined by correlating the fluctuating velocities u'_x with u'_z , see (Figure 8). These profile curves show a very interesting behavior. On both sides of the interface the fluid are in turbulent motion and momentum is transported by turbulence. Upon reaching the boundary layer the interfacial turbulence is largely suppressed and molecular diffusion dominates the transport process. Modern boundary layer theories (see *Kraus and Businger* [1994]) predict a constant flux into the water bulk. Our measurements indicate however a significant enhancement of the friction velocity at the water surface (Figure 8). While the friction velocity is constant in the bulk, an abrupt enhancement of the Reynolds stress from the bulk towards the water surface up to a factor of 2-6 is observed. This suggests, that the orbital movement of wind waves significantly enhances turbulent dissipation near the water surface (Figure 8d).

Previously *Agrawal et al.* [1992] measured *enhanced dissipation* of kinetic energy beneath strongly breaking waves at the lake Ontario. They found an enhancement factor of 5-60. Our measurements now indicate that micro-scale wave breaking is sufficient to produce significant turbulence enhancement.

Figure 9 show the dependency of the bulk velocity and friction velocity (computed in the bulk) on wind speed and fetch. The bulk shows a linear increase with the fetch, the friction velocity however does not show this behavior, and remains nearly constant. In addition these values show lie in good agreement to previously measured friction velocity using a momentum balance method [*Jähne et al.*, 1997].

Acknowledgements

Financial support for this research from the National Science Foundation (OCE91 15994) and the German Science Foundation DFG (Wi 1029/2-1) is gratefully acknowledged.

References

- Agrawal, Y. C., Terray, E. A., Donelan, M. A., Hwang, P. A., Williams III, A. J., Drennan, W. M., Kahma, K. K., Kitaigarodskii, S. A., Enhanced Dissipation of kinetic energy beneath surface waves, *Nature*, 359, 219-220, 1992
- Hering, F., Wierzimok, D., Jähne, B., Particle Tracking and its Application of Turbulence beneath Water Waves, *submitted to Experiments in Fluids*, 1995
- Jähne, B., Münnich, K. O., Siegenthaler, U., Measurement of gas exchange and momentum transfer in a circular wind-water tunnel, *Tellus*, 31, 321-328, 1979
- Kraus, E.B., Businger, J.A., Atmosphere-Ocean Interaction, *Oxford university press*, 2nd edition, New York, 137-180, 1994
- Thais, L., Magnaudet, J., A triple decomposition of the fluctuating motion below laboratory wind water waves, *Journal of Geophysical Research*, 100, No. C1, 741-755, 1995

Digital Particle Tracking Velocimetry Measurements Very Near a Free-Surface

Edwin A. Cowen, Stephen G. Monismith, and Jeffrey R. Koseff

Environmental Fluid Mechanics Laboratory
Department of Civil Engineering, Stanford University

Abstract

Gas transfer at an air-water interface is generally limited by the aqueous near-interface turbulence structure. Wavy open-channel flow is an ideal flow for investigating the effects of *free-surface* waves on turbulence structure near the free-surface since identical flows with and without waves can easily be compared. We report the preliminary results of an experimental investigation of the turbulence in the very near free-surface region of an *open-channel flow* in the absence of waves. The measurements were made using *digital particle tracking velocimetry* (DPTV) which allowed the mean and fluctuating velocity profiles to be resolved accurately at spatial resolutions of 100 microns right up to and on the free-surface. Our results show that the *vertical velocity fluctuations* decay linearly very near the free-surface. We also report evidence of an increase in the mean streamwise velocity in the first 500 microns below the water surface. This may result from a streamwise tangential stress on the free-surface originating at the outlet boundary. Prior to presenting these results we introduce the DPTV technique and present measurements, along with LDA and DNS measurements, from a validation experiment in a zero pressure gradient flat plate boundary layer. The validation experiment demonstrates the excellent resolution and accuracy of our DPTV technique.

1 Introduction

The exchange of mass, momentum, and energy across an air-water interface is controlled by the aqueous near free-surface turbulence structure. One of the major obstacles to investigating the turbulence associated with this region is the difficulty of making good experimental measurements close to a free-surface. Traditional point measurement instruments such as the laser-Doppler anemometer (LDA) and hot-wire and hot-film anemometers have two major drawbacks: limited spatial resolution, and the difficulty of using them to make measurements very near a free-surface. The recent development of *digital particle image velocimetry* (DPIV) techniques [e.g., Willert & Gharib, 1991] allows these obstacles to be overcome. Cowen and Monismith have developed a *digital particle tracking velocimetry* (DPTV) technique and demonstrated that it is possible to measure not only the velocity field but the vorticity, Reynolds stress, and dissipation fields beneath free-surface flows

[Cowen & Monismith, 1995] (hereinafter *CM*). Using DPTV, an experimental investigation of the effects of a free-surface (both steady and wavy) on the turbulence in an open-channel flow is presently underway. Wavy open-channel flow is an ideal flow for investigating the effects of free-surface waves on turbulence structure near the free-surface since identical flows with and without waves can easily be compared. In this paper we introduce *CM*'s DPTV technique, discuss its validation, and present and discuss preliminary results in the absence of waves from our ongoing free-surface study.

2 Digital Particle Tracking Velocimetry

Particle tracking velocimetry (PTV) is simply the tracking of illuminated particles in a flow field. In its simplest form two images of an illuminated plane are captured in a seeded flow a short time, Δt , apart. By tracking a particle's displacement from the first image to the second and dividing by Δt , the instantaneous velocity field can be measured. Previous PTV implementations have relied on large search windows in the second image to find the pairing particle [e. g., *Hassan et al.*, 1992], necessitating low seeding densities to avoid pairing ambiguity and thus resulting in low spatial resolution. However, the size of this search window can be significantly reduced if an accurate estimate can be made of the particle's location in the second sub-window. *CM* have developed a DPTV technique that uses the results of cross-correlation-based DPIV to guide the search process for the particle-pairs. The method uses a cross-correlation-based technique originally adapted from the work of *Willert & Gharib* [1991] to determine a function which estimates the displacement of any first image particle in the second image. The tracking algorithm searches a small region around the estimated second image location of a first image particle. Since only a small region is searched for the pairing particle significantly higher seeding densities can be used allowing for much greater spatial resolution.

DPTV offers other advantages over traditional correlation-based PIV. For example, correlation-based PIV suffers from bias errors associated with the presence of velocity gradients [*Keane & Adrian*, 1990]. These bias errors are eliminated by tracking individual particles and hence DPTV has the potential for reduced error relative to correlation-based PIV. We say "potential" because historically, unlike correlation-based PIV, PTV algorithms suffer from interpolation error. (Actually, there is an argument for interpolating correlation-based PIV data too but this is generally not done.) This is because PTV data is randomly located and previous researchers have had to interpolate the data onto regular spaced grids to look at turbulence statistics [*Agüí & Jiménez*, 1987; *Spedding & Rignot*, 1993]. The interpolated PTV data often has larger error than correlation-based PIV since the interpolation error is generally larger than the bias errors associated with PIV [*CM*].

DPTV however, allows for a novel approach to using PTV data that elim-

inates the need for interpolation. *CM* have demonstrated that by collecting hundreds or even thousands of velocity fields in a stationary or periodic flow (which is only feasible using a digital technique) it is possible to use the PTV data in-place. *CM*'s algorithm constructs a small three-dimensional measurement volume and calculates the statistics of all the particles that fall in this volume over all the images. This measurement volume is bounded by the light sheet thickness and a user defined area of the image, typically a hundred to several hundred microns. The number of images and size of the measurement volume are set so that typically 10,000 or more velocity vectors are used to calculate each statistic. In this way the mean quantities and components of the Reynolds Stress tensor are calculated as well as mean gradients and mean vorticity fields. Using a Monte Carlo simulation *CM* have demonstrated that this technique has better error characteristics than either correlation-based PIV or interpolated PTV data. By applying an interpolator to the data it is possible to calculate higher order statistics such as the dissipation components (mean squared fluctuating velocity gradients) as well as velocity spectra. As discussed above these statistics will have a larger uncertainty due to the interpolation of the data.

2.1 Hardware

The DPTV algorithm interrogates two singly-pulsed images. These images are captured on a cooled 12-bit digital slow-scan camera manufactured by Patterson Electronics in Tustin, CA. The camera is a full-frame transfer camera which allows two images to be captured on the CCD chip before they are downloaded. The minimum time between images is 3.5 milliseconds. The active image area of the chip contains 1134×485 pixels. The chip is typically cooled to -20°C which minimizes thermal noise as well as nonlinearities in individual pixel response. The flow is illuminated with two Continuum Minilite Nd:YAG lasers. The lasers are combined into a single optical path via a polarizing beam splitter and a half-wave retarder before passing through a cylindrical lens to form a light sheet. The laser and camera triggers are all controlled with National Instruments LabVIEW software running on a Macintosh IIfx computer. The digital images are collected and processed on an Intel i860 based processing card manufactured by Alacron and hosted in a Pentium-based PC.

2.2 Validation

To validate our DPTV technique we made measurements in a developed free-surface channel flow with both the DPTV technique and a Dantec two-component LDA. This flow is a good approximation of a zero pressure gradient *flat plate boundary layer*. The flow facility used was a constant head type recirculating flume fitted with a flat bottom and is discussed in detail in *O'Riordan et al.* [1993]. The Reynolds number of the flow based on momen-

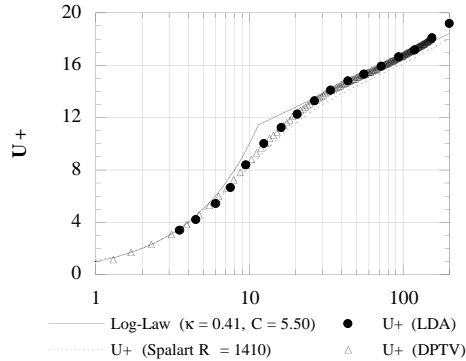


Figure 1: \bar{U} (+ units)

tum thickness (R_θ) was 1340 allowing the data to be compared directly to the zero-pressure gradient flat-plate boundary layer direct numerical simulation at $R_\theta = 1410$ of *Spalart* [1986]. Figures 1 and 2 show the mean velocity profile and the fluctuating velocity component profiles respectively as determined by the three techniques. As is apparent from the plots the DPTV technique has both excellent accuracy and resolution. Spalart's DNS mean streamwise profile has a lower value of C in the log-law region which is the result of a thinner viscous sublayer. This is not surprising since our facility's bottom plate had several joints that were not perfectly smooth. The effect of this slight roughness is evident in the streamwise velocity fluctuation profile as a small overshoot in the peak predicted by the DNS. The LDA measurements verify that these small variations from the DNS data are real in the sense that they are true characteristics of the flow in our facility. The flow was assumed to be homogeneous in the streamwise direction in the calculation of the turbulence statistics. For further details of this validation experiment see *CM*.

3 Experiments

The initial focus of our study is the effect of the free-surface on the near free-surface region turbulence. This study is taking place in a recently completed facility that we are still in the process of validating but we have made some interesting preliminary measurements very near the *free surface*. Presently we have three similar data sets that show the same results and we will only report one of them here.

3.1 Experimental Facility

The experiments were conducted in a new *wave-current channel* recently completed at the Environmental Fluid Mechanics Laboratory shown in Figure

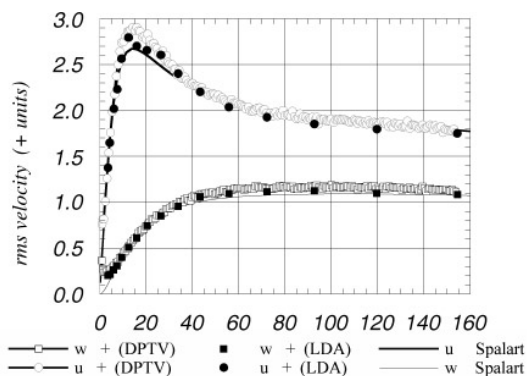


Figure 2: u' and w' (+ units)

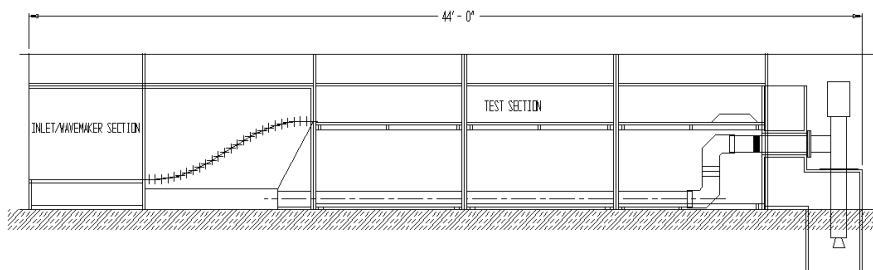
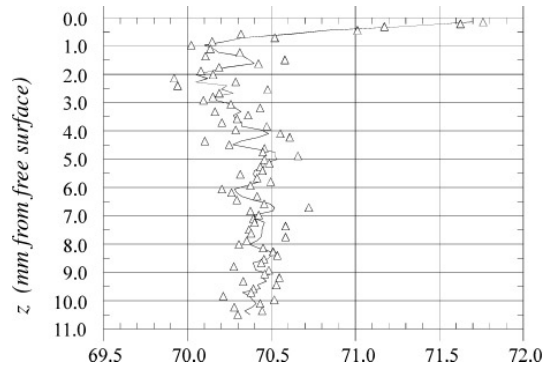
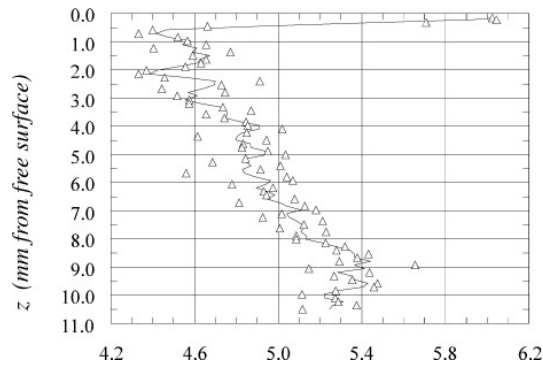


Figure 3: New wave-current flume.

3. It is a recirculating type flume with a 1.22 m wide and 7.32 m long cast acrylic test section. This allows for excellent optical access to flows from both the sides and bottom. The entrance section is 4.58 m long and pre-conditions the flow from a ten inch diameter pipe at its bottom through a horizontal expansion and three conditioning screens. The flow upwells and is turned downstream through a vertical contraction that was operated at 4.4:1. The outlet end of the test section is terminated by a broad crested weir, of height 23.5 cm, that forces the flow through critical depth, thus minimizing reflected wave energy. The outlet section and the pump are isolated from the rest of the facility to minimize vibrations. The pump is capable of delivering up to 3.8 m³/min but was run at approximately 1.4 m³/min.

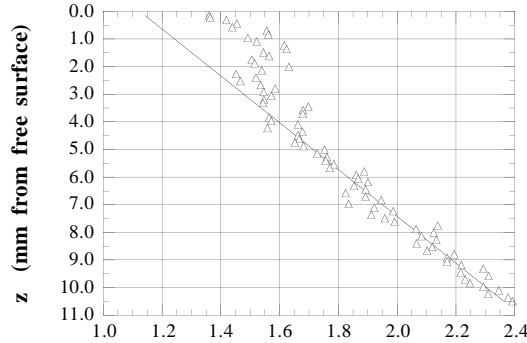
A coordinate system is defined based on the channel where x is the stream-wise distance from the beginning of the test section, y is the span-wise distance from the left wall (looking downstream), and z is the vertical distance below the free-surface. The upstream wall of the flume is a wave paddle. It is a cantilevered Lexan sheet that is unsupported for 18 inches below the mean free-surface position but was held in its fixed mean position for these experiments. All data was taken with the image area centered at

Figure 4: \bar{U} (mm/s)Figure 5: u' (mm/s)

$x = 3.23$ m and $y = 0.61$ m. The area imaged was 1.2 cm \times 1.0 cm and included about 1.0 cm below the free-surface. The flow depth was set at 28.5 cm and the bulk free-stream velocity was about 7.0 cm/sec (Froude number = 0.042). The flow was seeded with hollow glass spheres with a median diameter of about 11 micron and a median specific gravity of roughly 1.1 .

3.2 Preliminary Results

The mean (ensemble) streamwise near-surface *velocity profile* is presented in Figure 4. The solid line is a nearest-neighbor smoothed profile of the data. The mean velocity is approximately constant at 70.3 mm/sec up to the last half millimeter from the free-surface where a clear gradient to the free-surface begins. At the free-surface the free stream velocity is 71.7 mm/sec for a net increase of 1.4 mm/sec or 2.0 %. This pattern across the top millimeter of the flow was present in all three of our data sets. The mean vertical velocity profile is not shown but is zero to within ± 0.1 mm/s. Figures 5 and 6 show the fluctuating component of the streamwise and vertical velocities

Figure 6: w' (mm/s)

respectively. Again the solid line is a nearest-neighbor smoothed profile of the data. We should note that the fluctuating velocities in these data sets have a constant background noise source due to relatively low light conditions compared to an ideal DPTV image. This was primarily do to the small diameter of the particles and the relatively long light path through water. The *vertical velocity fluctuations* decay nearly linearly with depth over the entire region imaged. The streamwise fluctuations also decay linearly with depth over the majority of the depth measured but show a sharp increase over the top 0.5 mm. The Reynolds stress component, $\overline{u'w'}$, is not shown but is zero to within $\pm 0.3 \text{ mm}^2/\text{s}^2$.

3.3 Discussion

The gradient of the streamwise velocity very close to the free-surface is an interesting feature that we were not expecting and can find no previous evidence of in the literature. We are confident that it is not an aberration of the DPTV technique and have ruled out sampling bias by examining the free-surface position in many of the images collected. Our tentative hypothesis as to the source of this acceleration is centered on the *outflow boundary condition*. The flow is forced through critical depth at the outflow by the weir. At the weir y_c was estimated to be 3.3 cm which gives U_c of 57 cm/sec. Thus the free-surface is accelerated over the weir to more than eight times the mean bulk velocity. We hypothesize that the acceleration of the free-surface results in a net streamwise tangential stress being transmitted to the surface via the *surface tension*. This *tangential stress* is weak, but significant at our measurement station 3.91 m upstream from the weir's crest and acts to accelerate the flow adjacent to the free-surface.

Our theory seems to be supported by the fluctuating velocity data. There is no evidence of an increase in the vertical fluctuations near the free-surface which would be a signature of capillary waves or uncertainty in the location of the free-surface. However, there is an increase in the streamwise fluctu-

ations which suggests that the applied free-surface streamwise tangential stress is unsteady, which is to be expected if the stress arises from surface tension in a turbulent flow. The mean stress applied by the acceleration at the weir is modified on the local scale by eddies colliding with the free-surface, that cause local deformations in the free-surface and thus local fluctuations in the tangential component of the surface stress.

We attempted to change the outflow boundary conditions to test our theory by submerging an underflow gate over the weir. This traps a Reynolds ridge that advanced upstream to a steady state position about 1.2 m upstream of the weir. We collected data at the same position as for the critical overflow case above but the results were ambiguous. The elimination of the critical outflow resulted in the presence of very long, small amplitude waves and thus the free-surface position was unsteady. Examining the data without trying to account for this unsteadiness resulted in a roughly uniform velocity profile at the free-surface but the uncertainty in the convergence of the mean was too large (due to the presence of the waves) for us to be confident that there was no free-surface acceleration buried in the background signal from the waves.

The decay in the vertical fluctuations strength at the free-surface is not surprising and has been measured by other researchers [e.g., *Komori et al.*, 1982; *Davies*, 1972] and simulated by DNS [*Borue et al.*, 1995]. *Davies* [1972] derives an analytic expression (1) for w' from continuity showing that this decay should be linear. In this expression λ represents the thickness of the surface layer of damped turbulence and $w' = w_0$ at $z \geq \lambda$ near the surface.

$$w' = z w_0 / \lambda; \quad z < \lambda \quad (1)$$

Figure 6 has been fitted with a least squares linear fit from 10 mm through 4 mm from the free-surface ($R = 0.98$) which gives a ratio $\lambda/w_0 = 8.5$ sec. and demonstrates excellent agreement with the linear decay predicted by (1). The offset, $w'(0) = 1.1$ mm/s, is a measure of the constant background noise discussed above.

The decay in the streamwise fluctuations as the free-surface is approached (except for the top 0.5 mm) also surprised us since we expected an increase in u' to compensate for the decay in w' thereby conserving turbulent kinetic energy (q^2). While we do not have measurements of the transverse fluctuating component it is doubtful that it has increased enough to compensate for the decreases in u' and w' both and thus conserve q^2 . It appears that free-surface is acting to dissipate q^2 , probably working against the surface layer which suggests that our surface may not have been entirely clean, which is not surprising even in a laboratory environment, as these deformations were not elastic.

4 Conclusions

We have introduced a particle image velocimetry method that allows for very accurate high resolution measurements to be made in a flow field. We have not explored the power of this technique to look at spatial turbulence structure but as our DPTV technique is a full field technique this power clearly exists [see *CM*]. The above experimental work demonstrates the ability of DPTV to make highly resolved measurements in the top centimeter of a free-surface flow, an historically challenging region to make measurements in. This work verifies that the free-surface modifies the turbulence structure as the free-surface is approached. The vertical fluctuations decay linearly with distance from the free-surface as predicted by *Davies* [1972]. It appears that in laboratory scale facilities the outflow boundary condition may set the free-surface mean velocity profile. We hypothesize that the acceleration of the free-surface over an outfall applies a streamwise tangential stress on the entire free-surface that effects the mean flow even meters upstream. This work suggests that researchers interested in surface tension and near free-surface phenomena should pay close attention to the outlet boundary conditions of their facilities/models. In the near future we plan to look at the streamwise development of the mean velocity profile at the free-surface as a function of distance from the outfall to see if we can verify this mechanism.

The measurements presented in this paper represent our initial effort to quantify the turbulence structure below the free-surface in an open-channel flow. Upon completion of this effort we will apply free-surface waves to the flow. Our DPTV technique is well suited to making measurements at a wavy free-surface [see *CM*] and the comparison of the turbulence structure in the presence of waves to that in the absence of waves should yield insight into the effect of waves on gas transfer.

Acknowledgments

The authors gratefully acknowledge the support of our facility construction and of our research effort by the Fluid Dynamics Program, Office of Naval Research [Scientific Director: Dr. E. Rood, grant N00014-94-1-0190] and by the Marine Boundary Layer Program, Office of Naval Research [Dr. Wayne Patterson, grant N0014-93-1-0377]. Under a High Performance Computing Challenge Grant [ASC 9318166], the NSF High Performance Computing and Communication Program [Dr. A. Thaler] has provided support for the development of the DPTV algorithm and software.

The authors wish to thank Bob Street for his valuable input, John Crimaldi for making and processing the detailed LDA measurements in the DPTV validation, Bob Brown for his design of and incredible dedication to completing the new flume, and Emily Pidgeon for her assistance in constructing it.

References

- Agüi, J. C. & J. Jiménez, On the performance of particle tracking, *J. Fluid Mech.*, 185, 447-468, 1987
- Borue, V., S. A. Irszag, & I. Staroselsky, Interaction of surface waves with turbulence: direct numerical simulations of turbulent open-channel flow, *J. Fluid Mech.*, 286, 1-23, 1995
- Cowen, E. A. & S. G. Monismith, A hybrid digital particle tracking velocimetry technique, to be submitted to *Exp. Fluids*.
- Davies, J. T., *Turbulence Phenomena*, 412 pp., Academic Press, San Francisco, 1972
- Hassan, Y. A., T. K. Blanchat, C.H. Seeley Jr., & R. E. Canaan, Simultaneous velocity measurements of both components of a two-phase flow using particle image velocimetry, *Int. J. Multiphase flow*, 18, 371-395, 1992
- Keane, R. D. & R. J. Adrian, Optimization of particle image velocimeters. Part I: Double pulsed systems, *Meas. Sci. Technol.*, 1, 1202-1215, 1990
- Komori, S., U. Hiromasa, O. Fumimaru, & T. Mizushima, Turbulence structure and transport mechanism at the free surface in an open channel flow, *J. Heat Mass Transfer*, 25, 513-521, 1982
- O'Riordan, C. A., S. G. Monismith, & J. R. Koseff, An Experimental study of concentration boundary layer formation over a bed of model bivalves, *Limnol. Oceanog.*, 38 (8), 1712-1720, 1993
- Spalart, P. R., Direct simulation of a turbulent boundary layer up to $Re_{\delta_2} = 1410$, *NASA Technical Memorandum 89407*, 1986
- Spedding, G. R. & E. J. M. Rignot, Performance analysis of grid interpolation techniques for fluid flows, *Exp. Fluids*, 15, 417-430, 1993
- Willert, C. E. & M. Gharib, Digital particle image velocimetry, *Exp. Fluids*, 10, 181-193, 1991

Measurements of Velocity Profiles in the Aqueous Boundary Layer at a Wind-Driven Water Surface

Jochen Dieter^{1,2}, *Frank Hering*², *Roland Bremeyer*²,
and *Bernd Jähne*^{1,2,3}

¹Scripps Institution of Oceanography, Physical Oceanography Res. Div.
La Jolla, CA 92093-0230, USA, email: jdieter@ucsd.edu

²Institute for Environmental Physics, University of Heidelberg
Im Neuenheimer Feld 366, 69120 Heidelberg, Germany

³Interdisciplinary Center for Scientific Computing, University of Heidelberg
Im Neuenheimer Feld 368, 69120 Heidelberg, Germany

doi: 10.5281/zenodo.10393

Abstract

A two-dimensional flow-visualization technique for the investigation of wind-induced currents in the boundary layer beneath the water surface is presented. Experiments were conducted at the Heidelberg wind-wave facility at conditions where either wave motion was suppressed by surfactants or was not present because of low wind speeds. A PIV setup enables the calculation of flow vector fields and velocity profiles in an area of 4 mm beneath the interface. Parameters of this layer, such as the friction velocity were deduced from these profiles.

1 Introduction

The investigation of micro-scale turbulence near the free air/sea interface is important to understand wind-driven small-scale transport processes across the water surface. Flow measurements at different scales on both sides of the interface reveal information about the turbulent transport of momentum and the turbulent dissipation of energy as well as the influence of waves on these processes.

Of particular interest is the layer down to the first millimeter beneath the water surface, where viscous transport processes exceed the turbulent. Most parameters of the transport processes in this layer, can be deduced from mean velocity profiles in that layer. Measurements in this part of the flow are very rare, since the velocities are high in respect to the area of interest. The presence of waves makes the observation even more difficult. Therefore hardly any measurements of this area are available, except some pioneer work by *Okuda* [1992] for the air side and *Sivakumar* [1984] for the water side layer.

A setup for high-resolution *particle image velocimetry (PIV)*-measurements in the Heidelberg wind-wave flume was developed. Investigations of the flow, with wave motion being suppressed by the use of surfactants

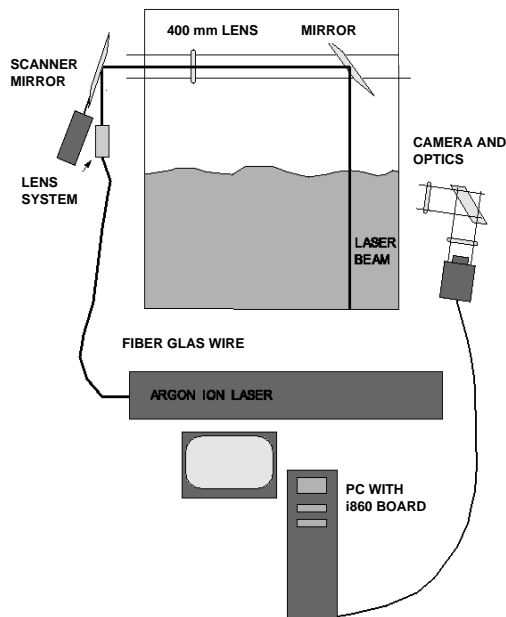


Figure 1: The setup used for PIV-measurements in the viscous boundary layer.

(Triton X100), were made. Low wave amplitudes at low wind speed make measurements with no surfactants also feasible.

Eulerian vector fields were extracted by a multi-grid PIV algorithm, especially designed for the processing of large displacements vectors. Velocity profiles and parameters of the viscous boundary layer, the friction velocity and the surface velocity are deduced from these vector fields.

2 Experimental Setup

Experiments are conducted at the Heidelberg wind-wave flume, with a setup very similar to one developed by *Münsterer and Jähne* [1995] for the acquisition of gas exchange rates. The circular Heidelberg facility provides the possibility to investigate events in the middle of a 35cm broad channel through windows in the flume wall from outside. Thus it is possible to place delicate equipment very close to the observed area with no interaction between the air/water stream and the optical instrumentation. This feature enables a setup of a high resolution optic beneath the water level of the flume. Two achromatic 200 mm lenses picture an area of $4\text{ mm} \times 4\text{ mm}$ on a 256×256 pixel CCD-array of a high-speed non-interlaced camera (Dalsa CA-D1). This yields a spatial resolution of $16\ \mu\text{m}$ and a frame rate of 200

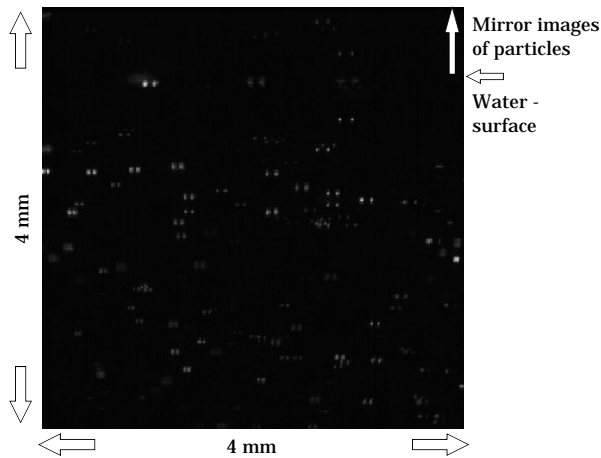


Figure 2: Image of particles in the viscous boundary layer taken at a wind speed of 1 m/s. The velocity decrease with the water depth is easy to verify by the distance of particle image pairs. It is also easy to determine the water surface. All particle images above the water surface are mirror images reflected at the interface.

frames/sec. The angle between the optical axis of this image acquisition equipment and the water surface was chosen 8° to avoid disturbances of the image by the interface outside the area of interest.

The flow was visualized by small seeding particles produced by electrolysis. Hydrogen bubbles are generated on the cathode, of a tungsten wire of $50\ \mu\text{m}$ diameter. In order to get a sufficient number of particles in the observed volume, the wire is placed close (about 10 cm upstream) to the area of interest. There is a potential voltage drop of 60 V between the wire and the anode at 10 cm distance at the flume wall. Since the flume is filled with deionized water, 0.15 g/l NaSO_4 is added to enable electrolysis [Oertel and Oertel, 1989].

For illumination a TEM_{00} 1 W argon ion laser (American Laser Corp., model 909) with a wavelength of 488 nm is used. The light is guided through a fiber glass wire. A lens system at the end of the wire and an additional 400 mm lens enables an adjustable beam diameter between $60\ \mu\text{m}$ and 2 mm. Corresponding to the depth of focus of $400\ \mu\text{m}$ a beam diameter of about $300\ \mu\text{m}$ is used. A scanner mirror generates a light sheet, which is directed by a second mirror into the water (see Figure 1). The scanner mirror is driven by a sinusoidal signal, that also synchronizes the camera each period. This yields two dots for every particle in one image frame. The light sheet is chosen larger than the picture frame. Although intensity is lost, a nearly linear laser beam velocity in the picture area is gained.

The camera is connected to a digital camera interface of a Hyperspeed XPI-i860 board. The images are stored in the RAM of the board during the

measurement. 34 MByte RAM allow 450 pictures ($\equiv 2$ s) to be taken consecutively.

3 Image Processing for PIV

Two-dimensional flow fields from sequential images of seeding particles in the flow are extracted with a Particle Image Velocimetry (PIV) algorithm. In contrary to particle based algorithms, as for example Particle Tracking Velocimetry (PTV), where special characteristics of the image of one particle is used to solve the correspondence problem, in PIV the characteristics of groups of particles is taken as standard for the calculation of displacement vectors (see also *Adrian* [1991], *Willert and Gharib* [1991]). Therefore the pattern created by particle images in a small part of the whole frame taken at the time τ was correlated to the next frame of the sequence taken at $\tau + \Delta t$. The mean velocity in this two-dimensional area is calculated dividing the shift of that pattern by the time Δt given by frame rate of the image acquiring system. The vector displacement was evaluated by using the spatial discrete correlation of these two areas.

The coordinates of the maximum of the correlation function is the most probable spatial shift vector and yields the mean displacement vector of the particles in the window. Typically a square area of 32×32 pixels is chosen as the matching window size for PIV measurements on digital images. The crosscorrelation is calculated in Fourier space using a discrete Fourier transformation done by a fast fourier algorithm FFT.

The detection of the peak in the cross correlation is often difficult, because of noise in the correlation function. In addition the peak tends to broaden, due to the gaussian form of the particles and from velocity gradients in the picture area. On the other hand this broadening is used for sub pixel accuracy processing via a center of mass algorithm. The noise results from:

- noise in the picture areas,
- three dimensional movement in and out of the light sheet,
- two dimensional movement of particles beyond the interrogation window,
- other particle patterns that randomly match up with the sampled picture area.

In other words sometimes the detected peak did not correlate to the real displacement vector. The quotient of the highest peak with the next lower is used as a measure of confidence for the results [*Keane and Adrian*, 1990]. Displacements larger than half the interrogation window can not be separated from displacements in the opposite direction, when the correlation is calculated in the Fourier space (Nyquist theorem).

Corresponding to the relatively high velocities of 10 cm/s in the boundary

layer spatial displacements up to 32 pixels are expected. In order to enable the evaluation of these shift vectors a multi grid algorithm was developed [Dieter et. al., 1994]. It divides the processing in two steps. First an estimate of the displacement vector is evaluated. This processing step was done on higher levels (in this case on the second level) of a Gaussian pyramid of the image [Jähne, 1995]. The estimate is used to match the second window over the first. Thus it is possible to calculate displacement vectors of up to 32 pixel, without loosing resolution of the vector field.

4 Results

The next step is the calculation of the water flow velocity as a function of the water depth. These *velocity profiles* are computed by averaging over all horizontal (parallel to the main wave propagation) velocity components and image sequences of two seconds (Figure 3). Centrifugal forces, which are present in the Heidelberg wind/wave flume because of its circular shape, induce secondary flows perpendicular to the main flow direction. Thus the form of the profiles is not logarithmic. An Airy-Function, as predicted by the *surface renewal model*, is used to fit the velocity profiles. There are two kinds of transport processes present in the boundary layer: diffusive and turbulent transport. The second process is described in the surface renewal model by a probability λ that turbulences reach into the boundary layer at a water depth h . This is normally done by using the power p of h . p is a real number and $p \geq 0$.

$$\lambda = \gamma_p h^p. \quad (1)$$

γ_p denotes a constant. The case $p = 0$ leads to the classic surface renewal model [Higbie, 1935; Münnich and Flothmann, 1975], often used to describe transport processes in the mass boundary layer at a wavy interface. The flow at a smooth water surface, as examined in experiments presented in this paper, is very similar to currents at a plane wall. Therefore p is set to one, so that λ is proportional to the water depth and no turbulences are present at the water surface. Therefore the solution of the transport equation is the Airy Function (Figure 3, right, small graphic):

$$u(h) = \frac{(u_{Wo} - u_{Bulk})}{Ai(0)} Ai \left(\frac{Ai(0)}{h \sqrt{\gamma_p / \nu Ai'(0)}} \right) + u_{Bulk}. \quad (2)$$

$Ai(0)$ and Ai' are constant, and u_{Wo} , u_{Bulk} are velocities at the surface and far away from the interface. ν is the viscosity of water.

The *surface velocities* extrapolated with the Airy Function from PIV-data are compared to direct surface velocity measurements as obtained by Reinelt [1994] using an imaging active IR technique (Figure 4, left). The friction velocity measured in Heidelberg wind/wave flume and by Sivakumar in a linear

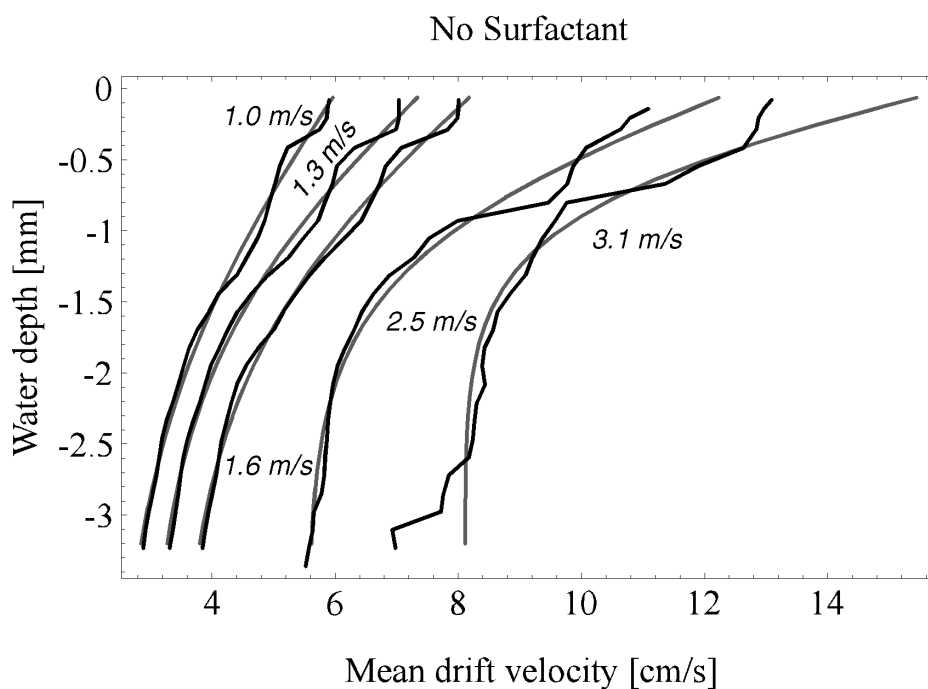
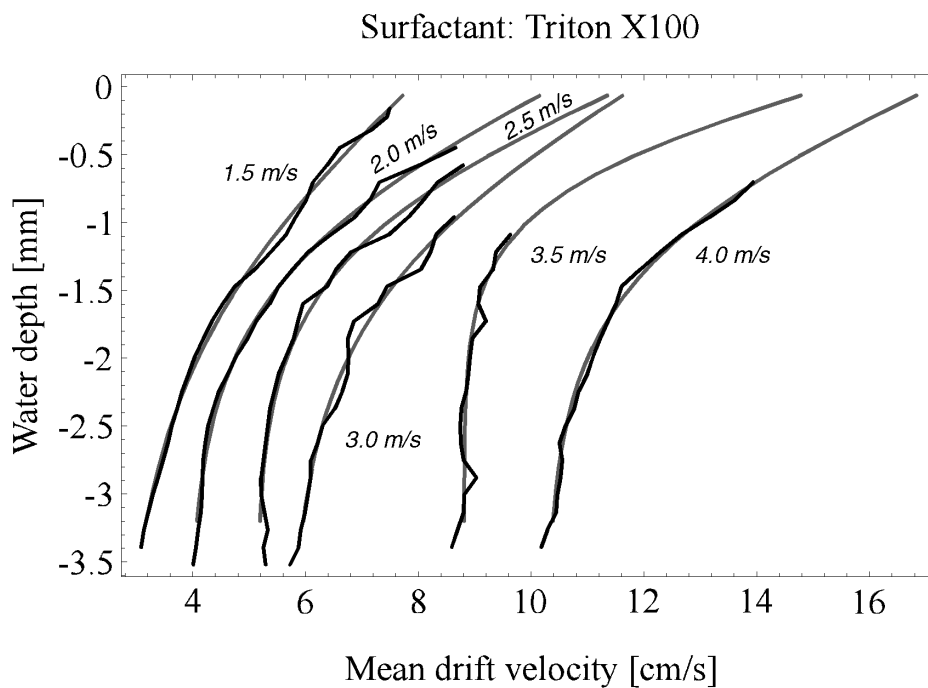


Figure 3: Velocity profiles in the aqueous viscous boundary layer, measured at the Heidelberg circular wind/wave flume. The Airy-Functions fitted in the profiles are shown as gray plots.

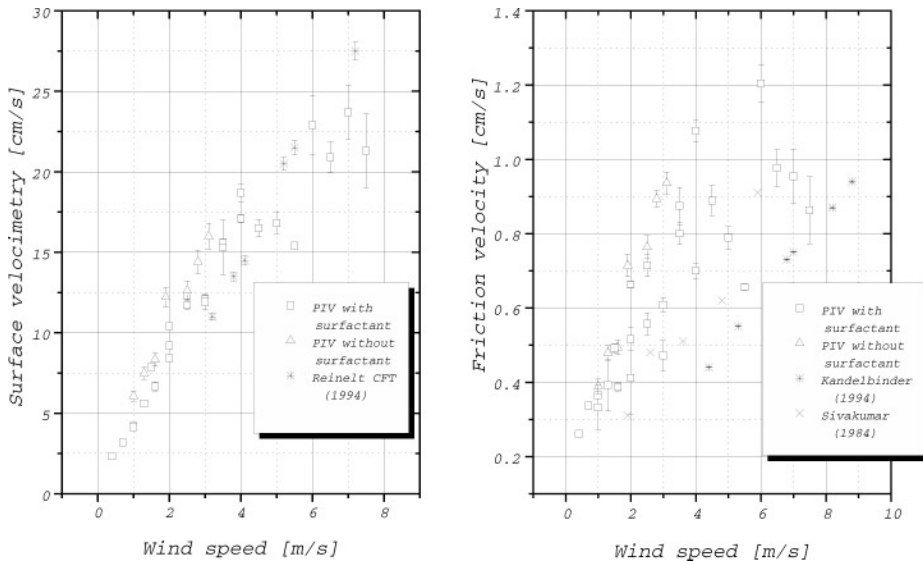


Figure 4: Left: Surface velocity as measured in the Heidelberg wind-wave flume. Right: Friction velocity measured in Heidelberg wind/wave flume and by Sivakumar in a linear wind wave tank of the University Newcastle.

wind wave tank of the University Newcastle are shown in Figure 4, right. Experiments by *Kandelbinder* [1994] were made using a momentum balance method in the Heidelberg flume. The lower values of the measurements by *Kandelbinder* can be explained, because the average over a much larger area close to the middle of the channel, where wind and water speed are lower, was taken into account. *Sivakumar* [1984] acquired his friction velocity data by flow measurements with floats near the interface and hot films away from the surface. Contrary to the other experiments, this data was taken at a wavy interface.

5 Conclusions

We successfully demonstrated a high-resolution PIV-flow visualization system to measure vertical velocity profiles within the viscous boundary layer. The results, are comparable to those gained by other techniques. This research is a first step in applying advanced imaging techniques for quantitative flow visualization techniques in the aqueous viscous boundary layer at a wavy interface. The next steps will be:

1. Improving the spatial resolution for measurements at higher wind speeds.
2. Incorporation of the optical system into a wave follower for measurements at a wavy interface.

References

- Adrian, R. J., Particle-Imaging Techniques for Experimental Fluid Mechanics, *Ann. Rev. Fluid Mech.*, 23, 261-304, 1991
- Dieter, J., R. Bremeyer, F. Hering, and B. Jähne, Flow measurements close to the free air/sea interface, *Proceedings to the Seventh International Symposium on Applications of Laser Techniques to Fluid Mechanics*, 1994
- Higbie, R., The rate of absorption of a pure gas into a still liquid during short periods of exposure, *Trans. A.I. Ch. E.* 31, 365-389, 1935
- Jähne, B., *Digital Image Processing, Concepts, Algorithms and Scientific Applications*, pp. 289-293 and 200-205, 3rd edition, Springer-Verlag, Berlin, 1995
- Kandelbinder, T., *Gasaustauschmessungen mit Sauerstoff*, Diploma thesis, Universität Heidelberg, 1994
- Keane, D. K., and R. J. Adrian, Optimization of particle image velocimeters. Part 1: Double pulsed systems, *Meas. Sci. Technol.*, 1, 1202-1215, 1990
- Münnich, K. O., and D. Flothmann, Gas exchange in relation to other air-sea interaction phenomena, *SCOR Workshop on Air/Sea Interaction Phenomena*, Miami, Dec 8-12, 1975
- Münsterer, T., and B. Jähne, A Fluorescence Technique to Measure Concentration Profiles in the Aqueous Mass Boundary Layer, in *The Air-Sea Interface*, M. A. Donelan, W. H. Hui, W. J. Plant, eds. The University of Toronto Press, Toronto, 1995, in press.
- Oertel, H. sen., and H. Oertel, jun., *Strömungsmesstechnik*, 413-415, G. Braun, Karlsruhe, 1989
- Okuda, K., Internal Flow Structure of Short Wind Waves, Part 1. On the Internal Vorticity Structure, *Journal of the Oceanographical Soc. of Japan*, 44, 28-42, 1982
- Reinelt, S., *Bestimmung der Transfergeschwindigkeit mittels CFT mit Wärme als Tracer*, Diploma thesis, Universität Heidelberg, 1994
- Sivakumar, M., Reaeration and wind induced turbulence shear in a contained water body, in: *Gas transfer at water surfaces*, W. Brutsaert and G. H. Jirka eds., Reidel, Dordrecht, 369-377, 1984
- Willert, C., and M. Gharib, Digital particle image Velocimetry, *Exp. in Fluids*, 10, 181-193, 1991

Spatial Measurements of Small-Scale Ocean Waves

P. A. Hwang

QUEST Integrated, Inc.
21414 68th Ave. South, Kent, Washington 98032

Abstract

Obtaining the spatial and wavenumber structure of small-scale waves is a difficult task even in a controlled laboratory environment. A scanning slope sensing technique has been developed to measure the two-dimensional spatial structure of surface slopes in the ocean. To reduce flow disturbance in field deployment, a wave-following open-frame structure is used as the instrument platform. The most significant step to reduce artificial wave generation is to perform the experiments with the instrument platform in free drift, thus minimizing the relative velocity between the platform structure and the flowing water. With this experimental design, the quality of the acquired data is found to be excellent. Characteristics of the mean square slope and two-dimensional wavenumber spectra in the range of wavelengths from 4 mm to 6.2 cm are presented.

1 Introduction

Small-scale waves serve as the *roughness elements* of the ocean's surface. They contribute to the transfer of heat, mass, momentum, and energy between air and water. For more than three decades, it has been observed in laboratory measurements that the gas transfer velocity increases significantly at the onset of surface wave generation. Laboratory measurements have established that the gas transfer enhancement correlates very well with short wind waves [Cohen *et al.*, 1978; Jähne *et al.*, 1979; Hasse, 1980]. However, the physical mechanism contributing to the observed enhancement of gas transfer by short waves is unknown. The study of the effects of short waves on gas transfer is progressing slowly due to the lack of understanding of small-scale wave characteristics. Because our knowledge of the processes governing the momentum balance of the wave spectral energy in the *capillary-gravity wave* region is at most qualitative, much of our understanding of the short-wave properties still relies on experimental evidence. In this respect, spatial measurements are most pertinent for two major reasons. First, the small-scale waves are subject to convection by the surface current, causing a nontrivial Doppler frequency shift. Interpretation of the frequency structure and attempts to derive the spatial scales from the frequency spectra have been found to be very difficult and the results are controversial. Second, the theoretical framework on the spectral energy balance is built upon the wavenumber domain. To combine the theoretical

development and experimental measurements to advance our knowledge of the short-wave structure, the spatial resolution is necessary.

In Section 2, a scanning slope sensing technique to measure the spatial structure of short surface waves is presented. The length scale of the resolved wave components is from 4 mm to 10 cm, covering the spatial region where both gravity and capillary effects are important as the restoring forces of the surface undulation. This is also the region where the wave phase speeds are the slowest and active momentum exchange between air and water is most likely to be initiated.

The scanning technique was tested successfully in the laboratory to measure the space-time evolution of small-scale waves [Hwang *et al.*, 1993]. However, the attempt to deploy in the field requires consideration of a very different issue — the disturbance caused by the instrument platform. Because short waves can be easily modified or modulated by the change of many environmental parameters, whether natural or man-made, the insulation of the sensing area from platform disturbances is critical to successful data acquisition in oceanic conditions. Our approach to reduce the flow disturbance is to mount the scanning slope sensor on a free-drifting open-frame buoy structure [Hwang *et al.*, 1995]. The results of the field data obtained using this approach are discussed in Section 3. The conclusions and summary of this experiment are presented in the final section of this paper.

2 Scanning Slope Sensing Technique and Instrument Platform

The optical refraction laser *slope sensing* technique is one of the most common techniques for measuring small-scale waves. The basic design projects a laser beam vertically from underwater. As the light penetrates the undulating air-water interface, the beam path in the air also undulates following Snell's law governing the refraction process. Recording the meandering refracted laser beam at a fixed distance (the image plane) from the mean water surface, the surface slope at the point where the laser beam penetrates the air-water interface can be calculated.

Because this is a single-point device, the time series and frequency spectra are collected [e. g., Tang and Shemdin, 1983; Shemdin and Hwang, 1988]. As mentioned previously, the interpretation of the frequency spectra is quite difficult due to the large Doppler frequency shift. Even though the kinematic aspect of the Doppler shift is well understood [Hughes, 1978], the conversion from frequency to wavenumber domain requires a priori knowledge of the surface current and directional distribution of the wave motion. Furthermore, wave blockage by surface drift can suppress slow-moving waves [Banner and Phillips, 1974; Phillips and Banner, 1974]. Such a process is irreversible and further complicates the frequency to wavenumber conversion.

One way to resolve the problem of the Doppler frequency shift is to perform spatial measurements, therefore, providing directly the spatial and

wavenumber information of the small-scale waves on the water surface. Because optical response is considerably faster than surface wave undulation, spatial information can be obtained from a single laser beam by scanning. In the scanning technique, instead of dwelling at a fixed point, the laser beam moves along a designated pattern. The technique was tested in the laboratory, using an acousto-optical modulator to scan the laser beam along a 12-cm linear segment to perform transect measurements of surface waves [Hwang *et al.*, 1993]. Figure 1a shows an example of the obtained space-time images of the wave patterns at six different wind speeds in a straight wind-wave facility.

Following the success in the laboratory, a field system was built. A scanning mirror was used to project the laser beam into eight lines to cover a two-dimensional rectangular area at the air-water interface. An important consideration for ocean deployment was the flow distortion caused by the mounting structures on ships or tower members. Disturbance from such sources was found to be quite apparent and created some doubt about the quality of earlier ocean data [Dobson, 1985]. To alleviate the flow distortion problems, the free-drifting operation was adopted to minimize the relative velocity between the mounting structure and the ambient current. The *scanning slope sensor* was mounted on a thin open-frame buoy, which also serves as a wave-following instrument platform (Figure 2). The system was deployed in the Atlantic Ocean in June 1993 and September-October 1994. The capillary-gravity wave data obtained from these two experiments cover wind gusts of up to 17 m/s. An example of the two-dimensional images of the ocean surface is shown in Figure 1b and 1c. Selected results from these field experiments are discussed in the following section.

3 Field Data

3.1 Mean Square Slope

Since the milestone paper of Cox and Munk [1954] on the sea surface statistics from *sun glitter* measurements, there have been continuous efforts to acquire more detailed information beyond the *mean square slopes* of the sea surface. These later measurements can be grouped into two major categories: point measurements and area imaging. Only a few of these ocean measurements reported the mean square statistics. Altogether, these data sets include measurements derived from aerial photographs of sun glitter near the Island of Maui [Cox and Munk, 1954, 1956]; surface slope measurements by a laser slope gauge, mounted 10 m ahead of the ship's bow, at Bute Inlet and with the wind fetch ranging from 4 to 77 km [Hughes *et al.*, 1977]; surface slope measurements by a laser slope gauge mounted on a mechanical wave-follower, carried out on a tower during the MARSEN Experiment in the North Sea [Tang and Shemdin, 1983] and during the TOWARD Experiment offshore of Mission Bay, California [Hwang and Shemdin, 1988];

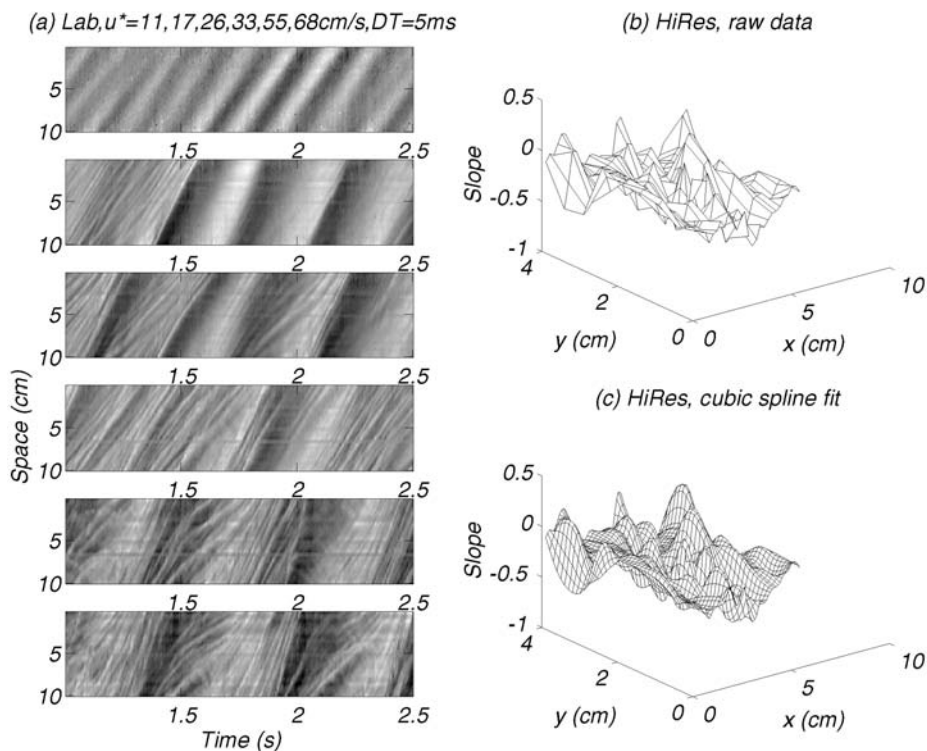


Figure 1: Examples of Scanning Slope Sensor Output. **a** Space-time images of small-scale waves in a laboratory wind-wave facility [Hwang *et al.*, 1993]; **b** the raw data and **c** cubic spline fitting of the two-dimensional structure of surface slopes of ocean waves.

and the data from the scanning slope sensor described above and partially reported in Hwang *et al.* [1995]. Due to the large quantity of the scanning slope sensor data (about 5 gigabytes), only the upwind slope component of these data has been processed. This component of the mean square slope is also reported in all the other studies cited above. The average ratio of the upwind component to the total mean square slope is found to be 0.57 ± 0.043 in Cox and Munk [1954, 1956], 0.59 ± 0.035 in Hughes *et al.* [1977], 0.48 ± 0.071 in Tang and Shemdin [1983], and 0.64 ± 0.078 in Hwang and Shemdin [1983]. The larger data scatter of the ratio from the wave follower measurements may be partially attributed to the flow disturbance by the instrument platform, which is carried by a servo motor to compensate for the motion of large waves in the ocean [Dobson, 1985]. Although some of the disturbance may be removed by the high-pass procedure during the data processing stage, a quantitative measure of disturbance removal is not available. In the following, the data of the upwind component and total mean square slope are presented. To obtain the total mean square slope of the

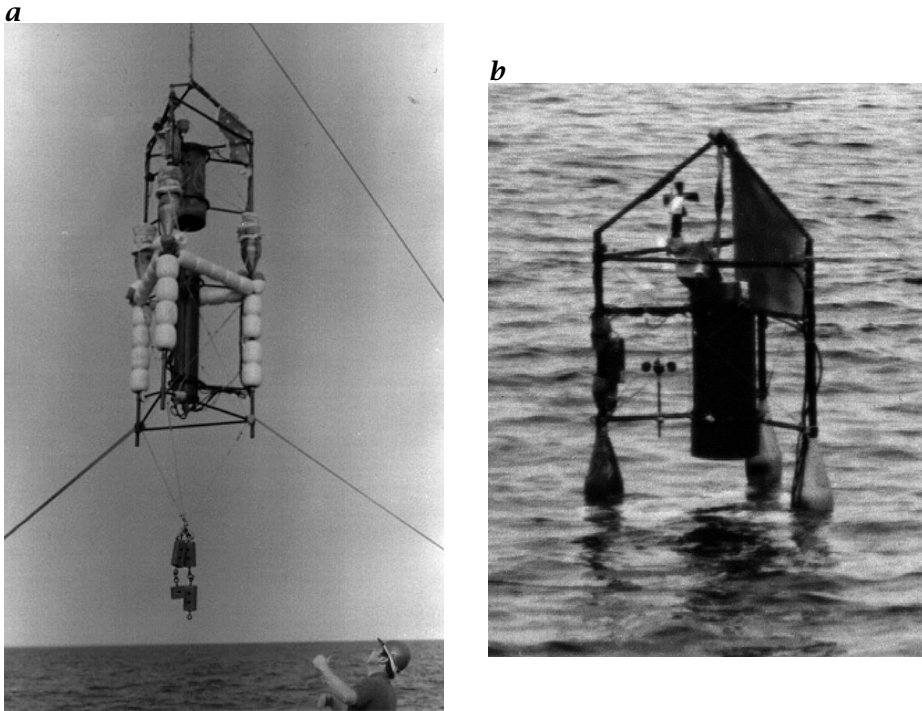


Figure 2: The Scanning Slope Sensor Buoy. *a* In the process of deployment, and *b* in free-drifting operation [Hwang et al., 1995].

scanning slope sensor data set, a ratio of 0.57 will be applied.

The data of *Cox and Munk* [1954, 1956] include measurements in both clean water and in slicks (one natural and eight artificial). The primary effect of the slicks is to suppress the presence of very short waves, leaving only the contribution from gravity wave components. The logarithmic dependence on wind speed is found to be satisfactorily explained by the dynamics of ocean wave generation [Phillips, 1977].

In clean water, the measured mean square slope is typically 2 to 3 times that observed in slicks. The wind speed dependence is empirically found to be linear. As illustrated in Figure 3, most of the data points obtained from sun glitter and laser beam refraction are in agreement within a factor of 2 (that is, within 3 dB). There are two groups of data above threshold wind speed that deviate obviously from the linear wind-speed dependence, as discussed below.

The lower-wind cases of Cox and Munk. This is probably an indication of the greater contribution by longer waves to the mean square slope at low wind conditions. Because these long waves may not be locally generated, the

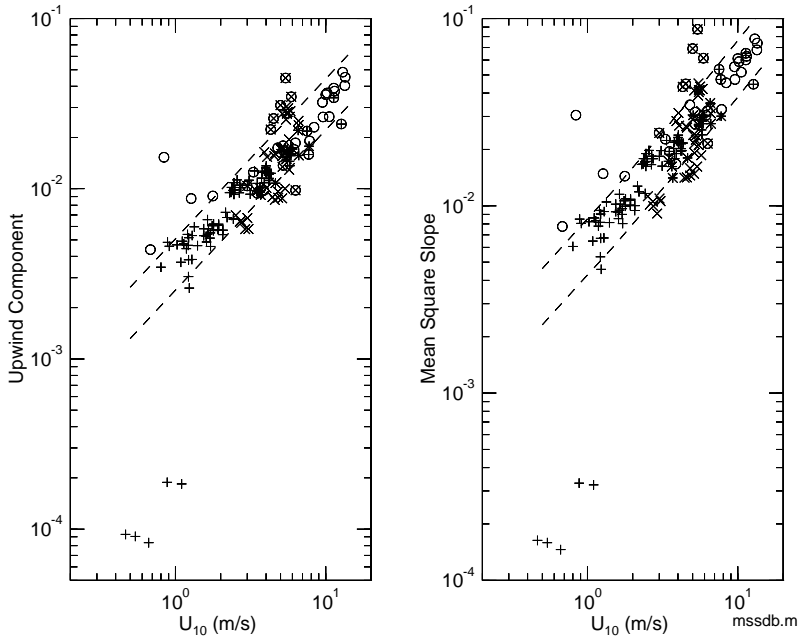


Figure 3: Field Measurements of **a** Upwind Component of the Mean Square Slope, and **b** Total Mean Square Slope, as a Function of Wind Speed. The symbols used in all the plots are: o : Cox and Munk [1954, 1956]; $*$: Hughes et al. [1977]; \oplus or \otimes : Tang and Shemdin [1983]; \times : Hwang and Shemdin [1988]; $+$: The scanning slope sensor data from the present experiment. The factor-of-two envelopes are shown in dashed curves.

wind dependence of the total mean square slope becomes less meaningful at lower wind velocities unless the long-wave components can be filtered out. To illustrate this point, the reported significant wave periods, T_s , of the four low-wind cases in the Cox and Munk [1954, 1956] data set are compared with the theoretical calculation of the saturation wave periods at these wind speeds [Pierson and Moskowitz, 1964; Phillips, 1977]. The results are listed in Table 1.

The large discrepancy in the measured and the predicted magnitudes of the significant wave period strongly supports the suggestion that little correlation with the local wind condition can be expected for these low-wind cases, as reflected from the data plotted in Figure 3.

In contrast, the measurements from the scanning slope sensor show considerably less data scatter with wind speed over the range from 0.7 to 6 m/s. Because detrending of the scanning slope data was performed in the space domain over the 6.2-cm scanning distance, the contribution from longer

Table 1: Comparison of the Measured and Predicted Significant Wave Periods of the Four Low-Wind Cases (Clean Water) of Cox and Munk [1954, 1956]

$U_{41'}$ (m/s)*	0.72	0.89	1.83	1.39
U_{10} (m/s)	0.68	0.84	1.77	1.27
Measured T_s (s)	3	not reported	4	4
Predicted T_s (s)	0.44	0.53	1.1	0.81

* $U_{41'}$ is the wind speed measured at 41 ft height, as reported in Cox and Munk [1954, 1956]

waves was largely removed. The results reveal that the linear wind dependence extends to wind speeds as low as 0.7 m/s.

A small group of MARSEN [Tang and Shemdin, 1983] and TOWARD data [Hwang and Shemdin, 1988] near $U_{10} = 5$ m/s. This is the “mixed-sea” case defined in Tang and Shemdin [1983], but the exact mechanism is probably due to the mechanical resonance of the instrument platform [Hwang, 1995].

The majority of the data points in Figure 3 can be represented by Eq. (1) for the total mean square slope,

$$s = 5.12 \times 10^{-3} U_{10} + 1.25 \times 10^{-3} \quad (1)$$

and by Eq. (2) for the upwind component of the mean square slope,

$$s_u = 3.04 \times 10^{-3} U_{10} + 3.41 \times 10^{-4} \quad (2)$$

Both equations are accurate to within 1.5 dB (i. e., $\sqrt{2}$), based on the comparison with the available ocean data. The linear wind dependence observed in the ocean data is not found in laboratory simulations and radar measurements. More detailed discussions on this topic are presented in Hwang [1995] and Hwang *et al.* [1995].

3.2 Wavenumber Spectrum

The one-dimensional (transect) *wavenumber spectra* of short waves in the ocean derived by the scanning slope sensor are presented in Hwang *et al.* [1995]. In the same paper, these field results are compared with laboratory measurements reported in Jähne and Riemer [1990] and Hwang *et al.* [1993]. The main conclusions of Hwang *et al.* [1995] are as follows:

- A pronounced peak at the transect wavenumber $k_1 = 900$ rad/m is evident in the curvature spectra.

- The slopes of the *curvature spectra* are 1 and -1 on the two sides of the spectral peak.
- The spectral density and *mean square roughness* properties increase linearly with wind speed.
- These observations suggest a spectral function of the form $\chi(k_1) = Au_*c^{-2}c_mk_mk_1^{-4}$, which is proportional to $u_*k_1^{-3}$ in the short gravity wave region and $u_*k_1^{-5}$ in the capillary wave region, where u_* is the wind friction velocity, c_m the minimum phase velocity of surface waves, and k_m the corresponding wavenumber. The dimensionless spectral coefficient A reaches an asymptotic constant at each end of the capillary-gravity wave spectra, with a magnitude of 0.0023 in the gravity region and 0.021 in the capillary region.

While comparing the field and laboratory data, it was found that the characteristics of the spectra collected from the ocean are very different from those obtained in the laboratory. The differences include nearly all the major features of wave spectra: the spectral density level, the threshold wind condition, the wind dependence of mean square roughness and individual spectral components, the apparent spectral slope, and the variation of spectral slopes in the gravity and capillary regions. These observations are summarized in Figure 4 [reproduced from Figure 7 of *Hwang et al.*, 1995], where the short-wave properties in the wavenumber range between 100 and 1600 rad/m are displayed.

The scanning slope sensor projects a rectangular grid pattern composed of eight scanning lines with each line sampled at 50 equal intervals. The two-dimensional wavenumber spectrum can be derived from the scanning slope data. The results for the six cases reported in *Hwang et al.* [1995] are plotted in order of increasing surface roughness in Figure 5.

For the lowest wind velocity case (1213, $U_{10} = 0.84$ m/s, Figure 5a), there is very little structure in the two-dimensional wavenumber spectrum. The ocean surface was observed from the research vessel to be very smooth during this period. The next two cases (1810 and 2422, Figures 5b and 5c) have essentially the same mean wind velocity ($U_{10} = 1.3$ m/s), but the wind fluctuations are much larger for case 2422. The environmental conditions are further complicated by the observation of slick bands on the water surface on both days (see discussion in *Hwang et al.* [1995]). In any event, the spectral intensities near the peaks of these two cases differ by a factor of 10. The energy distribution of the two-dimensional spectra is very narrow (i. e., very localized in the wavenumber domain), showing strong peaks near $k_x = 800$ rad/m. As the wind speed increases, the spectral level continues to increase; at the same time, the directional distribution broadens. In general, the peak spectral energy aligns with the wind direction (along $k_y = 0$), with the exception of the last case (1223, $U_{10} = 5.7$ m/s), where two local spectral peaks are found to be on the opposite sides of the mean wind direction. This may be an indication of bimodal distribution.

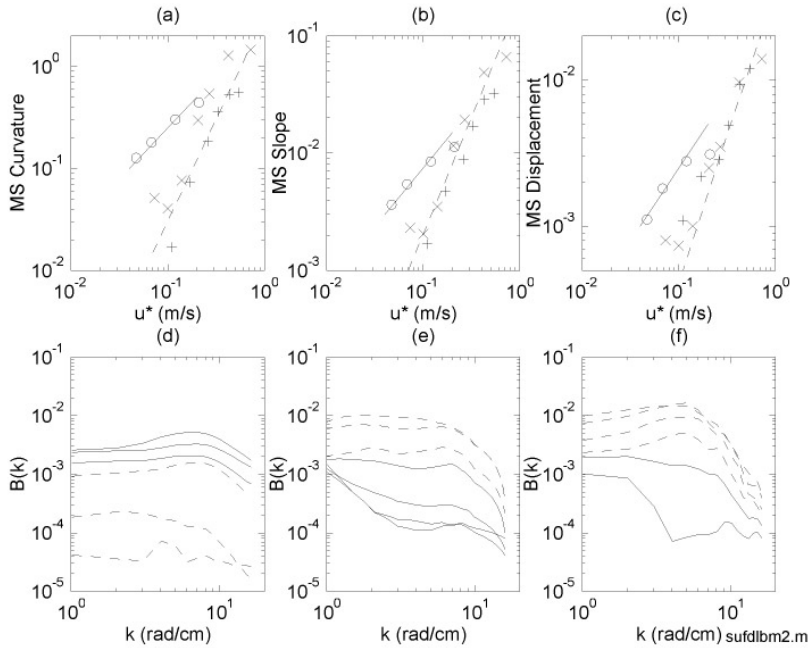


Figure 4: Comparison of Field Data and Laboratory Measurements. The mean square roughness in terms of curvature, slope, and displacement are shown in **a**, **b**, and **c**, respectively. o : Field data from this experiment; \times : Laboratory data [Jähne and Riemer, 1990]; $+$: Laboratory data [Hwang et al., 1993]. The wavenumber spectra of the degree of saturation, $B(k)$, are shown in **d**, **e**, and **f** for the field experiment, laboratory [Jähne and Riemer, 1990], and laboratory [Hwang et al., 1993], respectively. Solid curves represent cases with overlapping wind friction velocities among the three data sets [Hwang et al., 1995].

From these two-dimensional wavenumber spectra, the directional distribution of individual short-wave components can be calculated. Examples of the results are shown in Figure 6. There is an indication of progressive narrowing of the directional distribution toward higher wavenumbers for a given wind speed. For individual wave components, there is a trend of broadening of the directional distribution toward higher wind speeds in the first four cases shown in this figure ($U_{10} = 1.3$ to 3.5 m/s). The wind dependence appears to be stabilizing: the distributions between the last two cases ($U_{10} = 3.5$ and 5.7 m/s) are quite similar. A more quantitative study of the variation of directional distribution as a function of wavenumber and wind speed is in progress. (Note that there is an apparent offset between the directions of wave propagation and wind vector in all the cases presented in Figure 6. This directional offset indicates a misalignment of the buoy orientation due to asymmetric wind and current loadings on the instruments mounted on

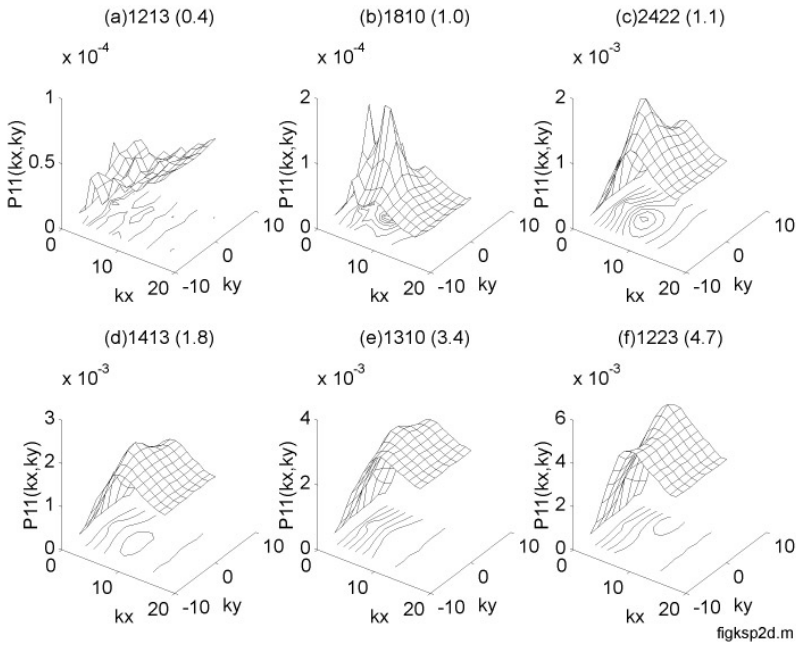


Figure 5: Two-Dimensional Wavenumber Spectra of Capillary-Gravity Waves Measured in the Ocean.

the structure. At lower wind conditions, the oscillatory wave-induced drag dominates the buoy orientation. The magnitude of the directional offset reduces toward higher wind speed, showing the effectiveness of wind vane for aligning the scanning direction with wind. This offset should not be interpreted as that the waves are not propagating in the wind direction.)

4 Conclusions

This article outlines a technique to obtain spatial information of sea surface small-scale waves by recording the refraction of a single scanning laser beam. The method was tested in the laboratory with success, and a system was built for field deployment. Because of the sensitive response of short waves to changes in environmental parameters, whether natural or man-made, attentive care is required to reduce the flow disturbance induced by the instrument platform. The scanning slope sensor presented here was mounted on a *free-drifting* open-frame *buoy* to reduce the relative motion between the flowing water and the members that penetrate through the air-water interface.

Field data collected from one ocean experiment were presented. Excel-

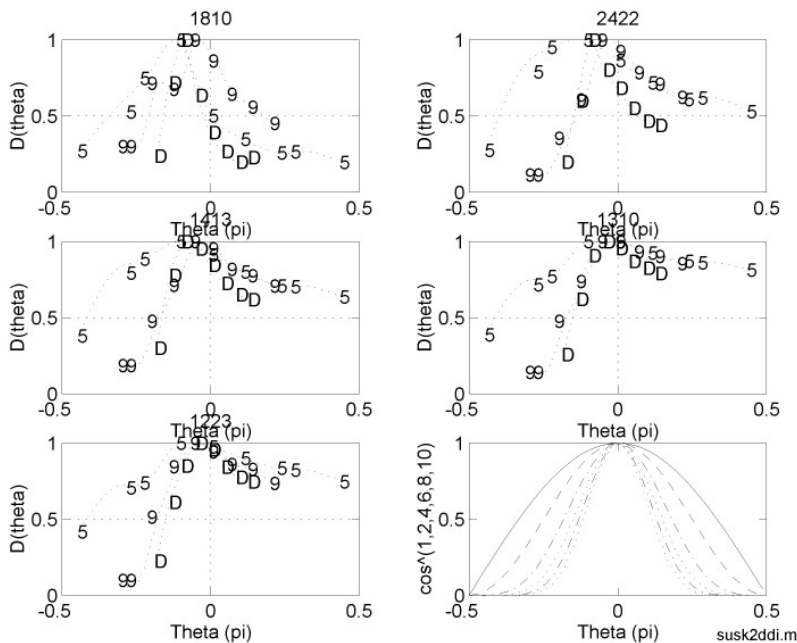


Figure 6: Directional Distributions of the Last Five Cases Shown in Figure 5. **a-e** The wavenumber components shown in each panel are $k = 500, 900$ and 1300 rad/m and are identified by the symbols "5", "9", and "D", respectively. **f** The function $\cos^n \theta$, $n = 1, 2, 4, 6, 8,$ and 10 .

lent agreement of the mean square slope with earlier results, including the measurements of *Cox and Munk* [1954, 1956], *Hughes et al.* [1977], *Tang and Shemdin* [1983], and *Hwang and Shemdin* [1988], reconfirms that the mean square slopes of small-scale waves increases linearly with wind speed. The spatial filtering inherent in the scanning slope technique permits removal of the long-wave contribution to the mean square slopes, which is particularly significant in the low-wind conditions, as found in the measurements of *Cox and Munk* [1954, 1956]. All the field results show remarkable agreement, and most data points fall within the factor-of-two envelopes.

Some preliminary results of the two-dimensional wavenumber spectra were also presented. There is a strong indication of progressive narrowing of the directional distribution toward shorter wavelengths for a given wind speed and a gradual broadening of the *directional distribution* toward high-wind velocities for a given wavenumber. Work is continuing to derive a more quantitative description of these changes. A detailed discussion of the one-dimensional wavenumber spectra and the comparison of field and laboratory measurements has been presented elsewhere [*Hwang et al.*, 1995]. Some key results from that study were summarized in this paper.

Acknowledgements

This work is sponsored by the Office of Naval Research under Contract No. N00014-93-C-0083.

References

- Banner, M. L., and O. M. Phillips, On the incipient breaking of small scale waves, *J. Fluid Mech.*, 65, 647-656, 1974
- Cohen, Y., W. Cocchio, and D. Mackay, Laboratory study of liquid-phase controlled volatilization rates in presence of wind waves, *Env. Sci. and Tech.*, 12, 553-558, 1978
- Cox, C. S., and W. Munk, Statistics of the sea surface derived from sun glitter, *J. Mar. Res.*, 16, 199-225, 1954
- Cox, C. S., and W. Munk, Slopes of the sea surface deduced from photographs of sun glitter, *Bull. Scripps Inst. Oceanogr.*, 6, 401-488, 1956
- Dobson, F., Comment on "Measurement of high-frequency waves using a wave-follower" by S. Tang and O. H. Shemdin, *J. Geophys. Res.*, 90, 9203-9204, 1985
- Hasse, L., Gas exchange across the air-sea interface, *Tellus*, 32, 480-481, 1980
- Hughes, B. A., The effect of internal waves on surface wind waves. 2. Theoretical analysis, *J. Geophys. Res.*, 83, 455-465, 1978
- Hughes, B. A., H. L. Grant, and R. W. Chappell, A fast response surface wave-slope meter and measured wind-wave moment, *Deep-Sea Res.*, 24, 1211-1223, 1977
- Hwang, P. A., A study of the wavenumber spectra of short water waves in the ocean. Part 2. Spectral model and mean square slope, subm. to *J. Phys. Oceanogr.*, 1995
- Hwang, P. A., and O. H. Shemdin, The dependence of sea surface slope on atmospheric stability and swell conditions, *J. Geophys. Res.*, 93, 13903-13912, 1988
- Hwang, P. A., D. B. Trizna, and J. Wu, Spatial measurements of short wind waves using a scanning slope sensor, *Dyn. Atm. and Oceans*, 20, 1-23, 1993
- Hwang, P. A., S. Atakturk, M. A. Sletten, and, D. B. Trizna, A study of the wavenumber spectra of short water waves in the ocean, *J. Phys. Oceanogr.*, 1995 (in press)
- Jähne, B., and K. S. Riemer, Two-dimensional wavenumber spectra of small scale water surface waves, *J. Geophys. Res.*, 95, 11531-11546, 1990
- Jähne, B., K. O. Münich, and U. Siegenthaler, Measurements of gas exchange and momentum transfer in a circular wind-wave tunnel, *Tellus*, 31, 321-329, 1979
- Phillips, O. M., *The Dynamics of the upper ocean*, 2nd ed., Cambridge Univ. Press., 1977
- Phillips, O. M., and M. L. Banner, Wave breaking in the presence of wind drift and swell, *J. Fluid Mech.*, 156, 505-531, 1974
- Pierson, W. J., and L. Moskowitz, A proposed spectral form for fully developed wind seas based on the similarity theory of S. A. Kitaigorodskii, *J. Geophys. Res.*, 69, 5181-5190, 1964
- Shemdin, O. H., and P. A. Hwang, Comparison of measured and predicted sea surface spectra of short waves, *J. Geophys. Res.*, 93, 13883-13890, 1988
- Tang, S., and O. H. Shemdin, Measurements of high-frequency waves using a wave follower, *J. Geophys. Res.*, 88, 9832-9840, 1983

Measurements of Short Ocean Waves during the MBL ARI West Coast Experiment

Jochen Klinke¹ and Bernd Jähne^{1,2}

¹ Scripps Institution of Oceanography, Physical Oceanography Res. Div.
La Jolla, CA 92093-0230, USA
email: jklinke@ucsd.edu

² Interdisciplinary Center for Scientific Computing, University of Heidelberg
Im Neuenheimer Feld 368, 69120 Heidelberg, Germany
email: bjaehne@giotto.iwr.uni-heidelberg.de

doi: 10.5281/zenodo.10399

Abstract

Within the framework of the *Marine Boundary Layers Accelerated Research Initiative (MBL ARI)* a buoy-mounted optical system was developed for the measurement of the small-scale structure of the ocean surface with high spatio-temporal resolution. The system is capable of measuring two wave slope components in an area of 15×20 cm with a dynamic slope range of more than ± 1.25 at a sampling rate of 30 Hz. Wave number spectra up to a maximum wave number of 8000 rad/m can be measured with the instrument. During the MBL ARI West Coast Experiment the system was successfully deployed in the field for the first time. Here, we provide a detailed description of the instrument and present first results from the West Coast Experiment 1995.

1 Introduction

Since the beginning of the century, oceanographers have attempted to measure the shape of the ocean surface with different optical techniques, including the sun glitter technique [Cox and Munk, 1954], the Stilwell technique [Stilwell, 1969], and stereophotography [Shemdin, 1988; Banner, 1989]. Although the various techniques have been greatly improved over the years, until now, no instrument has provided the spatial resolution to recover the full directional spectrum of the oceanic capillary waves. Estimates of the equilibrium spectra oceanic capillary-gravity and capillary waves therefore still rely mainly on wave number spectra obtained from laboratory experiments [Jähne and Riemer, 1990; Jähne and Klinke, 1994; Zhang, 1994; Zhang, 1995].

Short wind waves play an important role in air-sea interaction. They strongly influence the transfer of heat, mechanical energy, momentum, and mass across the atmosphere-ocean interface. Especially the gas exchange rate is correlated with the *mean square slope* of the waves [Coantic, 1980; Jähne et al., 1987]. Until now, much of the knowledge about short wind waves has been largely based on measurements conducted in wind/wave

facilities. The field data available today have mostly been acquired with point measuring devices such as wave height gauges and laser slope gauges. The resulting frequency spectra cannot be readily converted to wave number spectra due to the large Doppler frequency shift of the capillary-gravity waves by the orbital velocity of low frequency waves. In addition, frequency spectra ignore the directionality of the propagation of the waves. Unfortunately, in the field spatial measurements are considerably more difficult than point measurements. Thus only a few spatial measurements of capillary-gravity waves in the field have been published [Lee *et al.*, 1992; Hara *et al.*, 1994, Hwang, 1995]. In those studies *scanning laser slope gauges* were used to obtain the fine structure of the water surface. These systems impose some severe limitations on the measurement of small waves. The system used by Hara *et al.* [1994], for example, scans the water surface on the outline of a 10×10 m square with 129 samples. From laboratory measurements we know that the resulting wave number range from 31 to 990 rad/m is not sufficient to resolve the full spectrum of capillary waves. In addition, since no 2-D data is acquired, the 2-D spatial structure of the waves cannot be revealed. In order to gain deeper insight into the dynamics and the energy balance of ocean wind waves, i.e., the energy input by the wind, nonlinear wave-wave interaction, and energy dissipation, it is necessary to measure the spatio-temporal characteristics of short waves with the same kind of sophistication as it is currently available in laboratory settings.

In this paper we introduce a new system for the optical measurement of the fine structure of the water surface in the field. Section 2 contains a detailed description of the new system and its principle of operation. In the following sections, we present first results from the MBL ARI West Coast Experiment including a preliminary comparison of field and laboratory data. An outlook on necessary improvements of the instrument is given in the last section.

2 Description and Principle of Operation

The new system is based on an *imaging slope gauge* used in previous laboratory experiments to obtain a single slope component of the water surface [Jähne and Klinke, 1994]. This technique had been limited to laboratory settings due to the power constraints of optical light source involved. Now, the light source consists of two LED arrays which generate perpendicular intensity wedges. By pulsing the LED arrays shortly after each other, but in different fields of an interlaced video frame, quasi-simultaneous measurements of both the alongwind and crosswind slope can be performed with a single camera. In order to avoid velocity smearing in the images, the length of the pulse can be chosen between 0.2 and 2 ms. For an image sector of 15.1×19.2 cm, a maximum slope of ± 1.25 can be measured. This is significantly larger than the slope range of the available scanning laser slope gauges. With a resolution of 240×640 pixel per video field the recoverable

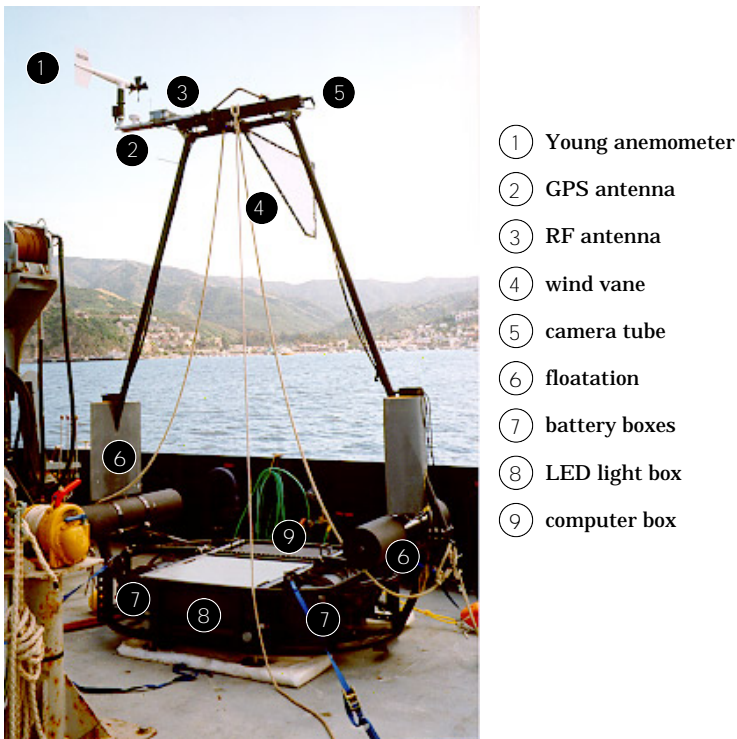


Figure 1: Instrument package on the stern of the R/V New Horizon during the MBL ARI West Coast Experiment in April 1995. The instrument weighs approximately 500 kg and overall dimensions of the instrument are $2.5 \times 1.7 \times 3.4$ m.

wave number range is at least 170–4000 rad/m.

The whole optical system is mounted on the frame of a buoy (see Figure 1) which follows the orbital motion of the longer waves and is critically damped to prevent instability in rougher conditions. The buoy is designed with rather shallow frame to provide minimum flow distortion in both the water and the air. The onboard computer for data and image acquisition is remotely controlled via a radio link from a distance of up to 20 km. Battery power allows free-floating operation for a duration of approximately eight hours. In addition to the 2-D imaging slope gauge, the buoy is equipped with a Young wind speed anemometer, a Global Positioning System receiver (GPS), as well as a digital gyro sensor system which provides stabilized pitch, roll, and magnetic azimuth data. An ultrasound distance meter is used to measure the distance of the camera to the water surface at a rate of 7 Hz.

The system is launched from the R/V New Horizon with the help of a crane. Once deployed, the wind vane forces the instrument to turn into the wind (Figure 2). Due to the effect of ambient and direct sunlight, the operating period for the imaging slope gauge is currently limited to the time from



Figure 2: Freely drifting instrument after deployment from the R/V New Horizon during the MBL ARI West Coast Experiment 1995.

dusk to dawn. Through a radio link, the GPS receiver and the Young wind speed anemometer on the buoy are monitored constantly, to provide the position and drift of the buoy as well as the local wind speed. This is especially important since the instrument was mostly deployed at night. During a single deployment period a total of 6000 single image frames can be recorded digitally at any time. The maximum length of an image sequence at 30 Hz sampling rate is 6.7 s, or 200 image frames. The image data is downloaded to a shipboard computer via Ethernet after recovery of the instrument.

3 First Results

During several deployments from the R/V New Horizon more than 20000 images were recorded. Figure 3 shows examples of corresponding alongwind and crosswind images from deployment in Monterey Bay on May 3, 1995 with wind speeds around 5 m/s. The image pair on the left several trains of capillary waves on the front face of a shorter gravity waves are visible. The image pair on the right shows microscale wave breaking.

The short wave image sequence in Figure 4 illustrates the potential of the instrument for the study of intermittent phenomena and the measurement of phase velocities of capillary waves. The consecutive images show the evolution of several capillary wave trains with different propagation directions. The time delay between the first and the last image is just 100 ms.

In a preliminary analysis of the acquired image data, directional satura-

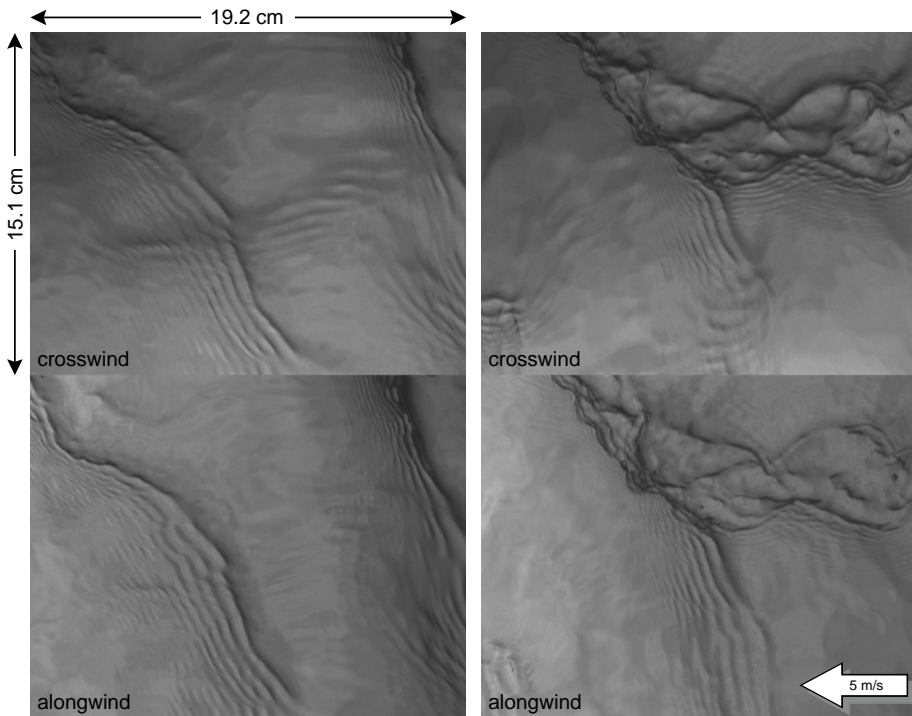


Figure 3: Two image pairs taken at a wind speed of about 5 m/s. The wind is blowing from right to left. Crosswind images are shown in the top half and the corresponding alongwind images are shown in the bottom half. The image sector is 15.1 cm in crosswind and 19.2 cm in alongwind direction.

tion wave number spectra for wind speeds around 5 m/s were obtained from 12 5 s image sequences (150 along/crosswind image pairs at 30 Hz sampling rate). The spectra were averaged to produce the directional spectrum in Figure 5 f. The laboratory spectra in Figures 5 a-e show how the wave field develops with increasing fetch.

An overall similarity in the spectral shape of the lab and field data with regard to the wave number dependence exists, however, several differences are noticeable. First, the angular dispersion of the field data is much wider and not symmetric with regard to the wind direction. This asymmetry, however, may have been caused by a swell system propagating obliquely to the main wind direction. Also, we find an increased saturation level at high wavenumbers for the field data.

The unidirectional wave number spectra shown in Figure 6 confirm this finding. The lab spectra on the left are ensemble averages of 200 images over a 5 min period, while the ocean spectra on the right are averages of 150 images over a 5 s period. It is noteworthy to point out that the spectral

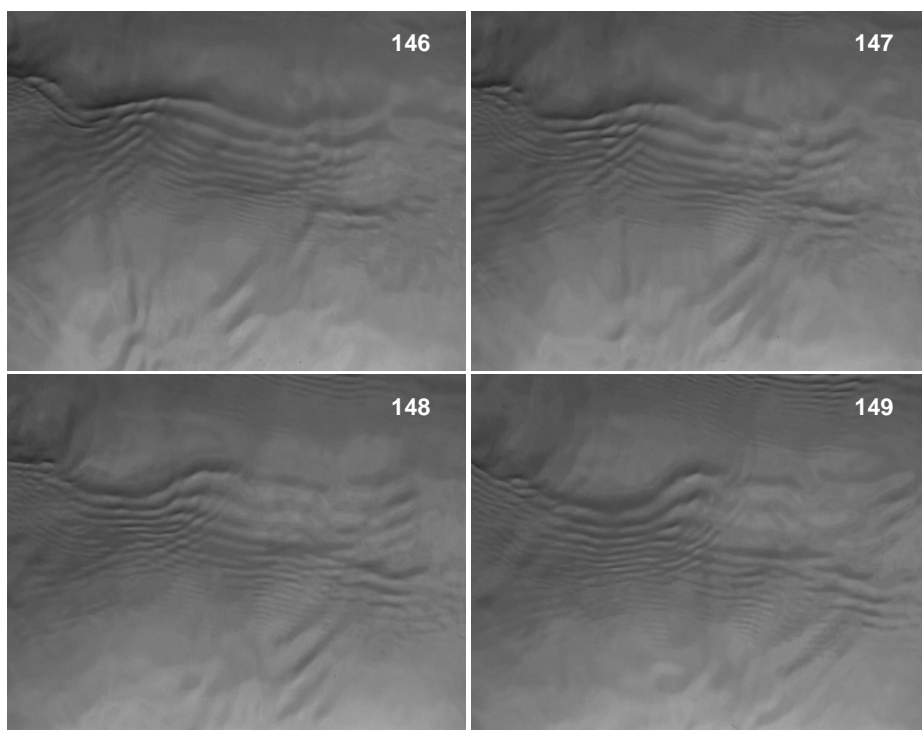


Figure 4: Four consecutive crosswind images out of a sequence of 150 images. The time delay between each images is 33 ms.

cutoff in the unidirectional spectra occurs around the same wave number for the lab and the field data.

4 Conclusions and Outlook

From the shortcomings of the existing scanning laser slope gauges stemmed the need for a field- suitable optical instrument with increased wave number resolution. The presented instrument allows the measurement of the sea surface fine structure with unrivaled spatial and temporal resolution. Additional sensors on the buoy provide the necessary meteorological data as well as information on the background wave conditions.

It turned out that instrument needs to be modified to facilitate the deployment and recovery from a ship. However, once deployed, the buoy rides very stable on the larger waves, even in wind speeds up to 12 m/s; the wind vane helped to steer the buoy into the wind. One drawback is that currently the stabilizing weight is mounted relatively high and requires trimming of the system for different wind forcing. Another disadvantage is that oper-

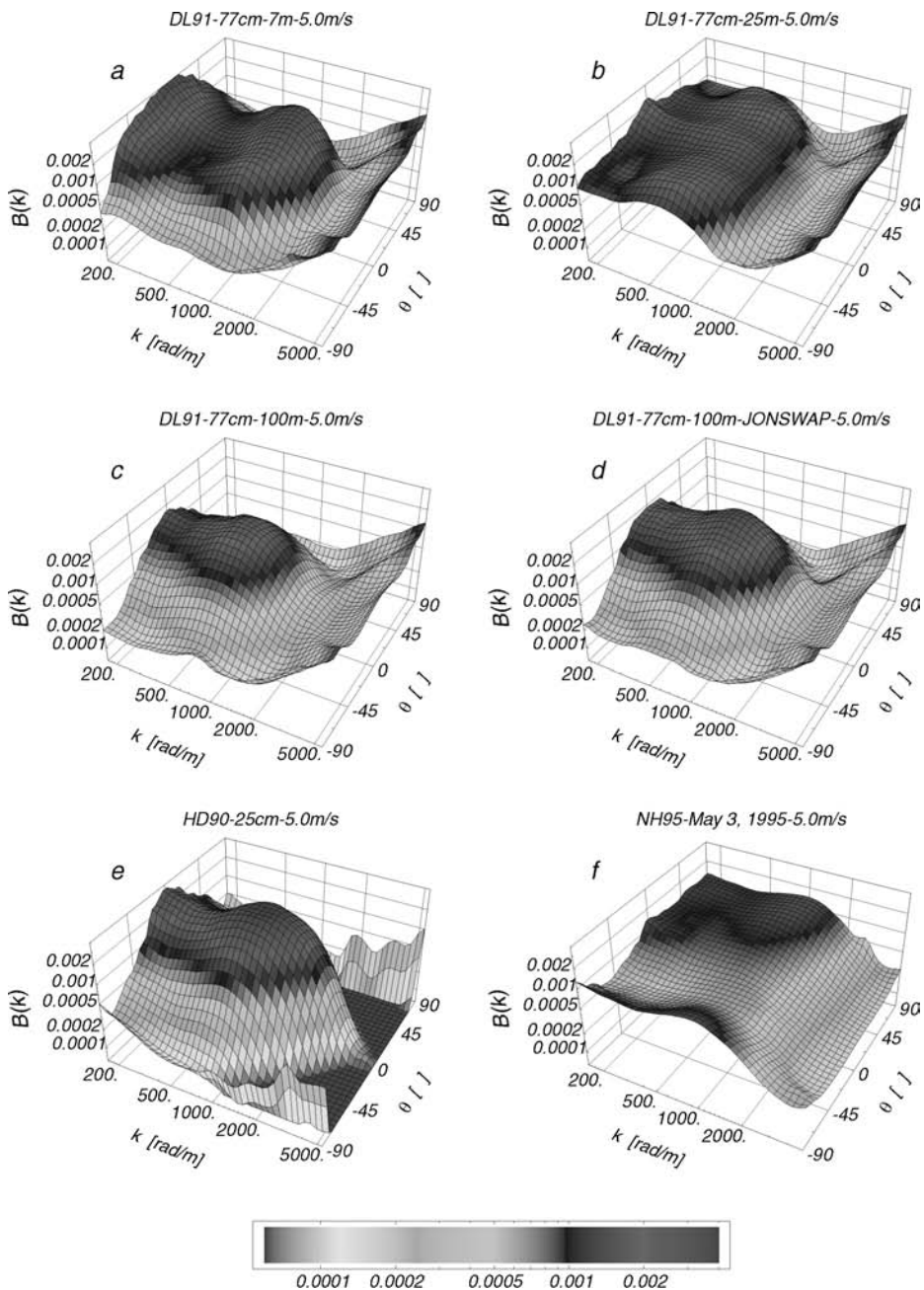


Figure 5: Comparison of directional wave number spectra at 5 m/s wind speed: **a** Delft facility (1991) at **a** 7 m fetch; **b** 25 m fetch; **c** 100 m fetch; **d** 100 m fetch with JONSWAP-type mechanically generated waves; **e** Heidelberg facility infinite fetch (1990); **f** MBL ARI West Coast Experiment 1995. The spectra are twelve 5 s averages for the field and 5 min averages for the lab data. (For color figure, see Plate 11.)

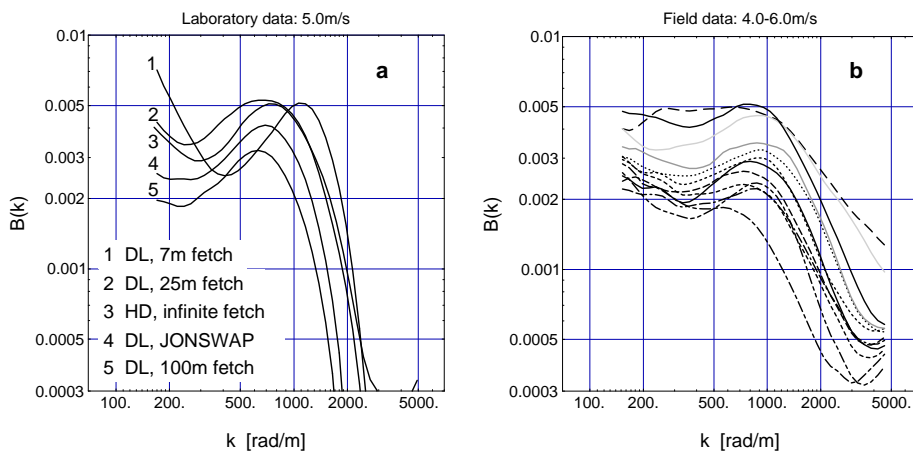


Figure 6: Comparison of unidirectional wave number (integrated over all propagation angles): a) laboratory experiments at wind speeds of 5.0 m/s. Facilities and conditions as indicated; b) MBL ARI experiment 1995 at wind speeds between 4.0 and 6.0 m/s.

ation of the imaging slope gauge is possible only between dusk and dawn. By using multiple cameras with electronic shutter it should be possible to overcome this constraint and to utilize the instrument also in broad daylight conditions.

A first data set of wave slope image sequences was acquired during the MBL ARI West Coast Experiment 1995, the data only provide a first insight into high resolution ocean wave spectra and are neither sufficient for a more quantitative comparison with the available laboratory data, nor are they sufficient for a systematic study of intermittent processes.

However, these first deployments of the buoy in open ocean conditions provided valuable hints for the improvement of the system. We found that especially for deployment of the buoy in higher wind conditions it is necessary to lower the center of mass in order to counteract the torque by the wind drag on the upper structure. Currently, these modifications are incorporated into the system so that it will be available for additional field measurements off the Scripps Pier in fall of 1995. These measurements should allow for a more systematic study of short ocean wave spectra, especially with regard to wind speed dependence and the effect of wind speed variation.

Acknowledgements

This research was performed within the framework of the ONR MBL ARI and the NSF CoOP projects. Financial support from the U.S. Office of Naval Research (N00014-93-J-0093) is gratefully acknowledged. The authors would like to express their sincere thanks to their colleagues from Woods Hole Oceanographic Institution for the excellent cooperation during the West

Coast Experiment off the Coast of California in April 1995. Special thanks are due to Dr. Erik Bock, chief scientist on the R/V New Horizon during the MBLARI cruise, Jochen Dieter, Horst Haussecker, and Sven Weber for their invaluable help in preparation of and during the actual field experiment. In addition, we would like to acknowledge the support by David Malmberg and the other personnel of the Scripps Marine Science and Development Shop.

References

- Banner, M. L., I. S. F. Jones, and J. C. Trinder, Wavenumber spectra of short gravity waves, *J. Fluid Mech.*, 198, 321-344, 1989
- Barter, J., K. L. Beach, D. Kwok, M. Ludwig, H. Rungaldier, J. C. Schatzman, I. Stonich, R. N. Wagner, and A. B. Williams, TRW surface truth measurement system, TRW Internal Report 53563-6005, 1990
- Coatic, M., Mass transfer across the ocean/air interface: small scale hydrodynamic and aerodynamic mechanisms, *Physicochemical Hydrodynamics*, 1, 249-279, 1980
- Cox, C., and W. Munk, Measurement of the roughness of the sea surface from photographs of the sun's glitter, *J. Opt. Soc. Am.*, 44, 838-850, 1954
- Hara, T., E. J. Bock, and D. Lyzenga, In situ measurements of capillary-gravity wave spectra using a scanning laser slope gauge and microwave radars, *J. Geophys. Res.*, 99, 12,593-12,602, 1994
- Hwang, P. A., Spatial measurements of small-scale ocean waves, this volume, 1995
- Jähne B., and K. O. Münnich, R. Bösinger, A. Dutzi, W. Huber, and P. Libner, On the parameters influencing air-water gas-exchange, *J. Geophys. Res.*, 92, 1937-1949, 1987
- Jähne B., and K. Riemer, Two-dimensional wave number spectra of small-scale water surface waves, *J. Geophys. Res.*, 95, 11,531-11,546, 1990
- Jähne, B. and J. Klinke, Wave Number Spectra of Short Wind Waves -Laboratory Results and Extrapolation to the Ocean, submitted to *JGR Oceans*, 1994
- Keller, W. and B. L. Gotwols, Two-dimensional optical measurement of wave slope, *Appl. Opt.*, 22, 3476-3478, 1983
- Lee, P., J. D. Barter, K. L. Beach, C. L. Hindman, B. M. Lake, H. Rungaldier, J. C. Schatzman, J. C. Shelton, R. N. Wagner, A. B. Williams, and H. C. Yuen, Recent advances in ocean surface characterization by a scanning laser slope gauge, in *Optics of the Air-Sea Interface: Theory and Measurements*, L. Estep, ed., *Proc. Soc. Photo-Opt. Instrum. Eng.* 1749, 234-244, 1992
- Shemdin, O. H., H. M. Tran, and S. C. Wu, Directional measurements of short ocean waves with stereophotography, *J. Geophys. Res.*, 93, 13891-13901, 1988
- Stilwell, D., Directional energy spectra of the sea from photographs, *J. Geophys. Res.*, 74, 1974-1986, 1969
- Zhang, X., Wavenumber spectrum of very short wind waves — An application of two-dimensional Slepian windows to spectral estimation, *J. Atmos. & Oceanic Technol.*, 11, 489-505, 1994
- Zhang, X., Capillary-gravity and capillary waves generated in a wind wave tank: observations and theories, *J. Fluid Mech.*, 289, 51-82, 1995

Wind-Wave Coupled Downward-Bursting Boundary Layer Below the Sea Surface — In Relation to Penetration Depth of Bubble Clouds

*Yoshiaki Toba*¹ and *Hiroshi Kawamura*²

Physical Oceanography Group, Tohoku University,
Sendai, 980-77 Japan

¹Concurrently affiliated with Earth Observation Research Center (EORC) of National Space Development Agency of Japan (NASDA) Tokyo, 106 Japan and Japan Marine Science and Technology Center (JAMSTEC), Yokosuka, 237 Japan

²Center for Atmospheric and Oceanic Studies, Faculty of Science, Tohoku University, Sendai 980-77, Japan

Abstract

By re-examination of data of the turbulent structure beneath *wind waves* in laboratory tanks by *Yoshikawa et al.* [1988], we propose the existence of a particular *turbulent boundary layer* which is directly coupled with wind waves, a “*downward-bursting boundary layer (DBBL)*” in water beneath wind waves. The data indicates that the depth of this layer is from 3 to 7, or about 5 times the significant wave height of wind waves. This agrees with data of acoustic observations of bubble clouds under breaking wind waves in the sea made by *Thorpe* [1986, 1992]. It is inferred, using other data also, that DBBL is formed in equilibrium with the local wind waves, as a common feature from initially generated wind waves, young laboratory wind waves to mature wind waves in the sea. Some discussion on the physical basis for this nature is also given.

1 Introduction

In recent years, it has been reported that there exists the ocean surface zone where *wave-enhanced turbulence* is recognized. The depth of this layer was reported as 10 times the wave amplitude [*Kitaigorodskii et al.*, 1983; *Thorpe*, 1984], or about 0.2 times the surface wave length [*Thorpe*, 1992]. *Craig and Banner* [1994] proposed a theoretical model for this layer, and referred to the wave enhanced layer, with the shear layer in the deeper water.

Yoshikawa et al. [1988] demonstrated, by a laboratory wind-wave tank experiment, that turbulence in this layer was produced primarily by downward bursting of water from the vicinity of wind-wave surfaces, even though there was no visible wave breaking with air entertainment, and that this downward bursting is the principal mechanism for the downward momentum and heat fluxes within this layer. They reported that the depth of this layer was 0.5 times the representative wavelength of wind waves in the laboratory cases.

Ebuchi et al. [1992] made a *flow visualization* study of this downward bursting, and made a model simulation.

Considering the systematic difference in wave steepness from young laboratory wind waves to mature ocean wind waves, it is shown in this paper, by re-examination of the data by *Yoshikawa et al.* [1988] and others, that thickness of this layer is of the order of five times the significant wave height of wind waves. Data of flow visualization of turbulence beneath very young laboratory wind waves by *Toba et al.* [1975], *Okuda et al.* [1976], and data of CO₂ concentration boundary layer in a gas exchange experiment by *Komori and Shimada* [1995] indicate the same thickness of this special boundary layer. Measurement data of the depth of bubble clouds in the sea by using acoustic devices by *Thorpe* [1986; 1992] also indicate a similar depth. Consequently, it is inferred that the above-described depth of the downward bursting boundary layer holds equally for laboratory wind waves to windsea in the sea.

A discussion on the physical basis for this depth to be proportional to the significant wave height is also given.

2 Re-Examination of Past Experiment and Observation Data

2.1 Data by *Yoshikawa et al.* [1988]

Structure of the turbulent boundary layer underneath laboratory wind waves was studied by using a combination of a two-component sonic flowmeter with a high-sensitivity thermometer array, in a wind-wave tank of 20 m length and 60 cm width of Tohoku University, by *Yoshikawa et al.* [1988]. The turbulence energy was dominant in a frequency range of 0.01 to 0.1 Hz, which was much smaller than the wind-wave frequency of 2 to 5 Hz, and in which the turbulence was anisotropic. By analyses of the time series, it was found that conspicuous events related to this main turbulence energy band were the downward bursting from the vicinity of the wave surface.

For the values of turbulent fluctuation, u' and w' , components of wind-wave motion had been thus eliminated by filtering out. They noted the existence of a layer with constant turbulence intensity and constant Reynolds stress, with depths different for differing wind conditions, and reported that these depth values collapsed when normalized by using wave length of the peak frequency waves, λ_p and reported that this layer was confined to about 0.5 of λ_p .

Their data have been re-analyzed and are shown in Figure 1. The depth z is normalized by the *significant wave height* H_s , in the ordinate instead of the wave length in their case, and in the abscissa turbulence intensities are here normalized by the *Stokes drift velocity* of the peak frequency waves, u_0 , as will be explained a few sentences later.

From the ordinate of Figure 1, it is inferred that the depth of the layer of constant turbulence intensities is about $5 H_s$, rather than $0.5 \lambda_p$. In very

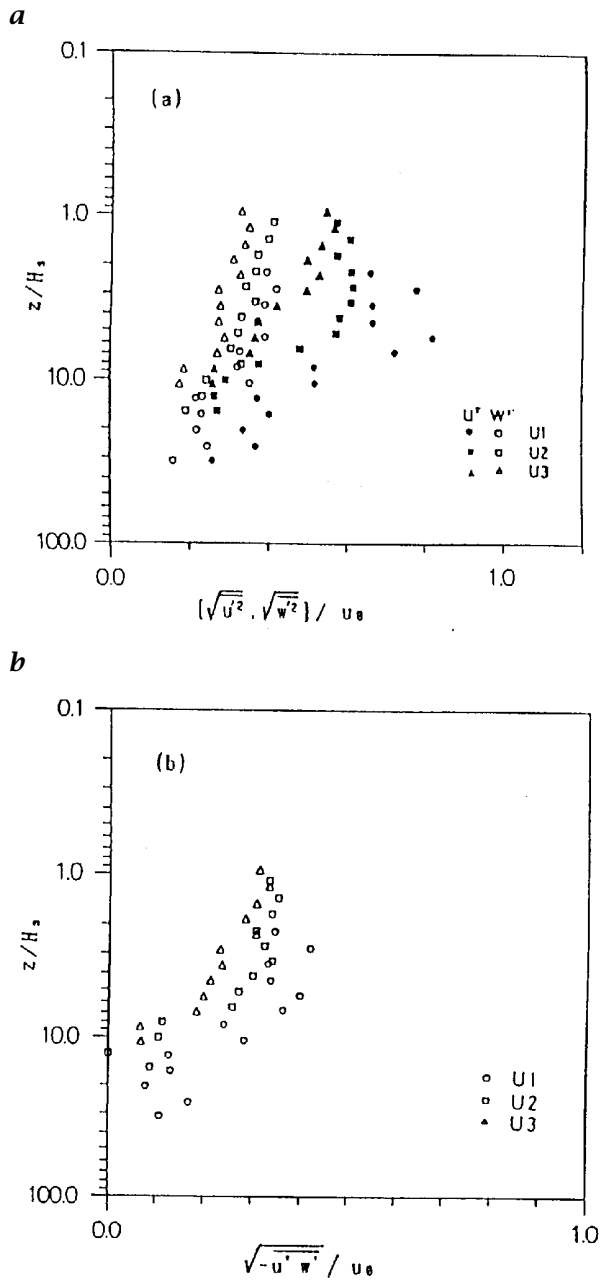


Figure 1: Re-analyzed non-dimensional presentation of Yoshikawa et al. [1988] data. Profiles of turbulence intensities (a) and Reynolds stress (b) beneath laboratory wind waves for three wind conditions.

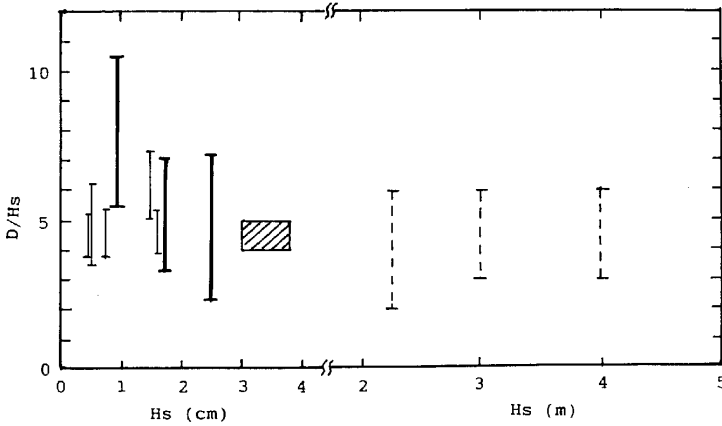


Figure 2: A composite data set of the range of the wind-wave coupled downward bursting boundary layer (DBBL), normalized by the significant wave height of wind waves, H_s . Thin segments are from data of Toba et al. [1975], thick ones from Yoshikawa et al. [1988], a rectangle from Komori and Shimada [1995], and broken segments from data of Thorpe [1986; 1992].

young laboratory wind waves, the steepness is close to 0.1, and it decreases down to about 0.03 for ocean waves of mature wave ages. It seems more reasonable to consider that the depth of the wind-wave coupled special turbulent boundary layer is related to the wave height rather than the wave length. In fact, there are many other data besides ours which indicate that this observation is common to wind-wave conditions from very young laboratory wind waves to mature windsea.

The ranges of depth where sharp decreases of the abscissa values occur in Figure 1 are shown in Figure 2 by thick segments for the three wind cases, together with other data. As for the abscissa of Figure 1, collapse of the data points is nothing but the indication of the satisfaction of the $3/2$ -power law for growing wind waves, as written down by the following relations [Toba, 1988]:

$$(\overline{-u'w'})^{1/2} = u_{*w} \propto u_0 = \pi \delta H \sigma_p / 2 = 2\pi^3 H^2 / gT^3 \quad (1)$$

where u_{*w} is the water friction velocity, δ the wave steepness defined as the ratio of wave height and wave length, g is the acceleration of gravity, H and T are average wave height and period, respectively. The data points indicate that $u_{*w}/u_0 = 0.33$, which may be converted to $u_0/u_* = 0.115$. In Toba [1972], it was shown that the $3/2$ -power law may also be written by $u_0/u_* = \pi^3 B^2 = 0.12$. This agrees closely with the observation from Figure 1.

2.2 Depth of Gas Concentration Boundary Layer in a Laboratory Tank by Komori and Shimada [1995]

Komori and Shimada [1995] made an experiment of air-water CO₂ exchange in a wind-wave tank. The range of their measurement was from 5 to 14 m/s in the mean wind speed, and the range of data points is shown in Figure 2 by a triangle area. The data indicates that the depth of the *gas concentration boundary layer* was between 4 and 5 times the representative wind-wave height.

2.3 Bubble Distribution Analysis in a Wind-Wave Tank by Toba [1961]

In his earlier study by using a wind-wave tank of a similar size with Tohoku, Toba [1961] measured bubble distribution below breaking wind waves. The range of the bubble distribution was up to 3 times the average wind-wave height. However, since the bubbles observed were only large ones to be photographed, it is considered that the rising speed of the air bubbles caused the smaller depths observed.

It should be noted that Toba estimated from this bubble distribution an average *eddy diffusivity* within this layer, by assuming the diffusion-buoyancy rising equilibrium of bubbles. The values were of the order of 50 cm²/s. If we estimate the value of eddy diffusivity by using a conventional equation of $K = ku_*z$, where $k = 0.4$ is the von Kármán constant, it becomes one order of magnitude smaller than this value.

2.4 Bubble Cloud Observation Data in the Sea by Thorpe [1986; 1992]

Recent years, *bubble cloud* measurements by using an acoustic system have become effective. Thorpe's [1986; 1992] data of bubble clouds produced by breaking wind waves in the sea, showed a depth of 3 to 6 times the significant waves. Figure 2 contains these values as broken segments, obtained by reading from the data of his paper [1992]. It is noticeable that these values are in very good agreement with the above described wind-wave tank data.

It should be noted that Kitaigorodskii *et al.* [1983] reported, from data of observation by using a drag sphere velocity probe in Lake Ontario by Donelan [1978], that there was a *two-layer structure*, and that in the upper layer with a thickness of the order of 10 times the rms wave amplitude, intense turbulence generation by waves was observed. This is also in agreement with our 5 times the significant wave height.

3 Interpretation and Physical Considerations

3.1 Interpretation of the Experimental and Observational Results

The description of the previous section indicates the existence of a particular turbulent boundary layer which is directly coupled with wind waves, with the

depth of from 3 to 7, or about five times the significant wave height, H_s .

We call it “the downward bursting boundary layer (DBBL)” beneath wind waves. In analogous to our studies of the ordered motion above wind waves [Kawamura and Toba, 1988], we may consider that the depth of $3 H_s$ corresponds to the inner boundary layer, and that of $7H_s$ the outer boundary layer.

It is also inferred that, in this layer, the value of eddy diffusivity is much larger than the values estimated from the usual wall law, and that it is characterized by turbulent conditions where the wind and wind waves are strongly coupled, and that it is closely related with the mechanism of the existence of the $3/2$ -power law. The usual boundary layer of the upper ocean will begin underneath this special layer.

Since the depth of DBBL of the order of $5H_s$ is common for various stages of wind-wave generation from initial wavelets to wind waves in the sea, it is considered that the DBBL exists in local equilibrium with the wind waves, just like the existence of the $3/2$ -power law.

3.2 Physical Consideration of the H_s - Proportionality of DBBL

The situation that the depth of DBBL is given only by H_s may be interpreted as follows. The origin of the ordered motion below wind waves are in penetration of very local wind-drift shear flow, which is distributed along the phase of wind waves, together with breaking of wave crests. Consequently, the energy of these ordered motions is of the surface origin. The undulation of the wind-wave surfaces is confined within the vertical range H_s . This should be the origin of the H_s - proportionality of the depth of DBBL.

3.3 Relationship with Langmuir Circulation

It is often considered that bubble clouds are carried down by *Langmuir circulation*. However, there is no definite theory to predict this depth. According to Craik and Leibovich [1976], Langmuir Circulation is formed by conversion of the wind-shear vorticity to the vorticity in the direction of the wind. If we consider this mechanism, the depth of Langmuir Circulation may be determined by the depth of the direct action causing *ordered motions* by downward bursting, as observed in the wind-wave tanks.

Bubbles as detected by Thorpe's [1986] acoustic devices were of the size of the order of $10 \mu\text{m}$ in diameter, and their terminal velocity of rising by buoyancy force is expected negligible compared to the turbulence velocities. Consequently, we may assume that the depth of penetration of bubble clouds in the sea, in this case, is same as the depth of DBBL, in a similar way as the observation in the wind-wave tanks.

Acknowledgements

The authors express many thanks to Mr. Shoichi Kizu and Mr. Ikuo Yoshikawa for their help in the course of the analyses of data.

References

- Craig, P. D., and M. L. Banner, Modeling wave-enhanced turbulence in the ocean surface layer. *J. Phys. Oceanogr.*, 24, 2546-2559, 1994
- Craik, A. D. D. and S. Leibovich, A rational model for Langmuir circulations, *J. Fluid Mech.* 73, 401-426, 1976
- Donelan, M. A., Whitecaps and momentum transfer, in *Turbulent Fluxes Through the Sea Surface, Wave Dynamics and Prediction*, eds., A. Favre and K. Hasselmann, Plenum, 273-287, 1978
- Ebuchi, N., H. Kawamura and Y. Toba, Bursting phenomena in the turbulent boundary layer beneath the laboratory wind-wave surface, in *Natural Physical Sources of Underwater Sound*, ed. by B. Kerman, pp. 263-276, Kluwer, Morwell, Mass., 1993
- Kawamura, H. and Y. Toba, Ordered motion in the turbulent boundary layer over wind waves, *J. Fluid Mech.*, 197, 105-138, 1988
- Kitaigorodskii, S. A., M. A. Donelan, J. L. Lumley and E. A. Terray, Wave-turbulence interactions in the upper ocean. Part II: Statistical characteristics of wave and turbulent components of random velocity field in the marine surface layer, *J. Phys. Oceanogr.*, 13, 1988-1999, 1983
- Komori, S. and T. Shimada, Laboratory estimation of CO₂ transfer velocity across the air-sea interface. in *Biogeochemical processes and Ocean Flux in the Western Pacific*, ed. Y. Nozaki, Terra Sci. Pub. Co., Tokyo, 1995
- Okuda, K., S. Kawai, M. Tokuda and Y. Toba, Detailed observation of the wind-exerted surface flow by use of flow visualization methods. *J. Oceanogr. Soc. Japan*, 13, 53-64, 1976
- Thorpe, S. A., On the determination of K_v in the near-surface ocean from acoustic measurements of bubbles. *J. Phys. Oceanogr.*, 14, 855-863, 1984
- Thorpe, S. A., Measurements with an automatically recording inverted echo sounder; AIREX and the bubble clouds, *J. Phys. Oceanogr.*, 16, 1462-1478, 1986
- Thorpe, S. A., Bubble clouds and the dynamics of the upper ocean, *Quart. J. Roy. Meteor. Soc.*, 118, 1-22, 1992
- Toba, Y., Drop production by bursting air bubbles on the sea surface (III) Study by use of a wind flume, *Mem. Coll. Sci. Univ. Kyoto, Ser. A*, 29, 313-344, 1961
- Toba, Y., Local balance in the air-sea boundary processes I. On the growth process of wind waves. *J. Oceanogr. Soc. Japan*, 28, 109-120, 1972
- Toba, Y., M. Tokuda, K. Okuda and S. Kawai, Forced convection accompanying wind waves, *J. Oceanogr. Soc. Japan*, 31, 192-198, 1975
- Toba, Y., Similarity laws of the wind wave and the coupling process of the air and water turbulent boundary layers, *Fluid Dyn. Res.*, 2, 263-279, 1988
- Yoshikawa, I., H. Kawamura, K. Okuda and Y. Toba, Turbulent structure in water under laboratory wind waves, *J. Oceanogr. Soc. Japan*, 44, 143-156, 1988

Energy Dissipation through Wave Breaking and the Air-Sea Exchange of Gases

D. K. Woolf

Department of Oceanography, University of Southampton,
Southampton Oceanography Centre, Waterfront Campus, European Way,
Southampton, SO14 3ZH, UNITED KINGDOM
email: dkw@willow.soton.ac.uk

Abstract

Previous experiments have shown that large enhancements of air-sea transfer are likely as a result of “whitecapping” breaking waves. Transfer will be enhanced by the additional near-surface turbulence, by exchange through the surface of bubbles, and by disruption of the sea surface microlayer by surfacing and bursting bubbles. The description of each mechanism remains incomplete, and uncertainties in estimates of air-sea transfer velocities are correspondingly large. Knowledge of wave energy loss and the resultant turbulent dissipation rates in the upper ocean can be used to estimate the contribution of near-surface turbulence to air-sea gas transfer. *Kitaigorodskii* [1984] has previously applied results of laboratory experiments on homogenous turbulence to air-sea transfer; he assumed a reasonably uniform dissipation rate would be sustained by breaking waves. Recent results show that dissipation rates are only intermittently high and suggest that it is more reasonable to describe most of the upper ocean as a shear layer, with only a few patches where breaking-wave-generated turbulence dominates. The contribution of this turbulence to air-sea gas transfer is strongly dependent on the fractional surface coverage of these patches. Assuming a correspondence to whitecap coverage, the contribution of highly turbulent patches to the surface-averaged transfer is generally modest but highly wind speed dependent. Senescent but growing patches of turbulence several wave periods after wave breaking, though accounting for only a few percent of dissipation associated with wave breaking, make a more significant contribution to transfer. On the basis of this model, the turbulence due to wave breaking has a significant effect on air-sea gas transfer but is unlikely to be a dominant mechanism. If a significant fraction of wave energy loss is initially expended in submerging bubbles to a small depth (~10 cm) then the resulting bubble-mediated transfer is likely to dominate at high wind speeds. Consideration of the dissipation of wave energy is useful, but the individual and combined effect of breaking wave processes on air-sea gas transfer remain difficult to calculate.

1 Introduction

Most theories of the transfer of gas across the marine microlayer compare the oceanic surface layer to the *shear layer* in flow over a rigid surface. In particular, the simplest boundary layer theories [e. g., *Deacon*, 1977] equate the transfer of a gas or heat across the marine microlayer to transfer across the turbulent shear boundary layer next to a rigid surface for any particular Schmidt/Prandtl number and friction velocity. These theories have been modified by various workers in consideration of a different hydrodynamic boundary condition (i. e., a free rather than a rigid surface) and the roughness and deformability of the surface [*Jähne et al.*, 1987], but the basic analogy to a turbulent shear layer remains. *Kitaigorodskii* [1984] pointed out that consideration of shear-produced turbulence alone appears mistaken when in most sea conditions wave breaking will greatly influence the character of the subsurface turbulence. A number of studies [e. g., *Merlivat and Memery*, 1983] have shown that “whitecapping” appears to strongly enhance gas transfer. In a wave tunnel, this “wave breaking regime” is commonly only encountered at high wind speeds, but detailed observational and statistical studies of whitecapping [*Monahan and O’Muircheartaigh*, 1986] suggest wave breaking may be important even at moderate wind speeds.

The increase in transfer velocities associated with the onset of large-scale wave breaking has commonly been solely identified with transfer mediated by the bubbles entrained by the breaking waves. In fact, at least three quite distinct mechanisms of gas transfer are associated with large-scale *wave breaking* and *air entrainment*:

1. Transfer associated with patches of turbulence in the upper ocean generated by breaking waves.
2. Transfer mediated by bubbles, where gas is within a bubble during an interval of its exchange between atmosphere and ocean.
3. Transfer across the sea surface where the microlayer has been “internally disrupted” by a surface process (in comparison to the essentially external forcing described in (1)), such as a bubble surfacing and bursting.

There have been several important theoretical, laboratory and field studies of the energy input into waves, the loss of this energy due to wave breaking and the statistics of *turbulent dissipation* in the upper ocean. It has also been discovered by *Lamarre and Melville* [1991] that a very considerable fraction of the energy dissipated in a breaking wave can initially be expended in entraining air beneath the surface (gravitational potential energy). In this paper, the efficiency of the first “simple turbulence” mechanism is considered. It is also confirmed that an estimate of the surface flushing of the upper ocean by bubbles [*Woolf*, 1993], upon which estimates of the importance of the second and third mechanisms can be based, is consistent with energy considerations. The effect of turbulent plumes on the dynamics of

bubbles is also briefly discussed.

2 A Model of Gas Transfer by Turbulent Patches

A fluid dynamical theory of air-sea gas transfer in the presence of breaking waves has been presented by *Kitaigorodskii* [1984]. He estimated transfer using “the idealised picture of a continuously existing *turbulent patch*, supported by the sequence of breaking events”. Thus, the description of the near-surface ocean as a shear layer was entirely abandoned in his model. This theory further assumes that this turbulence is isotropic and the surface is fluid. There have been several laboratory measurements of the gas transfer across a free surface in the presence of mechanically-generated, isotropic turbulence. For instance, one of these studies [*Dickey et al.*, 1984] supports the following formula for transfer velocity,

$$K = 0.17[\epsilon(0)\nu/Sc^2]^{1/4} \quad (1)$$

where $\epsilon(0)$ is the near-surface dissipation, ν is kinematic viscosity and Sc is the Schmidt number of the gas. Note that the transfer velocity, K , is proportional to the quarter power of the dissipation rate. Equation (1) and an estimate of the near-surface dissipation rate sustained by the loss of wave energy is sufficient to estimate transfer velocity in the style of *Kitaigorodskii*. As discussed in the next section, the “dissipation term” in the wave energy budget is the subject of much scientific discussion, and probably has quite a complicated dependence on sea state. For our simple model, we adopt the following simple estimate of the rate of wave energy dissipation, E , solely as a function of the friction velocity in the water, w_* , attributed to Banner [in *Craig and Banner*, 1995],

$$E = 100w_*^3 \quad (2)$$

An integration depth, H , is defined so the mean near-surface dissipation is given by,

$$\xi = E/H \quad (3)$$

Assuming (as *Kitaigorodskii*) that the dissipation rate is uniform over the sea surface ($\xi = \epsilon(0)$) and combining (1), (2) and (3),

$$K = 0.17[100w_*^3\nu/Sc^2H]^{1/4} \quad (4)$$

An approximate dependence of transfer velocity on wind speed, U , can be deduced, by equating the atmospheric and oceanic stresses

Transfer Velocities versus Wind Speed

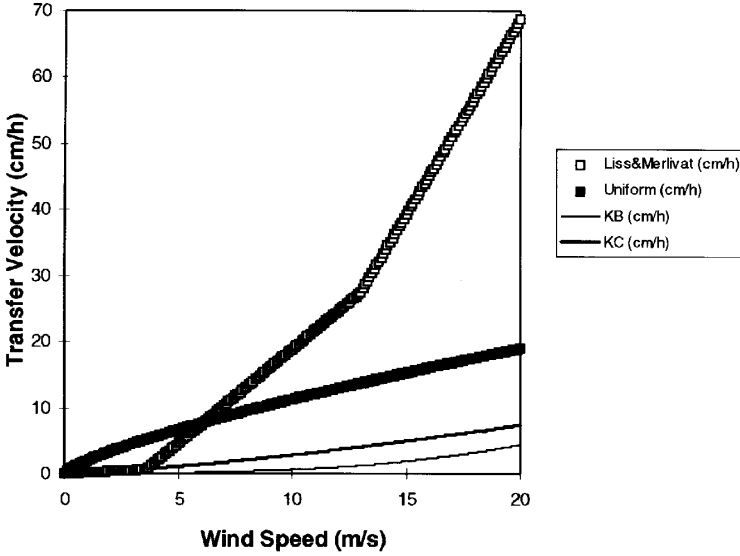


Figure 1: The variation of transfer velocity with wind speed according to the parameterisation of Liss and Merlivat [1986], a model with uniform dissipation rates supported by breaking waves, equation (7), and for a model of patches of turbulence separated into two contributions, K_B and K_C , (12) and (17). (Calculated with the constants: $Sc = 600$, $\nu = 10^{-6} \text{ m}^2 \text{ s}^{-1}$, $H = 1 \text{ m}$).

$$\rho_a u_*^2 = \rho_w w_*^2 \quad (5)$$

where, u_* is the friction velocity of the wind and the ratio of densities, $\rho_w/\rho_a \approx 800$, and inserting a drag coefficient, $C_D = 2 \times 10^{-3}$ say, where

$$u_*^2 = C_D U^2 \quad (6)$$

Combining (4), (5) and (6),

$$K = 0.0043 U^{3/4} [\nu / Sc^2 H]^{1/4} \quad (7)$$

This result (assuming also $H = 1$ metre) is plotted in Figure 1.

Consider the possibility that though the mean dissipation rate is the same, the dissipation is restricted to a fraction, f , of the sea surface. The dissipation rate within a patch is raised compared to the uniform case ($\xi =$

$f\epsilon(0)$), but transfer is only enhanced over a fraction of the sea surface. The contribution to the mean air-sea transfer velocity is thus given by the following modification of (4),

$$K = 0.17[100f^3w_*^3\nu/Sc^2H]^{1/4} \quad (8)$$

The mean transfer velocity is reduced by a factor $f^{-3/4}$ compared to the uniform case, for example if the dissipation is restricted to 1% of the sea surface then the mean transfer velocity associated with this mechanism would be reduced by a factor of thirty. Also, if the fractional area, f , increases in proportion to the rate of energy input from the wind (as is commonly supposed for whitecap coverage [Wu, 1979]), then the transfer velocity will be very strongly dependent on wind speed (approximately as friction velocity cubed). Thus, one of the most important features of turbulent dissipation rates is their patchiness. Measurements in the ocean suggest that it is neither satisfactory to assume a uniform dissipation rate, nor that the extent of breaking wave patches is entirely limited, reality is somewhere between these two simple idealised pictures, though it is probable that very high dissipation rates are limited to a small fraction of the surface layer. Agrawal *et al.* [1992] reported that while dissipation was generally enhanced above the "law of the wall" values expected for a shear flow in a surface layer, the modal value of dissipation remained at the law-of-the-wall value. Osborn *et al.* [1992] found some correspondence between (acoustically-detected) bubble clouds and higher dissipation rates.

Far more detail on the statistics of dissipation near the sea surface are required. In the meantime, it is interesting to apply the laboratory results of Rapp and Melville [1990], to the question of the efficiency of breaking-wave-generated turbulence in the air-sea exchange of gases. Rapp and Melville report that only 2-4% of the energy lost in breaking remains in the plume after 4 wave periods. Only after this development period does the plume approximate a decaying turbulent patch (even then it is non-isotropic). The total kinetic energy in the patch then decays inversely with time (as expected in the "initial period" [Batchelor and Townsend, 1948]) while also entraining more fluid at a scale velocity. It is clear that application of results for simple, homogenous turbulence to this complex turbulent phenomenon is unsatisfactory, but we shall apply the above model (equation (8) and preceding). In very crude mimicry of the behaviour reported by Rapp and Melville, we consider patches of this type, generated by n breaking waves (per unit area \cdot unit time) forming homogenous, intense patches of surface area A , and depth, H with 96% of the energy dissipated uniformly during a period, T , after which time the remainder of the energy dissipates slowly as the patch decays and expands. For simplicity we equate the coverage of the intense patches to that of mature whitecaps [Monahan, 1993],

$$W_B = nAT \quad (9)$$

The contribution of the intense patches to the mean air-sea transfer velocity, K_B , is then estimated as,

$$K_B = 0.17[96W_B^3 w_*^3 \nu / Sc^2 H]^{1/4} \quad (10)$$

Using a simple approximation of the environmental dependence of white-cap coverage [Wu, 1988],

$$W_B = 0.2u_*^3 \quad (11)$$

we can again deduce an approximate wind speed dependence,

$$K_B = 1.2 \times 10^{-6} U^3 [\nu / Sc^2 H]^{1/4} \quad (12)$$

which is also plotted in Figure 1.

While most of the energy is dissipated in the intense patch, the increasing surface coverage of the patch in its later development counteracts the decreased dissipation rate. *Rapp and Melville* [1990] reported the growth and decay of the senescent patch for a two-dimensional breaking wave, where the lateral growth of the patch was restricted, so we must surmise the growth of a patch associated with a three-dimensional breaking wave. Assuming that the turbulent kinetic energy, Q , of the patch will decay inversely with time and the patch will entrain outwards at a velocity proportional to the scale velocity, u (where $Q = u^2 V$, V being the volume of the patch), of the patch it is found algebraically that the dissipation rate, ξ , area, a , and depth, h , at time, t , are related to the characteristics at time, T , (ϵ, A, H), for $t > T$, by,

$$\xi = \epsilon(t/T)^{-13/5} \quad (13)$$

$$a = A(t/T)^{2/5} \quad (14)$$

$$h = H(t/T)^{1/5} \quad (15)$$

Using (4), the contribution of the patch to the air-sea transfer velocity integrated over surface area, $\int K dA$, will vary with time as,

$$\int K dA \propto t^{-1/4} \quad (16)$$

This contribution decays only slowly and the mean contribution of all patches can only be calculated with an assumption about the interaction and final decay of patches. A simple scheme in which only one patch contributes in a particular area at any one time is solved algebraically with the preceding equations, to give the following estimate of the contribution of the remaining 4% of breaking wave energy to the mean transfer coefficient, K_C ,

$$K_C = 2.5 \times 10^{-4} U^{39/28} [\nu / S c^2 H]^{1/4} \quad (17)$$

which is also plotted in Figure 1.

The transfer coefficients derived from the "uniform model", (7), are quite comparable to estimated air-sea transfer coefficients [e. g., *Liss and Merlivat*, 1986], but cannot explain the upturn at high wind speeds; see Figure 1. Taking into consideration the inhomogeneity of the breaking-wave-generated turbulence, the contribution of these patches is much reduced. In particular, the calculated effect of intense patches, (12), is very small, though sensitive to wind speed. The effect of larger, decaying patches is more substantial, (17), but cannot explain very high transfer coefficients at high wind speeds.

3 Discussion

In the last section, we have described a model which allows crude estimates of the effect of turbulent patches generated by breaking waves on air-sea gas transfer. This model has two principal elements: a description of the distribution of turbulent dissipation rates within these patches, and a relationship (from a laboratory study) of gas transfer coefficients to the near-surface dissipation rates. Both of these elements are in fact quite speculative as discussed briefly below.

There has been considerable discussion of the dissipation of wave energy and there are a few estimates of its rate in various wind and sea conditions [*Phillips*, 1985; *Thorpe*, 1993; *Melville*, 1994]. It seems likely that a large fraction of the energy in moderate and high winds will be lost through large "whitecapping" breaking waves, but the exact fraction is unknown. The frequency and coverage of whitecaps should be a fair indication of at least the initial characteristics of the energy flux, but it is improbable that there is an exact one-to-one relationship between the surface area of mature whitecaps and the area of the most intense patches (another estimate of the coverage of these patches was derived by *Thorpe* [1993]). The scale depth, "H", is also difficult to estimate, but fortunately the transfer coefficient is only weakly sensitive to it ($\propto H^{-1/4}$). A fraction of the energy will create a turbulent bubble plume, in its mature (or actually senescent) state crudely approximating classical, decaying, homogenous, isotropic turbulence [*Batchelor and Townsend*, 1948; *Speziale and Bernard*, 1992]. This patch will continue to expand as it decays as a result of turbulent entrainment, and interaction with shear flow and large scale organised motions (Langmuir circulation). Many characteristics of the plumes can be imaged through acoustic measurements of bubbles. *Thorpe* [1986] and others have described how a "stratus layer" of small bubbles develops, but it is important to realise that though on a time scale of 100 seconds or so bubbles may spread throughout this layer, there are clusters of exceptionally high bubble density associated with individual

breaking waves (as well as typically a large scale modulation associated with Langmuir circulation). There is a great deal still to learn about the distribution and character of subsurface turbulent patches.

The existence of a reliable relationship between mass transfer coefficients and the turbulent dissipation rate is doubtful. Reviews of various laboratory studies [Asher and Pankow, 1986; George *et al.*, 1994], show that the coefficient in Equation (1) deviates from 0.17 in other experiments. Surface films are implicated in some variations, but the structure of the turbulence may also be important. A unique coefficient can only be expected if small eddies are largely responsible for transfer. There is some evidence that large eddies are important [George *et al.*, 1994]. The most appropriate coefficient for oceanic breaking waves is uncertain, and plausibly could be an order of magnitude higher than in (1). Furthermore, there is evidence of a quite different relationship in the most vigorous conditions [Kishinevsky and Serebryansky, 1956; Khoo and Sonin, 1992], with transfer coefficients that are much higher than one would expect from (1) and independent of the Schmidt number. This might be relevant to transfer very close to a breaking wave. If the transfer on the liquid side is locally extremely efficient (this appears unlikely but not impossible), atmospheric transfer would become limiting for some additional gases in these patches, introducing a solubility dependence to air-sea gas transfer coefficients. Such possibilities not only make it difficult to rule out the importance of the intense breaking wave patches to gas transfer, but add further to uncertainties in the parameterisation of air-sea transfer as a whole (particularly Schmidt number and solubility dependence).

Transfer coefficients with a complicated dependence on solubility and molecular diffusion constants have been attributed to bubble-mediated transfer. A significant bubble-mediated transfer of many fairly soluble gases, including carbon dioxide, requires a very large flux of bubbles. In particular, Woolf [1993] calculated *bubble-mediated gas transfer* coefficients resulting from a "volume flux" (V , litres $m^{-2}s^{-1}$) of bubbles proportional to fractional *whitecap coverage*,

$$V = 6.25W_B \quad (18)$$

initially submerged to a depth of 10 cm, which requires an energy flux (E_a , Wm^{-2}),

$$E_a \approx 6W_B \quad (19)$$

From equations (2), (5) and (11) an approximate relationship of the total rate of wave energy loss to whitecap coverage is derived,

$$E \approx 23W_B \quad (20)$$

Thus, the predicted flux of bubbles requires that approximately 25% of the energy loss in breaking waves estimated by Banner [in *Craig and Banner*, 1995] is initially expended in submerging bubbles. This seems to be a reasonable result given the results reported by *Lamarre and Melville* [1991]. The transfer across the surface of a rising bubble is usually related to the flow around the bubble generated by its rise ("self-ventilation"), but bubble-mediated transfer may be enhanced in highly turbulent regions [*Thorpe*, 1982]. The high predicted levels of turbulence within newly-formed plumes (dissipation $\approx 2 \times 10^{-2} \text{m}^2 \text{s}^{-3}$, if $H = 1 \text{m}$) are sufficiently high to produce an enhancement, and this fact should be incorporated in future models of bubble-mediated gas transfer. The disruption of the surface microlayer by surfacing and bursting bubbles may also strongly influence gas transfer, and merits further investigation.

4 Conclusions

The simple model described in this paper is clearly inadequate in many respects, but it does suggest that though sub-surface turbulence from breaking waves is a significant mechanism of air-sea gas exchange, it is unlikely to be the dominant mechanism in any circumstance. The description of the initial, highly energetic period is particularly crude, but it is interesting to note that the contribution to transfer calculated for this period is actually very small (<1 cm/h averaged over the sea surface) except at very high wind speeds. It is possible that the nature of the turbulence is paramount, for instance if there are organised overturning motions this may transfer gas more "efficiently" than the mechanically-generated turbulence typical of laboratory experiments. Surface films are another complication, especially as it is unclear what conditions are "typical" of the ocean surface. The transfer associated with more realistic turbulent patches and surface conditions needs to be established experimentally. The contribution of the turbulent patches, particularly in the first phase, is also very sensitive to the area of the patch (or the fractional coverage of all patches). Thus, the character of oceanic turbulence and the statistics of near-surface dissipation rates must be established as a priority. The senescent patch remaining tens of seconds after a breaking wave appears to be fairly important. The behaviour of the senescent plumes and their effect on "the shear layer" is an important consideration in modelling transfer across the remainder of the sea surface. The direct influence of breaking-wave-generated turbulence on air-sea gas transfer should not be neglected, and should be considered together with bubble-related mechanisms.

Acknowledgements

Our research on bubbles and air-sea gas transfer is supported by the EC MAST II programme ("Bubbles", contract MAS2-CT93-0056).

References

- Agrawal, Y. C., E. A. Terray, M. A. Donelan, P. A. Hwang, A. J. Williams III, W. M. Drennan, K. K. Kahma, and S. A. Kitaigorodskii, Enhanced dissipation of kinetic energy beneath surface waves, *Nature*, 359, 219-220, 1992
- Asher, W. E., and J. F. Pankow, The interaction of mechanically generated turbulence and interfacial films with a liquid phase controlled gas/liquid transport process, *Tellus*, 38B, 305-318, 1986
- Batchelor, G. K., and A. A. Townsend, Decay of turbulence in the initial period, *Proc. R. Soc. Lond.*, A193, 527-543, 1948
- Craig, P. D., and M. L. Banner, Modeling wave-enhanced turbulence in the ocean surface layer, *J. Phys. Oceanogr.*, 24, 2546-2559, 1994
- Deacon, E. L., Gas transfer to and across an air-water interface, *Tellus*, 29, 363-374, 1977
- Dickey, T. D., B. Hartman, D. Hammond, and E. Hurst, A laboratory technique for investigating the relationship between gas transfer and fluid turbulence, in *Gas Transfer at Water Surfaces*, edited by W. Brutsaert and G. H. Jirka, pp. 93-100, 1984
- George, J., F. Minel, and M. Grisenti, Physical and hydrodynamical parameters controlling gas-liquid mass transfer, *Int. J. Heat Mass Transfer*, 37, 1569-1578, 1994
- Jähne, B., K. O. Münnich, R. Bösinger, A. Dutzi, W. Huber, and P. Libner, On the parameters influencing air-water gas exchange, *J. Geophys. Res.*, 92, 1937-1949, 1987
- Khoo, B-C. and A. A. Sonin, Scalar rate correlation at a turbulent liquid free surface: a two-regime correlation for high Schmidt numbers, *Int. J. Heat Mass Transfer*, 35, 2233-2244, 1992
- Kishinevsky, M. Kh., and V. T. Serebryansky, The mechanism of mass transfer at the gas-liquid interface with vigorous stirring, *J. Appl. Chem. U.S.S.R.*, 29, 29-33 (English translation), 1956
- Kitaigorodskii, S., On the fluid dynamical theory of turbulent gas transfer across an air-sea interface in the presence of breaking wind waves, *J. Phys. Oceanogr.*, 14, 960-972, 1984
- Lamarre, E., and W. K. Melville, Air entrainment and dissipation in breaking waves, *Nature*, 351, 469-472, 1991
- Liss, P. S., and L. Merlivat, Air-sea gas exchange rates: Introduction and synthesis, in *The Role of Air-Sea Exchange in Geochemical Cycling*, edited by P. Buat-Menard, pp. 113-127, 1986
- Melville, W. K., Energy dissipation by breaking waves, *J. Phys. Oceanogr.*, 24, 2041-2049, 1994
- Merlivat, L., and L. Memery, Gas exchange across an air-water interface: Experimental results and modeling of bubble contribution to transfer, *J. Geophys. Res.*, 88, 707-724, 1983

- Monahan, E. C., Occurrence and evolution of acoustically relevant sub-surface bubble plumes and their associated, remotely monitorable, surface whitecaps, in *Natural Physical Sources of Underwater Sound, Sea Surface Sound*, Vol. 2, edited by B. R. Kerman, pp. 503-517, Kluwer Academic Publisher, Dordrecht, 1993
- Monahan, E. C., and M. C. Spillane, The role of oceanic whitecaps in air-sea gas exchange, in *Gas Transfer at Water Surfaces*, edited by W. Brutsaert and G. H. Jirka, pp. 495-503, Kluwer Academic Publisher, Dordrecht, 1984
- Monahan, E. C., and I. G. O'Muircheartaigh, Whitecaps and the passive remote sensing of the ocean surface, *Int. J. Remote Sensing*, 7, 627-642, 1986
- Osborn, T., D. M. Farmer, S. Vagle, S. A. Thorpe, and M. Curé, Measurements of bubble plumes and turbulence from a submarine, *Atmosphere-Ocean*, 30, 419-440, 1992
- Phillips, O. M., Spectral and statistical properties of the equilibrium range of wind-generated gravity waves. *J. Fluid Mech.*, 156, 505-531, 1985
- Rapp, R. J., and W. K. Melville, Laboratory measurements of deep-water breaking waves, *Phil. Trans. R. Soc. London*, A331, 735-800, 1990
- Speziale, C. G., and P. S. Bernard, The energy decay in self-preserving isotropic turbulence revisited, *J. Fluid Mech.*, 241, 645-667, 1992
- Thorpe, S. A., On the clouds of bubbles formed by breaking wind-waves in deep water, and their role in air-sea gas transfer, *Phil. Trans. R. Soc.*, A304, 155-210, 1982
- Thorpe, S. A., Measurements with an automatically recording inverted echo sounder; ARIES and the bubble clouds, *J. Phys. Oceanogr.*, 16, 1462-1478, 1986.
- Thorpe, S. A., Energy loss by breaking waves, *J. Phys. Oceanogr.*, 23, 2498-2502, 1993
- Woolf, D. K., Bubbles and the air-sea transfer velocity of gases, *Atmosphere-Ocean*, 31, 517-540, 1993
- Wu, J., Oceanic whitecaps and sea state, *J. Phys. Oceanogr.*, 9, 1064-1068, 1979
- Wu, J., Variations of whitecap coverage with wind stress and water temperature, *J. Phys. Oceanogr.*, 18, 1448-1453. 1988

Whitecap Measurements and Whitecap Dissipation Modelling

C. Kraan, W. A. Oost, and P. A. E. M. Janssen

Royal Netherlands Meteorological Institute
de Bilt, the Netherlands

Abstract

With video equipment and image processing software we have measured the whitecap coverage of the sea surface near the Dutch coast. We also developed a model that produces a theoretical estimate of the whitecap percentage as a function of the wave age. The comparison between the measured whitecap coverage and the model results shows an order of magnitude correspondence for most of the data. A group of outliers appears to be connected to the strength of the current. A more extended version of this paper ("Wave energy dissipation by whitecaps") has been accepted for the Journal of Atmospheric and Oceanic Technology.

1 The Data

During the ASGASEX '93 experiment, performed in September '93 at Meetpost Noordwijk (MPN), a research platform 9 km off the Dutch coast, we used two black and white video cameras for *whitecap* detection. One camera (indicated as 'WC', for WhiteCaps) was installed at the helideck, 18 m above mean sea level. This camera was looking over the sea surface in a more or less horizontal plane. The second camera ('BR', for BReaking waves) was looking straight down from a mean height of 6m.

The whitecaps we wanted to detect are the crests of *breaking waves* ("A"-type *whitecaps* according to *Monahan*, [1969]), characterized by a brightness (grey level) exceeding a threshold value. Determining that value was the most critical part of the processing.

We tried to make our analysis as objective as possible by scanning the tape several times, using different thresholds, by avoiding areas in the pictures with strong reflections and by using three different analysis methods.

2 Data Treatment

In the first of the three methods we used we straightforwardly calculated, for a selected threshold value of the grey level, the *whitecap percentages* (WCP's, the percentages of the area selected for analysis covered with whitecaps) as well as their progressive mean, for as many frames of a run as possible. At a maximum we can calculate each second the WCP's of 2 frames, i. e., 8% of

the data offered to the system, that produces its pictures at the usual speed of 25 Hz. The procedure was repeated with different threshold values, until a grey level was found where the WCP varied very little with changes in the threshold. The WCP's in this range were considered as the actual ones.

For the second approach we measured the WCP after subtracting, pixel by pixel, the grey level values of two frames. This resulted in a new frame in which only pixels at positions where changes occurred have a value different from zero. The time lag between the pictures was adjustable. With this method we intended to eliminate the effects of *foam*, which is more or less stationary on the surface, whereas the whitecaps move with the velocity of the wave. With this second method we needed two seconds to calculate a WCP.

In the third approach we took the average of an adjustable number of frames and calculated the WCP of the result. Here again we needed about two seconds for the calculation of a WCP.

The three methods gave consistent results for a timelag of 0.4 s (in the second method) and with averaging over 7 frames (with the third method).

The stability of the results of our three independent methods gave us the conviction that these results have physical significance. Whether the resulting values are actually the areal percentages or fractions of type A whitecaps cannot be determined as long as we have no generally accepted and straightforward method to determine that quantity.

To further check the reproducibility of our analysis we analyzed a number of times different areas of the same pictures, to see whether the resulting whitecap percentages were consistent. This turned out to be the case within 5%. The data we present here were obtained with the first approach.

In most cases the (area averaged) WC data agreed well with the (time averaged) BR data of the same run. The results show an RMS error in the mean WCP of a run of 5 to 10%, with the BR results somewhat higher than those from the WC camera. The best estimate of the overall accuracy is probably found by comparing the results of the three analysis methods, which shows differences of about a factor two.

No error bars are plotted in the figures: it is difficult to estimate the error of the measured WCP's. The plotted values are averages per run and have, in general, the indicated standard deviation of 5 to 10%, due to variations in the WCP itself and changes in the circumstances during the run. The error in the model values is difficult to assess. If our assumptions about the homogeneity and stationarity of the whitecap phenomena during a run are correct, the scatter should mainly be caused by inadequacies of the measurement techniques used. The correlation coefficients between the modelled and measured whitecap percentages are 17% and 26% for respectively the WC and the BR camera. These numbers are based on data produced with the first ("direct") type of analysis method.

3 Modelling the Dissipation of Wave Energy by Whitecaps

The dissipation source function (effectively a sink) is given by *Komen et al.* [1984] and by the WAMDI-group [1988] as:

$$S_{ds} = -\beta\omega^2 F \quad (1)$$

where

$$\beta = \frac{c_0}{\bar{\omega}} \left(\frac{\bar{\alpha}}{\bar{\alpha}_{PM}} \right)^2 \quad (2)$$

with the constant $c_0 (= 3.35 \times 10^{-5})$, $\bar{\omega}$ the mean frequency and $\bar{\alpha}$ and $\bar{\alpha}_{PM}$ wave steepness indicators. $\bar{\alpha}_{PM} = 4.57 \times 10^{-3}$ is the value for the saturated (Pierson-Moskowitz) spectrum.

If we factor the *spectral function* F in a normalized frequency part $G(\omega)$ and a directional part $H(\theta)$, we can derive formal expressions for the wave variance E , the mean frequency $\bar{\omega}$ and the integral wave steepness parameter $\bar{\alpha}$ in terms of G .

The *energy dissipation* per unit time is given by

$$\varepsilon_{ds} = \rho_w g \int S_{ds} d\omega \quad [W/m^2] \quad (3)$$

with ρ_w the specific density of water and ω the circular frequency of the wave.

The contribution of whitecaps to wave energy dissipation can be approximated as

$$\varepsilon_{ds} = -\gamma \rho_w g WCF \omega_p E \quad [W/m^2] \quad (4)$$

where γ is the average fraction of the total wave energy dissipated per whitecapping event. WCF is the *WhiteCap Fraction* (the fraction of the sea surface covered with whitecaps) and ω_p the (circular) peak frequency. $\bar{\omega} = c_1 \omega_p$, where the c_1 coefficient depends on the definition of $\bar{\omega}$ and the spectral shape.

With the foregoing we can find an expression for the WCF from

$$\int \beta \omega^2 G d\omega = \gamma WCF \omega_p E \quad (5)$$

or

$$WCF = \frac{\beta \int \omega^2 G d\omega}{\gamma \omega_p E} = \frac{c_0 c_1}{\gamma} \frac{\int G d\omega \int \omega^2 G d\omega}{(\int \omega G d\omega)^2} \left(\frac{\bar{\alpha}}{\bar{\alpha}_{PM}} \right)^2 \quad (6)$$

where the latter expression was found with the definition of β and the formal expression for E ($E = \int G d\omega$).

Our whitecap measurements show a large scatter. Therefore we can approximate the measured spectra to an accuracy well within that of the whitecap percentages by the simple expression [WMO, 1976, section 2.8]

$$\begin{aligned} G(\omega) &= \alpha g^2 \omega^{-5} (\omega \geq \omega_P) \\ &= 0 (\omega < \omega_P) \end{aligned} \quad (7)$$

where α is the Phillips 'constant'. Integrating over all frequencies we find expressions for ω_P and $\bar{\omega}$, resulting in $c_1 = 4/3$. Substituting the values of c_0 , c_1 and $\bar{\alpha}_{PM}$ the expression for WCF becomes

$$WCF = \frac{2.4}{\gamma} \bar{\alpha}^2 \quad (8)$$

During the video recordings we made simultaneous wind and wave measurements, so we know the *significant wave height* (H_s , in m), the *peak frequency* (f_p , in Hz) and the atmospheric *friction velocity* (u_* , in m/s). These data allow us to estimate $\bar{\alpha}$ as:

$$\bar{\alpha} = E \bar{\omega}^4 g^{-2} = \frac{(2\pi c_1)^4}{16g^2} H_s^2 f_p^4 = 3.2 H_s^2 f_p^4 \quad (9)$$

if we take $E = H_s^2/16$ and $\bar{\omega} = c_1 \omega_P = 2\pi c_1 f_p$.

If we eliminate the fetch from the JONSWAP spectral formula [Hasselmann *et al.*, 1973], it appears appropriate to write $\bar{\alpha} = a \xi^b$ with $\xi = c_P/u_* = g/(2\pi u_* f_p)$, the *wave age*. From a regression analysis we find

$$a = 0.20 \pm 0.02 \quad \text{and} \quad b = -1.04 \pm 0.2, \quad (10)$$

with a correlation of 69%.

So from the wind and wave measurements we find an expression for the wave steepness as a function of wave age:

$$\bar{\alpha} = 0.2 \xi^{-1.04}. \quad (11)$$

Comparable values for a and b are found in the literature; e. g., *Komen et al.* [1994] give $a = 0.57$ and $b = -1.5$.

Combination of the two expressions for $\bar{\alpha}$ gives us the whitecap percentage (WCP) as a function of the wave age. To compare these theoretical values with the field measurements we have to make an estimate of the fraction γ .

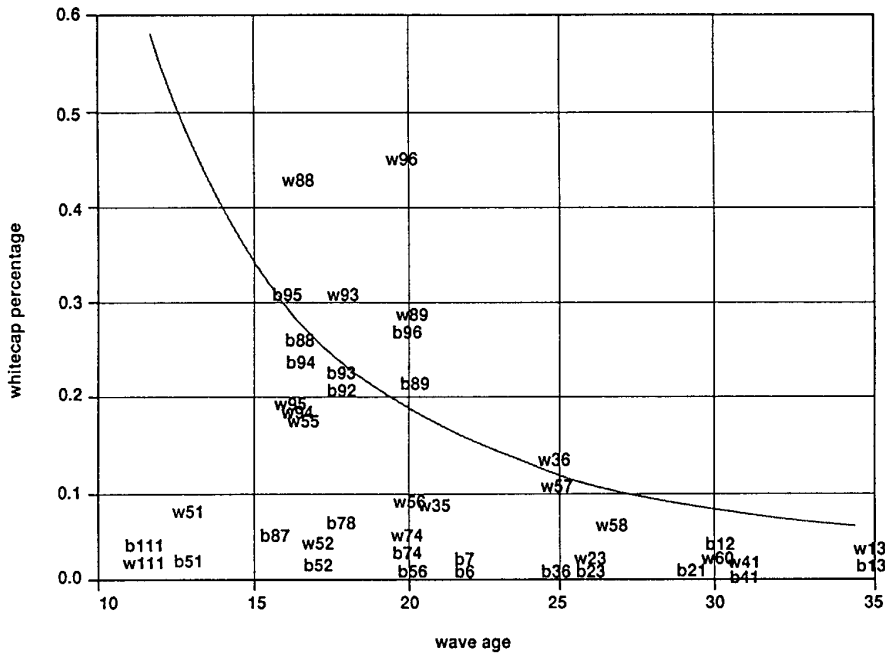


Figure 1: Measured whitecap percentage (WCP, the percentage of the sea surface covered with whitecaps) vs. measured wave age $\xi = c_p/u_*$. c_p is the phase velocity of the spectral peak, u_* the atmospheric friction velocity. Wnn are data measured with the whitecap camera, Bnn data with the breaker camera, with “nn” indicating the run number. For reasons of clarity two points were left out in this figure: B35 is almost identical to B6 and W61 to W41. The line corresponds to $WCP = 96 \xi^{-2.08}$. Note the “outliers” for low wave ages.

From Melville and Rapp [1985] we find, taking a value of 0.2 for the wave steepness in their figure 4, that whitecaps are responsible per event for the loss of about 10% of the total wave energy, so $\gamma = 0.1$. Then

$$WCP = 100 \frac{2.4}{0.1} 0.2^2 \xi^{-2.08} = 96 \xi^{-2.08} \tag{12}$$

4 Comparing Model and Data

If we plot the measured WCP as a function of the wave age, we can compare the field data with the WCP formula (figure 1). From the figure it is clear that theory and experiment give values of the same order of magnitude, although there is a large scatter in the experimental values.

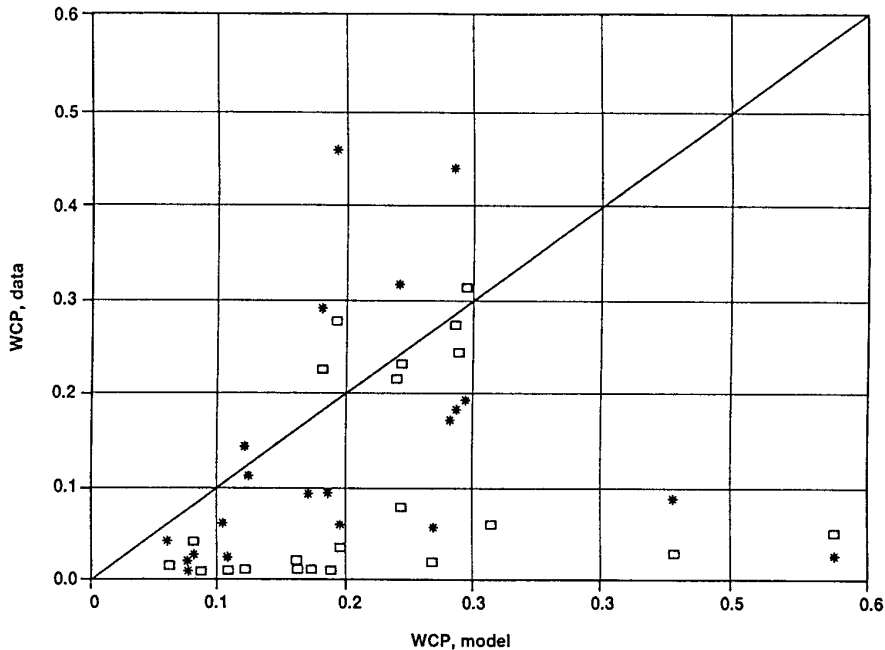


Figure 2: Direct comparison between the modelled and measured whitecap percentages (WCP's). *: WC-camera; □: BR-camera. Despite the large scatter the data suggest a separation into two main groups.

In figure 2 the same results are compared directly. The figure again shows that theory and experiment lead to whitecap percentages of the same order of magnitude. Figures 1 and 2 give the impression that there are two different kinds of field data: one with a high (WCP \approx 0.25%) and one with a low (WCP \approx 0.05%) whitecap percentage. We therefore scrutinized our data in order to find a connection with other parameters.

By visual observation we had noted two situations where no whitecaps were visible, though the wind speed was in the range 7-8 m/s. In one of these instances the air/sea temperature difference was measured as 6 °C (very stable), in the other case it was 0 °C (near neutral), but on both occasions there was a strong *tidal current* (about 1 m/s). This suggested that the absence of the whitecaps was not caused by e. g., the atmospheric stability, but by the current.

Inspired by these occurrences we plotted our WCP values against the speed of the (mainly tidal) current (fig.3). The plot indeed suggests a descending maximum value for the WCP as a function of the current velocity, with two exceptions, a WC and a BR value that belong to the same run. The figure is not very convincing, due to the limited number of data points. However, if we compare figs.1 and 3 we find the data points at high current

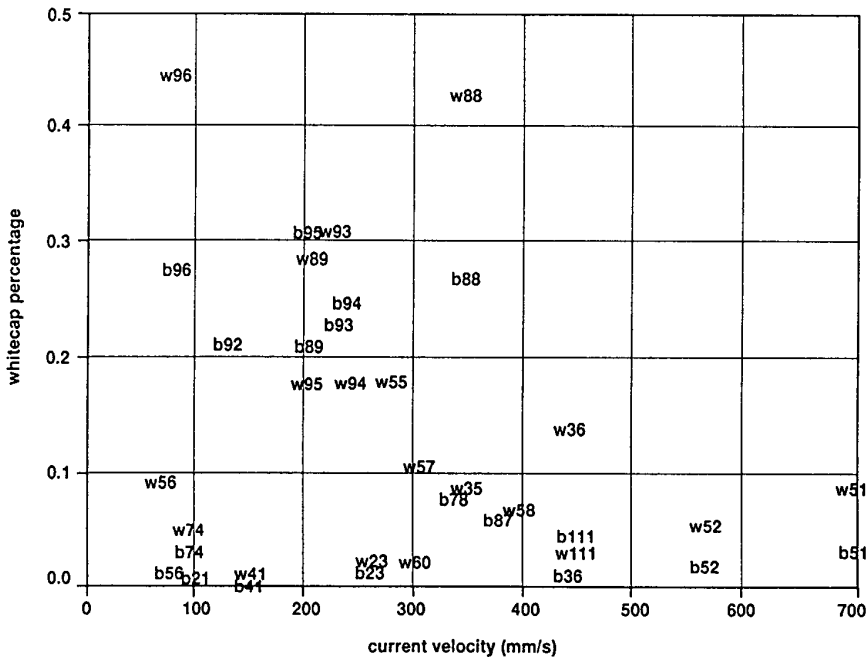


Figure 3: The measured whitecap percentage as a function of the current velocity. Symbols as in fig.2. Note the position of the outliers of fig.2 in this figure, suggesting an effect of the current velocity on the WCP's.

velocities in fig.3 in fig.1 as the group with the low whitecap percentage at low values of the wave age.

A tentative conclusion therefore is that in these fairly shallow tidal waters the current speed puts an upper limit to the WCP value, but that below this limit the wave age appears to be the determining factor. The mechanism through which the current affects the WCP is at the moment a matter of speculation. A possibility in this respect could be interaction of the current shear and the long waves, which both can extend over the full water depth (18 m) in the MPN area.

We have not been able to detect any relationship between the WCP values and wind direction, wave height, wave direction, angle between camera and wave direction, atmospheric stability, current direction or the angle between waves and current.

References

- Hasselmann, K., T. P. Barnett, E. Bouws, H. Carlson, D. E. Cartwright, K. Enke, J. A. Ewing, H. Gienapp, D. E. Hasselmann, P. Kruseman, A. Meerburg, P. Müller, D. J. Olbers, K. Richter, W. Sell, H. Walden, Measurements of wind-wave growth and

- swell decay during the Joint North Sea Wave Project (JONSWAP), *Dtsch. Hydrog. Zeitschr.* A12 (supplement), 1973
- Komen, G., L. Cavaleri, M. Donelan, K. Hasselmann, S. Hasselmann and P. A. E. M. Janssen, Dynamics and modelling of ocean waves, Cambridge University Press, Cambridge, 532 pp., 1994
- Komen, G., S. Hasselman and K. Hasselman, On the existence of a fully developed wind-sea spectrum. *J. Phys. Oceanogr.* 14, 1271-85, 1984
- Melville, W. K. and R. J. Rapp, Momentum flux in breaking waves, *Nature* 317, 514-516, 1985
- Monahan, E. C., Fresh water whitecaps *J. Atmos. Sci.* 26, 1926-29, 1969
- WAMDI Group (Wave Model Development and Implementation Group), The WAM model - a third generation ocean wave prediction model. *J. Phys. Oceanogr.* 18, 1775-1810, 1988
- WMO, *Handbook on wave analysis and forecasting*, World Meteorological Organization, Geneva, No. 446, 1976

Measurement of Gas Transfer, Whitecap Coverage, and Brightness Temperature in a Surf Pool: An Overview of WABEX-93

W. E. Asher¹, B. J. Higgins¹, L. M. Karle¹,
 P. J. Farley¹, C. R. Sherwood¹, W. W. Gardiner¹,
 R. Wanninkhof², H. Chen², T. Lantry²,
 M. Steckley², E. C. Monahan³, Q. Wang³,
 and P. M. Smith⁴

¹ Pacific Northwest Laboratory/Marine Sciences Laboratory
 1529 W. Sequim Bay Road, Sequim Washington 98382, U.S.A.

² National Oceanic and Atmospheric Administration, Atlantic Oceanographic
 and Meteorological Laboratory, Miami Florida 33149, U.S.A

³ University of Connecticut, Avery Point
 Marine Sciences Institute, Groton Connecticut 06340, U.S.A

⁴ Naval Research Laboratory/Stennis Space Center,
 Code 7240 Stennis Mississippi 39529, U.S.A

Abstract

Toward a method for estimating air-sea gas transfer velocities, k_L , from remote measurements of fractional area whitecap coverage, W_C , a gas exchange experiment was conducted in an outdoor surf pool during the October 1993 Wave Basin Experiment (WABEX-93). For both spilling and plunging breaking waves, measurements were made of W_C ; air-water fluxes of carbon dioxide, helium, nitrous oxide, oxygen, and sulfur hexafluoride; microwave brightness temperature of the water surface, σ ; aqueous-phase turbulence velocities; and bubble size spectra. The data show that k_L scales as a common, linear relation with W_C for both spilling and plunging breaking waves. The gas transfer data have been used to develop an empirical parameterization for predicting k_L from W_C , Schmidt number, and solubility.

1 Introduction

Ocean regions that global carbon cycle models show are large sinks of carbon dioxide (CO_2) are known to have high wind speeds. Therefore, estimates of the global ocean uptake of CO_2 could be improved through better prediction of the air-sea gas transfer velocity, k_L , at high wind speeds. Because high winds are also associated with increased whitecapping, development of an accurate method for estimating k_L for CO_2 from measurements of *whitecap coverage*, W_C , could provide a method for predicting k_L at high wind speed. Additionally, it could be possible to measure W_C using the remote-sensing technique of passive *microwave radiometry*.

Gas transfer data from laboratory experiments conducted in a tipping-bucket whitecap simulation tank (WST) have been used to develop a parameterization of k_L in terms of W_C ; Schmidt number, Sc ; and aqueous-phase solubility, α (given as the dimensionless Ostwald solubility) [Asher *et al.*, 1995a, 1995b]. The parameterization partitions k_L into a fraction due to turbulence generated by mechanical mixing, k_M , a fraction due to turbulence generated by the breaking wave, k_T , and a fraction due to *bubble-mediated transfer* processes, k_B . Before the functional form of the parameterization from the WST can be applied to air-sea gas exchange under oceanic conditions, it must first be shown that a parameterization derived from data acquired using the WST can be applied to more realistic breaking waves.

Extension of the WST results to oceanic conditions should be made using direct oceanic measurements of k_L and W_C . This would require a dual-tracer gas exchange experiment, with its associated cost and difficulty. In addition, with field measurements there is a risk that wind speeds during the experiment would not be high enough to cause significant whitecapping. As an alternative to an oceanic experiment, gas transfer measurements were made during the October 1993 Wave Basin Experiment (*WABEX-93*) in a large outdoor surf pool capable of generating breaking waves that were very similar to ocean whitecaps. The use of a surf pool provided the additional benefit of a controlled, reproducible field of breaking waves.

Although use of the *surf pool* is not a direct replacement for the oceanic measurements necessary to generate a parameterization of k_L in the presence of breaking waves, it allowed an empirical relationship developed from the WST data to be tested using breaking waves that were more characteristic of oceanic whitecaps. The reproducible waves in the surf pool also allowed a systematic study of the effect of breaking waves on air-water transfer. In addition, the surf pool was outdoors, so a passive microwave radiometer could be used to measure microwave brightness temperature, σ . These measurements enabled correlation of σ with W_C and preliminary development of a method for estimating k_L directly from σ [Wang *et al.*, 1995].

2 Experimental Techniques

2.1 Physical Measurements

The surf pool used is located at Wild Rivers Waterpark in Irvine, California and is called "Hurricane Harbor". Hurricane Harbor is an unheated, fresh-water recreational pool approximately 20-m wide by 70-m long, with an average depth of 0.8 m (Figure 1). Waves were generated with four pneumatic plenum chambers at the deep end of the pool. The pressurization sequence of the chambers could be programmed to generate a "roller" pattern, characteristic of plunging *breaking waves* (Figure 2), and a "diamond" pattern, characteristic of spilling breaking waves (Figure 3). The wave period in the basin was 4.2 s, and the wave generators were set to generate waves with

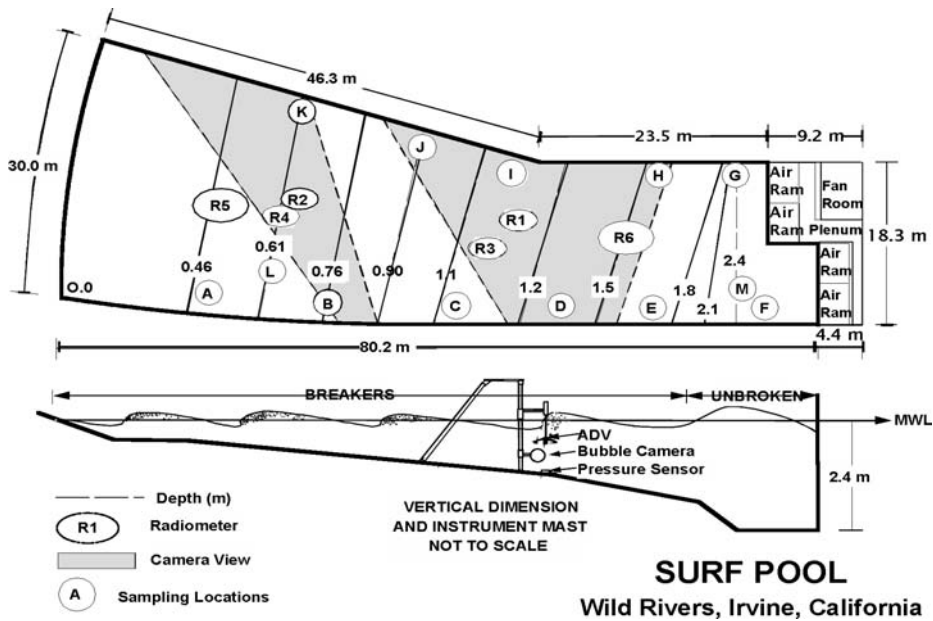


Figure 1: Schematic diagram of the surf pool “Hurricane Harbor” showing the locations of the 11 water sampling stations (listed as A-M), the 6 radiometer positions (listed as R1-R6), whitecap coverage video camera footprints. Also shown is a schematic diagram of the instrument mast used to mount the acoustic Doppler anemometer (ADV) and underwater video camera.

one of the following wave heights: 0.3 m; 0.6 m; 0.9 m; and 1.2 m (wave heights were measured before breaking at the 2.4-m depth contour).

Microwave radiometric measurements were made at an incidence angle of 53° using a 19-giga-Hertz single-polarization radiometer with a beam width of 7° (3-dB antenna pattern). The corresponding 3-dB footprint of the radiometer was an ellipse on the water surface. The radiometer was mounted on the platform of a man-lift crane (Figures 2 and 3) with a maximum extension of 20 m. The radiometer measured σ at the six locations shown in Figure 1 (Positions R1 through R6). Positions R1, R2, R5, and R6 were used for the plunging breaking waves, and positions R3, R4, R5, and R6 were used for the spilling breaking waves. The elevations (given as nadir distance from radiometer to the water surface) and the major and minor axes of the antenna footprints for the six positions are listed in Table 1. Although the radiometer could only measure one polarization component of the microwaves at a time, it could be rotated on an axis parallel to the main lobe of the antenna pattern so that either vertically or horizontally polarized radiation could be measured. The radiometer output was digitized and stored by an MS-DOS computer at a sampling frequency of 100 Hz.

An 8-mm Hi-8 video camcorder was mounted axially and boresighted



Figure 2: Photograph of a typical 1.2-m high plunging breaking wave generated by the Roller Pattern. The crane arm holding the radiometer is seen in the center of the picture.

Table 1: Radiometer elevations and antenna footprints

Position	Elevation meters	Footprint Axes	
		Major meters	Minor meters
R1	3.6	1.2	0.73
R2	3.6	1.2	0.73
R3	3.7	1.3	0.76
R4	3.4	1.2	0.70
R5	14.0	4.8	2.9
R6	14.3	4.9	2.9

with the radiometer to provide collocated video records of whitecap coverage in the radiometer footprint. Time-coding of the video images allowed the time series of whitecap coverage to be synchronized with the time series of σ .

The radiometer was calibrated at the beginning and at the end of each day using a two-point hot and cold reference temperature procedure. A sheet of microwave absorber immersed in a liquid nitrogen bath was used as a cold microwave reference temperature, and a similar sheet of material at ambient temperature was used as a warm reference temperature. Ambient temperatures were measured using a National Institute of Standards



Figure 3: Photograph of typical 0.9-m high spilling breaking waves generated by the Diamond Pattern. The crane arm holding the radiometer is seen in the center of the picture.

and Technology-traceable mercury thermometer. The temperature of the cold reference was taken to be the boiling point of nitrogen at the local atmospheric pressure. Atmospheric pressure was measured using a digital electronic barometer.

Two fixed-position video cameras mounted at an elevation of 18 m above the surf pool were used to measure fractional area coverage of the actively breaking waves, W_C , in the deep and shallow ends of the pool. The field of view of each camera is shown as a hatched region in Figure 1. W_C was determined from the video records using the grey-scale procedure of Monahan [1989]. Table 2 gives W_C for the two cameras along with an area-weighted average W_C for the entire surf pool. The output from each of these cameras was time-stamped using a time-code generator and stored on VHS-format videocassette recorders (VCR).

Water velocities in the breaking waves were measured with an *acoustic Doppler velocimeter (ADV)* that measured three orthogonal velocity components of the flow. The tripod used to mount the ADV in the pool is shown schematically in Figure 1. The tripod could be easily positioned to sample water velocities in the core of the breaking wave. Velocities from the ADV were used to study the turbulence structure beneath the breaking waves and to model turbulence-driven gas transfer. Wave heights were measured concurrently using a digital pressure gauge mounted below the ADV (see Figure 1). The ADV sampling locations, turbulence results, and their use in model-

Table 2: Fractional area whitecap coverage in the surf pool

Wave Type	Wave height (m)	W_C (Shallow)	W_C (Deep)	W_C (Average)
Plunging	0.3	0	0	0
Plunging	0.6	0.050	0.0019	0.020
Plunging	0.9	0.045	0.036	0.040
Plunging	1.2	0.048	0.086	0.072
Spilling	0.3	0	0	0
Spilling	0.6	0.014	0	0.0054
Spilling	0.9	0.057	0.0057	0.025
Spilling	1.2	0.053	0.014	0.029

ing gas transfer velocities in the surf pool are discussed in detail in *Ogston et al.* [1995].

Size-segregated bubble concentrations were measured using video micrographs of bubble populations recorded by an underwater video camera. The optics of the video imaging system were similar to that described in *Asher and Farley* [1995], except that the video camera, imaging optics, and light source were mounted in waterproof housings. The camera was mounted on the instrument tripod that held the ADV. The video output from the camera was time-stamped using a time-code generator and recorded on an S-VHS VCR. The time-code generator was synchronized manually with the clock of the computer acquiring the radiometer data and with the time-code generators of the other video cameras. Bubble sizes were analyzed by digitizing the video images using a commercial image processing software package.

Bubble populations were measured at the three locations in the surf pool where the ADV was located (see *Ogston et al.* [1995]). Available bubble data are discussed in *Wanninkhof et al.* [1995].

2.2 Gas Exchange Measurements

Air-water transfer velocities of CO_2 , *helium* (He), *nitrous oxide* (N_2O), *oxygen* (O_2), and *sulfur hexafluoride* (SF_6) were measured in the surf pool. Concentrations of N_2O and SF_6 were elevated by adding water saturated with each into the pool. The concentration of He was raised by bubbling pure gas into the pool. This process sparged O_2 so that invasion rates of O_2 were measured. CO_2 concentrations were adjusted by changing the pH of the pool using hydrochloric acid. Further details on preparation of the pool water before an experiment are given in *Wanninkhof et al.* [1995].

Depending on height and type of the breaking waves, gas concentrations were monitored in the pool for a total time of 3600 s to 7200 s (the longer total times correspond to the smaller and less energetic waves). Water was collected for He and SF_6 analysis every 300 s during the first 1200 s of the

experiment and every 600 s thereafter. Samples for N₂O and O₂ analysis were collected every 1200 s. The sampling strategy for CO₂ is discussed in detail in *Wanninkhof et al.* [1995].

Because the gas exchange time constants were on the order of 600 s, resolution of possible lateral concentration gradients required a sampling array consisting of 13 submersible pumps mounted to the bottom of the pool (pump locations are shown in Figure 1). Samples collected in the deep end of the pool at depths of 2.4 m and 1.2 m indicated that the pool was vertically well mixed. Each pump delivered a flow of $6.7 \times 10^{-5} \text{ m}^3 \text{ s}^{-1}$ to the side of the pool. A specially designed manifold allowed this stream to be sampled using $3 \times 10^{-4} \text{ m}^{-3}$ glass bottles or $5 \times 10^{-5} \text{ m}^{-3}$ glass syringes equipped with luer-lock syringe valves.

Samples were stored prior to analysis in coolers filled with wave basin water. He, N₂O, and SF₆ were analyzed chromatographically using a syringe-headspace method [*Wanninkhof et al.*, 1991]. O₂ was measured by Winkler dissolved-O₂ titration and with two polarographic dissolved-O₂ probes calibrated by comparison with O₂ concentrations determined by Winkler titration. The procedure for calculating k_L and analysis methods for CO₂, He, N₂O, and SF₆ are described in detail in *Wanninkhof et al.* [1995].

3 Results and Discussion

The spatial pattern of the whitecaps for both the spilling and plunging waves was not uniform over the tank surface (Figures 2 and 3). Because it was assumed that k_L in the pool was a function of measurement location, the sampling array described above was used to resolve lateral differences in k_L . Figure 4 shows k_L values for He and SF₆ calculated at each of the 13 stations for two different wave heights and wave breaking patterns (in the figure, k_L has been normalized by the average k_L for all thirteen stations from that experiment). As seen in Figure 4, there were no significant systematic differences in k_L values from different locations in the pool. Pool-averaged k_L values were then calculated as the linear average of k_L from the 13 stations.

Figure 5 shows the pool-averaged k_L values for CO₂, He, N₂O, O₂, and SF₆ plotted versus the pool-averaged fractional area whitecap coverage, W_C , from Table 2. The k_L data were taken from Table 2 of *Wanninkhof et al.* [1995] and when available, k_L values for the same gas from different experiments with the same wave size and type have been averaged together. Representative error bars (plus or minus one standard deviation) are shown for He and CO₂ for spilling and plunging breaking waves. The data in Figure 5 show that increases in k_L are correlated with increasing W_C .

The k_L data for both spilling and plunging breaking waves follow a common relationship with respect to W_C . This shows that both types of breaking wave had the same effect on enhancing gas transfer per unit area of coverage. Further, this means that the turbulence and bubble plumes generated by breaking waves that enhance gas transfer are not strong functions of

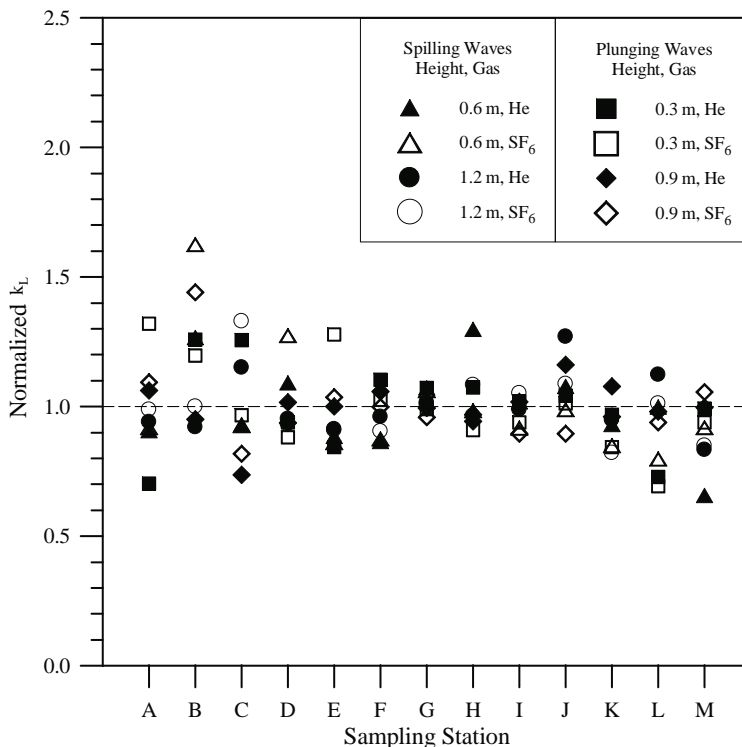


Figure 4: Plot of the gas transfer velocity, k_L , of helium (He) and sulfur hexafluoride (SF₆) measured as a function of position in the surf pool. Sampling stations A through M correspond to the locations shown in Figure 1. All k_L values have been normalized to k_L averaged over all stations for the particular gas in question at that wave condition.

breaking wave type. The similarity in physical characteristics between the waves in the surf pool and oceanic breaking waves provides further evidence that k_L could be correlated with W_C under oceanic conditions. However, it is understood that it is unlikely that a parameterization of bubble-mediated gas exchange developed using this data from freshwater could be applied directly to air-sea gas transfer.

In the absence of bubbles, k_L is proportional to $Sc^{-1/2}$. Therefore, during transfer across a flat water surface, k_L measured for SF₆, $k_L(\text{SF}_6)$, will be less than k_L measured under the same conditions for CO₂, $k_L(\text{CO}_2)$, because $Sc(\text{SF}_6) > Sc(\text{CO}_2)$. When $W_C < 0.5\%$, the surf pool data agree with this analysis, because Figure 5 shows that $k_L(\text{SF}_6) < k_L(\text{CO}_2)$. In contrast to the flat-surface case, bubble-mediated transfer processes cause k_L to be a function of both Sc and α , with k_L increasing as α decreases at constant Sc . At constant α however, k_L will decrease with increasing Sc . Although $Sc(\text{SF}_6)$ is 1.8 times larger than $Sc(\text{CO}_2)$, $\alpha(\text{SF}_6)$ is 200 times smaller than $\alpha(\text{CO}_2)$.

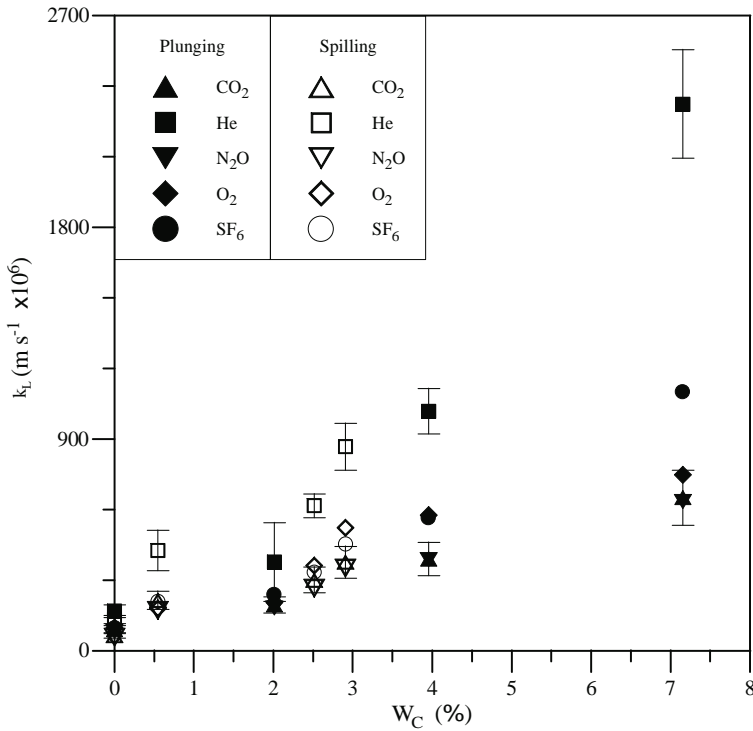


Figure 5: The gas transfer velocity, k_L , of carbon dioxide (CO_2), helium (He), nitrous oxide (N_2O), oxygen (O_2), and sulfur hexafluoride (SF_6) measured in the surf pool plotted versus the fractional area coverage of the actively breaking waves, W_C .

When bubble-mediated transfer processes are important, the effect due to decreases in α will dominate the effect of the increase in Sc , and $k_L(\text{SF}_6)$ will be greater than $k_L(\text{CO}_2)$. The data in Figure 5 support this conclusion and show that $k_L(\text{SF}_6) > k_L(\text{CO}_2)$ when $W_C > 0.5\%$. This demonstrates that bubbles were an important gas transfer pathway in the surf pool.

Gases with equal Sc and α should have equal k_L , regardless of bubble-mediated transfer effects. As discussed in Wanninkhof et al. [1995] (see also Figure 5), k_L values for CO_2 and N_2O agree with this prediction and their k_L values over the range of W_C studied are nearly identical.

One of the goals of WABEX-93 was to determine whether an empirical parameterization of k_L for bubble-plume driven gas transfer developed using data collected in a WST could be applied to breaking waves. For seawater, the WST data have shown that k_L can be written in terms of W_C as [Asher et al., 1995a, 1995b]

$$k_L = [k_M + W_C(k_T - k_M)] + W_C k_B \tag{1}$$

where k_M is defined by transfer from mechanically generated turbulence, k_T defines transfer from turbulence generated by the breaking wave, and k_B is due to transfer from the bubble-mediated gas flux. Additional gas transfer measurements in the WST have shown that (1) is applicable in freshwater and that k_B in freshwater is given by [Asher, unpublished results]

$$k_B = b\alpha^{-0.045}Sc^{-0.35} \quad (2)$$

where the exponents for α and Sc were determined by linear regression of the WST data at a fractional area bubble plume coverage of 0.4%. For a clean water surface, both k_M and k_T have the form

$$k_X = A_X Sc^{-1/2} \quad (X = M \text{ or } T) \quad (3)$$

where A_X is determined by the turbulence dissipation rate [Ogston *et al.*, 1995]. In the presence of breaking waves, combining (1), (2), and (3) gives

$$k_L = [A_M + W_C(A_T - A_M)]Sc^{-1/2} + W_C(b\alpha^{-0.045}Sc^{-0.35}) \quad (4)$$

As applied to the WABEX-93 data, A_M , A_T , and b in (4) were determined by minimizing the reduced chi-square of the pool-averaged k_L values for CO₂, He, N₂O, and SF₆ to (4) using W_C measured in the surf pool and the Sc and α values from Wanninkhof *et al.* [1995] (k_L [O₂] could not be used to determine A_M , A_T , and b because it was measured for gas invasion rather than evasion). For k_L in units of meters per second, $A_M = 7.49 \times 10^{-4} \text{ m s}^{-1}$, $A_T = 0.037 \text{ m s}^{-1}$, and $b = 0.093 \text{ m s}^{-1}$. Figure 6 shows the experimentally determined values for CO₂, He, N₂O, and SF₆ plotted versus k_L calculated from the measured W_C values and (4) using the coefficients listed above.

Overall, (4) adequately estimates k_L in the wave basin. This shows that the functional form of the parameterization developed using data from the WST can be applied to more realistic wave conditions. However, at lower W_C values, the method underpredicts the observed transfer velocities by a factor of 2 to 3. Ogston *et al.* [1995] show that the underprediction of k_L at low W_C is caused by the assumption of constant k_M and k_T .

4 Conclusions

It has been shown that a recreational surf pool can be used to study air-water gas transfer in the presence of breaking waves. The benefit of using the surf pool was that it generated reproducible breaking waves that were similar in appearance to plunging and spilling whitecaps. The reproducibility of the wave field greatly simplified measurement of gas transfer rates, whitecap coverage, microwave brightness temperature, and aqueous-phase

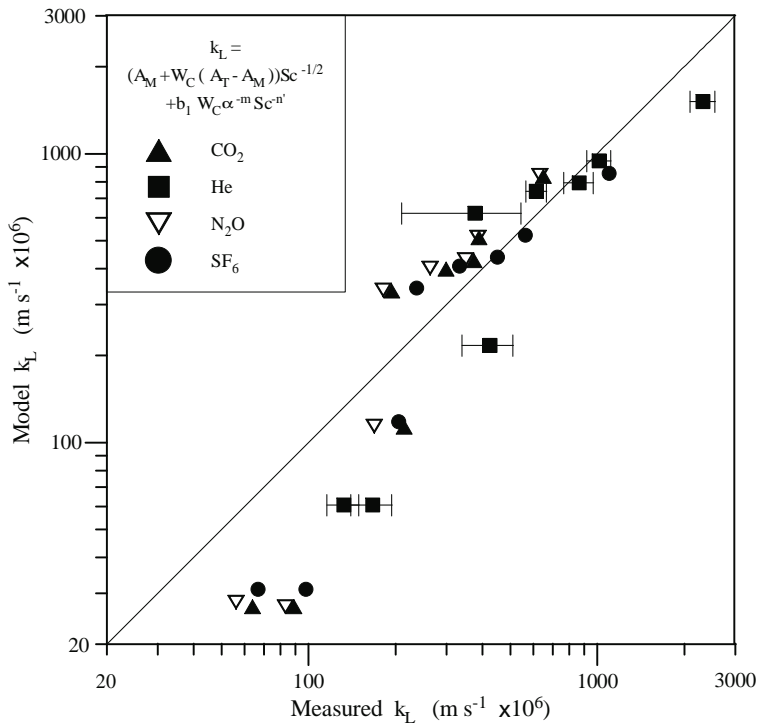


Figure 6: The experimentally determined gas transfer velocity of carbon dioxide (CO₂), helium (He), nitrous oxide (N₂O), oxygen (O₂), and sulfur hexafluoride (SF₆) plotted versus the transfer velocity for the corresponding gas as estimated from (4).

turbulence. The gas transfer data were used to show that a parameterization of the bubble-mediated transfer velocity derived independently from data collected in a whitecap simulation tank could be used to estimate transfer velocities in the surf pool. Further discussions of related aspects of the data from WABEX-93 can be found in *Ogston et al.* [1995], who discuss the turbulence structure beneath the breaking waves, *Wang et al.* [1995], who discuss the microwave radiometric data, and *Wanninkhof et al.* [1995], who model the bubble-driven gas flux.

Acknowledgements

This research was supported by the U.S. Department of Energy (DOE), Office of Health and Environmental Research, Environmental Sciences Division under Contract DE-AC06-76RLO 1830. Pacific Northwest Laboratory is operated for DOE by Battelle Memorial Institute. The assistance of Mr. Gregg Briggs and the rest of the staff at Wild Rivers Waterpark in conducting this experiment is also acknowledged.

References

- Asher, W. E., and P. J. Farley, Phase-Doppler anemometer measurement of bubble concentrations in laboratory-simulated breaking waves, *J. Geophys. Res.*, *100C*, 7045–7056, 1995
- Asher, W. E., L. M. Karle, B. J. Higgins, P. J. Farley, I. S. Leifer, and E. C. Monahan, The influence of bubble plumes on air/seawater gas transfer velocities, submitted to *J. Geophys. Res.*, 1995a
- Asher, W. E., L. M. Karle, B. J. Higgins, P. J. Farley, I. S. Leifer, and E. C. Monahan, [1995b] The effect of bubble plume size on the parameterization of air/seawater gas transfer velocities, *This volume*, 1995b
- Monahan, E. C., From the laboratory tank to the global ocean, in *Climate and Health Implications of Bubble-Mediated Sea-Air Exchange*, edited by E. C. Monahan and M. A. Van Patten, pp. 43–64, Connecticut Sea Grant College Program, 1989
- Ogston, A. S., C. R. Sherwood, and W. E. Asher, Estimation of turbulence dissipation rates and gas transfer velocities in a surf pool: Analysis of the results from WABEX-93, *This volume*
- Wang, Q., E. C. Monahan, W. E. Asher, P. M. Smith, Correlations of whitecap coverage and gas transfer velocity with microwave brightness temperature for plunging and spilling breaking waves, *This volume*
- Wanninkhof, R., J. R. Ledwell, and A. J. Watson, Analysis of sulfur hexafluoride in seawater, *J. Geophys. Res.*, *96C*, 8733–8740, 1991
- Wanninkhof, R., W. E. Asher, and E. C. Monahan, The influence of bubbles on air-water gas exchange: Results from gas transfer experiments during WABEX-93, *This volume*

Correlations of Whitecap Coverage and Gas Transfer Velocity with Microwave Brightness Temperature for Plunging and Spilling Breaking Waves

Q. Wang¹, E. C. Monahan¹, W. E. Asher², and P. M. Smith³

¹ Marine Sciences Institute, University of Connecticut
1084 Shennecossett Road, Groton, CT 06340-6097 USA

² Pacific Northwest Laboratory / Marine Sciences Laboratory
1529 W Sequim Bay Road, Sequim WA 98382 USA

³ Naval Research Laboratory, Stennis Space Center, Code 7240
Stennis, MS 39529 USA

Abstract

The correlations of whitecap coverage, gas transfer velocities with water-surface microwave brightness temperature have been examined in an air-water gas exchange experiment conducted in an outdoor surf pool. The regression analyses show that both horizontal-polarization (H-pol) and vertical-polarization (V-pol) microwave brightness temperatures have linear correlations with whitecap coverage and gas transfer velocities. The correlation of microwave brightness temperature with whitecap coverage is found to be the same for spilling breaking waves as for plunging breaking waves. This suggests the correlation does not depend upon the surface wave pattern. The regression results also show that brightness temperature is more sensitive to the changes in whitecap coverage at H-pol than V-pol. The H-pol and V-pol microwave emissivities of whitecap and non-whitecap surface water are estimated.

1 Introduction

Bubbles and bubble plumes generated by wind-induced breaking waves significantly enhance gas exchange across the interface between the ocean and atmosphere under high-wind conditions. *Whitecaps*, or active spilling wave crests, are the sea-surface manifestation of the bubbles and bubble plumes in the subsurface mixed layer. This suggests that the air-sea gas transfer velocity could be estimated at high wind speed from whitecap coverage. The fractional area of the sea surface covered by whitecaps has been proposed to correlate linearly with the air-sea gas transfer velocity [Monahan and Spillane, 1984]. The presence of whitecaps substantially increases the microwave brightness temperature of the sea surface [Droppleman, 1970]. If *whitecap coverage* (W) could be estimated from *microwave brightness temperature* (σ), and if *gas transfer velocity* (k_L) is correlated with W , k_L could be estimated from σ . Therefore, it could be possible to estimate k_L from

the sea-surface microwave brightness temperature measured from satellite-borne sensors. A better understanding of the correlations of W and k_L with σ would also be very helpful in developing a remote-sensing model for predicting k_L from σ . The study presented below investigates these correlations for plunging and spilling breaking waves using gas exchange, whitecap coverage and passive microwave brightness temperature made in a surf pool.

2 Experimental Setup

As a part of an air-water gas exchange experiment conducted in an outdoor surf pool, measurements were made that were designed to investigate the correlations of gas transfer velocity and whitecap coverage with microwave brightness temperature [Asher *et al.*, 1994]. The pool was filled with fresh water with an average depth of 0.8 m. A mechanical wave maker was located at the deep end of the pool, and the generated waves propagate and break towards the shallow end of the pool. Two wave patterns characteristic of *plunging* and *spilling breaking waves* at wave heights of 0.3 m, 0.6 m, 0.9 m, and 1.2 m were produced.

A 19-GHz single-polarization microwave radiometer with a beam angle of 7° mounted at an elevation of 3.4 m and at an incidence angle of 53° was used to measure the H-pol and V-pol microwave brightness temperatures of water surface while a whitecap camera located near the radiometer was looking at the same footprint as that of the radiometer. Therefore, the correlation of brightness temperature with whitecap coverage from this low-elevated camera can be estimated. In addition, two additional whitecap video cameras focused on the pool surfaces of a deep-water zone and a shallow-water zone, respectively. Whitecap coverage in the shallow-water zone was recorded by a video camera at an elevation of 6.71 m while whitecap coverage in the deep-water zone was recorded by a camera at an elevation of 10.67 m. Therefore, a pool-averaged whitecap coverage can be estimated from the measurements of these two high-elevated cameras. In addition to these measurements, air-water fluxes of *helium* (He) and *sulfur hexafluoride* (SF_6), bubble size distributions, and other environmental parameters were simultaneously measured [Asher *et al.*, 1994].

3 Correlation Between Brightness Temperature and Whitecap Coverage

The microwave brightness temperature measured at 19 GHz ranged from 155°K to 210°K for vertical polarization (V-pol) and 100°K to 160°K for horizontal polarization (H-pol) with the microwave brightness temperature increasing with wave height.

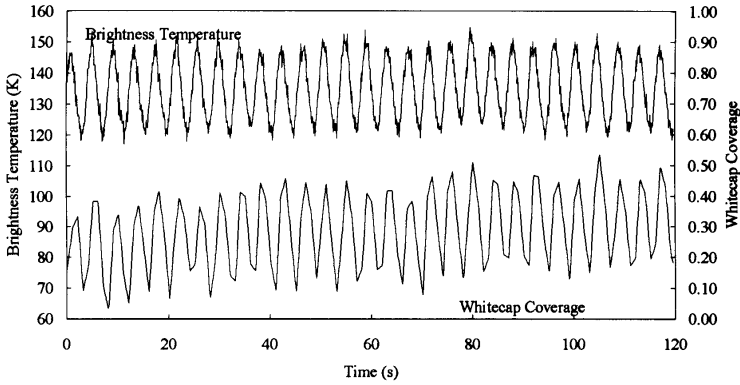


Figure 1: Time sequences of H-pol microwave brightness temperature and whitecap coverage for a plunging breaking wave with wave height of 0.9 m.

The time sequences of H-pol microwave brightness temperature and whitecap coverage from the low-elevated camera for a plunging breaking wave with wave height of 0.9 m are plotted, as an example, in Figure 1. It clearly shows that microwave brightness temperature has a positive correlation with whitecap coverage and has a same periodicity of 4.17 second as that of whitecap coverage.

From the data, it was found that time-averaged whitecap coverage (W_L) from low-elevated camera was linearly correlated with H-pol/V-pol microwave brightness temperature (σ_h or σ_v) and *linear regression* was used to investigate this correlation. The regression analysis showed that at each polarization line relating σ_h to W_L is the almost same for plunging breaking waves as for spilling breaking waves (see Figure 2). This suggests that the correlation between W_L and σ_h does not depend upon the surface wave pattern. Similar correlation is obtained for σ_v .

The linear regression yields the following relationship between σ_h (or σ_v) and W_L (see Figure 3),

$$\sigma_h(^{\circ}K) = 126.9 W_L + 109.5 \quad (1)$$

$$\sigma_v(^{\circ}K) = 111.6 W_L + 170.5 \quad (2)$$

The regression results also showed that the slope for H-pol is larger than that for V-pol and the correlation coefficient for σ_h is greater than that for σ_v . This indicates that σ is more sensitive to changes in W_L at H-pol than at V-pol. Therefore, H-pol could be the preferred radiometer polarization for *remote sensing* of W_L . These results are consistent with the aircraft measurements [Webster *et al.*, 1976], in which an aircraft-mounted *microwave radiometer* was used to measure the sea-surface brightness temperature under

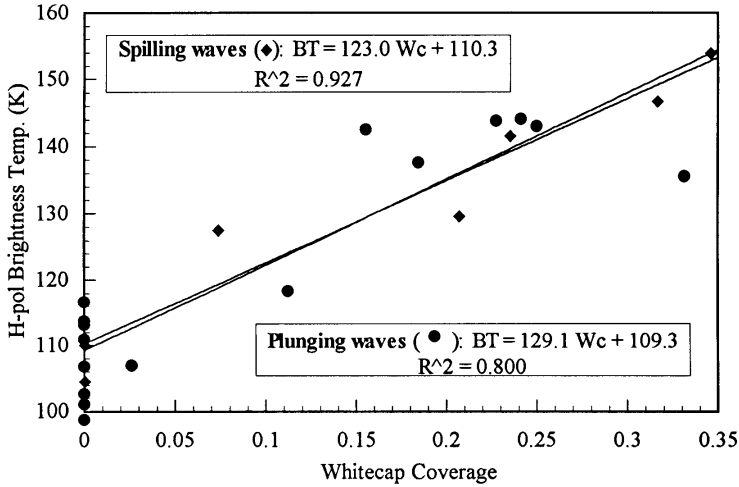


Figure 2: Correlation of σ_h with W_L for both spilling and plunging breaking waves.

various wind conditions. Webster et al. reported that the V-pol brightness temperature of sea surface is substantially greater than that of the H-pol for same wind conditions, and that the H-pol brightness temperature has higher sensitivity to changes in sea-surface wind speed.

Microwave brightness temperature (σ) is mainly dependent upon whitecap coverage, water temperature, wave slope steepness and atmospheric moisture [Pandey and Kakar, 1982]. By neglecting effect of atmospheric moisture, σ can be expressed by the product of the microwave emissivity (E) of water surface and water temperature (T_s),

$$\sigma = ET_s \quad (3)$$

The brightness of water surface partially-covered with whitecaps may be expressed as the sum of the microwave contributions from whitecap water surface and non-whitecap surface [Smith, 1988],

$$\sigma_h = E_{sh}(1 - W_L)T_s + E_{wh}W_LT_s \quad (4)$$

$$\sigma_v = E_{sv}(1 - W_L)T_s + E_{wv}W_LT_s \quad (5)$$

where E_{sh} (E_{sv}) denotes the H-pol (V-pol) microwave emissivity of non-whitecap water surface and E_{wh} (E_{wv}) represents H-pol (V-pol) emissivity of whitecap surface.

These emissivities may be estimated from the fitting curves of (1) and (2). The averaged water temperature was about 20 °C (293 °K) during the

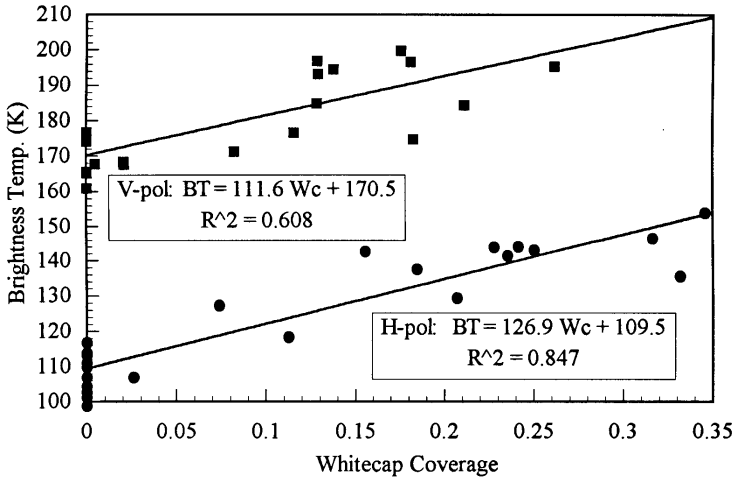


Figure 3: Correlation of σ_h and σ_v with W_L .

Table 1: Estimations of microwave emissivities

	E_{sh} or E_{sv}	E_{wh} or E_{wv}
H-pol	0.374	0.807
V-pol	0.582	0.963

experiment. Therefore, the emissivities can be calculated as shown in Table 1.

As expected, the estimated microwave emissivity of whitecap surface is much larger than that of non-whitecap surface. The estimated emissivities are slightly greater than the emissivities obtained at sea by *Smith* [1988]. This slight overestimation is due probably to the fact that the camera looked at larger area than the radiometer did. The influence of wave slope steepness has not been separated from whitecap coverage and, therefore, the estimated emissivities may include the contributions from the wave slope steepness.

In order to view a larger area, the radiometer and video camera were raised to an elevation of 15 m above the water surface. At this elevation, σ was measured at the deep and shallow ends of the pool (positions R5 and R6, respectively, in *Asher et al.* [1995]). The measurements of σ and W_L at these two stations are plotted as open circles (V-pol) and diamonds (H-pol) in Figure 4. The emissivities estimated from the low-elevated radiometer/camera are used to predict σ from W_L collected at the elevation of 15 m and the two lines in Figure 4 present the $\sigma_h - W_L$ and $\sigma_v - W_L$ relationships from the modeling. It can be seen that the predictions are consistent with the measurements of σ and W_L from the radiometer/camera at the higher elevation.

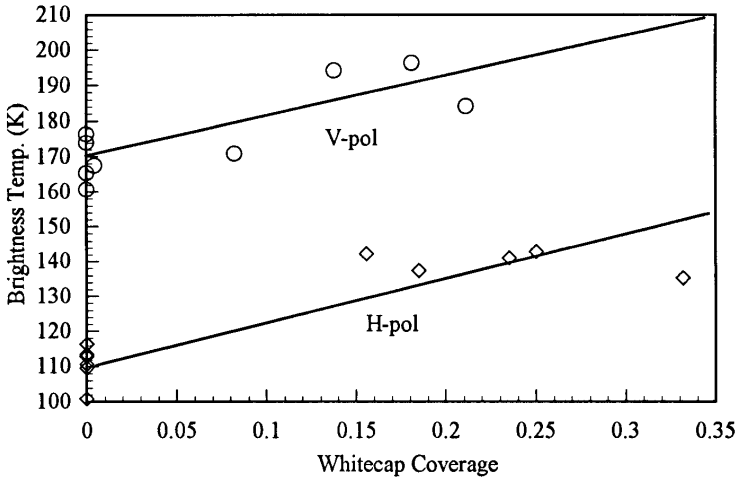


Figure 4: Comparison between model predictions and measurements of σ and W_L from the radiometer/camera at an elevation of 15 m.

This supports that the $\sigma - W_L$ correlations in (1) and (2) obtained from the low-elevated radiometer/camera can be applied to predict pool-averaged σ from pool-averaged whitecap coverage.

4 Correlation of Brightness Temperature With Gas Transfer Velocities

The transfer velocities (k_L) of many environmental gases (e.g., He and SF₆) were measured during the experiment. The k_L measurements were taken at eleven stations along the surf pool near both sides. The turbulence and bubble plumes generated by breaking waves made the gas concentration horizontally and vertically homogeneous within the pool. The gas transfer velocity averaged over all sampling stations can represent a pool-averaged gas transfer velocity. The measured k_L substantially increases with wave height.

The average whitecap coverage obtained from the two high-elevated video cameras focusing on the shallow- and deep-water zones significantly increase with wave height for a given wave pattern. Compared between patterns, the whitecap coverage for the plunging breaking waves was markedly greater than that for the spilling breaking waves. The whitecap analysis showed that the whitecap coverage in shallow-water zone was nearly constant as wave height increased from 0.6 m to 1.2 m for plunging breaking waves and wave height increased from 0.9 m to 1.2 m for spilling breaking waves. This suggests that wave breaking was saturated in the shallow-water zone at those wave conditions. However, the whitecap coverage increased

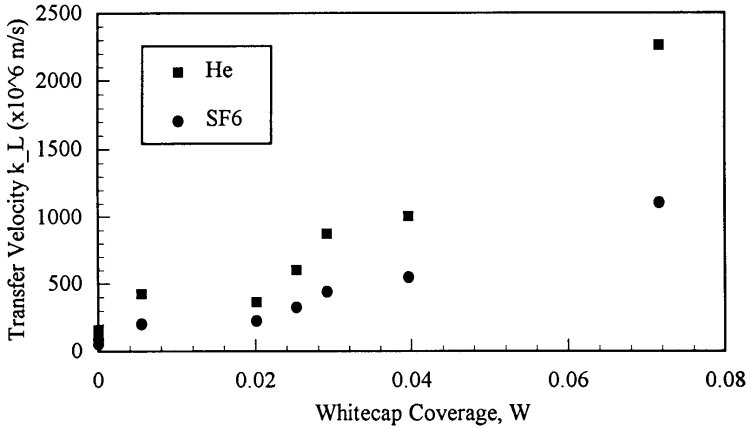


Figure 5: Correlation of gas transfer velocity (k_L) with whitecap coverage (W).

with wave height in deep-water zone. Because the high-elevated cameras looked at large areas of pool water surface, the whitecap coverage averaged over two water zones can represent a pool-averaged whitecap coverage. The averaged values increase with wave height.

In Figure 5, the pool-averaged transfer velocities of He and SF₆ gases are plotted against the pool-averaged whitecap coverage (W) obtained from these two high-elevated cameras. The regression analysis shows that $k_L - W$ correlations have fairly-high correlation coefficients (R^2) of 0.936 for He and of 0.964 for SF₆. The transfer velocity $k_L(\text{He})$ of He gas is almost twice as large as $k_L(\text{SF}_6)$. This is because the *Schmidt number* $Sc(\text{He})$ of He gas is smaller than $Sc(\text{SF}_6)$ and the gas transfer velocity is proportional to Sc^{-n} with $n = 0.3 \sim 0.5$ [Asher et al., 1992].

The correlation of gas transfer velocity with microwave brightness temperature may be determined through their relationship to whitecap coverage. The correlation between whitecap coverage and brightness temperature was known as described in (1) and (2), and the microwave emissivities were calculated as listed in Table 1. The brightness temperature corresponding to pool-averaged whitecap coverage (W) from the high-elevated cameras can in turn be estimated. Therefore, the transfer velocity of gases (e. g., He and SF₆) can be correlated with the estimated brightness temperature. The resulting correlations between H-pol brightness temperature (σ_h) and the transfer velocities of He and SF₆ gases can be expressed as,

$$k_L(\text{He}) = 220.27 \sigma_h - 24047 \quad (6)$$

$$k_L(\text{SF}_6) = 109.80 \sigma_h - 11966 \quad (7)$$

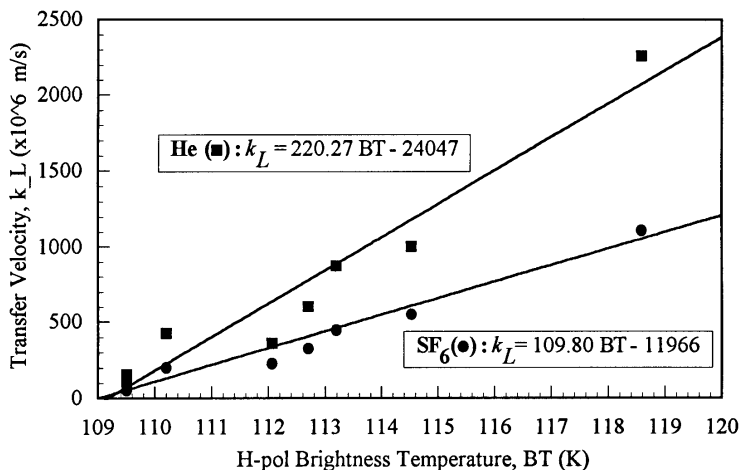


Figure 6: Correlation of gas transfer velocities (k_L) with brightness temperature (σ).

The k_L measurements and the σ_h estimations, and their linear regression analysis are showed in Figure 6.

5 Conclusions

The linear regression approach was applied to analyze the measurements of gas transfer velocities, whitecap coverage and microwave brightness temperatures which were concurrently measured during the surf-pool experiment. The data analyses show that both H-pol and V-pol microwave brightness temperatures have linear correlations with whitecap coverage as well as gas transfer velocities. This supports the feasibility of remote determination of gas transfer velocity and whitecap coverage from microwave remote sensing techniques. The microwave brightness temperature is more sensitive to the changes in whitecap coverage at H-pol than V-pol. This may conclude that the H-pol brightness temperature, not the V-pol, is the preferred parameter for remote sensing of whitecap coverage and gas transfer velocity. The experimental data indicate that the correlation of microwave brightness temperature with whitecap coverage is the same for spilling breaking waves as for plunging breaking waves, which suggests the correlation does not depend upon the surface wave pattern. Although the spilling breaking waves produce different whitecap dimensions on water surface from the plunging breaking waves, the brightness temperature from the microwave radiometer is mainly proportional to the area covered by whitecaps rather than the volume of whitecaps since microwave can only penetrate a few millimeters of water column. The H-pol and V-pol microwave emissivities of whitecap-covered water surface were noted to be much larger than those of

the non-whitecap water surface.

Acknowledgements

This study was supported by the U.S. Department of Energy (DOE) under Contract DE-AC06-76RLO 1830. Pacific Northwest Laboratory is operated for DOE by Battelle Memorial Institute.

References

- Asher, W. E., P. J. Farley, R. Wanninkhof, E. C. Monahan, and T. S. Bates, Laboratory and field measurements on the correlation of fractional area whitecap coverage with air/sea gas transport, In *Precipitation Scavenging and Atmosphere-Surface Exchange*, Volume 2 — The Semonin Volume: Atmosphere-Surface Exchange Processes, S. E. Schwartz and W. G. N. Slinn, eds., Hemisphere, Washington, DC, 815-828, 1992
- Asher, W. E., L. M. Karle, B. J. Higgins, P. J. Farley, C. R. Sherwood, W. Gardiner, R. Wanninkhof, H. Chen, T. Lantry, and M. Steckley, E. C. Monahan, Q. Wang, and P. M. Smith, Measurement of gas transfer, whitecap coverage, and brightness temperature in a surf pool: An overview of WABEX-93, *This volume*
- Droppleman, J. D., Apparent microwave emissivity of sea foam, *J. Geophys. Res.*, 75(3), 696-698, 1970
- Karle, L., W. Asher, B. Higgins, P. Farley C. Sherwood, W. Gardiner, R. Wanninkhof, H. Chen, T. Lantry, M. Steckley, E.C. Monahan, M. B. Wilson, Q. Wang, and P. Smith, Measurement of gas exchange, whitecap coverage and microwave brightness temperature in a surf pool, AGO, San Diego, 1994
- Monahan, E. C. and M. C. Spillane, The role of oceanic whitecaps in air-sea gas exchange. In *Gas Transfer at Water Surface*, W. Brutsaert and G. H. Jirka, Eds., D. Reidel Pub., Dordrecht, Holland, 495-503, 1984
- Pandey, P.C. and R. K. Kakar, An empirical microwave emissivity model for a foam-covered sea, *IEEE J. Ocean Engrg.*, 7, 135-140, 1982
- Smith, P. M., The emissivity of sea foam at 19 and 37 GHz, *IEEE Trans. Geosci. Remote Sens.*, 26, 541-547, 1988
- Webster, W. Jr., T. T. Wilheit, D. B. Ross, and P. Gloersen, Spectral characteristics of the microwave emission from a wind-driven foam-covered sea, *J. Geophys. Res.*, 81, 3095-3099, 1976

The Effect of Bubble Plume Size on the Parameterization of Air-Seawater Gas Transfer Velocities

W. E. Asher¹, L. M. Karle¹, B. J. Higgins¹, P. J. Farley¹, I. S. Leifer², and E. C. Monahan³

¹ Pacific Northwest Laboratory/Marine Sciences Laboratory
1529 W. Sequim Bay Road, Sequim, Washington 98382, USA

² Earth and Atmospheric Sciences Department
Georgia Institute of Technology, Atlanta, Georgia 30332, USA

³ Marine Sciences Institute, University of Connecticut, Avery Point
Groton, Connecticut 06340, USA

Abstract

Laboratory results have demonstrated that bubble plumes are a very efficient air-water gas transport mechanism. Because breaking waves generate bubble plumes, it could be possible to correlate the air-sea gas transfer velocity, k_L , with whitecap coverage. However, the functional form for a parameterization of k_L in the presence of breaking waves is not definitively known at present. A whitecap simulation tank (WST) was used to measure k_L for evasion of carbon dioxide, helium, oxygen, and sulfur hexafluoride through cleaned seawater surfaces. Fractional area bubble plume coverage, B_C , in the WST was varied by changing the size of the simulated breaking waves. An empirical model has been developed from the data that can predict k_L from B_C , diffusivity, and solubility. The results show that B_C can be used to scale the effects of whitecaps on k_L when the size of the simulated whitecap is not constant.

1 Introduction

The air-sea flux of a slightly soluble gas is calculated as the product of its concentration difference across the air-sea interface and the air-sea transfer velocity, k_L . In the absence of bubbles, k_L is dependent on the intensity of the near-surface aqueous-phase turbulence and the molecular diffusivity or Schmidt number, Sc , of the gas. Because most of the turbulence in the ocean surface is generated by wind stress, past studies have attempted to parameterize k_L in terms of wind speed, U [Liss and Merlivat, 1986; Wanninkhof, 1992]. High wind speeds are also associated with the presence of *whitecaps*, which can increase the gas flux by generating intense patches of turbulence and by creating *bubble plumes*. The bubble plumes will provide increased surface area for gas exchange and generate additional turbulence.

Whitecap-related turbulence and bubble processes are very effective at promoting gas transfer, and it has been proposed that k_L will increase linearly with increasing fractional area whitecap coverage, W_C [Monahan and Spillane, 1984]. More importantly however, it is not definitively known how the presence of breaking waves and bubble plumes affect the dependence of k_L on Sc and aqueous-phase solubility, α (given as the dimensionless Ostwald solubility [Reid *et al.*, 1987]). Knowledge of this dependence is necessary to determine the best method for parameterizing k_L in the presence of breaking waves.

Using data collected in a tipping-bucket *whitecap simulation tank* (WST), Asher *et al.* [1995] have shown that k_L for evasion when the transferring gas is far from equilibrium can be partitioned into a component due to turbulence generated by a small homogenization pump in the WST, k_M , a component due to turbulence generated by the simulated breaking waves, k_T , and a component due to bubble-mediated transfer, k_B . If $k_M = A_M Sc^{-n}$ and $k_T = A_T Sc^{-n}$ (where A_M and A_T are constants determined by the pump- and whitecap-generated turbulence, respectively, and n is between 1/2 for a clean water surface and 2/3 for an interface covered by a surface film), k_L can be written as

$$k_L = (A_M + B_C(A_T - A_M))Sc^{-n} + B_C(a_1\alpha^{-1} + b_1\alpha^{-m_1}Sc^{-n_1}) \quad (1)$$

where $n = 1/2$ for transfer through a clean water surface and B_C is bubble plume coverage (i. e., B_C is the laboratory analog of W_C). The bubble-mediated transfer velocity, k_B , is the second term on the right-hand side of (1) and has been proposed previously by Merlivat *et al.* [1993]. The set of coefficients A_M , A_T , a_1 , b_1 , m_1 , and n_1 were determined for gas evasion by Asher *et al.* [1995] using chi-square optimization of (1) to measurements of k_L made in a WST for evasion of *carbon dioxide* (CO_2), *helium* (He), *oxygen* (O_2), *sulfur hexafluoride* (SF_6), and *dimethylsulfide*.

It is not clear that the functional form for k_B given in (1) can be applied to oceanic conditions. Although Asher and Farley [1995] showed that the bubble populations in the WST were similar to oceanic bubbles, B_C in the WST was increased by increasing the frequency at which bubble plumes were generated while the size of each plume remained constant. In contrast, available field data indicate that W_C in the ocean increases because both frequency of breaking and whitecap size increase [Monahan and Monahan, 1986]. This difference could affect the functional form of the parameterization given in (1).

When the size of a breaking wave increases, it generates a larger bubble plume and more turbulence. If the number of bubbles and turbulence energy generated per unit area of plume remain constant as whitecaps grow larger, the net effect of this increase in size on gas exchange can be accounted for by the increase in W_C . This is equivalent to the proposition that the fraction of surface that is whitecap-covered increases, but the transfer velocity of a

patch of ocean covered by a whitecap remains constant. In this case, A_T , a_1 , b_1 , m_1 , and n'_1 will be constant with W_C and (1) could be used to estimate k_L . Alternatively, it is possible that the bubble population and turbulence per unit area will increase as whitecap size increases, and A_T , a_1 , b_1 , m_1 , and n'_1 would be functions of W_C . Therefore, (1) would have to be modified to include the functionality of the coefficients with respect to W_C .

In this paper, the WST used by Asher *et al.* [1995] was modified so that bubble plumes of different size could be generated using the tipping bucket. Evasive transfer velocities for CO₂, He, O₂, and SF₆ were measured in seawater as a function of B_C , where B_C was increased by increasing the plume size while keeping the frequency of generation constant. These k_L values were then used to determine whether (1) could be used to model the dependence of k_L on B_C , Sc , and α . The data were also used to investigate whether changes in plume size caused A_T , a_1 , b_1 , m_1 , and n'_1 to be functions of B_C .

2 Experimental

The gas exchange measurements reported here were made in the tipping-bucket WST described in detail by Asher and Farley [1995]. Briefly, the WST used was a 1.2-m by 1.2-m by 1.8-m acrylic tank with a water depth of 1.2 m and a water volume of 1.7 m³. It generated bubble plumes by releasing a volume of water vertically onto the tank water surface using a tipping bucket. Water temperature, T_W (K), was regulated to within 0.5 K using a flow-through chiller/heater (Acry-Tech, San Diego, California). Water in the WST was homogenized by means of a small submersible pump; dye studies and position-dependent sampling showed that the characteristic mixing time was 300 s in the absence of bubble plumes. A schematic diagram of the WST is shown in Figure 1.

The WST was filled with seawater that had been filtered through a 5- μ m spun-fiber filter and then sterilized using a flow-through ultraviolet sterilizer. This procedure removed particles, helped prevent biologically-produced bubbles, and reduced water surface contamination. Interfacial contamination was further reduced by vacuuming the water surface prior to the start of each experiment. Salinity in the WST was measured by refractometry and found to be between 29 ‰ and 32 ‰. T_W and air temperature were measured using platinum thermistors.

Fractional-area bubble plume coverage, B_C , was measured in the WST by video analysis of the surface expression of the bubble plumes [Asher *et al.*, 1991]. B_C was a function of the volume of water in the bucket, F_V (m³), and the time between successive bucket tips, T_B (s). In Asher *et al.* [1995], B_C was varied by changing T_B at a constant F_V . Here, in order to study the effect of changes in wave size on the parameterization of k_L , B_C was varied by changing F_V at a constant T_B . Table 1 shows T_B , F_V , and the resulting B_C for the experiments described here.

Evasive k_L values were measured for CO₂, He, O₂, and SF₆. Sc and α for

Table 1: Fractional area bubble plume coverage

T_B (s)	F_V ($\times 10^{-3} \text{ m}^{-3}$)	B_C (fraction)
n.a.	0	0
36	8.2	0.0040
36	12.6	0.0064
36	17.3	0.0087

each gas were calculated using the relations from *Wanninkhof* [1992]. He, CO₂, and O₂ were added to the tank by bubbling through a diffuser tube mounted at a depth of 0.75 m. SF₆ was added by injecting a small volume of saturated aqueous solution to the tank water.

Glass syringes with a volume of $5.0 \times 10^{-5} \text{ m}^3$ were used to collect $3.0 \times 10^{-5} \text{ m}^3$ water samples from a port 0.25 m below the water surface. Aqueous-phase concentrations of SF₆ and He in these samples were analyzed using the syringe-headspace method of *Wanninkhof et al.* [1991]. Concentrations were determined chromatographically using an electron-capture detector (ECD) for SF₆ and a thermal conductivity detector (TCD) for He.

SF₆ standards with concentrations of 24 pptv (parts-per-trillion by volume), 138 pptv, and 969 pptv SF₆ were used to calibrate the response of the ECD. The three SF₆ standards were made in-house by volumetric dilution of a commercially-prepared 101-parts-per-million by volume (ppmv) SF₆ in nitrogen (N₂) standard (So-Cal Airgas, Los Angeles, California). Their concentrations were determined by comparison with the standards described in *Wanninkhof et al.* [1991]. The TCD response for He was calibrated using a commercially-prepared 10⁴-ppmv He in N₂ standard (Airco, Vancouver, Washington).

Aliquot samples of water were collected in $3.0 \times 10^{-4} \text{ m}^3$ glass bottles to determine aqueous-phase O₂ concentrations during each experiment. O₂ concentrations were measured in these samples by Winkler titration.

CO₂ evasion experiments were conducted by lowering the pH of the WST to below 5.0 using hydrochloric acid. For pH < 5, the total concentration of all dissolved CO₂ species, $t\text{CO}_2$, is approximately equal to the concentration of dissolved CO₂, [H₂CO₃*]. In the WST, [H₂CO₃*] was determined from Henry's law by measuring the partial pressure of CO₂ in the aqueous phase. All CO₂ acid-base constants and the Henry's Law constant (in units of moles of CO₂ dissolved per cubic meter of water per atmosphere of CO₂ pressure) were obtained from DOE [1994].

The atmospheric partial pressure of CO₂ was measured by sampling the air 0.5 m above the water surface in the WST using a gas-tight $3.0 \times 10^{-5} \text{ m}^3$ nylon syringe. The partial pressure of CO₂ dissolved in the aqueous phase was measured using an air-water gas equilibrator suspended in one corner of the WST (see Figure 1). A pump provided a water flow of $5 \times 10^{-3} \text{ m}^3 \text{ min}^{-1}$

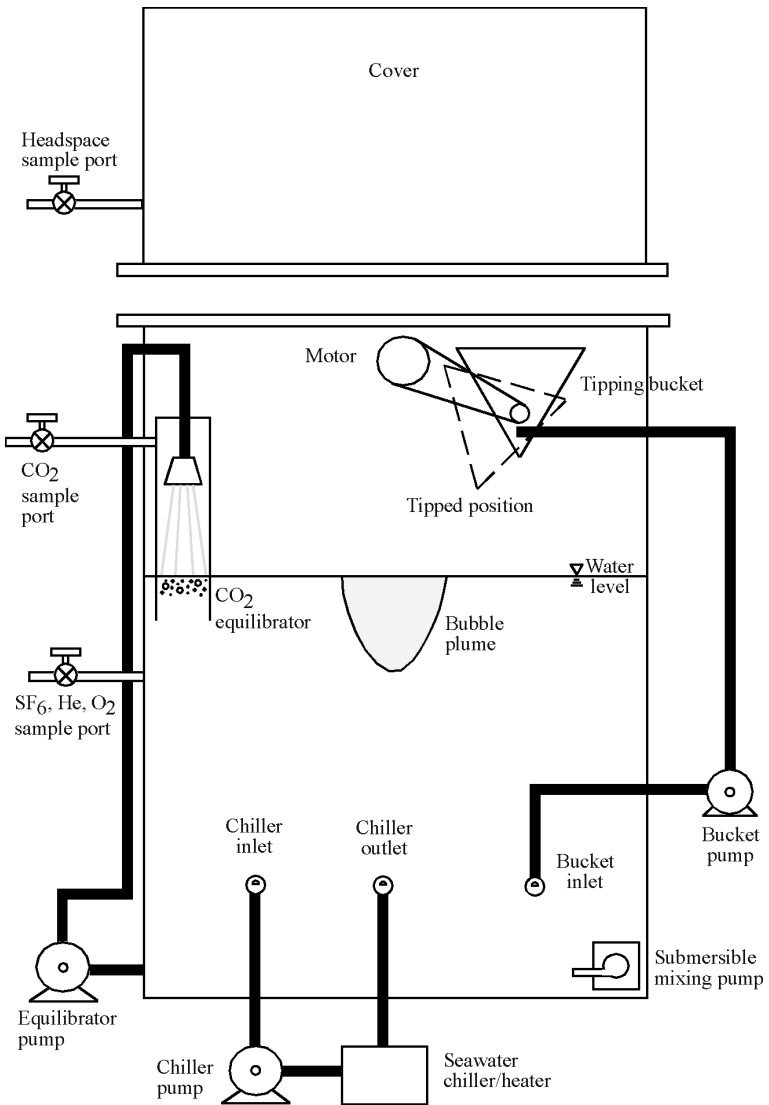


Figure 1: Schematic diagram of the whitecap simulation tank. The tank cover was left open during the experiments described here.

Table 2: Coefficients for empirical parameterization of k_L

Equation	n	A_M (m s^{-1})	A_T (m s^{-1})	a_1 (m s^{-1})	b_1 (m s^{-1})	m_1	n'_1
(1)	0.56	7.9×10^{-4}	0.20	-6.1×10^{-5}	0.032	0.25	0.21
(2) †	0.56	7.9×10^{-4}	0.34	3.0×10^{-5}	0.52	n.a.	0.66

† See text for explanation of (2)

through a shower head into the equilibrator, and the resulting response time of the equilibrator to step changes in aqueous CO_2 concentrations was less than 600 s. The air phase in the equilibrator was sampled with a 3.0×10^{-5} - m^3 nylon syringe. Concentrations of CO_2 in the syringes were analyzed on a TCD-equipped gas chromatograph. The TCD was calibrated using 350-ppmv and 1050-ppmv CO_2 in He standards (Airco, Vancouver, Washington).

3 Results and Discussion

Figure 2 shows k_L for He, $k_L(\text{He})$, k_L for CO_2 , $k_L(\text{CO}_2)$, k_L for O_2 , $k_L(\text{O}_2)$, and k_L for SF_6 , $k_L(\text{SF}_6)$, plotted versus B_C . In agreement with the measurements by Asher *et al.* [1992, 1995], k_L for all four gases correlates linearly with B_C . This shows that B_C can be used to scale the effect of breaking waves on gas transfer when the size of the breaking wave increases. In addition, the linear relationship between k_L and B_C suggests that the whitecap-related coefficients A_T , a_1 , b_1 , m_1 , and n'_1 in (1) are constant with increasing B_C . Therefore, (1) can be used to model k_L in the presence of simulated breaking waves.

The initial step in determining the coefficients in (1) is to estimate the transfer velocity due to turbulence generated by the submersible mixing pump, k_M . As was discussed above, k_M is equal to $A_M Sc^{-n}$ where A_M is a constant and the value for n is between 1/2 and 2/3. Therefore, n and A_M were estimated by linear regression of $\log(k_L)$ for $B_C = 0.0$ with $\log(Sc)$. For the k_L data at $B_C = 0.0$ in Figure 2, a linear regression of $\log(k_L)$ versus $\log(Sc)$ resulted in a coefficient of determination of 0.98 and $n = 0.56$ and $A_M = 7.9 \times 10^{-4} \text{ m s}^{-1}$. These values will be used in (1) in the following calculations.

The constant defining transfer due to whitecap-generated turbulence, A_T , and the four constants, a_1 , b_1 , m_1 , and n'_1 , that define the bubble-mediated transfer velocity, k_B , were determined by nonlinear chi-square minimization of (1) to the data in Figure 2 using a Levenberg-Marquardt algorithm [Press *et al.*, 1992]. Table 2 shows the resulting values for the five coefficients and Figure 3 shows the measured k_L value from Figure 2 plotted versus k_L calculated from (1) and the coefficients listed in Table 2. Figure 3 shows that (1) can be used to parameterize k_L in the WST.

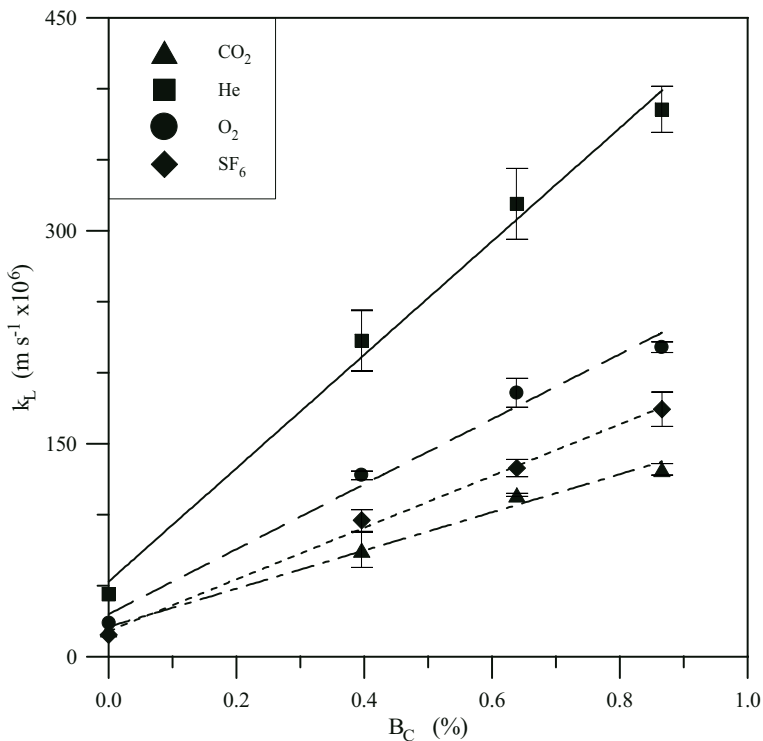


Figure 2: The air-seawater gas transfer velocity, k_L , of carbon dioxide (CO_2), helium (He), oxygen (O_2), and sulfur hexafluoride (SF_6) measured in the whitecap simulation tank plotted versus fractional area bubble plume coverage, B_C . Error bars show plus or minus one standard deviation of the average k_L value for at least three measurements.

Asher et al. [1995] developed the functional form of (1) from the models for bubble-driven gas transfer proposed by Memery and Merlivat [1985] and Keeling [1993]. In the case of evasion, the bubble-mediated flux is due to bubbles, the gas composition of which equilibrates with the surrounding water, and which then return to the surface, and to bubbles that continue to exchange gas over their entire subsurface lifetime. Based on the discussion in Memery and Merlivat [1985], Asher et al. [1995] reasoned that the term a_1/α in (1) defines the fraction of the gas flux due to equilibrating small bubbles, and $b_1\alpha^{-m}Sc^{-n}$ defines the gas flux from larger bubbles. If this physical interpretation is correct, the constants a_1 and b_1 should be positive because both equilibration and the flux due to the larger bubbles will increase the net gas flux. However, a_1 for (1) listed in Table 2 is negative. This suggests that the individual terms in (1) defining k_B cannot be related to specific physical processes.

However, both Merlivat et al. [1993] and Asher et al. [1995] have shown

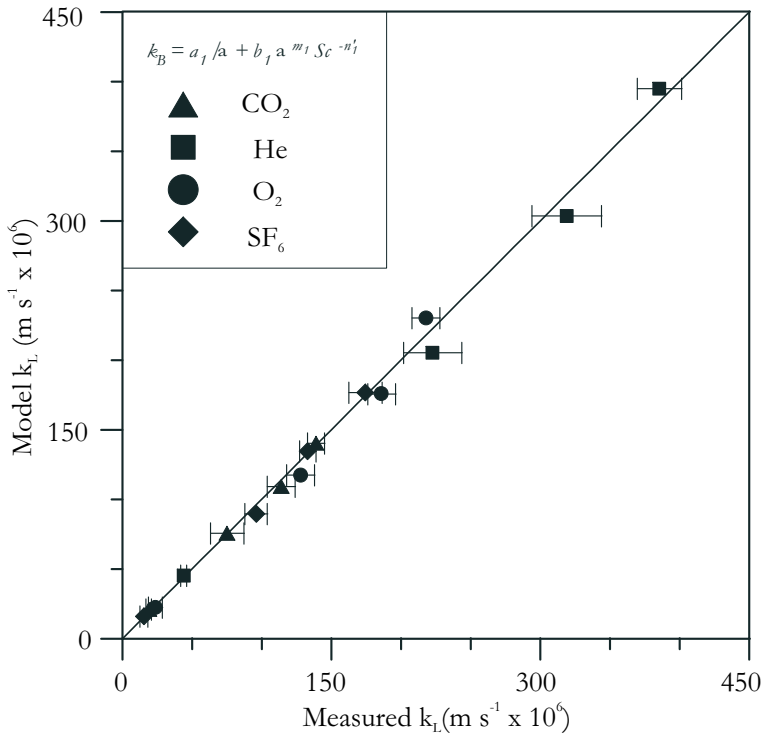


Figure 3: The air-seawater gas transfer velocity, k_L , of carbon dioxide (CO_2), helium (He), oxygen (O_2), and sulfur hexafluoride (SF_6) estimated in the whitecap simulation tank using (1) and the corresponding coefficients listed in Table 1 plotted versus the directly measured values. The horizontal error bars show plus or minus one standard deviation of the average k_L value for at least three measurements. The uncertainty in k_L predicted by (1) was not calculated.

that k_B as parameterized in (1) does a very good job of estimating the transfer velocity resulting from bubble-mediated processes.

One possible solution to the problem of negative coefficients in the definition of k_B is to develop an alternative parameterization for k_L based on (1) and the approximate form for k_B given by *Memery and Merlivat* [1985]. *Memery and Merlivat* showed that for evasion of a gas whose concentration is far from equilibrium, k_B is equal to $a/\alpha + b$. The term a/α results from the flux due to equilibrating bubbles. The term b is derived from the gas flux due to non-equilibrating bubbles. If a bubble does not equilibrate, its net gas flux can be described by a transfer velocity that is proportional to Sc^{-n} but independent of α . Therefore, if b is proportional to $Sc^{-n'}$, (1) can be rewritten as

$$k_L = (A_M + B_C(A_T - A_M))Sc^{-n} + B_C(a_1\alpha^{-1} + b_1Sc^{-n'}) \quad (2)$$

where A_M and A_T are defined identically to (1).

The coefficients A_T , a_1 , b_1 , and n'_1 in (2) were determined by chi-square optimization of (2) to the data in Figure 2 with the results listed in Table 2. Both a_1 and b_1 are positive and therefore, in principle, are physically significant. In fact, it could be possible to estimate them in the WST using the model of *Memery and Merlivat* [1985] with the bubble population data from *Asher and Farley* [1995]. However, these results are not yet available. It is interesting that n'_1 for (2) was found to be 0.66, which implies that the transfer velocity to nonequilibrating bubbles had an Sc dependence characteristic of a film-covered water surface. This suggests that the bubbles in the WST were covered by a surface film and should be modeled as rigid spheres.

Figure 4 shows the k_L values determined by the coefficients plotted versus the experimentally measured values. Also shown in Figure 4 are $k_L(\text{CO}_2)$, $k_L(\text{He})$, $k_L(\text{O}_2)$, and $k_L(\text{SF}_6)$ measured by *Asher et al.* [1995] plotted versus the corresponding k_L values estimated using (2). Although the fit of (2) to the WST data is excellent for $k_L(\text{He})$, $k_L(\text{CO}_2)$, and $k_L(\text{SF}_6)$, the resulting coefficients significantly underpredict $k_L(\text{O}_2)$. The reasons for this are not clear at present. However, Figure 4 shows that (2) accurately estimates k_L for the data of *Asher et al.* [1995]. This is significant because *Asher et al.* [1995] varied B_C by adjusting the frequency of wave breaking, and the coefficients in Table 2 for (2) were derived using the variable-plume size data measured here.

The limiting behavior of k_B as given in (2) with respect to α and Sc does not agree with that proposed by *Woolf* [1995]. *Woolf* has stated that when $\alpha \gg 1$, k_B will be proportional to $1/\alpha$ and that when $\alpha \ll 1$, k_B will be proportional to D^n , where $1/2 < n < 2/3$, but independent of α . Although the form for k_B given in (2) does not give this behavior, *Asher et al.* [1995] have shown that k_B for SF_6 measured at $T_W = 278$ K and 293 K (i. e., $\alpha \ll <1$) estimated from measurements of k_L in the WST was proportional to $D^{0.27}$. The $n < 1/2$ dependence suggests that k_B was also a function of α even for an insoluble gas. Furthermore, *Asher et al.* [1995] have shown that k_B for $\alpha > 1$ was proportional to α^{-m} where m was between 0.35 and 0.8. This suggests that k_B was still a function of diffusivity. Because the available experimental evidence indicates that the bubble-mediated transfer velocities in the WST do not obey the limiting behavior with respect to Sc and α proposed by *Woolf* [1995], there is no compelling reason to require a parameterization of k_B in the WST to follow that limiting behavior either.

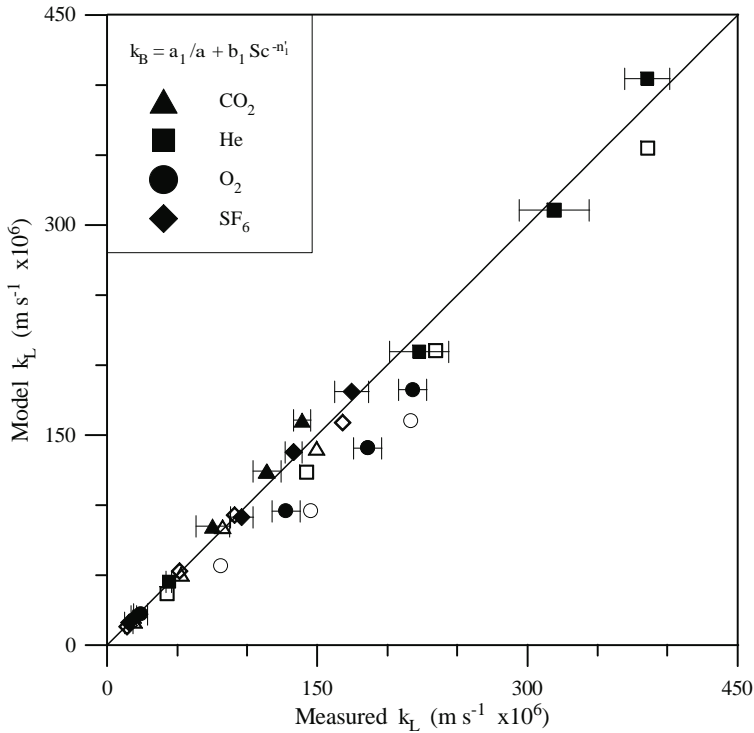


Figure 4: The air-seawater gas transfer velocity, k_L , of carbon dioxide (CO_2), helium (He), oxygen (O_2), and sulfur hexafluoride (SF_6) estimated in the whitecap simulation tank using (2) and the corresponding coefficients listed in Table 1 plotted versus the directly measured values. The horizontal error bars show plus or minus one standard deviation of the average k_L value for at least three measurements. The uncertainty in k_L values predicted by (2) was not calculated.

4 Conclusions

The empirical relation defining k_L in terms of B_C , Sc , and α proposed by *Merlivat et al.* [1993], developed in *Asher et al.* [1995], and given in (1) has been shown to be applicable to the case where increases in B_C are caused by increasing wave size. In addition, the modified version of the parameterization given in (2) has been shown to have physically realistic coefficients. It has also been shown that (2) can be used to predict the k_L values measured by *Asher et al.* [1995]. These results show it is possible to estimate k_L in the presence of bubbles using a relatively simple relation. Although it is unlikely that the WST results will be directly applicable to the oceans, the similarity of bubble populations in the WST to those measured in the ocean [*Asher and Farley*, 1995] suggests that a relation similar in functional form to (1) or (2) could be developed to estimate oceanic k_L values.

Acknowledgements

This research was supported by the U.S. Department of Energy (DOE), Office of Health and Environmental Research, Environmental Sciences Division under Contract DE-AC06-76RLO 1830. Pacific Northwest Laboratory is operated for DOE by Battelle Memorial Institute.

References

- Asher, W. E., and P. J. Farley, Phased-Doppler anemometer measurement of bubble concentrations in laboratory-simulated breaking waves, *J. Geophys. Res.*, 100C, 7045-7056, 1995
- Asher, W. E., E. C. Monahan, R. Wanninkhof, and T. S. Bates, Correlation of fractional foam coverage with gas transport rates, in *Air-Water Mass Transfer*, edited by S. E. Wilhelms and J. S. Gulliver, pp. 536-548, A.S.C.E., New York, New York, 1991
- Asher, W. E., P. J. Farley, R. Wanninkhof, E. C. Monahan, and T. S. Bates, Laboratory and field measurements concerning the correlation of fractional area foam coverage with air/sea gas transport, in *Precipitation Scavenging and Atmosphere-Surface Exchange: Volume 2-The Semonin Volume: Atmosphere-Surface Exchange Processes*, edited by S. E. Schwartz and W. G. N. Slinn, pp. 815-828, Hemisphere, Washington D.C., 1992
- Asher, W. E., L. M. Karle, B. J. Higgins, P. J. Farley, I. S. Leifer, and E. C. Monahan, The influence of bubble plumes on air/seawater gas transfer velocities, submitted to *J. Geophys. Res.*, 1995
- DOE, *Handbook of Methods for the Analysis of the Various Parameters of the Carbon Dioxide System in Sea Water*; version 2, edited by A. G. Dickson and C. Goyet, ORNL/CDIAC-74, 1994
- Keeling, R. F., On the role of large bubbles in air-sea gas exchange and supersaturation in the ocean, *J. Mar. Res.*, 51, 237-271, 1993
- Liss, P., and L. Merlivat, Air-sea gas exchange rates, introduction and synthesis, In *The Role of Air-Sea Exchange in Geochemical Cycling*, edited by P. Buat-Menard, pp. 113-127, D. Reidel, Hingham, Massachusetts, 1986
- Memery, L., and L. Merlivat, Modeling of the gas flux through bubbles at the air-water interface, *Tellus*, 37B, 272-285, 1985
- Merlivat, L., L. Memery, and J. Boutin, Gas exchange at the air-sea interface. Present status: the case of CO₂, Paper 27, The Fourth International Conference on CO₂, Carqueiranne, France, September 13-17, 1993
- Monahan, E. C., and C. F. Monahan, The influence of fetch on whitecap coverage as deduced from the Alte Weser light-station observer's log, in *Ocean Whitecaps and Their Role in Air-Sea Exchange Processes*, edited by E. C. Monahan and G. MacNiocaill, pp. 275-277, D. Reidel, Hingham, Massachusetts, 275-277, 1986
- Monahan, E. C., and M. C. Spillane, The role of whitecaps in air-sea gas exchange, in *Gas Transfer at Water Surfaces*, edited by G. H. Jirka and W. Brutsaert, pp. 495-504, D. Reidel, Hingham, Massachusetts, 1984
- Press, W. H., B. P. Flannery, S. A. Teukolsky, and W. T. Vetterling, *Numerical Recipes in FORTRAN: The Art of Scientific Computing*, Second Edition, 963 pp., Cambridge University, New York, New York, 1992

- Reid, R. C., J. M. Prausnitz, and B. E. Poling, *The Properties of Gases and Liquids*, 4th ed., McGraw-Hill, New York, New York, 1987
- Wanninkhof, R., Relationship between wind speed and gas exchange over the ocean, *J. Geophys. Res.*, *97C*, 7373-7382, 1992
- Wanninkhof, R., J. R. Ledwell, and A. J. Watson, Analysis of sulfur hexafluoride in seawater, *J. Geophys. Res.*, *96C*, 8733-8740, 1991

The Influence of Bubbles on Air-Water Gas Exchange: Results from Gas Transfer Experiments during WABEX-93

*R. Wanninkhof*¹, *W. Asher*², and *E. C. Monahan*³

¹ NOAA/Atlantic Oceanographic and Meteorological Laboratory
Miami, FL 33149

² PNL/Marine Sciences Laboratory
Sequim, WA 98382

³ University of Connecticut, Marine Science Institute Groton, CT 06340

Abstract

Bubble mediated gas transfer velocities were determined in a fresh water surf pool during WABEX-93. Gas transfer of N₂O, CO₂, He, and SF₆ were measured under eight different mechanically generated breaking wave conditions. Contrary to gas transfer across an air-water interface, where the transfer is solely controlled by surface turbulence and the molecular diffusion coefficient of the gas, exchange through bubbles is also a function of the solubility of the gas, bubble size and bubble penetration depths. The relative rates of gas transfer through bubbles of N₂O, CO₂, He, and SF₆ for the experiment are compared with models developed by *Woolf* [1995] and *Keeling* [1993]. The model of Woolf shows reasonable agreement with the observed results while that of Keeling overpredicts the exchange of N₂O. The trend suggests that in the surf pool experiments the solubility dependence of the model of Keeling is too strong while that of Woolf is slightly too weak compared to the observations.

1 Introduction

Gas transfer under rough and windy conditions, when whitecaps are present, contributes disproportionately to the global flux of environmentally important gases such as carbon dioxide (CO₂), carbonyl sulfide (COS), and dimethyl sulfide (DMS). Field, laboratory, and theoretical studies have been performed to study bubble mediated exchange [*Atkinson*, 1973; *Asher et al.*, 1995b; *Broecker and Siems*, 1984; *Farmer et al.*, 1993; *Merlivat and Memery*, 1983; *Woolf*, 1995] but some important questions remain. Key pragmatic issues are how to parameterize gas exchange in presence of bubble plumes, what the absolute magnitude of gas transfer is, and how the relative rates of exchange of gases differ in presence of bubbles compared to exchange over an unbroken surface. This study, in which the exchange rates of helium (He), sulfur hexafluoride (SF₆), nitrous oxide (N₂O) are compared in a freshwater

surf pool, addresses the difference in relative exchange rates of gases with different physical properties.

Gas transfer across rough unbroken surfaces has been parameterized by *Jähne et al.* [1987]:

$$k = BSc^{-0.5}U_w^* \quad (1)$$

where B is a constant, Sc is the *Schmidt number* defined as the kinematic viscosity divided by the diffusion coefficient, and U_w^* is the (water) friction velocity. Laboratory and field studies have lent support to this parameterization [*Holmen and Liss*, 1984; *Jähne et al.*, 1984; *Upstill-Goddard et al.*, 1990; *Wanninkhof and Bliven*, 1991]. Gas transfer velocities over the ocean only have been determined for a select suite of gases (^{222}Rn , $^{14}\text{CO}_2$, and $\text{SF}_6/{}^3\text{He}$) but as long as (1) is applicable, k for a particular gas may be normalized to any other gas provided their Sc are known.

Bubble mediated exchange exhibits a different dependence on Sc , and the *solubility* of the gas becomes a factor with gases of lower solubility exhibiting a stronger enhancement [*Asher et al.*, 1995b; *Wolf*, 1995]. Bubble penetration depth, bubble size, surface cleanliness, gas composition in the bubble, and bubble rise time also influence bubble mediated gas exchange. Since all these parameters are seldom measured simultaneously under oceanic conditions, models of bubble mediated exchange contain many approximations and frequently use "universal" bubble spectra and bubble penetration depths.

Several models for *bubble mediated gas transfer* have been developed [*Keeling*, 1993; *Memery and Merlivat*, 1985; *Wolf*, 1995]. Transfer velocities using the bubble models of *Keeling* [1993] and *Wolf* [1995] are compared with experimental results of CO_2 , He, SF_6 , and N_2O exchange from the 1993 surf pool experiment (*WABEX-93*) [*Asher et al.*, 1995a]. The *WABEX-93* study was performed in a freshwater surf pool with bubble size spectra that differed from those in seawater. Because of this difference, the comparison of the surf pool results with the models is for characterization of the processes that are important for bubble mediated exchange rather than as an indication of the validity of a particular model. The model of *Keeling* [1993] was specifically developed for large bubbles ($>50 \mu\text{m}$) at small hydrostatic pressure in seawater. The model of *Wolf* [1995] applies to gas exchange over the ocean with a bubble spectrum characteristic of seawater rather than freshwater bubble plumes.

In the model of *Keeling* [1993] the gas transfer velocity for evasion from bubbles, k_b^{out} , is of the form:

$$k_b^{out} \sim \alpha^{-0.3}Sc^{-0.35} \quad (2)$$

where α is the Ostwald solubility.

Woolf [1995] created a model for oceanic whitecaps in which:

$$k = k_s + k_b \quad (3)$$

where k_s is gas transfer across the unbroken air-water interface ($\approx 2U_{10} Sc^{-0.5}$, where U_{10} is the wind speed at 10 m height) and k_b is the transfer due to bubbles parameterized as:

$$k_b = 2450W_b / \left[\alpha [1 + (14\alpha Sc^{-0.5})^{-0.833}]^{1.2} \right] \quad (4)$$

where W_b is the total or mature whitecap coverage. W_b is about ten times larger than the coverage of whitecaps that are actively entraining air (W_a) [Monahan and Lu, 1990]. W_a , and not W_b , was measured during WABEX-93 [Asher *et al.*, 1995a].

2 Methods

The details of the operation of the surf pool are given in Asher *et al.* [1995a]. Briefly, the *surf pool* was a 60 m by 20 m basin with a sloping bottom (Figure 1). Four pneumatically driven chambers at the deep end of the pool generated waves that propagated and broke as they neared the shallow end. Waves with a mean height before breaking of 0.3 m, 0.6 m, 0.9 m, and 1.2 m were generated. Two wave patterns were used; a roller pattern that was characteristic of plunging breaking waves; and a diamond pattern, that was characteristic of spilling breaking waves. The total volume of the pool was 1600 m³.

The gas transfer experiments were performed by supersaturating the water in the surf pool with *helium* (He), *sulfur hexafluoride* (SF₆), *nitrous oxide* (N₂O), and *carbon dioxide* (CO₂). Helium was added to the water by injecting approximately 500 moles into the deep end of the pool over a period of 4 hours. After the injection of He, 80 l of water saturated with N₂O and 0.3 l of water saturated with SF₆ were added to the pool. The partial pressure of CO₂ (pCO₂) of the water was raised to a level of approximately 2000 μ atm (500% saturation) by adding 12 l of 12-N hydrochloric acid to the pool. The pool was homogenized using its filtration system and by running the wave maker at its lowest setting (0.3 m wave height with diamond pattern) several times over a period of two hours. The filtration system was shut off 30 minutes before the start of each experiment.

Gas transfer velocities (k) for He, SF₆, N₂O in the surf pool were determined by measuring the concentration decrease with time at 13 locations, labeled with letters in Figure 1. Small sump pumps located approximately at mid-depth on the side supplied water to shore for sampling. Preliminary studies during the previous year did not show any significant depth dependence in concentrations. The gas transfer velocity (k) is defined in terms of concentration decrease as:

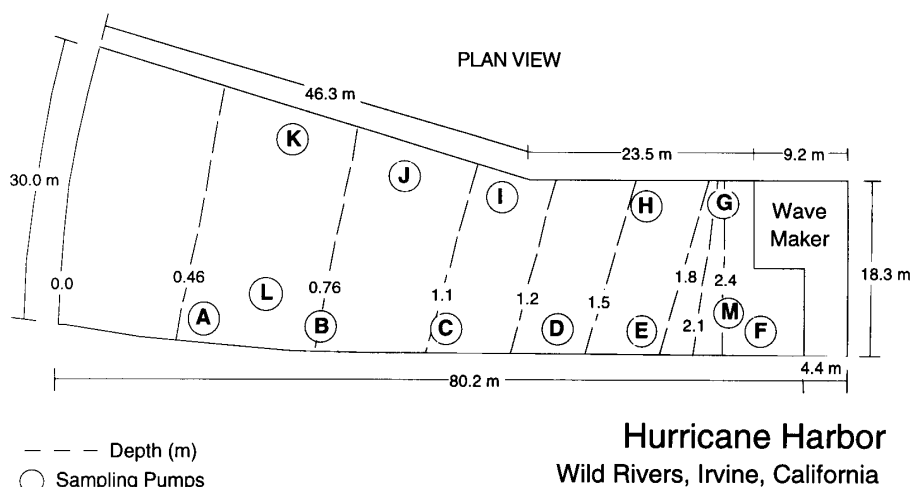


Figure 1: Plan view of the surf pool with dimensions and depths in m.

$$k = h \ln \left[(C_i - C_o) / (C_f - C_o) \right] dt^{-1} \quad (5)$$

where h is the average depth of the pool (≈ 0.84 m), dt is the time interval between sampling, and $(C_i - C_o) / (C_f - C_o)$ is the ratio of initial to final concentration over the time interval with the background concentration (C_o) subtracted. The background concentrations for He, SF₆, and N₂O were measured prior to injection of the gases. They were below detection limit for He and SF₆, and at saturation with ambient air for N₂O and CO₂. Four to eight samples were obtained at each location for each run and the k at each sampling point was obtained by a least squares linear regression of the right-hand side of (5) versus time.

The gas transfer velocity of CO₂ (k_{CO_2}) had to be determined in a different manner because the decrease in pCO_2 is buffered by the (bi)carbonate concentration in the water. k_{CO_2} was calculated according to:

$$k_{CO_2} = \frac{h dDIC/dt}{S(pCO_{2w} - pCO_{2a})} \quad (6)$$

where h is the depth of the water, $dDIC/dt$ is the change in water concentration of total dissolved inorganic carbon (DIC) over time, S is the solubility [$\text{mol L}^{-1} \text{atm}^{-1}$], and $pCO_{2w} - pCO_{2a}$ is the partial pressure difference of CO₂ in water and atmosphere.

In calculating the gas transfer velocities, it is assumed that mixing of water in the pool is significantly faster than gas transfer. Under this assumption, the whole pool has the same rate of concentration decrease with

Table 1: Summary of physical characteristics of gases used in experiment (@ 20 °C).

Gas	Mol. Weight (gr mol ⁻¹)	Ostwald Sol.	Diff. Coeff. (10 ⁻⁵ cm ² s ⁻¹)	Schmidt Number
He	2	0.0094	6.73	149
O ₂	32	0.033	1.89	529
CO ₂	44	0.942	1.67	599
N ₂ O	44	0.693	1.66	604
SF ₆	146	0.0066	1.05	958

time. For most runs, this was a good assumption as k for each sampling location was generally within 10% of the average of all 13 stations (see Figure 4, Asher *et al.*, 1995a). For experiments with high gas transfer velocities the pool showed concentration gradients that were in quasi-steady state. That is, the areas with rapid concentration decreases (shallow areas near locations of wave breaking), showed lower concentrations but the change in the natural log of concentration with time was similar to that of the deep area.

Thirty ml of water were drawn in 50-ml glass syringes and were subsequently equilibrated with 20 ml of N₂ for SF₆ analysis. The headspace was injected into a gas chromatograph equipped with an electron capture detector (ECD-GC) [Wanninkhof *et al.*, 1987]. Analytical precision based on replicates was 3%. Nitrous oxide samples were processed for analysis in a similar manner except that the equilibration occurred by shaking the syringe in a water bath at 20.0 °C. Nitrous oxide has a higher solubility than SF₆ (Table 1) and a significant fraction remains in the water phase during equilibration. The partitioning is a function of temperature necessitating good temperature control. The ECD-GC for N₂O was similar to the setup described in Butler *et al.* [1989]. Helium analyses were performed on an aliquot of the headspace remaining after SF₆ analysis using a gas chromatograph equipped with a thermal conductivity detector (TCD-GC). Detector response for each instrument was determined by running compressed gas standards with concentrations bracketing the samples. For each gas the response of the detector was linear for the concentration range in question.

For interpretation of the CO₂ results both the partial pressure and the DIC had to be measured. The pCO₂ was determined at two locations (L and M in Figure 1) by pumping water through an equilibrator at a rate of 10 l min⁻¹. The headspace attained the same concentration as the water phase with a response time (e-folding time) of 2 minutes [Wanninkhof and Thoning, 1993]. The headspace gas was sampled at three-minute intervals and the location from which the water was sampled (L or M , Figure 1) was changed every 10 to 20 minutes. 500-ml samples for DIC were drawn at every location while more frequent sampling was done from the sampling lines L and M connected to the equilibrator. DIC was analyzed by acidifying an aliquot of water and measuring the evolved CO₂ quantitatively using a

Table 2: Summary of results (A)

Date	Exp. #	Cond.	W_a	Location	He [cm hr ⁻¹]	
					k	s.d.
1 Nov	7-A	0.3m-Diamond	0	L	38.1	3.3
				M	28.8	0.0
				av.	37.0	5.7
2 Nov	8	0.3m-Diamond	0	L	44.9	1.5
				M	44.0	1.9
				av.	53.1	7.6
27 Oct	2-A	0.3m-Roller	0	L	37.9	2.3
				M	64.6	4.9
				av.	56.8	7.9
26 Oct	1	0.6m-Diamond	0.00716	L	89.6	5.4
				M	89.3	3.3
				av.	147.3	29.1
1 Nov	7-B	0.6m-Diamond	0.00716	L	160.0	8.9
				M	119.9	6.9
				av.	129.0	23.9
27 Oct	2-B	0.6m-Roller	0.02582	L	63.8	0.0
				M	92.3	0.0
				av.	156.2	55.7
4 Nov	10	0.6m-Roller	0.02582	L	130.2	14.8
				M	109.8	1.1
				av.	134.4	67.9
28 Oct	3	0.9m-Diamond	0.03127	L	215.3	5.4
				M	211.0	12.7
				av.	208.6	18.2
3 Nov	9	0.9m-Diamond	0.03127	L	230.3	10.0
				M	207.9	13.5
				av.	210.8	10.0
29 Oct	4	0.9m-Roller	0.04061	L	248.0	17.8
				M	350.7	10.3
				av.	358.5	47.8
30 Oct	5	1.2m-Diamond	0.03374	L	270.5	13.3
				M	245.2	13.1
				av.	301.2	40.5
31 Oct	6	1.2-Roller	0.06704	L	1036.7	101.1
				M	1118.6	22.2
				av.	809.1	89.3

Location= Location of sampling (see Figure 1); av. = average of all 13 sampling locations; k = gas transfer velocity; s.d.=standard deviation.

Table 3: Summary of results (B)

Date	Exp. #	SF6 [cm hr ⁻¹]		CO ₂	N ₂ O [cm hr ⁻¹]	
		<i>k</i>	s.d.	[cm hr ⁻¹] <i>k</i>	<i>k</i>	s.d.
1 Nov	7-A	18.9	0.9	no data	30.4	0.0
		8.9	0.7	no data	23.6	0.0
		19.1	1.4	—	21.5	2.3
2 Nov	8	28.3	0.5	20.8	27.3	0.2
		29.3	3.3	31.9	27.2	1.2
		24.9	2.5	26.3	26.7	1.2
27 Oct	2-A	26.3	2.8	52.8	37.7	3.8
		40.9	2.1	31.5	33.2	3.9
		31.0	4.6	42.2	28.6	9.6
26 Oct	1	60.3	5.4	26.7	66.9	8.9
		59.3	10.4	64.0	70.5	1.8
		77.4	15.0	45.4	76.2	8.9
1 Nov	7-B	68.1	1.2	no data	65.5	3.5
		65.6	0.7	no data	58.6	1.3
		49.5	9.8	—	61.9	3.1
27 Oct	2-B	113.7	5.0	66.1	69.3	6.1
		80.0	10.0	62.0	62.4	3.9
		94.8	12.1	64.1	64.9	6.8
4 Nov	10	89.7	2.4	86.6	77.4	3.7
		62.6	2.5	81.9	71.8	4.2
		78.7	23.7	84.2	69.8	6.6
28 Oct	3	108.0	17.7	100.4	103.8	2.3
		102.7	6.6	79.7	74.8	4.0
		120.6	12.6	90.1	96.5	10.3
3 Nov	9	99.4	1.1	121.3	109.4	4.2
		118.1	8.5	86.7	95.5	2.6
		111.0	6.4	104.0	101.0	6.2
29 Oct	4	182.1	23.4	137.2	142.1	5.9
		176.3	8.4	115.0	150.8	8.5
		183.7	15.3	126.1	141.7	10.0
30 Oct	5	133.4	3.6	78.7	122.4	1.3
		129.1	4.9	134.3	123.8	2.3
		149.1	12.1	106.5	124.1	3.1
31 Oct	6	388.7	48.5	188.3	226.5	6.5
		561.4	59.2	129.9	229.4	5.3
		354.5	22.4	159.1	229.7	7.7

Location= Location of sampling (see Figure 1); av. = average of all 13 sampling locations; *k*= gas transfer velocity; s.d.=standard deviation.

coulometer equipped with a Single Operator Multi-Parameter Metabolic Analyzer (SOMMA) [Johnson *et al.*, 1993]. Precision based on replicate DIC analyses of reference material was $2 \mu\text{mol}/\text{kg}$ or 0.2% of the DIC signal observed during the experiments. Since pCO_2 measurements were only performed at 2 locations, the CO_2 gas transfer velocities are discussed separately in comparison with the N_2O results at these locations.

The areal coverage of actively breaking waves, W_a was determined from gray scale analysis of video images of the pool surface for each wave condition [Asher *et al.*, 1995a]. Bubble spectra were obtained from a backlit underwater video microscope [Asher *et al.*, 1995a]. The nominal range of radii of bubbles that were measured using this system was from $30 \mu\text{m}$ to $2000 \mu\text{m}$. Only data from the 1.2-m wave height roller pattern at depths of 30 and 45 cm have been analyzed to date.

3 Results

The gas transfer velocities for each experiment averaged over all sampling stations are summarized in Tables 2 and 3. For most experiments the first sampling time was omitted because of large concentration variability throughout the pool. It is possible that this first sample at the start of an experiment was taken before steady state conditions were reached. Tables 2 and 3 also shows the k measured in the shallow end of the pool at location L , and the deep end of the pool at location M using an average depth for the entire pool (≈ 0.84 m). Differences in k observed for the two locations, that diminish with increasing wave size, suggest that mixing of water increased at a greater rate than the localized variability in the concentration caused by gas loss. Gas concentrations in experiments with diamond patterned waves showed less variation than for roller patterned waves because the diamond pattern was more uniform over the surface of the pool than the roller pattern. The standard deviation of k at a particular sampling site was determined by the standard error in the slope of $\ln(C)$ versus t . The standard deviation of the average k (av. in Tables 2 and 3) was obtained from the standard error from the average of the 13 sampling stations. No attempt was made to invoke a spatial or volumetric weighting scheme, or to propagate the error in k for each location. Whitecap coverage was significantly higher for the rolling waves and the coverage increased nearly linearly with intensity of wave making for the rollers. The diamond pattern showed a much lower whitecap coverage for the same energy input and leveled off between intensity 3 and 4.

4 Discussion

The effect of the bubble mediated gas flux on the Schmidt number exponent is illustrated by normalizing k for N_2O , He, and SF_6 to $Sc = 600$ assuming

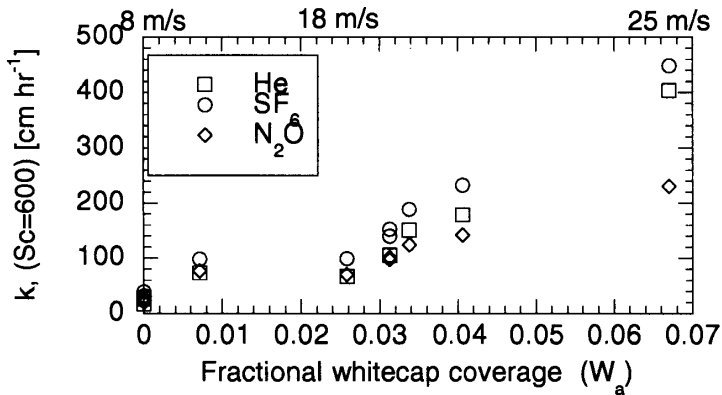


Figure 2: Gas transfer velocities normalized to $Sc = 600$ using $k \propto Sc^{-1/2}$.

k is proportional to $Sc^{-0.5}$. Figure 2 shows the normalized k values for the three gases plotted versus W_a . At the lowest wave height (0.3 m), when wave breaking was not significant, the Sc normalized k values for N_2O , He, and SF_6 converge.

With increasing whitecapping differences in the normalized values become large. The enhancement of gas transfer by bubbles is inversely related to solubility [Memery and Merlivat, 1985; Woolf, 1995]. SF_6 has the largest normalized gas transfer velocities because it has the smallest solubility; while N_2O , which has the highest solubility, shows the lowest normalized k . The normalized k_{SF_6} values show enhancement compared to He at fractional whitecap coverages less than 0.03 suggesting that small differences in solubility of the very insoluble gases He and SF_6 (see Table 1) have a large effect on their relative gas transfer velocities. Small anomalies in normalized SF_6 gas transfer velocities have in the past been attributed to uncertainties in the estimates of the diffusion coefficient. However, recent direct measurement of Sc by King and Saltzman [1995] yields the same value for SF_6 at 20 °C as the semi-empirical equation of Hayduk and Laudie [1974] used in this analysis. It is unlikely therefore that the behavior of k_{SF_6} at the lower W_a values is an artifact of the uncertainty of the Sc of SF_6 . Asher et al. [1995b] have indicated that the $Sc^{-1/2}$ dependence effectively breaks down at W_a values as low as 0.002. On the top axis of Figure 2 the equivalent wind speeds are given corresponding to the k of N_2O using the parameterization for steady winds of Wanninkhof [1992]: $U_{10} = (k_{600}/0.31)^{0.5}$. Thus, the gas transfer velocities measured in the surf pool were within environmental range anticipated for large storms.

The bubble size spectra for the experiments in the freshwater surf pool are different from those observed in seawater [Asher and Farley, 1995]. Figure 3 gives the bubble concentration for plunging breaking waves of 1.2 m height. The bubble spectrum for an experiment with seawater in a whitecap

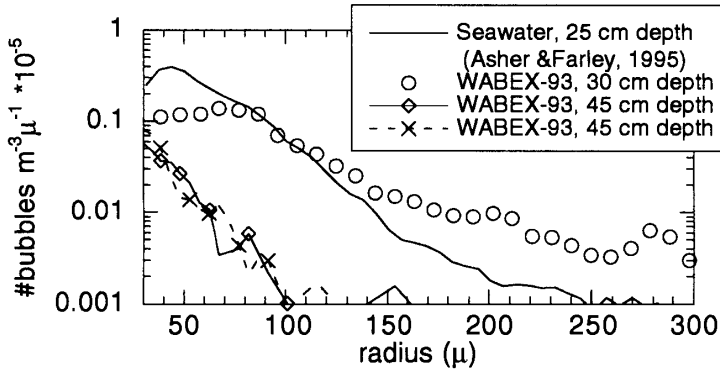


Figure 3: Bubble populations at different depths for a 1.2 m roller wave for WABEX-93 and for a seawater experiment in a WST normalized to $W_a = 0.0031$.

simulation tank (WST) is included for comparison.

Asher and Farley [1995] showed that the seawater bubble population in the WST is very similar to bubble populations measured in the ocean. The bubble concentrations in Figure 3 all have been normalized to a fractional whitecap coverage of 0.0031 assuming a linear relationship with whitecap coverage. The seawater data shows a peak in number of bubbles near a radius of 50 μm while the freshwater results show a broad maximum at 100 μm and a slower decrease in bubble concentrations with increasing bubble radius. Since the smaller bubbles contribute most to enhancement by the solubility effect, due to deeper penetration and complete dissolution, the freshwater surf pool results are likely to show a lower solubility dependence of bubble mediated gas exchange than seawater.

4.1 Comparison of Results with Models

Two models of air-sea gas flux due to bubbles have been developed recently by Keeling [1993] and Woolf [1995]. The model of Keeling [1993] has a parameterization unique for gas evasion from water with gas concentrations far from equilibrium with the atmosphere. The gas flux from bubbles is expressed by Keeling as:

$$F = (k_s + k_b^{out})S(P_g - P_l) + (k_b^{in} - k_b^{out})SP_g \quad (7)$$

where k_s is the gas transfer velocity over the air-sea interface; k_b^{out} is the water-to-air gas transfer velocity through bubbles; P_g and P_l are the partial pressures of the gas in air and water, respectively; S [$\text{mol l}^{-1} \text{atm}^{-1}$] is the solubility of the gas, and k_b^{in} is the air-to-water gas transfer velocity through bubbles. The equation collapses into transfer across the air-water interface

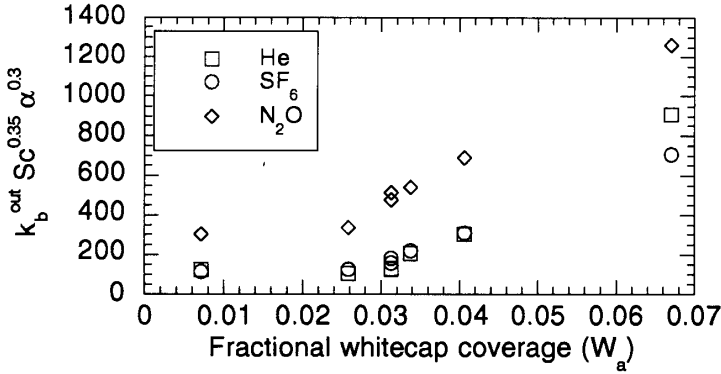


Figure 4: $k_b^{out} \alpha^{0.3} S_c^{0.35}$ for N_2O , SF_6 , and He .

when the bubble gas transfer velocities are set to zero. After making certain (simplifying) assumptions about bubble populations and bubble dynamics, Keeling suggests that k_b^{out} scales as $\alpha^{-0.3} S_c^{-0.35}$ where α is the Ostwald solubility ($\approx SRT$, where R is the ideal gas constant and T is temperature (in K)).

N_2O , SF_6 , and He levels in water were fifty to one hundred fold supersaturated. The result of this supersaturation is that the $(k_b^{in} - k_b^{out}) SP_g$ term in (7) is much smaller than the $(k_s + k_b^{out})S(P_g - P_l)$ term in (7) and can effectively be ignored for the experiments. For comparison of our data with (2) as proposed by Keeling [1993], the measured k has to be separated in k_b and k_s . k_s is calculated from the wave turbulence data according to Ogston et al. [1995]:

$$k_s = 2113\nu^{1/4} S_c^{-1/2} (\varepsilon_m^{1/4} + W_a^* (\varepsilon_t^{1/4} - \varepsilon_m^{1/4})) \quad (8)$$

where k_s is in $[cm \text{ hr}^{-1}]$, ν is kinematic viscosity, ε_m is dissipation rate of mechanically generated turbulence $[cm^{-2} s^{-3}]$, and ε_t is dissipation rate of whitecap-generated turbulence $[cm^{-2} s^{-3}]$. k_b^{out} is obtained by subtracting k_s from the observed k . The WABEX-93 results for N_2O , SF_6 , and He are normalized to: $k_b^{out} \alpha^{0.3} S_c^{0.35}$ for each gas, and plotted against fractional whitecap coverage in Figure 4.

If the model accurately predicted the k of N_2O , SF_6 , and He , all results of this scaling would converge to a single line. The normalized He and SF_6 values agree well with each other except for the highest whitecap coverage. This suggests that the Keeling model is reasonably robust for these gases. Normalized N_2O values fall above the normalized SF_6 and He values. The Schmidt number of N_2O lies in between that of SF_6 and He (Table 1) while the α is two orders of magnitude greater. The data suggests that the solubility dependence of the Keeling parameterization is too strong when used for the

surf pool data. This also explains why the He has a higher normalized k than SF₆ at high whitecap coverage. A possible explanation is that the model was developed for seawater with smaller bubble sizes.

In contrast to *Keeling and Woolf* [1995] parameterizes the net gas flux including bubbles as:

$$F = (k_s + k_b)S(P_g(1 + \Delta) - P_l) \quad (9)$$

where Δ is the equilibrium supersaturation caused by bubble mediated transfer. This parameterization avoids separate terms for gas transfer for invasion and evasion. Since $P_g \ll P_l$ for the WABEX-93 work, (7) and (9) reduce to the same expression: $F = (k_s + k_b)S(-P_l)$. However, the functional form for k_b for each model differs because of differing assumptions about how bubble dynamics, bubble size spectra, and depth of bubble penetration influence the gas flux. Woolf used the laboratory data of *Cipriano and Blanchard* [1981] and assumed that gas transfer occurred from clean bubbles rising through quiescent water. From these assumptions he derived the following relationship for k_b under oceanic conditions:

$$k_b = 2450W_b \left[\alpha [1 + (14\alpha Sc^{-0.5})^{-0.833}]^{1.2} \right]^{-1} \quad (10)$$

where W_b is the total whitecap coverage. Since k_b is scaled to W_b , an absolute comparison can be made between gas transfer velocities from WABEX-93 and the Woolf model, in addition to comparing relative rates, if the fractional whitecap coverage is converted from W_b to W_a measured in this study [*Asher et al.*, 1995a]. Although the W_a to W_b ratio varies depending on the parameterization (and wind speed), $W_b \approx 10W_a$ for active whitecapping [*Monahan and Lu*, 1990]. Substituting W_a for W_b in (10) and using the whitecap fractions from Table 2, k_b is calculated and compared with the observed values in Figure 5b. Figure 5a shows the gas transfer velocity scaled to:

$$\alpha [1 + (14\alpha Sc^{-0.5})^{-0.833}]^{1.2} \quad (11)$$

which is the same exercise as performed in Figure 4.

The trend is significantly different than that in Figure 4 with SF₆ rather than N₂O showing the largest normalized k . The normalized values for He, SF₆, and N₂O (Figure 5a) agree to within 20% even at the highest whitecap coverage suggesting that the parameterization with Sc and α is reasonably robust. The difference in absolute magnitude (Figure 5b) is attributed to differences in the surf pool environment compared to the ocean. The bubble spectra are different and the gas transfer in the surf pool is driven exclusively by breaking waves compared to the ocean where a significant fraction of gas exchange is driven by wind generated turbulence. The normalized values show better agreement than the normalization of Keeling despite that

the model of Woolf was constructed for oceanic conditions with different bubble spectra. However, if the solubility effect is greater for seawater than freshwater, (10) would underpredict the influence of the solubility effect on bubble mediated exchange in the ocean.

4.2 Comparison of N₂O and CO₂ Exchange

Nitrous oxide was used as a proxy for CO₂ in the WABEX-93 work since transfer of CO₂ could not be determined at every location. Although this appears warranted based on the similarity of *Sc* numbers and solubilities (Table 1), the analogy could break down by, for instance, the chemical enhancement of CO₂ gas exchange by reaction with water and hydroxide ions [Hoover and Berkshire, 1969; Smith, 1985]. The decrease of N₂O, pCO₂, and DIC with time was monitored at a shallow and deep site (locations *L* and *M*, respectively, in Figure 1) and gas transfer velocities at these sites were calculated using (5) and (6). The gas transfer velocities of N₂O and CO₂ at locations *L* and *M* are very similar (Figure 6).

A least-squares linear fit forced through the origin yields a relationship:

$$k_{N_2O}(\pm 26) = 1.14(\pm 0.06)k_{CO_2} \quad r^2 = 0.79 \quad (12)$$

where the standard errors are in parentheses. The slight enhancement of N₂O exchange could be caused by the 36% lower solubility of N₂O. Indeed, the model of Woolf predicts an 11%, and that of Keeling predicts a 9% enhancement of k_{bN_2O} based on the solubility difference. This is within the standard error of the comparison in (12). Thus, in the presence of bubbles N₂O exchange can be used as a reasonable proxy of CO₂ exchange if the (small) difference in solubility is taken into account.

5 Summary

The solubility dependence of gas exchange in presence of bubbles is apparent in the WABEX-93 surf pool study with low solubility gases (He and SF₆) showing a significantly stronger enhancement of their gas transfer velocities than N₂O which has a solubility that is two orders of magnitude higher (Table 1). The solubility dependence suggests that the smaller bubbles have a significant influence on gas transfer even in freshwater. Comparison of the relative rates of exchange with the gas transfer rates from the models of Keeling [1993], and Woolf [1995] show that the latter model has better agreement with the observations. This is surprising as the model was formulated for seawater while the model of Keeling emphasizes the influence of larger bubbles. The model of Woolf overpredicts the absolute magnitude of k_b but obvious differences between the ocean and the surf pool, and the conversion from active breaking (W_a) to total whitecap coverage (W_b) are

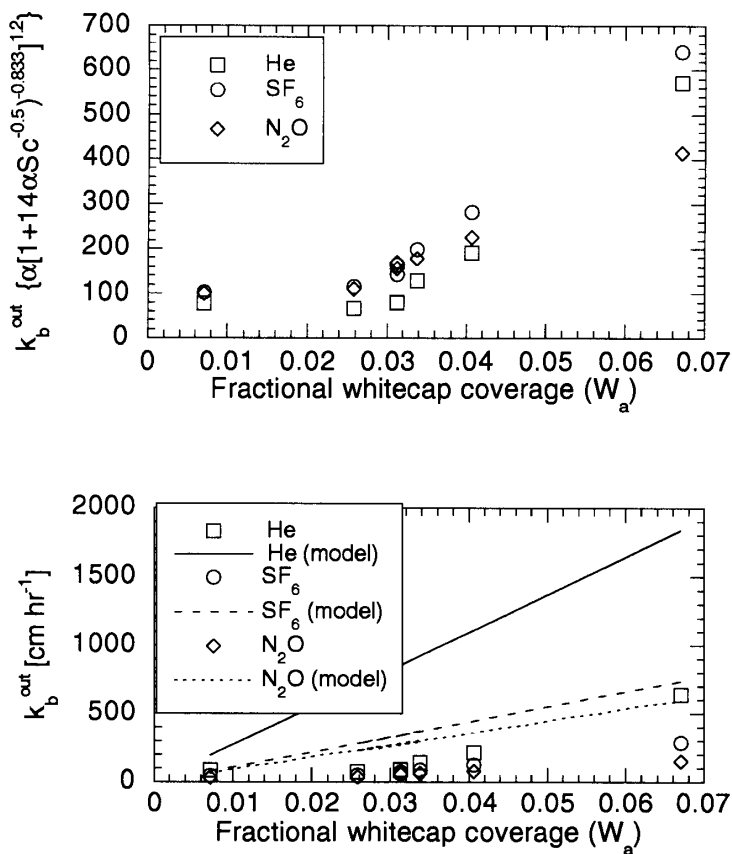


Figure 5: **a** $k_b^{out} \alpha [1 + (14\alpha S_c^{-0.5})^{-0.833}]^{1.2}$ for N_2O , SF_6 , and He; **b** k_b^{out} versus W_a . The solid lines are the Woolf model results and the symbols are the experimental results.

likely causes for the discrepancy. Comparison of N_2O and CO_2 exchange at two locations in the pool show good agreement suggesting that N_2O results are a reasonable proxy for CO_2 for the WABEX-93 work. The $14 \pm 6\%$ enhancement of N_2O exchange over CO_2 exchange can be largely explained by the lower solubility of N_2O .

Acknowledgements

The authors wish to thank Hua Chen, Paul Farley, Bruce Higgins, Lisa Karle, Tom Lantry, Matt Steckley, Qin Wang, and Martin Wilson for assistance during the WABEX-93 experiments. This research was supported by the U.S. Department of Energy (DOE), Office of Health and Environmental Research, Environmental Sciences Division under contract DE-AC06-76RLO 1830. Pa-

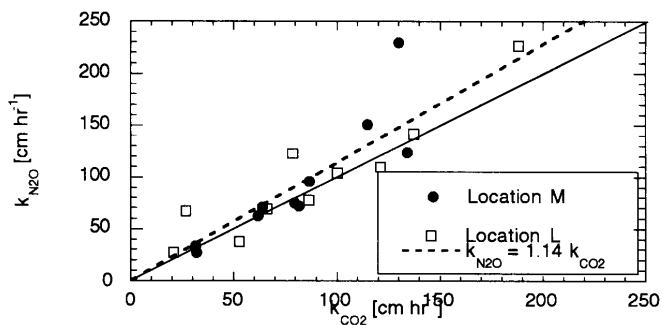


Figure 6: Gas transfer velocity of CO_2 compared to that of N_2O . The squares are the results for location M, and the circles are for location L. The least squares linear fit is the dashed line while the solid line is the 1:1 relationship.

cific Northwest Laboratory is operated for DOE by Battelle Memorial Institute. RW was supported by the NOAA Climate and Global Change program.

References

- Asher, W.E., and P.J. Farley, Phase-Doppler anemometer measurement of bubble concentrations in laboratory-simulated breaking waves, *J. Geophys. Res.*, 100, 7045-7056, 1995
- Asher, W., L. Karle, B. Higgins, P. Farley, C. Sherwood, W. Gardiner, R. Wanninkhof, H. Chen, T. Lantry, M. Steckley, E. Monahan, Q. Wang, and P. Smith, Measurement of gas transfer, whitecap coverage, and brightness temperature in a surf pool: An overview of WABEX-93, *This volume*, 1995a
- Asher, W.E., P.J. Farley, B.J. Higgins, L.M. Karle, E.C. Monahan, and I.S. Leifer, The influence of bubble plumes on air/seawater gas transfer velocities, *J. Geophys. Res.*, 1995b (submitted)
- Atkinson, L.P., Effect of air bubble solution on air-sea gas exchange, *J. Geophys. Res.*, 78, 962-968, 1973
- Broecker, H.C., and W. Siems, The role of bubbles for gas transfer from water to air at higher windspeeds; Experiments in the wind-wave facility in Hamburg, in *Gas Transfer at Water Surfaces*, edited by W. Brutsaert, and G.H. Jirka, pp. 229-238, Reidel, Hingham, Mass., 1984
- Butler, J.H., J.W. Elkins, and T.M. Thompson, Tropospheric and dissolved N_2O of the West Pacific and East Indian Oceans during the El Niño Southern Oscillation event of 1987, *J. Geophys. Res.*, 94, 14,865-14,877, 1989
- Cipriano, R.J., and D.C. Blanchard, Bubble and aerosol spectra produced by a laboratory "breaking wave", *J. Geophys. Res.*, 86, 8085-8092, 1981
- Farmer, D.M., C.L. McNeil, and B.D. Johnson, Evidence for the importance of bubbles increasing air-sea flux, *Nature*, 361, 620-623, 1993
- Hayduk, W., and H. Laudie, Prediction of diffusion coefficients for non-electrolytes in dilute aqueous solutions, *AIChE J.*, 20, 611-615, 1974

- Holmen, K., and P.S. Liss, Models for air-water gas transfer: An experimental investigation, *Tellus*, 36B, 92-100, 1984
- Hoover, T.E., and D.C. Berkshire, Effects of hydration in carbon dioxide exchange across an air-water interface, *J. Geophys. Res.*, 74, 456-464, 1969
- Jähne, B., W. Huber, A. Dutzi, T. Wais, and J. Ilmberger, Wind/wave-tunnel experiment on the Schmidt number - and wave field dependence of air/water gas exchange, in *Gas Transfer at Water Surfaces*, edited by W. Brutsaert, and G.H. Jirka, pp. 303-309, Reidel, Hingham, Mass., 1984
- Jähne, B., K.O. Münnich, R. Börsinger, A. Dutzi, W. Huber, and P. Libner, On parameters influencing air-water gas exchange, *J. Geophys. Res.*, 92, 1937-1949, 1987
- Johnson, K.M., K.D. Wills, D.B. Butler, W.K. Johnson, and C.S. Wong, Coulometric total carbon dioxide analysis for marine studies: maximizing the performance of an automated continuous gas extraction system and coulometric detector, *Mar. Chem.*, 44, 167-189, 1993
- Keeling, R.F., On the role of large bubbles in air-sea gas exchange and supersaturation in the ocean, *J. Mar. Res.*, 51, 237-271, 1993
- King, D.B., and E.S. Saltzman, Measurement of the diffusion coefficient of sulfur hexafluoride in water, *J. Geophys. Res.*, 100, 7083-7088, 1995
- Memery, L., and L. Merlivat, Modeling of gas flux through bubbles at the air-water interface, *Tellus*, 37B, 272-285, 1985
- Merlivat, L., and L. Memery, Gas exchange across an air-water interface: Experimental results and modeling of bubble contribution to transfer, *J. Geophys. Res.*, 88, 707-724, 1983
- Monahan, E.C., and M. Lu, Acoustically relevant bubble assemblages and their dependence on meteorological parameters, *IEEE J. of. Oceanic Eng.*, 15, 340-349, 1990
- Ogston, A.S., C.R. Sherwood, and W.E. Asher, Estimation of turbulence dissipation rates and gas transfer velocities in a surf pool: Analysis of results from WABEX-93, *This volume*
- Smith, S.V., Physical, chemical and biological characteristics of CO₂ gas flux across the air-water interface, *Plant, Cell and Environment*, 8, 387-398, 1985
- Upstill-Goddard, R.C., A.J. Watson, P.S. Liss, and M.I. Liddicoat, Gas transfer in lakes measured with SF₆, *Tellus*, 42B, 364-377, 1990
- Wanninkhof, R., J.R. Ledwell, W.S. Broecker, and M. Hamilton, Gas exchange on Mono Lake and Crowley Lake, California, *J. Geophys. Res.*, 92, 14,567-14,580, 1987
- Wanninkhof, R., and L. Bliven, Relationship between gas exchange, wind speed and radar backscatter in a large wind-wave tank, *J. Geophys. Res.*, 96, 2785-2796, 1991
- Wanninkhof, R., Relationship between gas exchange and wind speed over the ocean., *J. Geophys. Res.*, 97, 7373-7381, 1992
- Wanninkhof, R., and K. Thoning, Measurement of fugacity of CO₂ in surface water using continuous and discrete sampling methods, *Mar. Chem.*, 44, 189-205, 1993
- Wolf, D.K., Bubbles and their role in gas exchange, in *The Sea Surface Microlayer and Global Change*, edited by P.S. Liss, Cambridge U. Press, London, 1995 (in press)

Estimation of Turbulence-Dissipation Rates and Gas-Transfer Velocities in a Surf Pool: Analysis of the Results from WABEX-93

A. S. Ogston¹, C. R. Sherwood², and W. E. Asher²

¹School of Oceanography University of Washington
Seattle Washington 98195, U.S.A.

²Pacific Northwest Laboratory/Marine Sciences Laboratory
1529 W. Sequim Bay Road, Sequim Washington 98382, U.S.A.

Abstract

As part of the 1993 Wave Basin Experiment (WABEX-93), water velocities and gas fluxes were measured in a surf pool in Irvine, California, under plunging and spilling waves with heights up to 1.2 m. Vertical profiles of turbulence-dissipation rates were estimated from velocity measurements made with an Acoustic Doppler Velocimeter (ADV). The ADV measured three components of velocity at a sampling rate of 25 Hz. Turbulence-dissipation rates were estimated from the magnitude of the wavenumber spectra of vertical velocity using the universal form for the inertial subrange. Dissipation rates beneath unbroken waves were found to be low in magnitude and uniform in the vertical. Beneath broken waves, dissipation rates were found to be significantly higher in magnitude throughout the water column and to increase toward the water surface. Near-surface dissipation rates beneath breaking waves were found to follow an exponential dependence on whitecap coverage for all but one wave height condition. This suggests that whitecap coverage can be used to scale increases in dissipation rate for breaking waves. The gas transfer velocity due to turbulence generated by near-surface currents and nonbreaking waves, and the gas transfer velocity due to turbulence generated by breaking waves have been estimated from their respective dissipation rates. These transfer velocities have been used with the bubble-mediated transfer velocity to predict the total gas transfer velocity in the surf pool. Predicted gas transfer velocities agree well with measured gas transfer velocities.

1 Introduction

The flux of gases to or from bodies of water can be estimated as the product of the air-water concentration difference, ΔC , of a gas and its transfer velocity, k_L . Because of the difficulties associated with direct oceanic measurements of k_L , it is often calculated from parameterizations derived empirically from wind speed. High surface winds generate surface currents and breaking waves, which generate bubbles and affect mixing. As part of an experiment designed to help develop a method for estimating k_L at high

wind speed, gas fluxes and turbulence were measured in a large outdoor surf pool. A more complete description of the experiment and the gas-flux measurements can be found in *Asher et al.* [1995] and *Wanninkhof et al.* [1995].

Results from the gas-exchange measurements suggest that k_L can be partitioned into a component due to near-surface turbulence generated by currents and nonbreaking waves (k_M), one due to turbulence generated by breaking waves (k_T), and one due to bubble-mediated transfer (k_B). For gas evasion with ΔC much less than zero, k_L can be written in terms of the fractional area of whitecap coverage, W_C , as

$$k_L = (k_M + W_C(k_T - k_M)) + W_C k_B \quad (1)$$

Asher et al. [1995] showed that (1) could be applied to gas transfer measured in the surf pool using an explicit functional form for k_B developed using data collected in a whitecap simulation tank. Although (1) provided reasonable estimates of k_L in the surf pool, it was observed to systematically underpredict k_L when W_C was small. *Asher et al.* [1995] hypothesized that this discrepancy was caused by incorrectly parameterizing the dependence of k_M and k_T on W_C .

Equation 1 was derived by assuming that k_M and k_T were constant and not functions of W_C . Because k_M and k_T are determined by the vertical structure and intensity of the near-surface aqueous-phase turbulence, they are constant only if the turbulence in the surf pool is constant as W_C changes. However, it is reasonable to expect that the turbulence associated with breaking waves increases with wave height and that the background turbulence levels in the surf pool will increase with increasing wave energy. The present study confirms that the turbulence-dissipation rate increases with wave height. Furthermore, the increase in dissipation rate can be scaled using the whitecap coverage of the breaking waves, and inclusion of turbulence-dissipation rates in estimating k_M and k_T improves the ability of (1) to predict gas transfer velocities.

2 Experiment

As part of the 1993 Wave Basin Experiment (*WABEX-93*), estimates of turbulence-dissipation rates were made in the Hurricane Harbor *surf pool* at Wild Rivers Waterpark in Irvine, California, under breaking waves with heights up to 1.2 m (see *Asher et al.* [1995] for details of the surf pool and wave generation). The objective of the measurements described here was to obtain velocity profiles and pressure measurements at multiple locations in the surf pool with resolution sufficient to estimate profiles of turbulence-dissipation rate.

Turbulence-dissipation rates were estimated from velocity measurements made with a SonTek acoustic-*Doppler velocimeter* (*ADV*). The *ADV* measured

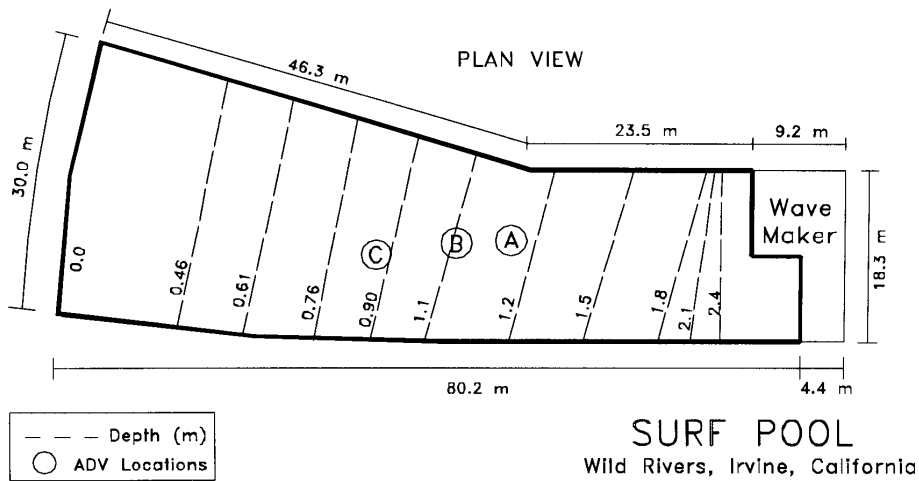


Figure 1: Plan view of the surf pool at Wild Rivers Waterpark in Irvine, California, showing the three ADV measurement locations.

three components of velocity in a 0.5-cm^3 sampling volume located 10 cm below the probe, minimizing the effect of the sensor on the flow field. Measurements were recorded at 25 Hz for runs lasting approximately 300 s (70-100 waves). Because the wave field was highly repeatable, profiles were made by compositing data from three to seven runs, each with the instrument mounted at the same horizontal location but at a different elevation. Profiles were obtained at three locations across the surf zone under spilling and plunging waves generated at four energy levels by the wavemaker, with nominal unbroken wave heights of 0.3, 0.6, 0.9 and 1.2 m. Figure 1 is a schematic drawing of Hurricane Harbor showing the three ADV measurement locations, denoted A, B, and C. Simultaneous measurements of pressure were made with a precision strain-gage located on the bottom directly beneath the ADV. When ADV measurements were made very close (<15 cm) to the bottom the pressure transducer was located ~ 30 cm to the side. Video images of the water surface were recorded and later used to determine wave type and breaker location.

3 Data Analysis

Flow beneath waves can be separated into three components: mean, periodic (wave), and fluctuating (turbulence) components. The objective of the data analysis was to quantify the turbulence component. Several approaches were considered. In laboratory studies with highly repeatable waves, all velocity deviations from the ensemble-mean wave velocity can be attributed to turbulence (Nadaoka et al. [1983]). Although waves in the surf pool

appeared quite regular, the detailed pressure measurements showed wave-to-wave variations in pressure. Irregularity in the wave field was most likely caused by the combined effects of variability in the wavemaker, seiching of the pool, reflected waves, and episodic outbreaks of a rip current. Estimates of turbulence based on deviations from the ensemble-mean velocity were precluded because they would overestimate turbulence by including non-turbulent, pressure-induced fluctuations. An alternative approach for extracting turbulence from velocity records involves the portion of the records associated with wave-induced variations of the water-surface (*Kitaigorodskii et al.* [1983], *Agrawal and Aubrey* [1992]). This frequency-domain method assumes that velocity variations that are coherent with pressure fluctuations are caused by two-dimensional progressive waves, and that noncoherent velocity fluctuations can be attributed to turbulence. However, the technique is prone to error if waves have directional spread (*Herbers and Guza* [1993]). We instead used the *inertial dissipation method* of *George et al.* [1994], modified to take advantage of the nearly regular wave field and the measurement capabilities of the ADV.

3.1 Data Processing

One advantage of the ADV was its ability to rapidly re-establish good velocity measurements after the loss of acoustic signals in bubble plumes or during subaerial exposure in the trough of a wave. Initial processing identified and rejected data from times when the ADV was exposed or large amounts of bubbles were present. A preliminary criterion for rejection was based on the correlation coefficient between the transmitted acoustic signal and the received backscattered signal. Data-rejection rates increased from near zero at depth to as much as 37% near the surface under larger waves. Acceptable data for 70 to 100 successive waves were phase aligned using the peak in the cross covariance of the slope of the pressure signal, and ensemble means and standard deviations for three velocity components and pressure were estimated (Figure 2). An iterative check on data was then performed: data were rejected if the velocity magnitude exceeded 3.7 standard deviations about the ensemble mean at each phase in the wave, and ensemble statistics were recalculated. Finally, mean and root-mean-square (RMS) velocities were determined for acceptable data from each data run.

3.2 Estimates of Dissipation Rates

In steady flow with isotropic, fully-developed turbulence, kinetic energy is transferred from the mean flow to large eddies, then to small eddies, and is finally dissipated by viscosity. Under these conditions, the turbulence-dissipation rate can be estimated by the magnitude of the wavenumber spectra in the inertial subrange, which takes the form:

$$E(\kappa) = \alpha \varepsilon^{2/3} \kappa^{-5/3} \quad (2)$$

where κ is wavenumber, $E(\kappa)$ is wavenumber spectral density, ε is the turbulence-dissipation rate, and α is the Kolmogorov constant. The inertial subrange extends from large eddies, the scales of which are typically determined by physical dimensions of the flow (e. g., depth) to the Kolmogorov microscale, which is determined by kinematic viscosity and dissipation rate.

Estimates of dissipation rate were made for the surf pool data using (2), and assume that the turbulence was fully developed and isotropic. The vertical component of the ADV velocity signal was used to calculate dissipation rates because it had the highest signal-to-noise ratio of the three components. Spectral estimates were obtained using a windowing and ensemble-averaging (Welch) method. Because data were removed during initial processing, the spectra for each windowed time series was computed using a method appropriate for irregularly spaced data (*Press et al.* [1992]). Entire data windows were omitted if more than 50% of the data points were missing. Spectral estimates were obtained by first detrending the data by subtracting out the ensemble-mean periodic (wave) velocity component, then computing spectra on a windowed data segment extending over three successive waves, and finally ensemble-averaging the spectra. Windowed segments were overlapped 67%. This procedure yielded spectral estimates with resolved bandwidths of 0.16 Hz and 156 degrees of freedom for typical time series containing 80 waves.

The time-series data at a fixed point were used to estimate the energy-density spectrum as a function of frequency, not wavenumber. The frequency spectra were converted to wavenumber spectra using Taylor's hypothesis of frozen turbulence, assuming that the time scale of turbulent fluctuations was long compared with the time scale of the motion advecting the eddy past the sampling point. The RMS orbital velocity was used as the advective velocity for the conversion from measured frequency spectra to wavenumber spectra (*Agrawal et al.* [1992]). An example of the wavenumber spectra generated from the vertical velocity data is shown in Figure 3.

Turbulence-dissipation rates (ε) were estimated from the magnitude of the wavenumber spectra in the inertial subrange using (2). For each data run, the wavenumber spectra were individually inspected and the magnitude of the spectra in the range over which the theoretical -5/3 slope was found was used to estimate the dissipation rate (typically between radian wavenumbers of 0.4 and 1.5 cm^{-1}).

4 Turbulence Dissipation Results

Profiles of ε beneath plunging waves are shown in Figures 4a and 4b, and beneath spilling waves in 4c. Elevation is normalized by the water depth,

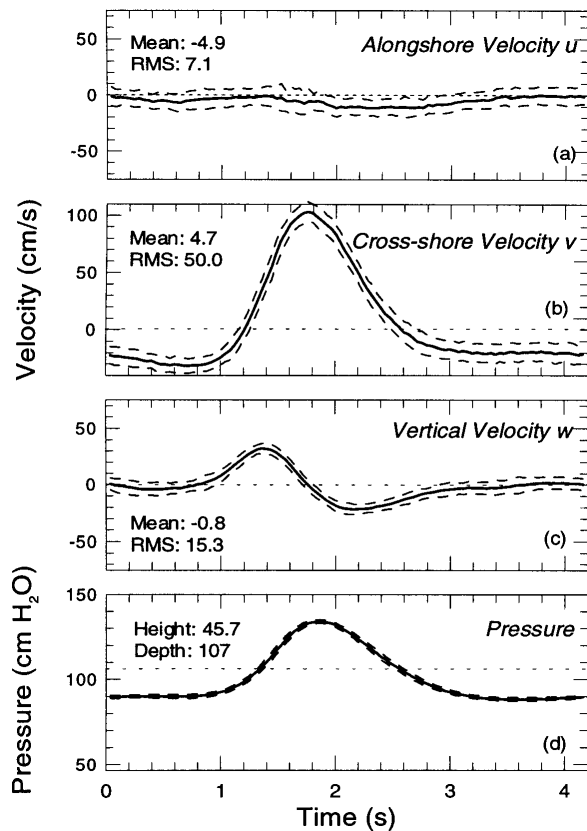


Figure 2: Ensemble-average velocities and pressure under plunging wave of nominal height 0.9 m at location A, 53 cmab: **a** Alongshore velocity. **b** Cross-shore velocity. **c** Vertical velocity. **d** Pressure.

so that a normalized elevation of 1.0 is at the mean water surface. Under unbroken waves, ε profiles were generally low in magnitude and vertically uniform. Beneath plunging waves measured at location A (Figure 4a), ε was highest near the surface and increased with increasing wave height. Dissipation rates were also seen to increase with increasing wave height throughout the water column.

Profiles of ε at location B (Figure 4b) are similar to profiles at location A (Figure 4a), although the mid-water column ε are higher at B, and there is at B little difference in ε between the 0.9-m and 1.2-m wave conditions. Strong rip currents at B could be responsible for the increase in the ε for the mid-water column compared with A. Alternatively, the increased distance from breaking (cross-shore location) at B could have allowed homogenization of turbulence through the water column. Similar values of ε for wave heights

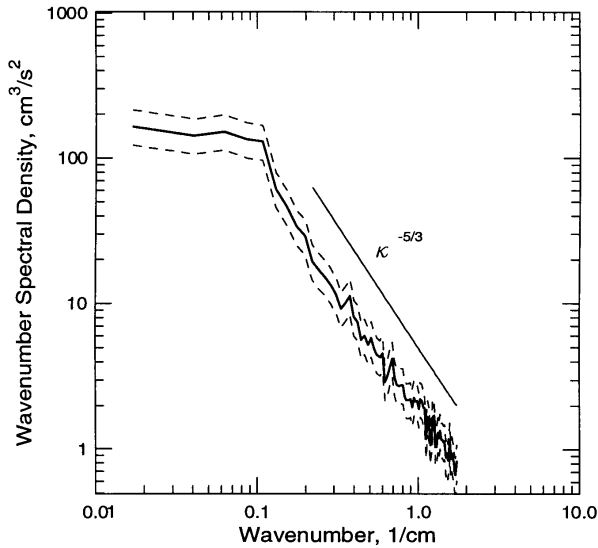


Figure 3: Representative wavenumber spectrum of vertical velocity showing inertial subrange ($\kappa^{-5/3}$ slope) under plunging wave of nominal height 0.9 m at location A, 53 cmab.

of 0.9 m and 1.2 m could indicate a saturation value for ε at some distance from the break point. At B, velocity measurements were made very close to the pool bottom, and observed increases in ε are likely associated with shear-induced turbulence in the bottom boundary layer (Figure 4b).

Beneath spilling waves at location C (Figure 4c), profiles of ε show more variation, possibly because spilling waves were less regular. Like ε measured beneath plunging waves at B, ε was high in the middle of the water column but, in contrast to measurements of ε at B, ε measured beneath spilling waves at C did not appear to reach saturation near the surface.

4.1 Characteristic Dissipation Rates

Dissipation rates from two depths were used to characterize turbulence generated by breaking waves (ε_T), and background mechanical turbulence generated by currents and nonbreaking waves (ε_M). The ε_T was taken to be the ε interpolated at a normalized elevation of 0.8 for the plunging waves, and 0.65 for the spilling waves (upper limit of measurements). These depths are consistent with the assumption that the dominant length scale for turbulence generated by wave breaking is proportional to the breaking wave amplitude. It was assumed that the characteristic ε_T and ε_M for gas exchange in the entire surf pool were less than ε_T and ε_M at location A and greater than ε_T and ε_M at location B beneath plunging waves, and that the characteristic

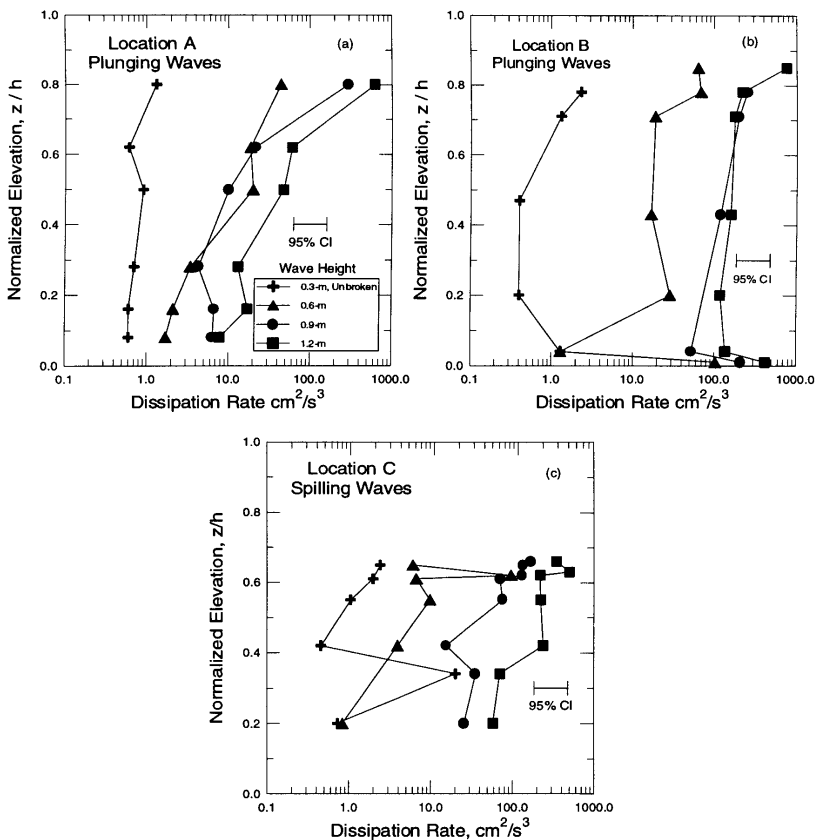


Figure 4: Vertical profiles of turbulence-dissipation rate, ϵ , beneath **a** plunging waves at location A, **b** plunging waves at location B, and **c** spilling waves at location C, of nominal waveheights 0.3, 0.6, 0.9, 1.2 m.

ϵ_T and ϵ_M were approximately equal to ϵ_T and ϵ_M at location C beneath the spilling waves. Values for ϵ_T are listed in Table 1 for the two wave types and four wave heights. The dissipation rate for turbulence generated by non-breaking waves and currents, ϵ_M , was determined at a normalized elevation of 0.2 (Table 1). This level was generally below the region of large gradients in the ϵ profiles. Turbulence generated in the bottom boundary layer was observed below this level (Figure 4b), but does not appear to influence ϵ above normalized elevations of 0.1.

4.2 Dissipation Rates and Whitecap Coverage

The area-weighted fractional coverage of actively breaking waves, W_C , was measured in the pool (Asher *et al.* [1995]), and values are listed in Table 1.

Table 1: Turbulence-dissipation rates and whitecap coverage

Wave Type	Nominal Height	ε_M (cm ² /s ³)	ε_T (cm ² /s ³)	W_C (%)
Plunging	1.2 m	75	499	7.15
Plunging	0.9 m	45	299	3.96
Plunging	0.6 m	2	66	2.01
Plunging	0.3 m	0.6	0.8	0.00
Spilling	1.2 m	65	428	2.90
Spilling	0.9 m	21	152	2.51
Spilling	0.6 m	5	6	0.54
Spilling	0.3 m	1	2	0.00

Figure 5 is a log-normal plot of ε_T versus W_C from the data in Table 1. ε for spilling waves at all four heights and ε_T for breaking waves with heights of 0.3 m, 0.6 m, and 0.9 m were found to follow the same exponential dependence on W_C . This suggests that W_C can be used to scale increases in ε_T caused by breaking waves. It is not clear why ε_T for the 1.2-m plunging breaking waves does not follow the same dependence as the other seven wave conditions, but it should be noted that these conditions presented the most difficult data-analysis problems, and many data points during the times of high velocities were eliminated. As a result, maximum dissipation rates could have been underestimated.

5 Parameterization of Gas Transfer Velocities

Lamont and Scott [1970] showed that for gas exchange across an unbroken water surface, k_L could be estimated using ε . Using their relation, k_M and k_T can be written as

$$k_X = BSc^{-1/2}(\varepsilon_X\nu)^{1/4} \quad (X = M, T) \quad (3)$$

where B is a dimensionless constant, Sc is the Schmidt number of the gas (equal to the ratio of kinematic viscosity to molecular diffusivity), ν is the kinematic viscosity of water, and ε_M and ε_T are the dissipation rates of the wave-current-generated turbulence and the breaking-generated turbulence, respectively. In support of (3), Asher and Pankow [1986] found that k_L for transfer of carbon dioxide (CO₂) through a cleaned water surface scaled linearly with $\varepsilon^{1/4}$. They also found that B was equal to 0.65.

Asher et al. [1995] measured k_L for CO₂, helium (He), nitrous oxide (N₂O), and sulfur hexafluoride (SF₆) as a function of W_C in the surf pool. They developed an empirical parameterization of k_L using (1) by assuming k_M and k_T were constant with increasing W_C and taking $k_B = b_1\alpha^{-0.043}Sc^{-0.35}$. As

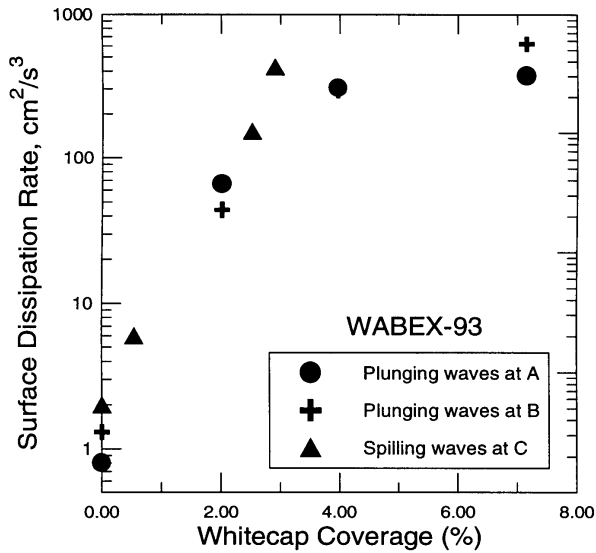


Figure 5: Whitecap coverage, W_C , versus surface turbulence-dissipation rate, ε_T , for plunging waves at locations A and B and spilling waves at location C.

can be seen in Figure 5 however, ε_M and ε_T were not constant with increasing W_C , and (3) shows k_M and k_T will also increase. Therefore, it is not surprising that *Asher et al.* [1995] found that parameterizing k_L using (1) and assuming that k_M and k_T were constant was unsatisfactory.

The dissipation rates listed in Table 1 were used to calculate k_M and k_T using (3) and assuming B would be a constant fit by the data. These transfer velocities were substituted into (1) to account for the effect of the increase in turbulence with increasing W_C . Written explicitly, k_L in the wave basin can be parameterized as

$$k_L = B(\varepsilon_M \nu)^{1/4} + W_C \left((\varepsilon_T \nu)^{1/4} - (\varepsilon_M \nu)^{1/4} \right) S_C^{1/2} + b_1 W_C \alpha^{-0.043} S_C^{-0.35} \quad (4)$$

The resulting model was then fit using least-squares linear regression to the measured k_L data from *Asher et al.* [1995] to determine the coefficients b_1 and B in (4). This fit results in $B = 0.58$ and $b_1 = 6.30 \text{ m s}^{-1}$ with a coefficient of determination of 0.84. The value of B found for the WABEX-93 data is in good agreement with that determined by *Asher and Pankow* [1986].

Figure 6 shows the result of fitting (4) to the surf pool data by plotting k_L for CO_2 , He, N_2O , and SF_6 calculated using (4) versus the experimentally determined value. There is excellent agreement between the calculated and measured k_L values. *Asher et al.* [1995] found a reduced chi-squared (χ^2) of

192 for the constant k_M and k_T parameterization. The χ^2 for the data in Figure 6 was 70, which shows that including the effects of increasing turbulence with increasing W_C improves the predictive accuracy of a parameterization based on (1).

The parameterization given in (4) can also be used to estimate the fraction of k_L that is due to turbulence and the fraction of k_L that results from bubble-mediated processes. For SF₆ for a 0.9-m spilling wave, turbulence processes accounted for 38% of the total transfer velocity and bubble processes were 62% of the total. In contrast, the turbulence fraction for CO₂ under the same conditions was 46% and the bubble fraction was 54%. The decreased importance of bubble-mediated transfer for CO₂ compared with SF₆ agrees with the model predictions of *Memery and Merlivat* [1985]. Their results indicated that k_B for a soluble gas such as CO₂ would be less than k_B for an insoluble gas like SF₆.

6 Conclusion

Turbulence dissipation rates were found to increase with increasing wave height for spilling and plunging waves. The surface dissipation rates scaled as an exponential function of whitecap coverage for spilling waves with nominal heights of 0.3 m, 0.6 m, 0.9 m, and 1.2 m and for plunging waves with nominal heights of 0.3 m, 0.6 m and 0.9 m. For reasons that are not clear at present, the surface dissipation rate for plunging waves with a height of 1.2 m did not follow this exponential scaling.

Asher et al. [1995] found that parameterizing k_L for CO₂, He, N₂O, and SF₆ assuming k_M and k_T were constants did not provide a satisfactory fit with the measured surf pool data ($\chi^2 = 192$). Substitution of the direct estimates of k_M and k_T from (3) and dissipation rates estimated from the surf pool measurements improved the agreement between measured and predicted k_L values ($\chi^2 = 70$).

In the surf pool, increases in W_C were caused by increases in height of the breaking wave. It could be expected that a similar process occurs under oceanic conditions, where increasing wind speed leads to larger wave size and higher whitecap coverage. The success of the approach described here suggests that successful application of (1) to ocean conditions will require knowledge of k_B and the dependence of k_M and k_T on wind speed. Although this complicates the parameterization of k_L in the ocean, it will provide an accurate estimation of the effect of the turbulence and bubbles generated by breaking waves on air-sea gas fluxes.

Acknowledgements

This research was supported by the U.S. Department of Energy (DOE), Office of Health and Environmental Research, Environmental Sciences Division under Contract DE-AC06-76RLO 1830. Pacific Northwest Laboratory (PNL) is

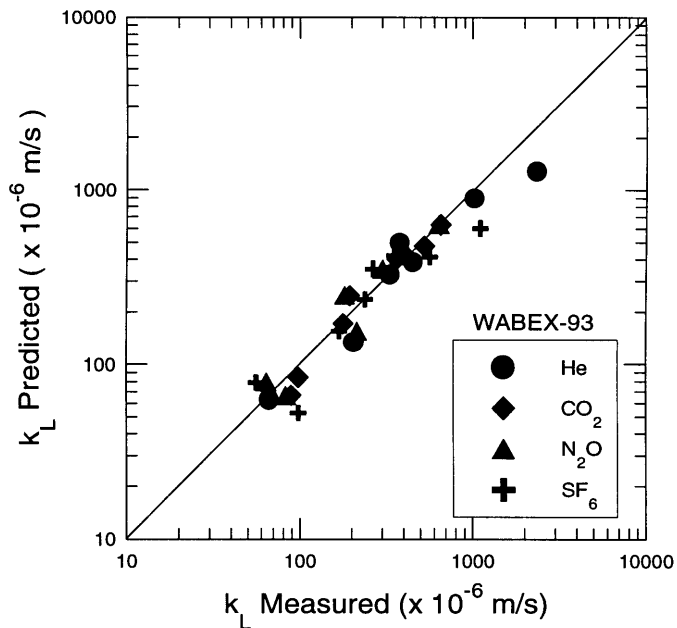


Figure 6: Measured versus predicted total gas transfer velocity, k_L , for He, CO₂, N₂O, and SF₆.

operated for DOE by Battelle Memorial Institute. We appreciate the assistance of Atle Lohrmann of SonTek, Inc., who provided an early model of the ADV. Andrea Ogston is a graduate fellow at PNL under the Associated Western Universities Northwest program and has also been supported by the Office of Naval Research.

References

- Agrawal, Y. C., and D. G. Aubrey, Velocity observations above a rippled bed using laser Doppler velocimetry, *J. Geophys. Res.*, 97, 20249-20259, 1992
- Agrawal, Y. C., E. A. Terray, M. A. Donelan, P. A. Hwang, A. J. W. III, W. M. Drennan, K. K. Kahma, and S. A. Kitaigorodskii, Enhanced dissipation of kinetic energy beneath surface waves, *Nature*, 359, 219-220, 1992
- Asher, W. E., and J. F. Pankow, The interaction of mechanically generated turbulence and interfacial films with a liquid phase controlled gas/liquid transport process, *Tellus*, 38B, 305-318, 1986
- Asher, W., L. Karle, B. Higgins, P. Farley, C. Sherwood, W. Gardiner, R. Wanninkhof, H. Chen, T. Lantry, M. Steckley, E. Monahan, Q. Wang, and P. Smith, Measurement of gas transfer, whitecap coverage, and brightness temperature in a surf pool: an overview of WABEX-93, *This volume*
- George, R., R. E. Flick, and R. T. Guza, Observations of turbulence in the surf zone, *J. Geophys. Res.*, 99, 801-810, 1994

- Herbers, T. H. C., and R. T. Guza, Comment on "Velocity observations above a rippled bed using laser doppler velocimetry" by Y. C. Agrawal and D. G. Aubrey, *J. Geophys. Res.*, *98*, 20331-20333, 1993
- Kitaigorodskii, S. A., M. A. Donelan, J. L. Lumley, and E. A. Terray, Wave-turbulence interactions in the upper ocean. Part II: Statistical characteristics of wave and turbulent components of the random velocity field in the marine surface layer, *J. Phys. Oceanogr.*, *13*, 1988-1999, 1983
- Lamont, J. C., and D. S. Scott, An eddy cell model of mass transfer into the surface of a turbulent liquid, *A.I.Ch.E.J.*, *16*, 513-519, 1970
- Memery, L., and L. Merlivat, Modeling of the gas flux through bubbles at the air-water interface, *Tellus*, *37B*, 272-285, 1985
- Nadaoka, K., M. Hino, and Y. Koyano, Structure of the turbulent flow field under breaking waves in the surf zone, *J. Fluid Mech.*, *204*, 359-387, 1989
- Press, W. H., S. A. Teukolsky, W. T. Vetterling, and B. P. Flannery, Numerical Recipes in FORTRAN: the Art of Scientific Computing, *Cambridge University Press*, New York, 963 pp., 1992
- Wanninkhof, R., W. E. Asher, and E. C. Monahan, The influence of bubbles on air-water gas exchange: Results from gas transfer experiments during WABEX-93, *This volume*

A Validation Study of Bubble Mediated Air-Sea Gas Transfer Modeling for Trace Gases

*Ira S. Leifer*¹, *William E. Asher*², and *Paul J. Farley*²

¹ School of Earth and Atmospheric Sciences
Georgia Institute of Technology, Atlanta, GA 30332

² Pacific Northwest Laboratory/Marine Sciences Laboratory
Sequim, WA 98382

Abstract

Laboratory results have demonstrated the importance of bubble plumes to air-water gas transfer [Asher *et al.* 1995]. Bubble plumes enhance gas transfer by directly transporting a gas and by creating turbulence. Models of bubble gas transfer have been developed by Atkinson [1973], Memery and Merlivat [1985], and Woolf and Thorpe [1991] to determine the gas flux due to bubbles. A new model has been developed here based upon principles and relations from the three earlier works. Using bubble distributions, ϕ , measured in a whitecap simulation tank (WST) by phase Doppler anemometry (PDA) this new model was used to estimate bubble driven gas transfer velocities. The predicted transfer velocities are then compared with transfer velocities directly measured in the WST.

The comparison has shown that the new model developed here underpredicts the measured gas transfer velocity by several orders of magnitude. However, the model correctly simulates the sign of the asymmetry between invasion and evasion for bubble mediated gas transfer. In addition, the model correctly predicts the time evolution of the number size spectrum of small bubbles in the WST. Initializing the model with photographically measured ϕ , rather than PDA measured ϕ , has shown that large bubbles ($r > 500 \mu\text{m}$) are primarily responsible for bubble gas transfer. Underprediction of the asymmetry for insoluble gases suggests small bubbles ($r < 50 \mu\text{m}$) may also be important.

1 Introduction

Oceanic whitecaps entrain air and generate bubble plumes through the breaking process. The bubbles in these plumes can be very efficient at transferring gas across the air-sea boundary. For bubble-mediated gas exchange, the air-sea gas transfer velocity, k_L , is a function of both molecular diffusivity and aqueous-phase solubility of the transferring gas. In contrast, for transfer across an unbroken surface, k_L is only a function of molecular diffusivity.

Understanding this change in the functionality of k_L is important due to the difficulty in making direct measurements of air-sea gas fluxes under oceanic conditions. In many cases, the flux of the species of interest cannot

be measured with a high enough precision to be useful in determining k_L . Therefore, the flux of a more easily measured reference gas is determined. Then, the k_L value of the primary gas is determined from the k_L for the reference gas based on an assumed dependence on molecular diffusivity.

Although this reference technique can be used successfully at low to intermediate wind speeds where the fractional area whitecap coverage is low, the presence of bubble-mediated transfer processes can change the functional dependence of k_L on diffusivity. Understanding the magnitude of the effect of bubbles on the functionality of k_L is therefore important in interrelating k_L measurements for different gases at high wind speeds. This functionality could be determined from numerical models of bubble-driven air-water gas transfer. However, none of the more sophisticated bubble gas transfer models have been verified by comparing the calculated fluxes with direct laboratory or field measurements.

In this paper, a model for calculating the bubble-driven gas flux of trace gases is used to estimate air-seawater fluxes of carbon dioxide (CO_2), dimethyl sulfide (DMS), helium (He), and sulfur hexafluoride (SF_6). The k_L values derived from these fluxes are then compared to k_L values measured in a whitecap simulation tank (WST). Initializing the bubble gas transfer model with bubble populations measured using a phase-Doppler anemometer (PDA) in the WST shows the model underpredicts the measured fluxes. If a bubble population is used in the model that has higher concentrations of large bubbles, there is reasonable agreement between the calculated and measured gas fluxes.

2 Bubble Mediated Gas Flux

The partial pressure of a trace gas, i , in a bubble with atmospheric mole fraction X_i is equal to its atmospheric partial pressure plus the added *hydrostatic pressure* and the excess pressure due to *surface tension* (i. e., the Laplace pressure). This is given by,

$$P_i = X_i \left(P_{atm} + \rho g z + \frac{2\sigma}{r} \right) \quad (1)$$

where P_i is the partial pressure of gas i , P_{atm} is the local atmospheric pressure, ρ is the density of water, g is the gravitational acceleration, z is the depth of the bubble, σ is the surface tension of water in contact with air, and r is the bubble radius. Inspection of (1) shows that increasing depth or decreasing radius will increase P_i . As will be shown below, the effect of surface tension and hydrostatics on P_i have interesting consequences in terms of the bubble gas flux.

When the partial pressure of a gas in the bubble is not in equilibrium with the aqueous gas concentration, the net change in the molar composition of a gas in the bubble is given by,

$$\frac{dn_i}{dt} = k_{Bub_i} 4\pi r^2 \{C_i - P_i/H_i\} \quad (2)$$

where n_i is the number of moles of the gas in the bubble, k_{Bub} is the individual bubble gas transfer velocity through the bubble-water interface, C_i is the aqueous concentration of the gas, and H_i is the Henry's Law constant. In similarity with k_L for gas transfer across an unbroken surface, k_{Bub} is a function of the molecular diffusivity of the gas, the size of the bubble, the flow field surrounding the bubble, and the presence of surfactants. The flow field around a bubble is a function of radius, r , so k_{Bub} is also a function of r . Here, k_{Bub} was estimated using the parameterization of Clift et al. [1978] Eqn. 5-26 for dirty bubbles behaving as rigid spheres at high Reynolds number, Eqn. 5-39 for clean bubbles behaving as fluid spheres at high Reynolds number, and Eqn. 3-52 for clean bubbles at low Reynolds number. In the case where $C_i < P_i/H_i$ (i. e., outflow of gas from the bubble), the increase in P_i will increase dn_i/dt . Conversely, if $C_i > P_i/H_i$ (i. e., inflow of gas to the bubble), the increase in P_i will reduce dn_i/dt . Because $C_i < P_i/H_i$ is the defining condition for invasion (i. e., net transfer of gas from the atmosphere to the ocean), and $C_i > P_i/H_i$ is the defining condition for evasion (i. e., net transfer of gas from the ocean to the atmosphere), the increase in P_i leads to an asymmetrical preference for invasion compared to evasion.

In the case of an air bubble, a significant outflow of both oxygen (O_2) and nitrogen (N_2) from the bubble will cause r to decrease. As shown by (1), this decrease in r will increase P , which will in turn increase the gas flux from the bubble (see [2]). The interaction between flux, r , and P creates a positive feedback loop for gas outflow that can cause bubbles to dissolve completely. Because of this dissolution process, and the increased bubble pressure from hydrostatic and Laplace contributions, there will be a slight supersaturation of the bulk water compared to the thermodynamic equilibrium condition of $C_i = P_i/H_i$. If the bubble-mediated gas flux is constant with time, this supersaturation will reach a dynamic equilibrium. At dynamic equilibrium the excess flux into the water due to bubble dissolution will be matched by the flux of gas into the atmosphere through the unbroken surface and through bubbles returning to the water surface.

When a bubble-mediated transfer process is in dynamic equilibrium with respect to N_2 and O_2 , the change in bubble radius due to changes in bubble composition are minimized. This is important because the effect of atmospheric gas flux upon trace gases is minimized, as is the effect of uncertainties in the parameterization of k_{Bub} . In addition, assuming dynamic equilibrium minimizes the sensitivity of the calculated trace-gas fluxes to the aqueous concentrations of N_2 and O_2 .

3 Description of the Model and a Simple Example

The model used to calculate the air-water gas flux due to bubbles was based on the models of *Memery and Merlivat* [1985], and *Woolf and Thorpe* [1991]. It solves the set of coupled differential equations that describe the bubble rise, the change in the bubble size due to changes in internal bubble composition, changes in the hydrostatic pressure, and the effect of the Laplace pressure. The model includes a random walk simulation of one-dimensional (vertical) turbulence advection of the bubbles. The differential equations were solved using a standard fourth-order Runge-Kutta routine.

The effects of turbulence on bubble advection were included in the model by assuming the bubbles are continually advected by eddies with a three-dimensional turbulence velocity scale Q_t in a randomly chosen direction. Horizontal advection is ignored, and the bubble velocity in the vertical direction is the vector sum of the bubble rise velocity and the vertical velocity component of a randomly chosen three-dimensional turbulence velocity. Because using discretized random velocities in the model produced numerical instabilities, the time series of the discretized velocities was smoothed by spline interpolation to ensure numerical stability. The method used to determine Q_t is discussed in Section 4.

The gas flux from a bubble is defined by (2) where the time evolution of P_i in (2) is described by the differential form of (1). Even though changes in r due to the gas flux have been minimized, it is still necessary to describe its time evolution due to changes in hydrostatic pressure and gas flux. This requires that a third differential equation for r as a function of time be solved simultaneously with dn/dt and dP_i/dt .

$$\frac{dr}{dt} = \left(\frac{dn}{dt} \frac{1}{k} + \rho g r \frac{dz}{dt} \right) / \left(3(1 - \rho g z) + \frac{4\sigma}{r} \right) \quad (3)$$

where dz/dt is the *bubble rise velocity*, and k is equal to

$$k = 4\pi r^3 / 3RT \quad (4)$$

where R is the universal gas constant, and T is the temperature. Bubble rise is the vector sum of the vertical turbulence velocity component and the rise velocity.

Figure 1 shows the time evolution of n_i in a 50- μm and a 1000- μm bubble rising from a depth of 0.5 m for CO_2 , He, and SF_6 at 20 °C. The results for a 50- μm bubble are shown in Figures 1a and 1b where Figure 1a is for net outflow of the three gases by the bubble and Figure 1b is for net inflow of the gases from the bubble. Figure 2 shows the results of identical calculations for a 1000- μm bubble rising to the surface. The results in both Figures 1 and 2 were obtained by setting $Q_t = 0$.

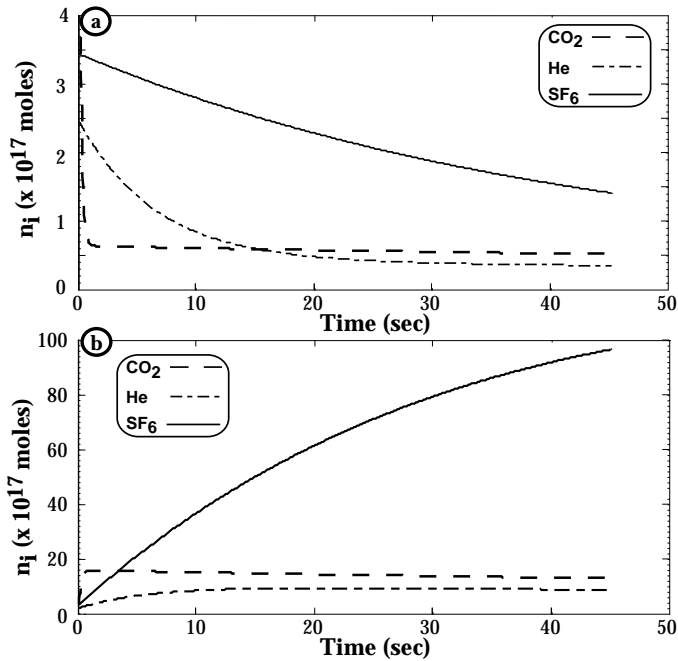


Figure 1: Time evolution of n_i for CO₂, He, and SF₆ in a 50- μ m bubble rising from $z = 0.5$ m. **a** $C_i < P_i/H_i$. **b** $C_i > P_i/H_i$. Data key on figure.

Comparison of the time to reach a steady state n_i for CO₂, He, and SF₆ in Figures 1a and 1b shows that the molar composition of a soluble gas in a small bubble reaches equilibrium much faster than an insoluble gas. In fact, Figure 1b shows that CO₂ equilibrates so rapidly that the outflow of N₂ and O₂ causes outflow of CO₂ after the initial rapid inflow of CO₂.

The results for a large bubble in Figures 2a and 2b show that although CO₂ equilibrated more rapidly than He and SF₆, none of the gases actually reach equilibrium. Comparison of the net total change in n_i for the three gases for a small and large bubble shows that large bubbles transfer far more gas than small bubbles.

The model was tested by calculating the total gas flux from a plume of monodisperse bubbles with $r = 50 \mu\text{m}$ for invasion ($C_i = P_i/5H_i$) and evasion ($C_i = 5P_i/H_i$) of CO₂, He, and SF₆ at 20 °C. These results were compared to identical calculations performed on a monodisperse plume of bubbles with $r = 1000 \mu\text{m}$. The total volume of bubbles in each plume was equal which meant that the plume of small bubbles contained approximately 570,000 bubbles. In contrast, the plume of large bubbles contained only 1,400 bubbles. In both cases the effect of turbulence advection was ignored. The entire plume in each case was formed at a depth of 0.5 m.

The change in C_i due to the bubble-mediated gas transfer was equal to,

Table 1: Normalized k_B and invasion/evasion asymmetry for large and small bubbles*

	k'_B evasion	k'_B invasion	asymmetry	k''_B evasion	k''_B invasion	asymmetry
CO ₂	0.266	0.274	3.01 %	0.003	0.013	450 %
SF ₆	0.311	0.321	3.22 %	0.039	1.490	3846 %
He	0.965	1.000	3.62 %	0.298	1.000	335 %

* $k'_B = 1000 \mu\text{m-plume}$ was 1400 bubbles,
 $k''_B = 50 \mu\text{m-plume}$ was 570,000 bubbles.

$$\Delta C_i = \frac{\Delta n_i}{V} \quad (5)$$

where ΔC_i is the change in C_i , Δn_i is the change in n_i and V is the total volume in the simulation. From ΔC_i , the overall transfer velocity due to the plume, k_B , can be estimated as,

$$k_B = \frac{h}{\Delta t} \ln \left(\frac{C_i(t_0) - P_i/H_i}{C_i(t) - P_i/H_i} \right) \quad (6)$$

where h is the water depth, Δt is the elapsed time ($\Delta t = t - t_0$), $C_i(t_0)$ is the concentration at t_0 , and $C_i(t)$ is equal to $C_i(t_0) + \Delta C_i$. Table 1 shows k_B for invasion and evasion for CO₂, He, SF₆ calculated from the bubble gas flux as described above. In Table 1, all k_B invasion and evasion values have been normalized to k_B for He invasion for 1000- μm and 50- μm bubbles. The asymmetry is listed as the per cent difference between invasion and evasion. Table 1 shows that k_B is smallest for the soluble gas CO₂; a result that agrees with the laboratory measurements of *Asher et al.* [1995]. Also, the asymmetry between evasion and invasion is much larger for the 50- μm bubbles than for the 1000- μm bubbles. This is caused by the larger Laplace pressure term for the smaller bubbles, and their greater time submerged. Furthermore, the 50- μm bubbles have a much larger surface area-to-volume ratio than the 1000- μm bubbles. As a result P_i for each gas in the smaller bubbles equilibrate much faster than P_i in the larger bubbles, causing the asymmetry to increase for less soluble gases.

4 Bubble Population and Turbulence Measurements

The bubble populations used were measured by *Asher and Farley* [1995] in a *whitecap simulation tank* (WST) using a phase-Doppler anemometer (PDA). The WST generated reproducible bubble plumes using a tipping bucket. The

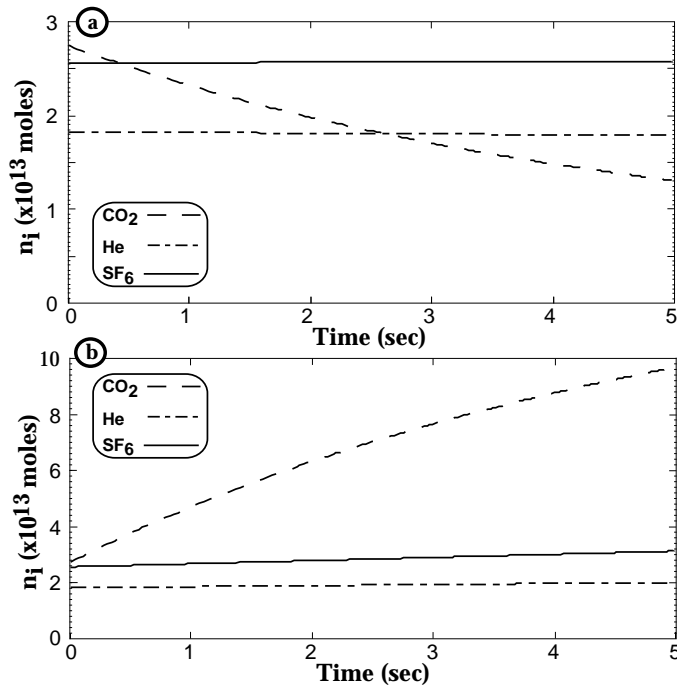


Figure 2: Time evolution of n_i for CO_2 , He, and SF_6 in a bubble rising from $z = 0.5$ m. **a** $r = 1000 \mu\text{m}$ and $C_i < P_i/H_i$. **b** $r = 1000 \mu\text{m}$ and $C_i > P_i/H_i$. Data key is on figure.

PDA is a technique based on well-known laser Doppler anemometric methods. A complete description of the WST, the PDA, their operating characteristics, and the calculation method for estimating bubble concentrations can be found in Asher and Farley [1995]. The bubble measurements can be made with very good spatial resolution, allowing *bubble concentrations* in the plume to be mapped as a function of depth and lateral position. The bubble measurements reported here were all taken under conditions of dynamic equilibrium with respect to N_2 and O_2 . This minimized changes in bubble size caused by dissolution or growth (see Section 3).

The PDA provides an estimate of the size-segregated bubble spectrum and the vertical and one horizontal component of the bubble velocities in the WST. The raw PDA data consists of a series of bubble radii and velocities measured as a function of time after the initial generation of the plume. By combining the time series from at least 50 sequential bubble plumes, an average distribution of the bubble concentration as a function of t , r , and depth, z at one lateral position can be calculated. This distribution will be denoted $\phi(t, r, z)$ and has units of number of bubbles per cubic meter per micrometer increment of r . The bubble gas flux model requires the

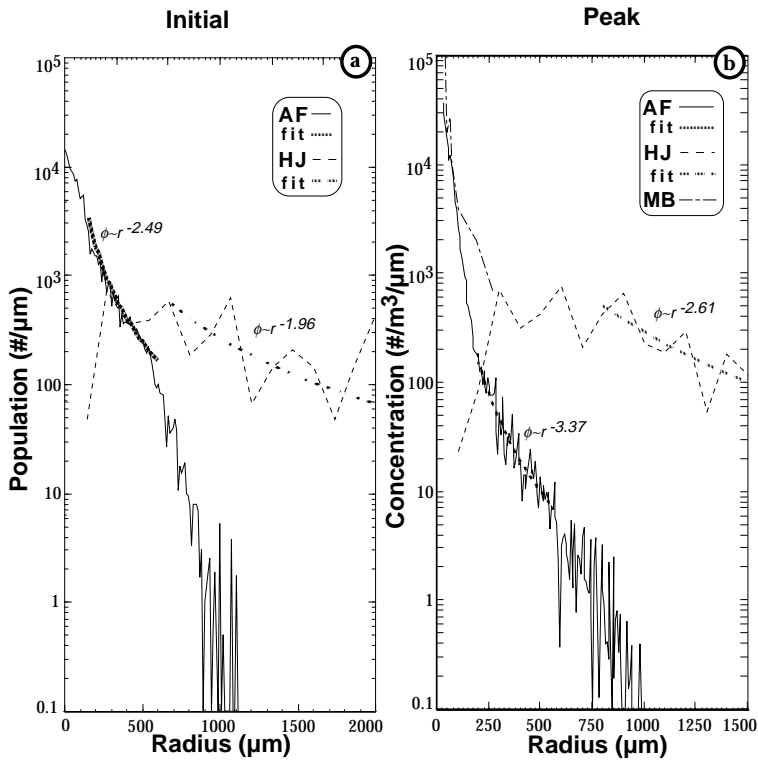


Figure 3: Initial and peak bubble plume concentrations. **a** The initial bubble concentration at $z = 0.25$ m from the data of Asher and Farley [1995] (AF) and Haines and Johnson [1995] (HJ). **b** Peak, time-averaged plume concentration at $z = 0.25$ m for AF, HJ, and the data of Medwin and Breitz [1989] (MB). Data key is on figure.

initial distribution of bubbles in the plume as one of its input variables. This distribution, $\phi_o(r, z)$, is defined as $\phi(t, r, z)$ at the instant the plume is generated. Unfortunately, the high bubble densities in the interior of the plume prevented measurement of $\phi(t, r, z)$ at $t = 0$. The maximum value of $\phi(t, r, z)$ was found for $t = 2.375$ s and this value was assumed equal to the true $\phi_o(r, z)$. Although it is likely this assumption underestimated $\phi_o(r, z)$ both near the surface and for very large bubbles ($r > 500\mu\text{m}$), measurements of $\phi(t, r, z)$ at depths near the maximum penetration of the plume (approximately at $z = 0.30$ m) showed $\phi(t, r, z)$ remained constant during the generation phase of the plume for $t < 2.375$ s. Extrapolation to the surface, to small radii and for large bubbles at the initial time is a good first estimate of these regimes.

Because for homogeneous (i. e., well mixed) aqueous phase gas concentration gas transfer is only dependent upon vertical position, and independent of horizontal position, the need to track horizontal bubble motions was elim-

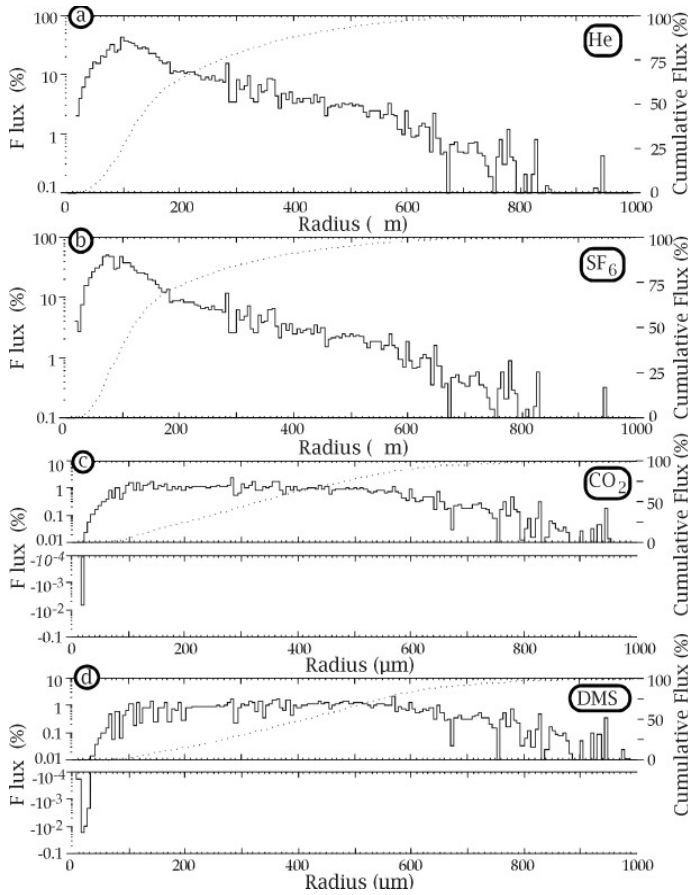


Figure 4: Time and depth-averaged, normalized percent trace gas flux (left hand side axis), and percent cumulative flux (dotted line, right hand side axis) showing the relative importance of different radius sizes. **a** He; **b** SF₆; **c** CO₂; and **d** DMS. Positive flux is bubble outflow corresponding to k_B invasion. Trace gas flux is for k_B evasion. **c** and **d** include a lower panel for bubble outflow due to small bubble dissolution.

inated. This assumption also increased the precision of the $\phi_o(r, z)$ because PDA measurements at different lateral plume locations could be averaged together. Thus the laterally summed $\phi_o(r, z)$ is the total bubble population in the plume, and has units of bubbles per increment of r .

Although the PDA provided very good measurements of $\phi_o(r, z)$ for $z > 0.1$ m, shallower depths could not be measured because surface waves in the WST interfered with the laser beams. Therefore, $\phi_o(r, z)$ for $z < 0.1$ m was estimated by extrapolating the measured $\phi_o(r, z)$ for $0.1 \text{ m} < z < 0.35 \text{ m}$ to shallower depths using a linear least squares regression of the $\log(\phi_o(r, z))$ with respect to z at each r . Figure 3a shows $\phi_o(r, z)$ integrated over z to

give the total water column bubble population, $\phi_o(r)$.

Figure 3a shows $\phi_o(r, z)$ for $z = 0.25$ m from the measurements of *Asher and Farley* [1995] (referred to hereafter as AF). Also shown for comparison in Figure 3 are the measurements of oceanic bubble concentrations made by *Medwin and Breitz* [1989] (referred to hereafter as MB) and the bubble data from the tipping-bucket whitecap apparatus used by *Haines and Johnson* [1995] (referred to hereafter as HJ). The HJ data has been scaled to the AF plume. There is good agreement between the MB and AF data. However, the concentration of large bubbles in the HJ data set is several orders of magnitude larger than the AF and MB data.

The HJ bucket was approximately twice as large (50 liter versus 20 liter), tipped from approximately twice as high (0.7 m versus 0.3 m) and three times less frequently (90 s versus 30 s). The HJ data was scaled by assuming $\phi(t, r)$ scales as the energy of the plunging mass of water, and the inverse of the tipping rate. Thus $\phi(t, r, z)$ was scaled by 0.057 while $\phi_o(r, z)$ was scaled by 0.17. In addition, $\phi_o(r, z)$ was scaled to the total volume of the AF plume based upon the HJ- $\phi_o(r, z)$ concentration.

The $\phi(t, r)$ can be described by $\phi(t, r)\alpha r^{-s}$ where s is the power law exponent. Observations show that s increases with t from of approximately $s = 2$ to $s > 7$ at 9 s, with $s = 3.37$ in the average plume for $r < 550\text{-}\mu\text{m}$ bubbles. The low HJ- $\phi_o(r, z)$ value of s is partially due to the early time of the initial plume, although the $s = 2.6$ of the average HJ- $\phi(r, z)$ may be due to measuring in the formation zone [*Haines and Johnson*, 1995].

The difference between the AF and HJ data may be due to scaling differences between the data sets; different measurement techniques; different initial plume times (i. e., the HJ- $\phi(t, r, z)$ was at $t = 1.7$ s versus 2.5 s for the AF- $\phi(t, r, z)$); or different turbulence.

Attempts were made to estimate Q_t in the WST from the PDA data records. However, after high pass filtering out the large wave orbital velocities the accuracy of the turbulence velocities was severely degraded. Therefore, Q_t was estimated using the bubble advection calculations from the model. Because the evolution of $\phi(t, r, z)$ with respect to t is a function of Q_t , comparison of the predicted $\phi(t, r, z)$ at different t with the experimentally-observed $\phi(t, r, z)$ at the same t will show the Q_t used in the advection calculations is reasonable. The model was run for Q_t values ranging from 0 cm/s to 10 cm/s. This showed that for steady state turbulence, using $Q_t = 3$ cm/s was reasonable.

5 Gas Fluxes in the Whitecap Tank

The model described in Section 3 was used to calculate air-seawater fluxes of trace amounts of CO_2 , DMS, He, and SF_6 in the whitecap simulation tank using $\phi_o(r, z)$ measured using the PDA (See Section 4). The model calculated the net gas inflow or outflow from each bubble as it rose to the surface from its initial depth and was advected in the vertical direction by turbulence.

Table 2: Physical-chemical constants for the gases in Figure 4 and the importance of different radii bubbles to dirty bubble gas transfer.

	α	Sc	$Sc^{0.67}/\alpha$	$r(25\%)$ μm	$r(75\%)$ μm	Δr μm
SF ₆	0.0043	1066	24,838	80	220	140
He	0.0076	165	4026	100	280	180
CO ₂	0.746	666	104.5	200	500	300
DMS	14.1	918	6.9	250	570	320

The concentration change in the WST was calculated from the individual gas fluxes by

$$\Delta C_i = \frac{1}{V} \int_r \int_z \phi_0(r, z) * \Delta n(t, r, z) dr dz \quad (7)$$

where V is the volume of the WST and $\Delta n(t, r, z)$ is the change in the number of moles of the gas in a bubble with radius r at depth z and time t . As defined in Section 3 for a monodisperse plume, k_B for the plume can be calculated using (6). In the presence of turbulence, a minimum of four bubble plumes were simulated to increase the precision of the estimate of k_B .

The normalized gas flux integrated over the depth and life of the plume as a function of r , for evasion of CO₂, DMS, He, and SF₆ is shown in Figure 4. Also shown in Figure 4 is the per cent cumulative flux as a function of r . In Figure 4, a positive flux denotes bubble gas inflow, which corresponds to net evasion from the bulk water. Because the normalized invasion flux of a trace gas is indistinguishable from evasion on the scale shown in the figure, normalized fluxes for invasion are not shown.

The relative importance of different radii to bubble gas transfer is shown in Table 2. Also shown in table 2 is the Ostwald solubility, α , Schmidt number, a quantity proportional to the equilibration time, Sc^n/α , the radius of the first $r(25\%)$ and third $r(75\%)$ quartile of trace gas flux, the middle two quartile radius width, Δr . For a clean bubble, $n = 0.5$, while for a dirty bubble, $n = 0.67$.

The model calculations show that the flux due to bubbles with $r > 500 \mu\text{m}$ accounts for less than 10 percent of the total flux for soluble (CO₂, DMS) and insoluble (He, SF₆) trace gases. For soluble gases, small bubbles are less important than for insoluble gases. However, Δr and $r(25\%)$ for SF₆ is less than that for He despite the lower solubility of He, indicating the greater importance of smaller bubbles. Both $r(25\%)$ in conjunction with Δr indicate the relative importance of different bubble sizes. Thus, the importance of small and large bubbles is better determined by $Sc^{0.67}/\alpha$ than α alone. When $dr/dt = 0$, Woolf and Thorpe [1991] have shown that the equilibration time, τ_{eq} , is equal to

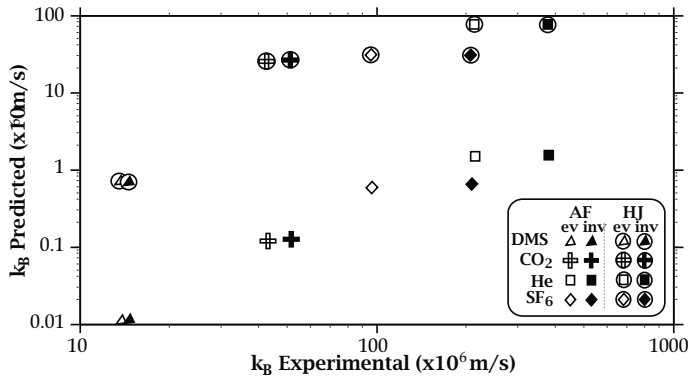


Figure 5: Comparison of the experimental k_B values for CO_2 , DMS, He, and SF_6 in the WST with k_B values predicted by the model using both the AF bubble data and the HJ bubble data. Data key is on the figure.

$$\tau_{eq} = r(\alpha k_{Bub})^{-1} \quad (8)$$

where k_{Bub} is proportional to $Sc^{-0.5}$ for clean bubbles and $Sc^{-0.67}$ for dirty bubbles. Gases with large τ_{eq} are more efficiently transferred by small bubbles that are submerged longer. Gases with small τ_{eq} are more efficiently transferred by larger bubbles. Slowly equilibrating gases are more efficiently transferred by small bubbles which are submerged longer, and more numerous with larger surface area. Rapidly equilibrating gases are more efficiently transferred by larger bubbles that have greater total volume despite being submerged for shorter time periods. For very small bubbles, ($r < 50 \mu\text{m}$) dissolution becomes important, as can be seen in Figures 4c and 4d by the negative flux for DMS and CO_2 . Thus the constant radius assumption used in the derivation of (6) is inappropriate for bubbles that dissolve ($r < 50 \mu\text{m}$).

Because smaller bubbles exhibit a greater invasion/evasion asymmetry (Table 1) the model predicts an increased invasion/evasion asymmetry for slower equilibrating gases. This is in agreement with the observations of Asher *et al.* [1995].

The fluxes calculated from the model were used to derive k_B for evasion and invasion of CO_2 , DMS, He, and SF_6 . These were compared to k_B values derived from gas exchange measurements in the WST. Asher *et al.* [1995] have shown that k_B in the WST for CO_2 , DMS, He, and SF_6 for evasion can be estimated from,

$$k_B = B_c \left(\frac{a_1}{\alpha} + b_1 \alpha^{-m} Sc^{-n'} \right) \quad (9)$$

where B_c is the fractional area coverage of the bubble plumes responsible for the gas exchange, and a_1 , b_1 , m and n' are constants determined using

Table 3: Parameters for (9) from WST for evasion and invasion.

	a_1 (m/sec)	b_1 (m/sec)	m	n'
invasion	1.03×10^{-4}	0.017	0.374	0.183
evasion	1.02×10^{-4}	0.029	0.41	0.24

a nonlinear optimization procedure by Asher *et al.* [1995] and are functions of the flux direction. Table 3 lists a_1 , b_1 , m , and n' for evasion and invasion in the WST [Asher *et al.*, 1995].

The k_B values calculated using the fluxes from the bubble-mediated model and (6) and (7) are shown in Figure 5 plotted against the k_B values for the WST calculated using (9) for CO₂, DMS, He, and SF₆. The model-derived k_B estimates are approximately two orders of magnitude less than the experimentally determined k_B for all four gases for both invasion and evasion. One possible explanation for the low k_B values calculated by the model is that the k_{Bub} parameterization from Clift *et al.* [1978] gives k_{Bub} values that are too low. However, increasing k_{Bub} to a level necessary to match k_B values leads to unrealistically rapid bubble dissolution. Two alternative explanations for the underestimation of k_B values in the WST by the model are that the transfer velocities in the WST were not measured at dynamic equilibrium or that the total plume population of large bubbles was underestimated by the PDA. However, modeling runs performed with difference values for the total gas tension showed that the effect of gas tension on k_B is too small to account for the underprediction.

The sensitivity of the model to total gas tension was examined by calculating the fluxes of CO₂, He, and SF₆ for total gas tensions of 10% above and below dynamic equilibrium. The calculations showed that this range in gas tension resulted in a 7%, 3.7% and .08% change in the SF₆, He and CO₂ fluxes, respectively.

This leaves underestimation of the concentration of large bubbles as the most likely cause of underprediction of k_B in the WST by the bubble-flux model. This was tested by using the bubble concentrations measured in a tipping bucket bubble plume by Haines and Johnson [1995] to estimate $\phi_o(r, z)$. Haines and Johnson used a photographic system to measure bubble concentrations, and as shown in Figure 3, they measured far more bubbles with $r > 500\mu\text{m}$ than were measured by Asher and Farley [1995]. Bubble gas fluxes were calculated for evasion and invasion of CO₂, He, and SF₆ using $\phi_o(r, z)$ estimated from the HJ data set. The HJ bubbles were assumed clean. These were used to calculate k_B in the WST as described above. Figure 5 also shows these k_B values plotted versus experimental k_B estimated using (9). Using the HJ- $\phi(r, z)$ significantly improved the agreement between k_B calculated using the bubble-flux model and k_B estimated from Asher *et al.* [1995].

The invasion/evasion asymmetry observed by Asher *et al.* [1995] in the

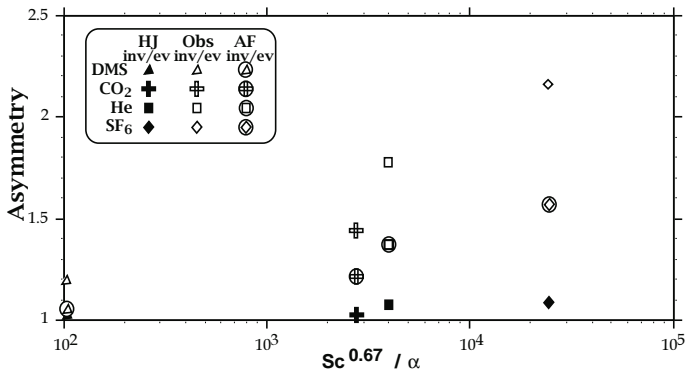


Figure 6: $k_B(\text{Inv.})/k_B(\text{Evas.})$ for CO_2 , DMS, He, and SF_6 from the WST experimental data and model predicted results plotted versus $Sc^{0.67}/\alpha$. Both results from the AF and HJ data sets are shown. Data key on figure.

data from the WST is also seen in the k_B values calculated by the model with the PDA bubble data. Figure 6 shows the ratio of k_B for invasion to k_B for evasion plotted versus $Sc^{0.67}/\alpha$ values listed in Table 2. Also shown in Figure 6 are the invasion/evasion asymmetries resulting from k_B values calculated using (9) and the parameters in Table 3 plotted versus $Sc^{0.67}/\alpha$.

The bubble model correctly predicts the decrease in the asymmetry with increasing $Sc^{0.67}/\alpha$. However, the model underpredicts the magnitude of the observed asymmetry. Furthermore, using the bubble concentrations measured by *Haines and Johnson* [1995] to estimate k_B further reduces the magnitude of the asymmetry.

6 Conclusions

The bubble gas transfer model reasonably simulates the time evolution of the bubble concentrations observed in the WST. However, using the bubble concentrations measured in the WST by *Asher and Farley* [1995], the model underpredicts the observed overall bubble-mediated gas transfer velocities by two orders of magnitude. Bubble gas transfer velocities calculated using bubble concentrations measured by *Haines and Johnson* [1995] for similar tipping-bucket bubble plumes improves the agreement between the model predictions and the experimental data. However, using the *Haines and Johnson* [1995] bubble data, with its larger relative fraction of bubbles with radii greater than $500 \mu\text{m}$, results in a lower invasion/evasion asymmetry than observed experimentally. Because this asymmetry is caused primarily by small bubbles, it is possible that small bubbles are under-represented in the *Haines and Johnson* data.

Acknowledgements

This research was supported by the U.S. Department of Energy (DOE) under contract DE-AC06-76RLO 1830. Pacific Northwest Laboratory is operated for DOE by Battelle.

References

- Asher, W. E., L. M. Karle, B. J. Higgins, P. J. Farley, E. C. Monahan, and I. S. Leifer, The influence of bubble plumes on air-seawater gas transfer velocities, submitted to *J. Geophys. Res.*, 1995
- Asher, W. E., and P. J. Farley, Phase-Doppler anemometer measurement of bubble concentrations in laboratory-simulated breaking waves, *J. Geophys. Res.*, 100C, 7045-7056, 1995
- Clift R., J. R. Grace, and M. E. Weber, *Bubbles, Drops and Particles*, Academic Press, New York, New York, pp. 380, 1978
- Haines, M. A., and B. D. Johnson, Injected bubble populations in seawater and fresh water measured by a photographic method, *J. Geophys. Res.*, 100C, 7057-7068, 1995
- Medwin, H., and N. D. Breitz, Ambient and transient bubble spectral densities in quiescent seas and under spilling breakers, *J. Geophys. Res.*, 94C, 12,571-12,759, 1989
- Memery, L., and L. Merlivat, Modeling of the gas flux through bubbles at the air-water interface, *Tellus*, 37B, 272-285, 1985
- Wanninkhof, R., Relationship between wind speed and gas exchange over the ocean, *J. Geophys. Res.*, 97C, 7373-7382, 1992
- Woolf, D. K., and S. A. Thorpe, Bubbles and the air-sea exchange of gases in near saturation conditions, *J. Mar. Res.*, 49, 435-466, 1991

Field Measurements of Air Entrainment by Breaking Waves

W. K. Melville, E. Terrill, and L. Ding

Scripps Institution of Oceanography
University of California, San Diego, La Jolla, CA 92093-0213

Abstract

We report on the use of acoustic techniques to measure the void fraction and bubble size distribution in the surface layers of the ocean. During the winter of 1993–94 a sound speed profiling buoy was moored in the North Atlantic for a period of three months. Low-frequency sound speed data is inverted to give volume fraction of air (or void fraction) in the first seven metres below the surface. This data demonstrates that the void fraction field is intermittent and marked by injection events associated with breaking waves. A simple inversion of broad-band sound speed and attenuation data from a separate experiment is shown to give credible measurements of bubble size distribution near the surface.

1 Introduction

Breaking waves entrain air at the ocean surface. The entrained air breaks up into bubbles which may contribute to air-sea gas transfer. Models of bubble-mediated gas transfer depend on reliable estimates of the initial bubble size distribution, turbulent transport, bubble break-up and dissolution. At this time such models are highly speculative since they involve many untested assumptions and hypotheses which together are compared with sparse data sets from the field. Laboratory studies of air-water gas transfer are useful for process-oriented studies but do not fully model the complexity of the air-sea interface with its wide range of scales of fluid dynamic, thermodynamic and chemical phenomena. While more complete information on the evolution of the bubble size distribution in the surface layers of the ocean is our goal, the less ambitious goal of measuring the volume of entrained air (or void fraction) is also worthy of pursuit. Measurements of void fraction impose an integral constraint on the measurements of bubble size distribution and can also be used to infer other features of the surface layer relevant to air-sea gas transfer. In this paper we present our preliminary attempts to measure void fraction and bubble size distributions in the ocean surface layer.

The void fraction in the surface layer depends on the incidence of breaking which in turn depends on the evolution of the wind-generated waves and swell. At present we do not have a good model for the incidence of breaking and current research is still concerned with correlating breaking statistics

with wind and wave variables. This implies that a similar approach is needed for the measurement of the bubbly layer. It follows that long time series of measurements will be needed to obtain reliable statistical correlations between void fraction, bubble size distributions and the other environmental variables. Shorter process-oriented studies will also prove important, but ultimately there is a need to make measurement over weeks and months, not minutes and hours. Given these constraints we believe that at present acoustical rather than optical techniques are more suited to long-term ocean deployments.

The sound speed and attenuation in a bubbly mixture is a function of the size distribution of the bubbles and the acoustic frequency. At sufficiently low acoustic frequencies, below the resonant frequency of the largest bubbles, the sound speed is non-dispersive and just a function of the void fraction. This relationship between void fraction α and low-frequency sound speed is known as Wood's equation [Wood, 1941]. Thus measurements of low frequency sound can be used to infer the void fraction. Measurements of sound speed and attenuation at higher frequencies can be inverted to give the bubble size distribution.

This paper reports on measurements of void fraction made from a moored buoy in the North Atlantic during the winter of 1993–94. We also describe the application of a technique for the inversion of broad-band sound speed and attenuation data to give the bubble size distribution.

2 The Experiments

2.1 Void Fraction

During the winter of 1993–94, a *spar buoy* was moored in approximately 5 km water depth during the *ASREX experiment* in the North Atlantic between Woods Hole and Bermuda. The spar extended to a depth of 7 m along which seven acoustic source/receiver pairs with horizontal acoustic path lengths in the range 0.5–1 m were spaced at depths extending from 0.7–6.9 m. The sources transmitted pulses centered at a fixed frequency of 3, 5 or 10 kHz at a 2 Hz repetition rate continuously for 40 minutes of every 90 minutes. Cycling through the three frequencies gave 40 minutes of data at each frequency every 4.5 hours. Following *Lamarre & Melville* [1994], correlation techniques were used to process the received pulse to give sound speed. The processed data were stored on a hard disk. In addition to the sound speed modules the spar was equipped with three temperature and conductivity modules, to provide calibration data for the calculation of bubble-free sound speeds during quiet periods between storms. The buoy was powered by solar panels and batteries, and summary data were recovered by transmissions via Argos satellites during the course of the experiment. After seven weeks of continuous operation the buoy suffered a power failure and no further data was collected.

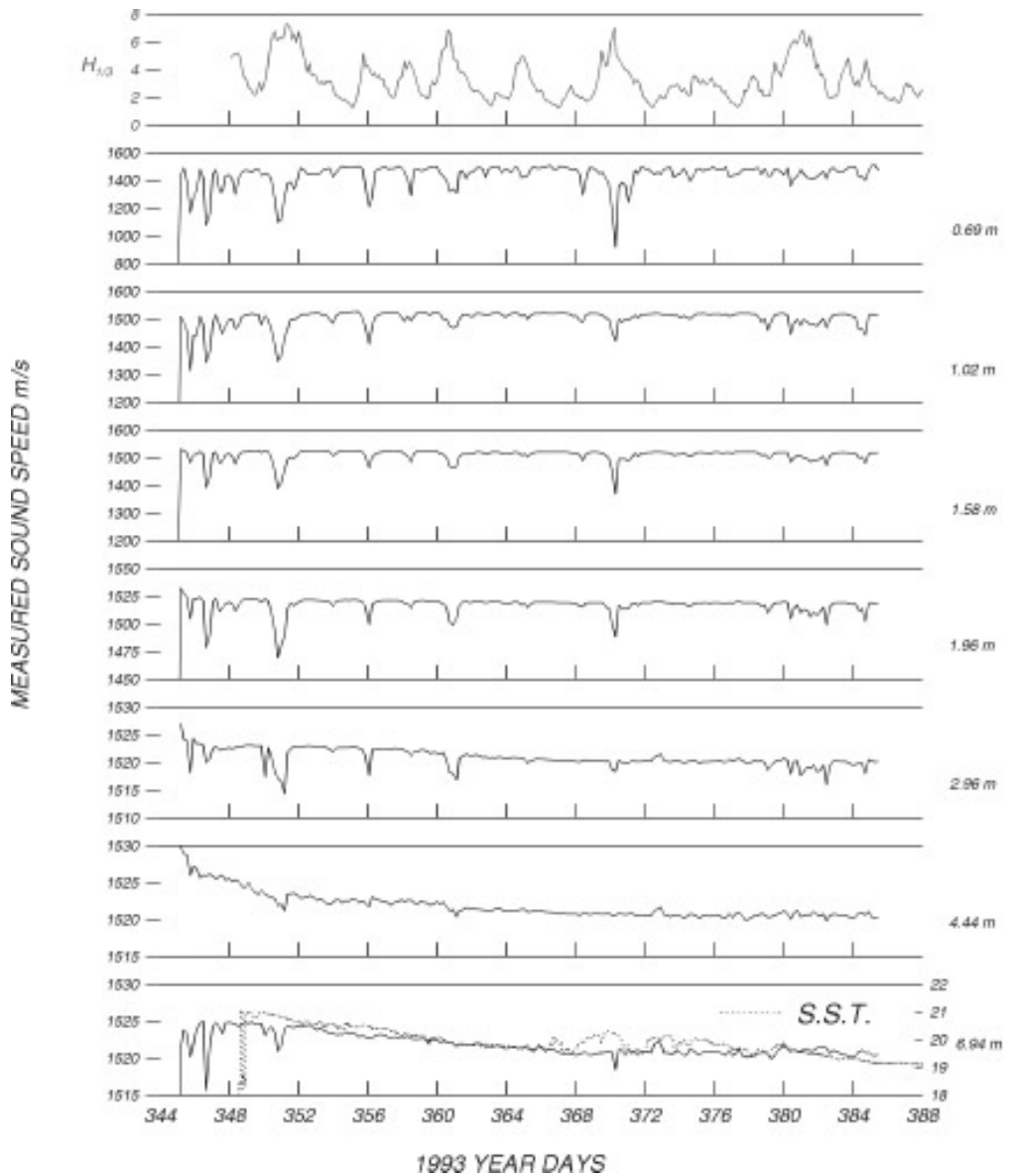


Figure 1: Time series of 40 minute averages of sound speed (3 kHz) at various depths, along with significant wave height and SST. Note that the influence of the storms on the averaged data is limited to the first few metres. By 7 m the average sound speed is dominated by secular changes associated with temperature. Note the vertical scale varies with depth.

2.2 Bubble Size Distribution

The data which are inverted to give *bubble size distributions* have been reported earlier [Lamarre & Melville, 1994]. They are broad band measurements of sound speed and attenuation at frequencies in the range 6–40 kHz taken at a depth of approximately 0.5 m off the entrance to Buzzards Bay, Massachusetts, in winds of 8 m/s and significant wave heights of 0.5 m. The data show that at frequencies below approximately 15 kHz the sound speed is approximately non-dispersive, and there is little attenuation. At higher frequencies the sound speed increases as does the attenuation.

The procedure for obtaining bubble size distribution from acoustic measurements requires solving the following integral equation:

$$\int_{a_1}^{a_2} k(a, f)N(a)da = M(f) \quad (1)$$

where $N(a)$ is bubble size distribution, $M(f)$ is either sound speed anomaly¹ or attenuation measured at frequency f (or a function of these measurements), and $k(a, f)$ is the kernel, the form of which depends on the specific variable M . Early solutions to the equation have been based on the assumption that major contributions to backscattering or attenuation come from bubbles with a resonance frequency near the frequency of incident waves [Wildt, 1946]. Recent work by Commander and Moritz [1989] has however shown that off-resonance contributions are also important. This indicates that the equation must be solved including contributions due to all bubble sizes.

Equation (1) is a Fredholm equation of the first kind, which is in general ill-posed, i.e., small errors in $M(f)$ may cause large changes in the solution $N(a)$. Field measurements of $M(f)$ naturally have many sources of errors, which are likely to make the solution unstable. In order to obtain a stable solution, we have to impose physical constraints (e.g., a positive $N(a)$ and a finite void fraction). This process is termed regularization of the problem. Generally speaking, the more physical constraints are imposed on the solution, the more stable the solution is likely to be. While there has been extensive literature on *inverse problems* in many fields, very few papers have directly addressed this bubble size inversion problem.

Recently Duraiswami [1993] proposed a linear optimization approach which allows convenient addition of constraints to the problem. The problem is formulated as a standard linear programming problem [Press et al, 1992] which is easy to implement and compute. We rewrite Eq.(1) as

$$\mathbf{KN} = \mathbf{M} \quad (2)$$

where \mathbf{K} is an integration operator (usually in the form of summation) on the size distribution at a number of frequencies, and \mathbf{M} is the measurement

¹The sound speed anomaly is $c - c_0$, where c_0 is the sound speed in bubble-free water.

vector at those frequencies. The linear optimization approach is formulated as

$$\text{Min} \quad |\mathbf{K}_2 \mathbf{N} - \mathbf{M}_2| \quad (3)$$

$$\text{subject to} \quad \mathbf{K}_1 \mathbf{N} = \mathbf{M}_1 \quad (4)$$

$$N(a) > 0 \quad \sum N < C_1 \quad (5)$$

$$\int_{a_1}^{a_2} N(a) a^2 da < C_2 \quad \int_{a_1}^{a_2} N(a) a^3 da < C_3 \quad (6)$$

where \mathbf{K}_1 and \mathbf{K}_2 are operators for different kernel functions, and \mathbf{M}_1 and \mathbf{M}_2 are different measurements, C_1, C_2, C_3 are physical constraints on $N(a)$. In our case \mathbf{K}_1 and \mathbf{M}_1 correspond to the sound speed anomaly kernel and measurements, respectively, and \mathbf{K}_2 and \mathbf{M}_2 the attenuation kernel and measurements.

The forms of the kernels are determined by the acoustic properties under investigation. In our case, measurements of phase speed and amplitude attenuation of sound waves in bubbly liquids are available. *Commander and Prosperetti* [1989] derived the following complex dispersion relation

$$\frac{c_0^2}{c^2} = 1 + 4\pi c_0^2 \int_{a_1}^{a_2} \frac{aN(a)}{\omega_0^2 - \omega^2 + 2ib\omega} da, \quad (7)$$

where c_0 is the speed of sound in pure liquid and c that in the bubbly mixture. ω is the frequency of incident waves, ω_0 the resonance frequency of a bubble of radius a at the frequency ω , b bubble damping coefficient. a_1 and a_2 are the smallest and largest bubble size in the mixture. They compared the model with experimental data and found that it worked well for void fractions up to 1-2% if bubble resonances play a negligible role. This condition holds when there are many bubble sizes in the mixture. Eq.(7) may be used to derive the kernels for the inversion. Eqs.(3)-(6) can now be posed in the standard form for linear programming and can be solved using the Simplex method [*Press et al*, 1992].

3 Results

3.1 Void Fraction

Since the 3 kHz data best represents the low frequency limit we shall limit our analysis of the data to this acoustic frequency. Figure 1 shows a summary plot of the sound speed at the seven depths ranging from 0.69-6.94 m, along with significant wave heights and sea surface temperatures (*Gnanadesian & Weller*, personal communication). The acoustic data corresponds to 40 minute averages every 4.5 hours. During this period the significant wave height ranged up to approximately 7 m and the wind speed (not shown) up to approximately 18 m/s, as wind and wave events recurred on a 4-5 day cycle.

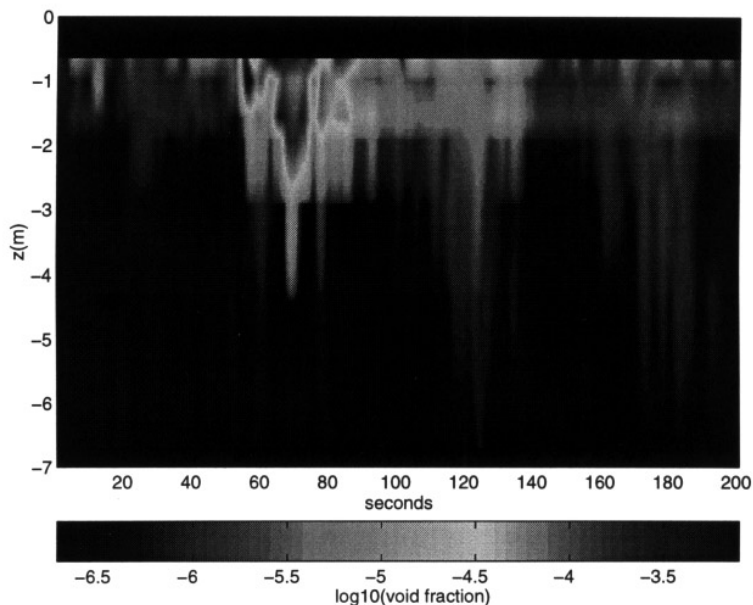


Figure 2: Contour plot of void fraction due to a breaking event. Note that the primary event lasts for approximately 30-40s near the surface, with somewhat lower void fractions persisting for perhaps another 50s. (For color figure, see Plate 12.)

What is apparent from the data is that the storm events are accompanied by significant reductions in the average sound speed; by as much as 600 m/s, or 40%, at the shallowest depth around year day 370. This corresponds to a void fraction of $O(10^{-4})$. At the surface the variability in the sound speed is dominated by the storms, whereas by a depth of 7 m, the variability due to the slow change in sea surface temperature (SST) is comparable to that due to the direct effects of air entrainment during storms. The slow change in the sea surface temperature is due to surface cooling associated with the decreasing air temperature, wind mixing, thermal convection and radiative cooling.

While the average data shows the gross effects of storms and secular changes during the experiment, they do not demonstrate that the sound speed reductions due to air entrainment are intermittent events associated with breaking. Figure 2 shows a contour plot of the void fraction associated with a breaking event. Near the surface the primary event lasts for 30-40s with void fractions of $O(10^{-3})$ at a depth of 0.7 m. The event reaches to a depth of approximately 4.5 m but by that depth the void fraction is reduced to $O(10^{-5})$ and lasts for perhaps only a few seconds. Following the primary event a secondary event is evident with void fractions elevated above the noise down to 5 m or so, and some suggestion of a periodic fluctuation.

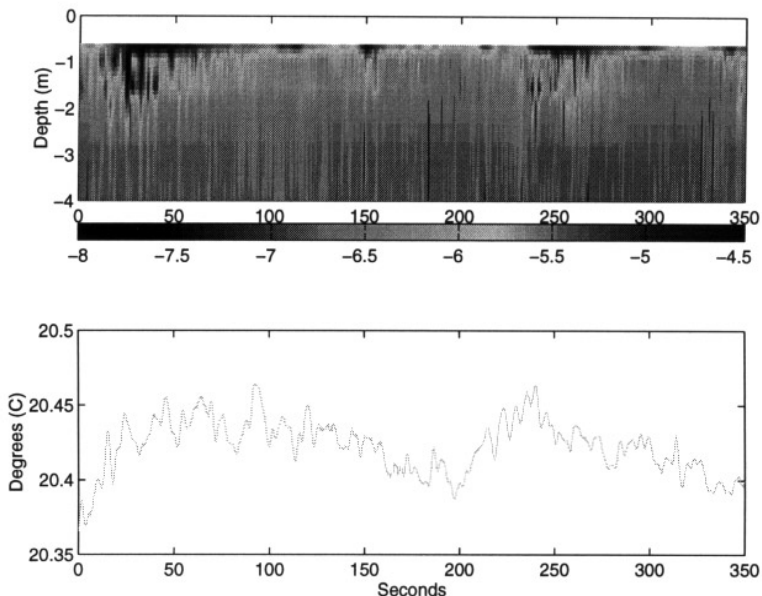


Figure 3: Contour plot of void fraction due to several major injection events and the associated temperature time series at 1.5 m. The time between major events is of the order of the period of the surface-wave groups. (For color figure, see Plate 13.)

This may be the remnants of the primary event being advected by the orbital motion of the waves, leading to an apparent quasi-periodicity in the data. The 40 minute averages are dominated by the contribution from these injection events.

Preliminary analysis of the void fraction and wave data suggests that during some periods there is significant contribution to the variance of the void fraction data at frequencies corresponding to the group frequencies of the waves. Figure 3 shows contours of void fraction due to two injection events along with temperature data at a depth of approximately 1.5 m. Notice that the primary injection events are separated by approximately 200 s, as are the local extreme in the temperature signal. Others have noted the influence of breaking on temperature in the wave zone.

There is considerable interest in developing one-dimensional models of air entrainment and related processes, although the availability of 3D numerical codes for boundary-layer processes may rapidly overtake the simple models. Nevertheless, it is of interest to determine whether the average void fraction can be described by simple functions of the depth. Our preliminary analysis of the data implies that the exponential profile which has been used by *Vagle and Farmer* [1992] and *Lamarre & Melville* [1994] may give a good fit during active storm events but the correlation is significantly reduced

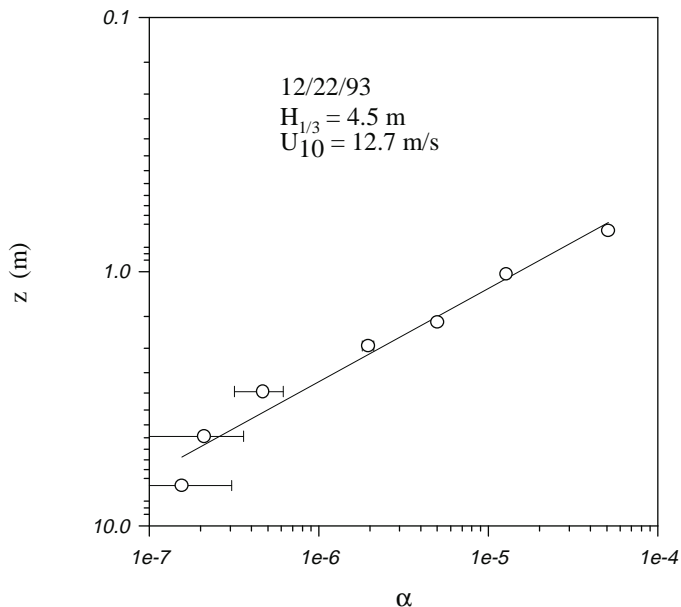


Figure 4: An example of a 40 minute mean void fraction profile showing an approximate z^{-3} decay.

during quieter periods. The exponential decay scale was found to be $O(1$ m) despite the fact that the significant wave height varied over an order of magnitude. Figure 4 shows that power laws may also provide a good fit to the data: In this case approximately z^{-3} . Given the intermittency of the data (e.g., Figures 2 and 3) it may prove difficult to derive simple rational models which adequately represent the physical processes.

We believe that we can resolve void fractions as small as $O(10^{-7})$ corresponding to errors in sound speed of ± 5 m/s. With vertical profiles of void fraction we can integrate to obtain the total volume of air per unit surface area. With the present data we do not have measurements above 0.7 m depth, and given the uncertainty of the exact form for the vertical profiles we have not extrapolated the data to the surface. Figure 5 shows the void fraction at 0.7 m and the corresponding vertically integrated void fraction during one storm event. Analysis of this data continues, but the figure suggests that surface measurements of void fraction along with supplementary data on the decay scale of the void fraction may be useful for inferring the total volume of air in the surface layer. The data in this figure are also consistent with a decay scale of $O(1$ m).

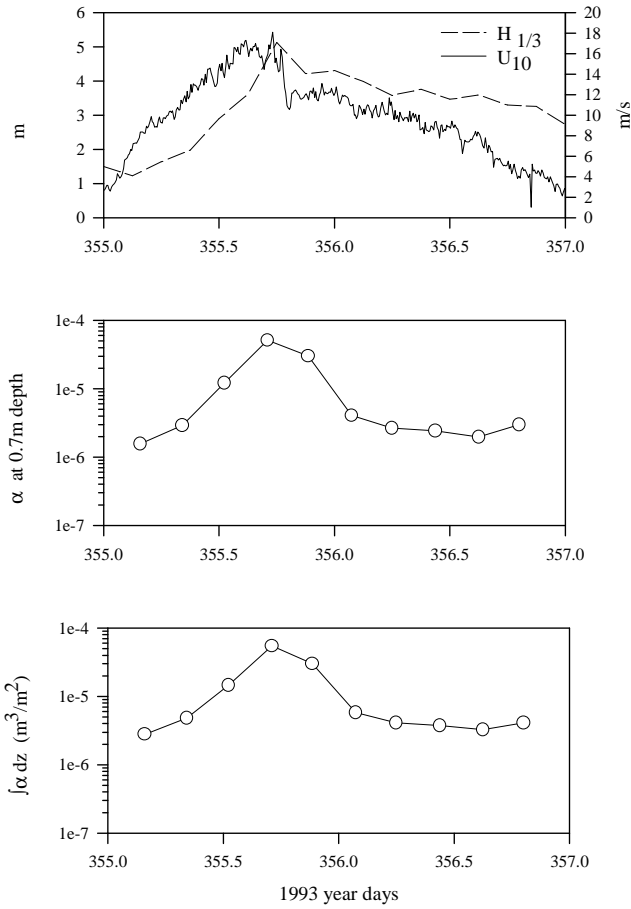


Figure 5: Plots of wind speed, U_{10} , significant wave height, $H_{1/3}$, α (0.7 m), and the void fraction integrated from 0.7-7 m around the peak of a storm.

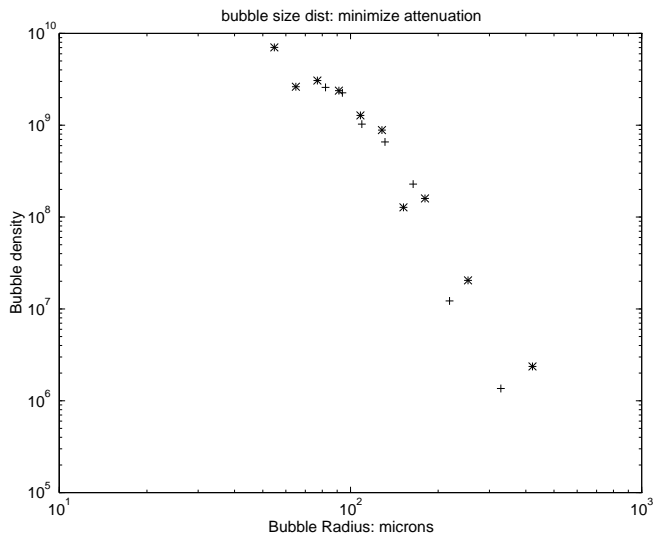


Figure 6: Inversions of the Buzzards Bay data using the simplex method (*) and the resonant approximation (+). Note the significant differences at larger bubble sizes.

3.2 Bubble Size Distribution

Figure 6 presents an example of the inversion of the sound speed and attenuation data for acoustic frequencies in the range 6–40 kHz using both the full simplex method and a resonant approximation which neglects the off-resonant contributions to the measured data. The differences are significant, corresponding to a slope difference of approximately -2 to -3. Both estimates give an approximately constant slope region at larger bubble radii, and appear to be approaching a maximum at radii smaller than those accounted for by the range of acoustic frequencies. It is not clear whether this behavior at small slope is also due to end effects associated with the high frequency cut off.

4 Discussion

In this paper we have presented preliminary results from moored measurements of void fraction in a North Atlantic winter experiment (ASREX), and inversions of acoustic data to give bubble size distribution. We anticipate that the final analysis of our ASREX data along with environmental data collected by others will provide new insight into the entrainment of air by breaking waves and its correlation with the relevant environmental variables. These measurements clearly demonstrate that autonomous acoustic instrument systems which include both data acquisition and significant on-board pro-

cessing, and data transmission are feasible in some of the harshest oceanic conditions.

The inversion of the limited broad-band data set demonstrates that credible inversions of acoustic data can be made and are sufficiently simple to permit the incorporation of the software into autonomous systems for field deployment. We plan to develop this capability to give bubble size distributions for bubble radii in the range $O(10 - 10^3) \mu\text{m}$.

4.1 Acknowledgments

We thank our colleagues and friends at Woods Hole Oceanographic Institution for making possible our successful participation in ASREX. We are particularly grateful to John Kemp, George Tupper, and the Captain and crew of RV Knorr for deploying our buoy before the almost incessant storms of the December 1993 cruise. This research was supported by a grant from the Office of Naval Research (Acoustics) in the Acoustic Reverberation Special Research Program.

References

- Commander, K. W., and E. Moritz, Off-resonance Contributions to Acoustical Bubble Spectra, *J. Acoust. Soc. Am.* 85(6), 2665-2669, 1989
- Commander, K. W., and A. Prosperetti, Linear pressure waves in bubbly liquids: Comparison between theory and experiment, *J. Acoust. Soc. Am.*, 85,732-746, 1989
- Duraiswami, R., Bubble Density Measurement Using an Inverse Acoustic Scattering Technique, in *ASME Cavitation and Multiphase Flow Forum*, Washington, D.C., 1993
- Lamarre, E., *An experimental study of air entrainment by breaking waves*, Ph.D dissertation, MIT/WHOI Joint Program, Cambridge, Massachusetts, 1993
- Lamarre, E. & W. K. Melville, Sound speed measurements near the ocean surface. *J. Acous. Soc. Am.*, 96, 3605-3616, 1994
- Press, W. H., S. A. Teukolsky, W. T. Vetterling and B. P. Flannery, *Numerical Recipes*, 2nd edition, Cambridge University Press, 1992
- Vagle, S. and D. M. Farmer, The measurement of Bubble Size Distributions by Acoustical Scatter, *J. Atmos. Oceanic Tech.*, 9, 630-644, 1992
- Wildt, R., Ed. *Physics of sound in the sea*, Chap. 28 "Acoustic theory of bubbles," N. D. R. C. Summary Tech. Rep., Div. 6, Vol. 8, Department of Defense, Washington, DC., 1946
- Wood, A. B. *A Textbook of Sound*, G. Bell & Sons, 1941

Breaking Waves, Bubbles and Langmuir Circulation: a Measurement Strategy for Studying Bubble Enhanced Air-Sea Gas Transfer

D. Farmer

Institute of Ocean Sciences
Sidney, BC, Canada
email: dmf@ios.bc.ca

Abstract

Determination of the role of bubbles in enhancing air-sea gas transfer depends on adequate measurements of the near surface velocity field, the bubble distribution in space, and the bubble size distribution. An approach to this measurement problem is described.

1 Introduction

The role of *bubbles* in the transfer of gas between atmosphere and ocean remains a challenging but poorly understood problem. It is certain that bubbles can enhance the transfer of the weakly soluble primary constituents, N_2 and O_2 [Farmer, McNeil & Johnson, 1993]. It also appears that the larger bubbles may contribute to the transfer of CO_2 when there is significant partial pressure difference across the bubble surface [Woolf, 1993, Keeling, 1993]. However, the extent to which bubble enhanced transfer occurs is difficult to calculate accurately because of the paucity of information on bubble distributions and the near surface motions which contribute to bubble dissolution.

A convenient expression of the problem is in the formulation of a coupled system of equations describing the source of bubbles, the gas exchange through the bubble wall, and the flow field within which they move before dissolution or release at the air-water interface [Thorpe, 1982, 1984b]. These equations may be solved numerically in a stochastic model for which the source function, flow field and partial pressure field are prescribed, thus leading to a prediction of the bubble distribution and the resultant gas transfer. The challenge lies in specifying realistic source distributions and flow fields. As shown by Farmer, McNeil & Johnson [1993], even the change in partial pressure associated with wind driven entrainment can be a significant factor in bubble enhanced gas transfer.

Particularly difficult from an observational point of view is the problem of adequately accounting for horizontal advection of property gradients. Observational approaches that minimize this problem, or address it directly, are particularly appropriate.

Here we outline a measurement strategy for studying bubble enhanced *air-sea gas flux*. At this time, although data have been acquired, the full problem of measurement and analysis remains incomplete. The purpose here is to report on measurement technologies that have been developed which should contribute to our understanding of the problem.

2 Statement of the Problem

The observational task proposed here is to measure the bubble source and near surface circulation, together with the partial pressure field, sufficiently well to account for the observed spatial and size distribution of subsurface bubbles. Implicit in this description is the assumption that there is sufficient order in the surface flow field to justify useful description in terms of representative hydrodynamic features. It is a remarkable result of recent studies of the near surface waters of lakes and oceans that this is indeed the case: bubbles injected by breaking waves are advected through the mechanism known as *Langmuir circulation* [Langmuir, 1938] into long parallel rows where they sink and may dissolve [Thorpe, 1984a]. While the details of Langmuir circulation are not yet predictable in terms of a comprehensive hydrodynamic model, the orderly velocity and bubble field that results can be measured. Specifically we need to measure the bubble injection process, the velocity field within the upper few meters and the detailed properties of the bubble field.

3 Measurement Strategy

In order to minimize problems with advection of horizontal property gradients and to simplify data collection in the open ocean, our approach has been to develop self-contained recording instruments that drift with the prevailing current; however the instruments may also be deployed for extended periods from fixed point moorings. Four distinct systems have been developed, although more than one sensor system may be deployed on any one drifting instrument.

3.1 Breaking Wave Sensor

This instrument is specifically designed to follow the surface waves accurately. A light vertical bar supporting various sensors has two buoyancy blocks at the surface so that it closely follows surface motions. A preliminary description is given in *Farmer & Gemmrich* [1995]. The bar is connected by hinged supports to a spar buoy containing batteries, recorders and associated electronics, and is drogued so as always to point into the wind (see Figure 1). The sensor includes four conductivity probes and fast response thermistors at fixed depths, as well as a mechanically driven profiling thermistor

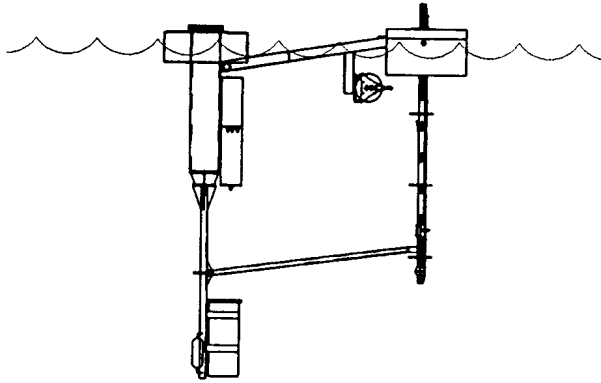


Figure 1: A breaking wave detecting instrument. Conductivity, temperature and velocity sensors are mounted on a hinged vertical bar.

that runs up and down the sensor support at 60 s intervals. Additional sensors include a 3-axis acoustic current meter, capacitance wire gauge, compass and accelerometers and also a sound speed sensor/resonator which is discussed subsequently.

3.2 Bubble Distribution and Velocity Field

The horizontal distribution of bubbles is detected with back scatter sonar using 4 fan beam sonars with orientation controlled by stepping motors [Farmer, Teichrob, Elder & Sieberg, 1990, and Trevorrow & Teichrob, 1994]. The instrument platform is suspended at a depth of 25-30 m by rubber cord from a surface float (Figure 2). The sonars may be programmed to sweep in azimuth, in which case they generate a 360° image, analogous to a radar image, every 30 s. Alternatively they may be programmed to face in prescribed directions, actively correcting for instrument motions. Different modes may be programmed to operate in sequence.

Both transmission signals and sample timing on all of the sonar systems are derived from a single clock, allowing synchronous detection and Doppler estimation. The velocity field may be analyzed in different ways. After correction for measured instrument motion the dominant wave orbital velocity field can be used to generate directional wave spectra. Azimuthally scanned Doppler fields can also be used to generate surface horizontal velocity fields. Of particular interest from the point of view of bubble advection is the much smaller signal associated with larger scale (10-100 m, >10 s) motions due to near surface circulation. Wave number-frequency filters can separate these signals from the higher frequency motions due to waves.

Vertical velocities associated with Langmuir convergence zones are more difficult to separate from wave orbital velocities. Nevertheless this separa-

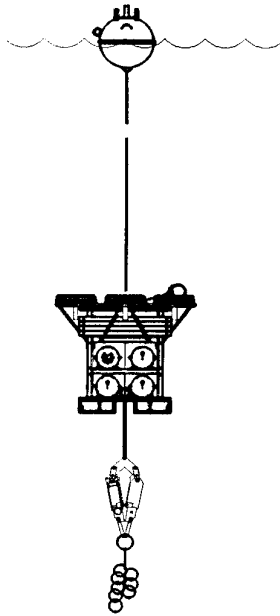


Figure 2: Sonar platform with azimuthally scanning and fixed vertical sonars. In addition to the horizontal sonars, vertically oriented sonars are used to obtain vertical profiles of the bubble distribution. These can be used simultaneously with the horizontally scanning sonars. Six frequencies (28 kHz - 400 kHz) are used simultaneously so as to take advantage of frequency discrimination by resonant bubble radius [Vagle & Farmer, 1992].

tion is possible and can be achieved by a combination of correction based on the acoustically measured surface elevation above the sonar using the linear dispersion equation and measured instrument motion, with appropriate filtering.

3.3 Bubble Size Distributions

Except for the largest bubbles, size distributions can be measured acoustically in various ways. Multiple frequency target strength is one approach; however, for linear systems the size range that can be measured is strictly limited by the sonar frequency range. Practical narrow beam sonars suitable for self-contained instruments are limited to about 25 kHz.

In situ sensors can more conveniently span the lower frequencies. We employ two approaches; one makes use of a travel time *sonar* similar to that described by Lamarre & Melville [1994]. A second approach is to use an *acoustic resonator*. Breitz & Medwin [1989] devised a resonator with which

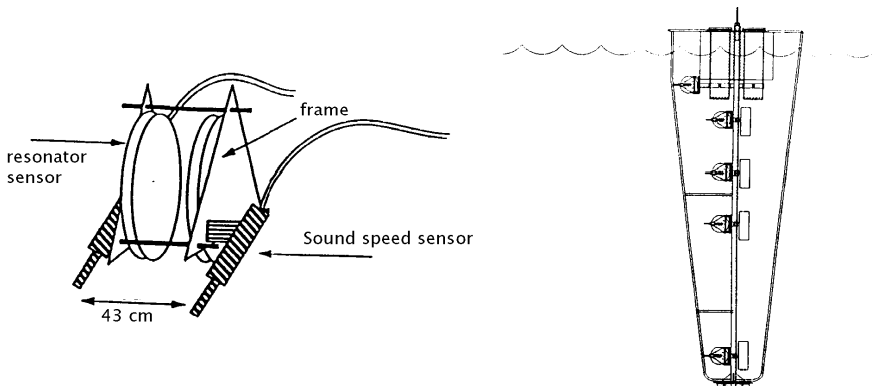


Figure 3: Bubble size detection sensor including both resonator and travel time sonars on surface drifter.

they probed bubble distributions; the same design has also been used by *Su and Cartmill* [1995]. We have recently developed the resonator concept in a somewhat different way so as to achieve both a high Q factor and high resonant peak stability. While a description of the operational details of this sensor lie beyond the scope of this paper, it is relevant that its resolution and stability readily allow detection of sound speed at 39 frequencies up to 197 kHz. Bubble populations may be inferred both from the acoustic dispersion and from the change in resonator Q , thus allowing a check on the inversion algorithms. The simultaneous use of both a simple travel time sonar and the resonator also allows a check on the measurement approach.

The sensors are mounted at various depths on a freely drifting platform, drogued so that they point into the prevailing wind (Figure 3). Each sensor has its own real time processing and disc storage unit allowing convenient deployment on alternative platforms. For example, resonators have also been mounted on the breaking wave measurement device shown in Figure 1.

3.4 Lagrangian Measurement of Subsurface Motions

An additional approach involving acoustically tracked neutrally buoyant floats has also been used for measuring the deeper motions associated with Langmuir circulation. A preliminary application has been described by *Farmer, D'Asaro, Trevorrow & Dairiki*, [1995], but the concept has been extended to include real time tracking of the floats using surface drifting buoys suitable for operation in the ocean (Figure 4). Up to 4 surface buoys are deployed, each fitted with differential GPS tracking and an acoustic transponder for positioning the subsurface float(s). The subsurface floats, being neutrally buoyant and having a large drag, follow the 3-dimensional motions thus providing Lagrangian paths. They therefore provide an additional means of

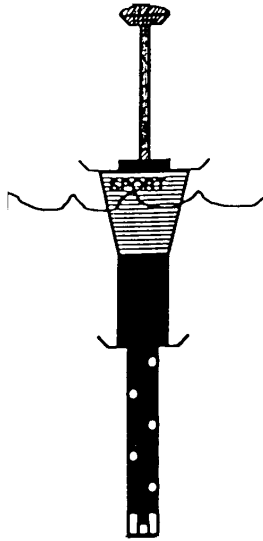


Figure 4: DGPS/acoustic surface buoy for tracking neutrally buoyant floats.

characterizing the circulation responsible for advection and downwelling of bubble plumes.

3.5 Dissolved Oxygen and Nitrogen

The combined use of a *dissolved oxygen sensor* and a *gas tension device* to separate the dissolved nitrogen is discussed elsewhere in this volume [McNeil, Farmer & Johnson, 1995]. The GTD-O instrument is conveniently attached to the bubble size distribution sensor platform shown in Figure 3. However, extensive bottle samples and oxygen titrations remain an essential component of field operations.

4 Summary

Confidence in bubble enhanced air-sea gas transfer models depends on adequate environmental measurement. The relevant measurements must span the bubble source (wave-breaking), subsurface horizontal advection into convergence zones and subsequent downwelling. In addition, the spatial distribution and the size distribution must be established and the dissolved gas partial pressures must be measured. All such observations must be supplemented with more traditional oceanographic measurements of salinity and temperature profiles. Moreover, the observational approach must

minimize effects of, and preferably include measurements of, the horizontal advection of property gradients.

These requirements present a formidable challenge. Our approach to this problem has been to develop a suite of instruments designed to measure wave breaking, the directional surface wave spectrum, the nearsurface horizontal divergence field responsible for advecting bubbles into the downwelling zones, profiles of the vertical velocity of the bubbles, larger scale subsurface motions within the surface mixing layer, bubble size distributions and dissolved nitrogen and oxygen partial pressures. When used in combination with appropriate supporting measurements, the resulting data set should provide a basis for testing models that relate bubble formation, dispersion and dissolution, and consequently the role of bubbles in air-sea gas flux. An initial data set has been acquired for this purpose in the Marine Boundary Layer Experiment off the California coast in April 1995.

Acknowledgements

This brief description does not do justice to the efforts of students, research associates, colleagues and technical staff who developed and operated the instrumentation. I am especially grateful to all of the IOS Ocean Acoustics Group, including especially Svein Vagle, Craig McNeil, Mark Trevorrow, Vadim Polonichko, Johannes Gemmrich, Dan Veenstra, Victor Mao, Ron Teichrob, Nick Hall-Patch and Al Adrian. Funding was provided by the National Scientific and Research Council of Canada and the US Office of Naval Research.

References

- Breitz, N., & H. Medwin, Instrumentation for in situ acoustical measurements of bubble spectra under breaking waves. *J. Acoust. Soc. Am.* 86(2): 739-743, 1989
- Farmer, D. M., E. A. D'Asaro, M. V. Trevorrow, & G. T. Dairiki, Three-dimensional structure in a tidal convergence front, *Continental Shelf Research Vol 15*, No. 13, 1995
- Farmer, D. M., & J. Gemmrich, Breaking waves and vertical heat transport in the upper ocean, submitted to *J. Phys. Oceanogr.* (1994 01 18), 1995
- Farmer, D. M., C. McNeil, & B. Johnson, Evidence for the importance of bubbles to the enhancement of air-sea gas flux, *Nature* 361: 620-623, 1993
- Farmer, D. M., R. C. Teichrob, C. J. Elder & D. G. Sieberg, Novel acoustical instrumentation for the study of ocean surface processes, *IEEE-OCEANS '90*, 1990
- Keeling, R. F., On the role of large bubbles in air-sea gas exchange and supersaturation in the ocean, *Journal of Marine Research*, 51: 237-271, 1993
- Lamarre, E. & W. K. Melville, Sound-speed measurements near the ocean surface, *J. Acoust. Soc. Am.* 96 (6): 3605-3616, 1994
- Langmuir, I., Surface motion of water induced by wind. *Science*, 87: 119-123, 1938
- McNeil, C., D. M. Farmer & B. Johnson, Development and testing of in situ N₂ and O₂, and gas tension sensors for oceanographic studies, *This volume*

- Su, M.-Y., and J. Cartmill, Effects of salinity on breaking wave generated void fraction and bubble size spectra. *This volume*
- Thorpe, S. A., The effect of Langmuir circulation on the distribution of submerged bubbles caused by breaking wind waves, *Journal of Fluid Mechanics*, 142: 151-170, 1984a
- Thorpe, S. A., The role of bubbles produced by breaking waves in super-saturating the near-surface ocean mixing layer with oxygen, *Annual Reviews in Geophysics* 2(1): 53-56, 1984b
- Trevorrow, M., & R. Teichrob, Self-Contained Acoustics Platforms for Probing Ocean Surface Processes, *Journal of Oceanic Engineering* (19) No. 3: 483-492, 1994
- Vagle, S., & D. M. Farmer, The measurement of bubble size distributions by acoustical backscatter, *J. Atmosph. & Ocean. Technology*, 9 (5): 630-644, 1992

Effects of Salinity on Breaking Wave Generated Void Fraction and Bubble Size Spectra

M.-Y. Su ¹ and J. Cartmill ²

¹ Naval Research Laboratory
Stennis Space Center, MS 39529-5004, USA
email: su@nrlssc.navy.mil

²Planning Systems Incorporated
Slidell, LA 70458, USA email: cartmill@nrlssc.navy.mil

Abstract

The chemical composition of seawater has profound effects on the size distribution of bubbles formed by breaking waves in the ocean. The purpose of this experiment was to quantify these effects by measuring bubble size spectra and total void fraction in both saltwater and freshwater under identical breaking conditions. Mechanically generated waves in a large wave tank were used to produce breaking wave groups in freshwater and then in saltwater with a salinity of 30 parts per thousand. Measurements of the bubble size spectra in the range of 34-1200 microns showed a 10 fold increase for the saltwater case, whereas the total void fraction showed a negligible difference.

1 Introduction

This paper highlights the results of a recent experiment performed at the Hinsdale Wave Research Facility located at Oregon State University in Corvallis, Oregon. Mechanically generated wave groups were used to produce breaking waves and bubble plumes comparable in scale with ocean waves. Bubble size distributions, over the range of 34-1200 μm in radius, were measured by an acoustic resonator in *freshwater* and in *saltwater* with a *salinity* of 30‰.

The acoustic resonator used in the experiment measures the extinction as a result of air bubbles of a sound field in a resonant cavity formed by two parallel plates. This acoustic extinction is then inverted to produce a bubble size spectrum (number $\text{m}^{-3} \mu\text{m}^{-1}$ vs. radius). Over 30 discrete bubble sizes can be measured simultaneously with this method. Direct void fraction measurements were made during the experiment with a resistance gage sensor system developed at NRL.

2 Measurement Techniques

There is no question that bubble plumes generated in freshwater and in saltwater, even by the same techniques, are qualitatively different [Scott, 1975]. The bubbles are finer in saltwater aquaria than in freshwater, as freshwater bubbles coalesce easily, whereas saltwater bubbles repel each other as a result of their surface physical-chemical properties.

2.1 Void Fraction Meter

The *void fraction meters* consist of two square gold electrodes 2.5 cm on a side separated by a gap of 2 cm. The sensor forms one leg of a Wheatstone bridge circuit to measure the resistance. The void fraction p can then be determined with Equation 1 from the relation derived by Maxwell:

$$p = \frac{(r/r_0) - 1}{(r/r_0) + 1/2} \quad (1)$$

where r is the measured resistance in bubbly water and r_0 is the resistance in water without bubbles.

2.2 Bubble Size Spectra Sensor

The *acoustic resonator array* was constructed by the Naval Research Laboratory (NRL), on the basis of a design originally developed by Herman Medwin and Nigel Breitz of the Naval Postgraduate School [Breitz and Medwin, 1989; Medwin and Breitz, 1989]. The system consists of a capacitive transducer plate and a reflector plate held in a parallel configuration. The transducer consists of a 0.5 mm sheet of aluminized Mylar stretched over an aluminum disk 26 cm in diameter. The aluminum disk is embedded in a 2.5 cm disk of PVC and on the front of the Mylar is a 2 mm coating of Eccothane, which forms a waterproof seal. The reflector plate consists of a stainless steel disk 6 mm in thickness mounted on PVC. A ceramic disk hydrophone, also coated with Eccothane, is embedded in the surface of the reflector plate. The transducer and reflector are separated by a distance of 24.1 cm.

The operating principle of the acoustic resonator is based on two types of resonance: the first type is the geometrical cavity resonance induced by the open space between the transducer and the reflector, which are parallel to each other. When white noise is produced by the source transducer and reflected partially back and forth between these two plates, a series of standing acoustic waves is created within this open cavity. For the separation of 24.1 cm currently used in our system, the fundamental frequency of the standing waves is close to 3 kHz and has 32 higher harmonics in the 100 kHz bandwidth of the white noise. The second type of resonance is individual bubble resonance as a result of excitation by acoustic waves. This

resonance has an equivalent cross-section about a thousand times larger than the corresponding pure geometrical cross-section of the bubble. For the fundamental frequency of 3 kHz, the resonant bubble radius is about 1200 μm , and for the highest harmonic frequency of 99 kHz, the resonant bubble radius is about 34 μm .

The complete system was constructed and integrated by NRL for use at sea. The transducer is connected to a 300 V d.c. polarizing battery and amplified white noise. The white noise is produced from the output section of an HP-3561A dynamic analyzer and is amplified by an Instruments Incorporated Model L2 power amplifier. The signal received by the hydrophone is fed into an Ithaco Model 143 preamplifier, which provides 20 dB of gain and matches the high impedance of the hydrophone to the low impedance of the transmission cable. The signal is then input into the HP-3561A dynamic analyzer, where its power spectrum is calculated by Fast Fourier Transform (FFT) and averaged. The time is about equally divided for raw data acquisition and for FFT computation. The conversion of the acoustic resonator data to bubble size distribution is based on the formula [Breitz and Medwin, 1989]

$$\eta_0(a) = \frac{2\pi\Delta f}{c\sigma 10^6 \delta a} \quad (2)$$

where η_0 is the zeroth-order bubble density, c is the speed of sound in water, σ is the extinction cross-section at resonance, Δf is the increase in resonance width, δ is the damping constant at resonance and a is the bubble radius.

The differences in resonance heights between the spectra with bubbles and a bubble-free reference case are then used to compute the Δf used in equation (2). An initial bubble distribution, η_0 , is then computed for each case. A correction for the contribution of off-resonance bubbles is then computed by integrating the equation

$$a_B(f) = -4.3 \int_0^\infty a\eta(a)da \quad (3)$$

with $\eta(a) = \eta_0(a)$ and then substituting into

$$\eta_1(a_\eta) = \eta_0(a_\eta) [a_B(f_\eta)/a(f_\eta)] \quad (4)$$

This produces the modified and corrected first-order bubble distribution, $\eta_1(a)$. This last correction can then be carried to a higher order, if desired.

3 Breaking Wave Facility

The main features and dimensions of the wave channel we employed for our experiment are shown in Fig. 1. A programmable paddle type wave generator

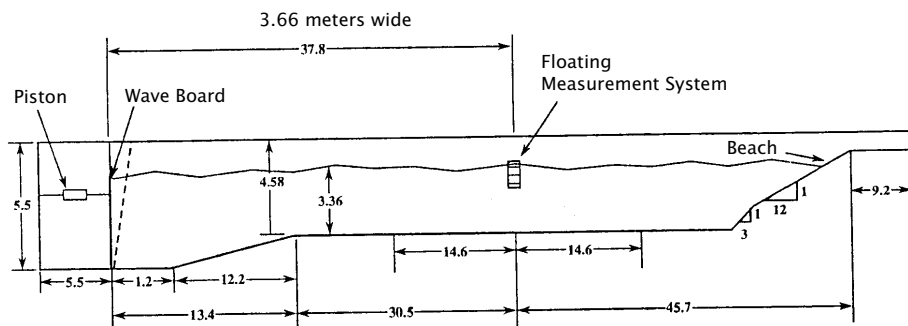


Figure 1: The dimensions of the wave tank used in this experiment (all dimensions in meters).

is located on one end of the channel, and at the other end is a beach with a 1-in-12 slope. The mean water depth was maintained at 3.5 m for the main test section in the middle of the channel. The time series of the wave profile was measured by two ultrasonic wave height sensors placed 1.1 m above mean water level.

4 Method of Salt Mixing in the Wave Tank

In order to achieve a salinity approaching the level found in the ocean, 40 one ton bags of salt had to be added to the water in the wave tank. A weir was constructed at the beach end of the tank, and a recirculating pump was used to mix the salt. An electrical stirring mechanism was also employed. The wavemaker was turned on during the mixing procedure to further enhance the mixing. A final salinity of 30‰ was achieved using this process. The photograph in Figure 2 illustrates a portion of the process.

5 Results of Experiments

The photograph in Figure 3 shows the measurement system after a breaking wave has passed with a number of bubble plumes surrounding the instruments. *Bubble spectra* for both saltwater and freshwater measured at a depth of 0.3 m are shown in Figure 4. An order of magnitude difference in the number of bubbles is apparent for bubble radii greater than 100 μm , with a smaller difference for bubble radii less than 100 μm . Figure 5 presents spectra measured at a depth of 1.22 m. Over the entire range an order of magnitude difference exists between the number of saltwater and freshwater bubbles. A strikingly similar appearance between the saltwater and freshwater spectra is also apparent. A -3 power law fits the data reasonably well in the 100-1200 μm range.



Figure 2: A photograph of the salt mixing section with a one ton bag of salt being added.

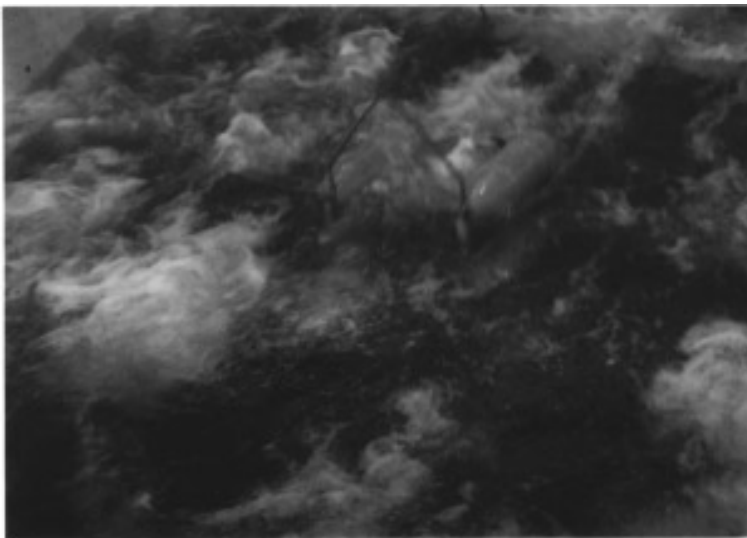


Figure 3: A photograph of the system after a large breaking wave has passed several bubble plumes may be seen surrounding the instruments.

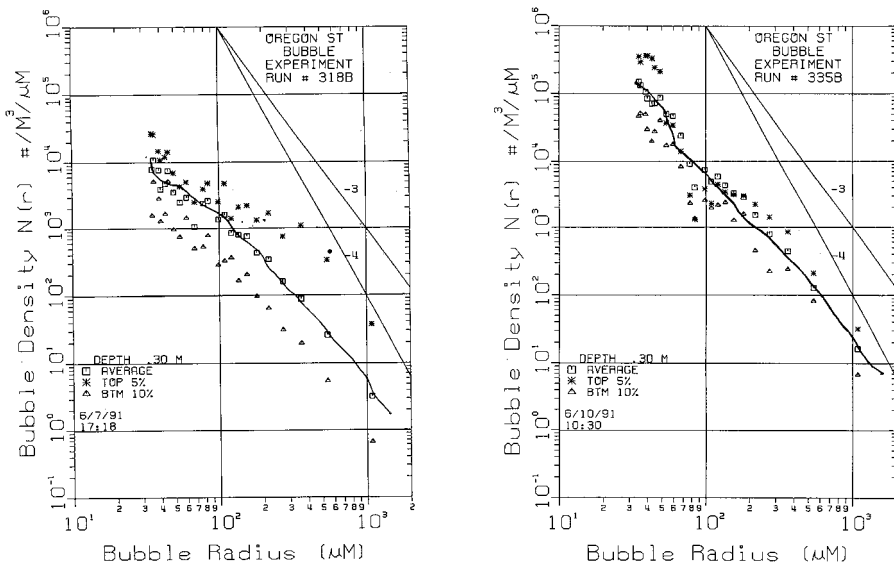


Figure 4: Bubble size distributions for fresh (left) and salt (right) water at a depth of 0.30 meters.

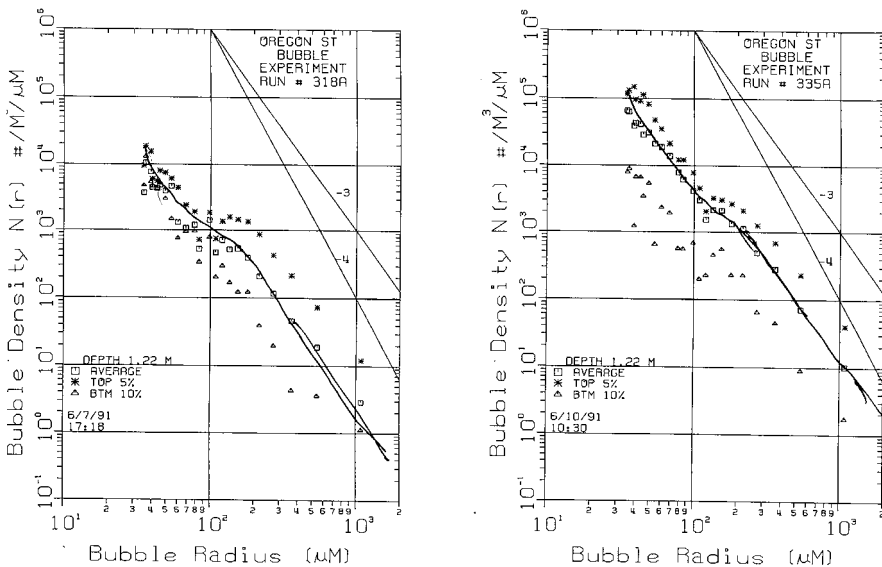


Figure 5: Bubble size distributions for fresh (left) and salt (right) water at a depth of 1.22 meters.

The large difference in the number of bubbles produced by saltwater vs. freshwater breaking waves over this size range is attributed to the coalescence of small bubbles in freshwater. This process is inhibited by ionic repulsion in saltwater.

6 Summary and Conclusions

The microbubble size spectra in the radius range of 34 to 1200 microns, generated by a continuous breaking wave train in a $12 \times 15 \times 400$ ft tank, are about ten times higher in oceanic-like saltwater than in fresh tap water for the top depth of about five feet. The exact physical mechanism for this large difference is still uncertain.

Total *void fractions* in the range of 0.5% or higher and in the vicinity of breaking waves do not show much difference between the fresh and saltwater. This very weak dependence on salinity may imply that void fraction is directly in proportion to the energy/momentum loss of breaking waves, and the fact that the difference in surface tension of fresh and saltwater is small.

Acknowledgements

The authors would like to acknowledge the efforts of Raymond Burge of NRL and Dr. C.K. Sollitt and the staff of the Hinsdale Wave Facility of Oregon State University throughout the experiment. We would also like to thank Dr. Marshall Orr who was the program manager at the Office of Naval Research for funding this experiment.

References

- Cartmill, J. and M. Y. Su, Bubble size distribution under saltwater and freshwater breaking waves, *Dynamic Atmos. and Ocean.*, 20, 25-31, 1993
- Breitz, N. D. and H. Medwin, Instrumentation for in-situ acoustical measurements of bubble spectra under breaking waves, *J. Acoust. Soc. Am.*, 86 (2), 739-743, 1989
- Medwin, H. and N. D. Breitz, Ambient and transient bubble spectral densities in quiescent areas and under spiling breakers, *J. Geophys. Res.*, 94, 12751-12759, 1989
- Scott, J. C., The role of salt in whitecap persistence, *Deep Sea Res.*, 22b, 653-657, 1975
- Su, M. Y. et al., Laboratory comparisons of acoustical and optical microbubble measurements, *J. Atm. Oceanic Tech.*, 11 (1), 170-181, 1994

Effects of Waves and Heat Fluxes on Bubble Patch Structure and Gas Exchange

A. Gnanadesikan

Department of Physical Oceanography
Woods Hole Oceanographic Institution, Woods Hole, MA 02543

Abstract

This paper considers when and how oceanic mixing processes affect gas exchange. The two processes considered are wave breaking and Langmuir circulations. The approach taken is to predict the strength of the Langmuir cell overturning as a function of surface forcing. It is demonstrated that although the cells are capable of producing large alterations in the structure of the bubble layer, that on average they are too weak to greatly alter the amount of air entrained, since the majority of the bubbles which make up the deep patches would have eventually have gone into solution anyway. The depth to which the initial breaking event deposits bubbles, on the other hand, is shown to be of much more importance.

1 Introduction

Injection of gasses into the ocean occurs when waves break, creating bubbles which are injected into the surface layer. The fate of these bubbles depends on the injection depth of the bubbles and the strength of the mixing which they experience after injection. If the mixing is very strong, bubbles can be entrained into deep patches and drawn down to depths of up to 10 meters [Zedel and Farmer, 1991; Plueddemann *et al.*, 1995]. Suppose that a patch of bubbles 10 m deep has a mean void fraction of 10^{-5} (a total air content of 0.1 l/m²). Then assuming that the air within that patch is absorbed at a rate of 0.01 s⁻¹ (reasonable given the values in Thorpe [1982]) and that such patches cover approximately 1/2 the ocean surface area, then the air absorbed in such patches could amount to 40 l/day. The bubble layer may also play an important role in removing relatively insoluble, photochemically produced gasses such as carbon monoxide from the surface layer [Gnanadesikan, 1995a]. Bubble patches also play an important role in causing acoustic backscatter [McDaniel, 1993].

Does the detailed structure of such patches matter for air-sea gas transfer? The answer depends primarily on the strength of the mixing which maintains the patches. The principal means by which persistent bubble patches are maintained appears to be the quasi-two dimensional vortices known as Langmuir circulations. This paper draws on and expands upon recent work to argue that although Langmuir cells are important in determining the structure of the bubble layer do not appear to determine the gas

exchange rate to $O(1)$. The depth to which bubbles are initially injected is shown to be of far greater importance in this respect. This work differs from previous work in that the cell strength is predicted rather than being specified, enabling the relative importance of Langmuir cells and wave breaking to be estimated.

2 Basic Equations and Important Parameters

The basic equations governing the development of *Langmuir cells* are taken from *Craik and Leibovich* [1976] and *Huang* [1979]. The fundamental assumption is that when the flows associated with the cells are small and slowly varying in comparison with the surface gravity waves, a consistent averaging over the waves which takes into account the stretching and tilting of vortex lines by the wave field gives the following equation.

$$\frac{\partial}{\partial t} \mathbf{u} + \nabla(\mathbf{u} \cdot \mathbf{u}/2) + (\omega + f\mathbf{k}) \times (\mathbf{u} + \mathbf{u}_s) = -\frac{1}{\rho_0} \nabla p + \rho g \mathbf{k} + \nabla K_V \nabla \mathbf{u} \quad (1)$$

where the bold letters denote vectors, f is the planetary vorticity, \mathbf{k} is the unit vector in the vertical direction, \mathbf{u}_s is the Stokes drift associated with the surface gravity waves, and K_V is the eddy viscosity. The key point is that the Stokes drift can advect filaments of planetary and relative vorticity, but since it is a residual flow from an irrotational wave field it cannot serve as a source of vorticity itself. The bubbles are assumed to obey the following equation (similar to *Thorpe*, [1982, 1984])

$$\frac{\partial B}{\partial t} + (\mathbf{u} + \mathbf{u}_s) \cdot \nabla B = S e^{z/L_i} - \alpha z B - w_{rise} \frac{\partial B}{\partial z} + \nabla K_V \nabla \mathbf{u} \quad (2)$$

A numerical code developed in *Gnanadesikan* [1994] is used to integrate these equations.

There are a number of key length and frequency scales which emerge from these equations.

- The depth over which the bubbles are injected L_i .
- The strength of “subgrid-scale” turbulence, parameterized as $u_* L_t$.
- The rise velocity of the bubbles w_{rise} .
- The consumption rate αz .
- The depth at which the bubbles are entrained L_e .
- The cell penetration depth D .
- The overturning rate associated with the cells Ω .

Recent measurements and modelling studies have advanced understanding of the final quantity, which turns out to play a key role in bubble patch

dynamics. A summary of what has been learned is presented in the following section.

3 Langmuir Cells and the Turnover Time

The key to linking Ω , the *overturning rate*, to surface forcing may be found in the *energy balance equations*. The energy balance can be shown to be (Leibovich [1977]; Gnanadesikan, [1994])

$$\int -\langle u'w' \rangle \frac{\partial u_s}{\partial z} dz - \int \frac{g}{\rho} \langle \rho'w' \rangle dz = \int \epsilon dz \quad (3)$$

Wave-current interaction + Buoyant Production = Dissipation

Gnanadesikan [1994] argues that if a “typical” Stokes drift shear $\delta U_s/\delta z$ is chosen, that the first term of the energy balance can be parameterized

$$\text{Wave-current interaction} \sim K_V \frac{\partial U}{\partial z} \frac{\partial U_s}{\partial z} \quad (4)$$

where $\partial U/\partial z$ is a typical Eulerian shear in the absence of cells. Gnanadesikan [1994, 1995b] argues that if the cells penetrate over some depth D , that the Stokes drift shear at $D/3$ is an appropriate value to use in this equation (unless D is much larger than $1/k_w$ the inverse wavenumber of the surface gravity waves). The second and third terms scale as

$$\text{Buoyancy production} \sim K_V N_0^2 \quad (5)$$

$$\text{Dissipation} \sim K_V \Omega^2 \quad (6)$$

where Ω is a typical shear scale associated with the Langmuir cell overturning and N_0 is a typical buoyancy frequency in the absence of cells. Thus the turnover time for a given depth scales as

$$\Omega = C \sqrt{\frac{\partial U_s}{\partial z} \frac{\partial U}{\partial z} - N_0^2} \quad (7)$$

where the constant of proportionality is yet to be determined.

The upper ocean can be thought of as containing three separate regimes, a high shear surface layer, a low-shear mixed layer interior, and a high-shear upper thermocline. Figure 1 shows sample profiles of a mixed layer. Figure 1a shows a sample profile of the shear in the mixed layer from the Surface

Waves Processes Program (see *Weller et al.* [1991]) for a description of the experiment. Figure 1b shows a profile of the shear from a numerical model of Langmuir cells (given a mean stress of $0.12 Pa$, a mean viscosity of $0.0235 m^2/s$, an entrainment heat flux of $40 W/m^2$ and waves given by a Pierson-Moskowitz spectrum with a mean amplitude of $1.4 m$ and a peak period of $11.2 s$) which displays similar features. The surface shear layer (which in the presence of buoyancy flux is also stratified), gives the appropriate scaling for $\delta u/\delta z$ in (8) Within the shear layer, one can estimate a local eddy viscosity by assuming that

$$K_V \frac{\partial U}{\partial z} = \frac{\tau}{\rho} \quad (8)$$

The *eddy viscosity* is well approximated by assuming that

$$K_V = \kappa u_* \min(z, L_{mo}) \quad (9)$$

where L_{mo} is the Monin-Obhukhov length $L_{mo} = \rho c_p u_*^3 / \kappa g \alpha_T Q$ (c_p the specific heat, α_T the coefficient of thermal expansion, g gravity, Q the heat flux, and κ the Kolomogorov constant 0.4). A comparison of the (9) and the estimated eddy viscosity is shown in Figure 2a.

Gnanadesikan [1994] argues that the shear variance in a frequency band from 1-36 cph across depths of 2.25 and 6.75 m is dominated by high-frequency cells with wavelengths of 10-30 m and penetration scales of 5-15 m. Assuming a mean penetration depth of about 10 m, the Stokes drift shear at about 3 m and the measured mean shear between 2.25 and 4.5 m to estimate $\delta U/\delta z$ and N_0 , then the observed and predicted shear can be compared (Figure 2b). The predicted and observed levels of shear are quite strongly correlated. Note that on March 5 the wind is low but the waves remain high. During this time period, enhanced levels of shear are seen which correspond to increased levels of Langmuir cell activity. This day provides one of the first pieces of quantitative evidence for wave-current interaction actually driving Langmuir cells. Note also that the prediction for Ω goes to zero on the following day. This occurs because N_0 becomes large.

4 Langmuir Cells and Bubble Patches

The scaling for Ω outlined in Section 3 has a number of implications for *bubble patch dynamics*. In order for cells to create patches, they must be able to entrain bubbles faster than they can rise, this means that either

$$E_{in} \sim \Omega L_i / w_{rise} \sim O(1) \quad (10)$$

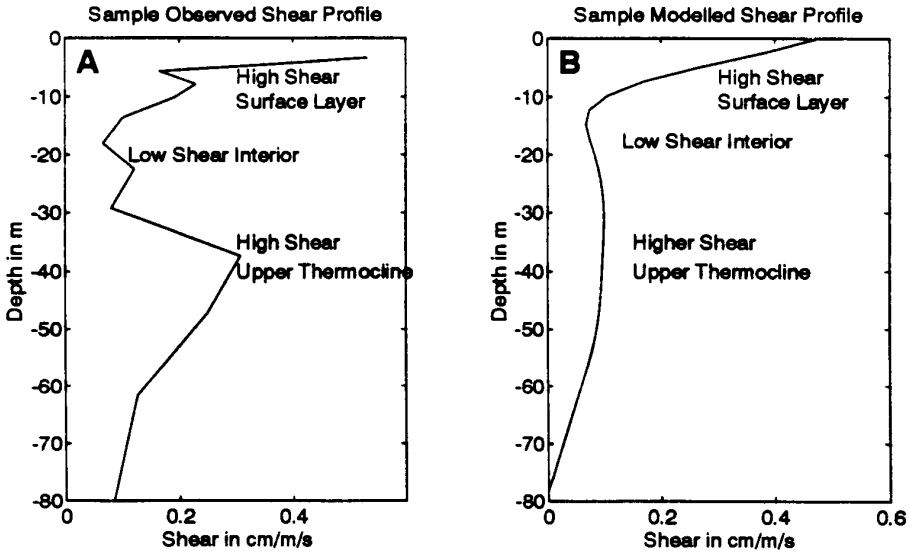


Figure 1: Shear profiles from data and models. (A) Daily-averaged shear from March 4th during the Surface Wave Processes Program (SWAPP). (B) Daily-averaged shear from a numerical model run with the mean conditions during SWAPP showing similar features.

so that the cells entrain the bubbles directly after they are injected by the waves or

$$E_{diff} \sim \Omega u_* L_t / w_{rise} \sim O(1) \quad (11)$$

so that diffusive processes bring the bubbles down to a depth where the cells can entrain them. Additionally, the bubbles must be able to survive being transported to depth

$$C = \alpha z / 2\Omega \sim O(1) \quad (12)$$

Given $\alpha = 0.0015$ /s/m and $w_{rise} = 0.01$ m/s [Thorpe 1982, 1984] then for the parameterization of diffusion in (8), $L_i = 1$ m, and $\Omega \sim 0.005$ /s, it can be seen that the cells primarily entrain bubbles which are diffused downwards and that they are capable of transporting these bubbles to depths of order 7 m. This value is in line with the results of Zedel and Farmer [1991] and Plueddemann et al. [1995]. When stratification shuts off the cells, the bubble layer is more dominated by small-scale turbulence (the transition between “columnar” and billow bubble clouds referred to in Thorpe [1982]).

A numerical model run with bubbles and Langmuir cells is presented in Figure 3. The velocity field produced by these runs yields a similar level

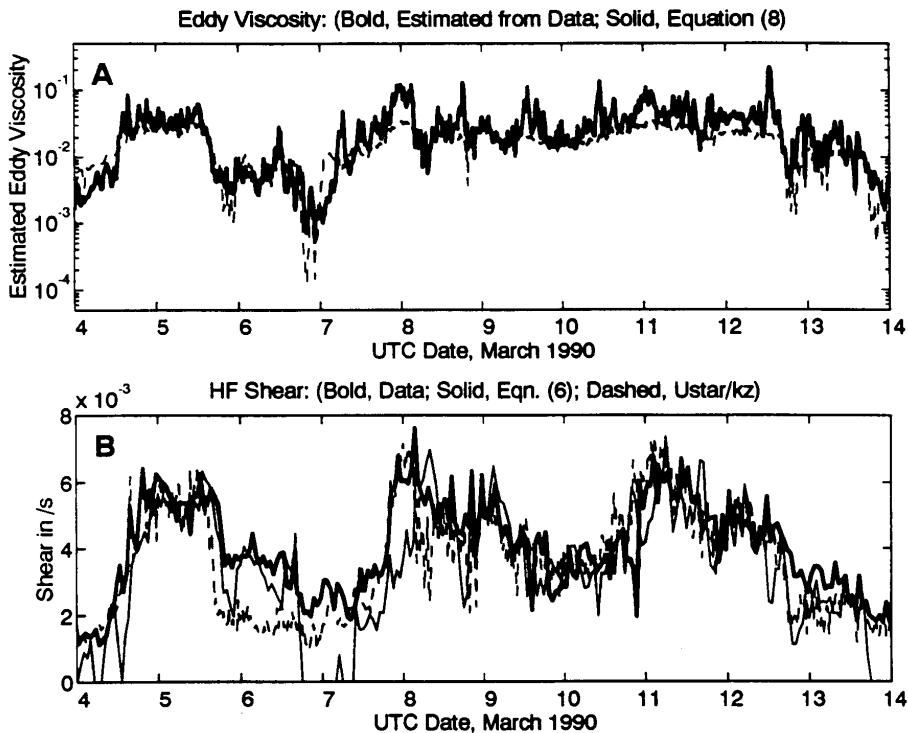


Figure 2: Eddy viscosity and shear in a band (1–36 cph) thought to be related to Langmuir cells. (A) Bold line is eddy viscosity (m^2/s) estimated from (7) using current meters at nominal depths of 2.25 and 4.5 m below wave trough (estimated actual depths are 1.125 m larger). Dashed line is equation (8) with $z = 4.5$ m. (B) HF shear (proportional to the overturning rate). Bold line is from current meters at nominal depths of 2.25 and 6.75 m. Solid line is Ω estimated from (6) with $C = 2$. Dashed line is u_*/kz , with $z = 6.75$ m. Note March 5th, a day when the wind is low, but waves are high.

of mean shear (and thus “eddy viscosity”) between 2.25 and 4.5 m. Narrow patches of bubbles move downward in downwelling zones, with broader upwelling zones in between being associated with decreases in bubble concentration. Two different bubble fields are computed, longer-lived but more quickly rising $100 \mu\text{m}$ bubbles in the top panel show deeper penetration than the slower-rising but shorter-lived $50 \mu\text{m}$ bubbles in the middle panel.

Despite the fact that Langmuir cells do create and maintain persistent deep patches on bubbles, they do not have a major impact on the gas flux. Figure 3c and d show profiles of gas absorption for the two size classes in Figures 3a and b respectively. For both classes of bubbles, concentrations are lowered at the depth of maximum gas flux, but increased below. The

total effect is to shift the gas flux lower into the water, but not to increase it substantially (the vertically integrated gas flux is 10% higher for the 100 μm bubbles and less than 1% higher for the 50 μm bubbles). In order for Langmuir cells to significantly enhance gas transfer, the cells must draw down significant numbers of bubbles which otherwise would have escaped the system, rising before they were absorbed. This requires

$$C_e = \alpha L_e^2 / w_{rise} \ll 1 \quad (13)$$

$$E_{ad} = \Omega L_e / w_{rise} > 1 \quad (14)$$

For the values of Ω shown here (which it should be noted are relatively large in comparison with $\kappa u_* / z$, the classical scale for overturning in a wall layer) and given a rise velocity of 0.005–0.01 m/s, for E_{ad} to be large L_e must be of order 2 m. At such depths, however, C_e is of order 1. Another way of putting this is that most of the bubbles entrained into the cells have diffused down to the entrainment depth and that they are unlikely to diffuse back up to the surface in time.

This result is a strong function of boundary conditions (a fact which came as a nasty surprise to the author). The results here assume a fixed bubble input which is balanced by absorption and bubble rise at the surface. Because vertical velocities associated with the cells are small at the surface, relatively few bubbles are removed by the cells and so the effect is to simply redistribute where gas absorption occurs. When instead a fixed value of concentration is maintained on the upper surface, the bubbles drawn down by Langmuir cells are replaced by other bubbles (in a rather unphysical way), and the flux increases.

Thus wave-current interaction, though important for bubble cloud structure, is less important for gas exchange. What about the injection length (which following *Rapp and Melville* [1990] may be strongly dependent on the wave height)? Figure 4 demonstrates that varying the injection length may be extremely important. In both 4a and 4b, the mixing is assumed to be given by a wall layer with $K_v = \kappa u_* \min(L_{mo}, z)$. Figure 4a demonstrates that when L_i is small, the strength of the mixing (which in this case goes solely as the friction velocity) plays a major role in determining how much gas enters the water column. However, when L_i is large (2 m) the gas flux has a much weaker dependence on mixing. The effects of heat fluxes are even less significant. Heat fluxes will only play a role if L_{mo} is of the same size as L_i . But as shown in Figure 4b, given a reasonable range of heat fluxes, the friction velocity must be very small before any effect is seen. When the mixing is very weak, the injection depth rather than the mixing sets the rate of gas transfer.

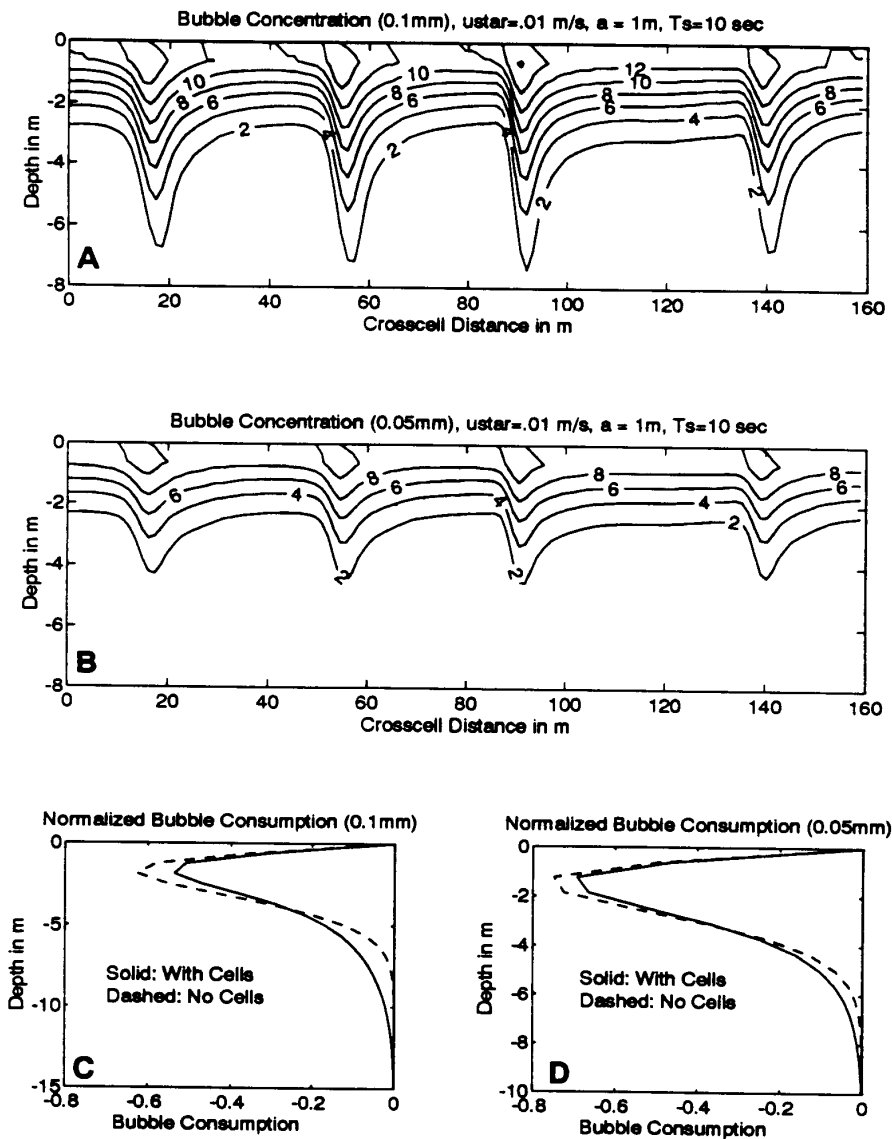


Figure 3: Langmuir cells with bubbles. Runs shown are for $u_{*} = 0.01$ m/s, wave height of 1 m, peak period of 10 sec, and a grid spacing of 0.63 m. (A) Bubble concentration (normalized to surface input), for 100 μ m bubbles. ($w_{rise} = 0.01$ m/s, $\alpha = 0.0015$ /m/s). (B) Bubble concentrations for 50 μ m bubbles, ($w_{rise} = 0.005$ m/s, $\alpha = 0.003$ /m/s). (C) Bubble absorption with (solid) and without (dashed) cells vs depth. (D) Bubble absorption with (solid) and without (dashed) cells vs. depth.

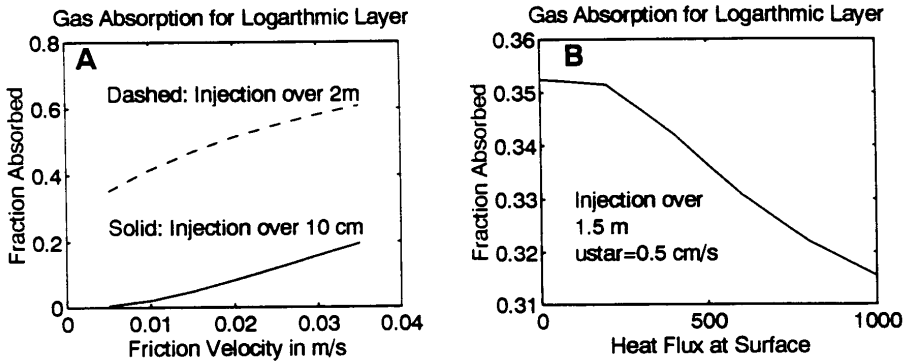


Figure 4: Fraction of bubble input absorbed predicted from one-dimensional model runs for equation (2) with $\alpha = 0.0015$ /s/m, $K_v = u_* \min(L_{mo}, z)$. (A) Two cases with no heat flux (L_{mo} infinite), but different values of L_i . For small L_i , the mixing is very important, but for larger values, the mixing plays less of a role. (B) Illustration of the weak dependence of outgassing fraction on heat flux when L_i is large enough so that $L_{mo} < L_i$.

5 Discussion and Conclusions

This paper has used observations and models of Langmuir cells to evaluate their importance in gas exchange relative to wave breaking. The new portion of this work is that it links on the spatial and temporal overturning scales associated with the cells to the surface forcing and demonstrates how these scales determine the structure of the bubble layer. In the presence of strong surface warming (particularly from insolation) and weak surface gravity waves, the spatial scales associated with turbulent overturns will become small (of the same size as the bubble layer) and a more uniform layer of bubbles will be seen. As waves become stronger and heat fluxes become more and more destabilizing, larger-scale Langmuir cells take over the transport of bubbles and create heterogeneous patches of bubbles.

As indicated by previous investigators [Thorpe, 1982, 1984] the effects of Langmuir cells on gas exchange, however, are quite weak. On average, large-scale Langmuir cells do not have fast enough overturning rates to remove bubbles from the surface. Large downwelling velocities extending right to the surface yield near surface vorticities which cannot be sustained for long given observed levels of forcing. It seems likely that observations of such large downwelling velocities coupled with bubble patches may be capturing part of the wave breaking event rather than the slower advection of bubbles associated with Langmuir cells. The length over which breaking waves inject bubbles (corresponding to the period when the boundary layer deepens quickly in the work of Rapp and Melville [1990]) is probably the most important part of the mixing cycle for gas exchange. Nonetheless Langmuir cells

still can play an important role since they are responsible for stirring the mixed layer on short time scales. As argued by *Gnanadesikan* [1994, 1995a] this fact may play an important role for gasses such as carbon monoxide, which can be rapidly consumed within the mixed layer. Additionally, it is possible that the cells may enhance the retention of larger, faster rising bubbles, if they can be transported to great enough depths. Lastly smaller-scale Langmuir cells may play a role in stirring the bubble layer, although the balance between the small-scale cells, shear-driven turbulence, and turbulence driven by wave breaking remains to be established.

Acknowledgements

This work was supported by the Office of Naval Research under grants N00014-90J-1495 and N00014-91J-1891. The data reported here was collected by the Upper Ocean Processes Group at Woods Hole Oceanographic Institution under the direction of Bob Weller and Al Plueddemann.

References

- Craik, A. D. D., and S. Leibovich, A wave-current interaction model for Langmuir circulation, *J. Fluid Mech.*, 73, 401-426, 1976
- Gnanadesikan, A., Langmuir circulations in the oceanic surface layer, Ph. D. Thesis, 354 pp., MIT/WHOI Joint Program in Oceanography and Oceanographic Engineering, *WHOI Tech. Report* 94-23, 1994
- Gnanadesikan, A, Modelling the diurnal cycle of carbon monoxide: Effects of physics, chemistry, biology, and optics, subm. to *J. Geophys. Res.*, 1995a
- Gnanadesikan, A, Mixing driven by vertically variable forcing: An application to the case of Langmuir circulations, subm. to *J. Fluid Mech.*, 1995b
- Huang, N., On the surface drift currents in the ocean, *J. Fluid Mech.*, 91, 191-208, 1979
- Leibovich, S., Convective instability of stably stratified water in the ocean, *J. Fluid Mech.*, 82, 561-583, 1977
- McDaniel, S.; Sea surface reverberation: A review. *J. Acoust. Soc. Am.*, 94, 1905-1934, 1993
- Plueddemann, A. J., J. Smith, D. M. Farmer, R. A. Weller, W. R. Crawford, R. Pinkel, S. Vagle, and A. Gnanadesikan, Structure and variability of Langmuir circulation during the Surface Waves Processes Program, subm. to *J. Geophys. Res.*, 1995
- Rapp, R. J., and W. K. Melville, Laboratory measurements of deep-water breaking waves, *Phil. Trans. R. Soc. Lon. A.*, 331, 735-800, 1990
- Thorpe, S. A., On the clouds of bubbles formed by breaking wind-waves in deep water and their role in air-sea gas transfer, *Phil. Trans. R. Soc. Lon. A.*, 304, 155-210, 1982
- Thorpe, S. A., The effect of Langmuir circulations on the distribution of submerged bubbles caused by breaking wind waves, *J. Fluid. Mech.*, 142, 141-170, 1984
- Weller, R. A., M. A. Donelan, M.G. Briscoe, and N. E. Huang, Riding the crest: A tale of two wave experiments, *Bull. Amer. Met. Soc.*, 72, 163-183, 1990

Zedel, L., and D. M. Farmer, Organized Structures in subsurface bubble clouds: Langmuir circulation in the open ocean, *J. Geophys. Res.*, *91*, 8889–8900, 1991

Bubble Size Distributions in Coastal Seas

Gerrit de Leeuw and Leo H. Cohen

TNO Physics and Electronics Laboratory
P.O. Box 96864, 2509 JG The Hague, The Netherlands
Phone +31 70 326 42 41
FAX +31 70 328 09 61
email: deleeuw@tnofel.fel.tno.nl

Abstract

Bubble size distributions have been measured with an optical system that is based on imaging of a small sample volume with a CCD camera system, and processing of the images to obtain the size of individual bubbles in the diameter range from 30 to 1000 μm . This bubble measuring system is deployed from a buoy which is either self-contained or which is connected to a ship or platform and uses electrical cables to receive power and transmit data. Results are presented from bubble measurements at the North Sea, the North Atlantic and the Baltic. The influence of meteorological parameters on the bubble size distributions and the bubble concentrations is discussed.

1 Introduction

Bubbles are produced by the entrainment of air by breaking waves. The air breaks up into bubbles which are dispersed throughout the water column by turbulent transport and other processes such as Langmuir circulation. The vertical extension of the bubble plume may be 10–20 m in high wind speeds. The evolving bubble plume, consisting of bubbles with a wide spectrum of sizes, rises to the surface. The bubble rise time depends on the bubble size. Large bubbles reach the surface very fast due to their large buoyancy. Small bubbles are near-neutrally buoyant and have a very small rise speed. The spectral distribution of the smaller bubbles is affected by processes such as coagulation and gas exchange at the bubble surface. Through coagulation, the small bubbles may be taken up into larger bubbles, while on the other hand the bubbles may go into solution and thus disappear. The suspended bubbles affect the propagation of acoustic radiation due to scattering and absorption.

When the bubbles reach the surface, they burst and produce acoustic noise [Spiel, 1991]. The bursting bubble cap may break up into a large number of small film *droplets* and subsequently jet drops are ejected from the rising hydrostatic jet [Blanchard, 1983; Spiel, 1994]. The *aerosol* limits the propagation of electro-magnetic radiation at wavelengths in the visible and infrared, plays a role in chemical transformations in the atmospheric boundary layer, while they can also act as cloud condensation nuclei. Furthermore,

sea spray aerosol may be important in the air-sea exchange of moisture and latent heat at high wind speeds [Andreas, 1992; Katsaros and De Leeuw, 1994; Fairall et al., 1995].

The importance of bubbles for air-sea gas exchange has been indicated [Lamarre and Melville, 1991; Wallace and Wirick, 1992; Farmer et al., 1993]. Climatologically and environmentally important gases are involved. For a greenhouse gas such as CO₂, the ocean is an important reservoir and acts as a buffer. The air-sea exchange of both aerosols and gases plays a role in the geochemical cycles affecting the Earth climate.

The above summary indicates the importance of bubbles for various processes. However, detailed knowledge on the effects of bubbles is still lacking. The study of this influence is one of our objectives to measure the bubble size distributions in combination with gas fluxes near the air-sea interface. Another objective is to derive a quantitative source function for sea spray aerosol as function of meteorological and oceanographic parameters, from simultaneous measurements of aerosol and bubble size distributions. In this contribution results are presented from measurements of bubbles in the *North Sea*, the *North Atlantic* and the *Baltic*. Bubble size distributions are compared with data available from the literature and the dependence on meteorological parameters of both the bubble concentrations and the shape of their size distributions is discussed.

2 The Bubble Measuring System

Bubble size distributions are measured with an optical system that has been described in De Leeuw and Cohen [1994]. The bubble measuring system (BMS) was developed by the TNO Physics and Electronics Laboratory (TNO-FEL) to measure the size of single bubbles in sea water, in the diameter range from 30 to 1000 μm , from which the bubble size distribution can be obtained. It uses a diode laser to illuminate the sample volume that is imaged by a telescope on a CCD camera. The length of the sample volume is limited by conical tubes in which windows and lenses are mounted. The length of these tubes has been chosen such that bubbles cannot pass through the laser beam outside the sample volume and cause erroneous signals. The conical shape has been chosen to reduce the creation of turbulence near the sample volume. The camera signal is fed into a dedicated processing board for on-line analysis of the size and shape of objects in the sample volume. The images are also recorded on S-VHS video tape as a back-up. The BMS was calibrated with simulated bubbles, i.e. circles drawn on paper which were reduced photographically to a known size. By using several simulated bubble sizes a calibration curve could be obtained. Based on this exercise, the smallest bubble size that we can reliably measure has been determined as 30 μm .

2.1 Data Processing

The data processing is based on discrimination between bubbles and other objects in the video image by their aspect ratio, i. e. the ratio between the horizontal and vertical dimensions of the object. Based on many visual observations the bubbles are assumed spherical whereas other objects would not be. Objects with non-spherical shapes are assumed to be particles or algae. The total number of such objects is retained in the data files, but their size distributions are not.

However, in conditions of very little or no wave breaking in shallow water near the Danish coast, large numbers of 'bubbles' were counted. Obviously the above selection criterion was not adequate. Therefore other criteria have been implemented in the processing algorithm that not only look at the shape of the object but also consider the 'fill factor', i. e. the amount of shading inside the bubble [Coonen, 1995]. Visual inspection indicated that many biological objects are transparent. Bubbles, due to their spherical shape, reflect and refract the light and thus appear as a dark homogeneous sphere in an image, apart from a small central spot where the light is transmitted through the bubble. In addition, the calibration algorithm has been modified resulting in a higher accuracy which allows for detection of bubbles that are about a factor 2 smaller than with the original software [De Leeuw and Cohen, 1994]. These changes have recently been implemented and the first tests have shown that the detection of bubbles and the discrimination between bubbles and other objects is satisfactory.

3 Deployments

For the deployment of the BMS at open sea or in coastal waters, two different buoy systems were developed. One is self-contained and transmits the data (images) to a receiver ashore. This allows for the deployment of the BMS at distances up to 18 km with line of sight to the receiver station (ship or ashore). This large buoy system has a total length of 7 m, including the antenna. Power is supplied by batteries mounted in a box at the bottom, that also provides the required counterweight. The float is a 2-m wide toroid. The BMS can be mounted at depths between 1 m and 3 m. The other buoy system was designed for measurements at close range from a ship or platform, to which it is connected with electrical cables with a length of 100 m for power and data transmission. Floatation is provided by a life-buoy. The BMS is mounted at the bottom of the pole extending 0.5-2 m (adjustable) below the surface. Both buoy systems have a gimbal construction to allow the float to follow the motions of the water surface while the BMS is kept horizontal at a fixed depth below the instantaneous water surface. The bubble measuring system has been deployed in the North Sea, in the North Atlantic and in the Baltic. The conditions at these locations were quite different, both in an oceanographic sense and meteorologically. Hence different influences on

Table 1: Overview of deployments of the TNO-FEL bubble measuring system

Experiment	Location		period	water depth m	bubble depth m	wind speed m/s	water temp °C	air temp °C
ASGASEX/ MAPTIP	MPN tower	North Sea	Sep/ Oct 93	18	0.5, 1	3-17	15.3- 17.2	10.9- 19.1
BUBBLES I	Inisheer	North Atlantic	Sep 94	70	1.5	2.5- 12	14.5- 16.3	11.7- 16.4
Lolland I	Vindeby	Great Belt (Baltic)	Oct/ Nov 94	2	0.38	2-12	8	5-12
OMEX	Belgica	North Atlantic	Mar 95	> 100	0.38	7-14	11.3- 12.2	8.8- 11
Lolland II	Vindeby	Great Belt	Apr 95	2	0.38	0- 10.5	8- 13.8	1.2- 18.6
OMEX	Valdivia	North Atlantic	Jul 95	> 100	0.4	—	—	—

the bubble size distributions would be revealed from results at these locations. Details are briefly discussed below. An overview of the deployments is presented in table 1.

3.1 North Sea Deployment: ASGASEX and MAPTIP

The North Sea deployment, during the experiments *ASGASEX* [Oost, 1994] and *MAPTIP* [Van Eijk et al., 1994] from Meetpost Noordwijk (MPN, a tower 9 km off the Dutch coast) in September and October 1993, was the first field test of the BMS. The objective was to test the system in open sea, to use the data in conjunction with acoustically measured bubble plumes for the analysis of simultaneously measured air-sea gas fluxes, and to derive aerosol source functions. Although quite some problems were encountered, the results were encouraging. The bubble spectra compare favorably with other data in similar conditions. The variations in the bubble concentrations could be qualitatively explained in terms of meteorological parameters [De Leeuw and Cohen, 1994]. Unfortunately the data set was too small for quantitative analysis.

3.2 North Atlantic Deployment (Inisheer)

The deployment of the BMS in the North Atlantic was in the framework of a dedicated study on the effect of bubbles on air-sea gas exchange. The study was made off the Irish coast, 5.4 NMi SW of the Island of Inisheer (Aran Islands), in 70 m deep water, in September 1994. Other participants (UCG, Galway, Ireland and SUDO, Southampton, UK) measured bubble plumes with

acoustical methods, gas saturation, wave spectra and made STD soundings. TNO-FEL measured aerosol particle size distributions from the Inisheer Lighthouse. The BMS was deployed at about 1.5 m below the water surface. This was the first deployment of the large buoy system and the signal was much weaker than expected over this distance. Although an additional amplifier was applied for the data recording and a software filter was used to reduce the noise, the quality of the recorded data was not sufficient to reliably derive bubble size distributions. Some qualitative results are available. The system has been improved for the deployments planned at the same site in August/September 1995.

3.3 Lolland Experiments

The 'Baltic' deployments were in the Danish coastal seas, off the coast of Lolland, in an off-shore windmill park near the village Vindeby, in October/November 1994 and in April 1995. The BMS was deployed on the small float, which was attached to one of the wind mills where the data were recorded via the cable. The system was operated unattended. This deployment was made in the framework of a study on the influence of sea spray aerosol on ammonia (NH_3) profiles. Previous observations of NH_3 profiles over water have shown that the gradients near the surface are very large [Asman *et al.*, 1993]. Thus the NH_3 fluxes determined from the profiles are unrealistically high. NH_3 is known to react rapidly with sea salt aerosols. The objective of this project was to test the hypothesis that the higher concentrations of sea spray aerosol near the surface are responsible for the scavenging of NH_3 , thus causing the strong gradients. The bubble size distributions were measured for modeling the air-sea gas transfer and the sea salt aerosol production. Aerosol size distributions were simultaneously measured and are used for testing the above hypothesis and for modeling the aerosol production. CO_2 fluxes were measured for comparison of the fluxes of reactive and highly solvable NH_3 with those of the inert and slowly dissolvable CO_2 . In addition, a new technique was tested to measure CO_2 fluxes with two IR CO_2 concentration fluctuation meters [Larsen *et al.*, 1995].

3.4 OMEX Cruises: North Atlantic

The main objective of our involvement in the OMEX program is to describe the general flux structure and in particular the exchange of CO_2 between the ocean and the atmosphere in the OMEX areas. The purpose of these efforts is to contribute to the study of the exchange processes at the ocean margins (OMEX=Ocean Margin EXchange), and in particular the carbon cycle [Wollast, 1993]. In the framework of the OMEX program three cruises are planned in 1995 to study the geochemical cycling of biogases. The Belgica cruise took place in March, from Boulogne via Bayonne to Zeebrugge. The Valdivia cruise takes place in July, from Cork via Lisbon to Hamburg. The

Poseidon cruise is planned for September, from Reikjavic to Lisbon. On all these cruises CO₂ fluxes have been or will be measured with the two sensors method [Larsen *et al.*, 1995]. Bubbles are measured only from the Belgica and the Valdivia.

4 Results

A detailed analysis of the results from the North Sea deployments during ASGASEX and MAPTIP was presented in *De Leeuw and Cohen* [1994]. Our data compare favorably with those published in the literature. However, as discussed in *section 2.1*, the results from the Lolland I experiments showed that objects/species were often counted as bubbles because the processing software did not reliably discriminate between bubbles and other spherical objects. After implementation of the new algorithm the ASGASEX data were re-processed, but the size distributions were not significantly different. Hence the observations and conclusions presented in *De Leeuw and Cohen* [1994] are still valid. In summary, a wind speed dependence was clearly observed, but also a dependence on wind direction (fetch). Because the data set is too small for a sub-division based on fetch, a quantitative relation for the dependence of the bubble concentrations on wind speed could not be derived.

Examples of ASGASEX bubble size distributions are presented in Figure 1. With the new processing algorithm, we have confidence that bubbles with sizes down to about 30 μm can reliably be measured. The data in Figure 1 are for wind speeds (U_{10}) ranging from 6.2 m/s to 14.3 m/s. The spectra do not show a clear variation with wind speed, although the concentrations are lower for the lowest wind speed, whereas the concentrations for wind speeds of 10.5, 11 and 14.3 m/s are all similar. This is in agreement with the observations presented in *De Leeuw and Cohen* [1994] that were summarized above.

The spectral shape of the bubble size distributions is similar, with a clear peak at 50-60 μm diameter and a sharp drop-off toward the larger bubbles. Describing this drop-off as a power law, $dN/dD = CD^n$, where N is the number of bubbles per size interval per cm^3 and D is the bubble diameter, we see that in our spectra the value of n is approximately -3. At the lowest wind speed n is closer to -4, at the highest wind speeds n could be somewhat larger than -3. The stronger drop-off at lower wind speeds is confirmed by the data obtained at wind speeds of 8-10 m/s. The data presented above were from the ASGASEX/MAPTIP experiments in shallow coastal water (depth 18 m). The OMEX data presented in Figure 2 are for deep water near the ocean margins. Figures 2a and 2b show results obtained in wind speeds of 7-8 m/s and 10-13 m/s, respectively. Obviously, the concentrations are much smaller at the lower wind speed while the spectra seem to be wider. Describing the spectra for bubbles larger than about 100 μm again as a power law distribution, the value for n in the higher wind speed is close to -3, whereas in the lower wind

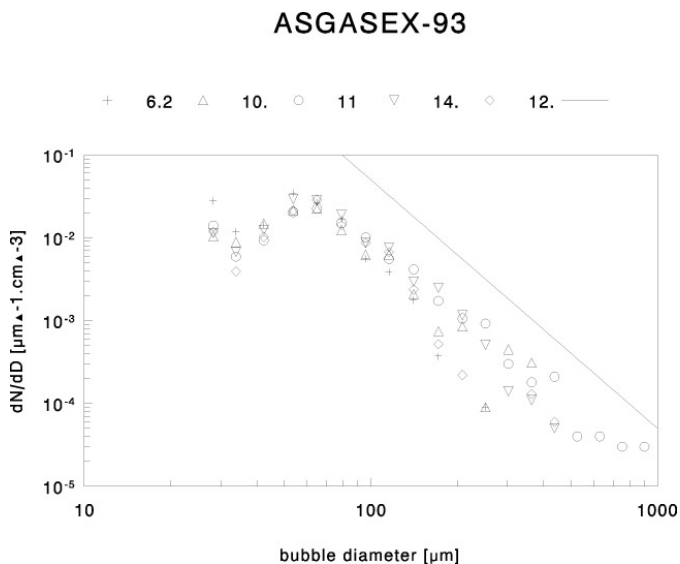


Figure 1: Bubble size distributions measured in the North Sea during the ASGASEX/MAPTIP experiments, for wind speeds ranging from 6 to 14 m/s (see legend)

speed n seems closer to -2 . This may be a consequence of the absence of larger bubbles, which biases the fit because it cannot be extended to sizes large enough to determine the drop-off with some confidence.

We also note that the spectral distribution at the lower wind speed is more peaked than at the higher wind speed. In both cases the spectra peak at diameters of about $50\text{--}70\ \mu\text{m}$ but for most of the spectra at the higher wind speed this peak is not really clear and the concentrations of bubbles with sizes between 40 and $100\ \mu\text{m}$ do not change much. The differences between the spectral shapes of the data presented in Figure 2 are confirmed when we consider the wind speed dependence of the bubble concentrations, Figure 3. Data are shown for bubbles with diameters from 42 to $209\ \mu\text{m}$. The concentrations of the bubbles increase faster with wind speed as the bubble size becomes larger. Hence the spectral shape of the bubble concentrations also changes with wind speed.

5 Discussion

Bubble size distributions measured in the North Sea and in the North Atlantic were analyzed according to their spectral shape and their dependence on meteorological parameters. Since at present not enough data are available for a statistically reliable analysis, only the effect of wind speed could quantitatively be analyzed. Qualitative results for other parameters have been indicated. Data from the Baltic were only qualitatively taken into account.

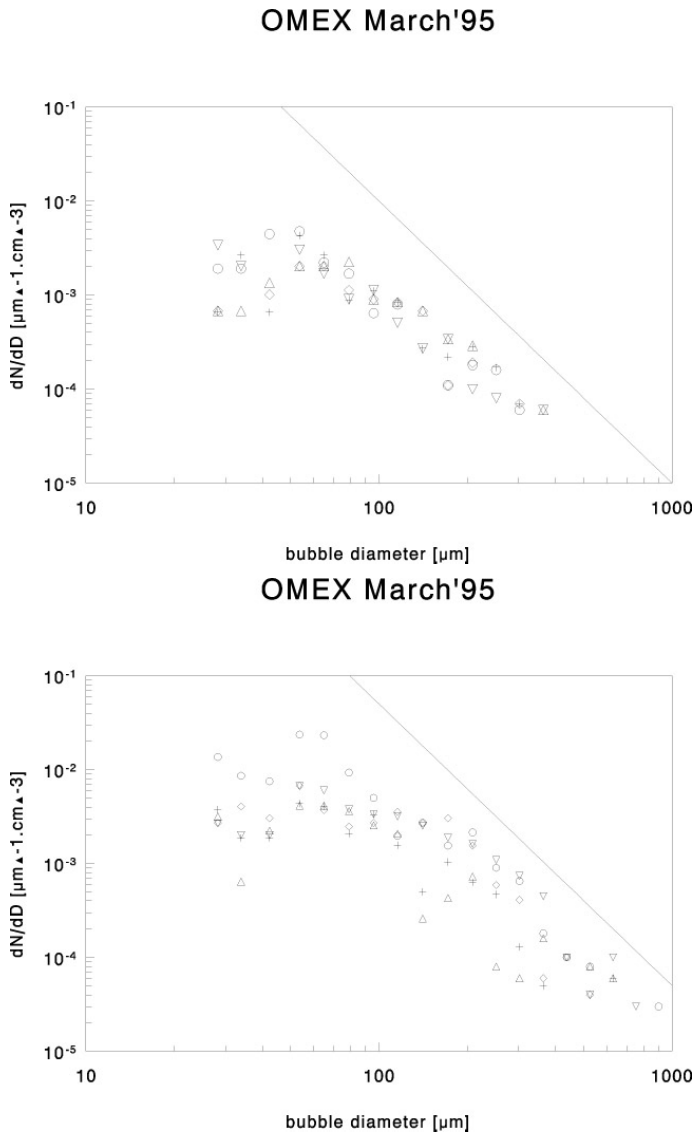


Figure 2: Bubble size distributions measured during the OMEX experiments in deep water at the North Atlantic, in wind speeds of 7-8 m/s (top) and 10-13 m/s (bottom).

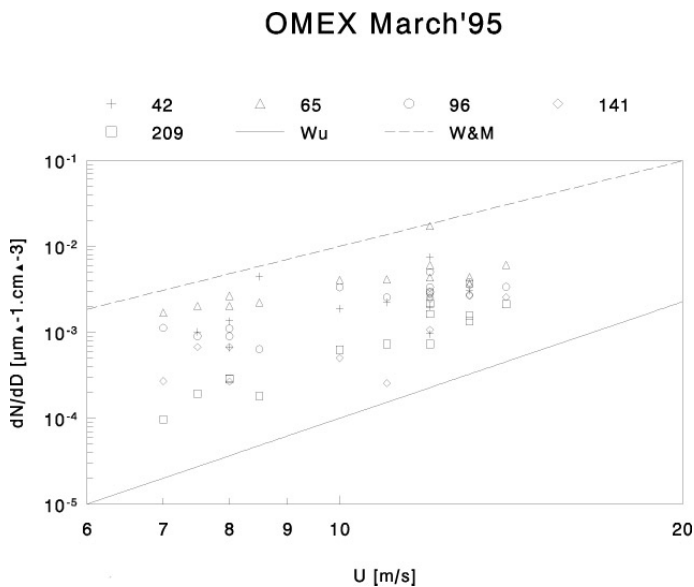


Figure 3: Bubble concentrations dN/dD as function of wind speed, for bubbles with diameters ranging from 42 to 209 μm (see legend). The relations presented by Wu [1981] (thick line) and Walsh and Mulhearn [1987] (dashed line) are indicated.

Spectral shape. The spectral shape of the bubble size distributions is similar for the North Sea and the North Atlantic. The spectra were observed to peak at diameters of 50-70 μm , the drop-off at larger sizes can be approximated by a power law distribution with a power of approximately -3. However, significant excursions from this value were observed and for individual spectra n can vary between -2 and -4. A clear wind speed dependence of the spectral shape cannot be given at this stage. In fact, the data from the North sea and the North Atlantic are contradictory. The North Sea data do not show any clear wind speed dependence, due to a large variation in wind directions resulting in different fetches in this coastal area. Therefore we presume that the large drop-off at higher wind speeds is due to other processes than in the North Atlantic. These processes need to be identified. Considerations are the young waves at the short fetches, the steeper and lower waves, and the resulting mixing processes. Also the atmospheric stratification (large air-sea temperature differences occurred during the North Sea experiments) may be important. The physics of the processes in and over the open ocean is usually less complicated than in coastal areas. Therefore we tend to believe that the wind speed dependence of both the spectral shape and the concentrations observed at the North Atlantic is a real phenomenon, whereas the observations over the North Sea present complications that need further investigation. Another observation which has to be explained is that the bubble concentrations in the North Sea are higher than in the North Atlantic, for

similar wind speeds (compare figures 1 and 2).

The spectral shape of the bubble size distributions is in reasonable agreement with data published in the literature. The spectral peak was observed for bubble sizes of 68 μm [Walsh and Mulhearn, 1987], 60–70 μm [Kolovayev, 1976], 40–50 μm [Johnson and Cooke, 1976] and 30–93 μm [Baldy and Bourguel, 1987]. A wide range of power law distributions were reported, with values of n ranging from -2 to -6. We note here that data in the literature are presented as $N(D)=CD^n$, i.e. the number of bubbles per cm^3 , whereas we have plotted the number of bubbles per size increment per cm^3 , dN/dD . Hence we should compare the values for n that we obtained with literature values of -3 to -7. Thus our values of about -3 are in reasonable agreement with some of those found in the literature: e. g., [Medwin and Breitz 1989] report an average value of -3.7, [Walsh and Mulhearn 1987] report an average value of -5 (with data ranging between -3.9 and -7), [Medwin 1970] reported $n = -3$, and [Kolovayev 1976] reported $n = -4.5$. [Blanchard and Woodcock 1957] reported $n = -4.7$, but also $n = -5.6$, however, which latter value is close to those reported by, e. g., [Johnson and Cooke 1976] ($n = -5.5$) and [Wu 1988] ($n = -5$).

Wind speed dependence. The North Atlantic wind speed dependence is similar to the sparse quantitative information in the literature. For the variation of the total bubble concentration with wind speed, [Wu 1981] obtained $N=Cu_{10}^{4.5}$ (7–11 m/s), and [Walsh and Mulhearn] found $N=Cu_{10}^{3.3}$ (6–14 m/s). These relations have been plotted in Figure 3. The wind speed dependence of the larger bubbles is similar to the that presented by Wu, whereas the increase of the concentrations of the smaller bubbles with wind speed is better described by the relation of Walsh and Mulhearn. The increase of the concentrations of the smallest bubbles with wind speed is actually somewhat weaker. Since the total concentrations are determined by those of the smaller bubbles, our data indicate a wind speed dependence given by $N=Cu_{10}^n$, where n is about 3.3 or somewhat smaller.

6 Conclusion

The above comparisons show the wide range of values that were observed for the spectral shape of the bubble size distributions. In view of these differences, unique answers can not yet be expected from studies on the effects of bubbles on the various processes described in the introduction. Much research still has to be done to determine the causes of these differences to come to a more reliable prediction of the bubble size distribution as function of depth, and as a function of meteorological and oceanographic conditions, to eventually determine the resulting bubble fluxes at the sea surface and the effects that these bubbles have on air-sea exchange processes.

Acknowledgement

The bubble measuring system was developed with support from the TNO Central Organisation and the Netherlands Ministry of Defence (assignment A92KM714). The ASGASEX measurements and the North Atlantic deployment were supported by EC DG XII (contract MAS2-CT93-0056) and the Netherlands Ministry of Defence (assignment A93KM635), the MAPTIP experiments were carried out with support from NATO (commitment numbers 6056 and 6092), the US Office of Naval Research ONR (contract N00014-91-J-1948) and the Netherlands Ministry of Defence (assignment A92KM715). The Baltic experiments were supported by the US Office of Naval Research ONR (contract N00014-91-J-1948). The OMEX measurements were carried out with support from EC DG XII (contract MAS2-CT93-0063) and the Netherlands Ministry of Defence (assignment A93KM676)

References

- Andreas, E. L. Sea spray and the turbulent air-sea fluxes, *J. Geophys. Res.* 97, 11,429-11,441, 1992
- Asman, W. A. H., L. L. Sorensen, R. Berkowicz, K. Granby, H. Nielsen, B. Jensen, E. Runge and C. Lykkelund, Dry deposition processes (In Danish: Processer for tordeposition). *Under the series Marine research from the Danish Environmental Protection Agency*, 1993
- Baldy, S., and M. Bourguel, Bubbles between the wave trough and the wave crest levels, *J. Geophys. Res.* 92, 2,919-2,929, 1987
- Blanchard, D.C., The production, distribution, and bacterial enrichment of the sea-salt aerosol, in *The air-sea exchange of gases and particles*, edited by P. S. Liss and W. G. N. Slinn, pp. 407-454, D. Reidel, Dordrecht, 1983
- Blanchard, D. C., and A. H. Woodcock, Bubble formation and modification in the sea and its meteorological significance, *Tellus* 9, 145-158, 1957
- Coonen, V.H., Modificaties op bubble processing software versie 3.0 t.o.v. versie 3.2 (in Dutch). Unpublished manuscript, 1995
- De Leeuw, G., and L.H. Cohen, Measurements of oceanic bubble size distributions, *Proc. Oceans* 94, 1994
- Fairall, C. W., G. J. Holland and J. D. Kepert, The effect of sea spray on surface energy transports over the ocean, *Atmos.-Ocean System*, in press
- Farmer, D. M., C. L. McNeil and B. D. Johnson, Evidence for the importance of bubbles in increasing air-sea gas flux, *Nature*, 361, 620-623, 1993
- Johnson, B. D., and R. C. Cooke, Bubble populations and spectra in coastal waters: A photographic approach, *J. Geophys. Res.* 84, 3,761-3,766, 1979
- Katsaros, K. B., and G. de Leeuw, Sea spray and the turbulent air-sea heat fluxes — Comments, *J. Geophys. Res., Oceans* 99 (C7), 14,339-14,343, 1994
- Kolovayev, P. A., Investigation of the concentration and statistical size distribution of wind-produced bubbles in the near-surface ocean layer, *Oceanology*, 15, 659-661, 1976
- Lamarre, E., and W. K. Melville, Air entrainment and dissipation in breaking waves, *Nature*, 351, 469-472, 1991

- Larsen, S. E., F. Aa. Hansen, G. de Leeuw and G. J. Kunz, Physical parameters controlling the fluxes in the marine atmospheric surface layer. *Ocean Margin Exchange OMEX*, Second Annual Report, 1995
- Medwin, H., In-situ acoustical measurements of bubble populations in coastal ocean waters. *J. Geophys. Res.* 75, 559-611, 1970
- Medwin, H., and N. D. Breitz, Ambient and transient bubble spectral densities in quiescent seas and under spilling breakers, *J. Geophys. Res.* 94, 12,751-12,759, 1989
- Oost, W. A., The ASGASEX experiment, KNMI Technical report TR-161, 1994
- Spiel, D. E., Acoustical measurements of air bubbles bursting at a water surface: bursting bubbles as Helmholtz resonators, *J. Geophys. Res.* 97, 11,443-11,452, 1991
- Spiel, D. E., The number and size of jet drops produced by air bubbles bursting on a fresh water surface, *J. Geophys. Res.* 99, 10,289-10,296, 1994
- Van Eijk, A. M. J., D. R. Jensen and G. de Leeuw, MAPTIP experiment, Marine Aerosol Properties and Thermal Imager Performance, in *Atmospheric Propagation and Remote Sensing III*, W. A. Flood and W. B. Miller, Eds., SPIE Proc. Vol. 2222, 299-315
- Wallace, D. R., and C. D. Wirick, Large air-sea gas fluxes associated with breaking waves, *Nature*, 356, 694-696, 1992
- Walsh, A. L. and P. J. Mulhearn, Photographic measurements of bubble populations from breaking wind waves at sea, *J. Geophys. Res.* 92, 14,553-14,565, 1987
- Wollast, R., Interactions of carbon and nitrogen cycles in the coastal zone, in *Interactions of C, N, P, and S biogeochemical cycles and global change*, R. Wollast, F. T. Mackenzie and L. Chou, Eds., NATO ASI series, Vol. 14, pp. 195-210, 1993
- Wu, J., Bubble populations and spectra in near surface ocean: summary and review of field experiments, *J. Geophys. Res.* 86, 457-463, 1981
- Wu, J., Bubbles in the near-surface ocean — a general description, *J. Geophys. Res.* 93, 587-590, 1988

Laboratory Measurements of Bubble Size Distributions Beneath Breaking Waves

M. R. Loewen¹, M. A. O'Dor¹, and M. G. Skafel²

¹Department of Mechanical Engineering
University of Toronto, Canada

²National Water Research Institute
Canada Centre for Inland Waters

Abstract

Measurements of the size distributions of large bubbles entrained by mechanically generated breaking waves in fresh- and saltwater are presented. Bubble size distributions were obtained by analyzing digital video images of the region immediately beneath and behind the breaking wave crest. This imaging technique was accurate for bubble radii, $r \geq 0.8$ mm. The bubble size spectra (N the number of bubbles per μm radius increment per m^3 plotted as a function of bubble radius r) were essentially the same in fresh- and saltwater. The bubble spectra are well represented by an exponential equation of the form $N \sim e^{-1.5r}$ or by a power law equation of the form $N \sim r^{-3.3}$. There were no significant differences between the depth distribution of the bubbles in salt- and freshwater. In both cases the data can be represented by $N = N_o e^{-z/h}$ where z is the distance below the free surface, h is the entrainment depth and N_o is the total bubble concentration at the free surface. N_o and h were found to be 4×10^5 and 1.0 cm, respectively. The fact that significant numbers of large bubbles are entrained by relatively small *breaking waves* (wavelength ~ 1.5 m) suggests that gas transfer due to large entrained bubbles may be important even at low sea states.

1 Introduction

Several studies have recently compared field measurements of air-sea gas exchange with model predictions [Farmer, McNeil and Johnson, 1993; Wallace and Wirick, 1992]. Wallace and Wirick [1992] found that estimates of the air-sea flux of oxygen, based on measurements of the dissolved oxygen, were up to three orders of magnitude greater and in some cases of opposite sign to predictions based on the thin film model and the Liss-Merlivat equations. They observed sudden increases in the dissolved oxygen concentrations followed by gradual decreases. A numerical simulation, in which the conventional thin-film model was coupled with a semi-empirical equation developed by Thorpe [1984] for calculating the gas exchange due to entrained air bubbles, predicted dissolved oxygen time series that were in qualitative agreement with the observations. Based on these results, Wallace and Wirick [1992] concluded that sudden increases in dissolved oxygen were caused by

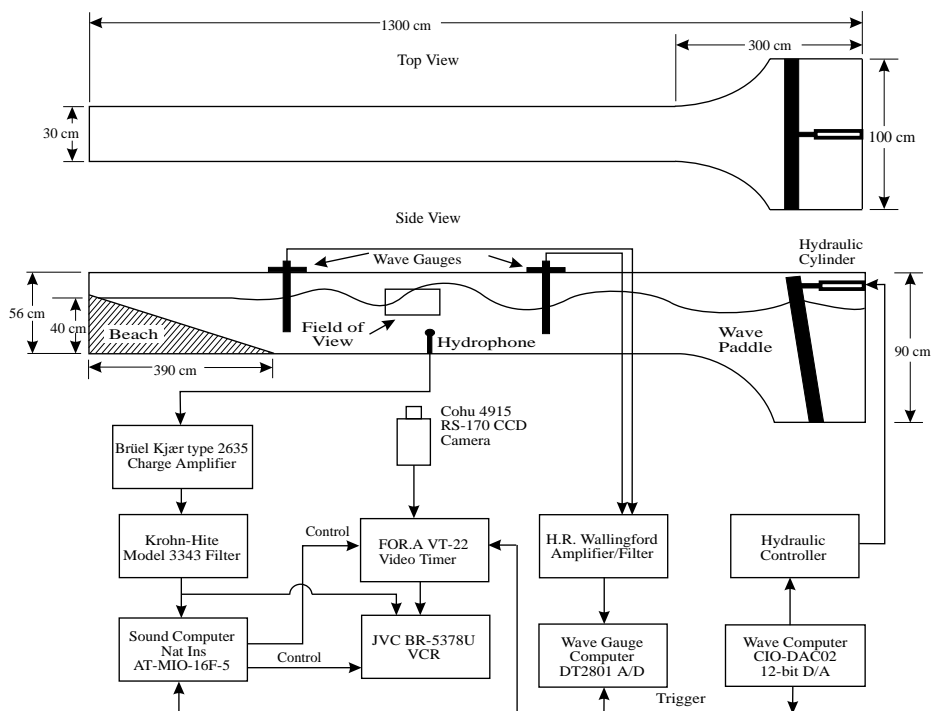


Figure 1: Schematic of the wave channel and experimental equipment.

the increased *air entrainment* associated with *breaking waves*. *Farmer et al.* [1993] measured a variety of parameters including dissolved oxygen during a storm in the Georgia Strait. They computed oxygen fluxes based on dissolved oxygen measurements and compared them to predictions derived from (a) the thin-film model which does not include the gas transfer due to bubble entrainment, and (b) the model of *Woolf and Thorpe* [1991] which parameterizes the gas transfer due to bubble entrainment. Both models under-predicted the observed dissolved oxygen levels by wide margins. These two studies clearly demonstrate the need for continued research into the effect of air entrainment by breaking waves on air-sea gas transfer.

Keeling [1993] used a model of bubble-induced gas exchange to investigate the role of *large bubbles* in air-sea gas exchange. He concluded that bubbles greater than 0.5 mm in radius contribute significantly to bubble-induced air-sea gas exchange. In addition, his results suggest that the majority of the enhanced air-sea gas transfer observed at windspeeds greater than 13 m/s is due to bubble entrainment by breaking waves.

Measurements of the size distributions of large bubbles have been made under simulated breaking waves such as waterfalls and tipping buckets by *Monahan and Zietlow*, [1969], *Cipriano and Blanchard* [1981] and *Haines and*

Johnson [1995]. Observations of the large bubbles entrained by breaking wind waves have been reported by Baldy and Bourguel [1987], Baldy [1988] and Hwang *et al.* [1990]. Baldy and Bourguel [1987] and Baldy [1988] used a laser-based single particle technique to measure bubble sizes in freshwater between the troughs and crests of wind waves in a wind-wave channel. Their main conclusions were:

- A bubble generation layer exists immediately below the free surface and below this is the dispersion layer dominated by turbulence and buoyancy effects;
- In the generation layer the slope of the bubble size spectrum is constant and approximately equal to -2;
- In the dispersion layer the slope of the size spectrum increases with depth approaching a value of -4;
- In the generation layer the bubble concentration increases exponentially with elevation as the free surface is approached.

Hwang *et al.* [1990] used an optical sensor based on the light blocking principle to measure bubble sizes in freshwater in a wind-wave channel. Their measurements were restricted to the region below the troughs of the waves. They observed an exponential decrease in the total bubble concentration with depth and found that the entrainment depth h (the e-folding depth) increased with wave amplitude. The slope of the bubble size spectrum increased with increasing depth from approximately -2 to -4.

Keeling [1993] noted that there is large degree of uncertainty in predictions of the bubble-induced air-sea gas exchange because of a lack of data on the production rates and size distributions of large bubbles (radius greater than 0.5 mm). We have addressed this issue by conducting a series of laboratory experiments to measure the bubble size distributions of large bubbles (0.8 - 5.0 mm radius) produced by mechanically generated breaking wave packets in fresh- and saltwater.

2 Experimental Procedure

The experiments were conducted in a *wave channel* located at the Canada Centre for Inland Waters, Burlington, Ontario. The glass walled channel was 10 m long and the test section of the channel where the measurements were made was 30 cm wide and was filled with water to a depth of 40 cm. A computer controlled hinged hydraulic *wave paddle* was located in an enlarged steel-walled section at the end of the channel. The larger section was smoothly contracted to the dimensions of the test section as shown in figure 1. The wave paddle was programmed to focus a dispersive wave packet at a point $x_b = 5.8$ m from the wave paddle. This technique has been extensively used to investigate the behavior of spilling and plunging deep-water breaking waves [Chan and Melville, 1988; Rapp and Melville, 1990; Loewen

and Melville, 1991]. Measurements were made of the water and air temperatures, surface displacement (fractional energy dissipation) and underwater sound. A detailed schematic of the experimental equipment is plotted in figure 1. Video recordings of the breaking waves were used to determine the size and location of entrained bubbles. Experiments were conducted in both fresh- and saltwater. The saltwater was 3.4% concentration by weight produced by adding NaCl to fresh tap water.

2.1 Breaking Wave Generation

A wave packet was synthesized from 32 sinusoidal components of constant slope ak , where a is the component amplitude and k is the component wavenumber. The wave components were equally spaced over a frequency bandwidth of $\Delta f = 0.7$ Hz and centred at a frequency of $f_c = 1.12$ Hz. Linear wave theory predicts a range in wavelengths from 0.64 m to 2.16 m for frequencies of $1.12 \text{ Hz} \pm 0.35 \text{ Hz}$. Breaking waves were generated using a personal computer and DAC (digital to analog converter) to convert a synthesized digital signal to an analog signal which was transmitted to the wave paddle hydraulic controller, see figure 1. This technique produces very repeatable breaking events and allows measurements to be averaged over repeated runs with the same breaking wave.

2.2 Surface Displacement Measurements

The surface displacement in freshwater was measured with a set of resistance wave gauges and digitally sampled at a rate of 40 Hz. The wave gauges and signal conditioning electronics were purchased from HR Wallingford Limited (Wallingford, U.K.). The sensing elements were two 610 mm long, 6 mm diameter stainless steel rods mounted 50 mm apart on a supporting frame. Aliasing of the signals was prevented by filtering the analog signals with a low pass filter with -3 dB cut-off frequency of 20 Hz prior to digitizing.

The wave gauges were calibrated by sampling the still water level for 20 seconds at 6 vertical positions from -8 cm to +10 cm. A linear equation was fitted to the average voltage at each amplitude to give a calibration equation relating the voltage to the surface displacement. The correlation coefficient was always ≥ 0.99999 indicating that the gauges response was linear. The gauges were calibrated approximately every three hours in order to minimize the errors due to variations in the calibration coefficients. Runs were separated by three minutes to allow surface oscillations in the channel to decay to negligible amplitudes.

The repeatability of the wave packets was monitored by measuring the position of the wave paddle. The wave maker system included a position transducer which produced an analog signal proportional to the linear position of the paddle. This signal was sampled at 40 Hz along with the wave

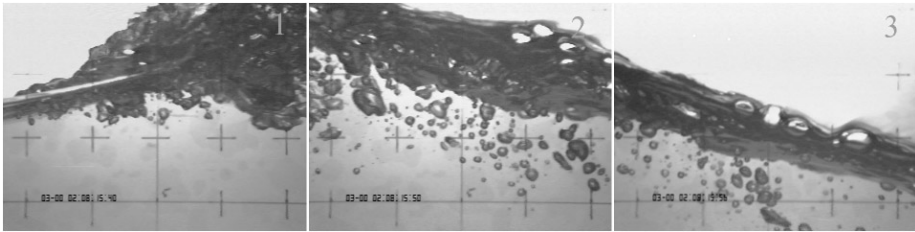


Figure 2: Three digital video images of the freshwater wave with $G = 0.76$ at horizontal position 6. Image 1 was at $t = 15.40$ s after the initiation of paddle movement. The wave is moving from right to left in all the images. Image 2 is at $t = 15.50$ s, 3 frames after image 1. Image 3 is at $t = 15.56$ s, 2 frames after image 2.

gauge signals and the variance was checked to ensure that repeated runs of the same wave packet slope produced equal variances.

2.3 Video Recordings and Image Analysis

A Cohu 4915 RS-170 CCD video camera equipped with a Computar 1:1.2 / 12.5-75 mm TV zoom lens was mounted on a tripod so that it viewed the breaking waves from the side through the glass sidewall. The camera was mounted so that it looked up at the underside of the free surface at an angle of approximately 5 degrees. This helped to prevent the rippled and folded surface of the breaking wave crest from obscuring bubbles. A FOR.A VT-22 Video Timer imprinted a time base accurate to 1/100 second directly into the corner of every recorded image. The video signals were recorded in VHS format using a JVC BR-5378U VCR. The breaking waves were backlit by placing a 150 watt spotlight approximately 50 cm behind the far channel wall. A sheet of drafting Mylar was taped to the backside of the far channel wall to diffuse the light. The spotlight was positioned so that the brightest spot of light coincided with the vertical location of the crest as the breaking wave moved through the field of view. This arrangement provided enough light that the aperture of the camera lens could be almost completely closed at the shutter speed of 1/2000 second thus maximizing the depth of field. It also provided more light near the free surface where bubbles were harder to distinguish against the dark background of the free surface.

Three digital images are shown plotted in figure 2 for the freshwater wave with $G = 0.76$. The three images were recorded at the same camera position. Image 1 shows the breaking wave crest advancing from right to left. Bubbles are being entrained near the leading edge and are left behind by the fast moving crest. Images 2 and 3 show the entrained bubbles after the crest has passed i.e. beneath the rear face of the breaking wave. A grid (2×2 cm), as seen in figure 2, was drawn on the glass wall of the channel as an aid in positioning the camera and as a length scale for sizing the bubbles.

The camera was positioned so that the lens was 118 cm from the near edge of the channel. The zoom lens was adjusted so that the field of view was 9.4 cm by 6.7 cm. The width of the field of view was smaller than the length of the breaking region and therefore the camera and light were moved along the channel to image the entire wave. Six to eight camera locations were required to cover a given wave. At each location ten repeats of the same amplitude wave were recorded. With this set-up it was impossible to determine the position of a bubble across the channel. When computing the bubble size it was assumed that all the bubbles were located at the middle of the channel. Therefore, the computed size of bubbles at the near and far walls are over- and underestimated by 6% respectively. The smallest radius bubbles that could be resolved with this set-up was estimated to be 0.2 mm.

The depth of field was difficult to determine exactly because the aperture of the camera was opened such that without a wave in the field of view the picture was over-exposed. When a breaking wave was present the bubbles and free surface scattered and reflected enough light that the image was not over-exposed, see figure 2. Based upon visual examination of the images the depth of field for bubbles larger than 0.8 mm radius was estimated to be the entire width of the channel, 30 cm. Image quality (i.e. contrast and sharpness) was not constant for all images therefore in some cases the depth of field may have been reduced to approximately 75% of the width or 23 cm. For all the image analysis the depth of field was taken to be 30 cm.

Bubble sizes and locations were determined by first digitizing the video images using a DT3851 frame grabber board and Global Lab Image software (Data Translation). The images were then processed using a Matlab program (The Mathworks Inc.). Images were displayed on the computer screen and bubbles and other features were visually identified. The computer mouse was used to locate and size specific features. The size and location of bubbles was found by clicking the mouse on two or four points (for spherical or ellipsoidal bubbles respectively) on the circumference of the bubble and then fitting a circle or ellipse to the selected points. The length scale for an image was determined by selecting three of the intersection points of the grid drawn on the near wall of the channel, see figure 2. The lines where the free surface intersected the front and rear glass walls of the channel were determined by selecting approximately ten points along each line. The location of the free surface was taken to be the average of the two lines. The vertical location of the bubbles was computed as the distance below this average free surface location. Using this procedure the vertical location of some bubbles is negative (i.e. above the free surface) and for these cases the bubbles were assumed to be at the free surface.

Bubble size distributions were computed by summing the number of bubbles in 0.2 mm radius increments centred at $r = 0.1, 0.3, 0.5 \dots 4.9$ mm. The volume occupied by the bubbles in each image was computed by dividing the image into ten vertical strips and locating the highest and lowest elevation bubbles in each strip. The volume occupied in each strip equals the height

(the elevation difference between the highest and lowest bubbles) times the width of the strip (1/10 of the image width) times the depth of field (channel width, 30 cm). The total volume in each image is the sum of the ten strip volumes. Then for each image the number of bubbles per mm radius bin per m^3 is computed.

3 Results

The water temperature was measured with a Newport model 267B digital thermometers calibrated to $\pm 0.1^\circ\text{C}$. During the course of the experiments the water temperature varied by a maximum of 2°C for a given wave amplitude and for all wave amplitudes was within the range 20.1°C to 22.8°C . These temperature variations are considered negligible because variations this small do not have a significant effect on the process of air entrainment [Hwang et al., 1991].

The fractional energy dissipated by breaking is given by

$$D = (\eta_0^2 - \eta_f^2) / \eta_0^2 \quad (1)$$

where η_0^2 and η_f^2 are the surface displacement variances upstream and downstream of the breaking event [Rapp and Melville, 1990]. Video images of waves with gains of, $G = 0.75, 0.76$ and 0.77 , were analyzed. These amplitudes produce spilling and small plunging breaking waves and correspond to fractional dissipation values of 4% to 6% due to breaking. Larger amplitude waves which dissipated more energy produced bubble clouds that were too dense to analyze accurately with this imaging technique. Ten repeats of each amplitude wave were repeated at each horizontal location of the camera. The third or fourth frame after the breaking wave crest first appeared in the field of view was digitized. In figure 2 image 2 was analyzed because it is the fourth frame after the crest first appeared in the field of view. The images from every other horizontal position were analyzed. A total of 30 to 50 images were analyzed for each wave.

A plot of a typical bubble size distribution (N the number of bubbles per mm radius increment per m^3 versus the bubble radius r) of a freshwater wave with $G = 0.77$ is shown in figure 3. The data are averaged over ten images or repeats of the wave at horizontal position 6 (position 8 is the farthest upstream and position 1 the farthest downstream). The variance in the data is greater at larger bubble sizes because of the smaller number of larger bubbles. The bubble size distributions (i.e. the number of bubbles per mm radius per m^3) for all six waves are shown plotted in figure 4. The freshwater data in figure 4b clearly show that for a given radius the number of bubbles per unit volume is independent of the amplitude or steepness of the wave packet. The steeper freshwater waves entrain more bubbles but the volume over which they are dispersed also increases and therefore the

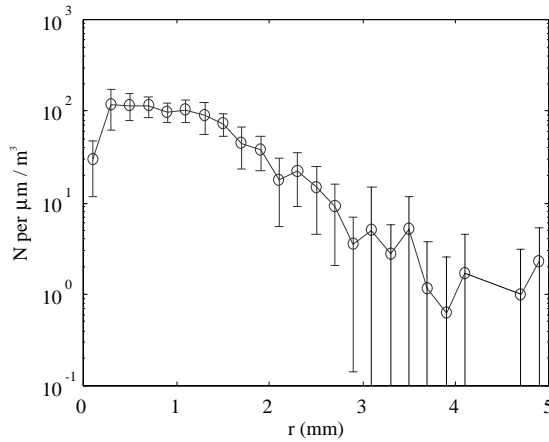


Figure 3: The bubble size spectrum, N the number of bubbles per mm radius increment per m^3 versus r the bubble radius, for the freshwater wave with $G = 0.77$. The data were obtained by averaging over ten repeats i.e. ten images. The radius bins are 0.2 mm wide centred at 0.1, 0.3 ... 4.9 mm. The error bars denote plus or minus one standard deviation.

density of bubbles remains approximately constant. This is not the case for the saltwater data in figure 4a where the size distributions for the largest amplitude packet $G = 0.77$ has consistently higher bubble densities than the two lower amplitude packets for $r > 0.8$ mm.

For all six waves the bubble density increases as the bubble radius r decreases until a maximum value is reached and it then decreases as r decreases further. The location of the maximum bubble density varies from $r = 0.3$ mm - 0.9 mm. Previous investigations have shown that the maximum bubble density should occur at a much smaller radius than indicated in figure 4 [Johnson and Cooke, 1979; Baldy, 1988]. The smallest bubble size which could be detected based on the resolution of the video recordings was $r = 0.2$ mm. However, the data in figure 4 indicate that the imaging technique used here is only consistent down to a bubble radius of $r = 0.8$ mm because some of the bubble size spectra have a maximum at radii as large as 0.9 mm (note that the bin centred at $r = 0.9$ mm covers the range $r = 0.8$ -1.0 mm). In these experiments it was not possible to detect and accurately size all of the bubbles entrained because; (i) smaller bubbles may be hidden behind larger ones, (ii) bubbles very close to the free surface were difficult to detect because of the lack of contrast between the background (the underside of the free surface) and the bubbles, see figure 2, and (iii) the depth of field for bubbles less than $r = 0.8$ mm was less than the full width of the channel and therefore small bubbles near the rear channel wall were not detected.

The salt- and freshwater data are directly compared in figure 5. The

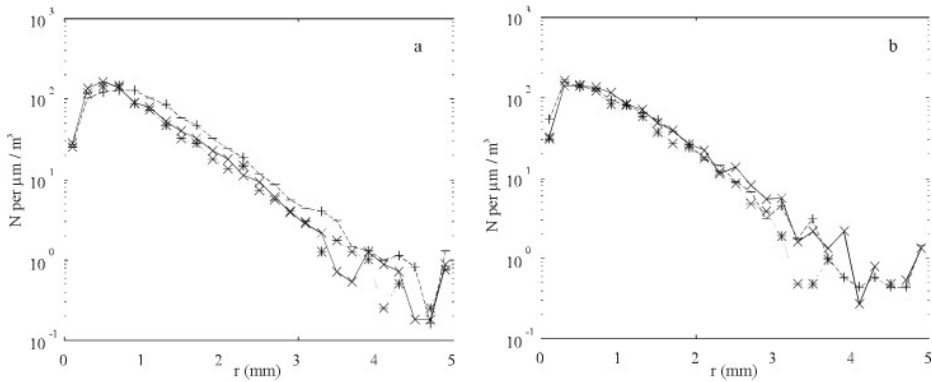


Figure 4: The bubble size spectrum for the three saltwater waves in (a) and the three freshwater waves in (b). +, × and * correspond to $G = 0.77, 0.76$ and 0.75 respectively.

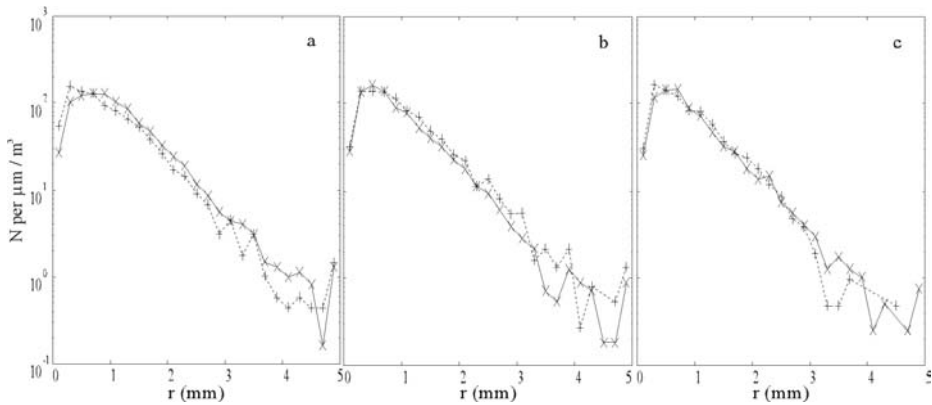


Figure 5: A comparison of the salt- and freshwater bubble size spectra. Figures (a) $G = 0.77$ (b) $G = 0.76$, and (c) $G = 0.75$, × saltwater, + freshwater.

differences between the salt- and freshwater size distributions are small particularly for the two smaller amplitude packets. The largest saltwater wave does have consistently larger bubble densities but given the variance in the data (see figure 3). These differences may not be significant.

In figure 6 the bubble size distribution for the saltwater wave with $G = 0.76$ is plotted. Figure 6a is a semilog plot of N versus r and an exponential equation of the form

$$N = A_1 e^{\beta r} \tag{2}$$

where A_1 and β are constant has been fitted to the data. Figure 6b is a log-log plot of N versus r and a power law equation of the form

Table 1: List of constants in the exponential and power law equations, see equations 2 and 3. A least squares procedure was used to fit the equations to the data.

Wave ¹	Exponential Fit			Power Law Fit		
	β	A1	Correlation coefficient	α	A2	Correlation coefficient
S77	-1.454	467	0.9779	-3.2539	149	0.9475
S76	-1.540	382	0.9721	-3.4821	117	0.9514
S75	-1.501	332	0.9782	-3.3598	104	0.9617
F77	-1.463	363	0.9688	-3.3202	120	0.9514
F76	-1.424	377	0.9643	-3.1805	125	0.9463
F75	-1.729	490	0.9698	-3.4095	104	0.9375

¹S = salt water, F = fresh water

$$N = A_2 r^\alpha \quad (3)$$

where A_2 and α are constants has been fitted to the data. It is evident from figure 6 that the exponential equation is a better fit to the data than the power law equation. In table 1 the constants A_1 , β , A_2 and α and the correlation coefficients for the exponential and power law equations are listed for the six waves. The average value of the exponents for the six waves are, $\beta = -1.5$ and $\alpha = -3.3$. The correlation coefficients for the power law fits are in the range from 0.94 to 0.95 and for the exponential fits they are consistently higher in the range from 0.96 to 0.98. Note that only the data for $r \geq 0.8$ mm was included in the correlations (i.e. the first four data points corresponding to bins at $r = 0.1, 0.3, 0.5$ and 0.7 mm were excluded).

The distribution of the total number of bubbles (i.e. of all sizes) as a function of depth below the free surface is shown plotted in figure 7. There are no significant differences between the depth distribution in saltwater and freshwater. The two depth distributions can be fitted with equations of the form

$$N(z) = N_o e^{-z/h} \quad (4)$$

where N_o is the total bubble density at the free surface and h is the entrainment depth [Hwang *et al.*, 1990]. For the saltwater depth distribution $N_o = 3.9 \times 10^5$ per m^3 and $h = 1.0$ cm and for the freshwater depth distribution $N_o = 4.7 \times 10^5$ per m^3 and $h = 0.94$ cm.

4 Discussion

These are the first measurements of bubble size distributions beneath mechanically generated dispersive wave packets therefore detailed compar-

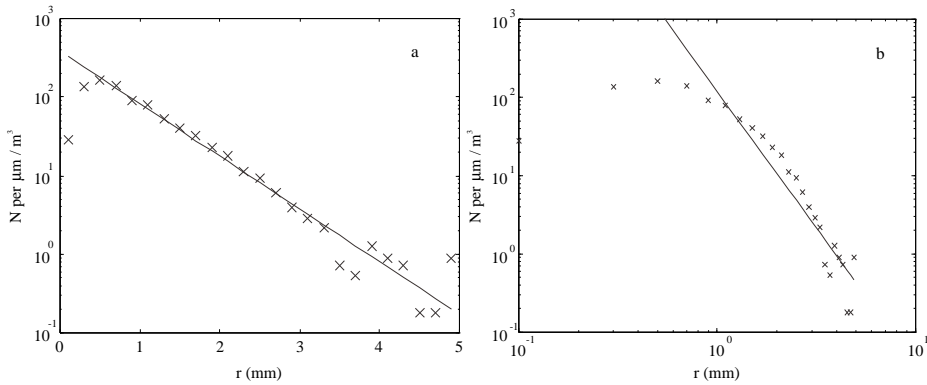


Figure 6: Bubble size spectrum for the saltwater wave with $G = 0.76$. **a** An exponential equation has been fitted to the data. **b** A power law equation has been fitted to the data. Note the points corresponding to the smallest four radius bins (0.1 - 0.7 mm) have not been used in the least squares computations.

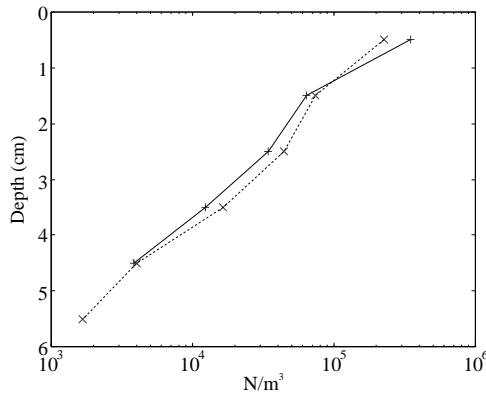


Figure 7: The total number of bubbles N per m^3 ($r < 0.8$ mm) plotted as a function of z the depth below the free surface. \times freshwater, $+$ saltwater.

isons to previous measurements is difficult. However, comparisons with the averaged quantities from the breaking wind wave measurements of *Hwang et al.* [1990] and *Baldy and Bourguel* [1987] may prove useful. Both *Hwang et al.* [1990] and *Baldy and Bourguel* [1987] observed slopes in the bubble size spectra that varied from -2 to -4 depending on the depth. In both studies the slope closer to the free surface was -2. In this study we found that the slope of the bubble size spectrum was approximately -3.3 for bubble radii > 0.8 mm. However, an exponential equation was found to represent the data better with $N \sim e^{-1.5r}$. The difference in the slopes may be due to: (i) the fact that in the two previous experiments the maximum radius of bubbles observed was 1.5 mm considerably less than the maximum of 5 mm ob-

served in our experiments, (ii) there may be significant differences between the entrainment of air bubbles by wind waves and mechanically generated dispersive wave packets, and (iii) the previous experiments both presented data averaged over long time periods compared to the period of the waves and in our experiments the bubble size measurements are all snapshots of the distributions in the water just behind the leading edge of the breaking crest.

The depth to which bubbles are entrained is characterized by the entrainment depth or e-folding depth of the bubble depth distribution (figure 7). *Hwang et al.* [1990] found that h varied from 5.4–10.8 cm for wind waves with rms wave amplitudes from 1.7–2.7 cm. *Baldy and Bourguel* [1987] did not compute the entrainment depth but it can be computed from the data in their figure 12 for wind waves with a significant wave height of 9.2 cm at a wind speed of 14 m/s. The entrainment depth for this case is $h = 1.1$ cm. In our experiments we found $h = 1.0$ cm and 0.94 cm for the salt- and freshwater waves respectively in agreement with the measurements of *Baldy and Bourguel* [1987]. It should be remembered that *Hwang et al.* [1990] did not make any measurements above the minimum trough level and therefore their estimate of the entrainment depth may be biased.

5 Conclusions

We have reported on the measurements of the large bubble size distributions in fresh- and saltwater beneath mechanically generated breaking wave packets. It was found that the size distribution for large bubbles, $r > 0.8$ mm, are essentially the same in salt- and freshwater. The bubble spectra are best represented by an exponential equation of the form $N \sim e^{-1.5r}$ or alternatively by a power law equation of the form $N \sim r^{-3.3}$. The depth distributions in salt- and freshwater are very similar and may be represented by an exponential equation, $N = 4 \cdot 10^5 e^{-z/h}$ where $h \sim 1$ cm. These measurements demonstrate that significant numbers of large bubbles are entrained beneath small-scale breaking waves (wavelengths of ~ 1.5 m and amplitudes of ~ 10 cm). These results combined with *Keeling's* [1993] predictions suggest that air-sea gas transfer due to the entrainment of large bubbles may be significant even when the sea surface is relatively calm.

Acknowledgements

We would like to thank D. Doede for assisting in the experiments and the data processing. This research was funded by a grant from the Natural Sciences and Engineering Research Council of Canada.

References

- Baldy, S., Bubbles in the close vicinity of breaking waves, *J. Geophys. Res.*, *93*, 8239-8248, 1988
- Baldy, S. and M. Bourguel, Bubbles between the wave trough and wave crest levels, *J. Geophys. Res.*, *92*, 2919, 1987
- Chan, E. S. and W. K. Melville, Deep-water plunging wave pressures on a vertical plane wall, *Proc. R. Soc. Lond.*, *A417*, 95-131, 1988
- Cipriano, R. and D. C. Blanchard, Bubble and aerosol spectra produced by a laboratory breaking wave, *J. Geophys. Res.*, *86*, 8085-8092, 1981
- Farmer, D. M., C. L. McNeil and B. D. Johnson, Evidence for the importance of bubbles to the enhancement of air-sea gas flux, *Nature*, *361*, 620-623, 1993
- Haines, M. A. and B. D. Johnson, Injected bubble populations in seawater and freshwater measured by a photographic method, *J. Geophys. Res.*, *100*, 7057-7068, 1995
- Hwang, P. A., Y.-H. L. Hsu and J. Wu, Air bubbles produced by breaking wind waves: A laboratory study, *J. Phys. Oceanogr.*, *20*, 19-28, 1990
- Hwang, P. A., Y.-K. Poon and J. Wu, Temperature effects on generation and entrainment of bubbles induced by a water jet, *J. Phys. Oceanogr.*, *21*, 1602-1605, 1991
- Johnson, B. D. and R. C. Cooke, Bubble populations and spectra in coastal waters: A photographic approach, *J. Geophys. Res.*, *84*, 3761-3766, 1979
- Keeling, R. F., On the role of large bubbles in air-sea gas exchange and supersaturation in the ocean, *J. Marine Res.*, *51*, 237-271, 1993
- Loewen, M. R. and W. K. Melville, Microwave backscatter and acoustic radiation from breaking waves, *J. Fluid Mech.*, *224*, 601-623, 1991
- Monahan, E. C. and C. R. Zietlow, Laboratory comparisons of freshwater and saltwater whitecaps, *J. Geophys. Res.*, *74*, 6961-6966, 1969
- Rapp, R. J. and W. K. Melville, Laboratory measurements of deep water breaking waves, *Phil. Trans. Royal Society of London*, *A331*, 735-800, 1990
- Thorpe, S. A., The role of bubbles produced by breaking waves in super-saturating the near-surface ocean mixing layer with oxygen, *Ann. Geophys.*, *2*, 53-56, 1984
- Wallace, D. W. R. and C. D. Wirick, Large air-sea gas fluxes associated with breaking waves, *Nature*, *356*, 694-696, 1992
- Wolf, D. K. and S. A. Thorpe, Bubbles and the air-sea exchange of gases in near-saturation conditions, *J. Marine Res.*, *49*, 435-466, 1991

Measurements of Bubble Size Distributions with an Optical Technique Based on Depth from Focus

Peter Geißler¹ and Bernd Jähne^{1,2}

¹Interdisciplinary Center for Scientific Computing, University of Heidelberg
Im Neuenheimer Feld 368, 69120 Heidelberg, Germany
email: pgeiss@giotto.iwr.uni-heidelberg.de

²Scripps Institution of Oceanography, Physical Oceanography Res. Div.
La Jolla, CA 92093-0230, USA
email: bjaehne@ucsd.edu

doi: 10.5281/zenodo.10400

Abstract

An optical sensor for bubble size measurements is presented. It is based on the combination of light blocking visualization and depth from focus techniques and allows for the measurement of single bubbles. The degree of blur in the images of single bubbles is used to compute the distance from focal plane and thus to determine a virtual measuring volume that is increasing with bubble size. The image sequences are evaluated using digital image processing to calculate bubble size distributions. Experiments performed in the linear wind/wave facility of Delft Hydraulics are presented. For different wind speed conditions and depths bubble spectra in fresh water have been measured.

1 Introduction

Air bubbles are produced in the upper regions of the ocean by air entrainment due to breaking waves. These bubbles play an important role in various small-scale air-sea interaction processes, especially for the exchange of climate relevant trace gases such as O₂ and CO₂ at high wind conditions. By offering an additional route for gas exchange, the presence of bubbles leads to a significantly enhanced transfer velocity [*Liss and Merlivat*, 1986]. This has recently confirmed in field experiments [*Farmer*, 1993], as well as in several laboratory studies in whitecap simulation tanks by *Monahan* [1990] and *Asher* [1991]. The influence of bubbles depends greatly on parameters as buoyancy (and thus lifetime) and amount of gas carried by the bubble, which are given by the size of the bubble. Small bubbles tend to completely disappear by dissolution in the water. Large bubbles exchange gas through their surface towards equilibrium. The importance of large bubbles to gas exchange has first been pointed out by *Jähne*, [1984]. Recently, *Keeling*, [1993] introduced a detailed model for bubble mediated gas exchange. It indicates that bubbles with radii greater than 500 μm contribute significantly

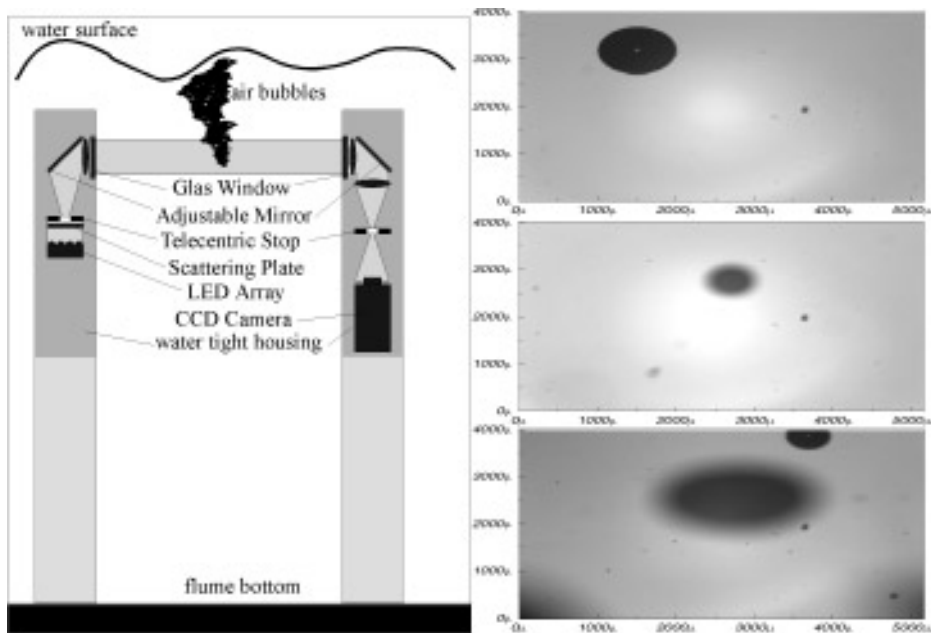


Figure 1: left: Sketch drawing of the optical bubble measuring device used during the second campaign in the Delft facility. right: Three images taken with the direct light illumination technique. Both well focused and out of focus bubbles can be seen.

to bubble induced gas transfer and oceanic supersaturation of more soluble gases. Furthermore, the transfer velocity becomes dependent on both molecular diffusivity and solubility. Uncertainties in the model arise from the lack of information about bubble distributions in the open sea. Therefore it is necessary to measure both bubble spectra and depth distributions at various wind speed conditions, especially for larger bubble sizes.

We have developed an optical device to measure the sizes of single bubbles in a diameter range of $50 \mu\text{m}$ to $1000 \mu\text{m}$. It was used during a measuring campaign in the large wind wave facility of Delft Hydraulics in the fall of 1991 and 1994. The main feature of the device is that the measuring volume can be defined without the help of mechanical delimiters. Furthermore, it increases linearly with bubble size. Due to the typical decrease of the bubble density with the radius ($\sim r^{-2} - r^{-4}$), this significantly enhances the statistics for large bubbles. Recently, *de Leeuw* [1994] used a similar system for field measurements in the North Sea. It uses a similar illumination technique, but the measuring volume is defined by mechanical delimiters and independent of bubble size.

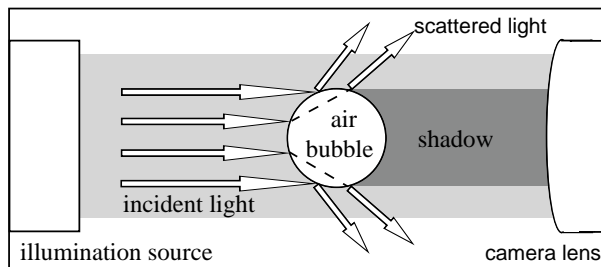


Figure 2: Visualization principle: bubbles scatter light so that it does not reach the lens (not drawn to the scales).

2 The Measuring System

The device consists of two water tight housings, mounted to the bottom of the flume in a distance of 40 cm (Figure 1). The vertical position of the device can be changed, thus allowing the measurement of bubble size distribution at various depths to the mean water surface. One of the housings contains the illumination system, while the optical receiver is located in the other one. The sample volume is located in between the both towers. The air bubbles are imaged using a CCD camera looking directly into the light source. Light hitting an air bubble in the measuring volume is scattered so that it does not reach the camera lens. Therefore, a dark image of the bubble is obtained on the image plane, allowing the determination of the shape of each individual bubble (Figures 2 and 1).

The illumination consists of an array of 7 LED's. Synchronized with the image acquisition, they were pulsed with a duration of 20 μs . In addition, the camera is shuttered to an acquisition time of 1/2000 s to completely suppress scattered light from the environment. The short illumination time avoids any motion blur in the images of fast moving bubbles. With a single pixel imaging an area of $10.1 \mu\text{m} \times 16.7 \mu\text{m}$, bubble velocities up to 0.5 m/s (x-direction) and 0.8 m/s (y-direction) cause motion blur less than one pixel. Images sequences of 5000 to 8000 images were taken for each measuring condition. They were stored on laser video discs for later processing.

Due to the fact that the depth of field is small compared to the distance between the two towers, most bubbles are not in focus and thus imaged blurred. The measurement of the amount of the blur is used to calculate their position along the optical axis. From this the measuring volume can be determined. A principal problem of this approach is that it is not possible to distinguish whether a bubble is located in front or behind the focal plane. The calculation of the true size of a bubble from its blurred size and the amount of blur may therefore result in an ambiguity of the radius measurement. To overcome this problem, we used with the device of the 1994 campaign a telecentric path of rays both on the illumination side as well as

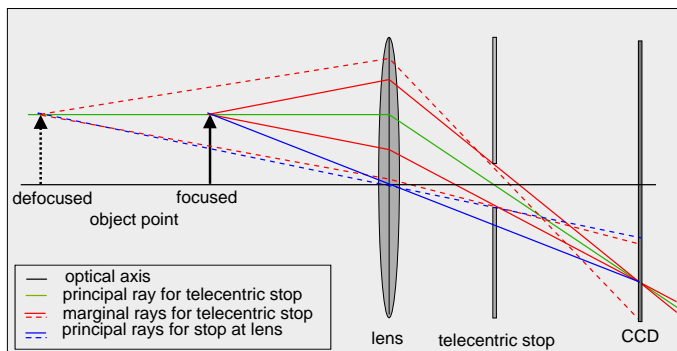


Figure 3: Principle of the telecentric optics: the displacement of an object point along the optical axis does not cause changes in the size of the image.

on the camera side. With this setup, the aperture stop is located at the rear focal point of the respective optics. The effect is that all principal rays in object space are parallel to the optical axis. Only narrow and axis-parallel ray bundles contribute to image formation. Then, the size of blurred bubbles becomes independent from the grade of the blur or the location along the optical axis (Figure 3). The size of a blurred bubble is hereby defined at the gray values that are the half of the maximum gray value. Furthermore, the grade of blurring becomes independent from whether the position is in front or behind the focal plane. Because of the symmetry introduced by the telecentric path of rays, the position ambivalence can be completely disregarded in the measurements.

3 Determination of Bubble Size Distributions

3.1 Principle

Bubble size distributions can be calculated from the image sequences if both the size of each individual bubble as well as the measuring volume is known. The volume can be calculated if the 3D-positions of every bubble are known. The calculation of the position perpendicular to the optical axis is trivial: it is directly given by the gray value center of the bubble in the image. The position along the axis can be determined from a single two-dimensional image using a *depth-from-focus* technique [Jähne and Geißler, 1994]: because the depth of field of the optical system is small compared to the distance between the focal plane and the lens, only the images of bubbles closed to the focal plane appear sharp. The blur in the image increases with the distance of the bubble from the focal plane. Therefore, the measurement of the blur allows us to determine the position along the optical axis. Because a large bubble at the same distance from the focal plane appears less blurred

than a smaller one, a “minimum sharpness” criterion yields a measuring volume with is roughly proportional to the bubble diameter. Furthermore, the “virtual volume boundaries” avoid all the disadvantages of flow distortions caused by mechanical volume delimiters close to the measuring volume.

3.2 Model of Image Formation

An air bubble can be modelled by its light absorbing coefficient $\tau(\vec{x})$ in the object plane. A circular bubble at the position \vec{X}_0 and with the radius r is then described as a circular box function $\tau(\vec{X}) = \Pi(|\vec{X} - \vec{X}_0|/2r)$ where $\Pi(x)$ is the unit step function. The capital letters indicate object plane coordinates. The Z axis of the system coincides with the optical axis of the system. The image of the bubble is given by the convolution of the well focused image with the *point spread function* $PSF(\vec{x})$ of the optical system:

$$I(\vec{x}) = \left(1 - \Pi\left(\frac{|\vec{x} - \vec{x}_0|}{2r}\right) \right) * PSF(\vec{x}). \quad (1)$$

In this equation, the object coordinates have been replaced by the image coordinates. With the telecentric path of rays, the geometrical magnification is independent of z and is taken here as 1 for convenience. With increasing z , the point spread function does not change its shape but only its extension. Therefore, the normalized PSF is given by

$$PSF_z(\vec{x}) = kB \left(\frac{\vec{x}}{V_p(z)} \right) \quad (2)$$

with the normalization factor $k^{-1} = \int d\vec{x}B(\vec{x})$.

At the focal plane ($z = 0$), V_p is 0 resulting in delta peak for the PSF. The resulting brightness distribution on the CCD sensor plane is then

$$I(\vec{x}) = v(\vec{x}) [1 - \tau(\vec{x}) * PSF_z(\vec{x})] \quad (3)$$

with $v(\vec{x})$ being the vignetting function.

3.3 Gray-Scale Normalization

First, the quantity of interest $\tau(\vec{x}) * PSF_z(\vec{x})$ has to be extracted from the acquired images. This is done by applying a linear illumination model assuming that the image shows a background level $b(\vec{x})$ and that the measured gray values $g(\vec{x})$ are further proportional to the irradiance $I(\vec{x})$. Then

$$g(\vec{x}) = a(\vec{x})I(\vec{x}) + b(\vec{x}). \quad (4)$$

The unknown quantities $b(\vec{x})$ and $a(\vec{x})$ are obtained by taking a background image $g_b(\vec{x})$ with illumination switched off ($I(\vec{x}) = 0$) and a zero image $g_z(\vec{x})$ in which no bubbles are present ($I(\vec{x}) = I_0(\vec{x})$).

Then, the linear inhomogeneous point operation

$$n(\vec{x}) = \frac{g_z(\vec{x}) - g(\vec{x})}{g_z(\vec{x}) - g_b(\vec{x})} = \tau(\vec{x}) * PSF_z(\vec{x}) \quad (5)$$

results in a normalized gray value $n(\vec{x})$ in the range of 0 to 1. It is important to note that this procedure removes any type of inhomogeneities caused by uneven illumination or small dust particles on the CCD chip or the lenses.

3.4 Measurement of Size and Distance from Focal Plane

As mentioned above, the size of a bubble can be calculated from its blurred image if the boundary is defined to be at the gray values which are 1/2 of the maximum gray value. The radius is calculated from the segmented area A as the area equivalent radius $\sqrt{A/\pi}$.

To determine the distance from the focal plane, it is necessary to measure the amount of blurring in the image. A good integral measure of the blur of a bubble is the mean gray value g_m on the 1/2-area, which is one for a well focused bubble and decreases with increasing distance from the focal plane. All bubbles with the same ratio between the radius r and the size V_p of the point spread function have the same mean gray value g_m , because their images differ only in size and are of the same shape. Thus,

$$\frac{V_p(z)}{r} = const \Leftrightarrow g_m = const. \quad (6)$$

Denoting the constant in the above equation by $\gamma(g_m)$, g_m is given by

$$g_m(z, r) = \gamma^{-1} \left(\frac{V_p(z)}{r} \right) \quad (7)$$

Because due to the telecentric path of rays, $V_p(z)$ is a symmetric and linear function of z . Therefore, g_m depends only on the normalized distance z/r :

$$g_m(z, r) = \gamma^{-1} \left(\frac{a|z|}{r} \right) = g_m \left(\frac{|z|}{r} \right) \quad (8)$$

Thus, together with the direct radius measurement g_m allows the measurement of the distance $|z|$ from the focal plane.

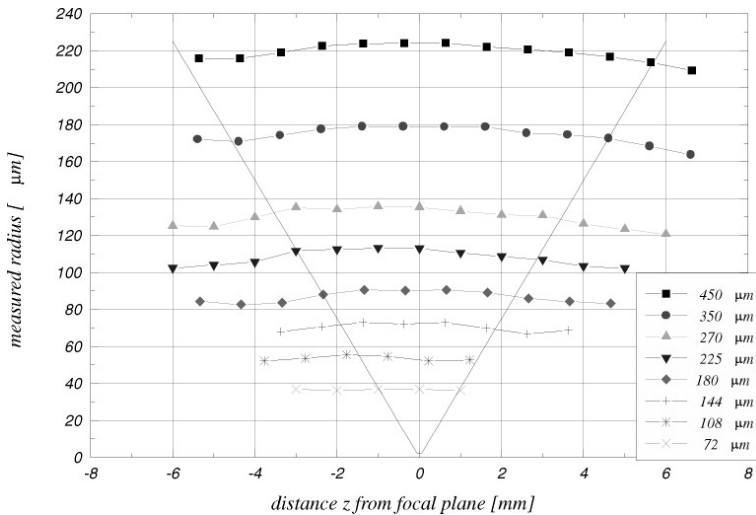


Figure 4: Independence of the size of blurred bubbles with the distance from the focal plane. The thin lines indicate the size of the virtual measuring volume.

4 Calibration

Calculating bubble size distributions from the image sequences with the depth from focus approach requires that the instrument is calibrated with a focus series of calibration targets of known size. Patterson reticles were used as calibration targets.

This standard target for microscopic calibration consists of a series of black circles in a diameter range from $18 \mu\text{m}$ up to $450 \mu\text{m}$ on a glass plate. Because Patterson globes are not absolutely accurate, the true size of each circle has to be measured independently, e.g. using a calibrated microscope. A black circle is a very good approximation of the focused image of a bubble, since with the optical setup used in the experiments more than 99.6% of the incident light is scattered away from the receiver. Nevertheless, the bright dot which appears in the center of well focused bubbles can be easily removed by applying a median filter to the normalized image before computing the mean gray value. To perform the calibration, an optical bench is mounted on top of the device. The calibration target is then fixed to the bench with a precision positioning table. Depth series centered to the focal plane are taken with a step size of 1 mm. Figure 4 shows the radii measured from different circles of the patterson target. Within the measuring volume, the difference between the measured and the true radius is in the order of 10 to $15 \mu\text{m}$, which is about the size of one pixel. The variation of the mean gray value with increasing depth is shown in Figure 5. A linear model $g(z, r) = g_0 - \alpha(r)|z|$ fits well to the data. Because a small axis offset and slight tilt of the target can often not be avoided, the axis offset for each

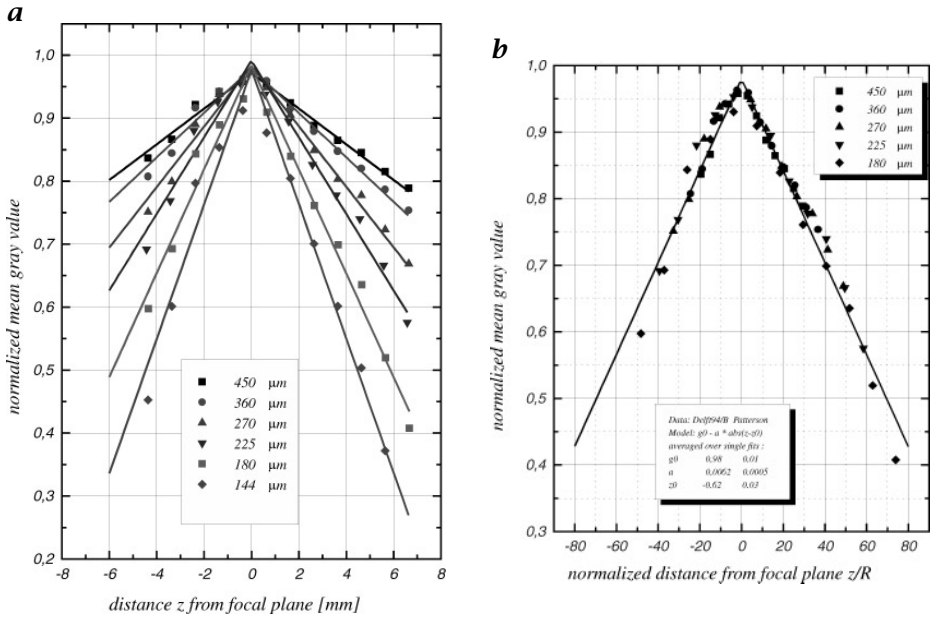


Figure 5: **a** mean gray value calculated for different patterson globes; **b** mean gray value versus normalized distance z/R . This validates the fact that g_m only depends on z/R .

circle is corrected by finding the center of symmetry in its depth series.

5 Measuring Volume

The decrease of the mean gray value with increasing distance from the focal plane can now be used to define the measuring volume by a lower limit for g_m . Only bubbles with mean gray values above this limit are taken into account for the calculation of the size distribution. Thus the linear dependence of g_m on the normalized distance

$$g(z, r) = g_0 - \alpha(r)|z| = g_0 - \alpha_0 \frac{|z|}{r} \quad (9)$$

gives the volume boundary:

$$z_{max} = \frac{1}{\alpha(r)}(1 - g_{min}) = \frac{r}{\alpha_0}(1 - g_{min}). \quad (10)$$

The measuring volume is then given by

$$V(r) = 2z_{max}(r)A_0 \quad (11)$$

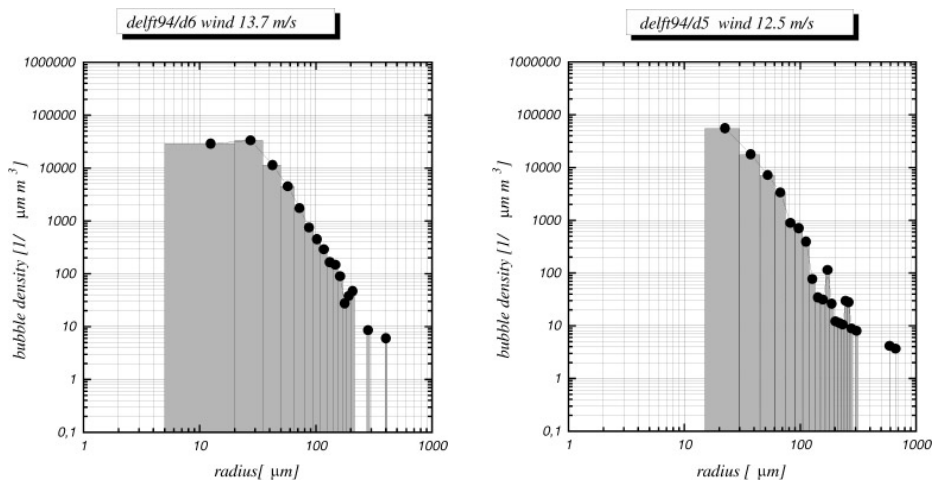


Figure 6: Size distributions of bubbles measured 5.5 cm below the mean water surface at wind speeds of 13.7 m/s and 12.5 m/s in the wind/wave flume of Delft Hydraulics, The Netherlands. The gray bars indicate the width of the histogram bins.

with A_0 being the area imaged by the CCD at the focal plane.

Due to the fact that bubbles touching the border of the image cannot be processed at the moment, the measuring volume increases approximately linear with the radius for smaller bubbles (up to a radius of approx. 300 μm) only.

6 Results

The bubble measuring device has been used in the large wind wave facility of Delft Hydraulics. Bubble spectra were measured under wind speed conditions from 7 m/s up to 14 m/s and depths from 3 cm to 30 cm. For all measuring conditions, fresh water was used. The flume is described in detail in *van Vliet et al.* [1995].

Two sample spectra are shown in Figure 6. These were measured at wind speeds of 13.5 m/s and 12.5 m/s in a mean water depth of 5.5 cm. Both show a steep decrease of the bubble density towards larger radii approximately with $r^{-3.3}$.

The bubble size distributions were calculated from the number $N(r, dr)$ of bubbles found in the radius interval $[r, r + dr]$ by

$$\psi(r, dr) = \frac{N(r, dr)}{N_I dr V(r)} \quad (12)$$

where N_I is the total number of images. A bin size of 15 μm has been used to calculate the size distributions. In Figure 7 size distributions are shown

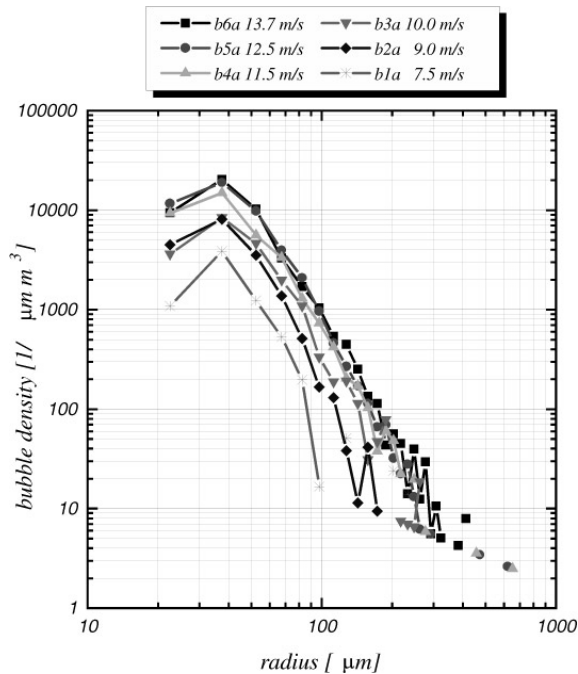


Figure 7: Size distributions of bubbles measured at different wind speeds 17.5 cm below the mean water surface in the wind/wave flume of Delft Hydraulics, The Netherlands.

over a wider wind speed range. These spectra have been measured at the same location within the flume, but at a depth of 17.5 cm.

All spectra show a cutoff at small bubble sizes. Because all cutoff radii are in the range of 20 - 40 μm and thus belonging to a pixel area of less than 25 pixels, it is very likely that the cutoff is an artifact introduced by the fact that the segmentation is performed on a coarse grid. No subpixel accurate segmentation can be done at the moment. For bubble radii greater than 500 μm , the number of bubbles per bin is too small to allow for the computation of the size distribution. The comparison between bubble spectra measured at different depth to the mean water level implies that the total number of bubbles does not change with depth. In fact, this is not true because for the smaller depth the measuring volume comes up in wave tridges. Instead of the number of acquired images the number of in-water images has to be used in (12). A coarse estimate shows that then the total number of bubbles is different by about a factor of 30 - 40 %.

7 Conclusions

In this paper an optical sensor for bubble size measurements has been introduced. It has been showed that the combination of direct visualization of single bubbles and a depth from focus approach to define a non-mechanical delimited measuring volume allows the construction of a rugged bubble measuring device.

The use of a telecentric path of rays is a significant improvement compared to the device we used in the first measuring campaign. It allows for easier calibration and direct measurement of bubble radii. A not yet solved problem is the fixed measuring position that does not allow for measurements of bubble size distributions in a constant distance to the water surface, but averages over a depth range according to the wave height. This problem can be solved by either parallel measuring of the actual wave height or by mounting the device on a float which moves with the larger waves. Therefore it is intended to use the sensor on a drifting buoy to measure bubble spectra at sea.

Acknowledgements

Financial support of the European Community (Large Installation Program) that enabled us to perform measurements at the wind/wave flume of Delft Hydraulics, The Netherlands, is gratefully acknowledged.

References

- Asher, W., E. Monahan, R. Wanningkof, and T. Bates, Correlation of Fractional Foam Coverage with Gas Transport Rates, *Air-Water Mass Transfer*, selected papers from the 2nd International Symposium on Gas Transfer at Water Surfaces, Minneapolis, S. Wilhelms and J. Gulliver, eds., pp. 536-548, ASCE, New York., 1990
- Farmer, D. M., C. L. McNeil, and B. D. Johnson, Evidence for the importance of bubbles in increasing air-sea gas flux, *Nature*, 361, 620-623, 1993.
- Jähne, B., T. Wais, and M. Barabas, A New Optical Bubble Measuring Device; A Simple Model for Bubble Contribution to Gas Exchange, *in: Gas Transfer at Water Surfaces*, W. Brutsaert and G. Jirka, eds, pp. 237-246, Reidel Publishing Company, 1984
- Jähne, B., and P. Geißler, Depth from focus with one image, *Proc_Conference on Computer Vision and Pattern Recognition (CVPR'94)*, Seattle, 20.-23. June 1994, 713-717, 1994
- Keeling, R., On the role of large bubbles in air-sea gas exchange and supersaturation in the ocean, *Journal of Marine Research*, 51, 237-471, 1993.
- Liss, P. S., and Merlivat, L. Air-Sea gas exchange rates : introduction and synthesis, *The Role of Air-Sea Exchange in Geochemical Cycling*, edited by P. Buat-Menard, pp. 113-127, Reidel Publishing Company, 1986
- de Leeuw, G., and L. Cohen, Measurements of oceanic bubble size distributions, *Oceans 94*, 13-16 Sept. 1994

- Monahan, E., and T. Torgersen, The Enhancement of Air-Sea Gas Exchange by Oceanic Whitecapping *Air-Water Mass Transfer*, selected papers from the 2nd International Symposium on Gas Transfer at Water Surfaces, Minneapolis, Minnesota, S. Wilhelms and J. Gulliver, eds, pp. 608-617, ASCE, New York., 1990
- van Vliet, P., F. Hering, and B. Jähne, Delft Hydraulic's large wind/wave flume, *This volume*

Mass Transfer from Gas Bubbles in Fresh and Seawater

W. R. McGillis, E. J. Bock, and N. M. Frew

Woods Hole Oceanographic Institution
Woods Hole, MA 02543, USA

Abstract

A gas transfer rate equation has been derived to include the effect of bubble mediated gas transfer. In addition, a model based on three components of bubble mediated gas transfer was applied to discern the contribution from direct wave influenced gas transfer, bubble absorption, and turbulence induced by surfacing bubbles. Because bubble supersaturation can be significant, it was included in the rate equation to more accurately predict the relative contributions of these mechanisms. The developed model was used to analyze O₂ gas exchange experiments performed in fresh and seawater. Soluble surfactants were added to the fresh water to explore the relative impact on bubble absorption and bubble surface mixing gas transfer. Results indicated good agreement between the model and the experiments. Results also showed that soluble surfactants have a greater effect on bubble surfacing than on bubble absorption. An increase in bubble absorption from fresh to seawater was also observed.

1 Introduction

The mechanisms of gas exchange at the air-sea interface are of considerable importance in estimating fluxes of gas absorbed or released by the ocean. The air and the water are usually in turbulent motion, and the interface between them is irregular, and disturbed by waves, sometimes accompanied by breaking, spray, and bubble formation. A significant increase in gas transfer is known to occur under conditions of *breaking waves*. Breaking waves produce sub-surface *bubble plumes* which contribute to the overall gas transfer rate by several mechanisms. Bubbles exchange gas directly with the liquid, generate turbulence which diffuses to the interface producing fluctuations in surface divergence, and disrupt the diffusive sublayer to produce a patch of *near surface turbulence*.

In order to determine the role of bubbles on air-sea gas exchange, a formulation for the gas transfer rate equation had to be modified. Since bubbles are exposed to both hydrostatic and Laplace pressures, the degree of *bubble overpressure* can be significant. Four models [Merlivat and Memery, 1983; Woolf and Thorpe, 1991; Keeling, 1993; Haines, 1994] have included bubble overpressure and identified its role in augmenting the bubble gas transfer velocity. We have also attempted to determine the role that bubbles might

have on enhancing the surface gas exchange rate by contributing to the surface mixing.

Next, a series of laboratory experiments was performed to investigate the relative contribution of bubble mediated gas exchange in fresh and seawater. The first set of experiments used artificially-injected bubble plumes with both O_2 evasion and invasion in fresh water with and without surfactants. The second set of experiments used artificially- injected bubble plumes with both O_2 evasion and invasion in seawater. A third experiment was performed to determine if the proposed gas transfer formulation could be extended to direct wave-injected bubbles.

2 Gas Transfer Rate Model

Injected subsurface bubble plumes contribute to the overall gas transfer rate by two mechanisms. Bubbles exchange gas directly with the liquid and disrupt the diffusive sublayer and produce a patch of near surface turbulence. Previously, two component models were used to estimate the total gas flux including the combined effects of the sea surface and *bubble absorption*

$$F_{tot} = F_s + F_b \quad (1)$$

However, if bubbles effect the surface gas exchange mechanism due to near surface mixing, F_s should include both a wave contribution and a bubble mediated surface mixing contribution. Therefore, the total flux may be given as

$$F_{tot} = F_w + F_t + F_b \quad (2)$$

where F_w is the contribution from waves, F_t is the contribution of turbulence near the surface caused by bubbles, and F_b is the contribution from bubble absorption. The flux of gas across the surface is now given as

$$F_s = k_w(C - C_s) + k_t(C - C_s) \quad (3)$$

where $C_s = SP_a$, $C = SP_w$ (S is the solubility of the gas, P_a is the partial pressure of the gas in the air, and P_w is the partial pressure of the gas in the water), and k_w and k_t are the transfer velocities for the waves and the bubble mediated surface turbulence, respectively. A simple form for the flux of gas across the bubble interface is given as

$$F_b = k_b(C - C_b) \quad (4)$$

where $C_b = SP_b$ (P_b is the gas pressure inside the bubble ($= p + \rho g z + 2\sigma / r$) and k_b is the bubble absorption transfer velocity. The individual bubble

absorption transfer velocity is only a function of bubble size, velocity, gas diffusivity, and bubble surface film. The bubble size is a function of depth, z , and gas transfer rate.

Combining the individual contributions, the total flux of gas becomes

$$F_{tot} = k_w(C - C_s) + k_t(C - C_s) + k_b(C - C_b) \quad (5)$$

In a controlled tank experiment, the total flux of gas is determined from a mass balance on the bulk water, giving

$$-\frac{V}{A_s} \frac{dC}{dt} = k_w(C - C_s) + k_t(C - C_s) + k_b(C - C_b) \quad (6)$$

If there are no bubbles present, equation (6) reduces to the well-known differential equation predicting the gas transfer velocity across a wavy surface

$$-\frac{V}{A_s} \frac{dC}{dt} = k_w(C - C_s) \quad (7)$$

which has a solution

$$C = C_o e^{-k_w t/H} \quad (8)$$

where $H (= V/A_s)$ is the mean water height and C_o is the initial concentration. The full solution to equation (6) is given as

$$C = \frac{b_2}{b_1} \left[1 - e^{-b_1(t-\zeta)} \right] + C_\zeta e^{-b_1(t-\zeta)} \quad (9)$$

where ζ is initial time, $b_1 = (k_w + k_t + k_b)/H$, and $b_2 = ((k_w + k_t)C_s + k_b C_b)/H$.

3 Experimental Methods

Experiments were performed in the annular *wind-wave tank* at the Woods Hole Oceanographic Institution. The tank has a small annular polycarbonate channel (0.25 m mean radius; 0.1 m width; 0.1 m depth) with a gas-tight headspace to allow both gas invasion and evasion experiments. Headspace gases included nitrogen and air. For artificial injection of bubbles, the tank was equipped with a stainless steel frit. A frit was used to produce reproducible bubble plumes while being able to control the bubble concentration and volume flux. The bubble size variation with volume flux was measured optically by post-processing photographs of the bubble field. The tank also

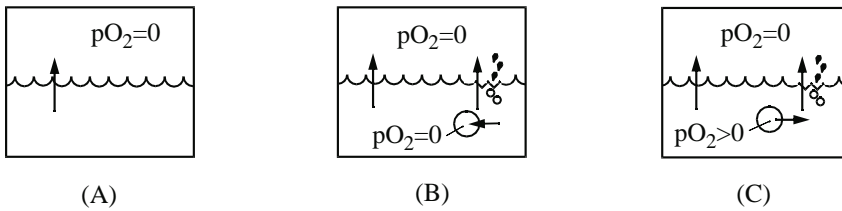


Figure 1: Schematic of representative processes: (A) Evasion through surface waves only; (B) Surface wave evasion, bubble absorption evasion, and bubble turbulence evasion; and (C) Surface wave evasion, bubble absorption invasion, and bubble turbulence evasion.

had multiple ports for headspace purging, sampling of both liquid and gas phases, and for surface skimming to remove surface films. Wind-driven waves were generated by a rotor with ten vertical paddles (0.1 m length and 0.03 m height) around the perimeter. Instrumentation in this wave tank includes a fixed-point laser slope gauge, acoustic current meter, and an oxygen probe. The laser slope gauge allowed point measurements of mean square slope.

Seawater measurements were made with samples taken from a 1000 m depth in the Sargasso Sea. Although the *surface active material* present from this location was small, there was a measurable increase in wave damping at a given wind speed. Therefore, the seawater results could not be directly compared to the clean water case. The effect of surface films on bubble mediated gas transfer was explored systematically in fresh water using varying bulk concentrations of *Triton-X-100*.

Figure 1 shows three different conditions with different gas transfer contributions. Figure 1A shows the contribution of O_2 evasion for waves only. Figure 1B shows O_2 evasion from surface waves, bubble absorption, and bubble surface turbulence. Figure 1C shows O_2 evasion through surface waves, O_2 invasion through bubble absorption, and O_2 evasion through bubble surface turbulence. For each case, equation (6) is applicable. This results in the following system of equations that can be solved for k_w , k_t , and k_b .

$$\begin{bmatrix} (C - C_s) & 0 & 0 \\ (C - C_s) & (C - C_s) & (C - C_b) \\ (C - C_s) & (C - C_s) & (C - C_b) \end{bmatrix} \begin{bmatrix} k_w \\ k_t \\ k_b \end{bmatrix} = \begin{bmatrix} -\frac{V}{A_s} \frac{dC}{dt} \\ -\frac{V}{A_s} \frac{dC}{dt} \\ -\frac{V}{A_s} \frac{dC}{dt} \end{bmatrix} \quad (10)$$

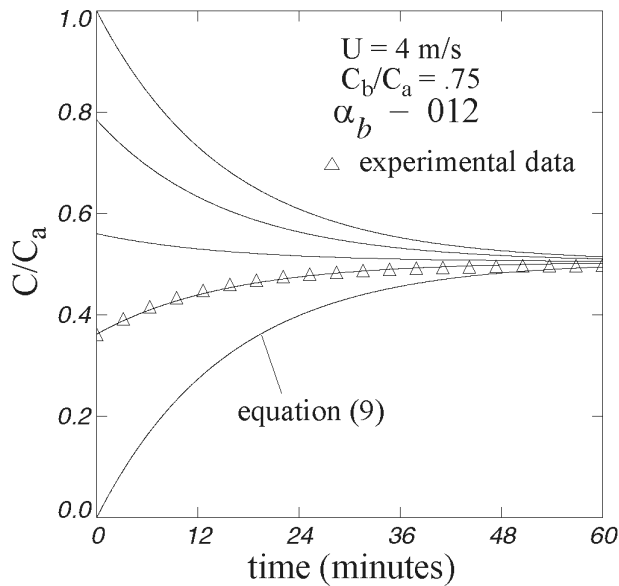


Figure 2: Comparisons of O₂ bulk concentration predictions and experimental data.

4 Results and Discussion

In a series of experiments, the concentration of O₂ in the artificially-injected bubbles was varied by mixing air and nitrogen. Matrix experiments were performed by changing the headspace gas or the O₂ concentration of the artificially-injected bubbles. For the artificially-injected bubble plumes containing O₂, the mean bubble size was approximately $r = 0.5 \text{ mm}$. The bubble time constant shown by *Motarjemi and Jameson* [1978] is much larger than its residence time [*Jähne et al.*, 1984]. For this reason, C_b remains almost uniform in time. For a given wind speed and bubble plume, k_w , k_t , and k_b are constant and equation (10) can be applied to the system. Figure 2 shows a comparison of equation (9) and experimental results for a bubble with $C_b/C_a = .75$ and a headspace of $C_s/C_a = 0$. For any initial condition in concentration, the prediction converges to an equilibrium value. When the experimental concentration is used as the initial condition, equation (9) shows very good agreement with experimental data.

Figure 3 shows the bulk concentration (C/C_a) plotted as a function of bubble concentration (C_b/C_a). Depending on the value of C_b/C_a , C/C_a asymptotes to different concentrations. The bulk concentration will equilibrate when the flux of gas across the surface is balanced by the flux of gas across the bubble. If the surface transfer velocity was equal to the bubble transfer velocity, the equilibrium concentration would be the mean of the concentration at the surface and the concentration at the bubble wall. This is similar to oceanic conditions when the bulk water concentration equili-

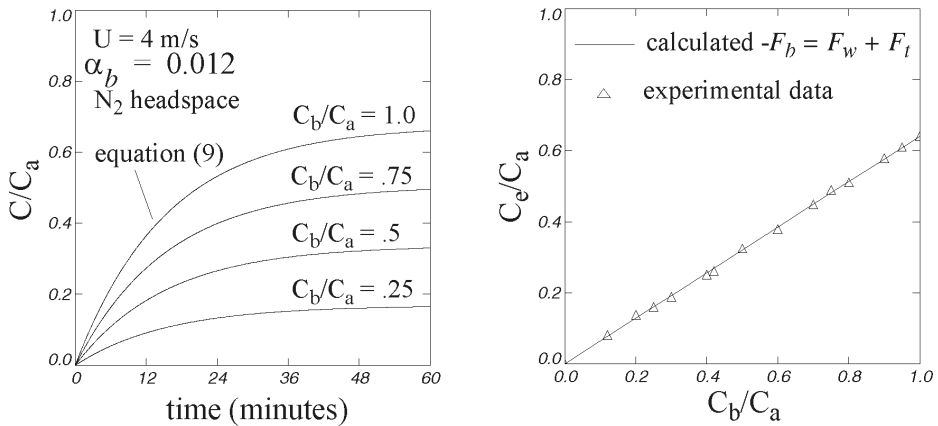


Figure 3: **a** Predictions of bulk concentration time response with bubble concentration. $C_s/C_a = 0$. **b** Comparison of measured and calculated equilibrium saturation conditions. $C_s/C_a = 0$.

brates. The bulk concentration is in equilibrium with the atmosphere and the bubbles. The exact departure from equilibrium is determined, in part, by the bubble characteristics. Figure 4 shows measurements of equilibrium concentrations (C_e/C_a) versus C_b/C_a for a constant wind speed and bubble volume. Equilibrium occurs when the net flux is zero and the bubble absorption gas flux is equal to the flux due to waves and bubble turbulence. Predicted C_e/C_a is shown to be in excellent agreement with the experimental results.

Figure 5 shows k_b and k_t as a function of bubble volume fraction (α_b). As expected, both k_b and k_t increase with an increase in α_b . An increase in α_b , results in an increase in the number of bubbles and therefore the surface area of bubbles. The increase in k_t may have been a result of the increased disruption of the surface diffusive sublayer. Good agreement was found between k_b and Levich [1962], where Levich [1962] gives the bubble flux to be

$$F_b = 8\sqrt{\frac{\pi}{2}} \left[\frac{DU}{r} \right]^{1/2} r^2 \Delta C \tag{11}$$

and D is the gas diffusivity, U is the bubble rise velocity, and r is the bubble radius. With the same volume flux of bubbles, the following table provides comparisons between fresh water and seawater.

The seawater k_b was increased from that of fresh water because of the enhanced bubble surface area due to smaller bubbles generated in seawater. Also, as shown in equation (11) the individual bubble gas transfer velocity is larger for small bubbles. The surface mixing contributions, k_t and k_w , were reduced for seawater. This was probably due, in part, to the dissolved

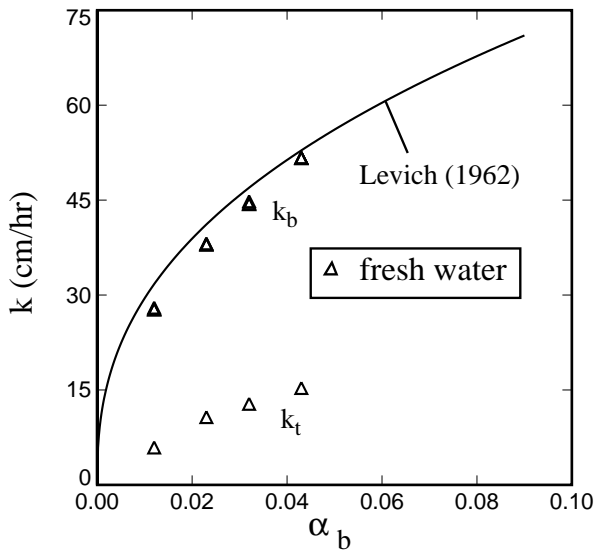


Figure 4: Gas transfer velocity versus bubble volume fraction.

Table 1: Gas Transfer Velocity Comparisons between Sea and Fresh Water.

	seawater	fresh water
k_b (cm/hr)	118.7	44.9
k_t (cm/hr)	7.4	17.9
k_w (cm/hr)	4.3	5.6

organic material in the seawater which tends to dampen surface fluctuations and waves.

The significant impact from surface films was explored more systematically by using variations of bulk concentrations of Triton-X-100. For a constant wind speed and bubble volume fraction, Figure 6 shows the equilibrium concentration decrease with an increase in soluble surfactant. Because the decrease in k_t (and k_w) shown in Figure 7 was greater than the decrease in k_b , the surface invasion flux was reduced more than the bubble evasion flux. This resulted in a decrease in the equilibrium concentration. This was consistent with the results observed for seawater. A large reduction in k_w and k_t with surfactant concentration implies that bubble surface turbulence and waves are damped equally.

Figure 8 shows the O_2 gas transfer velocity determined using equation (8) versus friction velocity (u_*) in seawater. A line is fit through the data where there is a linear relationship between k and u_* . At a u_* greater than about 4, there is a deviation from the linear relationship due to the effect

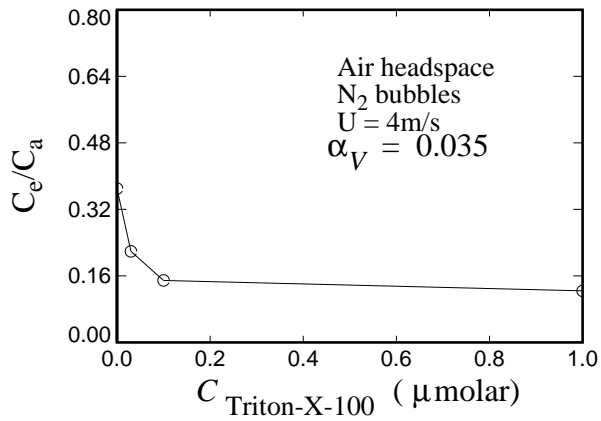


Figure 5: Measured bulk equilibrium versus surfactant concentration.

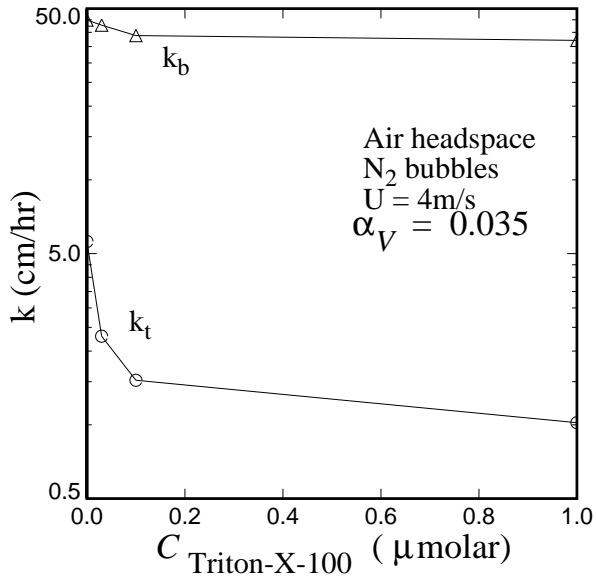


Figure 6: Gas transfer velocity versus surfactant concentration.

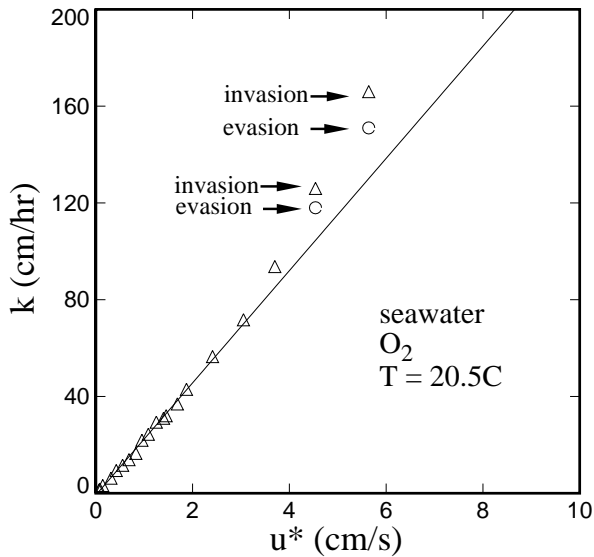


Figure 7: Gas transfer velocity versus friction velocity.

of bubbles. Shown at several u_* is the result from evasion and invasion experiments. When bubbles are not present, evasion and invasion gas transfer velocities are symmetric. Using equation (9), the contributions from all the mechanisms were estimated for $u_* = 4.7$. The contribution from the surface was calculated to be 103.7 cm/hr and the degree of *supersaturation* was calculated to be 1.14%. This corresponds to a $k_w = 95.1$, $k_b = 20.1$, and $k_t = 8.6$ cm/hr.

5 Conclusions

A technique to estimate the contributions of direct wave influenced gas transfer, bubble absorption, and turbulence induced by surfacing bubbles has been developed. Bubble supersaturation was included in the gas transfer rate equations. At the same volume flux of bubbles, bubble gas transfer in seawater was much greater than that in fresh water because of the enhanced surface area and smaller bubble size. Soluble surfactants were found to have a greater effect on bubble surface mixing than on bubble absorption.

Acknowledgements

This work was supported by the National Science Foundation under Grant OCE-9301334 and the Woods Hole Oceanographic Institution (contribution No. 9072).

References

- Haines, M. A., Gas exchange velocities: The bubble contribution, submitted to the *Journal of Marine Research*, 1994
- Jähne, B., Wais, T., and Barabas, M., A new optical bubble measuring device: A simple model for bubble contribution to gas exchange, W. Brutsaert and G. H. Jirka (eds.), *Gas Transfer at Water Surfaces*, pp. 237-246, 1984
- Keeling, R. F., On the role of large bubbles in air-sea gas exchange and supersaturation in the ocean, *Journal of Marine Research*, 51, pp. 237-271, 1993
- Levich, V. G., *Physico-Chemical Hydrodynamics*, Englewood Cliffs, NJ: Prentice Hall, 1962
- Merlivat, L., and Memery, L., Gas exchange across an air-water interface: Experimental results and modeling of bubble contribution to transfer, *Journal of Geophysical Research*, 88, pp. 707-724, 1983
- Motarjemi, M., and Jameson, G. J., Mass transfer from very small bubbles - the optimum bubble size for aeration, *Chemical Engineering Science*, 33, pp. 1415-1423, 1978
- Woolf, D. K., and Thorpe, S. A., Bubbles and the air-sea exchange of gases in near-saturation conditions, *Journal of Marine Research*, 49, pp. 435-466, 1991

Laboratory Measurements of Seawater CO₂ Gas Fluxes

*M. D. DeGrandpre, W. R. McGillis,
N. M. Frew, and E. J. Bock*

Woods Hole Oceanographic Institution
Woods Hole, MA 02543 USA

Abstract

Carbon dioxide air-water exchange has been extensively studied in wind-wave tanks, flumes, and wind tunnels. Interestingly, correlations used to determine CO₂ gas transfer velocities (K_T) for seawater are almost exclusively based upon studies of fresh or distilled water and/or by use of other gases as analogs. Because CO₂ fluxes can be enhanced through chemical reaction at high pH, it is important to use seawater (pH~8) rather than fresh water (pH~6). We have determined K_T s, and their relationship to mean square wave slope, for distilled water (pH~5.5), spring water (pH~7.7), and seawater (pH~8.1). We found that the K_T s level off at approximately 1 cm/hr, 3 cm/hr, and 4 cm/hr for the distilled, spring and sea water respectively at low wind speeds (low mean square slope). The seawater enhancement compares well with theoretical predictions by others.

1 Introduction

The oceans absorb significant quantities of atmospheric CO₂ [Siegenthaler and Sarmiento, 1993], but because the mechanisms of exchange are not yet well understood, both CO₂ uptake since the industrial revolution and future projections remain highly uncertain. It is therefore very important to study the processes that control CO₂ air-sea exchange under the most realistic conditions possible, ideally in the field, but also in the laboratory where gas exchange can be reproducibly studied. Two critical pieces of information needed for estimating gas fluxes are 1) the CO₂ gradient across the air-sea interface ($\Delta p\text{CO}_2$) and 2) the *gas transfer velocity* (K_T). Much work has focused on determining and understanding K_T , yet estimates of K_T based on wind speed differ by over a factor of 5 at 10 m/s from different laboratory and field experiments [Wanninkhof, 1992]. A large uncertainty in K_T leads to an equivalent uncertainty in CO₂ flux estimates. The scatter in K_T has a number of origins, the major source being the assumption that winds of similar magnitude generate the same sea state or wave field. Ocean fetch, surface layers, wave tank geometries, all of which influence interfacial turbulence to some degree, are examples of field and/or laboratory variables that can alter the K_T -wind speed relationship. A second source of error in K_T

arises from the correction used to put the K_T for different gases on the same basis. Gas exchange is assumed to scale by Sc^n where Sc is the Schmidt number (kinematic viscosity/gas diffusivity) with n between -0.5 and -0.67. Gas diffusivities and their temperature dependence must be accurately known or errors are introduced when this correction is applied. A third source of variability in K_T arises from using tracers that respond on widely different time scales. Comparing instantaneous estimates with long-term averages is not necessarily valid. Globally averaged K_T s are useful for climate models, whereas, more instantaneous measurements of K_T give insights into the actual mechanisms that are driving gas exchange.

Considering all the variables involved, it is problematic to compare K_T between different field and laboratory experiments. The field would obviously benefit from a more realistic representation of gas exchange based upon surface wave properties, rather than wind speed. Promising trends have appeared in the literature, with studies of gas exchange relationships to wave height [Wallace and Wirick, 1992], bubbles [Farmer et al., 1993], whitecap coverage [Asher et al., 1992], and wave slope [Jähne et al., 1987].

Our research involves field and laboratory measurements of dissolved gases (CO_2 and O_2), interfacial properties (surface films) and wave properties (wave spectra). The focus of our recent work has been to refine our understanding of gas transfer through experiments in a small annular wind-wave tank (described below). This particular study has been motivated by our discovery that, although CO_2 exchange has been extensively studied in wind-wave facilities, few experiments have actually used seawater (i.e., a realistic pH and alkalinity). Because CO_2 can undergo reactions that augment fluxes at low wind speeds [Hoover and Berkshire, 1969; Liss, 1973; Emerson, 1975; Broecker and Peng, 1974; Wanninkhof, 1992], and because these reactions are pH dependent, it is important to use seawater rather than distilled water. In addition few experiments have combined seawater CO_2 flux measurements with measurements of wave slope. Therefore, we felt that a closer look at CO_2 gas exchange in wind-wave tanks was warranted. In the experiments described herein, we measured CO_2 and O_2 fluxes and wave spectra and determined simultaneous K_T s for both gases. Gas exchange was measured using distilled water, a commercial spring water, and seawater.

2 CO_2 Gas Exchange in Wind-Wave Tanks

Most studies of CO_2 gas exchange in wind-wave tanks have used distilled water and, hence, most have not addressed the possibility of chemical reactions [e.g., Ocampo-Torres and Donelan, 1994; Jähne et al., 1979; Broecker et al., 1978]. We have found remarkably few reported measurements of CO_2 exchange in seawater in wind-wave tanks or flumes (i.e., with controlled air flow over the surface). Most of the reported seawater data has been from CO_2 exchange in stirred tanks [e.g., Liss, 1973; Broecker and Peng, 1974; Goldman and Dennett, 1983]. The lack of systematic studies of seawater

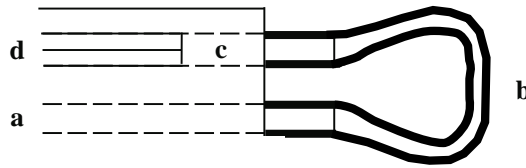


Figure 1: Schematic of *in situ* pCO₂ sensor used in the wind-wave experiments. The sensor OD is 3.2 mm. **a**-capillary tube inlet from syringe pump, **b**-tubular silicone rubber membrane, **c**-optical cell, **d**-fiber optics and indicator capillary tube outlet.

CO₂ exchange in wind-wave tanks is puzzling, but we speculate that it is due to the difficulty in measuring seawater CO₂ fluxes. The major obstacles are: 1) because of the carbonate buffering action of seawater, the rate of change of pCO₂ (the partial pressure of CO₂) is small and difficult to measure compared to other gases, especially on discrete samples and 2) because most of the CO₂ exists as bicarbonate in seawater, the change in total CO₂ (TCO₂ = CO₂ + HCO₃⁻ + CO₃²⁻) not pCO₂ is needed to determine fluxes. In this study we have utilized a newly developed pCO₂ sensor [DeGrandpre, 1993] to measure pCO₂ directly in the wind-wave tank (described below). The pCO₂ measurements were combined with the total alkalinity (TA) to determine the change in TCO₂ [Millero et al., 1993a] and hence, the flux of CO₂ into or out of the water.

3 Experimental

Both pCO₂ and O₂ were measured in the *wind-wave tank* with *in situ* sensors. The pCO₂ sensor uses a colorimetric *acid-base indicator* (*bromothymol blue*) that is periodically pumped into a *gas permeable membrane* connected to a 2 μl fiber-optic cell (Figure 1). The fiber optics and capillary exit tube are epoxied into a 0.5 mm ID capillary tube to form a single-ended probe.

Calibrations were performed using CO₂ gas standards as described in DeGrandpre [1993]. The measurement precision is approximately ±1 μatm. The 4–5 min. response time is limited by the time required for the indicator solution to reach equilibrium with the ambient CO₂. The following sequence takes place during each measurement cycle: 1) detector dark signals are recorded, 2) the light source (tungsten lamp) and pump (syringe-type) are turned on, 3) the light signals are recorded at the absorbance maxima of the base form of the indicator (620 nm) and at a wavelength where the indicator does not absorb (720 nm) for reference, and 4) the pump is turned off and the newly pumped indicator solution resides in the membrane until the next measurement cycle (approx. 5 minutes).

O₂ measurements were made using a polarographic O₂ electrode. Both O₂ and pCO₂ sensors were inserted directly into the bulk water through ports in the tank. A laser slope gauge was used for continuous measurements of

Table 1: Water properties used in gas exchange experiments

Water type	Alkalinity ($\mu\text{eq/kg}$)	Initial pH
Distilled water	0	5.5
Spring water	650	7.7
Sargasso Sea 1000 m water	2350	8.1

mean square slope $\langle S^2 \rangle$.

All gas exchange experiments were performed in a 0.5 m radius, 0.1 m wide, 0.1 m deep annular wind-wave tank equipped with a rotor and ten vertical paddles to create wind above the annular channel. Temperature was controlled by circulating water in a jacket that surrounds the tank. A small suction tube continuously skimmed the water surface to help prevent build up of surfactants during each experiment. Gas evasion and invasion experiments were performed by flushing the head space with CO_2 -free N_2 and filtered air, respectively. Head space CO_2 was monitored by circulating head space air through an infrared CO_2 analyzer (Model 6251, Licor, Inc.). During the evasion and invasion experiments the CO_2 head space typically did not vary by more than $10 \mu\text{atm}$. All experiments were run at $20.7 \pm 0.2^\circ\text{C}$.

Gas transfer velocities were calculated using,

$$H \frac{dC_T}{dt} = K_T S \Delta C \quad (1)$$

where H is the water depth, S is the gas solubility, ΔC is the partial pressure difference between the head space and bulk water and C_T is the TCO_2 concentration in the bulk. By combining the total alkalinity (TA), which is constant for CO_2 gas exchange, and bulk pCO_2 , TCO_2 can be estimated to within $\pm 3 \mu\text{mol/kg}$ [Millero *et al.*, 1993a] assuming precisions of $\pm 2 \mu\text{atm}$ pCO_2 and $\pm 2 \mu\text{mol/kg}$ TA. Note that since we are interested in changes in TCO_2 (i.e., dC_T), it is the precision in TCO_2 that is important rather than the absolute accuracy. TA was measured by titration [Millero *et al.*, 1993b]. Equation (1) was also used to calculate O_2 K_{TS} , except that in this case C_T was equal to the bulk O_2 partial pressure. Experiments typically lasted 2 hours. To improve the measurement precision, the instantaneous K_{TS} were averaged for the experiment duration.

4 Results and Discussion

We measured CO_2 and O_2 gas exchange in distilled water, a commercial spring water and seawater (Table 1). The initial pH (i.e., before gas exchange) was estimated from the initial pCO_2 , assuming atmospheric equilibrium ($360 \mu\text{atm}$), and TA [Millero *et al.*, 1993a]. As described earlier, water

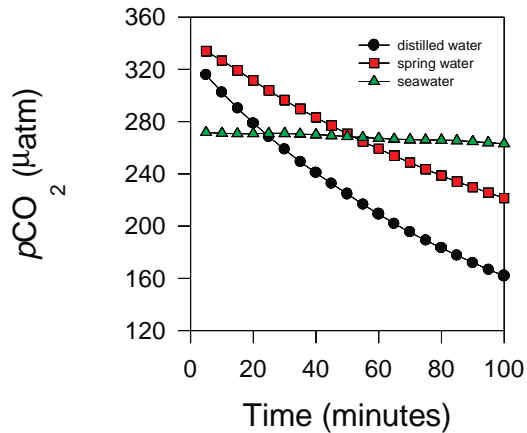


Figure 2: Change in pCO₂ versus time for distilled water, spring water, and seawater for the same rotor speed. The mean square slopes were similar for each case.

with significant TCO₂ will buffer the rate of change of pCO₂ because of the carbonic acid equilibria,



Figure 2 illustrates this buffering action. It is evident that the rate of change of pCO₂ increases dramatically with decreasing TCO₂.

The CO₂ and O₂ K_Ts are plotted versus mean square slope in Figure 3 for all evasion and invasion experiments. K_T standard deviations at low wind speeds (calculated from the instantaneous K_Ts) were typically < ±1 cm/hr for distilled and spring water and from ±0.5 – 1.9 cm/hr for seawater. The seawater standard deviation is larger due to the very small pCO₂ changes at low wind speeds.

While the different water K_Ts for O₂ all fall on the same curve, the CO₂ K_Ts diverge at low mean square slope, leveling off at approximately 1, 3, and 4 cm/hr for the distilled, spring and seawater, respectively. To better illustrate the differences between O₂ and CO₂ gas transfer, the CO₂ and O₂ K_Ts are plotted together in Figure 4. The Schmidt number dependence (Sc⁻ⁿ), which assumes that K_T between different gases scales with the gas diffusion coefficients, is also plotted. If there is no chemical enhancement, CO₂ and O₂ K_Ts should have an approximately linear relationship on a log plot. It is readily apparent that seawater CO₂ gas exchange deviates from the Sc number model. Gas exchange for the spring water case is also significantly different from the distilled water case (Figure 3 and 4) although not distinctly nonlinear in Figure 4.

If it is assumed the distilled water gas transfer approaches 1 cm/hr at low mean square slope [Wanninkhof, 1992], then the spring water and seawater fluxes are approximately 3 and 4 times the distilled water case, respectively.

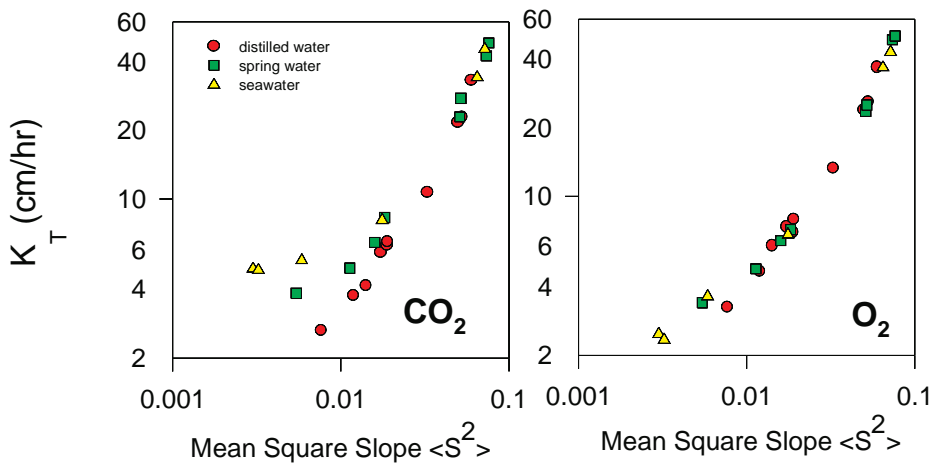


Figure 3: Gas transfer velocities (K_T) for CO_2 and O_2 versus mean square wave slope $\langle S^2 \rangle$. Rotor speed ranged from 100–325 rpm. $T = 20.7 \pm 0.2^\circ \text{C}$.

Because hydration of CO_2 is slow (the left side of (2)), and because at high pH, the faster reaction,



becomes significant, the flux can be increased at high pH or when the boundary layer thickness exceeds $100 \mu\text{m}$ (the point at which diffusion and reaction times are similar) [Hoover and Berkshire, 1969; Liss, 1973; Broecker and Peng, 1974; Emerson, 1975; Wanninkhof, 1992]. The CO_2 K_T s are plotted in Figure 5 against the boundary layer thickness (δ), calculated from the O_2 K_T s and O_2 diffusion coefficient D_{O_2} (i.e., $\delta = D_{\text{O}_2}/K_T$ where D_{O_2} is the O_2 diffusion coefficient at 21°C).

The enhancement appears to occur when δ is 100–150 μm , in agreement with the theoretical predictions. Table 2 shows the reported theoretical and measured flux enhancements.

Predicted chemical enhancements for seawater range from 2.7–5.0 and measured values range from 1.6–4.0. Our data fall at the high end of the seawater range, but it is important to note that all other results are from stirred tanks which may have different turbulent mixing.

5 Summary

As stated by Wanninkhof, [1992], low wind speeds are common over large areas of the ocean. Our results show that the seawater K_T is significantly larger at low wind speeds than K_T for non-reactive gases; and, therefore, at low wind speeds the chemical enhancement of CO_2 fluxes must be taken

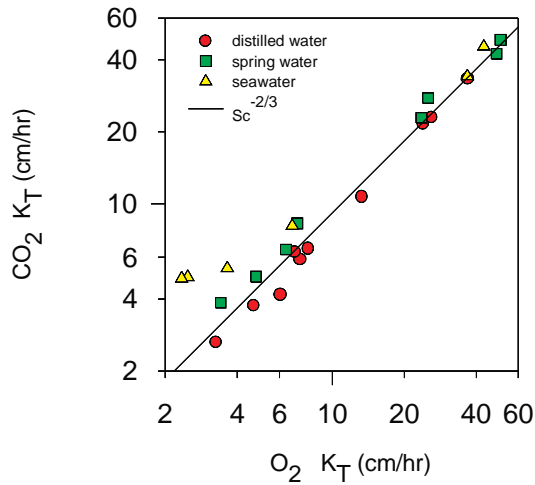


Figure 4: K_T s for CO_2 and O_2 . The Schmidt number curve, $K_T(\text{CO}_2) = K_T(\text{O}_2) \times [\text{Sc}(\text{CO}_2)/\text{Sc}(\text{O}_2)]^{-n}$ with $n = 2/3$ at low wind speeds, is also plotted.

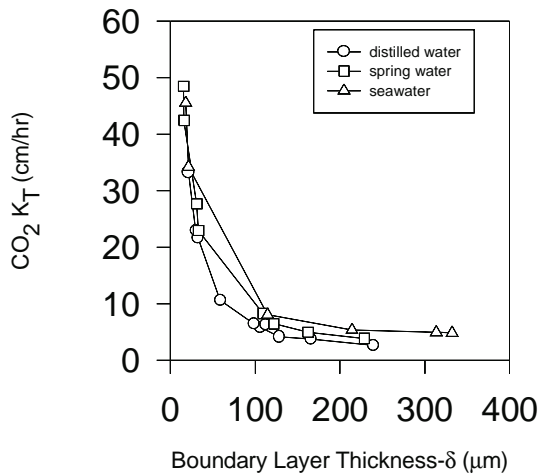


Figure 5: CO_2 K_T versus boundary layer thickness calculated from the O_2 K_T s. Theoretical predictions by others (see text) show that chemical enhancements occur when the boundary layer reaches $100 \mu\text{m}$.

Table 2: Predicted and observed chemical enhancements [$K_T(\text{CO}_2)/K_T(\text{low pH or O}_2)$] reported by others and for this study. Values were taken from tables or estimated from figures within cited text.

Water type	Predicted	Observed	Boundary layer thickness (μm)	Reference
pH = 6.5	1.3	1.4	300	[Hoover and Berkshire, 1969]
Seawater	2.7	—	300	[Hoover and Berkshire, 1969]
Seawater	2.9	3.0	310	[Broecker and Peng, 1974]
Seawater	—	1.6	—	[Liss, 1973]
pH = 6.4	1.4	1.6	—	[Liss, 1973]
pH = 10	5.0	3.7/6.5	300	[Emerson, 1975]
Seawater	5.0	—	—	[Wanninkhof, 1992]
Seawater	—	4.0	300	[this study]
pH = 7.7	—	3.0	300	[this study]

into account in flux calculations. In addition, we have shown some of the first correlations for seawater CO_2 exchange and mean square wave slope. We are currently working towards making simultaneous field measurements of wave slope and dissolved gases to compare our laboratory results with "real-world" estimates. We hope these efforts lead to a more coherent representation of gas transfer than presently possible using wind speed alone.

Acknowledgements

We thank Terry Hammar and Steve Smith (WHOI) for technical assistance. We also thank Ernie Lewis (Brookhaven National Lab) for alkalinity analyses. This work was supported by NSF grant OCE-9410914 and DOE Ocean Margins Program grant DE-FG02-92ER61437.

References

- Asher, W. E., Farley, P. J., Wanninkhof, R., Monahan, E. C., and T. S. Bates, Laboratory and field experiments on the correlation of fractional area whitecap coverage with air/sea gas transport, in *Precipitation Scavenging and Atmosphere-Surface Exchange*, vol. 2, edited by S. E. Schwartz and W. G. N. Slinn, pp. 815-827, Hemisphere Publ., 1992
- Broecker, H. C., Peterman, J., and W. Siems, The influence of wind on CO_2 exchange in a wind-wave tunnel, including the effects of mono layers, *J. Mar. Res.*, 36, 595-610, 1978

- Broecker, W. S. and T.-H. Peng, Gas exchange rates between air and sea, *Tellus*, 26, 21-35, 1974
- DeGrandpre, M. D., Measurement of seawater pCO₂ using a renewable-reagent fiber optic sensor with colorimetric detection, *Anal. Chem.*, 65, 331-337, 1993
- Emerson, S., Chemically enhanced CO₂ gas exchange in a eutrophic lake: A general model, *Limnol. Oceanog.*, 20, 743-753, 1975
- Farmer, D. M., McNeil, C. L., and B. D. Johnson, Evidence of the importance of bubbles in increasing air-sea gas flux, *Nature*, 361, 620-623, 1993
- Goldman, J. C. and M. R. Dennett, Carbon dioxide exchange between air and seawater: no evidence for rate catalysis, *Science*, 220, 199-201, 1983
- Hoover, T. E. and D. C. Berkshire, Effects of hydration on carbon dioxide exchange across an air-water interface, *J. Geophys. Res.*, 74, 457-464, 1969
- Jähne, B., Münnich, K. O., Bösinger, R., Dutzi, A., Huber, W. and P. Libner, On the Parameters Influencing Air-Water Gas Exchange, *J. Geophys. Res.*, 92, 1937-1949, 1987
- Jähne, B., Münnich, K. O., and U. Siegenthaler, Measurements of gas exchange and momentum transfer in a circular wind-water tunnel, *Tellus*, 31, 312-329, 1979
- Liss, P. S., Processes of gas exchange across an air-water interface, *Deep-Sea Res.*, 20, 221-238, 1973
- Millero, F. J., Byrne, R. H., Wanninkhof, R., Feely, R., Clayton, T., Murphy, P., and M.F. Lamb, The internal consistency of CO₂ measurements in the equatorial Pacific, *Mar. Chem.*, 44 269-280, 1993a
- Millero, F. J., Zhang, J.-Z., Lee, K. and D. M. Campbell, Titration alkalinity of seawater, *Mar. Chem.*, 44, 153-165, 1993b
- Ocampo-Torres, F. J. and M. A. Donelan, Laboratory measurements of mass transfer of carbon dioxide and water vapour for smooth and rough flow conditions, *Tellus*, 46B, 16-32, 1994
- Siegenthaler, U. and G. Sarmiento, Atmospheric carbon dioxide and the ocean, *Nature*, 365, 119-125, 1993
- Wallace, D. W. R. and C. D. Wirrick, Large air-sea gas fluxes associated with breaking waves, *Nature*, 356, 694-696, 1992
- Wanninkhof, R., Relationship between wind speed and gas exchange over the ocean, *J. Geophys. Res.*, 97, 7373-7382, 1992

Development and Testing of In Situ N₂, O₂ and Gas Tension Sensors for Oceanographic Studies

C. McNeil¹, D. Farmer², M. Trevorrow², and B. D. Johnson³

¹L.O.D.Y.C., Université Pierre & Marie Curie, Paris, France
(email: mcneil@lodyc.jussieu.fr)

²Institute of Ocean Sciences, Sidney, B.C., Canada

³Dalhousie University, Halifax, N.S, Canada

Abstract

In this paper we present new measurements obtained in Lake Biwa, Japan, of dissolved nitrogen gas. The dissolved nitrogen concentration is calculated from simultaneous measurements of dissolved oxygen and gas tension. The data set show the robustness of the instrumentation and technique and indicate the potential of such measurements for use in bio-physical gas exchange studies.

1 Introduction

The air-sea interface and the upper ocean mixed layer have globally significant roles in the redistribution and recycling of dissolved atmospheric gases and their organic and inorganic derivatives. However, the detailed mechanisms by which the redistribution and recycling processes occur and the magnitude of the resultant fluxes are poorly known. This motivated a study to measure simultaneously dissolved nitrogen and oxygen concentrations under a wide range of oceanographic and meteorological conditions. The chief advantages of studying oxygen and nitrogen simultaneously are two-fold. First, because dissolved nitrogen, unlike dissolved oxygen, has a low biological activity [e.g., *Mague et al.*, 1974], simultaneous measurements of these two gases provide a differential indicator of the magnitude of *biological* versus non-biological processes affecting these gases [e.g., *Emerson et al.*, 1991]. Second, the dissolved concentrations of these two primary atmospheric gases will directly influence bubble dissolution rates and hence bubble mediated air-sea gas exchange rates. Bubble dissolution is an important contribution to gas exchange at higher wind speed [*Thorpe*, 1984; *Woolf*, 1993; *Woolf and Thorpe*, 1991; *Keeling*, 1993; *Farmer et al.*, 1993]. To this end, novel dissolved gas sensors are being developed. Operating in situ, these devices can be moored or placed on freely drifting arrays to obtain extended time series measurements of dissolved oxygen, nitrogen and gas tension.

2 Gas Tension and Nitrogen Measurements

Gas tension is a measurement of the sum of the partial pressures of all the dissolved gases (i. e., the water phase analogue of barometric pressure). The measurement is obtained by equilibrating a small sample volume of air, separated by a gas-permeable membrane, with all the dissolved gases in the water [D'Aoust *et al.*, 1975; Anderson and Johnson, 1993]. The sample volume is designed to be independent of hydrostatic pressure variations. Measurement of the air pressure in the equilibrated sample volume is then the gas tension of the water (we call the instrument a *gas tension device*, GTD). Previous to our use of this measurement in air-sea gas exchange studies, the gas tension measurement was used in water quality control of natural waters and reservoirs [e.g., D'Aoust and Clark, 1980]. This measurement alone, however, provides no discrimination of the dissolved gases present in the water. Because naturally occurring water masses, typically, are in approximate equilibrium with the atmosphere (composed of 78% N₂ and 21% O₂), the gas tension measurement is primarily that of the partial pressure of nitrogen and *oxygen*. By subtracting the contribution of oxygen to the gas tension measurement one obtains the partial pressure of *nitrogen*. Dissolved gas concentrations are related to partial pressures by solubility coefficients which depend on the temperature and salinity of the water.

Our first such nitrogen measurements were made in the N.E. Pacific [McNeil *et al.*, 1995]. These results are reproduced in Figure 1. The calculation of the nitrogen saturation levels (Fig. 1d) were performed using dissolved oxygen measurements at 30 m depth and gas tension measurements at 40 m depth. This difference in depth between the two measurements combined with various diurnal physical and biological oceanographic processes [McNeil and Farmer, 1995] resulted in an artificial *diurnal cycle* in the dissolved nitrogen saturation levels (Fig. 1d). These first results were significant, however, in testing the *instrumentation* and methodology. Use was also made of the nitrogen measurements to infer that air-sea gas exchange was of secondary importance to the interpretation of the dissolved oxygen measurements [McNeil and Farmer, 1995]. In this paper we present new measurements obtained with a fully integrated GTD/CTDO₂ system to show the robustness of the nitrogen subtraction process and the state of instrumentation development.

3 Lake Measurements

As part of our participation in the BITEK study in Lake Biwa, Japan during August 1993, we deployed a newly developed GTD/CTDO₂ combined sensor (shown in Figure 2) at 4–6 m depth. The water temperature and *dissolved gas measurements* are shown in Figure 3. At present, dissolved oxygen measurements have a rather large uncertainty in absolute magnitude of $\pm 10\%$ saturation. Figure 3d shows the results of the nitrogen subtraction process.

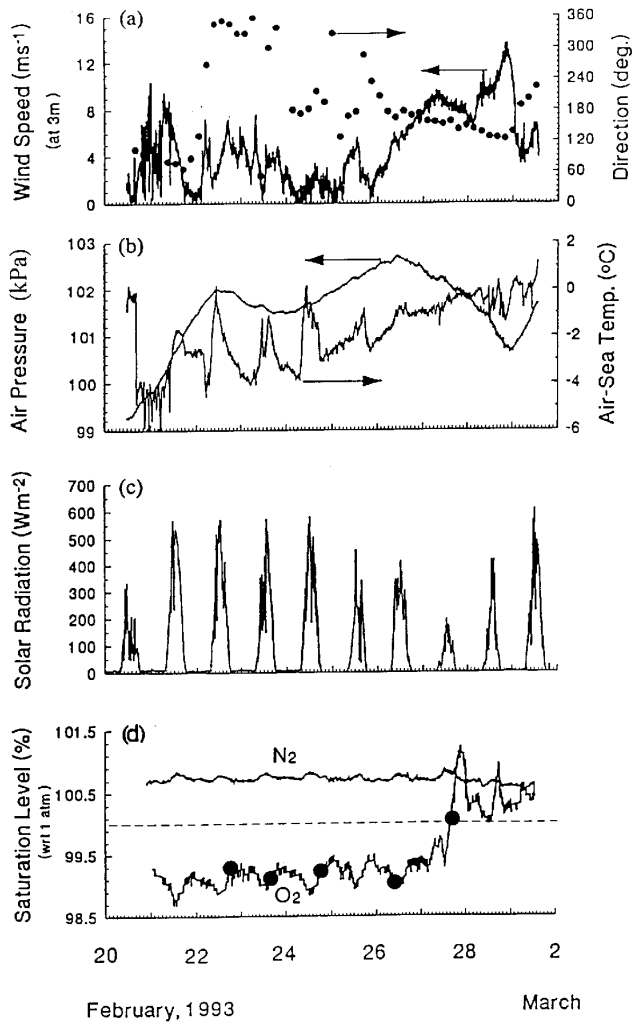


Figure 1: Measurements made in the N.E. Pacific, showing: (a) wind speed and direction; (b) air pressure and air-sea temperature; (c) solar radiation intensity; and (d) dissolved oxygen and nitrogen saturation levels (w.r.t. 1 standard atmosphere of moist air) at 30–40 m depth.

Dissolved Gas Sensor

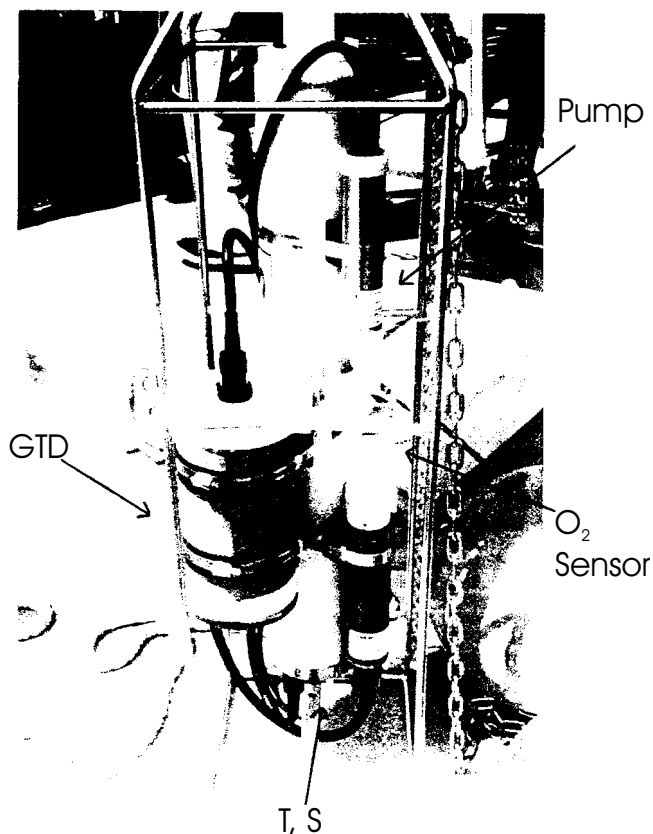


Figure 2: A photograph of the fully integrated dissolved gas sensor, consisting of a pumped Sea-Bird Electronics, Inc. (Seattle, USA) SBE16DO CTD modified to record the output of a Paroscientific, Inc. (Seattle, USA) pressure sensor, the primary measurement of the gas tension device (GTD). The system is completely autonomous and can be deployed for more than a year.

The bold lines indicate *dissolved oxygen* and nitrogen saturation levels; the dashed lines indicate the error in the dissolved nitrogen saturation level for a $\pm 10\%$ error in the dissolved oxygen saturation level. The time invariance of the dissolved nitrogen signal is quite remarkable, showing less than 0.5% variability over time scales of a day, in contrast to more than 10% diurnal variability of the dissolved oxygen saturation level. These results are consistent with the known biological inactivity of dissolved nitrogen gas [e.g., *Mague et al.*, 1974]. As the nitrogen subtraction process is performed for gas tension and oxygen measurements at the same location in the water column, there is no problems of incomplete nitrogen separation previously

encountered with the N.E. Pacific data set.

The saturation level anomaly between the dissolved oxygen and nitrogen provides an indication of net community *production/respiration*. Low frequency variability of the nitrogen measurements indicate the importance of physical processes affecting the dissolved gas saturation levels, e. g., gas transfer and net heating/cooling. Without the dissolved nitrogen measurements it would be difficult to assess what contribution to oxygen saturation level is derived from physical processes and what contribution is derived from biological processes. From this preliminary investigation of the data set, and the associated large uncertainty in the absolute value of the dissolved oxygen concentration, one cannot conclude confidently a value for net community production/respiration within the lake. However, the data do indicate the potential for using simultaneous nitrogen and oxygen time series measurements, in combination with simple budget models of air-water gas exchange (including some Schmidt number dependency), to understand the processes and magnitudes of fluxes of gases to and within water masses.

4 Future Developments

The main measurements used to infer nitrogen concentration in sea water are gas tension, dissolved oxygen, temperature and salinity. The accuracy and resolution of the gas tension measurement depends only on the pressure sensor once the sensing volume of air behind the membrane is equilibrated. Bio-fouling of the membrane under prolonged exposure to biologically active conditions will lead to a decrease of the membrane diffusivity and hence decrease the gas tension device response time; the accuracy and resolution of the gas tension measurement is not compromised. For the gas tension pressure measurement we make use of a Paroscientific Inc. (Seattle, US) pressure sensor which has a rated accuracy of 0.01 % per year and a resolution of 10^{-8} . This accuracy and resolution greatly exceeds that of any commercially available *oxygen probe*, such as the YSI probe supplied by Seabird Electronics on their CTDs. As the nitrogen measurement accuracy and time dependent stability depends on the specifications of the oxygen sensor, we are investigating the exciting possibility of developing a highly stable oxygen sensor based on the gas tension device technology. Preliminary results from laboratory experiments conducted at Dalhousie University are encouraging. If successful, this will provide highly stable nitrogen and oxygen measurements, to the time dependent stability of the Paroscientific pressure sensor and associated electronics, for applications in long term moorings.

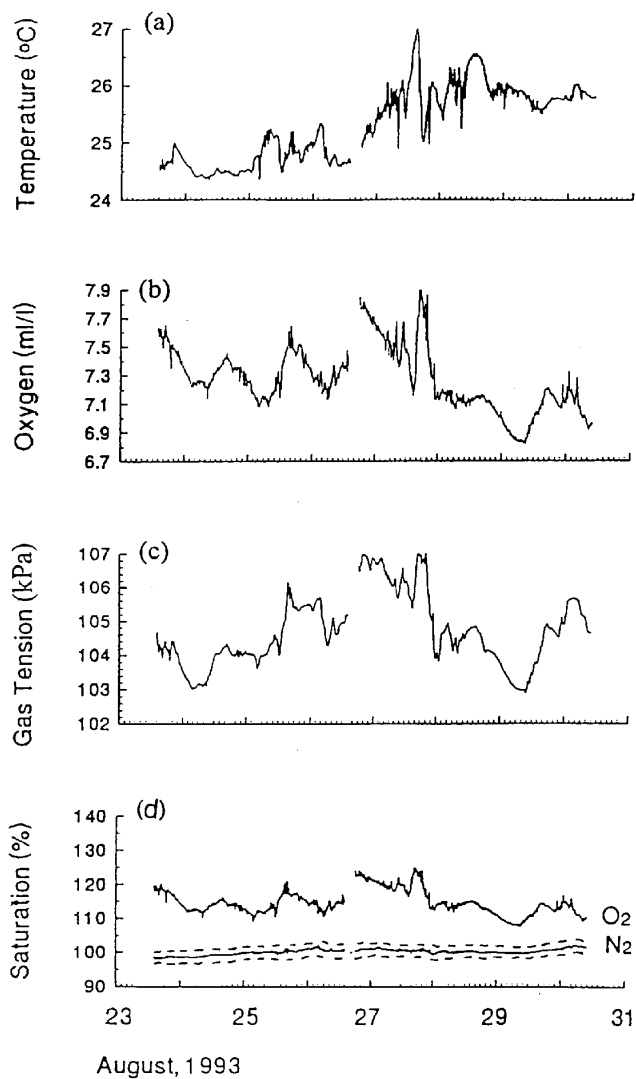


Figure 3: Measurements made in Lake Biwa, Japan, at 4 to 6 m depth, showing: (a) water temperature; (b) dissolved oxygen concentration; (c) gas tension and (d) dissolved oxygen and nitrogen saturation level (w.r.t. 1 standard atmosphere of moist air). The dashed lines indicate the error in the dissolved nitrogen saturation level associated with a $\pm 10\%$ error in the oxygen saturation level.

References

- Anderson, M. L. and B. D. Johnson, Gas transfer: a gas tension method for studying equilibration across a gas water interface, *Journal of Geophysical Research*, 97, C11, 17899-17904, 1992
- D'Aoust, B. G. and M. J. R. Clark, Analysis of supersaturated air in natural waters and reservoirs, *Transactions of the American Fisheries Society*, 109, 708-724, 1980
- D'Aoust, B. G., H. Siebold and R. White, Direct measurements of total dissolved gas pressure, *Undersea Biomedical Research*, 2, 141-149, 1975
- Emerson, S., P. Quay, C. Stump, D. Wilbur and M. Knox, O₂, Ar, N₂ and ²²²Rn in surface waters of the subarctic Pacific Ocean: Net biological O₂ production, *Global Biogeochemical Cycles*, 5, 49-69, 1991
- Farmer, D. M., C. L. McNeil and B. D. Johnson, Evidence for the importance of bubbles in increasing air-sea gas flux, *Nature*, 361, 620-623, 1993
- Keeling, R. F., On the role of large bubbles in air-sea gas exchange and supersaturation in the ocean, *Journal of Marine Research*, 51, 237-271, 1993
- Liss, P. S. and L. Merlivat, Air-sea gas exchange rates: Introduction and synthesis. In Buat-Menard, P. (ed.), *The Role of Air-Sea Exchange in Geochemical Cycling*, pp. 113-127, D. Reidel Pub. Co., Dordrecht, Holland, 1986
- Mague, T. H., Weare, M. M., and Holm-Hansen, O., Nitrogen fixation in the North Pacific Ocean, *Marine Biology*, 41, 213-227, 1974
- McNeil, C. L. and D. M. Farmer, Observations of the influence of diurnal convection on upper ocean dissolved gas measurements, *Journal of Marine Research*, 53, 151-169, 1995
- McNeil, C. L., B. D. Johnson and D.M. Farmer, In situ measurement of dissolved nitrogen and oxygen in the ocean, *Deep-Sea Research*, 42(5), 819-826, 1995
- Thorpe, S. A., The role of bubbles produced by breaking waves, *Geophysics*, 2(1), 53-56, 1984
- Wolf, D. K., Bubbles and the air-sea transfer velocity of gases, *Atmosphere-Ocean*, 31(4), 517-540, 1993
- Wolf, D. K. and S. A. Thorpe, Bubbles and the air-sea exchange of gases in near-saturation conditions, *Journal of Marine Research*, 49, 435-466, 1991

Propane as a Tracer Gas for Reaeration Tests

B. E. Boumansour, H. Jupsin, and J. - L. Vasel

Fondation Universitaire Luxembourgeoise
186, av. de Longwy; B - 6700 Arlon, Belgium

Abstract

The aim of this study was to examine the possible applications of propane as a tracer when the gas of interest is air or propane. The influences of various factors on the transfer coefficient $kl \cdot a$, i. e., surfactant, inert suspended solids and biological suspended solids, were also studied. The effects of these factors on $kl \cdot a$ were characterized but the ratio between oxygen transfer coefficient and propane transfer coefficient proved not to be affected by those factors. Applications of propane as a tracer in various biosystems are illustrated.

1 Introduction

Using gaseous tracers for *reaeration* coefficient measurement was first suggested by *Tsivoglou et al.* [1965]. Developed first in order to quantify the reaeration coefficients of rivers, the method utilized radioactive krypton 85 as the tracer gas, tritium as the dispersion and dilution tracer and rhodamine wt in order to provide information about sampling times. However, this technique was not pursued because of constraints linked to radioactive tracers. Another method that did not require radioactive tracer was suggested by *Rathbun and Shulz* [1975]. It employs a low-molecular-weight tracer — either ethylene or *propane* — as the gaseous tracer and *rhodamine wt* as the dispersion and dilution tracer.

Under certain conditions this technique yields accurate reaeration measurements and has been applied successfully to small rivers [*Vander Borgh*, 1980]. *Rathbun et al.* [1978] conducted a detailed laboratory study of ethylene and propane as tracer gases. If the ratio of transfer coefficients between oxygen and tracer gas is examined, one obtains a 1.15 ± 0.0226 average value with ethylene as the tracer gas and 1.39 ± 0.0281 with propane. The authors also showed that these ratios were not affected by the presence of phenol, oil, or detergent (sodium alkylaryl sulfonate) in water. *Swee*ris [1979] examined the possibility of helium, hydrogen, argon, nitrogen and krypton as tracer gases for reaeration capacity measurement in activated-sludge sewage treatment plants. The author suggested argon and helium as usable tracers. His results indicate a slight ratio dependence on the aeration system, that is, surface aeration or diffused air system. On the other hand, the presence of cellulose powder (10 g/l) does not particularly affect the ratio. A weak effect

is recorded, but is due more to associated surfactants compounds than to the cellulose itself.

Using a tracer gas provides a transfer coefficient value for a gas that is not consumed by the biological reactions occurring in the system. If the oxygen/tracer gas transfer coefficient ratio is known, we can quantify oxygen exchanges in the presence of biological reactions. Propane is at first sight an interesting tracer gas: it is naturally absent in water and in air, easily available and inexpensive, and can be measured easily. Our purpose is to test propane as a tracer gas for reaeration tests and examine the influence of factors such as gas flow, surfactants or suspended solids — particularly biological sludge — on the oxygen and propane transfer coefficients ratio. We shall examine whether the method is applicable to other sewage treatment systems, particularly trickling filters and activated sludges systems.

2 Theory

To describe mass transfer between gas phases and liquid phases one often uses the well known Adeney's equation, which expresses the transfer as being proportional to the concentration gradient in the liquid phase. When applied to oxygen this gives:

$$\frac{dC}{dt} = kl \cdot a(C_s - C) \quad (1)$$

with $kl \cdot a$ = mass transfer coefficient for oxygen (time^{-1}), C_s = dissolved oxygen content at saturation (mg/l), C = dissolved oxygen content in the liquid phase (mg/l).

When applied to propane, Adeney's equation gives:

$$\frac{dP}{dt} = kl \cdot a_p(P_s - P) \quad (2)$$

with $kl \cdot a_p$ = mass transfer coefficient for propane (time^{-1}), P_s = dissolved propane content at saturation (mg/l), P = dissolved propane content in the liquid phase (mg/l).

The saturation values for oxygen (C_s) and propane (P_s) depend on both the component's partial pressure in the gas phase and the temperature. It is necessary to distinguish two cases depending on the composition of the gaseous phase that is in contact with the liquid.

2.1 Air Injection

In this case, the propane concentration at saturation (P_s) is equal to zero, and as mentioned further oxygen saturation in oxygen (C_s) can be estimated by different ways. Equation (1) is integrated as follows:

$$\ln(C_s - C) = -kl \cdot a \times t + \ln(C_s - C) \quad (3)$$

with C_0 = Initial oxygen concentration (mg/l)
and the solution of equation is (2) is:

$$\ln P = \ln P_0 - kl \cdot a_p t \quad (4)$$

with P_0 = Propane concentration in the reactor at $t = 0$

2.2 Propane Injection

In this case, given that $C_s = 0$ and P_s has been determined, the equations then become:

$$\ln(P_s - P) = -kl \cdot a_p t + \ln(P_s - P_0) \quad (5)$$

$$\ln C = -kl \cdot a t + \ln C_0 \quad (6)$$

From these equations it can be deduced that propane could be utilized as tracer during absorption or desorption. The transfer coefficients ratio is defined as:

$$R = \frac{kl \cdot a}{kl \cdot a_p} \quad (7)$$

According to *Tsivoglou* [1965], R is equal to the square root of the diffusion coefficients ratio.

$$R = \frac{kl \cdot a}{kl \cdot a_p} = \sqrt{\frac{D_a}{D_p}} \quad (8)$$

If the resistance to the transfer of propane is also located in the liquid film, then $kl \cdot a_p$ should depend on $V_L^{1/3}$, $\mu_L^{-2/3}$ and $\rho_L^{1.16}$ corresponding respectively to the local liquid velocity, liquid viscosity and liquid density [*Calderbank & Moo-Young*, 1961]. The $kl \cdot a$ and $kl \cdot a_p$ would depend on temperature.

3 Bench Scale Equipment

The tests were conducted in a 3.2 liter plexiglass pilot placed in a thermostatic tank. Gas flow rate was measured and regulated with a rotameter. A three-way valve allowed us to select propane or air as the working gas

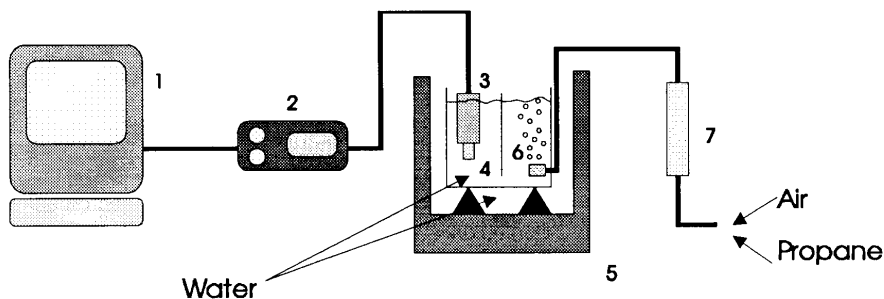


Figure 1: Bench scale equipment. (1) microcomputer (2) oxygen and temperature meter (3) thermistor and oxygen polarographic probe (4) laboratory pilot (5) thermostatic tank (6) porous stone (7) gas flowmeter

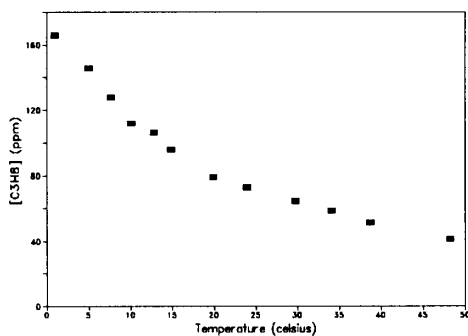


Figure 2: Saturation value of propane in pure water ($P = 1 \text{ atm}$).

or to obtain a constant flow as soon as the valve opens. The gas was injected through a porous stone that produces medium-size bubbles. Thanks to the shallow injection depth (15 cm) it was not necessary to correct the oxygen concentration at saturation, as the pressure varied with hydrostatic pressure.

4 Propane Solubility

No saturation data for propane at various temperature (P_S value) were available in the literature. The curve was thus obtained as follows: Propane was injected through a porous stone into 250 ml of water. The bottle was in a bath equipped with a thermostat, and the whole apparatus was located in a tank, also with a thermostat. Gas injection was maintained for 30 minutes, after which the water was sampled and the propane concentration analyzed by gas chromatography. The result is the curve in Figure 2.

From the observed data a nonlinear regression could be calculated as

follows:

$$\begin{aligned}
 P_S \text{ (ppm)} &= 170.08917 - (7.01445T) + (0.15516T^2) \\
 &- (0.001354T^3) \quad (R^2 = 0.99) \\
 \text{or} & \\
 P.S. \text{ (ppm)} &= 229.3902 - (48.152643 \ln(T)) \\
 &- (62.89265/T) \quad (R^2 = 0.99)
 \end{aligned}
 \tag{9}$$

where T = temperature in °C, P_S = propane concentration at saturation (mg/l)

Another way to express saturation values is to provide Bunsen coefficients β . In our case,

$$10^3\beta = 84.8325 - (3.4985T) + (0.07739T^2) - (0.00067528T^3) \quad (R^2 = 0.99) \tag{10}$$

$$10^3\beta = 114.4091 - (24.0163 \ln(T)) - (31.3679/T) \quad (R^2 = 0.99) \tag{11}$$

With β expressed as $\left(\frac{\text{volume of gas in standard conditions } 0^\circ\text{C, } 1 \text{ atm}}{\text{volume of liquid}} \right)$

5 Determination of Sampling Times

The samples should be taken when both curves for oxygen and propane (ln(deficit) versus time) are still straight lines but as late as possible to provide a better estimation of the slope. Similar results may be observed during air injection. The results for air and propane injection prompted us to sample as follows: At least three or more samples would be taken within 180 seconds after injection of gas. In both test types we could choose propane sampling time by observing on a computer screen the real-time plot of the logarithm of the dissolved oxygen deficit.

6 Effect of Compounds on $kl \cdot a$

Figures 3-5 show the influences of various factors — surfactant (lauryl sulfate, Figure 3) and inert (clay; Figure 4) and biological suspended (Figure 5) solids — on transfer during air and propane injection.

Biological suspended solids were provided by activated sludge from a sewage treatment plant. The respiration was then stopped by using mercuric chloride (HgCl_2). Suspended solids were measured by standard methods.

7 Ratio Study

For both gas phases (air and propane), classic analysis of variance with one, two, or three criteria and a replicate [Dagnelies, 1980] led us to accept the

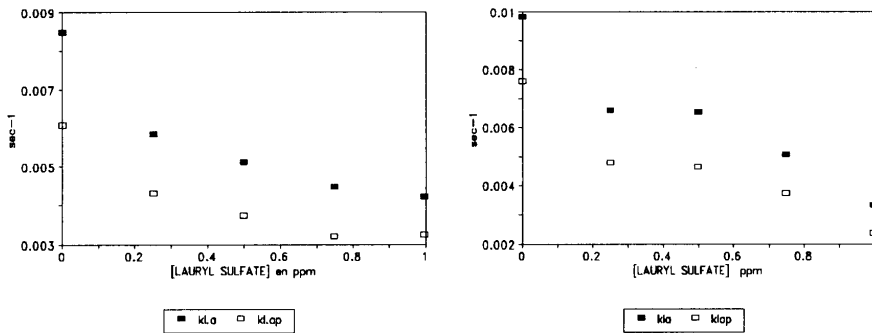


Figure 3: Effect of surfactant (ppm) on $k_L \cdot a$ gas flow rate: 90 lN/hr. (a) propane injection, (b) air injection

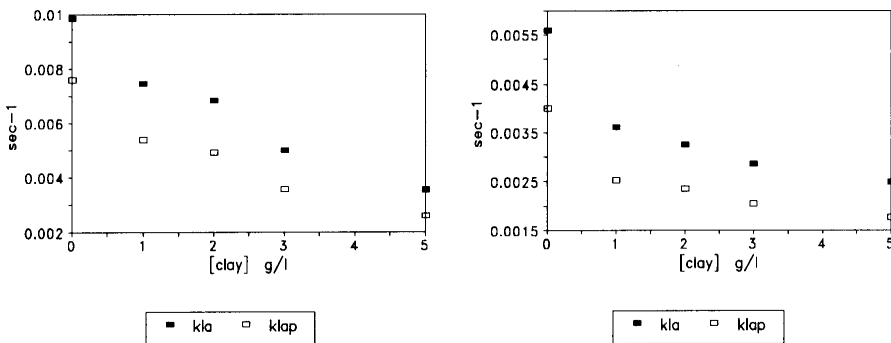


Figure 4: Effect of inert suspended solids (g/l), on transfer coefficient (gas flow rate = 90 lN/hr). (a) air injection, (b) propane injection

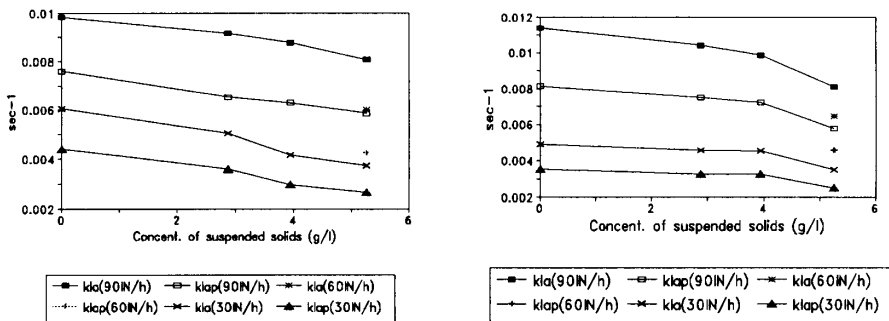


Figure 5: Influence of flocculated biological suspended solids (g/l) at different flow rates. (a) air injection, (b) propane injection

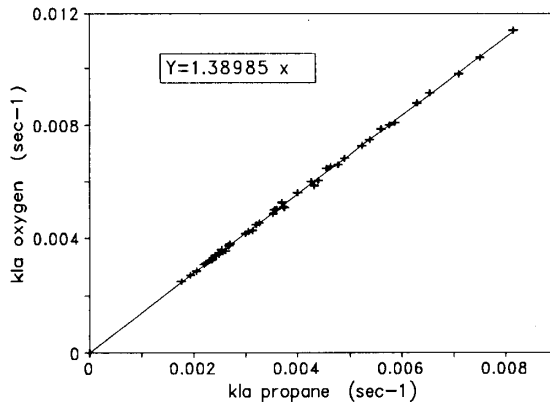


Figure 6: Correlation between $kl \cdot a$ and $kl \cdot a_p$ on cumulative experimental data.

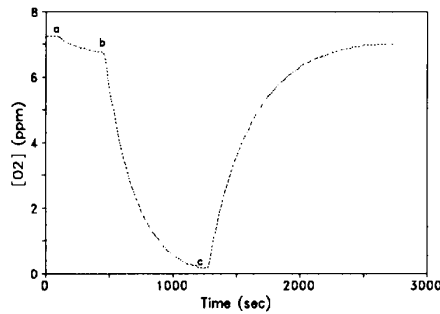


Figure 7: Experimental results in an activated sludge reactor. (a) substrate injection, (b) propane injection, © air injection.

hypothesis that the ratios were independent of state variables. From these results we deduced that flow rate, surfactants, suspended solid, and air and propane injection did not modify the value of the transfer coefficients (oxygen and propane) ratio. We can consider the ratio to reflect a random distribution characterized by the following parameters: Average = 1.389, standard deviation = 0.0252, Max = 1.42, Min = 1.2934. Another way to present the results is illustrated in Figure 6. The regression calculated from our experimental data yielded a slope of 1.3898 and $r^2 = 0.99$. These results are very close to those of Rathbun et al., 1.39 ± 0.0281 [1978].

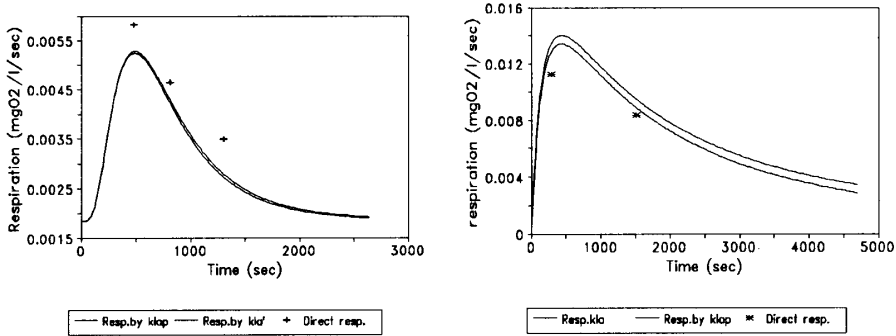


Figure 8: Calculated respiration rates. (a) First test. (b) Second test.

8 Applications

8.1 Respiring Bioreactor

An experiment is realized as shown in Figure 7. In a batch reactor continuously aerated substrate is first injected (a), then propane is injected (b) to decrease oxygen concentration and to get enough propane for analysis. Then air is again provided back stationary state. Figure 7 shows (c) dissolved oxygen in the reactor during the experiment.

The oxygen balance for the reactor is described by the following equation:

$$\frac{dC}{dt} = kl \cdot a' (C_s - C) - R_t \quad (12)$$

with $kl \cdot a' =$ transfer coefficient in waste water (s^{-1}).

The respiration rates calculated from the reactor's oxygen balance are given in Figure 8.

As observed in Figure 8, the respiration rates calculated by the oxygen balance using either $kl \cdot a'$ or $kl \cdot a'_p \times 1.39$ are very similar. In both experiments the overall tendency is confirmed by direct measurements (respiration rates on samoles from the reactor). The discrepancies between the three methods are due partly to the reproducibility of the respirograms between two substrate injections.

Be that as it may, it appears from these experiments that $kl \cdot a$ may be estimated for a respiring biosystem by using propane as a tracer [Boumansour, 1994].

8.2 Tests on Trickling Filters

The method was first proposed and developed by *Vasel and Schrobiltgen* [1991]. Propane is useful to measure oxygen transfer efficiency when the

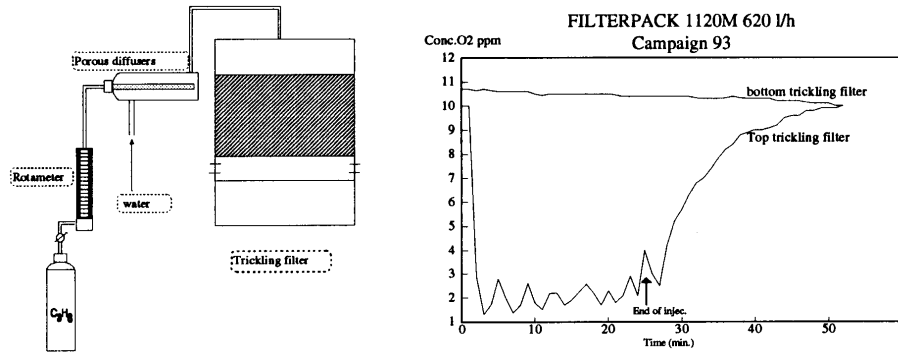


Figure 9: (a) Propane injection device in tap water. (b) Example of an experiment on trickling filter dissolved oxygen at top and bottom of trickling filter during propane injection.

media is covered with biomass. Using a plug flow model to describe the hydrodynamics of the trickling filter, the equations for propane and oxygen become:

$$\ln \frac{P_{out}}{P_{in}} = kl \cdot a_p \bar{t} \tag{13}$$

and

$$\frac{\ln kl \cdot a' (C'_S - C_{in}) - r_A / \delta}{\ln kl \cdot a' (C'_S - C_{out}) - r_A / \delta} = kl \cdot a' \bar{t} \tag{14}$$

where r_A = respiration rate per unit area ($\text{mgO}_2/\text{m}^2 \text{ s}$), δ = liquid film thickness (m).

$kl \cdot a'$ has been estimated as $kl \cdot a'_p * 1.39$, and from this a global oxygen balance could be calculated.

The tests were conducted on a pilot trickling filter installed in a full scale facility. The installation included a trickling filter ($H = 1.73 \text{ m}$, $A = 2 \text{ m}^2$). The filtration medium was a random plastic packing material (Filterpak 1120 M; $A_s = 95 \text{ m}^2/\text{m}^3$). The ventilating holes had a total surface area of 0.028 m^2 . The experiments were run using tap water. Propane was injected into the water through a porous diffuser as indicated on figure 9a.

A tank supplied with an automatic purger was located after the gas injection to avoid injecting bubbles with the liquid.

The measurements were made at four different flow rates. We injected the propane once hydraulic steady state had been reached. Dissolved oxygen was measured at the top and bottom filter using oxygen probes (Orbisphère 2603). The signal from the oxygen probes was recorded until steady state

Table 1: Oxygen transfer in trickling filter [Vasel 1988]

SOTR(kgO ₂ /kWh)	Irrigation rate (m ³ /m ² · h)			
	0.125	0.250	0.375	0.5
Clean media	1.44	1.54	1.67	2.10
Media covered with biomass	8.61	13.61	13.47	12.84

was reached. At completion the water was sampled and state variables (temperature, pressure, etc.) were measured. The water was sampled at the top and bottom of the trickling filter using airtight vials.

Results are as given in Table 1.

From those results it can be deduced that oxygen transfer in a trickling filter is highly enhanced by microbial respiration.

9 Conclusion

Propane was already known as a useful tracer gas but its main application was for measuring K_2 coefficients in rivers. In our work the methodology has been adapted to artificial biosystems, i. e., trickling filters and activated sludge pilot plants.

Before using propane in such systems it was necessary to ascertain whether the ratio between oxygen transfer coefficient and propane transfer coefficient was not affected by the water's composition. Thus the main parameters that may affect the transfer were tested, namely, surfactant and suspended solids (both inert and biological). It appears that $kl \cdot a$ and $kl \cdot a_p$ decrease when the concentrations of these compounds increase but the coefficients' ratio remains unchanged.

Another result is that the methodology can be applied using air or propane as the gas phase, which means that it can be utilized during absorption as well as desorption of propane.

The methodology has been applied to trickling filters and activated sludge. For trickling filters the method is easy to handle on clean media. For media covered by biomass the method is more difficult. From our first results it is obvious that there is a huge increase of oxygen transfer in the liquid film flowing in the media. This transfer increase is due to the respiration rate in the liquid film. For activated sludge it appears that the method with propane provides values of respiration rates very close to those deduced from the oxygen balance after $kl \cdot a$ determination. These values are not very different from the values measured directly on sampled mixed liquors. The method is now being tested with other systems such as RBC and hydraulic structures.

NOTATION

A	trickling filter section	(m ²)
A_s	specific support surface area	(m ² /m ³)
SOTR	Standard oxygen transfer rate	(kgO ₂ /kWh)
C	dissolved oxygen concentration	(mg/l)
C_o	initial oxygen concentration	(mg/l)
C_s	oxygen concentration at saturation	(mg/l)
C_{in}	oxygen concentration in water at inlet	(mg/l)
C_{out}	oxygen concentration in water at outlet	(mg/l)
D_a	oxygen diffusion coefficient	(cm ² s ⁻¹ 10 ⁻⁵)
D_p	propane diffusion coefficient	(cm ² s ⁻¹ 10 ⁻⁵)
H	trickling filter height	(m)
$kl \cdot a$	oxygen transfer coefficient	(s ⁻¹)
$kl \cdot a'$	transfer coefficient in waste water	(s ⁻¹)
$kl \cdot a_p$	propane transfer coefficient	(s ⁻¹)
P	propane concentration at inlet	(mg/l)
P_o	propane concentration at outlet	(mg/l)
P_{in}	injection concentration of propane in water at entry	(mg/l)
P_{out}	concentration of propane in water at exit	(mg/l)
P_s	propane concentration at saturation	(mg/l)
R	adim transfer coefficient ratio	
r_A	respiration rate per unit area	(mgO ₂ /m ² s)
R_t	biomass respiration rate	(mgO ₂ /l s)
\bar{t}	average residence time as measured by a tracer dye (rhodamine wt)	
t	time	(s)
T	temperature	(°C)
δ	liquid film thickness	(m)
β	Bunsen coefficient	

Acknowledgements

The first author was awarded a combined grant for this research by the Ministry of Environment and Ministry of Education of Luxembourg.

References

- BOUMANSOUR, B. E., Utilisation du propane comme gaz traceur pour la détermination des coefficients de réaération dans les écosystèmes aquatiques, master degree, FUL, Belgium, 1994
- CALDERBANK, P. H., MOO - YOUNG, M. B., *Chem. Engrg. Sci.*, 16, pp 39, 1961
- DAGNELIES, P., Théorie et méthodes statistiques, Vol II, Presses agronomiques de Gembloux
- RATHBUN R. E., STEPHENS D. W., SHULTZ D. J. & TAI D.Y., Laboratory studies of gas tracers for reaeration, *J. Env. Eng. Div.*, EE2, pp 215-229, 1978

- RATHBUN, R. E. & SCHULTZ D. S., Preliminary experiments with a modified tracer technique for measuring stream reaeration coefficients, *US Geol. Survey Open File Report 256*, 36 pp, 1975
- SWEERIS S., New developments for measuring the oxygenation capacity, *Prog. Wat. Techn.*, Vol 11 (3), pp 37-47, 1979
- TSIVOGLU et al., Trace measurement of atmospheric reaeration I: Laboratory studies, *JWPCF*, Vol 10 (33), pp 1343-1362
- VANDERBORGHT, P., Etude physico-chimique des eaux de la Semois en vue d'une gestion qualitative, Ph. D. thesis, FUL, 1980
- VASEL, J. - L., Contribution à l'étude des transferts gazeux en gestion des eaux, Ph. D. thesis, FUL, 1988
- VASEL, J. - L. & SCHROBILTGEN P., Oxygen transfer in Trickling filters, *Water Research*, Vol 25 (1), pp 53-60, 1991

Heat as a Proxy Tracer for Gas Exchange Measurements in the Field: Principles and Technical Realization

H. Haußecker^{1,3}, *S. Reinelt*², and *B. Jähne*^{1,3}

¹Scripps Institution of Oceanography, Physical Oceanography Res. Div.
La Jolla, CA 92093-0230, USA, email: bjaehne@ucsd.edu

²Institute for Environmental Physics, University of Heidelberg
Im Neuenheimer Feld 366, 69120 Heidelberg, Germany

³Interdisciplinary Center for Scientific Computing, University of Heidelberg
Im Neuenheimer Feld 368, 69120 Heidelberg, Germany
email: horst.haussecker@iwr.uni-heidelberg.de

doi: 10.5281/zenodo.10401

Abstract

An infrared technique to investigate the transfer processes across the aqueous mass boundary layer is presented. This controlled flux technique (CFT) uses heat as a proxy tracer for gases to allow for fast and local measurements of the gas transfer rate. Three different ways of gas transfer velocity measurements are investigated. The first one, the steady state method is a straightforward way to probe the basic unknowns needed to directly compute the gas transfer velocity k . The other two proposed techniques are model based but also yield a deeper insight into the mechanisms of air-sea gas exchange. The decay method works only in a lab environment while the spatio-temporal temperature fluctuation method is well suited for both lab and ocean measurements. The mathematical foundations of the underlying models are introduced together with their practical application.

1 Introduction

The transfer rate k for any species (heat, gases or momentum) in water is directly related to the tracer flux across the interface and the resulting concentration difference across the aqueous boundary layer by

$$k = \frac{j}{\Delta c}, \quad (1)$$

with j = flux density of the observed species and Δc = concentration difference across the boundary layer. For heat Δc has to be replaced by the temperature difference ΔT , with $\Delta c = \rho C_p \Delta T$. The relation between k and the characteristic time constant t_* of the transport process is given by

$$t_* = \frac{D}{k^2}, \quad (2)$$

independently of the underlying model. Heat – like a dissolved gas tracer – is a scalar. Thus convective transport of both is the same, only the molecular transport differs. The ratio between gas and heat exchange rates, k_g/k_h , can be expressed as [Jähne *et al.*, 1989]

$$\frac{k_g}{k_h} = \left(\frac{D_g}{D_h}\right)^n = \left(\frac{Sc_g}{Sc_h}\right)^{-n}, \quad (3)$$

where the (dimensionless) *Schmidt number* Sc is defined as the ratio of kinematic viscosity ν to the diffusion coefficient D , $Sc = \nu/D$. The exponent ranges between 1/2 and 2/3 depending on the friction velocity and the mean square slope of the waves. Using this relation, the transfer velocity of any gas can be estimated if the transfer velocity of heat is known. Only the diffusion coefficients of the tracer and the Schmidt number exponent n have to be known accurately enough. Using a ± 0.02 uncertainty for n and a relative error for the diffusion coefficient D of 5%, the maximum absolute error of the gas exchange rate calculated from the heat transfer is about 12%.

In the following section, three different methods are introduced to measure the transfer velocity for heat exchange k_{heat} . These are:

- *steady state method*
- *decay method*
- *spatio-temporal temperature fluctuation method.*

2 Techniques, Models and Simulation

2.1 Steady State Method

If a known *heat flux* density of artificial *infrared radiation* is used to heat up the water surface, the transfer rate for heat in water can directly be determined from the resulting temperature response at the surface by (1). If the heat flux density j is well known k is inversely proportional to the temperature difference ΔT in the state of equilibrium. With the heat source turned on and off periodically ΔT can be measured directly out of the temperature increase right at the surface. The temperature response itself can very easily be measured with an infrared camera that observes the temperature distribution at the water surface.

2.2 Decay Method

The second method is to determine the time constant t_* of gas transfer out of the systems' response to a short temperature increase. This time the radiation is focused on a small spot that is heated up for a short time. If this heat spot can be tracked with an imaging thermography system the temporal decay of the temperature right at the surface yields t_* and therefore k since D is well known (2). Analytical and numerical solutions for the temporal

decay of a heat blob for different boundary layer models have already been developed by *Reinelt* [1994].

He solved the differential equations for the two boundary models *diffusion model* and *surface renewal model* [*Dankwerts*, 1951] for the one-dimensional case:

$$\frac{\partial C_d(z,t)}{\partial t} = D \frac{\partial^2 C_d(z,t)}{\partial z^2} \quad \text{and} \quad (4)$$

$$\frac{\partial C_{sr}(z,t)}{\partial t} = D \frac{\partial^2 C_{sr}(z,t)}{\partial z^2} - \lambda C_{sr}(z,t), \quad (5)$$

with the statistical renewal rate λ and a constant diffusion coefficient D . The time constant of the renewal effect $\tau = 1/\lambda$ describes the mean life span of a water surface element in between two surface renewal effects. Let $f(z,t)$ be a solution of (4) and $g(z,t)$ a solution of (5). Then f and g automatically are related by $g(z,t) = f(z,t)e^{-\lambda t}$.

Thus for a given initial concentration distribution within the boundary layer $C(z,0)$ the temporal solution $C(z,t)$ of (4) and 5 is given by

$$C_d(z,t) = \frac{1}{2\sqrt{\pi Dt}} \int_{-\infty}^{\infty} C(\xi,0) e^{-\frac{(z-\xi)^2}{4Dt}} d\xi \quad \text{and} \quad (6)$$

$$C_{sr}(z,t) = \frac{1}{2\sqrt{\pi Dt}} e^{-\lambda t} \int_{-\infty}^{\infty} C(\xi,0) e^{-\frac{(z-\xi)^2}{4Dt}} d\xi, \quad (7)$$

as a superposition of the elementary solutions of (4) and (5).

The instrumental setup consisted of a CO₂ infrared laser at a wavelength of 10.6 μm as heat source. The beam was focused and scanned in cross-wind direction producing a uniform flux distribution in this direction over a length of 13 cm and a laser profile shaped distribution in wind direction. Thus the whole decay process can be considered to be one-dimensional with the wind direction defining the time axis. The spatial distribution of the laser flux density is determined within the temperature images by means of digital mage processing techniques and subsequently used as spatially inhomogeneous boundary conditions in the simulation. The resulting temperature depth profile after the surface element has left the irradiated area can best be approximated by the Gaussian distribution

$$C(z,0) = C_o e^{-\frac{z^2}{h^2}}, \quad -\infty < z < 0, \quad (8)$$

with the penetration depth $h/2$. This is used as the initial temperature distribution within the boundary layer. Combining (6), (7) and (8) yields

$$C_d(z,t) = C_o \frac{h}{\sqrt{h^2 + 4Dt}} e^{-\frac{z^2}{h^2 + 4Dt}} \quad \text{and} \quad (9)$$

$$C_{sr}(z,t) = C_o \frac{h}{\sqrt{h^2 + 4Dt}} e^{-\frac{z^2}{h^2 + 4Dt} - \lambda t}, \quad (10)$$

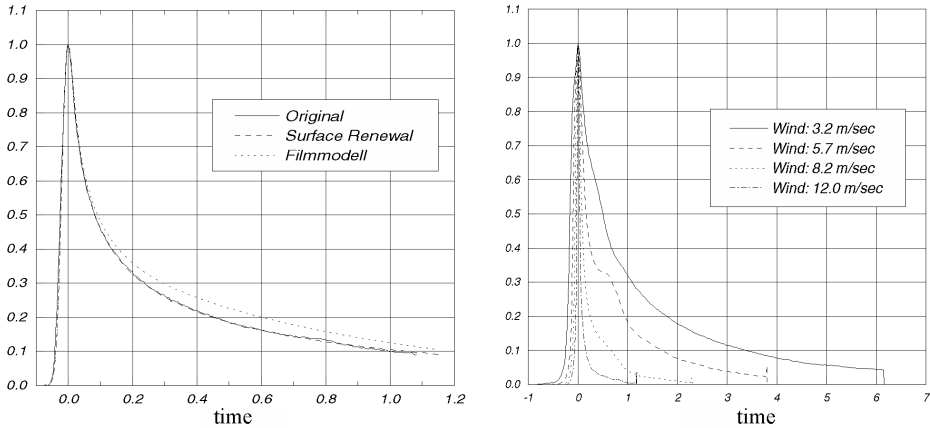


Figure 1: Decay curves of the water surface temperature after leaving the irradiated area. Left: Measurements with surface film. Data fitted with the two possible model-based decay functions for a wind speed of 8.8 m/s. Right: Decay curves for different wind speeds, measured without surface films.

for the two different boundary layer models. The infrared camera is sensitive in the 3–5 μm wavelength region. The corresponding penetration depth is about 20 μm , less than 5% of the typical heat boundary layer depth. Thus the temperature observed by the camera can be considered to be the surface temperature $T(0, t)$. The measured spatio-temporal temperature distribution therefore consist of the solutions (9) or (10) at $z = 0$:

$$C_d(0, t) = C_o \frac{h}{\sqrt{h^2 + 4Dt}} \quad \text{and} \quad C_{sr}(0, t) = C_o \frac{h}{\sqrt{h^2 + 4Dt}} e^{-\lambda t}. \quad (11)$$

One of them should reflect the real averaged temperature development observed by the camera.

The unknown parameters of (11) are C_o , h and λ . C_o is the temperature of the decay curve at any time chosen as a starting point. Fitting the data to the decay curve yields the two remaining parameters. It shows that the surface renewal solution always provides better fits to the data than the diffusion model curve (Figure 1). Therefore the surface renewal decay curve is used for all further data evaluation with the *decay method*. The heat transfer rate k_{heat} can directly be computed out of (2) with $t_* = \lambda^{-1}$. Figure 2 shows some results of heat transfer rates computed with the decay method out of data from different wind-wave facilities. They are in good agreement with previously measured mass transfer values.

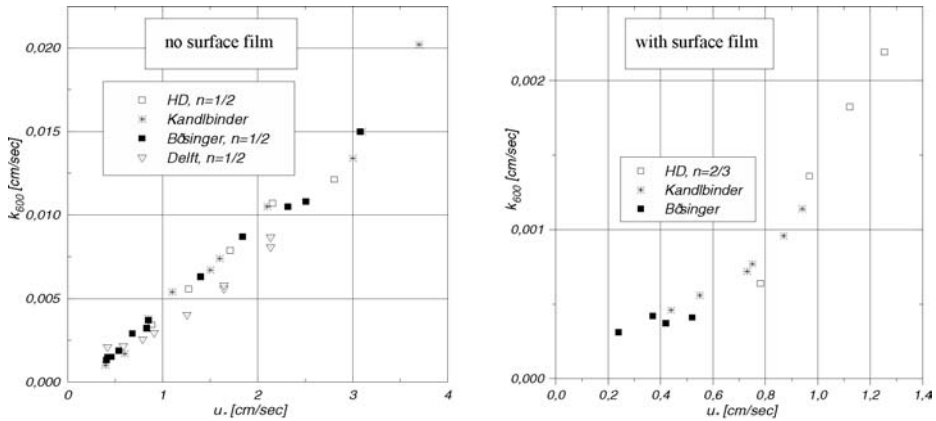


Figure 2: Gas transfer rates computed with the decay method for measurements at different wind wave facilities (Triangles: Linear Tank of Delft Hydraulics, The Netherlands. Rest: Circular Heidelberg facility). Open squares and triangles: decay method. Rest: previous mass transfer measurements.

2.3 Spatio-Temporal Temperature Fluctuation Method

The fact that the heat distribution at the water surface can directly be observed with a high spatial and temporal resolution offers another possibility to measure k and to get information about the transport mechanisms themselves. It was a main discovery during the first measurements with a new AMBER Radiance 1 infrared camera, that the typical natural heat fluxes across the water surface due to *radiative cooling* and *evaporation* are sufficiently large to cause significant temperature variations at the water surface. Since these variations are due to vertical mixing processes the heat patterns consist of both, the surface temperature and upwelling bulk water. With this discovery it is possible to estimate the temperature difference across the heat boundary layer out of the spatial temperature distribution. In this way the transport mechanisms become visible without any further application of external radiation. Nevertheless a model is needed to interpret the image content appropriately.

Previous measurements with the *decay method* showed that the surface renewal model is in best correspondence with the measured data. Therefore we use this model for a numerical simulation of the anticipated temporal temperature distribution. The concept of the surface renewal theory is that the fluid on the surface is periodically renewed by bulk fluid with a statistical renewal rate λ . The time constant of the renewal process τ is given by $\tau = 1/\lambda$. It has the physical meaning of the mean live span of a surface water patch. Given a constant tracer flux density j across the interface, the difference between water surface temperature and bulk temperature, $\Delta T(t)$ is directly proportional to the square root of the elapsed time since the last

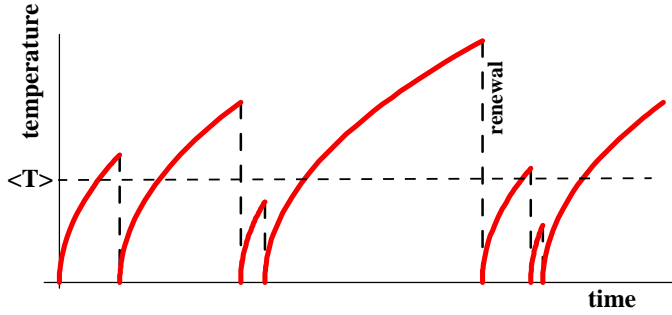


Figure 3: Qualitative sketch of temporal surface temperature evolution for the surface renewal model with randomly distributed renewal effects.

renewal effect. Combining equations (1) and (2) yields

$$\Delta T(t) = \frac{j_{heat}}{\rho C_p \sqrt{D}} \sqrt{t} = \alpha \sqrt{t}. \quad (12)$$

For a typical heat flux density of $j = 150 \text{ W/m}^2$, $\alpha = 0.0959$. Numerical simulations of the temperature evolution for the same heat flux density as boundary condition yield $\alpha = 0.1088$. Without surface renewal effects the surface temperature would continuously decrease according to (12). Introducing a statistical renewal, the temperature randomly drops back to the initial bulk water temperature T_o . Figure 3 shows a qualitative sketch of the surface temperature increase with renewal drop offs for a heat flux heating up the water surface.

The probability $P(t, \lambda)$ that a surface element would have an age of t , for a certain renewal rate $\lambda = 1/\tau_o$, is given by [Dankwerts, 1951, Gulliver, 1991]

$$P(t, \tau_o) = \lambda e^{-\lambda t}. \quad (13)$$

With this distribution the expectation value $\langle \Delta T \rangle$ of the surface temperature can be computed. This should be the mean temperature visible in the infrared images (Figure 3). The mean value $\overline{\Delta T}(\tau)$ of a single temperature increase in between two surface renewal effects with the temporal distance τ is given by

$$\overline{\Delta T}(\tau) = \tau^{-1} \int_0^\tau dt \Delta T(t). \quad (14)$$

The expectation value for ΔT is computed as the expectation value for all mean values $\overline{\Delta T}$ for all possible τ with $p(\tau, \tau_o)$ given in (13):

$$\langle \Delta T \rangle_{\tau_o} = \int_0^\infty d\tau \overline{\Delta T}(\tau) p(\tau, \tau_o) \quad (15)$$

$$= \int_0^\infty d\tau \left[\tau^{-1} \int_0^\tau dt \Delta T(t) \right] p(\tau, \tau_o). \quad (16)$$

For a periodical renewal effect, i.e. $p(t, \tau_o) = \delta(t - \tau_o)$, (15) reduces to $\langle \Delta T \rangle_{\tau_o} = \overline{\Delta T}(\tau_o)$. The variance σ^2 of the temperature distribution is given by

$$\sigma_{\tau_o}^2 = \int_0^\infty d\tau \left[\tau^{-1} \int_0^\tau dt (\Delta T(t) - \langle \Delta T \rangle_{\tau_o})^2 \right] p(\tau, \tau_o). \tag{17}$$

For the temperature difference in (12) equations (15) and (17) reduce to

$$\langle \Delta T \rangle_{\tau_o} = \frac{2\alpha}{3\tau_o} \int_0^\infty d\tau \sqrt{\tau} e^{-\frac{\tau}{\tau_o}} \quad \text{and} \tag{18}$$

$$\sigma_{\tau_o}^2 = \frac{\alpha^2}{2\tau_o} \left[\int_0^\infty d\tau \tau e^{-\frac{\tau}{\tau_o}} \right] - \langle \Delta T \rangle_{\tau_o}^2, \quad \text{respectively.} \tag{19}$$

A numerical evaluation of equations (18) and (19) for different τ_o shows that the ratio y between the expectation value of the temperature difference $\langle \Delta T \rangle_{\tau_o}$ and the standard deviation of the temperature distribution σ_{τ_o} is independent from τ_o :

$$y = \frac{\langle \Delta T \rangle_{\tau_o}}{\sigma_{\tau_o}} = 0.657393 \approx \frac{2}{3} \quad \forall \tau_o. \tag{20}$$

This result opens up a very simple opportunity to estimate the temperature difference across the interface. Instead of directly measuring the difference between the mean surface temperature and some estimated bulk temperature it is sufficient to compute the standard deviation σ of the surface temperature distribution. The mean temperature difference across the interface is given by (20) and thus

$$k_{heat} = y \frac{j}{\rho C_p \sigma}. \tag{21}$$

These results are used to estimate the heat transfer rate out of the image temperature distribution. Since the surface renewal is a statistical effect it should be equally distributed in space and time. Therefore every image is supposed to contain a variety of surface temperature states in between recent renewal and long periods of undisturbed cooling. The significance of this statistical assumption increases if the camera moves over the water surface and thus shows a variety of heat patterns with time.

A further test for the validity of the underlying model can be undertaken comparing the temperature distribution within the infrared images with the theoretical distribution for the modelled process. Given the temporal evolution of the surface temperature (12) the relative frequency $h(\Delta T, \tau)$ of ΔT for a certain τ computes as

$$h(\Delta T, \tau) = \frac{2}{\alpha^2} \frac{\Delta T}{\tau}. \tag{22}$$

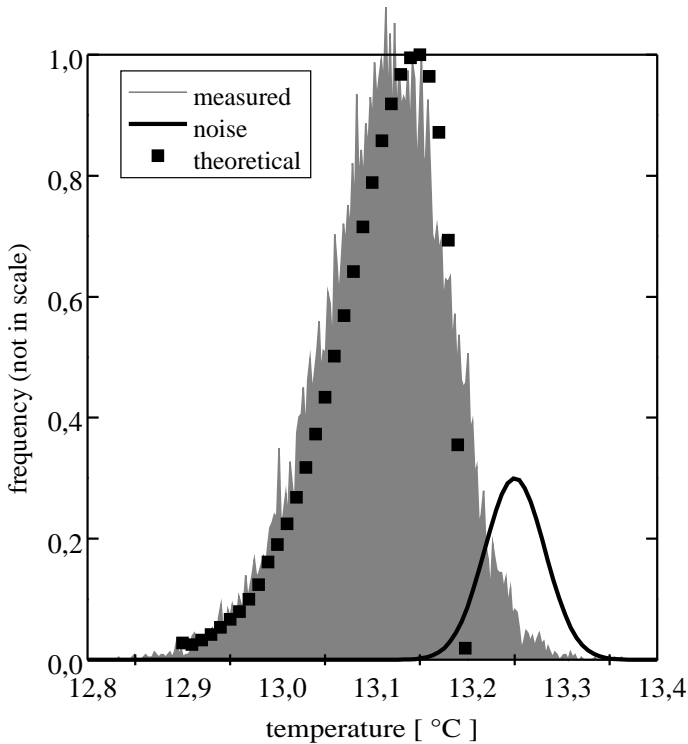


Figure 4: Measured temperature distribution within one single image (grey area plot) together with the theoretical distribution (black squares). The corresponding noise variance is indicated by the solid black curve. The image was acquired during night time with clear sky at a wind speed of 5 m/s east of Catalina island, California.

The total frequency $h(\Delta T, \tau_o)$ of a certain τ_o is given by

$$h(\Delta T, \tau_o) = \frac{2}{\alpha^2} \Delta T \int_{\Delta T^2/\alpha^2}^{\infty} d\tau \frac{p(\tau, \tau_o)}{\tau}. \quad (23)$$

Figure 4 shows both the theoretical and the measured frequency distribution of one single image. Both are in good correspondance. This clearly supports the assumed boundary layer model. Also the temperature distribution within one single image seems to be representative for the process and thus allows to compute k out of (21) for each image, i. e., 60 times per second!

Haußecker et al. [1995] have successfully used this technique in the field during the MBL/COOP West Coast experiment in April/May 1995 aboard R/V New Horizon. Preliminary results are discussed in this paper together with the experimental setup of the sea-going instrument.

3 Conclusions

The various possibilities proposed in this article make the CFT a very versatile instrument to probe the gas transfer velocity and to get an insight into the mechanisms governing gas exchange. With three different techniques the results can mostly be verified against each other. The setup used within the lab experiments and the field going instrument proved to work well. However, some more detailed simulations have to be done to model the physical properties of the camera and water surface (e. g., finite penetration depth of both camera sensitive radiation and radiative cooling). A very promising result is the fact, that even a rough model seems to reflect the main principles of air-sea gas exchange.

Acknowledgements

Financial support of this research by the Office of Naval Research (N00014-93-1-0515 and N00014-94-1-0050) and by the National Science Foundation (OCE 89 11224) is gratefully acknowledged.

References

- Dankwerts, P. V., Significance of Liquid-Film Coefficients in Gas Adsorption, *Industrial and Engineering Chemistry*, Vol. 43(6), pp. 1460–1467, 1951
- Gulliver, J. S., Introduction to Air-Water Mass Transfer, *Air-Water Mass Transfer*, selected papers from the 2nd International Symposium on Gas Transfer at Water Surfaces, September 11–14, 1991, Minneapolis, Minnesota, S. C. Wilhelms and J. S. Gulliver, eds, pp. 244–256, ASCE, New York., 1991
- Haußecker, H., and B. Jähne, In situ measurements of the air-sea gas transfer rate using heat as a proxy tracer, *Second International Conference on Air-Sea Interaction and Meteorology and on Oceanography of the Coastal Zone*, Lisbon, September 22–27, 1994, Lisbon, Portugal, 1994
- Haußecker, H., and B. Jähne, In situ measurements of the air-sea gas transfer rate during the MBL/COOP West Coast Experiment, *this volume*.
- Jähne, B., P. Libner, R. Fischer, T. Billen, and E. J. Plate, Investigating the transfer processes across the free aqueous viscous boundary layer by the controlled flux method, *Tellus* (1989), *41B*, pp. 177–195, 1989
- Jähne, B., From mean fluxes to a detailed experimental investigation of the gas transfer process, *Air-Water Mass Transfer*, selected papers from the 2nd International Symposium on Gas Transfer at Water Surfaces, September 11–14, 1991, Minneapolis, Minnesota, S. C. Wilhelms and J. S. Gulliver, eds, pp. 244–256, ASCE, New York, 1991
- Reinelt, S., Bestimmung der Transfargeschwindigkeit mittels CFT mit Wärme als Tracer, *Diploma thesis*, Institute for Environmental Physics, University of Heidelberg, August 1994

Radiometric Measurement of Diffusion Zone Thickness

W. McKeown

Naval Research Laboratory Code 7253
4555 Overlook Ave. SW Washington, D.C. 20375-5351 202-767-2352
waltm@ltn.nrl.navy.mil

Abstract

A new radiometric technique to measure air/water interface temperature gradients is presented with an example of its use for gas flux research. Inherent radiometric characteristics in the water molecule cause absorption coefficient variations in the 2.2 and 3.8 micron region. These variations allow emerging radiation to carry information about subsurface temperatures. Near these frequencies, emitted radiance/frequency variations measure temperature/depth variations. Laboratory experiments have produced radiance spectra indicating these crucial temperature gradients can now be studied in detail.

This technique has the potential to sense the thickness of the thermal conduction zone during known gas transfers. The conduction zone's linear temperature gradient becomes non-linear where eddy motion dominates heat flow. This point of non-linearity measures the conduction zone's thickness. This thickness and a ratio of Schmidt and Prandtl numbers may be used to calculate the diffusion zone thickness because the transfer velocity of different gases varies as their respective diffusivities. Since heat can be considered a passive tracer in water with an effective molecular diffusivity (Prandtl number), the relative movement of heat and gas should be the ratio of their Schmidt and Prandtl numbers.

The sample experiment manipulates wind speed, heat flux and gas concentration differences across an interface to stabilize the Schmidt and Prandtl numbers. Simultaneously, a radio-metrically stable interferometer measures the conduction zone thickness by sensing temperature gradients down to 0.0408 cm. Gas transfer velocity and gas concentration differences across the interface gives gas flow. Outputs are conduction zone thickness, diffusion zone thickness and wind speed. These data will allow comparisons of conduction & diffusion zone thicknesses and gas/heat transfer velocities to the advantage of gas flux theory.

1 Introduction

The water molecule's inherent radiometric characteristics cause natural frequency variations of the absorption coefficient in the 2.2 and 3.8 micron region [*IR Handbook*, 1989]. These variations cause the water to be more

transparent to subsurface radiation in some frequencies than others. Radiation at frequencies with low absorption coefficients carries information about subsurface water temperatures. As a result, radiance/frequency variations can measure the temperature/depth variations.

A radiometer looking down at the water senses radiation with two origins: the water surface and the intervening atmosphere. This is formalized by the radiation transfer equation, the fundamental principle of radiometric sounding.

$$I = \underbrace{R_{sfc} \tau_{atmos}}_{\text{surface term}} + \int_{p_s}^p \underbrace{B \left[T_{atmos}(z) \frac{d\tau_{atmos}(z)}{dp} \right]}_{\text{atmospheric term}} dp \quad (1)$$

where I = upwelling radiance spectrum entering the sensor, R_{sfc} = surface radiance, τ = atmospheric transmittance between the instrument and the surface, $B[T(z)]$ = Planck function corresponding to air temperature at height z , $d\tau_{atmos}/dp$ = change in transmittance with atmospheric pressure level, p_s = surface pressure, p = atmospheric pressure at the instrument.

If the surface material is opaque at a frequency (large absorption coefficient), the first term is a simple multiple of the surface emissivity with Planck radiance generated by the surface temperature. Subsurface radiation cannot reach the instrument. This is the case for water in most of the infrared frequencies.

However, as frequencies approach the visible light regions, water's absorption coefficient begins to vary with frequency starting at 5 microns, dropping 2 orders of magnitude by 1.0 micron and another 3 orders of magnitude by 0.5 microns. As a result, the transparency of water varies strongly with wavelength, allowing subsurface radiation to emerge.

Since emitted radiation from a 300 K object peaks at 11 microns and decreases exponentially as wavelength decreases, emitted radiation is very weak at wavelengths smaller than 2 microns. However, measurable radiation is still carried in the 2.0–5.0 micron region. In addition, the absorption coefficient variations allow subsurface radiation to emerge. Frequency variations of radiation measure subsurface temperature gradients in the air/water interface.

To represent this physical reality, the surface term of (1) is replaced by an integral similar to the atmospheric term. This integral represents the sum of the emerging radiation from all levels in the water. Subscripts refer to parameter values at pressure levels in the respective fluid.

$$\begin{aligned} I &= \int_{p_s+\delta}^p B \left[T_{water}(z) \frac{d\tau_{water}}{dp} \right] dp + \int_{p_s}^p B \left[T_{atmos}(z) \frac{d\tau_{atmos}(z)}{dp} \right] dp \\ &= \int_{p_s+\delta}^p B \left[T(z) \frac{d\tau^*}{dp} \right] dp \end{aligned} \quad (2)$$

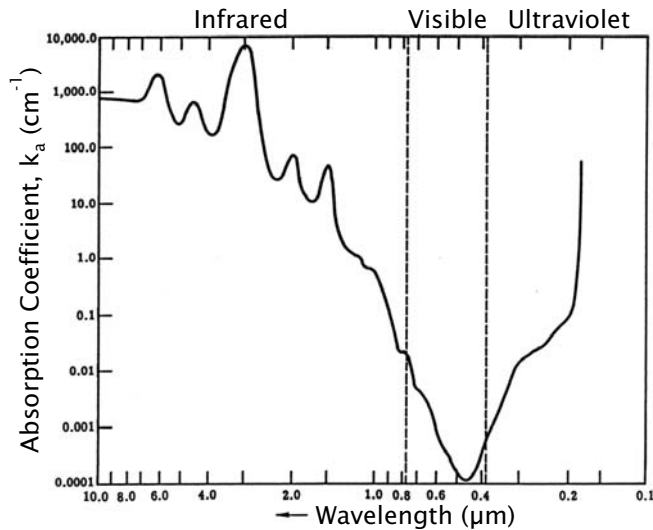


Figure 1: Variation of the absorption coefficient of water 10–0.1 microns [Infrared Handbook, 1989, pp. 3–107]

where δ = water pressure depth where transmittance is zero at every wavenumber, τ^* = multiple of the transmittance through water and atmosphere = “effective” transmittance, p , p_s = pressure at the instrument and at the water surface, respectively.

The emerging radiation is predominantly sensitive to temperatures down to the “effective optical depth” (EOD = inverse of the absorption coefficient).

Measurement of these small variations of radiation requires the performance of the low noise radiometrically stable instruments already used in atmospheric sounding. The use of high spectral resolution increases the temperature profile’s vertical resolution in the same way as atmospheric sounders [Huang et al., 1993]. High spectral resolution ($\lambda/\delta\lambda = 1000$), a characteristic of *Michelson interferometers*, have already allowed gradient measurements at very fine vertical resolution (600+ data points in 1/10 mm).

The air/water interface can be considered as divided into zones within which heat flows primarily by radiation, conduction or eddy diffusion [McAlister et al., 1969]. A high vertical resolution interface gradient should show nonlinearities where the gradient enters the eddy diffusion zone from the conduction zone. The depth of this nonlinearity will determine the conduction zone thickness.

Measurement of these temperature gradients has been attempted with fine wire probes [Mammen et al., 1992]. However, such mechanical measurements do not allow the fine vertical resolution required to determine conduction zone thickness for the purposes outlined here.

Laboratory experiments in the 2.2 and 3.8 micron spectral regions have

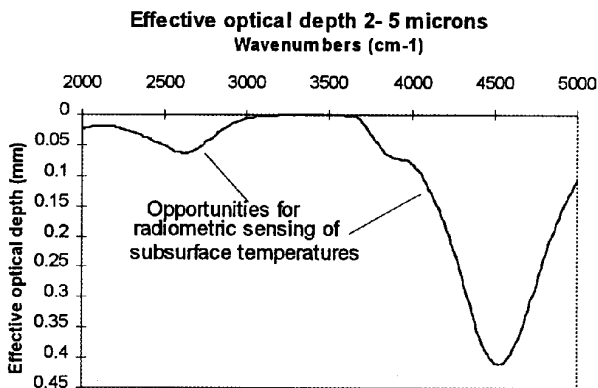


Figure 2: Variation of effective optical depth in the 2.0-5.0 micron region. The water surface is at the top [Wieliczka et al., 1989]

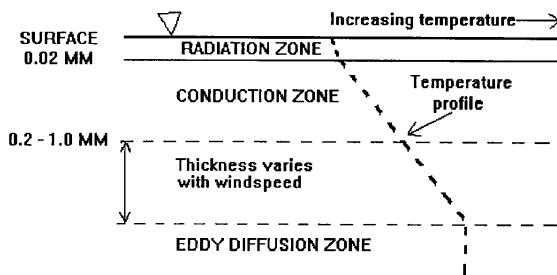


Figure 3: Heat flow in the air/water interface (after McAlister [1969]). Each zone indicates the primary but not exclusive means of heat motion.

produced radiance spectra indicating that these elusive *temperature gradients* can now be studied in detail. Radiance spectra changed with evaporation and heat flux magnitude, indicating that the gradient driving the heat flow was being sensed. The spectra were corrected for frequency variations of water's emissivity and reflection characteristics and for atmospheric absorption. During the experiments, correlations were observed between spectra and interface temperature gradients inferred from calorimetry.

Examples of air/water interface temperature gradients measured at 3.8 microns during 1992 laboratory experiments at the University of Wisconsin-Madison are shown in Figure 4. The straight line is the linear temperature gradient expected for the *heat flux* measured independently. To compare this gradient with that sensed radiometrically, brightness temperatures are plotted at the effective optical depth (EOD = inverse of the absorption coefficient) of the frequency rather than the frequency itself. Measured spectra are corrected for frequency variations of emissivity/reflectivity and smoothed

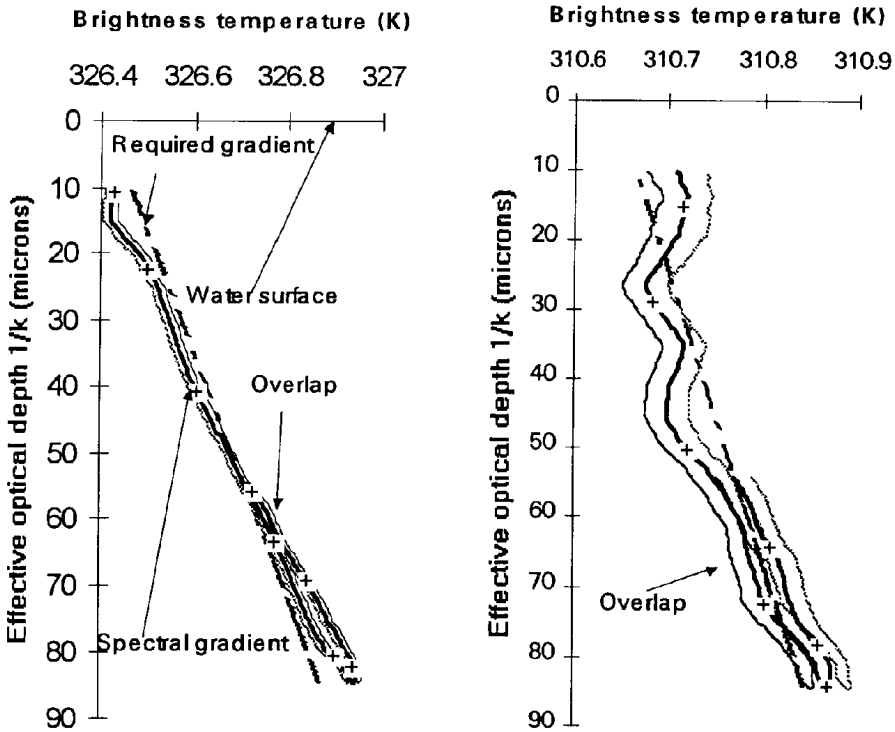


Figure 4: Typical interface temperature gradients sensed at 3.8 microns.

over 41 channels.

An internal check on the theory is the appearance of the overlap feature with a non-zero gradient. While this feature is not evident in conventional spectra of brightness temperature vs frequency, it becomes obvious in these spectral gradients (brightness temperature vs effective optical depth of the frequency). The overlap feature appears when frequencies with the same optical depth measure the same brightness temperature. This would only occur if a gradient were being observed. While flat spectra (brightness temperature invariant with frequency) would also show an overlap, such spectra must also show a zero gradient. The overlap feature with a non-zero gradient appeared consistently in hundreds of experimental spectra gathered at 3.8 and 2.2 microns.

The technique at 2.2 microns was more difficult because the emitted radiance of a 300 K object peaks at 11 microns, dropping exponentially with wavelength. This weak radiance was sensed by a cold-filtered indium antimonide detector. Frequencies with optical depths less than ~ 0.1 mm were cut off by the cold filtering, leaving the 0.1–0.408 mm range for observation.

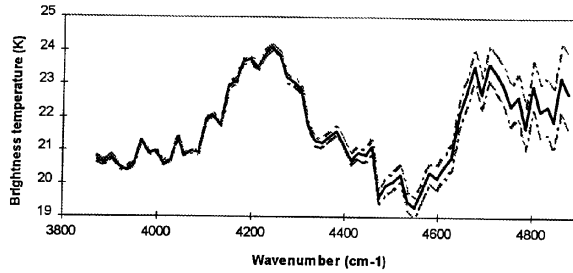


Figure 5: Averaged 2.2 micron spectrum (Spectral gradient and further description, see Fig. 5).

The instrument was automatically recalibrated before and after each water view. Radiance spectra were taken while holding the heat flux constant. Evidence that thermal structures in the water were sensed include consistent appearance of an overlap feature with a non-zero gradient, spectral shape variations with wind speed and heat flux magnitude and spectral features corresponding to the refractive index of water. Details of the experiment in a paper submitted to the Journal of Geophysical Research are available from the author.

The “peaks and valleys” in the spectrum in Fig. 5 are significant because of optical depth variations (Fig. 2). Peaks at ~ 4200 and ~ 4700 cm^{-1} share the same absorption coefficient. The valley occurs where absorption coefficients reach a minimum. The spectral gradient (Fig. 6) shows that many different frequencies with the same absorption coefficient are measuring the same brightness temperatures. The reverse gradient in Fig. 6 below 0.25 mm may indicate evaporation-cooled water meeting the warmer water that is rising to replace evaporative losses. The actual water flow at these length scales was not recorded.

This technique may be used in gas flux research by sensing the thickness of the thermal conduction zone during a known gas transfer. While the gradient will be linear in a conduction zone, it should become non-linear as it enters the eddy diffusion zone where heat moves by convection (Fig. 3). This non-linear point measuring conduction zone thickness should vary with wind speed and thus may be easily manipulated. The gradient itself drives heat flux and is also affected by wind speed.

Gas diffusion and heat conduction are slow processes in water, operating over very small depths before shear forces dominate. The transfer velocity of different gases measured under the same hydrodynamic conditions will vary as their respective diffusivities [Brumley and Jirka, 1988]. In effect, this is a ratio of their Schmidt and Prandtl numbers. Since heat can be considered a passive tracer in water with an effective molecular diffusivity, the relative movement of heat and gas should be the ratio of their Schmidt and Prandtl numbers [Jähne et al., 1989]

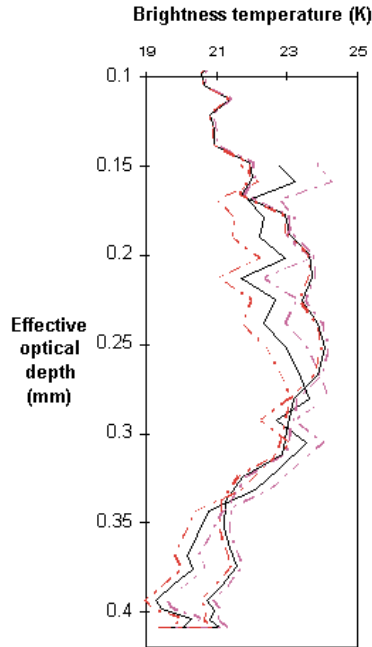


Figure 6: Spectral gradient. Measured brightness temperatures is the solid line. Measurement error is the dashed lines. This spectrum is 2.4×10^6 spectra averaged over 127 hours. Corrected for emissivity, reflection & atmospheric absorption.

$$\frac{Sc}{Pr} = \left(\frac{\text{gas diffusion}}{\text{heat conduction}} \right)^{-N} \quad (3)$$

where Sc = Schmidt number, Pr = Prandtl number.

Using a surface renewal model, the exponent N should be ~ 0.5 and allow the diffusion zone thickness to be calculated. Experimental determination of this exponent would help to refine gas flux models.

The experimenter must manipulate wind speed, heat flux and gas concentration differences across an air/water interface to control the Schmidt and Prandtl numbers. A high spectral resolution interferometer using the two spectral intervals in Fig. 2 would simultaneously sense the interface gradients from directly above. When the Prandtl and Schmidt numbers are stabilized, the radiance spectra would determine the interface temperature gradients: the 3.8 micron region down to 0.0063 cm and the 2.2 micron region down to 0.0408 cm. These depth ranges encompass most of the thermal conduction zone where a linear temperature gradient would occur. Manipulation of wind speed should cause a non-linear point to appear in the spectral gradient and measure conduction zone thickness.

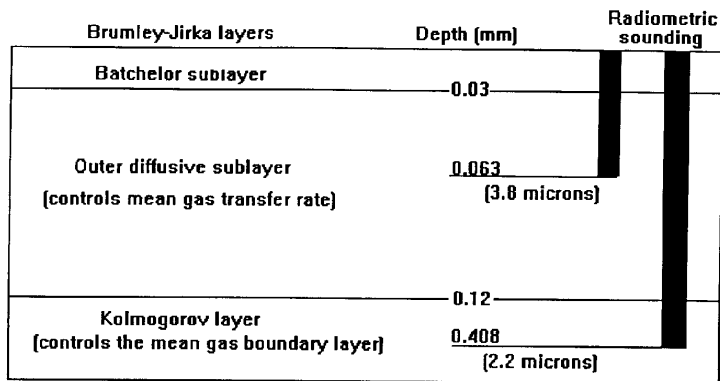


Figure 7: Coincident viscous sublayers and radiometric sounding capability.

The Brumley/Jirka model of the air/water interface [Brumley and Jirka, 1988] has dimensions which indicate an overlap of the viscous sublayers with the radiometric sounding capability. Under known hydrodynamic and gas flow conditions, detailed knowledge of the temperature gradients within these sublayers may be of interest to gas flux researchers.

The conduction zone thickness used with the Schmidt/ Prandtl number ratio can calculate the diffusion zone thickness. Known variations of conduction zone thickness, diffusion zone thickness and gas transfer velocities with wind speeds will allow the comparison of these thicknesses and gas/heat transfer velocities.

This technique may be of use in other experiments suitable in heat and gas flow.

Acknowledgments

While the theory and experiments exploring this technique were developed by the author, the application of the technique to gas flux research was worked out in conversations with Bill Asher of Battelle Laboratory. Without his insights into the relevant gas flux parameters and his generosity in explaining them, this experiment would have remained a vague dream.

References

- Brumley, B. and Jirka, G., Air-water Transfer of Slightly Soluble Gases: Turbulence, Interfacial Processes and Conceptual Models, *Physiochemical Hydrodynamics*, 10, 3, pp 295-319, 1988
- IR Handbook*, Infrared Information and Analysis Center (IRIA), University of Michigan, 1989

- Jähne, B, Münnich, K. O., Bösinger, R., Dutzi, A., Huber, W., and Libner, P., On the parameters influencing air/sea gas exchange, *J. Geophys. Res.* 92, pp 1937-1949, 1987
- Huang, H. - L., Smith, W. L. and Woolf, H. M., Vertical resolution and accuracy of atmospheric infrared sounding spectrometers, *J. Appl. Met.* 31, 3, 1992
- Mammen, T. C., von Bosse, N., STEP: A temperature profiler for measuring the oceanic thermal boundary layer at the ocean/air interface., *J. of Oceanic and Atmos. Tech.*, 7 312-322, 1992
- McAlister, W. and William McLeish, Heat Transfer in the top Millimeter of the Ocean. *J. Geophys. Res.*, 74, 13, pp. 3408, 1969
- McKeown, W., Bretherton, F., Huang, H. L., Smith, W. L. and Revercomb, H. L., Sounding the skin of water: sensing air/water interface temperature gradients with interferometry. *J. of Atmos. and Oceanic Tech.*, Dec. 1995
- Wieliczka, Weng and Querry, Optical constants of water in the infrared, *J. Appl. Opt.*, 28, pp. 1714-1719, 1989

An Innovative Air-Water Exchange Process for the Treatment of Waste Waters

J. S. Smith, K. T. Valsaraj, and L. J. Thibodeaux

Department of Chemical Engineering, Louisiana State University
Baton Rouge, LA 70803 U.S.A.

Abstract

Results of gas hold-up, bubble size, and dispersion experiments are reported as functions of gas velocity for two different types of *gas-bubble spargers*, namely, a fine porous glass frit (9 cm in diameter) and an annular bubble *shear sparger* (porous surface area = 0.1 ft²). The data suggest that the interfacial mass transfer areas generated by these spargers can be significantly larger than those observed from conventional spargers. Fractional removal data obtained from three-phase, continuous *solvent sublation* experiments demonstrate the effectiveness of these spargers. As much as 95 % removal of pyrene from 100 ppb aqueous solutions was observed for the shear sparger. It is speculated that the shear sparger has the potential to extend the bubbly flow regime to gas velocities greater than 4 cm/sec, the generally accepted upper limit. The implication is that low-pressure *adsorptive bubble* processes that operate in the bubbly flow regime, such as solvent sublation, may soon become viable options for industry.

1 Introduction

Hydrophobic organic compounds which possess very low aqueous solubilities and vapor pressures represent a significant portion of the pollutants found in the environment. These compounds are mostly neutral and non-polar and are often found in very dilute concentrations in aqueous systems. One of the challenges that faces environmental engineers today is the cost-effective separation of these compounds from aqueous systems. Adsorptive bubble processes, such as solvent sublation, have the potential to meet such a challenge. Although this paper is focused upon solvent sublation and its application to the environment, it is stressed that the results presented herein can be applied to other adsorptive bubble processes as well as other air-water processes in general.

Solvent sublation is a three-phase separation process. A water-immiscible solvent floats upon a column of polluted water while air is sparged into the bottom of the column. The air bubbles that are formed provide the means of mass transport of pollutant from the aqueous phase to the solvent phase. One feature of solvent sublation is that the surface-active nature of organic compounds results in an effective air-bubble concentration being higher than that predicted by Henry's law for air-water equilibrium.

The consequence is that the net transport of the rising bubbles to the solvent overwhelms the transport from the solvent to the water and the establishment of equilibrium is prevented. Thus, the fractional recoveries in solvent sublation processes can be as high as 95 % [Lu *et al.*, 1991; Shih *et al.*, 1990; Valsaraj *et al.*, 1991; Valsaraj and Thibodeaux, 1991a; Valsaraj and Thibodeaux, 1991b]. The advantages over conventional liquid-liquid extraction are, intimate contact of the solvent and water is avoided, less solvent is needed, and mixers and settlers are not needed [Valsaraj, 1995].

An important parameter in bubble column dynamics is the specific interfacial area, a_v . The specific interfacial area is comprised of two hydrodynamic properties, d_s , the Sauter mean bubble diameter and ϵ , the mean fractional gas hold-up ($a_v = 6\epsilon/d_s$). Gas holdup is defined as the volume fraction of the gas (air) in the two phase mixture (air and water) in the column. Both properties are functions of gas velocity. It is generally accepted that low gas velocities yield small bubbles, or equivalently, large interfacial areas per bubble. Traditionally, sublation columns have been operated at low gas velocity to exploit this fact; thus, sublation processes have been grouped into the small class of applications that operate in the so called "bubbly flow regime" (i. e., superficial gas velocities < 4 cm/sec). From an industrial perspective, it is generally desirable to operate at high gas velocity or in the "churn-turbulent regime" so as to maximize the interfacial area per unit volume by increasing ϵ ; however, increasing the gas velocity also increases d_s as well as increasing the mixing intensity. The traditional view has been that these adverse effects limit the industrial potential of solvent sublation [Valsaraj *et al.*, 1991]; however, the utilization of novel spargers [Johnson and Gershey, 1990; Johnson *et al.*, 1982; Marshall *et al.*, 1993] may make sublation a viable alternative. Such spargers employ shear forces which are applied parallel to the surface of bubble generation. Bubbles as small as 50×10^{-6} m have been produced at low gas flow rates (6 to 8 cm³/min) [Johnson *et al.*, 1982]. Since bubble coalescence does not occur at these flow rates, the bubble sizes are maintained. The potential consequences of these spargers in bubble column applications are the generation of smaller bubbles at high gas velocity (churn turbulent regime) or the generation of bubbles that are smaller than what is normally observed in the bubbly flow regime.

Another important hydrodynamic property in bubble columns is the extent of mixing or dispersion. It is often reported in terms of an axial dispersion coefficient, D (cm²/sec). In sublation columns, the effect of dispersion upon performance is not as significant as the effects of d_s or ϵ ; however, it is desirable to minimize axial dispersion.

In this paper, hydrodynamic properties obtained from a fine, porous glass frit and an annular shear sparger operating in a three-phase-continuous, countercurrent solvent sublation process are presented. The effects on the specific interfacial area and column flow regime are briefly discussed. Finally, to demonstrate the effectiveness of these gas spargers, fractional re-

moval data obtained from the solvent sublation of pyrene are presented.

2 Experimental

The process equipment consists of a 4" (0.1016 m) I.D. by 5' (1.524 m) long PYREX® glass bubble column, an overflow reservoir, a column mount, bubble spargers, and process ancillaries to accommodate three-phase continuous operation (Figure 1). Two types of bubble spargers are used. The first is a fine porous glass frit having a diameter of 0.090 m and an estimated mean pore size of 1.7×10^{-6} m. The second type is referred to as a bubble-shear sparger. It differs from a conventional sparger in that an external velocity field (typically a water jet) is set up parallel to the sparger surface. The sparger element used in these experiments is a cylinder made of 316SS having a porous area of 0.1 ft² (92.9 cm²) and mean pore size of 2.0×10^{-6} m (supplied by Mott Metallurgical Corporation). The element is placed in a 3/4" NPT-PVC pipe which provides an annulus for the water jet to flow. The external velocity field exerts a shear force on the bubbles as they protrude from the sparger surface, which results in a smaller mean bubble diameter.

Gas hold-up was determined by measuring the change in liquid height with and without air flow at various air flow rates. Bubble size measurements were determined from a photographic technique [Valsaraj et al., 1991], which employs the use of a video image analyzer (JAVA®) to estimate the cross-sectional areas of the bubbles. Liquid dispersion coefficients were estimated at different air flow rates by injecting a tracer (dye) into the top of the column and measuring the time for the tracer front to traverse a fixed distance. The dispersion coefficient was calculated as $D = x^2/4t$ [Smith et al., 1995].

For the sublation experiments, feed stocks were prepared by spiking containers of distilled water with pyrene from a gravimetrically prepared pyrene-MeCN solution. Most feed stocks were spiked to around 100 µg/L. An HP1046A fluorescence detector ($\lambda(\text{excitation}) = 237$ nm, $\lambda(\text{emission}) = 385$ nm) was used to determine both the influent and effluent concentrations of pyrene. Fractional removal was calculated from the ratio of these two concentrations to within a relative standard deviation (RSD) of 2.9%.

The materials used in the experiments were light, white mineral oil supplied by Sigma-Aldrich, pyrene supplied by Aldrich Chemicals, distilled water, and pressurized air supplied by LSU Plant Services.

3 Results and Discussion

3.1 Hydrodynamic Properties

Figure 2 shows the dependence of gas hold-up upon superficial air velocity u_g . Generally, such data conform to a power model of the type $\epsilon = \alpha u_g \beta$. The data from the porous glass frit have near linear behavior for $u_g < 2.1$

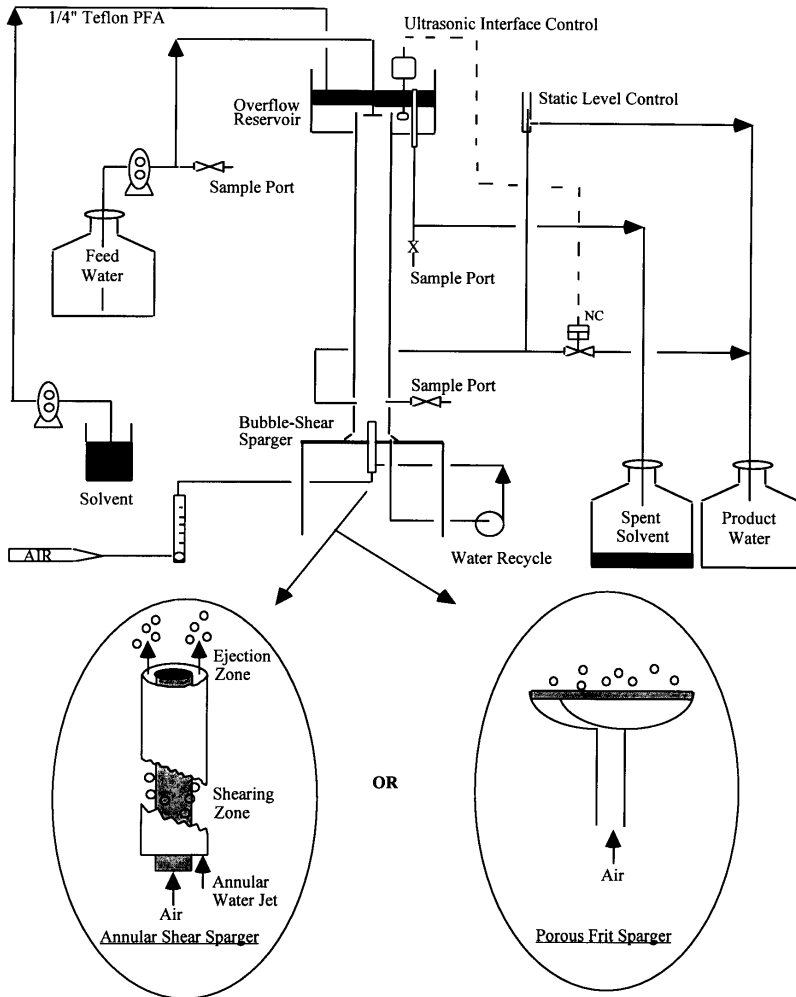


Figure 1: Schematic of Pilot Process for Solvent Sublimation

cm/s ($\alpha = 0.049, \beta = 1.21$) and then begin to transcend to the slug flow regime at $u_g > 2.1$ cm/s ($\alpha = 0.066, \beta = 0.71$). These features are characteristic of the bubbly flow regime and come as no surprise for a perforated or sintered-type sparger. As a point of reference, the correlations of Akita and Yoshida [1973] and Hikita *et al.* [1980] have been included in the figure. Deckwer and Schumpe [1993] have recently reported that these correlations provide good, conservative estimates of the gas hold-up in bubble columns; however, the authors stressed that such correlations do not apply to the limited number of applications involving the bubbly flow regime. The gas

hold-up data obtained from the annular bubble-shear sparger compare reasonably well with the correlations at low velocities. At velocities greater than 2.1 cm/s, however, the correlations underestimate the gas hold-up. The data imply that a linear relationship for gas hold-up is also applicable to bubble-shear spargers. It should be noted that in the case of the shear sparger, increasing the water jet velocity from 3.8 ft/sec to 6.3 ft/sec, the design limit of the apparatus, had only a small favorable effect on gas hold-up. However, initial studies from a larger process indicate that a water jet of ≈ 16 ft/sec yields gas holdup data which coincide with the data obtained from the porous glass frit [Smith *et al.*, 1995].

Evidence that these bubble spargers produce higher interfacial mass transfer area than conventional spargers is best illustrated in Figure 3, where the Sauter mean diameter (each point calculated from 200 individual measurements) is plotted versus u_g . Both spargers produce smaller bubbles than those predicted by the semi-empirical theory for a single orifice of Ruff [Clift *et al.*, 1978] and the correlation of Akita and Yoshida [1974]. In the case of the porous frit sparger, the data conform quite nicely to a power law model with a 0.57 dependence on velocity which is characteristic of the bubbly flow regime. The data from the annular shear sparger show a weaker dependence on velocity. In fact, for $u_g > 1.0$ cm/s, the Sauter mean diameter for the shear sparger is essentially constant. It should be noted that the data for both spargers were collected at a height of 2 ft from the column base. This is especially important for the annular shear sparger in which the 8 cm plume of bubbles and water leaving the ejection zone was observed to be very milky. This was the result of the bubbles being extremely small. Most of the bubbles were estimated to be on the order of 100 μm ; however, the bubbles could not be accurately measured since the milky white plume eliminated the contrast between the air and the water. Above the plume, a local CSTR region that was created by the water jet was observed. Essentially all the bubble coalescence in the column occurred in this region. The bubbles that left the CSTR region were near uniform in size and seemingly independent of gas velocity as the data in Figure 3 suggest. This dependence suggests that the mechanisms controlling bubble size in this range of gas velocities is bubble formation dynamics as opposed to coalescence and bubble breakage [Geary and Rice, 1991]. When formation dynamics are controlling, the flow tends to remain homogeneous (bubbly flow regime). Bubble size data, such as that predicted by the Akita-Yoshida correlation, where the size decreases asymptotically with increasing gas velocity, indicate that coalescence and breakage are the dominant mechanisms affecting bubble size. The consequence is that for the shear sparger, bubbly flow may be possible at gas velocities > 4 cm/sec. This possibility has a profound impact upon the industrial viability of solvent sublimation and other low-pressure, adsorptive bubble processes which require bubbly flow.

There was no significant difference in the observed axial dispersion for the two different spargers as Figure 4 shows; however, one may argue that

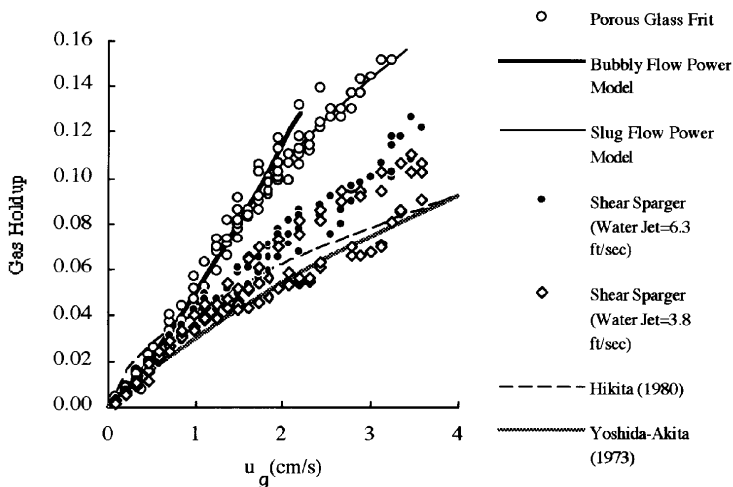


Figure 2: Functional Dependence of Gas Hold-Up on Superficial Gas Velocity

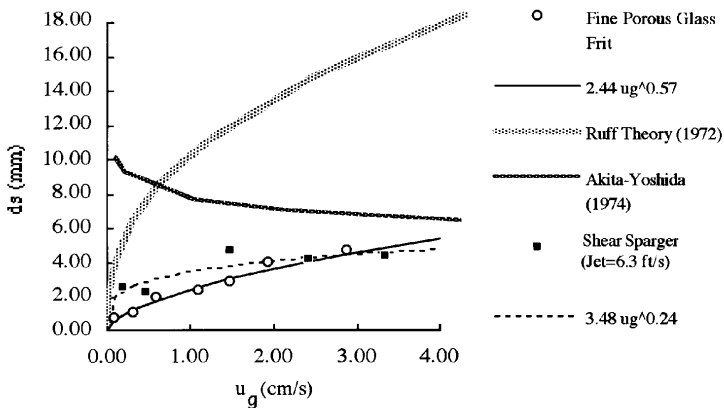


Figure 3: Sauter Mean Diameter versus Superficial Gas Velocity

small biases exist. Therefore, each data set appearing in the figure has been fit with its own power law to illustrate the small biases. Overall, the entire data set conforms to a power-law model with a 0.62 dependence on velocity. According to *Rice et. al.* [1981], this dependence falls between bubbly flow (linear dependence) and churn-turbulent (one-third dependence). At velocities greater than 1.0 cm/s, the dispersion in the column is effectively a constant equal to approximately 375 cm²/s which is not too surprising given the low L/D_c of 15. *Deckwer et. al.* [1974], using a better technique for dispersion measurement, has reported values in the range of 275-300 cm²/s for the same range of velocities studied here, but for columns with L/D_c

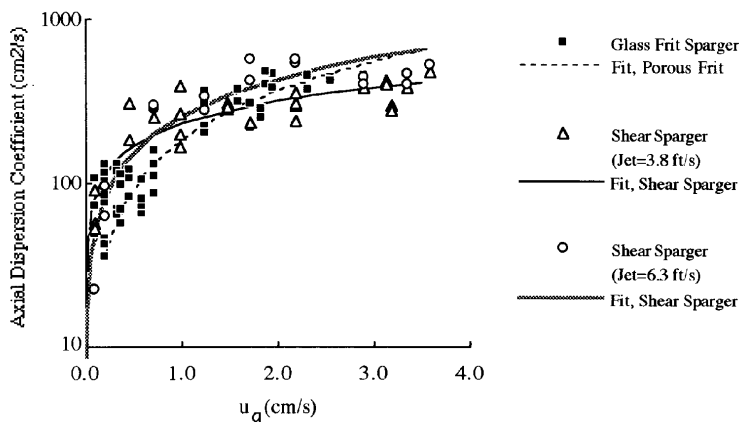


Figure 4: Liquid-Phase Axial Dispersion Dependence upon Superficial Gas Velocity

ratios around 30.

3.2 Solvent Sublation of Pyrene

To investigate the effects of these spargers in a practical application, sublation experiments were conducted in which *pyrene* (a polyaromatic hydrocarbon) was removed from simulated wastewater to an overlying layer of mineral oil. Experiments were conducted over a wide range of air, water, and solvent flow rates. For each experimental condition, influent and effluent water samples were collected periodically over time and analyzed for pyrene. Fractional removal was then determined and tracked with time. The experiment was terminated after steady-state had been maintained for at least 12 hours (the duration of most were 24 hours). The results of the experiments are shown in Figure 5 where fractional removal is plotted versus the ratio of the air flow rate to the water flow rate, $Q_A : Q_W$.

As anticipated, there was no observable effect of the solvent flow rate, Q_O , over the range studied; therefore, all of the data have been lumped into one figure. Most of the runs were conducted with $Q_W : Q_O = 14$. The reason why the solvent flow rate is unimportant is easily explained by comparing the solubility of pyrene in mineral oil, 1.3 mol% (UNIFAC), versus that in water, 1.2×10^{-6} mol% (135 $\mu\text{g/L}$). From this comparison, it is evident that only a small amount of solvent (a threshold) is necessary to recover the pyrene. This assumes nonequilibrium conditions for the solvent-water interface. As stated in the introduction, nonequilibrium is possible since the principal mechanism of mass transfer is the unidirectional transport by the air bubbles rising through the column. The solvent flow rate does not affect this mechanism. On the other hand, as one can see from Figure 5, increasing the air flow does indeed favor the transport of pyrene to the solvent phase.

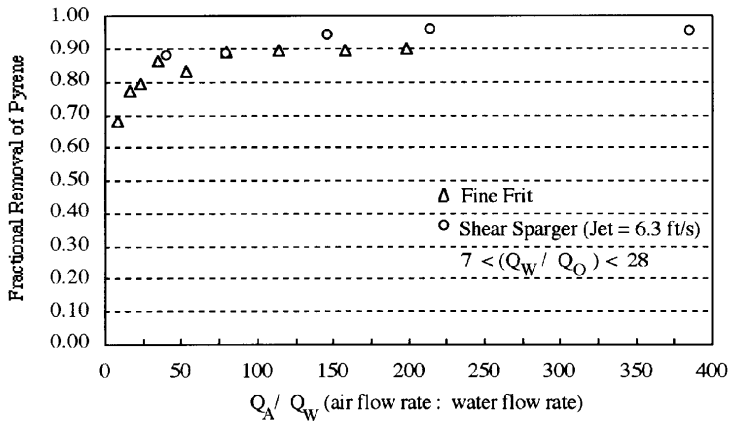


Figure 5: Fractional Removal Data obtained from the Solvent Sublimation of Pyrene

For the case of the porous frit, the fractional removal increased from about 70% to 90% as $Q_A : Q_W$ was increased from 8 to 80. However, for $Q_A : Q_W$ greater than 80, there was no further increase in fractional removal. The data collected from the shear sparger was nearly identical with that of the frit for $Q_A : Q_W = 40$ and 80. However, at a flow ratio of about 150 the fractional removal was 95%, which was a significant improvement over the frit. But just like the frit, as the flow ratio was increased no further benefit was observed.

The reason why the shear sparger outperformed the frit was attributed to the altered hydrodynamic properties associated with the shear sparger. The mass transfer at the bottom of the column may have been significantly enhanced due to the small bubbles (100 μm) present in the plume; however, it is difficult to accept this possibility without more data. A second possible explanation is that the weak bubble size dependence upon gas velocity may be indicative of a more radially uniform gas holdup distribution. That is to say, the interfacial area for mass transfer over the column cross section is more uniform; and consequently, for a gas velocity > 1 cm/sec, a_v is larger for the shear sparger than that for the porous frit. This argument is consistent with the speculation that bubble formation dynamics dominate more for the shear sparger than they do for the frit. As already mentioned, efforts are underway to operate at higher water jet velocities in order to determine if the shear sparger can extend the bubbly flow regime to higher gas velocities.

Acknowledgements

This work was supported in part by National Science Foundation / EPSCOR program NSF/LaSER [1992-96] ADP - 03.

References

- Akita, K. and F. Yoshida, Gas Holdup and Volumetric Mass Transfer Coefficient in bubble Columns, *Ind. Eng. Chem. Proc. Des. Dev.*, 12, p. 76, 1973
- Akita, K. and F. Yoshida, Bubble Size, Interfacial Area, and Liquid Phase Mass Transfer Coefficients in Bubble Columns, *Ind. Eng. Chem. Proc. Des. Dev.*, 13 p. 84, 1974
- Clift, R., J. R. Grace, and M. E. Weber, *Bubbles, Drops, and Particles*, Academic Press, INC., San Diego, p. 321-328, 1978
- Deckwer, W. D., R. Burckhart, and G. Zoll, Mixing and Mass Transfer in Tall Bubble Columns, *Chemical Engineering Science*, 29, p. 2177-2188, 1974
- Deckwer, W. D. and A. Schumpe, Improved Tools for Bubble Column Reactor Design and Scale-Up, *Chemical Engineering Science*, 48 (5), p. 889-911, 1993
- Geary, N. W. and R. G. Rice, Bubble Size Prediction for Rigid and Flexible Spargers, *AIChE*, 37 (2), 161-168, 1991
- Hikita, J., K. Asai, K. Tanigawa, K. Segawa, and M. Kitao, Gas Holdup in Bubble Column, *J. Chem. Eng.*, 20, 59, 1980
- Johnson, B. D. and R. M. Gershey, Bubble Formation at a Cylindrical Frit Surface in a Shear Field, *Chemical Engineering Science*, 46(10), 2753-2756, 1990
- Johnson, B. D., R. M. Gershey, R. C. Cooke, and W. H. Sutcliffe, A Theoretical Model for Bubble Formation at a Frit Surface in a Shear Field, *Separation Science and Technology*, 17 (8), 1027-1039, 1982
- Lu, X., K. T. Valsaraj, and L. J. Thibodeaux, Studies in Batch and Continuous Solvent Sublation. IV. Continuous Countercurrent Solvent Sublation and Bubble Fractionation of Hydrophobic Organics from Aqueous Solutions, *Separation Science and Technology*, 26 (7), 977-989, 1991
- Marshall, S. H., M. W. Chudacek, and D. F. Bagster, A Model For Bubble Formation From An Orifice With Liquid Cross-Flow, *Chemical Engineering Science*, 48 (11), 2049-2059, 1993
- Rice, R. G., J. M. Tupperainen, and R. M. Hedge, Dispersion and Holdup in Bubble Columns — Comparison of Rigid and Flexible Spargers, *The Canadian Journal of Chemical Engineering*, 59 (12), p. 677-687, 1981
- Shih, K. Y., W. D. Han, and S. D. Huang, Solvent Sublation of Hexachlorobutadiene and 2,4,6-Trichlorophenol, *Sep. Sci. Tech.*, 25 (4), 477-487, 1990
- Smith, J. S., L. F. Burns, K. T. Valsaraj, and L. J. Thibodeaux, Bubble Column Reactors for Wastewater Treatment Part II. The Effect of Sparger Design on Sublation Column Hydrodynamics in the Homogeneous Flow Regime, *Ind. Eng. Chem. Research*, 1995 (submitted)
- Valsaraj, K. T., Removal of Organics from Water by Non-foaming Flotation, in *Flotation-Science and Engineering*, K. A. Matis, Editor, Marcel-Dekker, NY. 365-383, 1995
- Valsaraj, K. T., X. Y. Lu, and L. J. Thibodeaux, Continuous Countercurrent Solvent Sublation for the Removal of Hydrophobic Organics from Water, *Water Research*, 25 (9), 1061-1072, 1991
- Valsaraj, K. T., X. Y. Lu, and L. J. Thibodeaux, Continuous Nonfoaming Adsorptive Bubble Separation Processes for the Removal of Hydrophobic Organic Compounds from the Aqueous Phase, In *Symposium on Separations Science in En-*

Environmental Chemistry, ACS National Meeting, 14-19 April 1991. Atlanta, GA, USA, 1991

Valsaraj, K. T. and L. J. Thibodeaux, Studies in Batch and Continuous Solvent Sublimation. I. A Complete Model and Mechanisms of Sublimation of Neutral and Ionic Species from Aqueous Solutions, *Separation Science and Technology*, 26 (1), 37-58, 1991a

Valsaraj, K. T. and L. J. Thibodeaux, Studies in Batch and Continuous Solvent Sublimation. II. Continuous Countercurrent Solvent Sublimation of Neutral and Ionic Species from Aqueous Solutions, *Separation Science and Technology*, 26 (3), 367-380, 1991b

Valsaraj, K. T., G. J. Thoma, L. J. Thibodeaux, and D. J. Wilson, Nonfoaming Adsorptive Bubble Separation Processes, *Separations Technology*, 1(5): 234-243, 1991

Development of Visualization Techniques for Motion of Surface Water Induced by Collision of a Vortex Ring

T. Etoh, K. Takehara

Department of Civil Engineering, Kinki University
Higashi-Osaka, JAPAN

Abstract

Microscopic observations of the fundamental processes of gas transfer via collision of a vortex ring against the water surface have been conducted. Three observation techniques are employed: use of the pH-dependency of fluorescent dye, particle tracking and coloring of vortex rings. A method to measure the disturbance at the water surface due to the collision of a vortex ring is also proposed.

1 Introduction

A vortex ring moving upward and colliding against a still water surface was employed as a model turbulence element, and the flow field near the water surface following the collision was observed. To do this, the authors designed and manufactured a system where vortex rings could be reproduced in various sizes and at different velocities. They then studied the collision of vortex rings and their impact on water surfaces.

Three observation techniques were used: use of the pH-dependency of fluorescent dye, particle tracking, and coloring of vortex rings.

The disturbance at the water surface due to the collision was observed by tracking spot images of a bundle of parallel laser beams crossing the surface using automatic particle tracking velocimetry (PTV).

A high-speed videocamera developed by the authors and color CCD video-cameras for the consumer market were used for the continuous capture of images.

2 Vortex Generator

2.1 Outline

To generate *vortex rings* of a uniform size, the authors manufactured a piston-type generator using a head of water as the drive source. The experimental vortex generator is shown in outline in Figure 1. The cylindrical water tank is acrylic and measures 290 mm in inner diameter and 300 mm

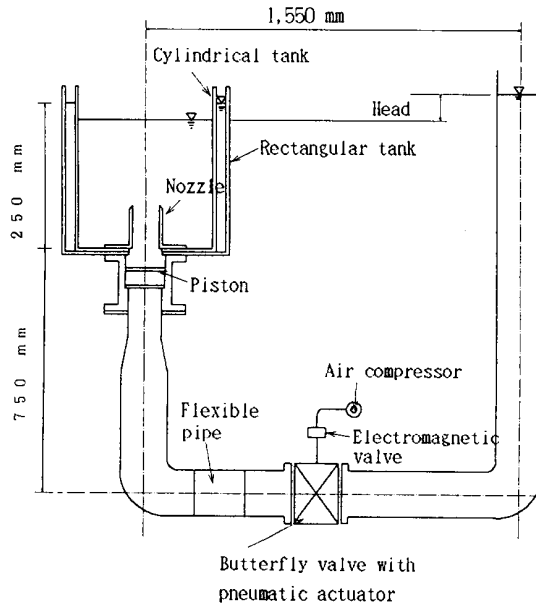


Figure 1: The vortex ring generator.

in height. To minimize observation distortion, a rectangular acrylic tank is placed around it. A nozzle with a circular blade-shaped tip is installed in the center of the bottom of the cylindrical tank through which water is ejected. As shown in Figure 1, after applying a head of water Δh , the valve is opened to allow the nozzle to eject water mass. The velocity of the water mass, or discharge flow rate, can be changed by adjusting the head of water.

The generator is designed so that the nozzle can be replaced with one of different inner diameter and/or length. The volume of water can also be changed by adjusting the piston stroke. An air cylinder butterfly valve controlled by an electromagnetic valve is used to ensure a constant valve operating rate. Furthermore, to eliminate vibration that could be caused when the butterfly valve opens, a buffer pipe with an inner diameter of 75 mm is installed between the water tanks and the valve.

This vortex generator is simple enough to be manufactured manually. To minimize vibration, it uses neither motor nor compressed air.

2.2 Piston

The following considerations are given to the piston section (see Figure 2):

- An adjustment screw is installed to allow the piston stroke to be changed (maximum stroke: 13 mm); changing the stroke varies the volume of water mass (maximum discharge volume: 27 cm³).

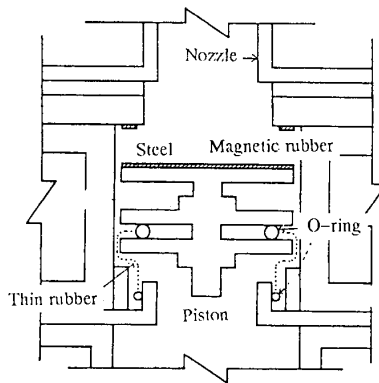


Figure 2: Detailed view of the piston.

- Water in the 0.3-mm gap between the piston and the cylinder serves as lubricant. The piston diameter is 51.1 mm and the cylinder diameter is 51.7 mm.
- A thin, cylindrical rubber membrane (indicated by the dotted lines in Figure 2) covers the lower part of the piston. The bottom edge is fixed to the lower piston stopper. This film prevents the water mass below the piston from leaking into the area above the piston.
- A thin steel plate is attached to the top surface of the piston and a magnetic rubber plate is attached to the upper piston stopper (both indicated by hatched areas in Figure 2). They serve as dampers to prevent the piston from rebounding strongly and to absorb vibration due to the collision.

3 Visualization of a Vortex Ring Colliding with the Water Surface

3.1 Motion of a Vortex Ring

Previous Studies

Cerra and Smith [1983] classified the reactions between vortex rings and water surfaces, collected from various references, into three groups. When a surface is solid, (1) a vortex ring that collides with the surface bounces back at a certain point, (2) a layer of secondary vorticity is formed along the periphery of the ring near the surface, and (3) the originally organized flow of the vortex ring suddenly changes into a disorganized one. If the surface is liquid, under some critical condition, a vortex ring slips on the water surface and behaves as though it had encountered a solid surface; *Cerra and Smith*

attribute this to surface tension. If the vorticity exceeds a critical point, the water surface is disturbed.

The effects of the surface tension upon gas transfer at the water surface still leave much to be clarified; there is discussion, for example, by *Asher and Pankow* [1991] and *Hanratty* [1991].

Observation

The movement of a vortex ring rising underwater is fairly simple. Released from the tip of the nozzle and taking on a stable shape, the diameter and the velocity of the vortex ring remain almost constant. Once it has collided with the water surface, however, its behavior becomes extremely complex. The vortex ring collapsing process is described below.

A collision was observed from the side and the top. Basically, the collision characteristics of a vortex ring obtained in the test correspond with the observation results reported by *Cerra and Smith*.

- Bouncing and reversing of a vortex ring Immediately after the collision, the vortex ring expands horizontally and shrinks vertically. The original vortex ring rebounds in the opposite direction.
- Formation of a layer of secondary vorticity Separation occurs inside the vortex ring that has expanded horizontally due to shear between the ring and the water surface. This generates a few secondary and tertiary vortex rings that rotate in opposite directions.

About one second after the appearance of secondary vortex rings, some of them are absorbed back into the original ring and the rest collapse downward.

- Transition of an organized vortex ring into a disorganized disturbance Immediately after the above, the organized collapse process turns into a disorganized disturbance.

3.2 Disturbance at the Water Surface

The disturbance at the water surface occurs depending on the velocity of the vortex ring.

With a head smaller than 30 mm, the water surface remains undisturbed and the vortex ring slides along the water surface after the collision because of the surface tension.

When the head is 40 mm, the water surface starts to be disturbed and a wave motion is observed. The disturbance becomes conspicuous with the increase in the head of water after this level. This is believed to be partly because of the impact of the collision and partly because of the shear flow due to the rotation of the ring itself. It is necessary to study which factor is dominant.

3.3 Visualization of Entrainment of a Thin Layer at the Water Surface

Observation using Micro-Particles

Fine particles made of EVA with a specific gravity of 0.95 and a diameter of $75\ \mu\text{m}$ or less were used. The particles were injected carefully into a water tank and allowed to spread evenly over the water surface overnight. Most of each particle was submerged in a thin layer a few scores of μm thick at the water surface.

Flow field and particle entrainment due to the collision was recorded by a CCD video camera with a macro lens; illumination was provided by a laser beam which was spread over the target area of 5.5 cm by 4 cm on the water surface. (Photos here show one half of the entire area, from the center axis of the vortex ring to the edge of the colliding ring.) Two imaging methods were used to help observation of the collision: in the first method, only floating tracer particles were visualized utilizing scattered light (Figures 3 and 4, left row), while in the second method both the vortex ring that was colored with a small amount of fluorescent dye excited by the laser and tracer particles were visualized (Figures 3 and 4, right row). Figures 3 and 4 show the examples with $\Delta h = 80\ \text{mm}$. These observations clarify the following points.

At a head of 20 mm, no entrainment or swelling of the water surface was observed. At 40 mm, a small number of tracer particles were entrained. At 80 mm, a large number of tracer particles were entrained in the following manner:

- As the vortex ring approaches the water surface, the latter rises [Figure 3a].
- After colliding with the water surface, the vortex ring expands in diameter and at the same time a secondary vortex ring starts to be formed due to an interaction with the original ring and the water surface. No entrainment of tracer particles has been observed at this point. For a moment, the particle image at the water surface vanishes for an unknown reason [Figure 3b].
- When a secondary vortex ring is sufficiently developed, tracer particles start to be entrained intermittently [Figure 3c].
- Entrained particles form a group and travel along the outer edge of the vortex ring to be included into the original ring [the clump shown in white in Figure 4a].
- At a certain point after the secondary vortex ring has been absorbed by the original ring, the number of entrained tracer particles suddenly increases [all the white dots shown in Figure 4b]. Entrainment takes place only outside the vortex ring.
- After the above, the organized vortex ring becomes a disorganized disturbance with many entrained particles starting to be distributed randomly [Figure 4c].

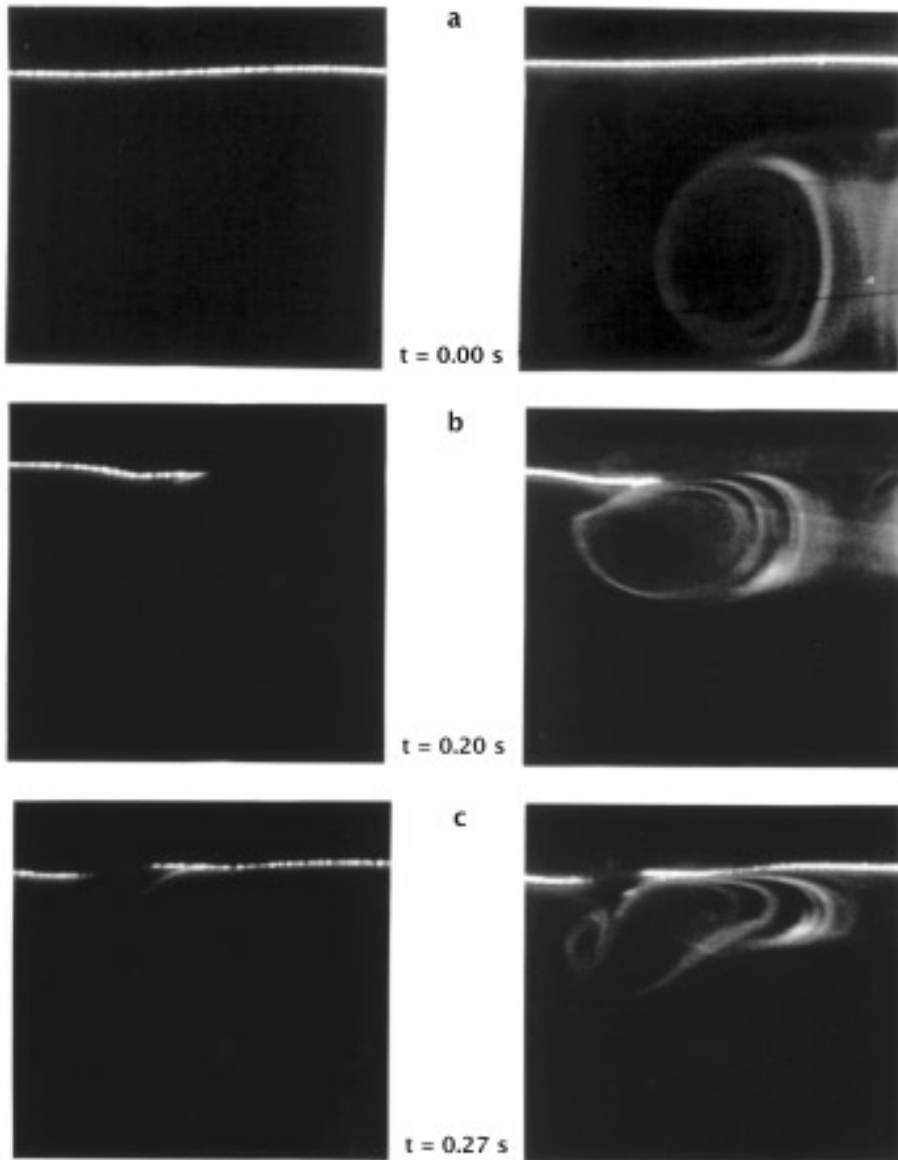


*Figure 3: Flow field and particle entrainment due to the collision. **Left** Floating tracer particles; **Right** The vortex ring and tracer particles*

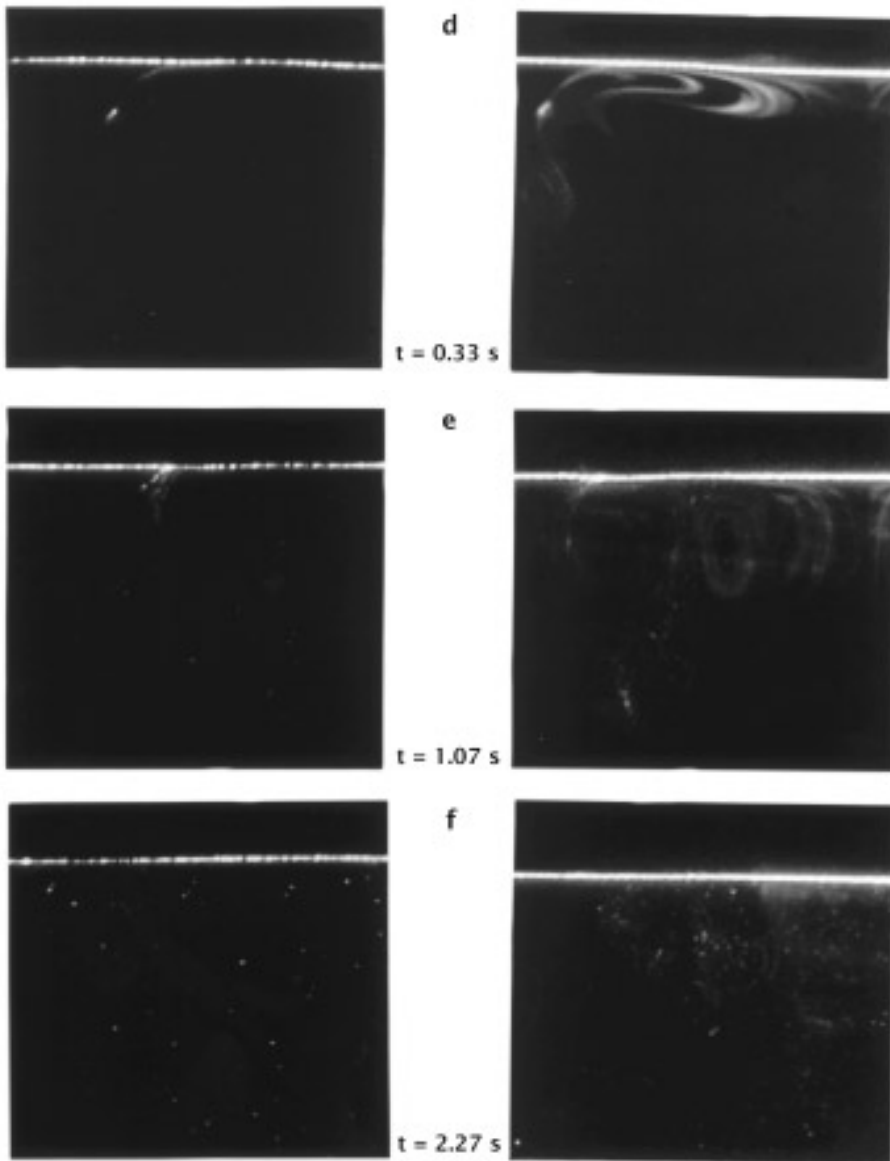


Figure 4: Flow field and particle entrainment due to the collision. **Left** Floating tracer particles; **Right** The vortex ring and tracer particles

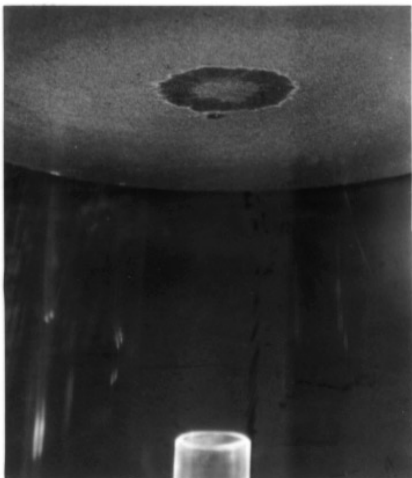
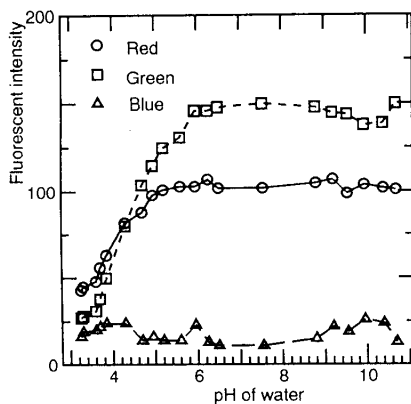
a*b*

Figure 5: *a* The water surface after the disturbance has dissipated. *b* Relationship between pH of a fluorescein solution and fluorescein intensity.

Figure 5a shows the water surface after the disturbance has dissipated. No tracer particles can be seen where the vortex ring collided but some are seen in the center. The dark ring is believed to be formed by water rising from the bottom.

Visualization by pH Dependency

pH Dependency by Fluorescent Light. It is known that the fluorescent characteristics of many substances vary with pH and temperature. In this experiment water-soluble fluorescein was used. The fluorescent intensity is maximum at an excitation wavelength of 494 nm and pH of 7.1, and the fluorescent spectrum is maximum at a wavelength of 518 nm. Slit light from a 488- and 514-nm argon-ion laser was employed as the excitation source to visualize the process of the dissolution of carbon dioxide. *Fluorescein* was dissolved in tap water to a concentration of 2.5×10^{-6} mol/l. The fluorescent spectrum of fluorescein is broader on the longer wavelength side than the spectrum peaks of the argon-ion laser. An optical filter that cut wavelengths below 520 nm was installed in front of the lens on the video camera to record only images due to fluorescence.

First, the relationship between the pH of the fluorescein solution and the fluorescent intensity was studied (see Figure 5b). In this measurement, the optical filter described above and a Toshiba 1/2-inch CCD video camera were used. RGB images recorded on a video tape were processed with an image

processor into digital images having 256 colors and 512×480 pixels.

The recording conditions were kept constant except pH; the water temperature was 17.7°C . The light intensity was averaged within a fixed area of 50×50 pixels for all the images recorded. In addition, three images were recorded at the same pH and the average values were employed. The pH was adjusted with 0.1N HCl and NaOH.

It was not possible to check accurately which wavelengths corresponded with the R, G and B outputs of the videocamera because detailed information on the color filters and the color response of the CCD video camera was not available. However, the following could be confirmed using Figure 3.

- Fluorescent intensity for blue: Weak. Little change within the pH range tested. This is because all the light with wavelengths below 520 nm is eliminated.
- Fluorescent intensity for green: With a pH of 6 or more, the fluorescent intensity for green is the highest of the three colors and does not depend on pH. With a pH of less than 6, however, the fluorescent intensity decreases rapidly with the drop in pH. This indicates that the fluorescent intensity for green depends most strongly on pH when the pH is less than 6.
- Fluorescent intensity for red: With a pH of 5 or more, the fluorescent intensity for red is the second highest next to green and barely changes with the increase in pH. With a pH of less than 5, the fluorescent intensity reduces in the same manner as that for green, though the rate of decrease is lower.

The above findings indicate that it is appropriate to set the initial pH around 6. As carbon dioxide starts to dissolve into the water, the pH and fluorescent intensity of that part of the water drop, which shows up as a dark area on the video screen.

Results of Visualization. Figure 6 (left row) shows a vortex ring colliding with the water surface. Figure 6 (right row) shows the results of the dissolution of carbon dioxide at the same water surface. The following are the comparative test results:

- Right after the collision of a vortex ring with the water surface, concentration boundary layers converge at the point where the external edge of the ring reaches the water surface and then enters the water. The concentration boundary layer where the external edge of the ring contacts the water surface is so thin that it could not be seen in the experiment.
- At some trigger, the concentration boundary layer starts to be entrained along the outer edge of the vortex ring. Once it starts, entrainment continues along the outer edge.
- Collision of the vortex ring generates a few secondary vortex rings and then leads to a disorganized disturbance. At the same time, the continu-

ously-entrained surface water is then dissipated in a disorganized manner in the water body.

4 Surface Slope Measurement

4.1 Description

Gas transfer is induced when the water surface is disturbed and entrained into the water body. The disturbance can be measured by assessing the change in *surface slope*.

To do this, *Hanratty* used a single laser beam. In order to obtain planer rather than an point data, the authors directed a number of laser beams vertically from the bottom of the water to hit a semi-transparent film placed above the water surface.

Any disturbance at the water surface generates a change in surface slope, shifting the beam spots. This shifting takes place so quickly that conventional videocameras for consumer use cannot possibly track the spots. Using the *high-speed videcamera* and the automatic particle tracking algorithm, it is only possible to accurately observe the changing shape of the water surface within a certain area.

4.2 Particle Tracking Velocimetry (KC Method)

Particle tracking velocimetry (PTV) estimates the position of particles in the water flow based on motion pictures of particle images. Many PTV algorithms, including the authors', have been developed so far.

The authors' method predicts information on a particle in the next step from its current data such as position, velocity, acceleration, size and brightness, using Kalman filtering. The probability that the predicted and observed particles are identical is judged objectively with a chi-square test.

Consequently, this has been named the APT-KC method, which stands for automatic particle tracking by Kalman filter and the chi-square test, or simply the KC method.

4.3 Experiments

Experiments to measure the change in surface slope by the method explained above are now in progress.

5 Concluding Remarks

Microscopic observations of the fundamental processes of gas transfer via the collision of a vortex ring against the water surface have been conducted. The following results have been obtained.

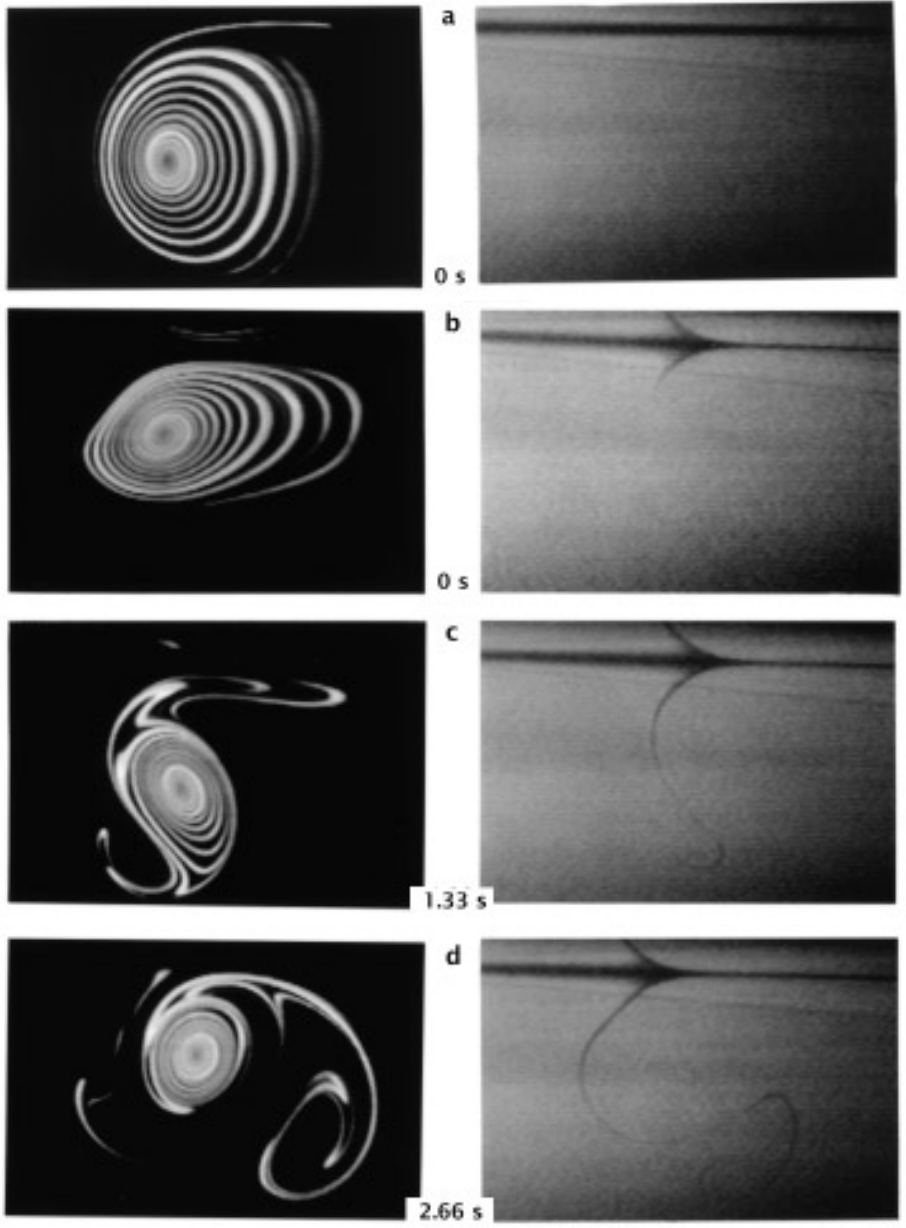


Figure 6: Collision of vortex ring (Left) and gas intrusion at the water surface (Right)

- A high-performance vortex ring generator has been designed and manufactured. It can produce vortex rings having a wide range of sizes and velocities, with high reproducibility.
- Some techniques have been developed to observe the motion of a vortex ring colliding against the water surface and entrainment of a thin surface layer that follows.
- A method to measure changes in surface slope due to the collision has been proposed. Disturbance at the water surface due to the collision of a vortex ring was observed by projecting a bundle of laser beams from the bottom of the water tank and tracking the movement of the beams with automatic particle tracking velocimetry and the world's fastest video-camera, developed by the authors.

Though the experiments have not reached the stage where the collision of a vortex ring and gas transfer can be directly correlated, it should be possible to apply the vortex ring generator and the visualization techniques developed here to future experiments on gas transfer at water surfaces.

References

- Asher, W. E. and Pankow J. F., The effect of surface films on concentration fluctuations close to a gas/liquid interface, *Air-Water Mass Transfer*, pp. 68-80, 1991
- Cerra, A. W, Jr. and Smith, C. R., Experimental observations of vortex ring interaction with the fluid adjacent to a surface, Rep. FM-4, 1983
- Etoh, T., High-speed Videocamera at 4,500 pps, *Japan Television Association*, Vol. 46, No. 5, pp. 543-545, 1992 (Japanese)
- Etoh, T. and Takehara, K., Development of a new algorithm and supporting technologies for PTV, Proc. of the International Workshop on PIV-Fukui '95, pp. 91-106, 1995
- Etoh, T. and Takehara, K., Needs, Requirements and New Proposals for Ultra-High-Speed Videocameras in Japan, Proc. of the 21st International Congress on High-Speed Photography and Photonics, Proc. SPIE2513, pp. 231-242, 1995
- Hanratty, J. H., Effect of Gas flow on physical absorption, *Air-Water Mass Transfer*, pp. 10-33, 1991.

High-Speed Video Capture of the Motion of Surface Water Induced by the Collision of a Droplet and the Collapse of a Bubble

T. Etoh, K. Takehara

Department of Civil Engineering
Kinki University, Higashi - Osaka, JAPAN

Abstract

Microscopic observations of the fundamental processes of gas transfer via the collision of droplets against water surfaces and the collapse of bubbles have been conducted. These two phenomena are closely related: collision of a droplet against a water surface causes gas entrainment in bubbles, and the collapse of a bubble and resultant water entrainment could produce droplets.

A droplet maker and a bubble generator having high reproducibility were designed and manufactured. Using the world's fastest videocamera, also developed by the authors, observations were made of the collisions of droplets against water surfaces and the collapse of bubbles.

1 Introduction

Gas transfer at air-water interfaces is enhanced by impacts which destroy the surface condition, such as the collision of droplets, vortex elements, rising bubbles and breaking waves. To understand the mechanism, it is useful to visualize water motion near air-water interfaces. However, it is difficult to capture such activity with consumer videocameras, because when taking pictures of water motion induced by impacts in a small area near the water surface, the frame rate of 30 pictures per second (pps) is too low, and the light sensitivity is inadequate. In 1991, the authors developed the world's fastest, and very sensitive, videocamera, with a frame rate of 4,500 pps at a resolution of 256×256 pixels. A very powerful image intensifier is attached directly to the image sensor, and the videocamera can capture moving images at 4,500 pps even in very dark conditions.

This paper shows frames from video sequences of the water motion near water surfaces following the collision of a droplet falling through air, taken by the videocamera developed by the authors. The motions are analyzed with an image processing computer. The paper also shows the motion of the water surface induced by the collapse of a bubble.

2 High-Speed Videocamera

2.1 Specifications

As a Kinki University Joint Research Center project in 1991, the authors developed a *high-speed videocamera* with an extremely sensitive internal MCP-type image intensifier and a recording speed of 4,500 pps [Etoh, 1992; Etoh and Takehara, 1995]. We reported on its use from the following three perspectives: past applications of the videocamera, mechanics developed after experience of the applications, and future improvements.

2.2 Applications

Table 1 lists current applications of the videocamera and those planned in the near future at Kinki University and in joint research at other universities and research laboratories, with the required frame rate, the success or failure of each application, and problem areas.

Since the development of the high-speed videocamera, we have been involved in further development of related technologies to make more effective use of it. Table 2 shows technologies already developed, planned for development, or planned for purchase at Kinki University.

The automatic image trigger, automatic trajectory tracking of tracer markers, the 3-way light splitter with filter holder, and a technique allowing the camera to track moving objects can be used in a variety of fields.

2.3 Further Improvements

Table 3 lists further points for improvement of the 4,500-pps videocamera. These include points discovered after some experience using the videocamera; others were known at the development stage, but were not pursued due to time limitations; and others are due to lack of communication between the authors and the hardware manufacturer.

3 Droplets

3.1 Previous Studies

Studies on phenomena that could take place when a *droplet* hits a water surface have been conducted since the middle of the last century. Two examples are Rogers [1858] and Thomson and Newmell [1885], who reported that a whirlpool could be generated when a colored droplet collides with the water surface at low speed. Worthington [1908] made detailed observations of the collision of a droplet dropped from 40–137 cm above the water surface using spark photography. Jayaratin and Mason [1964] observed the phenomenon of a droplet hitting the water surface and the top of a water

Table 1: Applications of the 4500-pps videocamera at Kinki University

Object	Evaluation of Imaging	Required Frame Rate (pps)	Problems/Difficulties	User
Measurement Accomplished/ Measurement Underway				
Laser Ablation	Difficult	10^5 - 10^7	Lack of speed	Electrical Engineering
Plasma Spray	Successful in measuring velocity field	10^4 - 10^5		Management Engineering
	Difficult to image spray particles	10^5 - 10^7	Lack of speed	
Interference in shock waves	Difficult	10^5 - 10^7	Lack of speed	Mechanical Engineering
Turbulence in flame	Possible	10^4 - 10^5	Lack of image resolution	Joint research
Star image fluctuation due to atmospheric turbulence	Possible	10^3 - 10^5	Lack of light	National Astronomical Observatory
Roll wave train	Possible	10^3 - 10^5		Joint research
Collision of a liquid droplet with water	Successful	10^3 - 10^4		Civil Engineering
Sedimentation of solid particles in water	Possible	10^3 - 10^4	Imaging with particles	Joint research
Cavitation	Difficult	10^5 - 10^7	Lack of speed	Mechanical Engineering
Two-phase liquid flow in a rotating pipe	Possible	10^4 - 10^6	Separation of air bubbles from water	Joint research
Deformation of tennis balls	Successful	10^3 - 10^4		Undergraduate physical exercise course
Movement of a runner's leg	Successful	10^3 - 10^4		Undergraduate physical exercise course
Planned in the future				
Turbulence in porous materials	Possible	10^3 - 10^5	Imaging within porous materials	Joint research
Blood flow in the fundus of the eye	Possible	10^3 - 10^5	Lighting	Joint research
Breaking waves and scattering of water in sprays	Possible	10^3 - 10^5	Separation of air bubbles from water	Joint research

Table 2: Related technologies under development at Kinki University Hydraulic Laboratory

Related technologies	Content and State
Completed	
Automatic image trigger	Trigger based on a change in brightness of the subject area.
Automatic particle tracking algorithm	Based on Kalman filter, Chi-square test, and Delaunay triangular net
3-way light splitter	3-way splitting of light using a 1/2 and 1/3 half prism.
Tracer particle with specific gravity and specific heat identical to water	Microcapsule of water covered with thin plastic film with a specific gravity of 1.
Under Development	
Colorization of MCP	Additional tests planned.
Glass, crystal, and plastics with refraction coefficients equal to that of water	Experiments and survey underway.
Device for tracking moving objects	Simple device under assembly.
Software to detect and track moving bodies	Further extension of automatic particle tracking algorithm.
Planned for purchase	
Postprocessor for image output	Necessary. However, available software can be used.

column separating from the main body, to collide with the water surface again. *Blanchard and Woodcock* [1957] studied the process of air bubbles entrained by a water droplet colliding with the water surface at terminal velocity and reported that the process depended on the size of the droplet. According to *Carroll and Wesler* [1981], a whirlpool that was created by a droplet starting 10 cm or less above the water surface and hitting the surface at low speed could play a great role in entraining air bubbles. Using high-speed film photography, *Pumphrey and Elmore* [1990] successfully visualized bubble entrainment at various collision speeds and with various droplet sizes, and analyzed the sounds generated in those collisions. Detailed research on droplets falling on a water surface, including numerical simulations, is also available by *Oguz and Prosperetti* [1990]. Gas transfer by a rain droplet was also studied by experiment and measurement [*Wilhelms and Gulliver*, 1990].

The authors have been engaged in reviewing these publications and also have set the following concrete aims in their research.

- Confirmation of phenomena that have been mentioned in the past.

Table 3: Points for improvement of the 4500-pps videocamera.

Points to consider	Notes
Internalization of an automatic trigger	At present, the external attachment is bulky.
Colorization	Simple. Colorization of internalized MCP type II under sutdy.
Higher resolution	Replacement of the imaging element is required.
Method to combine MCP and the imaging element	Movement due to vibrations, etc., is a source of noise.
Effects of vibration, temperature, and electromagnetic waves	A unified approach is needed.
Problem with cord length and connection	Cord is not long enough. Cause of noise. Monitoring by radio, etc.
Problem of transferring digital images	A way of transferring directly to a workstation is required.
Stripes in the image resulting from parallel readout	In addition to black correction (correction of the origin), it is necessary to have a simple gain correction mehtod.
Exposure time for frame speeds below 4500 frames/sec	Fixed at present.

- Analysis and evaluation of phenomena that have been observed previously but with insufficient definition and analysis.
- Finding unknown phenomena.

For example, it is stated in one of the above publications [Mesler *et al.*] that different results are obtained at low speed and high speed. However, no clear definition of the boundary between “high” and “low” is made.

3.2 Experimental Setup

A droplet maker has two electromagnetic valves which operate independently of each other so that liquid in a pipe can fall under its own weight, forming droplets (Figure 1). A nozzle was hand-made out of a commercially-available female pipet and attached to the end of the pipe. To store a certain amount of liquid inside the nozzle, a three-way cock was installed between the two electromagnetic valves. White poster color was used as the liquid to clearly show the phenomena taking place within the liquid. It must be noted therefore that the liquid droplet used in the experiment differed from a true raindrop in terms of viscosity, surface tension and other factors. The specific gravity of the poster color droplet was about 0.002 greater than that of the raindrop. The droplets and the water in the water tank were kept at 15 °C.

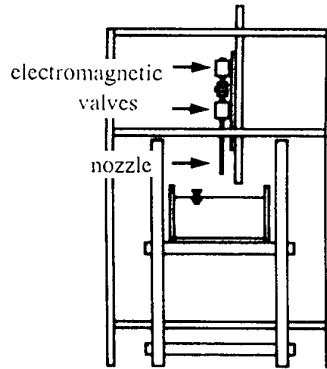


Figure 1: The droplet maker.

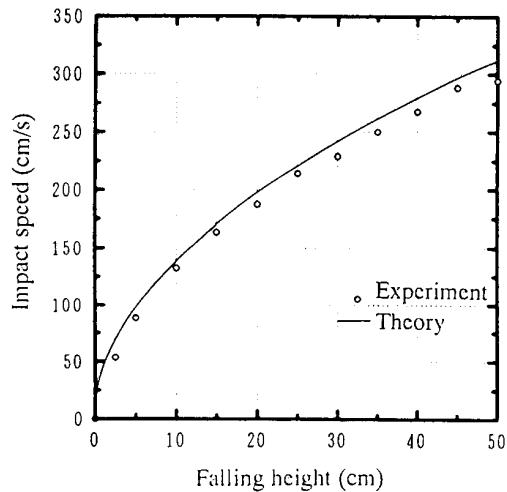


Figure 2: Freefall height vs. impact speed.

Two methods were used to measure the size of the droplets: (1) measuring the amount of liquid contained in one droplet with a scale on the nozzle, and (2) measuring via the image of a droplet while it fell.

Measurement of droplet size was conducted six times for each case under identical conditions. The diameter of a droplet based on measurement method (1), where droplets were assumed to be spherical, was an average of 4.76 mm with a standard error of 0.02 mm. With method (2), the results were an average of 4.81 mm in diameter with a standard error of 0.01 mm.

From the results obtained with these two methods, the reproducibility of the droplet maker employed in the experiment was determined to be less than 1%. The error in the diameter measured by method (2) in comparison

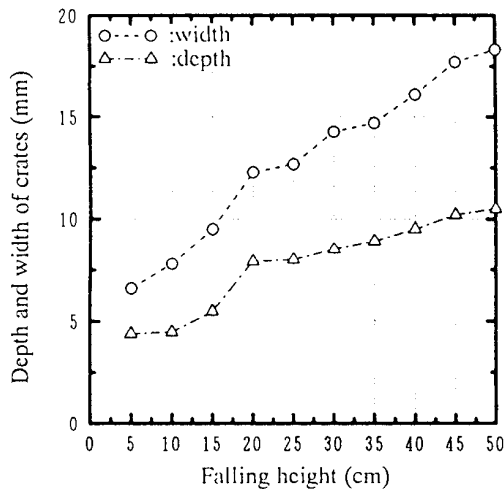


Figure 3: Freefall height vs. size of craters.

with the diameter obtained by method (1) was 1.1%.

The frame rate of the high-speed videocamera was set to 4,500 pps. The distance between the nozzle and the water surface was varied between 5 and 40 cm at intervals of 5 cm. The relationship between the fall height and the impact speed is shown in Figure 2. The impact speed was calculated from the time taken by the droplet to fall through the distance 1.0 to 0.5 cm immediately above the water surface. The circles in Figure 2 represent measured values and the solid line is a theoretical value $V = gh$ where air resistance is ignored.

All the experimental values obtained were smaller than the theoretical values because of air resistance. However, if this is actually true, the effects of friction should increase with increasing freefall height. Figure 2 indicates that the difference between the measured and theoretical values remains equal for all the different falling heights. Further work will have to be conducted to study this phenomenon.

3.3 Falling Height and Crater Size

The relationship between the droplet falling height and the size of the crater it generates when it hits the water surface was studied. In this experiment, normal non-colored water at 15 °C was used to produce droplets. The width of a crater was measured at the moment of maximum depth. The freefall height was varied between 5 and 50 cm at intervals of 5 cm. Measurements were conducted three times and the average was taken as the measured value. The falling height–crater size (depth and width) relationship shown in Figure 3 reveals the following:

- The relationship between the falling height and the crater size is significantly different at heights above and below 20 cm, indicating that the crater production mechanism may be different for the two cases.
- With a freefall height between 5 and 20 cm, the graph curve increases quadratically while between 20 and 50 cm, it increases linearly.

Visual observation confirms the difference in the phenomenon in the 5–20 cm and 20–50 cm regions. These could be interpreted as the “low speed” and “high speed” regions described by Mesler; the details are being investigated. Though the size of a crater produced at freefall height of less than 5 cm was not measured, the authors think the results would point to yet another different process, specifically one where the curve will bend drastically downward.

3.4 Example Frames

A few example frames are shown at the freefall height of 45 cm in Figure 4 (a) to (f). Time t is calculated from the moment the droplet hits the water surface. The position of the water surface is indicated alongside each photo.

The following phenomena were observed:

- The crater expands in a hemispherical shape.
- The original droplet colored by white poster paint assumes a flattened form at the bottom of the crater.
- A certain disturbing factor causes a vertical pattern in the crater.
- A wave motion expanding in the circumferential direction, which is probably a capillary wave, starts from the top edge of the crater, progressing downward (this phenomenon can be observed clearly on the moving image taken by the videocamera but not on a still image).
- At the same time, the bottom of the crater swells to form a water crown.
- Multiple projections appear at the crater bottom and dissolve into the water in the tank, leaving trails.
- As the bottom of the crater expands, the angle between it and the side walls tends toward the perpendicular. This interacts with the wave front coming down from the top, causing water from the droplet to dissolve into the water in the tank while leaving trails (this phenomenon, too, can be observed clearly on the moving image taken by the videocamera but not on a still image).

It has been found that remarkably different phenomena are observed at a freefall height of 15 cm, two of which are shown in Figure 5:

- A downward projection is observed at the bottom of a crater.
- The bottom of the crater is separated from the main body and pushed downward, where it drops underwater in the form of a vortex ring.

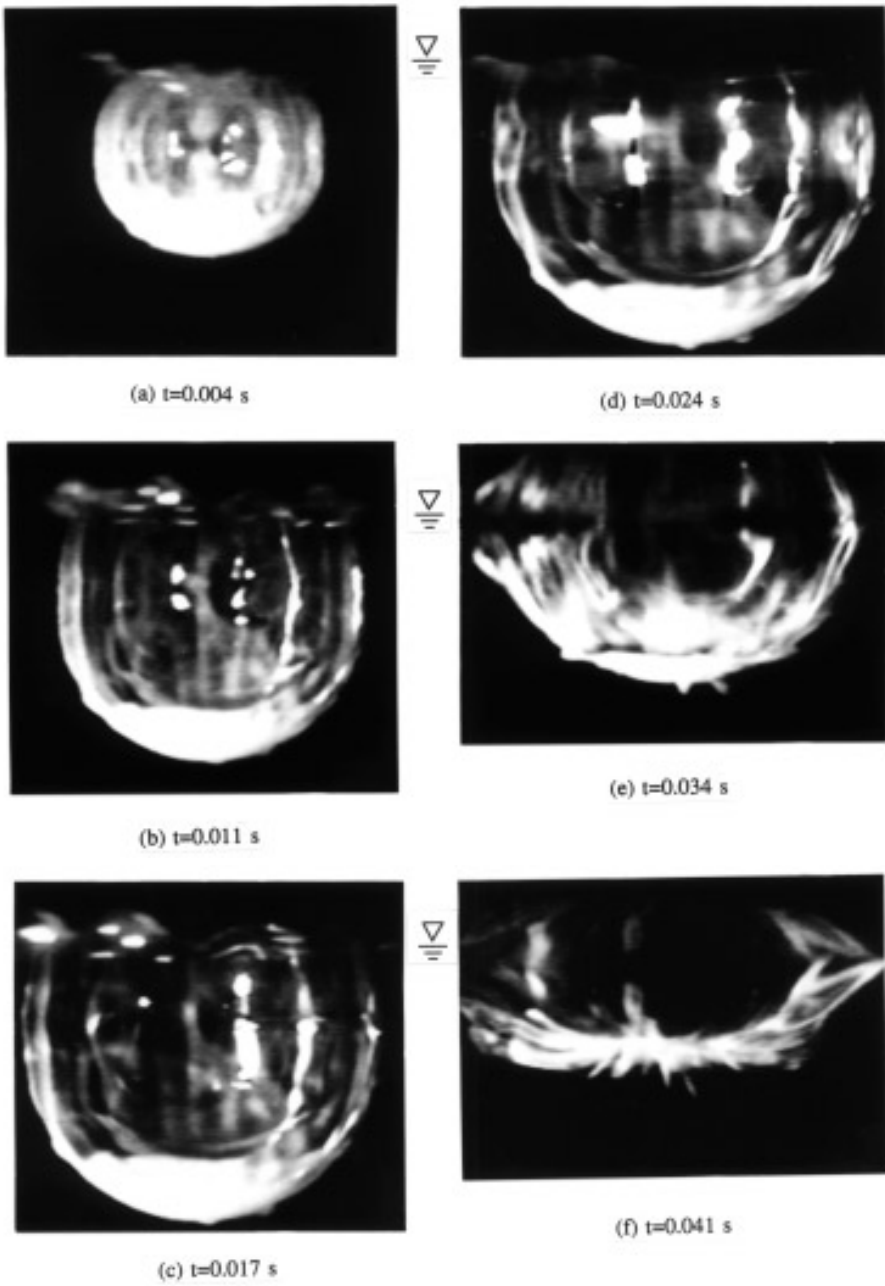


Figure 4: Surface deformation due to the impact of a droplet falling from 45 cm.

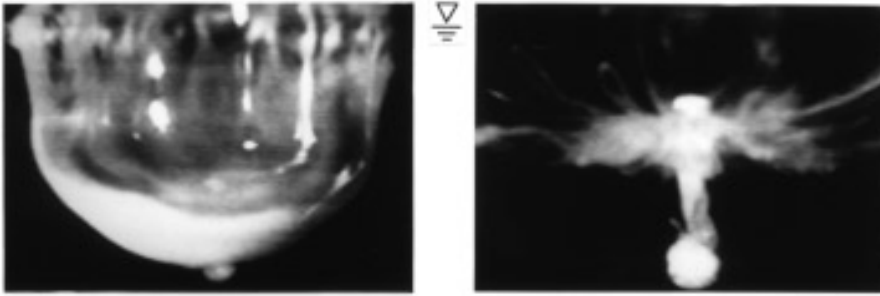


Figure 5: Surface deformation due to the impact of a droplet falling from 45 cm.

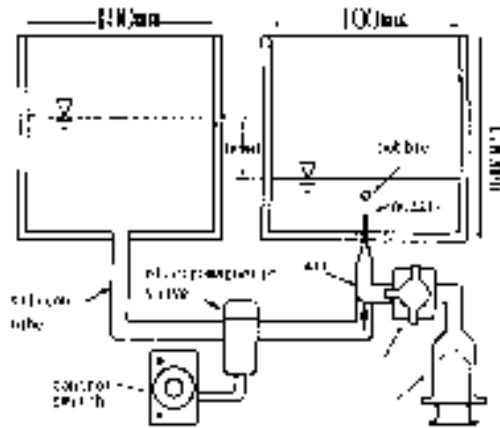


Figure 6: The bubble generator system.

4 Bubbles

4.1 Experimental Setup

Various physical factors can affect gas transfer at a water surface. One of them is the collapse of *bubbles* from below. To study the mechanism of bubble collapse, the authors developed a bubble generator and observed the collapsing with the high-speed videocamera.

The bubble generator was developed with the design objective of being capable of generating identical bubbles of 2 to 3 mm in diameter, one by one.

Figure 4 outlines the bubble generator system used in the experiment. Air fed from the injector collects under the nozzle and is released as bubbles due to the difference in the water heads of water tanks A and B. Uniform bubble sizes can be generated by adjusting the opening-closing time of the electromagnetic valve. Tanks A and B are $100 \times 100 \times 100$ mm, and the

Table 4: Bubble volume and reproducibility (accuracy).

	Average volume μ_V (mm ³)	Standard deviation σ_V (mm ³)	Volume accuracy ε (%)	Length accuracy $\varepsilon/3$ (%)	Diameter after spherical conversion (mm)
First bubble	8.61	0.33	3.46	1.15	2.638
Third bubble	8.97	0.22	2.43	0.81	2.578
Seventh bubble	8.28	0.18	2.14	0.71	2.510
Ninth bubble	7.88	0.13	1.65	0.55	2.470

silicone tube has an outer diameter of 6 mm and an inner diameter of 4 mm. A three-way cock is used to collect air efficiently in the injector, which keeps the amount of air inside the nozzle constant. The nozzle has an inner diameter of 0.4 mm and is inserted into tank A at the center of the tank base. An electromagnetic valve is used to provide the delicate opening/closing adjustment required for the generation of uniform bubbles. A switch that allows an on-time adjustment down to 0.01 s is used to control the valve open time. The valve opens when energized, and its minimum open time is 0.3 s. More than one dozen bubbles can be generated continuously once air has collected in the nozzle.

4.2 Reproducibility

Bubbles were produced in ten rounds, in each of which nine bubbles were generated. Ten images were observed for the first bubble. As the bubble is spheroidal, major and minor axis lengths were measured from all the obtained images and their volumes computed. Table 4 shows the results of the computation for the first, third, seventh and ninth bubbles, together with the reproducibility in terms of equivalent diameters obtained by converting the shape of the bubble into a sphere.

Table 4 makes the following clear:

- The bubbles that are produced earlier are bigger than those produced later. The average diameter of the first bubbles was 2.638 mm while that of the ninth was 2.470 mm.
- The length accuracy was 1.15% for the first bubbles and 0.55% for the ninth ones. Accuracy increases with bubbles produced later. Overall reproducibility of the generator is high.

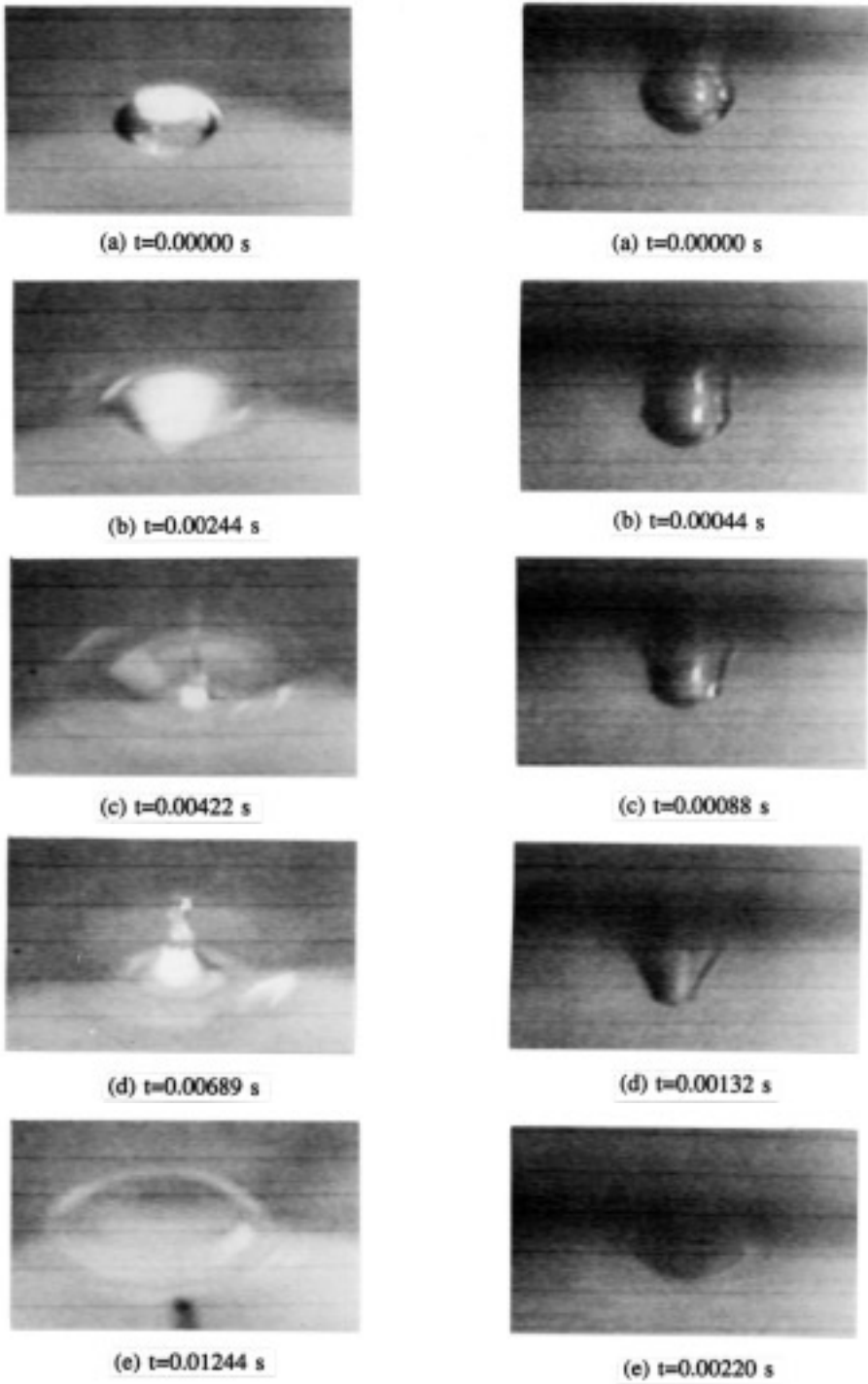


Figure 7: The collapse of a bubble at the water surface, viewed from above (left row) and the side (right row).

4.3 Example Frames

The collapse of a bubble was shot with the high-speed videocamera. Two examples are shown in Figure 7. In Figure 7 (left row), the moment the bubble collapsed was taken as time 0. In Figure 7 (right row), where it was difficult to determine the moment of collapse, time (a) was set to 0. The videocamera was positioned a little higher than the water surface and was focused downward on the water surface in Figure 7 (left row), and in Figure 7 (right row) it was positioned level with the water surface, with its focus inside the water.

The observation results can be summarized as follows:

- A bubble hitting the water surface from underneath does not collapse at once but bounces a few times (Figure 7a).
- The collapse itself takes place so quickly that it is difficult to record (Figure 7b).
- After the collapse, the water surface becomes cone-shaped and then the center is lifted vertically (Figure 7b).
- The lifted area blows upward and a small water droplet is ejected from the tip of it (Figure 7c).
- More droplets pull away from the raised center (Figure 7d).
- The central bulge disappears and waves ripple outwards (Figure 7e).

5 Concluding Remarks

Microscopic observations of the fundamental processes of gas transfer via collision of droplets against water surfaces and the collapse of bubbles has been conducted. These two phenomena are closely related; collision of a droplet against a water surface causes gas entrainment in bubbles, and the collapse of a bubble and resultant water entrainment could produce droplets.

A droplet maker and a bubble generator with high reproducibility were designed and manufactured. Using the world's fastest videocamera also developed by the authors, observations were made of the collisions of droplets against water surfaces and the collapse of bubbles.

Though direct correlations between the motions of droplets/bubbles and gas transfer have not yet been confirmed, the validity of the system used in the experiments has been verified for future study on gas transfer at the water surface.

References

- Blanchard, D. C. and Woodcock, A. H., Bubble nucleation studies Part II: Bubble entrainment by drop-formed vortex rings, *AIChE J.*, 27, pp. 853-856, 1957

- Carrol, K. and Wesler, R., Bubble nucleation studies - Part II: Bubble entrainment by drop-formed vortex rings, *AIChE J.*, 27, pp. 853-856, 1981
- Etoh, T., High-speed Videocamera at 4,500 pps, *Japan Television Association*, Vol. 46, No. 5, pp. 543-545, 1992 (Japanese)
- Etoh, T. and Takehara, K., Needs, Requirements and New Proposals for Ultra-High-Speed Videocameras in Japan, Proc. of the 21st International Congress on High-Speed Photography and Photonics, Proc. SPIE2513, pp. 231-242, 1995
- Jayeratin and Mason, The coalescence and bouncing of water drops at air water interface, Proc. Roc. Soc. London, A280, 545, 1964
- Oguz, H. N. and Prosperetti, A. Bubble entrainment by the impact of drops on liquid surfaces, *J. Fluid Mech.*, 219, pp. 143-179, 1990.
- Pumphrey, H. C. and Elmore, P. A., The entrainment of bubbles by drop impacts, *J. Fluid Mech.*, 220, pp. 539-567, 1990
- Rogers, W. B., On the formation of rotating rings by air and liquids under certain conditions of discharge, *Am. J. Sci. Arts, Second Series*, 26, 246, 1858.
- Thomson, J. J. and Newmell, H. F., On the formation of vortex rings by drops falling into liquids and some allied phenomena, *Proc. R. Soc. Lond.*, 39, p. 417, 1885.
- Wilhelms, S. C. and Gulliver, J. S. (editors), *Air-water mass transfer*, (selected papers from the Second International Symposium on Gas Transfer at Water Surfaces), ASCE, 1990
- Worthington, A. M., *A Study of Splashes*, New York: Longmans, Green and Co., 1908

A Bubbleless Hollow Fiber Membrane Aerator for Surface Waters

Peter T. Weiss and John S. Gulliver

Department of Civil Engineering, St. Anthony Falls Laboratory
University of Minnesota, Minneapolis, Minnesota

Abstract

Hollow fiber membranes have shown potential as a cost-effective technology for aerating surface waters. Two module designs have been developed to optimize fiber transfer rates in the different flow regimes found in lakes and rivers. Each design was tested under laboratory conditions using tap water to determine the effects of flow field parameters and oxygen feed pressure on mass transfer rates. Empirical relationships were developed in each case. Each module was also run for several weeks using diverted river water to examine the effect of fouling on long term use of the membranes in natural waters. The fiber performance was monitored over time and the rate and type of fouling was examined. These results may be used to predict fiber performance in future full scale applications.

1 Introduction

The reduction of point sources of *biochemical oxygen demand (BOD)* entering rivers, lakes, and streams can significantly increase *dissolved oxygen (DO)* concentrations, thereby greatly improving the water quality of surface waters. However, in many cases, the BOD input from non-point sources such as pastures, feed lot runoff and natural organic matter alone is great enough to reduce the DO in the receiving waters to dangerously low levels. The most effective treatment option of these non-point sources is often the aeration of the receiving water body. Unfortunately, the large volumes of water to be aerated adds greatly to operating expenses and traditional aeration technologies are often ineffective and/or cost-prohibitive. For example, the bubbling of compressed air through the water column typically produces ineffective oxygen transfer rates because air is only about twenty-one percent oxygen resulting in a relatively low driving force. Also, in shallow water bodies the bubbles rise to the water surface and escape to the atmosphere before much of the oxygen can be transferred. In deeper water bodies the air bubble can transfer more oxygen, due to a longer residence time and increased pressure, but it will also transfer nitrogen, which can result in harmful side effects on the aquatic life. Pure oxygen gas is sometimes used to increase transfer rates but again, the low residence time of the bubbles results in much of the manufactured oxygen simply being returned to the atmosphere.

Hollow fiber membranes filled with pressurized oxygen can provide significant oxygen transfer rates without bubbling or nitrogen supersaturation. Aeration occurs as the oxygen diffuses through a microporous membrane wall and into the passing water. Due to the small pore size, the surface tension of water, and the contact angle between the hydrophobic membrane material, water, and oxygen, pressures of greater than three atmospheres gage can be reached in the fiber without bubbling. Thus, using pure oxygen, the water phase oxygen concentration in equilibrium with the fiber is about fifteen times greater than that in equilibrium with a bubble of compressed air and there is essentially no loss of oxygen.

Two design orientations of hollow fiber membrane aerators are cross flow and parallel flow. In cross flow, the fiber axes are perpendicular to the water flow direction, whereas in parallel flow, the fiber axes are parallel to the water flow. Most of the prior research on gas transfer from hollow fiber membranes has been conducted using compact module designs. These designs typically favor the parallel flow configuration since it is easily manufactured in tubular form, but they must operate at much higher velocities than cross flow systems to achieve the same rate of oxygen transfer.

To achieve effective oxygen transfer rates in a parallel flow system the water is usually pumped past the fibers. Considering the volume of water to be treated when aerating surface waters, the energy costs of such a system could be cost prohibitive. Thus, the research presented herein has focused on developing a cross flow membrane aerator which can provide significant oxygen transfer rates by utilizing the relatively slow, but naturally occurring water velocities present in surface waters.

2 Fiber Characteristics and Module Design

Hollow fiber membranes can be subdivided into two broad categories by wall type. Those with uninterrupted micropores extending continuously through the fiber wall and those with a non-porous composite layer within a microporous wall. The first type results in pure gaseous diffusion from the fiber lumen to the outer surface, whereas the latter results in at least a portion of the transport process being solid diffusion through the composite layer.

Of the fibers tested, the composite fibers were found to be superior, primarily because they had a higher bubble point which resulted in higher attainable oxygen pressures without bubbling. The composite membranes used had essentially elliptical shaped pores with a long axis of approximately 0.3–0.4 microns and a short axis of approximately 0.1 micron, as shown in Figure 1.

Each module consisted of several separate fibers that were individually sealed at one end and potted together at the opposite, unsealed end. The base of the fiber module, containing the open end of the potted fibers, was connected to an oxygen supply. The fibers were pressurized with pure oxy-

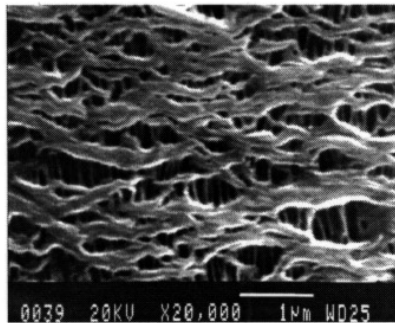


Figure 1: Electron micrograph of hollow fiber composite membrane (20,000X)

gen, resulting in oxygen transfer to the water. Due to the vastly differing flow velocities that exist in *lakes* and *rivers*, two different module designs were developed to provide a cross flow configuration in each case, thereby optimizing fiber performance regardless of water velocity.

The lake hypolimnetic aerator design consists of several pots, each holding 50–400 fibers, connected to a common oxygen supply. Thus, the fibers are fixed at the base, but can move freely and individually at the sealed end. Each fiber stands essentially vertical due to buoyancy. This design, which results in nearly 100% cross flow is shown in Figure 2. If this module design were installed in the much faster flow field of streams and rivers, the fibers would tend to bend downstream as the buoyant forces, which act to keep the fibers vertical, are overcome by the increasing drag forces exerted by the water. The result would be a mostly parallel flow orientation and a nearly tenfold drop in oxygen transfer rates. Thus, to maximize fiber performance, a second module design has been developed to insure cross flow in high velocity flow fields.

The high velocity design consists of sixteen or more fibers folded back on themselves several times and sewn together at the folds, forming a fiber mat. As in the previous design, the downstream end of each fiber is individually sealed and the opposite ends are potted to an oxygen supply. The fiber mat is attached to a hollow vertical pole and the open fiber ends proceed through a hole in the pole wall, down the center of the pole, and openly face the oxygen supply. The mat therefore resembles a flag, and the device has been named a flag aerator. The entire module design is shown in Figure 3. Finally, the modules are sealed to prevent oxygen from escaping through the center of the vertical pole. The net result is more of a cross flow configuration which increases fiber performance.

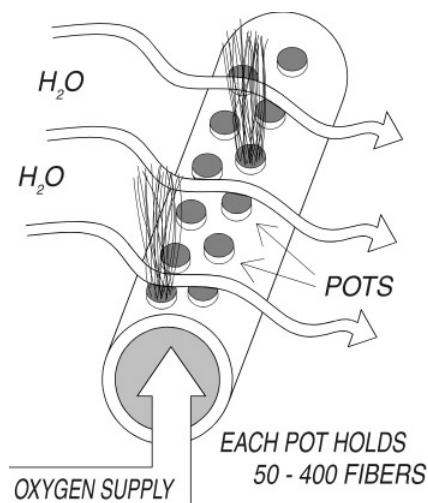


Figure 2: Schematic of typical full scale lake hypolimnetic aerator.

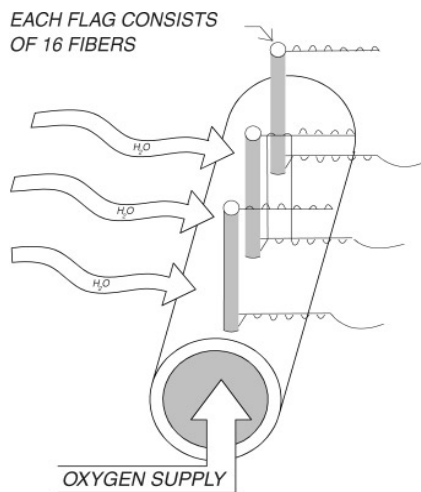


Figure 3: Schematic of a typical full scale instream aerator.

3 Oxygen Transfer Results

Both module designs were tested under laboratory conditions using tap water. Water velocities and oxygen pressures were varied to determine the effects of these parameters on oxygen transfer rates. A computer model was developed to estimate oxygen partial pressure profiles in the fiber lumen and to extract a bulk average mass transfer coefficient for the entire fiber module based on total fiber area [Weiss *et al.* 1994]. The objective was to develop empirical relationships to predict mass transfer coefficients based

on flow field conditions. These relationships could be use in future experiments and full scale aerator design to help predict membrane performance and guide the design process.

The result of the experiments was a mass flux rate of oxygen into the water. A numerical model was needed, however, to determine the experimental bulk mass transfer coefficient, \bar{K} because the oxygen concentration varied with distance along the fiber lumen. Therefore, a computer model was developed to estimate the shape of the fibers in a given flow field. Once the shape of the fibers was estimated the model used previous relationships between fiber angle and mass transfer coefficients to estimate a mass transfer coefficient for each incremental length of fiber. The model used the previous results to estimate a oxygen partial pressure profile within the fiber and total flux rate of oxygen out of the fiber. If the total oxygen transfer rate predicted by the model did not equal the observed rate the model iterated on the value of K for each fiber element until the predicted and observed rates were within acceptable limits. Finally, the computer model used the results to determine a bulk Sherwood number, Sh_B , for each experimental run [Weiss *et al.* 1994].

If it is assumed that mass transfer from a microporous fiber in a cross flow is similar to that from a cylinder in a cross flow, an appropriate relationship for fitting the experimental data is (Eckert and Drake, 1972).

$$\frac{\bar{K}d_o}{D_w} = Sh_B = \beta_1 Re^{\beta_2} Sc^{\beta_3} \quad (1)$$

where d_o = outer diameter of the fibers, D_w = diffusivity of oxygen in water, Re = Reynolds number, Sc = Schmidt number, and β_1 , β_2 , β_3 , are fitted constants.

The theory developed for heat and mass transfer around cylinders and similar convective heat transfer relationships suggest that the exponents should be in the range $0.3 \leq \beta_2 \leq 0.9$ and $0.33 \leq \beta_3 \leq 0.36$. Since the Schmidt number did not change significantly during the experiments, the power of 0.33 was chosen from parametric relationships for heat and mass transfer. In the current study the bulk Sherwood number was also found to be a strong function of pressure. For most fibers, the pressure difference is not considered to be a factor in increasing Sherwood number because the thickness of the concentration boundary layer is large compared to the spacing between pores. For the experiments described herein, the thickness of the concentration boundary layer was computed to be between 0.1 and 1.2 microns. Figure 1, however, which shows an electron micrograph of the fiber surface, shows that the pore spacing is at least on the same order of magnitude as the estimated thickness of the concentration boundary layer and in many cases it is much larger. Thus, it is possible that the protrusion of the meniscus into the boundary layer and the increase in the meniscus surface area, as influenced by a pressure increase, would have an

impact upon the bulk average Sherwood number. In other words, a pressure increase could push the gas-water interface further into the boundary layer, effectively reducing the boundary layer thickness and increasing mass transfer. The interfacial area for oxygen transfer would also increase with increasing pressure as the interface moves from the shape of a flat disk to a more hemispherical shape. Both of these effects would tend to increase oxygen flux if the pores are spaced significantly apart. Since the disruption of the boundary layer and the interfacial surface area are both related to the ratio of pressure and the pressure drop created by surface tension, the parameter $WeEu = \Delta P dp / \sigma$, where ΔP = the pressure drop across the gas-water interface, dp = the mean pore diameter, and σ = surface tension of water, was added to equation (1). We and Eu are the Weber number and Euler number, respectively.

Hence, the equation fit to experimentally determined Sh_B was:

$$\frac{\bar{K}d_o}{D_w} = Sh_B = \beta_1 Re^{\beta_2} [WeEu]^{\beta_4} Sc^{0.33} \quad (2)$$

3.1 Hypolimnetic Aerator

The hypolimnetic modules were tested under laboratory conditions using tap water. Three modules containing 50 fibers, 25 cm in length, were placed one in front of the other and water was passed by the pressurized fibers at different velocities and oxygen feed pressures. The best fit of equation (2) for the lake hypolimnetic aerator modules are :

$$\beta_1 = 0.387 \quad \beta_2 = 0.292 \quad \beta_4 = 0.388$$

Equation (2), with the three fitted coefficients, may now be used to predict the performance of this passive hollow fiber membrane aerator in the cross flow orientation described. The predictions from equation (2) and the best fit coefficients are compared with the measurements in Figure 4.

3.2 Instream Flag Aerator

The experiments were repeated using the instream modules. Each experiment consisted of a single membrane flag with sixteen, 210 cm effective length, fibers. The fiber pores were chemically plugged along the top and bottom of the membrane flag to prevent bubbling in areas of significant fiber-to-fiber contact.

This resulted in the effective length of fiber being less than the actual length. The experimental results were once again fit to equation (2) to determine the best fit coefficients. The results for the instream aerator design are :

$$\beta_1 = 0.0864 \quad \beta_2 = 0.601 \quad \beta_4 = 0.295$$

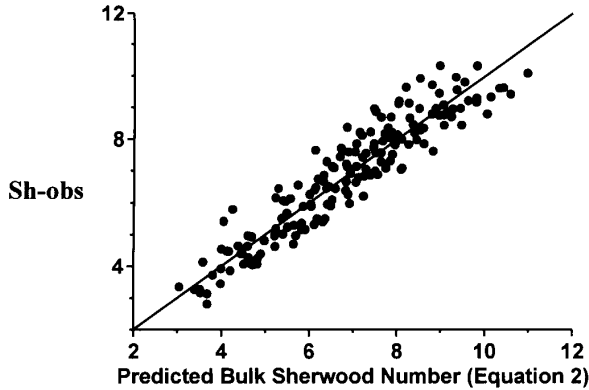


Figure 4: Comparison of observed and predicted bulk Sherwood numbers for the lake hypolimnetic aerator.

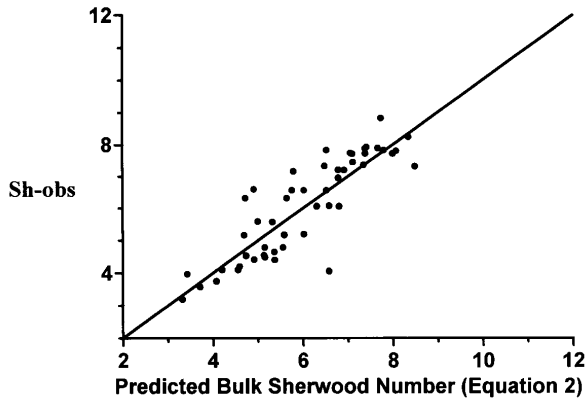


Figure 5: Comparison of observed and predicted bulk Sherwood numbers for the instream (flag) aerator.

The Sh_B predicted for the instream aerator, obtained from equation (2) and the coefficients shown above, are plotted against measured bulk Sherwood number in Figure 5.

In both designs there is no observable trend in the residuals of the curve fit to equation (2), which indicates a good match throughout the experimental range of velocities (Reynolds number) and pressure differentials (Weber-Euler number factor). One interesting point about equation (2) is the power of 0.388 and 0.295 on the $WeEu$ parameter. The value of the two powers on the pressure term means that if the pressure differential is increased by a factor of 3 (say from one to three atmospheres), Sh_B would increase by 53 and 38 percent, respectively. Thus, both the transfer coefficient and the

concentration gradient increase with pressure inside the fibers.

4 Membrane Fouling

A legitimate concern of extended membrane use in natural waters is that of *fouling*. Fouling can occur by biological attachment to and/or chemical precipitation on the fiber surface. In order to better characterize membrane performance in these situations, both module designs were run continuously for several weeks in diverted Mississippi River water.

4.1 Hypolimnetic Aerator

Six modules containing 396 fibers each (35 cm effective length) were installed side by side in diverted river water with velocities of approximately 1–2 cm/s. The performance of the system was monitored over time. During the time span of the experiment the flow field conditions (i. e., Re , We , Eu , Sc) varied slightly. Since the bulk average Sherwood number is a function of the experimental conditions, a simple plot of the mass transfer coefficient or Sherwood number versus time would not accurately represent variations in performance due only to fouling. In order to obtain a true measure of the impact of fiber fouling, it was assumed that the exponents on equation (2) for each module design were constant with time. With this assumption equation (2) was solved for the leading coefficient, β_1 , and β_1 was plotted versus time.

Figure 6 shows a plot of β_1 from equation (2) for the hypolimnetic module as a function of time. The performance of the fibers drops with time, apparently due to fouling. Over the time span of the experiment a slime layer developed on most of the fiber surface area. An electron micrograph of a sample of this layer, revealed that it is most likely a biofilm consisting of external polysaccharides, diatoms, and bacteria. The biofilm impedes diffusion of the oxygen to the passing water and the performance drops. The fouling, however, also raised the bubble point of the fibers by 50 percent. This increase allowed for larger concentration differences across the fiber without bubbling and somewhat offset the drop in Sherwood number due to fouling.

At 1779 hours the biofilm was sheared off by increasing the velocity of the water moving past the fibers to approximately 10–15 cm/s. This accounts for the jump in fiber performance at that time. The fiber performance, however, quickly dropped to previous levels as the biofilm reformed on the surface of the fibers. Presumably, a thin layer of biological attachment was not sheared off by the increase in water velocity and the biofilm was able to grow much more rapidly on the unclean surface.

In full scale, extended uses, the modules would most likely have to be periodically cleaned with a weak acidic solution to maintain their performance. The acid kills any biological growth attached to the fiber surface,

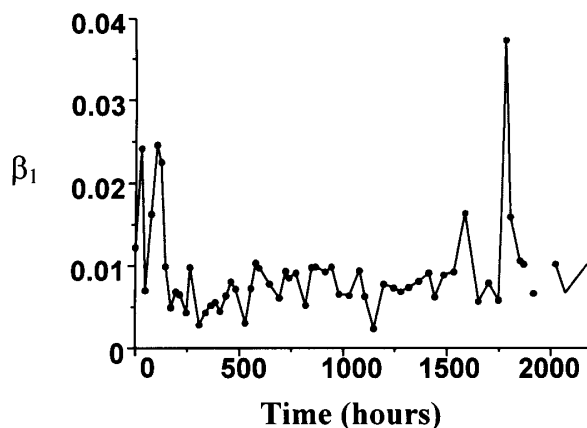


Figure 6: Performance of the lake modules as a function of time.

the goal being to revert back to the slower rate of fouling observed in the initial stages of the experiment.

4.2 Instream Flag Aerator

A single membrane flag was installed in diverted river water with a velocity of approximately 30 cm/s. Fiber performance was monitored over the course of several weeks. Equation (2) was again solved for the leading coefficient, β_1 . The results are shown in Figure 7. It can be observed that the fouling rate for the instream module is slower than that of the hypolimnetic aerator. The performance does not drop as quickly or to the same extent in comparison with the lake modules. Electron micrographs of several sections of fiber after continuous use, such as given in Fig. 8, revealed limited biological attachment. The figure shows some attachment of diatoms and possibly some chemical precipitation (angular, white deposits). Electron micrographs at a magnification of 20,000–30,000, as well as staining with acradine orange revealed no significant biofilm growth or bacterial attachment. The slow reduction in fiber performance can thus be attributed to the significantly higher water velocities present during the instream tests, where the shearing forces of the higher water velocities prevented any significant attachment of biological material. Although the lack of biological fouling is encouraging, the performance of the fibers was still dropping with time at the end of the experiment. Thus, if this were to continue indefinitely, at some time the fibers would have to be cleaned with a weak acidic solution to restore performance.

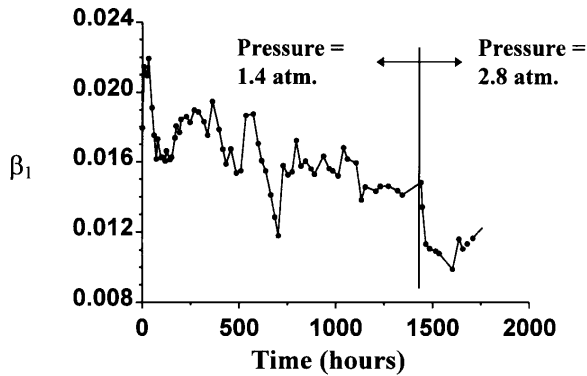


Figure 7: Performance of the instream modules as a function of time.

4.3 Results of Tests in Natural Waters

As expected the performance of the membrane modules dropped with time. However, as a result of fouling, the bubble point increased. Therefore, the drop in performance associated with fouling can be at least partially compensated for by an accompanying increase in the internal oxygen pressures attainable without bubbling.

The previous experiments certainly do not answer all of the questions concerning extended use of hollow fiber membranes as an aeration device in natural water bodies. For instance, a ruptured fiber can be sealed off, resulting in the loss of that fibers contribution to the aeration process, but eliminating the need to replace the entire module. If, however, the rate of fiber rupture were significantly large, entire modules may have to be replaced too often to provide cost-effective aeration. Also, it is reasonable to assume that there is a limit to the number of times a module can be acid washed and retain its effectiveness. Thus, modules may have to be replaced periodically even if no fibers rupture. These factors will certainly add to the operating and maintenance costs, but if they can be minimized, there is a strong potential for a full scale cost-effective hollow fiber membrane aerator.

5 Conclusions

Hollow fiber membrane aeration is a potentially cost-effective method of surface water aeration. Significant oxygen transfer to the water can be obtained with no bubbling and no detrimental side effects due to nitrogen supersaturation.

Two different module designs have been developed to optimize oxygen transfer rates in the vastly different flow velocities found in lake and rivers.

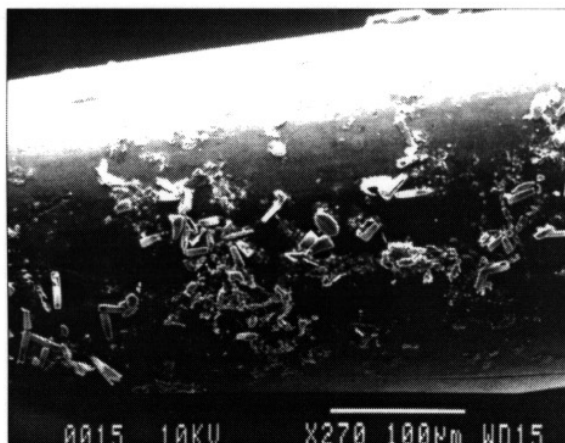


Figure 8: Representative electron micrograph (270X) of an instream modules hollow fiber membrane after over 1700 hours of use.

In slower velocity waters, such as lakes, fiber fouling was more significant due to biofilm growth on the fiber surface. Due to increased shearing forces, no observable biofilm was found at higher velocities and fiber performance dropped at a slower rate. To use either design for extended periods in a natural water body, the fibers would have to be periodically cleaned to maintain their performance.

Although hollow fiber membrane aeration has a large potential for cost savings, the cost-effectiveness of the system will depend on fouling rates and the frequency at which the modules will need to be replaced due to damage and breakage. If these rates can be minimized, hollow fiber membrane aeration can provide a cost-effective, advantageous alternative to conventional aeration technologies.

Acknowledgements

This paper is based upon work supported by the National Science Foundation under Grant No. BCS-9123175 and by the Minnesota Legislature ML 1991, Ch 254, Art. 1, Sec 14, Subd. 4K as recommended by the Legislative Commission on Minnesota Resources from the Minnesota Future Resources Fund. Any opinions, findings, and conclusions or recommendations expressed are those of the authors and do not necessarily reflect the views of either the National Science Foundation or the Minnesota State Legislature.

References

- Ashley, K. I., Hypolimnetic aeration research in British Columbia, *Veh. Internat. Verein. Limnol.*, Vol. 23, pp. 215-219, 1988
- Eckert, E. R., and Drake, R. M., *Analysis of Heat and Mass Transfer*, McGraw Hill, New York, NY., 1972
- Fast, A. W. and Lorenzen, M., Synoptic survey of hypolimnetic aeration, *Jour. Environmental Engineering, ASCE*, Vol. 102(EE6), pp. 1161-1174, 1976
- Macaitis, W., et al., Sidestream elevated pool aeration station design, in *Air-Water Mass Transfer*, S. C. Wilhelms and J. S. Gulliver, eds., American Society of Civil Engineers, New York, NY, pp. 670-681, 1991
- McQueen, D. J. and Lean, D. R. S., Hypolimnetic aeration: An overview, *Water Pollution Research Jour.*, Canada, Vol. 21(2), pp. 205-217, 1986
- Weiss, P. T., Oakley, B. T., Gulliver, J. S., and Semmens, M. J., The performance of a vertical fiber membrane aerator, in *Aeration Technology*, R.E.A. Arndt and A. Prosperetti, eds., American Society of Mechanical Engineers, New York, NY, FED. Vol. 187, pp. 59-66, 1994

Model of Reaeration at Permeable Breakwaters

Y. Hosoi¹ and H. Murakami²

¹ Department of Social Systems Engineering, Tottori University
Tottori, Japan

² Department of Civil Engineering, University of Tokushima
Tokushima, Japan

Abstract

Recently, permeable breakwaters through which water can flow have been constructed. Not only can they decrease wave reflections but also a reaeration function is expected at their open areas. From the view point of reaeration, oxygen absorption and replacement of aerated water with fresh water are important. To examine both functions of permeable breakwaters, experimental and theoretical analyses were carried out. It was indicated quantitatively that the oxygen absorption is more important for the reaeration at permeable breakwaters.

1 Introduction

According to increasing concerns about the water environment, not only disaster prevention, but also environmental protection is expected from breakwaters. Recently *permeable breakwaters* which can reduce wave reflection compared with impermeable ones have been often constructed. From the environmental point of view, they can contribute to *water purification* by sea water exchange through the slit and reaeration due to *wave breaking*. Several studies on the reaeration near coastal structures have been carried out. They indicate that far larger oxygen transfer due to wave breaking at permeable breakwaters as compared with other areas occurs. However most of them treat only oxygen transfer from air to water.

The oxygen flux N across the air-water interface can be written as $N = K_L(C_s - C)$, where C and C_s are the concentration of *dissolved oxygen (DO)* and the saturation concentration of DO, respectively. K_L is called the *oxygen transfer coefficient*. Previous studies have examined K_L or the *reaeration coefficient* k_2 which includes in addition to K_L the effects of the area of the air-water interface and of the water volume where reaeration takes place. But the concentration of DO also influences the oxygen flux. For that reason the oxygen flux depends not only on the oxygen transfer across the air-water interface but also on the longitudinal transfer of aerated water; i. e., quick replacement of aerated water with fresh water at the reaeration area is important.

In this study the reaeration function of the vertical silt type permeable breakwater was investigated. In addition to the evaluation of reaeration

function of breakwaters, i. e., the oxygen transfer from air to water at the reaeration area, the removal of the aerated water from the reaeration area is examined.

2 Reaeration at Permeable Breakwater

In this study vertical slit type permeable breakwaters were considered. These breakwaters have horizontal cross section geometries in their chamber sections. For the purpose of this study, we called the gaps between solid sections, chambers. Through the slits, water can flow, and waves are transformed and broken. At the slits there is water turbulence due to wave breaking, thus reaeration efficiency is high compared with other areas. Water with a high concentration of DO is transferred by exchange flow to outer area, and fresh water is supplied. The oxygen absorption efficiency is higher when the DO concentration is lower. Therefore, from a viewpoint of the oxygen supply to the water, both the function of oxygen absorption at the slit of the breakwater and water exchange between the slit and outer area should be examined.

3 Oxygen Transfer Model

A one-dimensional model, as shown in Figure 1, was considered. A *two-step renewal model* is presented as follows. The oxygen is transferred from the atmosphere to the water body across the water surface and quickly mixed vertically at the reaeration area. Therefore, the DO concentration at the aerated area is assumed to be uniform. This water is replaced with water from the outer area. From this assumption, the mass conservation equation of oxygen at the reaeration area is written as

$$V \frac{dC'}{dt} = K'_L A (C_s - C') - q(C' - C) \quad (1)$$

where V and A are water volume and surface area of the reaeration area, respectively, and q represents the longitudinal exchange flow between the reaeration area and the outer area. C' and C are the DO concentration of the aerated area and the outer area, respectively. K'_L is the local oxygen transfer coefficient which represents the oxygen transfer efficiency across the water surface of the reaeration area.

DO transferred to the outer area is assumed to be quickly mixed to become a uniform concentration. The aerated area is limited and small compared with outer area. Since the DO conveyed with aerated water from the slit is diluted by a far great volume of water, C' is assumed to be constant. In this case, a steady state condition where oxygen is transferred through

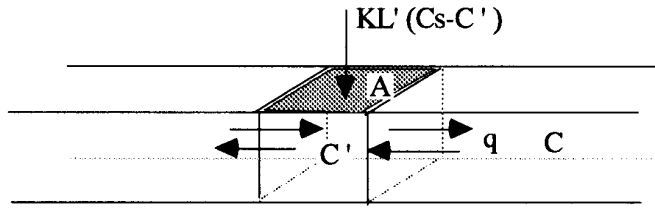


Figure 1: Oxygen transfer model

the slit of a permeable breakwater to a greater water body can be assumed. The steady state solution of Eq. 1 is

$$C' = \frac{K'_L A C_s + q C}{K'_L A + q} \tag{2}$$

The steady state oxygen flux is given as

$$N = \frac{K'_L}{K'_L A + q} q (C_s - C) = \frac{1}{\frac{A}{q} + \frac{1}{K'_L}} (C_s - C) \tag{3}$$

As the reaeration area is limited, it is suitable to use C to represent the concentration of DO. This situation is similar to that the concentration of DO of bulk flow is used in the surface renewal model. We define the overall transfer coefficient, K_L . The oxygen flux, N , is described by K_L and C instead of C' . The oxygen flux is given as

$$N = K_L (C_s - C) \tag{4}$$

From Eqs. 3 and 4 K_L is given as

$$K_L = \frac{1}{\frac{A}{q} + \frac{1}{K'_L}} \tag{5}$$

By considering the reaeration area produced by the breakwater, which also significantly affects the oxygen supply to water, the parameter K_{La} defined by $K_L A$ is suitable to describe the reaeration efficiency and is written as

$$K_{La} = K_L A = \frac{1}{\frac{1}{q} + \frac{1}{K'_L A}} \tag{6}$$

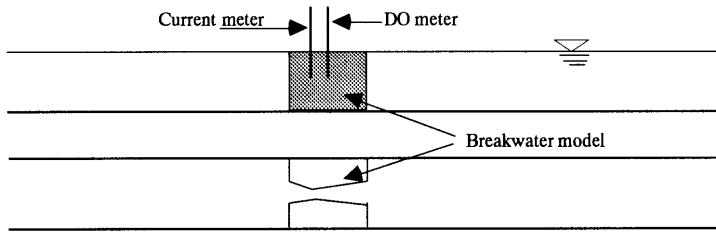


Figure 2: Experimental apparatus

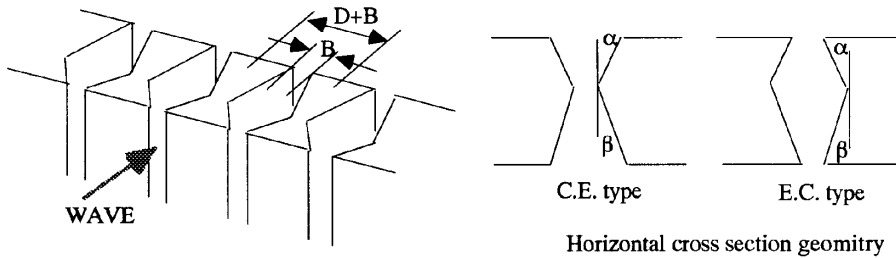


Figure 3: Vertical slit type permeable breakwater models

Eqs. 5 and 6 indicate the importance of q and A for reaeration. When $q/A \gg K'_L$, K_L is close to K'_L , i.e., the overall oxygen transfer is controlled by the oxygen transfer across the water surface at the reaeration area. Contrary, when $K'_L \gg q/A$, K_L approaches q/A : i.e., the water exchange between the reaeration area and the outer areas controls whole process.

4 Experimental Apparatus and Procedure

4.1 Experimental Flume and Breakwater Models

A wave tank (15 m long by 20 cm wide) with a flap-type wave generator at one end was used. The breakwater model was placed at a distance of 10 m from the wave generator. The vertical slit type permeable breakwater models are shown in Figure 3. Four combinations of angle α and β were used for the C. E. type: ($\alpha = 20$ degrees, $\beta = 20$ degrees), ($\alpha = 40$, $\beta = 20$), ($\alpha = 20$, $\beta = 40$) and ($\alpha = 40$, $\beta = 40$). For the E. C. type, four angle combinations were also used: ($\alpha = 20$, $\beta = 7$), ($\alpha = 40$, $\beta = 16$), ($\alpha = 46$, $\beta = 20$), and ($\alpha = 68$, $\beta = 40$).

4.2 Water Exchange Flow

Water exchange flow through the slit of the breakwater is caused by wave action. The horizontal water velocity at the smallest gap of the breakwater

was measured by a propeller type current meter at a point 7 cm below the water surface. The water exchange discharge per gap per unit of breakwater length caused by wave action is expressed as

$$q = \frac{2}{T} \int_0^{T/2} \frac{Dh}{D+B} V_{max} \cos\left(\frac{2\pi t}{T}\right) dt = \frac{2Dh}{\pi(D+B)} V_{max} \quad (7)$$

where V_{max} is the amplitude of water velocity at a gap and T is the wave period.

4.3 Reaeration

The experiment on reaeration was carried out. After the concentration of DO was reduced by sodium sulfite, waves were generated. The change in DO concentration under wave action was observed. There were one measuring point at the slit and several points in the outer area.

A similar experiment without the breakwater was also carried out. The temporal change of the concentration of DO was far smaller than that of the experiments with breakwaters. Here we assume that there is no reaeration due to breakwater in the outer area. Therefore, in the experiments with the breakwater, the increase in DO was assumed to be due to the reaeration at the breakwater. On the assumption of that the DO is absorbed only at the reaeration area, the concentration of DO in the experimental flume is described as follows:

$$V \frac{dC'}{dt} = K'_L A (C_s - C') - q(C' - C) \quad : \text{ reaeration area} \quad (8)$$

$$V^* \frac{dC^*}{dt} = q(C' - C_b) \quad : \text{ outer area} \quad (9)$$

where C^* is the mean DO concentration of the outer area, V^* is the water volume of the outer area and C_b is the DO concentration of outer area at the interface between the reaeration area and the outer area.

From these equations, temporal variation of the total mass of DO is described as

$$K'_L A (C_s - C') = \int V \frac{dC}{dt} dV. \quad (10)$$

In order to estimate K'_L strictly according to Eq. 10, the following procedure should be applied. Temporal variation of the concentration of DO is observed at the whole area of the flume. The right hand side of Eq. 10 (i. e., temporal change of total mass of DO in the flume) is calculated during

a time interval. The mean value of C' is calculated from the observed results during the time interval. Substituting these values for Eq. 10 yields K'_L .

On the other hand, if the second term of the right hand side of Eq. 1 is neglected, the following equation is obtained:

$$K'_L A = -\frac{V}{t} \ln \left(\frac{C_s - C'_2}{C_s - C'_1} \right) \quad (11)$$

where C_1 is the initial concentration of DO, and C_2 is the concentration after time t . According to this equation, K'_L can be estimated by the observation of DO at the permeable breakwater. It is easier than the above method. *Horie et al.* (1987) reported that Eq. 11 was applicable for a few tens of minutes from the beginning of the experiment when the concentration of DO is low and the effect of longitudinal transportation is small. It was also verified from the comparison of the estimated value yielded by Eq. 10 with that yielded by Eq. 11 for several cases in our preliminary experiments. Thus, Eq. 11 was used to estimate K'_L from the observed results in this study. Since there was strong mixing in the slit area, we assumed that there was no vertical and horizontal distribution of DO concentration.

5 Results and Discussion

5.1 Oxygen Transfer at the Permeable Breakwater

Figure 4 shows the local oxygen transfer coefficient obtained from the experiments. It is shown in relation to the volume of the slit. The larger slit size results in a decrease in the local oxygen transfer coefficient. It may be attributed to the mixing intensity of water at the reaeration area where energy is converted from waves through their breaking.

From the *surface renewal model*, the local oxygen transfer coefficient K'_L at the reaeration area is described by

$$K'_L = \sqrt{D_M r} \quad (12)$$

where D_M and r are the molecular diffusion coefficient and the surface renewal ratio, respectively.

The surface renewal model is based on the hypothesis that the gas diffuses into water elements located at the gas-water interface which are replaced with fresh bulk water. The *renewal ratio* r is closely related to the water turbulence. At the breakwater, it is produced by wave breaking. We assume that r is represented by the dissipated energy at the breakwater and the kinematic viscosity as follows:

$$r = \left(\frac{\varepsilon E_i}{\nu \rho V_d} \right)^{1/2} \quad (13)$$

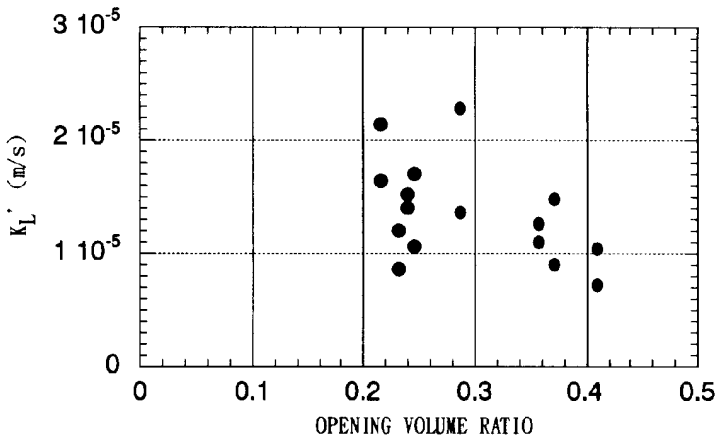


Figure 4: The local oxygen transfer coefficient

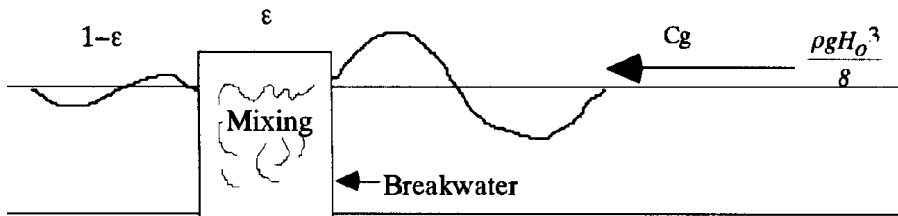


Figure 5: Description of reaeration due to dissipated wave energy

By substituting Eq. 13 for Eq. 12, the following equation is obtained:

$$K'_L = aD_M^{1/2} \left(\frac{\epsilon E_i}{\nu \rho V_d} \right)^{1/4} \tag{14}$$

where a is an experimental constant, $\epsilon, E_i, \nu, \rho, V_d$ are the energy dissipation ratio, the energy transported by incident waves, the kinematic viscosity, the water density, and the water volume at the site of *energy dissipation*. If V_d is assumed to be equal to the water volume of the slit, it is described by whole volume of the breakwater V which includes the slit as follows:

$$V_d = \alpha V \tag{15}$$

where α is the ratio of the volume of the slit to the whole breakwater volume. With the assumption that all the energy of offshore waves come to the

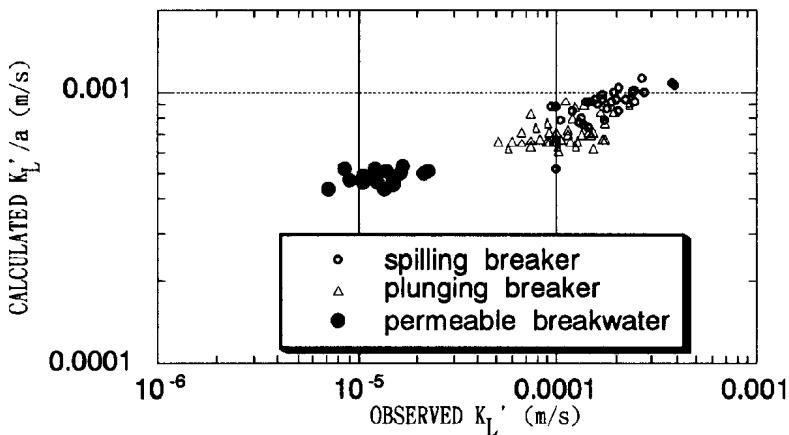


Figure 6: Comparison of observed and calculated K'_L

breakwater site, E_i is given by the energy and the group velocity of offshore waves as

$$E_i = \frac{1}{8} B \rho g H_0^2 \times \frac{1}{2} \left(\frac{gT}{2\pi} \right) = \frac{g^2 T B \rho H_0^2}{32\pi} \quad (16)$$

where H_0 , T , B and g are the offshore wave height, the wave period, the breakwater length measured perpendicular to the incident wave ray and gravitational acceleration, respectively. From Eqs. 14 and 15 we obtain

$$K'_L = a (D_M g H_0)^{1/2} \left(\frac{\varepsilon T}{32\pi \alpha S V} \right)^{1/4} \quad (17)$$

where $S = V/B$.

The comparison of calculated values yielded by Eq. 16 with observed ones is shown in

Figure 6. Also included are the results of experiments of reaeration by breaking waves on a uniformly sloping beach (Hosoi *et al.* [1984]). In the case of breaking waves on a beach, Eq. 16 was calculated by making $\varepsilon = 1$ and S the water volume from the breaking point to the shoreline. The oxygen transfer coefficient of breaking waves is greater than that at the permeable breakwater. However, the same theoretical equation can be used for prediction. By using regression analysis the following result is obtained:

$$K'_L = 0.0281 (D_M g H_0)^{1/2} \left(\frac{\varepsilon T}{32\pi \alpha S V} \right)^{1/4} \quad (18)$$

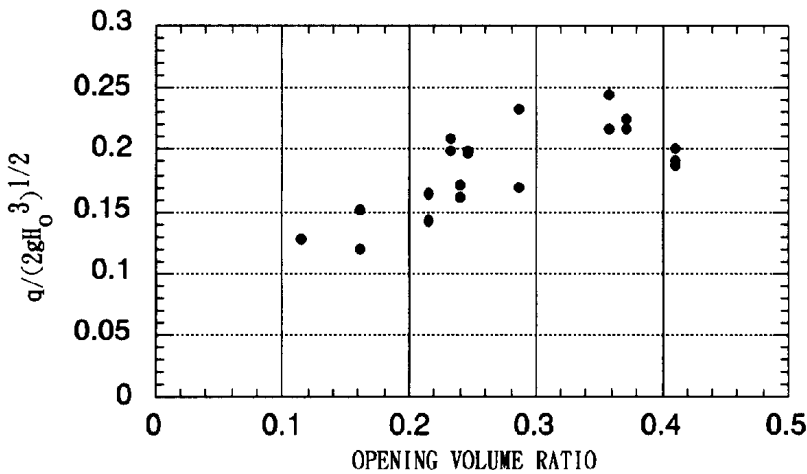


Figure 7: The exchange discharge

5.2 Exchange Flow through the Breakwater and Relationship with Reaeration

Figure 7 shows the water exchange discharge per unit of breakwater length in relation to the volume ratio of the slit. Regardless of the shape of the slit, the exchange discharge increases as the volume of the slit increases. By regression analysis the following equation is obtained:

$$\frac{q}{\sqrt{2gH_0^3}} = 0.634\alpha \quad (19)$$

The above equation is valid when the slit ratio is within the range of the performed experiments. When α approaches unity, q should be estimated by the small or finite amplitude wave theory.

From the viewpoint of the water exchange, the larger slit is preferable. But the larger slit induces wave transmission which is not favorable for breakwaters. As is seen in Figure 4, a large slit is disadvantageous for oxygen absorption.

Figure 8 is the relationship between K'_L and q/A . As K'_L increases, q/A decreases. The C. E. type has a larger function for water exchange. Since our experiments were carried out with only one water depth, the effect of the water depth could not be examined. For all breakwaters examined here, q/A is larger than K'_L . This means that reaeration is controlled by the oxygen absorption at the breakwater. Therefore, it is important to consider the shape of the slit which is more effective for oxygen absorption. Although Eq. 17 can be applied to estimate K'_L for wide range, it is not valid enough to describe in detail the effect of the shape of the slit of the permeable break-

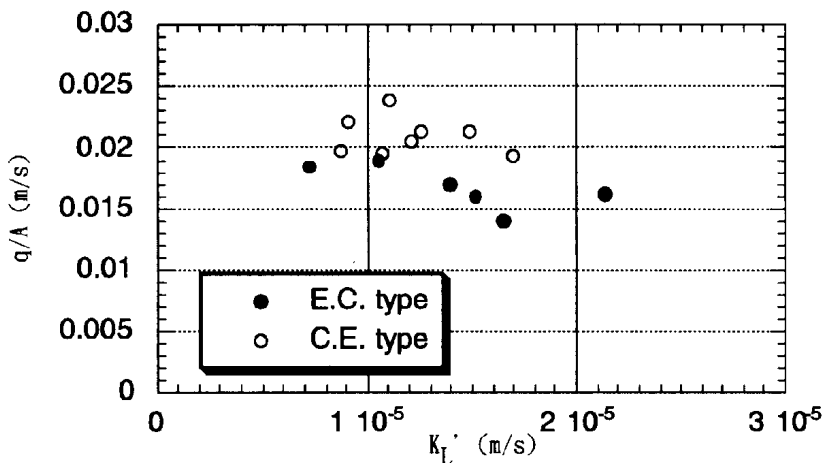


Figure 8: Comparison between K'_L and q/A

waters examined here. Here, for the time being, the following experimental equation is obtained from the results shown in Figure 4:

$$\frac{K'_L}{\sqrt{D_M/T}} = 0.106\alpha^{-0.646} \quad (20)$$

The comparison of oxygen absorption with water exchange is

$$\frac{K'_L A}{q} = \frac{0.167A}{\alpha^{1.646}} \sqrt{\frac{D_M}{2gH_0^3 T}} \quad (21)$$

where A is water surface area of the reaeration area per unit width. This equation indicates that water exchange discharge becomes relatively more effective as incident wave height becomes smaller. But as $0.167\sqrt{D_M/2g} = 1.7 \times 10^{-6}$ (meter-second unit), the oxygen absorption controls the entire process in general conditions.

6 Concluding Remarks

For reaeration at the permeable breakwater, both oxygen absorption and transport of aerated water are important. The two-step renewal model was presented to consider both effects. Both functions were evaluated by experiments, and some theoretical analysis was performed. As a result, it was demonstrated quantitatively that the oxygen absorption was more important than the longitudinal oxygen transport in the reaeration of permeable breakwaters.

References

- Hosoi, Y., Murakami, H. and Oto, V., Reaeration by spilling breaker, *Coastal Engineering in Japan*, Vol. 27, pp. 97-108, 1984
- Horie, T., Hosokawa, V., Miyoshi, E. and Sekine, Y., Hydraulic model experiments on reaeration capacity of seawall, *Technical note of the port and harbour research institute*, Ministry of Transportation, Japan, 1987 (in Japanese).

UConn's Sea Surface Physics Laboratory

Edward C. Monahan, Qin Wang, and Martin B. Wilson

Marine Sciences Institute, University of Connecticut at Avery Point,
1084 Shennecossett Road, Groton, CT 06340-6097, USA

The Sea Surface Physics Laboratory (SSPL) of the University of Connecticut, formally opened in October 1988, is dedicated to the investigation of *bubble-mediated air-sea exchange processes* in fresh- and sea-water. Among the major equipment items in this facility are two hooded *Whitecap Simulation Tanks* (WST's).

WST IV (3.0 m long \times 1.2 m wide), which is suitable for the study of *bubble plumes, whitecaps, air-sea gas transfer, aerosol generation* by the bursting of whitecap bubbles, and whitecap influence on *dry deposition*, is depicted in Figure 1 (from *Monahan and Van Patten*, 1989). An "exploded view" of this tank, along with its gantry, hood, and podium, is included as Figure 2 (from *Stramska et al.*, 1990). The gantry makes it possible to readily remove, service, and replace the hood and any associated measuring instruments. The hood serves to seal the head space above the tank proper, and the ports at each end of this hood, and the four small fans mounted on it, make it possible to readily flush the enclosed volume with virtually aerosol-free, or tracer-gas-free, air before an experiment begins, or alternatively, to continuously introduce "clean" air into the head space throughout the course of an experimental run.

WST IV can be equipped with a pair of opposing channels (see Figure 2 in *Stramska, et al.*, 1990) to generate bubble plumes by *wave-wave collisions* replicating the geometry in the Galway Whitecap Simulation Tank (II, *Monahan, et al.*, 1982), which itself represented an improvement on the original WST [I, *Monahan and Zietlow*, 1969]. This geometry, and the sequence of events as they transpired in WST II, are shown in Figure 3 [from *Cipriano, et al.*, 1987]. Alternatively, WST IV can be equipped with a *tipping bucket* mechanism, or a 48 air-stone bubbler mat of the IMST Marseille design (as can be seen in Figure 1), to produce transient, or steady-state, bubble clouds respectively.

An even broader range of techniques and mechanisms have been used to produce bubbles in the smaller (1.8 m \times 0.6 m) WST III. WST III was used in the "tipping bucket" laboratory gas evasion studies [*Monahan and Torgersen*, 1991] from which the first estimates of the gas transfer velocity to be associated with those portions of the sea surface covered by Stage-A whitecaps (spilling wave crests) were derived. Figure 4, taken from *Monahan and Torgersen* [1991], shows an end view of the prismatic trough ("tipping bucket") mounted above the water surface in WST III.

A large, oval (3.6 m \times 3.0 m) wooden tank (WST V), ideal for acoustic

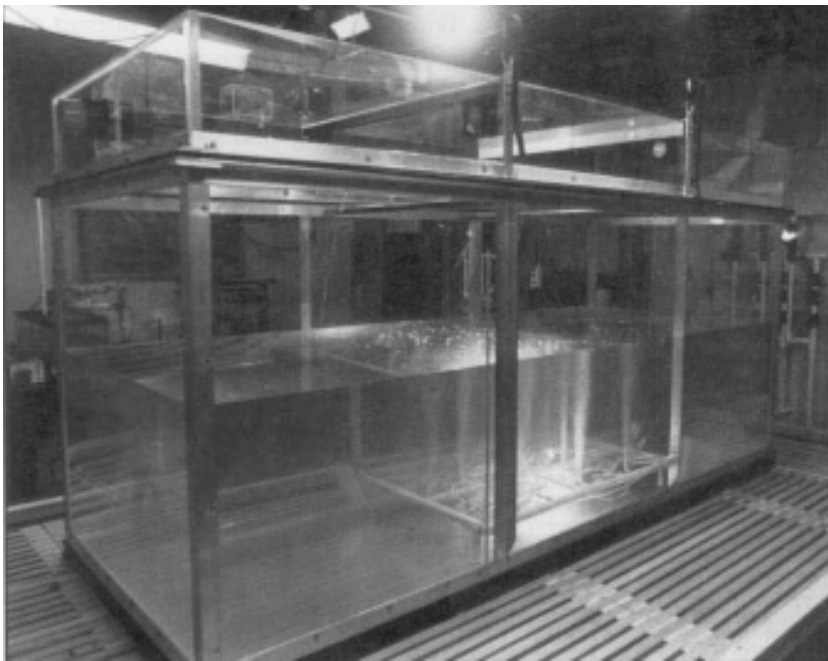


Figure 1: Whitecap Simulation Tank IV on its podium in the Laboratory for the Study of the Physics and Chemistry of the Sea Surface at the University of Connecticut Marine Sciences Institute. Visible near the bottom of the tank is an array of frits used to produce a continuous plume of bubbles as required in the series of Petit-CLUSE experiments, carried out to assess the contribution of bubble generated droplets to the sea-air moisture flux. Beneath the movable gantry, the hood that serves to enclose the space above the tank can be seen. The flexible duct which delivers filtered, virtually aerosol-free, air to the head space can also be seen in the far upper right of this photograph [from Monahan and Van Patten, 1989].

investigations of bubbles and bubble plumes is housed in the SSPL annex on the same campus.

Among the various special instruments developed for use in studying bubbles and bubble plumes in the several WST's is the bubble video microscope system. The latest version of this instrument is illustrated in Figure 5A. Two of these *bubble video microscope systems* are also incorporated in our "bubble stack", a device used to investigate the evolution, as a function of dissolved gas levels, water temperature, salinity, etc., of a bubble population as it rises two meters through a water column. The "closed" version of this system, which is used in the SSPL, is shown in Figure 5B. An "open" version of the "bubble stack" is used at sea to make in situ observations of the evolution of bubble spectra.

The informed reader will be able to get a sense of the capabilities of the

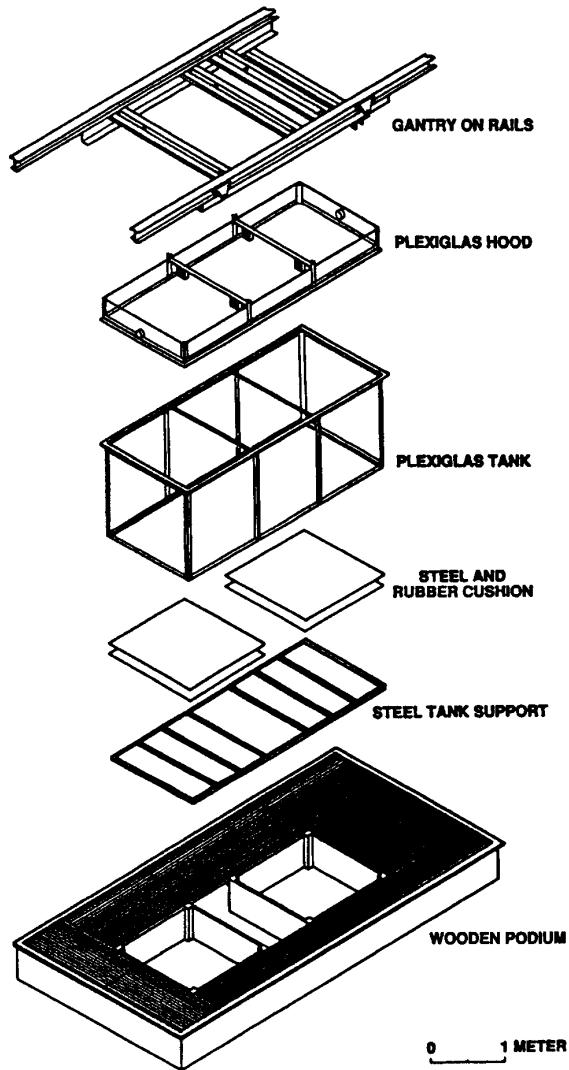


Figure 2: Exploded view of whitecap simulation tank IV, shown with its podium, hood, and gantry [from Stramska, Marks, and Monahan, 1990].

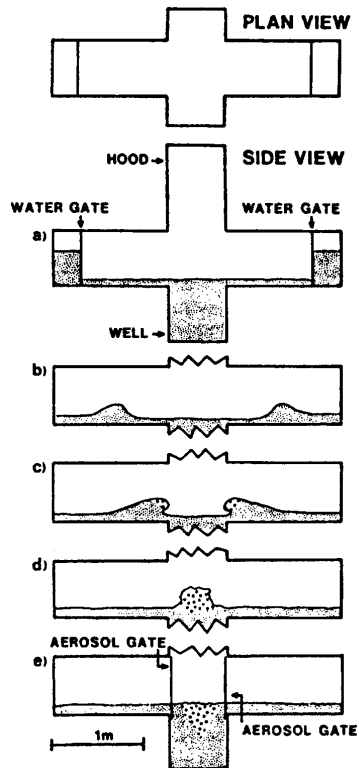


Figure 3: Scale drawing of the Galway whitecap simulation tank and sequence of events during an individual breaking wave event [from Cipriano, Monahan, Bowyer, and Woolf, 1987].

UConn SSPL from the foregoing catalogue of the major equipment items found in that facility. The SSPL research group welcomes further collaborations with other investigators of air-sea exchange phenomena.

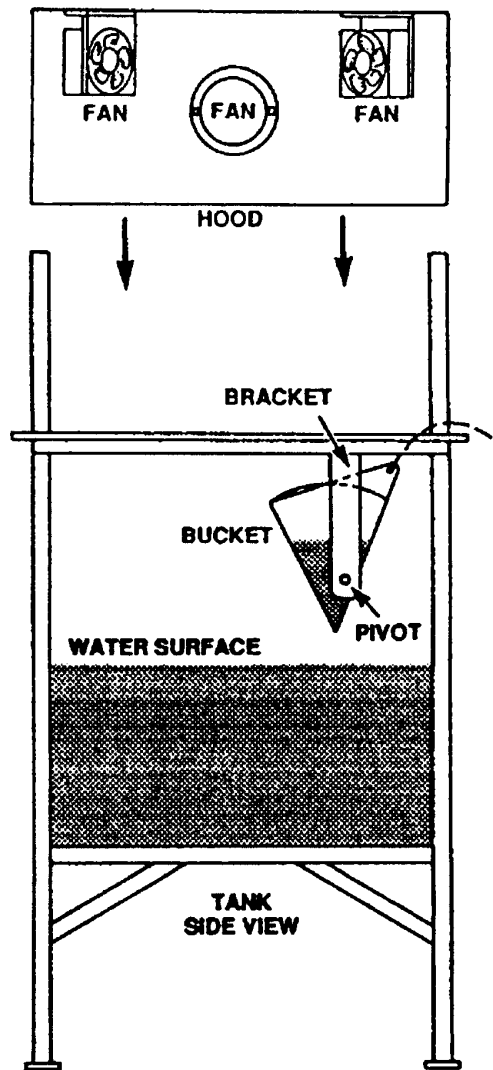


Figure 4: End of view of Whitecap Simulation Tank III (0.61 m wide \times 1.83 m long), with tipping bucket and covering hood. Note circular port in end of hood. Ports in both ends and fans facilitate flushing of enclosed space with trace-gas-less air [from Monahan and Torgersen, 1991].

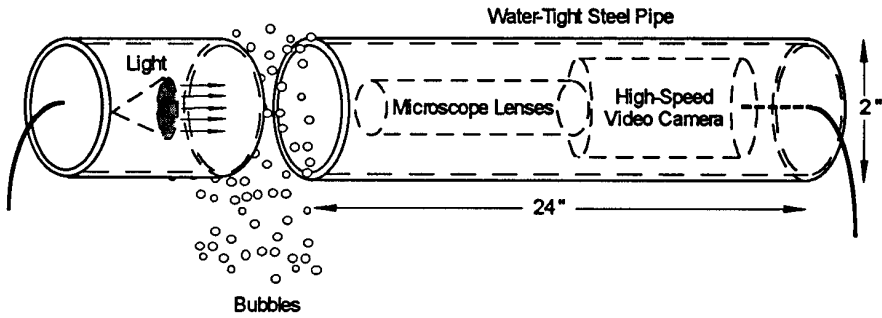
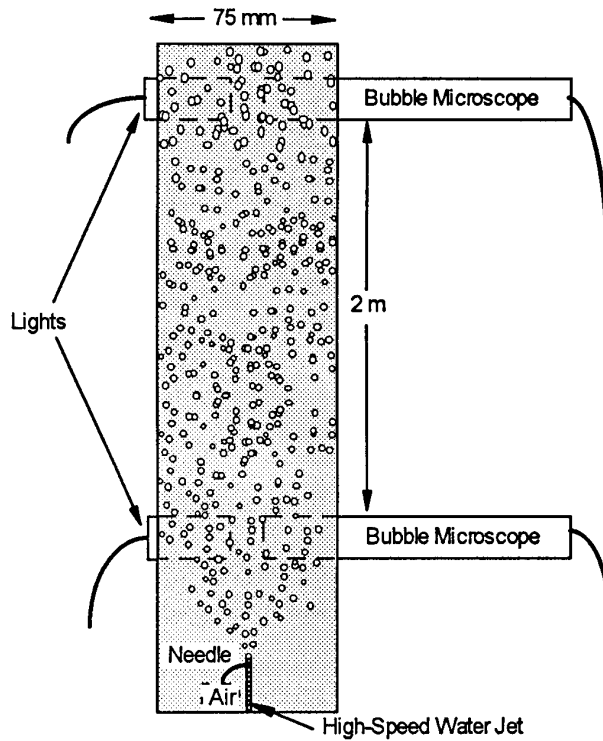
a*b*

Figure 5: *a* Bubble-video microscope system used to characterize bubble populations. *b* "Bubble Stack" for monitoring change in bubble spectrum as a result of two-meter rise through water of known dissolved gas content, salinity, temperature, etc.

References

- Cipriano, R. J., E. C. Monahan, P. A. Bowyer, and D. K. Woolf. Marine Condensation Nucleus Generation Inferred from Whitecap Simulation Tank Results, *Journal of Geophysical Research*, 92, 6569-6576, 1987
- Monahan, E. C., K. L. Davidson, and D. E. Spiel, Whitecap Aerosol Productivity Deduced from Simulation Tank Measurements, *Journal of Geophysical Research*, 87. 8898-8904, 1982
- Monahan, E. C., and T. Torgersen, The Enhancement of Air-Sea Gas Exchange By Oceanic Whitecapping, 608-617 in *Air-Water Mass Transfer*, Selected Papers from the Second International Symposium on Gas Transfer at Water Surfaces, S. C. Wilhelms and J. S. Gulliver, Eds., American Society of Civil Engineers, N.Y., N.Y., 1991
- Monahan, E. C., and M. A. Van Patten, Eds, Climate and Health Implications of Bubble-Mediated Sea-Air Exchange., Connecticut Sea Grant College Program, 1-170, 1989
- Monahan, E. C., and C. R. Zietlow, Laboratory Comparisons of Fresh-Water and Salt-Water Whitecaps, *Journal of Geophysical Research*, 74. 6961-6966, 1969
- Stramska, M., R. Marks, and E. C. Monahan, Bubble Mediated Aerosol Production as a Consequence of Wave Breaking in Supersaturated (Hyperoxic) Sea-Water, *Journal of Geophysical Research* 95, 18281-18288, 1990

Tilting Wind-Water Tunnel

Douglas B. Moog and Gerhard H. Jirka

DeFrees Hydraulics Lab., School of Civil & Environmental Engineering
Cornell University, Ithaca, NY 14853, USA

Abstract

The *Tilting Wind-Water Tunnel* (TWWT), located in the DeFrees Hydraulics Laboratory at Cornell University, is a flexible facility for the study of water and air flows - separate or combined, co-current or countercurrent - designed with a particular emphasis on air-water gas transfer research. Completed in 1990, it has been used for experiments on combined wind-water gas transfer and the effects of large scale roughness on stream reaeration. This presentation lays out its fundamental characteristics and special features.

1 History

The Tilting Wind-Water Tunnel (TWWT) was completed in 1990, designed in particular for air-water gas transfer experiments. It is a centerpiece of the DeFrees Hydraulics Laboratory, completed in 1984. Doctoral dissertations based upon TWWT research include:

- *Experiments on Gas Transfer and Turbulence Structure in Free Surface Flows with Combined Wind/Bottom Shear*, Chia-Ren Chu, Ph. D. Thesis, Cornell University, Ithaca, NY, 1993.
- *Stream Reaeration and the Effects of Large-Scale Roughness and Bed-forms*, Douglas B. Moog, Ph. D. Thesis, Cornell University, Ithaca, NY, 1995.

Other publications include:

- Chu, C. R. and G. H. Jirka, Reaeration in combined wind/stream driven flows, *This volume*
- Jirka, G. H. and C.-R. Chu, Surface gas transfer and turbulence structure in combined wind/bottom shear flow regimes, *Proc. Intl. Conf. on Hydrosience and Engineering*, Washington, D.C., June 7-11, 1993.
- Moog, D. B. and G. H. Jirka, Macro-roughness effects on stream reaeration, *This volume*

2 Dimensions

Size of test section	
Length	20 m
Width	1.000 m
Height	0.80 m
Water depth	0 to 0.30 m
Water volume	14.4 m ³ at full depth 7.0 m ³ at zero depth
Slope	-0.5% to 2.6% (-0.3° to 1.5°)
Overall size	
Length	27.1 m
Width	1.8 m
Height	4.3 m
Size of reservoir for preparation of test water	
Length	9.6 m
Width	1.8 m
Height	1.8 m
Volume	31 m ³

3 Materials

- Channel bed: stainless steel panels, removable.
- Channel sides: alternating plexiglass and optical glass (annealed plate) panels.
- Plexiglass permits taps for sampling and sensor access.
- Ceiling: two plywood layers, with adjustable bottom. Removable.
- Return piping: 30 cm and 41 cm PVC.
- Head box and tail box: stainless steel and plexiglass.

The lack of corrodible surfaces minimizes oxygen consumption.

4 Performance Characteristics

Water Flow

- Closed Recirculation Loop
- Pump: Variable speed, axial flow, 25 HP, Maximum discharge: 0.25 m³/s
- Maximum dimensionless parameters (approximate): Reynolds number: 2×10^6 (at 30 cm depth, 20 °C), 4×10^5 (at 10 cm depth) Shear (tur-

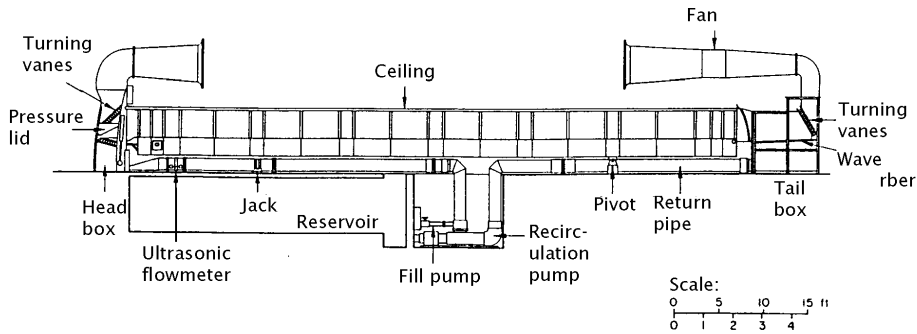


Figure 1: The tilting wind-water tunnel. Flow is from left to right. The ceiling may be removed.

bulent) Reynolds number: 2×10^5 (at 30 cm), 4200 (at 10 cm) Froude number: 2 (at 2.5 cm depth)

Air Flow

- Open Intake/Outlet Ducts
- Fan: Variable speed, reversible, 1 m diameter, 12 HP, Maximum flow: $11.8 \text{ m}^3/\text{s}$ Air flow may be co-current or countercurrent to water flow (if any). Shear velocities of 120 cm/s are sufficient for onset of capillary waves. Capable of generating strong wave action, breaking, and entrainment.

Special Features

A reservoir for preparation of test water contains a gas-bubbling system, for stripping oxygen or dissolving other gases.

A pressure lid in the head box lies above a series of turning vanes mounted on hinged, sliding parallelogram supports which move as the channel tilts, maintaining rectilinear water flow upon entrance to the channel. Air turning vanes are housed in both the head box and exit box. The ratio of head box and exit box surface areas is such as to maintain a constant water depth in the channel as it tilts.

A wave generator is provided by a motor-driven, vertically reciprocating wedge. A wave dissipator in the exit box may be adjusted to the water depth.

The TWWT features a low excess water volume outside the test channel. At 30 cm depth, the volume in the return system equals that in the test channel.

A false ceiling of adjustable plywood panels permits control of the pressure gradient for air flow. The panels are removable.

The tilt motor, pump and fan drives are computer controlled. The tilt may also be controlled by a hand-held remote.

Flow rates are provided by an ultrasonic, time-of-travel flowmeter (Nussonics 8400) mounted on the high-pressure side of the return pipe.

Delft Hydraulic's Large Wind-Wave Flume

*Paul van Vliet*¹, *Frank Hering*², and *Bernd Jähne*^{2,3}

¹Waterloopkundig Laboratorium, Delft Hydraulics Laboratory
Rotterdamseweg 185, NL-2692 HD Delft, Netherlands
Phone: (31) 015-569353

²Institute for Environmental Physics, University of Heidelberg
Im Neuenheimer Feld 366, D-69120 Heidelberg, Germany
email: fhering@davinci.uphys.uni-heidelberg.de

³Scripps Institution of Oceanography, Physical Oceanography Res. Div.
La Jolla, CA 92093-0230, USA
email: bjaehne@aeon.ucsd.edu

doi: 10.5281/zenodo.10402

1 Description of the Flume

Originally designed for the Dutch coastal research and protection program in the seventies, Delft Hydraulics large *wind wave flume* was totally overhauled to fit the needs of scientists working in the field of air/sea interactions. The facility consists of two main parts. A 90 m long, 10 m wide, and 2.7 m high corridor section. It contains a 8 m water channel and two side walks (Figure 1). The water height can be levelled between 0.3 and 0.8 m.

The corridor section ends in a 10 m long, 30 m wide and 5.5 m high wave basin giving the whole facility a T shape (Figure 2). The side basins can be parted from the main 8 m wide channel by removeable Plexiglass walls to keep the water channel 8 m wide up to the beach at 100 m fetch. The spending beach is adjustable (Figure 2) and provides 90% wave damping.

The water channel in the test section of the facility (75–100 m fetch) can quickly be emptied independently from the rest of the facility. This allows for a quick inspection or modification of submerged instrumentation. All places of the facility are easily accessible. The entire test section can be reached by a travelling crane. In this way even heavy equipment can easily be moved around in the facility (Figure 3). A complete set of standard measurement instruments such as wave height meters, flow meters, and pressure gauges are available.

Wind speeds between 0–15 m/s are generated by four large fans. The facility features a closed-circulation air system; the return flow is located beneath the water channel. One unique feature of this flume is the variable *fetch* limiter. The water surface can be covered from the wind entrance to any fetch with bubble foil. In this way, it is not required to replace any instrumentation in order to perform experiments at fetches between 0 and 90 m. A skimmer at the end of the flume is installed to clean the water surface from surface active materials.



Figure 1: A view from the sidewalk of the Delft wind/wave flume at about 90 m fetch in downwind direction while the facility is in operation at 12 m/s wind speed. The water channel is 8 m wide. (For color figure, see Plate 14.)

In addition the flume is also equipped with a hydraulic dual piston wave maker for the generation of mechanical waves. Waves are generated by a computer-controlled wave board of which the rotation and translation are adjustable. Wave frequencies between 0–3 Hz can be produced. The maximum wave height is 30 cm, the frequency ranges from 0 to 3 Hz. The maximum steepness of ≈ 0.1 can be reached for 0.5 Hz waves.

2 Projects and Funding

Specific investigations require special devices and equipment, and are normally brought along by the researchers. Apart from this, *Delft Hydraulics* can put a range of services and auxiliary devices at the visiting researchers' disposal. Various international projects have been successfully carried out at the large flume. This includes the Dutch/German VIERS-I program focusing on radar backscatter, an US/German project on gas exchange measurements at high wind speeds (B. Jähne and R. Wanninkhof), and two additional campaigns on air-water gas transfer that were founded by the EC within the European Large Installation Program. This EC research initiative provides access to large experimental facilities for European scientists. The large wind/wave flume is one of the experimental facilities at Delft Hydraulics that is recognized by the EC in the European Large Installation Program, which is currently in its third phase.



Figure 2: Close to the beach and air-flow return section, the 10 m wide corridor section of the Delft wind wave facility (see Figure 1) opens to a 30 m wide and 5.5 m high end section. Instruments can directly be built into the bottom of the facility, replacing $2 \times 2 \text{ m}^2$ large and 0.2 m high concrete plates. With a traveling bridge instruments can be mounted at the ceiling. (For color figure, see Plate 15.)



Figure 3: Heavy equipment can easily be moved around in the Delft wind/wave flume by a travelling crane. Here it is shown how the illumination unit of wave slope imaging is lowered to the bottom of the empty facility. (For color figure, see Plate 16.)



Figure 4: View of the instrumentation deck on the top of facility in the last part of the corridor section from 75–90 m fetch. Through several $1 \times 1 \text{ m}^2$ large openings, instruments can be mounted to make measurements from above. (For color figure, see Plate 17.)

Gas Transfer Flume Facility at CCIW

W. J. Cooper, M. A. Donelan, M. Alaei

National Water Research Institute, Canada Centre for Inland Waters
867 Lakeshore Road, P.O. Box 5050, Burlington, Ontario, Canada, L7R 4A6

The CCIW *Gas Transfer Flume* (GTF) is an airtight wind wave tunnel designed and constructed of aluminum to study wave and boundary layer mechanics influencing the mass transfer of specific chemicals including toxic contaminants. The wind tunnel of the GTF may be operated either open (ventilating mode) or closed (circulating mode). In the ventilating mode air is drawn from the surrounding laboratory and following one circuit through the flume is exhausted via charcoal filters and a roof vent to the atmosphere. In the circulating mode the tunnel is tightly closed and the air within circulates continuously, allowing experiments to be conducted with toxic chemicals which use may be strictly controlled. An interior vaneaxial fan generates air movement in the circulating mode, while both the interior and an exterior fan are combined in the ventilating mode. Both fans have external remote control capability permitting automated measurements at varying wind speeds. Water circulation independent of air speed is available in both directions. Paddle generated waves can be obtained in the flume utilizing an electro-hydraulic wave maker.

The GTF has three measuring stations located at different fetches: one at each end of the test section and one in the centre. At each station there are glass windows on both sides of the test section both in air and water. Each station is equipped with appropriate instrumentation for aerohydrodynamic and chemical measurements including air and water sampling ports. Profiling instruments and sensors are available at each station, featuring remote operation of the instruments utilizing computer controlled stepping motors. The chemicals of interest may be introduced into the GTF water in three ways: bubbled into the water as a gas, pumped directly into the water dissolved in a solvent or through the addition of spiked water from a separate tank. To date experiments have been done concerning the mass transfer of water vapour, carbon dioxide, monochlorobenzene, sulphur hexafluoride, halomethanes and naphthalene.

 Specifications of the CCIW Gas Transfer Flume Facility

Layout:	Three sampling stations are located at 5.3 m, 14.5 m, and 29.7 m from the upwind end of the test section.
Design Feature:	Flume may be operated either open to ambient air or sealed airtight.
Interior Fan:	25 H.P. vaneaxial
Exterior Fan:	25 H.P. vaneaxial
Water Pump:	15 H.P. inline
Dimensions:	32.2 metres long by 0.76 metres wide
Water Depth:	0.25 m (max.)
Total Water Volume:	10 m ³
Air Duct Height:	0.60 m
Total Air Volume:	66 m ³
Water Velocity:	0.60 m/sec (max.)
Air Speed:	22.5 m/sec (max.)

 Instrumentation

Air Measurements	Hot x-film anemometers, cold wire thermometers, pitot static tubes, thermistors, infrared gas analyzer (CO ₂ , and H ₂ O), humidity sensors. All or any of these may be profiled by remote computer control at the sample stations to different heights within the flume.
Air/Water Interface Measurements	Capacitance wave gauges, laser displacement gauge, laser slope gauge.
Water Measurements	Hot film sensors, thermistors.
Chemical Measurements	Gas chromatography, mass spectrometry, Fourier Transform infrared analyzer, fluorescence detector.
Water and air sample extraction points are provided at the three sampling stations.	Ambient flume air and water temperature and barometric pressure; remote fan operation for wind speed variation.
Miscellaneous	

References

- Merzi, N., M. R. Servos, and M. A. Donelan, Description of an air-tight gas transfer flume. National Water Research Institute, Technical Report 90-147, 1990

The circular wind/wave facilities at the University of Heidelberg

Dominik Schmundt^{1*}, *Thomas Münsterer*¹, *Hermann Lauer*²,
and *Bernd Jähne*^{1,2}

¹Institute for Environmental Physics, University of Heidelberg
Im Neuenheimer Feld 366, D-69120 Heidelberg, Germany
email: Thomas.Muensterer@iwr.uni-heidelberg.de

²Interdisciplinary Center for Scientific Computing, University of Heidelberg
Im Neuenheimer Feld 368, 69120 Heidelberg, Germany
email: Hermann.Lauer@iwr.uni-heidelberg.de
email: bjaehne@giotto.iwr.uni-heidelberg.de

doi: 10.5281/zenodo.10404

Abstract

At the University of Heidelberg circular wind/wave flumes are used to study small-scale air sea interaction processes under a wide range of conditions. The outer diameter of the large flume is 4 m and the channel width is 30 cm. Wind in the range of 0–12 m/s is generated by a rotating paddle wheel. The unique circular design yields to homogeneous quasi-infinite fetch conditions. Since the flume is gas tight and built from transparent PVC, it is suitable for experiments with various chemical species including acid gases and surface active materials. The flume accommodates a wide variety of techniques for noninvasive sensing of waves, water flow, air flow, and gas exchange. A brief summary of experiments performed within the last twenty years is given.

1 Introduction

In the early seventies, K. O. Münnich came up with the idea to build a small circular *wind/wave facility* for some basic studies in small-scale air sea interaction including isotope effects. Such a facility seemed to be more suitable for these such than conventional linear facilities:

- Homogeneous surface conditions in contrast to the *fetch*-dependent conditions in any linear facility. Homogeneous conditions are of special importance for studies of exchange processes since the transfer rates and other parameters based on mass balance methods can be measured only integrated over the whole facility.
- Compact, clean, and gas-tight facility. It is possible to work with corrosive gases, to use liquids other than fresh water, and to study the influence of surface active materials on air-water gas exchange and wind waves.

*Currently affiliated with Optoelectronics Research Centre, Southampton, GB



Figure 1: Detail view of the small circular facility at Heidelberg University. The cover with the wind paddle has been lifted to give view to the annular water channel with a cross section of $10 \times 10 \text{ cm}^2$. (For color figure, see Plate 18.)

- Independent control of wind speed and gas flush rate. In this way it is easy to control humidity and gas concentrations in the air space. In essence, the facility covers the conditions of closed-circulation and open-circulation linear facilities.
- It is still possible to study limited fetch conditions as in facilities by parting the annular water channel with a dam.

These significant advantages led to the construction of a small flume. Its annular water channel had a cross section of $10 \text{ cm} \times 10 \text{ cm}$ and outer diameter of 60 cm (Figures 1 and 2). The instrument was given the nickname “Windmühle” (wind mill) because of the paddle wheel used to generate the wind.

The circular design also has disadvantages. Unlike in linear channels surfactants do not get pushed towards the end of the flume by wind shear but stay on top of the water bulk. Therefore, it is much harder to remove surface active material; the water surface has to be thoroughly skimmed before each run. On the other side, it is much easier to experiment with surface active materials.

The most serious disadvantage is the influence of centrifugal forces which induce significant secondary currents. While these effects are quite significant in the bulk of the liquid and air, they tend to compensate each other at the interface in the viscous boundary layer. Therefore the study of air-water gas transfer and other processes close to the water surface is much less effected. The influence of secondary currents on the air-sea gas transfer rates could still be detected at low wind speeds in the small facility (up to 20%



Figure 2: The small circular wind-wave facility at Heidelberg University was contained in a thermostated box to run experiments between 4–35° C. The air space of the facility could be flushed with nitrogen at rates up to 60 l/min by evaporating liquid nitrogen from a tank with an electric heater (situated to the right of the thermostated box). (For color figure, see Plate 19.)

enhancement of the air-water gas transfer) [Jähne, 1980]. Therefore in 1977 work began to design and construct a larger circular facility. Unfortunately, the construction was delayed by a fire in the institute in 1981. The large circular facility was finally completed in 1985 and thoroughly renovated in 1994.

2 Experimental Conditions in the Large Flume

2.1 Wind Generation

The wind in the facility is generated by a paddle ring. This ring consists of a flexible 25 mm diameter PVC tube to which lightweight paddles are glued. The ring is held by 8 sets of 3 rubber-coated wheels each of which is directly driven by a 24 V, 25 W Faulhaber DC miniature motor. The maximum speed of the paddle ring is 12 m/s. The wind speed lags only slightly behind the paddle ring speed, 20% at high wind speeds and 33% at low wind speeds (Figure 5). The wind speed is monitored with a sensitive miniature propeller-type anemometer. The wind shear sets the water body into motion. It is (slowly) accelerated until the momentum input at the water surface is balanced by momentum loss to the channel walls and bottom.

The relation between the wind speed and *friction velocity* in the water, u_{*w} , measured at a clean, wavy water surface is shown in Figure 6.

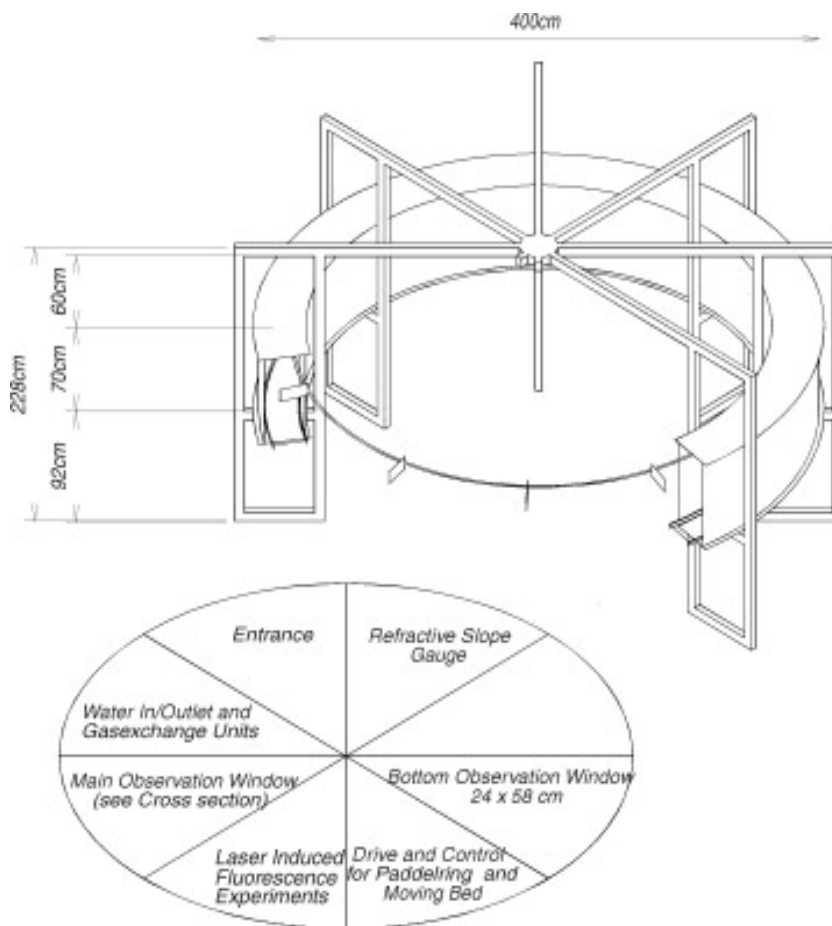


Figure 3: Schematic of the large circular wind/wave flume of the Institute for Environmental Physics at the University of Heidelberg. The outer diameter is 4 m, the channel width is 30 cm. The scheme in the lower part of the figure illustrates the position of the major instrumentation stations.

2.2 Air Circulation System

As already mentioned in *section 1*, the circular facility has the distinct advantage that the wind speed and air flush rate can be controlled independently. With a closed air circulation system, the channel is air tight for atmospheric pressure. In practice the leakages are low enough to achieve atmospheric residence times of more than an hour. In closed-circulation operation mode, experiments can be run with negligible heat exchange between air and water. The relative humidity is 100% and the air temperature quickly adjusts to the water temperature.

The air-space of the facility can be flushed with a rate of up to $1.5 \text{ m}^3/\text{min}$.

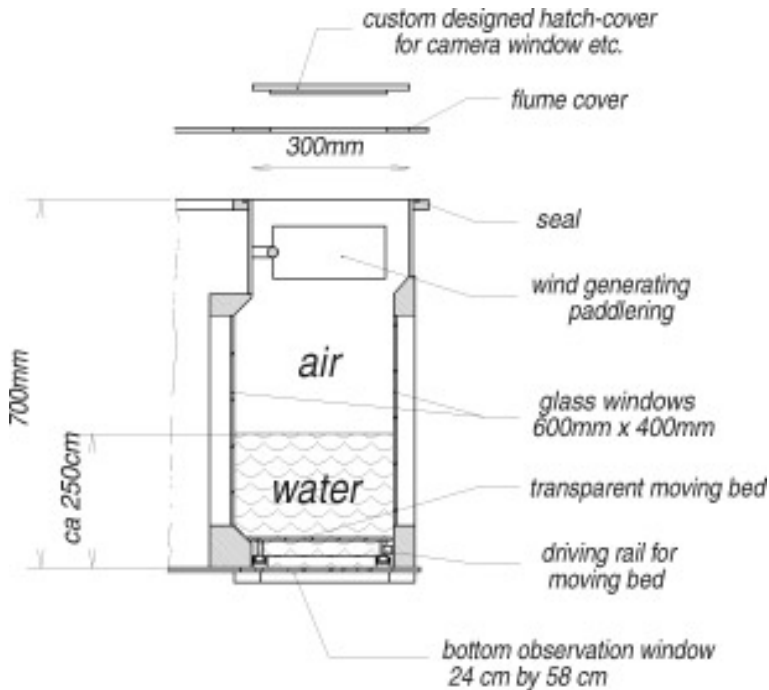


Figure 4: Cross-section of the flume at the position of the main observation windows. This section was specifically built for combined visualization studies of flow. It allows versatile imaging in the air and water from the inner and outer walls of the facility through (a) plane $0.6 \times 0.4 \text{ m}^2$ large optical quality windows, (b) a $0.24 \times 0.58 \text{ m}^2$ large bottom window, and (c) through exchangeable hatch-covers.

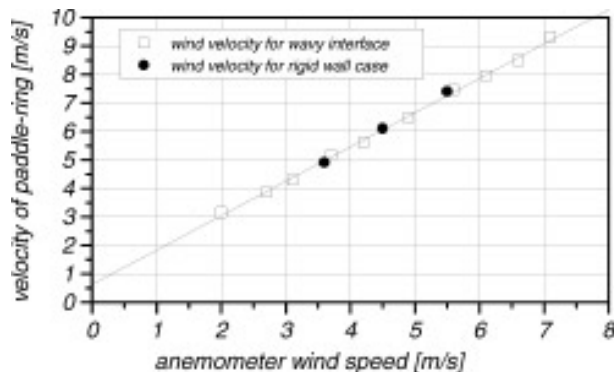


Figure 5: The wind velocity measured 23.5 cm above the mean water level with the standard water fill height of 0.25 m lags slightly behind the paddle ring speed.

Table 1: Dimensions of the large circular wind/wave flume at the Institute for Environmental Physics, Heidelberg University

Outer diameter of annular water channel	4 m \pm 0.002 m
Mean circumference	11.62 m
Cross section of the annular channel	0.30 m wide, 0.70 m high
Standard height of air space	0.45 m
Air volume	1.57 m ³
Maximum gas flushing rate	1.5 m ³ /min
Minimum residence time of atmosphere	1 min
Water surface area	3.49 m ²
Maximum water depth	0.30 m
Volume of the water body	0.349 m ³ at $h_w = 0.10$ m 0.872 m ³ at $h_w = 0.25$ m 1.046 m ³ at $h_w = 0.30$ m
Extra volume in the two circulation systems including the degasing/loading columns	0.080 m ³

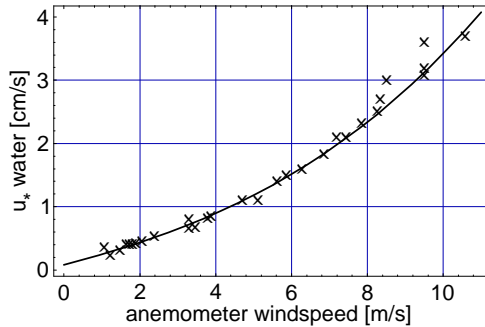


Figure 6: Friction velocity in water, u_{*w} , as measured with the momentum balance method as a function of the wind speed [Bösinger, 1986; Kandlbinder, 1994].

This leads to a minimum residence time of only a minute in the air space. In this way, gases can quickly be removed from the air space. The flush rate is also large enough to perform gas exchange experiments under evasion conditions, i. e., with negligible air concentrations even at high wind speeds. With the flushing-mode operation it is also possible to control and measure the evaporation rate. The total evaporative cooling can simply be computed from the humidities at the entrance and outlet of the air flush system and the flush rate.

2.3 Wind Wave Conditions

As the flume has an annular geometry, it features a quasi unlimited fetch. The principle advantage of this geometry has already been discussed in *section 1*. Wave growth is, of course, still limited by the shallow water depth (standard 0.25 m) and interference effects. Constructive interference occurs for wavelengths that are an integer fraction of the circumference and destructive interference otherwise. But with a circumference of only 12 m, wind waves still grow to significant larger wavelengths than in the largest linear wind/wave facility with 100 m fetch at Delft Hydraulics, the Netherlands [van Vliet et al., 1995].

The wave field in the circular facility appears much more random than in a linear facility. In this respect it is much more like the wave spectra in the ocean. A strong dominant peak in the gravity range is missing. The wave number spectra of waves in the capillary/gravity range look very similar to those in linear facilities at large fetches. A selection of 2-D wave number spectrum is shown in Figure 7.

Figure 8 shows the dependency between the *mean square slope* and the water-sided friction velocity u_* for clean water conditions as measured with two different optical techniques. Measurements of the two-dimensional wave slope distribution will become routine in all future experiments. The mean square slope can be measured with a temporal resolution of better than 5 min and is a very sensitive indicator for contamination by surface active material that tends to damp the short waves and thus the mean square slope in the course of an experiment.

2.4 Moving Bed

Tamburrino and Gulliver [1992] designed a *moving bed* facility in which the mean flow can be set to zero. This idea has been adapted for the annular channel by inserting a false bottom that can rotate with speeds of up to 0.6 m/s against or with the wind direction. Figure 9 shows a plot of the surface drift velocity vs. moving bed speed for no-wind conditions and a plot of the depth dependent induced drift.

2.5 Gas Loading and Degasing Facilities

The flume can be degased to 1/10 of the equilibrium concentration in approximately two hours (Figure 10) by means of a bubbleless hollow fiber membrane unit [Weiss and Gulliver, 1995]. With a second hollow fiber membrane unit, the water of the channel can be loaded with gases without losses in even shorter times. Dissolved oxygen concentration are measured with a temperature-compensated oxygen meter in a bypass of the water circulation system.

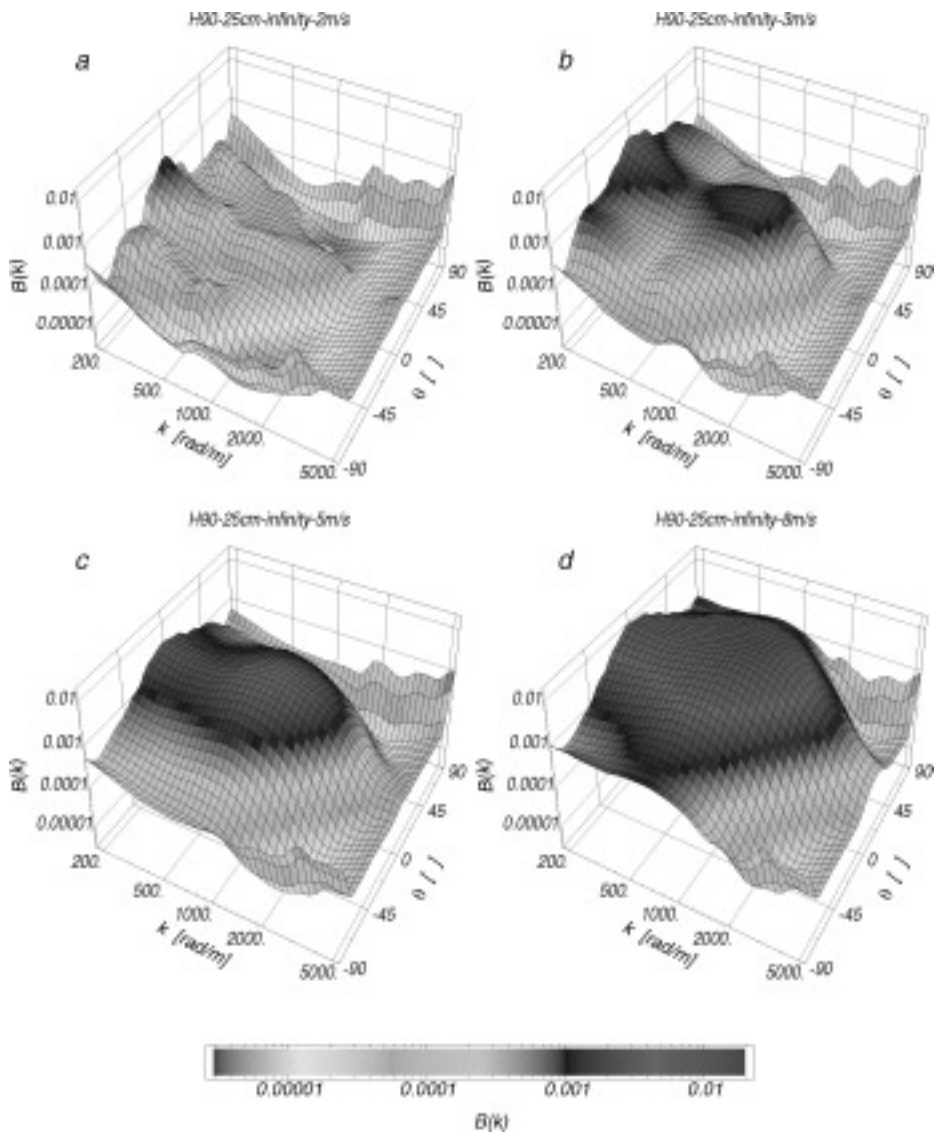


Figure 7: Selected 2-D wave number spectra from the Heidelberg facility at infinite fetch for wind speeds **a** 2.0 m/s, **b** 3.0 m/s, **c** 5.0 m/s, and **d** 8.0 m/s. (For color figure, see Plate 20.)

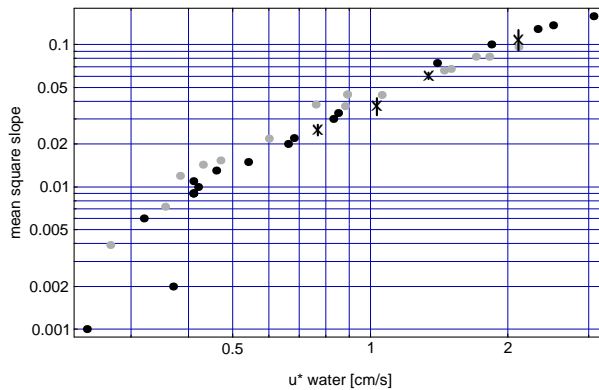


Figure 8: Mean square slope versus the friction velocity in water, u_{*water} , measured with a reflective slope gauge from slope distributions (crosses with error bars) and a laser slope gauge by integrating slope frequency spectra (black dots, large circular flume; grey dots: small circular facility).

2.6 Water Chemistry

Built entirely with non-corrosive and inert materials (PVC, stainless steel, and brass), the facility is ideally suited to perform delicate chemical experiments. It is filled with deionized water and the conductivity in the water can be maintained even for long experimental runs lower than $1\mu S$. Only because of these low residual water ionic water contaminations, the sensitive visualization techniques using low (in the 10^{-5} molar) pH indicator buffer solutions and acid gases reported by *Münsterer et al.* [1995] became feasible.

Experiments with *surfactants* are also possible. It requires, however, several water fill cycles because of slight surfactant bleeding from the plastic materials used in the flume, before sufficient clean water conditions can be achieved [*Frew et al.*, 1995].

Standard instrumentation of the facility includes high-precision conductivity measurements and a pH electrode suitable for low ionic strength solutions (i.e. deionized water) to monitor the pH-value.

3 Key Experiments

In this section, some key experiments that have been performed in the two circular facilities in last twenty years are briefly summarized:

3.1 Small Circular Facility

1975 Measurement of the *kinetic isotope separation* during evaporation [*Münnich and Flothmann*, 1977].

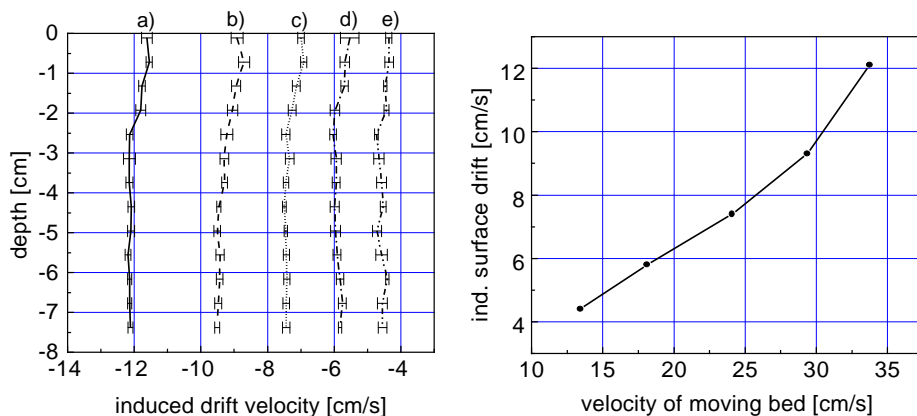


Figure 9: Left: Depth dependent drift velocity induced by different moving bed velocities: a) 33.8 cm/s, b) 29.4 cm/s, c) 24.1 cm/s, d) 18.1 cm/s and e) 13.5 cm/s. Right: induced surface drift vs. velocity of the moving bed [Hering, personal communication].

1979 Direct proof of the enhancement of the air-water gas transfer rate by wind waves. At the same friction velocity, data could be taken with and without waves [Jähne, Siegenthaler and Münnich, 1979].

1982 Development of an optical technique to measure the slope of capillary waves by refraction of a laser beam [Lange *et al.*, 1982].

1984 Measurements of the decrease of the *Schmidt number* dependency of the air-water gas transfer rate with a multi-tracer study including measurements of the transfer rates for heat, He, CH₄, Kr, Xe, and CO₂. With the transition from a smooth to a wavy surface the Schmidt number exponent decreases from 2/3 to 1/2 [Jähne *et al.*, 1984].

3.2 Large Circular Facility

1985 Development of a new optical technique to take images of the slope of wind waves and first attempt to visualize the penetration of a gas into the aqueous viscous boundary layer [Jähne, 1985, Jähne, 1986]

1989 Development of the "controlled flux" technique using heat as a proxy tracer for fast and local measurements of the gas transfer rate [Jähne *et al.*, 1989]

1990 Systematic study of two-dimensional wave number spectra of wind waves [Jähne and Riemer, 1990]

1991 Experimental studies of the turbulent flow beneath wind waves using particle tracking techniques [Wierzimok and Jähne, 1991]

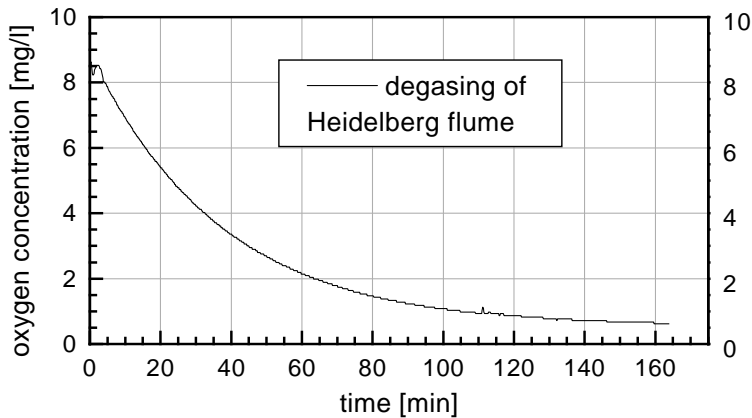


Figure 10: Degassing from equilibrium concentration to 10% of equilibrium concentration takes approximately 2 hours using a hollow fiber membrane unit.

1992 First measurements of high-resolution vertical profiles of the concentration of dissolved gases in the aqueous mass boundary layer using laser-induced fluorescence and a fluorescent indicator [Jähne, 1993; Münsterer and Jähne, 1993]

1994 Joint experiments with E. Bock, N. Frew, T. Hara and W. McGillis from WHOI on the influence of surfactants on gas exchange and wave fields. Combined experiments measuring gas exchange with SF₆, O₂ and the controlled flux technique and wave field measurements with the scanning laser slope gauge (WHOI), the RSG and the color imaging slope gauge.

Acknowledgments

The construction and instrumentation of the large wind/wave flume has been partly supported through grants from the German Science Foundation (DFG).

References

- Bösinger, R., Messungen zur Schmidtzahlabhängigkeit des Gasaustausches, Diploma Thesis, Institute for Environmental Physics, University of Heidelberg, 1986
- Frew, N. M., E. J. Bock, W. R. McGillis, A. V. Karachintsev, T. Hara, T. Münsterer and B. Jähne, Parameterization of Air-Water Gas Transfer using Wind Stress and Viscoelasticity, *this volume*
- Hering, F., personal communication.
- Jähne, B., K. O. Münnich, and U. Siegenthaler, Measurements of gas exchange and momentum transfer in a circular wind-water tunnel, *Tellus*, 31, 321-329, 1979

- Jähne, B., *Zur Parameterisierung des Gasaustausches mit Hilfe von Laborexperimenten*, Dissertation thesis, Fakultät für Physik und Astronomie, Univ. Heidelberg, 1980
- Jähne, B., W. Huber, A. Dutzi, T. Wais, and J. Ilmberger, Wind/wave-tunnel experiments on the Schmidt number and wave field dependence of air-water gas exchange, in *Gas transfer at water surfaces*, edited by W. Brutsaert and G. H. Jirka, pp. 303-309, D. Reidel, Hingham, Mass., 1984
- Jähne, B., *On the transfer processes at a free air-water interface*, Habilitation thesis, Faculty of Physics and Astronomy, Univ. Heidelberg, 1985
- Jähne, B., Bildfolgenanalyse in der Umweltphysik: Wasseroberflächenwellen und Gasaustausch zwischen Atmosphäre und Gewässern, in *Mustererkennung 1986*, Proceedings, 8th DAGM-Symposium, Paderborn, 30. Sep. - 2. Okt., 1986, Informatik-Fachberichte 125, pp. 201-205, Springer, Berlin, 1986
- Jähne, B., P. Libner, R. Fischer, T. Billen, and E. J. Plate, Investigating the transfer processes across the free aqueous viscous boundary layer by the controlled flux method, *Tellus*, 41B, 177-195, 1989
- Jähne, B., and K. Riemer, Two-dimensional wave number spectra of small scale water surface waves, *J. Geophys. Res.*, 95, 11,531-11,546, 1990
- Jähne, B., Imaging of gas transfer across gas/liquid interfaces, *Imaging in Transport Processes*, edited by S. Sideman and K. Hijikata, Begell House Publishers, New York, pp. 247-256, 1993
- Kandlbinder, T., Gasaustauschmessungen mit Sauerstoff, Diploma Thesis, Institute for Environmental Physics, University of Heidelberg, 1986
- Lange, P. A., B. Jähne, J. Tschiersch, and J. Ilmberger, Comparison between an amplitude-measuring wire and a slope-measuring laser wave gauge, *Rev. Sci. Instrum.*, 53, 651-655, 1982
- Lauer, H., Messung der Neigungsverteilung von Wasseroberflächenwellen mittels digitaler Bildverarbeitung, Diploma Thesis, Institute for Environmental Physics, University of Heidelberg, 1994
- Münnich, K. O., and D. Flothmann, Gas exchange and evaporation studies in a circular wind tunnel, continuous radon-222 measurements at sea and tritium/helium-3 measurements in a lake, NATO Symposium *Turbulent Fluxes through the Sea Surface, Wave Dynamics and Prediction*, Marseille, 12.-16. Sep. 1977, A. Favre and K. Hasselmann, eds., Plenum Press, New York, 1977
- Münsterer, T., and B. Jähne, A fluorescence technique to measure concentration profiles in the aqueous mass boundary layer, Proceedings, *Air-Sea Interface Symposium*, Marseille, 24.-30. June 1993, in press.
- Riemer, K., Scholz, T., und Jähne, B., Bildfolgenanalyse im Orts-Wellenzahl-Raum, *Mustererkennung 1991*, Proc. 13. DAGM-Symposium, 9.-11. Oktober 1991, ed. B. Radig, pp. 223-230, 1991
- Tamburrino, A., and J.S. Gulliver, Comparative flow characteristics of a moving bed flume, *Exp. in Fluids*, vol. 13, no. 5, 289-298, 1992
- Wierzimok, D., and B. Jähne, Measurement of wave-induced turbulent flow structures using digital image sequence analysis, *Air-Water Mass Transfer*, selected papers from the 2nd International Symposium on Gas Transfer at Water Surfaces, September 11-14, 1990, Minneapolis, Minnesota, S. C. Wilhelms and J. S. Gulliver, eds, pp. 200-209, ASCE, New York, 1991

The Effect of Breaking Waves on the Analysis of Dual-Tracer Gas Exchange Measurements

W. E. Asher¹ and R. Wanninkhof²

¹ Pacific Northwest Laboratory/Marine Sciences Laboratory
1529 W. Sequim Bay Road, Sequim WA 98382

² National Oceanic and Atmospheric Administration
Atlantic Oceanographic and Meteorological Laboratory, Miami FL 33149

Abstract

The dual-gaseous tracer technique is a new and reliable method for directly measuring air-sea gas transfer velocities. However, analysis of data from these experiments requires the assumption that the dependence of the transfer velocity on molecular diffusivity is constant. Modeling and laboratory studies indicate that this could be an invalid assumption when gas transfer through bubbles generated by breaking waves is a significant portion of the sea-to-air gas flux. Here, a parameterization of the transfer velocity in terms of wind speed and fractional area whitecap coverage is developed that includes the effects of bubble-mediated exchange processes. It is shown that transfer velocities estimated using this parameterization are consistent with available oceanic gas exchange measurements. The parameterization is then used to investigate the consequences of including whitecap-related transfer processes in the analysis of data derived from dual-tracer experiments. In the case of the tracer pair, sulfur hexafluoride and helium-3, it is shown that assuming a constant diffusivity dependence underestimates transfer velocities of helium-3 by up to 20% at high wind speeds. It is also shown that using the parameterization to normalize the transfer velocity for helium-3 to carbon dioxide results in a 6% decrease in the estimated transfer velocity compared to constant-diffusivity dependence estimates.

1 Introduction

Quantification of air-sea gas fluxes is important in understanding the global ocean carbon cycle and determining the atmospheric lifetimes of trace gases. In general, direct measurement of the flux, F (moles per area per time), of a sparingly soluble gas through the air-sea interface is extremely difficult. For this reason, F is often calculated as

$$F = k_L(K_h P_A - C_W) \quad (1)$$

where k_L (length per time) is the transfer velocity of the gas, K_h is the Henry's law solubility of the gas (moles per volume per pressure), P_A is the partial

pressure of the gas in the atmosphere, and C_B (moles per volume) is the concentration of the gas in the bulk liquid. In (1), $K_h P_A - C_B$ is called the air-sea concentration difference, ΔC (moles per volume), of the gas. In general, k_L is a function of the near-surface aqueous-phase turbulence and the molecular diffusivity of the gas. Although measurement of ΔC is relatively simple, oceanic determination of k_L is problematical, and k_L is estimated from wind speed at a 10-m reference height, U_{10} (length per time) using empirically derived relations.

The linear relation between F and k_L for constant ΔC implies that accurately parameterizing k_L in terms of U_{10} is critical in calculating F . This is especially true when U_{10} is large, since laboratory and field experiments suggest that k_L increases nonlinearly with U_{10} [Wanninkhof, 1992]. With the exact functional form of the relation between U_{10} and k_L being uncertain [Wanninkhof, 1992], estimation of k_L at high U_{10} could be inaccurate.

The functionality of k_L with respect to U_{10} could be resolved with further oceanic measurements of k_L at high U_{10} . Development of the purposeful *dual-gaseous tracer method* (DTM) [Watson *et al.*, 1991; Wanninkhof *et al.*, 1993] has provided a possible means for in situ measurement of k_L under these conditions. However, analysis of DTM data requires assuming that k_L is proportional to Sc^{-n} where Sc is the *Schmidt number* (i. e., the ratio of the kinematic viscosity of water to the molecular diffusivity of the gas) and n is expected to lie in the range of 1/2 for a clean water surface to 2/3 for a smooth surface or an interface that is severely contaminated by surfactants.

Although it is well known that $n = 1/2$ so that k_L is proportional to $Sc^{-1/2}$ for transfer through clean, unbroken wavy water surfaces, increases in U_{10} are also associated with increases in the frequency of wave breaking [Monahan, 1993]. The laboratory results of Asher *et al.* [1995a, 1995b] have shown that bubble-mediated transfer processes depend on both Sc and the aqueous-phase *solubility*, α (i. e., the dimensionless Ostwald solubility). In the absence of bubbles, the k_L values for different gases measured under the same conditions will scale as the ratio of their respective Sc raised to the power n . However, if the measured transfer velocities include contributions from transfer through *bubble-mediated processes*, the k_L values will not necessarily scale as Sc raised to the same power n that was observed in the absence of bubbles. Furthermore, the effect of bubbles on n will not be the same for all gases, but will be a function of Sc and α . This behavior with respect to Sc and α complicates analysis of DTM data collected at high U_{10} .

Here, a parameterization of k_L in terms of U_{10} and *fractional area whitecap coverage*, W_C , is developed using the bubble-mediated transfer data of Asher *et al.* [1995b]. By comparing k_L values calculated using this parameterization with oceanic k_L values measured by Watson *et al.* [1991] and Nightingale and Upstill-Goddard [1994], the model is shown to provide reasonable estimates of k_L over a range of wind and whitecap conditions. This whitecap-gas exchange model then can be used to include the effects of bubble-mediated transfer processes in the analysis of DTM data.

2 The Whitecap Gas Transfer Parameterization

Whitecaps can increase k_L by generating turbulence and bubble plumes. As the bubbles in the plume rise, they will generate additional turbulence, and the bubbles themselves can exchange gas with the surrounding water while they are beneath the surface. Asher *et al.* [1995a, 1995b] developed an empirical parameterization of k_L in the presence of bubble plumes by assuming that k_L could be partitioned into the fraction due to bubble-mediated transfer, k_B , and two terms resulting from turbulence-driven processes. For gas evasion, this relation can be written as

$$k_L = [A_M + W_C(A_T - A_M)]Sc^{-n} + W_C(a_1\alpha^{-1} + b_1\alpha^{-m_1}Sc^{-n_1}) \quad (2)$$

where A_M (length per time) and A_T (length per time) are constants defined by the turbulence generated by mechanical agitation (e. g., a circulation pump) and by the turbulence generated by whitecap processes, respectively. The term in (2) containing A_M and A_T represents the fraction of k_L due to turbulence-driven transfer processes. The mechanical-turbulence transfer velocity, k_M (length per time), is equal to A_MSc^{-n} and the whitecap turbulence transfer velocity, k_T (length per time), is equal to A_TSc^{-n} . The term in (2) that contains the constants a_1 , b_1 , m_1 , and n_1 , defines k_B , where both a_1 and b_1 have dimensions of length per time. For the remainder of this discussion, it will be assumed that $n = 1/2$ (i. e., the value at a clean surface) in further derivations of (2). However, it is acknowledged that n is a function of surface cleanliness and that n under oceanic conditions may be different from that found at a clean surface.

The constants A_T , a_1 , b_1 , m_1 , and n_1 in (2) have been determined empirically by Asher *et al.* [1995b] using data collected in a whitecap simulation tank (WST). Asher and Farley [1995] have shown that the bubble populations in the WST are similar to those in the ocean. Because the values for the bubble-transfer constants are determined by the bubble populations, the similarity between the WST and oceanic bubble populations suggests that the a_1 , b_1 , m_1 , and n_1 determined in the WST are good estimates of the oceanic values. Less is known about the relation of A_T determined in the WST to A_T for oceanic breaking waves. However, the data shown here suggest A_T from the WST is reasonable.

Direct application of the coefficients for bubble-mediated transfer, a_1 , b_1 , m_1 , and n_1 , from Asher *et al.* [1995b] to oceanic conditions includes the assumption that the four bubble-mediated parameters are constant with increases in turbulence generated by the whitecap and turbulence resulting from non-whitecap sources. This is valid because increases in whitecap-generated turbulence did not cause a_1 , b_1 , m_1 , and n_1 to vary. The surf pool data of Ogston *et al.* [1995] have shown that the dissipation rate of turbulence generated by a breaking wave is over an order of magnitude larger than the dissipation rate due to non-breaking wave turbulence. This implies

that it will be the turbulence generated by the breaking wave, and not the background turbulence, that will govern the dynamics of the bubble plume. Because a_1 , b_1 , m_1 , and n_1 are determined by the plume dynamics, turbulence due to processes unrelated to whitecapping will have little effect on a_1 , b_1 , m_1 , and n_1 for evasion under most conditions of interest.

The turbulence in the WST that was not related to the breaking wave processes was generated by mechanical mixing. This mixing was constant with increasing W_C , and therefore A_M was constant. However, in the ocean the near-surface aqueous-phase turbulence governing A_M is generated mainly by wind stress and non-breaking waves. Both wind stress and waves increase with increasing U_{10} , so under oceanic conditions, A_M will not be constant, but will increase with U_{10} . Therefore, the initial step in extending (2) to the ocean is to develop a relationship for estimating A_M from U_{10} . It is understood that near-surface turbulence can be produced in the ocean by mechanisms other than the wind stress. However, it is assumed here that in the absence of whitecapping, the majority of the turbulence responsible for gas exchange is generated through the wind stress.

There have been several relations proposed for calculating k_L in terms of U_{10} . Of these two deserve mention. *Wanninkhof* [1992] has proposed a relation where k_L is proportional to U_{10}^2 . In contrast, *Liss and Merlivat* [1986] have proposed a piece-wise linear form for k_L in terms of U_{10} . For the purposes of this study, the model of *Liss and Merlivat* [1986] is preferred because it partitions k_L into three different wind speed regimes based on wave state. In their model, for $U_{10} \leq 3.6 \text{ m s}^{-1}$ it is assumed there are no capillary waves and k_L is equal to (k_L in units of centimeters per hour)

$$k_L = 4.16U_{10}Sc^{-2/3} \quad (3)$$

where the exponent for Sc of $-2/3$ results from an assumption of transfer at a smooth surface. For $3.6 \text{ m s}^{-1} < U_{10} \leq 13 \text{ m s}^{-1}$, *Liss and Merlivat* assume capillary waves have formed on the water surface but that there is negligible wave breaking. In this case

$$k_L = (69.8U_{10} - 236)Sc^{-1/2} \quad (4)$$

with the same units as (3). The transition in the functional relation between k_L and U_{10} occurring at $U_{10} = 3.6 \text{ m s}^{-1}$ is caused by the generation of capillary waves [*Liss and Merlivat*, 1986]. The upper limit of $U_{10} = 13 \text{ m s}^{-1}$ for the applicability of (4) is associated with the onset of whitecapping. A third linear formula from *Liss and Merlivat* [1986] describes the relationship between k_L and U_{10} under conditions where whitecapping is a significant transfer pathway. However, the *Liss and Merlivat* relation for the breaking wave regime does not include the effect of bubbles on the dependence of k_L on Sc and α . Here, as shown below, the solubility effects caused by bubble-mediated transfer processes will be accounted for in the parameterization of k_L .

Comparing (4) with the form for $k_M (= A_M Sc^{-1/2})$ suggests that the relationship between A_M and U_{10} is linear. Assuming A_M can be modeled by (4) for $U_{10} > 3.6 \text{ m s}^{-1}$, A_M is equal to $69.8 U_{10} - 236$ for $U_{10} > 3.6 \text{ m s}^{-1}$ (with U_{10} given in meters per second and A_M in centimeters per hour). This relation for A_M can be substituted into (2) to give

$$k_L = ([69.8U_{10} - 236] + W_C[72000 - (69.8U_{10} - 236)])Sc^{-1/2} + W_C \left(\frac{-35.2}{\alpha} + 3023\alpha^{-0.42}Sc^{-0.13} \right) \quad (5)$$

for $U_{10} > 3.6 \text{ m s}^{-1}$ and k_L in centimeters per hour. In (5), the values for A_T , a_1 , b_1 , m_1 , and n_1 from Asher *et al.* [1995b] have been used. A formula similar to (5) can also be generated for $U_{10} \leq 3.6 \text{ m s}^{-1}$, but it has little practical application because there is insignificant whitecapping below $U_{10} = 3.6 \text{ m s}^{-1}$ [Monahan, 1993].

Monahan [1993] has shown that W_C can be estimated from U_{10} by

$$W_C = 1.25 \times 10^{-6} (U_{10} - 2.58)^3 \quad (6)$$

for W_C in fractional area coverage. This result can be substituted into (5) so that k_L can be estimated from U_{10} for any gas with known Sc and α . Figure 1 shows k_L for helium-3 (^3He), $k_L(^3\text{He})$, calculated using (5) and (6) for a seawater temperature, T_W , of 293 K plotted versus U_{10} . Figure 1 also shows the oceanic measurements of $k_L(^3\text{He})$ made using a DTM by Watson *et al.* [1991], Wanninkhof *et al.* [1993], and Nightingale and Upstill-Goddard [1994]. The experimentally determined $k_L(^3\text{He})$ have all been calculated and normalized to $T_W = 293 \text{ K}$ by assuming that k_L is proportional to $Sc^{-1/2}$. As discussed in detail in Section 3, using this assumption underestimates $k_L(^3\text{He})$ by 10% to 25% for U_{10} in the range of 10 m s^{-1} to 20 m s^{-1} .

Despite the lower $k_L(^3\text{He})$ caused by the $Sc^{-1/2}$ normalization, Figure 1 shows that there is good agreement between the $k_L(^3\text{He})$ estimated using (5) and the directly measured values. This shows that the parameterization developed here using the Liss and Merlivat [1986] model and the Asher *et al.* [1995b] data provides reasonable estimates of oceanic k_L values. In the following section, (5) will be used to examine the consequences of including bubble-mediated exchange processes in the analysis of DTM data.

3 Whitecaps and Dual-Gaseous Tracer Data Analysis

In a DTM experiment, sulfur hexafluoride (SF_6) and ^3He are injected into a parcel of water with a known initial aqueous-phase concentration ratio [e.g., Watson *et al.*, 1991; Wanninkhof *et al.*, 1993]. The concentration of each tracer will decrease by advection, dispersion, and the sea-to-air gas flux. Advection and dispersion of both gases will be equal when second-order

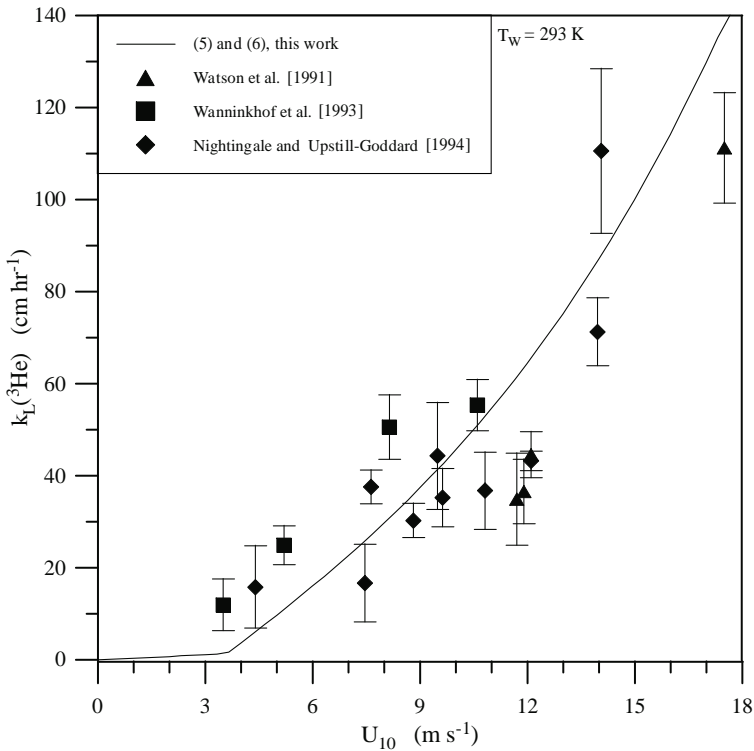


Figure 1: Dual-gaseous tracer measurements of the transfer velocity of helium-3, $k_L(^3\text{He})$, plotted versus wind speed measured at a height of 10 m, U_{10} , for the data of Watson et al. [1991], Wanninkhof et al. [1993], and Nightingale and Upstill-Goddard [1994]. Also shown are $k_L(^3\text{He})$ calculated using (5) and (6) at a seawater temperature, T_W , of 293 K. The $k_L(^3\text{He})$ have been normalized to $T_W = 293$ K assuming k_L is proportional to $Sc^{-1/2}$.

dispersion effects are negligible, and the time-evolution of their concentration ratio will be a function of the difference in their k_L values. Assuming the physical forcing functions for transfer are the same for SF_6 and ^3He , differences in their respective transfer velocities will be due to differences in their physico-chemical properties. When k_L is proportional to Sc^{-n} , $k_L(^3\text{He})$ can be calculated from

$$k_L(^3\text{He}) = (h/\Delta t) \ln(\Delta[^3\text{He}]/\Delta[\text{SF}_6]) \left[1 - (Sc(\text{SF}_6)/Sc(^3\text{He}))^{-n} \right]^{-1} \quad (7)$$

where h is water depth, $\Delta[\text{SF}_6]$ and $\Delta[^3\text{He}]$ are the concentration changes of SF_6 and ^3He , respectively, over the interval, Δt , and $Sc(\text{SF}_6)$ and $Sc(^3\text{He})$ are the Schmidt numbers of SF_6 and ^3He , respectively. In (7), the accuracy of $k_L(^3\text{He})$ depends on accurate knowledge of n .

Laboratory and field experiments have shown that n can range from $n = 1/2$ for transfer through an unbroken, clean water surface to $n = 2/3$ for transfer through a surfactant-influenced interface. The presence of white-caps may complicate DTM data analysis, because the laboratory data of Asher *et al.* [1995a, 1995b] show that there is not a simple power law relation between k_L and Sc when bubbles are present. However, it is possible to define an apparent Sc exponent, λ , for gas transfer in the presence of bubbles that is specific to a particular pair of gases under a particular set of physical conditions (i. e., T_W , bubble population, turbulence). In the case of SF_6 and 3He , λ is given by

$$\lambda = \frac{\ln[k_L(SF_6)/k_L(^3He)]}{\ln[Sc(^3He)/Sc(SF_6)]} \quad (8)$$

where the two transfer velocities must either be measured directly or are independently known. The two major differences between n and λ are that the latter is a function of the physical conditions under which $k_L(SF_6)$ and $k_L(^3He)$ are determined and that λ is not constrained to the range $1/2$ to $2/3$. Furthermore, λ as calculated using (8) is specific to the transfer of 3He and SF_6 under one particular set of conditions. For example, λ for SF_6 and 3He cannot be used to normalize $k_L(^3He)$ to give k_L for carbon dioxide, $k_L(CO_2)$, under equivalent conditions. Similarly, λ calculated for SF_6 and 3He at one T_W cannot be used to analyze DTM data for SF_6 and 3He collected at a different T_W .

Despite the fundamental differences between n and λ , λ could be used in place of n in (7) if it were known and constant over the interval Δt for the conditions associated with the dual-gaseous tracer experiment. The difficulty in using λ is that it must be determined from (8) using the measured transfer velocities, but calculation of $k_L(SF_6)$ and $k_L(^3He)$ using (7) requires that λ be known. This problem could be overcome if the transfer velocities used in (8) could be estimated independently for the conditions present during the DTM measurement.

Figure 1 shows that (5) provides reasonable estimates of oceanic k_L values. Because (5) was developed to include the effects of both turbulence- and bubble-mediated transfer processes, using k_L values calculated at a given U_{10} using (5) and (6) in (8) could give an estimate of λ at that U_{10} for oceanic conditions. Figure 2 shows λ calculated for SF_6 and 3He using (8) and transfer velocities calculated with (6) plotted as a function of U_{10} at $T_W = 278$ K and $T_W = 293$ K. Values for Sc and α were estimated from T_W and salinity (= 35 ‰) using the relations from Wanninkhof [1992]. The results demonstrate that λ is a function of U_{10} and T_W . For example, λ for 3He and SF_6 decreases from 0.50 at $U_{10} = 2.4$ m s⁻¹ to 0.46 at $U_{10} = 20$ m s⁻¹ at $T_W = 293$ K. At $T_W = 278$ K however, λ for 3He and SF_6 decreased from 0.50 to 0.40 over the same range in U_{10} .

Figure 2 also shows λ calculated for CO_2 and 3He for $T_W = 278$ K and $T_W = 293$ K. In contrast to λ for SF_6 and 3He , λ for CO_2 and 3He increases

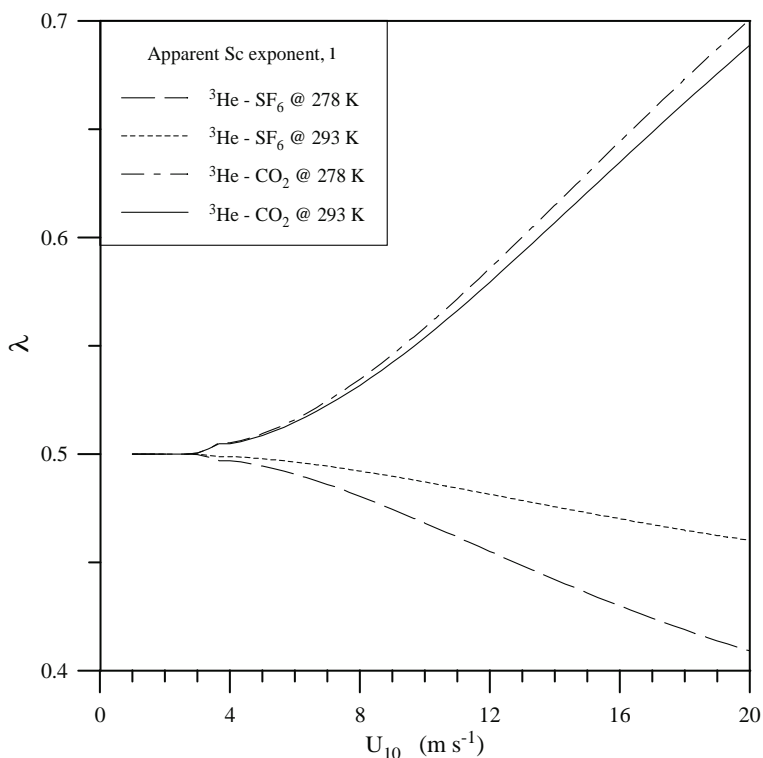


Figure 2: The apparent Sc exponent, λ , plotted versus wind speed measured at a height of 10 m, U_{10} for the gas pair helium-3, ${}^3\text{He}$, and sulfur hexafluoride, SF_6 , and the gas pair ${}^3\text{He}$ and carbon dioxide, CO_2 , at seawater temperatures, T_W , of 278 K and 293 K. All λ values have been calculated using (5), (6), and (8).

with increasing U_{10} . Additionally, the dependence of λ on T_W is weaker. Although the data are not shown in Figure 2, λ can also be calculated at $T_W = 278$ K and $T_W = 293$ K for CO_2 and SF_6 . In this case, bubble-mediated transfer decreases λ from 0.5 to -0.4 at $T_W = 293$ K and -0.7 at $T_W = 278$ K. The negative value of λ implies that $k_L(\text{SF}_6)$ is larger than $k_L(\text{CO}_2)$ even though $Sc(\text{SF}_6)$ is larger than $Sc(\text{CO}_2)$. This effect has been observed experimentally by Asher *et al.* [1995a, 1995b].

In order to account for the effect of whitecaps on the transfer process in analyzing DTM data, λ can be calculated for SF_6 and ${}^3\text{He}$ using the field measurements of U_{10} and T_W . Then, λ can be used in place of n in (7) to calculate $k_L({}^3\text{He})$. The DTM data of Watson *et al.* [1991] and Wanninkhof *et al.* [1993] can be reanalyzed using this method to show how large a difference is caused by using λ . Table 1 shows data interval, U_{10} , T_W , $k_L({}^3\text{He})$ calculated assuming $n = 1/2$, λ , and $k_L({}^3\text{He})$ calculated using λ for the data of Wanninkhof *et al.* [1993] and for the data of Watson *et al.* [1991]. Nightin-

Table 1: DTM Data from Wanninkhof et al. [1993] and Watson et al. [1991].

Source/Interval Start	U_{10} m s ⁻¹	T_W K	$k_{-L}({}^3\text{He})^*$ cm hr ⁻¹	λ ³ He/SF ₆	$k_L({}^3\text{He})^\dagger$ cm hr ⁻¹	λ^\ddagger CO ₂ / ³ He
Wanninkhof/April 8	8.1	278.5	36.2	0.478	37.1	0.567
Wanninkhof/April 10	10.6	278.5	39.7	0.461	41.5	0.625
Wanninkhof/April 12	5.2	278.5	17.8	0.493	18.0	0.520
Wanninkhof/April 14	3.5	278.5	8.53	0.497	8.56	0.514
Watson/March 20	12.1	280.5	33.9	0.458	39.6	0.645
Watson/March 22	17.5	280.5	84.7	0.428	103.	0.776
Watson/October 13	11.7	288.5	31.8	0.474	35.9	0.590
Watson/October 14	11.9	288.5	33.3	0.474	37.7	0.593

*Calculated assuming $n = 1/2$ in (7).

†Calculated using λ for ³He and SF₆ in (7).

‡Calculated for ³He at T_W and CO₂ at 293 K.

gale and Upstill-Goddard [1994] do not list T_W or the primary DTM data, so it is not possible to reanalyze their results here.

Comparison of the $k_L({}^3\text{He})$ values calculated using $n = 1/2$ with the corresponding $k_L({}^3\text{He})$ calculated using λ for ³He and SF₆ from Table 1 shows that including the effects of whitecap-generated bubbles increases $k_L({}^3\text{He})$. Because W_C and the bubble-mediated gas flux increase with increasing U_{10} , the difference in $k_L({}^3\text{He})$ between the two methods also increases with U_{10} . The largest increase in $k_L({}^3\text{He})$ occurs for the March 22 data point from the *Watson et al.* [1991] data set. In this case, for $U_{10} = 17.5$ m s⁻¹ there is a 22% increase in $k_L({}^3\text{He})$ calculated using λ for ³He and SF₆ compared with $k_L({}^3\text{He})$ calculated using $n = 1/2$. The data from *Wanninkhof et al.* [1993] show that there is little difference between $k_L({}^3\text{He})$ calculated using the two methods for $U_{10} < 10$ m s⁻¹.

The $k_L({}^3\text{He})$ listed in Table 1 have not been normalized to $Sc = 666$ (i. e., Sc for CO₂ in seawater at 293 K) using either λ for ³He and SF₆ or $n = 1/2$. While such a normalization could in principle be performed, the result would not be meaningful in terms of providing an estimate of $k_L(\text{CO}_2)$. Using the procedure proposed here, estimation of $k_L(\text{CO}_2)$ at 293 K would require normalization of $k_L({}^3\text{He})$ using λ calculated for CO₂ in seawater at $T_W = 293$ K and ³He at the measurement T_W . These are the λ values for CO₂ and ³He listed in the last column of Table 1. Figure 3 is $k_L({}^3\text{He})$ from the *Watson et al.* [1991] and *Wanninkhof et al.* [1993] data sets normalized to $k_L(\text{CO}_2)$ at $T_W = 293$ K plotted versus U_{10} . The open symbols in Figure 3 are $k_L(\text{CO}_2)$ determined assuming $n = 1/2$ throughout the calculation. The solid symbols are $k_L({}^3\text{He})$ calculated using the variable- λ approach and normalized to $k_L(\text{CO}_2)$ using λ for CO₂ and ³He from Table 1. The difference between $k_L(\text{CO}_2)$ calculated using the two procedures is not a constant function of wind speed due to differences in T_W and W_C between the *Watson et al.* [1991]

and *Wanninkhof et al.* [1993] data sets. Transfer velocities derived from the bomb- ^{14}C studies of *Broecker et al.* [1985] and *Cember* [1989] along with $k_L(\text{CO}_2)$ at $T_W = 293$ K calculated from (5) and (6) have been plotted for reference in Figure 3.

Using λ for ^3He and CO_2 to normalize $k_L(^3\text{He})$ to $k_L(\text{CO}_2)$ causes the estimated transfer velocity for CO_2 to be lower than that calculated assuming $n = 1/2$. The decrease in $k_L(\text{CO}_2)$ is a result of the decrease in effectiveness of bubbles in the transfer of a soluble gas. When normalized to CO_2 at $T_W = 293$ K, the *Watson et al.* [1991] data agree fairly well with $k_L(\text{CO}_2)$ predicted using (5). Although the *Wanninkhof et al.* [1993] data are in good agreement with $k_L(\text{CO}_2)$ derived from bomb- ^{14}C studies, the *Wanninkhof et al.* [1993] results are somewhat higher at a given U_{10} than both the *Watson et al.* [1991] data and the model predicted k_L values. This difference between the *Watson et al.* [1991] and *Wanninkhof et al.* [1993] data sets was also observed for $k_L(\text{CO}_2)$ calculated using the iterative approach described in *Wanninkhof et al.* [1993]. The reasons for this are not clear, although it should be noted the difference is not caused by the method of processing the DTM data. Both data sets in Figure 3 have been analyzed in an identical manner.

Figure 3 also shows $k_L(\text{CO}_2)$ estimated from the relation of *Liss and Merlivat* [1986] in (3) and (4). The whitecap parameterization in (5) results in a lower estimate of $k_L(\text{CO}_2)$ at high wind speed although the two are in reasonable agreement for intermediate U_{10} . This suggests that at intermediate wind speeds, bubbles have little effect on the net evasive flux of CO_2 . The decreased importance of bubbles in the air-sea exchange of CO_2 is expected because laboratory measurements have shown that the bubble-mediated transfer velocity decreases as α increases [*Asher et al.*, 1995a]. Therefore, including the effects of bubbles in the analysis of DTM data will have a larger effect on an insoluble gas like ^3He than a soluble gas like CO_2 .

4 Conclusions

Figure 1 shows that oceanic measurements of k_L agree reasonably well with the k_L values predicted using the parameterization developed in Section 2. This demonstrates that (5) can be used to estimate the effects of bubble-mediated gas transfer on the physico-chemical dependence of k_L . Using λ defined in (8), it has been shown that including the effects of whitecaps causes $k_L(^3\text{He})$ calculated from DTM data to be higher than $k_L(^3\text{He})$ calculated assuming $n = 1/2$ by 10% to 25%, depending on U_{10} . Unfortunately, this increase is of the same order of magnitude as the standard deviation associated with the DTM measurement for all but the highest wind speeds (see Figure 1). Figure 3 shows that bubble-mediated transfer processes cause $k_L(\text{CO}_2)$ estimated using λ for CO_2 and ^3He to be lower than $k_L(\text{CO}_2)$ calculated assuming $n = 1/2$.

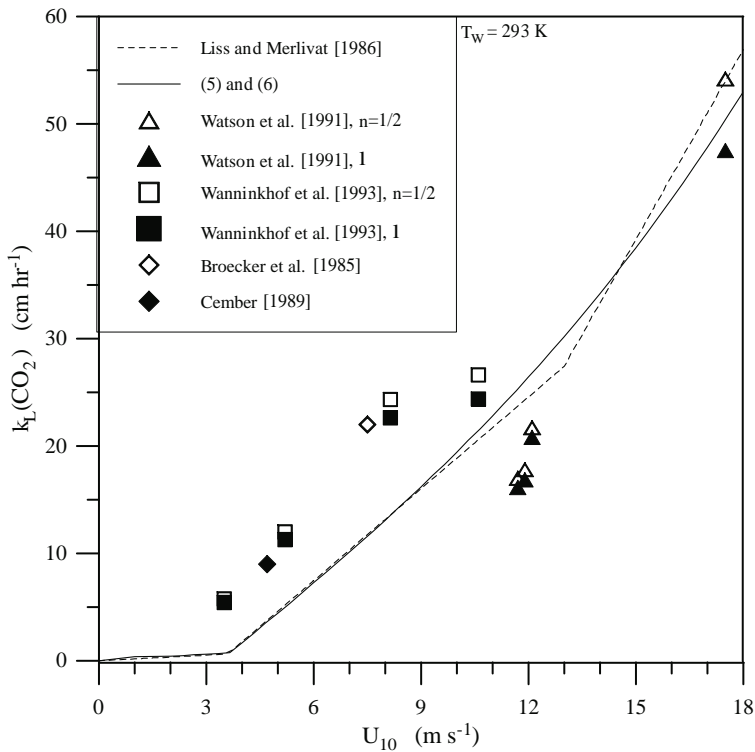


Figure 3: The transfer velocity of carbon dioxide, $k_L(\text{CO}_2)$, at a seawater temperature, T_W , of 293 K plotted versus wind speed measured at a height of 10 m, U_{10} . DTM derived estimates of the transfer velocity of helium-3, $k_L(^3\text{He})$, from Watson et al. [1991] and Wanninkhof et al. [1993] have been normalized to $k_L(\text{CO}_2)$ assuming $n = 1/2$ and using the apparent Sc exponent, λ , from Table 1. The bomb- ^{14}C $k_L(\text{CO}_2)$ values are taken from Broecker et al. [1985] and Cember [1989]. Also shown is $k_L(\text{CO}_2)$ calculated using (5) and (6) and $k_L(\text{CO}_2)$ calculated from the parameterization of Liss and Merlivat [1986].

Acknowledgements

W. E. Asher was supported by the U.S. Department of Energy (DOE), Office of Health and Environmental Research, Environmental Sciences Division under Contract DE-AC06-76RLO 1830. Pacific Northwest Laboratory is operated for DOE by Battelle Memorial Institute. R. Wanninkhof was supported by the Climate and Global Change Program of the National Oceanic and Atmospheric Administration.

References

- Asher, W. E., and P. J. Farley, Phased-Doppler anemometer measurement of bubble concentrations in laboratory-simulated breaking waves, *J. Geophys. Res.*, 100C, 7045-7056, 1995
- Asher, W. E., L. M. Karle, B. J. Higgins, P. J. Farley, I. S. Leifer, and E. C. Monahan, The influence of bubble plumes on air/seawater gas transfer velocities, submitted to *J. Geophys. Res.*, 1995a
- Asher, W. E., L. M. Karle, B. J. Higgins, P. J. Farley, I. S. Leifer, and E. C. Monahan, The effect of bubble plume size on the parameterization of air/seawater gas transfer velocities, *This volume*, 1995b
- Broecker, W. S., T.-H. Peng, G. Ostlund, and M. Stuiver, The distribution of bomb radiocarbon in the ocean, *J. Geophys. Res.*, 90C, 6953-6970, 1985
- Cember, R., Bomb radiocarbon in the Red Sea, a medium scale gas exchange experiment, *J. Geophys. Res.*, 94C, 2111-2123, 1989.
- Liss, P., and L. Merlivat, Air-sea gas exchange rates: introduction and synthesis, in *The Role of Air-Sea Exchange in Geochemical Cycling*, edited by P. Buat-Menard, pp. 113-127, D. Reidel, Hingham, Mass., 1986
- Monahan, E. C., Occurrence and evolution of acoustically relevant subsurface bubble plumes and their associated, remotely monitorable, surface whitecaps, in *Natural Physical Sources of Underwater Sound*, edited by B. R. Kerman, pp. 503-517, Kluwer, Dordrecht, The Netherlands, 1993
- Nightingale, P., and R. C. Upstill-Goddard, Measurement of air-sea gas exchange using the dual-tracer technique, in *Report of the ASGASEX-94 Workshop*, edited by W. A. Oost, pp. 52-53, KNMI Tech. Rep. TR-174, De Bilt, The Netherlands, 1994
- Ogston, A. S., C. R. Sherwood, and W. E. Asher, Estimation of turbulence dissipation rates and gas transfer velocities in a surf pool: Analysis of the results from WABEX-93, *This volume*
- Wanninkhof, R., Relationship between wind speed and gas exchange over the ocean, *J. Geophys. Res.*, 97C, 7373-7382, 1992
- Wanninkhof, R., W. E. Asher, R. Weppernig, H. Chen, P. Schlosser, C. Langdon, and R. Sambrotto, [] Gas transfer experiment on Georges Bank using two volatile deliberate tracers, *J. Geophys. Res.*, 98C, 20237-20248, 1993
- Watson, A. J., R. C. Upstill-Goddard, and P. S. Liss, Air-sea gas exchange in rough and stormy seas measured by a dual-tracer technique, *Nature*, 349, 145-147, 1991

Variation of Air-Water Gas Transfer with Wind Stress and Surface Viscoelasticity

Nelson M. Frew¹, Erik J. Bock¹, Wade R. McGillis¹,
Andrey V. Karachintsev¹, Tetsu Hara², Thomas Münsterer³,
and Bernd Jähne³

¹ Woods Hole Oceanographic Institution (WHOI)

² Graduate School of Oceanography, University of Rhode Island

³ Institute for Environmental Physics, University of Heidelberg (UH)

doi: 10.5281/zenodo.10405

Abstract

Previous parameterizations of gas transfer velocity have attempted to cast this quantity as a function of wind speed or wind-stress. This study demonstrates that the presence of a surface film is effective at reducing the gas transfer velocity at constant wind-stress. Gas exchange experiments were performed at WHOI and UH using annular wind-wave tanks of different scales. Systematic variations of wind-stress and surfactant concentration (Triton-X-100) were explored to determine their influence on gas transfer velocity. Attempts to characterize the surface properties of the surfactant solutions were performed using mechanically generated capillary-wave packets. Results indicate a strong inverse relationship between gas transfer velocity and enhanced wave damping.

1 Introduction

The exchange of gases by the oceans is an important component of global budgets for the cycling of climatically important gases, including carbon dioxide and other trace gases. Estimation of ocean-atmosphere gas fluxes requires a knowledge of gas concentration gradients and an accurate parameterization of the gas transfer velocity (k). Previous studies of gas transfer have shown a strong dependence of the gas transfer velocity on wind and a weaker dependence on gas diffusivity [Jähne *et al.*, 1987]. Thus, the exchange velocity is commonly parameterized as a function of *wind speed* (u) and *Schmidt number* (Sc). Field estimates of k using natural and bomb ¹⁴C inventories, radon and other gas tracers show considerable scatter as a function of wind, attributable in part to variable fetch, wave state and, owing to the nonlinearity of the $u - k$ relation, biases introduced by the use of averaged winds [Wanninkhof, 1992]. Laboratory measurements carried out under tightly controlled conditions in wind-wave tanks also show large variations in k at constant or nearly constant friction velocity, suggesting that wind stress alone is not sufficient to parameterize k , and that other factors enter into the exchange process [Jähne *et al.*, 1987].

Recent observations suggest that surface-active materials present naturally in lakes and seas and also adventitiously in laboratory wind-wave tanks have a significant effect on the gas transfer velocity [Frew, 1995]. From studies in turbulent systems, it is known that *surface films* affect near-surface turbulence length and velocity scales [Lee *et al.*, 1980]. The viscoelastic modulus introduced by the presence of surfactants at the gas-liquid interface represents an additional tangential stress that opposes surface divergence due to turbulent eddies [Davies, 1966]. Thus, the presence of a film inhibits surface renewal and the resultant exchange of gases between the two phases.

Wind-generated waves transfer energy to turbulence via wave-wave interactions [Jähne *et al.*, 1987]. Thus, factors that modify the spectral characteristics of the wave field are likely to affect turbulence and the transfer process. The effect of finite *surface viscoelasticity*, first introduced by Levich [1962], on wave propagation has been studied extensively in both laboratory experiments [Hansen and Mann, 1964; Bock, 1987], and field experiments [Alpers and Hühnerfuss, 1989; Bock and Frew, 1993]. Evidence has recently been obtained that surface viscoelasticity affects not only the dissipation terms of the wave energy budget, but also the wind-wave growth and mixing terms [Bock *et al.*, 1995]. Results obtained in a small annular wind-wave tank at WHOI, described in a companion paper in this volume [Hara *et al.*, 1995], indicate a well-behaved functionality between mean square *wave slope* and gas-transfer coefficient for waves on clean water surfaces. Several studies have been performed in annular tanks at WHOI and at UH in order to understand how films of surface-active molecules influence both waves and gas transfer. Results from these studies show that even for different *surfactants* and concentrations, a uniform correlation between mean square slope and gas transfer is found. In view of the effect of the viscoelastic modulus on the wave field, the dependence of k on the viscoelastic modulus has also been investigated and the initial results of these studies are reported here.

2 Experimental Methods

Measurements of k were carried out in very clean water and in dilute aqueous solutions of a synthetic surfactant (*Triton-X-100*, polyethylene glycol p-tert-octylphenyl ether, avg. mol. wt 628, ®Rohm and Haas, Philadelphia, PA) in two annular wind-wave tanks of different scales at WHOI and UH. The WHOI tank has a mean diameter of 0.5 m and is designed to be relatively free of surface-active contaminants. The UH tank has a mean diameter of 4 m and is capable of sustaining longer waves. Due to its size, the UH tank is more difficult to keep free of adventitious surfactants and requires more aggressive removal of contaminant films through the continuous use of a surface skimming device.

Gas transfer velocities were measured during evasion or invasion experiments using primarily *oxygen* as a gas tracer. O_2 measurements were made continuously using polarographic electrodes. *Sulfur hexafluoride* (SF_6) was

also measured in selected experiments in the UH tank. Aqueous concentrations of SF₆ in discrete samples were measured by gas chromatography with electron capture detection.

Wind speed in the WHOI tank was taken nominally to be the mid-channel speed of the wind generating rotor; an anemometer was used to measure u in the larger UH tank. Since an accurate knowledge of the wind stress was essential for interpretation of the effects of surfactant films, friction velocities were measured for all experiments in both wind-wave tanks. A hot-film anemometer probe was used to measure bulk velocity profiles in the liquid phase in the UH tank; similar measurements were made in the WHOI tank using a Sontek acoustic current meter. A relation for estimating the water-side *friction velocity* u^* from bulk fluid velocity u_b ($u^{*2} = u_b^2/\beta'$) was determined using the momentum balance method [Jähne *et al.*, 1987]. The drag coefficient β' was found to be relatively constant, except at low surface stress, where a transition from laminar to turbulent flow occurs.

Triton concentrations were varied from 0.03 - 2.0×10^{-6} mol ℓ^{-1} to provide a range of viscoelasticities. Since liquid phase volumes for the UH tank were known only approximately and losses occurred during surface skimming, water samples were collected at the beginning and end of each experiment for determination of Triton concentrations. These were determined by solvent extraction of sample aliquots and measurement of the concentration using gas chromatography.

Wave propagation in subsamples of the same water was studied simultaneously in a small linear tank. Estimates of wave damping coefficients were made by measuring the propagation characteristics of mechanically generated wave packets at a frequency of 28.0 Hz. A point laser slope gauge positioned at known distances from the wavemaker was used to determine wave amplitude and phase. The frequency dependence of the damping coefficient allowed determination of the viscoelastic modulus using a dispersion relation incorporating viscoelasticity.

3 Results and Discussion

3.1 Gas Transfer With Zero Viscoelastic Modulus

An objective of this study was to quantify the effects of synthetic surfactant films on gas transfer, which requires carefully controlled surface conditions. Experiments that are completely free of surfactant effects are difficult to achieve without extreme measures that unfortunately would be impractical for wind-wave tanks. Distilled waters typically contain significant amounts of surface-active organics that adsorb at the air-water interface. The presence of such adsorbable contaminants is reflected in a time-dependent decrease of wave slope and of mass transfer. Initial skimming of the surface only temporarily removes adsorbed films, which can quickly redevelop when skimming is discontinued. The experiments in the WHOI tank utilized

a commercially bottled spring water that, although not totally surfactant-free, contained very low amounts of organics and was significantly cleaner than the distilled water available in our laboratory. This allowed stable measurements over a period of hours. Filtered deionized water was used in the UH tank; initial experiments indicated that surface contamination developed within a short time of the initial skimming; therefore a skimmer was used continuously to remove adventitious surfactants and maintain relatively stable surface conditions.

Gas transfer velocities measured for different water surfaces in the WHOI tank are summarized in Figures 1-3. In Figure 1, k is shown to be a smooth function of wind speed in the case of the clean spring water surfaces, for which the viscoelasticity is expected to be negligible. Figure 2 shows the relation obtained between k and u^* . The transfer velocity increases as a smooth linear function of friction velocity. There is no pronounced transition from a smooth to wavy surface; waves were generally observed over the entire range of wind stress in the WHOI tank. A more stringent test for contaminants is to plot k normalized to u^* ($k^* = k/u^*$) as shown in Figure 3. Within experimental error, k^* is constant for $0.1 < u^* < 3.0 \text{ cm s}^{-1}$ in the clean case. This indicates that the near surface hydrodynamic regime was constant. Clean surface values for k^* measured in the UH tank are also plotted in Figure 3. For higher u^* , the UH clean water values are in close agreement with the WHOI values, suggesting that the scale of the tank is not a critical factor in comparing these measurements. At low to moderate u^* , the k^* values are suppressed relative to the WHOI values. This would be consistent with higher levels of organic matter in the water or from tank construction materials.

3.2 Gas Transfer With Non-Zero Viscoelastic Modulus

Transfer velocities were measured as a function of u^* for solutions of Triton at four different concentrations in the WHOI tank and three nominal concentrations in the UH tank; the latter varied from the nominal values due to depletions occurring during the measurements. Concentrations reported here are actual concentrations, measured as described in Section 2. Results for the WHOI tank are summarized in Figures 1-3. The observations for the UH tank were very similar and are included in Figures 3. Gas exchange was inhibited relative to clean water even for the lowest concentration measured ($3 \times 10^{-8} \text{ mol l}^{-1}$ Triton). In the presence of Triton, k increased more slowly and nonlinearly with increasing wind speed (Figure 1) and also with u^* (Figure 2). The relation between u and k becomes increasingly nonlinear with increasing surfactant concentration and is qualitatively very similar to results reported by *Asher and Pankow* [1986; 1991] for gas transfer in stirred grid turbulent systems and to the Liss-Merlivat multilinear parameterization of k with wind for in situ gas exchange in lakes and seas [*Liss and Merlivat*, 1986]. A *critical wind speed* necessary for development of waves becomes apparent,

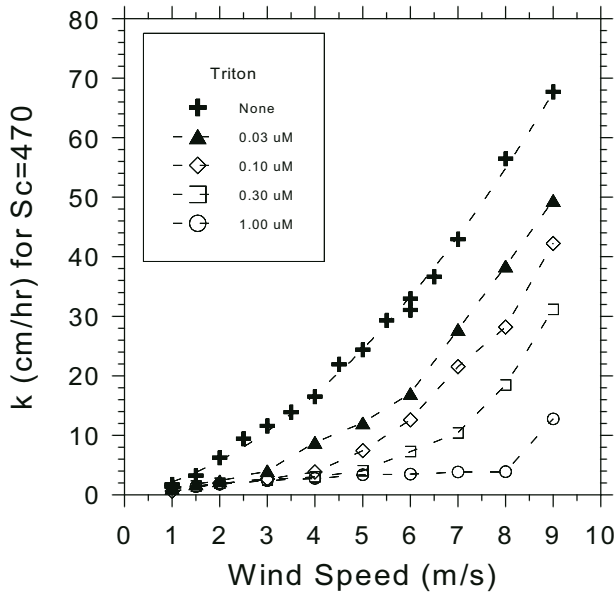


Figure 1: Dependence of gas transfer velocity, k , on wind speed, u , in the WHOI annular tank for clean water and dilute solutions of Triton-X-100.

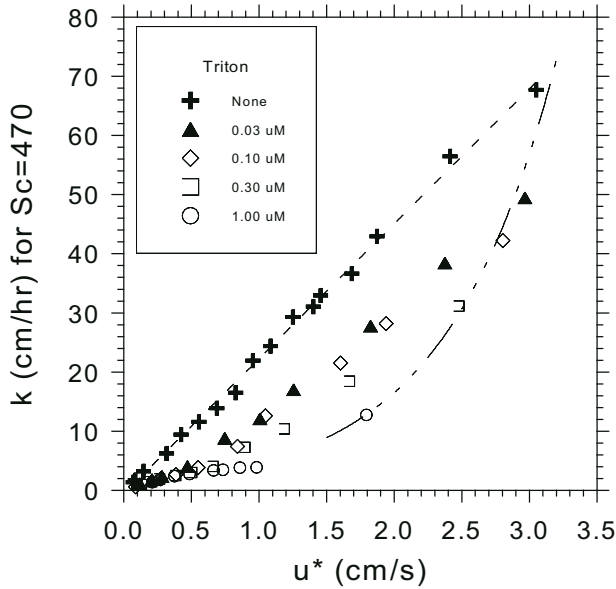


Figure 2: Gas transfer velocity as a function of water-side friction velocity, u^* , for clean water surfaces and for surfaces modified by different concentrations of Triton-X-100.

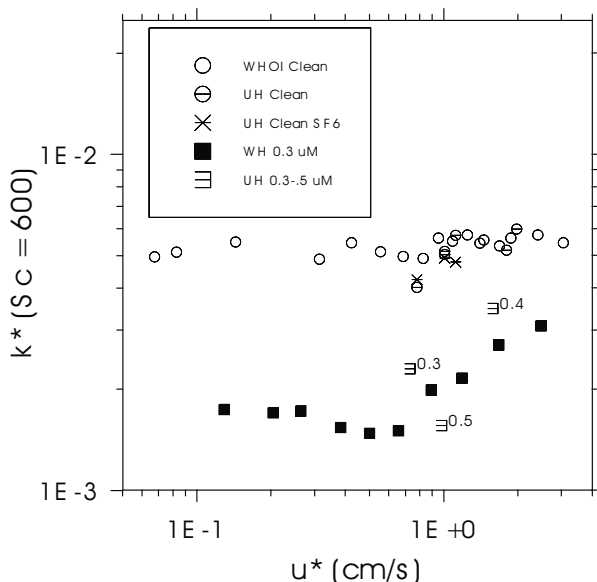


Figure 3: Dimensionless gas transfer coefficient, k^* , versus u^* for both clean water systems and for different concentrations of Triton-X-100. Data shown are from both WHOI and UH wind-wave facilities.

representing a transition between two hydrodynamic regimes. The *critical wind speed* increases with Triton-X-100 concentration. The inhibition of exchange is effective at the highest wind stress measured in the small tank ($u^* = 3 \text{ cm s}^{-1}$). Comparison of Figures 1 and 2 illustrates the striking effect of surfactants on the drag presented by the interface. The broken line curve in Figure 2 is fitted to k values for $u = 9 \text{ m/s}$. At a concentration of $1 \mu\text{mol l}^{-1}$, u^* is reduced to about 60% of the clean water value.

The transfer velocity can be expressed in terms of u^* as the dimensionless transfer velocity $k^* = k/u^* = \beta Sc^{-n}$. In Figure 3, the variation of k^* with u^* for a Triton solution ($0.3 \mu\text{mol l}^{-1}$) is compared with k^* values for clean water for the WHOI tank, along with data for similar concentrations in the UH facility. These have been normalized to $Sc = 600$ by assuming Schmidt number dependencies of $n = 1/2$ for wavy surfaces and $n = 2/3$ for smooth surfaces. However, the Schmidt number exponent is likely to have intermediate average values in the transition region, as shown by correlations of n with wave slope and by direct measurements of n using multiple gas tracers [Jähne *et al.*, 1987].

In contrast to the clean water values, k^* is strongly suppressed at low u^* and does not attain clean water values even at high u^* . A clear transition between hydrodynamic regimes (smooth surface to wavy surface) is observed. This transition occurred at different u^* for different surfactant

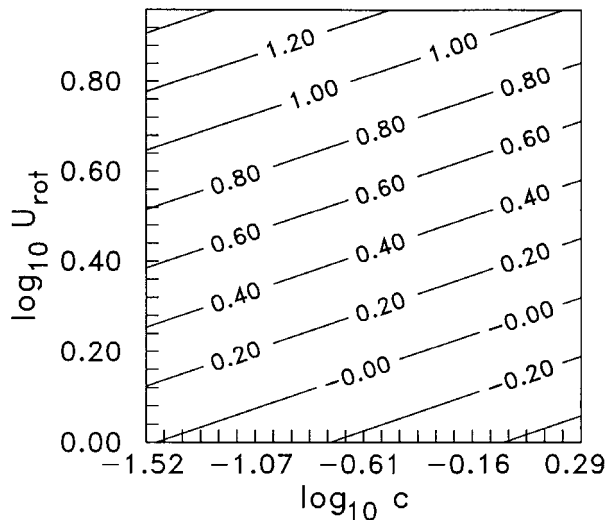


Figure 4: Surface contour plot of $\log_{10} k$ as a function of $\log_{10} c$ and $\log_{10} u_{rot}$. Data points represent measurements from both the WHOI and UH facilities. A planar surface fitted by means of least-squares-fit is depicted in the contour plot and explains the variance of 90% of the data.

concentrations.

As with surfactants that occur in natural waters [Frew and Nelson, 1992a; 1992b; Bock and Frew, 1993], Triton-X-100 is water-soluble, but forms films that are not reversibly adsorbed and desorbed at the interface. When Triton-X-100 films were allowed to accumulate in the absence of surface skimming, increased suppression of exchange was observed at a given surfactant concentration. Under conditions of constant surface skimming, the surface concentration of Triton-X-100 was expected to be in dynamic equilibrium with the bulk concentration, c , through diffusional exchange. Figure 4 shows the fitted three-dimensional plane that describes the $\log_{10}c$ - $\log_{10}u$ - $\log_{10}k$ relation that describes the experimental data for both the WHOI and UH wind-wave tanks. The plane describes within one standard deviation, the variance in 90% of the data points.

The results suggest that the Triton, a highly water-soluble surfactant, was capable of maintaining significant viscoelasticity at the interface despite the continuous disruption of the surface by the skimming device, which prevented accumulation of film material. This finding implies that natural soluble surfactants in seawater also could affect gas transfer under conditions where films of water-insoluble surfactants would be disrupted by wind shear and breaking waves.

3.3 Estimation of Wave Damping and Viscoelastic Modulus

A strong linear correlation between k and *mean squared surface slope* was observed for clean interfaces [Hara *et al.*, 1995]. The same relationship was also observed to apply in the presence of Triton-X-100. Apparently the surface roughness is an indicator of the turbulence phenomena governing the exchange. A study of the wave damping effects of the Triton was undertaken to try to correlate damping coefficients and k . An analysis of the data obtained from these experiments yielded values of the viscoelastic modulus.

Levich [1962] established early that the presence of a surface dilational elasticity caused damping of capillary and *capillary-gravity waves* by creating a surface tension gradient due to wave orbital motion. The hydrodynamic description was re-evaluated by Bock and Mann [1989] to eliminate spurious wave propagation modes and the resulting *dispersion relation* was formulated from the linearized Navier-Stokes relation and surface boundary conditions that include a dilational visco-elastic modulus. This dispersion relation is limited in the sense that surface shear viscoelasticity and other more complex surface rheological properties are omitted. Despite this, the formulated dispersion relation should be accurate for dilute gas-like surface films where shear viscoelasticities and surface plasticity should not exist. It relates the physical properties of the bulk fluid on which the waves propagate (namely the density, ρ , and the fluid viscosity, η), along with the *surface tension*, σ , and the gravitational constant, g , to waves with angular frequency, ω , that have a complex wavenumber, \hat{k} , that is defined as:

$$\hat{k} = \frac{2\pi}{\lambda} + i\beta \quad (1)$$

where λ is the wavelength of the wave and β is the distance damping coefficient. The dispersion relation takes the form of a determinant that is equal to zero when values of \hat{k} and ω are obtained that satisfy physically realistic wave propagation. The relation is given as:

$$\begin{vmatrix} (\rho\omega^2 - \rho g\hat{l} + 2i\omega\eta\hat{l}^2 - \sigma\hat{k}^2\hat{l}) & (-i\rho g\hat{k} - 2\omega\eta\hat{m}\hat{k} - i\sigma\hat{k}^3) \\ (2\omega\eta\hat{k}\hat{l} + i\hat{\epsilon}\hat{k}^3) & (i\omega\eta[\hat{k}^2 + \hat{m}^2] - \hat{\epsilon}\hat{k}2\hat{m}) \end{vmatrix} = 0 \quad (2)$$

where \hat{m} is defined as:

$$\hat{m} = +\sqrt{\hat{k}^2 - \frac{i\omega\rho}{\eta}} \quad (3)$$

and \hat{l} is defined as:

$$\hat{l} = +\sqrt{\hat{k}^2} \quad (4)$$

This dispersion relation predicts wave modes that correspond to the Laplace mode in which the primary restoring force for wave motion is the surface tension acting on the curvature of the wave. In the presence of a surface dilational viscoelasticity, a Marangoni mode is predicted, along with a modified Laplace mode. In this mode the primary restoring force is produced by local areas of compressed surface film that give rise to an oscillating compressional wave in the plane of the surface.

The dispersion relation can be solved to obtain the *viscoelastic modulus*, $\hat{\epsilon}$ by using experimentally obtained values for the remaining variables. To obtain the real and imaginary parts of \hat{k} , plane-wave packets are produced at the end of a 1.3 m linear wave tank. The packets propagate along the tank and a single-point slope gauge, that can be positioned at known locations along the tank, records its passage. Figure 5 shows a representative time series recorded at a point along the tank. Measurement of the phase of the wave packet at several 0.001 m spacings gives an accurate estimate of the real part of \hat{k} , and measurements of the packet amplitude at 0.05 m intervals give an estimate of the imaginary part, β . Separate measurement of surface tension is performed using a Wilhelmy plate and an electrobalance. Having experimentally fixed the frequency of the wave and using tabulated values for density, viscosity, and the gravitational constant, it is possible to solve iteratively the dispersion relation for $\hat{\epsilon}$. It is also possible to solve the dispersion relation assuming that the viscoelastic modulus is zero, corresponding to waves propagating on a clean surface with no surface film. This allows computation of β_E/β_T , the *damping ratio*, R .

For the wave damping experiments, three concentrations of Triton were tested. These concentrations were 0.01, 0.03, and 0.3 μM . The wave packet frequency was centered at 28.0 Hz, the density, viscosity, and gravitational constant used for the calculations were 0.998 g/cm^3 , 0.01 P, and 981 cm/s^2 , respectively. Because the results of these experiments were to be compared with the gas transfer measurements described above, it was important to create surface conditions in the linear tank that corresponded to the conditions in the annular wind-wave tank. Intrinsically, this could not be achieved because the quiescent conditions required for mechanically generated waves in the linear tank are not the same as the mixed, dynamical conditions obtained with wind stress generated over the surface in the annular tank. To simulate the effect that mixing would produce in the wind-wave tank, the surface of the linear tank was aspirated at one end while being re-supplied at the other end with a stream of solution of the same concentration in the tank. This process removed the very surface of the solution (and also incidentally caused a small surface drift) that resulted in a surface free of a statically adsorbed film. At the instant of the start of the wave measurements, the aspiration and re-supply were ended, and the surfactant was allowed to adsorb at its own pace. The surface tension was observed to decrease monotonically, indicating the re-adsorption of surfactant. While this took place, measurements proceeded at intervals of 10 minutes so that the

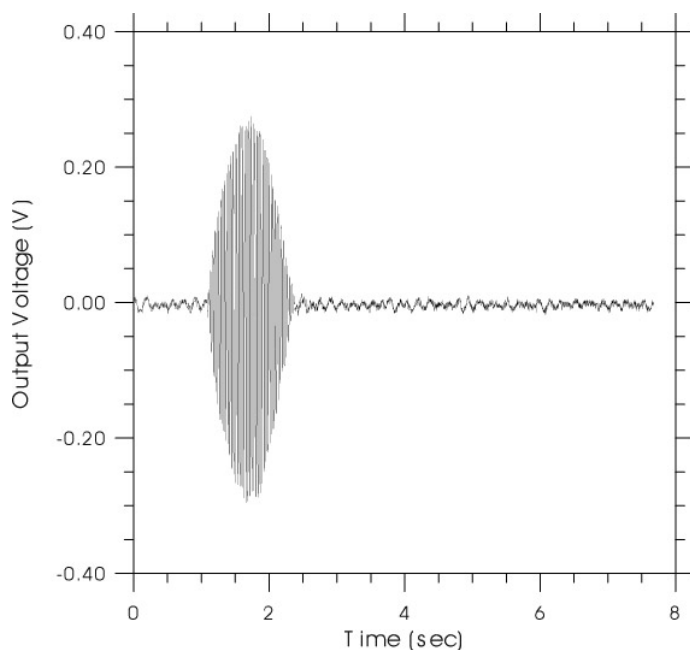


Figure 5: Representative wave packet from a 28 Hz wave produced in the linear wave tank. These data represent the time history of surface slope as observed at a fixed distance away from the mechanical wave generator.

calculated $\hat{\epsilon}$ and β_E/β_T values could be obtained. These values would then be extrapolated back in time to the start of the experiment to yield values representative of a fresh surface.

Results of these experiments were amplitude and phase versus distance at discrete points in time after the start of the experiment. In Figure 6, points are plotted representing packet amplitude as a function of distance away from the wave maker. Each of the lines represents a measurement made in 10 minute intervals from the start of the experiment. It is clear that the slope of these lines increases, indicating a larger value of distance damping coefficient. A similar phenomenon is demonstrated in the wavenumber ($2\pi/\lambda$), as a function of time. This evidence, along with the steady decrease in surface tension demonstrates how the surface of the solution ages. While it is not clear that the surface of the solution in the wind-wave tank is as efficiently stripped of a static adsorbed film under the conditions of wind-stress during a gas exchange measurement, we do not have the means to measure mechanically generated waves in the wind-wave tank.

The results in Table 1 include both measured and calculated properties for three different solutions of Triton-X-100. As stated above, these parameters are determined after thorough surface aspiration. Since the surface is initially stripped of adsorbed films, the initial surface tension, σ_0 is close

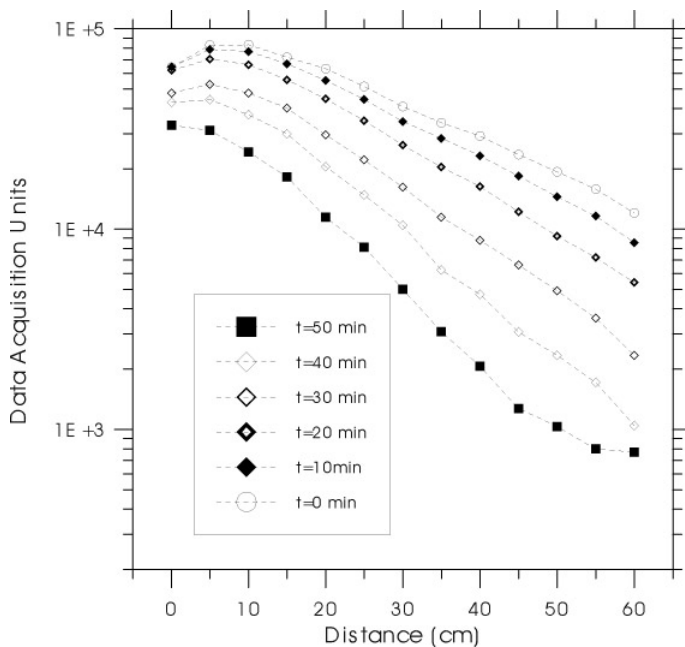


Figure 6: Damping curves (log amplitude versus distance) for wave packets at 28 Hz. The waves are propagating on a solution of $0.3 \mu\text{M}$ Triton-X-100. As the surface film adsorbs, the wave propagation is modified and the distance damping coefficient increases.

to that of pure water. For this reason, the theoretical wavenumber (calculated from the dispersion relationship with zero viscoelasticity) does not significantly vary with Triton concentration. For the $0.03 \mu\text{M}$ solution, the measured damping coefficient was not significantly different from the theoretical damping coefficient. Although small, the measured damping coefficient for the $0.1 \mu\text{M}$ solution was found to increase from the theoretical value. A much larger increase in the damping coefficient was measured for the $0.30 \mu\text{M}$ solution. A similar trend in the elasticity was observed. The uncertainty pertaining to the elasticity in the $0.03 \mu\text{M}$ solution was of the same order as the value itself. However, the $0.1 \mu\text{M}$ and $0.3 \mu\text{M}$ showed appreciable increases in elasticity. In all cases, the imaginary part of the viscoelasticity was negligible. This was probably due, in part, to the slow adsorption of Triton-X-100 at this concentration.

Comparison with the data in Figure 1 indicates that both R and ϵ_d are inversely correlated with k for a given u . However, the ability to correlate the wave damping characteristics and viscoelasticity with the gas transfer results is complicated by the ability to reproduce the same surface in separate experiments. This is a strong disadvantage of using Triton-X-100 and similar surfactants, that other researchers should be aware of. With the same

Table 1: Summary of wave damping and viscoelastic modulus

Concentration	0.03 μM	0.10 μM	0.30 μM
σ_0 (mN/m)	72.56	72.13	72.16
k_T (rad/cm)	6.9312	6.9456	6.9482
k_E (rad/cm)	6.9407	6.9177	6.6394
β_T (1/cm)	.02848	.02866	.02870
β_E (1/cm)	.02823	.02939	.03571
R	0.9912	1.0255	1.3425
ϵ_d (mN/m)	-0.3974	0.8709	2.7290
η_d (g/s)	-1.3E-4	1.1E-3	7.5E-3

bulk concentrations of absorbed surface active material, the actual surface concentration may vary substantially. This depends on many conditions which are difficult to control. If the surface is not continuously stripped of adsorbed films, the surface concentration will increase and both the damping coefficient and the viscoelasticity will also increase. There does remain a strong correlation between gas transfer velocity and bulk concentration. The results of this preliminary study indicate that the degree of the inverse relationship of gas transfer velocity and concentration may be determined by the surface viscoelasticity and the damping coefficient.

4 Concluding Remarks

Excellent agreement was obtained between the WHOI and UH facilities for determination of gas transfer velocity as a function of wind-stress. As expected, significant reduction of the gas transfer velocity was effected by surfactant films. A three-way power-law relation is seen in the data, which suggest a simple relation between gas transfer velocity, Triton-X-100 concentration, and wind. While it is not intuitive that concentration should form a simple relation to gas transfer velocity, there exists a strong inverse correlation between wave damping enhancement and gas transfer velocity.

Acknowledgements

The authors thank R. K. Nelson for his determinations of Triton-X-100 in the samples used, and C. G. Johnson, T. Donahue and J. Ledwell for their advice and assistance in developing the SF₆ gas chromatographic technique used at UH. This research was supported by the National Science Foundation under grants OCE-9301334 and OCE-9410537. Contribution No. 9071 of the Woods Hole Oceanographic Institution.

References

- Alpers, W. and H. Hühnerfuss, The damping of ocean waves by surface films: a new look at an old problem. *J. Geophys. Res.*, 94, 6251–6265, 1989
- Asher, W. E. and J. F. Pankow, The interaction of mechanically generated turbulence and interfacial films with a liquid phase controlled gas/liquid transport process. *Tellus*, 38B, 305–318, 1986
- Asher, W. E. and J. F. Pankow, The effect of surface films on concentration fluctuations close to a gas/liquid interface. In *Air-Water Mass Transfer*, S. C. Wilhelms and J. S. Gulliver eds, (pp.68–79): New York: American Society of Civil Engineers, 1991
- Bock, E. J., On ripple dynamics. I. Microcomputer-aided measurement of ripple propagation. *J. Colloid Interfac. Sci.*, 119, 326–33, 1987
- Bock, E. J., T. Hara and M. Donelan, Equilibrium spectra of wind waves in the presence of surfactants (in preparation)
- Bock, E. J. and N. M. Frew, Static and dynamic response of natural multicomponent oceanic surface films to compression and dilation: laboratory and field observations. *J. Geophys. Res.*, 98, 14599–14617, 1993
- Davies, J. T., The effects of surface films in damping eddies at a free surface of a turbulent liquid. Proceedings of the Royal Society of London, A290, 515–526, 1966
- Frew, N. M., The role of organic films in air-sea gas exchange. In: *The Sea Surface and Global Change*, P. S. Liss and R. A. Duce, eds., Cambridge University Press, 1995 (in press)
- Frew, N. M. and R. K. Nelson, Isolation of marine microlayer film surfactants for ex situ study of their surface physical and chemical properties. *J. Geophys. Res.*, 97, 5281–5290, 1992a
- Frew, N. M. and R. K. Nelson, Scaling of marine microlayer film surface pressure-area isotherms using chemical attributes. *J. Geophys. Res.*, 97, 5291–5300, 1992b
- Hansen, R. S. and J. A. Mann Jr., Propagation characteristics of capillary ripples. I. The theory of velocity dispersion and amplitude attenuation of plane capillary waves on viscoelastic films. *J. Appl. Phys.*, 35, 152–161, 1964
- Hara, T., E. J. Bock, N. M. Frew, and W. R. McGillis, Relationship between air-sea gas transfer velocity and surface roughness, *This volume*
- Jähne, B., O. Münnich, R. Bösinger, A. Dutzi, W. Huber and P. Libner, On the parameters influencing air-water gas exchange. *J. Geophys. Res.*, 92, 1937–1949, 1987
- Lee, Y. H., G. T. Tsao and P. C. Wankat, Hydrodynamic effect of surfactants on gas-liquid oxygen transfer. *AIChE Journal*, 26, 1008–1012, 1980
- Levich, V. G., [1962] *Physico-Chemical Hydrodynamics*. Englewood Cliffs, NJ: Prentice Hall, 1962
- Liss, P. S. and L. Merlivat, Air-sea gas exchange rates: introduction and synthesis, in *The Role of Air-Sea Exchange in Geochemical Cycling* (P. Buat-Menard ed.), Reidel, Dordrecht, pp. 113–127, 1986
- Wanninkhof, R., Relationship between wind speed and gas exchange over the ocean. *J. Geophys. Res.*, 97, 7373–7382

On the Influence of Fetch and the Wave Field on the CO₂ Transfer Process: Laboratory Measurements

*F. J. Ocampo-Torres*¹, *M. A. Donelan*²,

¹ C.I.C.E.S.E. Departamento de Oceanografía Física
Km. 107 Carretera Tijuana-Ensenada, Ensenada, B. C., MÉXICO

² N.W.R.I. Canada Centre for Inland Waters
867 Lakeshore Road, Burlington, Ontario L7R 4A6, CANADA

Abstract

Wind speed dependence of the gas transfer velocity is generally expressed in terms of power law relationships. Some studies however, have already shown the importance of other aspects besides wind speed: bubbles, spray, fetch, wave field, wind speed variability, etc., suggesting that a better parameterization of the gas transfer velocity is still needed. We aim to study further the influence of the wave field on the gas transfer process as it changes for different fetches under similar wind conditions.

The velocity of CO₂ transfer across the air-water interface (K_{CO_2}) has been measured in a wind-wave flume to study the influence of fetch and the wave field. A 32 m long gas transfer flume (GTF) has been used to generate two different wave fields for a determined wind speed (wind waves, and wind and paddle generated waves). Previously reported data from the same GTF, when an inverted beach was included in the middle of the tank (effective fetch of 16 m approximately), show generally lower transfer velocities for the same wind speeds than the new results from full length tank experiments (32 m fetch).

An increase of about 20% in K_{CO_2} is observed for 10 m/s reference wind speed (measured at about 30 cm above mean water level) from the full length tank experiments when compared to the case of 16 m fetch. Longer fetch is associated with higher waves for a particular wind speed. For 10 m/s for example, maximum significant wave height measured towards the end of the tank was nearly twice the value observed for the 16 m fetch experiments. The bulk transfer coefficients D_{CO_2} (equivalent to Dalton numbers) are shown to be relatively higher for the case of longer fetch. A minimum D_{CO_2} is also observed at a wind speed between 2 and 3 m/s, for the wind wave field. However, this minimum is not as pronounced when paddle generated waves are present. These results seem to stress the point that relationships using only the wind speed as the parameter to determine the gas transfer velocity might not be appropriate. A wave parameter might be included in a power law relationship and it will make for a better representation of laboratory and ocean observations.

1 Introduction

The exchange of gas between the ocean and the atmosphere influences substantially the overall cycle and budget of trace gases. Carbon dioxide (CO₂), specifically, is of primary importance as it might affect global scale processes that finally determine our planet's long term climate.

An enhancement of the gas transfer velocity due to the onset of waves has been noticed in some previous studies. Suggestions have been made that the waves at the high frequency end of the spectrum would be directly linked to the transfer rate [Coantic, 1986]. Further experimental work showed that the enhancement of the air-sea gas exchange rate is not closely linked to the spectral densities of small-scale water surface waves [Jähne, 1991], rather to the over-all stability of the wave field.

It is clear that waves influence the air-water gas transfer rate, however, how the wave field is linked to the transfer process and how to parameterize its effect is not so obvious.

It has been claimed that regular waves do not influence the gas transfer velocity, since significant enhancement had only been observed if close-to-unstable waves are added to the wind wave field, yielding significant breaking [Jähne, 1991].

Some controversy has arisen as different opinions emerged from experimental results using oxygen as tracer for instance, suggesting that mechanically generated waves could produce a significant air-water transfer. Results from a 19 m wind wave tank using oxygen as tracer [Downing and Truesdale, 1955], showed an approximate 28% increase in the gas transfer velocity for wind speeds of 5 m/s, and about 40% for winds of 10 m/s. Gas transfer velocity estimated in an 8 m tank increased about 30% when mechanically generated waves were added to the system [Merlivat and Memery, 1983]. More recently, the gas-transfer coefficient has been related to the vertical wave velocity at the water surface when estimated indirectly as the product of wave height and wave frequency [Daniil and Gulliver, 1991].

Influence of *fetch* on the gas transfer velocity was probably first reported when comparing results for NO₂ from an 8 m tank [Merlivat and Memery, 1983] with those obtained for CO₂ from an 18 m one [Broecker *et al.*, 1978]. Transfer velocities were about 30% higher for the larger fetch flume. Fetch dependence of the heat transfer process across the aqueous boundary layer has been observed with the controlled flux method [Jähne *et al.*, 1989]. For an increase in the fetch from 2 to 8 m, transfer velocities increased by 40% for low winds (4 m/s), and about 20% for winds of approximately 6 m/s. At higher wind speeds however, no significant change was observed. Nevertheless, it has already been claimed that comparing results from different flumes might not be appropriate since the obtained gas exchange rate are an average over the whole surface of the facility [Jähne, 1991]. Recently, this issue has been raised once again for accurate determination of gas fluxes from lakes and ponds, as it is suggested that fetch variations, lake size and

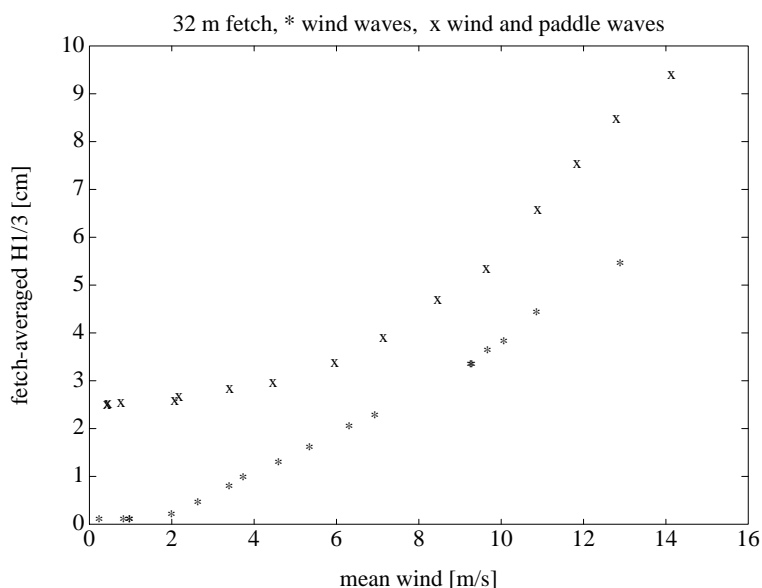


Figure 1: Fetch-averaged significant wave height $H_{1/3}$ for the 32 m long Gas Transfer Flume (GTF) experiments, as a function of the mean reference wind speed measured at 30 cm above mean water level. Wind waves (*), and wind and paddle waves (x).

shape and wind direction should also be taken into account [Kwan and Taylor, 1994].

It is the purpose of this work to explore the effect of the fetch and the wave field on the transfer process of carbon dioxide. In particular we present the results of some laboratory experiments carried out to estimate the mass transfer velocity K_{CO_2} for varying wind speeds under two different wave conditions; wind waves, and wind and paddle generated waves. Results from the wind wave cases are compared to those obtained previously when the fetch was half the size.

2 The Measurements

The experiments were performed in the *Gas Transfer Flume* (GTF) at the hydraulics laboratory of the National Water Research Institute [Merzi *et al.*, 1990]. A test section having a surface area of 32.2 m by 0.76 m permitted us to measure the transfer of CO_2 between 66 m³ of air and 10 m³ of water in a tightly closed system, where the water slowly circulated at a constant speed of approximately 10 cm/s. The fan system had the capability of delivering wind speeds up to 22.5 m/s. Instrumented measuring stations are located at about 5.3 m, 14.5 m, and 29.7 m from the upwind end of the test section.

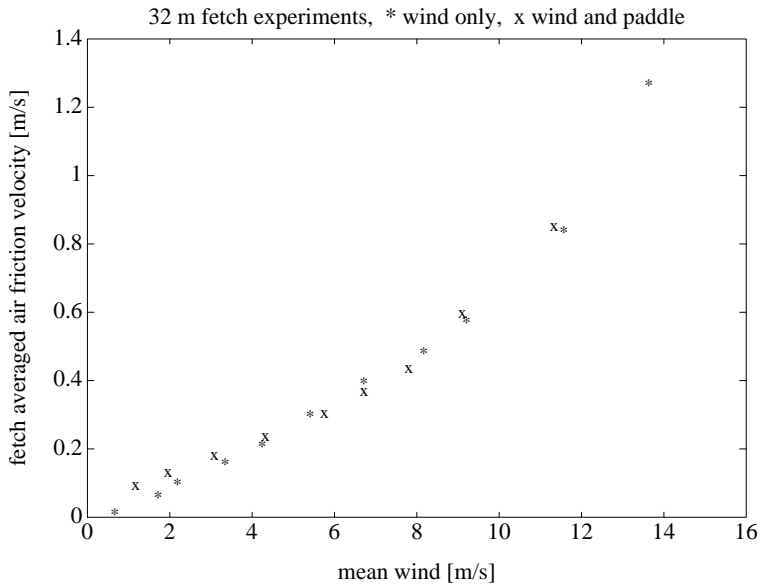


Figure 2: Fetch-averaged wind friction velocity as a function of the mean reference wind speed. Wind waves (*), and wind and paddle waves (x).

Details of the experimental procedures have been given previously elsewhere [Ocampo-Torres *et al.*, 1994], therefore, only a brief description is included for completeness.

Concentration of CO_2 in both aqueous and gaseous phases has been measured with a non-dispersive *infrared analyzer* (LI-6262, LiCOR). Previous results for 16 m fetch experiments [Ocampo-Torres *et al.*, 1994] are now complemented with those obtained from a 32 m full length fetch in the GTF. The estimation of the mass transfer velocity K_{CO_2} follows

$$\frac{\partial C_w}{\partial t} \frac{V_w}{A} = -K_{\text{CO}_2} (C_w - C_a/H) \quad (1)$$

where A is the surface area of the air-water interface exposed to the wind action (24.5 m^2), V_w the total volume of water (10 m^3), $\partial C_w / \partial t$ the rate of change of CO_2 concentration in water (C_w), and H the Henry's Law constant. Each experimental run yields a time series of the air-water CO_2 concentration difference ($C_a/H - C_w$) and the rate of change of concentration in both air and water phases (we use for simplicity only $\partial C_w / \partial t$). A linear fit allows us to calculate K_{CO_2} .

In addition, a different wave field was in effect, as mechanically generated waves were superimposed for a set of experiments with wind speeds up to 16 m/s. Wind speed and wave height were measured at stations 1, 2 and 3 by means of Pitot tubes and wave staffs, respectively. Separate experiments

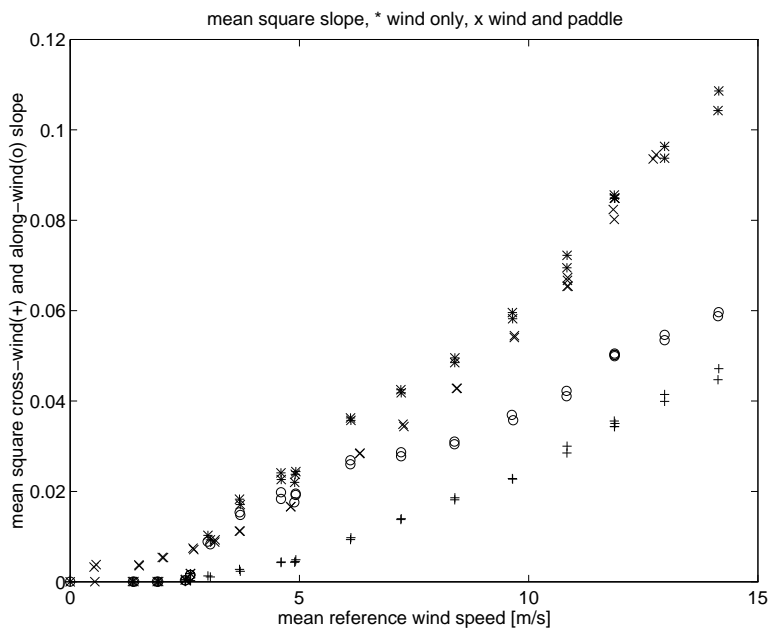


Figure 3: Mean square slope measured at station 2 for wind waves (*), and wind and paddle waves (x). Along-wind (o), and cross-wind (+) wave slopes are also shown for the wind wave cases.

were run to measure wave slope by a laser based system deployed at station 2 [Palm et al., 1977], and to estimate the wind friction velocity through wind speed profiles at the three measuring stations.

3 Results

Two different wave fields are obtained for any given wind speed by means of including paddle generated waves besides fan-induced wind waves. Fetch-averaged significant wave height as estimated from the wave staff measurements is a clear indication of these two rather different wave fields, as shown in figure 1. This fetch-averaged quantity properly characterizes the wave field incorporating the inherent fetch dependence associated with linear wind wave tunnel measurements. There we can observe that, on average, waves are not generated until wind speed reaches about 2 m/s. For the cases when the waves were also mechanically generated, significant wave heights of about 2.7 cm are detected for wind speeds lower than 3 m/s. In general, significant wave height is obviously greater for the wind and paddle cases in comparison to the only wind cases. The maximum (fetch-averaged) significant wave height observed is close to 10 cm for the highest wind speed at our experimental runs.

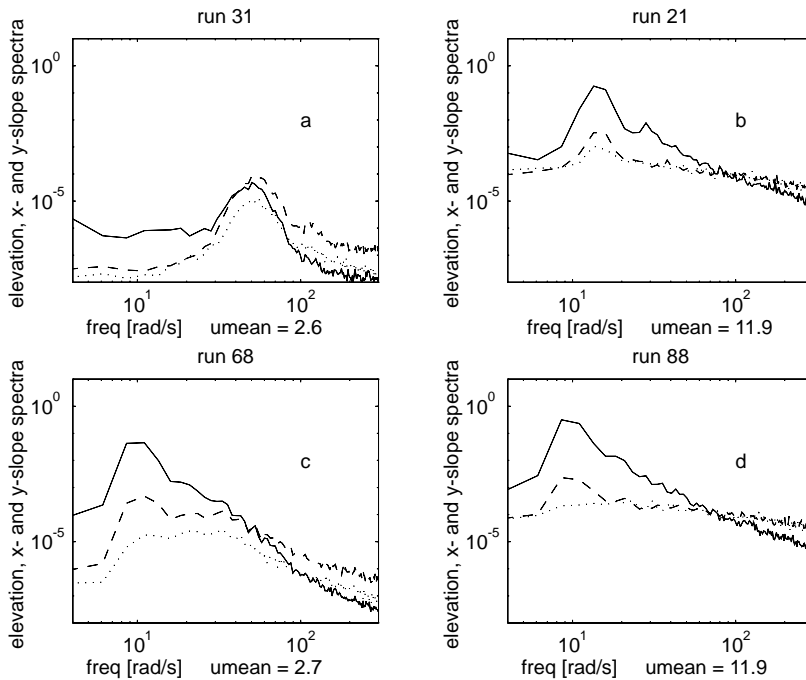


Figure 4: Surface elevation (-), and along-wind (- -) and cross-wind ($\cdot \cdot \cdot$) wave slope spectra. Example of two wind wave cases are shown for wind speed of a) 2.6 m/s, and b) 11.9 m/s. Two other cases when paddle generated waves are included are also shown for c) low wind speed (2.7 m/s), and d) higher wind (11.9 m/s). Run numbers are for specific experiments carried out to measure wave slopes.

Fetch averaged wind friction velocity is shown in figure 2. It seems that only at winds lower than 5 m/s, the cases when the paddle waves are included show slightly higher friction velocities. For moderate to strong winds there is no apparent difference.

Wave slopes were measured at station 2. Clear differences can be observed in the cases with and without paddle waves, up to wind speed of about 12 m/s (see figure 3). For stronger winds, the two cases show practically the same wave slope characteristics. From the wind wave cases, it is interesting to note a sudden increase in wave *mean square slope* for wind speed of about 3 m/s. For higher wind speed, mean square slope is higher for the only wind cases, in comparison to the wind and paddle cases. Details of the along- and cross-wind wave slopes are also shown for the wind only runs, where it can be observed that the sudden increase in the total mean square slope is practically due to the behaviour of the along-wind slope. A tendency for the along-wind slope to saturate is depicted in the wind speed

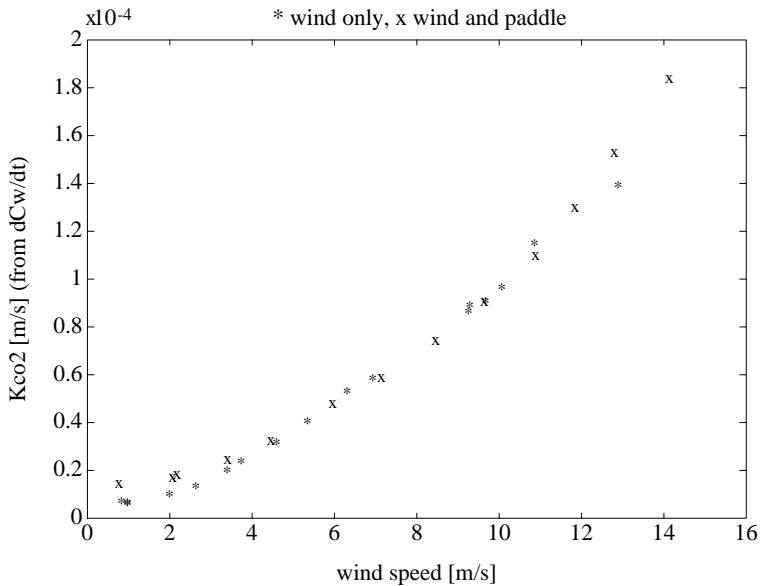


Figure 5: Mass transfer velocity for carbon dioxide K_{CO_2} adjusted for a Schmidt number equal to 600. Results for wind waves (*) and wind and paddle generated waves (x) are shown.

range of 6 to 10 m/s, although it increases further for stronger winds. This is not the case for the cross-wind wave slopes which show a monotonic increase with the wind for the speed range of the present experiments.

In order to better characterize the wave field present during our experiments, examples of surface elevation and wave slope spectra are shown in figure 4. Wave slope spectra under low wind conditions are rather broad when paddle generated waves are also present (compare figure 4 a and c). For the whole frequency range, low wind speed is characterized by inducing higher spectral levels for along-wind than for across-wind wave slopes. Stronger winds however, are associated with wave slope spectra which show noticeable differences only at the low frequency region of the spectra. Specifically, it is only at the spectral peak frequency, where the along-wind wave slopes are appreciably higher than cross-wind slopes.

Results of the CO_2 mass transfer velocity K_{CO_2} are shown in figure 5, after correction to their equivalent value for a Schmidt number (Sc) equal to 600, with the temperature influence on Sc taken into account. Subtle differences are observed in K_{CO_2} when expressed as a function of the reference wind speed, in particular for low winds; the mass transfer velocity is higher for the cases when paddle waves are present. The technique employed to determine the transfer velocity allows us to use either the rate of change of the gas concentration in water or in air [Ocampo-Torres *et al.*, 1994]. For simplicity

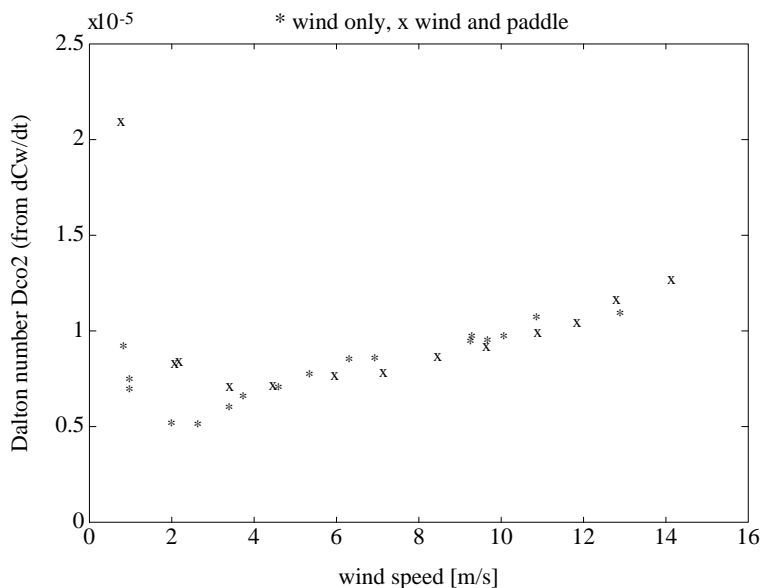


Figure 6: Dalton number for carbon dioxide D_{CO_2} adjusted for a Schmidt number equal to 600. Results for wind only waves (*) and wind and paddle generated waves (x) are shown.

however, we only show those results derived from the rate of change of the gas concentration in water.

Figure 5 indicates that paddle generated waves may increase the CO_2 mass transfer velocity for wind speeds lower than about 4 m/s. When comparing the present results of K_{CO_2} for the wind wave runs with those obtained from the 16 m fetch experiments (see figure 10 in [Ocampo-Torres et al., 1994]) the influence of the fetch is easily noticed. Generally higher mass transfer velocities are obtained from the longer fetch experiments.

Definite differences are observed between wind wave, and wind and paddle generated wave runs, in the exchange coefficient, so called Dalton number D_{CO_2} in analogy to the evaporation process (defined as the ratio between the transfer velocity K_{CO_2} and the wind speed), as it is shown in figure 6. Higher values for D_{CO_2} are obtained when paddle waves are superimposed on the wind wave field for low wind speeds. A minimum D_{CO_2} is detected for wind speed between 2 and 3 m/s for the wind only runs, similar to that obtained previously for the case of 16 m fetch [Ocampo-Torres et al., 1994]. We must however, indicate that the minimum value for D_{CO_2} from the 16 m fetch runs is considerably lower, approximately only 50% of its value from the 32 m fetch runs. Under moderate to strong winds, wind wave experiment results show D_{CO_2} about 20% higher when the full tank was used with a 32 m fetch. The presence of waves (paddle generated) under low wind

conditions seems to enhance the transfer and a less pronounced minimum in D_{CO_2} is observed.

4 Final remarks

Detailed measurements of waves and wind in the Gas Transfer Flume of the National Water Research Institute are reported, as an important component needed to study the transfer process of carbon dioxide between air and water. Accurate estimation of the mass transfer velocity is achieved from monitoring the rate of change of gas concentration in the water or in the air, inside the tightly closed system.

The data obtained using the full length tank (32 m fetch) complement those previously reported when an inverted beach was placed in the middle of the tank for an effective fetch of 16 m. The present results include cases when mechanically generated waves are superimposed on the wind wave field, allowing the possibility of exploring the influence of two different wave fields under similar wind and fetch conditions.

Comparing the present results (32 m fetch) with those previously reported from 16 m fetch experiments it has been shown that the mass transfer velocity for CO_2 increases with wave energy caused by the increase in fetch.

Significant wave height (fetch-average) as a function of wind speed clearly shows two different wave fields: wind waves, and wind and paddle generated waves. The fact that there is not much difference between the gas transfer velocities from the two different wave fields, tends to suggest that the significant wave height might not be an appropriate parameter to be included in the transfer velocity functional. These results support the idea once put forward by *Jähne* [1991] that gas exchange measurements do not show a significant effect of mechanically generated waves on the mass transfer velocity. Mean square slope on the other hand, shows a similar behaviour as the transfer velocity when viewed as a function of wind speed.

Acknowledgements

The technical support by D. Beesley and G. Voros during the experimental work is gratefully acknowledged. F. J. Ocampo-Torres would like to acknowledge the support and hospitality of the National Water Research Institute personnel. He also acknowledges CONACyT, México for funding through grant 3993-T9402. We are indebted to Julieta Castro who has provided excellent support on word processing and secretarial activities, and to E. Pavía for helpful comments on the manuscript.

References

- Broecker, H.-C., Petermann, J., and Siems, W., The influence of wind on CO₂ exchange in a wind-wave tunnel, including the effects of monolayers. *J. Mar. Res.* 36, 595-610, 1978
- Coantic, M., A model of gas transfer across air-water interface with capillary waves. *J. Geophys. Res.* 91, 3925-3943, 1986
- Daniil, E. I., and Gulliver, J. S., Influence of waves on air-water gas transfer. *J. Envir. Engin.* 117, 522-540, 1991
- Downing, A. L., and Truesdale, G. A., Some factors affecting the rate of solution of oxygen in water. *J. Appl. Chem.* 5, 570-581, 1955
- Jähne, B., New experimental results on the parameters influencing air-sea gas exchange. *Air-Water Mass Transfer* (eds. S. C. Wilhelms and J. S. Gulliver). Am. Soc. Civ. Eng., 582-592, 1991
- Jähne, B., Libner, P., Fischer, R., Billen, T., and Plate, E. J., Investigating the transfer process across the free aqueous viscous boundary layer by the controlled flux method. *Tellus* 41B, 177-195, 1989
- Kwan, J., and Taylor, P. A., On gas fluxes from small lakes and ponds. *Boundary-Layer Meteor.* 68, 339-356, 1994
- Merlivat, L., and Memery, L., Gas exchange across an air-water interface: experimental results and modeling of bubble contribution to transfer. *J. Geophys. Res.* 88, 707-724, 1983
- Merzi, N., Servos, M., and Donelan, M. A., *Description of an air-tight gas transfer flume and an experimental program for mass transfer at the air-water interface.* Tech. Rep. 90-147, National Water Research Institute, 1990
- Ocampo-Torres, F. J., Donelan, M. A., Merzi, N. and Jia, F., Laboratory measurements of mass transfer of carbon dioxide and water vapour for smooth and rough flow conditions. *Tellus* 46B, 16-32, 1994
- Palm, C. S., Anderson, R.C., and Reece, A. M., Laser probe for measuring 2-d wave slope spectra of ocean capillary waves. *Appl. Optics* 16, 1074-1081, 1977

Gas Transfer across a Wind-Driven Air-Water Interface and the Effects of Sea Water on CO₂ Transfer

S. Komori and T. Shimada

Department of Chemical Engineering, Kyushu University, Fukuoka 812-81, Japan

Abstract

The transfer mechanism of the carbon dioxide across a wind-driven air-water interface was investigated in terms of the turbulence structure in the interfacial region in a wind-wave tank. The CO₂ transfer velocity was measured against several wind speeds of $2 \text{ m/s} < U < 20 \text{ m/s}$ through desorption experiments in a wind-wave tank. To investigate the effects of natural sea water on the CO₂ transfer velocity, CO₂ absorption experiments were also carried out in a small oscillating-grid tank, and the CO₂ transfer velocities for five types of sea and fresh waters were measured. In addition to the measurements of the CO₂ transfer velocity, the frequency of appearance of surface renewal eddies was measured in both wind-wave and oscillating-grid tanks by means of a two-component laser Doppler velocimeter. The results show that the CO₂ transfer velocity rapidly increases with increasing wind speed or wind shear in the wind speed range of $U < 5 \text{ m/s}$, where capillary-like waves are present. However, the transfer velocity tends to level off in the high speed range ($5 \text{ m/s} < U < 12 \text{ m/s}$), where wind waves are rapidly developing. For higher wind speeds ($U > 12 \text{ m/s}$), the CO₂ transfer velocity again begins to increase rapidly. The behavior of the transfer velocity can be related to the variation of the frequency of the surface renewal eddies against the wind speed. It is also found that the CO₂ transfer velocity for sea water is damped to ~50% of the transfer velocity for fresh water. The reduction may be caused not by characteristic surface contaminants of sea water but by the effects of electrolytes apparently amplified by the presence of the invisible surface-active impurities common to both sea and fresh waters. From these results, the CO₂ transfer velocity across the air-sea interface was estimated by multiplying the transfer velocity measured in a wind-wave tank for fresh water by a factor of 0.5. The estimation suggests that the previous predictions based on the proportional relationship between the transfer velocity and the wind speed may underestimate the CO₂ exchange rate between the atmosphere and the ocean.

1 Introduction

It is of great importance to get more precise velocity of CO₂ transfer across the air-sea interface for estimating global atmospheric CO₂ budget, because the previous measurements of the CO₂ transfer velocity were uncertain. Although the CO₂ transfer velocity across the air-sea interface was measured

by a number of investigators in the field [Jähne, 1980; Roether and Kromer, 1984; Roether, 1986; Jähne et al., 1987; Watson et al., 1991], the field data were very scattered between investigations. The scattered data resulted in rough correlation that shows a linear proportionality between the transfer velocity and wind speed. In addition to the field measurements, a large number of laboratory measurements were conducted in wind-wave tunnels [e. g., Liss and Merlivat, 1986], but they also indicated a rough proportionality between the transfer velocity and wind speed or wind friction velocity. However, previous investigations could not physically explain the proportionality, and the proportional relation has been a mere best-fit curve for the measurements. Further, laboratory measurements have not been carefully compared with field measurements, since a quantitative disagreement between laboratory and field measurements was thought to be caused by the differences in both scale of the wind wave field and contamination of surface water [Broecker et al., 1986]. However, to discuss the differences, we should more quantitatively investigate how significantly surface contamination reduces the transfer velocity, before considering the difference of the wind wave field. Thus, important problems about both gas transfer mechanism across a wind-driven air-water interface and surface contamination need elucidation.

The purpose of this study is, therefore, to investigate the CO₂ transfer mechanism and the effects of sea water on the CO₂ transfer velocity through laboratory experiments. The CO₂ transfer velocity was measured in a wind-wave tank by carrying out the CO₂ desorption experiments, and instantaneous longitudinal and vertical velocities in both air and water flows were measured. To investigate the effects of the surface contamination, CO₂ absorption experiments were conducted for sea and fresh waters in a small oscillating-grid tank. From these laboratory measurements, the air-sea CO₂ transfer velocity was estimated, and they were compared with the field measurements.

2 Experiments

The first apparatus used in this study was a *wind-wave tank* with a glass test section which was 7 m long, 0.3 m wide and 0.8 m high. The water depth in the wind-wave tank was 0.5 m and the vertical height of the air flow above the air-water interface was 0.3 m. The details of the apparatus are described in Komori et al. [1993a, 1995]. Nonlinear three-dimensional waves with various conditions were driven in the wind-wave tank by winds with a free-stream velocity of $U = 2\text{--}20$ m/s. Wind waves intensively broke for a high free-stream velocity ($U > 14$ m/s), and many bubbles and spray droplets were entrained into water and air flows, respectively. The measurements were conducted in the region (*fetch*) of $x = 3\text{--}5$ m from the entrance ($x = 0$) of the test section. The effectiveness of the short fetch is discussed in Komori et al. [1993a, 1995] and Broecker et al. [1986]. Pure CO₂ was ex-

cessively dissolved into filtrated tap water of 20 °C stored in the wind-wave tank, and the CO₂ was desorped from water to air by wind effects. The CO₂ transfer velocity on the water side (k_L) was estimated by measuring the CO₂ desorption rate. The mean concentration of CO₂ desorped from water to air was measured vertically at two locations of $x = 3$ m and 5 m in the air flow by using two sampling tubes connected to the CO₂ analyzers (FUJI ELEC ZFP5). The analyzers employed infrared spectroscopy [Komori *et al.*, 1993a]. The bulk CO₂ concentration on the water side was measured using a sampling tube connected to a total organic carbon meter (SHIMAZU TOC-5000), and pH was measured by a pH meter (HORIBA F-16). From these concentration measurements, the desorption rate from water into air was estimated by taking the mass balance in the air flow, and the CO₂ transfer velocity on the water side was calculated by using the desorption rate and solubility of CO₂ in water. For small CO₂ fluxes, this measurement technique was superior to a conventional technique based on the CO₂ concentration measurements on the water side. However, mean CO₂ concentration measurements in air were limited to the wind speed range of $U < 14$ m/s because of many spray droplets entrained by intense wave-breaking. For the high wind speed range, the high mass transfer rate due to wave-breaking enabled us to estimate more precise CO₂ transfer rate by taking the mass balance on the water side. Thus, the desorption rate in the high wind speed range ($U > 14$ m/s) was estimated on the water side from the time derivative of the vertically-integrated value of the CO₂ concentration in the concentration boundary layer (i. e., by integrating the diffusion equation). The details of the CO₂ flux measurements are described in Komori *et al.* [1993a, 1995].

The second apparatus was an *oscillating-grid tank* with 0.5 m square cross section and 0.5 m water depth, similar to oscillating-grid tanks used in previous studies, e. g., Chu and Jirka [1992]; details of the apparatus are described in Komori *et al.* [1995]. Pure CO₂ or N₂O was filled in a 0.12 m-high, 0.5 m-square closed head-space over the air-water interface at the atmospheric pressure of 1 atm. An oscillating grid with the mesh size of 0.03 m and the rod diameter of 0.005 m was located at the depth of 0.09 m below the free surface and it was vertically oscillated at the stroke amplitude of 0.08 m and at a frequency of $\omega = 1.8$ –5.0 Hz. The oscillating conditions were determined to get the CO₂ transfer velocity for fresh water ranging from 1.0×10^{-5} m/s to 1.0×10^{-4} m/s that covers the measurements in a wind-wave tunnel. Five types of waters — pure water of pH = 6.2 (ion-exchange water), tap water of pH = 7.8 (filtered through a 5 μ m micropore filter), natural sea water of pH = 8.2 (sampled at the sea surface in the Tsushima Channel near Fukuoka city), artificial sea water of pH = 8.2 and saltwater of pH = 6.2 — were used in the oscillating-grid tank. The tank and grid were carefully washed to remove the contamination of the apparatus before each run by using plenty of pure water, and a constant value of the gas absorption rate was checked to confirm the same cleanliness of the apparatus before each run by carrying out pre-measurements of the gas absorption rate for pure

water. The CO₂ of 99.9% purity was mainly used as an absorption gas, but in some runs the N₂O of 99.9% purity was used to distinguish the effects of dissociation of CO₂ in water on the transfer velocity. The absorption rate per unit area was measured by a soap-film meter, and the gas transfer velocity k_L was calculated for the five waters.

Instantaneous longitudinal and vertical wind velocities in the air flow of $U < 14$ m/s in a wind-wave tank were measured at $x = 3$ m and 5 m by using a constant-temperature hot-wire anemometer (DANTEC 56C16) with a miniature X-probe (DANTEC 55P61). Longitudinal and vertical velocities in the water flow were measured using a two-color laser-Doppler velocimeter (DANTEC 55X) with a forward scattering mode for both wind-wave and grid-oscillating tanks. The frequency of appearance of large-scale surface renewal eddies was estimated by applying the variable interval time-averaging (VITA) technique to the instantaneous Reynolds stress signals in water flows [Komori *et al.*, 1993a, 1995].

3 Results and Discussion

3.1 CO₂ Transfer Mechanism across a Wind-Driven Air-Water Interface

Figure 1 shows the variation of the CO₂ transfer velocity k_L with wind speed U and friction velocity u_* together with previous measurements in a number of small and large wind-wave tunnels. Here, the friction velocity in air (u_*) was estimated from the measured values of the Reynolds stress in the interfacial region, and U and u_* were well correlated by $u_* = 0.02U^{1.5}$ [Komori *et al.*, 1993a]. Note that the previous measurements are plotted only against u_* . The present CO₂ transfer velocities rapidly increase with increasing U or u_* in the low wind speed region of $2 \text{ m/s} < U < 5 \text{ m/s}$ ($0.06 \text{ m/s} < u_* < 0.22 \text{ m/s}$), where capillary-gravity waves are present.

At $U = 5$ m/s, k_L reaches about ten times the values ($k_L < 2 \times 10^{-5}$ m/s) measured in open-channel flows with unsheared (zero-shear) air-water interfaces [Komori *et al.*, 1989, 1990]. This means that the mass transfer is intensively promoted in the presence of the interfacial wind shear. However, the increasing behavior of k_L becomes gentle in the high wind region of $U > 5$ m/s ($u_* > 0.22$ m/s), and k_L tends to level off. When the wind speed is over 12 m/s ($u_* > 0.83$ m/s), k_L again increases. In the high wind speed region, waves intensively broke, and many surface renewal (ripple-like) eddies with smaller scales than wave heights are generated. The wave-breaking phenomena may contribute to the rapid promotion of k_L in the region of $U > 12$ m/s ($u_* > 0.83$ m/s).

The behavior of the present measurements of k_L is rather different from the previous laboratory measurements against u_* in small [Liss, 1973; Mackay and Yeun, 1983; Plate and Friedrich, 1984; Jähne *et al.*, 1984] and large [Broecker *et al.*, 1978; Merlivat and Memery, 1983; Sivakumar, 1984; Jähne *et al.*, 1985] wind-wave facilities, and it does not at all follow the propor-

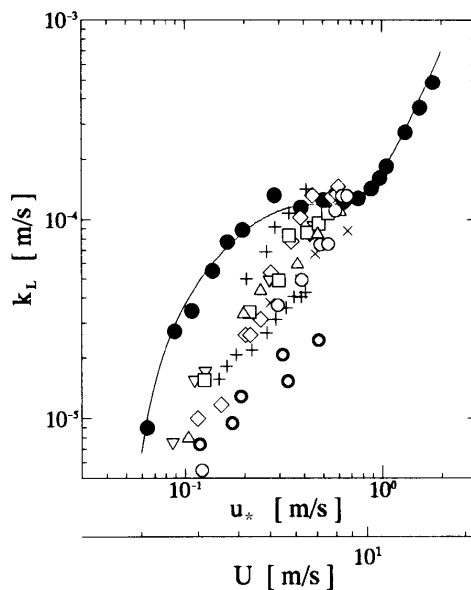


Figure 1: Comparison of the CO₂ transfer velocity between the present laboratory measurements (filled circles) and the previous laboratory measurements in large facilities by Broecker et al. [1978] (crosses), Merlivat and Memery [1983] (open squares), Sivakumar [1984] (open triangles) and Jähne et al. [1985] (open circles), and in small facilities by Liss [1973] (double circles), Mackay and Yeun [1983] (inclined crosses), Plate and Friedrich [1984] (open diamonds) and Jähne et al. [1984] (inverse open triangles). The solid line is a best-fit curve for the present measurements. The previous measurements are plotted only against the friction velocity u_* .

tionality between k_L and U . Although the previous measurements show the exponential increase against u_* , they are remarkably scattered among individual investigations. In particular, the previous data are smaller in the low wind speed region of $U < 6$ m/s ($u_* < 0.3$ m/s) than the present measurements. The difference may be caused by the measurement errors of gas flux due to two assumptions used in the previous experiments. The first is the assumption of the vertical homogeneity of the concentration field in the water flow beneath the interface, and most of the previous studies used the assumption to estimate CO₂ flux by taking the mass balance in the water flow [e.g., Wanninkhof and Bliven, 1991]. However, this assumption is wrong, since the CO₂ concentration gradient in the vertical direction was clearly observed up to the depth of 4-5 times the wave height. The presence of the concentration boundary layer is also indicated by Toba and Kawamura [1995]. The neglect of the vertical change of the concentration in the mass diffusion equation leads us to the underestimate of CO₂ flux, and in particular the effect may become significant in the low wind speed region

far from the well mixed condition. In fact, our estimation showed that the previous method underestimates about 70% at $U = 6.5$ m/s, compared to the present measurements of k_L . However, even if we consider the vertical change of the CO₂ concentration in the mass diffusion equation on the water side, the time derivative of the concentration in the boundary layer is small in the low speed region of $u_* < 0.8$ m/s, compared to the time derivative of the bulk concentration because of the small CO₂ exchange rate between air and water [Komori *et al.*, 1995]. This also led us to underestimate the mass flux in the low wind speed region. The second assumption is often used for experiments in recirculating wind-wave tunnels. In recirculating wind-wave tunnel experiments, the CO₂ flux was estimated from the long-time variation of the concentration of the CO₂ in well mixed bulk air or water, and the assumption of the constant flux over the whole test section was used. However, the CO₂ flux significantly changes in the inlet and outlet region where wind waves are not developed or deformed. That is, the estimation method on the second assumption gives an averaged value of k_L over the whole test section and the value may not reflect the exact behavior of k_L against U or u_* . Thus, the present estimation method based on the mass balance at two sections in the air flow is thought to be the most reliable way to estimate the CO₂ flux in the low wind speed region.

A kink of k_L in Figure 1 may be caused by the transition from two dimensional to three dimensional waves [Komori *et al.*, 1993a]. When the behavior of the present k_L is compared with that of the drag coefficient γ_{10}^2 by Toba and Kunishi [1970], it is found in Figure 2 that both behaviors against the Reynolds number based on u_* and wave height H well agree each other. Especially, the Reynolds number ranges showing the level-off agree well between k_L and γ_{10}^2 . Recent direct field measurements of k_L by an eddy correlation method [Donelan and Drennan, 1995] also showed a similar kink in the wind speed region of $7 \text{ m/s} < U < 12 \text{ m/s}$. These facts suggest that the present measurements of k_L are more reliable than the previous measurements.

The behavior of k_L in the region of $U < 12$ m/s ($u_* < 0.83$ m/s) can also be explained by estimating the frequency (f_S) of appearance of large-scale surface renewal eddies which predominate the mass transfer across the air-water interface [Komori *et al.*, 1993a, b]. Figure 3 shows the variation of $f_S^{1/2}$ against u_* or U . The solid line shows the values of f_S obtained from both the relation between k_L and u_* in Figure 1 and an empirical correlation between k_L and f_S based on the surface renewal concept:

$$k_L = 0.34\sqrt{D_L f_S}, \quad (1)$$

where D_L is the molecular diffusivity of CO₂ in water. Equation (1) was confirmed for both the present sheared interfaces and previous unsheread interfaces [Komori *et al.*, 1989, 1990, 1993a]. The variation of $f_S^{1/2}$ is quite similar to that of k_L in the region of $U < 12$ m/s ($u_* < 0.83$ m/s), and the

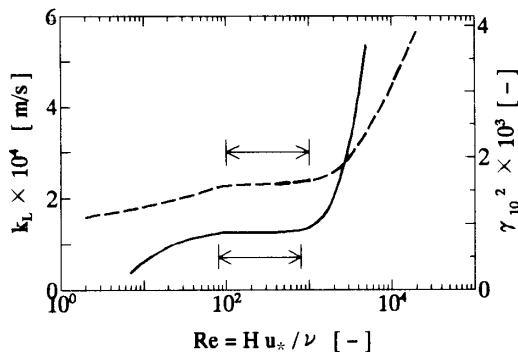


Figure 2: Comparison of the CO₂ transfer velocity k_L with the drag coefficient γ_{10}^2 of Toba and Kunishi [1970] (Komori et al. [1995]). The solid and dashed lines indicate best-fit curves for the present measurements of k_L and the measurements of the drag coefficient γ_{10}^2 by Toba and Kunishi [1970], respectively.

estimated values of $f_S^{1/2}$ well agree with the measured values. This means that the behavior of k_L is fluid-mechanically determined by the frequency of the surface renewal eddies. In the high wind speed region of $U > 12$ m/s ($u_* > 0.83$ m/s), the measured values of $f_S^{1/2}$ become smaller than the estimated values. The difference may be caused by the rapid promotion of the CO₂ transfer by a great number of ripple-like surface renewal eddies generated by intense wave-breaking. However, scales of the ripple-like eddies were smaller than half of wave heights, and the ripple-like motions could not be detected by means of the present velocity measurement technique below the valleys of the waves. This may result in the difference between the measured and predicted values of $f_S^{1/2}$ in Figure 3. Although the rapid increase of k_L in the high wind speed region is generally thought to be due to the entrainment of bubbles and spray droplets into the water and air flows, the amounts of bubbles and spray droplets may not be large enough to rapidly promote k_L . This will be clarified in our future work.

3.2 Difference of CO₂ Transfer Velocity between Sea and Fresh Waters

Figure 4 shows the variations of the CO₂ transfer velocity k_L for five waters at 13 °C against the oscillating frequency of grid ω . No differences are seen both between pure and tap waters and among natural sea water, artificial sea water and 0.62 mol/l (3.5 wt%) saltwater. Here, 3.5 wt% corresponds to 35 ‰. However, the transfer velocity for sea and salt waters (k_{LS}) is reduced to $\sim 50\%$ compared to that for fresh waters (k_{LF}), i.e., $k_{LS} = 0.5 k_{LF}$. These facts suggest that the effects of characteristic surface contaminant of natural sea water or tap water [Frew et al., 1990; Asher and Pankow, 1991] on the

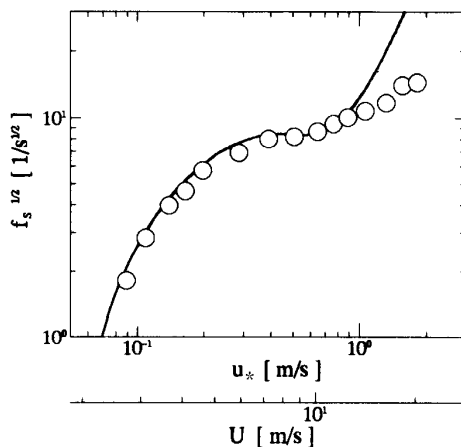


Figure 3: The square root of the frequency of appearance of surface renewal eddies as a function of the wind speed or the friction velocity [Komori et al., 1995]. The solid line shows the values estimated from (1) and the measurements of k_L in Figure 1.

transfer velocity can be neglected and the reduction of the transfer velocity is caused by any other reasons.

We first suppose two reasons; the effect of dissociation of CO_2 in sea and salt waters and the decrease of the molecular diffusivity due to the presence of electrolytes of Na^+ and Cl^- . In order to investigate the former effect, the transfer velocity ($k_{L,\text{N}_2\text{O}}$) of N_2O being undissociated in water was measured for pure and tap waters and 0.62 mol/l (3.5 wt%) saltwater. Figure 5 shows the comparisons of the CO_2 transfer velocity k_{L,CO_2} with $k_{L,\text{N}_2\text{O}}$ at the same oscillating frequency of grid ω . The proportionality between $k_{L,\text{N}_2\text{O}}$ and k_{L,CO_2} suggests that the dissociation of CO_2 is irrelevant to the reduction of k_L for sea and salt waters. Thus, the reason of the reduction of k_L for sea and salt waters may be focused on the change of the molecular diffusivity (D_L) due to the presence of electrolytes.

For air-water interfaces with not so weak liquid turbulence, k_L is proportional to $D_L^{1/2}$ [Wanninkhof et al., 1984; Watson et al., 1991; Chu and Jirka, 1992]. When the relation is applied to the present measurements, the fact of $k_{LS} = 0.5 k_{LF}$ leads to an assumption that the molecular diffusivity (D_{LS}) for sea and 0.62 mol/l (3.5 wt%) salt waters should be reduced to 25% of the molecular diffusivity (D_{LF}) for fresh waters, i. e., $D_{LS} = 0.25 D_{LF}$. According to the previous literature [Ratcliff and Holdcroft, 1963; Hikita et al., 1979; Yasunishi and Yoshida, 1978], D_{LS} is, however, about 95% of D_{LF} ($D_{LS} = 0.95 D_{LF}$). This suggests that the molecular diffusivity at the present air-water interfaces is apparently reduced by other factors in addition to the effects of electrolytes. To investigate other factors, the CO_2 transfer velocity in Figure 4 is replotted in Figure 6 against the frequency

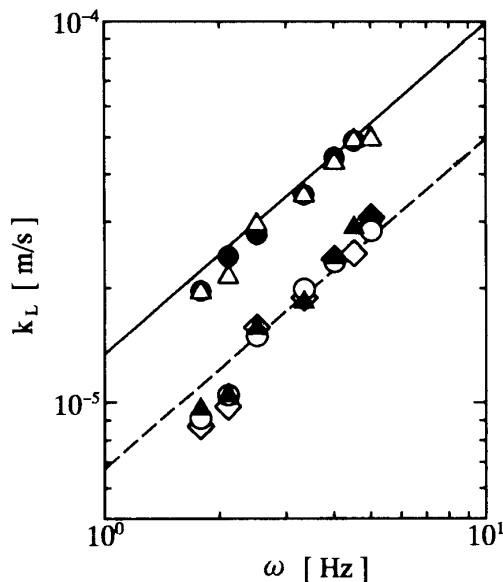


Figure 4: Variations of the CO₂ transfer velocity for five waters against the oscillating frequency of grid ω : tap water (filled circles), pure water (open triangles), 0.62 mol/l (3.5 wt %) saltwater (open circles), natural sea water (filled triangles) and artificial sea water (open diamonds). The solid line corresponds to the values calculated from (1) by using an empirical relation of $f_S = 1.14\omega^{1.74}$. The dashed line indicates the values of the solid line multiplied by 0.5.

of appearance of the surface renewal eddies f_S . The measured values of f_S were approximately correlated by $f_S = 1.14\omega^{1.74}$. The proportional relationship between k_L and $f_S^{1/2}$ showing the surface renewal concept is also applicable to the measurements in the oscillating-grid tank, and it is the same as (1) obtained in a wind-wave tank. However, for a really clean interface, a proportional constant in (1) is not 0.34 but it will be close to 1.0 as predicted by a cyclic eddy-cell model [Komori *et al.*, 1993a].

The difference between the proportional constants suggests that the apparent molecular diffusivity at the interface is reduced due to invisible tiny surface-active impurities that naturally cover the flat water surface and cannot be removed even by careful washing of the apparatus. Of course, if such extreme care as distillation of water or suction of surface water which is common in chemical engineering studies is taken, such contamination will be removed. However, really clean surfaces are not present in natural oceans, lakes or rivers, and such clean surfaces are no longer useful for estimating the air-sea transfer velocity from laboratory measurements. Because the tap water at best can be used in wind-wave tunnel experiments for air-sea interaction studies. Fortunately the present results in Figures 4 and 6

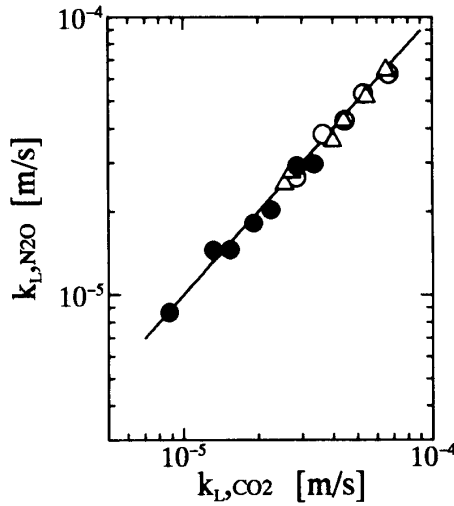


Figure 5: Comparison between the CO_2 transfer velocity k_{L,CO_2} and the N_2O transfer velocity $k_{L,\text{N}_2\text{O}}$ at the same oscillating frequency of grid ω . The open circles, the open triangles and the filled circles indicate the measurements for pure water, tap water and 0.62 mol/l (3.5 wt%) saltwater, respectively. The solid line shows the relation of $k_{L,\text{CO}_2} = k_{L,\text{N}_2\text{O}}$.

suggest that the surface-active impurities are equally involved in both fresh and sea waters, and they do not violate the proportionality between k_L and f_S in (1). Therefore, the present measurements affected by the impurities are more useful for estimating the air-sea transfer velocity than those for the really clean interface. Thus, we assume the apparent molecular diffusivity D_{La} at the interface by

$$D_{La} = D_L - D_{Lc}, \quad (2)$$

where D_L is the real molecular diffusivity at the really clean interface which is given in the previous literature and D_{Lc} is the reduction effect due to the surface-active contaminants. The ratios of $k_{LS}/k_{LF} = 0.5$ and $D_{LS}/D_{LF} = 0.95$ together with $k_L \propto (D_{La}f_S)^{1/2}$ give the value of $D_{Lc} = 0.93 D_{LF}$ under the assumption that D_{Lc} has a constant value in both sea and fresh waters. This suggests that the molecular diffusivity and the CO_2 transfer velocity at the present interfaces are apparently reduced to about 7% and 26%, compared to the values for the really clean interfaces, respectively. The constant (1) is also estimated to be 1.29 for the really clean interface. In particular, it should be noted that the reduction of the transfer velocity due to the surface-active impurities is in good agreement with the previous result that the invisible surface-active impurities reduce the gas transfer velocity to

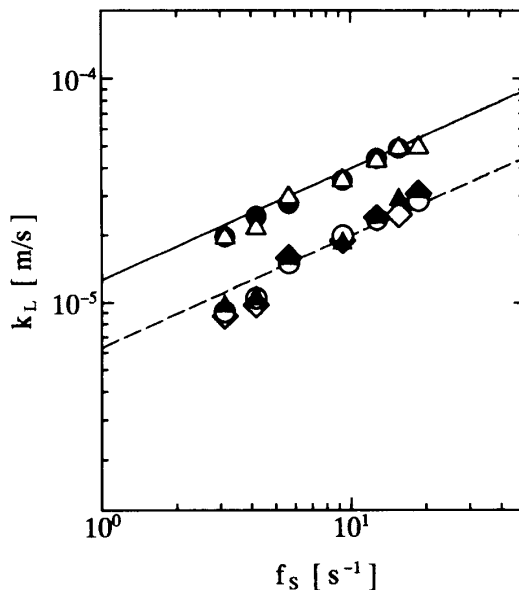


Figure 6: Variations of the CO₂ transfer velocity for five waters against the frequency of appearance of the surface renewal eddies f_s : tap water (filled circles), pure water (open triangles), 0.62 mol/l saltwater (open circles), natural sea water (filled triangles) and artificial sea water (open diamonds). The solid shows (1). The dashed line indicates the values of the solid line multiplied by 0.5.

27.6% in an agitated vessel [Fujinawa *et al.*, 1978].

The assumption in (2) that D_{LC} has a constant value equal to $0.93 D_{LF}$ can be verified by measuring the CO₂ transfer velocity against several salt concentrations. Figure 7 shows the ratio of the CO₂ transfer velocity for saltwater to that for fresh water (k_{LS}/k_{LF}) against the salt concentration C_s (mol/l). The solid line was obtained from (2) by using a best-fit curve for the real molecular diffusivities ratio D_{LS}/D_{LF} ($= 1 - 0.084 C_s$) [Ratcliff and Holdcroft, 1963; Hikita *et al.*, 1979; Yasunishi and Yoshida, 1978]. The measurements of k_{LS}/k_{LF} approximately support the assumption used in (2) in the salt concentration range of $C_s \leq 0.6$ mol/l, though the assumption becomes in-applicable in the high concentration range of $C_s > 0.6$ mol/l.

Thus, it is inferred that the remarkable decrease of k_{LS} is caused by the effects of the electrolytes that are apparently amplified by the presence of the surface-active impurities common to both sea and fresh waters. Of course, the above inference is very controversial, since it cannot directly be proved without using a sophisticated technique for seeing micro structure at the interface. However, the present results warn that the CO₂ air-sea transfer velocity conventionally estimated by using the relation $k_L \propto D_L^{1/2}$ from k_L of

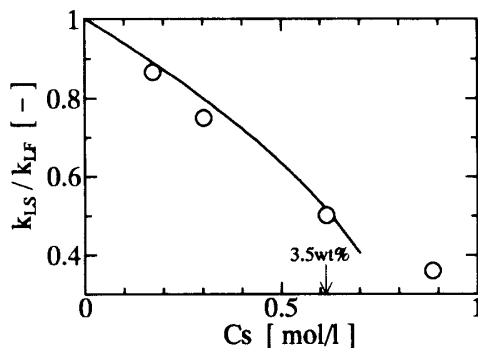


Figure 7: Variation of the ratio (k_{LS}/k_{LF}) of the CO_2 transfer velocity for saltwater to that for pure water against the salt concentration C_s . The open circles shows the measurements. The solid line indicates the ratio derived from (2) and the molecular diffusivity ratio D_{LS}/D_{LF} ($=1 - 0.084 C_s$).

other gases or tracers may include a significant error. To estimate the CO_2 transfer velocity by using the relation $k_L \propto D_{La}^{1/2}$, the apparent diffusivity D_{La} at the interface should be estimated for other gases.

3.3 Estimation of Air-Sea CO_2 Transfer Velocity

By using the above relation of $k_{LS} = 0.5 k_{LF}$ into k_L measured in the present wind-wave tank with tap water, the CO_2 transfer velocity across the air-sea interface may be estimated, since the temperature dependency on the ratio of k_{LS} to k_{LF} is very small. However, it should be investigated in a future study whether the relation of $k_{LS} = 0.5 k_{LF}$ obtained for non-breaking waves in the oscillating-grid tank is applicable to intensive breaking-waves in the high wind speed region of $U > 14$ m/s or not. Although this question has not been cleared, the CO_2 transfer velocity across the air-sea interface was estimated by using the relation of $k_{LS} = 0.5 k_{LF}$.

Figure 8 shows the estimated values together with the previous field measurements [Jähne, 1980; Roether and Kromer, 1984; Roether, 1986; Jähne *et al.*, 1987; Watson *et al.*, 1991] against the wind speed U . Here, for the previous measurements arranged only against u_* , U is estimated by $u_* = 0.02U^{1.5}$ [Komori *et al.*, 1993a], since the relation of $u_* = 0.02U^{1.5}$ was also confirmed in the field as shown by the measurements of Mitsuyasu *et al.* [1971]. The present estimated values stand among scattered previous field measurements, but they are larger than the estimation of Liss and Merlivat [1986] shown by the dashed line in Figure 8, especially in the region of $U < 12$ m/s ($u_* < 0.83$ m/s). The best-fit curve for the present estimated values is given by

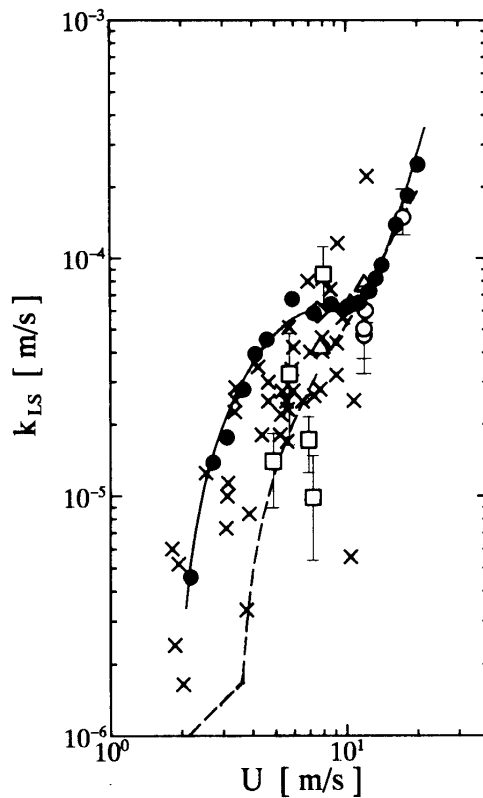


Figure 8: Comparison between the present laboratory estimated values of the air-sea CO₂ transfer velocity (filled circles) and the previous field measurements by Watson et al. [1991] (open circles), Roether [1986] (open triangles), Roether and Kromer [1984] (open squares), Jähne et al. [1987] (open diamonds), and Jähne [1980] (inclined crosses). The solid line shows a best-fit curve in (3) for the present estimated values, and the dashed line indicates the proportional relationship between U and k_L by Liss and Merlivat [1986].

$$k_{LS} = \begin{cases} 1.0031 \times 10^{-4} - 1.5157 \times 10^{-4} u_* + 1.3765 \times 10^{-4} u_*^2 & u_* > 0.5 \text{ m/s} \\ -2.5822 \times 10^{-5} + 5.5598 \times 10^{-4} u_* - 1.3059 \times 10^{-3} u_*^2 + 1.2459 \times 10^{-3} u_*^3 - 3.9019 \times 10^{-4} u_*^4 & u_* \leq 0.5 \text{ m/s} \end{cases} \quad (3)$$

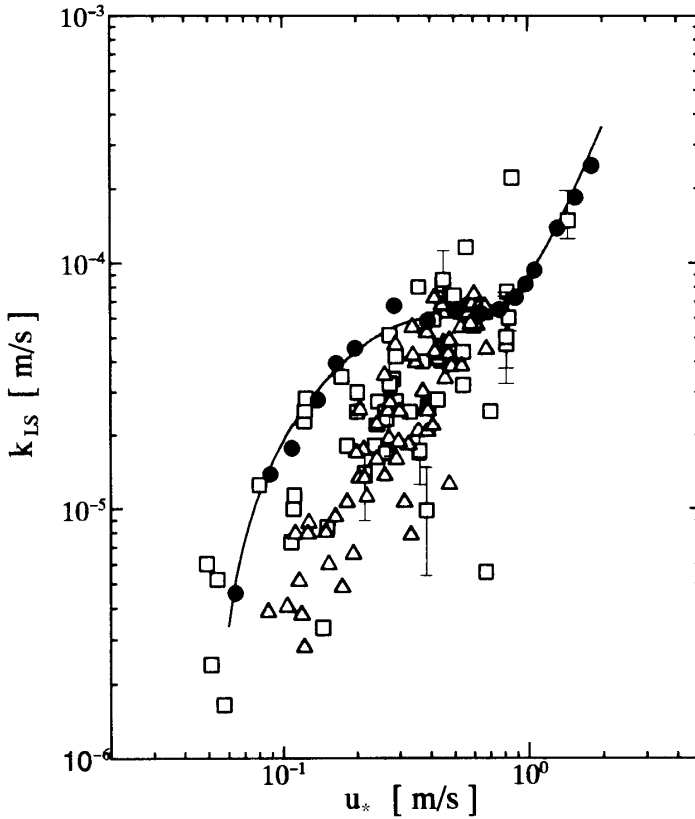


Figure 9: Comparison of the present (filled circles) and previous (open triangles) laboratory estimated values of the air-sea CO_2 transfer velocity with the previous field measurements (open squares). The solid line shows a best-fit curve in (3) for the present estimated values.

Furthermore, the previous laboratory measurements can be compared with the previous field measurements by using the relation of $k_{LS} = 0.5 k_{LF}$ as shown in Figure 9. Here, the field and laboratory measurements are shown by open squares and triangles without distinguishing each investigation, respectively, and the field data except for *Jähne* [1980] are plotted by using the relation of $u_* = 0.02U^{1.5}$. Although the data are scattered, the laboratory measurements corrected by the relation of $k_{LS} = 0.5 k_{LF}$ seem to span the field measurements. These results may support the independence of the wave field scale on the transfer velocity arranged by the friction velocity as well as in *Broecker et al.* [1986], although it is uncertain whether the friction velocity is only a predominant parameter or not.

4 Conclusions

The transfer mechanism of CO₂ across a wind-driven air-water interface and the difference of the CO₂ transfer velocity between fresh and sea waters were investigated through CO₂ desorption and absorption experiments in wind-wave and oscillating-grid tanks, respectively.

The CO₂ transfer velocity increased with increasing U in the wind speed region of $U < 5$ m/s, and it rapidly increased in the wave-breaking region of $U > 12$ m/s. However, the transfer velocity leveled off in the intermediate region of $5 \text{ m/s} < U < 12 \text{ m/s}$. The behavior of the level-off was quite different from previous measurements, but it was quite similar to the previous measurements of the drag coefficient in wind-wave tunnels.

The CO₂ transfer velocity for natural sea water was reduced to $\sim 50\%$ compared to that for fresh water. We inferred that the reduction is caused by the effects of electrolytes that are apparently amplified by the presence of the invisible surface-active impurities common to both sea and fresh waters, not by characteristic surface contaminants of sea water.

The transfer velocity across the air-sea interface was estimated by multiplying the CO₂ transfer velocity for fresh water measured in a wind-wave tank by a factor of 0.5. The estimated values were larger than the estimation by *Liss and Merlivat* [1986] in the wind speed region of $U < 10$ m/s.

Acknowledgments

The authors would like to thank Prof. Y. Murakami for his support on this study. This research was supported by the Japanese Ministry of Education, Science and Culture through Grants-in-Aid (No. 07455087).

References

- Asher, W. E. and J. F. Pankow, Prediction of gas/water mass transport coefficient by a surface renewal model, *Environ. Sci. Technol.*, 25, 1294-1300, 1991
- Broecker, H.-C., J. Petermann and W. Siems, The influence of wind on CO₂-exchange in a wind/wave tunnel, including the effects of monolayers, *J. Mar. Res.*, 36, 595-610, 1978
- Broecker, W. S., J. R. Ledwell, T. Takahashi, R. Weiss, L. Merlivat, L. Memery, T. H. Peng, B. Jähne and K. O. Münnich, Isotopic versus micrometeorologic ocean CO₂ fluxes: a serious conflict, *J. Geophys. Res.*, 91, 10517-10527, 1986
- Chu, C. R. and G. H. Jirka, Turbulent gas flux measurements below the air-water interface of a grid-stirred tank, *Int. J. Heat Mass Transfer*, 35, 1957-1968, 1992
- Donelan, M. A. and W. M. Drennan, Direct field measurements of the flux of carbon dioxide, *This volume*
- Frew, N. M., J. C. Goldman, M. R. Dennett and A. S. Johnson, Impact of phytoplankton-generated surfactants on air-sea gas exchange, *J. Geophys. Res.*, 95, 3337-3352, 1990

- Fujinawa, K., M. Hozawa and N. Imaishi, Effects of desorption and absorption of surface tension-lowering solutes on liquid-phase mass transfer coefficients at a turbulent gas-liquid interface, *J. Chem. Eng. Japan*, *11*, 107-111, 1978
- Hikita, H., S. Asai, H. Ishikawa, M. Seko and H. Kitajima, Diffusivities of carbon dioxide in aqueous mixed electrolyte solutions, *Chem. Eng. J.*, *17*, 77-80, 1979
- Jähne, B., Zur Parameterisierung des Gasaustausches mit Hilfe von Laborexperimenten, Dissertation, Institut für Umweltphysik, University of Heidelberg, 1980
- Jähne, B., W. Huber, A. Dutzi, T. Wais and J. Ilmberger, Wind/wave tunnel experiments on the Schmidt number and wave field dependence of air-water gas exchange, in *Gas Transfer at Water Surfaces*, edited by W. Brutsaert and G. H. Jirka, pp.303-309, Reidel, 1984
- Jähne, B., T. Wais, L. Memery, G. Gaulliez, L. Merlivat, K. O. Münnich and M. Coantic, He and Rn gas exchange experiments in the large wind/wave facility of IMST, *J. Geophys. Res.*, *90*, 11989-11997, 1985
- Jähne, B., G. Heinz and W. Dietrich, Measurements of gas exchange and momentum transfer in a circular wind-water tunnel, *J. Geophys. Res.*, *92*, 10767-10776, 1987
- Komori, S., Y. Murakami and H. Ueda, The relationship between surface-renewal and bursting motions in an open-channel flow, *J. Fluid Mech.*, *203*, 103-123, 1989
- Komori, S., R. Nagaosa and Y. Murakami, Mass transfer into a turbulent liquid across the zero-shear gas-liquid interface, *AIChE J.*, *36*, 957-960, 1990
- Komori, S., R. Nagaosa and Y. Murakami, Turbulence structure and mass transfer across a sheared air-water interface in a wind-driven turbulence, *J. Fluid Mech.*, *249*, 161-183, 1993a
- Komori, S., R. Nagaosa and Y. Murakami, Direct numerical simulation of three-dimensional open-channel flow with zero-shear gas-liquid interface, *Phys. Fluids A*, *5*, 115-125, 1993b
- Komori, S., T. Shimada and Y. Murakami, Laboratory estimation of CO₂ transfer velocity across the air-sea interface, in *Biogeochemical Processes and Ocean Flux in the Western Pacific*, edited by H. Sakai and Y. Nozaki, Terra Sci., Tokyo, 1995 (in press)
- Liss, P. S., Processes of gas exchange across an air-water interface, *Deep-Sea Res.*, *20*, 221-238, 1973
- Liss, P. S. and L. Merlivat, Air-sea gas exchange rates: introduction and synthesis, in *The Role of Air-Sea Exchange in Geochemical Cycling*, edited by P. Buat-Menard, pp.113-127, Reidel, 1986
- Mackay, D. and A. T. K. Yeun, Mass transfer coefficient correlations for volatilization of organic solutes from water, *Environ. Sci. Technol.*, *17*, 211-217, 1983
- Merlivat, L. and L. Memery, Gas exchange across an air-water interface; experimental results and modeling of bubble contribution to transfer, *J. Geophys. Res.*, *88*, 707-724, 1983
- Mitsuyasu, H., R. Nakayama and T. Komori, Observations of the wind and waves in Hakata bay, *Rep. Res. Inst. Appl. Mech.*, Kyushu Univ., *XIX*, 37-67, 1971
- Plate, E. J. and R. Friedrich, Reaeration of open channel flow, in *Gas Transfer at Water Surfaces*, edited by W. Brutsaert and G.H. Jirka, pp.333-346, Reidel, 1984
- Ratcliff, M. A. and J. G. Holdcroft, Diffusivities of gases aqueous electrolyte solutions. *Trans. Instn. Chem. Engrs.*, *41*, 315-319, 1963

- Roether, W. and B. Kromer, Optimum application of the radon deficit method to obtain air-sea gas exchange rates, in *Gas Transfer at Water Surfaces*, edited by W. Brutsaert and G. H. Jirka, pp. 447-457, Reidel, 1984
- Roether, W., Field measurements of gas exchange, in *Dynamic Processes in the Chemistry of the Upper Ocean*, edited by J. D. Buroton, P. G. Brewer and R. Chesselet, pp. 117-128, Plenum Press, 1986
- Sivakumar, M., Reaeration and wind induced turbulence shear in a contained water body, in *Gas Transfer at Water Surfaces*, edited by W. Brutsaert and G. H. Jirka, pp. 369-377, Reidel, 1984
- Toba, Y. and H. Kunishi, Breaking of wind waves and the sea surface wind stress, *J. Oceanogr. Soc. Japan*, 26, 71-80, 1970
- Toba, Y. and H. Kawamura, Wind-wave coupled downward-bursting boundary layer below the sea surface — in relation to penetration depth of bubble clouds, *this volume*
- Wanninkhof, R. H. and L. F. Bliven, Relationship between gas exchange, wind speed, and radar backscatter in a large wind-wave tank, *J. Geophys. Res.*, 96, 2785-2796, 1991
- Watson, A. J., R. C. Upstill-Goddard and P. S. Liss, Air-sea gas exchange in rough and stormy seas measured by a dual-tracer technique. *Nature*, 349, 145-147, 1991
- Yasunishi, A. and F. Yoshida, Diffusivities of carbon dioxide in aqueous solution of electrolytes, *Kagaku Kogaku*, 4, 190-194, 1978

Surface Deformation Measurement with Optical Sensor and Correlation with Reaeration Coefficient

Woodrow N. L. Roma

University of Sao Paulo, CP 359,
13560-970, Sao Carlos, SP, Brazil

Abstract

An optical sensor, for the detection of surface turbulence deformation was developed and used over two different turbulence generation systems. The sensor was built with a light beam emitter above the water surface collimated with a photo sensor under the surface. The electrical signal measured from the photo sensor is modulated by the water deformation, and presents a random behavior like the turbulence that generates the surface deformation. The statistical parameters calculated from the electrical signal have some correlation with the reaeration coefficient.

1 Introduction

Many authors are concerned with the *reaeration* problem in natural waters, mainly in the context of water quality. Several studies were performed looking for a way to quantify the reaeration coefficient as a function of the water turbulence. The instruments mostly used for this line of research have been the hot film anemometer and laser Doppler velocimetry, which can only measure water velocity far from the surface. The objective in this research has been the detection of the surface deformation that is associated with turbulent surface renewal.

2 Theoretical Considerations

The sensor is based upon the refraction of light crossing a surface separating two different media. The light path, vertical and uniform on the air side, is shifted when it crosses the surface and enters the water side, reaching a photo sensor with additive, or subtractive, behavior depending on the orientation of the spot where it strikes the surface. Figure 1 shows this behavior in a very simplified manner, using a bi-dimensional view of the physical model. As the system is a three-dimensional one, and has some axial symmetry, it is convenient to study it using cylindrical coordinates.

When the turbulence presents an upward movement, causing a *surface renewal* just over the sensor, there is an associated *surface deformation* building a topography that produces light scattering under the water surface. This scattered pattern of light rays will reach the sensor to produce

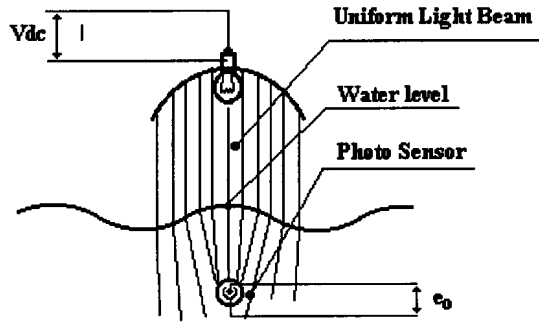


Figure 1: Simplified operating principle of the surface deformation optical sensor.

an electrical signal modulated by the surface deformation. If the sensor was a single point then its frequency resolution would be very narrow and the optical sensor would discriminate only a single frequency present in the turbulence, but, due to the sensor size being quite different from zero, several frequencies are present in the signal.

As the interface deformation comes from the energy of the turbulence near the surface, the modulated electrical signal produced contains information of the turbulence statistical parameters, and can be used to quantify the turbulence-dependent parameters.

Any surface element on the area over the sensor will contribute to the sensor signal if it has the correct angle with respect to the normal. This angle depends on the position from the center axis. Figure 2 presents the cylindrical coordinates over the measurement area. It is possible to observe that the closer to the center, the smaller is the correct angle of the surface that contributes to the sensor illumination. So the total amount of light on the sensor is given by the summation of all the light beams that reach the sensor, thus:

$$I_t = \int_A P(\alpha) I dA, \quad (1)$$

where $P(\alpha)$ is the probability that the element dA has the correct angle for light contribution. As I is a constant then the illumination I_t is given by

$$I_t = I \int_A P(\alpha) dA, \quad (2)$$

the integral representing the probability of the formation of a whole contributing pattern on the measurement area.

On the other hand, the Bernoulli equation can be applied between two points at the same vertical, in the near surface region, with one of them coincident with the surface position. Vertical velocity w' , at the point under

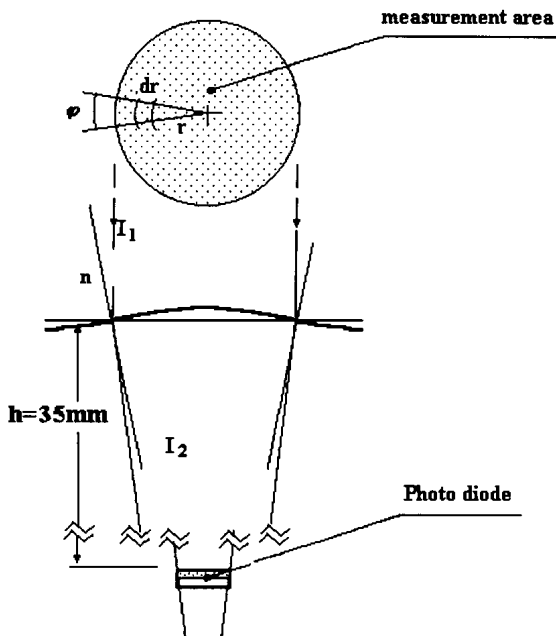


Figure 2: Path of light ray crossing the deformed surface on the measurement area.

the surface will reach the interface and be reduced to zero. Consequently, its energy will be converted to surface deformation, raising it. Then

$$\frac{w'^2}{2} = gz \quad (3)$$

This means that if w' must be zeroed at the surface, then the surface must suffer a deformation. Thus a measure of the surface deformation evolution contains information on the *RMS* value of the vertical velocity fluctuation w' , with consequent information on the random renewal distribution.

Jähne [1990] had detected that the surface deformation is small, with slope angles at the free surface less than 10° , so that it is possible, with a maximum deformation on the sensor area and using the refraction index for an air-water interface, the contribution area, for a 3.5 cm depth of the sensor, is close to 8 mm in diameter. Small deformations also contribute to the sensor illumination, due to its finite area.

As an ascending submerged jet causes a surface deformation that can be well represented by the Gaussian curve, we adopted this model to represent the small deformation caused by an upward velocity fluctuation w' .

A vertical light ray refracted by the surface will reach the sensor, adding to other rays, and the intensity of the illumination will depend on the amount of light that reaches the sensor, depending, thus, on the surface area that

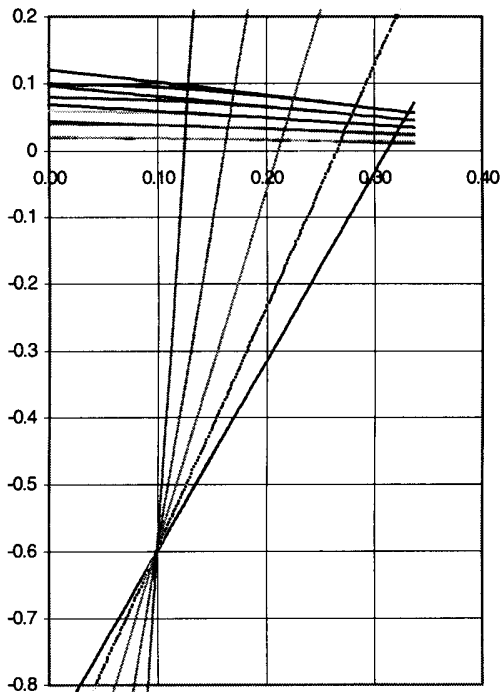


Figure 3: Refraction of light in a deformed surface.

contributes to the sensor illumination. The dependence upon the deformation height z was numerically investigated through a simulation of Snell's Law implemented in a spreadsheet. Figure 3 shows the graphical behavior obtained from a simulation of five different deformation heights z . As the illumination depends on the number of light rays reaching the sensor, it depends on the contributing area. Figure 4 shows the linear dependence between the elevation z and the radius R of the contributing area for the adopted model.

As the sensor presents a linear behavior, with the electric signal E proportional to the illumination I , then E must be linear with the contributing area, and so with the square of the radius. So we can write

$$w' = \kappa E^{0.25} \quad (4)$$

where κ is a constant.

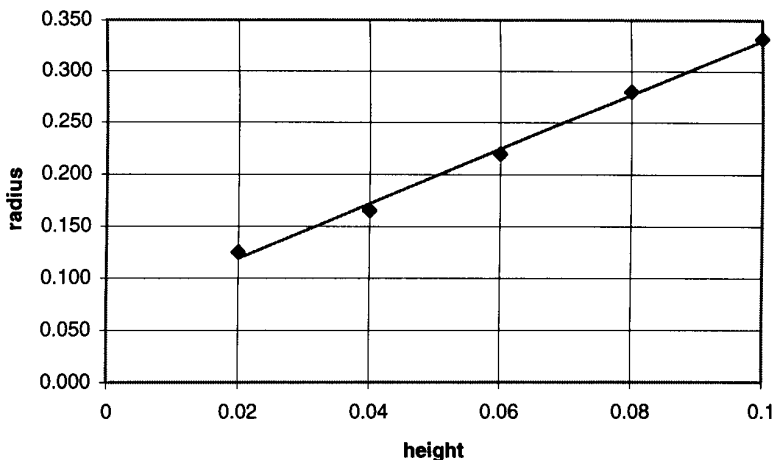


Figure 4: Linear dependence between illumination radius and height of surface deformation.

3 Experiments with the Optical Sensor

The optical sensor for measurement of the surface deformation in free surface turbulent flows is under experimental study and was used, until now, in two different turbulent systems to get some knowledge about its behavior. The first experiments were performed in a *stirred grid tank* for turbulence generation, Roma [1988]. This experiment was conducted in a $0.5 \times 0.5 \times 0.8$ m³ grid stirred tank, similar to the one used by *Brumley* [1984], with all measurements recorded in an 8 bit microcomputer. Data obtained in the grid stirred tank are shown in Figure 4, represented by square symbols. The horizontal axis represents the 0.25 power of the RMS value multiplied by the time scale, and the vertical axis represents the reaeration coefficient K_2 , in h^{-1} .

The second experiment was carried out in a circular tank agitated by rotating vanes, with the rotation rate varying from 60 to 276 rpm. Data from this measurement setup are represented in Figure 5 by dots.

4 Conclusion

The results depicted in Figure 5 show a good correlation between the electrical signal from the Deformation Optical Sensor and the reaeration coefficient K_2 . These are preliminary experiments with the sensor, and the improvement in the collecting data system for the second measurement set leads to a narrower dispersion with respect to the linear fit.

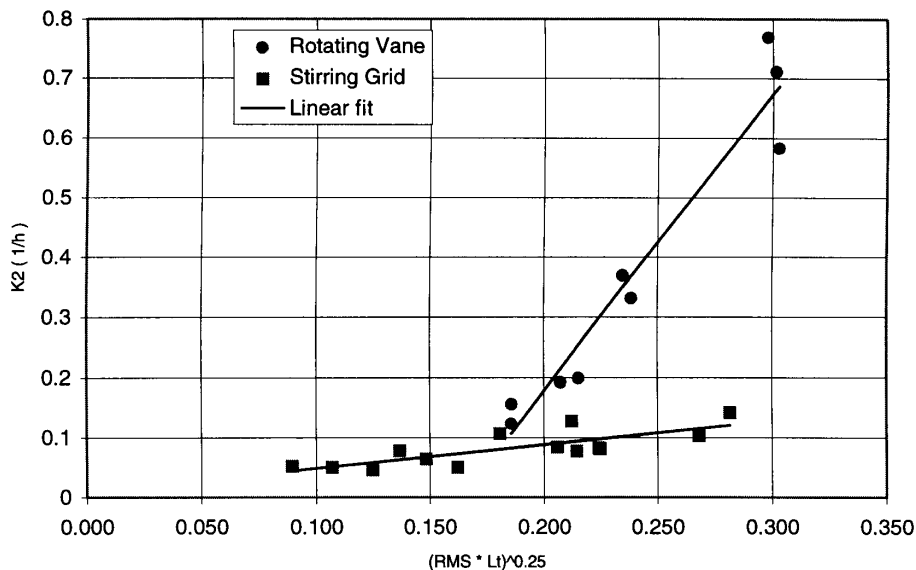


Figure 5: Correlation obtained between electrical signal from the Deformation Optical Sensor, and the reaeration coefficient K_2 . Squares are data measured in a grid stirred tank, and dots are data from a rotating vane tank.

Acknowledgements

We express our appreciation for the support granted by CNPq, Brazilian National Council for Scientific and Technological Development.

References

- Brumley, B., Turbulence measurements near the free surface in stirred grid experiments in gas transfer at water surface. In: Brutsaert, W. and Jirka, G. H. *Gas Transfer at Water Surface*, pp. 83-92, 1985
- Jähne, B., Libner, P., Billen, T., and Plate, E. J., Investigating the transfer Processes across the free aqueous viscous boundary layer by the controlled flux method. *Tellus*, 41B, 177-195, 1989
- Jähne, B., From mean fluxes to a detailed experimental investigation of the gas transfer process. In: Wilhelms, E. C. and Gulliver, J. S., *Air Water Mass Transfer*, ASCE, pp. 244-255, New York, 1990
- Maxwell, W. H. C. and Holley, E. R., A method for deaerating water. *Journal of the Hydraulics Division*, Vol. 95, No HY1, pp. 577-80, January, 1969
- Roma, W. N. L., Medida dos parametros de turbulencia na superficie da agua e sua relacao com o coeficiente de reaeracao. School of Engineering at Sao Carlos, Thesis, Sao Carlos, SP, BR, p. 62, 1988
- Thompson, J. S. and Turner, J. S., Mixing across an interface due to turbulence generated by an oscillating grid. *J. of Fluid Mech.*, 67, 349-368

The Air-Water Oxygen Transfer Coefficients with Waves Determined by Using a Modified Method

*Shohachi Kakuno, Mitsuru Saitoh,
Yoshihiro Nakata, and Kazuki Oda*

Dept. of Civil Engrg., Osaka City University
Osaka, Japan

Abstract

An experimental study on the air-water oxygen transfer coefficients air-water oxygen transfer through the still water surface, through the surfaces of non-breaking waves, and through breaker zone were carried out paying careful attention to the reaeration volume and the reaeration area in a wave tank. The reaeration volume in a wave tank was made by restricting a volume with vertical thin and loosely stretched film. The reaeration coefficients and the air-water oxygen transfer coefficients obtained with the present modified method are discussed.

1 Introduction

Dissolved oxygen in water is an essential matter not only for creatures inhabiting in the water but also for water quality and environmental pollution control related to organic matter. *Reaeration*, or air-water oxygen transfer through the sea surface, is one of the main sources of dissolved oxygen for surface waters in the sea.

Several studies are available on the air-water oxygen transfer through the surfaces of non-breaking waves or breakers generated in a wave tank. *Downing and Truesdale* [1955], *Hosoi, Ishida and Imoto* [1977], and *Daniil and Gulliver* [1991] investigated the air-water oxygen transfer through the surfaces of waves in a region of a constant water depth in a wave tank. In the experiments, however, it cannot be avoidable for experimental data to contaminate the effect of longitudinal dispersion caused by a wave maker or a wave absorber at an end of a wave tank. To overcome this unpreferable phenomenon, *Daniil and Gulliver* [1991] treated experimental data with an analysis of the longitudinal dispersion in a wave tank. *Hosoi et al.* [1977], on the other hand, measured dissolved oxygen concentration in a restricted volume made by placing vertical rubber screens in a wave tank. The Hosoi et al.'s method is direct method to obtain correct data and would be preferable for experiments to measure dissolved oxygen concentration in a wave tank. However, they demonstrated only few data.

To consider the air-water oxygen transfer due to breakers, *Hosoi, Murakami, and Oto* [1984], and *Moutzouris and Daniil* [1995] made experiments

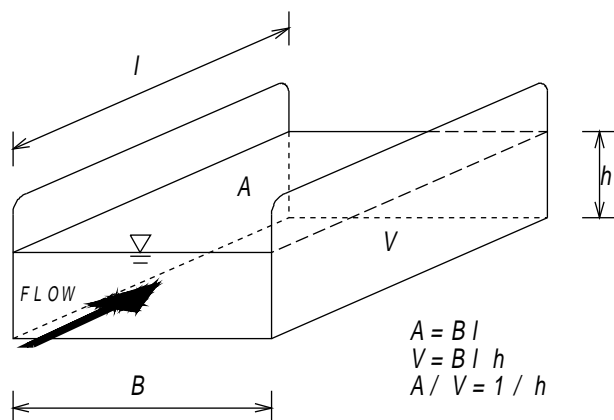


Figure 1: The reaeration area and the reaeration volume for an open channel flow.

generating breakers on a uniformly sloping bottom in a wave tank. In their experiments, they obtained the air-water oxygen transfer coefficients, or the *mass transfer* coefficient, K_L , through the relation $k_2 = K_L(A/V) = K_L(1/h)$, where k_2 is the reaeration coefficient which may be directly determined from time variation of dissolved oxygen concentration, A the projected surface area, or the reaeration area, V the volume with a projected surface area of A , or the reaeration volume, and h the water depth. However, it should be pointed out that the relation $A/V = 1/h$ used in their study can be used for only the case of a constant water depth like waves in a region of a constant water depth or an open channel flow (see Figure 1). For the case of region on a sloping bottom the relation could not be used because of its non-uniform water depth. In their experiments, moreover, it should also be pointed out that time variation of dissolved oxygen concentration must have been strongly affected by the longitudinal inhomogeneous oxygen distribution. Dissolved oxygen must concentrate amply at the breaker zone which is the main reaeration area, while little at the region offshore side of the breaking point in a wave tank.

The present study reconsiders the reaeration through the surfaces of the still water, of non-breaking progressive and *partial standing waves* in a constant water depth, and of breakers on a sloping bottom. Data was taken in a restricted volume made by placing two thin, 0.04 mm thick, vertical *vinyl screens* for cases of a constant water depth or a thin vertical vinyl screen at a point off the breaking point for cases of breakers on a sloping bottom. The vinyl screens used were loosely stretched and were confirmed to keep out a flux of oxygen and to transmit waves almost perfectly. They prevent from the effect of the dispersion from/to a wave maker, a wave absorber, and the main reaeration area. The volume of the restricted region made by the screens could be understood as the reaeration volume.

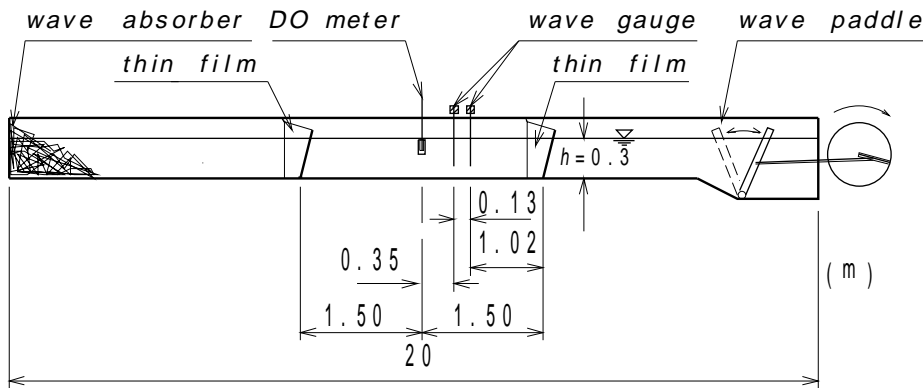


Figure 2: Experimental equipment for the case of a constant water depth.

2 Experimental Equipment and Procedure

All experiments were performed using a 20 m long, 50 cm wide, and 50 cm deep wave tank. Water depth was a constant $h=30$ cm for the most part of the experiments. A volume of 3 meter long was made using two vinyl screens for constant water depth conditions. Data for the case of the still water surface was also taken in the volume covering it with a sheet of vinyl. A uniformly sloping bottom whose inclination was $1/20$ was placed in the wave tank for the case of breakers. The experimental equipment for the case of a constant water depth is shown in Figure 2, and the one for the case of the breakers is shown in Figure 3. Figure 4 shows a setup of the vinyl screen on the sloping bottom and the reaeration area and the reaeration volume chosen.

Waves generated were regular. Experiments on the reaeration through the still water surface using a small tank, $58\text{ cm} \times 27.5\text{ cm} \times 34\text{ cm}$, covered by a sheet of vinyl and placed in a *constant temperature and humidity room* were also performed. Tap water was used, and was chemically deoxygenated by the addition of sodium sulfite and cobaltous chloride as a catalyst in all experiments. The dissolved oxygen meter used is the TYPE-58 made by YSI Co. The data from the dissolved oxygen meter was fed to a computer for 72 hours in maximum with a sampling period of 20 seconds. The reaeration coefficient k_2 was determined from the time variation of dissolved oxygen concentration. From the k_2 value the mass transfer coefficient, K_L , was determined through the relation

$$k_2 = K_L(nA/V). \quad (1)$$

In the relation, A was taken as the surface area of the restricted volume for the case of a constant depth. For the case of breakers on a sloping bottom, it was taken as the projected area of a breaker zone. V was taken as the

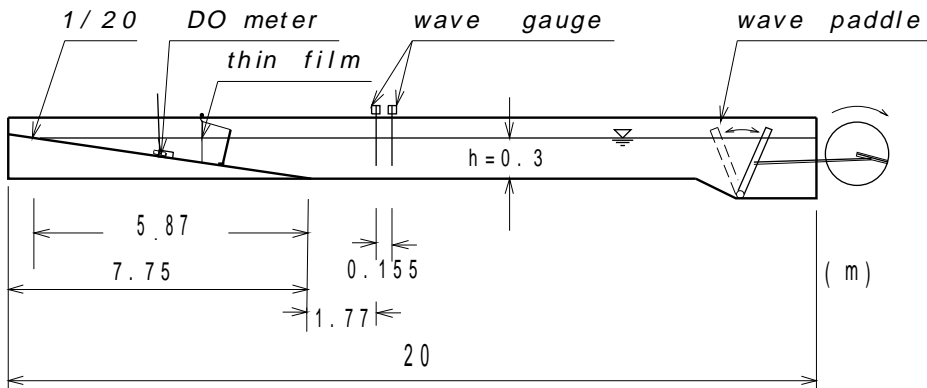


Figure 3: Experimental equipment for the case of a sloping bottom.

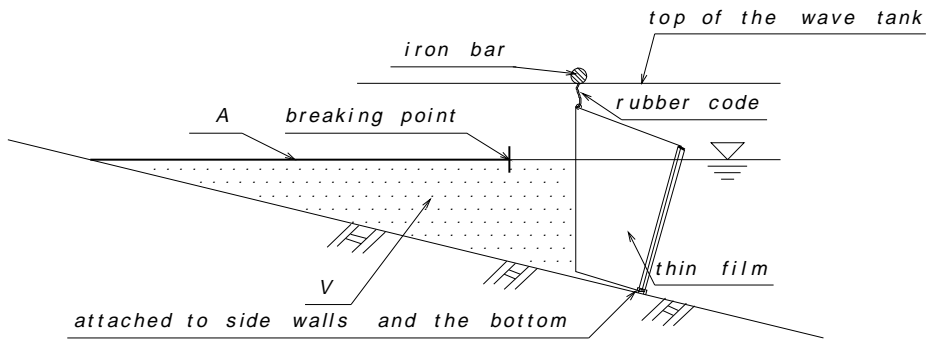


Figure 4: A setup of vinyl screen on a sloping bottom, and the reaeration volume and the reaeration area chosen.

volume of the restricted volume for all cases (see Figure 4). A constant n is the ratio of real surface area through which gas transfer occurs to the projected area. The value of n may be considered $n \approx 1$ for constant water depth conditions and $n > 1$ for the case of breakers which have complex water surfaces and many bubbles.

3 Air-Water Oxygen Transfer at the Still Water Surface

The reaeration at the still water surface is a basic phenomenon and gives us a kind of background value for other cases, say, the one at the surfaces of waves. As far as the authors surveyed, no reports have been presented on the reaeration at the still water surface.

The dissolved oxygen concentration was measured at the depth of 5 cm, 7 cm, 15 cm, and 21 cm in the wave tank, and at the depth of 7 cm and 21 cm in the small tank in a constant temperature and humidity room with the

water depth of 30 cm and 16 cm.

Figure 5 shows an example of the time variation of non-dimensional dissolved oxygen concentration deficit D^* taken in the wave tank, where

$$D^* = (C_S - C)/(C_S - C_0) \quad (2)$$

and C_S is the saturated dissolved oxygen concentration, C the dissolved oxygen concentration, and C_0 the initial dissolved oxygen concentration. As shown in the figure, $-\ln D^*$ increases linearly as time goes by, and the existence of the reaeration at the still water surface may be confirmed. The reaeration coefficient, k_2 , determined from the $D^* - t$ curve and the mass transfer coefficient, K_L , calculated from k_2 obtained in the wave tank tests were

$$k_2 \simeq 6.4 \times 10^{-6} \text{sec}^{-1} \quad \text{and} \quad K_L \simeq 1.9 \times 10^{-4} \text{cm/sec}$$

without regard to the depth of measuring points. The value of the mass transfer coefficient obtained is very much close to the one for an open channel flow of slow speed, $K_L = (2 \times 10^{-4} - 7 \times 10^{-4}) \text{cm/sec}$, which may be calculated from the value of the reaeration coefficient, $k_2 = (0.05 - 0.10) \text{day}^{-1}$, with water depth = (3.05 - 6.10)m, and velocity = (0.03 - 0.15)m/sec, measured by Chadderton et al. [1982]. From the small tank tests, the average value of the mass transfer coefficients was

$$K_L = 1.2 \times 10^{-4} \text{cm/sec} \quad (3)$$

which is about 60% of the value in the wave tank test.

4 Air-Water Oxygen Transfer at the Surfaces of Non-Breaking Waves

4.1 Experiments

The time variation of the dissolved oxygen concentration was taken in a volume restricted by two thin vinyl screens in the wave tank. Waves were progressive or partial standing. The partial standing waves were generated by placing a model of a structure which gives partial reflection, a slit type breakwater, at an end of the tank. The restricted volume was set apart from the model. The length of the volume was kept constant, 3 m, which is almost the same as the maximum wave length. The depth of measuring point was 7 cm beneath the still water surface in all cases. The separation of the incident wave heights and the reflected wave heights was carried out by applying the method developed by Goda and Suzuki [1976]. Table 1 shows experimental conditions and experimental results.

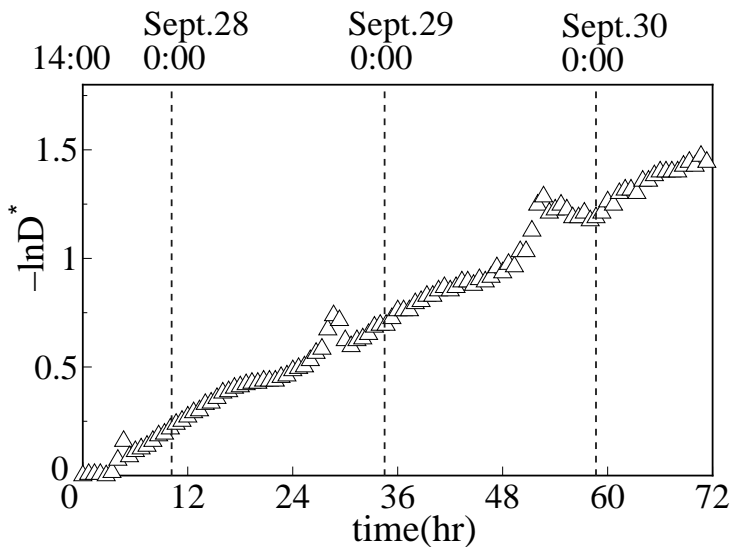


Figure 5: Time variation of dissolved oxygen concentration; still water surface in a wave tank.

Table 1: Experimental conditions and results; non-breaking waves on a horizontal bottom

RUN	T (sec)	H_i (cm)	L (m)	H/L	γ_R	t (°C)	$k_2(\text{sec}^{-1})$	K_L (cm/sec)
P1	0.88	1.1	1.13	0.010	0.09	12.0	6.26×10^{-6}	1.88×10^{-4}
P2	0.88	2.3	1.13	0.021	0.07	18.8	1.49×10^{-5}	4.48×10^{-4}
P3	0.88	3.3	1.13	0.029	0.05	11.7	1.93×10^{-5}	5.78×10^{-4}
P4	0.88	4.8	1.13	0.042	0.05	17.4	3.03×10^{-5}	9.09×10^{-4}
PR P5	1.25	5.3	1.87	0.028	0.05	14.4	2.80×10^{-5}	8.40×10^{-4}
P6	1.35	6.0	2.06	0.029	0.10	17.9	3.61×10^{-5}	10.8×10^{-4}
P7	1.50	4.6	2.34	0.020	0.09	17.9	2.58×10^{-5}	7.75×10^{-4}
P8	1.75	2.8	2.80	0.010	0.06	21.1	1.67×10^{-5}	5.01×10^{-4}
S1	0.88	2.2	1.13	0.019	0.34	14.2	1.56×10^{-5}	4.69×10^{-4}
S2	0.88	3.5	1.13	0.031	0.20	13.8	2.51×10^{-5}	7.52×10^{-4}
PS S3	1.35	4.6	2.06	0.022	0.60	11.1	2.91×10^{-5}	8.73×10^{-4}
S4	1.75	1.4	2.80	0.0051	0.85	9.8	9.78×10^{-6}	2.93×10^{-4}
S5	1.75	2.9	2.80	0.010	0.83	9.8	1.64×10^{-5}	4.93×10^{-4}

PR : progressive, PS : partial standing

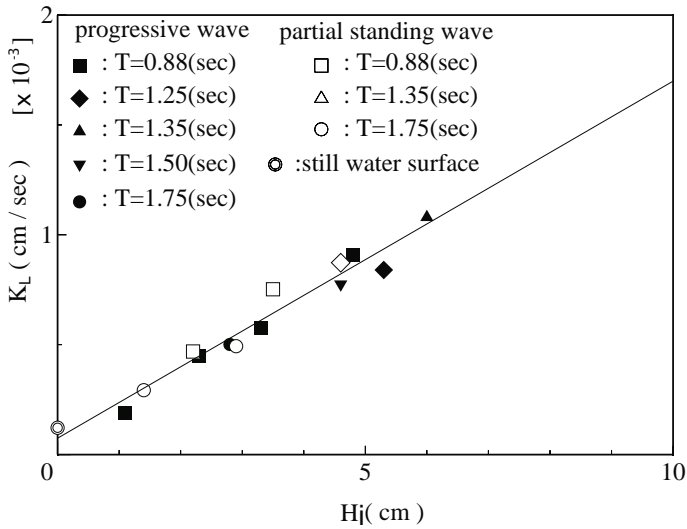


Figure 6: Correlation of K_L with H_i .

4.2 Results

Figure 6 shows the relationship between the mass transfer coefficient, K_L , obtained and the incident wave height, H_i . As shown in the figure, K_L has a strong and linear relationship with the incident wave height without regard to the wave period T and the type of waves of progressive or partial standing. The correlation coefficient is $r_c = 0.971$. It should be noted that the value of K_L corresponding to $H_i = 0$ almost coincides with it for the still water surface in a constant temperature and humidity room. The correlations between K_L and other parameters, say, the square root of the total energy of composite waves, are not strong compared to the relationship shown in Figure 6.

5 Air-Water Oxygen Transfer at Breaker Zone

Waves break strongly at the shore with many bubbles entrapped. Therefore, the reaeration at the breaker zone must contribute much to the dissolved oxygen in the nearshore where many kinds of creatures are inhabiting.

5.1 Experiments

Experiments to obtain the time variation of the dissolved oxygen concentration through the surface of breaker zone were carried out setting a restricted volume by a vinyl screen as shown in Figure 3 and Figure 4. The dissolved oxygen meter was placed at the breaking point. Breaking waves generated were plunging type and spilling type both. The location of the vinyl screen

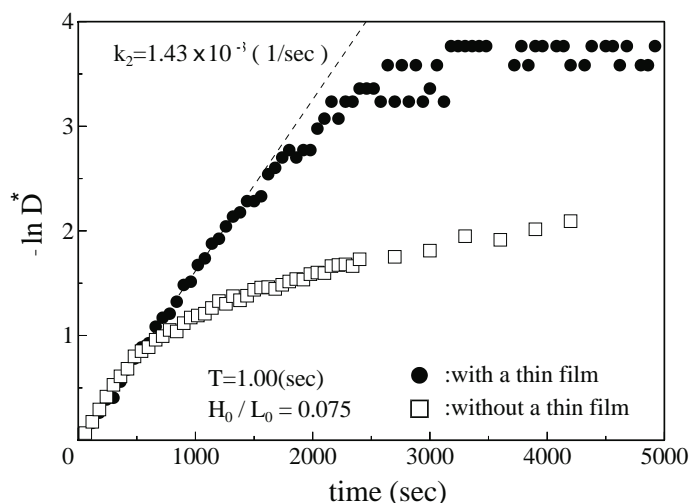


Figure 7: Time variation of non-dimensional DO concentration in the breaker zone on a sloping bottom.

was at the point whose depth was $h_b - 1.5h_b$, where h_b is the breaking water depth. For comparison, experiments with the condition where no restriction by vinyl screens were made were also performed. The incident wave heights were decided applying the method developed by *Goda and Suzuki* [1976]. Table 2 shows experimental conditions of breaking water depth, breaking wave height, the reaeration area, the reaeration volume, and the type of breaking. Experimental results are also shown in the table. Judgement of the type of breaking was done using a breaker type index [*Iwagaki*, 1987] drawn up using *Iversen's* data [1952] and other researchers' data.

5.2 Results

Figure 7 shows an example of the time variation of non-dimensional dissolved oxygen concentration deficit D^* obtained in the restricted volume with a screen placed and without a screen at the same conditions. As shown in the figure, the effect of the screen placed at the offshore site off the breaking point on a sloping bottom is clear. The data taken in the restricted volume with a screen shows steep and linear recovering in the dissolved oxygen concentration in the beginning and mild recovering towards the saturation after it. The reaeration coefficient, k_2 , therefore, may be without doubt and correctly determined from the first part of the curve. The data taken in the wave tank without a screen, on the other hand, shows a curve whose inclination is varied continuously due to the longitudinal dispersion of oxygen to the offshore direction in the wave tank. It would be difficult to determine k_2 from the curves as shown in the figure.

Table 2: Experimental conditions and results; breakers on a sloping bottom

RUN	T (sec)	H'_0 (cm)	H'_0/L_0	h_b (cm)	H_b (cm)	A (cm ² / cm)	V (cm ³ / cm)	t (°C)	TYPE	k_2 ($\times 10^{-3}$ 1/sec)	nK_L ($\times 10^{-2}$ cm/sec)
R1	0.88	7.3	0.060	10.2	7.8	204	1380	26.1	SP	1.87	1.27
R2	0.88	9.3	0.077	13.2	9.6	264	2740	29.9	SP	1.90	1.97
R3	0.88	11.1	0.092	16.2	11.3	324	6150	25.1	SP	1.39	2.64
R4	1.00	7.4	0.047	10.4	8.4	208	1380	24.4	SP	2.17	1.44
R5	1.00	9.0	0.058	12.6	9.7	252	2740	29.2	SP	1.81	1.97
R6	1.00	11.6	0.074	16.3	12.0	326	4970	25.4	SP	1.43	2.18
R7	1.10	5.3	0.028	7.8	6.9	156	770	26.1	PL	1.27	0.62
R8	1.10	7.1	0.038	10.3	8.5	206	2050	30.1	SP	0.78	0.77
R9	1.10	8.6	0.045	12.2	9.9	240	2050	28.7	SP	1.64	1.40
R10	1.20	4.9	0.022	7.5	6.6	150	770	24.1	PL	1.95	1.00
R11	1.20	6.7	0.030	9.9	8.5	198	1160	32.0	PL	1.43	0.84
R12	1.20	7.6	0.034	11.1	9.3	222	2500	30.7	PL	1.58	1.78
R13	1.40	3.5	0.012	5.9	5.8	118	770	23.0	PL	1.40	0.91
R14	1.40	4.6	0.015	7.4	6.9	148	1160	30.1	PL	1.04	0.81
R15	1.40	6.7	0.022	10.3	9.3	206	1160	30.6	PL	1.70	0.95

SP : spilling, PL : plunging

5.3 Mass Transfer Coefficient as a Function of Wave Characteristics

In Hosoi et al.'s study [1982 and 1984] on the reaeration at the surfaces of breaker zone, they expressed the reaeration coefficient as a function of the wave steepness in deep water condition, H'_0/L_0 , for the case of *plunging breakers* and as functions of relative breaking depth, h_b/L_0 , and H'_0/L_0 for the case of *spilling breakers*. In Moutzouris and Daniil's study [1994], $K_L S_C^{1/2}$, where S_C is the Schmidt number, was expressed as a function of H_i/T .

Figure 8 and Figure 9 show nK_L , which evaluated from k_2 through Eq.(1) as $nK_L = (V/A)k_2$, as a function of the deep water wave height, H'_0 , the square of the deep water wave height, $H_0'^2$, the deep water wave steepness, H'_0/L_0 , and H'_0/T , respectively. The square of the deep water wave height, $H_0'^2$, may be understood as the quantity proportional to the total dissipated energy at the breaker zone due to the wave breaking, while H'_0/T the quantity proportional to the water particle velocities. In the figures a type of breaking is specified and lines or a curve of second order which have strongest correlation in each relationship are shown with the value of the correlation coefficient, r_c .

As shown in the figures, there are definite and linear or second degree relationships between nK_L and the parameters mentioned above, some scattering may be seen for the case of plunging breakers, though. Except for the

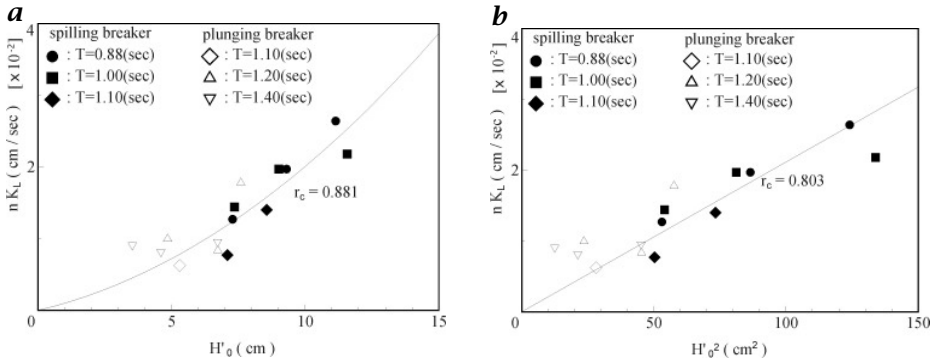


Figure 8: **a** Correlation of nK_L with H'_0 . **b** Correlation of nK_L with H'^2_0 .

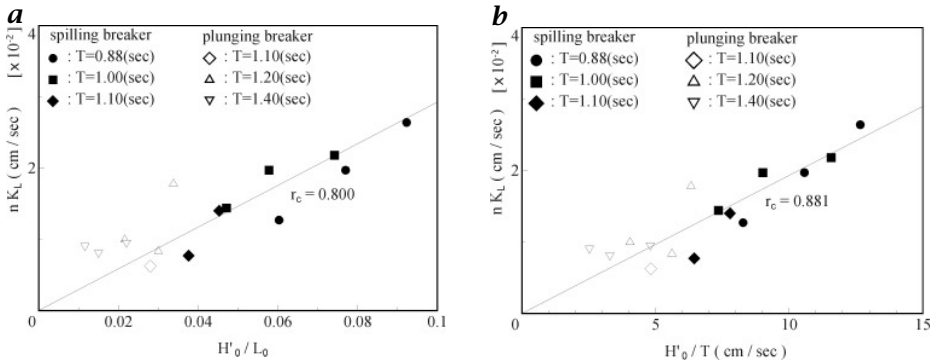


Figure 9: **a** Correlation of nK_L with H'_0/L_0 . **b** Correlation of nK_L with H'_0/T .

relationship as a function of H'_0 , linear relationship may be confirmed. In the linear relationships, the strongest correlation may be seen in the relationship as a function of H'_0/T with the correlation coefficient of $r_c = 0.881$. However, the difference among other cases is not so significant. Final judgment could be done after performing experiments with different inclination of the slope and experiments of larger scales. However, the expression of nK_L as a function of H'_0/L_0 seems not to be reasonable because we obtain the same value of nK_L in the wave fields of different scales, say, in the field or in the laboratory model, once the wave steepness is the same in the different wave fields.

6 Conclusion

It may be concluded from the present experimental study that experiments on reaeration at the surfaces of water waves in a wave tank with paying attention to the reaeration volume and the reaeration area are preferable to

obtain correct mass transfer coefficients.

From the experiments on the reaeration at the still water surface, the existence of the air-water oxygen transfer was observed.

From the experiments on the surfaces of non-breaking waves including partial standing waves, a linear relationship is observed between the mass transfer coefficient and the incident wave height without regard to the type of waves, progressive or partial, and the wave periods.

From the experiments with the modified experimental method presented herein on the surfaces of breakers, it was confirmed that definite and linear recovery in dissolved oxygen concentration could be obtained. The product of the ratio of real surface area through which gas transfer occurs to the projected area and the mass transfer coefficient, nK_L , has a linear relationship with the square of the deep water wave height, the deep water wave steepness, and the ratio of the deep water wave height to the wave period. It has a second order relationship with the deep water wave height.

Acknowledgements

This research has been supported in part by the Grant-in Aid for Scientific Research from the Ministry of Education, Science and Culture, Japan.

References

- Chadderton, R. A., Miller, A. C. and McDonnell, A. J., Uncertainty analysis of dissolved oxygen model, *Proc. ASCE*, **108(EE5)**, 1003-1013, 1982
- Daniil, E. I. and Gulliver, J. S., Influence of waves on air-water gas transfer, *J. Environmental Engrg., ASCE*, **117(5)**, 522-540, 1991
- Downing, A. L. and Truesdale, G. A., Some factors affecting the rate of solution of oxygen in water, *J. Applied Chemistry*, **5**, 570-581, 1955
- Goda, Y. and Suzuki, Y., Estimation of incident and reflected waves in random wave experiments, *Proc. the 15th Coastal Engrg.*, **15**, 828-845, 1976
- Hosoi, M., Ishida, A., and Imoto, K., Study on reaeration by waves, *Coastal Engrg. in Japan*, **20**, 121-127, 1977
- Hosoi, Y., Murakami, H., and Oto, M., A study on the reaeration by plunging breaker, *Proc. the 29th Japanese Conf. on Coastal Engrg.*, **29**, 565-569, 1982 (in Japanese)
- Hosoi, Y., Murakami, H., and Oto, M., Reaeration by spilling breaker, *Coastal Engrg. in Japan*, **27**, 97-108, 1984
- Iwagaki, Y., *Modern Coastal Engineering*, Morikita, p.111, 1987 (in Japanese)
- Moutzouris, C. I. and Daniil, E. I., Water oxygeneration in the vicinity of coastal structures due to wave breaking, *Proc. the 24th Intl. Conf. on Coastal Engrg.*, **24**, 3167-3177, 1995

Turbulent Surface Deformation and Their Relationship to Mass Transfer in an Open-Channel Flow

*John S. Gulliver*¹ and *Aldo Tamburrino*²

¹ St. Anthony Falls Laboratory, Department of Civil Engineering,
University of Minnesota, Minneapolis, MN

² Department of Civil Engineering, University of Chile,
Santiago, Chile

Abstract

The relationship between the flow field close to the *free surface* and the *liquid film coefficient* is investigated for a free surface flow. A technique to measure *free-surface turbulence* is used to infer the vertical *velocity gradient* at the surface, and ultimately quantify the liquid film coefficient.

1 Background

Many theories of mass transfer at a free interface are based upon the concept of *surface renewal* [Dankwerts, 1951]. The difficulty with the renewal theories is that they are conceptual, and not directly related to near-interface turbulence. Therefore, the measurements of “surface-renewal eddies” [Rashidi and Banerjee 1988; Komori *et al.* 1989; Komori *et al.* 1990; Davies and Khan 1965; Davies and Lozano 1984] are difficult to correlate with the liquid film coefficient because the investigators, themselves, define what constitutes a surface-renewal eddy.

The liquid film coefficient, however, can be more directly related to near-interface turbulence without the conceptual theories. For example, McCready *et al.* [1986] adapted the solid wall analysis of Sikar and Hanratty [1970] to develop the boundary layer equation for concentration in a turbulent flow field near a free surface.

$$\frac{\partial C}{\partial t} + \beta z \frac{\partial \bar{C}}{\partial z} = D \frac{\partial^2 C}{\partial z^2} \quad (1)$$

where C is solute concentration, \bar{C} is temporal mean solute concentration, z is distance from the interface, D is diffusivity, and β is the vertical velocity gradient very near the interface,

$$w = \beta z \quad (2)$$

where w is the velocity normal to the interface. The vertical velocity gradient is a function of time and distance parallel to the interface. This coordinate system moves with the interface, such that $z = 0$ always occurs at the interface, and the x and y coordinates are parallel to the surface.

The importance of the *normal velocity gradient*, β , to mass transfer is apparent in Eq. (2). The β parameter is a function of the turbulence in the flow. Continuity at the free surface gives

$$\beta = \frac{\partial w}{\partial x} = - \left[\frac{\partial u}{\partial x} + \frac{\partial v}{\partial y} \right] \quad (3)$$

McCready et al. then Reynolds decompose equation (1) and solve the linearized version for the concentration fluctuation. From this analysis, an expression for the fluctuating part of the mass transfer coefficient can be analytically found. The spectrum of the mass transfer coefficient and vertical velocity gradient at large ω are related as:

$$\frac{S_k(\omega)}{K^2} = \frac{S_\beta(\omega)}{\omega^2} \quad (4)$$

where S denotes spectrum, ω is angular frequency, and K is a dimensionless bulk liquid film coefficient. All terms in Eq. (4) are made dimensionless using the shear velocity and kinematic viscosity. From Eq. (4), the rms values of the mass transfer coefficient, relative to the temporary mean K , can be found:

$$\frac{\overline{k^2}}{K^2} = \int_0^\infty \frac{S_\beta(\omega)}{\omega^2} d\omega \quad (5)$$

The advantage of having an expression like Eq. (5) is that it provides a way of knowing the root mean square of the mass transfer coefficient without having to measure instantaneous concentrations.

McCready et al. [1986] solved the problem using both a linear and non-linear approach similar to the work of Campbell and Hanratty [1983] for a solid interface. By means of the linear approach, they were able to find an expression for the film thickness. Most important, they found the dependency of K_L on parameters that can be obtained from the spectrum of the gradient of the vertical velocity fluctuations. In both cases, the dependency of K_L with Sc agrees with experimental data. They assumed, however, that the turbulence measurements of Lau (1980) very near a solid boundary could be used to simulate those of a free surface generating shear stresses as long as the free surface boundary conditions were applied to bring the turbulence to the free surface via Eq. 1.

The *free-surface turbulence* measurements presented here will test McCready et al.'s hypothesis and be used to infer the parametric relationship between liquid film coefficient and free-surface turbulence in an open-channel flow where the turbulence is generated away from the interface.

2 Measurements of Free Surface Turbulence

Apparatus. The experiments were performed in the St. Anthony Falls *moving-bed flume*. It is a channel in which a polyester belt slides on a stainless steel plate. Two transverse vertical metal sheets define the test section, where a recirculating flow is produced by the belt motion. The channel is 15 m long, 76 cm wide and 69 cm deep, with transparent walls made from 1.3 cm thick glass. The belt is 71 cm wide and can reach a speed of 2 m/s. Details of that flume and its characteristics can be found in *Tamburrino and Gulliver* [1992]. The moving-bed flume facilitates the acquisition of certain types of data when compared with traditional laboratory flumes. For example, it is possible to set the cross-sectional mean velocity equal to zero at high Reynolds numbers. Then it is not necessary to displace the instrumentation with the flow in order to visualize the flow structures conveyed by the mean flow.

Technique. The primary data is obtained by means of time exposure photographs on the free surface using pliolite particles as tracers. The particles were previously sieved and only those smaller than 62 microns were used. Although these particles are considered neutrally buoyant, they float when they are introduced directly into the water surface. During the experiments, the particles were continuously poured on the free surface by means of a feeder located upstream. The photographs obtained in the experiments were enlarged to 16 × 20 inch prints and digitized in order to get the vector field on the free surface. The digitized streaks of one photograph are shown in Fig. 1. The data presented in Fig. 1 are randomly distributed in space, but statistical processing requires them to be equi-spaced along the transverse and longitudinal axes. Thus, the original data must be interpolated into the nodes of a grid. The data were interpolated into the nodes of a 5 mm × 5 mm grid using the kriging method, because it takes into account presence clusters of data and regions with low density of information in the interpolation process. A summary of the experimental conditions analyzed is given in Table 1.

A first-order, second-moment uncertainty analysis was undertaken to quantify measurement uncertainty. The manipulation of the surface streaklines into horizontal velocities assumes that the free surface is perfectly horizontal with an elevation that is constant over the exposure period, that the streaklines can be digitized accurately, and that interpolation of the streakline data into a square grid will sufficiently retain the accuracy. Therefore, the potentially significant sources of uncertainty in the measurements are 1) the bias that occurs because the free surface has some overall slope, 2) the precision due to a local curvature in the free surface, 3) the precision due to a vertical motion of the free surface, and 4) the precision uncertainty

Table 1: Experimental Conditions

Exp.	H cm	U_b cm/s	u^* cm/s	U_s cms	B/H	Re	Re*	T_{exp} s
61	12.65	18.30	0.89	2.20	6.0	22,884	1,113	0.2
81	9.36	19.07	0.96	2.41	8.1	17,163	864	0.2
103	7.12	66.44	2.78	6.58	10.7	45,486	1,903	0.2
121	6.07	15.04	0.83	2.35	12.5	8,532	471	0.2
122	6.00	41.53	2.02	4.88	12.7	23,289	1,133	0.2
123	5.96	55.60	2.60	5.96	12.8	30,970	1,448	0.1

H =flow depth; U_b =belt velocity; U_s =free surface mean velocity;
 u^* = shear velocity (computed from the logarithmic velocity distribution, Tamburrino and Gulliver [1992]); T_{exp} = time exposure; $Re = HU_b/\nu$;
 $Re^* = HU^*/\nu$; ν = kinematic viscosity.

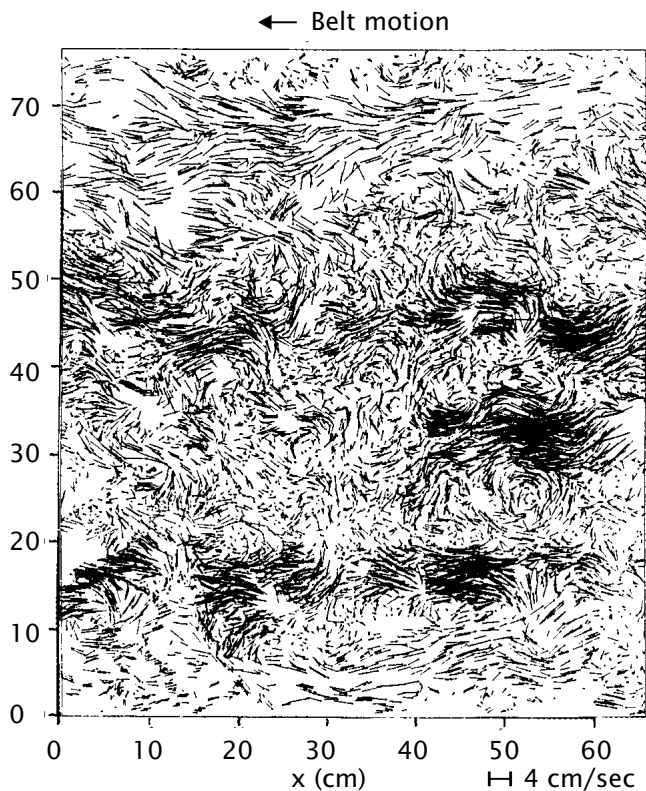


Figure 1: Velocity vector field for Experiment 61 with free surface mean velocity subtracted.

introduced in the digitizing and interpolation process. The details of this uncertainty analysis are given in *Tamburrino* (1994). For belt velocities greater than 60 cm/s, the uncertainties due to vertical motion are believed to be unacceptably large, and were not included in the current analysis.

3 Results

The most important kinematic variable affecting the mass transfer phenomenon across the free surface is the vertical gradient of the vertical velocity component, β , identified as the 2-D divergence in Eq. (3). High β values can be interpreted as the occurrence of surface renewal.

The gradient of the vertical velocity (2-D divergence) was computed from the interpolated values of u and v replacing the derivatives in Eq. (3) by finite differences. The β values, smoothed over 1 cm², are plotted versus longitudinal and transverse distances for a representative experiment in Fig. 2. The spatial scales of β seem to be correlated on a wavelength of between 2 and 3 cm. This wavelength is significantly smaller than that of the large upwelling events. In fact, a detailed inspection of the data indicates that large β values do not occur at the center of the upwelling regions but instead occur at the edges of these boils, where local vortices are formed by the spreading of fluid. Thus, the intense horizontal velocity gradients of the smaller vortices created by the upwelling is responsible for the high values of β , instead of the upwelling itself. This indicates that the long-term, low intensity upwelling zones traditionally viewed as surface renewal may be less important to mass transfer than free-surface vorticity.

4 Spectra of Vertical Velocity Gradient

Spectra of the *vertical velocity gradient*, S_β , computed from the measurements at each longitudinal location for the six experiments indicate that the dominant wave numbers are the smaller ones, $k/2\pi < 0.4 \sim 0.51/\text{cm}$, corresponding to wavelengths greater than 2.0 ~ 2.5 cm. A large peak at a $k/2\pi$ of 0.5 cm⁻¹, corresponding to wavelengths of 2 cm is especially persistent in the β spectra. At higher wave numbers, towards the small eddy model, the spectra decreases significantly. At lower wave numbers, the spectra decreases somewhat for flow depths of between 7 and 13 cm, and more quickly at flow depths of 6 cm. We believe that the scale of surface vorticity is limited by the depth of flow, such that the spectrum at smaller wave numbers become reduced. In general, there is no significant change in the dominant frequency of the β -spectra with a change in depth or boundary shear for these experiments. This is in direct contrast to longitudinal velocity, which was highly correlated on a scale equal to between two and three times the depth, due to large upwelling regions [*Tamburrino and Gulliver* 1994]. Apparently, the vertical velocity gradients of the large upwelling zones are overwhelmed

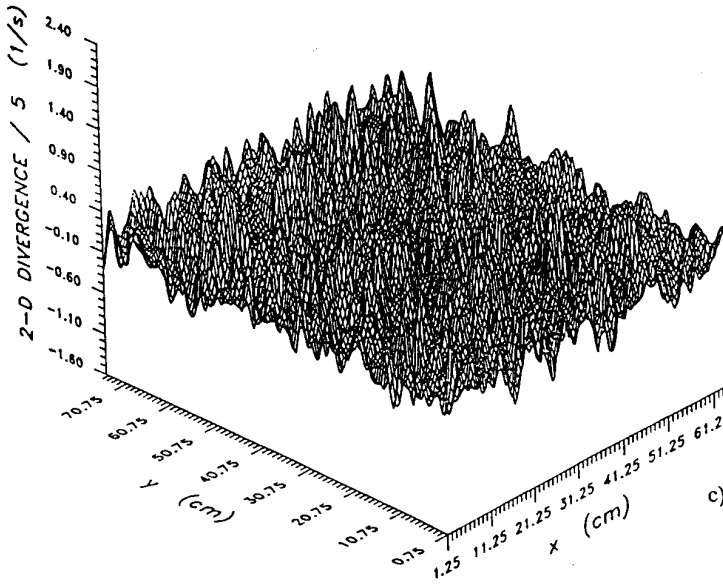


Figure 2: Distribution of the smoothed 2-D divergence, (β) for experiment 61.

by the vertical velocity gradients created by the two-dimensional vortices on the surface.

The velocity spectra of the six experiments were non-dimensionalized in the manner of *McCready et al.* [1986] and are plotted in Fig. 3. Wave numbers were converted to frequencies using the traditional frozen turbulence hypothesis of Taylor with the mean free surface velocity taken as the convection velocity. At the lower frequencies our β -spectra tend to decrease, indicating that the limitation of flume depth, as described previously, affects the large wavelength of β correlation. The spectra are also somewhat larger than *McCready et al.*'s, and tend to begin their high ω decrease at a different dimensionless frequency.

The differences between our velocity spectra and that used by *McCready et al.* [1986] were rectified through the use of the following relationship

$$S_{\beta}\omega = \frac{S_{\beta\max}}{1 + (\omega^+ - \omega_0^+)^2} \quad (6)$$

where $\omega^+ = \sigma\omega/\omega_m$, ω_0^+ is the non-dimensional frequency (ω^+) at the peak of the spectrum, σ is a constant of the spectrum, S_{β} is the dimensionless spectra and $S_{\beta\max}$ is the value of S_{β} at $\omega = \omega_0$.

In order to make all the spectra collapse into one curve, they were transformed into the parameters $S_{\beta}(\omega)/S_{\beta\max}$ and $\omega^+ - \omega_0^+$ instead of the normalization $S_{\beta}(\omega)/\beta^{+2}$ and ω^+ used in *McCready et al.* and employed in

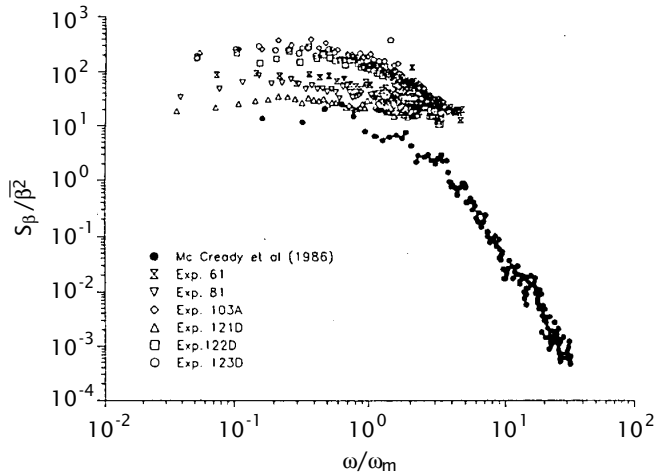


Figure 3: Experimental spectra obtained and spectrum used by McCreedy et al. [1986] in their computations. ω_m = mean frequency of all measurements.

Fig. 3. The normalized spectrum of the data employed by *McCreedy et al.* [1986] is presented in Fig. 4 together with the spectra corresponding to our experiments. McCreedy et al.'s data present more information in the high frequency range of the spectrum than the data obtained in the moving-bed flume. They are, however, based on measurements near a solid boundary, rather than at a free surface. It is seen that all of the spectra collapse onto one curve. Figure 4 validates McCreedy's et al. assumption that the damping of the gradient of ω close to a free surface occurs in a fashion similar to the damping close to a solid wall, although their magnitudes are different. In fact, the two flow situations are so different that it is likely that Fig. 4 represents a universal spectra for β . One still needs to determine the parameters $S_{\beta max}$, ω_0^+ and σ/ω_m for Eq. (6) from experiments on near-interface turbulence. The required techniques are described in *Tamburrino* [1994] and do not require measurements at very high frequency.

5 Relationship Between the β -Spectra and Mass Transfer Coefficient

The linearized theory as developed by *Vassilodeau* [1985] to relate the spectrum of vertical velocity to the liquid film coefficient at a free surface will be applied to the measured β -spectra of Fig. 4. Although the linearized theory overestimates K_L , it has been shown to provide the appropriate parameterization of K_L . The linearized theory also requires that a constant be fitted to other data, such as that from the disturbed equilibrium measurements of

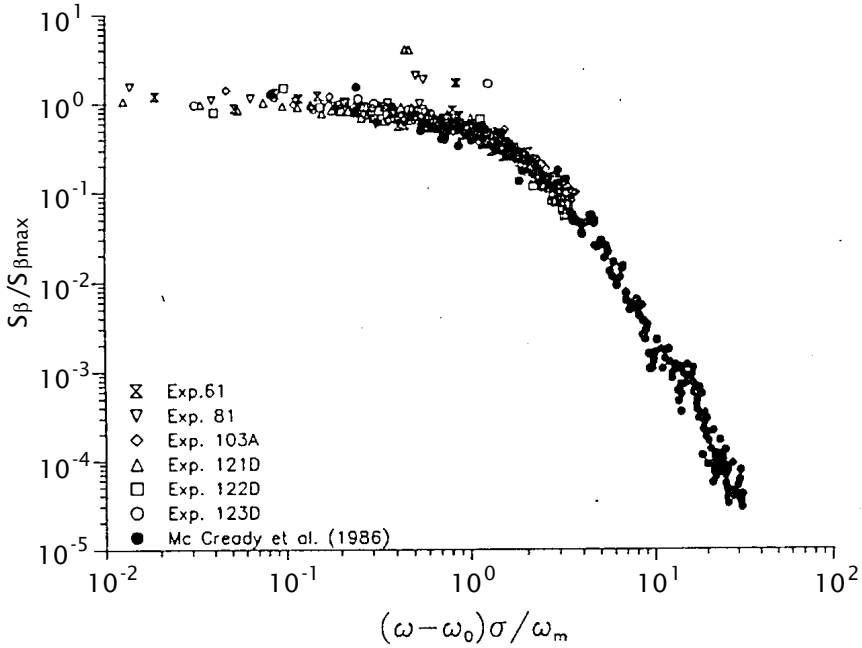


Figure 4: Normalized spectra of β .

concentration [McCreedy et al. 1986; Tamburrino 1994].

Vassilodeau [1985] developed the following expression for the spectrum, S_k , of dimensionless liquid film coefficient, K :

$$\frac{S_K \omega}{K^2} = \begin{cases} S_\beta(\omega) / \omega_c^2 & \omega \leq \omega_c \\ S_\beta(\omega) / \omega^2 & \omega > \omega_c \end{cases} \quad (7)$$

where ω_c is a cut-off frequency made dimensionless by ν and u^* that distinguishes the two regimes of the spectrum. For the spectrum given by Eq. (6), ω_c is given by the equation [Tamburrino 1994].

$$\begin{aligned} \frac{\omega_c}{S_{\beta max}} &= \frac{1}{\omega_c^+} \left[\tan^{-1}(\omega_0^+) - \tan^{-1}(\omega_0^+ - \omega_c^+) \right] \\ &+ \frac{1}{\omega_0^{+2} + 1} \left[\frac{1}{2} \ln \left((\omega_0^+ - \omega_c^+)^2 + 1 \right) - \ln(\omega_c^+) \right] \\ &+ \frac{\omega_0^+}{\omega_0^{+2} + 1} \left[\frac{\pi}{2} + \tan^{-1}(\omega_0^+ - \omega_c^+) \right] \end{aligned} \quad (8)$$

where $\omega_c^+ = \sigma \omega_c / \omega_m$. The cutoff frequency may also be related to the

mass transfer coefficient [Vassilodeau 1985]

$$\omega_c \propto K^2 S_c \quad (9)$$

If ω_c^+ is large Eqs. (8) and (9) give [Vasilodeau 1985]

$$K\sqrt{S_c} \propto (\beta^2)^{-1/4} \quad \omega_c^+ \gg 1 \quad (10)$$

A large ω_c^+ describes the co-current air-water mass transfer experiments of *McCready et al.* [1986] by fitting $S_{\beta_{max}}$ and $\overline{\beta^2}$ in their nonlinear model with the gradient of the vertical velocity inferred from measurements near a pipe wall to measurements of $K\sqrt{S_c}$ for the co-current experiments, *McCready et al.* [1986] estimated $K\sqrt{S_c} = 0.71(\overline{\beta^2})^{0.25}$.

At a small ω_c^+ , Eq. (8) does not reduce to as simple a form because both ω_c^+ and ω_0^+ can be small. Then Eqs. (8) and (9) give

$$K\sqrt{S_c} = AS_{\beta_{max}}^{1/2} F_{\omega}^{1/2}, \quad \omega_c^+ \ll 1 \quad (11)$$

$$\begin{aligned} F_{\omega} &= \frac{1}{\omega_c^+} \left[\tan^{-1}(\omega_0^+) - \tan^{-1}(\omega_0^+ - \omega_c^+) \right] \\ &+ \frac{1}{\omega_0^{+2} + 1} \left[\frac{1}{2} \ln(\omega_0^+ - \omega_c^+)^2 + 1 \right] - \ln(\omega_c^+) \\ &+ \frac{\omega_0^+}{\omega_0^{+2} + 1} \left[\frac{\pi}{2} + \tan^{-1}(\omega_0^+ - \omega_c^+) \right] \end{aligned} \quad (12)$$

where A = a constant of proportionality. Within the range of realistic parameters for an open-channel flow, F_{ω} does not appear to change significantly. In our experiments, $F_{\omega}^{1/2}$ varied from 2.46 to 2.62, a variation of 9%, while ω_0^+ and ω_c^+ varied over factors of 5 and 3.4, respectively. Therefore, F_{ω} was assumed to be constant ($F_{\omega}^{1/2} = 2.5$) and the value of A was determined to be 0.092 by comparison of Eq. (11) with the measurements of *Lau* [1975] and of *Gulliver and Halverson* [1989], as shown in Fig. 5 [*Tamburrino* 1994].

6 Applications

When reduced to the dimensional form, Eq. (11) becomes

$$K_L = 0.092(S'_{\beta_{max}} F_{\omega} D)^{1/2} \quad (13)$$

where K_L and $S'_{\beta_{max}}$ have units of length/time and time^{-1} , respectively. Shear velocity, which is a parameter used to represent the generation and

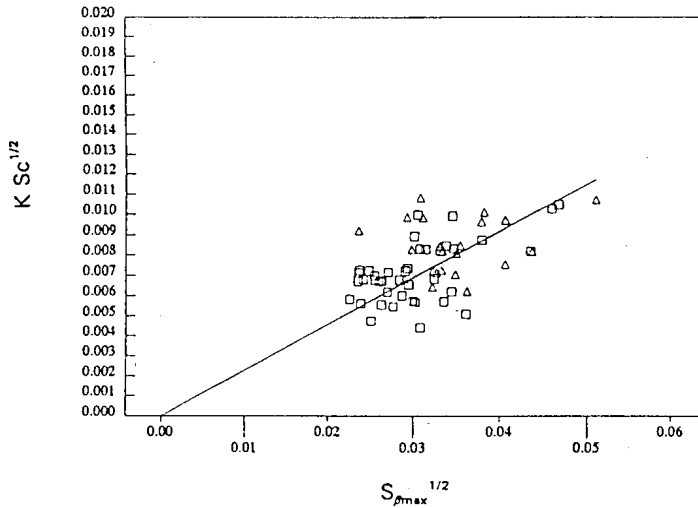


Figure 5: Relation of liquid film coefficient to free-surface turbulence used to determine the coefficient for Eq. (11). The $KSc^{1/2}$ are from the experiments of Lau (squares) and Gulliver and Halverson (triangles). The $S_{\beta_{max}}$ values are determined by a curve-fit of the experiments described herein to depth and shear velocity parameters [Tamburrino 1994]

dissipation of turbulence in the flow has been replaced by $S'_{\beta_{max}}$ and F_{ω} . These two parameters, however, can be measured in a stirred tank, while shear velocity measurements are more difficult to make and interpret. Equation (11), therefore, should predict the liquid film coefficient as long as turbulence is generated away from the interface and may be used to translate the results of a grid-stirred experiment, for example, into an equivalent open channel flow.

Another potential application of Eq. (11) would be the location-specific measurement of liquid film coefficient in natural streams. The great variation in turbulence with distance that occurs in a natural stream is typically averaged into bulk parameters that may not be representative of free-surface turbulence. It may be possible to photograph, or videotape, floating particles placed on the water surface to determine the $S_{\beta_{max}}$ and F_{ω} parameters to use in Eq. (11). The result would be a location-specific K_L measurement that could be compared to the morphology and other stream characteristics.

7 Conclusions

The hypothesis of *McCready et al.* [1986], that turbulence measurements near a solid boundary could simulate turbulence near a free surface as long as the proper free-surface boundary conditions are used, has been veri-

fied. In addition, a normalized spectra of β has been developed so that only $S_{\beta_{max}}$, ω_o , and σ/ω_m need to be determined for a given experiment.

The results of this and McCready et al.'s study can also be used to relate the surface renewal concept directly to free-surface turbulence. If the shear is generated at the water surface, such as a co-current or wind-influenced flow, both large and small eddies contribute and the mean surface renewal rate, $r \cong 0.5\bar{\beta}^{1/2}$. If the turbulence is generated away from the water surface, such as an open-channel flow, large eddies dominate and $r \cong 8.5 \times 10^{-3} F\omega S'_{\beta_{max}}$.

Acknowledgements

This paper is based on work partially supported by the National Science Foundation under Grant No. CES-8615279. Any opinions, findings, and conclusions or recommendations expressed are those of the authors and do not reflect those of the National Science Foundation. The second author would also like to acknowledge the partial financial support given by the Graduate School of the University of Minnesota as a Doctoral Dissertation Special Grant.

References

- Campbell, J. A. and T. J. Hanratty, Mass transfer between a turbulent fluid and a solid boundary: linear theory, *AiChE Jour.*, 29(2), 221, 1982
- Dankwerts, P. V., Significance of liquid-film coefficients in gas adsorption, *Ind. and Engr. Chemistry*, 43(6), 1460-1467, 1951
- Davies, J. T. and W. Khan, Surface clearing by eddies, *Chem. Engrg. Science*, (20), 713-715, 1965
- Davies, J. T. and F. J. Lozano, Turbulence and surface renewal at the clean surface in a stirred vessel, *AiChE Jour.*, 30(3), 502-504, 1984
- Gulliver, J. S., and M. J. Halverson, Air-water gas transfer in open channels, *Water Resources, Res.*, 25(8), 1783-1793, 1989
- Komori, S., Y. Murakami, and H. Ueda, The relationship between surface renewal and bursting motions in an open-channel flow, *J. Fluid Mechanics*, 203, 103-123, 1989
- Komori, S., R. Nagaosa, and Y. Murakami, Mass transfer into a turbulent liquid across the zero-shear gas-liquid interface, *AiChE Jour.*, 36(6), 957-960, 1990
- Lau, K. K., Study of turbulent structure close to a wall using conditional sampling techniques, Ph. D. thesis, Univ. of Illinois, Urbana, IL., 1980
- Lau, Y. L., An experimental investigation of reaeration in open channel flow, *Prog. Water Technol.*, 7(3/4), 519-530, 1975
- McCready, M.A., E. Vassiliadou, and T. J. Hanratty, Computer simulation of turbulent mass transfer at a mobile interface, *AiChE Jour.*, 32(7), 1108-1115, 1986
- Rashidi, M. and S. Banerjee, The effect of boundary conditions and shear rate on streak formation and breakdown in turbulent channel flows, *Phys. Fluids A*, (2)10, 957-960, 1990

- Sikar, K. K. and T. J. Hanratty, Relation of turbulent mass transfer to a wall at high Schmidt numbers to the velocity field, *Jour. Fluid Mech.*, 44, 589, 1970
- Tamburrino, A. and J. S. Gulliver, Comparative flow characteristics of a moving-bed flume, *Exp. in Fluids*, (13), 289-298, 1992
- Tamburrino, A., Free-surface kinematics: Measurement and relation to the mass transfer coefficient in open-channel flow, Ph. D thesis, University of Minnesota, Minneapolis, MN, 1994
- Tamburrino, A. and J. S. Gulliver, Free-surface turbulence measurements in an open-channel flow, in *Free-Surface Turbulence*, ASME, FED Vol. 181, 103-112, 1994
- Vassiliadou, E., Turbulent mass transfer to a wall at large Schmidt numbers, Ph. D. thesis, Univ. of Illinois, Urbana, IL, 1985

Dependence of the Skin Layer Recovery Rate on Heat Flux and Turbulence

A. T. Jessup^{1 2}, C. J. Zappa^{1 2}, V. Hesany²
M. R. Loewen³, and M. G. Skafel⁴

¹ Applied Physics Laboratory and ²Department of Civil Engineering
University of Washington, Seattle, WA USA 98105-6698;
jessup@apl.washington.edu

³ Department of Mechanical Engineering, University of Toronto
Toronto, Ontario, Canada M5S 1A4

⁴National Water Research Institute, Canada Centre for Inland Waters
Burlington, Ontario, Canada L7R 4A6

Abstract

The characteristic renewal time t_* utilized in the surface renewal model for heat or mass transfer has been equated to the time required for thermal recovery of the skin layer following artificial disruption. We present laboratory measurements using infrared imagery to demonstrate the dependence of the skin-layer recovery rate on heat flux and turbulence after the bulk-skin temperature difference is artificially destroyed by mechanically generated breaking waves. Supplemental measurements of wind waves in the absence of artificial disruption suggest that microscale wave breaking may provide an important surface renewal mechanism.

1 Introduction

The *surface renewal model* for heat or mass flux across an air-water interface is based on random replacement of fluid in the surface boundary layer with a characteristic renewal time t_* . If it is assumed that the mechanisms of heat and mass transport are similar, gas transfer velocities can be inferred from measurements of heat flux at the air-sea interface.

Using typical open-ocean values for heat flux and bulk-skin temperature difference, Hasse [1990] estimated t_* of $O(10 \text{ s})$ for a wind speed of 6 m s^{-1} . Hasse also noted this estimate was consistent with a thermal recovery time between 5 and 40 s following artificial disruption, as reported by Ewing and McAlister [1960]. Using a “controlled flux technique” to infer gas transfer velocities from infrared measurements of forced surface heating, Jähne *et al.* [1989] stated the thermal recovery time is of the order 0.1 to 10 s. Jessup [1995] reported a recovery time of $O(1 \text{ s})$ due to breaking waves in the field.

While Kitaigorodskii [1984] has modeled large-scale wave breaking as a source of turbulent dissipation contributing to enhanced gas transfer at high winds, Jähne *et al.* [1987] noted that the contribution from microscale wave

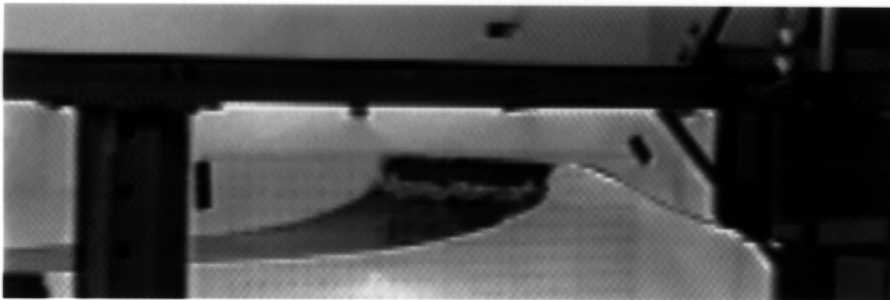


Figure 1: Photograph of individual, mechanically generated breaking wave used to artificially disrupt the thermal boundary layer. Wave propagation is from right to left.

breaking may be more significant. *Csanady* [1990] has modeled gas transfer due to *microscale wave breaking*.

Here, we present laboratory measurements using infrared imagery to demonstrate the dependence of the skin-layer recovery rate on *heat flux* and turbulence after the bulk-skin temperature difference is artificially destroyed by mechanically generated breaking waves. Supplemental measurements of wind waves suggest that microscale wave breaking may indeed provide an important surface renewal mechanism.

Our primary goal is to test the hypothesis that the recovery of the skin layer is dependent on (1) the heat flux, determined, in the absence of wind, primarily by the air-water temperature difference, $T_{\text{air}} - T_{\text{water}}$, and (2) the intensity of turbulence, given by the momentum dissipated by individual breaking waves of varying size.

The measurements were made at the Canada Centre for Inland Waters in Burlington, Ontario, in August, 1994. The wave tank was $10\text{ m} \times 0.3\text{ m}$, and the water depth 0.4 m . The spatial and temporal characteristics of the bulk-skin temperature difference, ΔT , were measured with and without wind using an infrared imager for individual breaking waves ranging in size from incipient to plunging and $T_{\text{air}} - T_{\text{water}}$ from $-11.1\text{ }^{\circ}\text{C}$ to $-4.3\text{ }^{\circ}\text{C}$.

The technique used to generate single breaking waves provides varying levels of *turbulence*, as quantified by the momentum dissipated [*Melville and Rapp*, 1985; *Rapp and Melville*, 1990]. Figure 1 shows an individual wave crest in the process of breaking. In practice, the *dissipation* is parameterized by a gain factor, G , employed to vary the amplitude of the wave packet used to generate the individual breaking wave. Figure 2 shows the relationship between G and the momentum dissipated.

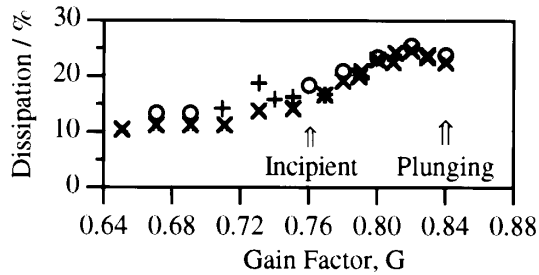


Figure 2: Relationship between momentum dissipation due to individual breaking waves and gain factor, G , used to parameterize breaker size.

2 Experimental Procedure

The spatial and temporal evolution of the *skin layer* following the passage of an individual breaking wave was measured by an Agema model 880LW *infrared imager* oriented along the length of the tank. The imager operates at wavelengths of 8–12 μm resulting in an effective measurement depth of roughly 10 μm . Reflection effects were minimized by shielding the tank with black cloth and poster board. The *bulk-skin temperature difference*, ΔT , was computed using the skin temperature measured by the imager and by taking the bulk temperature to equal the maximum skin temperature during the breaking process. This procedure assumes that the skin layer is completely destroyed by the breaking.

The infrared imagery consists of (1) time sequences of the water surface showing the spatial distribution of ΔT and (2) space-time plots derived from the time sequences. The time sequences consist of 10 images showing ΔT during and after the passage of an individual breaking wave. The vertical axis extends roughly 1.5 m along the tank. The breaking wave propagates from top to bottom; time is noted below each snapshot of the wave tank. The disruption of the skin layer by the passage of the breaking crest occurs early in the sequence, where the time step is a few tenths of a second. After the crest passes, a turbulent patch where $\Delta T \approx 0$ is left behind. The later snapshots, with a time step of 5 s, show the subsequent recovery of the skin layer up to a time of 30 s. The space-time images are a composite of single lines of ΔT along the center of the tank (vertical axis) plotted as a function of time (horizontal axis). The time step is 0.16 s and the plots extend out to 60 s.

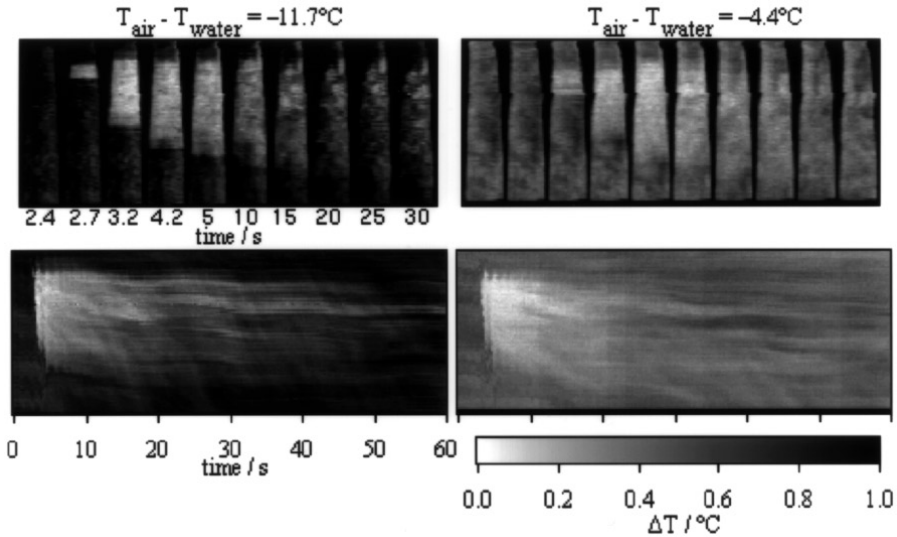


Figure 3: Time sequences (top) and space-time plots (bottom) of ΔT for $T_{\text{air}} - T_{\text{water}} = -11.7^\circ\text{C}$ (left) and -4.4°C (right), a fixed breaker size ($G = 0.76$), and no wind.

3 Results

3.1 Skin-Layer Recovery Rate without Wind

The images in Figure 3 illustrate the dependence of the *skin-layer recovery rate* on heat flux by comparing extremes of $T_{\text{air}} - T_{\text{water}}$ for a fixed breaker size ($G = 0.76$) without wind. The darker appearance of the images for the stronger $T_{\text{air}} - T_{\text{water}}$ (left) confirm that ΔT is greater for larger heat flux. The images also indicate that the skin layer recovery rate is greater for larger heat flux, since ΔT increases with heat flux and the recovery times for each case are comparable (this is shown more clearly later in Figure 5).

The images in Figure 4 illustrate the dependence of the recovery rate on turbulence by comparing extremes of breaker size for fixed $T_{\text{air}} - T_{\text{water}}$ ($\approx -7^\circ\text{C}$); clearly, the recovery time is greater for the larger breaking wave. Larger breaking waves disrupt a greater surface area and generate more turbulence, as quantified by increased momentum dissipation. More intense turbulence of longer duration prolongs the skin layer recovery.

To compare the skin-layer recovery rates for the two cases described above, time series of ΔT were computed from the spatial average over an area that covered roughly 1 m along the tank and 0.15 m across the tank and that was centered on the wake. Measurements of between three and five waves were ensemble averaged for each curve.

The time series of ΔT in the upper plot in Figure 5a show that the skin layer recovery rate, given by the slope, is dependent on $T_{\text{air}} - T_{\text{water}}$. The

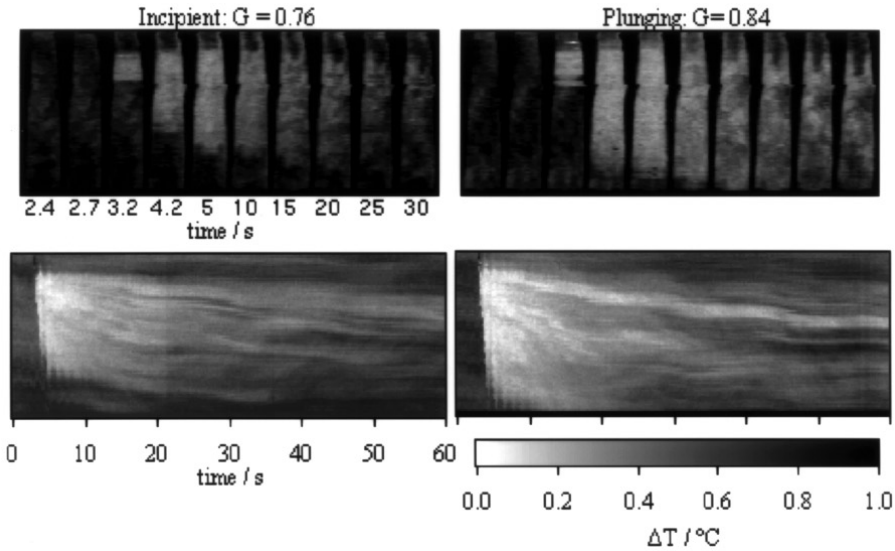


Figure 4: Time sequences (top) and space-time plots (bottom) of ΔT for different-sized breaking waves, described as incipient ($G = 0.76$, left) and plunging ($G = 0.84$, right), a fixed heat flux ($T_{\text{air}} - T_{\text{water}} \approx -7^\circ\text{C}$), and no wind.

skin layer recovers more rapidly for more extreme values of $T_{\text{air}} - T_{\text{water}}$, which correspond to a larger heat flux. The lower plot in Figure 5a shows the normalized bulk-skin temperature difference, $\Delta T_n = \Delta T / \Delta T_{\text{max}}$, where ΔT_{max} is the maximum ΔT measured during the passage of the breaking wave. If the skin-layer recovery rate is determined primarily by heat flux and turbulence, then one would expect a constant skin-layer recovery rate when ΔT is normalized by ΔT_{max} because the dissipation is held constant and, in the absence of wind, ΔT_{max} should be roughly proportional to the heat flux. Although the curves in the lower plot of Figure 5a do not collapse, their slopes are nearly the same.

Figure 5b shows time series of area-averaged ΔT_n for a fixed heat flux and a variable breaker size. The skin layer recovers most rapidly for the breaking waves with the lowest G . In all cases without wind, the disruption persisted for greater than 60 s.

The summary plot in Figure 5c shows the skin layer recovery rate, $d(\Delta T) / dt$, when (1) the breaking strength was varied and heat flux was fixed (+, bottom axis), and (2) the breaking strength was fixed and heat flux was varied (\times , top axis).

The skin-layer recovery rate was computed as the slope of a linear fit for $10 < t < 30$ s. These results show that the skin-layer recovery rate is dependent on both the heat flux and the turbulence resulting from disruption of the skin layer.

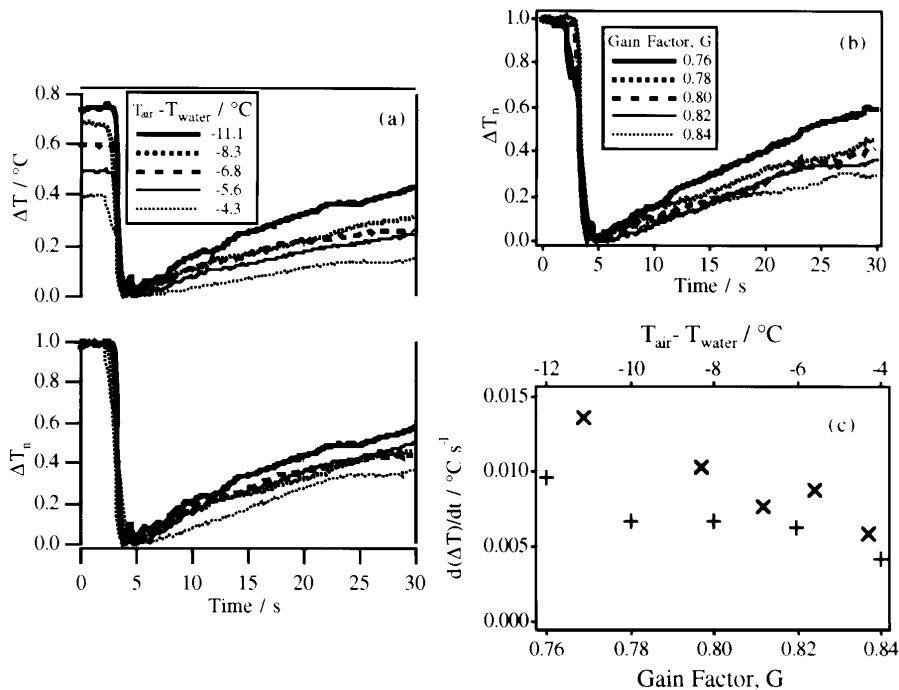


Figure 5: Summary of results for measurements without wind. **a** Time series of area-averaged ΔT and ΔT_n for a fixed breaker size ($G = 0.82$) and variable heat flux, **b** time series of ΔT_n for a variable breaker size and fixed heat flux ($T_{\text{air}} - T_{\text{water}} \approx -7^\circ\text{C}$), and **c** the dependence of the skin-layer recovery rate, $d(\Delta T)/dt$, on $T_{\text{air}} - T_{\text{water}}$ (\times) and G (+).

3.2 The Effect of Wind: Implications for Microscale Breaking

Figures 6 and 7 show the dramatic effect of wind on the spatial and temporal evolution of ΔT . The skin layer recovers to its “undisturbed” state much more rapidly compared with the no-wind cases, in which recovery remains incomplete after 60 s. The images in Figure 6 suggest that the skin layer is disrupted by the effect of the wind itself. Specifically, the space-time plots show temperature variations that propagate down the tank after the skin layer has recovered from the large-scale breaking wave.

The wind-related features shown in Figure 6 led us to investigate skin-layer disruptions due to individual wind waves without the artificial disruption caused by the mechanically generated breaking waves. Figure 8 illustrates the infrared signature of microscale wind-wave breaking. The video image in Figure 8 shows an individual wind-generated gravity wave of wavelength roughly 10 cm. The wave propagates from right to left, with capillary wave instabilities apparent on the forward face. The thermal images in Fig-

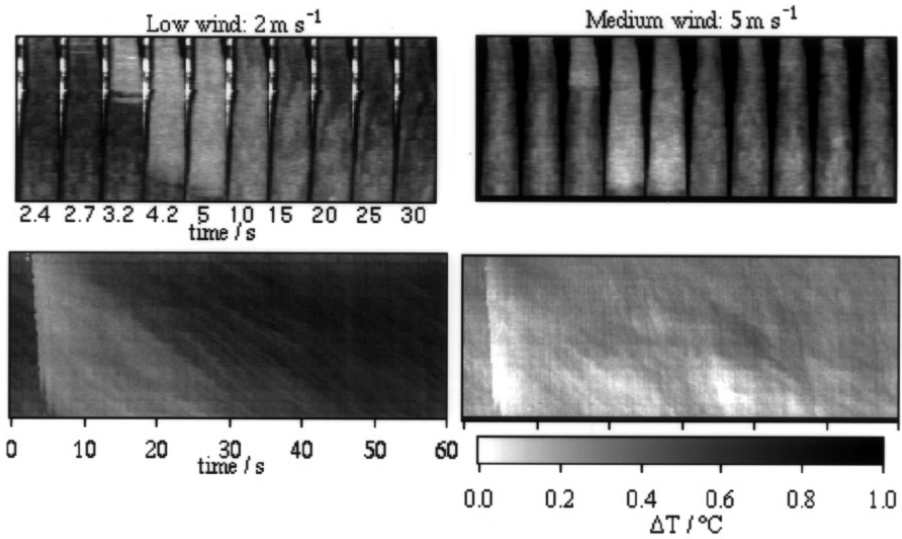


Figure 6: Time sequences of ΔT (top) and space-time plots (bottom) for near-surface wind speeds of 2 m s⁻¹ (left) and 5 m s⁻¹ (right) and a fixed breaker size ($G = 0.80$).

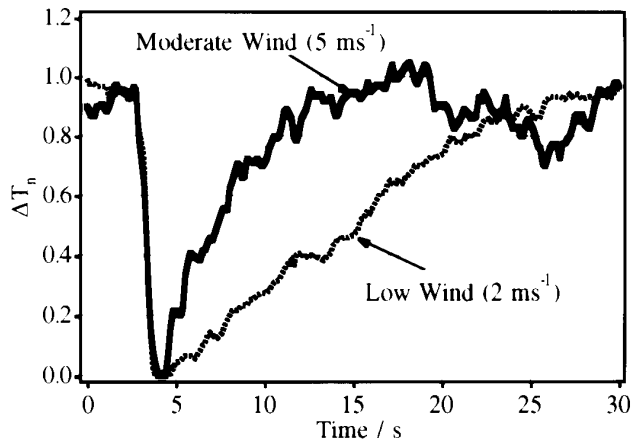


Figure 7: Time series of area-averaged ΔT_n for a fixed breaker strength ($G = 0.82$) and variable wind speed.

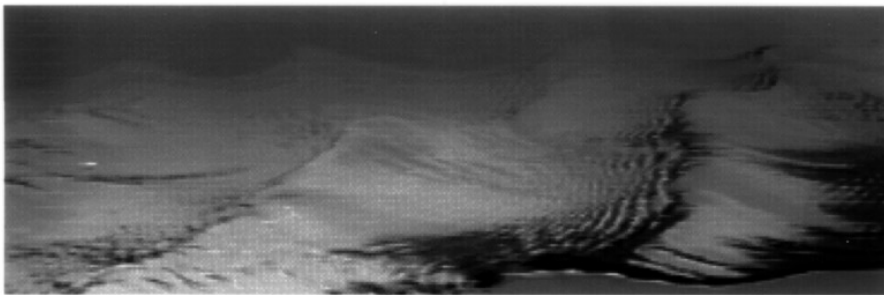


Figure 8: Wind-generated wave of wavelength roughly 10 cm showing capillary wave instabilities generated on forward face. This microscale breaking wave disrupts the thermal skin layer, momentarily destroying the bulk-skin temperature difference.

ure 9 were taken with the wind blowing from bottom to top. Time increases from left to right and spans approximately 2 s. A warm patch due to an individual microscale breaking wave is seen to grow in size and propagate along the tank. The extent of the patch in frame 12, denoted L_{\max} , is on the order of the wavelength. This example is typical of microscale breaking, which occurred continuously. The disruption is associated with the bore-like crest, as opposed to the capillary waves on the forward face. The plot in Figure 10 shows line profiles of temperature along the tank, centered on the warm patch, as indicated by the arrows below the thermal images in Figure 9. The amplitude of the temperature wave is roughly 0.5°C . These observations suggest that microscale wave breaking may provide an additional surface renewal mechanism not generally included in gas transfer models.

4 Summary and Conclusions

The dependence of the skin-layer recovery rate on heat flux and turbulence has been investigated in the laboratory. An infrared imager was used to measure the spatial and temporal evolution of the bulk-skin temperature difference after artificial disruption by individual, mechanically generated breaking waves. With no wind, the skin-layer recovery rate depended on both the heat flux and the turbulence. The skin-layer disruption persisted for at least 60 s.

The skin-layer recovery was significantly accelerated when wind was present, occurring within 10–15 s after disruption. The appearance of temperature fluctuations propagating in the direction of the wind after recovery led to measurements of wind waves without artificial disruption. Our observations of the infrared signature of wind waves suggest that microscale wave breaking may provide a surface renewal mechanism which is not generally included in gas transfer models.

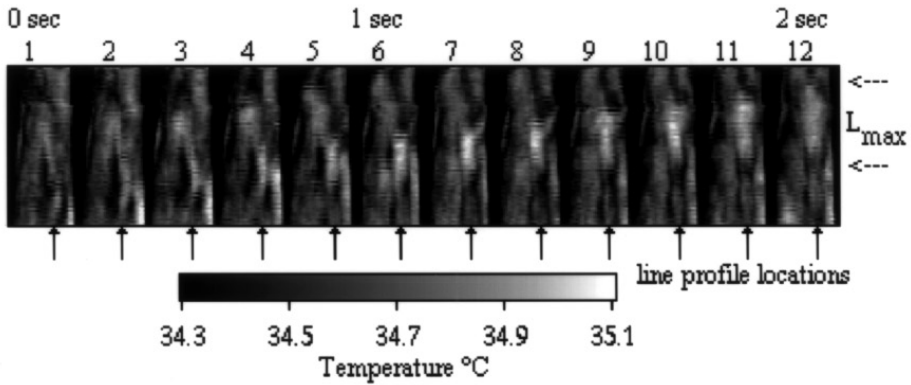


Figure 9: Mosaic of thermal images of water surface with wind-generated waves, looking down on the tank with wind blowing from bottom to top. Time increases from left to right and spans 2 s. A warm patch due to an individual microscale breaking wave is seen to grow in size and propagate along the tank. The extent of the patch in frame 12 is denoted L_{max} . Hatch marks show locations of line profiles in Figure 10.

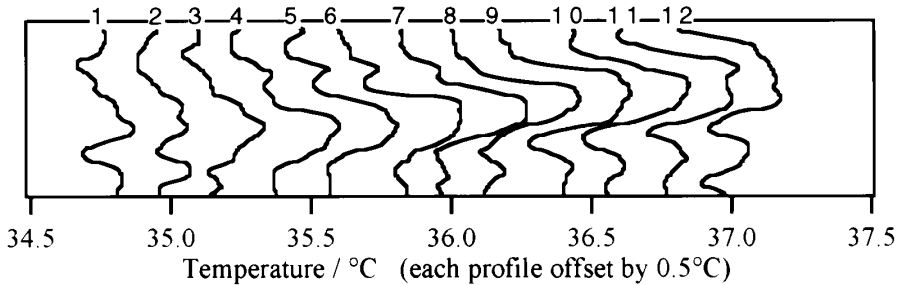


Figure 10: Line profiles of temperature along the tank, centered on the warm patch, for each frame in Figure 7b. The temperature wave with an amplitude of roughly 0.5°C is due to an individual microscale breaking wave crest.

Acknowledgements

Funding for this work was provided by the Office of Naval Research, the National Oceanic and Atmospheric Administration, and the Applied Physics Laboratory, University of Washington.

References

Ewing, G., and E. D. McAlister, On the thermal boundary layer of the ocean, *Science*, 1374-1376, 1960

Csanady, G. T., The role of breaking wavelets in air-sea gas transfer, *J. Geophys. Res.*, 95(C1), 749-759, 1990

- Hasse, L., On the mechanism of gas exchange at the air-sea interface, *Tellus Series B*, 42B, 250-253, 1990
- Jähne, B., K. O. Münnich, R. Börsinger, A. Dutzi, W. Huber, P. Libner, On the parameters influencing air-water gas exchange, *J. Geophys. Res.*, 92(C2), 1937-1949, 1987
- Jähne, B., P. Libner, R. Fischer, T. Billen, and E. J. Plate, Investigating the transfer processes across the free aqueous viscous boundary layer by the controlled flux method, *Tellus Series B*, 41B, 177-195, 1989
- Jessup, A. T., The infrared signature of breaking waves, In *The Air-Sea Interface*, M. A. Donelan, W. H. Hui, W. J. Plant (Ed.), University of Toronto Press, Toronto, 1995 (in press)
- Kitaigorodskii, S. A., On the fluid dynamical theory of turbulent gas transfer across an air-sea interface in the presence of breaking wind-waves, *J. Phys. Oceanogr.*, 14, 960-972, 1984
- Melville, W. K., and R. J. Rapp, Momentum flux in breaking waves, *Nature*, 317, 514-516, 1985
- Rapp, R. J., and W. K. Melville, Laboratory measurements of deep-water breaking waves, *Phil. Trans. Royal Soc. London A*, 331, 735-800, 1990

Relationship between Air-Sea Gas Transfer Velocity and Surface Roughness

Tetsu Hara ¹, Erik J. Bock ²,
Nelson M. Frew ², and Wade R. McGillis ²

¹ Graduate School of Oceanography, University of Rhode Island
Narragansett, RI 02882, USA

² Woods Hole Oceanographic Institution
Woods Hole, MA 02543, USA

Abstract

The relationship between short wind-waves and air-sea gas transfer velocity is studied using experimental results obtained in two laboratory wind-wave flumes. Although the transfer velocity increases linearly with the mean square slope in both experiments, the linear coefficient is much larger in a smaller flume. A close examination of wave fields using a scanning laser slope gauge suggests that only very short waves are related to the gas transfer velocity.

1 Introduction

Series of laboratory experiments have been conducted at the Woods Hole Oceanographic Institution (WHOI) and at the University of Heidelberg (UH) in order to investigate the effects of *wind stress*, *surface roughness*, *near-surface turbulence*, and *surface films* on the air-sea gas transfer velocity. In this article, we focus on the relationship between gas transfer velocity and surface roughness for clean water surfaces. Cases in the presence of surface films are reported in a companion article [Frew *et al.*, 1995].

An extensive summary of past laboratory measurements has been given in Jähne *et al.* [1987]. One of the important findings in their study is an unambiguous correlation between the *mean square slope* of short wind waves and the gas-transfer velocity. This conclusion was derived from experimental data collected in three very different wind-wave flumes. Many theoretical models have attempted to explain the strong effects of capillary-gravity waves on the gas-transfer velocity. Two models [Coantic, 1986; Back and McCreedy, 1988] have suggested that the interaction between surface waves and near surface shear (either in air or water) increases gas-transfer velocity. Csanady [1990] has shown that breaking wavelets may play a key role in the air-sea gas transport.

In order to investigate the role of short wind waves on the air-sea gas exchange, past laboratory experiments are not satisfactory for two reasons. The first is that past experiments at low wind speeds could be influenced by

the presence of surfactant. The second reason is that the method of previous wave characterization — using a point measurement of short wind waves — was ambiguous in clarifying the role of short wind waves, since frequency spectra of short wind waves are strongly influenced by Doppler shift due to near surface currents and larger gravity waves. Here, we report results from what we believe are the first measurements of gas-transfer across very clean air-water interfaces. We also attempt to determine the scale of waves which are most important for the air-sea gas exchange process. The application of a scanning laser slope gauge (SLSG) in the second half of our experiment may enable us to examine the role of wind-generated capillary-gravity waves on the gas-transfer coefficients in detail.

2 Experimental Methods

Experiments were performed in two *annular tanks* of very different scales. The first experiment took place at WHOI in a small annular polycarbonate channel (0.25 m mean radius; 0.1 m width; 0.1 m depth) with a gas-tight airspace to allow both gas invasion and evasion experiments. The tank had multiple ports for air phase purging, sampling of both liquid and gas phases, and for surface skimming to remove surface films. Wind-driven waves were generated by a disc with rows of vertical vanes arranged around the disc perimeter. Instrumentation in this wave tank included a fixed-point laser slope gauge, a current meter, an oxygen probe, and a surface tension electrobalance. The laser slope gauge allowed point measurements of wave slope spectra in the tank with a Nyquist frequency of 150 Hz. Wind stress was estimated by the momentum balance method [Jähne *et al.*, 1984].

The second experiments took place in an annular tank at UH (2 m mean radius; 0.3 m width; 0.25 m depth), which was equipped with a rotating paddle ring for wind generation and a degassing unit [Schmundt *et al.*, 1995]. The gas transfer velocity was measured by both oxygen-invasion and SF₆-evasion methods. Wind stress and near-surface turbulence were monitored using an X-film probe. Wind-waves were measured using a *scanning laser slope gauge* developed by Bock and Hara [1995]. The instrument is capable of measuring the three-dimensional wavenumber-frequency slope spectrum of capillary-gravity waves for wavenumbers between 30 and 1200 radian/m with a Nyquist frequency of 20.8 Hz. The instrument was successfully tested in a laboratory experiment and the associated instrumental errors were fully analyzed [Bock and Hara, 1995].

In order to keep the water surface free from surfactants, the surface was continuously skimmed during the experiment. Visual observations confirmed that the presence of the skimmer did not affect the wind-wave field. To further ascertain the cleanliness of the surface, water samples were drawn into a small linear tank during the course of experiments. Surface tension was measured with a Cahn 2000 electrobalance and a platinum Wilhelmy plate. Mechanically generated capillary-gravity waves were used to measure

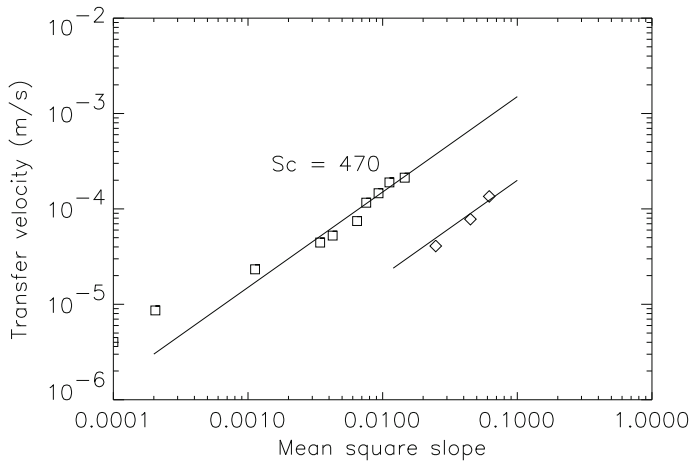


Figure 1: Gas transfer velocity versus mean square slope of wind waves. Squares, small tank at WHOI; diamonds, large tank at UH.

the surface viscoelasticity. In all cases reported here, the surface tension was close to the theoretical value (0.073 N/m) and the surface viscoelasticity was negligibly small.

3 Results and Discussion

In Figure 1 of the companion paper [Frew *et al.*, 1995] we report the relationship between the wind friction velocity and the gas transfer velocity. Our measurements do not support the concept that a critical wind velocity is necessary to initiate wind-waves on clean water. Such a *critical wind velocity* is associated with changes in near-surface turbulence regime as indicated by a change in Schmidt number dependency of gas exchange rate and is commonly observed in wind-wave tank studies and in situ studies [Jähne *et al.*, 1984; Liss and Merlivat, 1986]. However, for very clean surfaces, capillary ripples can be observed at the lowest wind speed attainable. The transfer velocity increases smoothly and linearly with friction velocity. This result is consistent with the finding of Scott [1972], who also found no evidence of a critical wind velocity for the initiation of wind-waves on assiduously cleaned water surfaces, using a completely different tank geometry. The excellent agreement between the results from the large flume (UH) and those from the small flume (WHOI) suggests that the finite size of the tank does not influence the air-water gas transfer process.

Next, we show the relationship between the gas transfer velocity and the mean square slope of wind-waves in Figure 1. Although linear relations are observed independently among the results in the small flume as well as among the results in the large flume, the transfer velocity values are much

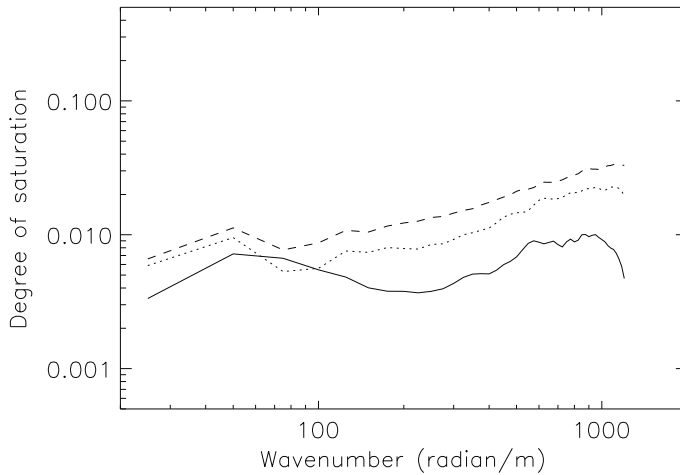


Figure 2: Degree of saturation of wind waves integrated over all directions. Solid line, friction velocity 0.23 m/s; dotted line, 0.42 m/s; dashed line, 0.57 m/s.

larger in the small tank than in the large tank at any given mean square slope. This fact suggests that the mean square slope alone does not provide a good parameterization of the transfer velocity. It does not support the argument by *Jähne et al.* [1987] that the transfer velocity is impacted by contributions to mean square slope at all wave frequencies.

Since neither a mean square slope or a frequency spectrum provides sufficient information on short wind-waves of different scales [*Hara et al.*, 1994], we use wavenumber spectra, obtained only in the larger flume at UH, in order to clarify what scale of waves are correlated most with gas transfer velocity. In Figure 2, the degree of saturation of wind waves (see *Jähne and Riemer* [1990] for definition) integrated over all directions are shown at three different wind friction velocities.

Although the values at lower wavenumbers (< 100 radian/m) are consistent with the large wind-wave flume results by *Jähne and Riemer* [1990], our results at higher wavenumbers are consistently higher. Also, our results do not show a cut-off wavenumber above which the degree of saturation decreases rapidly. In the large facility such cut-off wavenumbers were observed for a wide range of wind stress. It is not clear whether the discrepancy is because of the difference of the tank geometry or because of our careful cleaning of the surface.

In Figure 3 we plot the gas transfer velocity against the degree of saturation at three different wavenumbers. While the degree of saturation values at two higher wavenumbers (200 and 800 radian/m) correlate almost linearly with the transfer velocities, the values at the lowest wavenumber (50 radian/m) do not show any correlations. From these results, it is reasonable to assume that shorter waves are more directly related to the air-water gas

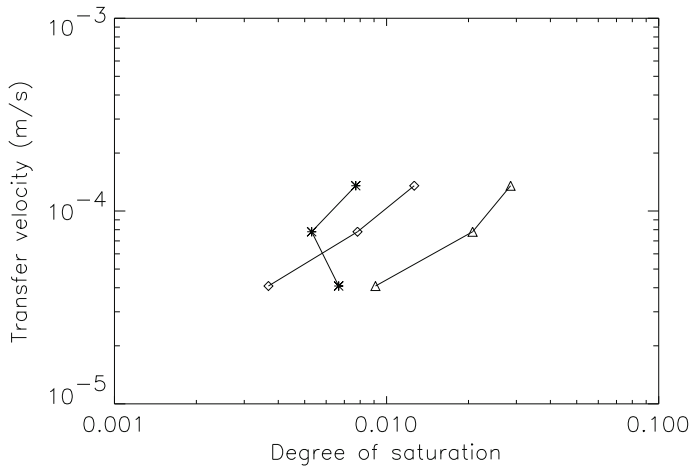


Figure 3: Gas transfer velocity versus degree of saturation of wind waves. Stars, wavenumber 50 radian/m; diamonds, 200 radian/m; triangles, 800 radian/m.

transfer process. This assumption may also explain why the relation between the mean square slope and the transfer velocity differs depending on the tank size. At a given wind stress longer waves are excited in a larger facility, and they contribute to the mean square slope even if the short wave fields are similar. Hence, the relation between the mean square slope and the gas transfer velocity is modified.

4 Concluding Remarks

Our careful analyses of the two laboratory results indicate that shorter wind-waves show a better correlation with the air-sea gas transfer, suggesting that shorter capillary waves might be responsible for the gas transfer, an observation consistent with the model by *Coantic* [1986]. Future extensions of this study include the analysis of the relation between wind-waves and gas transfer in the presence of surface films.

Acknowledgements

This work was supported by U.S. National Science Foundation, Grant OCE 9301334.

References

Back, D. D., and M. J. McCreedy, Effect of small-wavelength waves on gas-transfer across the ocean surface, *J. Geophys. Res.*, 93, 5143-5152, 1988.

- Bock, E. J., and T. Hara, Optical measurements of capillary-gravity wave spectra using a scanning laser slope gauge, *J. Atm. Ocean Tech.*, 12, 395-403, 1995.
- Coantic, M., A model of gas-transfer across air-water interfaces with capillary waves, *J. Geophys. Res.*, 91, 3925-3943, 1986.
- Csanady, G. T., The role of breaking wavelets in air-sea gas-transfer, *J. Geophys. Res.*, 95, 749-759, 1990.
- Frew, N. M., E. J. Bock, W. R. McGillis, A. V. Karachintsev, and T. Hara, Parameterization of air-water gas transfer using wind stress and viscoelasticity, this issue, 1995.
- Hara, T., E. J. Bock, and D. Lyzenga, In situ measurements of capillary-gravity wave spectra using a scanning laser slope gauge and microwave radars, *J. Geophys. Res.*, 99, 12,593-12,602, 1994.
- Jähne, B. K., W. Huber, A. Dutzi, T. Wais, and J. Ilmberger, Wind/wave tunnel experiments on the Schmidt number and wave field dependence of air/water gas exchange, in *Gas Transfer at Water Surfaces*, edited by W. Brutsaert and G. H. Jirka, pp. 303-309, Reidel, Dordrecht, Netherlands, 1984.
- Jähne, B. K., O. Mnich, R. Bsinger, A. Dutzi, W. Huber, and P. Libner, On the parameters influencing air-water gas exchange, *J. Geophys. Res.*, 92, 1937-1949, 1987.
- Jähne, B. K., and K. S. Riemer, Two-dimensional wave number spectra of small-scale water surface waves, *J. Geophys. Res.*, 95, 11,531-11,546, 1990.
- Liss, P. S., and L. Merlivat, Air-sea gas exchange rates: introduction and synthesis, in *The Role of Air-Sea Exchange in Geochemical Cycling*, edited by P. Buat-Menard, pp. 113-127, Reidel, Dordrecht, Netherlands, 1986.
- Scott, J. C., The influence of surface-active contamination on the initiation of wind waves, *J. Fluid Mech.*, 56, 591-606, 1972.
- Schmundt, D., T. Münsterer, H. Lauer, and B. Jähne, The circular wind/wave facilities at the University of Heidelberg, *This volume*

Wind and Wave Effects on Mass Transfer Velocities of Halomethanes and SF₆ Measured in a Gas Transfer Flume

M. Alaei, M. A. Donelan, and W. M. J. Strachan

National Water Research Institute, Canada Centre for Inland Waters
867 Lakeshore Road, P.O. Box 5050, Burlington, Ontario, Canada, L7R 4A6.

Abstract

The mass transfer velocities of gas tracer sulphur hexafluoride and of four halomethanes along with tetrachloroethene with Schmidt numbers ranging from 430 to 1100 were measured in a linear gas transfer flume under different wind speeds ($U_{0,3} = 1-15$ m/s) resulting in different wave fields (smooth, rough, and breaking). Simultaneous measurement of up to 3 compounds was achieved using a membrane inlet mass spectrometer. The mass transfer velocities were correlated with Schmidt numbers and with the ratios of diffusion coefficients.

1 Introduction

Estimation of *atmospheric fluxes* is an essential component in evaluating the role of contaminants such as carbon dioxide in global warming effects [Ocampo-Torres *et al.*, 1994] and in the transport of persistent organochlorine pollutants to cold climate regions such as the Arctic and Antarctic [Mackay and Wania, 1995]. *Gas exchange* across the air-water interface plays an important role in the determination of total atmospheric fluxes of contaminants into or out of a body of water. The atmospheric flux of gases (F) is described by equation (1) [Mackay and Leinonen, 1975]:

$$F = K_{ol}(C_w - \frac{C_a}{H}) \quad (1)$$

where K_{ol} is the mass transfer velocity, H is the dimensionless Henry's Law parameter, C_a and C_w are the concentrations in air and water. The magnitude of the flux gradient across the air-water interface is controlled by Henry's Law parameter, and by the difference of air and water concentrations from equilibrium. The rate of transfer across the air-water interface is also determined by the mass transfer velocity which is proportional to the diffusion coefficient of the molecules through the air and water. Air and water concentrations are determined directly, H can be estimated by various experimental procedures such as headspace analysis, sparging, or from

the ratio of vapour pressure to solubility, and the mass transfer velocity is determined under controlled laboratory or field experiments by:

$$L \frac{\partial C_w}{\partial t} = -K_{ol} \left(C_w - \frac{C_a}{H} \right) \quad (2)$$

where L is the ratio of water volume to surface area exposed to wind, and t is time. These types of determinations are costly and time consuming and only limited values for mass transfer velocities are available from laboratory or field determinations.

Another approach is to use a two film model to estimate the mass transfer velocity. Equations describing the two film resistance method were developed by *Whitman* [1923], further refined by *Liss and Slater* [1974], and modified for use with semi-volatile organic chemicals by *Mackay and Yeun* [1983], and *Baker and Eisenreich* [1990].

$$\frac{1}{K_{ol}} = \frac{1}{k_w} + \frac{1}{Hk_a} \quad (3)$$

where $1/k_w$ and $1/Hk_a$ are water and air film resistances respectively. Compounds such as CO_2 , where $1/k_w \gg 1/Hk_a$, are referred to as water phase controlled; on the other hand compounds such as water vapour, where $1/k_w \ll 1/Hk_a$, are air phase controlled.

Compounds with high molecular weights such as PCBs and DDTs, are controlled by both phases. Since mass transfer velocities for many compounds are not available from experimental sources, estimation methods are used. Air phase controlled compounds are usually determined from that of water vapour, and water phase controlled compounds are determined from CO_2 or SF_6 [*Hornbuckle et al.*, 1995]. The correlations are based on the Schmidt number which is the ratio kinematic viscosity of air or water to the diffusion coefficients of the compounds in the same medium. The mass transfer velocities of *chloromethanes* (mono-, di-, tri-, and tetra-) along with *sulphur hexafluoride* were determined in the *Gas Transfer Flume* (GTF) facility at the National Water Research Institute, and were used to compare with predictions using this approach.

2 Experimental

The GTF facility at NWRI is a linear recirculating gas tight flume (32 (l) \times 0.76 (w) \times 0.80 (h) m, water depth = 0.225 m). A detailed description of this flume is given by *Merzi et al.* [1990]. Briefly, this flume is equipped with two fans which deliver winds up to 25 m/s and can be operated in vented or circulating mode. A 15 hp pump is used to circulate the water; this pump is capable of circulating the water at mean speeds up to 60 cm/s, although during the course of these experiments the water was circulated

Table 1: List of the compounds and mass fragments.

Compound	Molecular Weight	Quantitation m/e	Mass Fragment	Confirmation m/e	Mass Fragment
SF ₆	146	127	M-F	108	M-2F
C ₂ Cl ₄	166	164	M	166	M+2
CCl ₄	154	119	M - Cl	117	M-2-Cl
CHCl ₃	119.5	84	M - Cl	86	M+2-Cl
CH ₂ Cl ₂	85	85	M	87	M+2
CH ₃ Cl	50.5	50	M	52	M+2
CH ₄	16	15	M-H	N/A	N/A

at 10 cm/s. Wind and wave data are collected at three sampling stations with 0.2 mm capacitance wave gauges and pitot tubes, and a laser system which measures wave height and slope. In these experiments the GTF was operated in its vented mode. With continuous use of fresh air in the flume, the concentrations of the analytes in the air are negligible (i. e., $[C_a] \approx 0$) for the species of interest in these experiments. Therefore equation (2) after integration will become:

$$\ln \frac{C_w}{C_{w0}} = -\frac{K_{ol}}{L} t \quad (4)$$

Mass transfer velocities can therefore be determined under these circumstances using time series of the concentration of analytes in water. Water concentrations as a function of time were determined using a MIMS (membrane inlet mass spectrometry) system. The experimental system consisted of a 300 atomic mass unit (amu) quadrupole mass spectrometer (Hidden, Hal) equipped with a siloxane membrane system for direct sampling of dissolved hydrophobic species in water. The probe was inserted into a 3.2 mm sampling loop with a flow of 50 ml/min taken from and returned to the GTF. Due to the interference of common mass fragments a maximum of only 3 species were introduced into the GTF. The mass spectrometer was set to follow up to 6 mass/ charge (m/e) ions (2 per compound) at 0.15 Hz for each m/e for a duration of 3 hours. The m/e values used for each compound are given in Table 1.

Methane (99%) and chloromethane (99%) were obtained from Matheson; dichloromethane was obtained from Caledon Laboratory (distilled in Glass). All other chemicals were obtained from Aldrich and were 99% pure. The species of interest were introduced into a tail box downstream of the sampling station. Liquid samples were introduced directly and gaseous samples were injected through a perforated stainless steel tubing. The water was recirculated at 60 cm/sec for mixing and reduced to 10 cm/sec after steady state at zero wind speed was achieved.

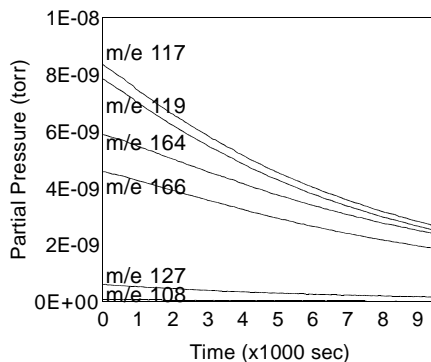


Figure 1: Raw data collected during the experiment.

Table 2: Diffusion coefficients (D) in air and water and Schmidt number in water for compounds used in this study at 25°C along with $R_{a/w}$ (k_w/Hk_a) at 1 m/sec.

Compound	D_{air} (m^2/sec)	D_{water} (m^2/sec)	$R_{air/water}$	Sc_{water}
SF_6	0.91×10^{-5}	11.6×10^{-10}	$<10^{-10}$	770
C_2Cl_4	0.86×10^{-5}	8.12×10^{-10}	1.6×10^{-3}	1100
CCl_4	0.89×10^{-5}	9.35×10^{-10}	2.5×10^{-3}	950
CHCl_3	1.0×10^{-5}	10.5×10^{-10}	1.7×10^{-3}	850
CH_2Cl_2	1.2×10^{-5}	12.3×10^{-10}	1.5×10^{-3}	720
CH_3Cl	1.6×10^{-5}	15.0×10^{-10}	4.6×10^{-4}	590
CH_4	2.8×10^{-5}	20.6×10^{-10}	4×10^{-5}	430

3 Results and Discussion

The compounds used in this study had relatively simple chemical structures and properties. These were: a limited number of elements, simple geometrical shapes with no aromatic rings or cyclic structures, non-ionic, water phase controlled, stable in water during the course of the experiments, minimum solubility of $1 \mu\text{g}/\text{ml}$ for detection by MIMS. As indicated in Table 2, the diffusivities of methane and chlorinated methane (mono, di, tri and tetra chloro) made them good candidates for this type of study. Sulphur hexafluoride was used as a benchmark compound for this study, and tetrachloroethene was examined because of its abundance in the environment.

Typical time series of partial pressure results from these experiments are presented in Figures 1-3. Figure 1 is the raw data collected from the mass spectrometer for six masses: 127 and 108 for SF_6 , 166 and 164 for C_2Cl_4 , 117 and 119 for CCl_4 . Due to interferences, which result from the loss of

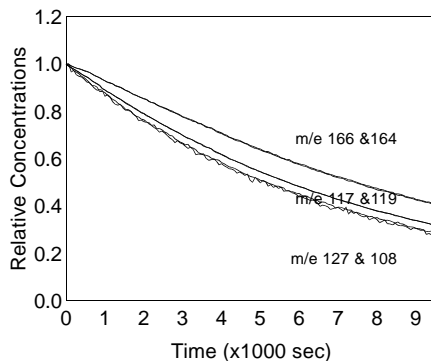


Figure 2: Normalized data (C/C_0).

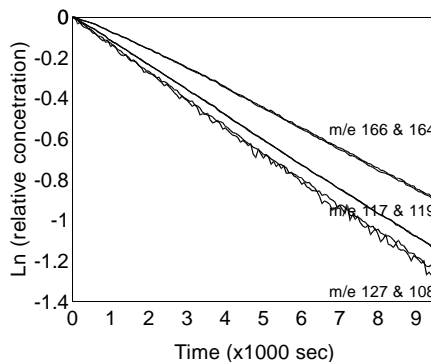


Figure 3: $\ln(C/C_0)$ as function of time.

a second chlorine, only two halomethanes were used simultaneously, i. e., one with an odd and the other with an even number of chlorines. The first step in data processing was to normalize the different mass fragments corresponding to the same compound collected during the course of experiment (Figure 2). Figure 3 is the logarithmic presentation of the relative concentration, straight lines corresponds to an exponential decay with time (Figure 3). R^2 (correlation coefficient) values for these experiment were >0.999 . In all cases except data collected for methane both signals converged to within 2%. The mass spectrum for methane consists of 3 main ions 16, 15, and 14; m/e 16 also corresponds to atomic oxygen and m/e 14 to atomic nitrogen. To avoid the interferences due to nitrogen and oxygen m/e 15 was selected to follow during the course of the methane experiment. However m/e 15 also corresponds to M - Cl in chloromethane. In this case the m/e 15 con-

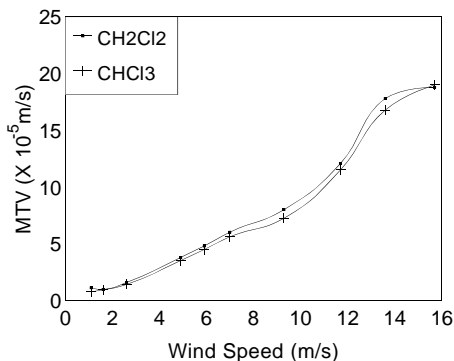


Figure 4: Wind speed dependence of Mass Transfer Velocity (MTV) for CH_2Cl_2 and CHCl_3 .

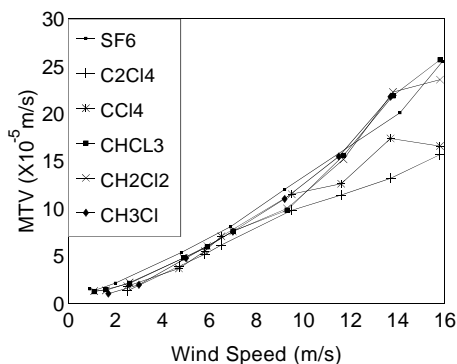


Figure 5: Wind speed dependence of MTVs for all compounds at $Sc \# 600$.

tribution from chloromethane was estimated from the ratio of fragments 50:15, and this was subtracted from the total signal to determine the signal due to methane. Unfortunately, after these data manipulations, the quality of the signal for methane was so deteriorated that the data was discarded.

The effect of wind on the mass transfer velocities of dichloromethane and trichloromethane is illustrated in Figure 4. Mass transfer velocity results from the experiments, along with appropriate conversion of these to *Schmidt number* of 600 are presented in Table 3. Variations in laboratory air temperature and water temperature were accounted for by adjusting the results to 20 °C using Schmidt number dependence. As shown, there are two distinct regions: a “smooth” region which is up to about 3 m/sec and a “rough” region which starts above 3 m/s. Due to the linear nature of the Gas

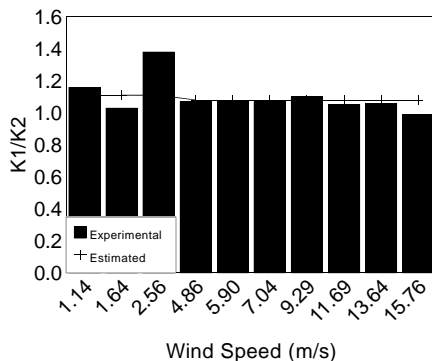


Figure 6: Comparison between ratios of MTVs and ratios of diffusion coefficients for CH₂CL₂ and CHCL₃.

Transfer Flume there is no definitive onset of breaking waves everywhere; as a result the third region is not pronounced. Similar results were observed in CO₂ studies performed previously [Ocampo-Torres et al., 1994].

Results from the Schmidt number conversion are presented in Figure 5. As shown there is good similarity among all mass transfer velocities for various compounds referred to Schmidt number of 600.

Ratios of the mass transfer velocities of the paired compounds *dichloromethane* and *trichloromethane* are presented in Figure 6 (bars), along with the ratio of the estimated diffusion coefficients (line). Di/trichloromethane system had an average ratio of 1.10 ± 0.11 and a median of 1.07 compared to the diffusion coefficient ratio of 1.08.

The *tetrachloromethane/tetrachloroethene* system on the other hand had an average ratio of 1.23 ± 0.18 , compared to the estimated value of 1.08. The main source of error associated with these values is in estimating the diffusion coefficients. Most of the current methods to estimate diffusion coefficients such as *Wielke and Chang* [1950] and *Hayduk and Laudie* [1974] have errors up to 25% associated with such estimates. Independent experimental measurement of diffusion coefficients will improve our capability to estimate mass transfer velocities for various compounds more accurately.

4 Summary and Conclusions

Mass transfer velocities of chloromethanes (mono-, di-, tri-, and tetra-), along with tetrachloroethene and sulphur hexafluoride, were measured in a linear gas transfer flume. Similar wind effects on mass transfer velocities of these compounds were observed. Differences in mass transfer velocity showed good correlation with diffusion coefficients. Better estimates of diffusion

Table 3: Mass Transfer Velocities obtained in the Gas Transfer Flume.

Compound	Temperature		Wind Speed (m/s)	Mass Transfer Velocity ($\times 10^{-5}$ m/s)	
	Air ($^{\circ}$ C)	Water ($^{\circ}$ C)		Raw data	Sc # 600
SF ₆	23.0	16.6	0.85	0.79	1.50
SF ₆	23.0	16.9	1.03	0.74	1.34
SF ₆	22.8	18.4	2.01	1.10	2.12
SF ₆	22.2	20.3	4.78	3.67	5.36
SF ₆	23.3	19.3	6.87	5.31	8.08
SF ₆	23.4	18.0	9.16	7.41	12.0
SF ₆	22.8	14.1	14.1	10.8	20.1
SF ₆	22.9	16.2	15.9	14.7	25.5
C ₂ Cl ₄	22.9	18.6	2.47	0.70	1.28
C ₂ Cl ₄	23.5	18.6	4.65	2.46	3.89
C ₂ Cl ₄	23.0	18.8	5.79	3.28	5.17
C ₂ Cl ₄	23.5	19.4	6.51	4.00	6.14
C ₂ Cl ₄	22.4	15.5	9.50	5.73	9.80
C ₂ Cl ₄	22.4	14.9	11.6	6.45	11.4
C ₂ Cl ₄	22.4	15.5	13.7	7.74	13.2
C ₂ Cl ₄	22.5	18.7	15.8	9.95	15.7
CCl ₄	22.9	18.6	2.47	1.08	1.80
CCl ₄	23.5	18.6	4.65	2.50	3.67
CCl ₄	23.0	18.8	5.79	3.74	5.49
CCl ₄	23.5	19.4	6.51	4.93	7.05
CCl ₄	22.4	15.5	9.50	7.23	11.5
CCl ₄	22.4	14.9	11.6	7.90	12.6
CCl ₄	22.4	15.5	13.6	11.2	17.4
CCl ₄	22.5	18.7	15.8	11.3	16.6
CHCl ₃	23.2	17.2	1.14	0.74	1.23
CHCl ₃	23.2	18.9	1.64	0.94	1.45
CHCl ₃	23.1	19.2	2.56	1.41	2.10
CHCl ₃	22.6	18.4	4.86	3.37	4.79
CHCl ₃	22.8	17.5	5.90	4.17	5.93
CHCl ₃	23.0	16.9	7.04	5.20	7.60
CHCl ₃	22.5	16.2	9.29	6.53	9.81
CHCl ₃	22.4	16.1	11.7	10.4	15.6
CHCl ₃	22.4	15.5	13.8	14.6	21.9
CHCl ₃	22.5	18.7	15.8	18.6	25.7

cont'd Table 4

Table 4: Mass Transfer Velocities obtained in the Gas Transfer Flume (continued from Table 3).

Compound	Temperature		Wind Speed (m/s)	Mass Transfer Velocity ($\times 10^{-5}$ m/s)	
	Air (°C)	Water (°C)		Raw data	Sc # 600
CH ₂ Cl ₂	23.2	17.2	1.14	0.86	1.28
CH ₂ Cl ₂	23.2	18.9	1.64	0.97	1.35
CH ₂ Cl ₂	23.1	19.2	2.56	1.57	2.18
CH ₂ Cl ₂	22.6	18.4	4.86	3.62	4.77
CH ₂ Cl ₂	22.8	17.5	5.90	4.46	6.04
CH ₂ Cl ₂	23.0	16.9	7.04	5.58	7.56
CH ₂ Cl ₂	22.5	16.2	9.29	7.21	10.0
CH ₂ Cl ₂	22.4	16.1	11.7	10.9	15.2
CH ₂ Cl ₂	22.4	15.5	13.8	15.6	22.3
CH ₂ Cl ₂	22.5	18.7	15.8	18.4	23.6
CH ₃ Cl	22.6	18.0	1.66	0.82	1.01
CH ₃ Cl	23.0	17.8	3.00	1.64	1.95
CH ₃ Cl	22.9	17.8	5.00	4.00	4.76
CH ₃ Cl	22.8	18.0	7.02	6.36	7.55
CH ₃ Cl	22.9	17.7	9.17	9.29	11.0
CH ₃ Cl	22.8	17.4	11.51	12.7	15.5
CH ₃ Cl	22.7	17.1	13.67	17.8	21.8

coefficients along with their temperature dependence are required to estimate the mass transfer velocity of different compounds.

Acknowledgements

The authors would like to acknowledge the technical contributions of J. Chisholm and D. Beesley. The MIMS system used in these experiments was supplied by B. Kerman. Financial support for this work was provided by the Great Lakes Action Plan of Environment Canada.

References

- Baker, J. E., and S. J. Eisenreich, Concentrations and fluxes of PCBs and PAHs across the air-water interface of Lake Superior, *Environ. Sci. Technol.*, 24, 342-352, 1990
- Hayduk, W, and H. Laudie, Prediction of diffusion coefficients for nonelectrolysis in dilute aqueous solutions, *AIChE J.*, 20, 611-615, 1974

- Hornbuckle, K. C., C. W. Sweet, R. J. Pearson, D. L. Swackhamer, and S. J. Eisenreich, Assessing Annual water-air Fluxes of polychlorinated Biphenyls in Lake Michigan, *Environ. Sci. Technol.*, 29, 869-877, 1995
- Jähne, B., W. Huber, A. Dutzi, T. Wais, and J. Ilmberger, Wind/wave-tunnel experiment on the Schmidt number - and wave field dependence of air/water gas exchange, In *Gas transfer at Water Surfaces*, W. Brutsaert, and G. H. Jirka, eds., 303-309, 1984
- Liss, P. S., and P. G. Slater, Flux of gases across the air-water interfece, *Nature*, 247, 181-184, 1974
- Makay, D., and A. T .K. Yeun, Mass transfer coefficient correlations for volatilization of organic solutes from water, *Environ. Sci. Technol.*, 17, 211-217, 1983
- Mackay, D. and F. Wania, Transport of contaminants to the Arctic, partitioning, processes, and models. *Sci. Total Environ.*, 160, 25-38, 1995
- Mackay, D., and P. J. Leinonen, Rate of evaporation of low solubility contaminants from water bodies to atmosphere. *Environ. Sci. Technol.*, 13, 333-337, 1975
- Merzi, N, M. R. Servos, and M. A. Donelan, Description of an air-tight gas transfer flume and experimental program for mass transfer at the air-water interface. *Technical Report 90-147*, National Water Research Institute, 1990
- Ocampo-Torres, F. J., M. A. Donelan, N. Merzi, and F. Jia, Laboratory measurements of mass transfer of carbon dioxide and water vapour for smooth and rough flow conditions. *Tellus*, 46 B:16-32, 1994
- Whitman, W. G., *Chem. Metall Eng.* 29, 146-148, 1923
- Wielkey, C. R. and P. Chang, Correlation of diffusion coefficients in dilute solutions, *AIChE J.*, 1, 264-270, 1955

Measurement of the Concentration Field Resulting from Oxygen Absorption at a Wavy Air-Water Interface

S. R. Duke and T. J. Hanratty

Department of Chemical Engineering
University of Illinois
Urbana, Illinois 61801 USA

Abstract

A technique is described which uses laser-induced fluorescence to measure the instantaneous two-dimensional concentration field of absorbing or desorbing oxygen just beneath an air-water interface. Wind waves have a profound influence on the time-averaged mass transfer rate. The fluorescence measurements show very large variations in the concentration field, which are believed to be related to variations of wave slope.

1 Introduction

Wind waves increase the mass transfer coefficient characterizing the exchange of gaseous components across an air-water interface by a factor of 3 to 5. The mechanism responsible for this enhancement has not been identified. Measurements of the local instantaneous *concentration field* in the liquid offer the opportunity of obtaining a better understanding of how absorption is related to the fluctuating velocity field in the liquid. However, such investigations are made difficult because of the thinness of the concentration *boundary layer* (20 to 300 μm).

The research described in this paper was undertaken to improve the technique described at the last conference on Air-Water Gas Transfer [Wolff, Liu, and Hanratty, 1990]. A *laser-induced fluorescence* method, which measured the time-varying one-dimensional *oxygen* concentration field in the liquid close to the interface, was described. Results for measurements in a stagnant fluid validated the relationship between the fluorescent signal and the local oxygen concentration. This arrangement has since been used to determine one-dimensional concentration fields for air and water flow in a *channel* [Wolff and Hanratty, 1994]. When measurements are compared for a flat interface and for an undulating interface, an interesting behavior of k/\bar{k} is found, where k is the local mass transfer coefficient and \bar{k} is the average mass transfer coefficient [measured with submerged O_2 probes, as described by McCready and Hanratty, 1985]. The ratio k/\bar{k} varies greatly for a wavy interface compared to what is found for a flat interface or a turbulent field. Thus, the waves cause large spatial variations in the thickness of

the concentration boundary layer. When k/\bar{k} was greater than 2, measurements of the boundary layer profile could not be made because it was too thin. The data suggest that the steepness of the interface is the main factor determining the variation in k/\bar{k} , because locations in the interface where measurements could not be made had steep slopes.

In recent work a laser-sheet was used in an attempt to study the two-dimensional concentration field. This paper reviews results obtained by *Wolff and Hanratty* [1994] and describes progress in using a two-dimensional light sheet.

2 Technique

The flow facility is a horizontal rectangular channel which has a height of 2.54 cm, a width of 30.5 cm, and a length of 11 m. The test section is 3.9 m from the liquid entrance. The concentration of dissolved oxygen in the recirculating water stream is controlled by bubbling nitrogen into the water holding tank. Air flowing over the water facilitates O₂ absorption through the interface. The liquid height is roughly 5 mm. The water and air flow concurrently. The temperature of the air and water are not controlled, but they remain between 20 and 24 °C.

Bulk O₂ concentrations were measured with submerged oxygen probes. The Beckman Monitor II system with a 39556 field oxygen sensor was used for measurements at two locations in the channel: 3.5 and 10 m from the liquid entrance (the upstream location near the optical test section). The time-averaged mass transfer coefficient \bar{k} was obtained from measurements of the liquid flow rate and the change in O₂ concentration between the metered locations.

The water contains *pyrene-butyric acid* (PBA). The vertical beam from a nitrogen laser ($\lambda = 337$ nm) excites the PBA molecules which, in turn, fluoresce. The fluorescence is quenched by dissolved O₂. Concentration is related to fluorescence intensity by the Stern-Vollmer equation:

$$\frac{F'_0}{F'} = 1 + k_{SV}C' \quad (1)$$

where F' is the fluorescence intensity, F'_0 is the intensity when no quencher is present, C' is quencher concentration, and k_{SV} is a constant. Near the interface, where the O₂ concentration is greatest (and determined by Henry's Law), the fluorescence intensity is weakest. In the bulk flow, where the O₂ concentration is smallest, the signal is strongest. Thus, a vertical concentration profile can be directly calculated from a vertical fluorescence intensity profile. When a vertical laser-sheet is used, a map of the two-dimensional fluorescence intensity is directly related to the two-dimensional concentration field. The PBA concentration is 4×10^{-5} M. A concentrated stock solution of PBA is prepared in warm 0.05 M NaOH to ensure that the PBA goes into solution [*Münsterer*, 1994].

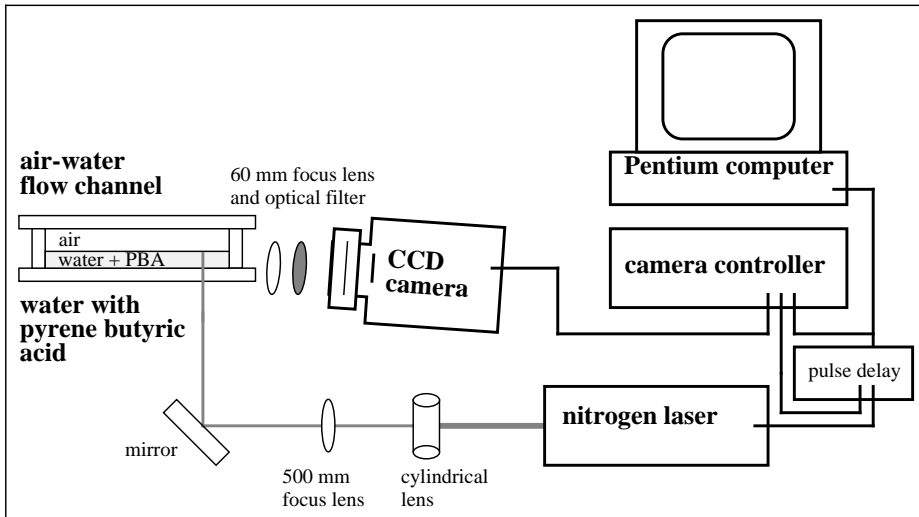


Figure 1: Apparatus sketch

Figure 1 shows the apparatus used to measure the two-dimensional fluorescence field. A nitrogen laser (9 mJ, 10 ns pulse) is expanded through a 254 mm cylindrical lens and focused through a 500 mm spherical lens to provide the thin vertical light sheet beneath the interface. The light sheet is 20.5 mm from the side wall. It has a thickness of less than 0.5 mm. An optical cut-off filter removes the light from the laser and the remaining fluorescent signal emitted from the sheet is focused through a Nikkor 60 mm 1-to-1 lens onto a high resolution CCD detector from Princeton Instruments. The detector is a KAF-1400 with 1035 x 1317 pixels, each $6.8 \times 6.8 \mu\text{m}^2$ (square aspect ratio). The Princeton Instruments ST-138 Controller operates in the non-interlace mode and allows 12-bit intensity resolution (4096 light levels). The detector is thermoelectrically cooled to -25°C . The chip face has been treated with a UV enhancing coating to improve sensitivity in the wavelength range for the fluorescence emitted from the PBA (the peak is at 410 nm). A variable electronic pulse delay synchronizes the laser firing and the camera shutter. The camera and focusing lens are tilted 7.3 degrees from the horizontal to avoid foreground interference.

The long axis of the camera is vertical. The vertical pixel coordinate Y ranges from 1 at the top of the image to 1317. The horizontal pixel coordinate X ranges from 1 at the upstream side of the image to 1035. Images of a ruler submerged in the channel in the plane of the laser sheet revealed that the lens arrangement results in a spatial magnification to $7.06 \mu\text{m}/\text{pixel}$. During image processing, the X, Y pixel coordinate system is replaced by the x, y distance coordinate system with the units of [mm]. The origin of the y -axis is the mean liquid level for the image and positive values of y

are for locations below the mean liquid level. The origin of the x -axis is the left-hand side of the image (where $X = 1$).

3 Image Processing

Figure 2 shows the raw intensities, $F'(Y)$, for vertical profiles from two images taken with a bulk O_2 concentration, C'_B , of 2.5 mg/L. The lower line is for conditions such that the imaging area is completely submerged and no interface is present. The upper line in figure 2 is for flowing air and water with a flat interface at roughly $Y_I = 360$. Intensities for a background image taken with the camera shutter disabled have been subtracted. The bottom third of the image ($Y > 850$) is discarded because a lip extending from the channel port blocks the view. For $Y < 850$ the intensity decreases exponentially. This is the Lambert-Beers effect described by

$$\frac{I}{I_0} = \exp(-\sigma C_{PBA} l) \quad (2)$$

where I is the energy of the laser in the fluid, I_0 is the intensity of the laser as it enters the fluid, σ is a molecule-dependent constant, C_{PBA} is the concentration of the fluorescent molecule, and l is the distance through the fluid. The PBA is well mixed, so C_{PBA} and σ are constant and I is found to decrease exponentially with increasing l (which is decreasing Y). The upper line in figure 2 shows that $F'(Y)$ departs from the exponential behavior due to reflection of the signal at the interface for $Y < Y_I$ and due to oxygen concentration variation for $Y > Y_I$.

The location of the interface is determined by exploiting the symmetry of the fluorescence signal and its reflection. A maximum symmetry filter (developed by *Münsterer and Jähne* [1995] for use on similar images) selects $Y_I(X)$ for each vertical profile. These surface locations are smoothed in X for each image with a 9-kernal rank filter. In theory, the interface should be along the minima of the vertical profiles. However, a method of locating the minima was ineffective because the scatter in the intensity measurements makes it difficult to distinguish the true minimum from a measurement near the interface which is a false minimum.

After the interface is identified, vertical profiles are corrected for signal variation not associated with changes in O_2 concentration. Sources include the variability of the PBA concentration, the laser pulse energy, the CCD controller signal gain, and the room light level. These effects can be removed by normalizing the images, that is, by dividing all intensities in each vertical profile by an intensity $F'_B(X)$ which is the average intensity for the Y range 750 to 850. The normalized intensity profiles $F_N(Y)$ for a portion of F' from figure 2 is seen in figure 3. The Lambert-Beers decay is determined for each profile by a least-squares fitting function $F_C(Y)$ which is a least-squares fit for $\ln(F_N)$ and Y for $750 < Y < 850$. Term $(1 - F_C(Y))$ is added to $F_N(Y)$. The

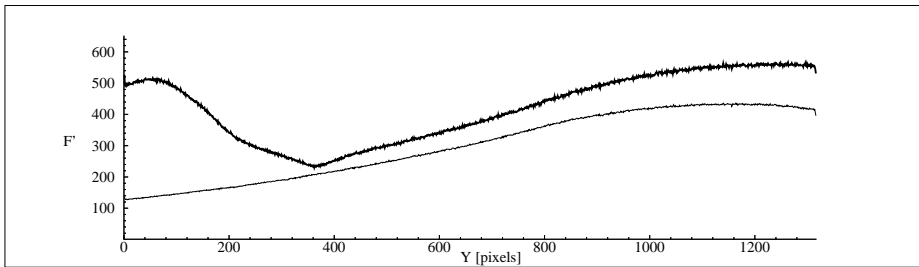


Figure 2: Vertical intensity profiles for images with and without a flat interface

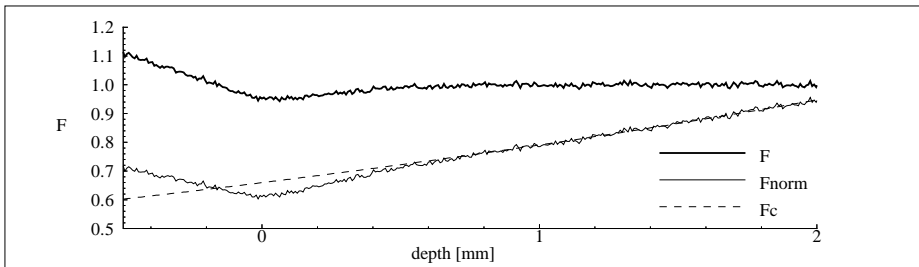


Figure 3: Normalized and corrected vertical intensity profiles for a flat interface

resulting profile, $F(Y)$, exhibits variation in fluorescence intensity solely due to variation in O_2 concentration. Figure 3 shows the normalized intensity profile $F_N(y)$, the function $F_C(y)$, and the corrected profile $F(y)$ obtained from a portion of the raw intensities shown by the upper line in figure 2. These are displayed in the distance coordinate system.

Figure 4 shows the normalized concentration profile $C(y)$ obtained from the corrected fluorescence profile in Figure 3. The symbols represent individual measurements and the line represents the slope of the concentration change at the interface predicted from the measurement of \bar{k} . The concentration is expressed as a dimensionless quantity which varies from 1 at the interface to 0 in the bulk flow.

$$C(y) = \frac{(C'(y) - C'_B)}{(C'_I - C'_B)} = \frac{F_I(F_B - F(y))}{F(y)(F_B - F_I)} \quad (3)$$

where C' are the dimensional concentration values. The subscripts B and I represent bulk and interfacial values. The O_2 concentration and the fluorescence intensity are related by equation 1. However, estimates for F_0 and k_{SV} are not needed when $C(y)$ is given in dimensionless form.

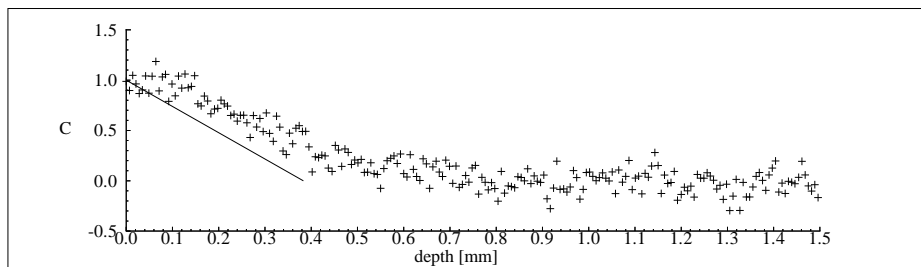


Figure 4: Normalized vertical concentration profile for a flat interface

4 Results for a Flat Interface

The measurements for $C(y)$ seen in figure 4 exhibit expected behavior. The maximum is near $y = 0$ mm and C is roughly constant at 0 for $y > 1$ mm (in the well-mixed low concentration bulk flow). The slope of the concentration change is close to $\frac{\partial C}{\partial y}$ predicted from measurements of \bar{k} . An unexpected behavior occurs in the region close to the interface where the concentration appears constant. This is where one would expect to see the largest value for $\partial C/\partial y$. This plateau region can be identified in the raw image profiles, so it is not an offset or an artifact of the image processing. The interface has been properly identified, so we are looking for an optical explanation.

The thickness of the concentration boundary layer, δ , is defined as the distance from the interface to a location where the concentration remains constant at the bulk value. The theoretical value for δ is D/k , where D and k are the coefficient of diffusion and the mass transfer rate. For O_2 in water at room temperature, $D = 2.1 \times 10^{-9}$ m²/sec. The position of the edge of the boundary layer in an image is $h - \delta$. This position is found by use of a linear curve fit for the concentration measurements between the interface and a point where the five-point running average of C is near 0.5. The boundary layer is assumed to begin at the intercept for this fit (where $C = 0$). In figure 4, $\delta = 0.61$ mm.

Figure 5 shows the surface locations and boundary layer edges measured for the image that produced the concentration profile in figure 4. There are 1024 profiles represented in this figure. The surface is flat with a standard deviation of 0.09 mm. The boundary layer depth, δ , has a mean value of 0.59 mm and a standard deviation of 0.05 mm. Two bubbles were identified on the interface near $x = 0.5$ mm and $x = 3$ mm; these raised the variation of the surface location and δ slightly. The value for δ obtained from the mass balance measurements is 0.38 mm. Nine additional images for these flow conditions were analyzed and produced similar profile and boundary layer behavior.

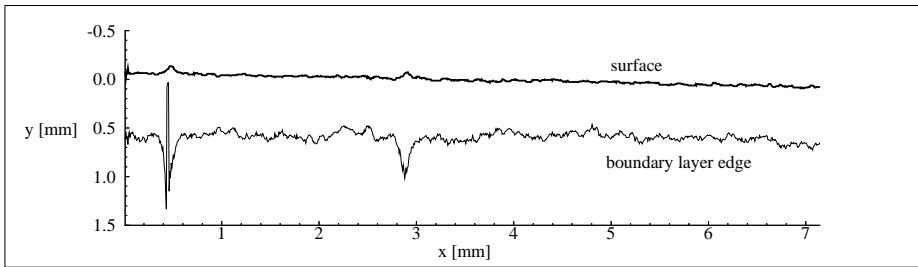


Figure 5: Surface and boundary layer depth locations for a flat interface

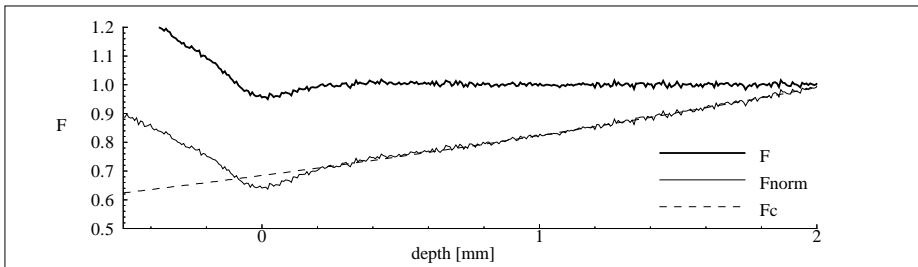


Figure 6: Normalized and corrected vertical intensity profiles for a wavy interface

5 Results for a Wavy Interface

Wolff and Hanratty [1995] reported variations in δ with time for a wavy interface that were an order of magnitude larger than found for a flat interface.

Figures 6 and 7 show normalized and corrected vertical intensity profiles for two horizontal locations in an image for a wavy interface. Figure 6 looks similar to the profile for a flat interface (figure 3); the interface and concentration change in the boundary layer are identifiable. Figure 7 displays a very different profile. The interface is still identifiable from the symmetry of the raw intensity signal. However, the change in fluorescence beneath the interface is not interpretable. It appears that the concentration rises toward the interface. The best explanation for this is that foreground waves shield the fluorescence sheet near the interface, a condition that we are trying to prevent by tilting the camera. Observation of several images for wavy surfaces shows that only about half of the vertical profiles are interpretable; there are regions where large sections of vertical profiles are interpretable and regions of adjacent profiles which appear shielded.

As mentioned previously, there is considerable noise scatter in the intensity measurements. If the magnitude of the signal is defined as the change in the intensity from the interface to the bulk, the signal-to-noise ratio is about 4 for the measurements presented in figure 4. This same level of noise appears for the image of fully saturated water, so the sources of the scatter

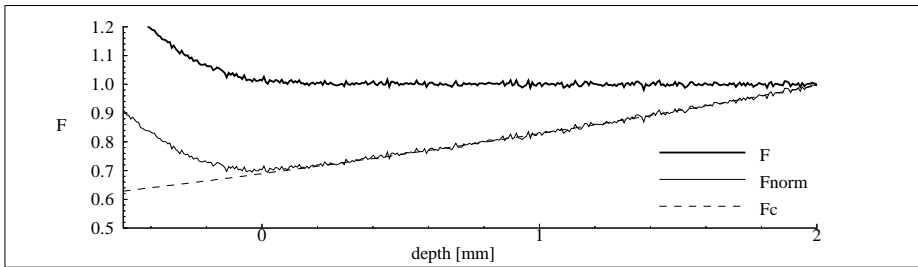


Figure 7: Normalized and corrected vertical intensity profiles for a wavy interface

are not due to variation in the concentration of O_2 . It is difficult to isolate a distinct frequency or energy level for the noise, so as to remove it without tampering with the measurements of concentration fluctuations. An additional source of noise is the discretization in the vertical and horizontal directions. The surface and the boundary layer locations are to the nearest pixel, so there is not a continuous length scale. The adaptive smoothing filters developed by *Braess and Jähne* [1995] are being explored.

6 Conclusions

The laser-induced fluorescence technique measures average boundary layer thicknesses which agree with the thicknesses predicted by time-averaged measurements of the mass transfer rates. The average thickness decreases when waves are present. The variation in the boundary layer thickness for a flat interface is 10 to 15 percent.

The goal of this work is to measure the variation of the concentration in the boundary layer when waves are present. This would allow comparison of the mean and statistical properties of the boundary layer thickness (which is proportional to the mass transfer rate) to various wavy surface conditions. We would also like to correlate directly the local mass transfer rate with the position and slope of the interface. The validity of the results for a flat interface indicate that the theory behind the approach is valid. However, complications in the fluorescence image introduced by waves have not yet been fully explained.

Acknowledgements

This work was supported by the Department of Energy under grant DOE DEF G02 86ER 13556 and the National Science Foundation under grant CTS-920877.

References

- Braess, H. and Jähne, B., Personal communication, 1995
- McCready, M.J. and Hanratty, T.J., Effects of air shear on gas liquid absorption by a thin film. *AICHE Journal*, 31, 2066, 1985
- Münsterer, T. Messung von Konzentrationsprofilen gelöster Gase in der wasserseitigen Grenzschicht. MS thesis. University of Heidelberg, 1994
- Münsterer, T. and Jähne, B., Personal communication, 1995
- Wolff, L. M. and Hanratty, T. J., Instantaneous concentration profiles of oxygen accompanying absorption in a stratified flow. *Experiments in Fluids*, 16, 385, 1994
- Wolff, L. M., Liu, Z. C, and Hanratty, T. J., A fluorescence technique to measure concentration gradients near and interface. *Air-water mass transfer*, 2nd International Symposium, 210, 1990
- Wolff, L. M., The study of gas absorption at a wavy air water interface. PhD thesis. University of Illinois, Urbana, 1991

Dual-Tracer Measurements of Concentration Profiles in the Aqueous Mass Boundary Layer

Thomas Münsterer¹, Hans Jürgen Mayer¹, and Bernd Jähne^{2,3}

¹Institute for Environmental Physics, University of Heidelberg
Im Neuenheimer Feld 366, 69120 Heidelberg, Germany
email: Thomas.Muensterer@iwr.uni-heidelberg.de

²Scripps Institution of Oceanography, Physical Oceanography Res. Div.
La Jolla, CA 92093-0230, USA, email: bjahne@ucsd.edu

³Interdisciplinary Center for Scientific Computing, University of Heidelberg
Im Neuenheimer Feld 368, 69120 Heidelberg, Germany

doi: 10.5281/zenodo.10406

Abstract

A combination of two laser-induced fluorescence (LIF) techniques for measurements of vertical concentration profiles of dissolved gases and thus the investigation of micro-turbulence in the aqueous mass boundary layer at a free interface is presented. The first one uses an acid-base reaction of the fluorescence indicator fluorescein at the water surface to visualize the concentration profiles. The second one uses fluorescence quenching of pyrenebutyric acid by oxygen. Both experiments are done simultaneously at the same location.

The advantage of a combined experiment is that the two techniques utilized here to visualize the concentration profiles are caused by different independent physical effects, i.e. an acid-base reaction and the fluorescence quenching by oxygen. Simultaneous measurements can help to detect possible systematic errors and offer the chance to learn more about the underlying gas exchange mechanisms.

Experiments performed at the circular facility of the University of Heidelberg using a surfactant to suppress waves are presented. For three wind speeds the mean and fluctuating boundary layer properties are investigated.

1 Introduction

Our understanding of the parameters influencing air-sea gas exchange has increased considerably in recent years, however, little is known about the mechanisms that control this process. There is limited data available with which to evaluate the different gas exchange models. To understand gas exchange mechanisms it is essential to investigate the processes within the aqueous *mass boundary layer*. This paper describes two laser induced fluorescence (LIF) techniques which measure vertical *concentration profiles* with high temporal and spatial resolution. One technique uses the dye *fluorescein*. A less fluorescent species of fluorescein anions is generated at the water surface through a reaction with an acidic gas. These species undergo

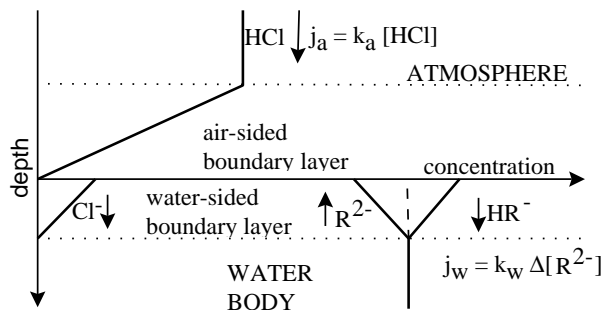


Figure 1: Schematic representation of the vertical concentration profiles at the air-water interface, when HCl is absorbed by a buffer solution.

no further reactions and are transferred into the bulk water flow. The second technique uses the dye pyrene butyric acid, whose *fluorescence* is quenched by *dissolved oxygen*. The research described in this paper was undertaken to make combined measurements with the two techniques at the same time and at the same location. Combined measurements have the advantage of allowing identification of systematic errors (the chemical and physical effects are very different) and investigation of the Schmidt number dependency of the underlying gas exchange mechanisms ($Sc \approx 2500$ for fluorescein and $Sc \approx 470$ for oxygen).

2 LIF Principles

This section describes how the two LIF techniques allow visualization of the concentration profiles in the aqueous mass boundary layer. It is crucial that the fluorescence intensity is a function solely of the concentration of the exchange component. This is fulfilled for both techniques.

2.1 The Fluorescein Method

The fluorescein technique uses an acid-base reaction at the interface to generate fluorescent molecules to visualize the concentration profiles (Figure 1). The *fluorescent indicator* sodium fluorescein is used at its buffer point in a 2×10^{-5} M solution. At the buffer point the solution contains equal concentrations of the two ionic species of fluorescein (abbreviated here as HR^- and R^{2-}). An *acid gas*, e.g. HCl, is then injected into an air-tight wind/wave facility in ppm concentration levels. The water surface acts as a perfect sink for the HCl. The HCl gas dissociates instantaneously and protonates the fluorescein anions at the water surface generating an excess number of the less fluorescent singly charged fluorescein anion HR^- . The disturbed equilibrium concentration of the two ionic forms of fluorescein at the water

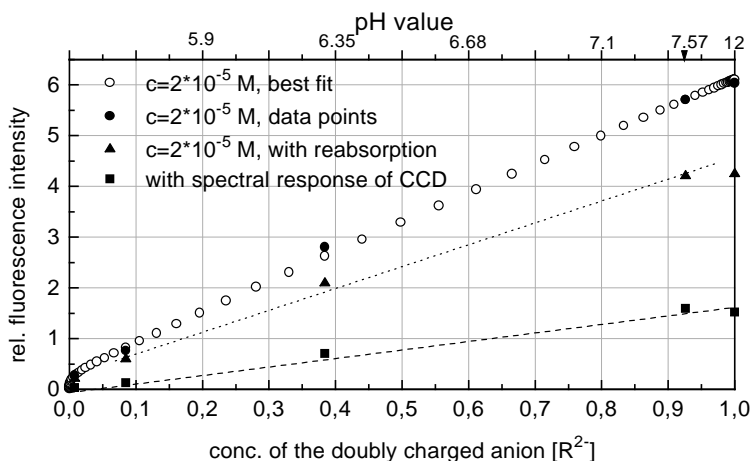


Figure 2: Intensity of the fluorescein fluorescence versus concentration of the doubly charged fluorescein anion. The curves are calculated from literature values for the absorbance at 488 nm [Martin and Lindqvist 1975], fluorescence spectra [Martin and Lindqvist 1975 and Razwadowski 1961] and quantum yields [Razwadowski 1961]. The circles show the response for an ideal system without reabsorption and an ideal CCD response. The upright triangles describe the system with reabsorption in a solution body as it is used in the experiments. The inverted triangles show the response taking into account reabsorption, the spectral response of the CCD and the dichroic mirror.

surface forces a flux of the different ionic forms of HR^- and R^{2-} across the aqueous mass boundary layer into the bulk flow.

This transfer process is equivalent to the transfer of an inert gas without influence by chemical reactions [Jähne 1991]. The only chemical reaction takes place directly at the water surface and is on a much shorter time scale than any transportation processes of interest here. Using rate constants by Yam et al. [1988] calculations show that 99% of the possible fluorescein protonation reactions take place within $0.5 \mu\text{m}$ from the water surface. Although the protonation changes the absorption and fluorescence spectra as well as the quantum yield, the fluorescence intensity is proportional to the concentration of the unprotonated ion over a wide range (see Figure 2). Below pH 8 the nonlinearity is less than 4%. An alkaline gas (e.g. NH_3) can be used in place of the acidic gas to produce the reverse effect (i.e. the highly fluorescent ions are depleted at the surface).

2.2 The Oxygen Quenching Method

The *oxygen quenching* technique was introduced by Wolff et al. [1991]. In this case, the dye concentration is constant, but the concentration of the

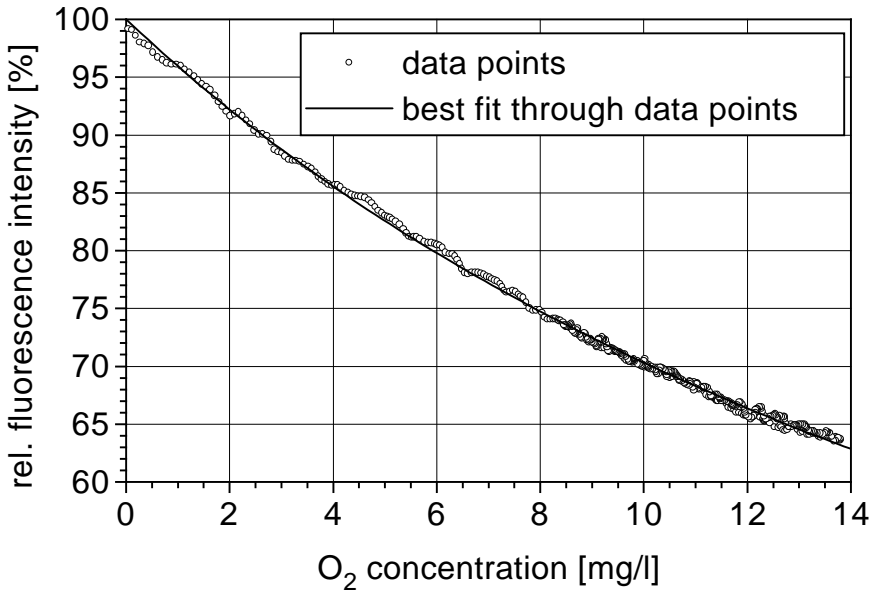


Figure 3: Fluorescence quenching of PBA fluorescence by the presence of dissolved oxygen (data from own experiments, $K = (683 \pm 70) \text{ l/mol}$ at $T = 298 \text{ K}$, within the margins of error of the K value first published by Vaughan and Weber [1970]; $K = (645 \pm 79) \text{ l/mol}$).

quenching molecule (oxygen) varies in the aqueous mass boundary layer. The presence of oxygen in the water causes the molecules to relax to their ground state through non-radiative collisions. The fluorescence intensity is described by the *Stern-Vollmer equation*:

$$I(c) = \frac{I_0}{1 + Kc}, \quad (1)$$

where I_0 is the fluorescence intensity with no quencher present, K is the quenching constant and c is the concentration of the quencher. The best fluorescent dye for this kind of experiments, described by Vaughan and Weber [1970] and Wolff *et al.* [1991], is *pyrene butyric acid* (PBA). It shows an approximately 20% loss of fluorescence intensity with dissolved oxygen concentrations increasing from 0.8 to 8 mg/l (see Figure 3) as is the case for the degased Heidelberg flume.

Experiments show that the two dyes exhibit a high degree of chemical and optical compatibility. Fluorescein fluorescence is neither affected by the presence of PBA in the solution nor significantly stimulated by the N_2 laser. The fluorescein fluorescence also shows only neglectable quenching by oxygen (much less than 1% over the concentration range investigated

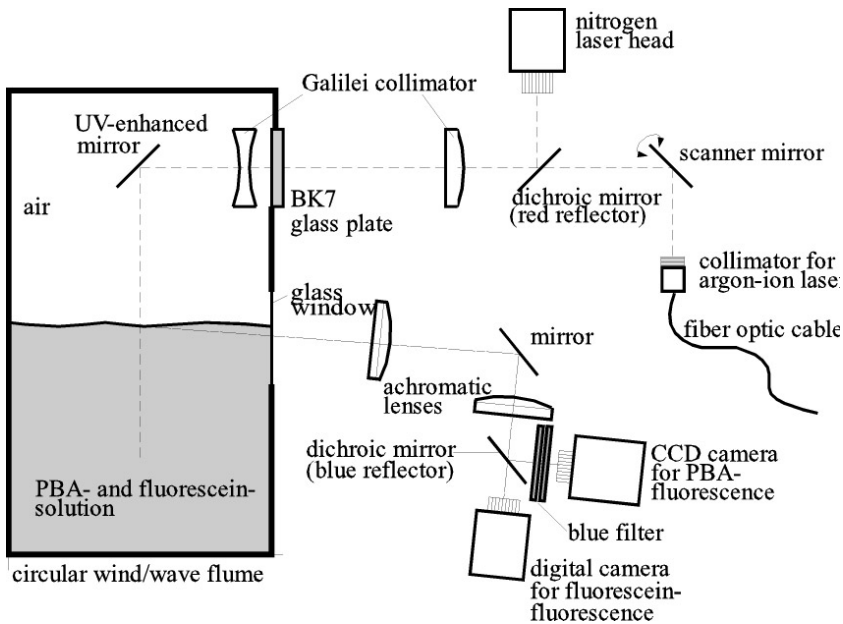


Figure 4: Sketch of the dual tracer experimental setup with imaging CCD-cameras and laser optics. The cameras as well as the laser optics are mounted on an optical wave follower.

here). The PBA fluorescence is not affected by the local pH value of the solution and is not stimulated by the argon ion laser. The possibility of further interferences is discussed in section 4.

3 Experimental Setup

The combined optical arrangement is mounted on an optical wave follower system. The laser optics are mounted on the same base plate as the imaging optics. Figure 4 shows the experimental setup at the circular wind/wave flume of the University of Heidelberg. This facility consists of a 30 cm wide and 70 cm high gas-tight annular channel with an outer diameter of 4 m. Wind is generated by a rotating paddle ring driven by 24 small DC motors. The channel is filled up to a height of 25 cm; so the water and air volumes are 0.88 and 1.6 m³, respectively. For more details on the flume see *Schmundt et al.* [1995].

A stock solution of PBA and fluorescein in a NaOH solution was prepared (*Wolff et al.* [1991] dissolved the PBA in an organic solvent). This stock solution was then diluted in the flume to give concentrations of 2×10^{-5} M for each of the dyes. In the flume HCl was added to titrate the solution to the fluorescein buffer point at pH 6.5 [*Guyot et al.* 1975]. The surfactant Triton

X-100 was used in a 5×10^{-6} M dilution to suppress waves in these first experiments. At the beginning of the experiment the water was degassed, using hollow fiber membranes (Membrane Corp.). The bulk concentration of oxygen in the flume was reduced to less than 1 mg/l. At the water surface the oxygen concentration is equal to the equilibrium concentration (approx. 8.5 mg/l). The PBA fluorescence is stimulated by a focussed nitrogen laser beam at 337 nm with a spot diameter of 200 μm . The oxygen concentration profile across the aqueous mass boundary layer is imaged with a standard NTSC camera. The pulse rate of the laser is 15 Hz resulting in exposure of every fourth field. By averaging over the width of the laser beam, each exposed field results in a one-dimensional profile. The horizontal averaging reduces the noise level. Juxtaposed sequential profiles result in a space-time image. The oxygen profiles were imaged with a 24 μm resolution in the vertical dimension. A stronger laser would be required to allow two dimensional imaging.

Fluorescence for the fluorescein experiment is stimulated by the focused beam of a 1 W argon ion laser (488 nm) piercing the water surface perpendicularly from above. To investigate a two dimensional area the beam is scanned, resulting in a light sheet 6 mm wide and 60 μm deep. Scanning the beam instead of widening it helps to avoid motion blur. Images of the concentration profiles are taken with a digital camera at a rate of 200 frames per second. The spatial resolution of the optical system is 16 μm .

A dichroic mirror allows the beams from the two lasers to travel the same optical path as they strike the water surface. The fluorescence spectra of fluorescein and PBA are separated using a different dichroic mirror in the imaging optical path.

4 Results

The experiments showed that when using HCl as an initiator for the fluorescein technique the two techniques cannot be combined. The PBA fluorescence was found to be severely quenched in the presence of HCl. This is probably due to fluorescence quenching by the chloride ions. Such effects are also known from the literature [Förster 1951] for other halogen ions. This results in the fact that two separate approaches have to be followed: a run using only the fluorescein technique with HCl as an initiator and a run using the combined method with NH_3 as an initiator for the fluorescein technique together with the oxygen quenching technique. Both runs were accompanied by a classical mass balance oxygen invasion experiment.

4.1 Fluorescein Experiments

Figure 5 shows a comparison of the boundary layer thicknesses (z_*) measured with fluorescein compared to those calculated from the oxygen invasion transfer velocities. The z_* values from the mass balance experiment

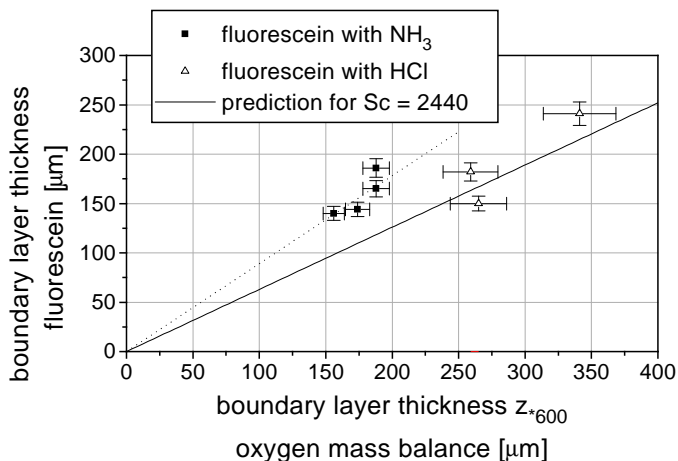


Figure 5: Comparison of the boundary layer thicknesses measured by the fluorescein method with those calculated from the oxygen transfer velocity.

were normalized to $Sc = 600$. The solid line shows the assumed Sc dependency for a diffusion constant for fluorescein of $D = 3.67 \times 10^{-6} \text{ cm}^2/\text{s}$ [Hodges and La Mer 1948]. The z_* values using NH_3 as an initiator deviate significantly from this line. The HCl values agree with this prediction within the margins of error ($\Delta z_*/z_* = 8\%$ for the oxygen mass balance value and $\Delta z_*/z_* = 5\%$ for the fluorescein value). The problem with the NH_3 probably results from the low rate constant for the dissociation reaction $\text{NH}_3 + \text{H}_2\text{O} \leftrightarrow \text{NH}_4^+ + \text{OH}^-$. The combined profile is affected by both the fluorescein and NH_3 transfer. The small rate constant for NH_3 violates one of the basic assumptions for the feasibility of the fluorescein technique: the time for the protonation reaction must be neglectable compared to any transportation processes. On the other hand this assumption is completely fulfilled for the HCl . More thorough investigations and numerical simulations have to be performed to be able to interpret the profiles obtained with NH_3 as an initiator for the fluorescein flux.

Figure 6 shows a comparison of averaged concentration profiles with the predictions by the small eddy and surface renewal models in dimensionless units. The profiles clearly show better agreement with the profiles for the Schmidt-number exponent $2/3$. At this point the concentration profiles cannot clearly distinguish between the predictions for the different models. Nevertheless such a distinction seems to be possible in the future.

Figure 7 shows three consecutive images of the two-dimensional fluorescein field. These have been normalized to the frame of reference of the water surface using image processing techniques. Although almost no waves were present, separated dark streaks indicate that parts of the boundary layer are being swept into the bulk.

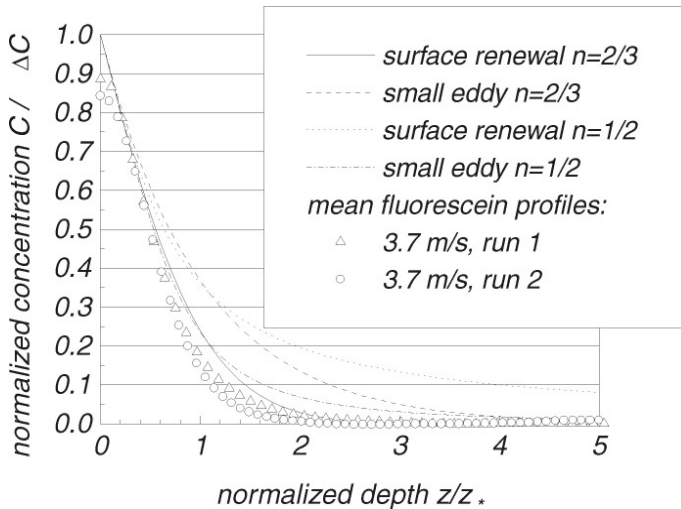


Figure 6: Comparison of the mean concentration profiles for fluorescein (using HCl as an initiator) with the predictions by the small eddy and the surface renewal models. The mean profiles are each averaged over 450,000 single profiles.

4.2 Oxygen Quenching

Figure 8 shows a space time image of the oxygen quenching technique normalized to the frame of reference of the water surface. The signal-to-noise ratio is much worse than for the fluorescein technique. The right hand side of Figure 8 shows a single profile at time 8 s. At this point it seems impossible to evaluate single profiles imaged with a standard CCD camera. Also the time resolution of 15 frames/s impedes the investigation of dynamic processes. A different approach has been taken by *Duke and Hanratty* [1995] imaging single two-dimensional fields with a thermo-electrically cooled *high resolution* camera.

In spite of the noise level mean profiles and mean boundary layer thicknesses can be obtained with the technique used here. Figure 9 shows a comparison of z_* values normalized to $Sc = 600$ for the oxygen quenching and oxygen mass balance technique. The values agree quite well, although larger differences can be seen for the values measured at 3.6 m/s. All of these values were measured on the same day and the deviation is probably due to a calibration problem with the oxygen probe.

Figure 10 shows a comparison of the averaged oxygen concentration profiles with the small eddy and surface renewal model predictions. As with the fluorescein profiles, the oxygen profiles clearly indicate the expected Schmidt-number exponent $2/3$. The profiles also show a flattening at the interface. The flattening at the interface is disturbing because all models predict a sharp concentration change at the interface. Since both techniques

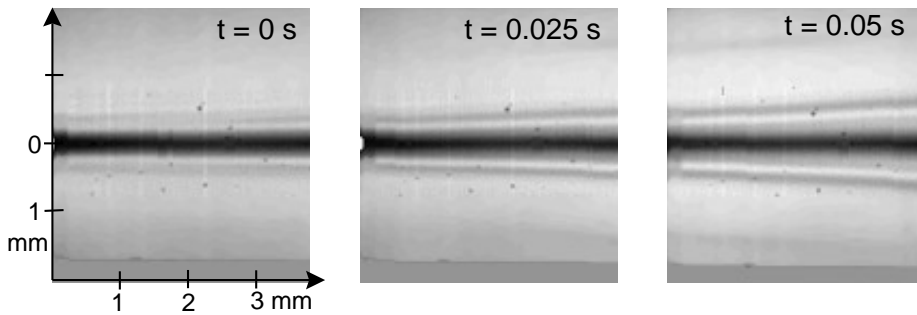


Figure 7: Three out of 1800 images taken with the fluorescein technique using HCl as an initiator. The wind speed is 3.6 m/s coming from the left side at a smooth interface. The aqueous mass boundary layer can be seen as a dark stripe in the middle of the image. The original profile is going down into the bulk. The top part of the image is caused by total reflection at the water surface.

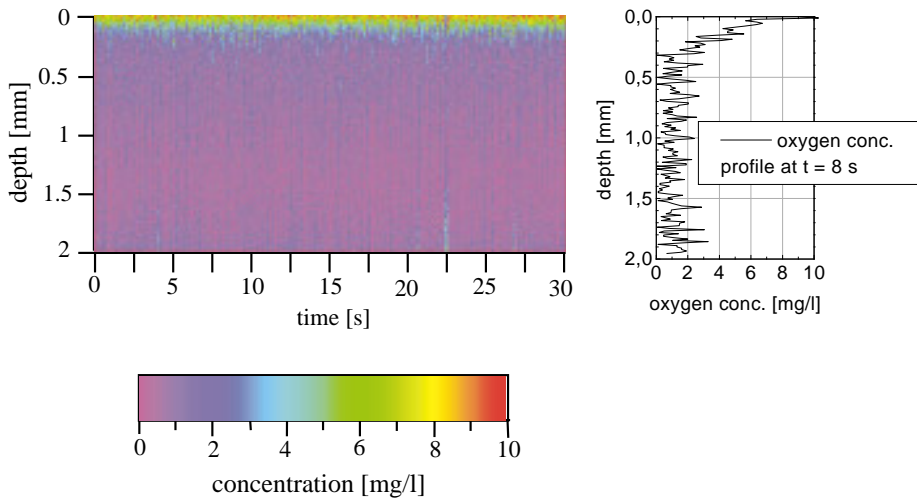


Figure 8: Left: Space time image of the oxygen concentration profile. The aqueous mass boundary layer is visible as a dark layer in the middle of the image. The image is converted to the frame of reference of the water surface using image processing techniques. Right: Cross section through the left hand image at time $t = 8$ s. (For color figure, see Plate 21.)

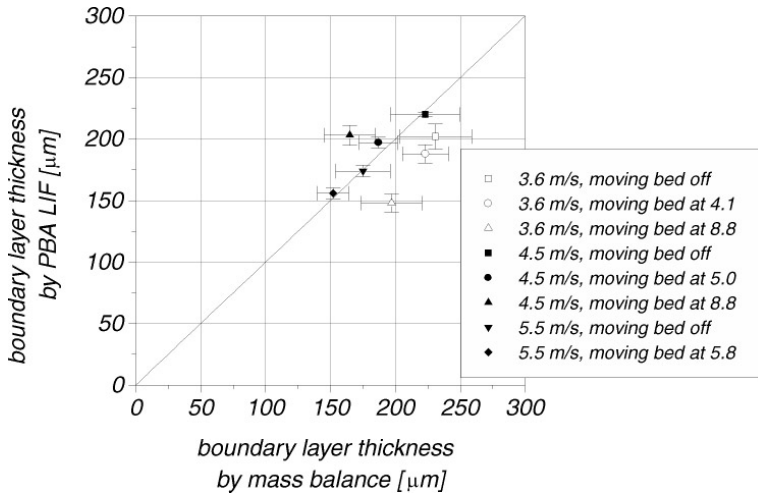


Figure 9: Comparison of the boundary layer thicknesses measured by the oxygen quenching method with those calculated from the oxygen transfer velocity.

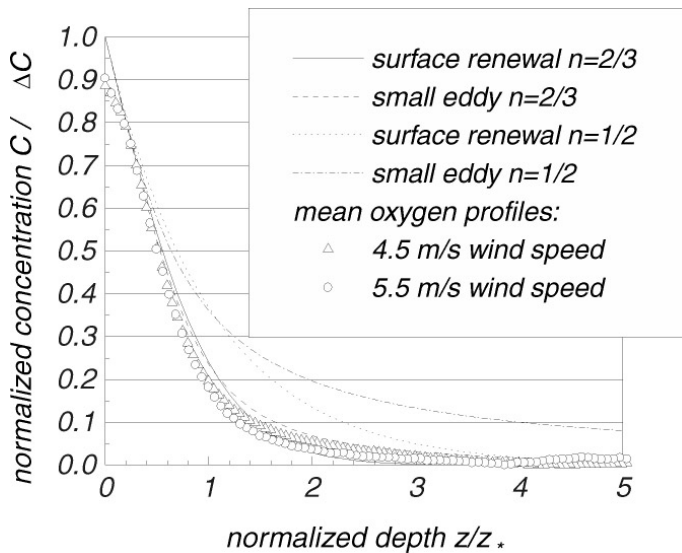


Figure 10: Comparison of the mean oxygen invasion concentration profiles with the predictions by the small eddy and the surface renewal model. The mean profiles are averaged over 16,200 and 10,800 single measurements, i.e. 18 and 12 minutes respectively.

measure such a flattening a chemical reaction of the fluorescein can be ruled out. The flattening is caused either by an optical effect (blur) or a "real" physical effect. The flattening is of the same scale in dimensionless plots although the actual mean boundary layer thicknesses differ by almost a factor of two. This is untypical for optical blur. Furthermore from the measured oxygen concentration in the bulk the surface concentration can be calculated using the Stern-Vollmer equation and the averaged fluorescence profiles. These calculations agree with the values calculated from the Ostwald solubility to within 3%. An optical blur should decrease this calculated surface concentration in the order of 15 to 20%.

5 Conclusions

The fluorescein technique using NH_3 as an initiator shows systematic deviations and needs further investigations. The oxygen quenching technique as well as the fluorescein technique using HCl as an initiator could be verified. For both techniques mean concentration profiles were calculated and compared to model predictions. The dynamic properties of the fluorescein profiles show that parts of the boundary layer are being swept into the bulk. The noise level for the oxygen profiles is too high to allow single profile evaluations. A combination of both techniques at the same time and location is not yet feasible because HCl interferes with the oxygen quenching. For a combination another acid or alkaline gas has to be found.

Acknowledgements

Financial support of this research by the National Science Foundation (Grant OCE9217002) is gratefully acknowledged.

References

- Duke, S. R. and T. J. Hanratty, Measurements of the concentration field resulting from oxygen absorption at a wavy air-water interface, *This volume*
- Förster, T., Fluoreszenz organischer Verbindungen, Vandenhoeck & Ruprecht, p. 184, 1951.
- Hodges, K. C. and V. K. La Mer, Solvent Effects of the Quenching of the Fluorescence of Uranin and Aniline, *Am. Soc.*, **70**, 724, 1948.
- Jähne, B., From mean fluxes to a detailed experimental investigation of the gas transfer process, *Air-Water Mass Transfer*, selected papers from the 2nd International Symposium on Gas Transfer at Water Surfaces, September 11-14, 1990, Minneapolis, Minnesota, S. C. Wilhelms and J. S. Gulliver, eds, pp. 244-256, ASCE, New York, 1991.
- Guyot G., R. Arnaud et J. Lemaire, Emission des différentes formes de la fluorescéine en solution aqueuse, *J. Chim. Phys.*, **72**, no. 5, 647-653, 1975.

- Martin M. M. and L. Lindqvist, The pH dependence of fluorescein fluorescence, *J. Luminescence*, **10**, 381-390, 1975.
- Razwadowski M., Effect of pH on the fluorescence of fluorescein solutions, *Acta Phys. Polonica*, **XX** (961), 1853-1854, 1961.
- Schmundt D., T. Münsterer, H. Lauer and B. Jähne, The circular wind/wave facility at the University of Heidelberg, *This volume*.
- Vaughan W. M. and G. Weber, Oxygen Quenching of Pyrenebutyric Acid Fluorescence in Water, *Biochemistry*, **9**, 464, 1970.
- Wolff, L. M., Z.-C. Liu and T. J. Hanratty, A fluorescence technique to measure concentration gradients near an interface, *Air-Water Mass Transfer*, selected papers from the 2nd International Symposium on Gas Transfer at Water Surfaces, September 11-14, 1990, Minneapolis, Minnesota, S. C. Wilhelms and J. S. Gulliver, eds, pp. 210-218, ASCE, New York, 1991.
- Yam R., E. Nachliel and E. Gutman, Time resolved proton-protein interaction. Methodology and kinetic analysis, *J. Am. Chem. Soc.*, **110**, 2636-2640, 1988.

Surfactant Effects on Vortex Flows at a Free Surface and the Relation to Interfacial Gas Transfer

A. Hirs¹, G. M. Korenowski², L. M. Logory¹,
S. Kim¹, and C. D. Judd²

¹Departments of Mechanical Engineering, Aeronautical Engineering & Mechanics
and ²Chemistry
Rensselaer Polytechnic Institute Troy, NY. 12180-3590

Abstract

Turbulence near an air-water interface was investigated by separately considering the interaction of surface-normal and surface-parallel components of vorticity with a free surface. The flow field during the collision of a vortex pair, with axes parallel to the free surface, was investigated experimentally. The *vortex pair* generator consisted of a pair of counter-rotating flaps. Surfactant effects in this case, are due to dilation/compression of the surface. Vortex pairs with Reynolds number (based on circulation) of 20,000 were generated which interact with the free surface. The Froude number for the vortex pair was small so that the surface remained nearly flat during the interaction and the vorticity generation was primarily due to surfactants and not surface curvature. The *velocity field* in the substrate was measured using a *digital particle image velocimetry* (DPIV) system down to a spatial resolution of the order of 0.1 mm and a temporal resolution of 2 ms. The surfactant concentration on the free surface was measured using the nonlinear optical method of *second-harmonic generation* (SHG) to a spatial resolution of less than 1 mm and a temporal resolution of 1/6 s. Prior to each experiment a known amount of an insoluble *surfactant*, hemicyanine, was spread on the surface as a monolayer. *Hemicyanine* was chosen because of its strong nonlinear optical response as well as its elastic properties which in the surface concentration ranges employed simulates many liquid-like surfactant films. Complete cleaning of the surface was observed for a range of initial surfactant concentration (with a surface pressure less than 7 dynes/cm) out to a distance comparable to the initial vortex pair separation.

The interaction of *surface-normal vorticity* with a contaminated surface was investigated by studying a columnar vortex. Stable columnar vortices were generated using a pair of co-rotating flaps with Reynolds number of 1,400 and the *laser-induced fluorescence* (LIF) method was utilized to study mass transfer from the gas phase. In the absence of highly viscous surfactants, the flow field on the surface remained nearly solenoidal, thus no surfactant concentration gradients were observed and the flow remained two-dimensional, with the vorticity vector normal to the surface. In this case, gas exchange was not observed to be enhanced, and was dominated by diffusion only. However, when a surfactant with a large surface shear viscosity (stearic acid) was present on the surface, a highly three-dimensional vor-

ticity field was observed. Along with the original swirling pattern, a flow directed toward the center of the vortex and away from the free surface was observed. This flow pattern is shown to enhance gas transfer into the bulk.

1 Introduction

Interfacial flow and in particular *turbulence* undoubtedly plays an important role in gas exchange at the air-sea interface. In this paper, we present our initial studies of how subsurface flow affects gas exchange rates at this interface. Inherent to and an integral part of this problem are surfactant (surface active agent) effects on free surface turbulence. We ignore for the present the role of wind-wave coupling in generating free surface turbulence at the air-sea interface and focus on characterizing the interplay between free surface turbulence, *surfactants*, and gas exchange rates. Our goal is a model capable of predicting the interfacial entrainment (gas and surfactant) that results from various *vortex flows* for different surfactant conditions. This model will be used as a foundation for describing entrainment for the important case of *free-surface turbulence*. The development of this model requires experimental quantification of flow behavior in both the bulk and the free-surface boundary layers, detailed knowledge of the interfacial rheological properties for various surfactant conditions, and quantitative measurement of gas exchange rates for selected flows and surfactant conditions. The following material describes our multifaceted approach to this problem.

2 Background

The observation of surface “striations” and “scars” characteristic of submerged *vortical structures* in turbulent flow were first reported by *Sarpkaya and Henderson* [1985]. In the interaction of subsurface turbulence with a free surface, vortex structures are observed to attach to the surface forming characteristic surface depressions or dimples [*Sarpkaya and Neubert*, 1994] which are indicative of surface normal vortical flows. It was also shown that a boundary condition of zero stress at a clean free surface requires vortex lines which terminate at the free surface to be surface normal [*Lugt*, 1987]. Based on these observations, a reasonable approach to the description of turbulent flow at a free surface is a combination of vortical flows, two orthogonal surface parallel components and one surface normal component. This description is depicted in Figure 1.

It is now well documented that surfactants alter vortical flows at the air-water interface. *Bernal et al.* [1989] demonstrated that a minute amount of surfactant causes the rebounding of a surface parallel vortex pair at a free surface. *Hirsa and Willmarth* [1994] subsequently explained this rebounding. Interfacial drag resulting from the surfactant generates opposite-signed vorticity which rolls up to form a secondary vortex pair forcing the initial

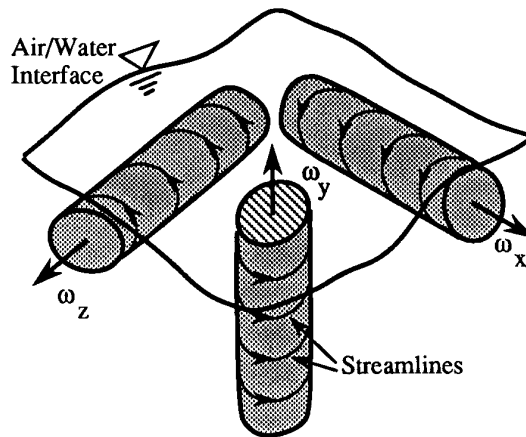


Figure 1: Vortex topology at a free surface. Note the components of the vorticity vector $\vec{\omega}$

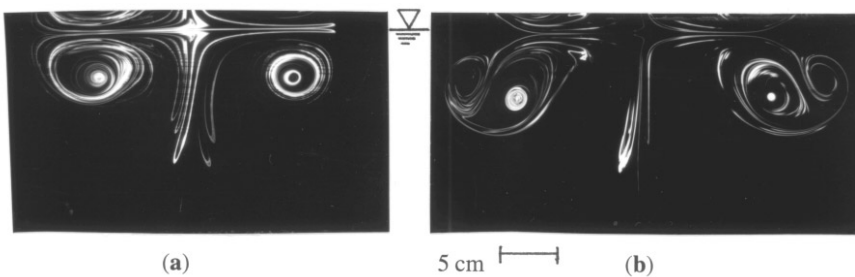


Figure 2: Photographs of vortex pair interaction with a free surface. The free surface is clean in (a) and covered with a monolayer of oleyl alcohol in (b), where the initial surface pressure was 2.5 dynes/cm. Note, the mirror image that appears on the upper portion of the photographs is due to total internal reflection at the free surface.

vortex to rebound away from the free surface. This behavior is shown in Figure 2 where the flow of a vortex pair at the air-water interface for a clean and a surfactant influence surface is contrasted using flow visualization.

When the surface is clean (Figure 2,a), the vortex pair rises and consequently interacts with its image and takes a diverging trajectory parallel to the surface. Figure 2(b) shows that when the surface is contaminated (in this case with oleyl alcohol at a surface pressure of $\pi = 2.5$ dynes/cm), secondary vorticity is generated which rolls up into a secondary vortex pair which drastically alters the trajectory of the primary vortex pair. Note that the mirror-image which appears at the top of each photograph is due to total internal reflection from the free surface.

More recently, Hirsa et al. [1995] demonstrated that surfactants can in-

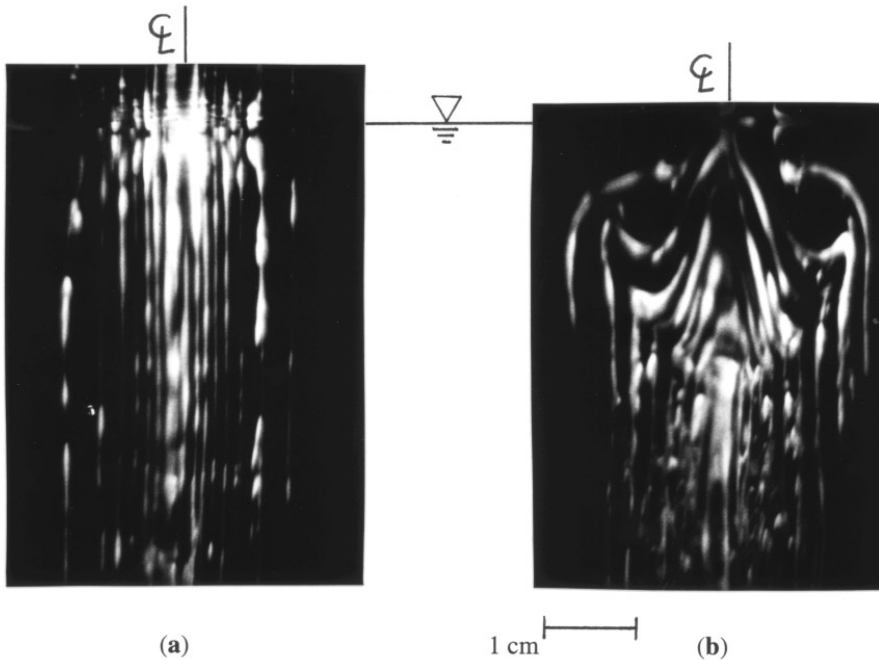


Figure 3: Photographs of columnar vortex interaction with a free surface visualized in a meridional plane. The free surface is clean in (a) and covered with a saturated monolayer of stearic acid in (b). The time in each case is $t = 10$ s following the termination of flap motion.

duce three-dimensional flow at the interface of an initially two-dimensional columnar (surface-normal) vortex flow. Flow visualization of a columnar vortex behavior at a clean and a surfactant-influenced free surface are presented in Figure 3. The photographs in Figure 3, show dye lines in a meridional plane through the columnar vortex, ten seconds after the termination of flap rotation. The vortex remains two-dimensional when the surface is clean, as depicted in Figure 3(a). Figure 3(b) shows the dye lines when the surface is contaminate with a saturated monolayer of *stearic acid*. The circulation (Γ) for this vortex was measured to be $14 \text{ cm}^2/\text{s}$, which results in a Reynolds number, Γ/ν , of 1,400, where ν is the kinematic viscosity.

In light of these laboratory studies demonstrating the effect of surfactants on free surface flow and because the ocean is a surfactant influenced surface, it is imperative that any description of turbulence and gas exchange at the air-sea interface incorporate surfactant effects. (The large Gibbs free energy of a clean water surface insures that an air-water interface will readily adsorb both soluble and insoluble organic surfactants. Organic materials from biological processes which are always present in the ocean lead to varying degrees of surfactant adsorption at the air-sea interface.)

3 Approach

In our approach, we independently study fully laminar surface-parallel and surface-normal vortex flows, the effects that surfactants have on these two types of vortical flows, and the effects on surfactant concentration profiles at the air-water interface. From the surface-parallel and surface-normal vortex experiments, we have determined that *surface rheological properties* can be extracted. These rheological properties (Gibbs elasticity, surface dilatational viscosity, and surface shear viscosity) are needed to characterize the interfacial hydrodynamic boundary conditions in the presence of insoluble surfactants. We have also explored how surfactant influenced vortex flows will result in entrainment of surfactant and gas at the free surface by inducing three-dimensionality (*vortex breakdown*) from what is initially a two-dimensional flow field.

4 Experimental Apparatus and Methodology

4.1 Digital Particle Image Velocimetry

The *digital particle image velocimetry* (DPIV) technique was utilized to obtain instantaneous velocity fields in a two-dimensional plane normal to the vortex pair axes. As employed here, the method is similar to that described by *Willert and Gharib* [1991]. Their technique involves cross-correlating sampling windows in consecutive video frames of a seeded flowfield in order to obtain particle displacements and hence particle velocity information. The specific features of the present DPIV system are described below; a more detailed description can be found in *Logory et al.* (1995). The size of the sampling window within the imaged field determines the spatial resolution of the velocity measurements. A method of sampling window refinement devised earlier [*Logory et al.*, 1995] was utilized here. Each DPIV measurement data produced approximately 4000 velocity vectors of which about 1000 are independent due to a 50% overlap of sampling windows utilized in the present system. The velocity vector field determined in this manner contains an uncertainty of $\pm 2\%$, and the vorticity calculation has an uncertainty of $\pm 4\%$. The magnification factor for the full-field measurements resulted in a spatial resolution of 4.8 mm. The spatial resolution in the high magnification measurements utilized for resolving the free-surface boundary layer, was 0.13 mm.

The general optical configuration depicted in Figure 4 was used for either full-field or high-resolution DPIV measurements. The beams from a pair of frequency-doubled Nd:YAG Lasers (Continuum Surelite I-10 and Powerlite NY 60-30) were combined and used for illumination. Laser outputs were electronically triggered to occur before and after camera frame transfer which allowed for a temporal spacing of 2 ms. A digital delay generator (Stanford Research Systems, model DG535) was used to synchronize the camera

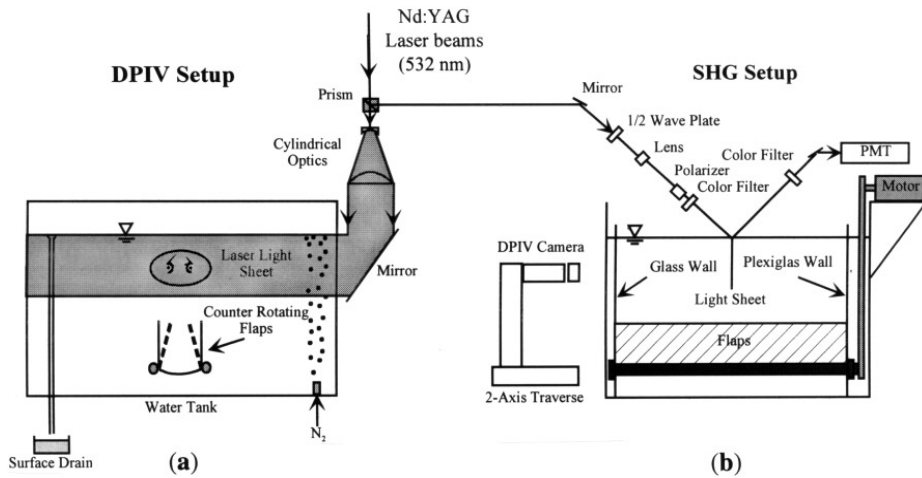


Figure 4: Schematic of the experimental setup for vortex pair measurements illustrating the vortex pair generator and the DPIV and SHG instrumentation; (a) front view, (b) side view.

frame transfer with the lasers. The short laser pulses (8 ns) ensured that the motion of particles was frozen in time. A digital video camera (Texas Instruments model 1134 P) with a 1134×486 pixel array produced a non-interlaced output at 30 Hz and was used for image acquisition. A 135 mm lens (Nikkor f/2) was used with bellows (Nikon model PB-6) to provide a good image quality and light intensity when placed 30 cm away from the image plane. The video signal was digitized using a frame grabber (Epix, model 12) and a personal computer was used to store and analyze the video images. For each realization of the experiment, the frame grabber video memory (16 MB) allowed 68 video frames to be recorded at a resolution of 512×486 pixels. For the high-resolution measurements, the water was seeded with $2.8 \mu\text{m}$ polystyrene particles (Polysciences Inc. s.g. 1.05) to a concentration of approximately 100,000 particles/ml. For the full-field measurements, $30 \mu\text{m}$ polycrystalline particles (Optimage, s.g. 0.98-1.02) were used with a concentration of approximately 150 particles/ml.

4.2 Second-Harmonic Generation

The laser based nonlinear optical technique of reflected second-harmonic generation was used to monitor surfactant concentrations at the air-water interface in the vortex pair experiments. Second-harmonic generation (SHG) is a second order nonlinear optical process in which two photons of light at frequency ω are converted to one photon at 2ω .

Second order nonlinear optical processes are symmetry forbidden in the bulk of optically isotropic media (electric dipole approximation). Fluids are

isotropic due to the random orientation of their component molecules. At an interface, the symmetry is broken and SHG is allowed for the interfacial layer, thus the technique is extremely surface selective. At an air/water interface, the SH signal originates in the top few molecular layers and can be used to study adsorbed species.

As utilized for the present study, the SHG signal intensity is directly proportional to the square of the surface concentration. Resonance enhancement at ω and/or 2ω can greatly enhance the SH signal intensity. Resonance enhancement occurs when the incident probe laser photon energy or the energy of the generated second-harmonic photon match the energy of an allowed molecular electronic or vibrational resonance in an interfacial molecule. In the experiment described in this paper, the incident laser light at 532 nm and the detected SH signal at 266 nm are both resonant with transitions of the hemicyanine molecule which was used as the surfactant.

Reflected SHG has become a popular method of surface analysis. It is non-invasive, and can in principle be applied to any optically accessible interface. The concentration-squared dependence of the signal makes it a sensitive probe of adsorbed species. SHG has been used to study surfactants adsorbed at solid/liquid, liquid/liquid, and liquid/vapor interfaces. A large number of experiments have been performed to characterize various surfactants at the air/water interface [Shen, 1989]. Excluding the use of SHG in probing the ocean surface [Korenowski *et al.*, 1993], few experiments have been performed to study systems which are dynamic on a macroscopic scale. The current experiment extends the application of SHG further into the realm of dynamic systems.

4.3 Present Experiment

The vortex pair experiments were conducted in a water tank with glass walls and floor which measures $1.2 \times 0.64 \times 0.76$ m, as shown in Figure 4. The tank was filled with distilled water which was passed through a UV filter. Prior to spreading the monolayer, ultra-pure nitrogen bubbles were used to bring any surfactants to the surface where they were removed by a stainless steel surface drain. Bubble life at the free surface provided a very sensitive measure of surface cleanliness [Scott, 1975]. All elements of the device which are below water are made of stainless steel, glass, or other non-surface active elements. Vortex pairs were generated 22 cm below the free surface by two counter-rotating flaps which are driven by a stepper motor through two lever control arms. A mylar sheet was connected between the bottom of the flaps to improve vortex pair stability [Hirsa and Willmarth, 1994]. A personal computer was used to control the stepper motor through a programmable indexer. A computer program generated a flap motion which simulated the circulation distribution behind an elliptically loaded wing. This resulted in a smooth rollup with minimal three-dimensional effects; for more details, see Locke *et al.* [1993].

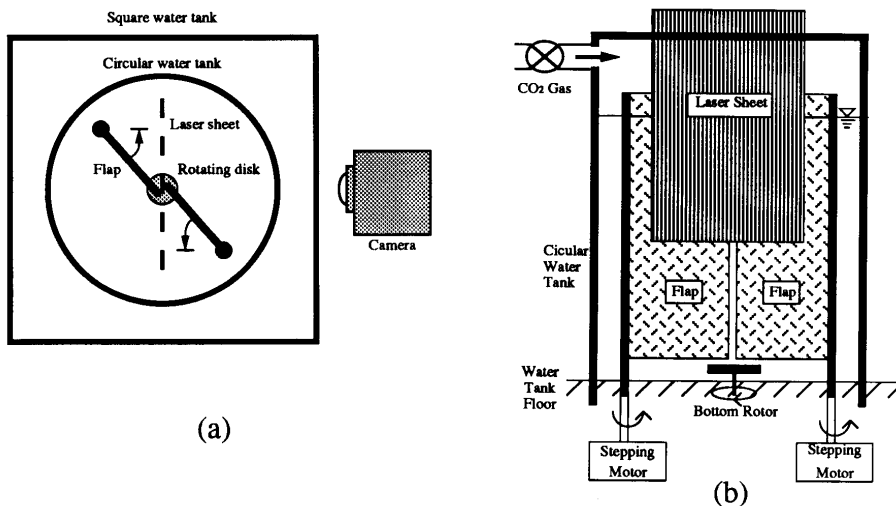


Figure 5: Schematic of the columnar vortex generator; (a) top view, (b) side view.

The columnar vortex was studied in a 25 cm diameter Plexiglas water tank which was also filled with distilled water passed through a UV filter. The vortex was generated by a pair of co-rotating stainless steel flaps, as illustrated in Figure 5. The surface of the water was cleaned by surface drainage. A larger square water tank was constructed around the circular tank to eliminate optical distortion caused by viewing through the circular tank. The flaps were initially positioned radially and were rotated a total of 67° as depicted in Figure 5(a). The flap rotation was accomplished by a computer-controlled stepping motor, similar to that described above. The detrimental effects at the tank bottom were minimized by use of a rotating disc as shown in Figure 5. The rotating disc was driven at a constant rate of 5.1 radians/s and its rotation is in the same direction as that of the columnar vortex.

The surfactant chosen for the vortex pair experiment (where SHG was utilized) was a hemicyanine dye, 4-[4-(dimethylamino)-styryl]-1-docosylpyridinium bromide. It was purchased from Aldrich Chemical Co., and used without purification. The hemicyanine was spread on the water surface from a chloroform solution. Hemicyanine dye was chosen because of its large second order optical nonlinearity. In addition, the behavior of monolayers of this surfactant on various sub-phases has been well characterized [Frysiner, 1992]. In the surface pressure range used in the following experiments, the hemicyanine surfactant is a well behaved monolayer. Oleyl alcohol and stearic acid were also utilized in some of the flow visualization experiments with vortex pairs and columnar vortices.

5 Results and Discussion

5.1 Gas Transport Measurements

The transport of *carbon dioxide* from the gas phase into the water was investigated in the columnar vortex flow. The entrainment of carbon dioxide was visualized using the *laser-induced fluorescence (LIF)* technique of Asher and Pankow [1991] and Münsterer and Jähne [1993]. The quenching of fluorescence from 2',7'-dichlorofluorescein (DCFS) with decreasing pH (in the range of 3.5 to 6.0) was used to visualize the transport of carbon dioxide into the bulk of the water. The fluorescence was stimulated by the 488 nm line of an argon-ion laser.

The results of the LIF study are shown in Figure 6. Presented in Figure 6(a) is the fluorescence during the interaction of the columnar vortex with a clean free surface. The first photograph (Figure 6,a,i) was taken at $t = 10$ s (compare this with Figure 3,a), where the termination of flap motion is defined at $t = 0$. The photograph shown in Figure 6(a,ii) was taken at $t = 22$ s. The fluorescence in the case of the columnar vortex interaction with a contaminated surface is presented in Figure 6(b) at the same respective times. In this case the surface was covered by a saturated monolayer of stearic acid. The relevant portion of these photographs is the vortex centerline in the near surface region. At the earlier time ($t = 10$ s), the rate of CO_2 intake into the bulk appears to be greater in the contaminated case as is evident by the dark streaks in the fluorescent light sheet (see Figure 6,b,i). The entrainment of CO_2 into the bulk becomes more evident at later times, as shown in Figure 6(b,ii). This is the result of the three-dimensionality in the substrate flow, which was illustrated in Figure 3(b). In the clean surface case, the flow remains two-dimensional and the rate of CO_2 intake appears to be diffusion limited. (It should be noted that away from the columnar vortex, secondary vortices exist. These secondary vortices are inherently three-dimensional regardless of the free surface condition, because of the bottom boundary condition. The three-dimensional flow induced by these secondary vortices also causes entrainment of CO_2 as is evident by the random dark streaks visible in Figure 6.)

5.2 Rheological Measurements

The results above illustrate the interplay between surfactants and subsurface flow and their effects on gas exchange. Based on this, it is apparent that rheological properties of surfactants are required for developing predictive models of gas exchange. Presently, an effort is made to quantify these rheological properties directly using vortical flows, in contrast with wave and bubble methods. In the following section, we discuss some of the measurements which can be used for obtaining rheological properties of a monolayer during the interaction of a vortex flow with a free surface.

Some of the rheological properties of a hemicyanine monolayer (an insoluble surfactant) were examined during the interaction of a vortex pair with a free surface. Full-field measurements of the vortex pair flow were made prior to the interaction with the free surface. Figure 7(a) shows the vortex pair instantaneous velocity vector field. At this time, the vortex pair separation, δ , is 8.3 cm and the vortex pair has begun a diverging trajectory because of the boundary. The circulation, Γ , associated with each vortex was calculated from the velocity field to be $205 \text{ cm}^2/\text{s}$, which results in a Reynolds number (Γ/ν) of 20,500. The Froude number, $\Gamma/(g\delta^3)^{1/2}$, was 0.27 which resulted in a nearly flat free surface [for comparison, see *Anathakrishnan & Yeung*, 1994 and *Ohring & Lugt*, 1991]; here, g is the gravitational acceleration. The vorticity (ω_z) for the same image is presented in Figure 7(b). The regularity of vorticity contours indicates that the flow is laminar, despite the relatively large Reynolds number.

High resolution measurements were made to resolve the free surface boundary layer during the interaction of the vortex pair with a hemicyanine-covered surface. The hemicyanine monolayer was at a film pressure of 3.2 dynes/cm. The measurements were made at a region centered at $x = 4 \text{ cm}$ (i. e., 4 cm to the right of the centerline). The small box drawn at the free surface edge of the plots in Figure 7 marks the region where the high resolution measurements were made. The velocity vector plot is presented in Figure 8(a) and the corresponding vorticity contours are shown in Figure 8(b). In the velocity vector plot (Figure 8,a), the boundary layer at the free surface appears as a narrow horizontal zone where the flow appears to be retarded. The total internal reflection at the free surface is responsible for the “image” vorticity observed in Figure 8(b). This serendipitous effect provides an exact means for locating the free surface. The magnitude of the vorticity measured in the boundary layer (of the order of 200 s^{-1}) is one order of magnitude larger than the initial vorticity in the core of each primary vortex (see Figure 7,b).

In order to extract rheological properties of surface (excess) shear viscosity (μ^s) and dilatational viscosity (κ^s), the tangential component of the stress boundary condition can be utilized [*Edwards et al.*, 1991]. This boundary condition expresses a balance between the stress exerted by the substrate, surface tension gradients, and a diffusion term due to the sum of the two surface viscosities ($\mu^s + \kappa^s$). If the surface tension gradients are available, the sum of the surface viscosities can be obtained using the velocity data. It should be noted, that although the vortex pair flow does not produce any shear in the plane of the surface, the effect of μ^s is not assessed and the term must be retained in the calculation.

In order to obtain the surface tension gradients (i. e. spatial derivative of the surface tension), time resolved SHG measurements were obtained. Figure 9 shows the concentration of hemicyanine measurements as a function of time made at a point on the free surface. The initial surface pressure in this case was $\pi = 3.2 \text{ dynes/cm}$. Measurements at two different locations are

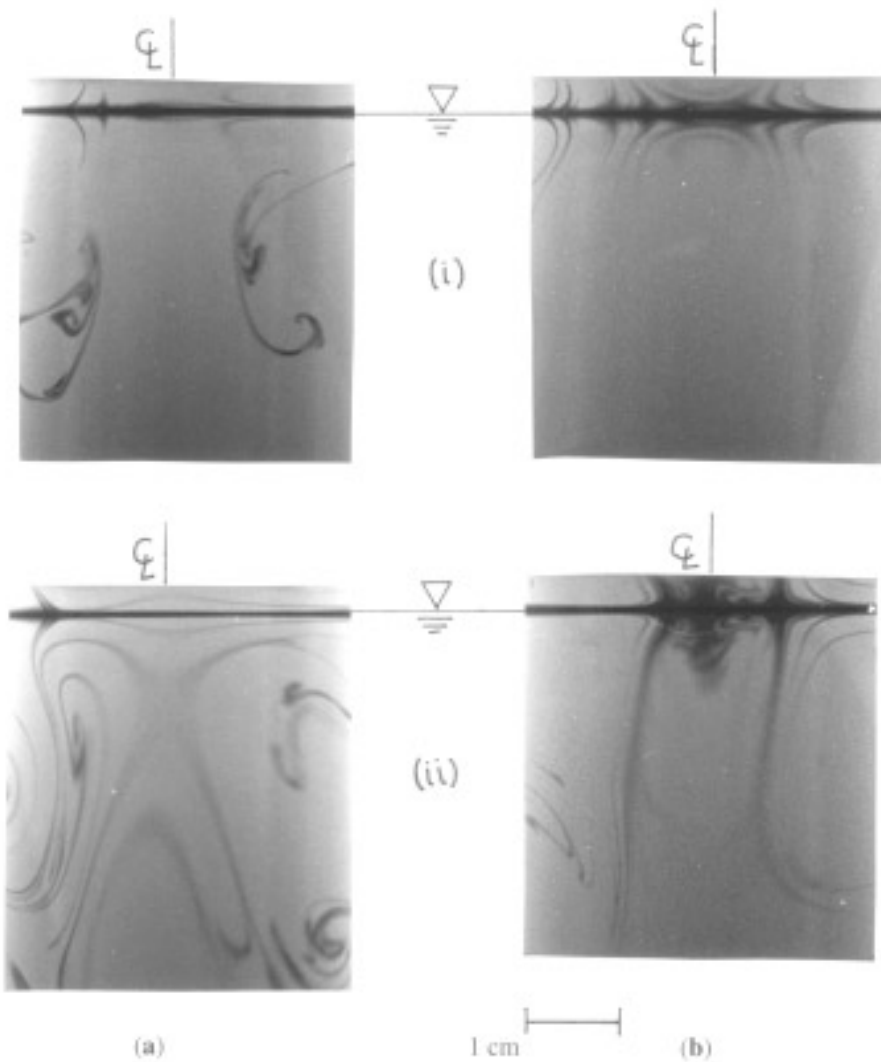


Figure 6: Photographs of columnar vortex interaction with a free surface visualizing the transport of CO_2 into water using a pH-sensitive LIF method. The free surface is clean in (a) and covered with a saturated monolayer of stearic acid in (b). The photographs in (i) were made at $t = 10$ s and the photographs in (ii) were made at $t = 22$ s.

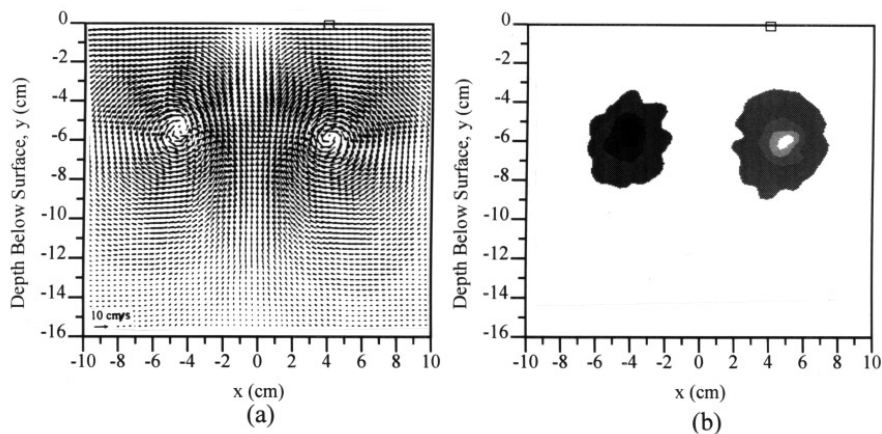


Figure 7: Full-field DPIV measurements of the vortex pair prior to the interaction with a clean free surface; (a) velocity vector plot, (b) vorticity contours. Vorticity contours range from a minimum level of -30 s^{-1} in the center of the right-hand vortex, to more than 24 s^{-1} in the left-hand vortex with increments of 6.7 s^{-1} . Note, the rectangular region shown at the top of each figure marks the location of high resolution measurements; see Figure 8.

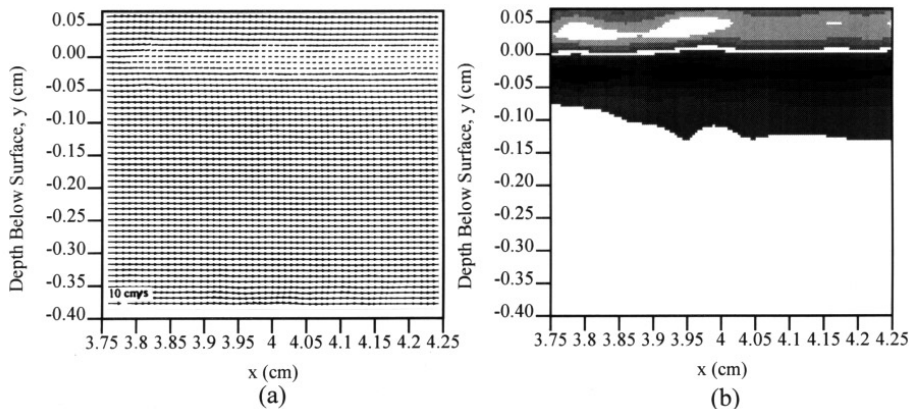


Figure 8: High resolution DPIV measurements of the free surface boundary layer formed during the vortex interactions with a contaminated surface ($\pi = 3.2 \text{ dynes/cm}$) centered at $x = 4 \text{ cm}$; (a) velocity vector plot, (b) vorticity contours. Vorticity contours range from a minimum level of -300 s^{-1} in the boundary layer, to more than 230 s^{-1} for the “image vorticity” with increments of 67 s^{-1} .

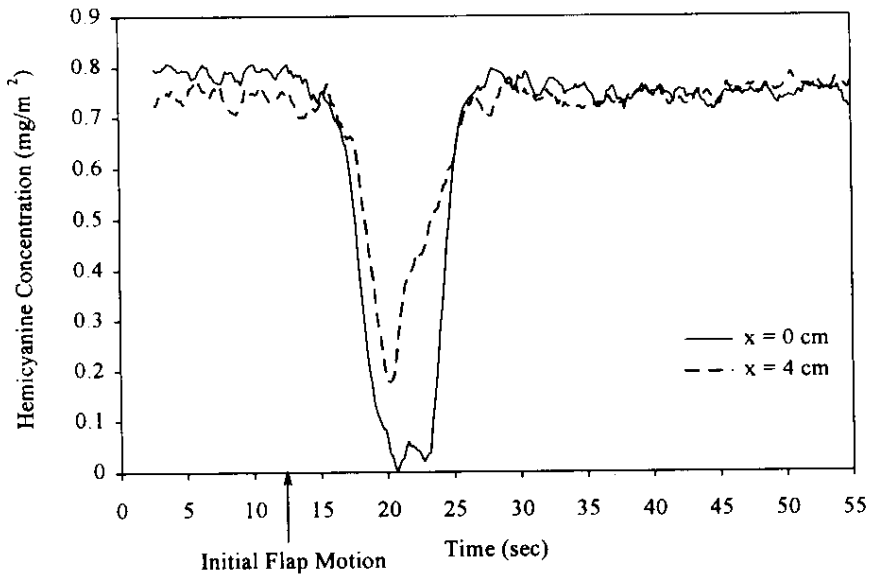


Figure 9: SHG measurements of the hemicyanine concentration as a function of time at $x = 0$, and 4 cm for an initial surface pressure of 3.2 dynes/cm.

shown, namely, the centerline ($x = 0$) and at $x = 4$ cm. The figure shows that the flow is initiated at 12.5 s when the vortex generation process begins. The vortex pair propagates toward the surface, which subsequently causes the transport of the surfactant away from the centerline. This process continues until the surface tension gradients increase while the vortex is rebounding from the free surface, which results in the return of the surfactant back to the center. Figure 9 indicates complete cleaning of the surfactant at the center for this initial surface pressure (3.2 dynes/cm). Additional measurements (not shown here) have illustrated that complete cleaning of the surfactant from the center is not achieved at an initial pressure of 7.3 dynes/cm [Hirsa et al., 1995].

The results of Figure 9 can be used to obtain the surface tension gradient, $\partial\sigma/\partial x$, knowing the equation of state for the surfactant, i.e., the relationship between the thermodynamic surface tension and surfactant concentration $\sigma = \sigma(c)$. Based on this, it is expected that the measurements presented here can be utilized along with the stress boundary condition to calculate the value of the viscous group ($\mu^s + \kappa^s$). Additionally, as illustrated by Hirsa et al. [1995], the columnar vortex flow can provide a relative measure of the surface shear viscosity (μ^s).

6 Conclusion

The interaction of turbulence with a free surface was studied by separately examining the interaction of surface-normal and surface-parallel vortices with a clean or contaminated free surface. Columnar vortex experiments have demonstrated that the three-dimensionality induced by a highly viscous surfactant (stearic acid) can enhance the rate of CO₂ transport into water. In the absence of the surfactant, CO₂ intake appeared to be diffusion dominated. The results of this experiment illustrate the importance of subsurface flow topology on the transport of CO₂ across the interface and supports the conjecture that the exchange of CO₂ is controlled by subsurface turbulence. As pointed out earlier, the importance of surfactants on the interaction of vortical flows with an air-water interface has been demonstrated. Therefore the results of the present experiment underscores the role of surfactants on gas exchange.

Velocity measurements in the bulk along with surfactant concentration measurements were made during the interaction of a vortex pair with a free surface. The thin (order of 1 mm) boundary layer formed beneath the surface was resolved. These measurements can be utilized along with *surfactant concentration* data to study the behavior of surface viscosities for a given surfactant. This information can, in principle, be used to understand the vortex dynamics at a contaminated surface, and develop predictive models of gas transport in free-surface turbulence.

Acknowledgements

We wish to acknowledge Mr. John E. Harper for assisting in many of the experiments with the columnar vortex. The authors would also like to acknowledge the support of the Office of Naval Research through grant no. N000149410062, N0001490J1537, and N0001491J1690.

References

- Anathakrishnan, P. and Yeung, R. P., Nonlinear interaction of a vortex pair with clean and surfactant-covered free surfaces, *Wave Motion*, 19, 343-365, 1994
- Asher, W. E., and Pankow, J. F., Prediction of gas/water transport coefficients by a surface renewal model, *Enviren. Sci. & Technol.*, 25, 1294-1300, 1991
- Bernal, L. P., Hirsa, A., Kwon, J. T., and Willmarth, W. W., On the interaction of vortex rings and pairs with a free surface for varying amounts of surface active agent, *Physics of Fluids A*, 1, No 12, 2001-2004, 1989
- Edwards, D. A., Brenner, H., and Wasan, D. T., *Interfacial transport processes and rheology* Butterworth-Heinemann, 1991
- Frysjinger, G. S., Nonlinear optical spectroscopy of air/water interface chemistry, Ph. D. Thesis, Rensselaer Polytechnic Institute, Troy, NY, 1992
- Hirsa, A., Harper, J. E., Kim, S., Columnar vortex generation and interaction with a clean or contaminated free surface, *Physics of Fluids*, 1995 (in press)

- Hirsa, A., Logory, L. M., Korenowski, G. M., Judd, C. D., Gaines, G.L., Velocity field and surfactant concentration measurement techniques as applied to the interaction of a vortex pair with a free surface, in *Laser Anemometry* (ed. T. T. Huang et al.), HTD-Vol. 229, ASME, New York, NY, 123-129, 1995
- Hirsa, A., and Willmarth, W. W., Measurements of vortex pair interaction with a clean or contaminated free surface, *J. Fluid Mech.*, 259, 25-45, 1994
- Jähne, B., and Münsterer, T., A fluorescence technique to measure concentration profiles in the aqueous mass boundary layer, *Air-Sea Interface Symp.*, Marseille, France, 1993
- Korenowski, G. M., Frysinger, G. S., and Asher, W. E., Noninvasive probing of the ocean surface microlayer using laser-based nonlinear optical methods, *Photogrammetric Engineering & Remote Sensing*, 59, No 3, 363-369, 1993
- Locke, C. A., Hirsa, A. and Rubin, M. D., Short-wave instability in a laminar vortex pair, *ASME Fluids Engrg. Conf., Forum on Unsteady Flows* (ed. W. L. Keith & T. Wei), FED-Vol. 157, 73-81, 1993
- Logory, L. M., Hirsa, A., and Anthony, D. G., Interaction of wake turbulence with a free surface, *Physics of Fluids*, 1995 (submitted)
- Lugt, H., Local flow properties at a viscous free-surface, *Phys. Fluids*, 30, No. 12, 3647-3652, 1987
- Ohring, S. and Lugt, H. S., Interaction of a viscous vortex pair with a free surface, *J. Fluid Mech.*, 227, 47-70, 1991
- Sarpkaya, T. and Neubert, D., Interaction of a streamwise vortex with a free surface, *AIAA J.*, 32, No. 3, 594-600, 1994
- Sarpkaya, T. and Henderson, D. O., Free surface scars and striations due to trailing vortices generated by a submerged lifting surface, *AIAA Paper* 85-0445, AIAA 23rd Aerospace Science Mtg. Reno, Nevada, 1985
- Scott, J. C., The preparation of water for surface-clean fluid mechanics, *J. Fluid Mech.*, 69, Part 2, 339-351, 1975
- Shen, Y. R., Surface properties probed by second-harmonic and sum-frequency generation, *Nature*, 337, 519-525, 1989
- Willert, C. E. and Gharib, M., Digital particle image velocimetry, *Experiments in Fluids* 10, 181-193, 1991

Hydrodynamics in a Jet-Agitated Vessel Close to the Gas-Liquid Surface

F. Minel and J. George

INP-ENSEEIHHT - Institut de Mécanique des Fluides URA 005 CNRS
Avenue du Professeur Camille Soula 31400 Toulouse. France

Abstract

The gas-liquid mass transfer phenomenon is quite complex and different characteristic velocities and length scales are involved. In order to study the size of the dominant eddies, laboratory experiments were carried out in a parallelepipedic jet-agitated vessel using a LDV device-2-directional. A direct estimation of the dissipation rate of the turbulent kinetic energy is performed, which shows a good agreement with results by *Brumley and Jirka* [1987]. Integral length scales are obtained both in the vertical and in the horizontal direction which show that there is a simultaneous increase of the horizontal macro scale and a collapse of the vertical one when the free surface is approached.

1 Introduction

There is a great demand for interfacial gas-transfer models in such domains as chemical engineering or in environmental studies. The mass transfer process is characterised by the mass transfer coefficient K_L which depends on the behaviour of the thin diffusive liquid layer inside which absorption of weakly soluble gases is controlled. The dynamics of the diffusive layer are closely dependent on the degree of agitation of the free surface. Interfacial agitation can be generated either from the gas side by the effect of wind and is characterised by the existence of waves, or inside the liquid phase by mechanical means. It is therefore of fundamental importance to understand the dynamics of the air-water interface, and more precisely to study the fate of liquid turbulence when the surface is approached.

In this paper, velocity measurements obtained by means of a two-component LDV are reported, which allowed the calculation of most third order moments of velocity fluctuations and, hence, a direct estimation of the *dissipation* rate ε of the *turbulent kinetic energy*.

2 Turbulence Measurements in a Microjets-Agitated Vessel

In order to study the fate of initially isotropic and homogeneous in horizontal planes turbulence as it reaches the vicinity of the air-water surface, an agitated vessel was designed by *Grisenti* [1991] (for more details see *Grisenti*

and George [1991], George *et al.* [1994]). In this vessel, turbulence is produced by a large number of upflowing liquid microjets. The vessel consists in a square based Plexiglas tank (Figure 1). Each nozzle diameter is 0.7 mm. The liquid flowrate is $q_L = 0.46$ l/s and pure deionized water is circulated in order to avoid the presence of contaminants at the surface. The flow hydrodynamics are presented in George *et al.* [1994].

According to the horizontal symmetry, the velocity profiles are explored only in the vertical z-direction (W, w') and in one horizontal x-direction (U, u'). It can be noted that the interface remained almost flat during experiments (capacitance probes disposed in the vessel did not show significant vertical fluctuations of the gas-liquid interface), therefore no wave motions had to be removed from the data set.

Thanks to the use of a two-components Laser Doppler velocity (LDV) device second and third order velocity moments have been measured ($u'^2, w'^2, u'w', u'w'^2, u'w'^2, u'^3, w'^3$) altogether with the mean and instant fluctuating values (U, W, u', w') (for more details see [Minel, 1994]). Time averaged values for each velocity component were obtained using a temporal averaging:

$$\bar{U} = \frac{\sum_i U_i(t_i - t_{i-1})}{\sum_i (t_i - t_{i-1})} \quad (1)$$

Each cross momentum was calculated when simultaneous particles were crossing the measurement domain (a 200 bursts window) within 10^{-3} ms. The third order moment $u'^2 w'$, for example, writes:

$$\overline{u'^2 w'} = \frac{\sum_i (U_i - \bar{U})^2 (W_i - \bar{W})(t_i - T_{i-1})}{\sum_i (t_i - t_{i-1})} \quad (2)$$

In order to be able to calculate power velocity spectra, time series obtained from the Burstware devices were rebuilt using the method proposed by Veynante and Candel [1988] (called SR method).

Power velocity spectra were obtained applying a FFT to reconstructed signals. The sampling frequency was 50 or 100 Hz, each block size was 2^{10} samples and average values were computed on the total number of blocks of each time series.

It has been verified that there is a good homogeneity in the horizontal plane and that the degree of isotropy is satisfactory (in fact the ratio u'/v' is of order of values reported by [Hopfinger and Toly, 1976]). Unfortunately, experimental results [Grisenti, 1991] have shown that secondary motions exist. The profiles show the expected trends, except for the mean velocity in the horizontal plane which is non zero at the free surface due to the presence of secondary mean motions. It can be added that the observed secondary motions do not seem to be created by a lack of symmetry of the vessel because they are sensitive only to the initial conditions and establish randomly each time.

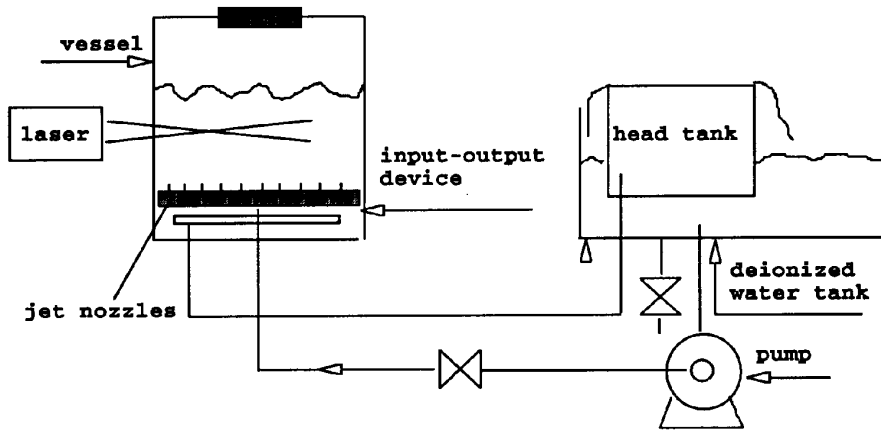


Figure 1: Experimental facility

3 Dissipation Rate of the Turbulent Kinetic Energy

Due to the random movements mentioned above, the classical hypothesis $U = V = 0$ does not hold and some symmetry hypothesis have to be made. That is also the reason why the turbulent kinetic energy budget cannot be written as a *diffusion/dissipation equilibrium*. Some advection and production terms are remaining and the dissipation rate ε can be deduced only from the whole turbulent kinetic energy equation.

The complete *turbulent kinetic energy* equation energy writes [Minel, 1994]:

$$\begin{aligned}
 & U \frac{\partial k}{\partial x} + V \frac{\partial k}{\partial y} + W \frac{\partial k}{\partial z} = \\
 & - \overline{u'^2} \frac{\partial U}{\partial x} - \overline{v'^2} \frac{\partial V}{\partial y} - \overline{w'^2} \frac{\partial W}{\partial z} \\
 & - \overline{u'v'} \left(\frac{\partial U}{\partial y} + \frac{\partial V}{\partial x} \right) - \overline{u'w'} \left(\frac{\partial U}{\partial z} + \frac{\partial W}{\partial x} \right) - \overline{v'w'} \left(\frac{\partial V}{\partial z} + \frac{\partial W}{\partial y} \right) \\
 & + \frac{\partial}{\partial z} \left(v \frac{\partial k}{\partial z} \right) + \frac{\partial}{\partial y} \left(v \frac{\partial k}{\partial y} \right) + \frac{\partial}{\partial x} \left(v \frac{\partial k}{\partial x} \right) \\
 & - \frac{\partial}{\partial z} \left(\frac{\overline{u'^2 w'} + \overline{v'^2 w'} + \overline{w'^3}}{2} + \overline{p'w'} \right) \\
 & - \frac{\partial}{\partial y} \left(\frac{\overline{u'^2 v'} + \overline{w'^2 v'} + \overline{v'^3}}{2} + \overline{p'v'} \right) \\
 & - \frac{\partial}{\partial x} \left(\frac{\overline{w'^2 u'} + \overline{v'^2 u'} + \overline{u'^3}}{2} + \overline{p'u'} \right) - \varepsilon
 \end{aligned} \tag{3}$$

Hypothesising planar symmetry of the flow such that

$$\frac{\partial U}{\partial z} + \frac{\partial W}{\partial x} = \frac{\partial V}{\partial z} + \frac{\partial W}{\partial y}, \quad v \frac{\partial k}{\partial y} = U \frac{\partial k}{\partial x} \quad (4)$$

and

$$-\overline{u'w'} \left(\frac{\partial U}{\partial z} + \frac{\partial W}{\partial x} \right) - \overline{v'w'} \left(\frac{\partial V}{\partial z} + \frac{\partial W}{\partial y} \right) = -2\overline{u'w'} \left(\frac{\partial U}{\partial z} + \frac{\partial W}{\partial x} \right) \quad (5)$$

and noting that theoretical considerations of the pressure-velocity fluctuation correlation for the case of turbulence that is inhomogeneous in the vertical direction, isotropy implies

$$\overline{p'w'} = -2/5\overline{k'w'} \quad \text{and} \quad \overline{p'u'} = -2/5\overline{k'u'} \quad (6)$$

[Magnaudet, 1993], the turbulent kinetic energy equation can finally be written as:

$$\begin{aligned} \varepsilon = & -2U \frac{\partial k}{\partial x} - W \frac{\partial k}{\partial z} + (\overline{u'^2} - \overline{w'^2}) \frac{\partial W}{\partial z} - 2\overline{u'w'} \left(\frac{\partial U}{\partial z} + \frac{\partial W}{\partial x} \right) \\ & + \frac{\partial}{\partial z} \left(v \frac{\partial k}{\partial z} \right) + 2 \frac{\partial}{\partial x} \left(v \frac{\partial k}{\partial x} \right) \frac{\partial}{\partial z} \left(\overline{u'^2 w'} + \frac{\overline{w'^3}}{2} - \frac{2}{5} \overline{k'w'} \right) \\ & - \frac{\partial}{\partial x} \left(\overline{w'^2 u'} + \overline{u'^3} - \frac{4}{5} \overline{k'u'} \right) \end{aligned} \quad (7)$$

Gradients both in the vertical and horizontal direction are deduced from measurements along the vertical axis and also from different horizontal positions. When all terms of the above equation are measured, it is possible to determine a direct estimation of ε .

Due to the large amount of measurements required, the vertical dissipation profile was performed only for one single experiment in the *jet-agitated vessel*.

As is shown in Figure 2, the profile of ε is quite similar to the one *Brumley and Jirka* [1987] obtained by different means in a grid-stirred vessel. However, the increase observed close to the free surface in the value of ε in some of their results does not exist, ε decreasing here regularly.

This last result can be due to the fact that in *Brumley and Jirka* [1987] experiments, a viscous layer seemed to be developing close to the free surface, and hence damping turbulence in the upper region. In our case, on the contrary, horizontal agitation seems to be remaining at the very surface, this is probably due to the fact that impurities have been removed carefully in order to prevent the formation of surface films.

It can be noted that, as observed in different situations by *Tamburrino and Gulliver* [1992] or by *Jähne* [1995] and *Münsterer et al.* [1995], large intermittent eddies are present at the free surface, which is in good agreement with the fact that there is no important damping of the horizontal velocity fluctuations, and hence, that the dissipation rate of the turbulent kinetic energy reaches a minimum at the interface.

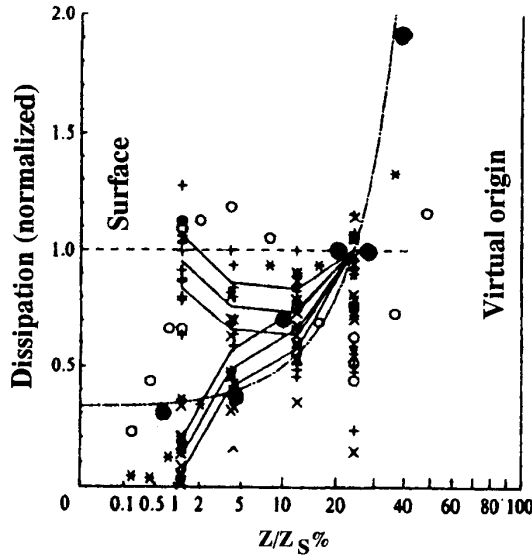


Figure 2: Vertical profile of ε , the dissipation rate of the turbulent kinetic energy. Broken line: constant dissipation rate; solid line: $\varepsilon \propto z^{-4}$; open circles, +: Brumley and Jirka [1987]; black circles: Minel [1994].

4 Characteristic Length Scales and Frequencies

As observed in the previous section, the dissipation rate ε seems to be reaching a minimum at the interface while, in the same hydrodynamic conditions, the turbulent kinetic energy is slightly increased [George *et al.*, 1994] when horizontal eddies can develop freely. In order to model gas transfer, it is important to understand what are the governing interfacial agitation parameters, it is therefore interesting to examine the size of characteristic length-scales present at the free surface.

A Kolmogorov microscale could be calculated from the classical relation

$$\eta = \left(\frac{\nu_L^3}{\varepsilon} \right)^{1/4} \tag{8}$$

where ν_L is the liquid kinematic viscosity. The result is: $\eta = 2.56 \cdot 10^{-4}$ m which is in agreement with the value of Chu [1990] who found $\eta = 3.8 \cdot 10^{-4}$ m.

As, in our experiments, time dependent power velocity spectra are available but not wave number ones, it is impossible to derive directly an horizontal macroscale, from the spectral density power, using the method proposed by Comte-Bellot [1965]. It was therefore necessary to use the method

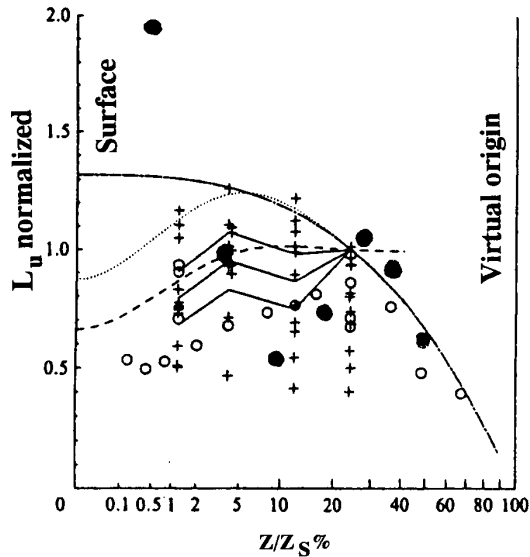


Figure 3: Vertical profile of the horizontal macro scale. Broken line: Hunt and Graham [1978]; solid line: Thompson and Turner [1975]; dotted line: Combined profile; open circles, +: Brumley and Jirka [1987]; black circles: Minel [1994].

proposed by Tennekes and Lumley [1972], that is:

$$L_U = \frac{(\sqrt{u'^2})^3}{2\varepsilon} \quad \text{and} \quad L_W = \frac{(\sqrt{w'^2})^3}{2\varepsilon} \quad (9)$$

At the interface, an increase in the estimated value of the horizontal macro scale (Figure 3) is observed altogether with a decrease of the vertical one (Figure 4), which tends to acknowledge the fact that large two dimensional eddies develop close to the free surface. It can be seen also that far away from the interface, L_U and L_W profiles follow Thompson and Turner [1975] predictions (linear law) while, when the surface is approached, eddies tend to become two-dimensional. It can be added that records of the instant velocity values close to the surface show some intermittence features, which confirms the existence of large eddies reaching the interface and renewing it.

Close to the free surface the respective values of L_U and L_W are: $L_U = 2.54 \cdot 10^{-2}$ m and $L_W = 3.08 \cdot 10^{-3}$ m, that is L_U is one order of magnitude larger than L_W .

This increase in the horizontal plane was confirmed when velocity spectra were obtained. When the interface is approached, part of the turbulent

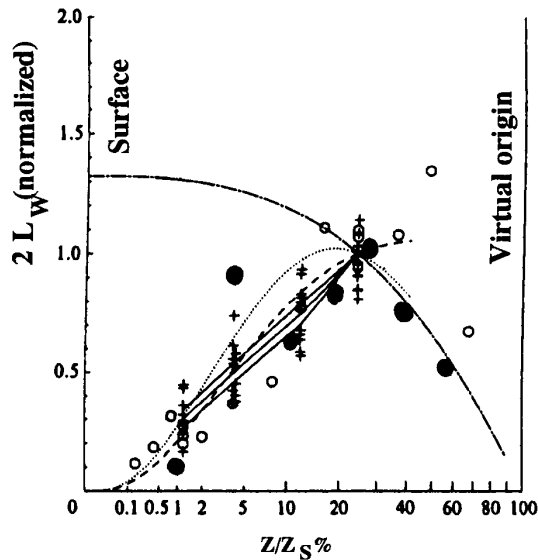


Figure 4: Vertical profile of the vertical macro scale. Broken line: Hunt and Graham [1978]; solid line: Thompson and Turner [1975]; dotted line: Combined profile; open circles, +: Brumley and Jirka [1987]; black circles: Minel [1994].

kinetic energy is transferred from the vertical direction towards the lower frequencies in the horizontal direction (Figures 5 a and b), the same trend was also observed by *Hannoun et al.* [1988] or by *Komori et al.* [1993].

Finally, the above results show that: when the interface is approached, the dissipation rate of the turbulent kinetic energy decreases altogether with the vertical rms. velocity and the vertical macro scale. On the contrary, the horizontal rms. velocity and macro scale are increased while lower velocity power density frequencies become more energetic. These results can be compared with the observed increase in the rms. concentration [*Prinos et al.*, 1995], which tends to acknowledge the fact that large horizontal eddies play a major role in the mass transfer phenomenon.

5 Conclusion

In conclusion, a method, believed original, was developed by *Minel* [1994] in order to obtain a direct estimation of ε the dissipation rate of the turbulent kinetic energy.

Results show a decrease of ε close to the free surface simultaneously with an increase of the integral scale and of the lower frequencies energy in the horizontal plane.

As reported earlier [*George et al.*, 1994], when a surfactant is added,

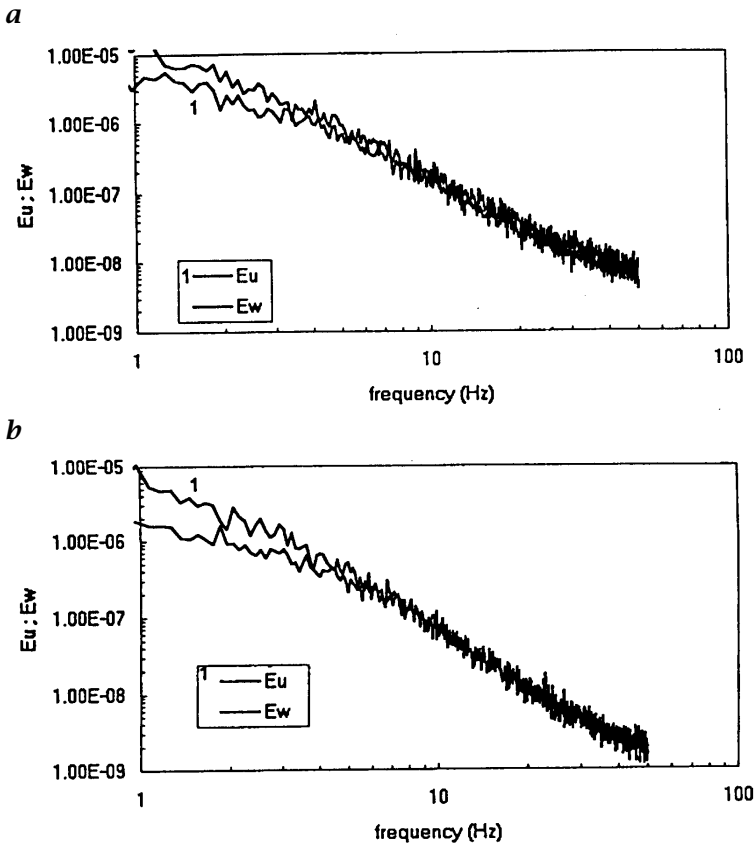


Figure 5: Power density spectra in the horizontal and vertical directions *a*) at $z/h = 0.942$ below the free surface, *b*) at the interface

the gas transfer rate is reduced and the relative importance of horizontal agitation compared to the vertical one is reduced, which also shows the importance of two dimensional eddies developing in the upper region.

References

- Brumley B., G. H. Jirka, Near-surface turbulence in a grid stirred tank, *J. of Fluid Mech.*, 183, 235-263, 1987
- Chu C. R., Near surface turbulent velocity and oxygen concentration measurements in a grid-stirred tank, Ph. D Thesis, Cornell University, 1990
- George J., B. Caussade, L. Masbernat, Conceptual modelling of interfacial gas-liquid mass transfer, *This volume*
- George J., F. Minel, M. Grisenti, Physico-chemical and hydrodynamic parameters controlling gas-liquid mass transfer, *Int. J. Heat Mass Transfer*, 37, 1569-1578, 1994

- Grisenti M., Etude de l'hydrodynamique et des transferts en cuve agitée par microjets, Thèse de Doctorat INP, 1991
- Grisenti M. and J. George, Hydrodynamics and mass transfer in a jet-agitated vessel, *Air-water mass transfer*, S.C. Wilhelms & J. S. Gulliver Eds, ASCE, 1991
- Hannoun I. A., H. J. S. Fernando, E. J. List, Turbulence structure near a sharp density interface, *J. of Fluid Mech.*, 189, 189-209, 1988
- Hopfinger E. J., Toly J. - A., Spatially Decaying Turbulence and its Relation to Mixing across Density Interfaces. *J.Fluid Mech.*, 78 (1), 155-175,1976
- Hunt J. C. R., Graham J. M. R., Free stream turbulence near plane boundary, *J. of Fluid Mech.*, 84, 2, 209-235, 1978
- Jähne B., Impact of quantitative visualization & image processing on the study of small-scale air-sea interaction, *This volume*
- Komori S., R. Nagaosa, Y. Murakami, Turbulence structure and mass transfer across a sheared air-water interface in wind-driven turbulence, *J. of Fluid Mech.*, 249, 161-183, 1993
- Magnaudet J., Modelling of inhomogeneous turbulence in the absence of mean velocity gradients, F.T.M. Neustadt (ed), *Advances in turbulence IV. Applied Scientific Research*, 51, 525-531, 1993
- Minel F., Transferts de masse et d'énergie en cuve agitée par microjets, Thèse de doctorat de l'INP de Toulouse, 1994
- Münsterer T., Mayer H. J., Jähne B., Dual-tracer measurements of concentration profiles in the aqueous boundary layer, *This volume*
- Prinos P., Atmane M., George J., Gas Flux Measurements and Modelling below an Air-Water Interface, *This volume*
- Tamburrino A., Gulliver J. S., Comparative flow characteristics of a moving bed flume, *Experiments in Fluids*, 13, 289-298, 1992
- Tennekes H., Lumley J. L., A first course in turbulence, *The MIT Press*, 1972
- Thompson S. M., Turner J. S., Mixing across an Interface due to Turbulence Generated by an Oscillating Grid, *J. of Fluid Mech.*, 67, 349-368, 1975.
- Veynante D., Candel S. M., Application of non linear spectral analysis and spectral reconstruction to Laser Doppler velocimetry, *Experiments in Fluids*, 6, 534-540, 1988.

Direct Field Measurements of the Flux of Carbon Dioxide

M. A. Donelan and W. M. Drennan

National Water Research Institute, Canada Centre for Inland Waters
Box 5050, Burlington, Ontario L7R 4A6 Canada

Abstract

Eddy correlation measurements of carbon dioxide (CO₂) flux have been made from a 15 m launch in Lake Ontario. Data were collected over a two week period in the fall, with 10 m wind speeds in the range of 3–16 m/s. At moderate wind speeds (3–7 m/s), the mass transfer rates of CO₂ are found to be similar to those measured using indirect tracer methods, but are twice as large at higher wind speeds.

1 Introduction

The understanding, and parameterizing, of the flux of CO₂ across the air-water interface is central to the success of climate modelling. Various attempts to measure the mass transfer velocity in laboratory tanks lead to widely different results (Figure 1). In the face of these differences, it is difficult to extrapolate laboratory results to make oceanic calculations of CO₂ flux. On the other hand the field measurements of CO₂ flux to date rest largely on indirect measurements in a relatively narrow range of wind speeds (3–12 m/s). Our purpose here is to report on direct field measurements of CO₂ flux and to compare the mass transfer velocities with established *field measurements* using indirect methods.

2 The AGILE Experiment

During the summer of 1994, the 15 meter launch AGILE was outfitted to measure *eddy-correlation* fluxes of *momentum*, *sensible heat*, *water vapour* and *carbon dioxide* – see Fig 2. The experiment took place in the western basin of *Lake Ontario* during the autumn of 1994. At this time of year, conditions are typically unstable with a net transfer of CO₂ out of the *lake*.

A Solent 3-axis sonic anemometer was mounted at the top of the AGILE's foremast, 6.8 m above the deck. Five centimeters behind the sonic sampling volume, dry and wet fast response thermocouples [Katsaros *et al.*, 1993] were positioned. Water was supplied to the wetbulb wick via gravity from a nearby 1 litre reservoir. In order to use the measured wind signals in an eddy correlation analysis, they must first be processed to remove the motion of

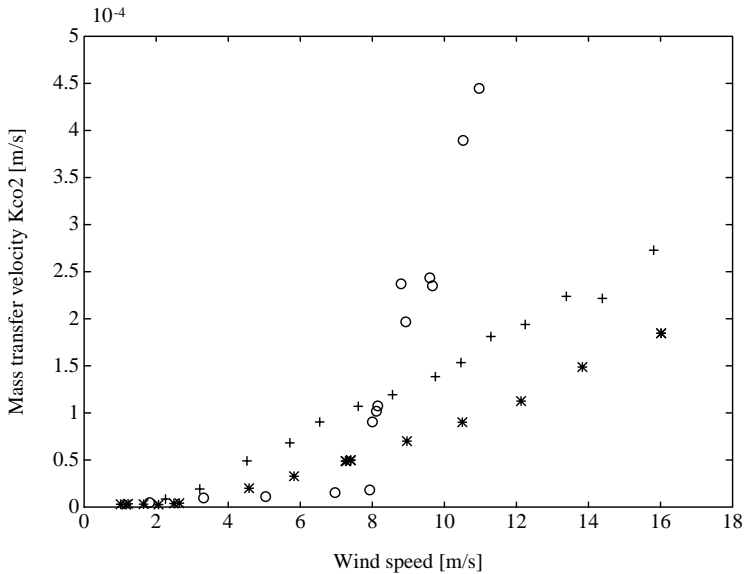


Figure 1: Laboratory data of CO₂ mass transfer velocity versus wind speed. Data are from Ocampo-Torres et al. [1994] (*), Jähne et al. [1979] (o) and Broecker et al. [1978] (+).

the ship [Anctil et al., 1994 and Katsaros et al., 1993]. To this end, a motion package, consisting of 3 linear accelerometers (measuring heave, surge and sway), 3 rate gyros (measuring the rate of change of pitch, roll and yaw) and a pitch-roll gyroscope, was installed near the bow of the AGILE. These signals were sampled at the same rate as the anemometer signals, allowing the anemometer signals to be corrected at each time step.

A LICOR LI-6262 CO₂/H₂O analyser was mounted in a sealed box on the foremast of the AGILE, 1 m below the anemometer. The LI-6262 is a non-dispersive *infrared* (NDIR) *gas analyser*. Bottled 350 ppm CO₂ was used as a reference, and the difference in IR absorption in the reference and sample volumes is used to determine the CO₂ concentration of the sample gas. The LICOR was operated in three 'modes', one for measurement of the CO₂ concentration in air, C_a , one for the CO₂ concentration in the water and a third for calibration.

A 2 m long tube was used to sample air at a position 20 cm behind the sampling volume of the sonic anemometer. In this mode of operation, air was pulled into the LICOR at the rate of 12 litres/min using a high speed pump, and then vented to the atmosphere after analysis. A comparison of the LICOR humidity variations with those calculated from the nearby wet/dry bulb sensors was made in order to estimate the time delay associated with the 2 meter long intake tube. The 0.32 s delay is accounted for

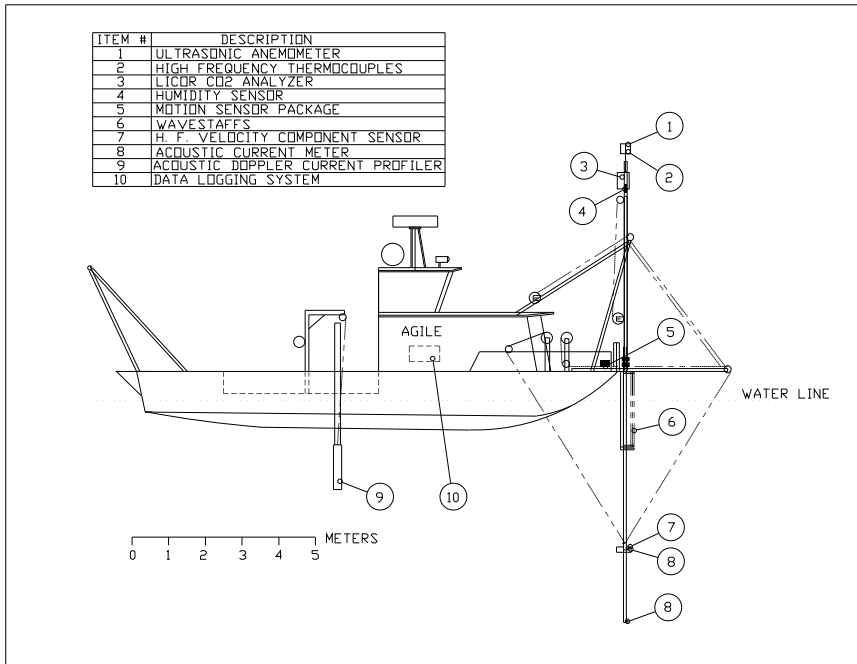


Figure 2: Schematic of research launch AGILE, showing equipment

in the analysis.

At least once each day, the LICOR was calibrated by passing in sequence N₂ (0 ppm CO₂), 350 ppm CO₂ and 1000 ppm CO₂ from pressurized bottles into the sampling volume.

In order to determine mass transfer rates, CO₂ concentrations in the water are also required. These were determined after each 30 min run in the following manner. Water was pumped from a point about 50 cm below the surface into a 2 litre glass column 110 cm high. A constant flow was maintained with the water entering near the top of the column and draining from the bottom. At the same time, air was bubbled through the column and then pumped into the LICOR for analysis. The vent from the LICOR served as the source of the sparging air, hence the air was maintained in a closed circuit. To establish a stable value, the sparging was carried out for 5 min, although typically equilibrium was achieved in less than a minute. We note that this method does not actually determine the CO₂ concentration in the water, C_w , but C_g , the concentration of CO₂ in air at equilibrium with the water. The two are related via the nondimensional Henry's law parameter, H , as

$$C_g = HC_w \tag{1}$$

where $H = H_{CO_2}R(T_w + 273)$. Here, H_{CO_2} is the Henry's law constant for CO_2 , R the universal gas constant and T_w the water temperature - see *Yin and Hassett [1986]*.

The CO_2 output signal was recorded in two forms: directly, and after passing through an amplifier. The amplifier was generally at a gain of 50, so that the resolution of the AtoD converter corresponded to 0.002 ppm, with an overall range of ± 4 ppm. With this added amplification, the recorded signals were never limited by the quantization resolution and the principal source of noise is the LI-6262 itself. The manufacturer's specifications give a noise level of 0.2 ppm peak-to-peak at 1 Hz or an rms noise of 0.07 ppm. Our measurements indicate that the noise is broadband and the level is as stated. Consequently, the signal-to-noise ratio (SNR) for CO_2 measurements with the LI-6262 is approximately

$$SNR = \left[(c_m/0.07)^2 - 1 \right]^{1/2} \quad (2)$$

where c_m are the fluctuations of the measured C_a in ppm. The intensity of c_m fluctuations, $\sigma_c/|C_g - C_a|$, was about 0.0035 so that in order to have SNRs in excess of 2 the air-water concentration difference must exceed 45 ppm in magnitude. Thus these direct flux measurements are difficult to make in the open ocean where typical ocean-atmosphere concentration differences are 20 ppm. However, in coastal regions and lakes, intense biological activity in the surface waters or upwelling of CO_2 rich bottom waters may greatly increase the concentration difference.

3 Results

During November 1994, we made 27 CO_2 flux measuring runs in the western end of Lake Ontario. To minimize the motion of the launch and provide the best exposure to the apparatus, we set course directly into the wind at about 5 knots. In 19 of the cases $|C_g - C_a| > 45$ ppm and we restricted our attention to these cases. Concentration differences were as large as 300 ppm in some cases, due almost entirely to CO_2 -enriched bottom waters being brought to the surface in the deep convective mixing characteristic of these lakes in the autumn.

Calculation of the fluxes by the eddy correlation method starts with the process of correcting the measured vertical velocity, w , to remove the motion of the ship. The total CO_2 flux is given by

$$F = \overline{\rho c w} = \bar{\rho} \overline{c' w'} + \bar{c} \overline{\rho' w'} + \overline{\rho' w' c'}, \quad (3)$$

where ρ is air density and the prime indicates the fluctuating components. The third term is of third order, and negligible compared to the other two. The first term is measured as described above, and the second is proportional to the flux of virtual temperature

$$\bar{c} \overline{\rho' w'} = -\bar{c} \bar{\rho} T_v^{-1} \overline{w' t'_v}, \quad (4)$$

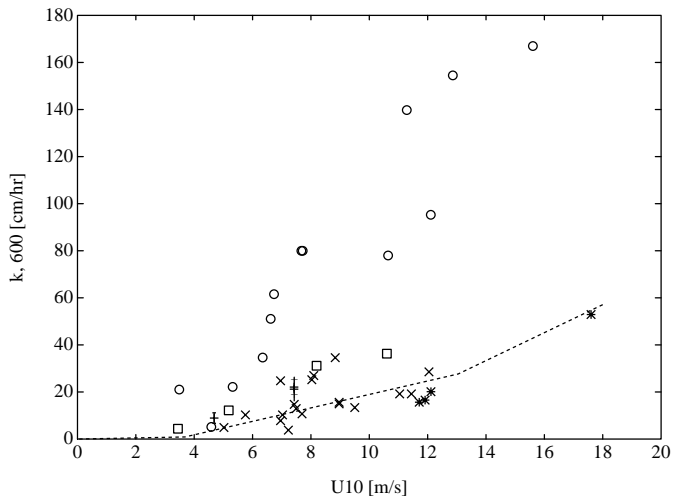


Figure 3: Mass transfer velocity, $k_{Sc=600}$ [cm/hr] vs wind speed, U_{10} [m/s]. Data from this experiment are shown by circles. Dual tracer studies in the North Sea [Watson et al., 1991] and Georges Bank [Wanninkhof et al., 1993] are shown by stars and boxes respectively. The curve is from Liss and Merlivat [1986]. Other data are summarized by Wanninkhof [1992].

where T_v is the virtual temperature, $T_v = T(1 + 0.61m)$, and m is the mixing ratio of water vapour in dry air. The mass transfer velocity was then calculated from

$$K_{CO_2} = F/\bar{\rho}(C_g - C_a). \tag{5}$$

For comparison with other results, we have adjusted these mass transfer velocities to a Schmidt number of 600, following the $Sc^{-0.5}$ behaviour established by Jähne et al. [1987].

The adjusted K_{CO_2} values are plotted against the (extrapolated) neutral wind at 10 m height in Fig. 3, along with the summary of field observations compiled by Wanninkhof [1992]. Our measurements are about a factor of two higher than the tracer experiments at high winds but show general agreement with them in the moderate wind speed range of 5–7 m/s. Chemical enhancement of CO₂ transfer is unlikely to be a significant factor at high wind speed and pH values of around 8, which are characteristic of Lake Ontario in this season [Portielje and Lijklema, 1995].

4 Discussion

The large discrepancy between our direct measurements of CO₂ flux and other indirect measurements may have many causes. It seems likely that the

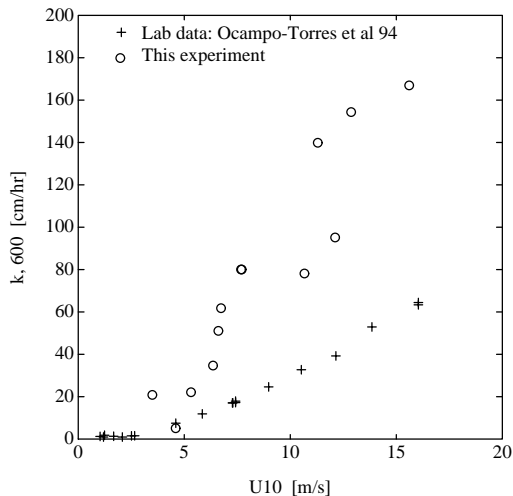


Figure 4: Mass transfer velocity ($k_{SC=600}$) vs wind speed for this field experiment (o) and laboratory experiment of Ocampo-Torres et al., [1994] (+).

differences arise because the wind speed is not the only flow variable that determines the ventilation rate of water phase limited gases across the interface. The increased turbulence intensity in the near surface waters caused by wave breaking must play a significant role in the process [c.f. Kitaigorodskii and Donelan, 1984]. The very great differences in mass transfer velocity between the laboratory experiments of Ocampo-Torres et al. [1994] and these field measurements (see Fig. 4) support the notion that the increased wave dissipation in the field provides a source of turbulence that acts to reduce the resistance to transfer of CO_2 in the very near surface layer.

Acknowledgements

We appreciate partial support for the AGILE experiments from the U.S. Office of Naval Research through grant N00014-94-1-0629.

References

- Anctil, F., M. A. Donelan, W. M Drennan and H. C. Graber, Eddy correlation measurements of air-sea fluxes from a Discus buoy. *J. Atmos. Oceanic Tech.*, 11, 1144-1150, 1994
- Broecker, H. C., J. Petermann and W. Siems, The influence of wind on CO_2 -exchange in a wind wave tunnel, including the effects of monolayers. *J. Mar. Res.*, 36, 595-610, 1978
- Jähne, B., K. O. Münnich and U. Seigenthaler, Measurements of gas exchange and momentum transfer in a circular wind tunnel. *Tellus*, 31, 321-329, 1979

- Jähne, B., K. O. Münnich, R. Börsinger, A. Dutzi, W. Herber and P. Libner, On the parameters influencing air-water gas exchange. *J. Geophys. Res.*, 92, 1937-1949, 1987
- Katsaros, K. B., M. A. Donelan and W. M. Drennan, Flux measurements from a Swath ship in SWADE. *J. Mar. Sys.*, 4, 117-132, 1993
- Kitaigorodskii, S. A. and M. A. Donelan, Wind-wave effects on gas transfer. In: *Gas transfer at the water surface*, Eds. W. Brutsaert and G.H. Jirka, D. Reidel, 147-170, 1984
- Liss, P. S. and L. Merlivat, Air-sea gas exchange rates: Introduction and synthesis. In: *The Role of air-sea exchange in geochemical cycling*, Ed. P. Buat-Ménard, D. Reidel, 113-129, 1986
- Ocampo-Torres, F. J., M. A. Donelan, N. Merzi and F. Jia, Laboratory measurements of mass transfer of carbon dioxide and water vapour for smooth and rough flow conditions. *Tellus*, 46B, 16-32, 1994
- Portielje, R. and L. Lijklema, Carbon dioxide fluxes across the air-water interface and its impact on carbon availability in aquatic systems. *Limnol. Oceanogr.*, 40, 690-699, 1995
- Smethie, W. M., T. T. Takahashi, D. W. Chipman and J. R. Ledwell, Gas exchange and CO₂ flux in the tropical Atlantic Ocean determined from ²²²Rn and pCO₂ measurements. *J. Geophys. Res.*, 90, 7005-7022, 1985
- Wanninkhof, R., Relationship between wind speed and gas exchange over the ocean. *J. Geophys. Res.*, 97, 7373-7382, 1992
- Wanninkhof, R., W. Asher, R. Weppernig, H. Chen, P. Schlosser, C. Langdon and R. Sambrotto, Gas transfer experiment on Georges Bank using two volatile deliberate tracers. *J. Geophys. Res.*, 98, 20237-20248, 1993
- Watson, A., R. Upstill-Goddard and P.S. Liss, Air-sea exchange in rough and stormy seas, measured by a dual tracer technique. *Nature*, 349, 145-147, 1991
- Yin, C. and J. P. Hassett, Gas partitioning approach for laboratory and field studies of mirex fugacity in water. *Environ. Sci. Technol.*, 20, 1213-1217, 1986

Over-Water Eddy Correlation Measurements of Fluxes of Momentum, Heat, Water Vapor and CO₂

G. J. Kunz¹, G. de Leeuw¹, S. E. Larsen², and F. Aa. Hansen²

¹TNO-Physics and Electronics Laboratory

P.O. Box 96864, 2509 JG The Hague, The Netherlands

²RISØ, National Laboratory, Department of Meteorology and Wind Energy

P.O. Box 49, DK-4000 Roskilde, Denmark

Abstract

Using a fast-response ultrasonic anemometer and a fast-response non dispersive infrared gas sensor for CO₂ and H₂O, fluxes of momentum, heat, water vapor and CO₂ were measured from a platform in the North Sea at 9 km from the coast of The Netherlands during the Air Sea GAS EXchange experiment ASGASEX. The instruments were mounted at the end of a 21 m long boom, about 6 m above the mean sea level. The results obtained for the fluxes of momentum, heat and water vapor compare favourably with earlier published data for similar conditions and with results obtained during the HEXOS experiment at the same location. The CO₂ fluxes varied between -0.03 and +0.07 mg/(m²s). This is only about a factor of 3 larger than the estimated minimum detectable CO₂ flux that can be measured with the utilized sensor package.

1 Introduction

The ASGASEX (Air Sea GAS EXchange) experiment was organized by the Royal Netherlands Meteorological Institute (KNMI), [Oost, 1994 and 1995a], with the objective to simultaneously measure CO₂ fluxes by independent and physically different principles, i. e., the chemical method and the eddy correlation method. Earlier studies indicated large discrepancies between the results from these methods. The present study, Oost [1995b] was aimed at resolving these discrepancies. The experiment took place from 1 to 30 September 1993 from the *MeetPost Noordwijk* (MPN), a research tower in the North Sea at 9 km off the coast of The Netherlands. During ASGASEX, the TNO-Physics and Electronics Laboratory (TNO-FEL) operated a micro-meteorological flux package consisting of an ultrasonic anemometer (Solent) and two identical open path infrared CO₂ and H₂O concentration fluctuation meters (Advanet E009A) in co-operation with RISØ National Laboratory, Denmark. This was the first field test of the common TNO-FEL/RISØ flux package that was developed for deployment on a ship. The instruments were mounted upside down on the south side of the prong at the end of a 21 m long boom that extended west from the tower. The sample volumes of the sensors were respectively 67 cm and 25 cm below the boom.

The horizontal separation between the two gas sensors was 20 cm and the distance to the anemometer was 25 cm. During the experiment, the CO₂ channels of the gas sensors were calibrated on a regular basis using N₂ and two factory-calibrated gas mixtures with respectively 250 ppm and 450 ppm CO₂ (balance nitrogen). For water vapor, the factory calibration was used. The ultrasonic anemometer was tested in a wind tunnel in collaboration with KNMI, prior to the experiment [Kunz, 1994a].

Additional meteorological and oceanographic data were made available from KNMI and from MPN, which is part of the North Sea observational network. Dalhousie and NIOZ (Netherlands Institute for Sea Research) measured, among others, the partial pressures of carbon dioxide both in the water and in the air [Bakker *et al.*, 1995].

The signals from the flux package were sampled with a frequency of 20 Hz in time slots of 45 minutes and converted to physical parameters using RISØ's data acquisition and pre-processing system PC-DAQ. The wind vector was transformed to a new orthonormal system with zero mean vertical wind speed and one horizontal streamwise wind component. Subsequently, one-minute mean values and covariances were derived. Several corrections were applied to calculate the desired results which in turn were compared with existing models, with results from other experiments and with results obtained by other groups participating in ASGASEX.

Because one of the gas sensors did not operate properly, the initially proposed method to suppress incoherent noise by combining two gas sensors, could not be tested. Evidently, the results presented in this paper are therefore based on only one gas sensor.

Discussions on the air-sea gas exchange coefficient are beyond the scope of this paper but can be found in, e. g., Broecker, Peterman and Siems [1978], Deacon [1981], Merlivat and Memery [1983], Liss and Merlivat [1986], Watson, Upstill-Goddard and Liss [1991] and Wanninkhof [1992].

2 Theoretical Background

The *eddy correlation* method is based on the correlation between the turbulent fluctuations of the quantity of interest with the turbulent fluctuations of the vertical wind speed, w' . Fluxes of momentum M , sensible heat H , water vapor E and carbon dioxide F_c , can be derived according to:

$$M = -\langle u' \cdot w' \rangle \rho \quad (1)$$

$$H = +\langle \theta' \cdot w' \rangle \rho c_p \quad (2)$$

$$E = +\langle q' \cdot w' \rangle \rho \quad (3)$$

$$F_c = +\langle c' \cdot w' \rangle \quad (4)$$

In these equations, the primed parameters are respectively the fluctuating parts of the horizontal wind speed, potential temperature, specific

humidity and concentration of carbon dioxide. ρ is the air density and c_p is the specific heat of air.

In micrometeorology, it is useful to define scaling parameters for modelling vertical *turbulent fluxes* of momentum, heat, *water vapor* and *carbon dioxide*. According to e. g. Hill [1989] and Donelan [1990] we write:

$$u_* \equiv -\langle u' \cdot w' \rangle / u_* \quad (5)$$

$$\theta_* \equiv -\langle \theta' \cdot w' \rangle / u_* \quad (6)$$

$$q_* \equiv -\langle q' \cdot w' \rangle / u_* \quad (7)$$

$$c_* \equiv -\langle c' \cdot w' \rangle / u_* \quad (8)$$

(note the symmetry in the above equations, especially with respect to u_*)

The fluxes of interest can also be estimated from the gradients in the bulk meteorological parameters according to:

$$M = +(U_s - U_z)(U_s - U_z)C_D\rho \quad (9)$$

$$H = -(U_s - U_z)(\Theta_s - \Theta_z)C_H\rho c_p \quad (10)$$

$$E = -(U_s - U_z)(Q_s - Q_z)C_E\rho \quad (11)$$

$$F_c = -(U_s - U_z)(C_s - C_z)C_c \quad (12)$$

in which the exchange coefficients C_D , C_H , C_E , C_c can be derived, for instance, from a combination of micrometeorological and bulk meteorological measurements using:

$$C_D = \frac{u_*}{(U_s - U_z)} \frac{u_*}{(U_s - U_z)} \quad (13)$$

$$C_H = \frac{u_*}{(U_s - U_z)} \frac{\theta_*}{(\Theta_s - \Theta_z)} \quad (14)$$

$$C_E = \frac{u_*}{(U_s - U_z)} \frac{q_*}{(Q_s - Q_z)} \quad (15)$$

$$C_c = \frac{u_*}{(U_s - U_z)} \frac{c_*}{(C_s - C_z)} \quad (16)$$

The subscript s refers to the value at the surface and the subscript z refers to the value at the measuring height z . The equations for carbon dioxide are assumed to be corrected for density variations due to heat and water vapor as pointed out e. g. by Webb, Pearman and Leuning [1980]. Note the symmetry of these equations especially with respect to the *drag coefficient* C_D .

For comparison of results obtained under different meteorological conditions and from different locations, the drag coefficient C_D is converted to

a neutral drag coefficient at a standard height of 10 m, generally expressed as $C_{DN}(10)$, C_{DN10} or simply C_{DN} . For that purpose, the wind speed at the measuring height z , must be converted to the wind speed at 10 m using the generally accepted model for the vertical profile of the horizontal wind speed:

$$U(z) = \frac{u_*}{k} \left[\ln\left(\frac{z}{z_0}\right) - \Psi_m\left(\frac{z}{L}\right) \right] \quad (17)$$

were z_0 is the *roughness length* (theoretically the height were the wind speed vanishes), $\Psi_m(z/L)$ the stability correction term, L the Monin-Obukhov length and k the von Kármán constant. A description of the stability term and the other two parameters is beyond the scope of this work and can be found in many standard works such as *Tennekes and Lumley* [1972], *Businger* [1973], *Panofsky and Dutton* [1984] or *Stull* [1988]. Knowing the stability, the roughness length can easily be derived from the ultrasonic anemometer data using equation (17) because both the wind speed and the friction velocity are directly measured.

Because the stability correction term in (17) vanishes under neutral conditions, the neutral drag coefficient at the standard height of 10 m becomes:

$$C_{DN} = \left[\frac{u_*}{U_N(10)} \right]^2 \quad (18)$$

Geernaert [1990] suggested to express the above mentioned quotient as $u_{*N}/U(10)$.

Substitution of equation (18) in equation (17) shows that the neutral drag coefficient can also be expressed in terms of the roughness length. This results in:

$$C_{DN} = \left[\frac{k}{\ln(10/z_0)} \right]^2 \quad (19)$$

In this case, it is not necessary to calculate explicitly the 10 m neutral wind speed.

Alternatively, the neutral drag coefficient can be estimated from the friction velocity using equation (19) and *Charnock's relation*:

$$z_0 = \frac{0.011u_*^2}{g} \quad (20)$$

where g is the acceleration due to gravity.

The other exchange coefficients can be derived in a similar way, taking into account that the roughness lengths for the temperature, water vapor and carbon dioxide are different from the roughness length for wind speed.

3 Results

Results derived from measurements with the TNO-FEL/RISØ micrometeorological package are presented and compared with fluxes obtained with the bulk method, with predictions from existing models and with results from other participants. Wind speeds are converted to the 10 m values in neutral stratification. During ASGASEX, the surface layer stability, z/L , varied from about -0.5 to about +0.1. Only in a few cases, the stability was between -1.0 and -0.5.

ASGASEX took place at the end of the summer, in a period in which westerly winds are expected to dominate. Therefore, the instrumented boom was pointed westwards for minimum flow distortion of the platform and other sensors on the boom. Other wind directions, which deviate more than about 60 degrees from this direction, induce some flow distortion (to a maximum of about 10 %). The effect of flow distortion can be observed in the data. These data are presented as open symbols and are not taken into account for curve fitting. No measurements were carried out when the wind had a truly easterly component (between about 30 and 160 degrees).

3.1 Momentum Flux and Related Parameters

The relation between the friction velocity and the 10 m neutral wind speed, derived from the ASGASEX data, is shown in Figure 1. From this relation the neutral drag coefficient can be derived (equation (18) and Figure 4). For comparison, we have also plotted some relations derived from other measurements at the North Sea. Figure 2 shows the variance of the stream wise wind component as a function of the kinematic *momentum flux*. The relation between these parameters is important for modelling diffusion over the sea [Geernaert, 1990]. Our data compared with the parameterization given by Geernaert.

In Figure 3, the roughness length for momentum flux, z_0 , is plotted as a function of the 10 m neutral wind speed. z_0 has been derived by several methods. The plus signs represent the roughness lengths as rest term of equation (17), using the measured streamwise wind components and the measured values of the friction velocity in combination with the calculated stability term. The solid dots represent the roughness lengths calculated from the friction velocity alone, using Charnock's relation (20). The dashed lines represent the roughness lengths calculated using (19) and the three indicated models for C_{DN} as published by Geernaert (1990). The solid lines represent the roughness lengths using (18) and (20). It is clear from the data presented in Figure 3 that a wide range of values can be obtained for z_0 depending on the equation used.

Figure 4 shows the measured and the modelled neutral drag coefficients as a function of the 10 m neutral wind speed. Again, different approaches have been applied to derive C_{DN} . The plus signs are derived from the ratio of

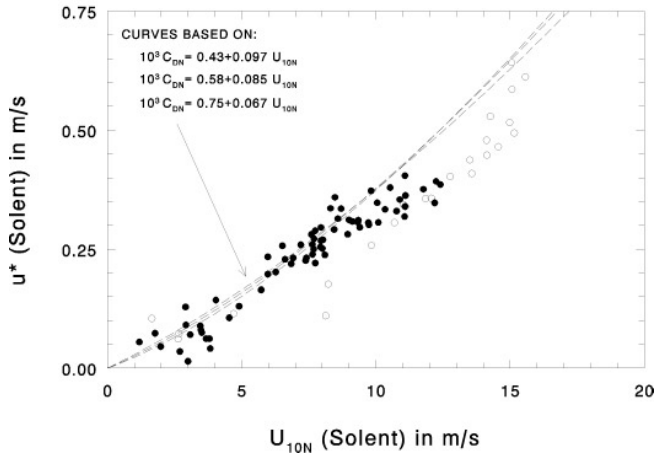


Figure 1: Friction velocity as a function of the neutral wind speed at 10 m. The lines are derived from a parameterization of C_{DN} [Geernaert, 1990] under neutral conditions from data also measured at the North Sea.

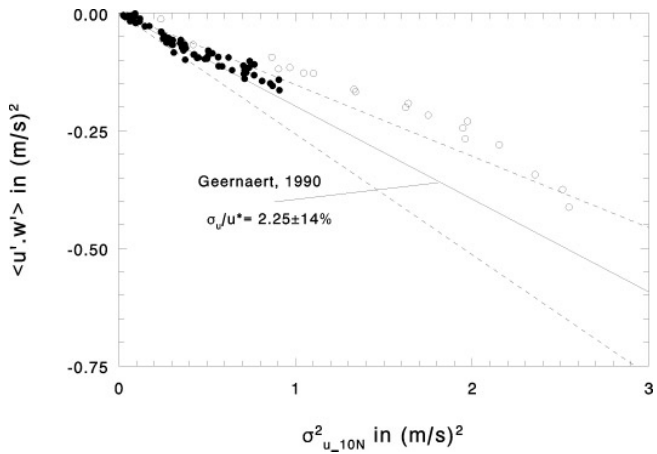


Figure 2: Relation between the kinematic momentum flux and the variance of the neutral horizontal 10 m wind speed. The mean parameterization is presented by the solid line with two dashed lines indicating the standard deviation [Geernaert, 1990].

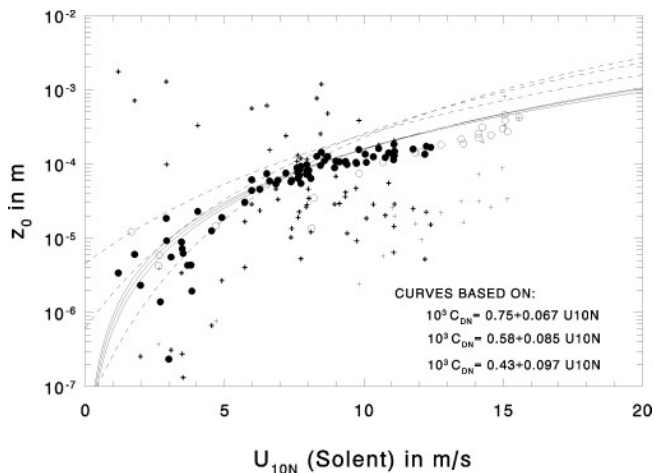


Figure 3: Roughness length as a function of the 10 m neutral wind speed calculated using different approaches (see text).

the friction velocity and the 10 m neutral wind speed according to equation (18) whereas the dots are based on the relation of u_* with the roughness length as shown in equations (19) and (20).

3.2 Sensible Heat Flux and Related Parameters

The mean air temperature and the turbulent variations were derived from the speed of sound measured with the ultrasonic anemometer. However, this temperature is almost equal to the virtual temperature and must therefore be corrected for the ambient humidity as was shown, e. g., by Schotanus, Nieuwstadt and DeBruin [1983] and Hignett [1992]. In Figure 5, we show the kinematic heat flux, $\langle \theta' \cdot w' \rangle$, as a function of the product of the air-sea temperature difference and the 10 m neutral wind speed, measured with bulk sensors. Because the wind speed vanishes for $z = z_0$, i. e., near the surface, the product reduces to $U_{10N}(\Theta_s - \Theta_{10})$. A linear relation is expected, with a slope equal to the exchange coefficient for temperature or Stanton number, C_{HN} . The relation proposed by Smith [1980] is indicated in Figure 5. Other values for the Stanton number have been published by Anderson and Smith [1981], Large and Pond (1982) and Geernaert [1990]. The differences between our results and Smith’s model might be due to the shallow water at the MPN location.

In surface layer bulk models, the temperature scaling parameter, θ_* , is often used instead of the kinematic heat flux $\langle \theta' \cdot w' \rangle$. A linear relation between θ_* and the air-sea temperature difference was suggested by Davidson [1978]. This follows from equation (14), by substitution of the friction velocity with the wind speed. In Figure 6, we compare our data with the relation

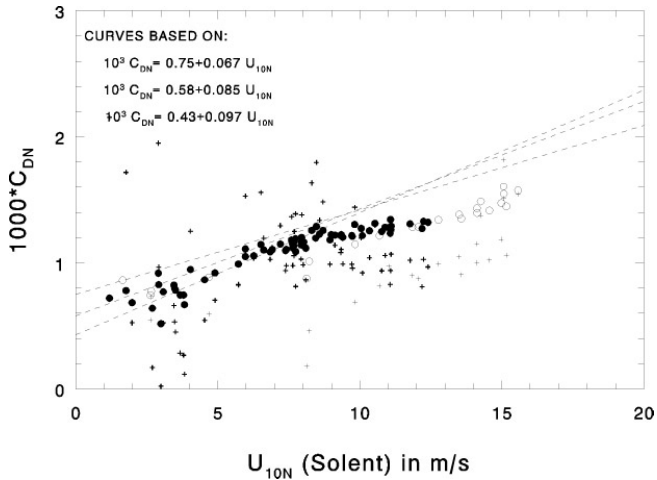


Figure 4: Measured and modelled neutral drag coefficient as a function of wind speed calculated using different approaches (see text).

proposed by Davidson. We observe a similar trend, although the slope in the experimental data indicates a larger Stanton number. This is in agreement with the data in Figure 5, as expected.

3.3 Humidity and Related Parameters

The water vapor exchange coefficient C_E , or *Dalton number*, relates the water vapor flux to the product of wind speed and the difference between the specific humidity at a certain level and at the surface (equation 11) and can thus be used to derive water vapor fluxes from standard meteorological observations. With reference to equations (7) and (15), we have plotted in Figure 7 the kinematic water vapor fluxes, $\langle q' \cdot w' \rangle$, as a function of the product of $U_{10N} \cdot (q_s - q_{10})$. Our data compare favorably with the relation obtained by Smith [1989] from data of the HEXOS experiment (broken line). Other values for C_{EN} were published by Anderson and Smith [1981], Large and Pond [1982], Geernaert [1990] and by Smith *et al.* (this volume). In analogy with the relation between the scaling temperature and the air-water temperature difference, the scaling humidity has been plotted versus the difference between the specific humidity at the 10 m level and near the water surface. This is shown in Figure 8. A linear least squares fit to the data yields the relation that is given in the figure.

3.4 Carbon Dioxide and Related Parameters

The CO₂ channel of the IR gas sensor was calibrated on a regular base (at least once a day) with two factory-calibrated gas mixtures and with N₂ gas. Cali-

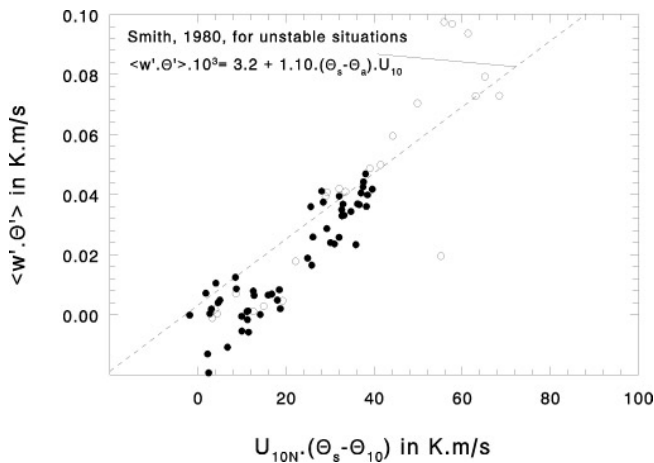


Figure 5: Relation between the kinematic sensible heat flux and the product of the 10m neutral wind and the sea-air temperature difference.

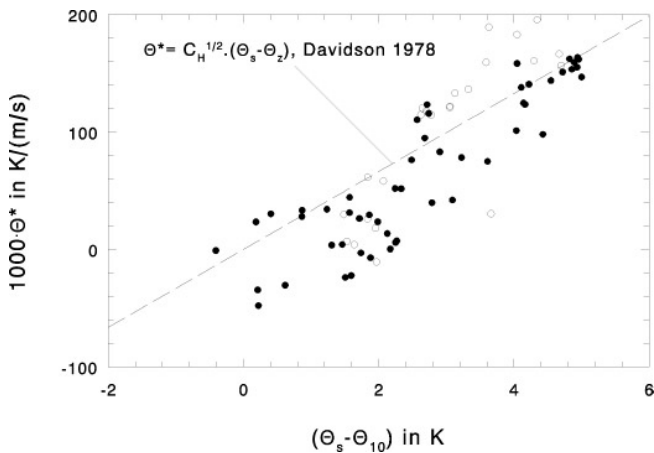


Figure 6: Scaling temperature as a function of the sea-air temperature difference.

bration is necessary to check the stability of the response. In addition, the absolute calibration allows us to measure the ambient concentration of CO₂. An independent measurement of the mean CO₂ concentration was available from the gas-chromatograph, operated by NIOZ [Bakker et al., 1995]. The 45-minute mean data from the IR gas sensor and the mean data from the gas-chromatograph in the same period were converted to absolute CO₂ concentrations using the actual air temperature, humidity and air pressure. Figure 9 shows a comparison between the data from the two instruments. We have no explanation for the differences in the results from the two gas sensors.

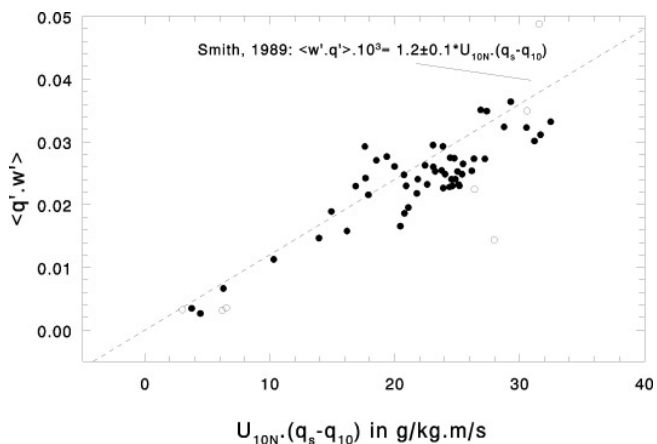


Figure 7: Kinematic water vapor flux, $\langle q' \cdot w' \rangle$ as a function of $U_{10N} \cdot (q_s - q_{10})$. The broken line gives the relation obtained by Smith [1989] from the HEXOS data.

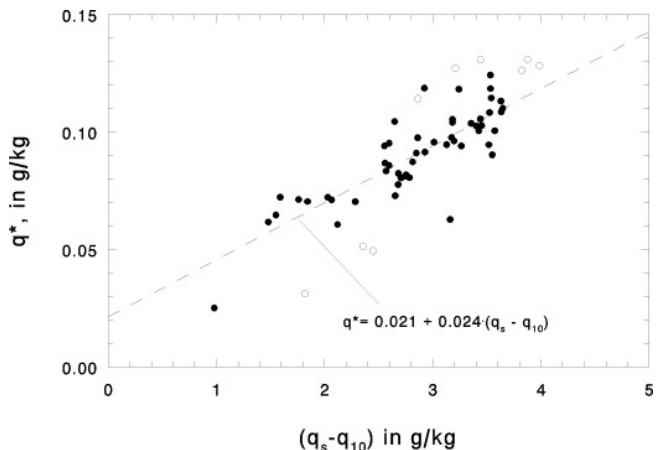


Figure 8: Relation between the scaling humidity and the difference of the specific humidity near the surface and the 10 m level. The indicated relationship was determined by a least squares fit to the solid data points.

The largest differences were observed during a brief period when the air temperature was relatively high (about 17 °C, as compared to the 12 °C during the previous days). In this period, the measured CO₂ concentrations dropped by about 15 % whereas the data from the gas-chromatograph did not show a similar decrease. An effect of water temperature on the atmospheric CO₂ concentration (both IR and GC) was not observed, is in agreement with earlier observations by Takahashi [1961]. The atmospheric CO₂ concentration and the specific humidity appear to be weakly correlated. This was observed both in the IR data and the GC data. Since the GC data were

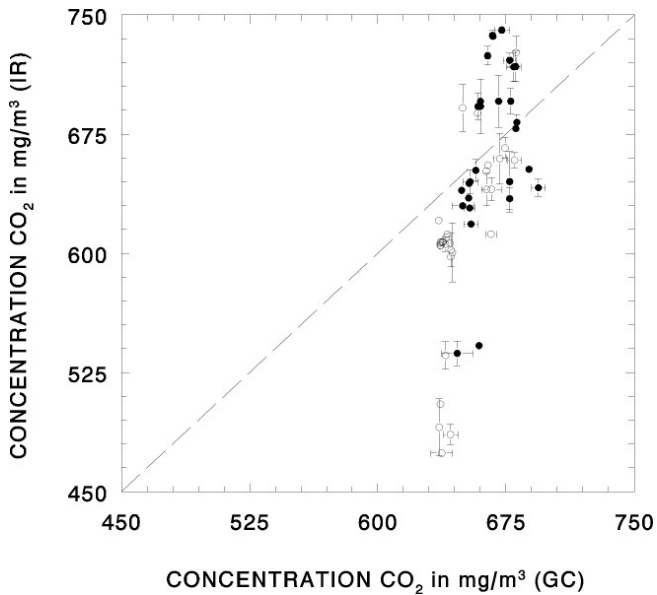


Figure 9: Comparison of 45-minutes mean atmospheric CO₂ concentration measured with the IR gas sensor and the gas-chromatograph, (GC), operated by (NIOZ).

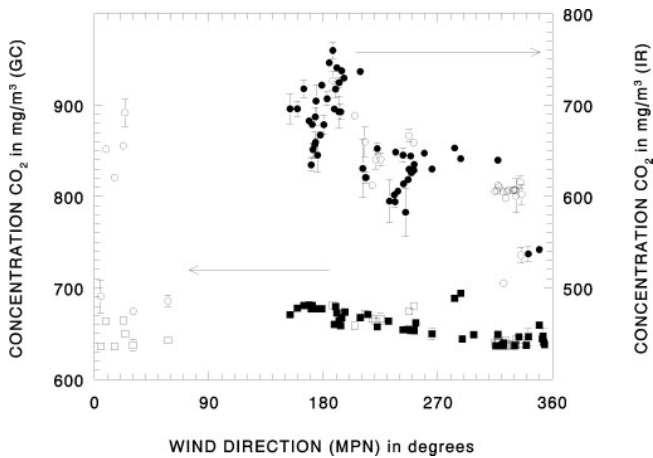


Figure 10: Mean atmospheric CO₂ concentrations during ASGASEX as a function of the wind direction. The squares (left scale) are from the gas-chromatograph, (GC), operated by (NIOZ) and the dots (right scale) are from the IR gas sensor (TNO/ RISØ).

from samples that were dried prior to analysis, the effect of cross talk in the IR gas sensor can be ruled out. We therefore concluded that the periods with high atmospheric CO₂ concentration occurred in periods with high specific humidity. The mean CO₂ concentration was not observed to vary with wind speed.

Figure 10 shows, more or less as expected, a variation of the atmospheric CO₂ concentration with wind direction, both in the data from the IR gas sensor and in the data from the GC. The largest CO₂ concentrations occur when the wind is from southerly directions (about 60 to 200 degrees), the Rotterdam industrial region. Also, when the wind is from the north-east, the Amsterdam industrial region and Velsen (steel factory), the mean concentrations of CO₂ seem to be enhanced.

Derivation of the carbon dioxide fluxes with the eddy correlation method is not straight forward because the air density varies with temperature and water vapor affects the CO₂ concentration too. Therefore, the turbulent fluctuations of the CO₂ concentrations must be corrected for these effects. The correction term depends on the mean atmospheric CO₂ concentration, the fluxes of sensible heat and water vapor and some other well-defined parameters. An extensive description of this 'Webb correction' can be found in *Smith and Jones* [1979], *Webb, Leuning and Pearman* [1980] and *Leuning et al.* [1982]. Because CO₂ fluxes over the sea are in general very small, the correction term often dominates the uncorrected 'raw' CO₂ fluxes. As a result, even the sign of the flux may change!

In Figure 11, we compare the net CO₂ fluxes with those derived by BIO and KNMI during ASGASEX. The latter data were obtained from independent measurements of the wind components and with different algorithms applied to the data from the IR gas sensor. Figure 11 shows that the CO₂ fluxes measured with micrometeorological methods are all in good agreement.

In Figure 12, the 'raw' (small solid squares) and 'net' (solid dots) CO₂ fluxes are compared with the product of the wind speed and the CO₂ gradient ($\Delta pCO_2 = CO_{2\text{water}} - CO_{2\text{air}}$), which is commonly believed to be the driving force for the CO₂ flux. The vertical gradient of the CO₂ concentration in the air is assumed to be negligible [*Ohtaki et al.*, 1989]. However, *Broecker, Petermann and Siems* [1978] observed gradients above the water surface in a laboratory experiment. In Figure 13, a relation between the 'raw' (small solid squares) and 'net' (solid dots) CO₂ fluxes are presented as a function of the water-air CO₂ partial pressure difference. The results presented in Figures 12 and 13 do not indicate any dependence of the CO₂ flux on either of the used parameters.

To calculate the scaling parameters for the CO₂ fluxes, c_* , similar to those for sensible heat and water vapor, the net CO₂ flux values were divided by u_* and compared with the values of ΔpCO_2 provided by NIOZ. Based on the assumption that scalars like CO₂, water vapor and heat would behave similarly, it was hoped that a regression line to the data would yield an

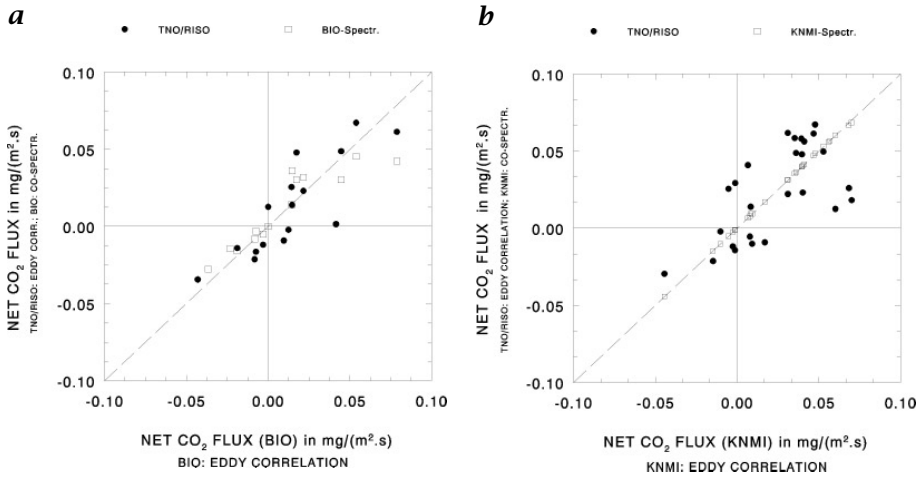


Figure 11: Comparison of the net CO₂ fluxes: TNO-FEL/RISØ (solid dots) versus BIO (a) and KNMI (b). The open squares represent the spectral analysis results from BIO and KNMI respectively. BIO and KNMI used different ultrasonic anemometers and different inversion algorithms.

exchange coefficient for CO₂, similar to C_H and C_E . However, it was not possible to fit a regression line that passed through the origin

4 Conclusions

During ASGASEX, data were obtained for the fluxes of momentum, heat, water vapor and CO₂ in the marine atmospheric surface layer. Values for C_D , C_H and C_E compare favourably with those earlier found at this location. The scaling parameters for temperature and humidity were calculated and compared with existing values. Despite the long boom, some of the results were apparently influenced by flow distortion by the MPN platform and by the instruments at the tip of the boom. These influences are well-known from previous experiments (HEXOS program). The required corrections have been applied.

Using a fast-response infrared gas sensor, which was calibrated on a daily base, the mean atmospheric concentration of CO₂ was measured and compared with the results from a slow responding gas-chromatograph. The results of both instruments show that the CO₂ concentration varies with the wind direction. When the wind advected air from industrial regions of Rotterdam and Amsterdam (at about 40 km), or from MPN itself, the mean CO₂ concentrations were higher than in winds from north-westerly directions.

Fluxes of CO₂ over the sea are very small and therefore difficult to measure with existing equipment. Integration times on the order of one hour are required. Even over such long periods, the standard deviations are of

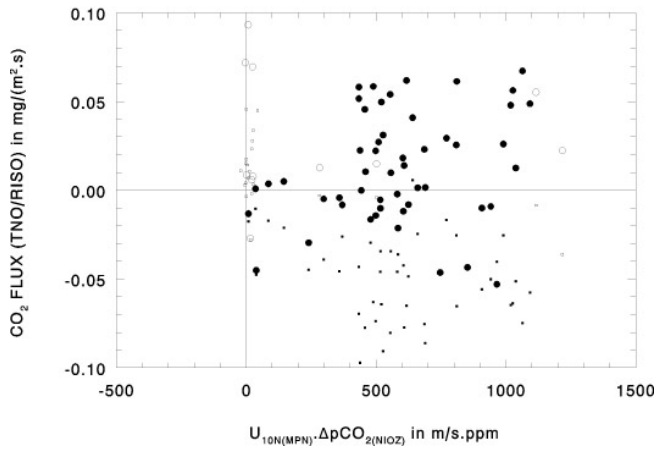


Figure 12: The ASGASEX net (solid dots) and raw (small squares) CO₂ fluxes as a function of the product of the wind speed U_{10N} and the (NIOZ) water-air CO₂ partial pressure difference.

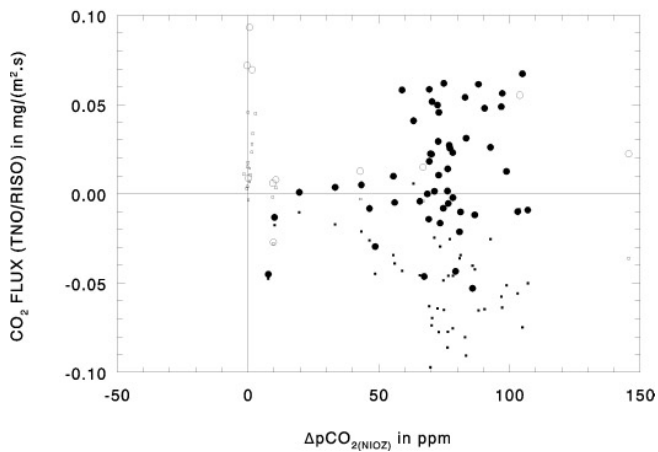


Figure 13: The ASGASEX net (solid dots) and raw (small squares) fluxes of CO₂, measured with TNO-FEL/RISØ micrometeorological package as a function of the water-air CO₂ partial pressure difference.

similar magnitudes as the mean value of the fluxes. Moreover, the fluxes calculated from the covariance of the vertical wind speed and the CO₂ concentration must be corrected for air density variations due to temperature fluctuations and effects of humidity. Over the sea, these correction terms often dominate the measured fluxes. During ASGASEX, net CO₂ fluxes were obtained with values varying between -0.03 to +0.07 mg/(m²s), but on average positive. From CO₂ flux measurements over land, Kunz [1994b], we estimated that the minimum detectable flux with the instrumentation package is about 0.02 mg/(m²s). We therefore conclude that during the ASGASEX experiments the signal-to-noise ratios were not larger than about a factor of 3. Nevertheless, because the net CO₂ fluxes calculated with the TNO-FEL/RISØ package compare reasonably well with the independently derived net fluxes from BIO and KNMI, we have confidence in our results. Comparison of other fluxes and bulk parameters derived from the observations with our micrometeorological package and with data from other experiments support this opinion. However, it was not clearly demonstrated that the CO₂ flux could be modelled in a similar way as the scalar fluxes of sensible heat and water vapor. Only a slight dependence on the wind speed was found.

Acknowledgements

We are grateful to KNMI (The Netherlands), in particular to Wiebe Oost, for the organisation of ASGASEX and for the technical assistance during the experiment. We acknowledge Stu Smith of BIO (Canada) for the close cooperation during the data analysis period and Dorothee Bakker of NIOZ (The Netherlands) for providing us with the gas-chromatograph data. The MPN crew is acknowledged for the hospitality and the logistical support during the experiment. Technical support was received from Leen Bruinsma, Leo Cohen and Marcel Moerman. Ken Davidson, from the NPS (USA) on sabbatical leave at TNO-FEL during the summer of 1994, learned us much about micrometeorology. We participated in ASGASEX with the financial support from the European Commission DGXII (contracts MAS2-CT93-0069 and with additional support from the Netherlands Ministry of Defence (contracts A92KM767).

References

- Anderson, R. J. and S. D. Smith, Evaporation coefficient for the sea surface from eddy flux measurements, *J. Geophys. Res.*, 86, 449-459, 1981
- Bakker, D. C. E., H. J. W. de Baar and A. A. J. Majoor, submitted. Dissolved carbon dioxide in Dutch coastal waters: hydrography and air-sea exchange. An ASGASEX paper
- Broecker, H. C., J. Petermann and W. Siems, The influence of wind on CO₂-exchange in a wind-wave tunnel, including the effects of monolayers, *J. Mar. Res.*, 36, 595-610, 1978

- Businger, J., Turbulent transfer in the atmospheric surface layer, in *Workshop on Micrometeorology*, edited by D. A. Haugen, pp. 67-100, American Meteorological Society, Boston, 1973
- Davidson, K. L., T. M. Houlihan, C. W. Fairall and G. E. Schacher, Observation of temperature structure function parameter, C_T^2 , over the ocean, *Bound.-Layer Meteorol.*, 15, 507-523, 1978
- Donelan, M., Air-sea interaction, in Ocean Engineering Science, *The Sea*, vol 9, part A, edited by B. le Méhauté and D.M. Hanes, pp. 239-292, Wiley and Sons, Inc. New York, 1990
- Deacon, E. L., Gas transfer to and across an air-water interface, *Tellus*, 29, 363-374, 1977
- Geernaert, G. L., Bulk parameterization for the wind stress and the heat fluxes, in *Surface Waves and Fluxes: Theory and Remote Sensing*, vol. 1, edited by G. L. Geernaert and W. L. Plant, pp. 91-172, Kluwer Academic Publishers, Dordrecht, 1990
- Hill, R. J., Implications of Monin-Obukhov similarity theory for scalar quantities, *J. Atmos. Sci.*, 46, 2236-2244, 1989
- Kunz, G. J., Test of a Gill ultrasonic anemometer in a wind tunnel, *TNO-FEL Report*, FEL-94-A118-1994a
- Kunz, G. J., TNO-FEL contributions to a pilot experiment for CO₂ flux measurement comparison, *TNO-FEL Report*, FEL-94-A163, 1994b
- Large, W. G. and S. Pond, Open ocean momentum flux measurements in moderate to strong winds, *J. Phys. Oceanogr.*, 11, 324-336, 1981
- Leuning, R., O. T. Denmead, A. R. G. Lang and E. Ohtaki, Effects of heat and water vapor transport on eddy covariance measurement of CO₂ fluxes, *Bound.-Layer Meteor.*, 23, 209-222, 1982
- Liss, P. S. and L. Merlivat, Air-sea gas exchange rates: introduction and synthesis, in *The role of air-sea exchange in geochemical cycling*, edited by P. Buat-Ménard, pp. 113-127, Reidel Publishing Company, Dordrecht, 1986
- Merlivat, L. and L. Memery, Gas exchange across an air-water interface: experimental results and modelling of bubble contribution to transfer, *J. Geophys. Res.*, 88, 707-724, 1983
- Oost, W. A., The ASGASEX experiment, KNMI, *Technical Report*, TR-161, 1994
- Oost, W. A., ASGASEX, *This volume*, 1995a
- Oost, W. A., On the discrepancies between CO₂ flux measurement methods, *This volume*, 1995b
- Ohtaki, E., O. Tsukamoto, Y. Iwatani and Y. Mitsuta, Measurements of the carbon dioxide flux over the ocean, *J. Meteor. Soc. Japan*, 67, 541-553, 1989
- Panofsky, H. A. and J. A. Dutton, *Atmospheric turbulence: models and methods for engineering applications*, 397 pp., John Wiley & Sons, New York, ISBN 0-471-05714-2, 1984
- Schotanus, P., F. T. M. Nieuwstadt, and H. A. R. DeBruin, Temperature measurements with a sonic anemometer and its application to heat and moisture fluctuations, *Bound.-Layer Meteor.*, 17, 375-379, 1979
- Smith, S. D. and E. P. Jones, Dry-air boundary conditions for correction of eddy flux measurements, *Bound.-Layer Meteor.*, 17, 375-379, 1979

- Smith, S. D., Wind stress and heat flux over the ocean in gale force winds, *J. of Phys. Ocean.*, 10, 709-726, 1980
- Smith, S. D., Water vapor flux at the sea surface; Review paper, *Bound.-Layer Meteor.*, 42, 277-293, 1989
- Smith, S. D., R. J. Anderson, O. Hertzman, W. Oost, W. Kohsiek, G. de Leeuw and G. J. Kunz, New measurements of eddy fluxes at the sea surface, *This volume*
- Stull, R. B., *An introduction to Boundary Layer Meteorology*, 666 pp., Kluwer Academic Publishers, 1988
- Takahashi, T., Carbon dioxide in the atmosphere and in Atlantic Ocean water, *J. Geophys. Res.*, 66, 477-494, 1961
- Tennekes, H. and J. L. Lumley, *A first course in turbulence*, 300 pp., The MIT Press, Cambridge, ISBN 0-262-20019 8, 1972
- Wanninkhof, R., Relationship between wind speed and gas exchange over the ocean, *J. Geophys. Res.*, 97, 7373-7382, 1992
- Watson, A. J., R. C. Upstill-Goddard and P.S. Liss, Air-sea gas exchange in rough and stormy seas measured by a dual-tracer technique, *Nature*, 349, 145-147, 1991
- Webb, E. K., G. I. Pearman and R. Leuning, Correction of flux measurements for density effects due to heat and water vapour transfer, *Q.J.R. Meteorol. Soc.*, 106, 85-100, 1980

New Measurements of Eddy Fluxes at the Sea Surface in ASGASEX

S. D. Smith¹, R. J. Anderson¹, O. Hertzman², W. A. Oost³, W. Kobsiek³, G. de Leeuw⁴, and G. J. Kunz⁴

¹Department of Fisheries and Oceans, Bedford Institute of Oceanography
P.O. Box 1006, Dartmouth, Nova Scotia, Canada B2Y 4A2

²Dept. of Oceanography, Dalhousie University, Halifax, N.S., Canada

³Royal Netherlands Meteorological Institute, de Bilt, the Netherlands

⁴Physics and Electronics Laboratory, TNO, den Hague, the Netherlands

Abstract

Air-sea fluxes have been measured in a series of experiments at and in the vicinity of Meetpost Noordwijk, a research platform in the North Sea 9 km off the coast of the Netherlands. The most recent of these, ASGASEX (Air-Sea Gas Exchange Experiment) in September of 1993, was a coordinated international study of CO₂ eddy flux and related parameters. Water vapour, sensible heat and momentum fluxes corroborate results of the HEXOS (Humidity Exchange over the Sea) Programme [Smith *et al.*, 1990] at the same site in 1986.

1 Instruments and Methods

1.1 Introduction to Eddy Fluxes in the Atmospheric Surface Layer

The *eddy correlation* method was used to measure surface fluxes in ASGASEX. The eddy flux of a property $X = \langle X \rangle + x'$ at a point in the atmospheric surface layer, carried by vertical wind gusts w' , is $\langle x'w' \rangle$. Angle brackets $\langle \dots \rangle$ denote averaging over a sufficient period (typically 15 to 60 min) to provide a stable average, but over which mean conditions remain nearly stationary. In the atmospheric surface layer the fluxes are nearly invariant with height and are equal to the surface fluxes. This method is widely used to measure wind stress which is equal to the *momentum flux*, $\tau = -\langle \rho u'w' \rangle$; *sensible heat flux* $H = \rho C_p \langle t'w' \rangle$; and *water vapour flux*, $E = \langle \rho'_v w' \rangle$ where ρ is air density, C_p is specific heat, $T = \langle T \rangle + t'$ is air temperature and $\langle \rho_v \rangle + \rho'_v$ is the partial density of water vapour in air.

The fluxes of sensible heat and water vapour are an integral part of the measurement of CO₂ *eddy flux* over the sea surface, and their contribution can be comparable to the “raw” eddy flux $\langle CO_2'w' \rangle$. Water vapour flux is itself a gas flux. It carries latent heat into the air, and leaves behind seawater of increased salinity. Sensible heat flux tends to reduce the temperature difference between the surface water and the overlying air. These processes,

resulting in the modification and formation of air and water masses, are crucially important in understanding and modelling the circulation of the atmosphere and oceans. For example, updating the *evaporation* formula in the the ECMWF atmospheric general circulation model [Miller *et al.*, 1992] has enhanced the ability of that model to forecast weather and to simulate climate, particularly over tropical and subtropical oceans.

1.2 The Bulk Formula for Evaporation

Water vapour flux is mainly driven by the wind U and undersaturation of ambient air, and also influenced by stratification of the air surface layer (affecting its turbulent structure) and the sea state (surface waves). The saturation water vapour density over seawater, determined by the water temperature T_s is taken to be $0.98 \rho_s(T_s)$. Taking the vapour flux (evaporation rate E) to vary linearly with wind speed and with undersaturation,

$$E = C_E(0.98\rho_s - \rho_v)U \quad (1)$$

The “bulk” *evaporation coefficient* C_E (also called the *Dalton Number*) is a function of measuring height, stratification, sea state, etc. Using empirical formulae to adjust the mean wind speed and humidity to values U_{10N} and ρ_{10N} that, at a standard 10 m height, would give the same surface flux with neutral density stratification,

$$E = C_{EN}(0.98\rho_s - \rho_{10N})U_{10N} \quad (2)$$

C_{EN} can be used to directly compare field measurements taken in varying conditions.

Prior to the *HEXOS* programme there were predictions that at high wind speeds (above about 15 m/s) the evaporation coefficient would increase rapidly due to evaporation of spray droplets, in addition to evaporation directly from the surface. Direct measurements at wind speeds above about 12 m/s were rare, precisely because the presence of spray made it impossible to operate Lyman-alpha or any other fast-response humidity sensors. In *HEXOS*, aspirated shields were used to extend the range of measurements to 19 m/s. It was found that the evaporation coefficient did not increase nearly as rapidly with wind speed as had been predicted [DeCosmo, 1991; DeCosmo *et al.*, 1996]. A linear regression indicated no significant increase with wind speed, and for 170 data runs the average value was $C_{EN} = 0.00112 \pm 0.00024$.

1.3 Instrumentation

In *ASGASEX* multiple sensors were placed on a boom extending 18 m to the west of *Meetpost Noordwijk* (MPN, Figure 1) to measure CO_2 , water vapour

and sensible heat fluxes by eddy correlation. Bedford Institute of Oceanography (BIO) and the Royal Netherlands Meteorological Institute (KNMI) operated *Lyman-alpha humidimeters* as in HEXOS; the former was directly exposed during periods of fine weather and the latter was in an aspirated shield to protect it from droplets. At the strong Lyman-alpha UV absorption line of the hydrogen in water vapour a path length of about 1 cm is needed, as opposed to typical path lengths of 40–60 cm (often folded in half using a mirror) for IR sensors. Smaller scales of turbulence can be sensed with the shorter UV path, and the more compact sensing head is more easily placed close to the vertical wind sensor. Careful attention was paid to cleanliness of the windows to maintain stable calibration.

KNMI and the Physics and Electronics Laboratory of the Netherlands Organization for Applied Scientific Research (TNO) each operated open-path multiple-wavelength infrared (IR) water vapour and CO₂ sensors.

Using the ratio of signal strength between an absorption and a reference band for each gas, these instruments are relatively insensitive to variations in source strength, detector efficiency and window transmission. The KNMI Infrared Flux Meter (IFM) was developed in-house. TNO operated two commercial Advanet sensors, one of which was borrowed from Risø National Laboratory, Denmark. The other, newly purchased, did not perform as expected for CO₂ measurements but did provide data for water vapour. An improved version of the infrared sensor used by Smith *et al.* [1991], under development for the Canadian participants, was unfortunately not ready in time for this experiment.

Each of the three groups deployed sonic anemometers and their own independent data logging and analysis systems. Many of the sensors were inter-connected so that each group could analyse fluxes from various combinations of sensors. This paper presents water vapour flux and also sensible heat flux and *wind stress*; at this Symposium Oost *et al.* [1995] and Kunz *et al.* [1995] report CO₂ eddy flux results.

Winds measured by the BIO sonic anemometer are used in the results to follow. Located on the south prong of the boom tip (Figure 1), this anemometer was well exposed for wind azimuths from 180 to 330 degrees. For northerly winds the KNMI sonic anemometer and pressure anemometers, on the north prong, were upwind of the BIO and TNO anemometers and were better exposed. Generally it was found that flux values were nearly the same regardless of which well-exposed anemometer was used to measure w' . Mean wind speeds have been corrected for flow distortion by MPN [Oost *et al.*, 1994], and currents measured at 5 m depth were subtracted so that wind speeds are relative to the water. In this paper corrections have not been made for local distortion of turbulence by the boom tip and its collection of sensors.



Figure 1: Sensors on the MPN boom in ASGASEX. Upper left and right, BIO and KNMI sonic anemometers are separated by 2 m. KNMI IFM water vapour and CO₂ sensor is attached just behind (to right of) KNMI sonic; BIO Lyman-alpha humidity meter and microbead thermistor are just behind base of BIO sonic. TNO sonic anemometer is at lower left, with two Advanet IR water vapour and CO₂ sensors just to the right and above it. KNMI pressure anemometer is at lower right. Boom is on west side of MPN; camera is pointing towards northwest.

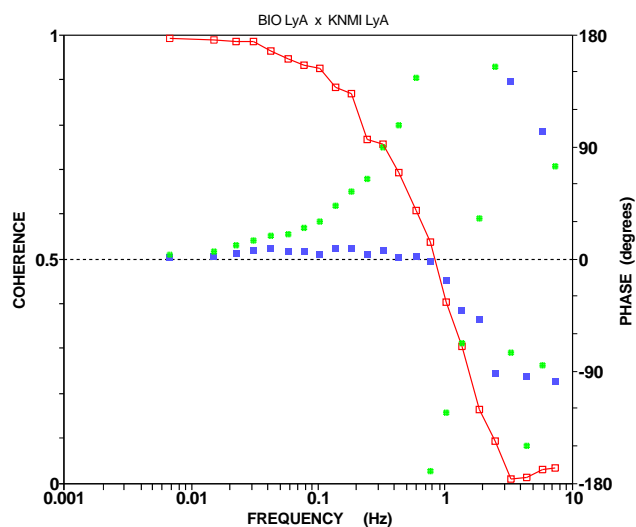


Figure 2: Coherence (open box) and phase (circle) of aspirated (KNMI) and bare (BIO) Lyman-alpha humidity signals for BIO Run 108 at 0020 UT, Sept. 29, 1993; phase (closed box) after correction of time delay; see text.

1.4 Phase Compensation

Where sensors are separated or respond with a time delay it becomes necessary to compensate for the phase shifts that ensue. Without compensation, contributions to eddy fluxes are multiplied by the cosine of the phase, and where phase shifts exceed 90 degrees, contributions to eddy fluxes can even be reversed in sign. Analysis of spectral coherence and phase showed that at low frequencies all humidity sensors in ASGASEX measured the same water vapour fluctuations, indicated by coherence nearly equal to 1.0.

The BIO data were logged at a rate of 16 samples per second, and spectra were analysed up to a Nyquist frequency of 8 Hz. In Figure 2 the phase lead of the bare BIO Lyman- α relative to the aspirated KNMI Lyman-alpha humidity increases with frequency, reaching 180 degrees at 0.72 Hz. This indicates a time delay of $1/(2 \times 0.72) = 0.69$ s, due to the southerly wind direction during this run, placing the KNMI sensors downwind, and also to the time for air to pass through its aspirated shield. This has been compensated by advancing the KNMI Lyman-alpha time series by 11 samples or $11/16 = 0.69$ s. Because the sensors were separated by 2 m there is a gradual loss of coherence at frequencies above about 1 Hz where the separation becomes comparable to the scale of the turbulent eddies, and higher-frequency contributions to the eddy flux are attenuated. The IR sensors also had time delays, possibly due to signal processing and D/A conversion of their output, and phase shifts

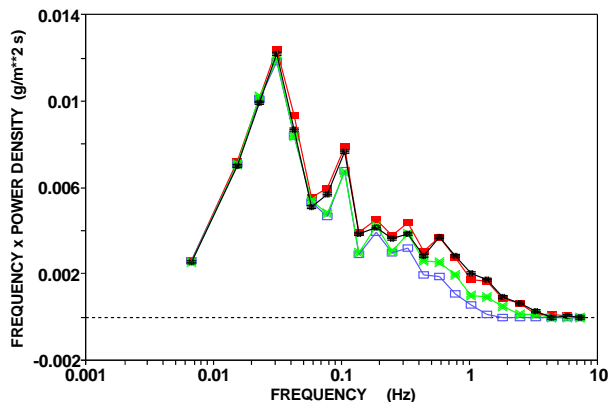


Figure 3: Cospectra of water vapour density from four sensors with vertical wind for BIO Run 108: BIO (black box) and KNMI Lyman-alpha (white box), and Risø Advanet (\times), KNMI IFM (grey boxes). Area under the cospectra is proportional to contributions to the water vapour flux.

were also seen where one sensor was upwind of another. These phase shifts have been compensated in the results to follow.

2 Results of ASGASEX

2.1 Evaporation Results

Cospectra of water vapour density and vertical wind (Figure 3) show the distribution in frequency (hence scale of turbulence) at the 6.3 m measuring height. The BIO Lyman-alpha humidimeter was adjacent to the BIO sonic anemometer (upper left in Figure 1) and its sensing path was open to the airflow. The KNMI IR sensor gave nearly identical results at all frequencies in spite of 2 m horizontal separation, while the cospectrum of the TNO-Risø Advanet, 1.3 m beneath the sonic anemometer, rolls off at frequencies above 0.5 Hz. Attenuation of the cospectrum of the aspirated KNMI Lyman-alpha seen at frequencies above about 0.2 Hz, a result of the above-noted reduction in coherence at higher frequencies, results in a small underestimation of eddy flux proportional to the missing area under its cospectrum in Figure 3.

Neutral evaporation coefficients are derived by correlating data of each of five water vapour sensors with vertical wind measured by the BIO sonic anemometer (Figure 4). Runs during which rain fell, and runs in which the denominator

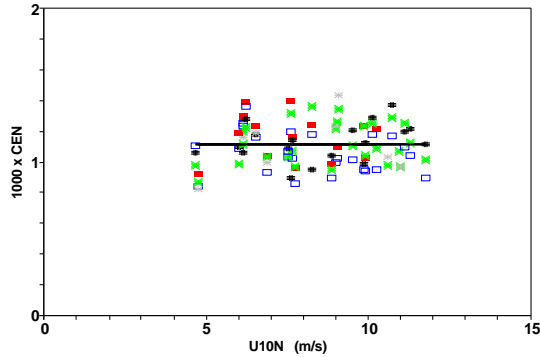


Figure 4: Neutral evaporation coefficients in ASGASEX from eddy fluxes with vertical wind from BIO sonic anemometer and five humidity sensors: BIO (black box) and KNMI Lyman-alpha (white box), TNO (*) and Risø Advanet (×), KNMI IFM (grey box). Line is mean value, 0.00111.

Table 1: Mean evaporation coefficients from four humidity sensors in ASGASEX, from BIO analysis with vertical wind from BIO sonic anemometer.

Humidity Sensor	1000 $\langle C_{EN} \rangle$	Std. Dev.	No. of runs
BIO Lyman-alpha	1.167	0.143	16
TNO-Risø Advanet IR	1.106	0.134	28
TNO Advanet IR	1.106	0.176	8
KNMI IFM IR	1.127	0.119	18
KNMI aspirated Lyman-alpha	1.057	0.133	25

$$(0.98\rho_s - \rho_v) < 1.0g/m^3 \quad (3)$$

have been deleted. The mean value from 70 data runs of all sensors, $C_{EN} = 0.00111 \pm 0.00014$, corroborates the HEXOS value (0.00112 ± 0.00024) [DeCosmo et al., 1996] and agrees with the average value, 0.0012, found by Smith [1989] from a compilation of data from a number of sites. Differences in mean values of C_{EN} among sensors are small, $\pm 5\%$ (Table 1). The highest mean C_{EN} , 0.00117, is from the BIO Lyman-alpha located by the anemometer. The KNMI aspirated Lyman alpha gave the lowest mean value, probably due to the above-noted attenuation of covariance at high frequencies. Because rain was absent in ASGASEX only during periods of low to moderate winds (4–13 m/s), we have no new information on the influence on C_{EN} of evaporating spray droplets at high wind speeds.

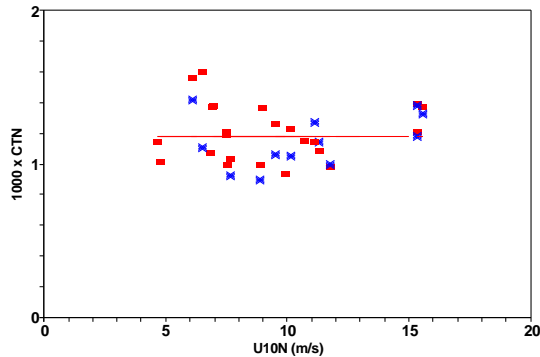


Figure 5: Heat flux coefficients in ASGASEX from BIO thermistor (closed box) and sonic thermometer (\times), adjusted to near-neutral stability. Line is mean value, 0.00118.

2.2 Heat Flux Results

Eddy fluxes of sensible heat from a microbead thermistor and the BIO sonic temperature (Figure 5) give heat flux coefficients (*Stanton numbers*), adjusted to near-neutral stability by removing the influence of stratification on the wind and temperature profiles,

$$C_{HN} = \langle t'w' \rangle / [U_{10N}(T_s - T_{a10N})] \quad (4)$$

having a mean value of 0.00118 ± 0.00019 . Runs with $abs(T_s - T_a) < 0.5^\circ C$ are deleted but rainy runs are not excluded, allowing a wider wind speed range of 4-16 m/s. This agrees with the HEXOS value of 0.00114 ± 0.00035 [DeCosmo *et al.*, 1995].

2.3 Wind Drag Coefficients

Neutral drag coefficients from the BIO sonic anemometer (Figure 6) clearly agree with the HEXOS results from the same site,

$$C_{10N} = 0.00027 + 0.00116U_{10N} \quad (5)$$

[Smith *et al.*, 1992, Eq. 11], but due to the limited range of wind speeds (5-12 m/s) and inherent scatter the correlation coefficient is only $r = 0.45$ and a new regression line would not have a well-determined slope. The scatter includes variation of C_{10N} with wave age [Smith *et al.*, 1992] and the influence of persistent structures in the boundary layer. Runs in south winds with the BIO sonic anemometer blocked by other sensors have been deleted. The KNMI pressure anemometer and the two other sonic anemometers gave similar wind stress results.

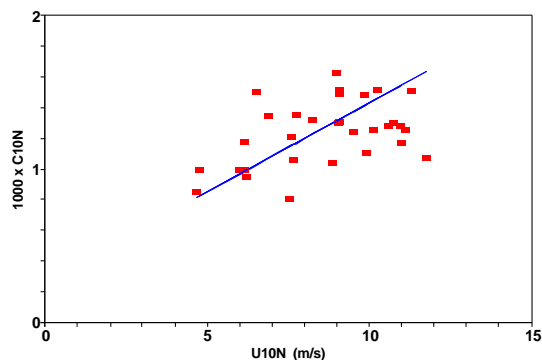


Figure 6: Drag coefficients from BIO sonic anemometer in ASGASEX, with HEXMAX line $1000 C_{10N} = 0.27 + 0.116 U_{10N}$ (Smith et al. [1992], Eq. 11).

3 Summary

Wind stress and eddy fluxes of water vapour and sensible heat measured at MPN during ASGASEX corroborate the HEXOS results. Intercomparisons verify the performance of new IR sensors for water vapour flux, which is important both in itself as a gas flux, and as a necessary part of CO₂ eddy flux measurements. Three independent systems for logging and analysing eddy flux data have been intercompared; all three give valid results and provide a sound basis from which to tackle the question of interpreting CO₂ eddy fluxes.

References

- DeCosmo, J., Air-sea exchange of momentum, heat and water over whitecap sea states. Ph. D. Thesis, Dept. of Atmospheric Sciences, University of Washington, Seattle, x + 212 pp. (Avail. from: University Microfilms, 300 North Zeeb Rd., Ann Arbor, MI 48106, USA), 1991
- DeCosmo, J., K. B. Katsaros, S. D. Smith, R. J. Anderson, W. Oost, K. Bumke and A. L. M. Grant, Air-sea exchange of sensible heat and water vapor: the HEXOS results, *J. Geophys. Res.* 101, 1996 (in press)
- Kunz, G., G. de Leeuw, S. Larsen and F. Hansen, Over-water eddy correlation measurements of fluxes of momentum, heat, water vapour and CO₂, *This volume*
- Miller, M. J., A. C. M. Beljaars and T. N. Palmer, The sensitivity of the ECMWF model to the parameterization of evaporation from the tropical oceans, *J. Climate*, 5, 418-434, 1992
- Oost, W. A., C. W. Fairall, J. B. Edson, S. D. Smith, R. J. Anderson, J. A. B. Wills, K. B. Katsaros and J. DeCosmo, Flow distortion calculations and their application to wind stress over the sea in HEXMAX, *J. Atmos. Oceanic Tech.*, 11, 366-386, 1994

- Oost, W., W. Kohsiek, H. J. W. de Baar, G. J. de Leeuw, G. Kunz, S. D. Smith, R. J. Anderson, O. Hertzman and M.-C. Bourque, On the discrepancies between CO₂ flux measurement methods, *This volume*
- Oost, W., The ASGASEX '93 experiment, *This volume*
- Smith, S. D., Water vapor flux at the sea surface (Review paper), *Boundary-Layer Meteorol.*, 47, 277-293, 1989
- Smith, S. D., R. J. Anderson, E. P. Jones, R. L. Desjardins, R. M. Moore, O. Hertzman and B. D. Johnson, A new measurement of CO₂ eddy flux in the nearshore atmospheric surface layer, *J. Geophys. Res.*, 96, 8881-8887, 1991
- Smith, S. D., R. J. Anderson, W. A. Oost, C. Kraan, N. Maat, J. DeCosmo, K. B. Katsaros, K. L. Davidson, K. Bumke, L. Hasse and H. M. Chadwick, Sea surface wind stress and drag coefficients: the HEXOS results, *Boundary-Layer Meteorol.*, 60, 109-142, 1992
- Smith, S. D., K. B. Katsaros, W. A. Oost and P. G. Mestayer, Two major experiments in the Humidity Exchange over the Sea program, *Bull. Amer. Meteor. Soc.*, 71, 161-172, 1990

Radon-222 Transfer Coefficients in Atlantic and Pacific Oceans. The Influence of Temperature and Wind

S. N. Kholouiski

P. P. Shirshov Institute of Oceanology RAS, Moscow

Abstract

Based on vertical profiles of radon-222, the transfer coefficients k_v across the sea surface were obtained at 33 stations in the Atlantic and Pacific Oceans. In the Atlantic, measurements were carried out at 13 stations in the Antarctic region, two stations were taken in subantarctic waters, and eight stations in the trade winds area. In the Pacific, measurements were taken at two stations in the Bering Sea, four stations in the Okhotsk Sea and four stations in the northern Pacific.

In the Antarctic, the k_v values ranged from 1.6 to 4.8 m/d with strong and variable winds at speeds generally from 8 to 12 m/s, and with near zero sea-surface temperatures. A functional dependence between k_v values and wind speed was not found. Comparison of the Antarctic data with those obtained in the trade winds region at a similar average wind speed of 10 m/s, but at a sea surface temperature of 27° C, reveals that the dependence of k_v on temperature through molecular diffusivity could be masked by water turbulence in natural sea conditions.

In the Pacific, the k_v values ranged from 1.8 to 5.4 m/d with weak and moderate winds of 4 to 8 m/s, and sea-surface temperatures from 4° C to 15° C. The maximum k_v value was measured in coastal waters at the intense by turbulent surface layer, but with weak wind. The normalized k_v values (at 20° C) were considerably higher in these regions than in low and temperate latitudes of the world ocean.

1 Introduction

The complexity of directly obtaining gas transfer coefficients (k_v) across the ocean-sea interface requires that instead the connections of k_v with the physical parameters that influence gas transfer be found. Under field conditions, the most easily determined of such parameters are the *sea-surface temperature* (T) and *wind speed* (W).

The results of laboratory experiments in wind-wave tanks [Wanninkhof and Bliven, 1991] and of the *dual tracer experiments* in lakes [Upstill-Goddard *et al.*, 1990] confirmed the existence of a functional connection k_v with surface temperature through a power-law dependence of the gas in the water on the *Schmidt number* (Sc). In addition, these experiments have shown a strong dependence of k_v on wind speed. In the natural sea, however, the

wind-speed dependence of k_v is still a problem. Recently, attempts to obtain this relationship were undertaken in coastal waters in the North Sea [Watson *et al.*, 1991] and in Georges Bank [Wanninkhof *et al.*, 1993] using a dual deliberate tracer technique.

One of the few methods used to give local short-term k_v values across the ocean surface is the *radon-deficit technique*, which is based on the distribution of this geochemical trace gas in ocean surface waters. Although results from use of this method, such as GEOSECS [Peng *et al.*, 1979] and TTO [Smethie *et al.*, 1985], showed considerable spatial and/or temporal radon gas k_v variations, the reasons for the variations are not clear. The obtained k_v values are likely to be a result of interaction of various factors affecting the gas exchange, rather than of a single factor [Wanninkhof, 1992]. Perhaps this could explain the failure to obtain the functional connection between k_v and wind speed based on the GEOSECS radon data [Peng *et al.*, 1979; Hasse and Liss, 1980]. Deacon [1980] reexamined GEOSECS results, and Smethie *et al.* [1985] looked again at the TTO results to try to find such a connection. However, in both cases the significant scatter of the results suggested only a possibility of correlation between k_v and wind speed. Therefore, the use of laboratory-determined functional dependence $k_v(W)$ is of limited application to air-sea gas flux determination in natural conditions.

The radon data were obtained in a wide range of wind and sea-temperature conditions, from 2 to 17 m/s and from -1°C to 30°C , respectively. However, most of the data concern tropical and temperate regions and reflect weak to moderate winds and sea-surface temperatures close to the world ocean average. Data for the high latitudes, shelf and coastal regions, and the seas are still insufficient.

Here we present three series of radon k_v measurements in the Atlantic and Pacific Oceans. Station locations and numbers are given in Figure 1.

The first series (in time sequence) was carried out during cruise number 10 of R/V *Vitiaz* in August to November 1985 at eight stations in the tropical Atlantic in the trade winds area. The second series was carried out during cruise number 43 of R/V *Dmitry Mendeleev* in February to April 1989 at 15 stations in the southern Atlantic, of which 13 were located to the south of the polar front in the following regions: Three stations along the 15°W transect (these stations were repeated in a month), three stations near South Orkney Islands area, two stations near Elephant Island, and one station in Bransfield Strait. Two more stations were sampled in the subantarctic waters. The third series was carried out during cruise number 21 of R/V *Academic Alexander Nesmeianov* in June to August 1992 at two stations in the Western Bering Sea, four stations in the Okhotsk Sea and four stations in the northern Pacific. The results are presented in Tables 1 and 2.

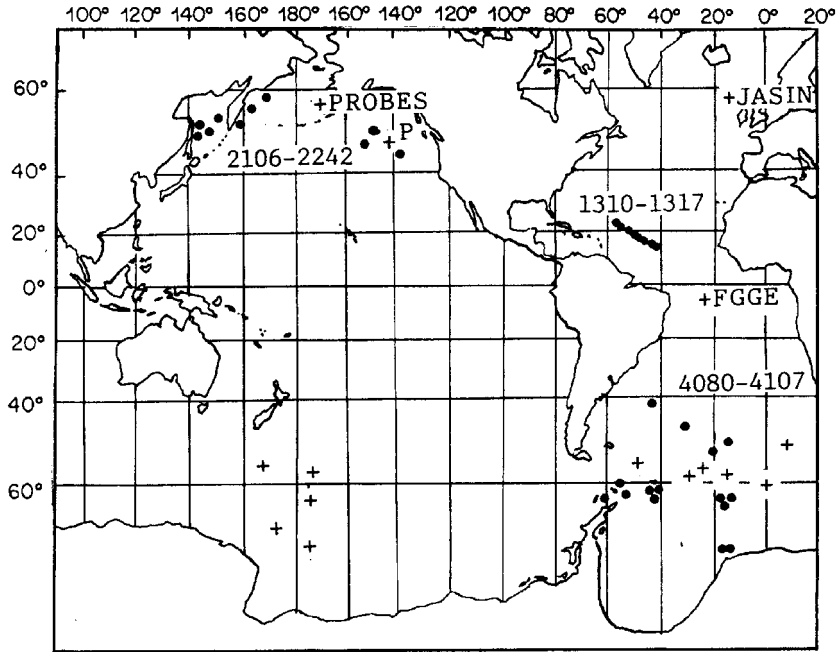


Figure 1: Locations of the radon profiles reported in this study (dots) and those reported by Peng *et al.* [1979] at GEOSECS Antarctic stations (crosses). The JASIN, FGGE, PROBES and station P locations (crosses) are also shown.

2 Method

Radon measurements in seawater were carried out using the instruments described in Kholujskij [1993]. The concentration of the parent radium-226 was measured in acidified (pH 2), hermetically sealed samples, after stationary amounts of radon had been accumulated. The reproducibility of our radon measurements in the water was less than ($\pm 5\%$), and radium made up ($\pm 8\%$ [Kholouiski *et al.*, 1988]. The vertical radon profiles resulted from measurements in 4 to 11 layers (8 layers in general) to the depth of 50 to 250 m. The k_v values are calculated according to the equation given elsewhere, for example, in Smethie *et al.* [1985]. These authors estimated the error of k_v determination from a single radon profile at not less than 20 to 35 %; this estimation is probably representative.

Because some of the stations were located not far from the coast, we had to evaluate the radon content in the atmosphere for these sites. The vacuum extractor of our device was filled with air from the atmosphere,

and the radon measuring procedure for seawater was reproduced. Radon content in the atmosphere was determined at nine points in the Bering and Okhotsk Seas along the sampling route and at nearshore stations N4080 and N4086 in the Antarctic. The radon value was close to analytical zero, and thus was not taken into account when calculating the k_v value.

Radium concentration in the upper layer was measured only at certain stations in the southern Atlantic [*Kholouiski and Lebedev*, 1991], and its vertical distribution only at stations number 4100, 4103, 4104, 4105 (Table 2). Radium distribution (in the mixed layer and beneath the radon deficit) at all of the stations was nearly homogeneous at depth. Thus, we assumed that the upper layer within the radon profiles in the southern Atlantic was homogeneous relative to radium. This assumption was extended to the other study areas. The equilibrium radon concentrations (C_e) were estimated at the stable lower parts of the radon profiles. Since the C_e values at replicate and neighboring stations did not differ significantly, their weighted mean values were used to calculate k_v (Table 2). The values are as follows: 18.8 dpm/100 L at stations NN 4083, 4084, 4102, 4103, 4104; 17.6 dpm/100 L at stations NN4086, 4089, and 4093; and 16.2 dpm/100 L at stations NN4096 and 4099 in the Antarctic region. At the western Bering Sea stations, the value was 13.6 dpm/100 L; at the Okhotsk Sea stations, it was 14.3 dpm/100 L; and at the northeastern Pacific stations it was 11.9 dpm/100 L.

In the surface mixed layer, the average activity (C_m) of homogeneously distributed radon was used for the k_v calculation; if the radon concentration increased considerably with depth, the mean from two near-surface samples was used. The sea-surface temperatures (T), salinities (S), and the average shipboard wind speeds (at the standard height 10 m above the water surface) 0 to 24 (W1) and 24 to 48 (W2) hours before radon profiles were taken are also given in Table 2.

3 Results

All of the antarctic k_v measurements were carried out at a sea surface temperature from -1°C to 3°C and in relatively strong winds, mainly from 8 to 12 m/s. During the period before the radon profiles were taken, wind speed averaged for 48 hours at all the antarctic stations was 10 m/s. The k_v values varied from 1.6 to 4.8 m/d, and they were 2.9 m/d, on average. This value is higher than the mean k_v values at the GEOSECS antarctic stations in the Atlantic Ocean (2.1 m/d, stations NN74 to 91), but lower than that of the Pacific stations (3.5 m/d, stations NN 282 to 290), calculated from [*Peng et al.*, 1979]. All our values were within the range of *Peng et al.*'s [1979] antarctic data.

For evaluation of the k_v dependence on wind speed under field conditions, it is desirable to compare the data obtained at nearly equal sea-surface temperatures and at a maximum possible range of wind speeds. These condition were ideally realized during JASIN and FGGE time-series k_v measure-

ments in the Atlantic [Kromer and Roether, 1983] and at station P in the northeastern Pacific [Peng *et al.*, 1974; Emerson *et al.*, 1991]. In the antarctic region, the influence of wind speed on k_v could be estimated from these data together with the GEOSECS results, because all were obtained in a narrow sea-surface temperature range, from -1°C to 5°C (Figure 2a). It is clear, however, that within the wind speed range from 5 to 15 m/s, there was no such correlation.

The influence of the sea surface temperature on radon k_v values is analyzed by comparing our antarctic data with similar results in the trade winds area (Table 2). This question was also discussed in Popov and Kholouiski [1993]. The mean wind speed for a 48-hour period before obtaining a radon profile was 10.4 m/s at the tropical stations; it was nearly the same as in the antarctic. However, the temperature difference between these series was 27°C on average; thus, the effect of temperature on k_v was close to the maximum observable for the world ocean surface waters. Assuming that the dependence of k_v is as indicated by laboratory studies, the similarity of wind speeds during the measurements in the tropics and antarctic indicates that k_v for the antarctic stations normalized to the temperature of the tropical stations should be equal to k_v measured in the tropics. According to the relationship $k_v \sim \text{Sc}^{-0.5}$ and the dependence of the radon Schmidt number in water on temperature [Jähne *et al.*, 1987], the decrease of the sea surface temperature by 27°C should result in a corresponding decrease in k_v values by a factor of two (from 2.8 m/d on average in the tropics to 1.3 m/d predicted in the antarctic). However, the observed k_v values in the antarctic were not lower, but rather, were somewhat higher on average (2.9 m/d) than those in the tropics. This increase in k_v with decreasing temperature cannot be explained using a power-law relation between k_v and the Schmidt number. In Figure 2b, the comparison of antarctic and tropical results normalized to 20°C (assuming $k_v \sim \text{Sc}^{-0.5}$) clearly shows the higher k_v values in the antarctic.

The results of the laboratory experiments described in Popov and Vodiana [1992] could probably provide an explanation of this phenomenon. Judging from these results, the carbon dioxide k_v dependence on water temperature strongly influenced the turbulence of the water. It could be described by several curves, with the slope increases depending on the degree of turbulence. The k_v value for the warm and slightly turbulent water could coincide with that of the cold and intensely turbulent water. The equality of the mean wind speed in our tropical and antarctic study areas could not be considered a confirmation of the equivalent surface mixing in these regions. On the contrary, at the antarctic stations, the wind speed varied widely in amplitude (often from 0 to 20 to 25 m/s in a gust) and in direction compared with the trade winds stations. Therefore, the greater wind stress and surface layer turbulence in the antarctic resulted in increased k_v values, even though the mean wind speeds were similar. Obviously, the influence of hydrodynamical factors on k_v is stronger than that of temperature.

Table 1: Sea surface temperature (T), salinity (S) and wind speeds (W_1, W_2).

Station Number	Location	Date	T ° C	S ‰	W1 m/s	W2 m/s
Atlantic Ocean. Trade winds. Cruise 10 R/V Vityaz						
1310	23° 00'N, 55° 48'W	28.09.85	28.20	36.36	9.7	9.4
1311	22° 00'N, 53° 18'W	30.09.85	27.87	37.03	10.4	9.1
1312	21° 00'N, 50° 18'W	01.10.85	27.31	37.33	11.5	8.8
1313	20° 00'S, 47° 36'W	03.10.85	27.28	37.40	12.3	10.5
1314	19° 24'N, 45° 48'W	04.10.85	26.94	37.04	15.0	12.1
1315	18° 36'N, 43° 48'W	05.10.85	26.78	37.15	12.0	11.4
1316	17° 36'S, 41° 12'W	06.10.85	26.86	36.78	8.3	8.4
1317	16° 36'S, 38° 42'W	08.10.85	26.61	37.00	9.3	8.1
Antarctic waters. Transect along 15° W. Cruise 43 R/V Dmitriy Mendeleev						
4080	52° 04'S, 15° 00'W	14.02.89	3.02	33.81	9	12
4105	55° 00'S, 19° 00'W	06.04.89	2.10	33.94	13	5
4083	62° 30'S, 15° 00'W	20.02.89	-0.27	34.06	6	9
4102	62° 30'S, 15° 00'W	26.03.89	-0.35	34.06	13	12
4104	62° 30'S, 14° 55'W	02.04.89	-0.39	34.05	11	11
4084	70° 50'S, 15° 23'W	23.02.89	-0.17	34.23	9	8
4103	70° 42'S, 15° 30'W	29.03.89	-0.96	34.22	8	10
South Orkney Islands						
4086	60° 50'S, 41° 10'W	02.03.89	-0.8	33.37	12	11
4090	60° 53'S, 41° 00'W	04.03.89	-0.9	33.40	12	11
4093	60° 45'S, 41° 00'W	05.03.89	0.5	-	9	12
Elephant Island						
4096	60° 51'S, 55° 30'W	08.03.89	1.22	34.13	8	9
4099	60° 44'S, 55° 51'W	10.03.89	3.01	33.79	12	10
Bransfield Strait						
4100	62° 24'S, 56° 54'W	12.03.89	1.47	33.72	8	11
Subantarctic waters						
4106	45° 50'S, 32° 50'W	10.04.89	11.32	34.34	13	12
4107	41° 50'S, 41° 37'W	12.04.89	15.4	34.37	11	15
Pacific Ocean. The Bering Sea. Cruise 21 R/V Academic Alexander Nesmeyanov						
2106	56° 27'N, 167° 41'E	17.06.92	5.21	33.03	2	4
2127	58° 07'N, 173° 48'E	21.06.92	4.5	33.18	6	7
The Okhotsk Sea						
2182	52° 40'N, 149° 40'E	26.07.92	10.53	32.81	6	5
2185	53° 33'N, 146° 02'E	27.07.92	12.23	28.29	7	6
2225	55° 10'N, 153° 47'E	03.08.92	10.99	32.89	8	4
2242	52° 47'N, 144° 23'E	06.08.92	9.58	30.38	8	11
The Pacific Ocean						
2166	52° 43'N, 148° 43'W	04.07.92	15.41	32.48	4	8
2169	47° 00'N, 138° 14'W	15.07.92	13.40	32.53	4	5
2171	49° 00'N, 150° 47'W	16.07.92	-	-	7	5
2174	52° 24'N, 158° 51'E	24.07.92	10.06	32.08	4	5

(^a) Deviation of the mean within the stationary part of a radon profile (2-7 sampling depths) (^b) Deviation of the mean of 2-7 sampling depths.

Table 2: Radon transfer coefficients (k_v) in dpm/l in the study areas.

Station Number	^{222}Rn beneath the deficit, C_e	^{222}Rn in the mixed layer, C_m	^{226}Ra in upper layer	k_v
Atlantic Ocean. Trade winds. Cruise 10 R/V Vityaz				
1310	9.1 ± 0.5	6.5 ± 0.3	-	1.8
1311	9.0 ± 1.2	6.5 ± 0.2	-	2.9
1312	9.0 ± 0.7	6.6 ± 0.2	-	3.2
1313	8.6 ± 0.7	6.5 ± 0.1	-	2.0
1314	8.6 ± 0.5	6.5 ± 0.3	-	2.2
1315	9.0 ± 1.0	5.8 ± 0.2	-	4.0
1316	9.0 ± 0.5	6.2 ± 0.4	-	4.1
1317	8.8 ± 0.8	6.6 ± 0.2	-	1.8
Antarctic waters. Transect along 15° W. Cruise 43 R/V Dmitriy Mendeleev				
4080	$13.8 \pm 0.1^{(a)}$	$8.4 \pm 0.6^{(b)}$	-	3.4
4105	17.0 ± 0.9	14.0 ± 0.9	$16.2 \pm 1.0^{(c)}$	2.9
4083	18.4 ± 0.6	11.7 ± 1.9	-	4.6
4102	19.0 ± 1.1	15.2 ± 0.7	-	2.0
4104	18.8 ± 1.0	15.8 ± 0.7	$18.9 \pm 2.1^{(c)}$	2.3
4084	18.5 ± 0.5	13.3 ± 1.4	-	4.8
4103	19.0 ± 0.7	14.7 ± 1.0	$19.0 \pm 0.7^{(c)}$	2.9
South Orkney Islands				
4086	17.5 ± 1.2	12.8 ± 1.0	$16.6 \pm 0.3^{(d)}$	2.4
4090	17.6 ± 1.2	12.6 ± 1.7	-	3.3
4093	-	12.8 ± 1.8	-	3.5
Elephant Island				
4096	17.2 ± 0.9	13.4 ± 1.0	-	1.6
4099	16.0 ± 0.4	12.1 ± 0.3	-	2.6
Bransfield Strait				
4100	18.2 ± 0.9	13.6 ± 0.7	$20.7 \pm 1.7^{(c)}$	2.0
Subantarctic waters				
4106	9.4 ± 1.8	7.8 ± 0.9	$9.5 \pm 0.5^{(d)}$	2.0
4107	10.2 ± 0.2	7.4 ± 0.9	-	3.1
Pacific Ocean. The Bering Sea. Cruise 21 R/V Academic Alexander Nesmeyanov				
2106	$13.5 \pm 0.5^{(a)}$	$9.5 \pm 0.1^{(b)}$	-	3.2
2127	13.9 ± 0.1	10.2 ± 0.6	-	2.7
The Okhotsk Sea				
2182	13.5 ± 0.6	9.1 ± 0.1	-	1.9
2185	14.8 ± 1.1	5.5 ± 0.8	-	4.3
2225	14.3 ± 1.1	6.1 ± 0.4	-	5.0
2242	14.3 ± 1.8	8.7 ± 0.1	-	1.8
The Pacific Ocean				
2166	12.1 ± 1.3	7.1 ± 0.5	-	4.2
2169	10.5 ± 0.8	6.5 ± 1.6	-	3.0
2171	11.7 ± 0.6	7.8 ± 0.2	-	3.6
2174	13.1 ± 0.7	7.0 ± 0.1	-	5.4

^(c) Deviation of the mean from 5–6 sampling depths in mixed layer and beneath the deficit. ^(d) The sea-surface sample with its counting error.

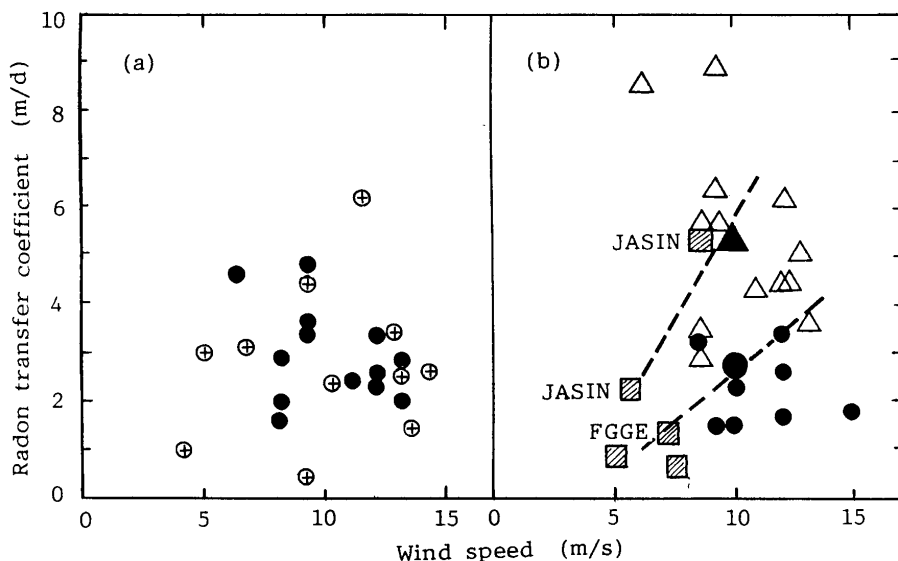


Figure 2: Observed radon transfer coefficients k_v vs wind speed 0 to 24 hours before sampling, W_1 . (a) Antarctic results. The solid circles are our data; the open circles with crosses are the GEOSECS data. (b) Normalized at 20° C, our antarctic data (open triangles) and tropical (solid circles) results. The large solid triangle and circle are the averaged k_v values vs averaged wind speeds in the antarctic and tropics, respectively. The squares are JASIN and FGGE data.

A similar effect was found in *Kromer and Roether's* [1983] comparison of FGGE and JASIN data. An increase of radon k_v values was observed from the FGGE trade wind area to the north Atlantic JASIN area at similar average wind speeds. The large wind variability in the JASIN data is a possible cause of this increase [*Kromer and Roether, 1983*].

Even if a dependence of k_v on wind speed exists in sea conditions, it could probably not be described with a single curve. It could be described instead by a number of curves (Figure 2b) specific to different ocean regions, the slope of which probably increase from the tropics to high latitudes. In any case, in view of this phenomenon, care should be taken to compare the k_v data sets obtained in different regions (see for example *Watson et al. [1991]*).

In the Pacific, the k_v values varied from 1.8 to 5.4 m/d in a relatively narrow range of weak and temperate winds, usually 4 to 8 m/s. Therefore, we cannot discuss the influence of wind speed on k_v in this region. The mean k_v value in the Bering Sea was 3.0 m/d; in the Okhotsk Sea it was 3.3 m/d, and in the north Pacific it was 4.1 m/d (these results were discussed in more detail in *Kholouiski et al. [1995]*).

In the natural environment, other hydrodynamical factors such as currents and free convection can influence gas transfer independently of wind, or there can be an interaction between wind and these factors. Such conditions exist in shelf and coastal waters, rather than in the open ocean. We observed such an effect in the northwestern Pacific, approximately 16 km off the coast of Kamchatka. There, the maximum from our Atlantic and Pacific k_v value of 5.4 m/d was obtained at permanent and slow wind speed of about 4 to 5 m/s, when the wind had been blowing for not less than two days. The ship was near the station during this period. However, taking into account abnormal salinity alterations at homogeneous temperature distribution, one could suggest that intensive turbulence was caused by near-shore currents, independent of the wind. This turbulence, perhaps, could be a reason for the high k_v value.

If we normalize the obtained k_v values to the sea surface temperature (we worked at 4° C-15° C, which is lower than the mean oceanic temperature) they would be considerably higher than the mean normalized GEOSECS data for the world ocean, 2.9 m/d, given in *Peng et al.* [1979]. To compare our results with those of GEOSECS, we normalized them to 20° C, assuming $k_v \sim Sc^{-0.5}$. On average, they were 4.7 m/d, which is considerably higher than the GEOSECS value of 2.3 m/d (recalculated in this manner from 2.14 m/d, [*Peng et al.*, 1979]) for the area to the north of 40° N in the Pacific. Similarly, normalized PROBES data obtained in the eastern Bering Sea by *Glover and Reerburgh* [1987] at the average sea surface temperature of 8.5° C were 3.1 m/d. In addition, the normalized station P data obtained by *Peng et al.* [1974] and *Emerson et al.* [1991] at 5° C to 13° C were 4.6 m/d, on average. Both of these results are also higher than the normalized GEOSECS average. Therefore, although the increase in k_v values from the Pacific region to the north of 40° N is evident, it is unclear whether it is a result of local hydrodynamics in the sea surface layer in marginal seas or of a more active wind regime in high latitudes.

References

- Deacon, E. L., Sea-air gas transfer: the wind speed dependence, *Boundary Layer Meteorol.*, 21, 31-37, 1980.
- Emerson, S., P. Quay, C. Stump, D. Wilbur, and M. Knox, O₂, Ar, N₂, and ²²²Rn in surface waters of the Subarctic Ocean: net biological O₂ production, *Global Biogeochem. Cycles*, 5, 49-69, 1991.
- Glover, D. M., and W. S. Reerburgh, Radon-222 and radium-226 in southeastern Bering Sea shelf waters and sediment, *Cont. Shelf Res.*, 7, 433-456, 1987.
- Hasse, L., and P. S. Liss, Gas exchange across the air-sea interface, *Tellus*, 32, 470-481, 1980.
- Jähne, B., G. Heinz, and W. Dietrich, Measurement of the diffusion coefficients of sparingly soluble gases in water, *J. Geophys. Res.*, 92, 10,767-10,776, 1987.
- Kholujskij, S., Radon evasion rates in the Atlantic sector of Southern Ocean, in *The Second Polish-Soviet Antarctic Symposium*, edited by R. Z. Klekowski and

- K.W.Opalínski, pp. 45-50, Institute of Ecology PAS, Dziekanów Lésny, Lomianki, Poland, 1993.
- Kholouiski, S. N., N. G. Lebedev, and V. I. Dobrinin, Radium-226 and radon in the water of the Lake Baikal (in Russian), *Geohimia*, 11, 1651-1655, 1988.
- Kholouiski, S. N., and N. G. Lebedev, The concentrations of radon-222 and radium-226 in the waters of Atlantic and Indian Oceans. Data report, obtained in cruise number 43 R/V Dmitry Mendeleev (January-April 1989) (in Russian), *VINITI*, N3623-B91, 1991.
- Kholouiski, S. N., V. V. Anikiev, and N. I. Popov, Radon-222 transfer coefficients across the sea surface in the Bering and Okhotsk Seas and in the Northern Pacific Ocean (in Russian), *Dokl. Akad. Nauk Rus.*, 344, 1995.
- Kromer, B., and W. Roether, Field measurements of air-sea gas exchange by the radon deficit method during JASIN 1978 and FGGE 1979, *Meteor Forschungsergeb., Reihe, A/B*, 24, 55-75, 1983.
- Peng, T.-H., T. Takahashi, and W. S. Broecker, Surface radon measurements in the North Pacific Ocean station PAPA, *J. Geophys. Res.*, 79, 1772-1780, 1974.
- Peng, T.-H., W. S. Broecker, G. G. Mathieu, Y. H. Li, and A. E. Bainbridge, Radon evasion rates in the Atlantic and Pacific oceans as determined during the GEOSECS program, *J. Geophys. Res.*, 84, 2471-2486, 1979.
- Popov, N. I., and E. G. Vodianaja, The influence of the temperature on the carbon dioxide transfer coefficients across the sea surface (in Russian), *VINIVI*, N1140-B92, 1992.
- Popov, N. I., and S. N. Kholouiski, On the influence of the temperature and the wind to the air-atmosphere gas transfer (in Russian), in *The Complex Study of the Basin of the Atlantic ocean*, proceedings of the 7-th regional conference, pp. 7-8, Kaliningrad, 1993.
- Smethie, W. M., Jr., T. Takahashi, D. W. Chipman, and J. R. Ledwell, Gas exchange and CO₂ flux in the tropical Atlantic Ocean determined from ²²²Rn and pCO₂ measurements, *J. Geophys. Res.*, 90, 7005-7022, 1985.
- Upstill-Goddard, R. C., A. J. Watson, P. S. Liss, and M. I. Liddicoat, Gas transfer in lakes measured with SF₆, *Tellus*, 42B, 364-377, 1990.
- Wanninkhof, R., Relationship between gas exchange and wind speed over the ocean, *J. Geophys. Res.*, 97, 7373-7381, 1992.
- Wanninkhof, R., and L. F. Bliven, Relationship between gas exchange, wind speed, and radar backscatter in a large wind-wave tank, *J. Geophys. Res.*, 96, 2785-2796, 1991.
- Wanninkhof, R., W. Asher, R. Weppernig, H. Chen, P. Schlosser, C. Langdon, and R. Sambrotto, Gas transfer experiment on Georges Bank using two volatile deliberate tracers, *J. Geophys. Res.*, 98, 20,237-20,248, 1993.
- Watson, A. J., R. C. Upstill-Goddard, and P. S. Liss, Air-sea exchange in rough and stormy seas measured by a dual tracer technique, *Nature*, 349, 145-147, 1991.

On the Discrepancies between CO₂ Flux Measurement Methods

Wiebe A. Oost ¹, Wim Kohsiek ¹, Gerrit de Leeuw ²,
Gerard J. Kunz ², Stuart D. Smith ³, Bob Anderson ³,
Owen Hertzman ⁴

¹ Royal Netherlands Meteorological Institute de Bilt, the Netherlands

² TNO-Physics and Electronics Laboratory, Den Haag, the Netherlands

³ Bedford Institute of Oceanography, Ocean Circulation Division
Dartmouth, N.S., Canada

⁴ Department of Oceanography, Dalhousie University
Halifax, N.S., Canada

Abstract

In 1993 the ASGASEX (for Air-Sea GAS EXchange) experiment took place at Meetpost Noordwijk, a research platform off the Dutch coast. One of the aims of the project was to try to find an explanation for the order of magnitude difference between transfer velocities for CO₂, measured with the eddy correlation technique, and those from other methods. After ascertaining the quality of our eddy correlation CO₂ flux data, we noted that the order of magnitude difference for the transfer velocity was again present. This drew our attention to the CO₂-fugacity, which showed large tide-related excursions, indicating fugacity gradients. Based on the contrast between the regularity of the fluxes and the more fluctuating character of the fugacities we make an argument that the gradients may be connected to a shallow pycnocline, in agreement with the results of earlier hydrographical work done in the area. This conceptual model can largely explain the transfer velocity discrepancy. It is stressed that, despite this agreement, the model is still hypothetical, that there are problems remaining and that confirmation is needed. This will be attempted as part of the ASGASEX MAGE (for Marine Aerosol and Gas Exchange, a subgroup of IGAC) experiment ASGAMAGE, to take place in 1996.

1 Introduction

In September '93 the ASGASEX (for *Air Sea GAS Exchange*) experiment took place at Meetpost Noordwijk (MPN, fig. 1), a research platform 9 km off the Dutch coast. One of the aims of the experiment was to try to find an explanation for the well-known, but not understood order of magnitude difference between *transfer velocities* for CO₂ measured over the sea by the *eddy correlation* (e-c) technique and those provided by all other methods.

For a good understanding of the problem, we repeat the steps that led to the discrepancy. A common way to find the CO₂ flux is to measure the in-

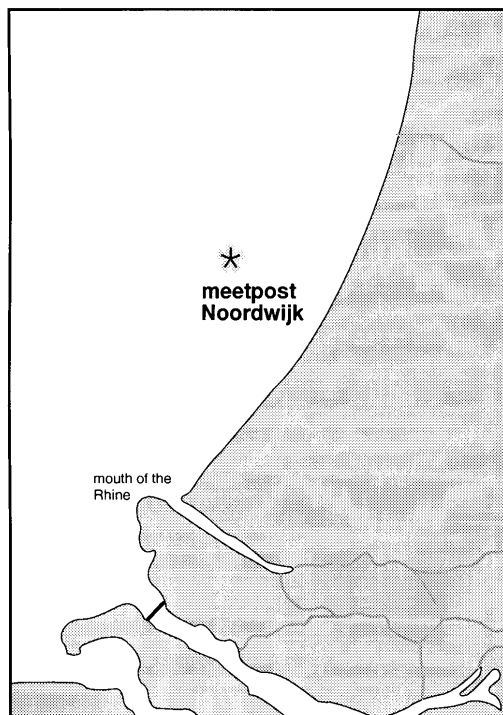


Figure 1: The position of Meetpost Noordwijk near the Dutch Coast (a picture of the platform is presented in the ASGASEX overview paper by Oost)

terfacial concentration difference ΔpCO_2 and to multiply it with the transfer velocity k_w to find the flux F :

$$F = k_w * \Delta pCO_2 \quad (1)$$

k_w is supposed to depend on a number of geophysical parameters, with the wind speed as the primary one. Values for k_w are derived from experiments with either natural or artificial tracers; well known functional relationships between k_w and wind speed for CO_2 are those of *Liss and Merlivat* [1986] and of *Wanninkhof* [1992].

The comparison of flux measurement methods has always been made in terms of the transfer velocity. The result of that comparison has been that the k_w values from e-c measurements were consistently an order of magnitude or more larger than those from other methods (e. g., *Broecker et al.* [1986]).

This result has often been considered as due to the inadequate sensitivity of the fast responding CO_2 sensors needed for the e-c measurements. With the availability of new and more sensitive detectors we wanted to make

another attempt to use the e-c technique, because it has some important advantages.

2 The Experiment

MPN was used for ASGASEX'93 because the e-c method requires a stable platform and this station is one of the very few bottom mounted platforms at sea available and suitable for research purposes.

Two independent CO₂ e-c flux measurement systems were used. These were operated by respectively the Physics and Electronics Laboratory of the (Dutch) Organization for Applied Scientific Research (TNO-FEL) and the Royal Netherlands Meteorological Institute (KNMI). The TNO-FEL contribution was a cooperative effort with the Danish Risø National Laboratories (Risø). The noise level is very important for this type of measurements, because the CO₂ sensors are functioning at the very limit of their sensitivity. This state of affairs is caused on one hand by the very low amplitude of the CO₂ concentration fluctuations, the basic quantity needed for the e-c technique, on the other by the need to apply a large correction to the initial data (the so-called Webb correction, *Smith and Jones* [1979], *Webb et al.* [1980]).

3 Flux Results

The values found for the CO₂ fluxes with the e-c method are plotted in fig. 2 as a function of wind speed. Some dubious data have been left out. It is clear that there is a lot of scatter, but the two fully independent sets of measurements, made with different types of instruments, show a good correspondence. A regression calculation gave a correlation coefficient for the TNO-Risø data of 0.65, for the KNMI data of 0.61. Assuming a power law dependence for the relation between the flux and the wind speed, $F = a \times U^n$, with U the neutral 10 m wind speed, we first fixed the exponent in that relationship by making fits to a combination of all accepted data, from TNO-Risø as well as KNMI, with $n = 1, 2, 3$ and 4, and compared the resulting rms errors. This gave an indication for a quadratic or third power dependence; we chose the quadratic one. Independent unweighted least squares fits with a quadratic function for both data sets produced the two almost identical curves in fig. 2 (we will return to the two remaining curves later). It should be stressed here that our choice for $n = 2$ is not a fundamental one: we could just as well have used $n = 3$ (the curves for that fit are only slightly more different than for $n = 2$). The important point is that the flux data show a regular dependence on the wind speed, despite the fact that they have been obtained at quite different times.

The uncanny (and probably slightly fortuitous) correspondence of the two fits strongly boosted our confidence in the data. At the same time it

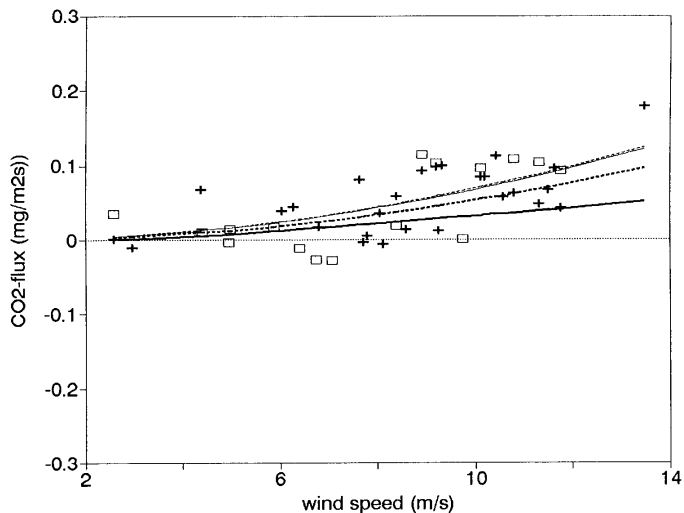


Figure 2: CO_2 fluxes as a function of wind speed. \square : FEL-TNO/Risø data; $+$: KNMI data; thin dashed line: quadratic fit to FEL-TNO/Risø data; thin solid line: id. to KNMI data; heavy solid line: values according to the Liss-Merlivat [1986] parametrization with $\Delta p\text{CO}_2 = 325 \mu\text{atm}$; heavy dashed line: id., according to Wanninkhof [1992].

indicated that the solution to the problem of the deviating k_w values had to be found elsewhere.

4 Concentration Gradients

Fig. 2 shows fluxes displaying a regular trend (within the scatter) to higher values for higher wind speeds, for both sets of data.

Fig. 3, however, shows that the relation between the (KNMI) CO_2 fluxes and $\Delta p\text{CO}_2$, measured by the Netherlands Institute for Sea Research, NIOZ, (Bakker *et al.*, submitted) is more or less random. The fluxes, calculated with the $\Delta p\text{CO}_2$ values of Bakker *et al.* (subm.) and the Liss-Merlivat [1986] and Wanninkhof [1992] parametrizations are also — again — far smaller than the e-c fluxes.

This state of affairs prompted us to take a closer look at the $\Delta p\text{CO}_2$ data.

To our surprise the $p\text{CO}_2$ data were clearly correlated with the tide (fig.4). This suggests the presence of — often pretty large — $p\text{CO}_2$ gradients in the MPN area. It is important to know the direction of these gradients because

- if the gradients are horizontal they can be considered as being caused by the *advection* and interplay of water masses and are only of local significance;
- if the gradients are vertical it may indicate that the water column can

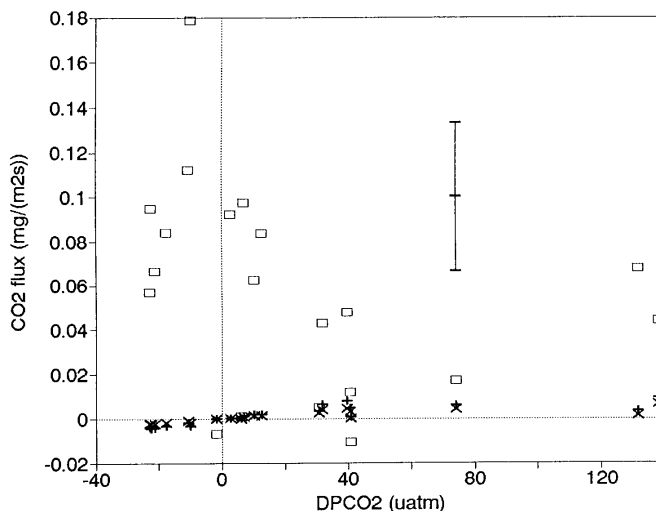


Figure 3: Relationship between $\Delta p\text{CO}_2$, as measured by the Netherlands Institute for Sea Research, NIOZ (Bakker et al., submitted) and CO_2 fluxes. \square : fluxes measured by KNMI using the e-c method; \times : fluxes according to Liss-Merlivat [1986]; $+$: fluxes according to Wanninkhof [1992]. $-$: rms error size of KNMI data (based on fig.2).

constitute a barrier for the gas flux, in contrast with an often made assumption.

The relative phase of concentration and tide can give us little information about the direction of the gradient, because the water displacement in the horizontal direction is more than 10000 times the vertical one, so a tiny horizontal gradient will fully mask a sizable vertical one.

Fig. 2 shows a fairly regular behavior of the CO_2 flux as a function of wind speed; a quadratic fit is close to optimal. Wanninkhof [1992] proposed a quadratic wind speed dependence of k_w (and the piecewise linear curve of Liss and Merlivat [1986] can be approximated in this way as well). Therefore, according to (1), $\Delta p\text{CO}_2$ should show only fairly small fluctuations, corresponding to the deviations of the data from the quadratic curve, for the whole period where we have flux measurements (with a strict quadratic wind speed dependence of both the flux and k_w it would have to be a constant). If we assume the concentration gradients to be purely horizontal, the average concentration differences for each and every run then have to average out to roughly the same values. Fig. 3 clearly shows that this is not the case.

If the CO_2 gradient should be mainly vertical, however, the almost constant CO_2 concentration we are looking for might be hidden deeper down, below the level where we sampled the water. This may be considered as being in line with the observation by van der Giessen et al. [1990] and de

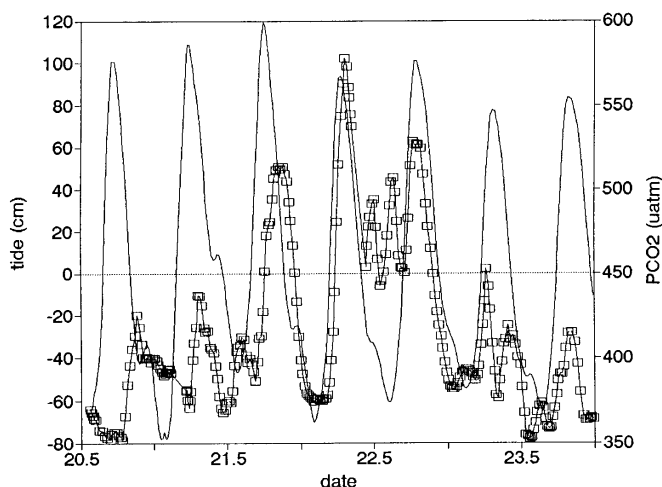


Figure 4: $p\text{CO}_2$ (\square , measured by NIOZ, Bakker et al., submitted) and tidal height (single solid line) as a function of time. The $p\text{CO}_2$ values have been filtered with a 2 h running average, to suppress short time fluctuations.

Ruijter et al. [1992] that density stratification is quite common near MPN. For the ASGASEX'93 period the values for the Rhine discharge are in the range average to low, which would have to result in weak stratification in the MPN area, according to de Ruijter et al. [1992]. Below the surface layer with partially mixed Rhine water, there would be the big mass of the water (95%) that entered the southern North Sea through the English Channel, the properties of which change only slowly in space and time. Unfortunately we measured no density profiles during the experiment, so we have no firm confirmation of any stratification.

During this conference Prof. Y. Toba introduced what he indicated as a "Downward Bursting Boundary Layer" (DBBL, Toba and Kawamura, [1995]), a surface layer with a depth of 3 to 7 times the wave height in which "... the value of the eddy diffusivity is much larger than the values estimated from the usual wall law ... The usual boundary layer of the upper ocean will begin underneath this special layer." If this layer is indeed as ubiquitous as the authors suggest, it could well be that the concentration gradient we have seen is at the underside of this DBBL in the area where the diffusion coefficient returns to its more usual values; the depth corresponds quite well with the range indicated by Toba and Kawamura [1995]. This would not only make our results of more general interest, but it would also explain the strength of the CO_2 flux, which is fairly high for a flux across even a weak pycnocline. Lacking data on the presence or absence of a DBBL we will continue our discussion in terms of stratification, keeping in mind that our surface layer could be interpreted as a possible DBBL.

What we hypothesize now is that an interface may exist between the surface water and the deeper water which impedes not only the vertical transport of heat and salt, but also that of CO₂. Of course the boundary between the two water layers is not strictly horizontal; slight tilts of this shallow pycnocline are sufficient to produce relationships between the concentrations and the tidal phases that agree with the data.

If we accept this point of view for the moment, we can compose a consistent picture. Essential is that the intermediate layer contains no important sources or sinks, or, to put it in a different way, that the transport through that layer and out into the air is too fast for any sources or sinks (that no doubt will be present) to have a significant effect. This is probably the case, due to the large values of the CO₂ fluxes (up to and over 0.1 mg/(m²s)). We have two main *flux barriers*: the lower one between the deep and the surface water and the upper one right at the surface. If we indicate the transfer velocities of these two barriers as, respectively, k_i for the lower one and k_s for the upper one and use k_w for the overall transfer velocity, eq. (1) can be replaced by (positive is upward)

$$F = k_i * \Delta pCO_{2_i} = k_s * \Delta pCO_{2_s} = k_w * \Delta pCO_{2_w} \quad (2)$$

with indices of the fugacities corresponding to those of the transfer velocities.

$$\Delta pCO_{2_i} + \Delta pCO_{2_s} = \Delta pCO_{2_w} \quad (3)$$

so ($\Delta pCO_2 = F/k$)

$$\frac{1}{k_w} = \frac{1}{k_i} + \frac{1}{k_s} \quad (4)$$

If under these circumstances we should — erroneously — use ΔpCO_{2_s} instead of the overall fugacity difference ΔpCO_{2_w} (for ΔpCO_2 in (1)), together with a correct value for the flux F , we end up with a value for k_w which is too high, as found before.

The surface layer will be most shallow at low wind speeds. According to our suppositions the deep water has the highest pCO₂ and our measurements were made at a depth slightly above the internal boundary, so we should find the highest pCO₂ values at the lowest wind speeds. In this way we can find an approximation to the deep concentration: because the CO₂ fluxes during ASGASEX'93 were in general from sea to air, the highest concentration at wind speed zero should be the best available approximation to the deep concentration. In fig.5 we have plotted ΔpCO_2 as a function of wind speed. The highest values are indeed at low wind speeds and by extrapolating to wind speed zero we found a maximum concentration difference of

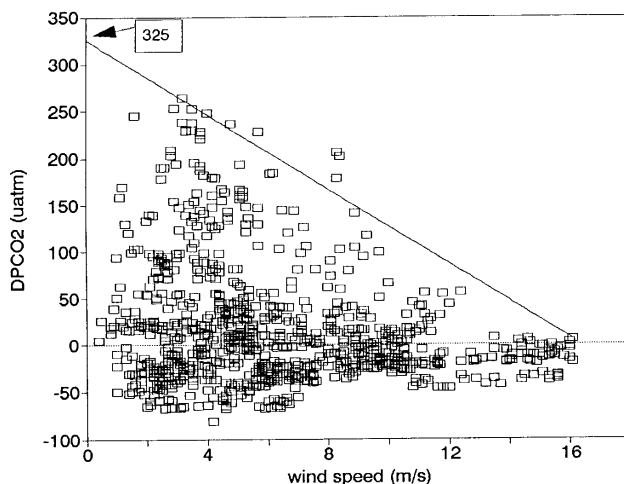


Figure 5: $\Delta p\text{CO}_2$, measured by NIOZ (Bakker *et al.*, submitted), as a function of wind speed.

about $325 \mu\text{atm}$. According to our conceptual model this should be the best available approximation to the concentration difference driving the fluxes. With this value and values for k_w , according to *Liss and Merlivat* [1986] and *Wanninkhof* [1992] we calculated the two remaining curves in fig.3. There still is a difference with the measurements, but it is now in a range where we can attribute it either to experimental inaccuracy, to the fact that the CO_2 flux in coastal waters may be higher than in the world oceans and/or to the fact that we have only a crude approximation to the driving concentration difference.

5 Sign of the Gradient

There still is an enigma left, however. Fig.3 shows that not only the size of the measured $\Delta p\text{CO}_2$ values, but also the sign bears no relationship with the fluxes. That would mean that in some cases we have a *counter-gradient flux* from the surface layer into the air.

To explain this phenomenon one could consider that the *footprint* for the flux is at a certain distance from MPN, so there may be little connection between the flux, originating at the footprint, and the local $\Delta p\text{CO}_2$ value. This explanation doesn't appear very probable as the single cause, though: According to *Schuepp et al.* [1992] the maximum of the footprint should be at a distance of some 60 to 100 meter and the distance to the point where 80% of the flux has been produced is about 1.6 km [*Schuepp et al.*, 1990]. With no data away from the platform, we made an (over-) estimate of the gradient by assuming the concentration change with time to be due

solely to a horizontal gradient (this is contrary to our earlier argument, but we only want to find the maximum possible gradient now) and then divided the concentration change by the current speed during the same period. With this procedure the horizontal pCO₂ gradient for the KNMI runs with negative $\Delta p\text{CO}_2$ gave both high (70 and 90 $\mu\text{atm}/\text{km}$) and low (2.4 and 3.3 $\mu\text{atm}/\text{km}$) maximum values for separate runs; the latter ones are too small to explain a concentration difference of some 20 μatm , needed to make $\Delta p\text{CO}_2$ at least zero.

This suggests that there indeed may be a counter gradient transport mechanism at work. A process that comes to mind in this respect is that of (dirty) air bubbles, rotating in Langmuir circulations and scavenging CO₂ from the water. The scavenging takes place in accordance with the conditions at the bubble surface, which may be slightly different from those at the water surface. When the bubbles surface, burst and add their contents to the atmosphere these contents would still reflect the conditions at the bubble surface when the bubble was some distance below the water surface.

Another possible explanation might be that the pCO₂ value in the upper part of the surface layer of the water is higher than the one lower down, due to local CO₂ production, possibly of biological origin. Formulae (2) - (4) are not valid anymore in this situation. In this option the pCO₂ values measured by NIOZ at 5 m depth have no connection with the flux across the water surface, which would be different from the one lower down. Taking the water surface as the most important barrier for the CO₂ flux in the air, the $\Delta p\text{CO}_2$ values across that surface regulate the flux in the air (which we measured), whereas the pCO₂ differences across the surface layer of the water cause a different CO₂ flux across that layer (which we didn't measure). A problem here is that a pCO₂ gradient across the surface layer would imply that this layer constitutes an significant barrier for CO₂, which is again at odds with the supposed overwhelming resistance of the surface.

Biological processes probably are important. As stated in the caption of fig.4, the pCO₂ values used in that figure are averaged ones. The difference between the initial and averaged data showed a daily rythm, with large fluctuating values in the early morning, tapering off to much lower amplitudes at night.

6 Conclusion

We have hypothesized a conceptual model that may explain to a large extent a problem that has been around for quite a number of years and solve a controversy that has blocked the use of a potentially very useful method for the study of the mechanisms of air-sea gas transfer. It should be stressed, though, that the ASGASEX '93 data are insufficient for a well-founded decision about the correctness of the model. To remedy this situation (and for several other purposes) we have planned another ASGASEX experiment at MPN in '96, called *ASGAMAGE*, because it is to be performed under the

aegis of the MAGE (= Marine Aerosol and Gas Exchange) subgroup of IGAC. One of the many things we will try to measure on that occasion is pCO₂ at two levels simultaneously, at least one of which will be varied over the full length of the water column.

Acknowledgements

ASGASEX was a corporate effort of a large number of people. We would like to thank especially Mr. J. A. M. Goossens and Mr. J. van der Horn of Rijkswaterstaat who, in their function as platform managers, not only took care that all basic systems of the platform were functioning, but also actively supported the smooth flow of the experiment itself. We are extremely grateful to D. C. E. Bakker of the Netherlands Institute for Sea Research, Den Burg, the Netherlands who provided the CO₂ concentration data without which this paper could not have been written. We would also like to thank her colleagues H. J. W. de Baar and H. de Wilde and D. K. Woolf of Southampton University, UK, who indicated some alternatives to our initial ideas.

References

- Bakker, D. C. E., H. J. W. de Baar and A. A. J. Majoor, submitted: Dissolved carbon dioxide in Dutch coastal waters: Hydrography and air-sea exchange. An ASGASEX paper
- Broecker, W. S., J. R. Ledwell, T. Takahashi, R. Weiss, L. Merlivat, L. Memery, Ts.-H. Peng, B. Jähne and K. O. Münnich, Isotopic versus micrometeorological ocean CO₂ fluxes: a serious conflict. *J. Geophys. Res.* 91, C9, 10517-0527, 1986
- Giessen, A. van der, W. P. M. de Ruijter and J. C. Borst, Three dimensional current structure in the Dutch coastal zone. *Neth. J. Sea Research* 25, 45-55, 1990
- Liss P. S. and L. Merlivat, Air-sea gas exchange rates: Introduction and synthesis. In: *The role of air-sea exchange in geochemical cycling*, ed. P. Buat-Menard, Reidel, 1986
- Ruijter, W. P. M. de, A. van der Giessen and F. C. Groenendijk, Current and density structure in the Netherlands coastal zone. In: *Dynamics and exchanges in estuaries and the coastal zone*, D. Prandle, ed. American Geophysical Union, Coastal and Estuarine Sciences. pp. 529-550, 1992
- Schuepp, P. H., M. I. Leclerc, J. I. Macpherson and R. L. Desjardins, Footprint prediction of scalar fluxes from analytical solutions of the diffusion equation, *Bound. Layer Meteorology* 50, 355-373, 1990
- Schuepp, P. H., J. I. Macpherson and R. L. Desjardins, Adjustment of footprint correction for airborne flux mapping over the FIFE site. *J. Geophys. Res.* 97, D17, 18455-18466, 1992
- Smith, S. D. and E. P. Jones, Dry-air boundary conditions for correction of eddy flux measurements. *Bound. Layer Meteorology* 17, 375-379, 1979
- Toba, Y. and H. Kawamura, Wind-wave coupled Downward-Bursting Boundary Layer below the sea surface — in relation to penetration depth of bubble clouds, *This volume*

- Wanninkhof, R., Relationship between wind speed and gas exchange over the ocean. *J. Geophys. Res.* 97, C5, 7373-7382, 1992
- Webb, E. K., G. J. Pearman and R. Leuning, Correction of flux measurements for density effects due to heat and water vapour transfer. *Q. J. R. Meteorol. Soc.* 106, 85-100, 1980

The Influence of Air-Sea-Exchange on the Partitioning of N-Species during Transport over Sea

E. Plate, T. Stahlschmidt, M. Schulz, and W. Dannecker

Universität Hamburg, Institut für Anorganische und Angewandte Chemie,
Martin-Luther-King-Platz 6, D - 20146 Hamburg, Germany

Abstract

Air-sea-exchange in the marine boundary layer influences the balance between the different nitrogen species. The nitrogen input into the sea depends on the actual evolution of the partitioning among different species. To investigate the splitting of nitrogen among the different species in the marine atmosphere, air samples were taken onboard a research vessel in the German bight and at a coastal station in Schleswig-Holstein, using the Lagrangian approach. HNO_3 , NH_3 , NO_3^- , SO_4^{2-} , NH_4^+ and Na^+ were determined using the denuder difference method. Only samples taken during easterly (offshore) and westerly (onshore) wind conditions are evaluated. The change in composition between the two stations was found to be significant for NH_3 and Na^+ . The effects leading to the evolution of the concentrations of the different nitrogen species are discussed. Air-sea-exchange velocities of 2-30 cm/s have been estimated using a logarithmic boundary layer structure. The evaluation of the onshore blowing conditions revealed that the coastal waters, the wadden sea and eventually also the salt marshes provide a significant source of NH_3 .

1 Introduction

The Nitrogen pool in the marine boundary layer is splitted among several gaseous and particulate species. The different reactivity and air-sea-exchange characteristics of N-species in the marine atmosphere determine their lifetime and hence their dispersion on a regional and global scale. Air-sea-exchange in the marine boundary layer influences the balance between the different species. It has been suspected that the deposition of the highly soluble gases NH_3 and HNO_3 to the sea surface causes with time the complete evaporation of the *ammonium nitrate* particles in the marine atmosphere [Otley and Harrison, 1992]. However, for both gases significant sources exist in the marine atmosphere. NH_3 may be emitted from seawater and HNO_3 may be formed by oxidation of nitrogen oxides. The nitrogen input into the sea depends on the actual evolution of the partitioning among different species. To provide better estimates of nitrogen input we have been investigating the splitting of nitrogen among the different species in the marine atmosphere. The experiment was performed within the German

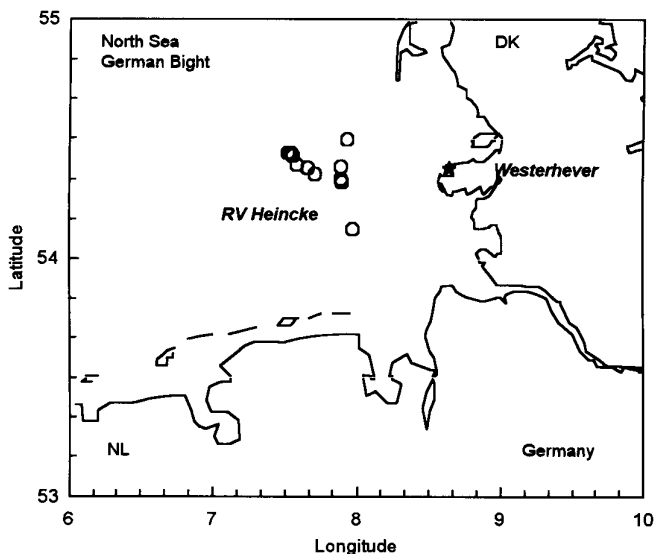


Figure 1: Positions of the ship during easterly and westerly wind and that of the coastal station near Westerhever lighthouse.

KUSTOS project, where coastal fluxes of matter and nutrients in the German Bight are to be investigated.

2 Experimental

Ambient air samples were taken onboard the research vessel Heincke in the German Bight and at a coastal station close to the Westerhever lighthouse on the Eiderstedt peninsula during the first experiment between 27.7. and 19.8.1994. The research vessel was kept close to a submersed drifting sail between $54^{\circ}31' \text{ N}/7^{\circ}18' \text{ E}$ and $54^{\circ}12' \text{ N}/8^{\circ}7' \text{ E}$ about 30 to 110 km to the West of Westerhever ($54^{\circ}23' \text{ N}/8^{\circ}25' \text{ E}$). Taking into account actual wind-speed, winddirection and position of the ship the time of sampling was coordinated between the two stations and delayed at the respective lee station. Under the assumption of horizontal homogeneity, the same air mass can be investigated twice according to a Lagrangian approach.

At both stations the gases HNO_3 and NH_3 and the particulate species NO_3^- , SO_4^{2-} , NH_4^+ and Na^+ were determined separately using the *denuder difference method* similar to that described by Shaw *et al.* [1982], Harrison and Kitto [1990] and Behlen [1995]. The denuder difference method consists of two filter packs running in parallel. One of the filter packs is preceded by two annular denuders to remove gaseous compounds (HNO_3 and NH_3) from the air stream. In this arrangement one filter pack collects only par-

ticulate species, while the other collects the sum of gaseous and particulate compounds. From the difference the amount of gaseous nitric acid and ammonia can be calculated. The annular denuder system is comprised of one coated with citric acid to remove NH_3 , and a second coated with magnesium oxide to remove HNO_3 . The filter packs consist of three filters in series. The air stream passes first a Teflon-filter (SATORIUS, pore width $0.45 \mu\text{m}$) to hold back particulate matter. Gaseous compounds of the air and volatilized matter from the Teflon-filter adsorb on the following two backup filters which have been a nylon filter (SATORIUS, pore width $0.45 \mu\text{m}$) for HNO_3 and a phosphorous acid impregnated paper filter (WHATMAN 41) for NH_3 . After sampling the Teflon- and paper filters are extracted in distilled water. The acids are stripped from the nylon filters by a $\text{CO}_3^{2-}/\text{HCO}_3^-$ buffer solution (2.5 mM/0.75 mM). All extractions were carried out for 45 minutes in an ultrasonic bath. The Teflon- and nylon filter extracts were analysed for NO_3^- and SO_4^{2-} with an ion chromatograph. Na^+ was determined via flame atomic absorption spectroscopy. All extracts, including the nylon filter ones, as suggested by Masia *et al.* [1994], were analysed for NH_4^+ using a gas diffusion method in a flow injection system. Non seasalt sulphate (NS-SO_4^{2-}) was calculated based on the sodium to sulphate ratio in seawater.

3 Results and Discussion

In the course of the experiment 24 12-hourly samples were taken at both stations. Not all of them were ideal to be evaluated according to a Lagrangian approach. Especially south-westerly winds are associated with large lateral concentration gradients, since air arriving at Westerhever is travelling over the coastal land areas while at sea the air might experience a considerable fetch over open sea waters.

Two subsets of sample pairs have been selected here. Easterly winds blowing offshore are known to bring polluted continental air masses to the German Bight. Westerly and northwesterly winds on the other hand are associated with clean air masses and a fetch of several hundred kilometres over the North Sea. The selection of cases is documented in Table 1. Air mass travel time has been calculated from actual wind speed and direction as well as positions of the ship and the coastal station.

Meteorological conditions varied little with moderate winds and only two drizzle rain events and one thunderstorm. Excluding the rainy cases did not change the overall picture. During easterly winds humidity increases from coast to sea as expected. The positive air/sea temperature gradient is a little more pronounced since continental warm air masses were advected over relatively cooler waters. Radiosoundings during easterly winds showed a stable boundary layer with heights ranging from 90 - 450 m [Michaelsen, 1995].

The mean concentrations of the gaseous and particulate N-species, sodium and NS-sulphate for the two sample subsets are shown in Table 2. For com-

Table 1: Overview on ambient air sampling during the KUSTOS central experiment 1994 (HEI: RV "Heincke", WHV: Lighthouse Westerhever).

FS HEINCKE Sampling periods (WHV delayed resp. preceded 1-3 hours)				air mass	HEI		HEI	WHV	HEI	
				travel-time	T air	T sea	Relat. Humid.	Relat. Humid.	Wind direction	Wind speed
				[h]	[°C]	[°C]	[%]	[%]	[°]	[m/s]
Easterly winds				lee						
28.07.	08:33	-	20:00	2.4	21.3	18.9	92.6	55.6	111.3	6.6
30.07.	23:00	- 31.07.	08:06	2.6	21.1	19.7	93.8	96.5	95.3	5.3
03.08.	09:56	-	20:07	3.5	21.5	20.4	78.8	60.5	72.5	4.9
03.08.	20:26	- 04.08.	08:05	2.5	21.5	20.5	83.5	87.5	111.0	6.7
04.08.	08:25	-	20:00	2.8	23.4	20.7	78.6	45.4	112.4	6.3
10.08.	20:18	- 11.08.	08:10	3.5	19.2	19.9	88.4	84.1	96.0	7.2
Westerly winds				lee						
29.07.	08:34	-	19:52	1.0	19.0	18.9	83.4	75.7	307.6	5.2
05.08.	08:26	-	20:42	4.0	22.0	20.6	87.4	71.5	273.8	5.1
05.08.	21:00	- 06.08.	08:35	2.6	20.1	20.6	84.3	87.2	298.2	7.4
06.08.	08:55	-	20:10	1.9	19.7	20.6	77.7	71.3	313.8	8.2
08.08.	20:06	- 09.08.	08:10	1.5	18.5	20.5	77.4	79.7	312.2	8.0
Average conditions										
westerly winds				2.2	19.8	20.2	82.1	77.1	301.1	6.8
easterly winds				2.9	21.3	20.0	86.0	71.6	99.8	6.2

parison the data published by *Ottley and Harrison* [1992] are incorporated in the table. From results of seven NERC-cruises in the southern North Sea they derived characteristic air mass concentrations for different transport sectors. The comparison shows that our concentrations of NH_4^+ , HNO_3 , NO_3^- , Na^+ and NS-SO_4^{2-} found for easterly winds are just slightly lower than those concentrations associated to European air masses by *Ottley and Harrison* [1992]. In westerly winds, with a longer fetch over the North Sea, the NH_4^+ - concentration resembles that of English origin. HNO_3 and NO_3^- - concentrations are lower in our samples, possibly because the NERC-samples were taken closer to the British isles. Possibly due to slow oxidation of SO_2 during transport over sea from England and marine emissions of biogenic sulphur in summer our samples show slightly increased values of NS-SO_4^{2-} .

The largest discrepancy is found for NH_3 . Our *ammonia* concentrations during westerly winds at sea in the German bight are almost identical to those of the air masses characterised as of marine origin by the above mentioned authors. All other ammonia concentrations are considerably enhanced. The large concentration at the coast in offshore blowing easterly winds is due to large ammonia sources nearby due to intensive farming in the coastal area. However, the high concentrations at sea in offshore winds

Table 2: Mean concentrations of gaseous and particulate N-species, sodium and NS-sulphate determined with the denuder difference method. Significant differences according to a pairwise t-test ($\alpha = 0.05$) between both stations are printed in bold letters.

	NH ₃	NH ₄ ⁺	HNO ₃	NO ₃ ⁻	Na ⁺	NS-SO ₄ ²⁻
	[nmol/m ³]					
Easterly wind (N=6)						
Westerhever (windward)	560.6	231.4	44.6	96.9	16.5	62.4
RV "Heincke" (lee)	98.0	252.5	41.2	114.9	49.9	62.9
West-north-westerly wind (N=5)						
RV "Heincke" (windward)	12.0	117.7	28.0	46.0	85.6	57.6
Westerhever (lee)	102.9	125.1	30.0	52.4	60.1	65.0
Europe*	29.4	245.0	48.3	138.2		69.0
England*	30.0	111.7	39.4	68.5		42.7
Scotland*	18.2	40.6	38.3	26.9		19.4
Marine*	9.4	24.4	10.6	22.9		23.0

*Ottley and Harrison, [1992]

and in Westerhever during onshore-wind conditions are remarkable and not that easy to explain.

The results show that at ground level more nitrogen in the coastal area is present as ammonia and ammonium than as nitrate plus nitric acid. The largest differences between the coastal and the seaward station are observed for ammonia. This lets us speculate that the air-sea-exchange of ammonia is of major importance. Ammonium, nitrate and nitric acid change only little from one station to the other.

For testing the statistical significance of the change in composition of the air masses between the two stations a pairwise t-test was conducted. This test can be applied here since each coastal measurement is related directly to one in the open sea (Table 3). For 6 respectively 5 cases a significant difference is found only for ammonia and sodium concentrations.

We believe three processes to be of major importance for the evolution of the concentrations of the different nitrogen species. Because of the large effect observed with regard to the ammonia concentrations the discussion will center on this effect.

3.1 Intensive Air-Sea Exchange of Ammonia in Coastal Marine Areas

As has been calculated recently by *Asman et al.* [1994] the net air-sea flux of ammonia can be both ways across the air-sea interface in the North Sea. Using the formulae given in that paper (1) we have calculated from sea water ammonium concentration [NH_x], pH and salinity - measured by *Brockmann et al.* [1995] during the same cruise - the corresponding equilibrium ambient air concentrations c_{eq} (Table 3).

Table 3: Parameters relevant to the two major processes involved in ammonia partitioning among seawater, gas and aerosol in the marine atmosphere.

		Westerly winds		Easterly winds	
		HEI windward	WHV lee	WHV windward	HEI lee
Ambient air conditions					
Air temperature	[°C]	19.8			21.3
Relative humidity	[%]	82.1	77.6	71.6	86.0
NH ₃ Concentration ±standard deviation	[nmol/m ³]	12.0 ± 16	102.9 ± 86	560.6 ± 169	98.0 ± 35
HNO ₃ Concentration ±standard deviation		28.0 ± 34	30.0 ± 25	44.6 ± 36	41.2 ± 29
NH₃-emission from seawater					
NH _x concentration seawater	[μmol/l]	1.3			1.2
pH seawater		8.4			8.4
Equilibrium surface air NH ₃ concentration ceq	[nmol/m ³]	45.3			44.7
Formation/evaporation of NH₄NO₃					
NH ₄ NO ₃ equilibrium constant	[ppb ²]	3.5	4.8	9.2	3.5
Measured concentration product		0.2	1.8	14.6	2.4

$$c_{eq} = \frac{M_{NH_3}[NH_x]}{RTH_{NH_3} \left[\frac{1}{\gamma_{NH_3}} + \frac{10^{-pH}}{\gamma_{NH_4}K_{NH_4}} \right]} \quad (1)$$

M_{NH_3} is the molecular mass of NH₃, R the gas constant, H_{NH_3} Henry's law constant for NH₃, γ_{NH_3} and γ_{NH_4} activity coefficients for NH₃ and NH₄ in seawater and K_{NH_4} the dissociation constant for NH₄⁺.

Results show that in westerly winds in the open sea emission from the sea or at least equilibrium taking into account the measured variability. However, the ammonia concentrations in Westerhever observed during westerly winds are well above the equilibrium concentration at sea. This indicates that the wadden sea and the salt marshes being between research vessel and the lighthouse sampling position act as a significant source for ammonia. There is no other process that could explain this increase in concentration.

In easterly winds the initial high ammonia concentration at the coast fall to almost the same value as that observed for onshore conditions in Westerhever. We might conclude that ammonia air concentrations are brought

into equilibrium with the sea water concentration of the coastal wadden sea waters. Of course, deposition of ammonia is needed to explain this feature. Although the equilibrium ammonia concentration calculated for the seaward station is even below the measured ammonia concentration, higher sea water concentrations are to be expected in the fetch area closer to the coast.

3.2 Particle Formation and Evaporation of NH_4NO_3

Depending on concentration product, humidity and temperature ammonium nitrate may evaporate or recombine to aerosol particles [Stelson and Seinfeld, 1982]. If one assumes thermodynamic equilibrium the concentration product of the gases HNO_3 and NH_3 can be predicted [Hamer and Wu, 1972]. For simplicity we have calculated the equilibrium constant for pure ammonium nitrate particles (Table 3). It shows that in easterly winds the formation of ammonium nitrate is still possible at the coastal site. The small increase of $20 \text{ nmol/m}^3 \text{ NH}_4\text{NO}_3$ and the small decrease in HNO_3 concentration (3.4 nmol/m^3) reflects this particle formation process (Table 2). It should be remarked that HNO_3 is steadily produced from nitrogen oxides, compensating for losses.

However in open sea conditions at the research vessel the measured concentration product reaches the equilibrium constant. Further deposition of ammonia, as indicated above, would force the ammonium nitrate particles to evaporate.

More pronounced departures from equilibrium are observed for westerly winds. In the large fetch over the North Sea air has probably been depleted from ammonia. Ammonium nitrate had then evaporated when arriving in the German Bight. Our impactor data confirm the absence of fine nitrate in westerly wind conditions. The ionic balance shows that the ammonium is attached to NS-sulphate, which is not evaporating. Ammonium concentrations might therefore stay almost as high as in easterly winds.

3.3 Vertical Mixing of NH_3 in the Marine Boundary Layer

Any quantitative estimate of the input of ammonia into coastal waters from the concentration decrease in offshore conditions is difficult because of possible mixing processes within the marine boundary layer and entrainment of free tropospheric air. However we have attempted to make some maximum assumptions for offshore blowing winds.

Dilution by entrainment of free tropospheric air into the boundary layer is probably insignificant since we found identical concentrations of NS-sulphate aerosol. Since these fine particles are very slowly depositing over sea they serve as a good tracer for other dilution processes. If we disregard advective interferences then the boundary layer structure remains as the main factor.

As mentioned above a stable boundary layer was observed with heights of less than 500 m which of course varied from case to case. Although turbulent mixing should be complete after 3 hours of transport as in our case, stable stratification could have limited the exchange to the first 100 m. We therefore assume two possible boundary heights in further calculations (100 and 500 m).

The budget of ammonia in the offshore transported air mass could be closed if we know the vertical profile over land and over sea. However, very few observations exist of vertical ammonia profiles. The high emissions over land coupled with a high deposition velocity of the reactive and soluble ammonia let us believe, that a considerable vertical concentration gradient exists over the coastal station. With the assumption of a logarithmic concentration profile and a certain top of the boundary layer concentrations ($c_{0,TBL}$) we can calculate from the boundary layer height z_H , and our measured coastal surface concentration ($c_{0,10m} = 560 \text{ nmol/m}^3$) the mean boundary layer concentration ($c_{0,BL}$). We have chosen two boundary layer top concentrations: First we assume the ammonia concentrations might have been as low as for westerly winds in the open sea. Secondly we assume that the concentration found at the research vessel reflects a well mixed profile and thus also provide information on the concentration at the top of the boundary layer. The top boundary layer concentration must have been at least 100 nmol/m^3 .

Over sea we can assume that a boundary layer is rather well mixed ($c_{10m} = c_{BL}$).

The removal velocities have then been calculated assuming an exponential decrease in concentration in the whole boundary layer from the coastal starting point with $c = c_{0,BL}$ to the arrival at the research vessel with a concentration equal to c_{BL} (2):

$$v = \frac{z_H}{\Delta t} \cdot \ln \left(\frac{c_{BL}}{c_{0,BL}} \right) \quad (2)$$

The results are to be found in Table 4. With our assumptions so far a large removal velocity of 2-30 cm/s is calculated. This suggests that dilution can not be the only reason for the large decrease in ammonia in offshore winds. However the large removal velocities calculated exceed momentum transfer rates and can thus not be taken as pure air-sea-exchange rates. So far our preliminary data analysis can not deliver much more insight. The large decrease in concentration however challenges further modeling efforts for its understanding.

4 Conclusions

Changes in ambient air composition with regard to nitrogen species have been measured during transport over sea. While major components of the

Table 4: Estimate of deposition velocity (v) for ammonia for different MBL structures, offshore winds and surface concentrations as in table 2.

Assumptions on BL structure Top conc.		Mean conc.	Removal velocity
$c_{0,TBL}$ [nmol/m ³]	z_H [m]	$c_{0,BL}$ [nmol/m ³]	v [cm/s]
12	500	107	4,2
100	500	180	29,1
12	100	129	2,6
100	100	198	6,7

aerosol like non seasalt sulphate and ammonium nitrate did not change significantly, a large effect was observed for ammonia. The large removal of ammonia in offshore blowing winds was attributed to a significant deposition of this component. Air-sea-exchange velocities of 2-30 cm/s have been estimated using a logarithmic boundary layer structure. Further quantification by modelling and additional data on vertical profiles of ammonia in the air is needed. The evaluation of the onshore blowing conditions revealed that the coastal waters, the wadden sea and also the salt marshes provide a significant source of ammonia.

Acknowledgements

This work was funded within the German BMBF-project grant No. 03F0111A, KUSTOS (Küstennahe Stoff- und Energieflüsse). We would like to thank Andreas Behlen for providing us with instrumentation and competent advise in utilizing the denuder difference method. Thanks are also due to Andreas Rebers and Holger Gerwig for help in taking the samples. We have to thank Uwe Brockmann and his co-workers for providing the sea water data and Kirsten Michaelsen having performed and analysed the radiosondings, allowing thus a first analysis of our data.

References

- Asman, W. A. H., R. M. Harrison, and O. J. Ottley, Estimation of the net air-sea flux of ammonia over the southern bight of the North Sea, *Atmos. Environ.*, 28, 3647-3654, 1994
- Behlen, A., dissertation, university of Hamburg, in preparation, 1995
- Brockmann, U., A. Pfeiffer, T. Raabe, and S. Rick, personal communication, 1995
- Hamer, W. J., and Y.-C. Wu, Osmotic coefficients and mean activity coefficients of uni-univalent electrolytes in water at 25 °C, *J. Phys. Chem. Ref. Data*, 1, 1047-1099, 1972

- Harrison, R. M., and A.-M. N. Kitto, Field Intercomparison of Filter Pack and Denuder Sampling Methods for Reactive Gaseous and Particulate Pollutants, *Atmos. Environ.*, 24A, 2633-2640, 1990
- Masia, P., V. Di Palo, and M. Possanzini, Uptake of ammonia by nylon filters in filter pack systems, *Atmos. Environ.*, 28, 365-366, 1994
- Michaelsen, K., personal communication, 1995
- Ottley, C. J., and R. M. Harrison, The spatial distribution and particle size of some inorganic nitrogen, sulphur and chlorine species over the North Sea, *Atmos. Environ.*, 26A, 1689-1699, 1992
- Shaw, R. W., R. K. Stevens, J. Bowermaster, J. W. Tesch and E. Tew, Measurements of atmospheric nitrate and nitric acid: The denuder difference experiment, *Atmos. Environ.*, 16, 845-853, 1982
- Stelson, A. W., and J. H. Seinfeld, Relative humidity and temperature dependence of the ammonium nitrate dissociation constant, *Atmos. Environ.*, 16, 983-992, 1982

The Potential of Vertical Profiling of Particulate Nitrogen Species to Investigate Air-Sea-Exchange of Nitrogen Species

M. Schulz, E. Plate, T. Stahlschmidt, and W. Dannecker

Universität Hamburg, Institut für Anorganische und Angewandte Chemie,
Martin-Luther-King-Platz 6, D - 20146 Hamburg, Germany

Abstract

Air-sea-exchange of *nitrogen gases* such as ammonia and nitric acid may be influenced by the presence and vertical distribution of aerosol particles. Filter pack sampling was employed to measure vertical concentration profiles of HNO_3 and HCl and NO_3^- , SO_4^{2-} , Cl^- , NH_4^+ and Na^+ . The profiles were measured at four heights between 2.5 and 10 m at a meteorological tower 1 km offshore near the Danish island of Lolland. Coarse aerosol profiles in easterly winds showed to be significantly kinked. The complex profile in these conditions with a concentration minimum at 5 m is explained by an evolving internal marine boundary layer. The correlation of the coarse nitrate profile with that of sea salt supports the hypothesis of a rapid transfer of nitric acid and/or ammonium nitrate to sea salt particles.

1 Introduction

Vertical concentration gradients in the atmosphere close to the air-sea interface are the result of limited turbulent mixing processes and sinks or sources within or at the border of the boundary layer. The air to sea transfer of a soluble gas like nitric acid may be enhanced if chemical reactions in the boundary layer remove it from the column. One of the processes involved is the reaction of *nitric acid* with sodium chloride to form coarse particulate nitrate. The uptake of nitric acid by sea salt droplets is enhanced due to its good solubility. This provides an additional downward flux of nitrate due to the high settling velocity of coarser particles. The higher sea salt content in the lower boundary layer may increase the removal rate of nitric acid there. This increases the concentration gradient in the boundary layer with the consequence of higher turbulent fluxes throughout the boundary layer. A second process involves the evaporation of NH_4NO_3 if nitric acid is removed from the gas phase [Stelson and Seinfeld, 1982]. Since thermodynamic equilibrium over the sea often favours this evaporation, it might be enhanced close to the sea surface where all nitric acid is removed either by deposition or reaction with sea salt [Ottley and Harrison, 1992]. The slow deposition of fine particulate NH_4NO_3 would indirectly be enhanced if it is transformed to nitric acid or further to coarser aerosol particles. However,

higher humidity near the sea surface stabilise NH_4NO_3 particles, since their molality decreases upon uptake of water.

It is not clear to what extent the above mentioned processes affect the deposition of nitrogen. However it is probable that the interaction between gases and particles affects the vertical concentration profiles of both. One major difficulty in investigating these profiles has been to obtain suitable experimental sites in marine conditions. Using towers at sea an undisturbed profile may be measured. The major purpose of this work was to provide new experimental data on marine vertical profiles of particulate nitrogen species during joint field experiments (ASEPS 1 and 2) in Lolland, Denmark, where micrometeorological and other chemical data were collected by other groups.

2 Experimental

Ambient air samples were taken during two experiments in October/November 1994 and April/May 1995. The micrometeorological tower used for these experiments has been built by the Risø National Laboratory and is located to the north west of the Danish island of Lolland at $54^{\circ}58' \text{N}/11^{\circ}9' \text{E}$ about 1 km from the coast.

The gases HNO_3 and HCl and the particulate species NO_3^- , SO_4^{2-} , Cl^- , NH_4^+ and Na^+ were collected with 4 identical filter packs made of PTFE at heights of 2.5, 5, 7 and 10 m. The filter packs consisted of three filters in series. The air stream passes first a Teflon filter (SATORIUS, pore diameter $5 \mu\text{m}$) to hold back particulate matter. The relatively large pore size was chosen to reduce filter resistance and increase the sampling volume. Gaseous compounds of the air and volatilised matter from the Teflon filter adsorb on the following two backup filters which were a prewashed nylon filter (SATORIUS, 50 mm diameter, pore width $0.45 \mu\text{m}$) for HNO_3 and HCl and a phosphorous acid impregnated paper filter (WHATMAN 41) for NH_3 . After sampling the Teflon and paper filters are extracted in distilled water. The acids are stripped from the nylon filters by a $\text{CO}_3^{2-}/\text{HCO}_3^-$ buffer solution (2.5 mM/0.75 mM). All extractions were carried out for 45 minutes in an ultrasonic bath. The Teflon and nylon filter extracts were analysed for Cl^- , NO_3^- and SO_4^{2-} with an ion chromatograph. Na^+ was determined by flame atomic absorption spectroscopy.

The filter packs were all attached to one low volume pump ensuring maximum coherence of flow rates of ca. $0.7 \text{ m}^3/\text{h}$ for each filter pack. Flow rates for each filter pack were checked, differed by 2% and were subsequently corrected. The overall pumped air volume was registered with a flow meter. Sampling intervals lasted from 5 to 24 hours. This mainly depended on whether a boat trip could be organised to the mast. In combination with the analytical precision this collection procedure results in ambient air detection limits of less than $1 \text{ nmol}/\text{m}^3$ for the major ions analysed here. To increase the accuracy of the measured profiles, related samples were anal-

used strictly in sequence. Full procedural field blanks showed no value above the detection limit.

After the first experiment, concern was raised that the inlet conditions for slightly tilted samplers might give rise to considerable bias between the filter packs. A special experiment in Hamburg with 4 filter packs being directed at different angles away and toward the wind resulted in an error of only 6% for the individual sodium determination. However, to improve sampler performance we have attached during the second experiment a downward facing cylinder of 10 cm length to exclude very coarse particles and fog droplets. In addition two extra samplers have been mounted during the second experiment at 2.5 and 10 m with quasi-isokinetic inlets facing into the wind. These were operated with a separate pump at the tower, resulting in slightly lower flow rates of 0.35 m³/h.

3 Results and Discussion

Sampling could only be performed during moderate wind conditions. While all samples from the 1994 experiment are incorporated, not all samples from the experiment of 1995 have been analysed yet. Preference in the analysis from the latter experiment was given to samples with a larger fetch and steady wind conditions. Sampling conditions and mean concentrations for all analysed sampling periods are given in Table 1. As a first attempt profiles were summarised by calculating the regression coefficient of concentration versus height for each profile. Averages of these values are also found in Table 1.

The use of 5 µm pore diameter Teflon filters appeared to allow for a rough estimate of the ratio of coarse to fine particles. Since we did not find in previous experiments sulphate on the nylon filters we can assume that the very fine sulphate particles could pass the Teflon filter and were collected on the subsequent nylon filter. For nitrate we have to consider additional sources of nitrate on the nylon filter. Nitric acid may be derived directly from the air or might result from evaporating ammonium nitrate already collected on the Teflon filter. Conditions for the latter artefact are not very likely to occur with our low flow rates and the high humidities present [see also *Harrison and Kitto*, 1990]. However no possibility exists to differentiate between nitric acid and fine particulate nitrate. Although nitric acid might have added to the nitrate found on the nylon filter we find a higher ratio of coarse nitrate to "fine" nitrate compared to sulphate. This expresses the generally coarser nitrate size distribution in the marine environment.

The reduced collection efficiency of the 5 µm Teflon filter for coarse particles is supported by the concentrations found with the isokinetic samplers. Here the fraction being collected on the nylon filter is larger than in the simultaneous ordinary filter pack samples both for nitrate and sulphate. This is readily explained by the reduced flow rates and thus a larger cut-off for particle collection on the Teflon filter.

Table 1: Overview on filter pack sampling during ASEPS 1 and 2.

		Mean ± Standard error
(N=23)		
Wind speed	[m/s]	5.6 ± 0.5
Temperature	[°C]	8.4 ± 0.3
Relative humidity	[%]	95.5 ± 1.6
Mean concentrations		
Na ⁺	[nmol/m ³]	22.7 ± 3.9
Cl ⁻		22.7 ± 3.6
SO ₄ ²⁻		42.5 ± 13.3
NO ₃ ⁻		62.6 ± 17.7
HCl		23.0 ± 2.9
fine SO ₄ ²⁻		24.0 ± 2.1
HNO ₃ + fine NO ₃ ⁻		20.7 ± 3.5
Mean concentration gradients		
Na ⁺	[% /m]	9.0 ± 3.1
Cl ⁻		5.6 ± 2.3
SO ₄ ²⁻		0.2 ± 1.3
NO ₃ ⁻		1.0 ± 0.5
HCl		-4.2 ± 4.9
fine SO ₄ ²⁻		-1.6 ± 0.7
HNO ₃ + fine NO ₃ ⁻		0.4 ± 0.2

The relatively low sodium concentrations reflect the low wind speeds. Sea salt sulphate thus is less than 5% of total sulphate.

The inspection of the 23 profiles reveals a considerable scatter. To reduce this we have identified 2 outliers and 3 incomplete profiles. We combined all those cases having a fetch of 20 to approximately 50 km being in the sector from 240° to 90° (N = 9). Another set of 9 samples represents the south-easterly transport with only 1 km fetch from Lolland. The 4 isokinetic samples analysed so far represent north-westerly conditions. Their absolute values can not be compared directly since they are only a subset of the north-westerly sample set. Figures 1–3 show the vertical profiles of the same components as mentioned in Table 1. We also tried to order samples by wind speed. By chance almost all easterly samples represent samples with wind speeds >5 m/s and all westerly samples represent rather smaller average winds. This of course is a consequence of the operating constraints on the tower.

Vertical profiles of the fine fractions of all major anions are rather indifferent. An exception is the profile of fine chloride plus HCl which shows a considerable increase in the lowest layer during easterly winds and in the

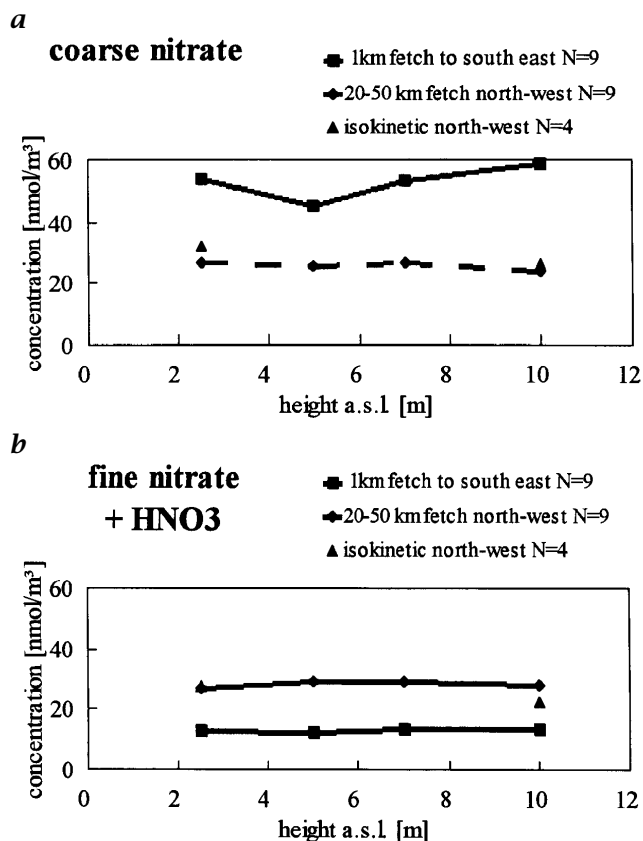


Figure 1: Average nitrate vertical profiles at the Lolland tower for selected cases.

isokinetic samples. The profiles of fine sulphate might be interpreted as following this trend. An explanation might be that in easterly winds the short fetch mobilises small sea salt particles only up to a height of 2 m.

Significantly differing from that are the profiles for the coarse aerosol fractions. For westerly winds small gradients are observed. A slight increase in concentration, especially in the isokinetic samples can be well explained by sea salt production. In easterly winds an inhomogeneous profile evolves. Differences are much larger than expected from our precision estimates stated above. Profiles of nitrate, chloride and sodium correlate well. A significant minimum is observed at a height of 5 m with 15–20% less than at 10 m. Since we have found no other reason we have to consider the mixing of two boundary layers in offshore winds as a possible source of this special profile. While the upper part reflects the profile evolving from turbulent mixing and deposition over land the influence of an emerging marine boundary layer with a production of sea salt is to be seen at the lowest height.

Interestingly the coarse nitrate follows the trend but, not surprisingly, the

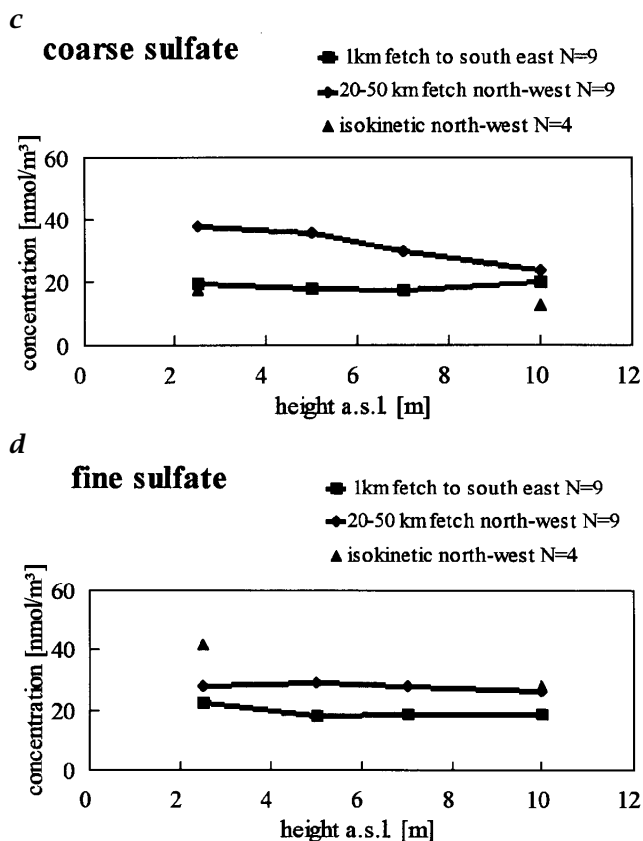


Figure 2: Average sulphate vertical profiles at the Lolland tower for selected cases.

effect is somewhat weakened. This is in contrast to the behaviour of coarse non sea salt sulphate. The correlation with sodium would be in accordance with the hypothesis of a significant and rapid transfer of nitric acid and fine ammonium nitrate into the coarse fraction of the aerosol when sea salt is present in sufficient quantities.

The importance of the interaction of nitrate compounds with sea salt is also reflected by the significantly higher coarse to fine nitrate ratio under easterly wind conditions. None of the other components shows this behaviour.

4 Conclusions

The measured profiles show significant deviations from homogenous profiles especially in the coarse aerosol mode and easterly winds. However no straight profile could be observed, probably because vertical homogeneity

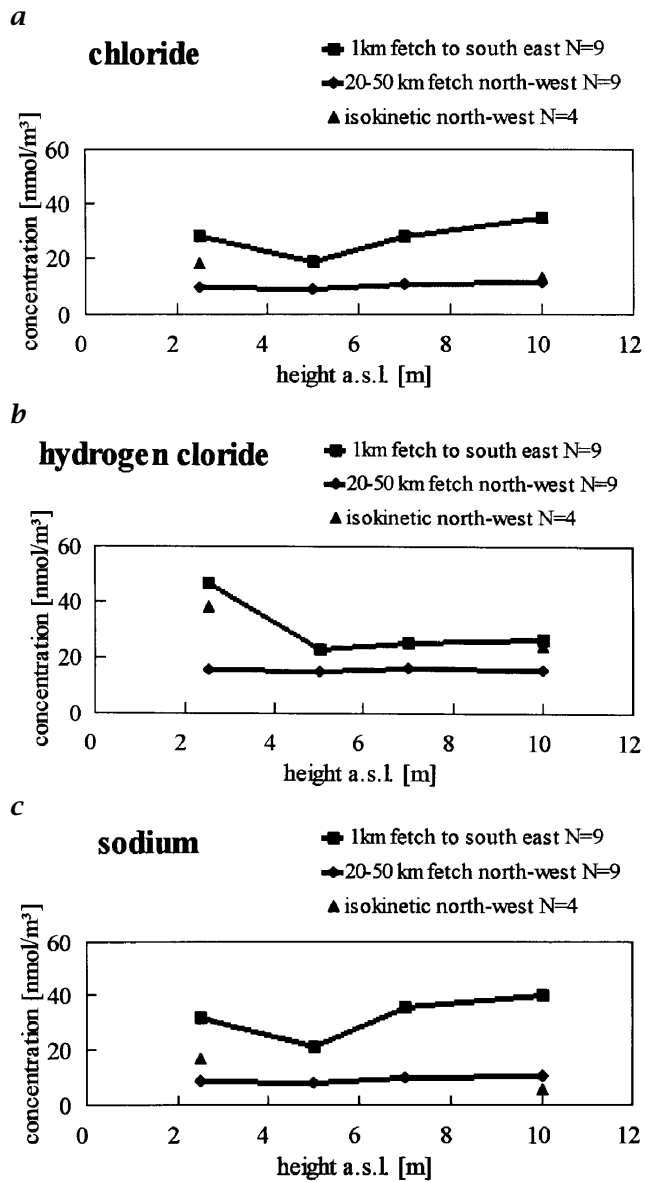


Figure 3: Average sea salt component and hydrogen chloride vertical concentration profiles at the Lolland tower for selected cases.

is not ensured in between the Danish isles. In easterly winds with a fetch of 1 km a complex profile emerges as a consequence of the evolving internal marine boundary layer. Sea salt production affects in these conditions only the concentration up to a height of a few meters. Coarse nitrate profiles correlate well with those of the sea salt component. The close interaction is also supported by the increased coarse to fine nitrate ratio under the more windy easterly conditions during the experiments. The measured aerosol profiles support the hypothesis of a significant and rapid transfer of nitric acid and fine ammonium nitrate into the coarse fraction of the aerosol when sea salt is present in sufficient quantities.

Acknowledgements

This work was supported by the US ONR- marine boundary layer programme R&T 241a122 and the German BMBF-project grant No. 03F0111A, KUSTOS (Küstennahe Stoff- und Energieflüsse). Thank is due to Andreas Behlen for his most valuable advice in filter pack sampling. We would also like to thank Lise-Lotte Soerensen and Jorgen Hojstrup and numerous other helping hands for their support during the experiment in Lolland/DK.

References

- Harrison, R. M., and A.-M. N. Kitto, Field Intercomparison of Filter Pack and Denuder Sampling Methods for Reactive Gaseous and Particulate Pollutants, *Atmos. Environ.*, 24A, 2633-2640, 1990
- Ottley, C. J., and R. M. Harrison, The spatial distribution and particle size of some inorganic nitrogen, sulphur and chlorine species over the North Sea, *Atmos. Environ.*, 26A, 1689-1699, 1992
- Stelson, A. W., and J. H. Seinfeld, Relative humidity and temperature dependence of the ammonium nitrate dissociation constant, *Atmos. Environ.*, 16, 983-992, 1982

Estimating Air-Water Transfer of Hexachlorocyclohexanes in Lake Ontario

Jeffrey J. Ridal^{1*}, Bryan Kerman¹, and William M. Drennan²

¹ Lake Meteorology Laboratory, Air Research Quality Processes Branch, Atmospheric Environment Service, Canada Centre for Inland Waters, 867 Lakeshore Road, Burlington, ON Canada L7R 4A6 email: bryan.kerman@cciw.ca

² National Water Research Institute, Canada Centre for Inland Waters, 867 Lakeshore Road, Burlington, ON Canada L7R 4A6 email: will.drennan@cciw.ca

* Current address: Station de Biologie des Laurentides, Université de Montréal, 440, Ave du Lac Croche, St. Hippolyte, QC, Canada J0R 1P0 email: ridalj@ere.umontreal.ca

Abstract

The air-water gas exchange of *hexachlorocyclohexane* (HCH) in Lake Ontario has been studied by comparing air and water concentrations from May–October in 1993. Results indicate that HCH air-water gas transfer is a dynamic process with reverses between volatilization and deposition occurring seasonally. Air-water HCH fluxes were calculated using the thin film approach. A comparison between two different sets of windspeed correlations used to estimate air- and water-side transfer coefficients was made and similar results for overall gas transfer rates were obtained. Net air to water fluxes of α -HCH ranged from averaged values of $-20 \text{ pg m}^{-2} \text{ day}^{-1}$ (deposition) in May to $18 \text{ pg m}^{-2} \text{ day}^{-1}$ (volatilization) in July, whereas net γ -HCH fluxes ranged from $-36 \text{ pg m}^{-2} \text{ day}^{-1}$ in May to $2.5 \text{ pg m}^{-2} \text{ day}^{-1}$ in August. During the six month period, we estimate that 12–16 kg of α -HCH volatilized and 33–46 kg of γ -HCH was deposited into Lake Ontario.

1 Introduction

Air-water gas transfer is an important pathway for the global transport of persistent organic pollutants in the environment [Baker and Eisenreich, 1990; Iwata *et al.*, 1993]. The ubiquitous organochlorine pesticides, α -HCH and γ -HCH (commonly known as lindane), are attractive compounds with which to study air-water gas transfer of organic pollutants due to their relatively high concentrations in both water and air, and low levels of binding by particulate matter in these phases [Ridal *et al.*, 1995]. A study of HCH gas transfer was undertaken by McConnell *et al.* [1993] for the Great Lakes. Fluxes of HCH isomers across the air-water interface in August 1990 were calculated from simultaneous air and water concentrations using a thin film model approach [Mackay and Yeun, 1983]. McConnell *et al.* [1993] found that Lakes Michigan, Huron and Erie volatilized HCH, while the flux of HCH was depositional into Lake Ontario. The authors hypothesized, however,

that the period of volatilization of HCH in the three upper lakes was short-lived, and suggested that the flux for all four lakes would be depositional during the majority of the year as surface waters cooled and the lake became unstratified.

We have further investigated the seasonality of HCH air-water gas exchange for *Lake Ontario* in 1993. Air and water concentrations have been determined on weekly cruises from May–October and HCH fluxes were estimated using the same approach as *McConnell et al.* [1993] for comparative purposes [*Ridal et al.*, 1995]. A question arising from this work was the appropriateness of the air-side mass-transfer coefficient (MTC) correlation used in these studies [*MacKay and Yeun*, 1983], particularly at low wind speeds. Since the air-water transfer of HCHs is predominately air-phase controlled [*MacKay and Leinonen*, 1975; *Ridal et al.*, 1995], the determination of k_a is particularly important in the calculation of HCH fluxes. Here we investigate modifications to the *MacKay and Yeun* [1983] air-side MTC correlation for use at low wind speeds. Resulting flux estimates are compared to those obtained using the MTC correlations suggested by *Schwartzbach et al.* [1993] and *Wanninkhof et al.* [1991], recently employed by *Hornbuckle et al.* [1994] to calculate air-water fluxes of PCBs for Lake Superior.

2 Methods

Sampling and analysis methods are provided in detail elsewhere [*Ridal et al.*, 1995]. Briefly, air and water samples were taken during weekly cruises on Lake Ontario from the first of May to the end of October, 1993. Air samples (100–200 m³) were taken by a calibrated high volume sampler mounted on the top foredeck of the research vessel. Polyurethane foam (PUF) plugs were used to collect HCHs from air and HCHs were extracted from the PUFs with hexane in the laboratory. HCHs were thrice extracted from surface water samples by stirring with dichloromethane. After sample concentration, clean-up to remove possible interferences, and solvent exchange to iso-octane, all samples were analysed by dual-column gas chromatography. Surrogate spikes using δ -HCH, generally not measurable in environmental samples, were added to air and water samples to monitor recovery. Recovery of surrogates (± 1 s.d.) averaged $85 \pm 13\%$ ($n = 62$) and $61 \pm 18\%$ ($n = 180$) for air and water samples, respectively.

Generally, 3 air and 6–9 water samples were taken during each 3–4 day cruise, with attempts to achieve both good temporal (day and night) and geographical sampling representation. Air sampling was initiated several kilometres offshore and the sampler run continuously for 8–16 hours per sample. Air temperature, barometric pressure, wave height, relative humidity, and surface water temperature were taken onboard ship at 3 hour intervals. Instantaneous wind speeds were generally taken shipboard as 5 minute averages on an hourly basis. Hourly wind speed data (10 minute averages) taken from shoreline meteorological stations on Lake Ontario were also used.

3 Results and Discussion

A summary of water and air HCH determinations are shown in Figure 1. Surface water concentrations of γ -HCH remained constant from May to October; weekly-averaged values ranged only from 317 to 417 pg/L with an overall mean value of 361 ± 33 pg/L. On the other hand, α -HCH values showed some seasonal variation with values averaging 922 ± 73 pg/L in May, during the sampling period when the lake was well-mixed, 679 ± 47 pg/L when the lake was stratified in July and August, and 895 ± 76 pg/L in October after fall lake turnover. Water samples taken beneath the thermocline (>20 m depth) during the course of the work do not show measurable seasonal differences. The range of α and γ HCH values measured in this study are in excellent agreement with levels of these compounds in other recent studies of Lake Ontario [Ridal *et al.*, 1995].

Mean vapour phase concentrations of α -HCH were 106 ± 25 pg/m³ and 50 ± 28 pg/m³ for γ -HCH. A springtime peak in γ -HCH values likely signifies recent agricultural applications of the compound in North America [Hoff *et al.*, 1992]. The most appropriate land-based determinations to compare with our Lake Ontario shipboard measurements are those taken at the Integrated Atmospheric Deposition Network (IADN) sampling site at Point Petre on Lake Ontario. A number of representative samples from May–October 1993 at Point Petre have been analysed and these results averaging 102 ± 18 pg/m³ and 40 ± 23 pg/m³ are excellent agreement with our shipboard samples [Ridal *et al.*, 1995].

4 Saturation Indexes

The level of saturation of α - and γ -HCH in the surface water relative to the overlying air determines the direction of air-water gas exchange. Percent saturation, % S, can be calculated using the expression:

$$\%S = (C_w / C_{HCH}^*) \times 100 \quad (1)$$

where

$$C_{HCH}^* = C_{air} \cdot RT / H \quad (2)$$

C_w and C_{air} are the respective dissolved and vapour phase (pg/m³) concentrations, R is the gas constant (Pa m³/mol K), T is the temperature at the air-water interface (K), H is the Henry's law constant (Pa m³/mol) calculated following Kucklick *et al.* [1991]. Under-saturation (i. e., values less than 100% saturation) implies net transfer of HCH into the water (deposition) whereas an over-saturated condition indicates net fluxes that are out of the water (volatilization).

Results of these calculations are also shown in Figure 1 together with surface temperature data. Both HCH isomers are under-saturated in May when the lake remains well-mixed and surface waters are cold. With onset of thermal stratification and warming of the surface waters, α -HCH becomes over-saturated owing to the temperature dependence of the air-water partition coefficient, H . This change in saturation indicates a reversal in net air-water exchange direction from depositional to volatilizational for α -HCH. On the other hand, the flux direction of γ -HCH remains depositional during June–July owing to relatively large air values in spring and early summer (Figure 1). Decreasing air values results in an over-saturated condition for γ -HCH in the surface waters and switch to volatilizational fluxes for August and early September. Near equilibrium conditions are observed for both HCH isomers in October.

5 Flux Calculations

Paired air and water data can be used to estimate instantaneous fluxes through the use of the two-film model for gas exchange [Liss and Slater, 1974; MacKay and Leinonen, 1975]. To review briefly, the flux of HCH (F_{HCH}) between the air and water is modelled to be limited by transport across stagnant films at the air-water interface, and not by turbulent transport in the bulk mixed layer, and is given by:

$$F_{HCH} = k_{ol}(C_w - C_a^*RT/H) \quad (3)$$

The overall transfer velocity, k_{ol} (m/s), is the overall mass-transfer rate through both air-side and water-side stagnant films and can be expressed in terms of k_a , the air side transport velocity, and k_w , the water-side transport velocity:

$$1/k_{ol} = RT/k_aH + 1/k_w \quad (4)$$

A number of correlations can be used to calculate k_a and k_w [Schwartzbach *et al.*, 1993], but some of the expressions most widely-used for estimating air-water fluxes of organic contaminants [e.g., Cotham and Bidleman, 1991; Iwata *et al.*, 1993; Ridal *et al.*, 1995] are based on those suggested by Mackay and Yeun [1983]:

$$k_a = 1 \times 10^{-3} + 46.2 \times 10^{-3} U_* Sc(a)^{-0.67} \quad (5)$$

$$k_w = 1 \times 10^{-6} + 34.1 \times 10^{-4} U_* Sc(w)^{-0.5} \quad (U_* > 0.3 \text{ m/s}) \quad (6)$$

$$k_w = 1 \times 10^{-6} + 144 \times 10^{-4} (U_*)^{2.2} Sc(w)^{-0.5} \quad (U_* < 0.3 \text{ m/s}) \quad (7)$$

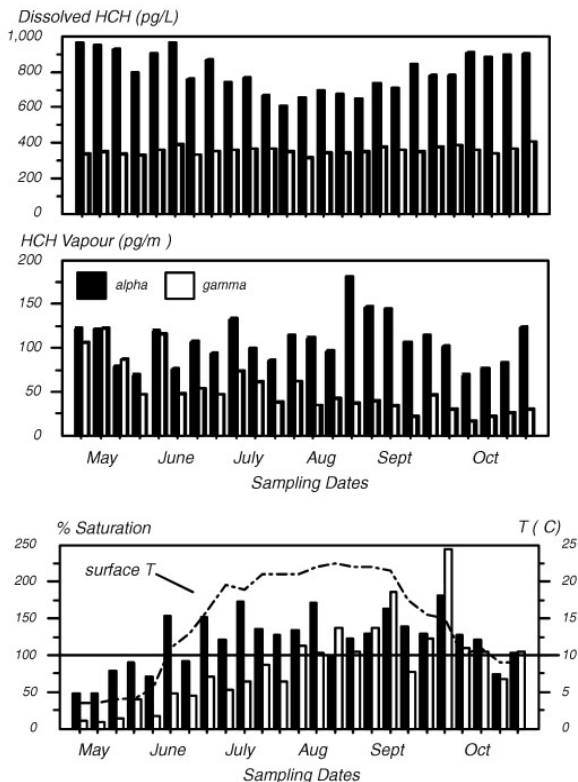


Figure 1: Average concentrations of α - and γ -HCH measured in surface water (top graph) and air (middle graph) of Lake Ontario during weekly cruises. Also shown are resulting levels of HCH saturation in surface waters (bottom graph).

where

$$U_* = [(0.61 + 0.063U_{10}) \times 10^{-3}]^{0.5} U_{10} \quad (8)$$

and U_{10} is the wind speed at 10 meters height above the water surface and $Sc(a)$ and $Sc(w)$ are the respective gas and water phase Schmidt numbers.

Expression (8) calculates the friction velocity following *Smith* [1980] at the air-water interface assuming conditions of thermal equilibrium between the air and the water. Thermal equilibrium is not always met in the environment so we furthermore correct U_* values for non-ideal cases following *Donelan* [1990]. This correction is relatively small during summer months

(<15%), but approaches 40% in certain cases during spring and fall when air-water temperature differences are relatively large. Following stability corrections, shipboard wind speed data ranged from 1.1 to 12.5 m/s with an average wind speed of 5.6 m/s. Meteorological station windspeed data, scaled up by a factor of 1.2 to correct for overland vs. overlake windspeed differences [Morton and Schwab, 1984], were similarly corrected for thermal stability and ranged from 1.9 to 13 m/s with an average of 6.0 m/s.

We note that equation (8) was based on U_{10} values between 6 and 18 m/s [Smith, 1980]. As approximately 50% of the wind speed data of this study fall below this range, we follow the suggestion of Donelan [1990] to use an expression for smooth flow for windspeeds below 6 m/s, which has the form:

$$U_* = K[\ln(10U_*/0.11\nu)]^{-1} \times U_{10} \quad (9)$$

where K is von Karman's constant (0.4) and ν is the kinematic viscosity of air. In further references we denote these modified MacKay and Yeun [1983] correlations as MTC model I.

Different MTC correlations (MTC model II) have been used to calculate air-water PCB fluxes in Lake Superior and these can be applied readily to calculate HCHs fluxes. Air-side transport is modelled using H_2O vapour flux as summarised by Schwartzbach *et al.* [1993]:

$$k_{a,HCH}(\text{cm/s}) = k_{a,H_2O}(D_{HCH}/D_{H_2O})^{0.61} \quad (10)$$

where

$$k_{a,H_2O} = 0.2U_{10} + 0.3 \quad (11)$$

where D_{HCH} and D_{H_2O} are the diffusivities of HCH and H_2O in air, respectively. Water-side transport is modelled using CO_2 following Wanninkhof *et al.* [1991]:

$$k_{w,HCH}(\text{cm/hr}) = k_{w,CO_2}(S_{CHCH}/S_{CCO_2})^{-0.5} \quad (12)$$

where

$$k_{w,CO_2} = 0.45U_{10}^{1.64} \quad (13)$$

Schmidt numbers were calculated using temperature-corrected viscosities and diffusivities using the methods of Fuller *et al.* [1966] and Hayduk and Laudie [1974].

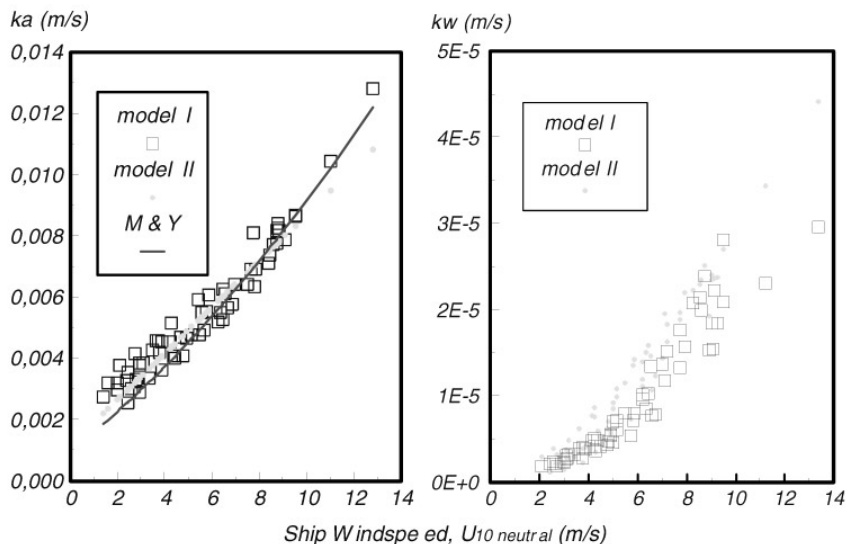


Figure 2: Comparisons of air- and water-side mass transfer coefficients calculated using models I and II. Also shown in the left graph is a fitted line to the k_a values calculated using MacKay and Yeun [1983] correlation.

A comparison of k_a values calculated by MTC models are shown in Figure 2. While models I and II do diverge slightly at high wind speeds, the agreement at low wind speeds is very good. A linear fit between the data produced by the two models was found to be:

$$k_a(I) = 1.01k_a(II) + 7.9 \times 10^{-5} \quad (14)$$

Also shown in Figure 2 is a fitted curve to the data produced from the unmodified MacKay and Yeun [1983] correlations. Interestingly, while this correlation does produce somewhat lower values at wind speeds <5 m/s than model I, the agreement between all three correlations remains within the variability of the geophysical data. Also shown for illustration are the resulting k_w values using the two models. Ratios of model I to model II averaged 0.88 ± 0.30 at wind speed <5 m/s and 0.76 ± 0.15 for wind speeds >5 m/s. Overall agreement between the models was very good for the HCHs, ratios of K_{ol} calculated with model I correlations to the model II correlations averaged 1.02 ± 0.13 for α -HCH and 1.03 ± 0.12 for γ -HCH (data not shown).

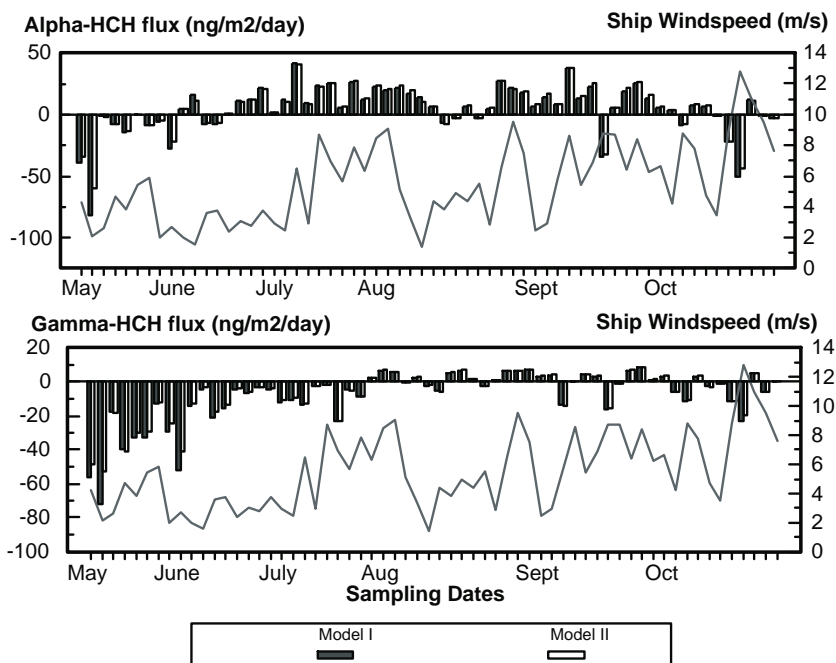


Figure 3: Shown are the instantaneous fluxes predicted for α - and γ -HCH using models I and II. Negative values denote deposition and positive values indicate volatilization.

The resulting fluxes of HCH compounds calculated from both correlations are shown in Figure 3 using ship windspeed data. Not surprisingly, good agreement is found between the fluxes using the two different correlation approaches. Instantaneous water to air fluxes range from 25 to $-80 \text{ ng/m}^2/\text{day}$ for α -HCH, and from 7 to $-71 \text{ ng/m}^2/\text{day}$ for γ -HCH. Mean fluxes for α - and γ -HCH of -6.1 and $-5.1 \text{ ng/m}^2/\text{day}$, respectively, were measured for Lake Ontario by McConnell *et al.* [1993] in August 1990. By August 1993 of this study, fluxes averaged 11.5 and $2.6 \text{ ng/m}^2/\text{day}$.

Ranges for semi-annual fluxes can be estimated from averaged instantaneous fluxes from each cruise using the two sets of K_{ol} determinations, as well as both ship and shoreline wind data. A semi-annual net volatilization of 590 to 824 ng/m^2 representing a loss of 12 – 16 kg from the lake over the study period is obtained for α -HCH. Similar estimates for γ -HCH gives a net deposition of 1650 to 2300 ng m^2 representing a transfer of 33 to 46 kg into Lake Ontario. These semi-annual values are of the same order or larger than wet deposition fluxes measured during the same months in 1992 at Point Petre, which were 21 and 22 kg for α - and γ -HCH respectively [Ridal

et al., 1995], indicating that air-water gas transfer plays a major role in the atmospheric deposition of these organic pollutants.

Acknowledgements

We thank Mike Fox, Louise Durham, Terry Bidleman, Ken Brice and Ray Hoff of Environment Canada and Lei Lin of the Université de Montréal for technical assistance and discussions.

References

- Baker, J. E. and S. J. Eisenreich, Concentrations and Fluxes of Polycyclic Aromatic Hydrocarbons and Polychlorinated Biphenyls across the Air-Water Interface of Lake Superior, *Environ. Sci. Technol.*, Vol. 24, pp. 342-352, 1990
- Cotham, W. E. and T. F. Bidleman, Estimating the Atmospheric Deposition of Organochlorine Contaminants to the Arctic Environment, *Chemosphere*, Vol. 22, pp. 165-188, 1991
- Donelan, M., Air-Sea Interaction, in *The Sea: Ocean Engineering Science*, Vol. 9. eds. Hanes and LéMehanté, John Wiley and Sons, N.Y., pp. 239-292, 1990
- Fuller, E. N., P. D. Schetter, and J. C. Giddings, A New Method for Prediction of Binary Gas-Phase Diffusion Coefficients, *Ind. Eng. Chem.*, 58, pp. 19-27, 1966
- Hayduk, W. and E. Laudie, Predictions of Diffusion Coefficients for Non-electrolytes in Dilute Solutions, *AIChEJ.*, 20, pp. 611-616, 1974
- Hoff, R. M., D. C. G. Muir, and N. P. Grift, Annual Cycle of polychlorinated Biphenyls and Organochlorine Pesticides in Southern Ontario Air, *Environ. Sci. Technol.*, 26, pp. 266-275, 1992
- Hornbuckle, K. C., J. D. Jeremiason, C. W. Sweet, and S. J. Eisenreich, Seasonal Variations in Air-Water Exchange of Polychlorinated Biphenyls in Lake Superior, *Environ. Sci. Technol.*, 29, pp. 1491-1501, 1994
- Iwata, H., S. Tanabe, N. Sakai, and R. Tatsukawa, Distribution of Persistent Organochlorines in Oceanic Air and Surface Water and the Role of the Ocean on their Global Fate and Transport, *Environ. Sci. Technol.*, 25, pp. 1075-1081, 1993
- Kuklick, J. R., D. A. Hinckley, and T. F. Bidleman, Determination of Henry's Law Constants for Hexachlorocyclohexanes in Distilled Water and Artificial Seawater as a Function of Temperature, *Mar. Chem.*, Vol. 34, pp. 197-209, 1991
- Liss, P. S. and P. G. Slater, Fluxes of Gases Across the Air-Sea Interface, *Nature*, 274, pp. 181, 1974
- Mackay, D. and P. J. Leinonen, Rate of Evaporation of Low-Solubility Contaminants from Water Bodies to Atmosphere, *Environ. Sci. Technol.*, Vol. 9, pp. 1178, 1975
- Mackay, D. and A. T. K. Yeun, Mass Transfer Coefficient Correlations for Volatilization of Organic Solutes from Water, *Environ. Sci. Technol.*, Vol. 17, pp. 211-216, 1983
- McConnell, L. L., W. E. Cotham, and T. F. Bidleman, Gas Exchange of Hexachlorocyclohexanes in the Great Lakes, *Environ. Sci. Technol.*, Vol. 27, pp. 1304-1311, 1993

- Ridal, J. J., B. R. Kerman, L. Durham, and M. E. Fox, Seasonality of Hexachlorocyclohexane Fluxes in Lake Ontario, *Environ. Sci. Technol.*, in review.
- Schwab, D. J. and J. A. Morton, Estimation of Overlake Wind Speed from Overland Wind Speed: A Comparison of Three Methods, *J. Great Lakes Res.*, pp. 68-72, 1984
- Schwarzenback, R. P, P. M. Gschwend, and D.M. Imboden, *Environmental Organic Chemistry*, Wiley Interscience, New York, pp. 228-238, 1992
- Smith, S. D. Wind Stress and Heat Flux Over the Ocean in Gale Force Winds, *J. Phys. Oceanogr.*, 10, 709-726, 1980
- Wanninkhof, R., Ledwell, J. R., and Crusius, J, in *Air-Water Mass Transfer*, S. C. Wilhem and J. S. Gulliver, eds, pp. 441-458, New York, 1991

Methane Emissions off the Dutch Coast: Air-Sea Concentration Differences Versus Atmospheric Gradients

*H. P. J. de Wilde*¹ and *J. Duyzer*²

¹ Department of Marine Chemistry and Geology, Netherlands Institute for Sea Research (NIOZ)

P.O. Box 59, NL 1790 AB Den Burg, The Netherlands

² Institute of Environmental Sciences, TNO Environmental and Energy Research
P.O. Box 6011, NL 2600 JA Delft, The Netherlands

Abstract

Air-sea fluxes of methane (CH₄) were determined by two different methods during the ASGASEX experiment in September 1993, on a research platform off the Dutch coast. Fluxes derived by the micrometeorological gradient method were on average 6 times larger than fluxes based on monitored air-sea concentration differences and estimated transfer velocities. This discrepancy, well-known from other studies, cannot be explained by experimental errors, nor by local variability in CH₄ concentrations.

The dissolved CH₄ distribution, ranging from 25 to 90 nmol l⁻¹, i. e., 10 to 35 times saturation, was dominated by the tidal cycle. Estimated emissions into the atmosphere, ranging from 0.01 to 0.5 μg m⁻² s⁻¹, are among the highest values reported for coastal areas. The inverse relationship between CH₄ and salinity suggested that river discharge was the major source of CH₄ in this region. Increasing CH₄ concentrations along the salinity gradient of the Scheldt river confirmed this hypothesis.

1 Introduction

Air-sea exchange of trace gases such as carbon dioxide (CO₂), nitrous oxide (N₂O) and *methane* (CH₄) is often estimated from the difference in concentration between air and water, multiplied with a transfer velocity. The transfer velocity is parameterised as a function of wind speed and temperature [Liss and Merlivat, 1986; Wanninkhof, 1992].

Although parameterised transfer velocities are of great practical value, large uncertainties exist about the actual forcing terms for air-sea gas transfer. Apart from wind speed and water temperature, gas exchange is also influenced by other geophysical variables, such as thermal stability, wind fetch, sea state, surface micro-layers, chemical reactions, bubbles, and cold skin layers [Ericson, 1993; Wanninkhof, 1992; Woolf and Thorpe, 1991; Robertson and Watson, 1992]. Consequently, parameterisations of transfer

velocities based on wind speed alone always contain significant uncertainties.

Micrometeorological methods enable direct measurement of fluxes [Dabberdt *et al.*, 1993], and therefore are independent of the underlying forcing terms for gas exchange. These techniques, which are not subject to the uncertainties of a transfer velocity, have been applied successfully for determination of trace gas emissions on land [Fowler and Duyzer, 1989]. Unfortunately, implementation of micrometeorological methods in the marine environment is complicated because it requires: (1) extreme analytical sensitivity as fluxes at sea are usually small (2) stable positioning of the equipment relative to the sea surface, or complex corrections for ship's movements, and (3) large corrections for water vapour fluxes. Nevertheless, improved technology has led to encouraging results. Especially eddy correlation measurements of CO₂ have been reported [e.g., Smith *et al.*, 1991; Donelan and Drennan, 1995; Kunz *et al.*, 1995; Oost *et al.*, 1995]. However, the micrometeorological eddy correlation method gives CO₂ fluxes about an order of magnitude larger than expected from air-sea concentration differences and isotopic methods. This discrepancy has initiated ongoing debate [Broecker *et al.*, 1986], indicating the need for direct comparisons of fluxes derived by micrometeorological methods and other techniques.

In September 1993 we participated in the international Air Sea GAS EXchange experiment (ASGASEX), organised on a research platform 9 km off the Dutch coast [Oost, 1995]. Our objectives were (1) to monitor the temporal variations of dissolved and atmospheric CH₄ and N₂O (2) to estimate the resulting air-sea gas fluxes, based on transfer velocities, and (3) to measure air-sea fluxes of CH₄ and N₂O by the micrometeorological gradient method. According to the *gradient method* the flux is derived from measurements of the concentration gradient of CH₄ in the air above the sea surface and the turbulence intensity. To our knowledge such measurements have not been carried out at sea before.

In this paper we focus on CH₄ fluxes, derived from the meteorological gradient method and from air-sea concentration differences. In addition, the temporal distribution of the CH₄ saturation is discussed in relation to local hydrography and river discharge.

2 Methods

2.1 Flux Calculations Based on Air-Sea Concentration Differences

The flux of CH₄ between the sea and the atmosphere was computed by multiplying the measured concentration difference ΔC with a transfer velocity K :

$$\text{Flux} = K \cdot \Delta C \quad (1)$$

Transfer velocities were estimated from wind speed and temperature according to the relationships of *Liss and Merlivat* [1986] and *Wanninkhof* [1992]. Local wind speed, averaged over 10 min intervals, was chosen because the surface water CH₄ concentration varied rapidly. Moreover, the time scale of the direct flux measurements by the gradient method was of the same order of magnitude (30 - 45 min). Calculation of CH₄ surface water concentrations was based on the solubility relationship of *Wiesenburg and Guinasso* [1979].

2.2 Flux Calculations Based on Atmospheric Gradients

The CH₄ flux by the gradient method is calculated from the turbulent exchange coefficient k_z for the sampling period, and the vertical CH₄ concentration gradient above the sea surface [*Fowler and Duyzer*, 1989]:

$$\text{Flux} = -k_z \cdot \frac{dc}{dz} \quad (2)$$

$$k_z = \frac{ku_*z}{\Phi(z/L)} \quad (3)$$

With dc/dz the CH₄ concentration gradient with height, k von Karman's constant, equal to 0.4 and z the height (taken here as the geometrical average of the sample heights z_2 and z_1). u_* is the friction velocity and $\Phi(z/L)$ a correction for atmospheric stability, described as a function of the Monin Obukhov length scale, L .

$$L = -\frac{u_*^3 T \rho c_p}{kgH} \quad (4)$$

In which T is air temperature, c_p specific heat, ρ air density, g acceleration by gravity, and H the sensible heat flux. Assuming similarity between transport of heat and mass, the following flux profile functions, Φ , were used.

$$\Phi_{h,z}\left(\frac{z}{L}\right) = \left(1 - 16\frac{z}{L}\right)^{-1/2} \quad L \leq 0 \quad (5)$$

$$\Phi_{h,z}\left(\frac{z}{L}\right) = 1 + 5\frac{z}{L} \quad L > 0 \quad (6)$$

The turbulent exchange coefficients were derived from equation (3) using friction velocities and heat fluxes measured with a three dimensional sonic anemometer, mounted at the end of a 21 m long boom. Using this long boom, bias in momentum and scalar fluxes resulting from flow obstruction by the platform was limited. Details of the turbulence measurements are given by *Kunz et al.* [1995].

2.3 Experimental

CH₄ Analysis. All CH₄ analyses were carried out with an automated gas chromatograph (Chrompack, model CP9000), equipped with stream selecting valves, a mini-pump, and a 500 μ l sample loop, enabling automated sequential sampling of surface water, air, and calibration gases in programmed repetitive duty cycles.

The sample loop, thermostated at 50.0 °C, was flushed with sample for 30 seconds at a flow of 50 ml/min, and vented for 4 sec to ambient pressure, prior to injection on a pre-column packed with 80/100 mesh Hayesep N. When the CH₄ peak had entered the main column, also packed with Hayesep N, the pre-column was back-flushed which prevented slowly eluting compounds from interference with the CH₄ from the next samples. At an oven temperature of 55 °C and a N₂ carrier gas flow around 20 ml/min, it took about 1.2 minutes for the CH₄ peak to reach the flame ionisation detector which was operated at 310 °C.

Gas chromatographic responses of samples were converted to CH₄ concentrations by using a quadratic calibration curve, based on the responses of standard gas mixtures, forced through zero. Working standards with CH₄ mixing ratios of 1.41, 2.78, 8.32, and 98.60 μ mol/mol in synthetic air were used. The first 2 standards were calibrated against primary CH₄ standards of 0.913 and 2.28 mmol/mol CH₄ in synthetic air (National Institute of Standards, USA). Samples were alternated with standards to reduce bias by drift in detector sensitivity.

Sampling of Dissolved CH₄. Surface water concentrations were monitored by means of a continuous equilibrating technique using a modified version of the system described by *Robertson et al.* [1992]. In short, sea water drawn from 5 m below mean water level, was continuously sprayed through a headspace of air. An atmospheric vent maintained the headspace at ambient pressure, but prevented contamination from outside. The headspace in this 'equilibrator' thus reflected the dissolved CH₄ concentration via the Henry coefficient. Every 15 min equilibrated air from the headspace was circulated through the sample loop of the gas chromatograph and subsequently analysed. The response time of the equilibrator was tested in the laboratory: after a change of the CH₄ concentration in the influent, 99% equilibrium was reached within 20 min. The temperatures at the sea water inlet and in the equilibrator were monitored to correct for solubility changes ($\leq 0.4\%$), due to warming of the equilibrator influent (≤ 0.2 °C). Atmospheric concentrations, measured at in situ humidity, were corrected to 100% humidity by applying the vapour pressure polynomial of *Weiss and Price* [1980]. The relative standard deviation of the equilibrator measurements was estimated at 1.1%.

Sampling of Atmospheric CH₄. Three adjustable air inlets were mounted upwind of the platform. In order to limit flow distortion by the platform, the upper and middle air-inlets were mounted at the end of long booms (11 and 21 m respectively). The lowest inlet was mounted on a small buoy. Typical operating heights of the inlets were about 0.5, 5, and 20 m above the sea surface. Air from these 3 inlets was pumped continuously through gas-impermeable tubing, at a flow of 5 l min⁻¹ to 5 l glass buffer vessels, which were vented to the laboratory under slight overpressure. Every 30 min, air from 2 of the 3 buffer vessels was sampled and analysed. Unfortunately, CH₄ concentrations in air drawn from the inlet at the buoy were biased by interference of seaspray and overcoming waves. These measurements were therefore discarded for the present analysis.

Atmospheric CH₄ Gradients. Gradient measurements were made by simultaneous sampling of air from the three air inlets described above. During runs of 30 to 45 minutes, air from each inlet was collected in 60 l gas-impermeable polyvinylfluoride sampling bags, at a flow rate of 1.3 to 2 l/min. In order to increase precision and to reduce bias by detector drift, samples were alternately taken from each bag, and analysed in about 50 repetitive cycles. Air samples were mostly dried and always brought to a temperature of 50 °C prior to analysis. This means that mixing ratios were measured, rather than concentrations. Consequently corrections for density effects, due to heat and water vapour gradients, were not required [Webb *et al.*, 1980]. Gradients were only measured when sensors and air inlets were upwind of the platform, in order to avoid bias of the turbulence measurements by flow distortion.

The relative standard deviation of the analysis of atmospheric samples was about 0.5%. Using 25 samples from each bag the random error could be reduced to 0.1%. For the flux measurements reported here, the random error in the flux varied (depending on wind speed) between 0.1 and 0.2 μg m⁻² s⁻¹.

3 Results and Discussion

3.1 Flux Estimates

The waters around the platform were strongly enriched in CH₄. During the study, CH₄ concentrations ranged from 25 to 90 nmol l⁻¹, corresponding with 10 to 35 times saturation with respect to the atmosphere (Fig. 1A). Resulting emissions into the atmosphere, estimated from the Wanninkhof windspeed relationship, ranged from 0.01 to 0.5 μg m⁻² s⁻¹. These results are in line with fluxes up to 0.2 μg CH₄ m⁻² s⁻¹, reported for the same area [Scranton and McShane, 1991]. A compilation of CH₄ fluxes from coastal and shelf areas, given by Bange *et al.* [1994], shows that the fluxes reported here, are among the highest in the world.

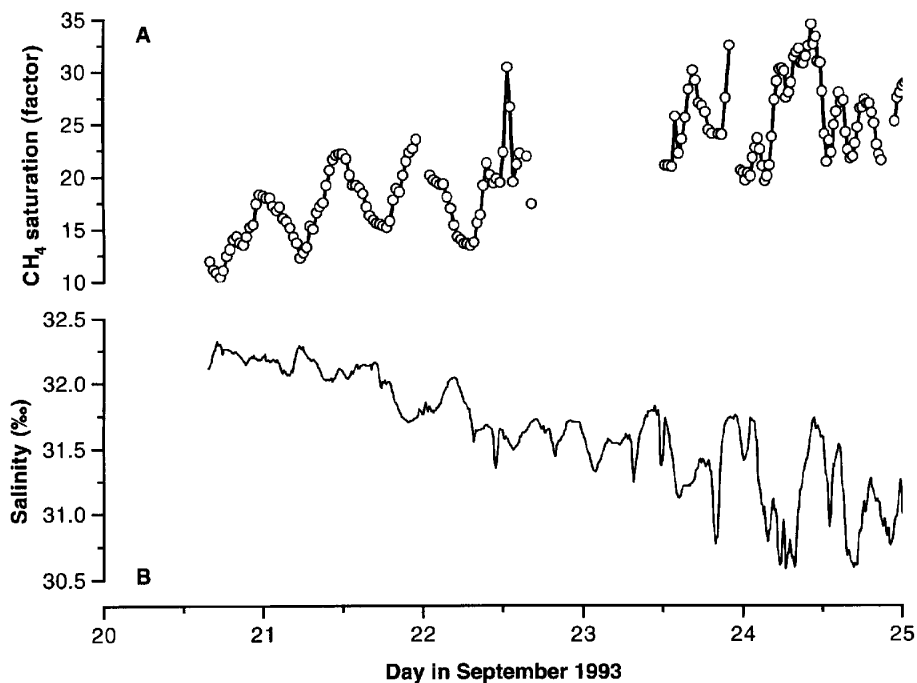


Figure 1: **a** Five days time series of dissolved CH_4 , showing strong and variable surface water saturations. A saturation factor of 1 corresponds with equilibrium relative to the atmospheric concentration. **b** Salinity, is negatively correlated with CH_4 , suggesting that freshwater discharge by rivers is an important source of coastal CH_4

3.2 Gradient Technique

The continuous registration of dissolved CH_4 and estimated emission into the atmosphere, was occasionally supplemented by *gradient measurements*. The concentration difference between air from the upper and middle inlet ranged from 1.4 to 7.9 ppb (mean 4.6 ppb; $n = 5$), relative to an atmospheric background concentration of 1786 ppb. Average values of u_* and L were 0.31 ms^{-1} and -235 m respectively. CH_4 fluxes derived from these data by the gradient method were on average 6 times larger then the fluxes based on the relationship of Wanninkhof (Fig. 2).

These results are rather conflicting. However, similar or larger discrepancies were reported for all studies in which micrometeorological measurements over the sea were compared with estimates based on surface water saturation [Broecker *et al.* 1986; Oost *et al.*, this volume]. An explanation for this phenomenon is not yet available. Bias, resulting from the inhomogenic distribution of dissolved CH_4 , was estimated less then a factor of 2, and thus too small to explain the large discrepancies observed. Variations in atmospheric CH_4 were insignificant on the time scale of the measurements.

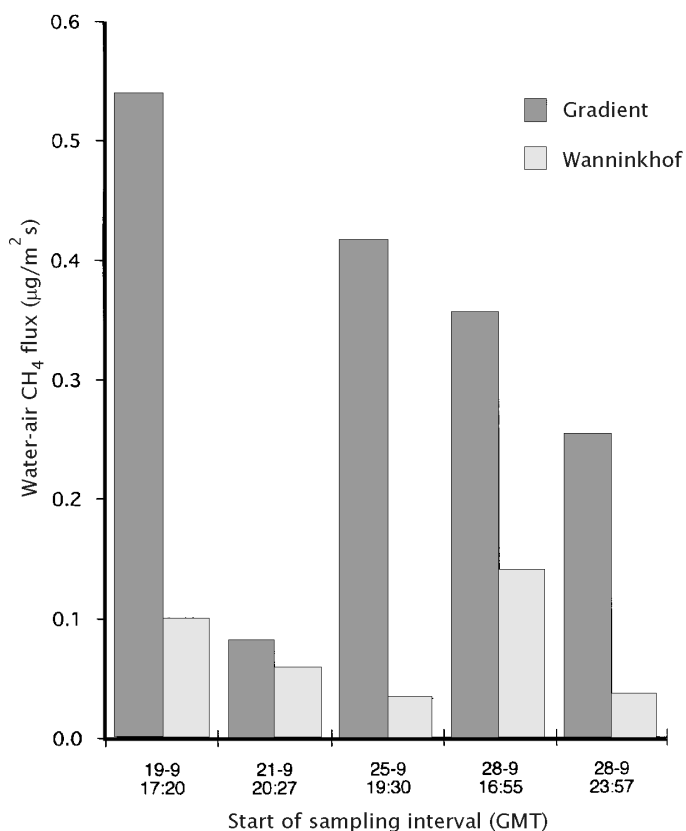


Figure 2: Comparison of CH₄ fluxes derived from the gradient method and from air-sea concentration differences.

The observed discrepancies between the gradient and transfer velocity methods are highly variable. Unfortunately, only 5 independent gradient measurements are available yet, because the measurements are rather labour intensive, whereas persisting easterly winds limited the possibilities for undisturbed measurements for long periods of time.

3.3 Origin of CH₄

Dissolved CH₄, and several other parameters oscillated diurnally in relation to the tidal cycle (Fig. 3). This pattern resulted probably from advection and mixing of different water masses. The influence of possible vertical gradients over the water column was limited, as extremes in CH₄ concentration did not coincide with extremes in water height (Fig. 3). However, the exact mechanisms underlying the diurnal oscillation are unclear yet, as the hydrographic structure in the area is complex, highly variable, and dominated by

II

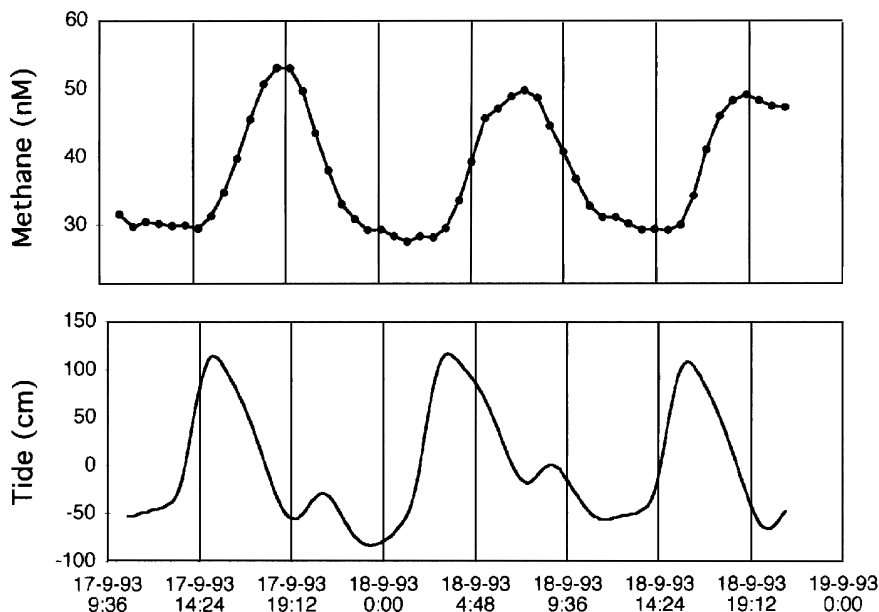


Figure 3: Relationship between dissolved CH_4 , and tide. Water height and CH_4 are out of phase, indicating the dominant influence of horizontal transport of water masses

freshwater discharge from the river Rhine. The region of freshwater influence, extends northeastwards along the entire Dutch coast, and out to 30 km offshore [Simpson *et al.*, 1993]. During the experiment, salinity ranged from 30.5 to 32.5 psu, corresponding with Rhinewater fractions of 7 to 13% (Fig. 1B).

Increasing CH_4 saturation, corresponded closely with decreasing salinity, indicating that salt and relatively CH_4 -poor water, was gradually replaced by less saline and CH_4 -rich water (Fig. 1 A,B). This apparent riverine origin of CH_4 was expected, since the importance of river discharge as a CH_4 source to the coastal sea, was shown by several studies. In October 1995, immediately after the ASGASEX experiment, we studied the CH_4 distribution in the Scheldt river, estuary, and adjacent coastal waters. Dissolved CH_4 increased from about 15 times saturation in the coastal waters off Vlissingen, up to as much as 350 times saturation in river waters upstream of Antwerp (Fig. 4). Similarly, *Scranton and McShane* [1991] reported extremely high CH_4 concentrations in the plume of the Rhine. These data suggest a major CH_4 supply by both Scheldt and Rhine rivers into the waters off the Dutch coast.

The role of other CH_4 sources is probably limited. Neither the sandy

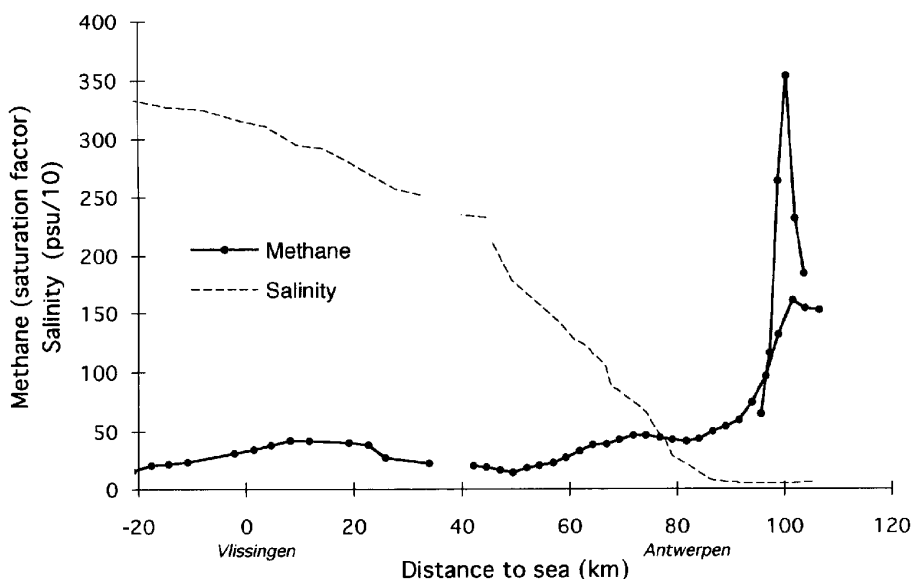


Figure 4: CH_4 along the salinity gradient of the Scheldt. Concentrations increase inland, reaching values over 350 times saturation, i. e., $1 \mu\text{mol l}^{-1}$.

sediments, nor the water column in this region are expected to produce substantial amounts of CH_4 . Even in areas where organic-rich sediments are known to sustain microbial CH_4 production, surface water saturations were much lower than in our study area [Bange *et al.*, 1994].

4 Concluding Remarks

Liss and Merlivat [1986] argued that the gradient method is difficult to apply for gases with low solubilities, such as CH_4 , N_2O , and CO_2 . Nevertheless, we succeeded in measuring significant and reproducible CH_4 gradients, primarily facilitated by the favourable combination of high analytical precision and huge local CH_4 air-sea concentration differences. CH_4 measurements were always accompanied by N_2O measurements with about the same precision. Nevertheless, it was difficult to measure significant N_2O gradients, because the N_2O saturation was almost 2 orders of magnitude lower than the CH_4 saturation. The applicability of the gradient method is thus largely determined by the water-atmosphere concentration difference and the available analytical sensitivity.

The CH_4 fluxes measured by the micrometeorological gradient method were on average 6 times larger than the fluxes estimated from the relationship of Wanninkhof [1992]. This discrepancy cannot easily be explained by experimental errors, nor by inhomogeneities in the dissolved CH_4 distribu-

tion. More simultaneous measurements by both methods are required to resolve this issue.

Despite the discrepancies observed, both methods confirm the global significance of the coastal zone in the marine CH₄ budget. Most probably, river discharge is the major source of CH₄ to the coastal sea.

Acknowledgements

We are grateful to the KNMI technical team for their support during the experiment. KNMI provided the turbulence measurements. Dorothee Bakker measured the surface water and equilibrator temperatures. This research was supported by the National Research Program on Global Air Pollution and Climate Change (NRP).

References

- Bange H. W., U. H. Bartell, S. Rapsomanikis, and M. O. Andreae, Methane in the Baltic and North Seas and a reassessment of the marine emissions of methane. *Global Biogeochemical Cycles*, 8, 465–480, 1994
- Broecker W. S., J. R. Ledwell, T. Takahashi, R. Weiss, L. Merlivat, L. Memery, T. H. Peng, B. Jähne, and K. O. Münnich, Isotopic versus micrometeorological ocean CO₂ fluxes: A serious conflict. *Journal of Geophysical Research*, 91 (C series, 9): 10517–10527, 1986
- Dabberdt W. F., D. H. Lenschow, T. W. Horst, P. R. Zimmerman, S. P. Oncley, and A. C. Delany, Atmosphere-Surface Exchange Measurements. *Science*, 260, 1472–1480, 1993
- Donelan M. and W. Drennan, Direct field measurements of the fluxes of carbon dioxide and water vapour. *This volume*
- Ericson D. J., A stability dependant theory for air sea gas exchange. *Journal of Geophysical Research*, 98 (C): 8471–8488, 1993
- Fowler, D. and J. H. Duyzer, Micrometeorological techniques for the measurement of trace gas exchange. In: *Exchange of trace gases between terrestrial ecosystems and the atmosphere*. M. O. Andreae, S. D. Schimel, editors. p. 189–207 John Wiley and Sons Ltd. D., 1989
- Kunz G., G. de Leeuw, S. Larsen, F. Hansen, Over-water eddy correlation measurements of fluxes of momentum, heat, water vapour, and CO₂. *This volume*
- Liss P. S. and L. Merlivat, Air-sea gas exchange rates: introduction and synthesis. In: *The Role of Air-Sea Exchange in Geochemical Cycling*, edited by P. Buat-Menard, Reidel, Dordrecht, pp. 113–127, 1986
- Oost W. A., The ASGASEX project. *This volume*
- Oost W. A., W. Kohsiek, G. de Leeuw, G. J. Kunz, S. D. Smith, R. J. Anderson, and O. Herzman, On the discrepancies between CO₂ flux measurement methods. *This volume*
- Robertson J. E. and A. J. Watson, Thermal skin effect of the surface ocean and its implications for CO₂ uptake. *Nature*, 358, 738–740, 1992

- Robertson J. E., A. J. Watson, C. Langdon, R. D. Ling and J. W. Wood, Diurnal variation in surface pCO₂ and O₂ at 60 °N, 20 °W in the North Atlantic. *Deep Sea Research*, 40, 409–422, 1992
- Scranton M. I. and K. McShane, Methane fluxes in the southern North Sea: the role of European rivers. *Continental Shelf Research*, 11, 37–52, 1991
- Simpson J. H., W. G. Bos, F. Schirmer, A. J. Souza, T. P. Rippeth, S. E. Jones and D. Hydes, Periodic stratification in the Rhine ROFI in the North Sea. *Oceanologica Acta*, 16, 23–32, 1993
- Smith S. D., R. J. Anderson, and E. P. Jones, A new measurement of CO₂ eddy flux in the nearshore atmospheric surface layer. *Journal of Geophysical Research*, 96 (C): 8881–8887, 1991
- Wanninkhof R., Relationship between wind speed and gas exchange over the ocean. *Journal of Geophysical Research*, 97 (C): 7373–7382, 1992
- Webb E. K., G. I. Pearman and R. Leuning, Correction of flux measurements for density effects due to heat and water vapour transfer. *Quart. J. R. Met. Soc.*, 106, 85–100, 1980
- Weiss R. F. and Price B. A., Nitrous oxide solubility in water and seawater. *Marine Chemistry*, 8, 347–359, 1980
- Wiesenburg D. A. and Guinasso N. L., *Journal of Chemical and Engineering Data*, 24, 356–360, 1979
- Woolf D. K. and Thorpe S. A., Bubbles and the air-sea exchange of gases in near saturation conditions. *Journal of Marine Research*, 49, 435–466, 1991

In Situ Measurements of the Air-Sea Gas Transfer Rate during the MBL/CoOP West Coast Experiment

H. Haußecker^{1,2} and *B. Jähne*^{2,1}

¹Interdisciplinary Center for Scientific Computing, University of Heidelberg
Im Neuenheimer Feld 368, 69120 Heidelberg, Germany
email: horst.haussecker@iwr.uni-heidelberg.de

²Scripps Institution of Oceanography, Physical Oceanography Res. Div.
La Jolla, CA 92093-0230, USA, email: bjahne@ucsd.edu

doi: 10.5281/zenodo.10407

Abstract

The controlled flux technique (CFT) uses heat as a proxy tracer for gases to measure air-sea gas transfer rates. It has been used during the MBL/CoOP West Coast experiment in April/May 1995 aboard R/V New Horizon for the first time at sea. In this paper the technical realization of the sea-going instrument is outlined and first measurements of the gas transfer rate in the field are shown. The high temporal resolution reveals that the gas transfer rates are intermittent with respect to space and time. Depending on surfactant concentration and the patchiness of surfactants they vary up to $\pm 25\%$ of their temporal average for a certain wind speed within some minutes.

1 Introduction

Conventional techniques to measure the transfer velocity k

$$k = \frac{j}{\Delta c} \quad (1)$$

of gases across the ocean interface are based on mass balance of the gas tracer in the water body. In order to determine the flux j the temporal change \dot{c}_w of the tracer concentration in a volume of water V_w has to be measured. The corresponding time constant τ_w is in the order of days to weeks in the ocean. This long integration time hinders empirical parameterization of the gas transfer rate with friction velocity and other parameters such as the wave field and prevents any insight into the mechanisms. Also the enormous difficulties in closing the mass balance for classical geochemical trace gases such as ^{222}Rn [Roether and Kromer, 1984], lead to systematic errors. Dual-tracer experiments as used by Wanninkhof [1993] and Watson [1991] partly overcome these problems but still suffer from the long time constant.

An alternative approach, the *controlled flux technique* (CFT) is based on the simple idea applying a controlled flux density j of a tracer across the interface. Now, the only unknown parameter according to equation (1) is the concentration difference Δc across the aqueous mass boundary layer.

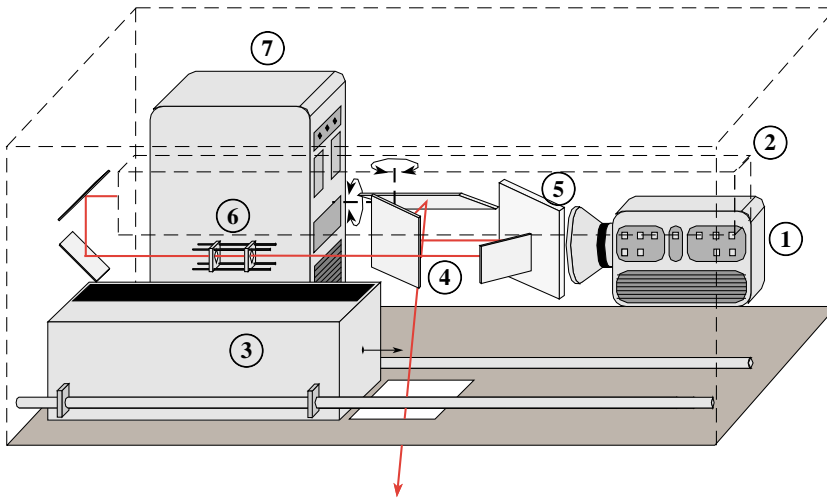


Figure 1: Schematic setup of the CFT field instrument (without detailed mountings, laser drawn transparent). 1: IR camera, 2: CO₂ laser, 3: calibration box, 4: x-y scan unit, 5: beamsplitter, 6: IR laser optic, 7: Computer.

With the assumption that the transport close to the interface is dominated by molecular diffusion, the time constant t_* for the transport across this layer with the thickness z_* is given by

$$t_* = \frac{z_*}{\langle k \rangle} = \frac{D}{\langle k \rangle^2}, \quad (2)$$

where D is the diffusion constant of the tracer in water [Jähne *et al.*, 1989]. The time constant t_* is of the order of only 0.1 to 10 s. In order to get a well defined tracer flux density, heat is used as a proxy tracer for gases. The heat concentration (temperature) at the water surface is measured with an infrared radiometer. The temperature difference ΔT can be determined by simply switching on and off the radiation. Knowing the *Schmidt number* dependency, the transfer velocity of any gas tracer can be estimated.

2 Experimental setup

Figure 1 shows the setup of the field instrument as it was used during the MBL/CoOP West Coast Experiment in April/May 1995. The main part consist of a 25 Watt CO₂ infrared laser at a wave length of 10.6 μm as a heat source and an AMBER Radiance 1 256 \times 256 focal plane array (FPA) *infrared camera* with a NETD of 0.025 K, sensitive in the 3 - 5 μm wave length region. The laser is used to heat up a small area on the water surface, either in continuous or in pulsed mode. The camera observes a footprint of about 140 \times 140 cm.



Figure 2: Photograph of the instrument at the boom on the foredeck of R/V New Horizon.

With an infrared optic, the size of the laser spot can be remotely adjusted from some centimeters up to the whole area observed. With this setup a large variety of heat patterns can be applied to the water surface and the temperature increase and temporal behavior of the heat distribution on the water surface can be observed.

The infrared camera has to be carefully calibrated in order to reliably use its temperature resolution of 25 mK. For this purpose a special calibration box was designed, which contains 3 different temperature standards with an extended aperture to cover the whole field of view of the camera. The geometrical arrangement of the calibration bodies, reference bodies and the box itself, together with a special IR-coating make it possible to reduce reflections of the incoming radiation flux significantly and make the calibration box almost behave like an ideal blackbody. With this special setup a relative temperature calibration can be performed with an accuracy of approx. 1 mK.

In our instrument both the camera and the laser together look via an x-y-scan unit at the water surface. The laser beam is aligned with the optical axis of the IR-camera with the help of a specially designed beamsplitter that has a reflectivity of $\rho > 0.95$ at the laser wave length ($10.6 \mu\text{m}$) and a transmittance of $\tau > 0.9$ at the camera wavelength ($3 - 5 \mu\text{m}$).

The CFT field instrument was used for the first time during the combined ONR 'Marine Boundary Layer' and NSF 'Gas Transfer in Coastal Waters' experiment (MBL/CoOP) at the US West Coast in April/May 1995 aboard the Research Vessel New Horizon (SIO). The instrumental setup was mounted at the end of a 7 m long boom right at the bow of the ship. The box was hanging 7 m above the water surface and looked under an angle of 20° off bow. This aluminum construction could be retrieved to reach the instrument and to secure it. Once deployed, the boom behaved very stably and did not shake or swing even under rough sea states. With this arrangement the influence of the ship could successfully be minimized. During the measurements the ship was steaming with a speed of 0.5 m/s headed up into the wind.

3 Preliminary Results of the MBL/CoOP CFT-Measurements

During the MBL/CoOP cruise off the West Coast from April 27, 1995 to May 16, 1995, extensive measurements were made with the new instrumentation aboard R/V New Horizon. The cruise covered an area that extends from Monterey Bay at the most northern position along the California coast down to San Diego within a range of up to 30 sea miles off shore.

The cruise on R/V New Horizon offered a unique variety of simultaneous measurements of key parameters influencing gas transfer velocity. The investigations focused on wind stress, dynamic surface viscoelasticity (surfactants of biological origin), short wind waves, gravity waves and atmospheric stability. Besides the CFT the instruments aboard R/V New Horizon included a catamaran (LADAS) with a scanning laser slope gauge (SLSG), a surface film sampler (SCUMS), a sonic anemometer and a meteorological package, a bouy with an imaging slope gauge (ISG) and a combined stereo height-slope-curvature imaging device (HSCI). The participating research groups were from Woods Hole Oceanographic Institution (WHOI), University of Rhode Island, Scripps Institution of Oceanography (SIO), and University of Heidelberg [Bock *et al.*, 1995].

Samples of the acquired infrared images at wind speeds from 2.5 to 13 m/s are shown in Figure 3. It is amazing to see how sensitive the camera imaging is at faint temperature differences at the water surface, giving major direct insight into the spacial structure of the micro turbulence at the ocean interface.

It was a main discovery of this cruise, that the typical heat fluxes across the air-water interface by radiative cooling, evaporation or sensitive heat transfer are sufficiently large to cause significant temperature variations at the water surface. Nevertheless the heat patterns in Figure 3 seem to be dominated by noise. A closer evaluation of the temperature standard deviation within single images shows that the temperature variations are well above the noise level even for high wind speeds. Figures 4-5 show a time series of single-image temperature standard deviations. A sequence of 8 images was acquired every 5 seconds. Because the image content is only

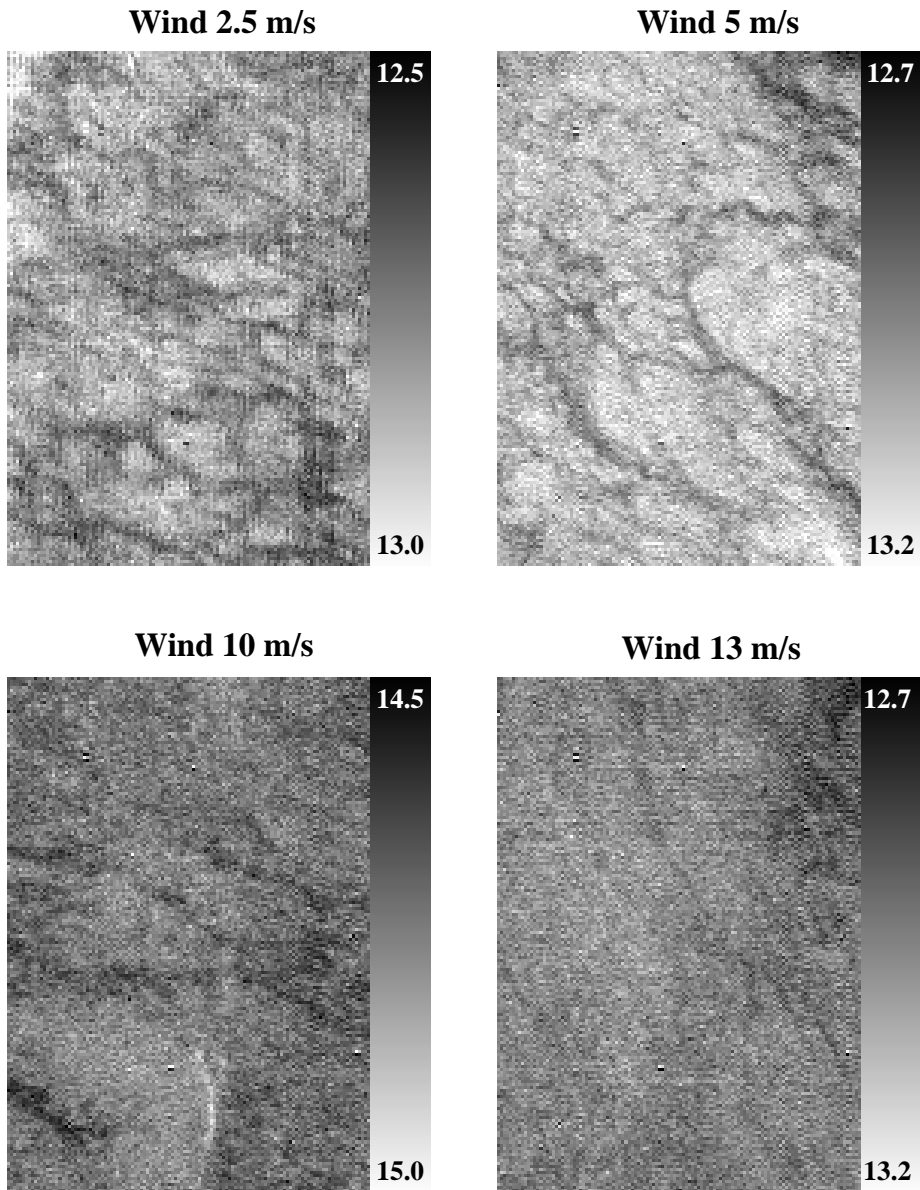


Figure 3: Examples of high resolution temperature images acquired during the MBL/CoOP West Coast experiment (temperature calibrated [$^{\circ}$ C]). The size of the images is about 1×1 m

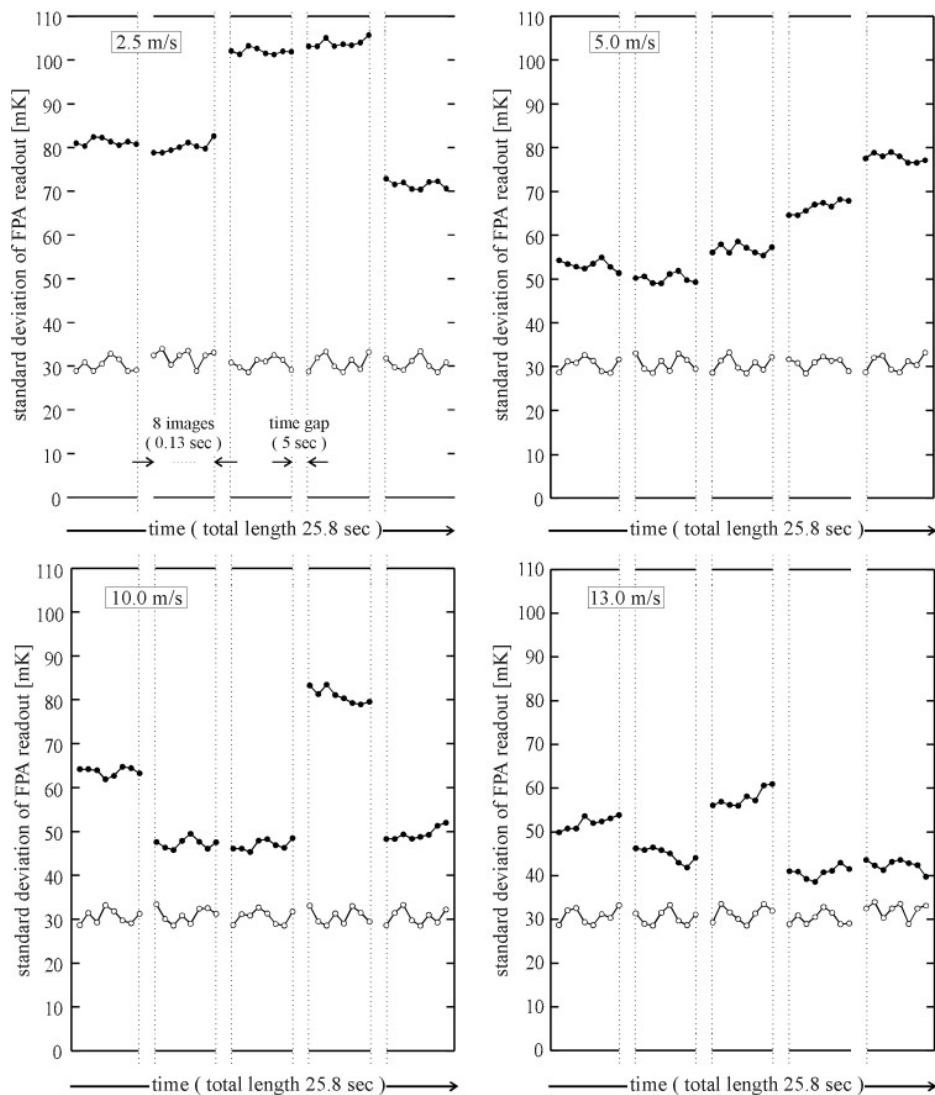


Figure 4: Standard deviation of the image temperature distribution for consecutive sequences of 8 images. The sequences were acquired at time steps of 5 seconds. Black circles: Ocean surface data for different wind speeds. Open circles: Uniformly heated calibration surface.

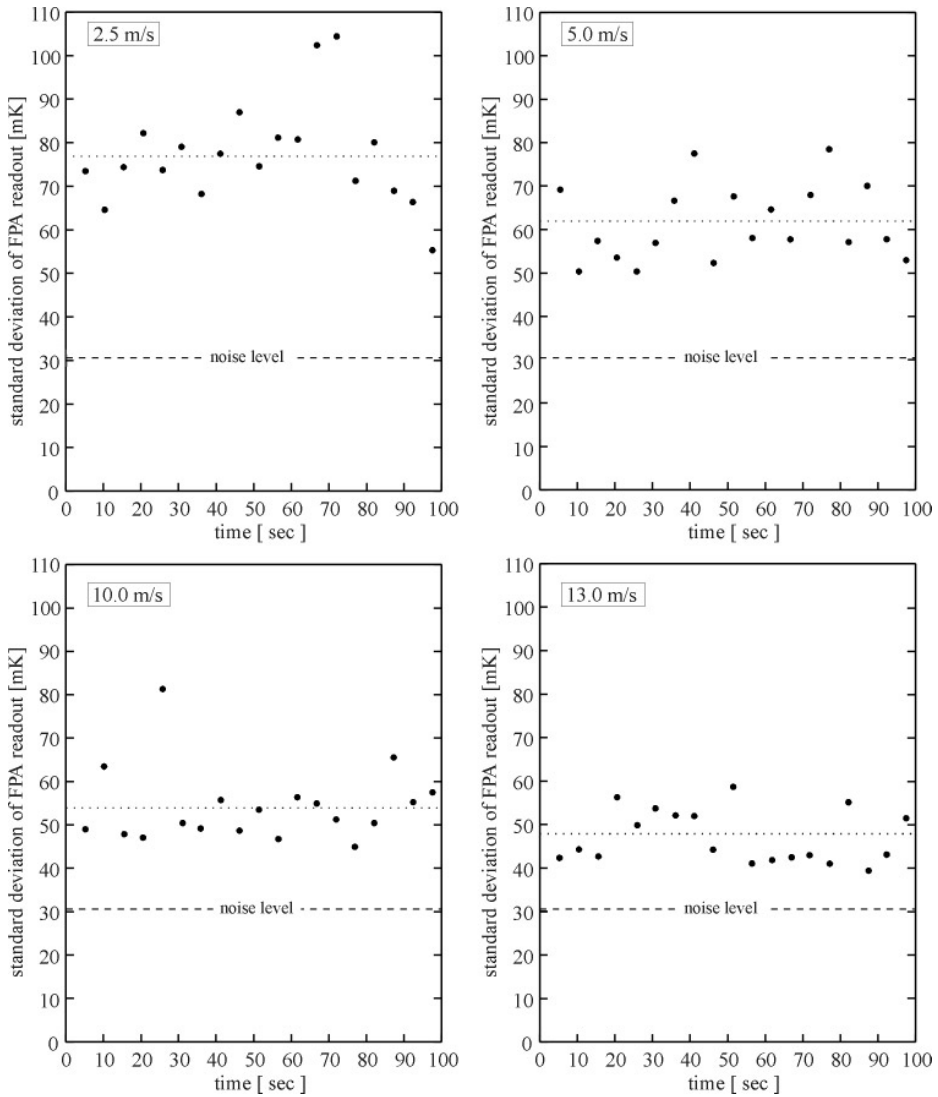


Figure 5: Standard deviation of the temperature distribution within a single image over a time interval of 100 seconds. Each dot represents the average value of one short sequence of 8 images in Figure 4. The dashed line indicates the temporal average of the camera noise in Figure 4. The dotted line shows the temporal average of the data, which is used to compute k .

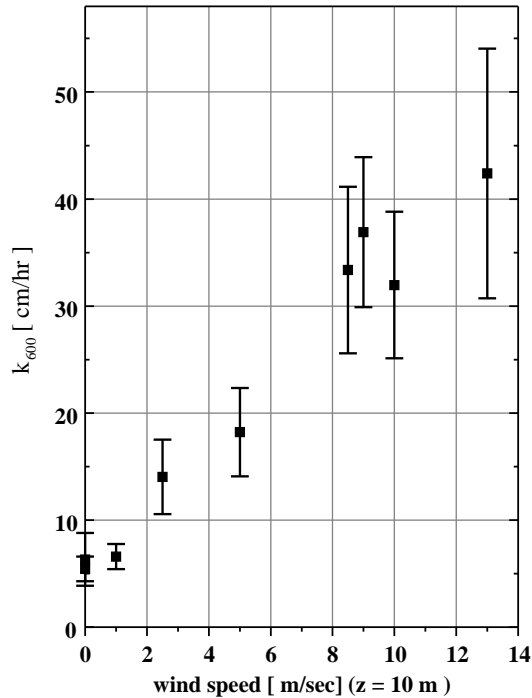


Figure 6: Gas transfer rates computed from the field data, normalized to Schmidt number Sc of 600 for different wind speeds. The error bars indicate the temporal variability (standard deviation) of the transfer rates during a period of 4 min. The black dots are the mean values of the transfer rates within this time span.

slightly shifted within 0.13 s the temperature distribution stays almost constant within the short sequences. After a time gap of 5 seconds the image content has changed and the camera observes another water surface element with different heat patterns. When the camera was pointed only at the homogeneously heated surface of the calibration device, a constant standard deviation of about 30 mK was measured. This shows the noise level of the camera in good accordance with the specifications of the manufacturer. It becomes obvious that the high temporal sensitivity of the camera is very important. A twice as high noise-equivalent temperature difference ($NE \Delta T$) would already suppress the heat patterns for wind speeds higher than 5 m/s!

The temporal averages of the temperature standard deviation were used to compute the gas transfer rate k_{600} with the *spatio-temporal temperature fluctuation method*, described in *Haußecker et al.*, [1995]. Figure 6 shows some preliminary results for k_{600} at different wind speeds. These data are in good correspondence with previous ocean measurements of other researchers (Figure 7). However, k seems to be slightly increased towards

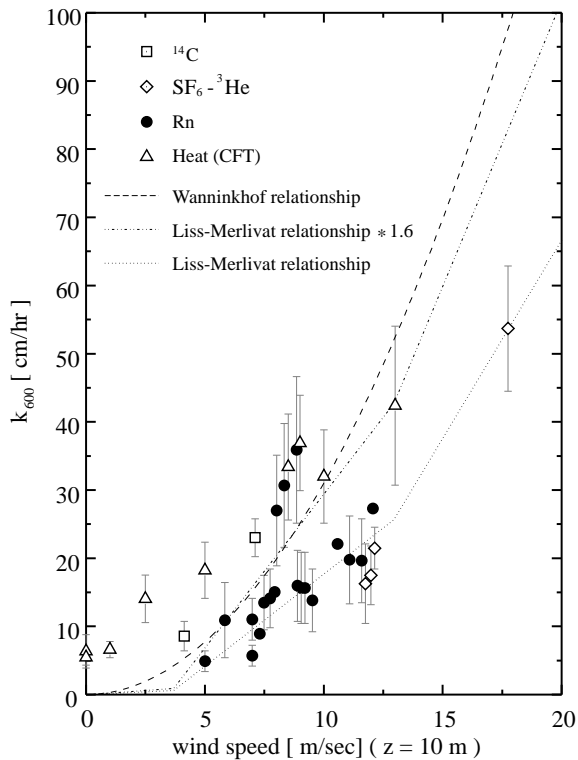


Figure 7: Summary of gas exchange measurements in the ocean and transfer velocity/wind speed relations, including some preliminary heat exchange data.

low wind speeds. This result is reasonable because at sea gravity waves are always present. One never gets a calm water surface as in wind wave facilities. There, the water surface is absolutely at rest if the wind is turned off. The data in Figure 6 shows some evidence of a slope change around a wind speed of 6 m/s, which has to be verified within further data evaluation.

The error bars in Figures 6–7 indicate the temporal variability of the transfer rate within 5 minutes. From Figures 4–5 it becomes obvious that the temperature standard deviation – and therefore the transfer rates – show fluctuations of up to 50% of the temporal average. This discovery clearly demonstrates the importance of gas exchange measurements with a high temporal resolution. A very important issue for future research projects will be to investigate, whether the temporal variability of gas transfer rates is due to an increased *intermittence* of parameters such as wind speed and the wave field or due to a spatially inhomogenous surfactant concentration.

4 Conclusions

The field going instrument proved to work well. Gas transfer rates could be computed with a high temporal resolution of less than a minute. However, not all data are yet evaluated. The measurements also have to be related to simultaneous measurements of other parameters influencing gas transfer, e. g., surfactant concentration.

Acknowledgements

Financial support of this research by the Office of Naval Research (N00014-93-1-0515 and N00014-94-1-0050) and by the National Science Foundation (OCE 89 11224) is gratefully acknowledged.

References

- Bock, E. J., J. Dieter, J. B. Edson, N. M. Frew, T. Hara, K. Hansen, H. Haußecker, B. Jähne, A. Karachintsev, J. Klinke, W. R. McGillis, R. K. Nelson, and M. Uz, Description of the Science Plan for the April 1995 CoOP Experiment, Gas Transfer in Coastal Waters, performed from the Research Vessel New Horizon, *This volume*
- Haußecker, H., and B. Jähne, In situ measurements of the air-sea gas transfer rate using heat as a proxy tracer, *Second International Conference on Air-Sea Interaction and Meteorology and on Oceanography of the Coastal Zone*, Lisbon, September 22-27, 1994, Lisbon, Portugal, 1994
- Haußecker, H., S. Reinelt, and B. Jähne, Heat as a proxy tracer for gas exchange measurements in the field: principles and technical realization, *This volume*
- Jähne, B., P. Libner, R. Fischer, T. Billen, and E. J. Plate, Investigating the transfer processes across the free aqueous viscous boundary layer by the controlled flux method, *Tellus*, 41B, pp. 177-195, 1989
- Roether, W. and B. Kromer, Optimum application of the radon deficit method to obtain air-sea gas exchange rates, In *Gas transfer at water surfaces* (eds. W.Brutsaert and G. H. Jirka), Dordrecht, Holland: Reidel, pp. 447-457, 1984
- Watson, A. J., R. C. Upstill-Goddard, and P. S. Liss Air-sea exchange in rough and stormy seas, measured by a dual tracer technique, *Nature*, 349, pp. 145-147, 1991
- Wanninkhof, R., Gas transfer experiment on Georges Bank using two volatile deliberate tracers, *Journal of Geophysical Research*, Vol. 98, No. C11, pp. 20,237-20,248, Nov. 1993

Relationship between Gas Transfer Velocities and Wind Speeds in The Tidal Hudson River Determined by the Dual Tracer Technique

J. F. Clark^{1*}, *P. Schlosser*¹, *H. J. Simpson*¹,
*Martin Stute*¹, *R. Wanninkhof*², and *D. T. Ho*²

¹Lamont-Doherty Earth Observatory,
Columbia University, Palisades, NY, 10964, USA

²Ocean Chemistry Division, NOAA/AOML, Miami, FL, 33149, USA

Abstract

Gas transfer velocities were determined using the dual tracer technique (³He and SF₆) for two 40–60 km reaches of the tidal Hudson River. The experiments were performed near Poughkeepsie, NY, in 1993 and near Catskill, NY, in 1994. During both experiments, wind speeds were measured above the river. The shape of daily axial SF₆ distributions and the evolution of peak concentrations followed patterns predicted by the one-dimensional advection-diffusion equation. Mean gas transfer velocities calculated from the 1994 data using the temporal change in SF₆ inventory ($4.6 \pm 0.4 \text{ cm hr}^{-1}$) and the tracer ratio ($5.3 \pm 0.2 \text{ cm hr}^{-1}$) are in good agreement, suggesting that the dual tracer technique yields reasonable results. The relationships between gas transfer velocity and wind speed found during these experiments are very similar to those observed previously for lakes, suggesting that wind is the primary source of surface turbulence in these reaches of the tidal Hudson River. The results of the 1993 and 1994 experiments agree very well, indicating that the local geometry of the river is of secondary importance.

1 Introduction

Exchange of dissolved gases across the air-water interface is an important physical process which influences many properties of natural waters. Water quality assessment often requires quantitative estimates of this parameter both for calculations of reaeration rates and for loss rates of volatile pollutants (e. g., *O'Connor* [1962], *Dyrssen et al.* [1990], *Thomann et al.* [1991]). Quantitative relationships which can be used to predict gas transfer velocities from easily measurable parameters such as wind and current speeds are particularly important. Such relationships can be used directly in model simulations and mass balance calculations. For instance, precise *gas transfer* velocities are needed to accurately measure whole-ecosystem respiration

*Now at: Department of Geological Sciences, University of California, Santa Barbara, CA, 93106, USA

rates using diurnal dissolved oxygen methods (*Odum [1956], Edwards and Owens [1962], Howarth et al. [1992]*) or to constrain mass balance calculations of volatile contaminants such as PCBs [*Thomann et al., 1991*].

Most experiments which quantified gas transfer velocities in estuaries have used either the helmet or mass balance methods (*Juliano [1969], Hartman and Hammond [1984], Clark et al. [1992], Marino and Howarth [1993]*). While such experiments can potentially lead to parameterizations of gas transfer velocities, the results are questionable because of a number of methodological uncertainties. The problem with the helmet method is that the surface turbulence regime, the physical driving force behind gas exchange, is disturbed during the measurement. Thus, the measured gas transfer velocity may be influenced by the helmet. Laboratory experiments have found little agreement between gas transfer velocities determined by the helmet method and other approaches (*Stephens [1978], Belanger and Korzum [1991]*), suggesting that the surface turbulence regime is indeed disturbed. A central weakness of the mass balance method is that the magnitude and variability of sources and sinks of the dissolved gas must be well known. Uncertainties associated with these terms influence calculated gas exchange rates. Despite these problems, both methods have shown that gas transfer velocities correlate well with wind speed in most estuaries (*Hartman and Hammond [1984], Kim and Holley [1988], Marino and Howarth [1993]*).

Recently, a new method, the *dual tracer technique* (*Watson et al. [1991], Wanninkhof et al. [1993]*), has been developed which can be used to quantify gas transfer velocities in large tidal rivers [*Clark et al., 1994*]. Because the surface turbulence regime is not disturbed during the measurements and because the gas tracers are added in a controlled fashion, the dual tracer technique does not have the methodological problems associated with the helmet and mass balance approaches. With the dual tracer technique, mean gas transfer velocities over periods of days to weeks can be estimated. By simultaneously measuring other environmental variables, parameterizations of the gas transfer velocity can be established for use in future experiments.

Here we present the results of two gas tracer experiments performed on the tidal *Hudson River* during summer and autumn months in 1993 and 1994. The focus will mainly be on the results of the 1994 experiment because the results of the 1993 experiment have been described earlier [*Clark et al., 1994*].

1.1 Principles of the Dual Tracer Technique

Most *tidal rivers* such as the Hudson can be approximated as one-dimensional systems. Dilution and first-order decay of a pulse of a non-reactive gas tracer added to such a system can be described by the following advection-diffusion equation:

$$\frac{\partial C}{\partial t} + u \frac{\partial C}{\partial x} = D \frac{\partial^2 C}{\partial x^2} - \alpha C \quad (1)$$

where C is the average cross sectional concentration of the gas tracer; u is the average cross sectional current velocity; D is the longitudinal dispersion coefficient; and α is the first order loss term due to transfer across the air-water interface (i. e., reaeration coefficient). *O'Connor* [1963] and *O'Loughlin and Bowmer* [1975] showed that the solution of equation (1) for an instantaneous injection of a gas tracer is:

$$C(x, t) = \frac{M}{A\sqrt{4\pi Dt}} \exp\left[-\frac{(x - ut)^2}{4Dt}\right] \exp(-\alpha t) \quad (2)$$

where M is the mass of trace gas added and A is the cross sectional area. This model predicts that longitudinal distributions of the tracer should be gaussian in shape and that the peak concentrations should decay linearly as a function of $e^{-\alpha t} t^{-1/2}$.

The gas transfer velocity, k , is defined in the following manner:

$$k = F / (C_{sur} - C_{eq}) = \alpha / h \quad (3)$$

where F is the mass flux of gas across the air-water interface, C_{sur} and C_{eq} are the concentrations of the gas in the water at the air-water interface and in equilibrium with the atmosphere, respectively, and h is the mean depth.

Solving the advection-diffusion equation with first order decay (eq. 1 and 2) for two instantaneously injected gases, such as ^3He and SF_6 , and assuming that the gas transfer velocities, $k_{^3\text{He}}$ and k_{SF_6} , are related by their Schmidt numbers [*Jähne et al.*, 1987]:

$$k_{\text{SF}_6} / k_{^3\text{He}} = \left(\text{Sc}_{(\text{SF}_6)} / \text{Sc}_{(^3\text{He})} \right)^{-n} \quad (4)$$

leads to the following expression for the gas transfer velocity of ^3He (*Watson et al.* [1991], *Wanninkhof et al.* [1993]):

$$k_{^3\text{He}} = \frac{1}{h} \frac{d}{dt} \left(\frac{\ln(\Delta[^3\text{He}] / \Delta[\text{SF}_6])}{1 - (\text{Sc}_{(\text{SF}_6)} / \text{Sc}_{(^3\text{He})})^{-n}} \right) \quad (5)$$

where $\text{Sc}_{(^3\text{He})}$, and $\text{Sc}_{(\text{SF}_6)}$ are the Schmidt numbers for ^3He and SF_6 calculated using the relationships given by *Wanninkhof* [1992] and the observed water temperature, $\Delta[^3\text{He}]$ and $\Delta[\text{SF}_6]$ are the differences between observed and atmospheric equilibrium concentrations for ^3He and SF_6 , respectively, and

n is the Schmidt number exponent. The Schmidt number is defined as the kinematic viscosity of water divided by the molecular diffusion coefficient of the gas in water. For wavy surfaces not broken by white caps, n has been determined to be 1/2 in both laboratory and field experiments (Ledwell [1984], Jähne *et al.* [1987], Watson *et al.* [1991]).

1.2 Study Location

The Hudson is a tidal river for more than 130 km south of the Federal Dam at Troy, NY (kmp 248¹) (Fig. 1). The position of the salt/fresh water interface varies seasonally. Typically, during spring runoff, it is located about 15 to 30 km north of New York City (kmp 25-40) and during late summer low runoff, it lies near Newburgh, NY (kmp 100).

Of the total freshwater discharge into the tidal Hudson River, 50-80 % enters at the Federal Dam. Flow from four large tributaries, Wappinger Creek (kmp 108), Rondout Creek (kmp 148), Esopus Creek (kmp 166), and Catskill Creek (kmp 183), account for most of the remaining freshwater discharge. Mean flow at the Federal Dam varies seasonally. Maximum ($> 800 \text{ m}^3 \text{ s}^{-1}$) and minimum flows ($50 \text{ to } 200 \text{ m}^3 \text{ s}^{-1}$) occur during spring and late summer respectively. Mean depths of cross sections vary between 4 and 9 m for most of the tidal river except for a 30 km reach downstream of Rondout Creek where the river deepens and mean depths of cross sections vary between 10 and 20 m (Fig. 2a). The cross sectional area of the channel increases downstream from $2,000 \text{ m}^2$ near the Federal Dam to $12,000 \text{ m}^2$ near the salt/fresh water interface (Fig. 2b).

The tracer release experiments were performed at different locations in the tidal Hudson River. During the 1993 experiment, a mixture of SF₆ and ³He was injected about 10 km south of Rondout Creek (kmp 138). The center of the tracer patch was confined to a 40 km reach of river between the injection point and Wappinger Creek. Here, the axis of the river trends north-south with only one significant bend in the river (Fig. 1). No major tributaries enter and no extended area of shallow water occurs along this stretch of river. The geometry is complicated only by Esopus Island, which lies about 3 km south of the injection point. The cross sectional area of the channel does not vary much along this reach (Fig. 2b). The mean depth and width of the channel is 14 m and 800 m, respectively (Fig. 2). During this experiment, the mean freshwater discharge rate over the Federal Dam was $160 \pm 24 \text{ m}^3 \text{ s}^{-1}$ and the temperature of the river averaged 26°C.

During the 1994 experiment, the injection point (kmp 227) was about 7 km south of Albany, NY. The center of the tracer patch was confined to a 60 km reach of the river between the injection point and Esopus Creek. The cross sectional area increases south of the injection point from about

¹Locations along the Hudson River are referred to by the axial distance, kilometer point (kmp), upstream (+) and downstream (-) from the Battery at the southern tip of Manhattan Island.

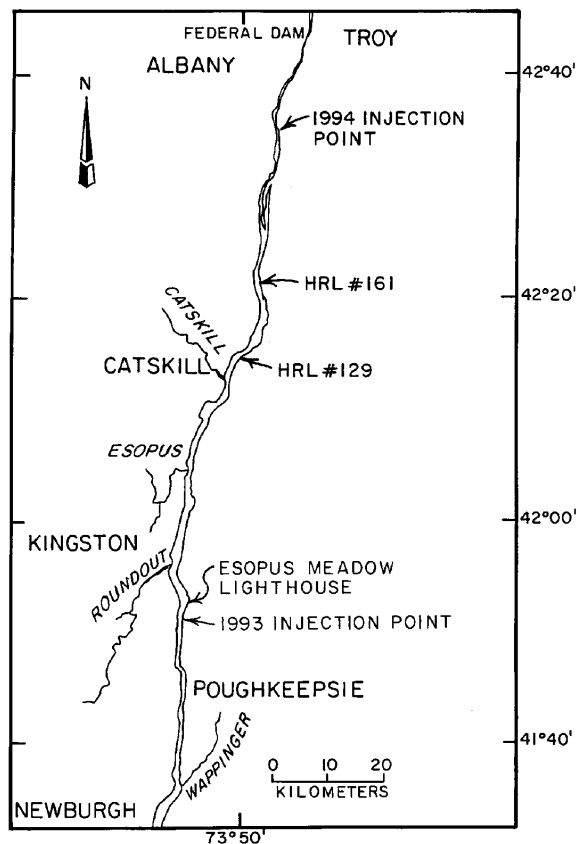


Figure 1: Map of the tidal Hudson River.

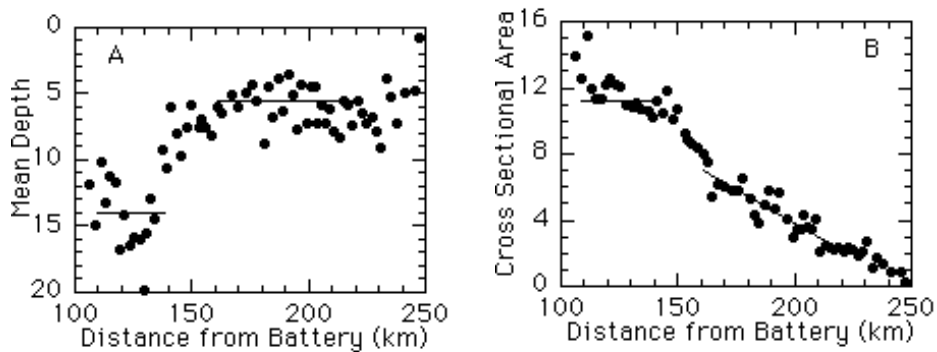


Figure 2: Geometry of Hudson River cross sections calculated from Stedfast (1980). **a** mean depth (m) and **b** cross sectional area (10^3 m^2). The lines represent the regions of the two tracer experiments.

Table 1: Results of Hudson River gas tracer experiments.

Time after Injection (day)	Peak SF ₆ (pmol l ⁻¹)	Peak Excess ³ He (10 ⁻¹⁶ ml STP g ⁻¹)	Excess ³ He/SF ₆	k ₆₀₀ (cm hr ⁻¹)	U ₁₀ (m s ⁻¹)
1993 Experiment					
1.1	3.28	1524	501 ± 15	-	-
2.0	1.98	1040	530 ± 16	-	0.7
3.1	1.64	791	483 ± 15	-	1.6
5.2	1.04	431	413 ± 12	3.9 ± 1.5	3.9
7.0	0.81	323	387 ± 12	1.5 ± 1.8	2.5
8.2	0.69	216	315 ± 10	9.0 ± 2.4	4.9
10.1	0.53	131	248 ± 7	6.3 ± 1.6	3.1
12.1	0.45	96	214 ± 6	3.5 ± 1.4	3.2
14.2	0.34	63	189 ± 6	3.6 ± 0.7	2.8
16.2	0.26	38	144 ± 4	5.9 ± 1.5	3.2
1994 Experiment					
1.1	41.3	-	-	-	-
2.1	20.0	-	-	-	-
3.1	11.6	-	-	-	-
4.1	7.84	2031	260 ± 5	-	-
5.2	4.73	940	199 ± 6	5.3 ± 1.0	-
6.3	3.06	437	143 ± 5	6.7 ± 1.3	2.9
7.3	2.24	251	109 ± 3	6.1 ± 1.4	3.1
8.2	1.79	166	92.4 ± 3	4.2 ± 1.5	2.7
9.2	1.42	115	81.1 ± 1	2.8 ± 1.0	1.3
10.1	1.17	77	65.5 ± 2	5.6 ± 1.2	2.4
11.0	0.86	38	43.9 ± 1	9.1 ± 1.2	5.1
12.0	0.66	21	32.5 ± 2	6.7 ± 1.9	4.2
13.1	0.51	12	24.1 ± 3	6.5 ± 4.2	3.4

2,000 m² to about 7,000 m² near Esopus Creek (Fig. 2b). Throughout this region, the main channel is dredged to a depth of about 10 m. However, because of extensive areas of shallow water (<2 m), the mean depth varied between 4 and 8 m and averaged about 5.5 m (Fig. 2a). Many islands and coves further complicate the geometry. During this experiment, the mean freshwater discharge rate over the Federal Dam was 210 ± 40 m³ s⁻¹. During the first week, the surface water temperature decreased from 19°C to about 15°C where it remained constant thereafter.

2 Methods

Prior to each Hudson River experiment, about 0.045 moles of 99.8 % pure ^3He gas and 31 moles of pure *sulfur hexafluoride* (SF_6) gas were mixed into a large gas cylinder (43.8 l). The gas mixtures were injected into the river on August 24, 1993 and September 28, 1994 through two diffusing stones which were suspended at a depth of 10 m behind a small boat. The injection occurred over a period of about 20 minutes as the boat crossed the channel perpendicular to the main axis of the river. During the 1993 experiment about 0.6 moles of the gas mixture were injected as the boat crossed the channel twice and during the 1994 experiment about 1.4 moles were injected as the boat crossed the channel 7 times. Approximately 20–40 % of the gases dissolved during the injection (see below; Clark *et al.* [1994]). Because of drag caused by the rope and diffusion stones, the injection depth of the gas mixture was shallower than 10 m.

For approximately two weeks after both injections, samples were collected in sequence along the main axis of the river from a small boat every 1 to 2 days using either a 1.5 l or 5 l Niskin bottle. Station locations were determined using a field Global Positioning System unit. During the 1993 experiment, stations were occupied at either slack high or slack low tide and spaced at intervals of 1 to 2 km. At each station, samples for SF_6 and ^3He were collected about 1 meter below the surface of the water and about 1 meter above the sediment. SF_6 samples were stored submerged in a bucket of river water and analyzed on shore 2 to 12 hours after collection.

During the 1994 experiment, the analytical equipment was set up in the cabin of our boat, enabling us to obtain nearly real time SF_6 data. Spacing between stations was determined by location within the tracer patch. At the edges, stations were separated by 2 to 4 km. This distance was shortened nearer to the center of the patch where the distance between stations was 0.3 to 0.5 km during the first week of the experiment and 0.5 to 1.5 km during the second week. Surface samples were collected at all stations, bottom samples were collected at every 3rd or 4th station and at all stations near the center of the patch, and mid-depth samples were collected at about one third of the center stations. While SF_6 was collected at all stations and measured on the boat, ^3He samples were collected only near the center of the patch and measured later on shore.

SF_6 samples were collected in either 50 ml glass syringes or 60 ml BOD bottles. All samples were analyzed with a gas chromatograph equipped with an electron capture detector using the head space method described by Wanninkhof *et al.* [1987, 1991]. SF_6 was separated from other gases with a molecular sieve 5A column held at room (cabin) temperature. All samples were measured within 12 h of collection. The reproducibility of the SF_6 measurements was ± 2 to 3 %.

^3He was analyzed from about 40 ml of water which was collected in copper tubes and sealed by pinch-off clamps. All samples were analyzed

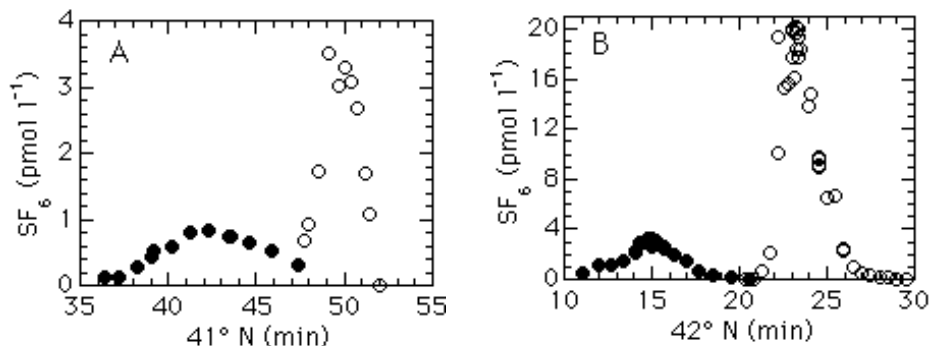


Figure 3: **a** Axial distributions of SF₆ from the 1993 experiment. Open circles = day 1 and solid circles = day 6. **b** Axial distributions of SF₆ from the 1994 experiment. Open circles = day 2 and solid circles = day 6.

on a VG-5400 helium isotope mass spectrometer using methods similar to those described by Bayer *et al.* [1989]. Precision of ⁴He concentrations and ³He/⁴He ratios were about ±0.5 % and ±0.2 %, respectively.

Excess ³He concentrations, [³He]_{exc}, were calculated from the measured ³He/⁴He ratio and ⁴He concentration in the following manner:

$$[{}^3\text{He}]_{\text{exc}} = [{}^4\text{He}]_s(R_s - R_a) + [{}^4\text{He}]_{\text{eq}}R_a(1 - a) \quad (6)$$

where ⁴He_s is the measured ⁴He concentration; ⁴He_{eq} is the atmospheric equilibrium concentration of ⁴He [Weiss, 1971]; R_s is the measured ³He/⁴He ratio; R_a is the atmospheric ³He/⁴He ratio (1.386 × 10⁻⁶; Clarke *et al.* [1976]); and *a* is the solubility isotope effect (0.983; Benson and Krause [1980]).

During each experiment an anemometer was placed within the river's channel (Fig. 1). In 1993, it was placed on top of the Esopus Meadow Lighthouse (kmp 141), 16 m above the high water mark. The lighthouse is located about 600 m from the western shore. In 1994, the anemometer was placed on Hudson River Light (HRL) #161 (kmp 203) for the first week and on HRL #129 (kmp 188) for the second week. The height of the anemometer above the high water mark was 9.6 m and 9.7 m, respectively. Both of these lights were more than one third of the way across the channel. Hourly mean wind speeds and prevailing wind direction (using 16 compass directions) were recorded. The same instrument was used during the two experiments.

3 Results

Because continental waters are potentially contaminated with SF₆ [Clark *et al.*, 1995a], background concentrations were measured prior to injecting the

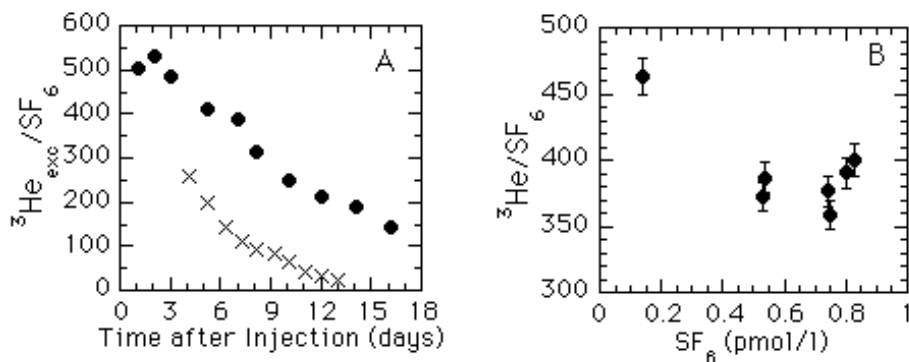


Figure 4: **a** Temporal change of the excess $^3\text{He}/\text{SF}_6$ ratios: solid circles = 1993 and crosses = 1994. **b** Excess $^3\text{He}/\text{SF}_6$ plotted as a function of SF_6 concentration. Transect collected on Aug. 31, 1993.

gas tracers. We found that background SF_6 concentrations were below our detection limit (0.01 pmol l^{-1}) in areas of our gas exchange experiments suggesting that the tidal Hudson River is free of any significant local contamination. At the same locations, ^3He was determined to be in solubility equilibrium with the atmosphere.

Daily distributions of SF_6 concentrations along the axis of the tidal Hudson River and the evolution of peak concentrations followed patterns predicted by the one-dimensional advection-diffusion equation (eq. 1 and 2) suggesting that this system can be approximated as a one-dimensional system. During both experiments, longitudinal distributions were approximately gaussian in shape (Figs. 3a and 3b) and peak SF_6 concentrations and excess $^3\text{He}/\text{SF}_6$ ratios decreased by 1 to 2 orders of magnitude (Tab. 1, Fig. 4a). The ratio observed near the center of the tracer patch ($[\text{SF}_6] > 0.5 * [\text{SF}_6]_{\text{max}}$) was approximately constant (Fig. 4b). Plots of peak SF_6 concentrations versus $e^{-\alpha t} t^{-1/2}$ were linear (Fig. 5). The change in slope in the 1994 data set appears to be related to a change in the longitudinal dispersion coefficient [Clark et al., 1995b].

While small vertical gradients in the tracer concentrations were observed during the 1993 experiment [Clark et al, 1994], they were not observed during the 1994 experiment.

Hourly mean wind speeds corrected to a height of ten meters, U_{10} , were highly variable during the two tracer experiments (Fig. 6). The wind speeds were corrected assuming a neutrally stable boundary layer, a logarithmic wind profile, and a drag coefficient of 1.3×10^{-3} (Large and Pond [1981]). Hourly mean wind speeds recorded during periods between sampling events varied by a factor of 3 to 6 and the prevailing wind directions were generally along the axis of the river. During the two experiments, mean U_{10} between

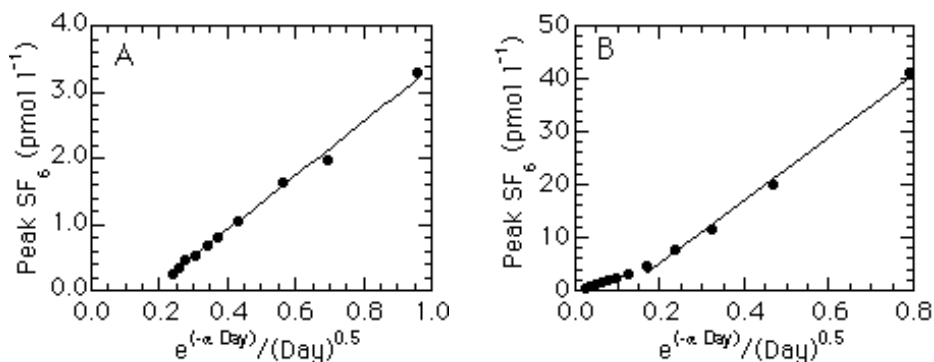


Figure 5: Peak SF₆ concentrations plotted as a function of $e^{-\alpha t} t^{-1/2}$: **a** results of the 1993 experiment and **b** results of the 1994 experiment.

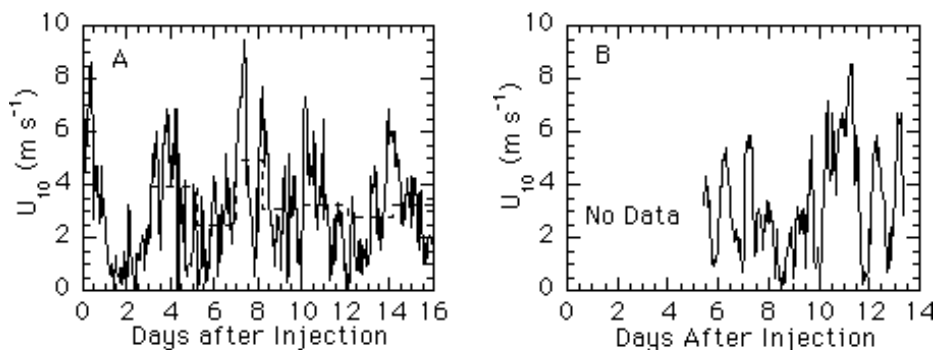


Figure 6: Mean wind speeds observed during the experiments, corrected to a height of 10 m. The solid and dashed lines are the hourly mean wind speed and the mean wind speeds between sampling events, respectively. **a** 1993 and **b** 1994.

sampling periods ranged between 0.7 and 5.1 m s⁻¹. Wind speeds over the river are not available for the first 5 days of the 1994 experiment because the anemometer failed to record the data.

Mean gas transfer velocities, k_{600} , were calculated from the change in the excess ³He/SF₆ ratio with time and normalized to a Schmidt number of 600 using equations (4) and (5) (Tab. 1). Daily ratios were determined from one station in 1993 and from 1 to 4 stations in 1994. In 1994, the mean standard deviation of the excess ³He/SF₆ ratios from stations near the peak was about $\pm 3\%$, approximately the same as the analytical error.

We have assumed that during the 1993 experiment, the error in the ratio was also approximately equal to the analytical uncertainty. Small corrections were applied to k_{600} calculated during the 1993 experiment to account

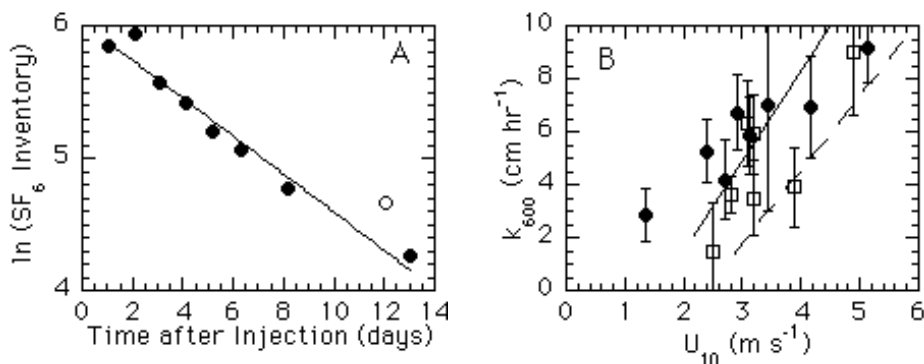


Figure 7: **a** SF₆ inventory (mmol) plotted as a function of time. The open circle was not used in the fit. **b** Results of Hudson tracer experiments. Open squares: 1993 data and filled circles: 1994 data. Dashed and plain lines represent trends from Rockland and Crowley lakes, respectively [Wanninkhof et al., 1985, 1987].

for observed vertical gradients [Clark et al., 1994]. Mean values of k_{600} calculated for the 1993 and 1994 experiments were $4.4 \pm 0.2 \text{ cm hr}^{-1}$ (day 3 to 16; $U_{10} = 3.1 \text{ m s}^{-1}$) and $5.3 \pm 0.2 \text{ cm hr}^{-1}$ (day 4 to 12; $U_{10} = 3.2 \text{ m s}^{-1}$), respectively.

Gas transfer velocities were not calculated for the initial period during either experiment for a variety of reasons. In 1993, an injection bias persisted for the first two days of the experiment [Clark et al., 1994]. In 1994, ³He samples were not measured during the first three days because of their high concentrations ($\delta^3\text{He} > 350\%$) and because of the failure of the anemometer during initial phase of the experiment.

4 Discussion

In 1994, the density of stations along the axis of the Hudson was sufficiently high to allow for examination of inventories of SF₆. These inventories were calculated assuming that cross sectional mean concentrations were equal to the observed concentrations in the center of the channel. The distributions were corrected for tidal movement which occurred during sampling in an attempt to provide synoptic distributions. Tidal current velocities, which were about 0.4 m s^{-1} during peak flow, were estimated from a hydrodynamic model developed by HydroQual, Inc. [Blumberg and St. John, 1995]. The corrections applied for tidal movement during sampling were as large as 20 % and averaged about 10 %. The assumption that the observed and cross sectional mean concentrations are equal is not entirely correct. Cross sectional surveys that were carried out on day 7 and 9 showed that concentrations outside of the channel and near the shore were often less than half

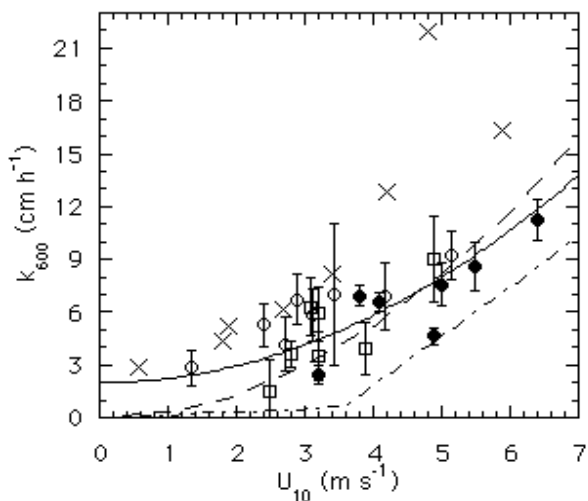


Figure 8: Relationship between gas transfer velocity, k_{600} , and wind speed, U_{10} , for estuaries. Open squares = 1993 Hudson River data [Clark et al., 1994]; filled circles = 1994 Hudson River data [this work]; open triangles = San Francisco Bay data [Hartman and Hammond, 1984]; crosses = Hudson River data [Marino and Howarth, 1993]. The dashed-dotted, dashed, and solid lines are the empirical relationships of Liss and Merlivat [1986], Wanninkhof [1992], and this study, respectively.

of those observed in the main channel. However, because the navigational channel typically made up 75-90 % of the cross sectional area [Steadfast, 1980], the error introduced by this assumption is probably small.

The SF_6 inventory decreased exponentially during the 1994 experiment (Fig. 7a) with a mean loss rate of SF_6 , α , of $0.144 \pm 0.011 \text{ d}^{-1}$. The mean gas transfer velocity, k_{600} , calculated from α is $4.6 \pm 0.4 \text{ cm hr}^{-1}$, using equation (3) and a mean depth of 5.5 m.

This value is slightly lower than the mean k_{600} , $5.3 \pm 0.2 \text{ cm hr}^{-1}$, calculated from the change in the excess $^3\text{He}/\text{SF}_6$ ratio between day 4 and day 12.

Daily mean gas transfer velocities calculated from the change in the excess $^3\text{He}/\text{SF}_6$ ratio with time correlate well with mean wind speed (Fig. 7b). Results from the 1993 and 1994 experiments were similar, suggesting that the local geometry of the channel has relatively little effect and that a single parameterization of k_{600} with U_{10} can be used for the entire tidal Hudson River. The observed trend is very similar to trends reported in lake experiments [Wanninkhof et al., 1985, 1987]. This agreement suggests that the tidal Hudson River behaves like a lake in terms of gas transfer across the air-water interface. Surface turbulence appears to be forced primarily by wind; surface turbulence resulting from boundary shear appears to be of minor importance.

Earlier gas exchange experiments in *estuarine* environments have found strong correlations between wind speed and gas transfer velocity (*Hartman and Hammond* [1984], *Kim and Holley* [1988], *Marino and Howarth* [1993]). *Hartman and Hammond* [1984] determined the relationship between gas transfer velocity and wind speed using both the mass balance and helmet methods in San Francisco Bay. The slope of the correlation ($\Delta k/\Delta U$) was higher for the results of the helmet experiment than for the mass balance experiment. Their results using the mass balance approach agree very well with our results using the dual tracer technique (Fig. 8). *Marino and Howarth* [1993] determined the relationship using the helmet method on the tidal Hudson River near the location of our 1993 experiment. Their results plot systematically higher than ours especially at high wind speed (Fig. 8). In both the tidal Hudson River and San Francisco Bay, results from helmet experiments tend to show higher gas transfer velocities than other approaches. This suggests that the helmet tends to increase the gas transfer rate.

Plotted in figure 8 along with the experimental data are the empirical equations of *Liss and Merlivat* [1986] and *Wanninkhof* [1992]. Liss and Merlivat's equation falls well below the tidal river and estuarine data. Wanninkhof's equation fits the estuarine results quite well at wind speeds above 4 m s^{-1} . However, at low wind speeds, it tends to underestimate the gas transfer velocity substantially.

A better relationship between wind speed and gas transfer velocity can be achieved by assuming a non-zero y-intercept. A number of studies in lakes suggest that at very low wind speeds k_{600} does not approach zero (*Wanninkhof et al.* [1985], *Clark et al.* [1995c]). In these settings a non-wind source of surface turbulence regulates gas transfer. Assuming that a similar process occurs in estuaries, we propose the following relationship for estuaries based on a 2^{nd} order polynomial fit of the empirical data determined with the dual tracer technique in the tidal Hudson River and mass balance method in San Francisco Bay (Fig. 8):

$$k_{600} = 2.0 + 0.24U_{10}^2 \quad R^2 = 0.58 \quad (7)$$

where k_{600} is in cm hr^{-1} and U_{10} is in m s^{-1} .

5 Conclusions

The dual tracer technique of determining gas transfer velocities has been successfully used in the tidal Hudson River. The daily distributions of SF_6 followed patterns predicted by the one-dimensional advection-diffusion equation. Mean gas transfer velocities calculated with the dual tracer technique and from the temporal change in SF_6 inventory agree quite well, verifying the accuracy of the dual tracer technique.

Gas transfer velocities in the tidal Hudson River were found to correlate strongly with wind speed. The relationship between wind speed and gas

transfer velocity falls close to those observed for lakes, suggesting that the tidal Hudson River behaves like a lake in terms of gas transfer.

Acknowledgements

We wish to thank S. Chillrud, B. Ekwurzel, and M. Taylor for helping with the field work. A. Ludin and R. Weppernig measured the ^3He samples. Special thanks go to T. P. Dernago, Jr., of the United States Coast Guard and A. Fitzpatrick for granting permission to place the anemometer on the Hudson River Lights and on the Esopus Meadow Lighthouse. The ^3He analyses were made possible by a generous donation by the W. M. Keck Foundation. Financial support was provided by the Hudson River Foundation (grant no. 011/92A and no. 009/94P) and by Columbia University through the Strategic Research Initiative Program. This is contribution no. 5394 from the Lamont-Doherty Earth Observatory of Columbia University.

References

- Bayer, R., P. Schlosser, G. Bönisch, H. Rupp, F. Zaucker, and G. Zimmek, *Performance and blank components of a mass spectrometric system for routine measurement of helium isotopes and tritium by the ^3He ingrowth method*. Sitzungsber. Heidelb. Akad. Wiss., Springer-Verlag, Math.-Naturwiss. KL., 5. Abhandlung: 241-279, 1989
- Belanger, T. V. and E. A. Korzum, Critique of floating-dome technique for estimating reaeration rates. *J. Environ. Eng., ASCE*, 117, 144-150, 1991
- Benson, B. B. and D. Krause, Jr., Isotopic fractionation of helium during solution: a probe for the liquid state, *J. Solution Chem.*, 9, 895-909, 1980
- Blumberg, A. and J. P. St. John, personal communication, 1995
- Clark, J. F., H. J. Simpson, W. M. Smethie, Jr., and C. Toles, Gas exchange in a contaminated estuary inferred from chlorofluorocarbons. *Geophys. Res. Lett.*, 19, 1133-1136, 1992
- Clark, J. F., R. Wanninkhof, P. Schlosser, and H. J. Simpson, Gas exchange rates in the tidal Hudson river using a dual tracer technique. *Tellus*, 46B, 274-285, 1994
- Clark, J. F., H. J. Simpson, R. F. Bopp, and B. L. Deck, Dissolved oxygen in the lower Hudson estuary since the late 1970s. *J. Environ. Eng., ASCE*, 121, 760-763, 1995a
- Clark, J. F., P. Schlosser, M. Stute, and H. J. Simpson, SF_6 - ^3He tracer release experiment: A new method of determining longitudinal dispersion coefficients in large rivers. *Environ. Sci. and Tech.*, 1995b (in press)
- Clark, J. F., P. Schlosser, R. Wanninkhof, H. J. Simpson, W. S. F. Schuster, and D. T. Ho, Gas transfer velocities for SF_6 and ^3He in a small pond at low wind speeds. *Geophys. Res. Lett.*, 19, 93-96, 1995c
- Clarke, W. B., W. B. Jenkins, and Z. Top, Determination of tritium by mass spectrometric measurement of ^3He , *Int. J. Appl. Radiat. Isotopes*, 27, 217-225, 1976
- Dyrssen, D., E. Fogelqvist, M. Krysell, and R. Sturm, Release of halocarbons from an industrial estuary. *Tellus*, 42B, 162-169, 1990

- Edwards R. W. and M. Owens, The effects of plants on river conditions, IV: The oxygen balance of a chalk stream. *J. Ecol.*, 50, 207-220, 1962
- Hartman, B. and D. E. Hammond, Gas exchange rates across the sediment-water and air-water interfaces in South San Francisco Bay. *J. Geophys. Res.*, 89, 3593-3603, 1984
- Howarth, R. W., R. Marino, R. Garritt, and D. Sherman, Ecosystem respiration and organic carbon processing in a large, tidally influenced river: the Hudson River. *Biogeochem.*, 16, 83-102, 1992
- Jähne, B., K. O. Münnich, R. Bössinger, A. Dutzi, W. Huber, and P. Libner, On parameters influencing air-water gas exchange. *J. Geophys. Res.*, 92, 1937-1949, 1987
- Juliano, D. W., Reaeration measurements in an estuary, *J. of San. Eng. Div. ASCE*, 95, 1165-1178, 1969
- Kim J. H. and E. R. Holley, *Literature survey on reaeration in estuaries*. Technical Memorandum 88-1, Center for Research in Water Resources, University of Texas. 75 p., 1988
- Large, W. P. and S. Pond, Open Ocean momentum flux measurements in moderate to strong winds. *J. Phys. Oceanogr.*, 11, 324-336, 1981
- Ledwell, J. R., The variation of the gas transfer coefficient with molecular diffusivity, in *Gas Transfer at Water Surfaces*, edited by W. Brutsaert and G. H. Jirka, pp. 293-302, D. Reidel, Hingham, Mass., 1984
- Liss, P. S. and L. Merlivat, Air-sea gas exchange rates: An introduction and synthesis, in *The Role of Air-Sea Exchange in Geochemical Cycles*, edited by P. Buat-Mánard, pp. 113-129, D. Reidel, Hingham, Mass., 1986
- Marino, R. and R. W. Howarth, Atmospheric oxygen exchange in the tidal Hudson River: Dome measurements and comparison with other natural waters. *Estuaries*, 16, 433-445, 1993
- Odum, H. T., Primary production in flowing waters. *Limnol. Oceanogr.*, 1, 102-117, 1956
- O'Connor, D. J., Organic pollution of the New York harbor - Theoretical considerations. *J. Water Poll. Control Fed.*, 34, 905-919, 1962
- O'Connor, D. J., Analysis of diffusion data of the Delaware river model. *Int. J. Air Wat. Poll.*, 7, 1073-1084, 1963
- O'Loughlin, E. M. and K. H. Bowmer, Dilution of aquatic herbicides in flowing channels. *J. of Hydrol.*, 26, 217-235, 1975
- Stedfast, D. A., Cross sections of the Hudson River estuary from Troy to New York City, New York. *U. S. Geol. Surv. Water Res. Inves.*, 80-24. 38 p., 1980
- Stephens, D. W., Preliminary evaluation of floating dome method of measuring reaeration rates. *J. of Res. of U. S. Geol. Surv.*, 6, 547-552, 1978
- Thomann, R. V., J. A. Mueller, R. P. Winfield, and C-R. Huang, Model of fate and accumulation of PCB homologues in Hudson Estuary. *J. Envir. Eng.*, 117, 161-178, 1991
- Watson, A. J., R. C. Upstill-Goddard, and P. S. Liss, Air-sea exchange in rough and stormy sea measured by a dual tracer technique. *Nature*, 349, 145-147, 1991
- Wanninkhof, R., Relationship between gas exchange and wind speed over the ocean, *J. Geophys. Res.*, 97, 7373-7381, 1992

- Wanninkhof, R., J. R. Ledwell, and W. S. Broecker, Gas exchange-wind speed relationship measured with sulfur hexafluoride on a lake. *Science*, 227, 1224-1226, 1985
- Wanninkhof, R., J. R. Ledwell, W. S. Broecker, and M. Hamilton, Gas exchange on Mono Lake and Crowley Lake, California. *J. Geophys. Res.*, 92, 14567-14580, 1987
- Wanninkhof, R., J. R. Ledwell, and A. J. Watson, Analysis of sulfur hexafluoride in seawater. *J. Geophys. Res.*, 96, 8733-8740, 1991
- Wanninkhof, R, W. Asher, R. Weppernig, H. Chen, P. Schlosser, C. Langdon, and R. Sambrotto, Gas transfer experiment on Georges Bank using two volatile deliberate tracers. *J. Geophys. Res.* 98, 20,237-20,248, 1993
- Weiss, R., Solubility of helium and neon in water and sea water, *J. Chem. Eng. Data*, 16, 235-241, 1971

Description of the Science Plan for the April 1995 CoOP Experiment, 'Gas Transfer in Coastal Waters', Performed from the Research Vessel New Horizon

*Erik J. Bock*¹, *James B. Edson*¹, *Nelson M. Frew*¹,
*Andrey V. Karachintsev*¹, *Wade R. McGillis*¹, *Robert K. Nelson*¹,
*Kurt Hansen*², *Tetsu Hara*², *Meté Uz*², *Bernd Jähne*⁴,
*Jochen Dieter*⁴, *Jochen Klinke*⁴, and *Horst Haußecker*³

¹ Woods Hole Oceanographic Institution (WHOI)

² Graduate School of Oceanography, University of Rhode Island (URI)

³ Interdisciplinary Center for Scientific Computing, University of Heidelberg (UH)

⁴ Scripps Institute of Oceanography (SIO)

doi: 10.5281/zenodo.10408 **Abstract**

A description of the scientific questions, the engineering approach to answering those questions and preliminary results from an experiment off the coast of southern California are presented. The experiment's main focus was on how local variability, caused primarily by nutrient availability (and hence surfactant concentration) and wind stress variability, influences gas exchange in coastal waters. To address this issue, a suite of instruments was developed to characterize interfacial phenomena in the coastal region off Monterey Bay, in conjunction with other platforms that intended to measure both atmospheric and ocean-mixed layer properties.

1 Introduction

Accurate estimates of air-sea gas-transfer rates are essential for understanding the global cycles of carbon dioxide, dimethyl sulfide and other trace gases that affect the earth's radiation budget. As part of the National Science Foundation's (NSF) Coastal Ocean Processes (*CoOP*) program, our main goal is to improve the understanding of air-sea gas-transfer under different environmental conditions at the real air-sea interface. Improved estimates require new advances in techniques to measure in situ gas transfer rates and governing environmental parameters. Jointly, groups from Woods Hole Oceanographic Institution (WHOI), University of Rhode Island (URI), Scripps Institute of Oceanography (SIO), and University of Heidelberg (UH) are developing a new in situ instrument suite that can measure the gas-transfer velocity on time scales (minutes to hours) that are much shorter than conventional tracer techniques (days or longer). The instruments are combined to provide coincident measurements of the gas-transfer velocity, small scale

roughness, wind stress, near surface turbulence and surface chemical enrichments.

In its first year, we participated in the joint NSF(CoOP)-ONR (*MBL-ARI*) field experiment off Monterey Bay in April – May, 1995. One of the main purposes of this operation was to integrate the intensive meteorological/oceanic measurements by MBL-ARI investigators into the measurements of air-sea gas exchange and related surface processes by CoOP participants. Such integration would provide necessary information to investigate the air-sea gas exchange processes in the coastal environment in detail. During the operation, we successfully accomplished all the measurements of the surface physical processes and the surface chemical characterization. We also maximized our possible opportunities to coordinate our measurements with those obtained from the R/P FLIP. Currently, preliminary data analyses are underway and we have started to integrate our data with MBL-ARI data. In the following sections, we summarize in detail the logistics of the experiment, and then report some preliminary data analyses.

A concise summary of past field studies of air-sea gas-transfer has been given by *Wanninkhof et al.* [1985]. The results have consistently exhibited a strong correlation between the gas-transfer velocity and the mean wind speed. In particular a sharp change in the wind speed dependence of the gas exchange coefficient was found at wind speeds of a few meters per second, which led to the so-called 'Liss-Merlivat' relationship [*Liss and Merlivat*, 1986]. Nevertheless agreement between different experiments are still within an order of magnitude at best. This is not surprising because the only available techniques for measuring air-sea gas-transfer in the field environment have been either the radon deficit method [*Broecker and Peng*, 1974] or purposeful tracer-injection techniques [*Wanninkhof*, 1985]. Both require time-averaging over days or longer. Since the wind field is never constant over such time scales, the correlation between the mean wind speed and k may likely be biased [*Wanninkhof*, 1992]. Another important factor that has been ignored is the presence of surfactant films. This effect is expected to be particularly important in coastal and inland waters where most of the past measurements have been performed.

In addition, the relation between wind speed and wind stress (drag coefficient) introduces a secondary effect that may further complicate the field observations. Although it is wind stress that is dynamically related to transfer velocity, the field measurements usually yield only the wind speed, and an empirical drag coefficient is used to estimate the wind stress. Recent studies [e. g., *Smith et al.*, 1992; *Geernaert et al.*, 1993] have shown that the drag coefficient may be strongly influenced by the nature of surface gravity waves and by the atmospheric stability. Therefore this factor can influence the estimate of the gas-transfer velocity unless direct stress measurements are performed in situ.



Figure 1: The LADAS air-sea interaction catamaran.

2 Experimental Techniques

2.1 Surface Characterization

Surface characterization is performed using the *LADAS* air-sea interaction catamaran that was developed at WHOI. Figure 1 shows *LADAS* during a typical deployment during the CoOP experiment. *LADAS* is equipped with a *scanning laser slope gauge* (SLSG), a surface *microlayer sampler* (SMS), a hot film probe for high frequency measurements of current fluctuations, an acoustic current meter, an attitude measuring unit, and a series of capacitance wire-wave staffs. These instruments are secured to the 4.8 m catamaran, which was then towed from the side of the R/V *New Horizon*. *LADAS* has electric motors and remotely actuated rudders that enable it to be maneuvered to maintain a position outside the disturbance caused by the bow wake of the research vessel.

Surface capillary and *capillary-gravity waves* are measured using the SLSG. A better description of the SLSG is given by *Bock and Hara* [1995]. The device makes use of the refraction of a narrow pencil-like beam from a laser beneath the air-sea interface, and uses a repetitive scanning pattern

to obtain temporal and spatial spectra of short waves. Another paper in this proceedings [Hara *et al.*, 1995] shows laboratory results confirming the relation between slope of short waves and gas transfer velocity.

A sample of the microlayer was obtained with the drum sampler first developed by Carlson *et al.* [1988]. The technique relies on a rotating glass cylinder that drags a sample of the sea surface into a drip cup that is drained by a pump and pushed through a fluorometer. The fluorometer measures emission at 450 nm and yields a measure of the *colored dissolved organic matter* (CDOM). There has been demonstrated a strong correlation between CDOM and surfactant concentration using polarographic techniques to quantify the surfactant concentration. Data from CDOM measurement during this experiment are presented below.

High-frequency measurements of water-side velocity fluctuations were obtained from the *hot film sensors* mounted at the bow of LADAS. These films were configured in a crossed geometry to measure two components of fluctuations, and frequency domain processing of the data produces estimates of ϵ , the dissipation. One intrinsic drawback common to hot-film sensors is that the sensors drift due to accumulation of surface films and contamination. Historically, this drawback has been combated by frequent calibration and cleaning. In the field, however, this is impractical and the problem of drift was solved by dynamically calibrating the long-term mean output of the hot films against measurements obtained from a Sontek current meter. This device was mounted in close proximity to the hot films and allowed the films to be used for periods in excess of six hours.

Additionally on LADAS was mounted an array of tantalum *wire-wave staffs*. These staffs were built in accordance to those described by Chapman and Monaldo [1991] and were used in conjunction with an attitude measuring unit (AMU, the inertial guidance system, MK50 AMU-200B, from a MK50 torpedo) to measure gravity waves in the earth's coordinate frame by means of complimentary filtering of the linear accelerometer signals and the outputs of the rotational rate gyros. This data will be useful for analysis of wave-wave interactions but will not be addressed in the context of this paper.

2.2 Meteorological Characterization

High frequency wind velocity and virtual temperature measurements were obtained from a *sonic anemometer*/thermometer mounted 10 m above the mean water height at the bow of the R/V New Horizon. The anemometer also had its own dedicated AMU, allowing stress and buoyancy flux calculations from both the direct covariance and inertial-dissipation methods. *Wind stress* measurements are limited to situations when the wind direction was within $\pm 45^\circ$ of the New Horizon's bow in order to eliminate records that are distorted by the ship's superstructure. Mean air and sea temperature and humidity measurements were also recorded in order to compute the sensi-



Figure 2: The Controlled Heat Flux boom on the R/V New Horizon during the April/May 1995 NSF CoOP cruise off Monterey Bay.

ble and latent heat fluxes from the bulk aerodynamic method. These fluxes will be used in conjunction with the LADAS and CFT measurement to study the effects of wind-wave coupling on the gas flux measurements.

2.3 Heat and Mass Fluxes

This experiment was the first time that the *Controlled Flux Technique* (CFT), developed by Jähne of SIO/UH and his group, was deployed in situ. The use of a pivoting extension boom from the bow of the research vessel enabled the CFT to image an area unaffected by reflections of the sky from the hull. A carbon dioxide laser was used to locally heat a patch of the ocean surface

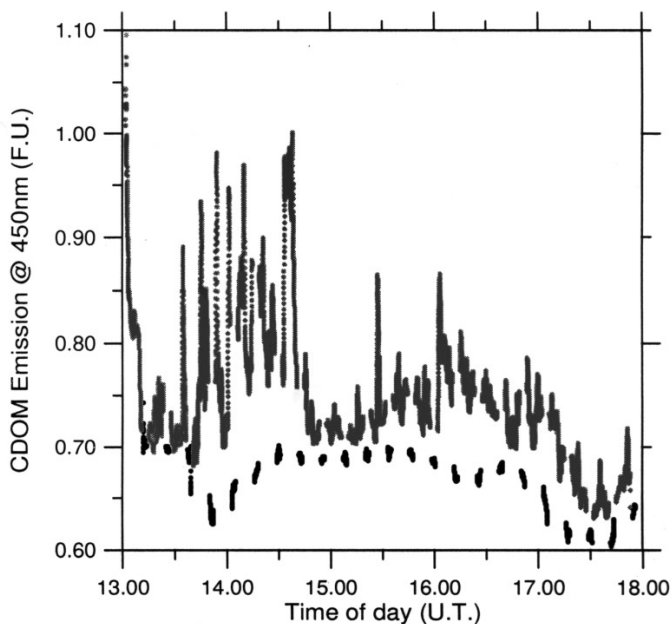


Figure 3: Data obtained on Julian Day 130 from the NSF CoOP cruise of April/May 1995 aboard the R/V New Horizon. Results are from the time period between 13:00 to 18:00 Universal Time. The enhanced surface enrichment observed during the period between 13:30 and 14:30 correspond to a transit across a visibly slicked area.

and an infra-red camera imaged the heated area in a range of wavelengths not encompassing the laser wavelength. Gas transfer coefficients can be derived from heat transfer coefficients obtained in this manner by scaling the mass transfer coefficient proportional to the relative diffusivities of mass and heat. We have successfully obtained both passive and active infrared images that can be used to investigate the heat/gas flux across the air-sea interface of the coastal ocean. Figure 2 shows the CFT boom as it was aboard the R/V New Horizon. *Haußecker et al.* [1995] describe the principle of the CFT, while preliminary results from the April/May 1995 CoOP cruise are reported by *Haußecker and Jähne* [1995].

3 Results and Discussion

3.1 Example of an Ocean Slick

Figure 3 shows the surface-microlayer CDOM (grey) and the subsurface CDOM (black) for the period of time between 13:00 and 18:00 U.T. on Julian Day 130. What is evident in this figure is the spatial variability that is common to coastal environments. The source of this variability lies in the sources

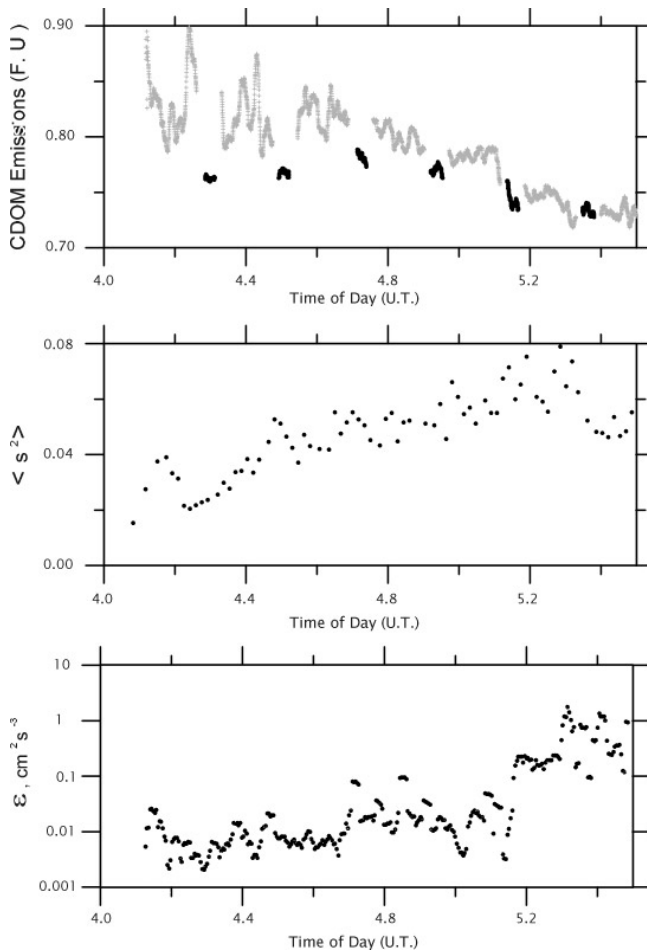


Figure 4: Data obtained on Julian Day 131 from the NSF CoOP cruise of April/May 1995 aboard the R/V New Horizon. Results are from the time period between 04:00 to 05:30 Universal Time.

and sinks of marine nutrients and phytoplankton distributions. Since the enhancement of CDOM has been well correlated to surfactant concentration, it is clear that surfactant modulation of gas transfer across the air-sea interface is a significant factor in coastal gas transfer. The need to be able to make gas transfer velocity measurements on time and space scales equal to the resolution of the variability observed in situ has initiated the study of using the CFT technique to estimate gas transfer velocity.

3.2 Example of a Steady Wind Stress

Preliminary analyses have been initiated, and some of these results are shown below. Figure 4 shows results of CDOM fluorescence, *mean-square surface slope*, $\langle S^2 \rangle$, and *turbulent dissipation rates*, ϵ for Julian Day (JD) 131. The top panel in this figure represents the surface microlayer sample ($< 100 \mu\text{m}$) sample in grey and the subsurface sample, taken at nominally 10 cm depth in black. During the time period between 04:00 and 05:00, the surface shows a significant enrichment relative to the subsurface sample. During the entire time period represented in the figure, the wind stress was nearly constant. For those times of significant surface enrichments, correspondingly low mean-square surface slope and turbulent dissipation were recorded. These enrichments progressively decreased along the ship's track, while the mean-square surface slope and turbulent dissipation increased correspondingly. This would suggest that the heat flux (and therefore gas flux) should also be increasing during this period. Results from the CFT studies are presently in progress and will be intercompared with these data.

3.3 Example of a Modulating Wind-Stress

The same measured quantities, namely CDOM, $\langle S^2 \rangle$, and ϵ are shown as a function of time of day for JD 135 in Figure 5. During this time frame, the wind speed varied, starting at 6 m/s at times between 01:30 to 02:30, then lowering to 3.5 m/s during the time frame between 02:30 and 03:30, and then increasing to 5 m/s after about 03:30. While trends consistent with this modulated wind speed are evident in the records, several issues need to be considered before a quantitative description of the situation is attained. For example, the decrease in surface enriched CDOM observed during the periods of higher wind correlates well with the increase observed in the mean square slope and turbulent dissipation. It is not immediately evident whether the causality of this correlation is explainable as a decrease in surfactant resulting in less damped waves and a higher mean square slope; or, conversely, that an increased wave and turbulence field was responsible for enhanced near-surface mixing that depleted the sea-surface of *surfactants*. These questions will be the object of further analyses.

Acknowledgements

The authors would like to thank Nick Witzell, Dave Schroeder, and Bob Nelson for their help in the preparation and execution of this cruise. They also thank the captain and crew of the R/V New Horizon for their assistance during this experiment. This research supported by the National Science Foundation, OCE-9410537.

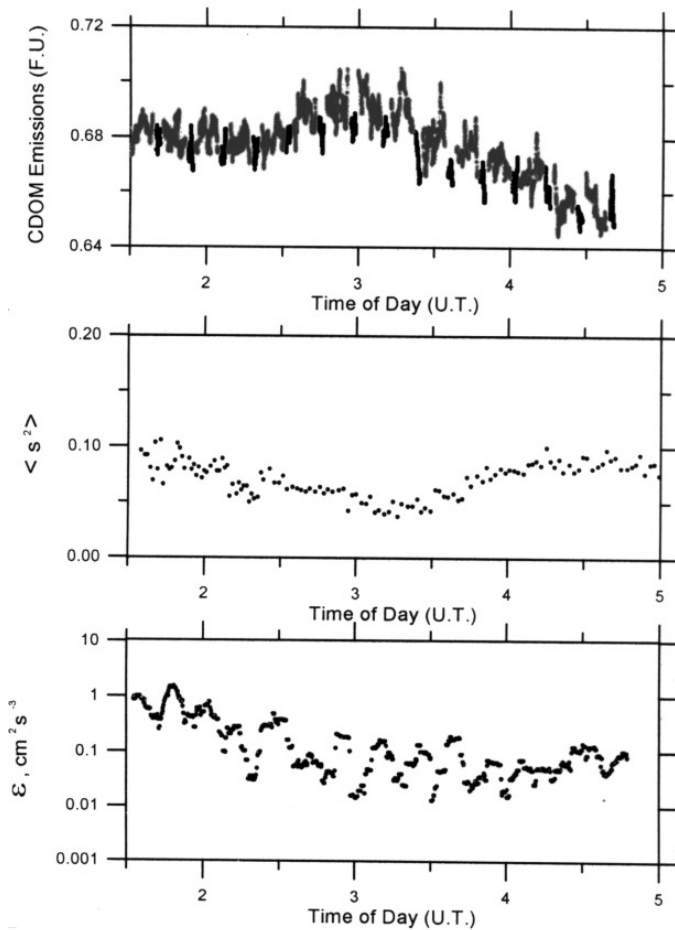


Figure 5: Data obtained on Julian Day 135 from the NSF CoOP cruise of April/May 1995 aboard the R/V New Horizon. Results are from the time period between 01:30 to 05:00 Universal Time.

References

- Bock, E. J., and T. Hara, Optical measurements of capillary-gravity wave spectra using a scanning laser slope gauge. *J. Atm. Ocean. Tech.*, 12, 395-40, 1995
- Broecker, W. S., and T. H. Peng, [1974] Gas exchange rates between air and sea. *Tellus*, 26, 21-35.
- Carlson, D. J., J. L. Canty, and J. J. Cullen, Description of and results from a new surface microlayer sampling device, *Deep-Sea Res.*, 35, 1205-1212, 1988
- Chapman, R. D., and F. M. Monaldo, Anodized tantalum wire wave gauges, *APL Technical Report S1R-91-041U*, August, 1991

- Geernaert, G. L., F. Hansen, M. Courtney, T. Herbers, Directional attributes of the ocean surface wind stress vector. *J. Geophys. Res.*, 98, 16571-16582, 1993
- Hara, T., E. J. Bock, N. M. Frew, and W. R. McGillis, Relationship between air-sea gas transfer velocity and surface roughness, *This volume*
- Haußecker, H., and B. Jähne, In situ measurements of the air-sea gas transfer rate during the MBL/CoOP West Coast Experiment, *this volume*.
- Haußecker, H., S. Reinelt, and B. Jähne, Heat as a proxy tracer for gas exchange measurements in the field: principles and technical realization, *this volume*.
- Liss, P. S. and L. Merlivat, Air-sea gas exchange rates: introduction and synthesis, in *The Role of Air-Sea Exchange in Geochemical Cycling* (P. Buat-Menard ed.), Reidel, Dordrecht, pp. 113-127, 1986
- Smith, S. D., R. J. Anderson, W. A. Oost, C. Kraan, N. Maat, J. DeCosmo, K. B. Katsaros, K. Bumke, L. Hasse and H. M. Chadwick, Sea surface wind stress and drag coefficients: the HEXOS results, *Bound. Layer Meteor.*, 60, 109-142, 1992
- Wanninkhof, R., Relation between wind speed and gas exchange over the ocean, *J. Geophys. Res.*, 97, 7373-7382, 1992
- Wanninkhof, R., J. R. Ledwell, and W. S. Broecker, Gas exchange-wind speed relation measured with sulfur hexafluoride on a lake. *Science*, 227, 1224-1226, 1985

The ASGASEX'93 Experiment

Wiebe A. Oost

Royal Netherlands Meteorological Institute, Department of Oceanographic Research, the Netherlands

Abstract

In September 1993 the first ASGASEX (for Air Sea GAS EXchange) experiment took place at Meetpost Noordwijk off the Dutch coast. Scientists from 8 institutes in 4 countries participated in an attempt to pin down the effects of as many parameters as possible on the gas exchange process at the sea surface. The results so far are presented in a number of talks and posters during this conference.

1 Rationale

There is a growing awareness that to successfully model turbulent transport (of momentum, heat and/or water vapor) at or near the ocean surface, dynamical processes need to be specifically included. Such processes include wave breaking, but other processes are also known to organise bubble plumes: Langmuir circulation, shear instability and forced convective plumes.

The ASGASEX (for Air Sea GAS Exchange) '93 experiment was held in September 1993 at *Meetpost Noordwijk* (MPN), a research platform 9 km off the Dutch coast, near the coastal resort of Noordwijk (fig.1). The experiment was intended to identify and quantify factors affecting the air-sea exchange of atmospheric trace gases, in particular CO₂, and to try to resolve the enigma of the eddy correlation (e-c) results for gas transfer at sea.

That enigma is the unacceptably large discrepancy between the values for the transfer velocity of CO₂, found with the e-c technique, and those obtained by other methods. One of the incentives to look into this problem is that the eddy correlation method is very attractive, because it allows, within certain restrictions, to measure the CO₂ transport directly and to do so within a relatively short time (with a minimum of about 20 min.). We started from the assumption that to solve the e-c problem we needed a thorough knowledge of the circumstances of the CO₂ transport. We therefore tried to measure as many environmental parameters as possible which could be expected to be relevant for gas exchange at the sea surface. This course of action made the experiment of interest for a larger group of institutes, each with its own research specialisations. A list of participating institutes, with their acronyms, is given in Table 1. The groups from the UK and Ireland, SUDO, UCG and IOSDL, as well as the Dutch TNO-FEL participants were interested in the amounts and properties of *bubbles* and *Langmuir circulations*,



Figure 1: Research station "Meetpost Noordwijk"

NIOZ in the amounts of CO_2 , CH_4 and N_2O in relation to the hydrographic situation. BIO together with DAL and KNMI and TNO-FEL in combination with NIOZ all aimed at a full description of the CO_2 transport (fluxes and concentrations). BIO, KNMI and TNO-FEL also measured the fluxes of momentum, heat and water vapor, partly because the latter two fluxes are also needed to find the net CO_2 flux, partly because of interest in the fluxes themselves. KNMI furthermore measured waves and whitecaps and was responsible for the organization and general technical support. RWS, formally not a participant, provided the platform and the facilities there. Table 2 contains a listing of the quantities that were measured during ASGASEX'93 and fig. 2 shows the distribution of the instruments over MPN. The TNO-FEL CO_2 eddy correlation measurements were a cooperative effort with the Danish Risø National Laboratories.

2 Course of the Experiment

The experiment was quite successful, despite some initial set-backs. We had to be content with two instead of the planned three independent systems for

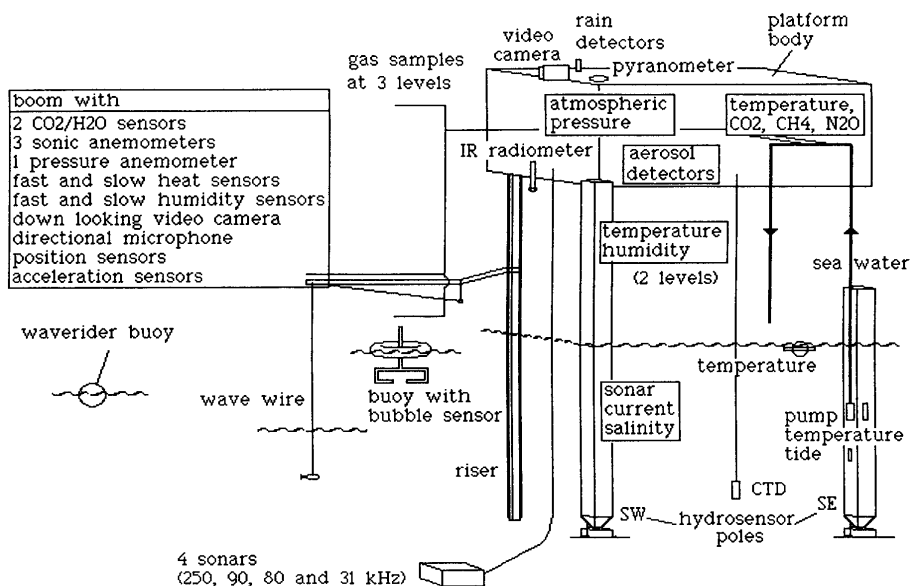


Figure 2: Measurements made during ASGASEX.

Table 1: Institutes and participants of ASGASEX'93.

BIO	Bedford Institute of Oceanography, Canada S. D. Smith, R. J. Anderson
DAL	Dalhousie University, Halifax, Canada O. Hertzman, M. Poliquin, M. - C. Bourque
TNO-FEL	Physics and Electronics Laboratory TNO, The Netherlands G. de Leeuw, G. J. Kunz, L. H. Cohen
KNMI	Royal Netherlands Meteorological Institute, The Netherlands W. A. Oost, W. Kohsiek, C. Kraan, C. v. Oort J. W. Schaap, H. Wallbrink, E. H. W. Worrell, R. Cornet
NIOZ	Netherlands Institute for Sea Research, The Netherlands D. C. E. Bakker, A. A. J. Majoor, H. de Wilde
RWS	Department of Harbours and Public Works J. A. M. Goossens, J. v. d. Horn
SUDO	Southampton University, Dept. of Oceanography, UK D. K. Woolf
UCG	University College Galway, Dept. of Oceanography, Ireland M. Curé, T. Furey
IOSDL	Institute of Oceanographic Sciences, Deacon Laboratory, UK A. Hall

Table 2: Measurements during ASGASEX (for institute acronyms see Table 1).

<i>Aerosol</i>	TNO-FEL
Air temperature	KNMI; BIO; TNO-FEL, RWS
<i>Alkalinity</i>	NIOZ
Bubbles	SUDO/UCG/IOSDL, TNO-FEL
CO ₂ flux	
eddy correlation technique	BIO, KNMI, TNO-FEL
gradient method	NIOZ
Current, strength and direction	RWS
Humidity	KNMI, BIO, TNO-FEL, RWS
<i>Humidity flux</i>	KNMI, BIO, TNO-FEL
Incoming short wave radiation	TNO-FEL
Langmuir circulations	SUDO/UCG/IOSDL
<i>Momentum flux</i>	KNMI, BIO, TNO-FEL
N ₂ O, CH ₄ in air and water	NIOZ
pCO ₂ in air and water	NIOZ, BIO/DAL
Rain	KNMI, TNO-FEL
Sea water temperature	KNMI, RWS, NIOZ
<i>Sensible heat flux</i>	KNMI, BIO, TNO-FEL
Total CO ₂ in water	NIOZ
Wave height	KNMI, RWS
<i>Whitecaps</i>	KNMI
Wind speed	KNMI, BIO, TNO-FEL, RWS

e-c CO₂ flux measurements, because one system was not available in time for the experiment. KNMI and TNO-FEL also had to find solutions for technical problems with their CO₂ sensors. The weather was not very cooperative either: during substantial parts of the experiment the wind was easterly, putting the outrigger with the e-c systems in the wake of the platform, thus precluding any measurements with this method, and on other occasions rain affected the optics of the CO₂ sensors.

In the end, however, a sizable amount of high quality CO₂ e-c flux data was collected, as shown in the papers by Oost et al. and by Kunz et al. in these proceedings. The fact that the CO₂ flux data from the independent KNMI and TNO-FEL systems show a very good correspondence is both a global first and a strong support for the validity of the measurements.

The e-c measurements of the fluxes of momentum, heat and water vapor are reported on in papers by Kunz et al. and by Smith et al. They again show a very good mutual correspondence, but are also in agreement with earlier data from the same location, measured during the 1986 HEXMAX experiment.

Participants not involved in the e-c measurements had no problems with wind directions or faulty instruments and measured continuously. The in-

stitutes operating sonar equipment (SUDO, UCG and IOSDL) noted already during the experiment the almost ubiquitous presence of the Langmuir cells they were looking for. At the time of writing the definitive results of these measurements are not yet available.

NIOZ measured by means of equilibration and gaschromatographic analyses the partial pressure differences of *carbon dioxide* (CO₂), *nitrous oxide* (N₂O) and *methane* (CH₄) between the air and the sea water, to calculate the fluxes of these greenhouse gases, using literature values for the transfer velocity. DAL also measured the partial pressure differences of CO₂, with the aim to combine them with the e-c measurements of BIO. Another KNMI activity during ASGASEX were video and sound recordings of white-caps. These data have been analyzed and the video results, which show a somewhat unexpected relationship with the current velocity, are presented in the symposium paper by Kraan et al.

3 The Results so Far and Future Activities

During the conference several papers were presented by ASGASEX '93 participants, both about their results from this experiment and related research. Indicating these papers by their authors we can mention contributions by D. K. Woolf, G. J. Kunz et al., S. D. Smith et al., H. J. de Wilde and J. Duyzer, G. de Leeuw, C. Kraan et al. and another one by the present author and a number of colleagues. The reader is referred to these papers for more detailed information (see references).

ASGASEX '93, as will be clear from these papers, has covered some ground, but it is still only part of the road. The problems with the CO₂ fluctuation sensors and the adverse weather conditions limited both the amount and the accuracy of the CO₂ flux data. More important, however, the ASGASEX data show some unexpected and exciting results which for their interpretation require additional information. Even the already large array of instruments that was used couldn't provide all the data needed and more and more extensive data are required. We hope to obtain these in *ASGAMAGE*, the '96 ASGASEX MAGE experiment (MAGE = Marine Aerosol and Gas Exchange, a working group of IGAC). That experiment will provide - we hope - the additional information we need, but it will also bring some fully new activities: direct measurement of the DMS flux, the use of a shipborne eddy correlation system and, at long last, a simultaneous dual tracer experiment, allowing a direct comparison of this technique with e-c flux data. We hope to inform you about the results during the 4th International Symposium on Air-Water Gas Transfer.

References

de Wilde, H. P. J., and J. Duyzer, Methane Emissions off the Dutch Coast: Air-Sea Concentration Differences Versus Atmospheric Gradients, *This volume*

- de Leeuw, G., and L. H. Cohen, Bubble Size Distributions in Coastal Seas, *This volume*
- Kraan, C., W. A. Oost, and P. A. E. M. Janssen, Whitecap measurements and whitecap dissipation modelling, *This volume*
- Kunz, G. J., G. de Leeuw, S. E. Larsen, and F. Aa. Hansen, Over-Water Eddy Correlation Measurements of Fluxes of Momentum, Heat, Water Vapor and CO₂, *This volume*
- Oost, W. A., W. Kohsiek, G. de Leeuw, G. J. Kunz, S. D. Smith, R. J. Anderson, and O. Hertzman, On the Discrepancies between CO₂ Flux Measurement Methods, *This volume*
- Smith, S. D., R. J. Anderson, O. Hertzman, W. A. Oost, W. Kohsiek, G. de Leeuw, and G. Kunz, New Measurements of Eddy Fluxes at the Sea Surface in ASGASEX, *This volume*
- Wolf, D. K., Vertical Mixing in the Upper Ocean and Air-Sea Gas Transfer, *This volume*
- Wolf, D. K., Energy Dissipation through Wave Breaking and the Air-Sea Exchange of Gases, *This volume*

The Joint Global Ocean Flux Study: Role of Gas Exchange

Bruce D. Johnson

Canadian JGOFS Program

Abstract

The oceans contain the major portion of the carbon actively circulating in the biosphere and are thought to be the principal sink for anthropogenic CO₂. The current build-up of CO₂ in the atmosphere and attendant threat of global warming are cause for concern, and especially since we do not understand the global carbon cycle sufficiently well to know how it will respond, and with what feedbacks, in a changing climate. Recognizing this problem and the special role of the oceans in CO₂ uptake, the Scientific Committee for Ocean Research (SCOR of ICSU) sponsored a meeting of experts in Paris in 1987. There, the goals and objectives of a program to study the ocean carbon cycle were established. Formal agreement between SCOR and the IGBP (International Geosphere Biosphere Program, also of ICSU) established the Joint Global Ocean Flux Study (JGOFS) under the auspices of SCOR and as one of the first Core Programs of the IGBP.

1 Introduction

The goals of *JGOFS* are (JGOFS Implementation Plan; *Fasham et al.*, [1991]):

- To determine and understand on a global scale the processes controlling the time varying fluxes of carbon and associated biogenic elements in the ocean, and to evaluate the related exchanges with the atmosphere, sea floor, and continental boundaries.

and

- To develop a capability to predict on a global scale the response of oceanic biogeochemical processes to anthropogenic perturbations, in particular those related to climate change.

or essentially, to increase our understanding of the *ocean carbon cycle*, its sensitivity to change and the regulation of the atmosphere ocean CO₂ balance.

Each of these goals has been divided into 4 objectives. Those with special relevance for understanding gas exchange include:

- To characterize the present geographical distribution of key biogeochemical properties and rate processes pertinent to the oceanic carbon system, as a necessary pre-requisite to predicting change in the system.

- To determine the role of the ocean in modifying the atmospheric increase in anthropogenic CO₂ and other gases affecting climate.
- To determine the response of the ocean carbon system to physical and chemical forcing from sub-seasonal events to decadal changes.
- To estimate the exchanges at ocean boundaries. These include air-sea exchanges (those most directly related to the rationale for JGOFS), exchanges with the bottom (with both benthic communities and buried sediments), and exchanges with continental margins.
- To establish strategies for detecting, above the background of natural seasonal and event-scale variability, longer term changes in ocean biogeochemical cycles in relation to climate change.

There are now 32 countries involved in JGOFS internationally who contribute through their national programs. As with all IGBP initiatives, participation is encouraged on a range of levels in a manner designed to maximize national contributions (see e. g., JGOFS Implementation Plan).

There are four kinds of studies designed to achieve the JGOFS objectives:

- Process studies involving the international JGOFS community are being conducted at field sites in areas of the world oceans chosen either because of their prominence in CO₂ fluxes or because of perceived sensitivities to climate change. Examples of the former are the North Atlantic and Equatorial Pacific and of the latter, the Southern Ocean and the Arabian Sea.
- Global survey using remote sensing and ship observations and long time series observations to improve basic descriptions of biogeochemical variability.
- Model studies to identify critical processes and variables, to assimilate observed parameters into basin and global scale fields, and to predict the future state of the ocean.
- Studies of the historical climate record by means of geochemical sampling of deep-sea and continental shelf sediments.

In order to use effectively the vast amount of high quality data obtained in JGOFS, a major international data archiving effort is in place.

2 Gas Exchange in JGOFS

Modelling studies [Sarmiento, 1992] suggest that for most regions of the world oceans, transfer of CO₂ across the air-sea interface is not the rate limiting step for oceanic uptake. The mixed layer equilibration time for a “normal” gas like N₂ is about 1 month, while about one year is required for CO₂ equilibration, because of its reactivity, and the buffer capacity of sea water [Broecker and Peng, 1982]. Despite this longer equilibration time for CO₂, model results indicate that it is still short compared to the time neces-

sary for transport of dissolved CO₂ through the thermocline from surface waters to the deep ocean.

Sarmiento et al. [1992] found that a doubling of the transfer velocity for CO₂ across the air sea interface would produce only a 9.2% increase in ocean uptake. If this view is correct, then the rate of global ocean uptake of anthropogenic CO₂ is controlled by vertical mixing.

However, even if not the rate determining step for ocean uptake, gas exchange does play an important role in JGOFS. Transfer of CO₂ across the air-sea interface represents a necessary flux for ocean uptake. Thus, estimates of this flux from $\delta p\text{CO}_2$ measurements and an appropriate transfer velocity relationship [e. g., *Liss and Merlivat*, 1986; *Wanninkhof*, 1992; *Monaahan and Spillane*, 1984, etc.] describe ocean uptake. These estimates though are not easy. The time scale of CO₂ equilibration in the surface layer is comparable to the annual cycles of biological activity and warming of surface waters. Add to this, patchiness in biological activity and processes such as upwelling, and fluxes may vary considerably, both spatially and temporally. This variability is perhaps exemplified in the large gross fluxes of CO₂, thought to be about 90 gtC/year from the ocean to the atmosphere, and about 92 gtC/year into the ocean (IPCC, Report of the Scientific Assessment Committee, 1994).

In surveying the temporal and spatial distribution of CO₂ fluxes, two kinds of information are needed - reliable relationships between physical forcing and gas transfer, and the distribution of $\delta p\text{CO}_2$, the difference between the partial pressures of CO₂ in the surface ocean and the atmosphere. While progress is being made in estimating sea state and hence piston velocity from remote sensing information [*Etcheto and Merlivat*, 1988], JGOFS has recognized that there is insufficient understanding of the global variability of $\delta p\text{CO}_2$ across the air-sea interface.

Lack of information, particularly on surface ocean pCO₂, may have contributed in the past to estimates of global ocean fluxes that are not consistent with modelling results. For example, *Tans et al.* [1990] concluded that in the period 1981-1987 the oceans absorbed <1 gtC/year, while model estimates indicate that uptake during the same period was about 2 gtC/year [*Sarmiento et al.*, 1992; *Keeling et al.*, 1989; *Stocker et al.*, 1994]. The uncertainty involved is a substantial portion of the 3.5 gtC currently taken up annually by global sinks other than the atmosphere. JGOFS therefore gives a high priority to making seasonal surveys of surface ocean pCO₂, with the result that pCO₂ and DIC are measured on many JGOFS cruises and cooperatively, on cruises of the WOCE Hydrographic Program.

There are, however, some regions of the world oceans in which air-sea gas transfer does appear to limit CO₂ uptake. For example, in regions of deep convection events, such as occur episodically at high latitudes, vertical mixing occurs on time scales too short for full equilibration of CO₂. For such events, gas transfer is considered to limit CO₂ uptake [*Broecker and Peng*, 1982]. Regions of the oceans where vertical mixing occurs rapidly account

for most of the sensitivity in ocean CO₂ uptake models to changes in gas transfer rates [Sarmiento, 1992].

Apart from improving the time and space resolution of δ pCO₂ measurements, we need to develop an increased confidence in our understanding of the relationship between piston velocity and wind speed. In measurements of fluxes or in inferences of fluxes, the relationships that describe piston velocities have received conflicting endorsements [Woolf and Thorpe, 1991; Farmer *et al.*, 1992; Wallace and Wirick, 1992; Spitzer and Jenkins, 1989; *etc.*]. Differences appear to be due to biases in the methods used in making the measurements and/or in variability in physical and biological conditions that affect mass transfer [Wanninkhof, 1992; Frew *et al.*, 1990].

3 Biological Processes

Increased levels of CO₂ in the atmosphere are not likely to directly stimulate increased plant production in the oceans. The principal plant species are single-celled organisms, phytoplankton, which, unlike land based plants are not subject to CO₂ fertilization, because they are not carbon limited in growth. Instead, they are limited by the macronutrients, nitrogen, phosphorous and silicon and in some parts of the oceans, perhaps, the micronutrients iron and zinc.

Most ocean models to date have contained the assumption that the ocean carbon cycle has not been affected by climate change. However, there is no certainty that this "steady state" approach is currently valid. This is especially a concern, because various modelling studies [e.g., Sarmiento, 1995] have shown that changes in the ocean carbon cycle are capable of causing large perturbations in atmospheric CO₂. For example, changes in the biological pump could have substantial effects on atmospheric CO₂ levels. Oeschger [1991] estimates that without marine biological activity, atmospheric CO₂ levels would reach about 450 ppmv, and conversely, if all nutrients were utilized, levels would reach about 150 ppmv. Consequently, understanding the current state of key biological processes, establishing the capability to detect changes, and providing the understanding necessary to predict the response of biological processes to climate change are all important components of JGOFS.

Studies of dissolved gases and gas transfer have a special role in efforts to understand the dynamics of biological and physical processes in the surface ocean. The seasonal cycle of the biological gas - O₂ in conjunction with measurements of inert gases, especially Ar and N₂ offer considerable promise for elucidation of surface ocean processes that include net biological production, gas exchange, bubble and temperature induced *gas supersaturations*, diurnal mixing and the fluxes of gases through the thermocline [Spitzer and Jenkins, 1989; McNeil and Farmer, 1995; Emerson *et al.*, 1991]. Accounts of rapid changes in gas fluxes [Wallace and Wirick, 1992; Farmer *et al.*, 1993] argue for sampling strategies that are continuous and in situ.

4 Gases Other Than CO₂

The oceans are variously a source or sink for other gases that are important in climate change, including CH₄, N₂O, methyl halides and DMS. As with CO₂, fluxes to or from the ocean for these trace gases are often estimated from measurements of disequilibrium and application of a transfer velocity relationship. Again, accurate estimates depend on well understood relationships between physical forcing and gas transfer.

While ocean exchanges of gases other than CO₂ have not to date been a major focus of JGOFS, a special interest in CH₄ and N₂O production and transfer is emerging from considerations of the effects of *iron fertilization*. In several large regions of the world oceans, i. e., the N. Pacific, Equatorial Pacific and Southern Oceans, availability of dissolved iron is thought to limit phytoplankton production. In theory, manipulation of the ocean carbon cycle, causing increased uptake of CO₂, can be accomplished by adding dissolved iron to surface waters in these iron limited regions, and thereby stimulate productivity. The result is increased sinking of particulate carbon to the deep ocean. However, recent modelling results (summarized in *Denman et al.*, IPCC, in review) suggest that while carbon uptake might be enhanced, this gain may be offset by increased respiration in the thermocline, depletion of O₂, and increased production of other radiatively active gas, N₂O and CH₄. The fates of these gases and especially the rate of transport to the atmosphere then become important considerations.

5 Special Challenges

A number of special challenges exist in the field of gas exchange for reaching JGOFS goals and objectives. Among these are:

- the need to improve our understanding of the global surface ocean distribution of $\delta p\text{CO}_2$. Our understanding is developing rapidly in this area [*Merlivat*, 1995] but because of temporal and spatial variability in $\delta p\text{CO}_2$, repeated measurements are necessary [*Watson*, 1991]. Clearly, what is needed is development of accurate stand-alone pCO₂ sensors for long term ocean deployment.
- the challenge of making better measurements of net production through modelling seasonal cycles of O₂ and correcting for gas exchange through the dynamics of inert gases. Here reliable remote sampling methods or accurate, stable sensors for dissolved gases and particularly dissolved O₂ and inert gases like N₂ and Ar are very much needed (e. g., McNeil et al. in press).
- the need to better understand the fundamental processes that control gas exchange. In particular, we need a better understanding of the role of wind, waves, bubbles, biological processes and near-surface dynamics including Langmuir cells, turbulence and breaking waves. Models

developed from this understanding can be used to identify some subset of measurements that must be made to accurately determine gas exchange rates.

- the requirement for instruments with sufficient sensitivity and long term stability to monitor changes in the concentrations or partial pressures of key gases, like the biological gases, CO₂ and O₂ and inert gases like Ar and N₂. Once we have characterized the present geographical distribution of key biogeochemical properties and processes, long term monitoring of the ocean will be needed to detect changes.

6 Progress in Instrument Development

Improved instrumentation and methods for measuring dissolved gases in situ are under development in a number of national JGOFS efforts. One example is the work we have been doing in developing gas tension instruments in a collaborative effort with David Farmer of IOS Canada and Craig McNeil, now working at the University of Paris with Liliane Merlivat [*Anderson and Johnson, 1992; McNeil et al., 1994*]. The present gas tension instrument provides microbar sensitivity and 0.2% per year stability. In practice, O₂ partial pressure and water vapor pressure are subtracted from gas tension to give what is very nearly the partial pressure of N₂ - a gas considered nearly inert in the oceans. This inference of N₂ is currently limited by the accuracy of the O₂ measurement, however, we are now working on an O₂ sensor based on the gas tension principal and plan to begin testing this summer.

References

- Broecker, W. S. and T. H. Peng, Tracers in the Sea, *Eldigo Press*, Palisades, New York, 1982
- Emerson, S., P. Quay and C. Stump, O₂, Ar, N₂ and ²²²Rn in surface waters of the subarctic ocean: net biological O₂ production, *Global Biogeochem. Cycles*, 5, 49-69, 1991
- Etcheto, J. and L. Merlivat, Satellite determination of the carbon dioxide exchange coefficient at the ocean-atmosphere interface: a first step, *J. Geophys. Res.*, 93, 15,669-15,678, 1988
- Farmer, D. M., C. L. McNeil and B. D. Johnson, Evidence for the importance of bubbles in increasing air-sea gas flux, *Nature*, 361, 620-623, 1993
- Fasham, M. J. R., K. Denman and P. G. Brewer, Global Environmental Change (R.W. Corell and P.A. Anderson, editors), *NATO ASI Series*, Springer-Verlag, Berlin, 1991
- Frew, N. M., J. C. Goldman, M. R. Dennet and A. S. Johnson, Impact of phytoplankton-generated surfactants on air-sea gas exchange, *J. Geophys. Res.*, 95, 3337-3352, 1990
- Keeling, C. D., S. C. Piper and M. Heimann [1989] A three dimensional model of atmospheric CO₂ transport based on observed winds, 4, Mean annual gradients

- and interannual variations, in *Aspects of Climate Variability in the Pacific and the Western Americas*, Geophys. Monogr. 55, (D.H. Peterson, editor) pp. 305-363, AGU, Washington, D.C,
- Liss, P. and L. Merlivat, Air-sea gas exchange rates: Introduction and synthesis, in *The Role of Air-Sea Exchange in Geochemical Cycling* (P. Baut-Menard, editor) pp. 113-127, D. Reidel, Norwell, Mass., 1986
- McNeil C. L. and D. M. Farmer, Observations of the influence of diurnal convection on upper ocean dissolved gas measurements, *J. Mar. Res.*, 53, 151-169, 1995
- McNeil, C. L., B. D. Johnson and D. M. Farmer, In situ measurement of dissolved nitrogen and oxygen in the ocean, in press in *Deep-Sea Res.*, 1994
- Merlivat, L., Carbon dioxide fluxes exchanged at the air-sea interface, in *JGOFS First Science Symposium; Abstracts*. Scientific Committee on Oceanic Research, 1995
- Monahan, E. C. and M. C. Spillane, The role of oceanic whitecaps in air-sea gas exchange, in *Gas Transfer at Water Surfaces* (W. Brutsaert and G.H. Jirka, editors) pp. 495-503, D. Reidel, Norwell, Mass., 1984
- Oeschger, H., Paleodata, paleoclimates and the greenhouse effect in Climate Change: Science, Impacts and Policy, (J. Jager and H.L. Ferguson, editors), *Cambridge University Press*, Cambridge, 1991
- Sarmiento, J. L., J. C. Orr and U. Siegenthaler, A perturbation simulation of CO₂ uptake in an ocean general circulation model, *J. Geophys. Res.*, 97, 3621-3645, 1992
- Sarmiento, J. L., Modeling the ocean uptake of anthropogenic carbon, *U.S. JGOFS News*, January 1995, 1995
- Spitzer, W. S. and W. J. Jenkins, Rates of vertical mixing, gas exchange and new production: estimates from seasonal gas cycles in the upper ocean near Bermuda, *J. Mar. Res.*, 47, 169-196, 1989
- Stocker, T. S., W. S. Broecker and D. G. Wright, Carbon uptake experiments with a zonally-averaged global ocean circulation model, *Tellus*, 46B, 103-122, 1994
- Tans, P. P., I. Y. Fung, and T. Takahashi, Observational constraints on the global atmospheric CO₂ budget, *Science*, 247, 1431-1438, 1990
- Wallace, D. W. R. and C. D. Wirick, Large air-sea gas fluxes associated with breaking waves, *Nature*, 356, 694-696, 1992
- Wanninkhof, R., Relationship between wind speed and gas exchange over the ocean, *J. Geophys. Res.*, 97, 7373-7382, 1992
- Watson, A. J., C. Robinson, J. E. Robinson, P. J. LeB. Williams and M. J. R. Fasham, Spatial variability in the sink for carbon dioxide in the North Atlantic, *Nature*, 350, 50-53, 1991
- Woolf, D. K. and W. A. Thorpe, Bubbles and the air-sea exchange of gases in near-saturation conditions, *J. Mar. Res.*, 49, 435-466, 1991

Estimating the Chemical Enhancement Effect on the Air-Sea CO₂ Exchange Using the ERS1 Scatterometer Wind Speeds

J. Boutin and J. Etcheto

Laboratoire d'Océanographie DYnamique et de Climatologie
UMR121 : CNRS/ORSTOM/ Université Pierre et Marie Curie, Paris, France
email: jb@lodyc.jussieu.fr

Abstract

The global coverage of satellite measurements of oceanic surface wind speed and sea-surface temperature has enabled us to compare various parametrizations of the air-sea CO₂ exchange coefficient. The *Wanninkhof* [1992] quadratic law is shown to induce regional biases when compared to more physical representations. The chemical enhancement could have a noticeable effect in equatorial regions but its existence in the ocean remains to be proven.

1 Introduction

The estimate of the CO₂ oceanic sink is of primary importance for climatological studies. One way to compute the global *air-sea CO₂ flux* is to globally integrate the local CO₂ flux which is commonly expressed as the product of the CO₂ transfer velocity, k , by the CO₂ solubility coefficient, S , and the partial pressure gradient between the ocean and the atmosphere, ΔP . Although this method is more direct than the ¹³C/¹²C estimates and can be used to validate biogeochemical model results, it suffers from several uncertainties. A recent study of *Van Soy et al.* [1995] reveals that neglecting the difference between the skin temperature and the temperature in the ocean subsurface may lead to a 0.17 to 0.39 GtC yr⁻¹ underestimate of the oceanic CO₂ uptake. The relationship between k and the surface wind speed, U , based on theoretical studies and on wind-tunnel and in-situ measurements [*Liss and Merlivat*, 1986] disagrees by a factor between 1.4 and 2.1 with the k estimates deduced from the ¹⁴C inventories [*Broecker et al.*, 1986] as reviewed by *Etcheto and Merlivat* [1989]. In order to reconcile both determinations, the possible effect of *chemical enhancement* on the CO₂ exchange over the ocean has recently been stressed by *Wanninkhof* [1992]. Taking a Rayleigh distribution function for the wind speed and the *Hoover and Berkshire* [1969] formalism to approximate the enhancement effect, he estimates that the CO₂ flux should be increased in equatorial regions by 6% to 20%. This effect occurs at low wind speed when a liquid film dominated by molecular diffusion can form at the surface of the ocean. The diffusion of CO₂ being 10⁴ slower

in water than it is in the air, the CO_2 concentration at the interface is different from that of the underlying ocean, which is dominated by turbulent mixing. Thus the hydration–dehydration reactions of CO_2 with water tend to change the CO_2 concentration in this film in such a way that the air–sea CO_2 concentration gradient is increased. This effect has been studied both theoretically and experimentally in wind–water tunnels.

In this paper, we estimate the possible effect of this chemical enhancement at a global scale according to the *Hoover and Berkshire* [1969] formulation using global wind fields deduced from the European Remote Sensing 1 (*ERS1*) scatterometer measurements and global sea surface temperature fields produced by *Reynolds and Smith* [1994]. We compare the results to what is obtained using the equation (8) proposed by *Wanninkhof* [1992].

2 Data

2.1 Wind Speed Data

The wind data are deduced from the ERS1 scatterometer measurements. The scatterometer is the most appropriate remote sensing instrument to estimate the sea surface wind speed and therefore the wind data are expected to be of good quality. They have been produced by IFREMER/CERSAT at BREST. The 10 m height wind speed, U , is retrieved using the final version of CERSAT algorithm from July 1992 to July 1993. The *rms* difference between the final retrieved wind speed and NOAA buoy measurements is equal to 1.2 m s^{-1} [*Quilfen and Bentamy*, 1994]. We take the best solution found by the CERSAT dealiasing algorithm. When no solution is found by the dealiasing algorithm, in particular in case of low wind speed, we take the rank 1 solution (provided that the three scatterometer antennas were functioning), that the Maximum Likelihood Estimator (MLE) is less than 60 and that the wind speed value is not 0. If the wind speed value is 0, we check that a solution has been found by the extraction algorithm since both wind speeds between 0 and 1 m s^{-1} and erroneous measurements are set to 0. Data in the presence of land and ice are discarded following the CERSAT flags. In order to completely eliminate the data polluted by the presence of ice, we add a test on the Maximum Likelihood Estimator (MLE) south of 50° S and north of 60° N : for the first and last 6 incidence angles, the wind data are discarded if MLE is less than 20. These sortings eliminate about 6 % of the oceanic data (not flagged as ice or land by CERSAT).

We compute global maps of the average, $\langle U \rangle$, and of the standard deviation, σ_U , of U at 1° and one week resolution using all the wind speeds located in a $1^\circ \times 1^\circ$ square (raster); only the rasters containing at least 10 observations per week are kept.

2.2 Sea Surface Temperature Data

Global fields of sea surface temperature, SST, are obtained from the *Reynolds and Smith* [1994] analyses. The analyses use in-situ and satellite SST measurements. They are produced weekly using an optimum interpolation on a 1° grid. The analysis includes a preliminary step that corrects any satellite biases relative to the in-situ data. This is particularly useful since the satellite observations are obtained from the Advanced Very High Resolution Radiometer (AVHRR) and biases of the AVHRR SST have been observed, in particular between daytime and nighttime retrievals and relative to in-situ observations during periods following volcanic eruptions.

As the SST variations are slow relative to those of the wind speed, in the following we use monthly SST fields that have been computed by taking the average of the weekly fields.

3 Exchange Coefficient Computation Methods

The CO₂ flux, when the thermal skin effect is neglected, can be expressed as the product of the CO₂ exchange coefficient, K which equals k multiplied by S , by ΔP . Given that with this formulation the flux can be directly deduced from K and ΔP without the knowledge of the temperature, all the results concerning large scale distribution of the CO₂ exchange will be shown in K .

3.1 K Without Chemical Enhancement Effect

We estimate K without chemical enhancement effect using two $k - U$ relationships: the *Liss and Merlivat* [1986] relationship and the one proposed by *Wanninkhof* [1992] which is calibrated on the ¹⁴C global estimates of K (relation (3) of his paper).

The global maps of the exchange coefficient computed using the *Liss and Merlivat* [1986] relationship, K_{LM} , are obtained by applying the relationship to each individual satellite wind speed measurement and by taking the average and the standard deviation of all K so obtained located in a 1° raster over one week. As for the wind speed maps, only the rasters containing at least 10 observations per week are kept. Since *Etcheto and Merlivat* [1988] have shown that the variations of k with temperature are nearly compensated by the variations of S with temperature so that K is nearly temperature independent, and since the introduction of the temperature parameter in the processing makes the computation time consuming, we compute K_{LM} at a constant temperature of 13° C and at a salinity of 35 ‰ corresponding to the average of the temperature dependent term of the *Liss and Merlivat* [1986] formula.

The relationship proposed by *Wanninkhof* [1992] has the following expression:

$$k_W = 0.31U^2(S_C/660)^{-0.5} \quad (1)$$

where S_C is the Schmidt number. Since this relationship is a quadratic function of U , the exchange coefficients average in 1° raster over one week, $\langle K_W \rangle$, is deduced from the global maps of $\langle U \rangle$ and σ_U as follows:

$$\langle K_W \rangle = 0.31(\langle U \rangle^2 + \sigma_U^2)(S_C/660)^{-0.5}S \quad (2)$$

S_C and S are estimated for a salinity of 35‰, using the Reynolds SST values and according to the temperature dependences given by *Jähne et al.* [1987] and *Weiss* [1974] respectively.

3.2 K Including Chemical Enhancement Effect

The transfer velocity without chemical enhancement, k_{un} , which is involved in the computation of the chemical enhancement factor (see below), is deduced from the global maps of K divided by S at the Reynolds SST. The K including chemical enhancement, K_{en} , will be deduced in the same way by multiplying the k including enhancement, k_{en} , by S .

We will follow the formalism of *Wanninkhof* [1992]: k_{en} will be expressed as the product of k_{un} by an enhancement factor, E . According to *Hoover and Berkshire* [1969], E is a function of pH, of salinity (Sal), of temperature (T), and of k_{un} but since E does not exhibit strong variations in Sal nor in pH around the Sal and pH values commonly found in seawater, we take a mean Sal value of 35 ‰ and a mean pH value of 8.3. The resulting k_{en} are shown on Figure 1 (dots) at four temperatures. We consider only the variations of E with k_{un} and T :

$$\begin{aligned} E(T, k_{un}) &= \frac{\tau(T)}{\tau(T) - 1 + \left[\tanh\left(\frac{A(T)}{k_{un}}\right) / \left(\frac{A(T)}{K_{un}}\right) \right]} \\ A(T) &= [\kappa(T)D(T)\tau(T)]^{1/2}; \\ \tau(T) - 1 &= \frac{(H^+)^2}{K_1K_2 + K_1(H^+)} \end{aligned} \quad (3)$$

where κ is the combined rate terms describing hydration as defined by *Hoover and Berkshire* [1969], D is the CO_2 diffusion coefficient, K_1 and K_2 are the ionization constants for carbonic acid. The temperature dependences are computed using the fits given by *Johnson* [1982] for the rate constants involved in κ computation, by *Jähne et al.* [1987] for D and by UNESCO [1987] for K_1 and K_2 . E is large for high T and low k_{un} .

In order not to compute E for each individual satellite measurement, which would be very heavy in computation time, we have established a computation method which makes use of only the 1° and one week average of

Table 1: Coefficients for least squares polynomial fit of $kE(k)$ versus k (Equations (4) and (5))

T °C	a ₀	b ₀	a ₁	b ₁	a ₂	b ₂
0	0.2462	0.0183	0.92663	0.99953	0.004881	0.000001
5	0.4771	0.0637	0.86286	0.99629	0.009042	0.000064
10	0.8712	0.1316	0.76295	0.99236	0.015273	0.000137
15	1.4794	0.2907	0.62517	0.98199	0.023466	0.000341
20	2.3599	0.5504	0.45510	0.96670	0.032734	0.000623
25	3.5577	1.0389	0.27212	0.93783	0.041314	0.001149
30	5.1316	1.9034	0.10416	0.88677	0.046725	0.002091

k_{un} , $\langle k_{un} \rangle$ and of its standard deviation, $\sigma_{k_{un}}$. First, we find that at a given temperature, k_{en} can be approximated by two least squares second-order polynomial fits versus k_{un} computed in two ranges of k_{un} values:

$$k_{en} = a_0 + a_1 k_{un} + a_2 k_{un}^2 \quad 0 \text{ cm hr}^{-1} < k_{un} < 12 \text{ cm hr}^{-1} \quad (4)$$

and

$$k_{en} = b_0 + b_1 k_{un} + b_2 k_{un}^2 \quad 8 \text{ cm hr}^{-1} < k_{un} < 30 \text{ cm hr}^{-1} \quad (5)$$

For the present study, fits have been determined for temperature ranging from -2° C to 31° C in 1° C temperature intervals. The fits found at 0°, 10°, 20° and 30° are shown on Figure 1 and the coefficients of the fits for 7 temperatures are indicated in Table 1.

Second, assuming that the same fit is valid for all the measurements inside a raster, the choice of the fit depends only on the $\langle k_{un} \rangle$ value: the one week and 1° average of k_{en} , $\langle k_{en} \rangle$ can be expressed as a function of $\langle k_{un} \rangle$ and $\sigma_{k_{un}}$:

$$\langle k_{en} \rangle = a_0 + a_1 \langle k_{un} \rangle + a_2 (\langle k_{un} \rangle^2 + \sigma_{k_{un}}^2) \langle k_{un} \rangle < 10 \text{ cm hr}^{-1} \quad (6)$$

and

$$\langle k_{en} \rangle = b_0 + b_1 \langle k_{un} \rangle + b_2 (\langle k_{un} \rangle^2 + \sigma_{k_{un}}^2) \langle k_{un} \rangle \geq 10 \text{ cm hr}^{-1} \quad (7)$$

This approximation is reasonable because the rasters containing both k_{un} individual values above 12 cm hr⁻¹ and k_{un} individual values below 8 cm hr⁻¹ are mostly located in regions of low temperature for which (4) and (5) outside the 8-12 cm hr⁻¹ region are very close to each other. We use relations (6) and (7) to compute weekly 1° maps of the enhanced exchange coefficient according to the *Liss and Merlivat* [1986] parametrization of k_{un} , $K_{LM_{en}}$. To compute the enhanced exchange coefficient obtained for a quadratic law calibrated with ¹⁴C, $K_{C14_{en}}$, we first compute:

$$\langle k_{un} \rangle = 0.304(\langle U \rangle^2 + \sigma_u^2)(Sc/660)^{-0.5} \quad (8)$$

using a 0.304 coefficient as suggested by *Wanninkhof* [1992]. We then use equations (6) and (7), neglecting $\sigma_{k_{un}}$. This approximation enables us to use wind speed data gridded at 1° , one week resolution instead of using the raw data. We tested on one week of data the resulting error: the difference of the exchange coefficients maps obtained by using equations (4) and (5) on the raw data and by using equations (6) and (7) and neglecting $\sigma_{k_{un}}$ is $-2.3 \times 10^{-4} \text{ mol m}^{-2} \text{ yr}^{-1} \mu\text{atm}^{-1}$ averaged over the world ocean, the standard deviation being $7.0 \times 10^{-4} \text{ mol m}^{-2} \text{ yr}^{-1} \mu\text{atm}^{-1}$. Compared to a ^{14}C global exchange coefficient of $6.2 \times 10^{-2} \text{ mol m}^{-2} \text{ yr}^{-1} \mu\text{atm}^{-1}$, we consider the error to be negligible.

To compute the enhanced exchange coefficient using equation (8) of *Wanninkhof's* [1992] paper, $K_{W_{enW}}$, we use our equation (8) and combine it with the temperature dependence proposed by *Wanninkhof* [1992].

4 Flux Computation Methods

In order to estimate the effect of the chemical enhancement on the air-sea flux, we have to combine the exchange coefficient maps to realistic ΔP maps. Since no measured monthly maps of ΔP over the global ocean exist, we use the outputs of an ocean model for the 1987 year provided to us by *Kurz and Maier-Reimer* [1995]. This can only be considered as a sensitivity test since these ΔP maps have been produced using a different K map as boundary condition to the ocean model and are therefore inconsistent with any other K map. The weekly K maps are averaged to obtain monthly maps and combined to the ΔP maps.

5 Results

5.1 K Without Chemical Enhancement Effect

We first compare the exchange coefficients without chemical enhancement effect, K_{LM} with K_W . Their yearly global averages are reported in Table 2. The K_W average is lower than the ^{14}C determination ($6.2 \times 10^{-2} \text{ mol m}^{-2} \text{ yr}^{-1} \mu\text{atm}^{-1}$) because the ERS1 wind speed average is 7.12 m s^{-1} , lower than the value taken by *Wanninkhof* [1992] to calibrate his parametrization (7.4 m s^{-1}). The 1992–1993 ERS1 wind speed average is not unusual since it is 7.17 m s^{-1} in 1993–1994. The ratio of the K global yearly average (K_W/K_{LM}) is 1.77.

When this ratio is computed in each 1° raster of a monthly map (July 1992), it varies with location from 1.5 at mid-latitude where the wind speed is moderate ($U \sim 7.5 \text{ m s}^{-1}$) to 2 at high latitude ($U \sim 13 \text{ m s}^{-1}$) and up to 2.3

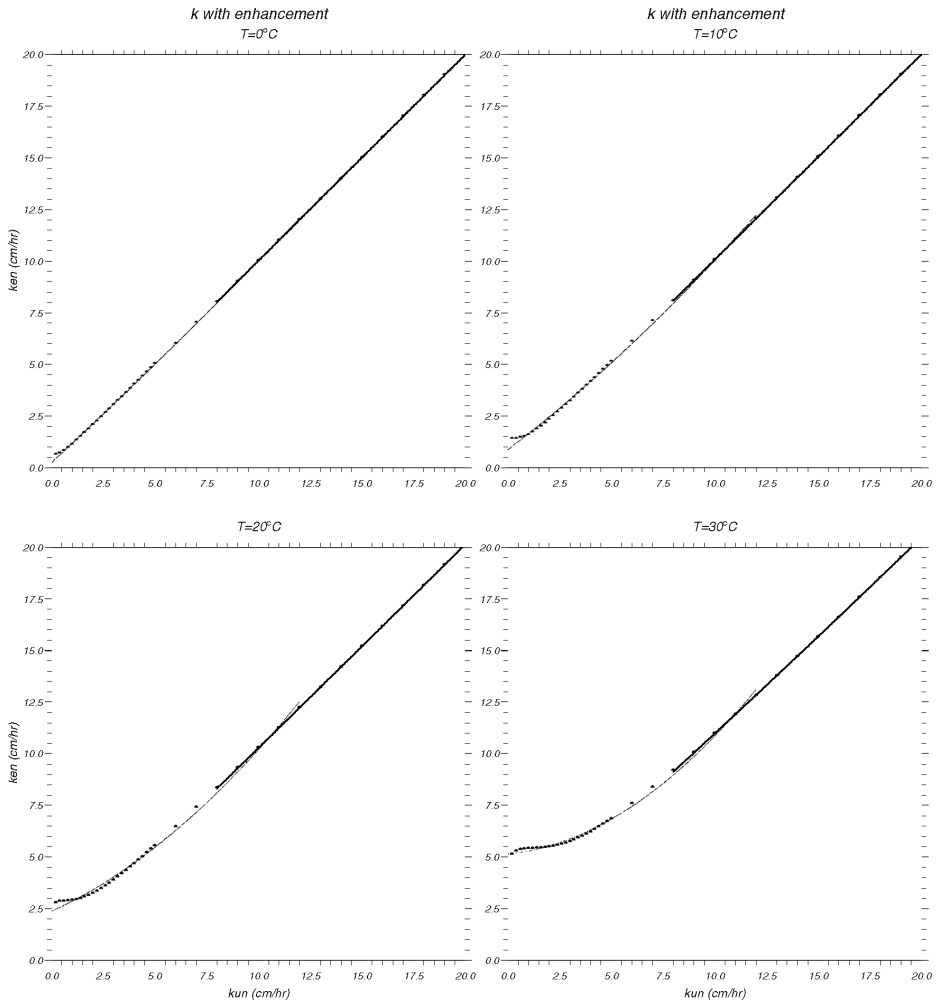


Figure 1: k_{en} versus k_{un} according to Hoover and Berkshire [1969] formalism (dots), to equation (4) (thin line) and to equation (5) (thick line). Top left: at 0°C ; top right: at 10°C ; bottom left: at 20°C ; bottom right: at 30°C .

Table 2: K global average ($10^{-2} \text{ mol m}^{-2} \text{ yr}^{-1} \mu\text{atm}^{-1}$) and (in parentheses) normalized global yearly flux

K_{LM} (F_{LM})	K_{LMen} (LM_{en})	K_W (F_W)	K_{C14en} ($FC14en$)	K_{WenW} ($FWenW$)
3.32 (-1.00)	3.55 (-0.95)	5.90 (-1.84)	5.88 (-1.77)	6.56 (-1.81)

in equatorial regions of very low wind speed ($U \leq 3 \text{ m s}^{-1}$). This is coherent with the wind speed dependence of the two parametrizations as noted by *Wanninkhof* [1992]: "a quadratic dependence of gas transfer and wind speed does not have any physical significance": below 3.6 m s^{-1} it overestimates the very low gas exchange observed in the smooth surface regime and at high wind speed, K_W is much larger than K_{LM} , as the quadratic law does not represent the breaking wave regime.

5.2 K Including Chemical Enhancement Effect

The global yearly averages of K determined as described in Section 3 and the global maps of the $K_{en} - K$ differences for the month of July 1992 are shown in Table 2 and on Figure 2 and 3 respectively. For the *Liss and Merlivat* parametrization: when the chemical enhancement is taken into account there is a 7% increase. On the $K_{LM_{en}} - K_{LM}$ map (Figure 2 top), the enhancement is maximum in the equatorial region, mainly in the western Pacific, where the temperature is high and the wind speed is low. The enhancement is mainly seen in the northern (summer) hemisphere. The reverse is true in January. There is no enhancement in the Antarctic ocean.

For the quadratic ^{14}C calibrated law (equation (8)), the global yearly average of $K_{C^{14}_{en}}$ is nearly the same as K_W , proving that the 0.304 calibration factor is correct. On the $K_{C^{14}_{en}} - K_W$ map (Figure 2 bottom), the maximum enhancement is seen in the same regions as for K_{LM} but it is smaller ($5 \cdot 10^{-3}$ instead of $7.5 \cdot 10^{-3} \text{ mol m}^{-2} \text{ yr}^{-1} \mu\text{atm}^{-1}$): for the same wind speed, k_{un} is larger for the quadratic law than it is for the *Liss and Merlivat* parametrization. For large regions of the ocean (most of the southern hemisphere) the "enhancement" is negative (blue colors). This is due to the ^{14}C calibration: since the ^{14}C inventories include the chemical enhancement effect, the ^{14}C calibrated K with and without enhancement must have the same global average. Therefore the enhancement at low wind speed must be compensated by a decrease at high wind speed.

The global yearly average of $K_{W_{en}W}$ is 11% larger than K_W : when integrated using measured quantities, the two parametrizations are not normalized to the same global value. The map of the difference $K_{W_{en}W} - K_W$ is plotted on Figure 3 top for the month of July 1992 while the $K_{C^{14}_{en}} - K_W$ difference map (same as Figure 2 bottom) is plotted at the bottom for comparison. The $K_{W_{en}W} - K_W$ difference is positive everywhere, giving all over the ocean an enhancement much larger than the *Hoover and Berkshire* [1969] formulation. Even in the Antarctic ocean where the SST is less than 5° C and the wind speed more than 10 m s^{-1} on most of the area, the enhancement effect is more than $2 \cdot 10^{-3} \text{ mol m}^{-2} \text{ yr}^{-1} \mu\text{atm}^{-1}$. It is maximum at $10^{-2} \text{ mol m}^{-2} \text{ yr}^{-1} \mu\text{atm}^{-1}$ in the western equatorial Pacific while it is only $0.5 \cdot 10^{-2} \text{ mol m}^{-2} \text{ yr}^{-1} \mu\text{atm}^{-1}$ for $K_{C^{14}_{en}}$ and $7.5 \cdot 10^{-2} \text{ mol m}^{-2} \text{ yr}^{-1} \mu\text{atm}^{-1}$ for $K_{LM_{en}}$ which should give the largest enhancement since for a given wind speed, the *Liss and Merlivat* [1986] parametrization gives the smallest k_{un} .

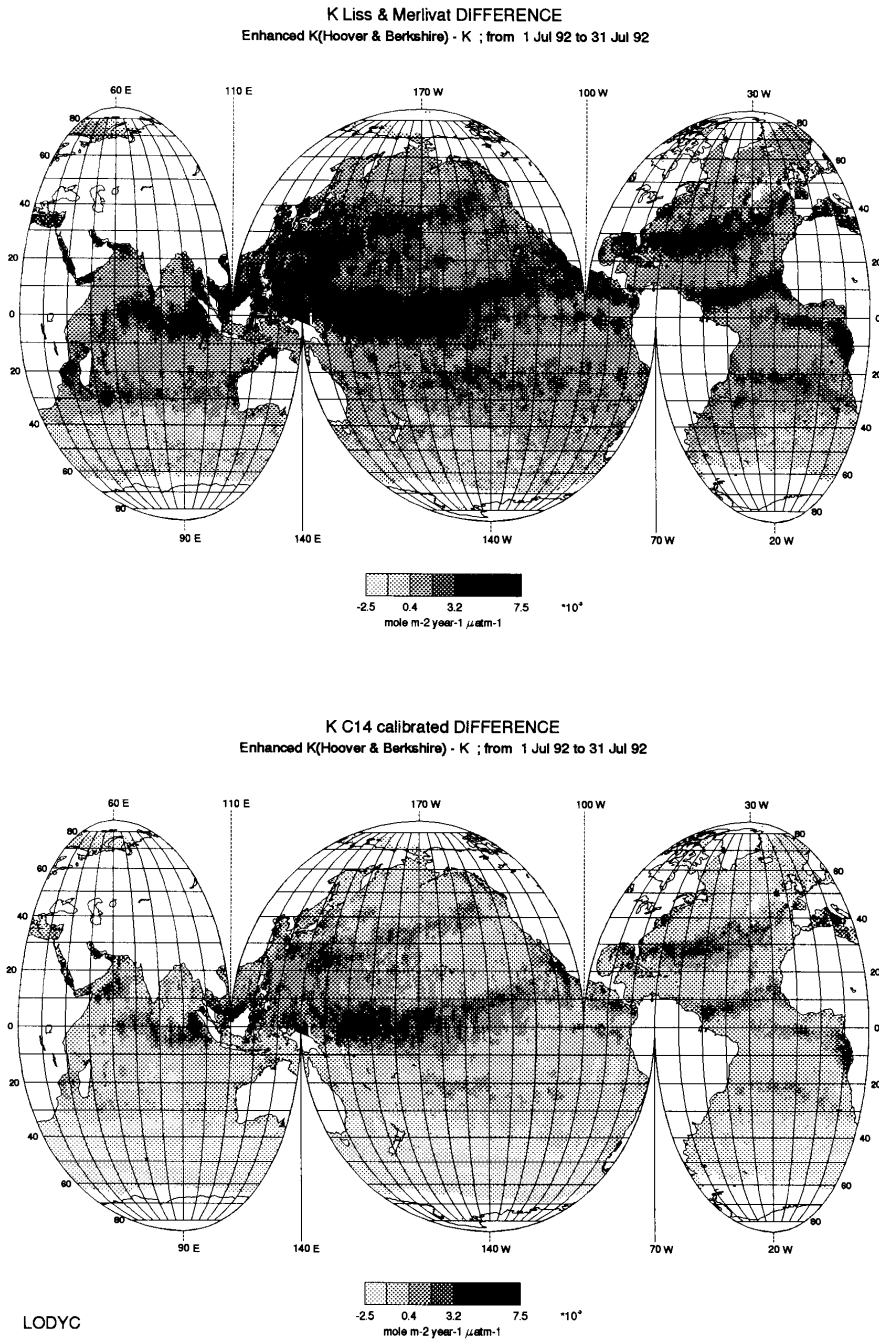


Figure 2: Difference map for the month of July 1992 of: $K_{LMen} - K_{LM}$ (top) and $K_{C14en} - K_W$ (bottom). The color scale varies over the range -2.5 to $7.5 \cdot 10^{-3} \text{ mol m}^{-2} \text{ yr}^{-1} \mu\text{atm}^{-1}$.

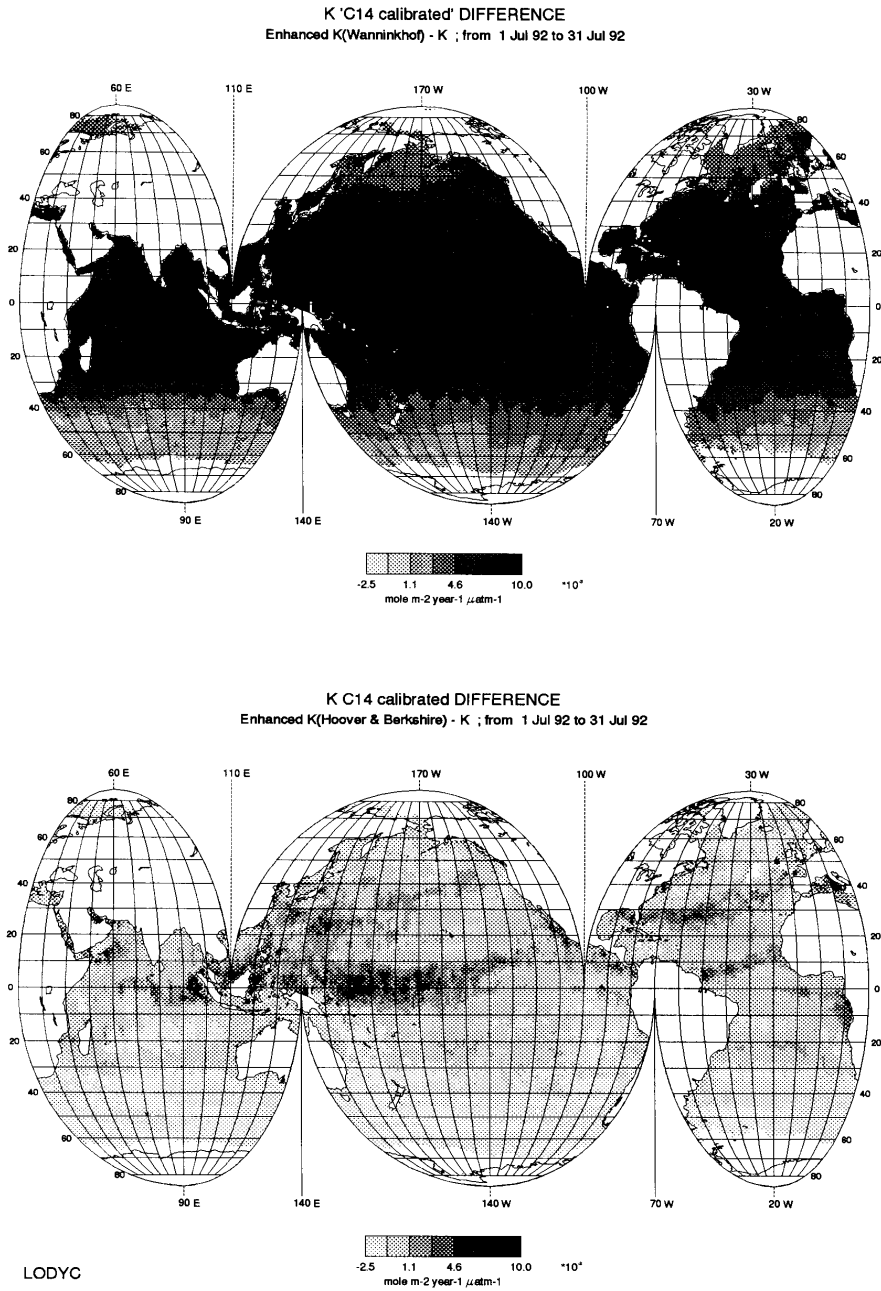


Figure 3: Difference map for the month of July 1992 of $K_{W_{enW}} - K_W$ (top) and $K_{C14_{en}} - K_W$ (bottom). The color scale varies over the range -2.5 to $10 \cdot 10^{-3} \text{ mol m}^{-2} \text{ yr}^{-1} \mu\text{atm}^{-1}$.

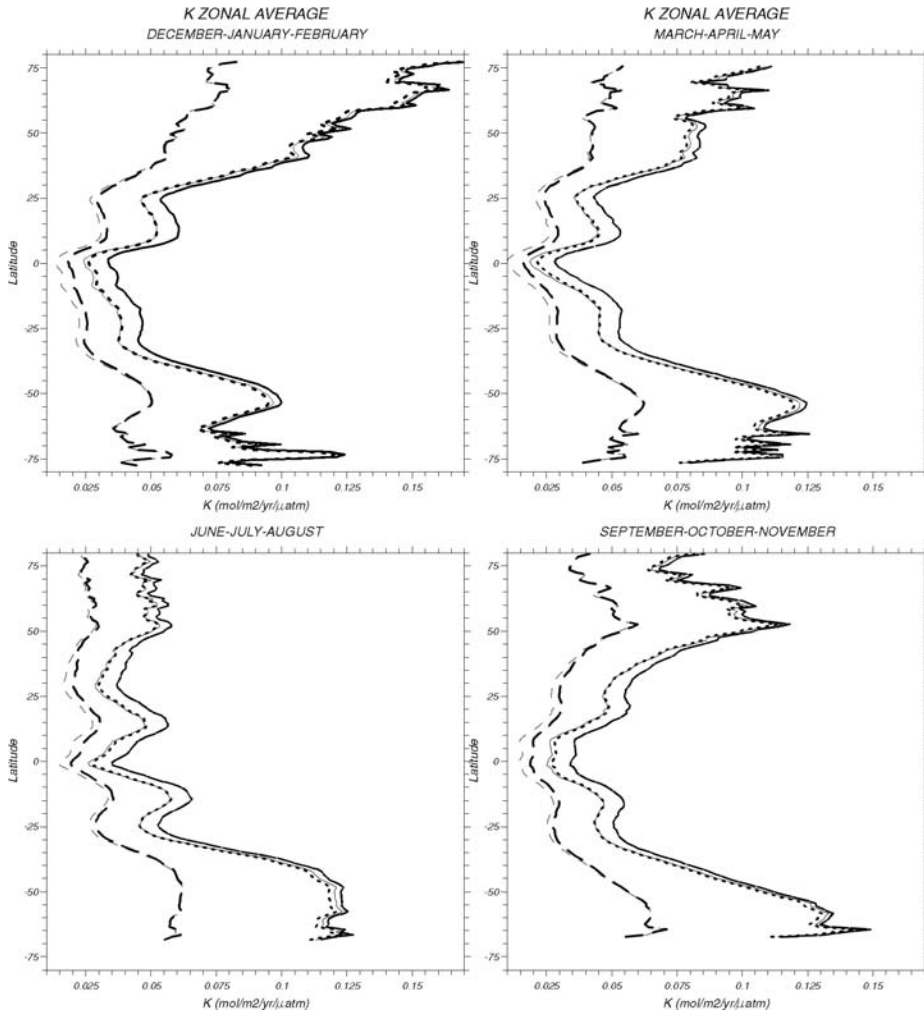


Figure 4: Seasonal variation of the K_{LM} (thin dashed line), $K_{LM_{en}}$ (thick dashed line), K_W (thin line), $K_{C14_{en}}$ (thick dotted line) and $K_{W_{enW}}$ (thick line) zonal average. Top left: December to February; top right: March to May; bottom left: June to August; bottom right: September to November.

The *Wanninkhof* [1992] parametrization of the chemical enhancement gives K values well above any other estimation: this is probably due to the fact that the enhancement factor has been computed for an unenhanced transfer velocity of 1 cm hr^{-1} , a low value observed only in few areas of the global ocean and for which the chemical enhancement is large (see Figure 1).

We have plotted on Figure 4, for the four seasons, the latitudinal profiles of K , zonally integrated over the global ocean, for our five K determinations. The seasonal variation can be clearly seen, maximum north of 50° N where K in summer is about one third of its winter value, while south of 50° S the winter value is only about 25% above the summer one with a K which is large all the year long. At low latitudes, the seasonal variation is weak, with the trade winds (equatorward of 25°) enhanced in the winter hemisphere.

The chemical enhancement according to *Hoover and Berkshire* [1969] is larger for the *Liss and Merlivat* [1986] formulation which gives lower k_{un} than for the ^{14}C calibrated quadratic law. As expected it exhibits a seasonal variation: maximum in equatorial regions, it extends further poleward in the summer hemisphere. The “enhancement” obtained for the ^{14}C calibrated quadratic law is a decrease poleward of 40° at all seasons.

The enhancement according to the *Wanninkhof* [1992] parametrization is present at all latitudes and all seasons, with a maximum in the equatorial region.

5.3 Effect of Chemical Enhancement on CO_2 Flux Determinations

We recall here that these results should only be taken as a sensitivity test since the ΔP fields used are inconsistent with any of the K maps that we obtain.

The monthly air-sea CO_2 flux maps have been averaged to obtain a yearly integrated flux. When K_{LM} is used, we obtain a yearly absorption by the ocean of 1.0 Gigatons of Carbon (GtC). In the rest of this text all the yearly fluxes will be normalized to this number. The normalized global yearly fluxes obtained with the five exchange coefficient formulations are written in parentheses in Table 2.

With K_W , the flux, F_W , is 1.84 the one obtained with K_{LM} , F_{LM} , a ratio slightly larger than the one of the exchange coefficients. In all cases, the absorbed flux obtained with the enhanced K , F_{en} , is smaller than the one obtained with the corresponding unenhanced K because the enhancement is maximum in the equatorial region which is also the main outgassing region of the ocean. The maximum decrease is for F_{LMen} (5%) since we have seen that its chemical enhancement is larger than for a ^{14}C calibrated quadratic law (4% decrease) due to the smaller k_{un} . For the flux computed with K_{WenW} , F_{WenW} , the decrease relative to F_W is less than 2% since we have seen that the enhancement extends to all latitudes in both outgassing and absorbing regions, increasing both outgassing and absorption which nearly compen-

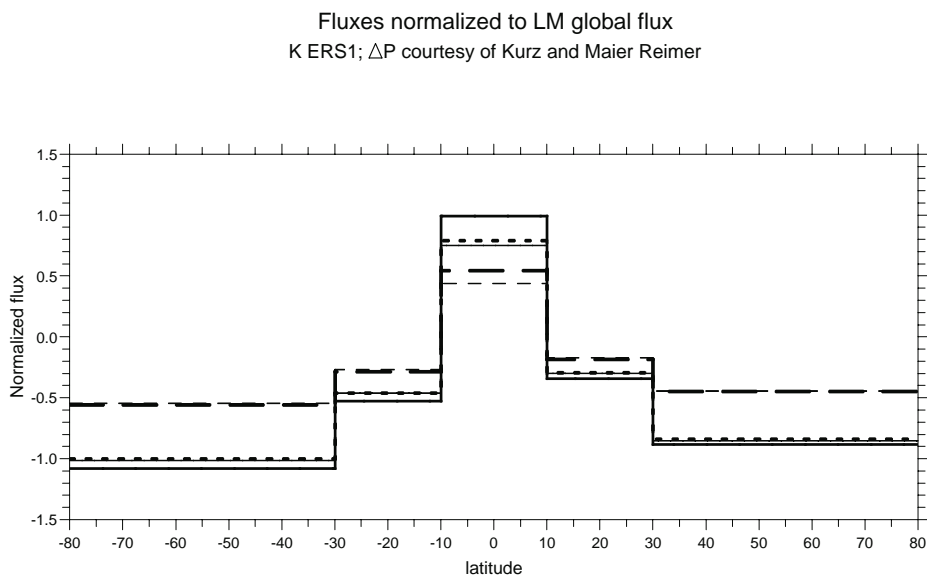


Figure 5: Integrated fluxes normalized to the LM global flux computed using ΔP fields from Kurz and Maier-Reimer and maps of K_{LM} (thin dashed line), K_{LMen} (thick dashed line), K_W (thin line), K_{C14en} (thick dotted line), K_{WenW} (thick line).

sate.

This can be clearly seen on Figure 5 where we plotted the normalized flux in five latitudinal bands computed with our five K determinations. The equatorial band (10S-10N) is the only outgassing one with a chemical enhancement larger for F_{LMen} than for F_{C14en} , the enhancement for F_{WenW} being even larger. The tropical bands (30S-10S; 10N-30N) are slightly absorbing, the chemical enhancement of F_{LMen} and of F_{C14en} being nearly zero while the F_{WenW} enhancement is still visible. The high latitude bands (80S-30S; 30N-80N) are more absorbing with a zero chemical enhancement for F_{LMen} and a very small "chemical decrease" for F_{C14en} , while in the southern ocean the F_{WenW} enhancement is of the same order as in the tropics, slightly smaller in the northern ocean.

6 Conclusions

Using satellite measurements, we have compared K_{LM} and K_W over the world ocean. Beside the difference in the global average due to the ¹⁴C normalization of K_W , important regional differences are observed due to the fact that a quadratic law cannot represent the three regimes of sea surface state.

We have evaluated too the possible effect of the chemical enhancement on the air-sea CO₂ exchange coefficient over the global ocean. We have also

made sensitivity test of the effect on the air-sea CO₂ flux. While the effect at global scale is only a few percent, it can be noteworthy in the equatorial region especially in the western pacific ocean. The formalism proposed by *Wanninkhof* [1992] to evaluate this effect which deconvolves the SST and the wind speed dependences, appears to widely overestimate it and to extend it to high latitude regions where it should not exist.

In any way, one should not forget that, as pointed out by *Hoover and Berkshire* [1969] the “wind tunnel results should not be extrapolated without qualification to the ocean”. They also reckon that “the average open ocean is far too turbulent to allow the sort of surface layer thicknesses observed in the experimental tank”. To our knowledge, no experiment has been conducted at sea to verify the existence of the chemical enhancement. Thence, even though our estimations have shown a possible noticeable effect in equatorial regions, the chemical enhancement should not be taken into account in oceanographic studies before in-situ experiments have been made.

Acknowledgements

We are grateful to L. Merlivat for helpful discussions and to K. Kurz and E. Maier-Reimer for providing ΔP fields. We thank M. Rafizadeh and S. Chauchereau for the processing of the ERS1 data. The authors are supported by the Centre National de la Recherche Scientifique. We are grateful to Ifremer/CERSAT and to Y. Quilfen for providing the ERS1 data. Most of this study was performed on the Centre National d'Etudes Spatiales (CNES) computer and we thank the CNES for giving us computer time. The work was performed with the support of the Programme National d'Etude Du Climat and under Commission of the European Communities contract EV5V-CT92-0124.

References

- Broecker, Wallace S., James R. Ledwell, Taro Takahashi, Ray Weiss, Liliane Merlivat, Laurent Memery, Tsung-Hung Peng, Bernd Jähne, and Karl Otto Münnich, Isotopic versus micrometeorologic ocean CO₂ fluxes: a serious conflict, *J. Geophys. Res.*, 91, 10517-10527, 1986
- Etcheto, J., and L. Merlivat, Satellite determination of the carbon dioxide exchange coefficient at the ocean-atmosphere interface: a first step, *J. Geophys. Res.*, 93, 15669-15678, 1988
- Etcheto, J., and L. Merlivat, Global determinations of the carbon dioxide exchange coefficient. Comparison of wind speed from different origins, *COSPAR proceedings*, 8 (9), 141-148, invited paper, 1989
- Hoover, T. E., and D. C. Berkshire, Effects of hydration in carbon dioxide exchange across an air-water interface, *J. Geophys. Res.*, 74, 456-464, 1969

- Jähne, B., G. Heinz, and W. Dietrich, Measurement of the diffusion coefficients of sparingly soluble gases in water with a modified Barrer method, *J. Geophys. Res.*, 92, 10767-10776, 1987
- Johnson, K. S., Carbon dioxide hydration and dehydration kinetics in seawater, *Limnol. Oceanogr.*, 27, 849-855, 1982
- Kurz, K., and E. Maier-Reimer, Effects of plankton dynamics on seasonal carbon fluxes, submitted to *Global Biogeochem. Cycles*, 1995
- Liss, P. S., and L. Merlivat, Air-sea gas exchange rates: Introduction and synthesis, in *The Role of Air-Sea Exchange in Geochemical Cycling*, edited by P. Buat-Ménart, pp. 113-127, D. Reidel Pub. Co, 1986
- Reynolds, R. W., and T. M. Smith, Improved global Sea Surface Temperature analyses using optimum interpolation, *J. Climate*, 7, 929-948, 1994
- Scoy, K. A. Van, K. P. Morris, J. E. Robertson, and A. J. Watson, Thermal skin effect and the air-sea flux of carbon dioxide: a seasonal high-resolution estimate, *Global Biogeochem. Cycles*, 9, 253-262, 1995
- UNESCO, Thermodynamics of the carbon dioxide sub-panel of the joint panel on oceanographic tables and standards, *Unesco Technical papers in Marine Science*, 51, 3-13, 1987
- Wanninkhof, R., Relationship between wind speed and gas exchange over the ocean, *J. Geophys. Res.*, 97, 7373-7382, 1992
- Weiss, R. F., Carbon dioxide in water and seawater: The solubility of a nonideal gas, *Mar. Chem.*, 2, 203-215, 1974

Modeling Global Air-Sea N₂O Fluxes A Sensitivity Analysis of the Gas-Exchange Formulation

P. Suntharalingam and J. L. Sarmiento

Atmospheric and Oceanic Sciences Program
Princeton University, Princeton, NJ 08540, USA

Abstract

Two models of the global oceanic N₂O flux distribution are presented, and the sensitivity of these models to the gas-exchange formulation is examined. The N₂O models discussed are a multi-variate regression method based on surface Δp N₂O measurements from *Weiss et al.* [1992], and a model of the oceanic N₂O cycle embedded in the ocean general circulation model (OGCM) of *Toggweiler et al.* [1989]. The gas-exchange parameterizations considered are from *Wanninkhof* [1992] and *Liss and Merlivat* [1986]. Results indicate that the formulation of *Wanninkhof* [1992] may be better suited for modeling oceanic N₂O fluxes using a data-based model or an OGCM.

1 Introduction

The ocean is considered a significant source of atmospheric N₂O (1-5 Tg N/year¹, *Houghton et al.* 1995]. Estimates of the global oceanic flux are usually derived by combining measurements of sea-air partial pressure differences with a parameterized gas-exchange coefficient, thus,

$$\text{Flux} = K_w \cdot \Delta p N_2O \quad (1)$$

where the partial pressure difference across the interface is given by

$$\Delta p N_2O = p N_2O_{\text{ocean}} - p N_2O_{\text{atmosphere}} \quad (2)$$

K_w , the gas-exchange coefficient, parameterizes the physical driving force, and is often defined to be dependent on such local factors as windspeed and temperature. Global estimates of the oceanic flux have traditionally relied on spatial extrapolation of local measurements of Δp N₂O to a global scale (e. g., *Butler et al.* [1989]). Such methods are, however, acknowledged to suffer from sampling bias due to the sparseness of the observational dataset, and to the large spatial and temporal variability of the surface N₂O distribution. Measurements suggest that the sub-tropical oceanic gyres are close

¹A more recent study extends the range to 1.8 - 6.5 Tg N/year [*Nevison et al.*, 1995]

to equilibrium with the atmosphere, and that the major part of the oceanic flux is derived from localized regions of upwelling and high biological productivity. In view of the difficulties in obtaining a *global flux estimate* from sparse measurements, models that predict the surface oceanic N₂O field by incorporating the effects of local biology and circulation, should prove valuable in identifying regions of high fluxes, and in constraining the oceanic source estimate. This study outlines two methods of deriving continuous *surface N₂O mappings*, and focuses on the sensitivity of the resulting flux distributions to the gas-exchange formulation. The N₂O models discussed in this exercise are (a) a non-parametric statistical regression model based on surface observations from *Weiss et al.* [1992], and (b) a model of the oceanic N₂O cycle embedded in an *ocean general circulation model* (OGCM).

2 Gas-Exchange Parameterization

A significant source of uncertainty in deriving oceanic flux estimates from surface partial pressure observations stems from the formulation of the gas-exchange coefficient K_w . For example, windspeed dependent relationships for K_w , based on tracer gas-exchange experiments in lakes and in the open ocean, yield values that differ by more than a factor of two, especially at higher windspeeds when factors such as bubble entrainment may play a role; (e.g., *Liss and Merlivat* [1986], *Wanninkhof* [1992]). These two formulations for K_w were compared in separate simulations to investigate the N₂O models' sensitivities to the parameterization of gas-exchange:

Simulation W	Wanninkhof [1992]	Quadratic windspeed dependence
Simulation LM	Liss and Merlivat [1986]	Linear dependence on windspeed; three windspeed regimes

The solubility parameterization employed for N₂O in both simulations was based on *Weiss and Price* [1980]; Schmidt numbers were taken from *Wanninkhof* [1992]. The climatological windspeed dataset from *Esbensen and Kushnir* [1981] is employed, and the temperature and salinity data are from *Levitus* [1982]. Figures 1a and 1b depict the global annual mean distribution of K_w ; as can be seen, the *Wanninkhof* [1992] formulation yields consistently higher K_w values than that of *Liss and Merlivat* [1986] with differences of over 100% at higher windspeeds.

3 Models of Oceanic N₂O Distribution

Several studies have observed negative correlations between dissolved O₂ and N₂O, and positive correlations between oxygen utilization and N₂O su-

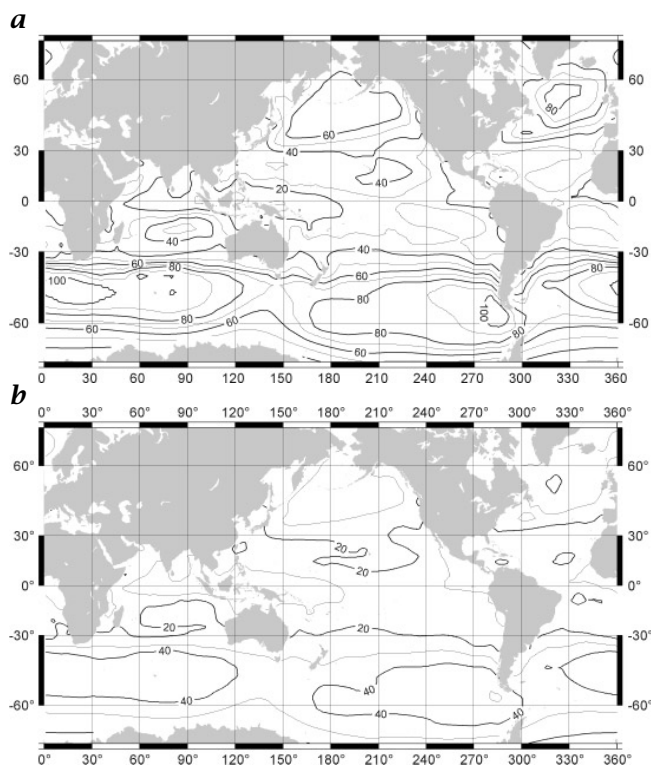


Figure 1: K_w Distribution: **a** Wanninkhof [1992] ($\mu\text{mol}/(\text{m}^2 \text{ year natm})$); **b** Liss and Merlivat [1986] ($\mu\text{mol}/(\text{m}^2 \text{ year natm})$).

persaturation at depth. These results suggest that the majority of oceanic N₂O is formed as a byproduct of the remineralization of organic matter into its inorganic constituents below the euphotic zone [Yoshinari, 1976, Cohen and Gordon, 1978]). Both models of N₂O distribution presented below are based on this premise that N₂O production is associated with O₂ depletion accompanying the oxidation of organic matter.

3.1 Model 1 : Multi-Variate Regression Model (MARS)

A continuous mapping of the annual-mean global distribution of Δp N₂O is obtained from a non-parametric regression model. The model uses two predictor variables: (a) Oxygen minimum level in upper 500 m of water column (used to incorporate the effect of organic matter remineralization. The choice of O₂ level rather than O₂ utilization is motivated by observations of enhanced N₂O production at low oxygen concentrations [Codispoti *et al.*, 1985]; (b) Wind-driven upwelling at the base of the mixed layer (N₂O equilibrates rapidly at the ocean surface and its distribution is characterized by

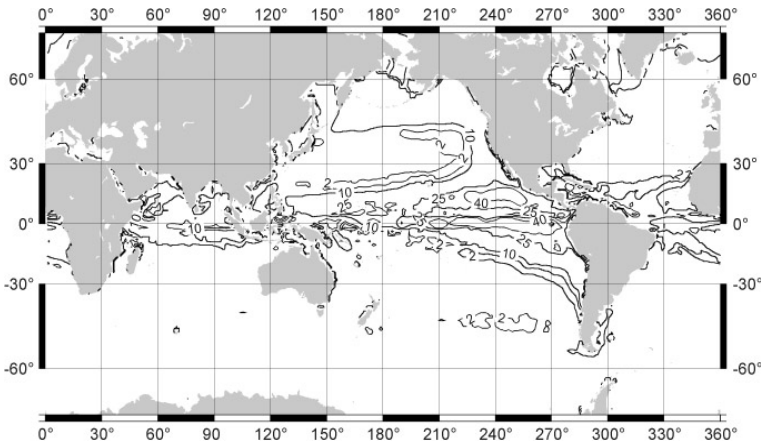


Figure 2: Annual-mean $\Delta p \text{ N}_2\text{O}$ (natm) field from MARS model based on data from Weiss *et al.* [1992].

significant high supersaturations in regions of strong upwelling).

The surface N_2O dataset from Weiss *et al.* [1992] is employed for estimation and prediction. The global datasets used for O_2 and windspeed are, respectively, Levitus [1982] and Esbensen and Kushnir [1981]. The non-parametric regression method is a multi-variate spline-fitting tool (Multivariate Adaptive Regression Splines (MARS), Friedman [1991]) which has previously been used to map surface distributions of phytoplankton and sea-ice [Morse, 1993, De Veaux *et al.*, 1993]. The global annual-mean $\Delta p \text{ N}_2\text{O}$ field predicted with the MARS model is shown in Figure 2, (correlation coefficient $r = 0.55$). Global N_2O fluxes are calculated by linking this field to the K_w formulations of W and LM via Equation 1.

3.2 Model 2 : Model of N_2O Cycle and Ocean GCM

N_2O is treated as a non-conserved tracer in an ocean GCM. It is subject to physical transport via ocean dynamics, biological sources and sinks in the ocean interior, and gas-exchange via the alternate formulations of W and LM at the ocean-atmosphere interface. The N_2O source function exploits the observed linear correlations between excess N_2O and Apparent Oxygen Utilization (AOU) at depths; i.e., we model an N_2O source based on oxygen consumption during the remineralization process. The N_2O production to O_2 consumption ratio used for this study is $1 : 10^4$ [Yoshinari, 1976]. The extent and magnitude of the remineralization processes are obtained from a model of marine organic matter cycling based on Najjar *et al.* [1992]. The organic matter cycling model and the N_2O model are embedded in the coarse resolution (4°) non-seasonal OGCM of Toggweiler *et al.* [1989]. For purposes of gas-exchange, the atmospheric partial pressure is maintained at a spatially constant pre-industrial level of 285 ppb.

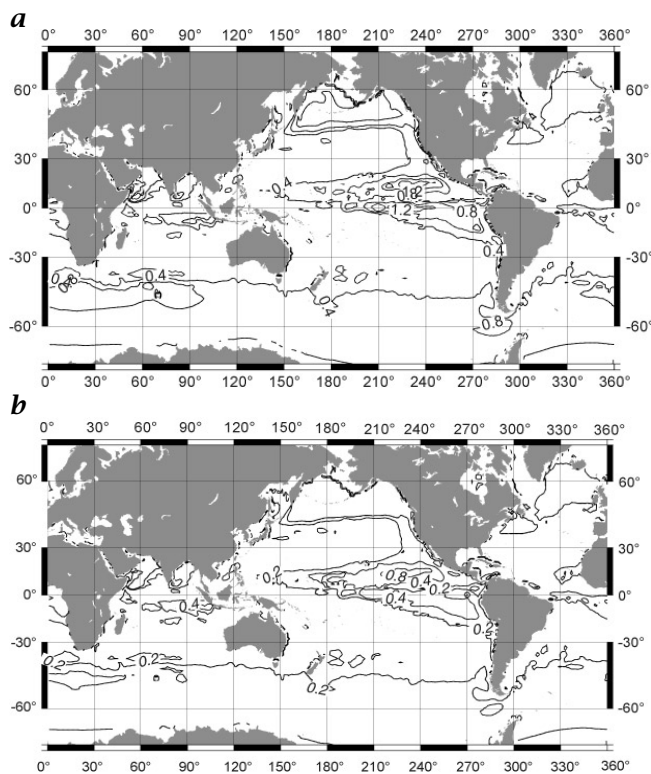


Figure 3: N₂O Flux: **a** Wanninkhof [1992] (mmol/(m² year)); **b** Liss and Merlivat [1986] (mmol/(m² year)).

4 Results

It should be noted that the two N₂O models (Model 1 and Model 2) display different sensitivities to the gas-exchange formulation. For Model 1 (MARS model), the Δp N₂O field is fixed, and the derived flux magnitude and distribution are dependent on the parameterization of K_w . However, for Model 2 (Ocean GCM), the global oceanic N₂O flux is determined by the embedded biological source function for N₂O; the global flux magnitude remains constant under W and LM, and variation in the formulation of K_w affects the local Δp N₂O field and N₂O distribution at depth. These effects are explored in more detail below.

4.1 Model 1 : MARS

As noted above, in this case, the Δp N₂O field is observationally based and invariant; the variations in sea-air N₂O flux directly reflect the gas-exchange formulation employed (see Figures 3a and 3b).

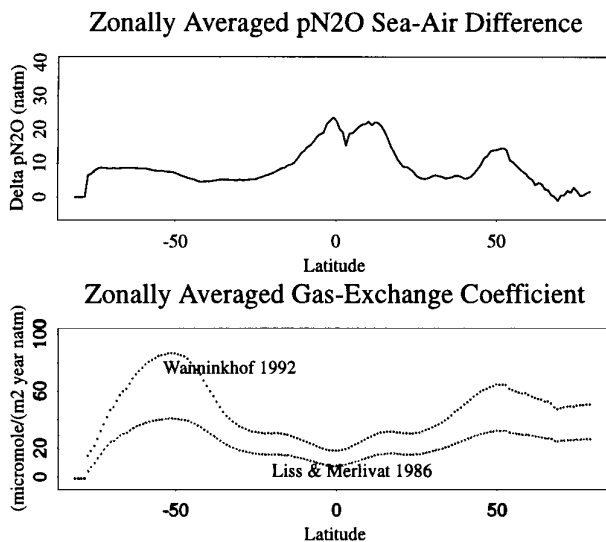


Figure 4: Model 1: Zonal averages, **top**: $\Delta p N_2O$ (natm), **bottom**: K_w ($\mu\text{mol}/(\text{m}^2 \text{ year natm})$).

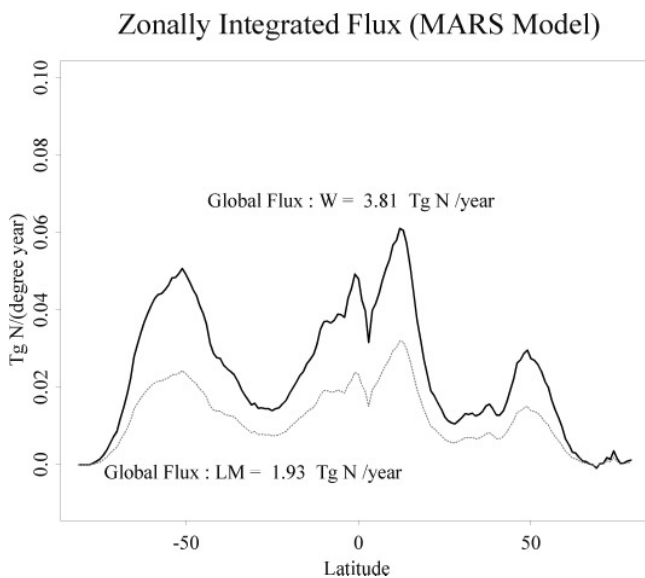


Figure 5: Zonally Integrated Fluxes (Tg N/(degree year)).

Figure 4 depicts the zonally averaged components of Equation 1, and Figure 5 the zonally integrated flux per latitudinal degree. The zonal flux distributions from both W and LM display a tri-modal pattern, with significant fluxes produced in equatorial and high-latitude regions (50°N, 50°S). Figure 6 indicates that the equatorial flux maxima are driven by elevated Δp N₂O levels due to high local biological productivity (especially in the Eastern Equatorial Pacific). However, large fluxes in the high latitudes, particularly in the Southern Ocean, are primarily a result of high windspeeds resulting in enhanced K_w values. Other regions of the ocean, notably, the sub-tropical gyres, yield minimal contribution to the global flux.

The most significant difference between the two gas-exchange formulations is the reflection of the varying magnitudes of K_w , especially at higher windspeeds, with W yielding local fluxes up to twice as large as LM. These differences lead to a variation in the global flux estimate of 1.9 Tg N per year (from LM) to 3.8 Tg N per year (from W). (Comparison of these flux magnitudes with other studies suggests that the higher flux from W is more consistent with previous estimates of the global oceanic N₂O flux. However, a large part of this agreement is due to the fact that the globally averaged K_w used in several studies is calibrated with radiocarbon data, as is the formulation of Wanninkhof [1992].)

4.2 Model 2: Ocean GCM

Figures 6a and 6b display the distribution of Δp N₂O obtained for the separate gas-exchange formulations. Results of the simulations indicate that the OGCM is successful in reproducing the large-scale features of the observed N₂O surface distribution. Notably, high surface saturation values are obtained in regions of upwelling and high biological productivity, and values close to equilibrium with the atmosphere are observed in the sub-tropical gyres. The global flux from this simulation is about 5 Tg N per year, which, though on the high side of the Houghton *et al.* [1995] estimate, is within the range reported by a more recent study Nevison *et al.* [1995].

Although the spatial distributions of Δp N₂O are similar for both gas-exchange simulations, LM yields higher levels, especially in high productivity regions. Since the N₂O source is identical for both W and LM, the ocean model responds to a lower gas-exchange coefficient (for LM) by correspondingly increasing the partial pressure difference, Δp N₂O, and hence the surface concentration. Comparison with observations suggests that, for Model 2, the surface concentrations from LM are generally too high, and that the gas-exchange formulation of W better reproduces the observed levels of surface N₂O.

Figure 7 depicts the zonally integrated fluxes for simulations LM and W. As with the data-based model, the highest fluxes are produced in the productive equatorial regions and in the high latitudes. For Model 2 the global flux magnitude and distribution is relatively insensitive to the gas-exchange for-

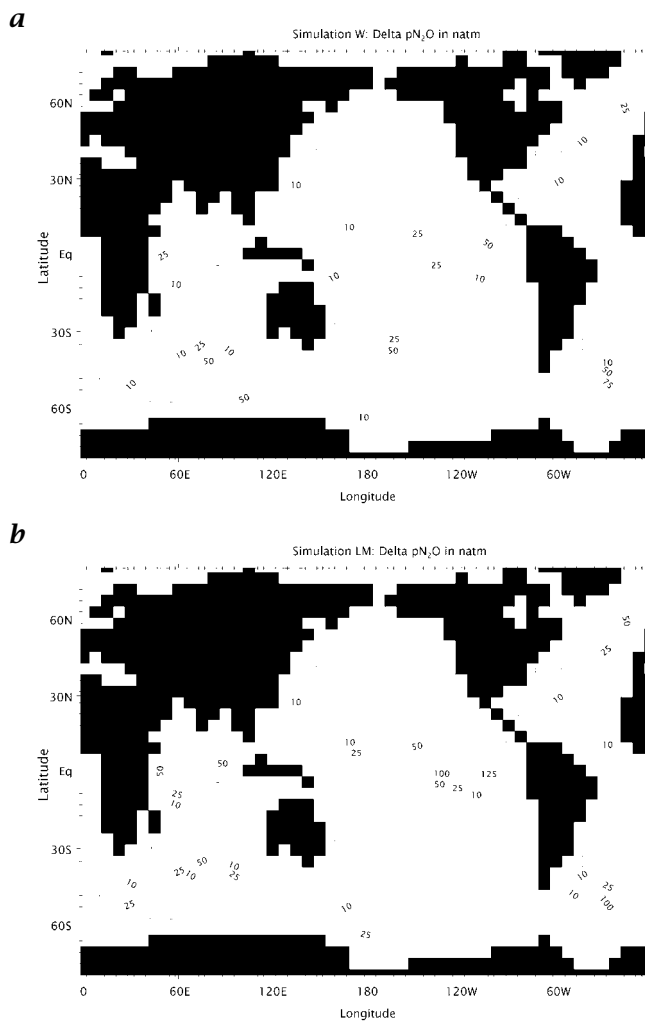


Figure 6: Model 2: $\Delta p N_2 O$ (natm): **a** Wanninkhof [1992], **b** Liss and Merlivat [1986]

mulation; however, as can be seen in Figures 7 and 8, significant variations are observed in regions of intense convection and upwelling (e.g., equatorial and Southern Ocean regions). Although $N_2 O$ equilibrates rapidly at the surface (timescale of a few weeks), the timescales of convective overturning and upwelling in these regions are even shorter. Hence in these locations of rapid resupply of $N_2 O$ to the surface from lower depths, the partial pressure difference is maintained at a higher level than it would be if the timescale of convection was longer; the simulation with a stronger gas-exchange coefficient (W) removes more of the upwelled surface $N_2 O$ than does LM, as these local regions have insufficient time to equilibrate. The higher fluxes

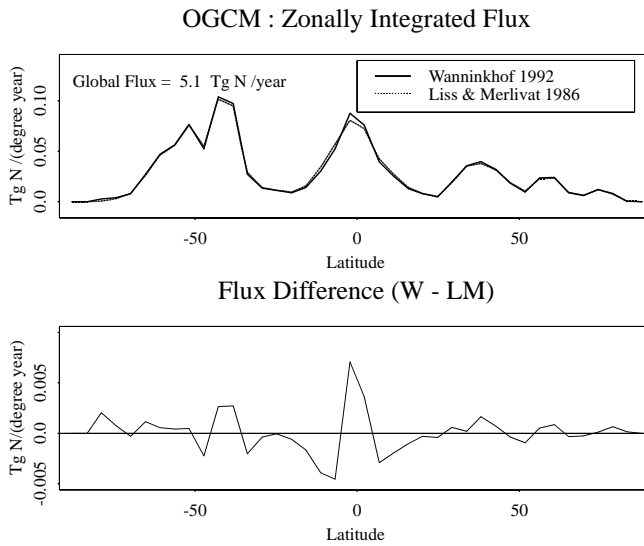


Figure 7: Model 2: Zonal Integrals, **a** Total Flux (Tg N / (degree year)) **b** Flux Difference W - LM

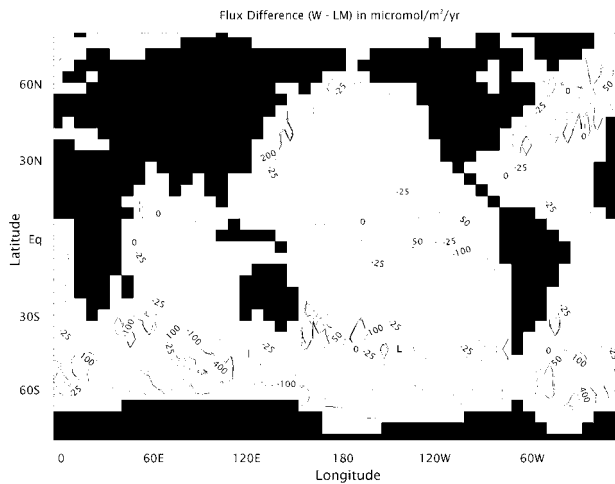


Figure 8: Model 2: Flux Difference (W - LM) $\mu\text{mol}/(\text{m}^2 \text{ year})$. Negative values are stippled.

in localized upwelling regions result in sharper spatial gradients in W than in LM; immediately outside the regions of intense convection and upwelling, W yields slightly lower fluxes than LM, thus ensuring that the globally integrated oceanic flux is the same in both cases. ²

5 Conclusions

Results from both N₂O models indicate high oceanic fluxes in regions of upwelling and high productivity; some of these regions, especially in the Southern Ocean, are particularly poorly represented in the observational N₂O database. The models respond differently to gas-exchange sensitivity analyses. Differences of over 100% are seen in the global flux estimates derived from the data-based Model 1, and variations of 100% are apparent in the modeled Δp N₂O field from the OGCM. Comparison of the W and LM simulations for Model 2 (OGCM) indicates that the modeled flux distribution only displays sensitivity to the gas-exchange parameterization in localized regions of intense convection. In general, simulation W (using a higher gas-exchange coefficient) yields more consistent fluxes from the two N₂O models and produces a better match to the available surface N₂O data. The *Wanninkhof* [1992] formulation may, therefore, be more suitable for modeling oceanic N₂O fluxes using both a data-based model and an OGCM.

References

- Butler J. H., J. W. Elkins, T. M. Thompson and K. B. Egan, Tropospheric and dissolved N₂O of the West Pacific and East Indian Oceans during the El Nino Southern Oscillation Event of 1987, *J. Geophys. Res.*, 94, 14865-14877, 1987
- Codispoti, L. A., and J. P. Christensen, Nitrification, denitrification, and nitrous oxide cycling in the Eastern Tropical South Pacific Ocean., *Mar. Chem.* 16, 277-300, 1985
- Cohen, Y., and L. I. Gordon, Nitrous oxide in the oxygen minima of the Eastern Tropical North Pacific; evidence for its consumption during nitrification and possible mechanism for its production., *Deep-Sea Res.*, 25, 509-524, 1978
- De Veaux, R. D., A. L. Gordon, J. C. Comiso and N. E. Bacherer, Modelling of topographic effects on Antarctic sea ice using multi-variate adaptive regression splines., *J. Geophys. Res.*, 98, 20307-20319, 1993
- Esbensen, S. K., and Y. Kushnir, The heat budget of the global ocean : An atlas based on estimates from surface marine observations, *Rep. 29, Clim. Res. Inst.*, Oreg. State Univ., Corvallis, 1981
- Friedman, J., Multivariate adaptive regression splines, *Ann. Stat.*, 19, (1), 1-141, 1991
- Houghton, J. T., L. G. Meira Filho, J. Bruce, et al., *Climate Change 1994 : Radiative Forcing of Climate Change and An Evaluation of the IPCC IS92 Emission Scenarios*, Cambridge University Press, 1995

²It should be noted that the OGCM produces some regions of intense convection (especially in the Southern Ocean) that may not be realistic [*Toggweiler et al.*, 1989]; these regions yield large local N₂O fluxes that should be regarded with caution.

- Levitus, S., Climatological Atlas of the World Ocean NOAA Professional Paper 13, U.S. Government Printing Office, Washington, D.C., 1982
- Liss, P. S., and L. Merlivat, Air-sea gas-exchange rates: Introduction and synthesis, in *The Role of Air-Sea Exchange in Geochemical Cycling*, edited by P. Buat-Menard, pp. 113-129, D. Reidel, Hingham, Mass., 1986
- Morse, R. L., Modelling the distribution of phytoplankton in the Southern Ocean using multi-variate adaptive regression splines and recursive partitioning, *Senior Thesis*, Princeton University, 1993
- Najjar, R. G., J. L. Sarmiento and J. R. Toggweiler, Downward transport and fate of organic matter in the oceans : simulations with a general circulation model, *Global Biogeochem. Cycles*, 6, 45-76, 1992
- Nevison, C. D., R. F. Weiss and D. J. Erickson III, Global nitrous oxide emissions, *J. Geophys. Res.*, 100, 15809-15820, 1995
- Toggweiler, J. R., K. Dixon and K. Bryan, Simulation of radiocarbon in a coarse resolution world ocean model, *J. Geophys. Res.* 94, 8217-8242, 1989
- Wanninkhof, R., Relationship between windspeed and gas exchange over the ocean, *J. Geophys. Res.* 97, 7373-7383, 1992
- Weiss, R. F. and B. A. Price, Nitrous oxide solubility in water and seawater, *Mar. Chem.* 8, 347-359, 1980
- Weiss, R. F., F. A. Van Woy and P. K. Salameh, Surface water and atmospheric carbon dioxide and nitrous oxide observations by shipboard automated gas chromatography: results from expeditions between 1977 and 1990. *Scripps Institution of Oceanography Reference 92-11*, 1992
- Yoshinari, T., Nitrous oxide in the sea, *Mar. Chem.* 4, 189-202, 1976

The Determination of CO₂ Difference of Partial Pressure in the North Pacific Ocean using SST by Ship and Satellite Data

Y. Sugimori¹, C. Zhao^{1,2}, M. Akiyama¹,
N. Itoh¹, and M. He²

¹ School of Marine Science and Technology, Tokai University,
Orido 3-20-1, Shimizu, Shizuoka Prefecture, Japan 424

² Ocean Remote Sensing Institute, Ocean University of Qingdao, P. R. China

Abstract

In this study, two approaches have been taken in estimating air-sea carbon dioxide (CO₂) flux; one makes use of the relationship between wind stress, roughness and wave parameters, and data obtained by using a waverider and a meteorological buoy, and a new relationship between u_* and u_{10} is derived after considering the state of wave development i. e., $u_* = 0.0360 u_{10}^{1.1832}$ or in the quadratic relationship $u_* = 0.0010u_{10}^2 + 0.0454u_{10} - 0.013$. This relationship is used in estimating the gas exchange velocity based on a whitecap model [Monahan and Spillane, 1984]. The other approach is to estimate the difference of carbon dioxide (CO₂) between atmosphere and ocean from SST data collected on the vessel Ryofu Maru. Finally, the distribution and variation of the CO₂ exchange coefficient in the North Pacific Ocean are estimated from satellite data (DMSP SSM/I and NOAA data).

1 Introduction

The earth's thermal regime is believed to be largely dependent on the concentration of greenhouse gas in the atmosphere. *Carbon dioxide* (CO₂), as the main greenhouse gas, is steadily increasing as people's activities and energy consumption increase [Keeling, 1995]. The possible climate change caused by this effect is the main research subject for many scientists. The ocean contains more than fifty times the carbon in the atmosphere and can be taken as a buffer limiting the concentration of CO₂ in the atmosphere. Since the growth of CO₂ in the atmosphere is less than the rate of the carbon release, some released carbon dioxide must be absorbed by either the terrestrial biosphere or the oceans (IPCC Report, 1990). However, CO₂ concentration in the ocean is controlled by physical, chemical and biological processes and all these processes are not well understood.

The direct measurement of carbon dioxide flux between atmosphere and ocean is quite difficult. For this reason, the flux is generally calculated from

$$F = \iint K_L \Delta P_{CO_2} ds dt \quad (1)$$

where K_L is the gas exchange velocity and ΔP_{CO_2} is the difference of gas concentration between air and sea. K_L is related to physical properties such as wind speed, wind stress, turbulence, wave breaking, etc., and chemical enhancement due to chemical reaction between CO_2 and water. Generally, chemical enhancement has an effect at low wind speeds according to theoretical and experimental results [Hoover and Berkshire, 1969; Liss, 1973; and Wanninkhof, 1992]. Physical processes are generally expressed in terms of wind stress [Deacon 1977; Monahan and Spillane, 1984; Komori et al., 1995] or wind speed [Liss and Merlivat, 1986; Tan et al., 1990; Wanninkhof, 1992]. However, the influence of wind wave in the estimation of wind stress is generally not considered. In this study, the relationship between wind stress and wind waves is investigated based on the published data set (experiment and field) and our in situ data set in Suruga Bay.

Another parameter, ΔP_{CO_2} , should be considered in estimating CO_2 flux between air and sea. In this paper, an initial result about the CO_2 partial pressure difference between ocean and atmosphere is derived from the SST distribution based on data collected aboard the Japanese Meteorological Agency ship Ryofu Maru. Finally the distribution of the CO_2 exchange coefficient in the North Pacific is estimated based on a whitecap model [Monahan and Spillane, 1984] by using DMSP SSM/I and NOAA AVHRR data.

2 Wind Waves, Wind Stress and Gas Exchange Velocity

The gas exchange velocity is generally related to wind speed or friction speed, and it is of great importance to know the relationship between friction speed, roughness length, and wave parameters over water surface. In neutral conditions, the mean wind speed near the water surface can be assumed to follow as a logarithmic profile:

$$u(z) = (u_* / k) \log(z / z_0) \quad (2)$$

where $u(z)$ is the wind speed at height z meters, u_* is the friction speed defined as $u_* = \sqrt{\tau_S / P_\alpha}$ (τ_S is the wind stress and P_α is the density of air) and z_0 is the roughness length and k is Karman's constant ($k = 0.4$). Until now, many observations have been analyzed but the results are still controversial.

Based on dimensional analysis and local wind wave equilibrium, Masuda and Kusaba [1987] proposed that the nondimensional roughness gz_0 / u_*^2 should be expressed as,

$$gz_0 / u_*^2 = \alpha (\sigma_P u_* / g)^\beta \quad (3)$$

where σ_p is the peak frequency of wind wave, and g is the acceleration due to gravity. α , β are constant. $\beta = 0$ is related to *Charnock* [1955] and *Wu* [1980] results. *Toba et al.* [1986, 1990, 1991] proposed $\beta = -1/2$ and -1 based on field and water tank data analysis. *Kusaba and Masuda* [1988, 1994] gave the result with $\beta = 1$. We can see that much effort should be expended in order to verify this equation.

Related to this problem, a waverider (made by *Datawell*, Netherlands) and a meteorological buoy have been deployed at a station in Suruga Bay (N34.5978, E138.5489, water depth 300 meters), more than one kilometer off the coast. The sea surface displacement is obtained by the double integration of measured acceleration, and is transmitted by an FM transmitter. A receiving system records the wind wave signal with a 400 ms sampling interval. The wind wave spectrum is calculated by the Fast Fourier Transform (FFT) and averaged using three raw spectra in order to estimate the peak frequency. Wind speed and direction is measured by one 3-cup anemometer and one wind direction sensor at the same time. Wind friction speed and roughness are derived from wind speeds at two heights by assuming a logarithmic profile.

With equations (2) and (3), it is possible to derive the relationship between friction speed, wind wave frequency and wind speed at 10 m above the ocean surface. However, the peak frequency of wind wave is not easy to measure globally. Here the data of three meteorological buoys deployed around Japan (see Fig. 1 St. A, B C) by the Japanese Meteorological Agency, where the wind-wave data are recorded every three hours, are used in order to obtain the empirical formula between friction speed and wind speed at 10 m height,

$$u_* = f(u_{10}) \quad (4)$$

Here the function f will be determined and shown in equation 8 and 9 below.

Finally, the gas exchange coefficient K_L can be calculated [*Deacon*, 1977, *Monahan and Spillane*, 1984; *Komori et al.*, 1995]. In this work, the whitecap model first proposed by *Monahan and Spillane* [1984] is used,

$$K_L = K_m(1 - W) + K_e W \quad (5)$$

where K_m is the transfer velocity associated with no whitecap area. K_e is the transfer velocity related with a turbulent whitecap area. W is the fraction of the sea surface covered by whitecaps due to wave breaking. K_m and K_e are estimated from GEOSECS and TTO radon data to have the value of 9.58 cm h⁻¹ and 475.07 cm h⁻¹. Whitecap W should be related to the energy flux from wind [*Wu*, 1988] and

$$W = \gamma u_*^3 \quad (6)$$

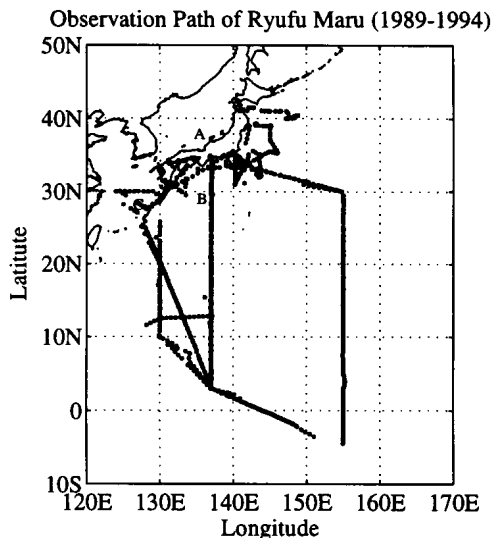


Figure 1: The observation path of the ship Ryofu Maru during 1989-1994. Japanese Meteorological Agency buoys are shown as A, B, C in this figure.

The coefficient γ will be determined from *Toba et al.* [1973] and *Monahan* [1981] data by using equation (4).

3 Ship, Buoy and Satellite Data

Three kinds of data set are used in this study. CO₂ data measured aboard the ship Ryofu Maru in 1989-1994 is provided by the WMO greenhouse data center (Tokyo) of the Japanese Meteorology Agency. The data distribution is shown in Figure 1.

Wind wave and wind data are measured using waverider and meteorological buoys, which are deployed in Suruga bay (N 34.5978, E 138.5489) in Oct., 1994. These data are used to study the roughness and wind wave relation, which is related to gas exchange coefficient by wind stress or friction speed [*Monahan and Spillane*, 1984; *Komori et al.*, 1995]. The data from the Japanese meteorological agency buoys are also used here in order to obtain an empirical relation between friction speed and wind speed at 10 m height. Satellite data, DMSP SSM/I data and AVHRR monthly mean data sets, are provided by JPL PODAAC data center and are used to estimate CO₂ gas exchange and *sea surface temperature* (SST) influence.

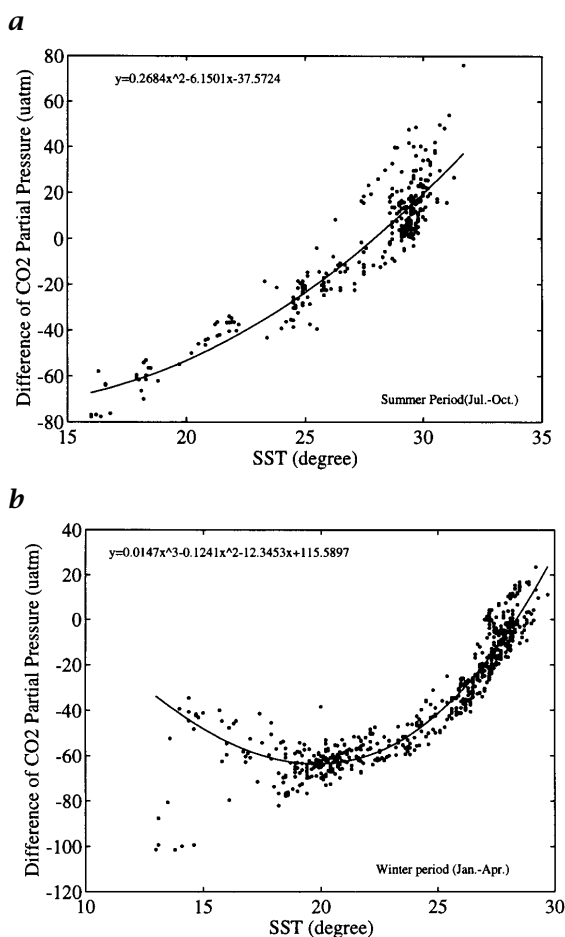


Figure 2: The relationship between SST and the difference of CO₂ partial pressure between air and ocean (μatm). **a** winter period (Jan.-Apr.) **b** summer period (Jul. - Oct.)

4 Data Processing and Results

4.1 CO₂ Difference of Partial Pressure and SST Relation

CO₂ difference of partial pressure between air and ocean (ΔP_{CO_2}) determines the gas exchange direction and any net flux across the sea surface. The partial pressure distribution (ΔP_{CO_2}) is controlled by physical, chemical and biological processes. The ship data are quite sparse, not only in spatial but in temporal distribution [Tans et al., 1990, Fig. 4].

The Ryofu Maru data in 1994 shows a good correlation between SST and the difference of CO₂ partial pressure between atmosphere and ocean, but

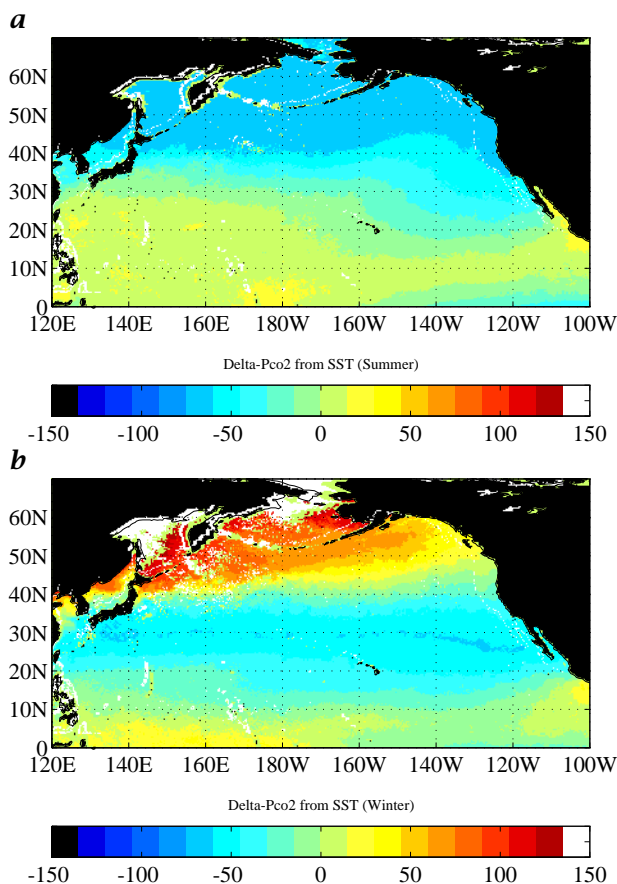


Figure 3: The distribution of CO₂ partial pressure difference in the North Pacific Ocean derived from SST data. **a** Summer period and **b** winter period.

the SST values lie in a rather narrow range.

Fig. 2 shows the relationship between SST and ΔP_{CO_2} (μatm) obtained by using the Ryofu Maru ship data in 1989 - 1994 (a: in summer period and b: in winter period). Here, CO₂ concentration has been corrected as fugacity value according to *Murphy, et al.* [1995]. The distribution of the CO₂ partial pressure difference (ΔP_{CO_2}) in the North Pacific is estimated based on AVHRR SST data and shown in Fig. 3.

Compared with the Takahashi data set published in 1990 (Fig. 4), the data around Japan and the pattern in mid- and high-latitudes shows a relationship with much variation found in low latitudes.

The reason is assumed to be the other factors controlling the CO₂ partial pressure difference between the ocean and atmosphere. This initial result shows the possibility of estimating ΔP_{CO_2} using satellite data, especially in certain regions with related ΔP_{CO_2} and SST relationship.

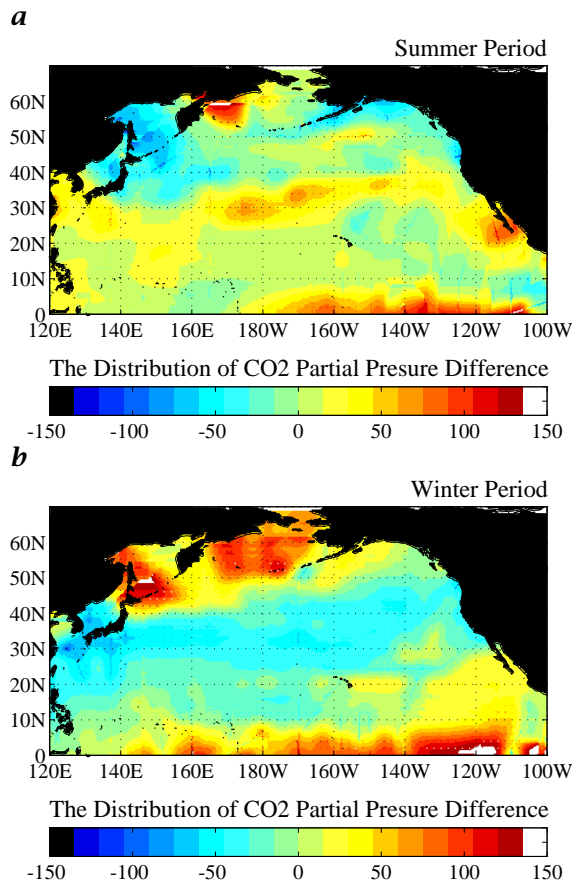


Figure 4: The distribution of CO₂ partial pressure difference in the North Pacific ocean. The result shown here is an objective analysis obtained by combining the Takahashi data set [Tans et al. 1990] and ship data from Japanese Meteorological Agency and Carbon Dioxide Information Analysis Center (CDIAC).

4.2 Wind Stress and its Dependence on Wind Wave

Fig. 5, 6 show the results of the relationship between non-dimensional *roughness* and the inverse of wave age based on wind wave data and wind data in Suruga Bay and the published experimental data in water tank. We can see that the roughness will become large as wave develops, and then decrease in the swell region. Fig. 6 is the same data as presented in Fig. 5 and the four difference lines shown are related to different conditions, i.e., total data, different inverse *wave age* greater than 0.05 and 0.08, and only field data in Suruga Bay. With the condition of inverse *wave age* greater than 0.05, the least-square-fit result is similar to *Toba et al.*, [1990] result.

Fig. 7 shows the result with the total published field and tank experimen-

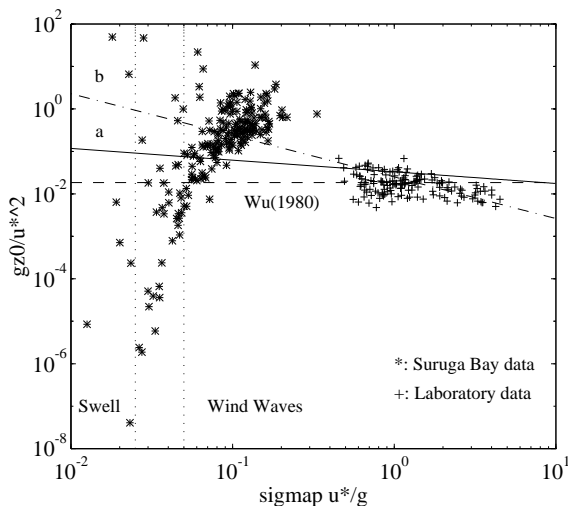


Figure 5: The relationship between the non-dimensional roughness and inverse wave age. The buoy data in Suruga Bay is shown in * and laboratory data in + which is provided by Ebuchi [1995].

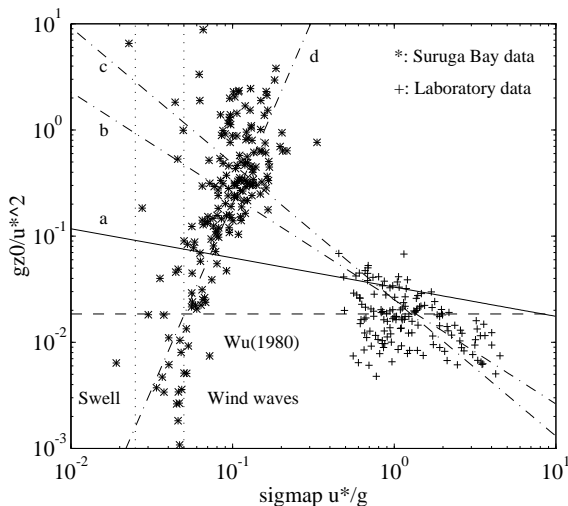


Figure 6: The same data as presented in Fig. 5. Four least-square-fit lines are shown: ($y = gz_0/u_*^2$ and $x = \sigma_P u_*/g$) a: $\log y = -0.2749 \log x - 1.4803$ total data (field data in Suruga Bay and laboratory data) b: $\log y = -0.9798 \log x - 1.6011$ $x > 0.05$ c: $\log y = -1.2831 \log x - 1.6096$ $x > 0.08$ d: $\log y = 3.50 \log x + 2.81$ only field data in Suruga Bay.

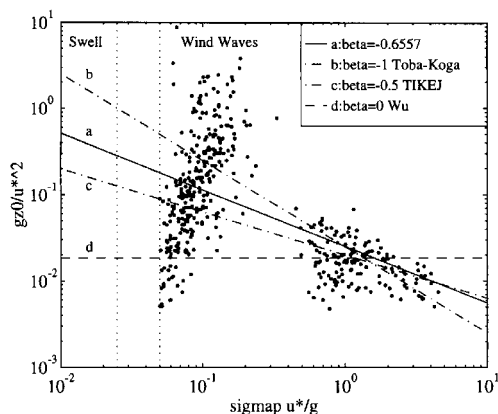


Figure 7: The non-dimensional roughness parameter versus inverse wave age including field (shown in Fig. 7 and our measurement data in Suruga Bay) and laboratory data. With the condition of $\sigma_p u_* / g > 0.05$, the least-square-fit is: $gz_0 / u_*^2 = 0.0252(u_* \sigma_p / g)^{-0.6557}$

tal data and our data in Suruga Bay. With all these data sets and with the condition of $u \sigma_p / g \geq 0.05$, the equation (3) should be written as,

$$gz_0 = u_*^2 = 0.0252(u_* \sigma_p / g)^{-0.6557} \tag{7}$$

and Fig. 8 shows a new empirical relationship between u_* and wind speed at 10 m above the sea surface by combining eq. (2) and eq. (7) based on JMA buoys data analysis. If the exponential relationship is assumed, u_* and u_{10} can be expressed as,

$$u_* = 0.0360u_{10}^{1.1832} \tag{8}$$

or a quadratic relationship can be used:

$$u_* = 0.0010u_{10}^2 + 0.0454u_{10} - 0.013 \tag{9}$$

Fig. 8 also shows Wu [1980], Komori et al. [1993a] relationship between u_* and u_{10} for comparison.

Based on eq. (6) and eq. (8) or (9), we reprocessed the data of Toba and Chaen [1973] and Monahan [1981], and found the coefficient y should be 0.0645 (shown in Fig. 9).

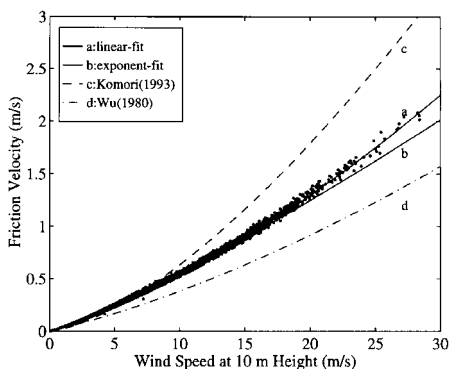


Figure 8: The relationship between u_* and u_{10} obtained by combining the equation shown in Fig. 8, the logarithmic profile assumption and JMA buoy systems data from Nov. 1, 1992 to May 31, 1994. a: $u_* = 0.0360 u_{10}^{1.1832}$ b: $u_* = 0.0010u_{10}^2 + 0.0454u_{10} - 0.013$. Lines c and d are results of Wu [1980] and Komori et al. [1993a] respectively and are plotted for comparison.

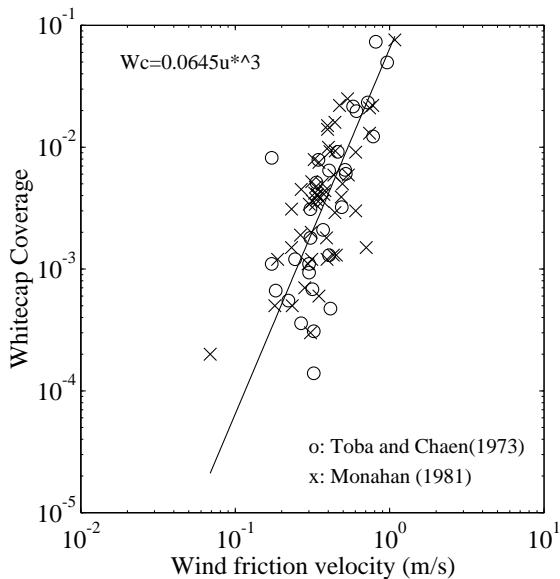


Figure 9: The relationship between friction velocity and whitecap coverage.

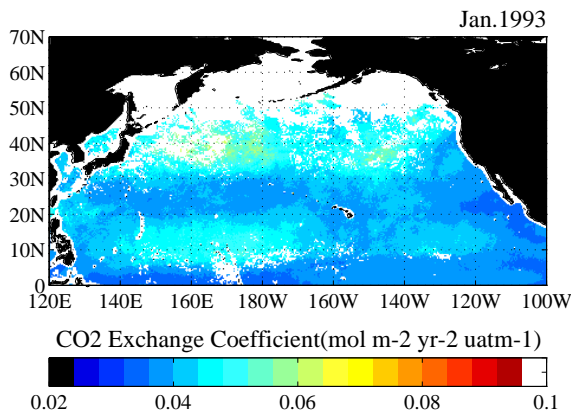


Figure 10: The CO₂ exchange coefficient distribution from SSM/I wind speed, NOAA SST and the whitecap model in Jan. 1993 (winter period).

4.3 The CO₂ Exchange Coefficient Distribution and SST Influence

The gas exchange coefficient is another factor controlling the CO₂ exchange between the atmosphere and ocean. It is controlled by physical properties such as *wind*, *wind wave*, *turbulence* and *wave breaking* and *chemical enhancement*. Chemical enhancement is effective at low wind speeds, based on theoretical analysis and experiment. Physical processes are the main mechanisms and the exchange coefficient is generally related to wind stress. With equation 8 or 9 and the whitecap model [Monahan and Spillane, 1984], the distribution of the CO₂ exchange coefficient in the North Pacific is estimated by using DMSP SSM/I data. In winter, the regions of maximum exchange are around 10–20 N and 30–40 N and its value varies from 0.04–0.07 mol m⁻² yr⁻¹ μatm⁻¹ (Fig. 10).

In summer, the region of maximum exchange is in the eastern part of North Pacific in 10–30 N and 130 W–170 W but with much smaller values than in winter (Fig. 11).

Generally, the maximum exchange coefficients exist in the western region in winter and the eastern region in summer in the North Pacific. The CO₂ exchange coefficient shows a clearly seasonal variation, shown in Fig. 12, with a maximum in Dec.-Jan. and a minimum in June-Sept.. The SST influence is also considered here by using AVHRR data and the exchange coefficient will have a smaller value, as shown in Fig. 12.

This result shows that the influence of SST on CO₂ exchange coefficient should be considered, otherwise a systematic error will be induced in CO₂ flux estimation.

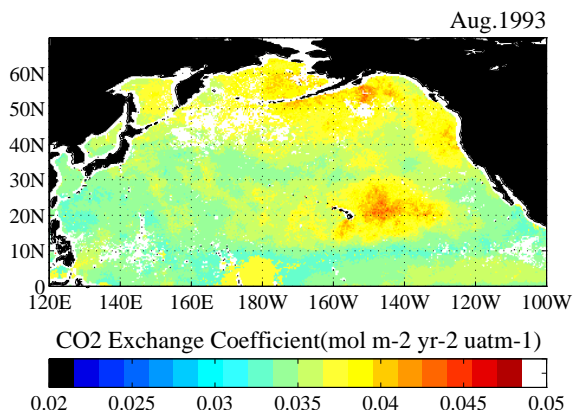


Figure 11: The CO_2 exchange coefficient distribution from SSM/I wind speed, NOAA SST and whitecap model in Aug. 1993 (summer period).

5 Conclusion

In this work, the wind wave and wind stress relationship is investigated using waverider and wind buoy data. The result shows the complicated relationship that exists between the nondimensional roughness and wave age, and a rather larger wind stress will be derived if wind wave influence is considered. With the new friction velocity and wind speed relationship, the distribution of the CO_2 exchange coefficient in the North Pacific ocean is estimated from satellite data. If the SST effect on Schmidt number and gas solubility is considered, the CO_2 exchange coefficient will possess a smaller value, especially in the winter season in the north Pacific Ocean. The initial result shows the possibility of obtaining CO_2 partial pressure differences from SST, especially in different ocean regions with related SST and ΔP_{CO_2} relationship. However, ΔP_{CO_2} distribution is not consistent with ship data in tropical area and the relationship between P_{CO_2} and SST, Chl_a is not clear. Even as to gas exchange coefficient, much more work is needed in future experiments to determine the dependence of gas exchange coefficient on PH value, turbulence, wave breaking, bubbling and Schmidt number.

Acknowledgements

References

Asher, W. E., P. J. Farley, R. H. Wanninkhof, E. C. Monahan, and T. S. Bates. Laboratory and field measurements concerning the correlation of fractional area foam covering with air/sea gas transport. In *Precipitation Scavenging and Atmosphere-Surface Exchange, Vol. 2*, The Semonin Volume: Atmosphere Surface Exchange

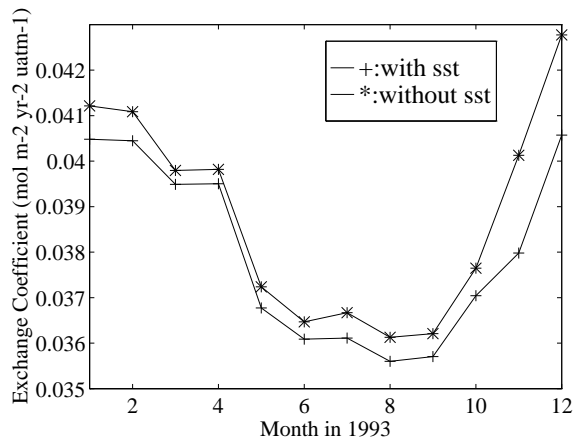


Figure 12: The seasonal variation of CO₂ exchange coefficient in the North Pacific ocean in 1993 and SST influence. Line * is the result by setting SST = 20° and line + by using AVHRR data.

- Processes, S. E. Schwartz and W. G. N. Slinn (eds.). Hemisphere, Washington, D.C., 815-828, 1992
- Keeling, C. D., 1995, Atmospheric carbon dioxide concentrations from Mauna Loa Observatory, Hawaii, 1958-1994. [NDP001R5 (July 1995) from Carbon Dioxide Information Analysis Center (CDIAC) FTP Archive]
- Komori S., Y. Murakami, and H. Ueda, The relationship between surface-renewal and bursting motions in an open channel flow, *J. Fluid Phys.* 203, 103-123, 1989
- Komori, S., R. Nagaosa and Y. Murakami, Turbulence structure and mass transfer across a sheared air-water interface wind driven turbulence, *J. Phys. Oceanogr.* 10, 727-740, 1993a
- Komori, S., T. Shimada and Y. Murakami, Laboratory estimation of CO₂ transfer velocity across the air-sea interface, In *Biogeochemical Processes and Ocean Flux in the Western Pacific*, edited by H. Sakai and Y. Nozaki, Terra Sci. Pub 1995
- Kusaba, T and A. Masuda, The roughness height and drag law over the water surface based on the hypothesis of local equilibrium, *J. Oceanogr. Soc. Japan*, 44, pp. 200 - 214, 1988
- Masuda, A. T. Kusaba and K. Komatsu, Two recent topics of wind-wave research in RIAM, Proceedings of the CREAM's 94 International Symposium, 24-26 Jan. 1994, Fukuka, Japan, p. 25-28, 1994
- Masuda, A., T. Kusaba, H. Mitsuyasu et al., The roughness and drag law over the water surface based on the hypothesis of local equilibrium, *Rep. Res. Inst. Appl. Mech., Kyushu Univ.* 64, pp. 49-60, 1987 (in Japanese)
- Monahan E. C., Oceanic Whitecaps, *J. Phys. Oceanogr. Vol. 1*, pp. 139-144, 1971
- Monahan, Edward C. and Michael C. Spillane, The role of oceanic whitecaps in air-sea gas exchange, Gas transfer at water surfaces, W. Brutsaert and G. H. Jirka (eds.), D. Reidel Publishing Company, 1984

- Murphy P. P., K. C. Kelly, R. A. Feely, and R. H. Gammon. Carbon Dioxide concentrations in surface water and the atmosphere during 1986-1989 NOAA/PEEL cruise in the Pacific and Indian Oceans. ORNL/CDIAC-75, NDP-047. Carbon dioxide information analysis center, Oak Ridge National Laboratory, Oak Ridge, Tennessee, pp. 139, 1995
- Tans, P. P., I. Y. Fung and T. Takahashi,, Observational constraints on the global atmospheric CO₂ budget, *Science*, 247, p. 1431-1438, 1990
- Toba, Y. and M. Chaen, , Quantitative expressions of the breaking of wind waves on the sea surface, *Rec. Oceanog. Works*, Vol. 12, pp 1-11, 1973
- Toba Y. and M. Koga, A parameter describing overall conditions of wave breaking, whitecapping, sea-spray production and wind stress, In *Oceanic whitecaps*, ed. by Monahan, E. C. and G. Mac Niocaill, (eds.), D. Reidel. pp. 37-47, 1986
- Toba, Y., N. Iida, H. Kawamura, N. Ebuchi anf I. S. F. Jones. Wave depence of sea-surface wind stress, *J. Phys. Oceangr.* 20(5), 705-721, 1990
- Toba Y. and N. Ebuchi, Sea-surface roughness length fluctuating in concert with wind and waves, *J. Oceanogr. Soc. Japan* 47, pp. 63-69, 1991
- Wanninkhof, R. H. Relationship between gas exchange and wind speed over the ocean. *Journal of Geophysical Research*, 97(C5) , 7373-7381, 1992
- Wu, J., Wind-stress coefficients over sea surface near neutral conditions-A revisit, *J. Phys. Oceanogr.* 10, 727-740, 1980
- Wu, J., Variations of whitecap coverage with wind stress and water temperature, *J. Phys. Oceanogr.* 18, pp. 1448-1453, 1988

A Note on Relationships between Sea Surface Roughness and Altimeter Backscatter

B. Chapron¹, K. Katsaros¹, T. Elfouhaily¹, and D. Vandemark²

¹Département d'Océanographie Spatiale
IFREMER, BP 70, 29280 Plouzané, France

²NASA/Goddard Space Flight Center, Laboratory for Hydrospheric Processes
Wallops Island, VA 23337, USA

Abstract

We present a sea scattering model for the radar altimeter. Central to this effort is definition of an idealized omnidirectional spectrum approximation in the high-wavenumber spectral domain. This spectrum is consistent with recent forms showing two distinct energy balance regimes and is constrained to the well-known optical slope observations made by *Cox and Munk* [1954]. Scattering prediction relies on the two-scale Kirchhoff method at vertical incidence to treat the dominant quasi-specular scattering but also to permit examination of diffraction caused by high-frequency waves. Using satellite altimeter data, attention is devoted to clarifying relationships between altimeter normalized cross section σ_0 , surface wind speed, and sea surface slope and height variance. Results indicate that Ku-band backscatter for wind speeds above 7 m/s is sensitive, as expected, to changes in total surface roughness, but also to changes in the more highly wind-dependent gravity-capillary range between 2 and 10 cm. Modeled frequency dependencies related to small-scale roughness are compared to global TOPEX Ku-band and C-band altimeter data showing promising agreement. For example, the physically-based development is able to reproduce a well-defined transition between the two frequencies of TOPEX measurements, observed near 7 m/s wind speed, presumably associated with the onset of boundary layer-flow separation and wave breaking events.

1 Introduction

Microwave altimeter ocean backscatter σ_0 is fundamentally related to *sea surface roughness*. An application is found in the robust, empirically-derived wind retrieval algorithm for Ku-band (13.9 GHz) instruments [Witter and Chelton, 1991]. Theoretical or physically-based scattering model studies [Barrick, 1968; Brown, 1978; Jackson *et al.*, 1992; Wu, 1994] suggest that there is a more direct altimeter inference to be made in terms of surface *mean square slope (mss)*, which should parallel the classical optical measurements of ocean *mss* versus wind speed provided by *Cox and Munk* [1954]. Uses for global *mss* data sets in air-sea interaction research are increasingly apparent. Indeed, wind induced wave motions tend to modify gas transfer

rates which are further enhanced when the waves break entraining bubbles and producing spray. It has been observed in laboratory conditions that gas transfer velocities significantly increase at the onset of surface wave generation. Moreover, measurements seem to indicate that gas transfer enhancement correlates well with surface roughness and *mss* parameters [Coantic, 1980; Jähne *et al.*, 1987; Wanninkhof and Bliven, 1991].

Potentially, information on gas transfer is thus available from the global satellite data sets, but, is altimeter backscatter solely related to integrated surface roughness? While strict adherence to specular-point scattering theory requires that this be the case, Thompson [1988] among others, have advanced the idea that some attenuation of near-vertical backscatter can be due to diffraction effects caused by small-scale waves. The theory is that under a two-scale Gaussian approximation for the surface, the predominant backscatter will come from quasi-specular reflections due to long-scale slopes, but short-scale waves below the high-frequency (or cut-off) limit will diffract radiation in proportion to their height spectral density. Such an effect may skew the traditional filtered-surface (mean square slope) interpretation and also indicates potential for a second frequency dependency in altimeter backscatter modeling. To investigate this idea, we employ the Kirchhoff integral equation approach (also termed the correlation function approach), use of a two-scale surface approximation, and consideration of the Rayleigh parameter associated with surface roughness and carrier frequency [Jackson *et al.*, 1992]. An integral part of this development is definition of the sea surface input to the scattering model. Much effort has gone into reconciling measurement and theory regarding the functional form for the *high-frequency wave spectrum* [e.g., Apel, 1994]. Our proposed omnidirectional form is representative of recent spectra indicating two distinct energy balance regimes, the gravity-capillary regime being more strongly wind-dependent than the short-gravity range as suggested by Donelan and Pierson [1987]. This spectrum is explicitly defined to conform to Cox and Munk's [1954] slick and clean surface slope measurements.

A key motivation for this study is the global dual-frequency (C and Ku-band) altimeter data set available from the TOPEX satellite. These data, combined with a representative, empirically-derived Ku-band altimeter wind speed algorithm, provide a sound basis for evaluation of specular-point and two-scale Kirchhoff solutions, in terms of both wind-speed and transmit-frequency dependencies. We note that our goal is not to analyze individual anomalies in altimeter data which might be due, among other processes, to wind variability, atmospheric stratification, sea state or fetch effects as well as erroneous atmospheric correction and instrumental noise. We chose a global data set including a large range of situations, but we limited it to cases with low atmospheric correction to permit us to extract mean tendencies.

2 Semi-Empirical Sea Spectrum

For examination of near-vertical incidence radar altimeter returns, accounting for wind directivity is not essential. Thus, the approximation presented here is an idealized one-dimensional form in the high-frequency spectral regime. To define this spectral tail region, we follow the approach used by *Rodriguez et al.* [1992]. For our investigation, we have only modified their proposed simplified analytical spectrum in order to further incorporate recent observations and theoretical developments. The spectral peak level is linearly dependent on the wind speed, U , 10 m above the surface. Although in the along-wind direction the directional spectrum may exhibit a classical Phillips' -4 power law dependence over the entire gravity wave range [*Banner et al.*, 1989], slope of the nondirectional spectrum is chosen to follow a -2.5 power law dependence for wavenumber greater than the peak and smaller than about 10 times the spectral peak wavenumber. Such a form follows *Kitaigorodski's* [1983] theoretical arguments and the Donelan and Pierson spectrum model. The peak spectral wavenumber is approximately given by g/U^2 , where g is the acceleration of gravity. To insure reasonable mean square slope estimates, we constrain the spectrum so we obtain the optical slope estimates of wind roughened natural clean and artificial slick sea surfaces made by *Cox and Munk* [1954]. For the slick surface, wave components shorter than a foot were almost absent, so a partial integration of our slope spectrum between the peak wavelength and 30 cm wavelength yield that result. For the clean surface, all wave components must contribute to the total mean square slope. The Cox and Munk clean and slick relationships are respectively [*Phillips*, 1977; *Wu*, 1990]:

$$m_{SS_{clean}} = .003 + 5.12 \times 10^{-3}U \quad m_{SS_{slick}} = .0046 \log(k_{slick}U^2/g) \quad (1)$$

where $k_{slick} = 2\pi/.3$ rad/m. In the high wavenumber pure capillary region, rapid decay, due mainly to viscous dissipation, is required so that contributions of millimeter waves can be ignored. Following recent *in situ* and laboratory optical measurements [*Klinke and Jähne*, 1994; *Hara et al.*, 1994], we set a secondary higher-wavenumber peak just before this fast decay. The analytical form of our spectral model for $U > 7$ m/s is then

$$F(k) = k^{-2.5} \times (s_1 e^{-k/k_1} + s_2 e^{-(k/k_2)^2}) \quad (2)$$

for $k > k_0 = g/U^2$ rad/m, and where $k_1 = 2\pi/.21 \times e^{-U/4.9}$ rad/m and $k_2 = 365$ rad/m. The spectral coefficients s_1 and s_2 are computed so the spectrum simultaneously satisfies (1) and a final condition

$$F(k_0) = 2.25 \times 10^{-3} \frac{U}{g^{1/2}} k_0^{-2.5} \quad (3)$$

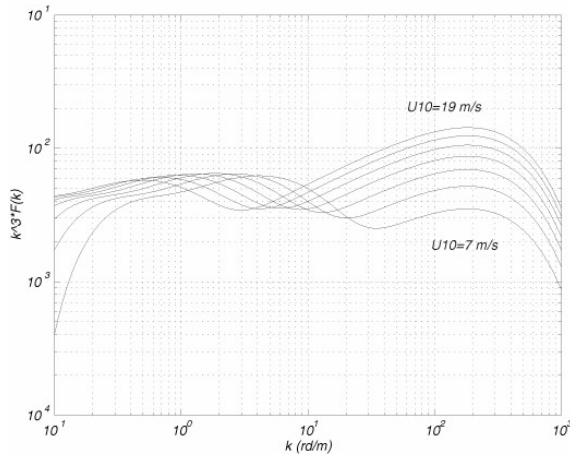


Figure 1: Omnidirectional saturation spectra for several wind speeds

to match data presented by Khama [Khama, 1981]. Figure 1 shows omnidirectional saturation spectra for several wind speeds ranging from 7 m/s to 19 m/s with a step of 2 m/s. A feature of this spectrum is that the mss computation can be analytically carried out to permit derivation of the constants, s_1 and s_2 .

3 A Two-Scale Scattering Model

The general problem of electromagnetic scattering from the rough sea surface can be approached in a variety of ways. Among them, Geometrical Optics (GO) (or specular-point) formulations have been proposed to describe ocean surface returns for small incidence angles. GO prediction works in the high-frequency limit, that is when surface roughness is large compared with the incident radiation wavelength, λ_i . Backscatter is treated as the incoherent addition of quasi-specular reflections from specular points associated with facets with dimensions $\geq 3\lambda_i$ [Brown, 1978]. Scattering from roughness scales below this dimension violates the theory's limitation. The GO solutions offers a simple, physically-intuitive expression relating the intensity of the return radiation in terms of joint pdf of surface height and specular slope. For Gaussian surface statistics and normal incidence, the GO approximation reduces to $\sigma_0 \propto 1./mss_{GO}$. mss_{GO} is the filtered mean square slope defined under GO theory, to differentiate between total mss and the partial mss available to the microwave altimeter because it cannot derive slope variance from waves of length below $3\lambda_i$. Ignoring wave directionality because of the normal incidence, this filtered slope variance is computed from our spectral model, as

$$m_{SSGO} = \int_{k_{peak}}^{k_{cut}} F(k) k^2 dk \quad (4)$$

where $k_{cut} = 2\pi/(3\lambda_i)$ is the cut-off wavenumber eliminating short-scale waves from the integration.

As a recognized alternative, the Physical Optics (PO) or Kirchhoff integral solution for the far-zone backscatter cross-section of a perfectly conducting Gaussian random isotropic rough surface can be written as

$$\sigma_0 = 2k_i^2 \int e^{-4k_i^2(\rho(0)-\rho(r))} r dr \quad (5)$$

with $k_i = 2\pi/\lambda_i$ incident radar wavenumber and ρ is the surface correlation function. Assuming perfect conductivity and the absence of shadowing effects, the PO solution reduces to the GO solution in the high-frequency limit [Brown, 1990]. However, the PO form will permit 'violation' of this limit. A frequently-cited approximation for the PO solution assumes that the surface can be spectrally decomposed into statistically independent large and small scale components. Such a decomposition is possible under Gaussian statistical description, and the correlation function can be written as $\rho(r) = \rho_L(r) + \rho_s(r)$. The break between scales is set by the high-frequency scattering limit to be k_{cut} . To simplify the large-scale contribution, one can expand the large-scale correlation function (Taylor series) and neglect the curvature (quartic) terms, leaving the parabolic second order terms containing the mean square slope. Expression (5) becomes

$$\sigma_0 = 2k_i^2 e^{-4k_i^2\rho_s(0)} \int e^{-k_i^2 m_{SSGO} r^2} e^{4k_i^2\rho_s(r)} r dr \quad (6)$$

In this expression, explicit accounting for diffraction effects is carried by the exponential term in front the integral. If the Rayleigh parameter, $k_i\sqrt{\rho_s(0)}$, becomes non-negligible, attenuation of radar cross section is predicted. Otherwise, (6) reduces to the GO solution.

This *two-scale Kirchhoff solution* is known [Thompson, 1988] and is analogous to two-scale scattering at moderate incidence angles. At those angles, diffraction dominates but specular contributions are added in the *ad hoc* two-scale methodology. That composite prediction was suggested to bring prediction in line with observations. As with scatterometry, we suggest that a 'violation', in this case, of the high-frequency scattering limit, appears justified when comparing data and model. The difference between GO and PO solutions in interpreting σ_0 versus wind speed is clear when examining figure 1 and considering the Ku-band microwave altimeter cut-off wavenumber of 100 rad/m. One can see that while slope in the large scale regime $< k_{cut}$

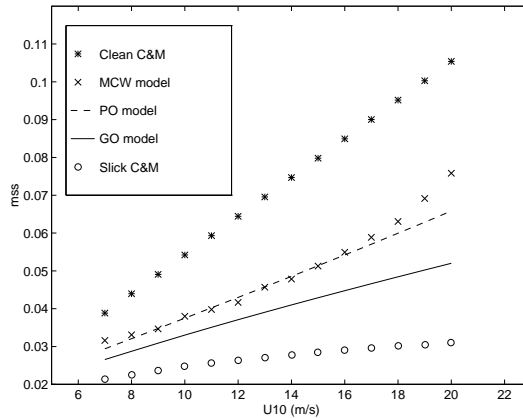


Figure 2: Mean square slope parameter versus wind speed U_{10}

increases, there is also a strong wind-dependence in the region above the cut-off (8–2 cm) gravity-capillary waves. This is borne out by scatterometer observations where the radar Bragg wavenumbers were at these short scales. In (6), the Rayleigh parameter will be quite small for Ku-band, but not negligible. Values should range from near 0 at 7 m/s to 0.4 at 20 m/s. At C-band, k_i is nearly three times smaller while small-scale height density changes little, therefore a C-band altimeter should be much less sensitive to wind changes entering into (6) through diffraction effects. Thus, the result of (6) is that while a C- and Ku-band altimeter should respond similarly to changes in large-scale slope variance, providing an almost redundant estimate, there will be additional, diffraction-caused attenuation evident in the Ku-band signal as wind increases. At this stage we note that we concentrate on $U > 7$ m/s for the reason that wind influence on the surface is better-understood above this level. Below this wind speed, both scattering and wind-wave theory require more attention than we can give here.

One test of a physically-based altimeter model should be its ability to reproduce observations and operational algorithms. Here, we consider the Modified Chelton-Wentz (MCW) operational wind speed retrieval algorithm [Witter and Chelton, 1991] for the Ku-band altimeter. To compare model results, figure 2 shows predictions as U_{10} against mss , where we define mss for the two-scale PO model (6) and MCW as $\propto 1./\sigma_0$ and mss_{GO} from (4). The spectral model of section 2 is used for GO and PO computations. The agreement between the model (7) and MCW is quite good, and is clearly better than the specular model. As discussed above, the added attenuation (seen here as increased mss) from the small-scale diffraction component of (7) is evident in comparing mss_{PO} to mss_{GO} . Increasing divergence between full integral model and filtered surface slope variances is interpreted as an increasing wind influence on small wave spectral density development.

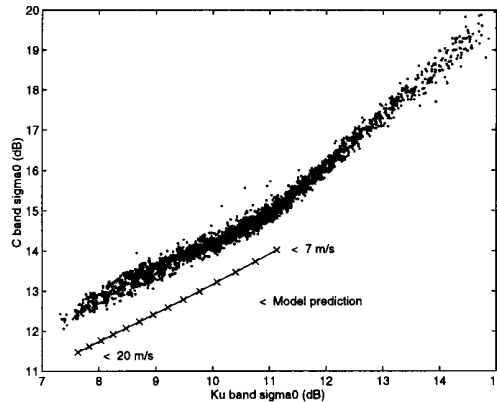


Figure 3: Predicted model results and global data

4 TOPEX Dual-Frequency Measurements

In the preceding section, we used the Kirchhoff model (6) in conjunction with an idealized short scale wave spectrum to predict wind dependent Ku-band altimeter returns. Results were close, particularly in form, to those predicted by the MCW operational empirical algorithm. The same physically-based model can be used to predict wind dependent C-band altimeter returns. Results can then be compared against a global C- and Ku-band data set from the TOPEX mission. Because absolute calibration information for C-band TOPEX data is unavailable, we will look at these comparisons in a relative manner. Selected TOPEX data correspond to a small subset of cycle 70 (10 orbits) acquired over deep-ocean areas. This cycle was chosen for its overall gain stability. Ku-band σ_0 data have been shifted (in dB) according to AVISO [1995]. Figure 3 presents predicted model results and data. Aside from a shift along the C-band axis (dB), our physically-based development reproduces the relationship between dual-frequency TOPEX measurements for even the lowest measured σ_0 (highest sea surface roughened case). A least-square adjustment between model prediction and data gives an *ad hoc* calibration constant for the TOPEX C-band data of about -1 dB.

Using this C-band calibration, figure 4 shows inferred altimeter and model results. Overall good agreement is clearly obtained for the highest *mss* parameters. This graph clearly reveals change in sensitivity between C- and Ku-band as sea surface roughness increases. However, C-band measurements do not dramatically saturate at high wind speed as would have been predicted by using the MCW algorithm to invert Ku-band data. The change in sensitivity occurs near 7 m/s wind speed. Such a transition may be associated with the transition from aerodynamically smooth to rough flow with onset of increased small scale wave breaking events [Banner and Melville,

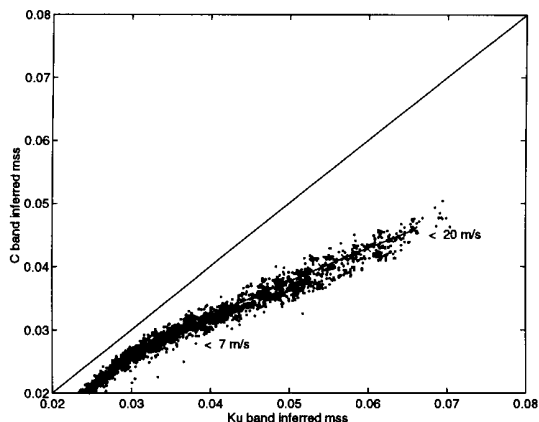


Figure 4: Inferred altimeter mean square slope parameter and model results

1976]. According to the scattering model development and the proposed idealized spectrum, increasing departure between C- and Ku-band data in the higher wind regime can be directly associated with increase in the integrated roughness but also, with changes in the more highly wind dependent gravity-capillary range between 2 and 10 cm waves. This is consistent with *in situ* and laboratory high resolution optical measurement as well as with the Donelan-Pierson spectral form in this range.

5 Summary

A *two-scale Kirchhoff scattering model* for the altimeter appears to provide a more consistent physical interpretation of satellite σ_0 data than a strict specular-point, or filtered-surface approach. A brief discussion of the model and implications indicate that, while the predominant altimeter backscatter is derived from large-scale slope variance, significant attenuation of the Ku-band signal can be attributed to diffraction effects of surface ripples below the large-scale cut-off wavelength. This was demonstrated with model comparison to the MCW wind speed retrieval algorithm. The effect of *small-scale wave growth* appears above about 7 m/s and is quantitatively derived based on the input wave spectral model provided in Section 2. This idealized wave model is in agreement with recent theory and optical measurements, particularly regarding high-wavenumber characteristics. The present development represents a first-order use of scattering theory and surface description that, while brief and incomplete in several aspects, points out important distinctions between optically-derived total *mss* and what the vertically-pointed microwave altimeter should be used to infer. The spectral model and integral equation approach are presently being tested for self-consistency through

comparisons against scatterometer algorithms and data sets.

Simultaneous dual-frequency TOPEX σ_0 data demonstrate the potential to go beyond empirical wind speed relationships. We observe that C- and Ku-band backscatter measurements show a large departure in the form of the wind-dependence function starting at about 7 m/s, a change, too abrupt to predict using a filtered-surface slope model and realistic wave spectrum. Even though the Ku-band model comparison with MCW in figure 3 suggests the growth of small-scale waves beyond this wind speed, the dual-frequency TOPEX data present an example where a two channel altimeter can clarify the picture considerably better. The observed data, interpreted using the Kirchhoff model, suggest a marker for the onset of small-scale wave growth, apparent in the Ku-band channel ($\lambda = 2.1$ cm) but not yet apparent at that wind speed for C-band ($\lambda = 5.5$ cm). We stress that we used global data, thus potentially indicating a fundamental change in the surface-roughness-to-wind relation near 7 m/s. Beyond this critical wind speed, it is known that generation of small-scale wind waves is responsible for a significant fraction of the mean sea surface wind stress [Makin *et al.*, 1995]. TOPEX data and the present scattering model should aid attempts to refine definitions of ultra-high wavenumber spectral densities.

In conclusion, acknowledging that an altimeter's areal coverage and non-directionality limit its contribution to wind field mapping, it is nevertheless clear that from a climatic standpoint global altimeter backscatter data are valuable. Defining momentum transfer to the ocean surface is a critical component in air/sea coupled modeling with inferences for both heat and gas transfer. A multiple (3 or 4) frequency altimeter could possibly allow differentiation between surface roughness changes among wavenumbers in the high-frequency wave regime (eg. $2 \text{ cm} > \lambda > 300 \text{ cm}$) for relating various air/sea processes. These waves seems to support most of the momentum transfer [Caudal, 1993]. Other scales may dominate heat and gas transfer, and such a multiple frequency instrument would help to better clarify a number of processes occurring at the interface contributing to these different transfers.

References

- Apel, J. R., An improved model of the ocean surface wave vector spectrum and its effect on radar backscatter, *J. Geophys. Res.*, 99, 16269-16291, 1994
- AVISO, AVISO CD ROM user guide: merged GDR status (cycles 1 to 90), *AVI-NT-02-102-CN*, 1995
- Banner, M. L., I. S. F. Jones and J. C. Trinder, Wavenumber spectra of short gravity waves, *J. Fluid Mech.*, 198, 321-344, 1989
- Banner, M. L. and W. K. Melville, On the separation of air-flow over water waves, *J. Fluid Mech.*, 77, 825-842, 1976
- Brown, G. S., Backscattering from a Gaussian distributed, perfectly conducting, rough surface, *IEEE trans. Anten. Propag.*, AP-26, 472-482, 1978

- Brown, G. S., Quasi-specular scattering from the air-sea interface, *Surface waves and fluxes*, Vol. II, Geernaert and Plant editors, 1-40, 1990
- Caudal G., Self-consistency between wind stress, wave spectrum and wind-induced wave growth for fully rough air-sea interface, *J. Geophys. Res.*, 98, 22743, 1993
- Coantic, M., Mass transfer across the ocean/air interface: small scale hydrodynamic and aerodynamic mechanisms, *Physicochemical Hydro.*, 1, 249-279, 1980
- Cox C. S., and W. H. Munk, Measurements of the roughness of the sea surface from photographs of the sun's glitter, *J. Opt. Soc. Am.*, 44, 838, 1954
- Donelan M. A., and W. J. P. Pierson, Radar scattering and equilibrium ranges in wind-generated waves with application to scatterometry, *J. Geophys. Res.*, 92, 4971, 1987
- Hara, T., E. J. Bock and D. Lyzenga, In situ measurements of capillary-gravity wave spectra using a scanning laser slope gauge and microwave radar, *J. Geophys. Res.*, 99, 12593, 1994
- Jackson, F. C., W. T. Walton and D. E. Hines, Sea surface mean square slope from Ku-band backscatter data, *J. Geophys. Res.*, 97, 11411-11427, 1992
- Jähne, B., K. O. Münnich, R. Böisinger, A. Dutzi, W. Huber and P. Libner, On the parameters influencing air-water gas-exchange, *J. Geophys. Res.*, 92, 1937-1949, 1987
- Jähne, B. and K. Riemer, Two-dimensional wave number spectra of small-scale water surface waves, *J. Geophys. Res.*, 95, 11531-11546, 1990.
- Khama, K. K., A study of the growth of the wave spectrum with fetch, *J. Phys. Oceanogr.*, 11, 1503-1515, 1981
- Kitaigorodski, S. A., On the theory of the equilibrium range in the spectrum of wind-generated gravity waves, *J. Phys. Oceanogr.*, 13, 816-827, 1983
- Klinke J. and B. Jähne, Measurements of small-scale structure of the ocean surface with new optical instrument, Preprints of 2nd Intl. Conf. on Air-Sea Interaction and on Meteorology and Oceanography of the Coastal Zone, *Amer. Met. Soc.*, 102-103, 1994
- Makin, V. K., V. N. Kudryavtsev and C. Mastenbroek, Drag of the sea surface, *Bound-Layer Meteo.*, 73, 159-182, 1995
- Phillips, O. M., The dynamics of the upper ocean, *Cambridge University Press*, 1977
- Rodriguez, E., Y. Kim and J. M. Martin, The effect of small-wave modulation on the electromagnetic bias, *J. Geophys. Res.*, 97, 2379-2389, 1992
- Thompson, D. R., Calculation of radar backscatter modulations from internal waves, *J. Geophys. Res.*, 93, 12371-12380, 1988
- Witter, D. L., and D. B. Chelton, A GEOSAT altimeter wind speed algorithm and a method for altimeter wind speed algorithm development, *J. Geophys. Res.*, 96, 8853, 1991
- Wanninkhof, R.H., and L. F. Bliven, Relationship between gas exchange, wind speed, and radar backscatter in a large wind-wave tank, *JGR* 96, 2785-2796, 1991.
- Wu, J., Mean square slopes of the wind-disturbed water surface, their magnitude, directionality and composition, *Radio Science*, 25, 37-48, 1990
- Wu, J., Microwave specular reflections from sea surface-A continuous altimeter-wind algorithm from breeze to hurricane, Preprints of 2nd Intl. Conf. on Air-Sea Interaction and on Meteorology and Oceanography of the Coastal Zone, *Amer. Met. Soc.*, 276-277, 1994

Transfer of CO₂ from Equatorial Latitudes to High Latitudes During the Late Quaternary

J. P. Jasper^{1*}, E. L. Sikes², and J. M. Hayes¹

¹ Biogeochemical Laboratories, Departments of Chemistry and of Geology, Indiana University, Bloomington IN 47405

² Institute for Antarctic and Southern Ocean Studies
University of Tasmania, Hobart, Tasmania 7001 Australia

* Now at: Marine Science and Technology Center
University of Connecticut, Groton, CT 06340

Abstract

In addition to existing low- and mid-latitude reconstructions of surface water PCO_2 , the completion of a northeast Atlantic (Feni Drift) deglacial record of PCO_2 indicates that overall there is (i) a high sea-to-air difference in pCO_2 (ΔpCO_2) in equatorial latitudes, (ii) near-equilibrium in mid-latitudes, and (iii) high air-to-sea difference in high latitudes. Unlike every other glacial-to-interglacial (deglacial) record of the carbon isotopic ratio of $C_{37:2}$ alkenones ($\delta_{37:2}$) measured to date, the Feni Drift ($\delta_{37:2}$) record *increased* by 3.7‰ rather than decreasing by 1–5‰ through this transition. Decreased values are consistent with increasing $CO_2(aq)$ concentrations and equilibrium PCO_2 which would support increasing deglacial atmospheric pCO_2 , as independently recorded by the ice core pCO_2 record. The increase in $\delta_{37:2}$ across the deglacial transition indicates that the northeast Atlantic has become a greater sink for atmospheric CO_2 over the last 16 kyr. The deglacial decrease in PCO_2 may be a result of increasing primary productivity (i. e., drawdown of $CO_2(aq)$) and decreasing vertical mixing of nutrients and $CO_2(aq)$. As CO_2 is absorbed and subducted into the deepwater formation regions of the north Atlantic, these processes may plausibly affect the earth's climate. While further calibration of the molecular isotopic PCO_2 barometer is required, the major global trends in paleoceanic CO_2 flux are beginning to emerge.

1 Introduction

Contemporary evaluations of the air-sea difference in molecular CO_2 levels (ΔpCO_2) show that oceanic waters are generally supersaturated in equatorial regions, near-equilibrium in mid-latitudinal regions, and undersaturated in high-latitude regions (e. g., *Tans et al.* [1990]). The global distribution of ΔpCO_2 indicates that CO_2 generally evades from the supersaturated equatorial ocean and invades back into the undersaturated high latitudinal oceans (Fig. 1). Over the last five years, the development of a molecular *isotope method* for the reconstruction of the paleoceanic partial pressure

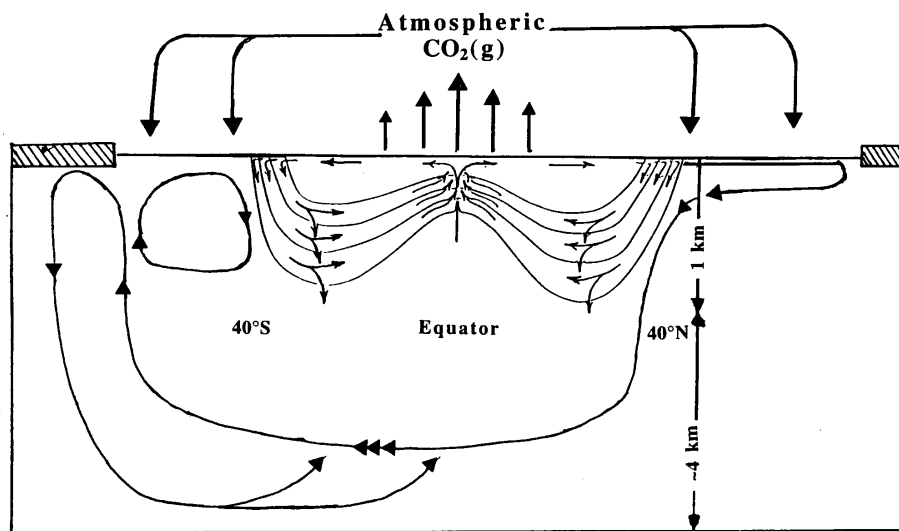


Figure 1: A generalized, pole-to-pole cross-section of the global ocean and atmosphere showing CO_2 fluxes out of the ocean at equatorial regions and back into the ocean in high latitudinal regions. (Composed from Broecker and Peng [1982], Imbrie et al. [1992], and Tans et al. [1990])

of CO_2 (PCO_2) permitted the reconstruction of temporal records of ΔpCO_2 in regions of supersaturation (the central equatorial Pacific: Jasper et al. [1994]), presumed equilibration (the northern Gulf of Mexico: Jasper and Hayes [1990]), and undersaturation (the northeast Atlantic). Combined evidence from the central equatorial Pacific (139°W , 1°N) and the northeast Atlantic (56°N , 13°W) suggests that there has been a net flux of CO_2 from the equatorial Pacific and into the northeast Atlantic.

Due to lack of calibration, the net flux into or out of the Circumantarctic Ocean [e.g., Shemesh et al., 1993] has not yet been determined. However, inspection of the diatom C_{org} and foraminiferal carbonate $\delta^{13}\text{C}$ records from the Southern Ocean indicates that the ΔpCO_2 decreased during the deglacial interval, as we show that it did in the northeast Atlantic.

Recent investigations have shown that the ^{13}C content of marine organic carbon is dependent on concentration of dissolved the CO_2 in ambient waters via the photosynthetic fixation of phytoplankton [Rau et al., 1989; Jasper and Hayes, 1990; Francois et al., 1993]. Since all the preceding water-column studies show an inverse relationship between marine $\delta^{13}\text{C}_{org}$ and $[\text{CO}_2(\text{aq})]$ provided that rates of growth remain constant, air-sea equilibrium considerations indicate that marine $\delta^{13}\text{C}_{org}$ values should have decreased since the last glacial maximum in oceanic regions which were at air-sea equilibrium for CO_2 . Previous and present data show the expected decrease (1.2–5.3‰) in the $\delta_{37:2}$ from the northern Gulf of Mexico [Jasper and Hayes, 1990]

Table 1: Samples used in this study

Location/Reference	Core	Coordinates	Depth (m)
North Atlantic Feni Drift [Sikes et al., 1991]	KNR51 29GGC	56° 13.1'N, 12° 37.7'W	2626
Gulf of Mexico Pigmy Basin [Jasper and Hayes, 1990]	DSDP 619	27° 11.61'N, 91.° 24.54'W	2259
Central Equatorial Pacific MANOP Site C [Jasper et al., 1994]	W8402A-14GC	0° 57.2'N, 138° 57.3'W	4287

and the central equatorial Pacific (MANOP Site C [Jasper et al., 1994]). However, if a site were found at which the $\delta^{13}\text{C}$ of marine C_{org} increased from the last glacial period from the present, it would indicate high $\text{CO}_2(\text{aq})$ concentration in the ice age and decreasing concentration toward the present. If concomitant variations in sea-surface temperature at the site indicated $\Delta\text{PCO}_2 < 0$, it would suggest that the region had been an important sink for oceanic CO_2 during glacial times (e. g., Keir [1993]).

Late Quaternary paleoatmospheric pCO_2 typically varies between approximately $190 \mu\text{atm}$ in glacial stages and $280 \mu\text{atm}$ in interglacial stages [Jouzel et al., 1993]. Potentially responsible mechanisms fall into three categories, reviewed by Keir in 1993: the “biological pump”, “alkalinity changes”, and the “solubility pump”. In the latter process, CO_2 is withdrawn from the atmosphere by dissolution in cold waters which then sink and are removed from contact with the atmosphere. Using a quantitative, circulation-dependent model of the solubility pump applied to the northern Atlantic, Keir [1993] could account for as much as 60% of the change in atmospheric pCO_2 from glacial to interglacial times.

2 Experimental

2.1 Samples

The samples used in this study come from the northeast Atlantic, the Gulf of Mexico, and the central equatorial Pacific, as detailed in Table 1.

2.2 Methods

The method employed here of estimating dissolved CO_2 concentration (c_e) is that diagrammed in Figure 2 [Jasper et al. 1994]. Concentrations of dissolved CO_2 are reconstructed via the relationship of the photosynthetic

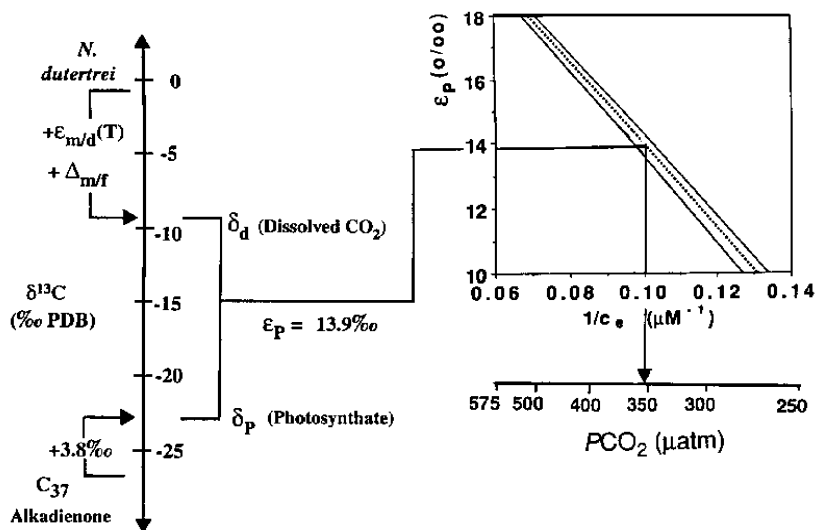


Figure 2: Diagram outlining the calculation of paleoceanic PCO_2 values from the photosynthetic fractionation of CO_2 (ϵ_P). From the $\delta^{13}C$ compositions of a planktonic foraminiferan (viz., *N. dutertrei*) and Prymnesiophyte microalgae (via a C_{37} alkadienone), values of ϵ_P are reconstructed. Calibration of water-column, coretop, and laboratory culture ϵ_P points against $1/c_e$ allows reconstruction of equilibrium PCO_2 values from sedimentary components. (Based on Jasper et al. [1994])

isotope effect (ϵ_P) to ambient sea-water dissolved $CO_2(aq)$ concentration. Molecular isotopic analysis permitted the measurement of the $\delta^{13}C$ of a specific marine biomarker compounds (viz., a $C_{37:2}$ alkenone) and from that the estimation of the $\delta^{13}C$ of bulk marine C_{org} (δ_P) of a specific class of phytoplankton, the Prymnesiophytes.

Carbon isotopic analysis of planktonic foraminiferal carbonates provides estimates of δ_d . Estimates of paleotemperatures are required to get the proper isotopic fractionation factors and to derive paleoceanic PCO_2 levels from $CO_2(aq)$ concentrations via Henry's Law. These are estimated from the alkenone-based UK'_{37} ratio of Brassell et al. [1986].

3 Results and Discussion

3.1 Quaternary Histories of PCO_2 by Latitudinal Region

Equatorial Latitudes: Supersaturated

MANOP site C (138 °W, 1 °N) in the central equatorial Pacific has been continuously supersaturated with $CO_2(g)$ relative to the (ice core) paleoatmosphere for the last ~ 255 kyr (Fig. 3). Counterintuitively, the largest ΔpCO_2

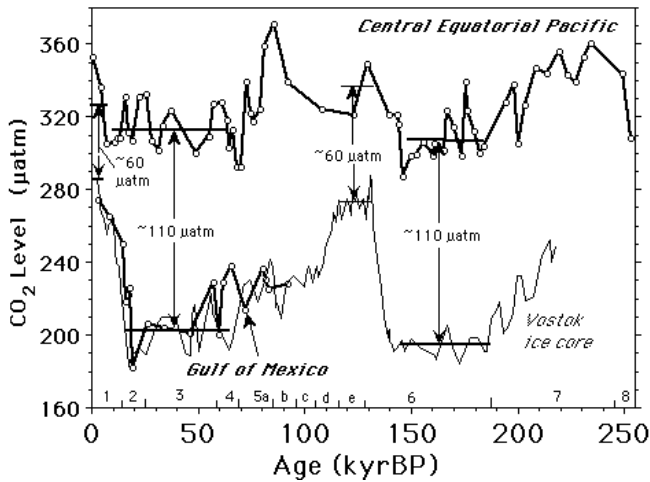


Figure 3: Reconstructed histories of PCO_2 in the central equatorial Pacific (MANOP site C at $138^\circ 57.3'W$, $0^\circ 57.2'N$; Jasper et al. [1994]) and in the northern Gulf of Mexico (Pigmy Basin at $27^\circ 11.61'N$, $91^\circ 24.54'W$; Jasper and Hayes [1990]) compared with the Vostok pCO_2 record [Jouzel et al., 1993]. These records indicate PCO_2 supersaturation at MANOP site C (equatorial latitudes) and near-equilibrium conditions at the Pigmy Basin (mid-latitudes). Compare with the conditions of the high-latitude region of the northeast Atlantic (Fig. 5a).

occurred in glacial periods and the smallest during interglacials. If the thickness of the stagnant boundary layer were the same or smaller during glacial times, this indicates higher sea-to-air fluxes of CO₂ during glacials. However, atmospheric pCO_2 was lower during glacials. Given only the MANOP site C paleoceanic PCO_2 - and paleoatmospheric pCO_2 records, one would infer that there has to be a larger glacial CO₂ sink elsewhere to account for the low ice age pCO_2 . Contemporary global maps of ΔpCO_2 show that there are large areas of CO₂ sources ($\Delta pCO_2 > 0$), equilibrium ($\Delta pCO_2 = 0$), and sinks ($\Delta pCO_2 < 0$) [Tans et al., 1990]. It is apparent that if the magnitude and direction of ΔpCO_2 may be both spatially and temporally variable, that different areas of the global ocean may respond differentially with climatic change.

Mid-Latitudes: Near Equilibrium

The Pigmy Basin in the northern Gulf of Mexico represents a “near-equilibrium” environment with respect to paleoceanic PCO_2 and paleoatmospheric pCO_2 [Jasper and Hayes, 1990] (Fig. 3). Deep Sea Drilling Project Core 619, spanning the last ~100 kyr, was the “test-of-concept” core for molecular isotopic PCO_2 reconstruction for a surface water environment that is presently near equilibrium [Tans et al., 1990]. With $\Delta pCO_2 \approx 0$, no net flux of CO₂

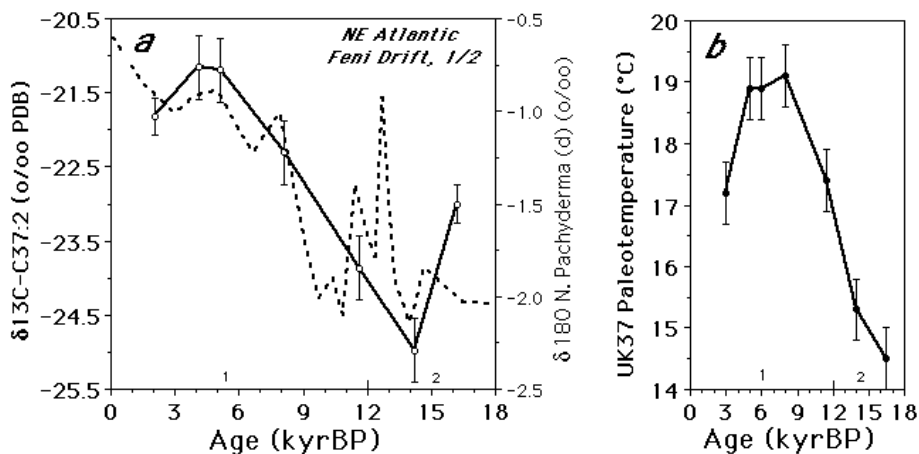


Figure 4: **a** Records of $\delta_{37:2}$ and foraminiferal $\delta^{18}\text{O}$ spanning the last deglacial transition at the Feni Drift in the north Atlantic (KNR51 29GGC; $56^{\circ} 13.1' \text{N}$, $12^{\circ} 37.7' \text{W}$). **b** Time-series records of alkenone-based UK'_{37} paleotemperatures at the Feni Drift (also, KNR51 29GGC; from Sikes [1990]).

would be expected from this region, similar to a vast region in the contemporary mid-latitude ocean has apparently no net air-sea flux of CO_2 [Tans *et al.*, 1990].

High-Latitudes: Undersaturated

The $\delta_{37:2}$ record from the northeast Atlantic shows a general increase of $\sim 3.7\%$ from glacial stage 2 into interglacial stage 1 (Fig. 4a). This observation contrasts sharply with that at other latitudes. Combined with the record of paleotemperatures (Fig. 4b), and either of the available paleobarometric calibrations ("oligotrophic", Pigmy Basin; "eutrophic", equatorial Pacific), it indicates (i) continued undersaturation with respect to the atmosphere (Fig. 5) and (ii) decreased concentrations of CO_2 in the waters in which the prymnesiophytes were growing. Provided that those waters were indeed then sinking to greater depths, this observation supports the solubility-pumping mechanism suggested by Keir [1993].

The deglacial record of UK'_{37} -based paleotemperatures of the Feni Drift shows a maximum increase over the transition of 4.6°C , with a cooling of $\sim 1.9^{\circ}\text{C}$ after the climatic optimum. The net temperature rise (2.7°C) is smaller than that estimated by a foraminiferal transfer function ($\sim 7^{\circ}\text{C}$: CLIMAP, 1976), but is larger than that used in the circulation-dependent solubility pump model ($1\text{--}2^{\circ}\text{C}$: Keir [1993]). The difference may be due to the different life histories of the temperature-indexing organisms [Fairbanks *et al.*, 1982; Honjo and Okada, 1974; Jasper and Gagosian, 1989; Sikes *et al.*,

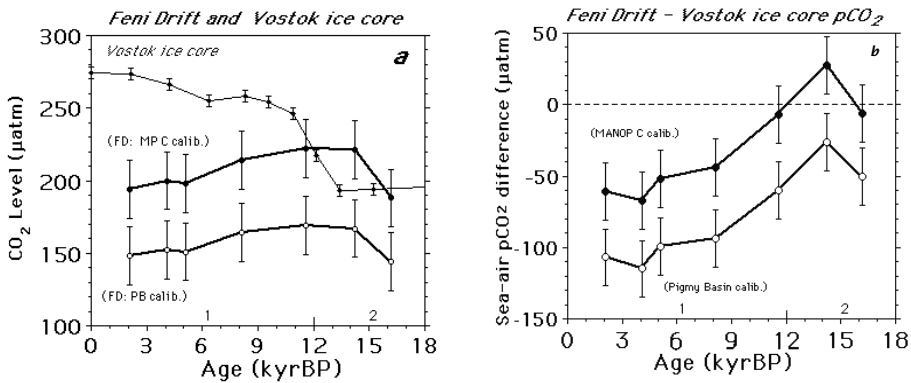


Figure 5: **a** Time-series records of ϵ_p -based pCO_2 from the Feni Drift and paleoatmospheric pCO_2 from the the Vostok ice core [Jouzel et al., 1993] for comparison. **b** Historical "air-sea" differences between paleoatmospheric pCO_2 from the Vostok ice core and paleoceanic pCO_2 from the Feni Drift (ΔpCO_2) over the last deglacial transition. By Fick's First Law of Diffusion, this difference (ΔpCO_2) is proportional to the air-to-sea flux of CO_2 , indicating increasing air-to-sea fluxes during the deglacial transition in the Atlantic.

1991].

A geochemical analogy can be made between the glacial-to-interglacial decrease in PCO_2 at the Feni Drift and the winter-to-spring decrease in oceanic PCO_2 in the Iceland Sea [Takahashi et al., 1985]. In the contemporary Iceland-Greenland Sea, high oceanic PCO_2 in winter is due to low biological drawdown and high vertical mixing, while low oceanic PCO_2 in the spring is due to high biological drawdown and decreased vertical mixing [Takahashi et al., 1985].

By analogy and based on present results, we suggest that deglacial north Atlantic had higher PCO_2 because of lower biological drawdown and high-er vertical mixing rates than the interglacial [Thomas et al., 1995 and McCave et al., 1995 for paleoceanographic comparisons].

Two lines of evidence support of the mixing/drawdown mechanism. First, Keir [1983] published a model which employed a 50% reduction in vertical circulation during the maximum rate of climate change (~11 kyrBP). This slowdown in circulation may have allowed the $[CO_2(aq)]$ to accumulate to the highest levels during the deglacial transition, as observed at ~10-15 kyrBP. Second, Mix and Fairbanks [1985] reported that the deep basins of the north Atlantic were filled by cold, nutrient-rich waters during glaciations and with warmer, nutrient-poor waters during interglaciations. These observations are consistent with lower glacial productivity (higher $[CO_2(aq)]$ due to lower drawdown) and higher interglacial productivity (lower $[CO_2(aq)]$).

4 Conclusions

A new deglacial $\delta_{37:2}$ record from the Feni Drift in the northeast Atlantic increases by $\sim 3.7\%$, unlike all previous lower-latitude deglacial transitions which showed decreases in $\delta_{37:2}$ values. While the latter data are consistent with the observed, increasing deglacial atmospheric $p\text{CO}_2$, the former indicated decreasing $p\text{CO}_2$. High $\text{CO}_2(\text{aq})$ concentrations during glacial periods near oceanic deepwater formation regions provides a mechanism by which to subduct CO_2 and to draw down paleoatmospheric $p\text{CO}_2$. Present estimates of PCO_2 at the Feni Drift are limited by other regional calibrations of ε_p versus $\text{CO}_2(\text{aq})$ concentration. To develop a more accurate record of northeast Atlantic, we are currently working on water-column calibration of the ε_p -based PCO_2 barometer for those waters. Our present model of the general deglacial decrease in PCO_2 is based on increases in both water-column mixing and phytoplanktonic fixation (drawdown) of $\text{CO}_2(\text{aq})$ as the main mechanisms. Molecular isotopic reconstruction of histories of paleo-oceanic PCO_2 in equatorial-, mid-, and high-latitudes show that, as in the contemporary ocean, there is a general efflux of CO_2 from equatorial regions and influx in high latitudinal regions. In addition to air-sea differences in the CO_2 levels ($\Delta p\text{CO}_2$), calculation of paleofluxes of CO_2 will require estimated gas transfer coefficients which are themselves functions of wind velocity. Since atmospheric $p\text{CO}_2$ is largely controlled by oceanic PCO_2 , understanding paleoceanic PCO_2 permits us to understand the main forcing functions which determined preindustrial atmospheric $p\text{CO}_2$ and serve as a baseline for preindustrial atmospheric $p\text{CO}_2$.

Acknowledgements

We particularly thank L. D. Keigwin (W.H.O.I.) for discussing the problem of latitudinal CO_2 fluxes and for directing us to samples for the study of the Feni Drift. We thank Oregon State University, Woods Hole Oceanographic Institution, Lamont-Doherty Geological Observatory for sediment samples; J. Fong, C. Walther, K. S. Duke, and A. Morey for technical assistance; N.S.F. Ocean Sciences (Chemical Oceanography) and N.A.S.A. support this research.

References

- Broecker, W. S. and T.-H. Peng, Tracers in the Sea, Eldigio Press, Columbia University, 690 pp., 1982
- CLIMAP Project Members, The surface of the ice-age Earth, *Science*, 191, 1131-1137, 1976
- Fairbanks, R. G., M. Sverdløve, R. Free, P. H. Wiebe, and A. W. H. Be, Vertical distribution and isotopic fractionation of living planktonic foraminifera from the Panama Basin, *Nature* 298, 841-844, 1982
- Francois, R., M. A. Altabet, R. Goericke, D. C. McCorkle, C. Brunet, and A. Poisson, Changes in the $\delta^{13}\text{C}$ of surface water particulate organic matter across the sub-

- tropical convergence in the S.W. Indian Ocean, *Glob. Biogeo. Cyc.* 7, 627-644, 1993
- Freeman, K. H. and Hayes, J. M., Fractionation of carbon isotopes by phytoplankton and estimates of ancient CO₂ levels, *Glob. Biogeo. Cyc.* 6, 185-198, 1992
- Honjo, S., and H. Okada, Community structure of coccolithophores in the photic layer of the mid-Pacific, *Micropaleontology* 20, 209-230, 1974
- Imbrie, J., E. A. Boyle, S. C. Clemens, A. Duffy, W. R. Howard, G. Kukla, J. Kutzbach, D. G. Martinson, A. McIntyre, A. C. Mix, B. Molino, J. J. Morley, L. C. Peterson, N. G. Pisias, W. L. Prell, M. E. Raymo, N. J. Shackleton, and J. R. Toggweiler, On the structure and origin and major glaciation cycles, 1, Linear response to Milankovitch forcing, *Paleoceanography* 7, 701-738, 1992
- Jasper, J. P. and J. M. Hayes, A carbon isotope record of CO₂ levels during the late Quaternary, *Nature* 347, 462-464, 1990
- Jasper, J. P., and R. B. Gagosian, Glacial-interglacial climatically forced $\delta^{13}\text{C}$ variations of sedimentary organic matter. *Nature* 342, 60-62, 1989
- Jasper, J. P., A. C. Mix, F. G. Prahl, and J. M. Hayes, Photosynthetic ^{13}C fractionation and estimated CO₂ levels in the Central Equatorial Pacific over the last 255,000 years. *Paleoceanography* 9, 781-799, 1994
- Jouzel, J., N. I. Barkov, J. M. Barnola, M. Bender, J. Chapellaz, C. Genthon, V. M. Kotlyakov, V. Lipenkov, C. Lorius, J. R. Petit, D. Raynaud, G. Raisbeck, C. Ritz, T. Sowers, M. Stievenard, F. Yiou, and P. Yiou, Vostok ice cores: extending the climatic records over the pen-ultimate glacial period, *Nature* 364, 407-412, 1993
- Keir, R. S., Cold surface ocean ventilation and its effect on atmospheric CO₂, *J. Geophys. Res.* 98, 849-856, 1993
- McGave, I. N., B. Manighetti, and N. A. S. Beveridge, Circulation in the glacial North Atlantic inferred from grain-size measurements, *Nature* 374, 149-152, 1995
- Mix, A. C. and R. G. Fairbanks, North Atlantic surface-ocean control of Pleistocene deep-ocean circulation, *Earth and Plan. Sci. Ltrts.* 73, 231-243, 1985
- Rau, G. H. Variations in sedimentary organic $\delta^{13}\text{C}$ as a proxy for past changes in ocean and atmospheric CO₂ changes in Carbon Cycling in The Glacial Ocean: *Constraints on the ocean's role in global climate change*, edited by R. Zahn, M. Kaminiski, M., L. D. Laberyie, and Pedersen, T. F., NATO ASI Series I: Global Environmental Change, Vol. 17, 307-321, Springer Verlag, Berlin, 1994
- Rau, G. H., P. N. Froelich, T. Takahashi, and D. J. DesMarais, Does sedimentary organic $\delta^{13}\text{C}$ record variation in Quaternary ocean c_e ? *Paleoceanography* 6, 335-347, 1989
- Shemesh, A., Macko, S. A., Charles, C. D., and Rau, G. H., Isotopic evidence for reduced productivity in the glacial Southern Ocean, *Science* 262, 407-410, 1993
- Sikes, E. L., Refinement and application of a new paleotemperature estimation technique, Ph. D., MIT/WHOI, Woods Hole, Mass., 1990
- Sikes, E. L., J. W. Farrington, and L. D. Keigwin, Use of the alkenone unsaturation ratio UK₃₇ to determine past sea surface temperatures: core-top SST calibrations and methodology considerations, *Earth Planet. Sci. Ltrts.* 104, 36-47, 1991
- Takahashi, T., J. Olafsson, W. S. Broecker, J. Goddard, D. W. Chipman, and J. White, Seasonal variability of the carbon-nutrient chemistry in the ocean areas west and north of Iceland, *Rit Fiskideildar* 9, 20-36, 1985

Tans, P. P., I. Y. Fung, and T. Takahashi, Observational constraints on the global atmospheric CO₂ budget, *Science* 247, 1431-1438, 1990

Thomas, E., L. Booth, M. Maslin, and N. J. Shackleton, Northeast Atlantic benthic foraminiferal during the last 45,000 years: changes in productivity as seen from the bottom up, *Paleoceanography* 10, 1995 (in press).

Author Index

- Akiyama, ML, 855
Alaee, M., 503, 617
Anderson, R. J., 703
Asher, W. E., 205, 217, 227, 239,
255, 269, 517
Atmane, M., 49
- Banner, M. L., 115
Bock, E. J., 363, 375, 529, 611, 801
Boumansour, B. E., 393
Boutin, J., 827
Bremeyer, R., 145
- Cartmill, J., 305
Caussade, B., 69
Chapron, B., 869
Chen, H., 205
Chu, C. R., 79
Clark, J. F., 785
Cohen, L. H., 325
Cooper, W. J., 503
Cowen, E. A., 135
- Dannecker, W., 735, 745
De Bryun, W. J., 13
de Leeuw, G., 325, 685, 703, 723
de Wilde, H. P. J., 763
DeGrandpre, M. D., 375
Dieter, J., 145, 801
Ding, L., 285
Donelan, M. A., 503, 543, 617, 677
Drennan, W. M., 677, 753
Duke, S. R., 627
Duyzer, J., 763
- Edson, J. B., 801
Elfouaily, E., 869
Emerson, S., 23
- Etcheto, J., 827
Etoh, T., 435, 447
- Farley, P. J., 205, 227, 269
Farmer, D., 297, 385
Frew, N. M., 363, 375, 529, 611, 801
- Gardiner, W. W., 205
Geißler, P., 351
George, J., 49, 69, 665
Gnanadesikan, A., 313
Gulliver, J. S., 461, 589
- Hanratty, T. J., 627
Hansen, F. Aa., 685
Hansen, K., 801
Hara, T., 529, 611, 801
Haußecker, H., 405, 775, 801
Hayes, J. M., 879
He, M., 855
Hering, F., 125, 145, 499
Hertzman, O., 703, 723
Hesany, V., 601
Higgins, B. J., 205, 227
Hirsa, A., 649
Ho, D. T., 785
Hosoi, Y., 473
Hwang, P. A., 153
- Itoh, N., 855
- Jähne, B., 3, 125, 145, 165, 351, 405,
499, 505, 529, 637, 775,
801
Janssen, P. A. E. M., 197
Jasper, J. P., 879
Jessup, A. T., 601
Jirka, G. H., 79, 89, 101, 495

- Johnson, B. D., 385, 817
 Judd, C. D., 649
 Jupsin, H., 393
- Kakuno, S., 577
 Karachintsev, A. V., 529., 801
 Karle, L. M., 205, 227
 Katsaros, K., 869
 Kawamura, H., 177
 Kerman, B., 753
 Kholouiski, S. N., 713
 Kim, S., 649
 King, D. B., 13
 Klinke, J., 165, 801
 Kohsiek, W., 703, 723
 Komori, S., 553
 Korenowski, G. M., 649
 Koseff, J. R., 135
 Kraan, C., 197
 Kunz, G. J., 685, 703, 723
- Lantry, T., 205
 Larsen, S. E., 685
 Lauer, H., 505
 Leifer, I. S., 227, 269
 Loewen, M. R., 337, 601
 Logory, L. M., 649
- Münsterer, T., 505, 529, 637
 Masbemat, L., 69
 Mayer, H. J., 637
 McGillis, W. R., 363, 375, 529, 611, 801
 McKeown, W., 415
 McNeil, C., 385
 Melville, W. K., 285
 Mikhailovsky G. E., 37
 Minel, F., 665
 Monahan, E. C., 205, 217, 227, 239, 487
 Monismith, S. G., 135
 Moog, D. B., 89, 101, 495
 Murakami, H., 473
- Nakata, Y., 577
 Nelson, R. K., 801
- O'Dor, M. A., 337
 Ocampo-Torres, F. J., 543
 Oda, K., 577
 Ogston, A. S., 255
 Oost, W. A., 197, 703, 723, 811
- Peirson, W. L., 115
 Plate, E., 735, 745
 Prinos, P., 49
- Reinelt, S., 405
 Rida, J. J., 753
 Roma, W. N. L., 571
- Saitoh, M., 577
 Saltzman, E. S., 13
 Sarmiento, J. L., 843
 Schlosser, P., 785
 Schmundt, D., 505
 Schulz, M., 735, 745
 Sherwood, C. R., 205, 255
 Shimada, T., 553
 Sikes, E. L., 879
 Simpson, H. J., 785
 Skafel, M. G., 337, 601
 Smith, J. S., 425
 Smith, P. M., 205, 217
 Smith, S. D., 703, 723
 Stahlschmidt, T., 735, 745
 Steckley, M., 205
 Strachan, W. M. J., 617
 Stute, M., 785
 Su, M.-Y., 305
 Sugimori, Y., 855
 Suntharalingam, P., 843
- Takehara, K., 435, 447
 Tamburrino, A., 589
 Terrill, E., 285
 Thibodeaux, L. J., 425
 Toba, Y., 177
 Trevorrow, M., 385
- Uz, M., 801
- Valsaraj, K. T., 425
 van Vliet, P., 499

Vandemark, D., 869

Vasel, J. - L., 393

Wang, Q., 205, 217, 487

Wanninkhof, R., 205, 239, 517, 785

Weiss, P. T., 461

Wierzimok, D., 125

Wilson, M. B., 487

Woolf, D. K., 59, 185

Yakushev E. V., 37

Zappa, C. J., 601

Zhao, C., 855

Zheng, M., 13

Index

- 3/2-power law, 180
- ^3He , 787
- “A”-type whitecaps, 197
- acid gas, 638
- acid-base indicator, 377
- acoustic, 209
- acoustic backscattering
 - cross-section, 63
- acoustic resonator, 300, 306
- acoustic scattering, 65
- activation energy, 16
- adsorptive bubble, 425
- ADV, 209, 256
- advection, 726
- aerosol, 325, 814
- aerosol generation, 487
- air entrainment, 186, 338
- air flow separation, 115
- Air Sea GAS Exchange (ASGASEX),
723, 811
- air-sea carbon dioxide flux, 827
- air-sea gas flux, 298
- air-sea gas transfer, 487
- air-water interface, 56
- alkalinity, 25, 814
- altimeter
 - microwave, 869
- ammonia, 738
- ammonium nitrate, 735
- annular tanks, 612
- area per unit volume, 426
- areas per bubble, 426
- ASGAMAGE, 731, 815
- ASGASEX, 197, 328, 685, 703, 723,
764, 811
- ASREX experiment, 286
- atmospheric flux, 617
- atmospheric $p_{\text{CC}} > 2$, 879
- attenuation depth, 63
- attenuation depth of bubble clouds,
65
- Baltic, 326
- biochemical oxygen demand, 461
- biological processes, 385, 820
- bioreactor, 400
- BOD, 461
- boundary layer, 627
 - downward-bursting, 177
 - gas concentration, 181
 - turbulent, 177
- boundary layer thickness, 29
- breaking waves, 197, 206, 218, 298,
337, 338, 363, 517
- bromothymol blue, 377
- bubble
 - adsorptive, 425
 - absorption, 364
 - cloud, 63, 181
 - concentrations, 275
 - distribution, 181
 - overpressure, 363
 - patch dynamics, 316
 - plumes, 227, 363, 487
 - rise velocity, 272
 - size distribution, 7, 288,
326, 342, 354
 - spectra, 308
 - video microscope system,
488
 - volume fraction, 368
 - mediated gas transfer, 192,
206, 240, 487, 518

- bubbles, 75, 297, 325, 456, 811
 - large, 338
- bubbly flow, 75
- bulk-skin temperature difference, 603
- buoyancy production, 315
- C_{37:2} alkadienones (*i*,_{37:2}), 879
- capillary-gravity waves, 153, 536, 803
- carbon dioxide, 19, 228, 241, 657, 677, 685, 687, 703, 815, 855
- carbon isotope fractionation, 31
- carbon isotopic analysis, 882
- carbon isotopic ratio, 879
- carbonate system, 26
- carbonic anhydrase, 30
- catalysis, 23
- central equatorial Pacific, 880
- CH₄, 812
- channel, 627
- characteristic velocity, 69
- Chamock's relation, 688
- chemical enhancement, 827, 864
 - of CO₂ gas transfer, 23
- chloromethanes, 618
- CO₂ exchange coefficient, 829
- CO₂ production
 - local, 731
- CO₂, 210, 228, 241, 375, 545
- CO₂ flux, 677, 723
- CO₂ laser, 407
- CO₂ transport, 812
- colored dissolved organic matter, 804
- concentration difference, 724
- concentration field, 8, 627
- concentration fluctuation, 54
- concentration gradients, 726
- concentration profiles, 53, 637
- conceptual modelling, 69
- constant temperature and humidity room, 579
- controlled flux technique, 775, 805
- CoOP, 776, 801
- counter-gradient flux, 730
- critical deficit, 104
- critical wind speed, 532, 534, 613
- curvature spectra, 160
- Dalton number, 692, 704
- damping ratio, 537
- Dco₂ minimum, 551
- decay method, 406
- deepwater formation regions of the north Atlantic, 879
- deglacial, 879
- density stratification, 728
- denuder difference method, 736
- deposition, 749
- depth-from-focus, 354
- device
 - gas tension, 386
- dichlorodifluoromethane (F-12), 15
- dichloromethane, 623
- difference of partial pressure, 859
- diffusion coefficient, 13
 - of gases in seawater, 19
- diffusion coefficients, 14, 16
- diffusion model, 407
- diffusion/dissipation equilibrium, 667
- digital particle image velocimetry (DPIV), 135, 649, 653
- digital particle tracking velocimetry (DPTV), 135
- dimethyl sulfide (DMS), 15
- dimethylsulfide, 228
- directional distribution, 163
- dispersion relation, 536
- dissipation, 51, 315, 602, 665
- dissipative structures, 69
- dissolved gas measurements, 386
- dissolved gas sensor, 388
- dissolved oxygen, 89, 101, 388, 461, 473, 577, 638
- dissolved oxygen sensor, 302
- diurnal cycle, 386
- DO, 101, 461, 473
- Doppler velocimeter, 209
 - acoustic, 256

- downward-bursting boundary layer (DBBL), 177, 728
- DPIV, 135, 653
- DPTV, 135
- drag coefficient, 687, 710
- droplet, 325, 448
- drops
 - freely falling, 73
- dry deposition, 487
- dual tracer experiments, 713
- dual tracer technique, 786
- dual-gaseous tracer method, 518
- dual-tracer, 637
- eddies
 - large, 69
 - small, 76
- eddy
 - horizontal, 75
- eddy correlation, 686, 703, 723
- eddy diffusivity, 181
- eddy model
 - small, 90
- eddy viscosity, 316
- eddy-correlation, 677
- emission from seawater, 740
- energy balance equations, 315
- energy dissipation, 199, 479
- enhanced dissipation, 134
- equatorial latitudes, 882
- error metrics, 103
- ERS1, 828
- estuaries, 79
- estuarine, 797
- Eulerian flow field, 127
- evaporation, 409, 704
- F-II, 19
- F-12, 19
- fetch, 499, 505, 544, 554, 749
- field measurements, 677
- filter pack, 748
- flat plate boundary layer, 137
- flow visualization, 178
- fluorescein, 442, 637
- fluorescence, 627, 638
 - laser-induced, 627
- fluorescence quenching, 628, 639
- fluorescent indicator, 638
- flux barrier, 729
- flux estimates, 767
- flux measurements, 677, 685, 703, 764
 - carbon dioxide, 814
- fluxes
 - turbulent, 687
- foam, 198
- footprint, 730
- form drag, 96, 116
- fouling, 468
- fractional area whitecap coverage, 518
- fractional-area bubble plume coverage, 229
- free falling film, 71
- free surface, 52, 70, 135, 138, 589
- free-drifting buoy, 162
- free-surface turbulence, 589, 590, 650
- freshwater, 305
- friction velocity, 130, 200, 369, 507, 531
- gas concentration boundary layer, 181
- gas exchange, 617
- gas flux, 54
 - bubble-mediated, 270
- gas permeable membrane, 377
- gas sensor
 - dissolved, 388
- gas supersaturations, 820
- gas tension, 386
- gas tension device, 302, 386
- gas transfer, 785
- gas transfer flume, 503, 545, 618
- gas transfer velocity, 217, 375
- gas-bubble spargers, 425
- GEOSECS, 714
- global flux estimate, 844
- gradient measurements, 768
- gradient method, 764

- gradients
 - concentration, 726
- grid-stirred vessel, 71
- Gulf of Mexico, northern, 880
- H₂, 16, 19
- Hayduk and Laudie relation, 15
- HCl, 638, 746
- He, 16, 19, 210, 218, 228, 241
- He-3, 521, 791
- heat flux, 8, 406, 418, 602
 - sensible, 691, 703
- heat flux coefficient, 710
- helium, 210, 218, 228, 241
- hemicyanine, 649
- hexachlorocyclohexane, 753
- HEXOS, 697, 704
- high resolution, 644
- high-frequency wave spectrum, 870
- high-latitudes, 884
- high-slope streams, 107
- high-speed videocamera, 444, 448
- HN0₃, 735, 746
- hollow fiber membranes, 462
- hot film sensor, 804
- Hudson River, 786
- Humidity flux, 814
- hydration rate constant, 30
- hydrolysis
 - CO₂, 24
- hydrostatic pressure, 270
- image processing, 630
- imaging slope gauge, 5, 166
- in situ, 385
- in situ sensors, 377
- indicator
 - acid-base, 377
- inertial dissipation method, 258
- infrared analyzer, 546
- infrared camera, 776
- infrared gas analyser, 678
- infrared imager, 603
- infrared radiation, 406
- instrumentation, 386
- interfacial gas transfer, 69
- interfacial turbulent kinetic energy, 70
- interfacial wind stress, 116
- intermittence, 783
- inverse problems, 288
- iron fertilization, 821
- isotope method, 879
- jet-agitated vessel, 668
- JGOFS, 817
- kinetic isotope separation, 513
- Kirchhoff scattering model
 - two-scale, 876
- Kirchhoff solution
 - two-scale, 873
- Kolmogorov microscale, 669
- KUSTOS, 736
- LADAS catamaran, 803
- Lagrangian measurement, 301
- Lagrangian trajectory, 127
- lake, 27, 79, 463, 677
- Lake Ontario, 677, 754
- Langmuir cells, 60, 314
- Langmuir circulation, 182, 298, 811
- large bubbles, 338
- large eddy model, 90
- laser, 627
- laser-induced fluorescence, 649, 657
- LDV, 665
- LIF, 657
- light sheet, 118
- linear regression, 219
- liquid film coefficient, 589
- liquid friction velocity, 69
- Lyman-alpha humidityrometer, 705
- macroroughness, 89
- MAPTIP, 328
- marine biota, 38
- marine boundary layer, 741
- Marine Boundary Layers Accelerated Research Initiative (MBL ARI), 165
- mass boundary layer, 637

- mass transfer, 578
- mass transfer velocity, 678
- material
 - surface active, 366
- mathematical model, 38
- MBL ARI, 776, 802
- mean square roughness, 160
- mean square wave slope, 5, 155, 165, 511, 536, 547, 548, 611, 808, 869
- Meetpost Noordwijk, 685, 704, 811
- methane, 15, 19, 763, 815
- methyl bromide (CH₃Br), 15, 19
- Michelson interferometers, 417
- micro-scale breaking, 118
- microlayer sampler, 803
- micrometeorological methods, 764
- microscale wave breaking, 602
- microwave brightness temperature, 217
- microwave radiometer, 219
- microwave radiometry, 205
- mid-latitudes, 883
- missing sinks, 37
- molar volume, 14-16
- molecular isotopic PCO₂ barometer, 879
- momentum, 677
- momentum flux, 689, 703, 814
- Mono Lake, 27
- Monte Carlo simulations, 126
- motion
 - ordered, 182
- moving bed, 511, 591
- multiplicative error, 105
- N₂, 297
- N₂O distribution, 845
- N₂O, 210, 241, 812, 843
- Ne, 16
- near equilibrium, 883
- near-surface turbulence, 363, 611
- NH₃, 639, 735
- nitric acid, 745
- nitrogen, 302, 386
- nitrogen cycle, 38
- nitrogen gases, 745
- nitrogen species, 735, 745
- nitrous oxide, 210, 241, 815
- normal stress, 116
- normal velocity gradient, 590
- North Atlantic, 326
- North Sea, 326
- northeast Atlantic, 879
- northern Gulf of Mexico, 880
- numerical model, 49, 60, 317
- O₂, 210, 228, 297, 377
- ocean, 79
- ocean carbon cycle, 817
- ocean carbonate system, 38
- ocean general circulation model, 844
- oceanic N₂O fluxes, 852
- OMEX, 329
- open-channel flow, 83, 135
- ordered motions, 182
- oscillating-grid tank, 555
- outflow boundary condition, 141
- overturning rate, 315
- oxygen, 210, 228, 302, 386, 530, 627
 - dissolved, 388
- oxygen probe, 389
- oxygen quenching, 639
- oxygen transfer coefficient, 473
- Pacific, central equatorial, 880
- paleoceanic CO₂ flux, 879
- partial standing waves, 578
- particle formation, 741
- particle imaging velocimetry (PIV), 7, 118, 145
- particle tracking velocimetry (PTV), 7, 125, 444
- PBA, 8
- pCO₂, 377
- peak frequency, 200
- permeable breakwaters, 473
- pesticides, 753
- pH, 442
- phosphorus cycle, 38

- photosynthetic fractionation of
 - CO_2 , 882
- phytoplankton bloom, 45
- PIV, 7, 145
- plunging breakers, 218, 585
- power-law
 - $3/2$, 180
- Prandtl number, 421
- processes
 - biological, 385
- production/respiration, 389
- propane, 393
- Prymnesiophyte microalgae, 882
- PTV, 7, 125, 444
- pycnocline, 728
- pyrene, 431
- pyrene butyric acid, 640, 628

- quenching, 8

- radar backscatter, 869
- radiative cooling, 409
- radiometry, 8, 416
- radium-226, 715
- radon-deficit technique, 714
- reaeration, 89, 101, 393, 571, 577
- reaeration coefficient, 473
- reaeration equations, 103
- reconstructions, 879
- remote sensing, 219
- renewal ratio, 478
- renewal theory, 90
- reservoir, 79
- Reynolds stress tensor, 129
- Rhine water, 728
- rhodamine, 393
- riffle-pool, 107
- rivers, 463
- roughness, 861
- roughness elements, 153
- roughness length, 688

- salinity, 305
- saltwater, 305, 559
- scanning laser slope gauge, 5, 155, 166, 612, 803

- scatterometer, 828
- Schmidt number, 14, 71, 223, 240, 406, 421, 514, 518, 529, 622, 713, 776
- sea surface roughness, 869
- sea surface temperature, 829, 858
- sea surface temperature variations, 778
- seawater, 559
- sea-surface temperature, 713
- sea-to-air difference in pCO_2 , 879
- seasonal variability, 44
- seawater, 364, 376
 - evasion, 364
 - invasion, 364
- second order modelling, 49
- second-harmonic generation, 649
- sedimentation flux, 46
- sensible heat, 677
- sensible heat flux, 691, 703, 814
- sensor, 385
 - in situ, 377
- SF_6 , 19, 210, 218, 228, 241, 530, 787, 791
- shear layer, 186
- shear sparger, 425
- short wind waves, 165
- significant wave height, 178, 200
- skin friction, 96
- skin layer, 603
- skin-layer recovery rate, 604
- slope sensing, 154
- small eddy model, 90
- small-scale wave growth, 876
- small-scale waves, 153
- solubility, 13, 14, 240, 396, 518
- solvent sublimation, 425
- sonar, 300
- sonic anemometer, 804
- spar buoy, 286
- spectral function, 199
- spilling breakers, 218, 585
- Stanton number, 691, 710
- stearic acid, 652
- stirred grid tank, 575

- Stokes drift velocity, 178
- stream reaeration, 89
- streams, 89
- stress
 - tangential, 116
- structure
 - two-layer, 181
- sulfur hexafluoride (SF₆), 15, 210, 218, 228, 241, 521, 530, 618, 791
- sun glitter, 3, 155
- supersaturation, 371, 882
- surf pool, 206, 241, 256
- surface active material, 366
- surface deformation, 571
- surface films, 530, 611
- surface N₂O mappings, 844
- surface renewal, 90, 571, 589
- surface renewal model, 149, 407, 478, 601
- surface rheological properties, 653
- surface roughness, 611
- surface slope, 444
- surface tension, 141, 270, 536
- surface velocity, 149
- surface viscoelasticity, 530
- surface-normal vorticity, 649
- surfactant, 513, 530, 649, 650, 808
- surfactant concentration, 662

- tangential stress, 116, 141
- temperature gradients, 418
- tetrachloroethene, 623
- tetrachloromethane, 623
- thermal imaging, 8
- tidal current, 202
- tidal rivers, 786
- Tilting Wind-Water Tunnel, 80, 91, 495
- tipping bucket, 487
- TOPEX, 870, 875
- total stream power, 96
- transfer
 - bubble-mediated, 206
- transfer velocities, 723
- trichloromethane, 623
- trichlorofluoromethane (F-11), 15
- trickling filters, 400
- Triton-X-100, 366, 530
- turbulence, 95, 602, 649, 650, 864
 - wave-enhanced, 177
- turbulent boundary layer, 177
- turbulent diffusion constant, 60
- turbulent dissipation, 186
- turbulent dissipation rates, 256, 808
- turbulent fluxes, 687
- turbulent kinetic energy, 51, 70, 665, 667
 - interfacial, 70
- turbulent patch, 187
- two-layer structure, 181
- two-scale Kirchhoff scattering model, 876
- two-scale Kirchhoff solution, 873
- two-step renewal model, 474

- undersaturated, 884

- velocity
 - characteristic, 69
 - liquid friction, 69
 - velocity field, 299, 649
 - velocity gradient, 589
 - velocity measurements, 662
 - velocity profile, 140, 149
 - vertical mixing processes, 59
 - vertical velocity fluctuations, 135, 141
 - vertical velocity gradient, 593
- vessel
 - jet-agitated, 49
- vinyl screens, 578
- viscoelastic modulus, 537
- viscosity, 14, 15, 19
- viscous sublayer, 116
- void fraction, 286, 311
- void fraction meters, 306
- vortex breakdown, 653
- vortex flows, 650
- vortex pair, 649
- vortex ring, 435
- vortical structures, 650

- WABEX-93, 206, 240, 256
- water purification, 473
- water vapor, 677, 687
- water vapor flux, 703
- wave age, 200, 861
- wave breaking, 186, 473, 864
- wave channel, 339
- wave dissipation, 682
- wave growth
 - small-scale, 876
- wave height
 - significant, 178
- wave number spectra, 169
- wave paddle, 339
- wave slope, 5, 530
- wave slope spectra, 548
- wave-current channel, 138
- wave-current interaction, 315
- wave-enhanced turbulence, 177
- wave-wave collisions, 487
- wavenumber spectra, 159
- waves
 - breaking, 363
 - small-scale, 153
 - wind, 177
- WCP, 197
- White Sea, 38
- whitecap coverage, 192, 205, 217, 262
- whitecap fraction, 199
- whitecap percentages, 197
- whitecap simulation tank, 228, 274, 487
- whitecaps, 197, 217, 227, 487, 519, 814
- Wilke and Chang relation, 15
- wind, 864
- wind drag coefficient, 710
- wind forcing, 785
- wind sheared interface, 70
- wind speed, 529, 713, 863
- wind stress, 8, 611, 705, 804
 - interfacial, 116
- wind stress enhancement, 115
- wind wave flume, 499
- wind waves, 177, 627, 864
 - short, 165
- wind-driven flows, 82
- wind-wave tank, 365, 377, 554
- wind/stream combined flows, 80
- wind/wave facility, 505
- wire-wave staff, 804
- zooplankton bloom, 45

A more complete understanding of the mechanisms involved in the exchange of gases between the atmosphere and the sea is needed if we are to address various environmental issues, and is essential to improved modeling of global climate. This volume contains selected papers from the Third International Symposium on Air-Water Gas Transfer, held at the University of Heidelberg, in Heidelberg, Germany from July 24 - 27, 1995. The papers are arranged into seven parts: Physical and Chemical Mechanisms, Waves and Turbulence, Breaking Waves and Bubbles, Measuring Technology, Laboratory Measurements and Facilities, Field Measurements, Remote Sensing, and Global Modeling. Emphasis is given to the transfer of carbon dioxide and other radiatively important gases, reflecting current interest in potential global warming. Breaking waves and the bubbles thereby generated play a prominent role in that regard. Also featured are non-invasive measurement technologies, many of which lend themselves to remote sensing applications. Those interested in chemical engineering, fluid mechanics, hydrology, hydraulics, environmental engineering, water quality engineering, climatology, meteorology, and oceanography will find this work a valuable resource.

ISBN 3-9804429-0-X



9 783980 442909